AD-A264 268

8

ARO 30430-1-PHCF

0

2nd International Conference on MILLIMETER WAVE AND FAR-INFRARED TECHNOLOGY

Editor

Carl M. Thicker

DTIC
ELECTE
MAY 14 1993
S E D

Reproduced From
Best Available Copy

[illegible]

PROCEEDINGS VOLUME OF ELECTRONICS INDUSTRY

DISTRIBUTION STATEMENT
Approved for public release
Distribution Unlimited

MASTER COPY KEEP THIS COPY FOR REPRODUCTION PURPOSES

REPORT DOCUMENTATION PAGE

Form Approved
OMB No 0704-0188

Public reporting burden for this collection of information is estimated to average 1 hour per response, including the time for reviewing instructions, searching existing data sources, gathering and maintaining the data needed, and completing and reviewing the collection of information. Send comments regarding this burden estimate or any other aspect of this collection of information, including suggestions for reducing this burden, to Washington Headquarters Services, Directorate for information Operations and Reports, 1215 Jefferson Davis Highway, Suite 1204, Arlington, VA 22202-4302, and to the Office of Management and Budget, Paperwork Reduction Project (0704-0188), Washington, DC 20503.

1. AGENCY USE ONLY (Leave blank)	2. REPORT DATE	3. REPORT TYPE AND DATES COVERED
	March 1993	Final 1 Aug 92-31 Jul 93

4. TITLE AND SUBTITLE

International Conference on Millimeter Wave and Far-Infrared Technology

5. FUNDING NUMBERS

DAAL03-92-G-0324

6. AUTHOR(S)

R.W. McMillan (principal investigator on project)

7. PERFORMING ORGANIZATION NAME(S) AND ADDRESS(ES)

Georgia Institute of Technology
Atlanta, GA 30332

8. PERFORMING ORGANIZATION REPORT NUMBER

9. SPONSORING/MONITORING AGENCY NAME(S) AND ADDRESS(ES)

U. S. Army Research Office
P. O. Box 12211
Research Triangle Park, NC 27709-2211

10. SPONSORING/MONITORING AGENCY REPORT NUMBER

ARO 30430.1-PH-CF

11. SUPPLEMENTARY NOTES

The view, opinions and/or findings contained in this report are those of the author(s) and should not be construed as an official Department of the Army position, policy, or decision, unless so designated by other documentation.

12a. DISTRIBUTION/AVAILABILITY STATEMENT

Approved for public release; distribution unlimited.

12b. DISTRIBUTION CODE

13. ABSTRACT (Maximum 200 words)

The conference was held as scheduled. The conference is recognized as a forum for the presentation of research results from the very capable scientists and engineers at China's universities, research institutes, and factories. In addition 95 papers were received from other countries. Conference sessions included radiometry/astronomy, plasma diagnostics, quasi-optics, atmospheric effects, gyrotrons, materials, spectroscopy, integral circuits, and optically-pumped lasers.

14. SUBJECT TERMS

Conference, Millimeter Wave Technology, Far Infrared Technology, Radiometry, Astronomy, Atmospheric Effects, Spectroscopy, Lasers, Integrated Circuits

15. NUMBER OF PAGES

689

16. PRICE CODE

17. SECURITY CLASSIFICATION OF REPORT	18. SECURITY CLASSIFICATION OF THIS PAGE	19. SECURITY CLASSIFICATION OF ABSTRACT	20. LIMITATION OF ABSTRACT
UNCLASSIFIED	UNCLASSIFIED	UNCLASSIFIED	UL

2nd International Conference on

MILLIMETER WAVE AND FAR-INFRARED TECHNOLOGY

Accesion For
NTIS CRA&I
DTIC TAB
Unannounced
Justification
By
Distribution /
Availability Codes
Dist | Avail and / or Special
A-1

Editor
Gail M. Tucker

93-10169

DISTRIBUTION STATEMENT A
Approved for public release;
Distribution unlimited

電子工業出版社
PUBLISHING HOUSE OF ELECTRONICS INDUSTRY

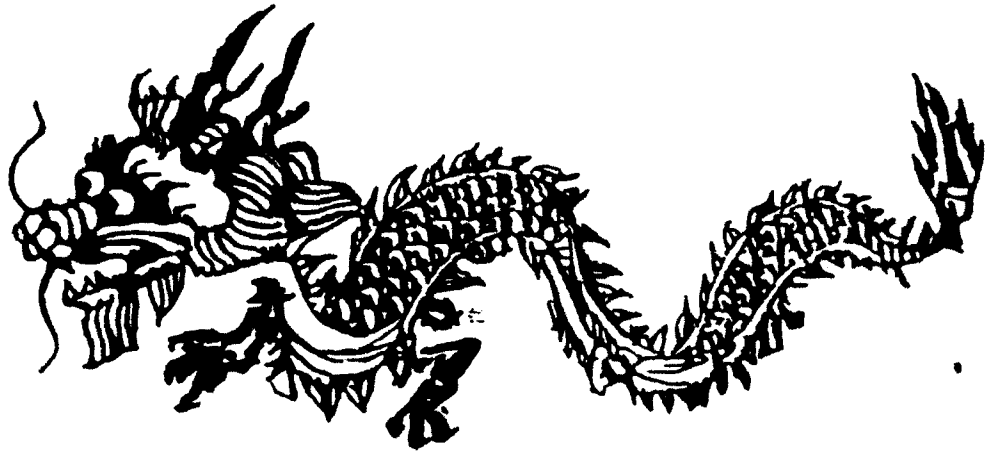

Sponsored By

CIE

Chinese Institute of Electronics

Georgia Tech

Georgia Institute of Technology

U.S. Army Research Office

National Natural Sciences Foundation of China

International Conference on Millimeter Wave and Far-Infrared Technology

August 17-21, 1992

Yanxiang Hotel
Beijing, China

CONFERENCE DIGEST

Gail M. Tucker
Editor

International Conference on Millimeter Wave and Far-Infrared Technology

ICMWFT '92

Yanxiang Hotel
Beijing, China

August 17-21, 1992

General Chairman
M. von Ortenberg, Technical University of Braunschweig, Germany

Program Committee
Han-Chuan Hu, Beijing Vacuum Electronics Research Inst. China, Co-Chairman
R. W. McMillan, Georgia Institute of Technology, Co-Chairman
I. Alexeff, University of Tennessee, USA
Zeng-Gui Chen, Institute of Electronics, Academia Sinica, China
N. Fourkis, Defence Science and Technology Organisation, Australia
C. J. Gibbins, Rutherford Appleton Laboratory, United Kingdom
B. D. Guenther, U.S. Army Research Office
K. Hisano, National Defense Academy, Japan
M. Kimmitt, University of Essex, United Kingdom
Fu-Jiang Liao, Beijing Vacuum Electronics Research Institute, China
Jin-Ting Lin, Nanjing Solid-State Devices Research Institute, China
Yi-Kun Lin, Zhongshan University, China
A. Raisanen, Helsinki University of Technology, Finland
J. E. Walsh, Dartmouth College, USA
Zhi-Ying Zhang, Beijing Institute of Radio Measurement, China
U-Ji Zhou, Beijing Dahua Radio Instrument Factory, China

Organizing Committee
Zong Sha, Chinese Institute of Electronics, Chairman
Zhi-Wu Li, Chinese Institute of Electronics
Mengqi Zhou, Chinese Institute of Electronics

International Advisory Committee
M. Afsar, Tufts University, USA
K. Chang, Texas A&M University, USA
P.D. Coleman, University of Illinois, USA
F.C. DeLucia, Ohio State University, USA
L. I. Fedoseev, Institute of Applied Physics, Russia
T. V. George, Department of Energy, USA
Tatsuo Itoh, University of California, Los Angeles, USA
P. Janssen, Laboratory for Low Temperature and High Field Physics, Belgium
F. K. Kneubühl, Swiss Federal Institute of Technology, Switzerland
A. F. Krupnov, Academy of Sciences, Russia
T.L. Lane, Georgia Institute of Technology, USA
J. Leotin, National Institute of Applied Sciences, France
Ying Li, Shanghai University of Science and Technology, China
Jin-Ting Lin, Nanjing Solid State Device Research Institute, China
Yi-Kun Lin, Zhongshan University, China
Shen-Gang Liu, University of Electronic Science and Technology, China
H. Meinel, Deutsche Aerospace, Germany
Y. Myasin, Institute of Radioengineering and Electronics, Russia
A. Nosich, Institute of Radioengineering and Electronics, Ukraine
Eizo Otsuka, Osaka University, Japan
H. Rothermel, Max-Planck Institute, Garching, Germany
S.C. Shen, Shanghai Institute of Technical Physics, China
Yi-Chun Shen, Chinese Institute of Electronics, China
C. J. Summers, Georgia Institute of Technology, USA
A. Vystavkin, Institute of Radioengineering and Electronics, Russia
Yi-Ping Wang, Xidian University, China
J. C. Wiltse, Georgia Institute of Technology
D. E. Wortman, U.S. Army Harry Diamond Laboratories
G. T. Wrixon, University College, Cork
Ming-Gao Zhang, China Research Institute of Radiowave Propagation, China
Wen-Xun Zhang, Southeast University, China
Zhi-Ying Zhang, Beijing Institute of Radio Measurements, China

FOREWORD

The International Conference on Millimeter-Wave and Far-Infrared Technology in 1992 (ICMWFT'92) is the second in the series of conferences following the highly successful ICMWFT'90 held in Beijing in June of 1990. Initial discussions for this series of meetings took place between H. C. Hu of the Beijing Vacuum Electronics Research Institute and J.J. Gallagher and R. W. McMillan of Georgia Tech during a visit by the latter two persons to China in 1984. Detailed planning for this first meeting took place beginning in 1988, and the technically successful and socially entertaining ICMWFT'90 was the result. During the plenary session of that meeting, which was held in the Chinese Year of the Horse, H.C. Hu showed a slide characterizing this series of conferences as a herd of horses following a lead horse, designated as ICMWFT'90, and expressed the hope that similar conferences would follow just as the herd followed the lead animal. It appears that his wish will be fulfilled, since there are now at least preliminary plans to hold conferences in China on this growing area of research every even-numbered year.

This conference is recognized as a forum for the presentation of research results from the very capable scientists and engineers at China's universities, research institutes, and factories, but it is an international forum in a very real sense. At last count, approximately 95 papers from Australia, Belgium, Canada, Egypt, France, Germany, India, Japan, Lithuania, Poland, Republic of China, Russia, Switzerland, Turkey, Ukraine, United Kingdom, and United States, in addition to 86 papers from the Peoples Republic of China, had been received. The conference organizers hope that this meeting will be an effective forum for the exchange of ideas between members of the international millimeter-wave and far-infrared community and that those who attend will find this exchange useful in their work.

The venue for the conference is the Yanxiang or "Flying Swallow" hotel, located about midway between the Beijing International Airport and the city center. The Yanxiang is a modern three-star hotel in the Chinese style. Its location is convenient for sightseeing and shopping, and a variety of dining rooms and recreational facilities are available in the hotel.

The conference organizers would like to thank the Georgia Tech Research Institute which has provided initial funding for the organization of this conference. The U.S. Army Research Office provided funding for partic support of some invited speakers from the West, and the Chinese Institute of Electronics and the National Natural Science Foundation of China have provided cooperative support. The program organizers and digest editor would also like to thank Mr. Rick Hoffner of Georgia Tech, who designed the First and Second Calls for Papers and aided in formulating this digest and the Advance Program.

M. von Ortenberg
General Chairman

H.C. Hu
Program Co-Chairman

R. W. McMillan
Program
Co-Chairman

Braunschweig, Beijing, and Atlanta
May 24, 1992

IN MEMORIAM

James J. Gallagher

1922 - 1991

Jim Gallagher was born in Albany, NY on November 15, 1922. He entered Siena College in the fall of 1941, enrolling in the School of Business. While at Siena, he played on the nationally ranked basketball team and was president of the sophomore class. He entered the Army in 1943 and served until the end of World War II, completing his tour in the Philippines. Gallagher graduated from Siena with a degree in physics in 1948 and earned a Master's Degree in Physics at Columbia University, studying under Nobel Laureates Charles Townes and Willis Lamb. After doing further graduate work at Johns Hopkins University, he worked for a time at the JHU Radiation Laboratory.

Jim was especially gifted and motivated to share his knowledge with younger scientists, engineers, and students. He was instrumental in establishing the interne research program at Georgia Tech Research Institute and served as the first chairman of the International Conference on Infrared and Millimeter Waves, held in Atlanta in 1974. This conference has been held every year since, alternating between locations in the U.S. and abroad. In 1990 he was General Chairman of the first International Conference on Millimeter Wave and Far Infrared Technology, held in Beijing, China. He served on program committees of several other international conferences and has more than 200 publications and meeting presentations.

Jim was a man of extraordinary warmth, a trait not evident in reading a list of his accomplishments. He helped and encouraged many students and young scientists in their careers, and was very generous with his time and abilities. He could be found on many Saturday mornings in the laboratory at Martin Marietta or Georgia Tech, helping some young scientist with a thesis problem or sharing his knowledge of millimeter wave science.

Mon AM	Plenary Session			
Mon PM	Plenary Session			
Tues AM	Radiometry/Astronomy	Atmospheric Effects I	FEL & Orotron I	Materials/Measurements I
Tues PM	Plasma Diagnostics	Sources I	Atmospheric Effects II	Materials/Measurements II
Wed AM	Detectors	Gyrotrons	Spectroscopy I	Integrated Circuits
Wed PM	Quasi-Optics	Materials/Measurements III	Spectroscopy II	Sources II
Thurs AM	Applications/Systems I	Sources III	Atmospheric Effects III	Materials/Measurements IV
Thurs PM	Applications/Systems II	FEL & Orotron II	Spectroscopy III	Optically-Pumped Lasers
Fri PM	Laboratory and Institute Tour			
	Room 1	Room 2	Room 3	Room 4

Registration Period

Sunday, August 16, 7PM - 10PM

Monday-Thursday, August 17-20, 8AM - 12PM

Monday AM August 17, 1992, 0830
Invited Plenary Session M1
Presider: H.C. Hu

Welcome and Introductory Remarks, M. von Ortenberg, H.C. Hu and R.W. McMillan

M1.1 **"Sub-Millimeter Microwave Spectroscopy with Primary Radiation Sources"** - A.F. Krupnov, Institute of Applied Physics, Academy of Sciences of Russia, 603600 Nizhny Novgorod, Russia

M1.2 **"Research on Millimeter Wave Propagation in China"** - M. G. Zhang, China Research Institute of Radiowave Propagation, Qingdao, P.R. China

Break

M1.3 **"Novel Strange and Ultrashort-Pulse Mid-and Far-Infrared Lasers and Their Applications"** - F. K. Kneubuhl, Swiss Federal Institute of Technology, Zurich, Switzerland

M1.4 **"Optical Phase and Frequency Control of FET Oscillator"**, F. J. Liao, Beijing Vacuum Electronics Research Institute, Beijing, P.R. China and R. W. McMillan, Georgia Institute of Technology, Atlanta, GA, USA

Lunch

Monday PM, August 17, 1992, 1330
Invited Plenary Session M2
Presider: R. W. McMillan

M2.1 **"A New Milestone of Active Device----Vacuum Microelectronics and Its Preliminary Research in P.R. China"**, Han C. Hu, Beijing Vacuum Electronics Research Institute, and Guang Yi Liu, Electronics Research Institute, Chinese Academy of Sciences, Beijing, P.R. China

M2.2 **"Study of the Dynamical Properties of E12 Centers in GaAs by Infrared and Millimeter Wave Measurements"**, Tyuzi Ohyama, Osaka University, Osaka, Japan

M2.3 **"Whispering Gallery Mode in Dielectric Waveguide and Dielectric Resonators"**, Sheng Gang Liu, University of Electronic Science and Technology of China, Chengdu, P.R. China

Break

M2.4 **"Millimeter-Wave Quasi-Optical Rectifying Antennas for Power Transmission Applications"**, Kai Chang, Texas A&M University, College Station, Texas, USA

M2.5 **"Interband Transition Modulated FIR Cyclotron Resonance in Semiconductors"**, S. C. Chen and Wei Lu, Shanghai Institute of Technical Physics, Shanghai, P.R. China, and Michael von Ortenberg, Institute of Semiconductor Physics and Optics, University of Braunschweig, Germany

Tuesday AM August 18, 1992
Session T1
Radiometry / Astronomy
Room 1
Presider: H. Rothermel 08:30

T1.1 **"A 345 GHz Open Structure SIS Receiver at the IRAM 30-m Telescope"**, Invited, H. Rothermel, Max Planck Institute for Extraterrestrial Physics, Garching, Germany; K.H. Grundlach and B. Lazaref, IRAM, Saint Martin D'Heres, France

T1.2 **"SIS Junction MM Wave Receivers"**, Invited, A. Vystavkin, M. Tarasov, V. Koshelets, S. Shitov, V. Belitsky, S. Kovtonjuk, O. Kaplunenko, G. Prokopenko, L. Filippenko, V. Kaplunenko, M. Khabipov, and S. Turygin, Institute for Radioengineering and Electronics, Moscow, Russia

Break

T1.3 **"Five mm Microwave Radiometer Receiver"**, Zhi Cai Xu, Purple Mountain Observatory, Academia Sinica, Nanjing, and Shu Sheng Peng, Xi'an Space Radio Technology Institute, Xi'an, P.R. China

T1.4 **"Far-Infrared Balloon-Borne Imaging of the Cygnus Region"**, A. P. Hoienstein, G. Schenker, St. Clerc, and F. K. Kneubuhl, Swiss Federal Institute of Technology, Zurich; and D. Huguenin, Geneva Observatory, Sauverny, Switzerland

T1.5 **"5 mm Microwave Radiometer Scanning Antenna"**, Zong Zhen Shen and En Hui Zhao, Xi'an Institute of Space Radio Technology, Xi'an, P.R. China

T1.6 **"Correlation Reflectometry Via Stochastic noise Signals"**, V.S. Korosteljov, K.A. Lukin, O.S. Pavlichenko, R.O. Pavlichenko, V.A. Rakityansky, and V.P. Shestopalov, Institute of Radiophysics and Electronics, Kharkov, Ukraine

Tuesday AM August 18, 1992
Session T2
Atmospheric Effects I
Room 2
Presider: C.J. Gibbins 08:30

T2.1 **"Inversion of Rain Distribution Along Earth-Space path by Meteorologic Radar and Satellite"**, Da Zhang Hu, China Research Institute of Radiowave Propagation, Qingdao, P.R. China

T2.2 **"Correlation of Cloudiness and Rain Components of Millimeter Radio Wave Attenuation in Hydrometeorological Formations in the Troposphere"**, V.V. Stroganov, Radiophysical Research Institute, Nizhny Novgorod, Russia

T2.3 **"Rain Induced Depolarization at Millimeter and Sub-Millimeter Waves in a Xi'an Environment"**, Y. Yan, Xidian University, Xi'an, P.R. China

Break

T2.4 **"Measurements of Atmospheric Attenuation in the Region of 300 GHz"**, N.I. Furashov, V.Yu. Katkov, and B.A. Sverdlov, Radiophysical Research Institute, Nizhny Novgorod, Russia

T2.5 **"The Integration Times and the Rainfall Climatic Classification in China"**, Qing Sheng Dong, Qingdao Research Center of CRIRP, Qingdao, P.R. China

T2.6 **"Millimeter Wave Propagation Experiment in Sand-Dust Storm and Smoke"**, Qing Sheng Dong, Qingdao Research Center of CRIRP, Qingdao, P.R. China

Tuesday AM August 18, 1992
Session T3
FEL and Orotron I
Room 3
Presider: Y. A. Myasin 08:30

T3.1 **"Comparison Between the FEL Radiation and Cyclotron Radiation"**, Yuan Zhao Yin, Institute of Electronics, Academia Sinica, Beijing, P.R. China

T3.2 **"Free Electron laser with Electron Ring and Electromagnetic Pumping Wave"**, Invited, Yuan Zhao Yin, Institute of Electronics, Academia Sinica, Beijing, P.R. China

T3.3 **"Simulation of FEL Pumped by Electromagnetic Wave in the Relativistic Backward Wave Oscillator"**, Tian Quan Deng, University of Electronic Science and Technology, Chengdu, P.R. China

Break

T3.4 **"Study of Centimeter and Millimeter Wave Range powerful Orotrons' Efficient Regimes at the IRE of the Academy of Sciences of the USSR"**, Invited, Ye. A. Myasin, V. D. Kotov, A. N. Solovjov, S. G. Tchigarev, L. M. Nutovich, I.I. Tsitson, U. V. Andreev, T. A. Litkina, Institute of Radioengineering and Electronics, Moscow, Russia

T3.5 **"The Space Charge Effects in Orbitron and EECRM Maser"**, Zhi Qing Liu, Institute of Electronic Product Reliability and Environmental Testing of China, Guangzhou, Cai Dong Xiong and Shen Gang Liu, University of Electronic Science and Technology of China, Chengdu, P.R. China

T3.6 **"Analysis of Instability in EECRM System"**, Cai Dong Xiong and Shen Gang Liu, University of Electronic Science and Technologyof China, Chengdu, P.R. China

Tuesday AM August 18, 1992
Session T4
Materials/MMW
Apparatus and Measurements I
Room 4
Presider: H.C. Hu 08:30

T4.1 **"Research on the Millimeter-Wave Radome"**, Cheng Gong and Ke Qin Chen, Shanghai Research Institute of Microwave Technology, Shanghai, P.R. China

T4.2 **"Shielded Suspended Coupled Dielectric Guide and Directional Coupler"**, Alok Kumar Rastogi, MVAM, and A. K. Tiwari, MACT, Bhopal, (M.P), India

T4.3 **"A Simple and Accurate Method for Analysis of Dielectric Periodic Structures"**, Invited, Shan Jia Xu, University of Science and Technology of China, Hefei, and Li Guo Sun, Institute of Remote Sensing Applications, Beijing, P.R. China

T4.4 **"Characteristic Impedance of Waveguides and a Design Method for Two-Section Quarter-Wave Transformers"**, Junichiro Hashimoto and Fujio Ishihara, Tamagawa University, Machida, Japan

T4.5 **"Dispersion Characteristics of a Circular Cylindrical Dielectric Waveguide with Periodic Metallic Strips"**, Shan Jia Xu and Xin Zhang Wu, University of Science and Technology of China, Hefei, P.R. China

Break

T4.6 **"Analysis of a Planar Transmission Line with Discontinuity Using the New Time-Domain Method of Lines"**, Invited, Ling Chen and Si Fan Li, Southeast University, Nanjing, P.R. China

T4.7 **"The New Approach of Full-Wave Analysis of Discontinuities in a Planar Transmission Line"**, Ling Chen and Si Fan Li, Southeast University, Nanjing, P.R. China

T4.8 **"Transient Analysis of Microstrip Step Discontinuities on Anisotropic Substrate Having a Tilted Optical Axis"**, Guo Wu Zheng and Kang Shen Chen, Zhejiang University, Hangzhou, P.R. China

T4.9 **"Efficient Analysis of Finline Structures by the Boundary-Element Method"**, Invited, Bin Song and Jun Mei Fu, Xi'an Jiaotong University, Xi'an, P.R. China

Tuesday PM August 18, 1992
Session T5
Plasma Detection/Diagnostics
Room 1
Presider: T. Tsukishima 13:30

T5.1 **"Development of a High-Power, Power-Modulated TEA CO_2 Laser System as a Driving Source of Electrostatic Plasma Waves"**, Invited, K. Sasaki, K. Takahashi, T. Fujii, M. Nagatsu, and T. Tsukishima, Nagoya University, Nagoya, Japan

T5.2 **"Non-Coherent Reflectometry Method for Measurement of Plasma Cut-Off Layer Position"**, V.V. Kulik, K.A. Lukin, V.A. Rakityansky, Institute of Radiophysics and Electronics, Kharkov, Ukraine

Tuesday PM August 18, 1992
Session T6
Sources, Source Technology I
Room 2
Presider: R. W. McMillan 13:30

T6.1 **"Dual-Band Millimeter Wave Oscillators for Medical Use"**, Shu Xian Song, Dong Cheng Liu, and Ci Ping Deng, Beijing Institute of Technology, Beijing, P.R. China

T6.2 **"Quasioptical Translator on Ruby"**, A.A. Verity, S.P. Gavrilov, S.I. Tarapov, Institute of Radiophysics and Electronics, Kharkov, Ukraine

T6.3 **"W-Band Harmonic Mode GaAs Gunn Diodes"**, Yan Mao Deng, Nanjing Electronic Devices Institute, Nanjing, P.R. China

T6.4 **"The Experimental Investigation of the Super-Slow Electromagnetic Waves in the Periodic Semiconductor Structure"**, A.A. Bulgakov, S.K. Kondrashin, V.V. Kutuzov, Institute of Radiophysics and Electronics, Kharkov, Ukraine

Break

T6.5 "MM-Wave Bi-Tuning VCO", Invited, Dong Jin Wang and Dun Fu Li, University of Science and Technology of China, Hefei, P.R. China

T6.6 "Ka-Band Gunn VCOs", Cheng Xi Li, the Institute of Electronic Engineering of PLA, and Yong Li, No. 16 Institute, Ministry of Machine-Building and Electronics Industries of China, P.R. China

T6.7 **"New Wave Processes in the Inhomogeneous Semiconductors and Superlattices"**, F.G. Bass, A.A. Bulgakov, and S.I. Khankina, Institute of Radiophysics and Electronics, Kharkov, Ukraine

T6.8 **"Continuous Radiation Generator's Utilization in Coherent Millimeter Radars: Radiation Properties, Construction Schemes, Results of Experiments"**, A.A. Kostenko, G.I. Khlopov, V.P. Shestopalov, U.V. Yakimchiyk, Institute of Radiophysics and Electronics, Kharkov, Ukraine

Tuesday PM August 18, 1992
Session T7
Atmospheric Effects II
Room 3
Presider: D.Z. Hu 13:30

T7.1 **"The Attenuation of Electromagnetic Waves Due to Fog"**, Invited, D.J. Harris, University of Wales College of Cardiff, Cardiff, United Kingdom

T7.2 **"A New Model of Frequency Scaling of Rain Attenuation"**, Invited, Jie Huang and Da Zhang Hu, China Research Institute of Radiowave Propagation, Qingdao, P.R. China

T7.3 **"Experimental Investigation of Atmospheric Gas and Cloud Absorption in Millimeter Wave Band"**, Rin Jin Jia, Feng Xia Wang, and YiGuang Zhao, China Research Institute of Radiowave Propagation, Qingdao, P.R. China

T7.4 **"Fluctuations of MMW Propagating in Layered Inhomogeneous Turbulent Thickness"**, G.A. Andreyev and S.A. Ogarev, Institute of Radioengineering and Electronics, Moscow, Russia

Break

T7.5 **"Scanning Radiometer and Atmospheric Attenuation at 3 mm Wave Band"**, Pei Yuan Xu and Yin Long Cao, Shanghai University of Science and Technology, Shanghai, Yi Ting Cao and Hui Bo Shen, Purple Mountain Observatory, Academia Sinica, Nanjing, P.R. China

T7.6 **"Investigation of Rain-Induced XPD by Using Differential Attenuation at 30 - 100 GHz"**, Zhen Wei Zhao, China Research Institute of Radiowave Propagation, Qingdao, P.R. China

T7.7 **"Measurement of Millimeter Wave Scintillation on a Terrestrial Path"**, Zhi Huang Wu and Ya Qing Tan, China Research Institute of Radiowave Propagation, Qingdao, P.R. China

T7.8 **"The Use of Atmospheric Molecular Emission Lines for Passive Remote Sensing of the Earth's Surface"**, A.A. Shvetsov, Institute of Applied Physics, Nizhny Novgorod, Russia

Tuesday PM August 18, 1992
Session T8
Materials/MMW
Apparatus and Measurements II
Room 4
Presider: K.H. Jian 13:30

T8.1 **"Soliton Solutions of Periodic and Nonperiodic Inhomogeneous Nonlinear Klein-Gordon Equations"**, F. K. Kneubuhl and J.Feng, Swiss Federal Institute of Technology, Zurich, Switzerland

T8.2 **"Complex Permittivity (ε) and Permeability (μ) Measurements at Millimeter Wavelengths"**, Kun Hua Jian, Zhong Chen, and Shi Zhi Li, Beijing Institute of Technology, Beijing, P.R. China

T8.3 **"Internal Matching Broadband Method of Millimeter Waveguide Circulator"**, Deng Guo Zhang, Southwest Jiaotong University, Chengdo, P.R. China

Break

T8.4 **"Solitons in Periodic Structures with Kerr-Nonlinearity"**, J. Feng and F. K. Kneubuhl, Swiss Federal Institute of Technology, Zurich, Switzerland

T8.5 **"Ka-Band NRD Guide Power Divider"**, Ming Li Zhu, Huazhong University of Science and Technology, Wuhan, P.R. China

T8.6 **"NRD Waveguide LSE Mode Exciter"**, Hong Ma and Lan Fen Qi, Huazhong University of Science and Technology, Wuhan, P.R. China

Wednesday AM August 19, 1992
Session W1
MMW Detectors
Room 1
Presider: J.T. Lin 08:30

W1.1 **"Wideband 8mm-Wave Mixer with High IF"**, Zhou Qi, No. 16 Institute, The Ministry of Machine-Building and Electronics Industries of China

W1.2 **"DC to 120 GHz Harmonic Mixers for Millimeter Wave Instrumentation"**, A. M. Shchitov, J. S. Zaitsev, and A. M. Lomakin, Institute of Electronic Measurements (KVARZ), Nizhny Novgorod, Russia

W1.3 **"Detector of Millimeter Waves Based on Inhomogeneous Electron Heating"**, A. I. Vakser, Institute of Radiophysics and Electronics, Kharkov, Ukraine

W1.4 **"A Thin-Film Antenna-Coupled MOM Detector of IR Radiation"**, I. Wilke, K. Gilles, W. Herrmann, and F. K. Kneubuhl, Swiss Federal Institute of Technology, Zurich; and Y. Oppliger, CSEM, Neuchatel, Switzerland

Break

W1.5 **"A Novel Room temperature Operated Fast-Response FIR Detector"**, A.P. Dmitriev, S.A. Emelyanov, S.V. Ivanov, P.S. Kop'ev, Ya.V. Terent'ev, and I.D. Yaroshetsky, A.F. Ioffe Institute, St. Petersburg, Russia

W1.6 **"MM-Wave InP Beam-Lead Schottky Diodes"**, V G. Bozhkov, O.Yu. Malakhovsky, T.N. Korablyova, G.N. Misevichus, Research Institute of Semiconductor Devices, Tomsk, Russia

W1.7 **"2D Electron Gas as a Far-Infrared and Millimeter-Wave Detector"**, V.A. Pogrebnyak, D.D. Khalameida, V.M. Yakovenko, Institute of Radiophysics and Electronics, Kharkov, Ukraine

Wednesday AM August 19, 1992
Session W2
Gyrotrons
Room 2
Presider: S.G. Liu 08:30

W2.1 **"Numerical Simulations of Operational Characteristics of Cusptron Tube with an Anti-Coaxial-Magnetron-Type Waveguide Circuit"**, Invited, Xiao Min Wang, Hong Zhou, and Kang Sheng Chen, Zhejang University, Hangzhou, P. R. China

W2.2 **"Simulation of Non-Adiabatic Collector for Gyrotrons"**, A.L. Goldenberg and V.N. Manuilov, Institute of Applied Physics of Academy of Sciences, Nizhny Novgorod, Russia

W2.3 **"A Study of Harmonic Gyrotrons with Two Structures"**, Hong Fu Li, Pin Zhong Du, and Jian Kai Hu, University of Electronic Science and Technology of China, Chengdu, P.R. China

W2.4 **"The Helical Cerenkov Effect and Harmonic Emission in a Medium"**, Josip Soln, Harry Diamond Laboratories, Adelphi, Maryland, USA

Break

W2.5 **"Submillimeter Cyclotron Resonance Lasers and Their Applications"**, Yu.B. Vasilyev, Yu.L. Ivanov, S.D. Suchalkin, A.F. Ioffe Institute, St. Petersburg, Russia

W2.6 **"Production and Study of Axis-Circling Electron Beams for Peniotrons"**, V.D. Yeremka, Institute of Radiophysics and Electronics, Kharkov, Ukraine, and I.I. Golenitsky, B.C. Djubua, O.W. Evtushenko, V.P. Sazonov, R & P Corporation, Fryazino, Russia

W2.7 **"Power and Band Characteristics of Autoresonant Amplifier-Peniotron"**, V.D. Yeremka and V.A. Zhurakhovsky, Institute of Radiophysics and Electronics, Kharkov, Ukraine

Wednesday AM August 19, 1992
Session W3
Spectroscopy I
Room 3
Presider: N. Miura 08:30

W3.1 **"The Concept and Performance of a Continuous Submillimeter Wave Spectrometer in the Range of 250 μm to 7.5 mm Wavelength"**, Invited, E.A. Vinogradov, General Physics Institute, Moscow, Russia

W3.2 **"Torsion-Rotation FIR Spectrum of $^{13}CD_3OH$"**, Li-Hong Xu and R. M. Lees, University of New Brunswick, Fredericton, N.B., And J.W.C. Johns, National Research Council of Canada, Ottawa, Canada

W3.3 **"Microwave Absorption and Complex Formation in Some Donor-Acceptor Mixtures"**, K.N. Abd El Nour, M.Z. El Sabee, and S.L. Abd El Messeh, National Research Centre, Cairo, Egypt

W3.4 **"Far Infrared Laser Stark Spectroscopy of O-18 Methanol: Determination of Electric Dipole Moment"**, G. R. Sudhakaran, State University of New York, Oswego, NY, USA; R. Gopalsamy, I. Mukhopadhyay, P.K. Gupta, and R. Prasad, Department of Atomic Energy, Indore, India; R. M. Lees, University of New Brunswick, Fredericton, N.B., Canada; and R.R.J. Goulding, Memorial University of Newfoundland, St. Johns, N.F., Canada

Break

W3.5 **"Submillimeter Magnetic and Dielectric Properties of the Rare-Earth Orthoferrites"**, V.B. Anzin, G.B. Kozlov, S.P. Lebedev, A.A. Mukhin, A.S. Prokhorov, Institute of General Physics, Moscow, Russia

W3.6 **"The Microwave Photoconductivity of a Gapless Semiconductor Produced as a Result of Formation of an Energy Gap"**, S.G. Gasan-Zade, E.A. Sal'kov, and G.A. Shepelsky, Institute of Semiconductors of Ukraine, Kiev, Ukraine

W3.7 **"Effect of the Magnetic Field on the Polarization of Thermal Emission from an Isotropic Semiconductor"**, A.G. Kollyukh and V.A. Morozhenko, Institute of Semiconductors, Kiev, Ukraine

W3.8 **"Transmission, Reflection, and Absorption in Truncated Superlattice"**, R. Brazis and L. Safonova, Institute of Semiconductor Physics, Vilnius, Lithuania

W3.9 **"Dielectric Characterization of Materials at Submillimeter Wavelengths using BWO Spectrometers"**, V.B. Anzin, Yu.G. Goncharov, B.P. Gorshunov, G.V. Kozlov, S.P. Lebedev, A.A. Volkov, Institute of General Physics, Moscow, Russia

W3.10 **"Characterization of Millimeter-Submillimeter Filters by Use of BWO Spectrometers"**, V.B. Anzin, Yu.G. Goncharov, B.P. Gorshunov, G.V. Kozlov, S.P. Lebedev, A.A. Volkov, Institute of General Physics, Moscow, Russia

Wednesday AM August 19, 1992
Session W4
Integrated Circuits
Room 4
Presider: K. Chang 08:30

W4.1 **"Design and Performance of a Ka-Band Integrated Circuit Mixer"**, Biao Wang, Bao Qing Zhou, and Lin Xie Bei, Institute of Technical Physics, Shanghai, P.R. China

W4.2 **"Ka-Band GaAs Gunn MMIC VCO"**, Invited, Ping Lai, Mao Sen Wang, and Jin Ting Lin, Nanjing Electronic Devices Institute, Nanjing, P.R. China

W4.3 **"Progress in Millimeter-Wave Integrated-Circuit Horn Antennas"**, Invited, Yong Guo, Clemson University, Clemson, South Carolina, Jung-Chih Chiao, Kent A. Potter, and David B. Rutledge, California Institute of Technology, Pasadena, California, USA

W4.4 **"Millimeter Wave Integrated Circuits Based on a Dielectric Slotted Waveguide"**, S. E. Bankov, V. D. Vasukov, M. D. Duplenkova, V. I. Kanichev, V. N. Kozin, U. V. Kuranov, I. V. Levchenko, E. V. Rodionova, The Moscow Power Engineering Institute, Moscow, Russia

W4.5 **"Application of CO2 Laser To Formation of Silicon Cobalt Resistive Films"**, A. Medvid, T. Purlis, J. Kaupuza, M. Ogrins, and A. Kalnacs, Riga Technical University, Riga, Latvia

Wednesday PM August 19, 1992
Session W5
Quasi-Optics
Room 1
Presider: R. W. McMillan 13:30

W5.1 **"Accurate Electromagnetic Simulation of Open Resonators Loaded with Dielectric Slabs and Periodic Gratings"**, Invited, Alexander I. Nosich, Bilkent University, Ankara, Turkey

W5.2 **"Optimization Design and Experiment for 3 mm Quasi-Optical Power Combiner of Solid-State Sources"**, Cheng Tian Xue, Li Ming Lei, Hui Zhen Li, Hai Wen Zhang, and Ying Liu, Nankai University, Qiao Min Wang, Tianjin University, P.R. China

W5.3 **"Design Frequency of the Near-Millimeter Wave Quasi-Optical Monolithic Diode-Grid Frequency Multiplier Array"**, R. J. Hwu and L.P. Sadwick, University of Utah, Salt Lake City, Utah, USA

W5.4 **"A New Kind of Compound Microstrip Quasi-Optical Power Combiner"**, Yi-Jun He and Quan-Rang Yang, Research Institute of EMF and Microwaves, Southeast University, Nanjing, P.R. China

Break

W5.5 **"A Solid-State Generator with a Quasioptical Dielectric Resonator"**, S. N. Kharkovsky and A. Yu. Krichenko, Institute of Radiophysics and Electronics, Kharkov, Ukraine

W5.6 **"Ferrite and Semiconductor Quasioptical Devices of Millimetric and Submillimetric Wave Band Isolators, Circulators, and Switches"**, Alexey A. Kostenko, Grigoriy I. Khlopov, Victor P. Shestopalov, and Uriy B. Yakimchuk, Institute of Radiophysics and Electronics, Kharkov, Ukraine

W5.7 **"Study on Quasi-Optical Spherecomerechelette Open Resonator Solid-State Oscillator"**, O.I. Bekous, A.I. Fisun, A.M. Fursov, A.A. Kirilenko, Institute of Radiophysics and Electronics, Kharkov, Ukraine

W5.8 **"The Calculation of the Transitions Between the Quasi-Optical Waveguides"**, Vladimir K. Kiseliyev and Taras M. Kushta, Institute of Radiophysics and Electronics, Kharkov, Ukraine

W5.9 **"A New Type of an Open Resonator for MM- and Sub-MM-Wavelength Range Electron Devices"**, V.P. Sazonov, Research and Production Corporation "Istok", Fryazino, Russia

W5.10 **"Elements of the Diffraction Quasioptics; Part 1: The Main Properties"**, I.V. Minin and O.V. Minin, Institute of Applied Physics, Novosibirsk, USSR

W5.11 **"Elements of the Diffraction Quasioptics; Part 2: The Main Applications"**, I.V. Minin and O.V. Minin, Institute of Applied Physics, Novosibirsk, USSR

Wednesday PM August 19, 1992
Session W6
Materials/MMW
Apparatus and Measurements III
Room 2
Presider: L.J. Zhou 1:30 PM

W6.1 **"Calculation of S-Parameters of Planar Junctions by Boundary-Element Method"**, Bin Song and Jun Mei Fu, Xi'an Jiaotong University, Xi'an, P.R. China

W6.2 **"On the Elimination of Infinities in the PO Component of Equivalent Edge Currents"**, Taner Oguzer, Ayhan Altintas, Bilkent University; and O. Metin Buyukdura, Middle East Technical University, Ankara, Turkey

W6.3 **"Analysis of Transmission Characteristics of Inhomogeneous Planar Dielectric Waveguides Using Method of Transfer Matrix"**, Fu Yong Xu, Ke Yu Zhao, Zhong Ying Yang, and Fen Li, Lanzhou University, Lanzhou, P. R. China

W6.4 **"Electromagnetic Whispering Gallery Modes in a Radial Layer Dielectric Resonator"**, Yu. F. Filippov, S. N. Kharkovsky, and Z. Ye. Yeremenko, Institute of Radiophysics and Electronics, Kharkov, Ukraine

W6.5 **"Dimensional Optimization of Corrugated Rectangular Flexible Waveguides in Millimeter Band"**, Yao Kun Chin, Hua Yao He, and Yi Xin Yang, Shanghai Transmission Lines Research Institute, Shanghai, P.R. China

W6.6 **"A New Calibration Method for the Four-Port Reflectometer"**, Hong Xing Wu, Da Quan Liu, and Chu Hua Pan, Zhongshan University, Guangzhou, P.R. China

Break

W6.7 **"Automatic Measurement for Dielectric Properties of Solid Material at 890 Ghz"**, Invited, Bing Sheng Qiu, Cheng Jia Liu, Jiang Jun Huang, and Ru Man Qiu, Zhongshan University, Guangzhou, P.R. China

W6.8 **"Higher Order Modes in Coaxial Chirowaveguides"**, Zhong Xiang Shen, Nanjing Aeronautical Institute, Nanjing, P.R. China

W6.9 **"Research on Improving Isolation of 8 mm PIN Switch"**, Chun Zhou, Yu Fang, Pu Ming Fang, Liang Chen Wang, Li Wang, and Dong Zheng, Institute of Semiconductors, Academia Sinica, P.R. China

Wednesday PM August 19, 1992
Session W7
Spectroscopy II
Room 3
Presider: F.K. Kneubuhl 13:30

W7.1 **"Far-Infrared Spectral Emission from Simple Ionic Films"**, Invited, Kumao Hisano, National Defense Academy, Yokosuka, Japan

W7.2 **"Interactions Between Millimeter Wave Polar and Nonpolar Molecules"**, Jian Bo Chen and Bin Hong Li, Shanghai Jiao Tong University, Shanghai, P.R. China

W7.3 **"Far IR Transmission Spectra of $YBa_2Cu_3O_{7-\delta}$ Thin Films"**, A. Hadni and X. Gerbaux, University of Nancy, Nancy, France

W7.4 **"Absorption Properties of Pure Water Vapor at 297, 343, 412, and 440 GHz"**, N.I. Furashov and V. Yu. Katkov, Radiophysical Research Institute, Nizhny Novgorod, Russia

Break

W7.5 **"Application of IR and FIR Radiation in High Magnetic Field Spectroscopy"**, Invited, N. Miura, University of Tokyo, Tokyo, Japan

W7.6 **"Experimental Study of Four-Sublattice Antiferromagnet $CuCl_2 \cdot 2H_2O$ Resonance Properties"**, V. V. Eremenko, S. A. Zvyagin, V. V. Pishko, Yu. G. Pashkevich, and V. V. Shakhov, Institute for Low Temperature Physics and Engineering, Kharkov, Ukraine

W7.7 **"E-Beam Ionizer-Sustainer Laser on Rotational Transitions of Molecules"**, E. Ya. Kogan and N. E. Molevich, Pedagogical Institute, Samara, Russia

Wednesday PM August 19, 1992
Session W8
Sources, Source Technology II
Room 4
Presider: J. T. Lin 1:30 PM

W8.1 **"Study of a Gunn Oscillator Workable in Dual Bands"**, Xing Hau Liu, Zhejiang University, Hangzhou, P.R. China

W8.2 **"Tuning Performance of Ka-Band Radial Line Varactor Controlled Oscillators"**, Nizar Sultan, Canadian Space and Telecom, Inc., Orleans, Ontario, Canada

W8.3 **"U-Band Highly Stabilized Gunn Oscillator"**, Invited, Ji Hua Cao and Jin Ming Zhang, University of Science and Technology of China, Hefei, P. R. China

W8.4 **"Wide Range Tunable Submillimeter Cyclotron Resonance Germanium Laser: Spectral Characteristics and Applications"**, Ya.A. Mityagin, V.N. Murzin, S.A. Stoilitsky, and O.N. Stepanov, P.N. Lebedev Physical Institute, Moscow, Russia

Break

W8.5 **"Varactor Tuning for 3 mm Harmonic Oscillators"**, Jun Liu Tai, Chongqing Institute of Posts and Telecommunications, Chongqing, Zheng De Wu, and Xiao Hong Tang, University of Electronic Science and Technology, Chengdu, P.R. China

W8.6 **"Superslow Waves in Periodic Structures"**, A.A. Bulgakov and V.D. Koroiev, Institute of Radiophysics and Electronics, Kharkov, Ukraine

W8.7 **"Highly Stable Ka-Band GaAs Gunn Microstrip Oscillator"**, Invited, Da De Zhao, Yan Mao Deng, Hong Gui Qin, Bin Qian Tang, Jia Ling Zhang, Xiao Peng Sun, and Kai Shao, Nanjing Electronic Devices Institute, Nanjing, P.R. China

W8.8 **"Open Resonators with Matching Excitation"**, I.G. Kuzmitchiev, A.A. Kostenko, G.I. Khlopov, V.P. Shestopalov, U.V. Yakimchiyk, Institute of Radiophysics and Electronics, Kharkov Ukraine

Thursday AM August 20, 1992
Session Th1
Applications/Systems I
Room 1
Presider: S.F. Li 08:30

Th1.1 **"The Quest for Antenna Elements for Wide Band Multifunction Phased Arrays"**, Invited, N. Fourikis, Defence Science and Technology Organisation, Salisbury, South Australia

Th1.2 **"HRR Profiles Processing Techniques for IFMCW Millimeter Wave Radar"**, Song Hua He, Gui Rong Guo, Xiu Huang Guo, and Wei Zhang, Changsha Institute of Technology, Hunan, P.R. China

Th1.3 **"The Longwave Radiation Around Buildings at Different Angles"**, H. Nowak and K. Cena, Technical University of Wroclaw, Wroclaw, Poland

Th1.4 **"Analysis of Singularity of EMP on Aperture with IOEM"**, Ka Ma Huang and Yong Xue Yu, Sichuan University, Chengdu, P.R. China

Break

Th1.5 **"A Function of Lateral Inhibition Spectrum and Neural Networks in Heat Image Handler"**, Yi Qian, Department of Space Physics, Wuhan University, Wuhan, P.R. China

Th1.6 **"Application of Millimeter-Wave Radar in the Trajectory Measurement of Guns"**, Guang Jin Zhang, Wen Xiang, and Ji Guang Wu, East China Institute of Technology, P.R. China

Th1.7 **"Universe, Human Beings, and Millimeter Waves"**, Wen Zhou Huang, Fu Cheng Mao, and Jin Zhen Hong, Fujian Light Industry Institute, P.R. China

Th1.8 **"Testing System for High Isolation of MM-Wave Darkroom"**, Dong Jin Wang, Dun Fu Li, and Yuan Zhu Dou, University of Science and Technology of China, Hefei, P.R. China

Th1.9 **"An Investigation of the RF Channel Coupling and the RF Space Coupling in a Multichannel Millimeter-Wave System"**, Ya Ming Wang, Luoyang Optoelectronic Institute, Luoyang, P.R. China

Thursday AM August 20, 1992
Session Th2
Sources, Source Technology III
Room 2
Presider: F. J. Liao 08:30

Th2.1 **"A Three-Cavity Relativistic Klystron Amplifier"**, H. C. Chen, R. A. Stark, and V. M. Ayres, Naval Surface Warfare Center, White Oak, MD, USA

Th2.2 **"3 mm Band (75 - 110 GHz) BWO Sweep Oscillator Development"**, Ye Mei Zhu and Li Gang Xu, Beijing Vacuum Electronic Device Research Institute, Beijing, P.R. China

Th2.3 **"Test of WRC-40 (3 mm) Millimeter-Wave Source"**, Shiu Fang Yang, Southwest Institute of Applied Magnetics, P.R. China

Th2.4 **"Millimeter-Wave Injection-Locked Frequency Dividers"**, Ru Shan Chen, Ming Song Sun, and Xing Guo Li, East China Institute of Technology, P.R. China

Th2.5 **"Investigation of the Cathode for Millimeter Wave Tube"**, Zhi Zheng Zhou and Ai Ju Chen, Beijing Vacuum Electronics research institute, Beijing, P.R. China

Break

Th2.6 **"Network Synthesis of RF Windows for MM TWTs"**, J. L. Zhang and G. J. Su, Beijing Vacuum Electronics Research Institute, Beijing, P.R. China

Th2.7 **"Millimeter-Wave Synthesizers"**, G.M. Altshuller, O.G. Anikin, O. P. Pavlovsky, E. M. Karyakin, V. P. Kazakov, and A. F. Krupnov, Institute of Electronic Measurements (KVARZ), Nizhny Novgorod, Russia

Th2.8 **"Negative High Frequency Conductivity in Submicron Semiconductor Structures"**, V. M. Yakovenko, Institute of Radiophysics and Electronics, Kharkov, Ukraine

Th2.9 **"Ballast Electron Beams in O-Type Devices with Distributed Interaction"**, G.A. Alexeev, Institute of Radiophysics and Electronics, Kharkov, Ukraine

Thursday AM August 20, 1992
Session Th3
Atmospheric Effects III
Room 3
Presider: Y.P. Wang 08:30

Th3.1 **"Statistics and Variability of Millimetre-Wave Propagation and Related Meteorology Over a 500 m Path"**, Invited, C.J. Gibbins, Rutherford Appleton Laboratory, Chilton, United Kingdom

Th3.2 **"Attenuation and Depolarization for 3 mm Wave Band Induced by Rain"**, Invited, Ji Ying Huang and Yi Ping Wang, Xidian University, Xi'an, P.R. China

Th3.3 **"3 mm Microwave Radiometer and Sky Radiometric Temperature Research"**, Zu Yin Zhang and Jun Deng, Huangzhong University of Science and Technology, Wuhan, P.R. China

Break

Th3.4 **"Monte Carlo Solution of Rain Attenuation for Millimeter Waves"**, Zhen Sen Wu, Yi Yan, and Li Hong Chen, Xidian University, Xi'an, P.R. China

Th3.5 **"Conversion of 10-Minute Rainfall Rate to Equivalent 1-Minute Value at Some Locations in China"**, Shen Bo Qiu and Xiu Wan Lin, China Research Institute of Radiowave Propagation, Qingdao, P.R. China

Th3.6 **"Backscattering Cross-Section of Sand and Snow Surfaces on Short Millimeter Waves"**, G.A. Andreyev and G.I. Khokhlov, Institute of Radioengineering and Electronics, Moscow, Russia

Th3.7 **"Experimental Investigation of Cloud Attenuation"**, Lan Li, China Research Institute of Radiowave Propagation, Qingdao, P.R. China

Thursday AM August 20, 1992
Session Th 4
Materials/MMW Apparatus & Measurements IV
Room 4
Presider: N. Fourikis 08:30

Th4.1 **"Rigorous Numerical Analysis of Quasi-TEM Transmission Lines"**, Bin Song and Jun Mei Fu, Xi'an Jiaotong University, Xi'an, P.R. China

Th4.2 **"Exact Singular Integral Equation Solution for the Mode Functions of Finned Guides"**, P.V. Ramakrisna and D. Chadha, Indian Institute of Technology, New Delhi, India

Th4.3 **"An Example of Millimeter Wave (8 mm) Scalar Network Measurements"**, Shiu Fang Yang, Southwest Institute of Applied Magnetics, P.R. China

Th4.4 **"Some Aspects Concerning Characteristic Parameters Calculating Algorithms for Main Transmission Lines in cm and mm Wave Range"**, R. K. Starodubrovsky, Institute of Electronic Measurements (KVARZ), Nizhny Novgorod, Russia

Th4.5 **"Optimum Design of Waveguide Taper from Rectangular to Grooved Cross Section"**, Jin Ying Liu and Jian Zhang Qin, Beijing Vacuum Electronics Research Institute, Beijing, P.R. China

Break

Th4.6 **"The Characteristic Equation of Asymmetric Double Circular Groove Guide"**, Jian Lei Ma, Hong Sheng Yang, and Zhong Zuo Lu, Southeast University, Nanjing, P.R. China

Th4.7 **"Scattering Characteristics of Epitaxial Layer on Lossy Dielectric Segment Partially Filled in Waveguide"**, Xu Shanjia and Wu Xinzhang, University of Science and Technology of China, Hefei, P.R. China; P. Greiner, C.R. Becker, and R. Geick, University of Wurzburg, Wurzburg, Germany

Th4.8 **"Research Progress in Grooved NRD Waveguides"**, Xun Zhong Wen, Lin Xiao Li, and Zhu Lei, Southeast University, Nanjing, P.R. China

Th4.9 **"A Millimeter-Wave Broadside Gap-Coupled Suspended Substrate Stripline Bandpass Filter"**, Yit-Chyun Chiang, Ching-Kuang Tzuang, and Shyang Su, National Chiao Tung University, Hsinchu, Taiwan, Republic of China

Thursday August 20, 1992
Session Th5
Applications/Systems II
Room 1
Presider: S. L. Johnston 13:30

Th5.1 **"Contemporary Millimeter Wave Radar"**, Invited. Stephen L. Johnston, International Radar Directory, Huntsville, Alabama, USA

Th5.2 **"W-Band Communication System and Electrical Wave Propagation Measurement System"**, Shu Yi Dong, Dong Gou Zhang, Yi Yan, Li Min Qiao, Xidian University, Xi'an, P.R. China

Th5.3 **"Applications of High-Temperature Superconductors in Millimeter-Wave Components"**, A. R. Jha, Jha Technical Consulting Services, Cerritos, California, USA

Th5.4 **"Study of Dual-Band and Dual-Polarization MMW Antenna Feed System"**, Ci Peng Deng, Xin Liu, and Zhen Li, Beijing Institute of Technology, Beijing, P.R. China

Break

Th5.5 **"New Excitation Method of Avalon Switch"**, Ling Qing Zhang and Ke Qin Wu, Shanghai Millimeter-Wave and Submillimeter-Wave Laboratory, Shanghai, P.R. China

Th5.6 **"Millimeter-Wave ECM - A New Field of Electronic Combat"**, Jin Xuan Gong, Southwest Institute of Electronic Equipment, Chengdu, P.R. China

Th5.7 **"Investigation of Frequency Scanning Characteristic of periodically Loaded Leaky-Wave Antenna with Metal Strips"**, Guo Ding Li, Chang Sheng Shi, and Zhi Hong Zeng, Tsinghua University, Beijing, P.R. China

Th5.8 **"Influence of Electromagnetic Wave on Encapsulated Semiconductor Devices"**, Ka Ma Huang and Yong Xue Yu, Sichuan University, Chengdu, P.R. China

Thursday PM August 20, 1992
Session Th6
FEL and Orotron II
Room 2
Presider: A. I. Nosich 13:30

Th6.1 **"Some Topics on ECRM Theory"**, Sheng Gang Liu, University of Electronic Science and Technology of China, Chengdu, P.R. China

Th6.2 **"Investigation of a Free-Electron Laser with an Electromagnetic Wiggler"**, Zheng Liang, Jia Yin Li, Bin Zhang, Jian Qiang Wu, Wen Duo Ma, Zi Qiang Yang, Tian Quan Deng, Xin Yu Chen, Xiao Lan Zhou, Jia Hong Sun, and Sheng Kong Liu, University of Electronic Science and Technology of China, Chengdu, P.R. China

Th6.3 **"The Clinotron"**, G. Ya. Levin, A. Ya. Krichenko, A. I. Borodkin, S. A. Churilova, and A. Ya. Usikov, Institute of Radiophysics and Electronics, Kharkov, Ukraine

Th6.4 **"Synchronous and Chaotic Oscillations in the Smith-Purcell Free-Electron Lasers"**, Dmitry M. Vavriv, Institute of Radio Astronomy, Kharkov, Ukraine

Break

Th6.5 **"Radiative Damping of Two-Dimensional Plasmons in an Open Structure with a Metal Grating"**, O.R. Matov, O.V. Polishchuk, and V.V. Popov, Institute of Radioengineering and Electronics, Saratov, Russia

Th6.6 **"Theory and Design of a New Smith-Purcell Amplifier"**, Yuriy A. Romantsov, Institute of Radio Astronomy, Kharkov, Ukraine

Th6.7 **"Distributed Interaction of Open Resonator Fields with Semiconductor"**, V.A. Abdulkadyrov, and I.D. Revin, Institute of Radiophysics and Electronics, Kharkov, Ukraine

Th6.8 **"Superslow Waves in Periodic Structures"**, A.A. Bulgakov and V.D. Korolev, Inst. of Radiophysics and Electronics, Kharkov, Ukraine

Index to Authors

Author	Session	Page
Abd El Nour, K.N.	W3.3	267
Abd El Messieh, S.L.	W3.3	267
Abdulkadyrov, V.A.	Th6.7	626
Afsar, M.H.	Th8.6	686
Alexeev, G.A.	Th2.9	509
Altintas, A.	W6.2	355
Altshuller, G.M.	Th2.7	502
Altukhov, I.V.	Th7.5	651
Andreev, U.V.	T3.4	94
Andreyev, G.A.	T7.4	178
Andreyev, G.A.	Th3.6	531
Anikin, O.G.	Th2.7	502
Anzin, V.B.	W3.5	274
Anzin, V.B.	W3.9	290
Anzin, V.B.	W3.10	294
Ayres, V.M.	Th2.1	479
Bankov, S.E.	W4.4	308
Bass, F.G.	T6.7	162
Becker, C.R.	Th4.7	559
Bei, L.	W4.1	297
Belavsky, B.A.	T3.4	94
Belitsky, V.	T1.2	43
Belous, O.I.	W5.7	334
Bernachevsky, G.A.	T3.4	94
Bockstal, L. Van	Th7.10	664
Bocquet, R.	Th7.4	646
Borodkin, A.I.	Th6.3	610
Boucher, D.	Th7.4	646
Bozhkov, V.G.	W1.6	230
Brazis, r.	W3.8	286
Bulgakov, A.A.	T6.7	162
Bulgakov, A.A.	Th6.8	630
Bulgakov, A.A.	T6.4	152
Bulgakov, A.A.	W8.6	433
Buyukdura, O.M.	W6.2	355
Cao, Y.	T7.5	182
Cao, Y.	T7.5	182
Cao, J.	W8.3	421
Cena, K.	Th1.3	451
Chadha, D.	Th4.2	542
Chan, C.P.	Th7.6	654
Chang, K.	M2.4	30
Chen, A.	Th2.5	495
Chen, L.	T4.6	116
Chen, H.C.	Th2.1	479
Chen, J.	W7.2	391
Chen, K.	T4.1	100
Chen, L.	Th3.4	523
Chen, L.	T4.7	120
Chen, K.	T4.8	124
Chen, K.	W2.1	236
Chen, Z.	T8.2	198
Chen, R.	Th2.4	491
Chen, X.	Th6.2	606
Chen, W.	Th7.4	646
Chi, H.	Th8.6	686
Chiang, Y.-C.	Th4.9	568
Chiao, J.-C.	W4.3	304
Chin, Y.K.	W6.5	367
Churilova, S.A.	Th6.3	610
D.J. Harris	T7.1	166
Deng, T.	T3.3	90
Deng, Y.	T6.3	148
Deng, Y.	W8.7	437
Deng, C.	T6.1	140
Deng, J.	Th3.3	519
Deng, C	Th5.4	584
Deng, T.	Th6.2	606
Dmitriev, A.P.	W1.5	227
Dong, Q.S.	T2.5	75
Dong, Q.S.	T2.6	78
Dong, S.	Th5.2	576
Dou, Y.	Th1.8	471
Du, P.	W2.3	243
Duplenkova, M.D.	W4.4	308
El Sabee, M.Z.	W3.3	267
Emelyanov, S.A.	W1.5	227
Eremenko, V.V.	W7.6	405
Evdokimov, V.V.	T3.4	94
Fang, P.	W6.9	384
Fang, Y.	W6.9	384
Feng, J.	T8.1	196
Feng, J.	T8.4	204
Filippenko, L.	T1.2	43
Filippov, Yu. F.	W6.4	363
Fisun, A.I.	W5.7	334
Fourikis, N.	Th1.1	444
Fu, J.	T4.9	128
Fu, J.	W6.1	351
Fu, J.	Th4.1	538
Fujii, t.	T5.1	132
Furashov, N.I.	T2.4	72
Furashov, N.I.	W7.4	398
Fursov, A.M.	W5.7	334
Gasan-zade, S.G.	W3.6	278
Gavrilov, S.P.	T6.2	144
Geick, R.	Th4.7	559
Gerbaux, X.	W7.3	395
Gibbins, C.J.	Th3.1	510
Gilles, K.	W1.4	223

Index to Authors

Author	Session	Page
Goldenberg, A.L.	W2.2	240
Goncharov, Yu. G.	W3.9	290
Goncharov, Yu. G.	W3.10	294
Gong, C.	T4.1	100
Gong, J.-X.	Th5.6	591
Gopalsamy, R.	W3.4	270
Gorshunov, B.P.	W3.9	290
Gorshunov, B.P.	W3.10	294
Goulding, R.R.J.	W3.4	270
Goulding, R.R.J.	Th7.6	654
Greiner, P.	Th4.7	559
Gundlach, K. H.	T1.1	35
Guo, Y.	W4.3	304
Guo, G.	Th1.2	447
Guo, X	Th1.2	447
Gupta, P.K.	Th8.2	672
Gupta, P.K.	W3.4	270
Hadni, A.	W7.3	395
Hashimoto, J.	T4.4	108
He, H.Y.	W6.5	367
He, Y.-J.	W5.4	325
He, S.	Th1.2	447
Herlach, F.	Th7.10	664
Herrmann, W.	W1.4	223
Hisano, K.	W7.1	387
Holenstein, A.P.	T1.4	50
Hong, J.	Th1.7	467
Hu, J.-K.	W2.4	247
Hu, H. C.	M2.1	17
Hu, D.	T7.2	169
Hu, D.-Z.	T2.1	61
Huang, K.	Th5.8	599
Huang, J.	T7.2	169
Huang, J.Y.	Th3.2	515
Huang, J.	W6.7	376
Huang, W.	Th1.7	467
Huang, K.	Th1.4	455
Huguenin, D.	T1.4	50
Hwu, R.J.	W5.3	321
Ishihara, f.	T4.4	108
Ivanov, S.V.	W1.5	227
Ivanov, Yu. L.	W2.5	249
Ja, R.J.	T7.3	173
Janssen, P.	Th7.10	664
Jha, A.R.	Th5.3	580
Jian, K-h.	T8.2	198
Johns, J.W.C.	Th7.6	654
Johns, J.W.C.	Th8.4	679
Johns, J.W.C.	W3.2	263
Johnston, S.L.	Th5.1	572
Kagan, M.S.	Th7.5	650
Kalinichev, V.I.	W4.4	308
Kalnaca, A.	W4.5	312
Kaplunenko, V.	T1.2	43
Kaplunenko, O.	T1.2	43
Karyakin, E.N.	Th2.7	502
Katkov, V. Yu.	T2.4	72
Katkov, V. Yu.	W7.4	398
Kaupuzs, J.	W4.5	312
Kazakov, V.P.	Th2.7	502
Khabipov, M.	T1.2	43
Khalameida, d.D.	W1.7	234
Khankina, S.I.	T6.7	162
Kharkovsky, S.N.	W5.5	328
Kharkovsky, S.N.	W6.4	363
Khlopov, G.I.	W5.6	331
Khlopov, G.I.	T6.8	163
Khlopov, G.I.	W8.8	440
Khokhlov, G.I.	Th3.6	531
Kirichenko, A. Ya.	Th6.3	610
Kirichenko, A. Ya.	W5.5	328
Kirilenko, A.A.	W5.7	334
Kiselyev, V.K.	W5.8	335
Kneubuhl, F.K.	M1.3	9
Kneubuhl, F.K.	W1.4	223
Kneubuhl, F.K.	T8.4	204
Kneubuhl, F.K.	T1.4	50
Kneubuhl, F.K.	T8.1	196
Kogan, E. Ya.	W7.7	409
Kollyukh, A.G.	W3.7	282
Komeda, R.	Th7.7	658
Kondrashin, S.K.	T6.4	152
Kop'ev, P.S.	W1.5	227
Korablyova, T.N.	W1.6	230
Korol'ov, K.A.	Th7.5	650
Korolev, V.D.	Th6.8	630
Korolev, V.D.	W8.6	433
Korosteljov, V.S.	T1.6	57
Koshelets, V.	T1.2	43
Kostenko, A.A.	T6.8	163
Kostenko, A.A.	W8.8	440
Kostenko, A.A.	W5.6	331
Kotov, V.D.	T3.4	94
Kovtonjuk, S.	T1.2	43
Kozin, V.N.	W4.4	308
Kozlov, G.V.	W3.10	294
Kozlov, G.V.	W3.9	290
Kozlov, G.C.	W3.5	274
Krevet, R.	Th7.9	663
Kriven, S.I.	Th7.2	638

Index to Authors

Author	Session	Page
Kriven, S.I.	Th7.3	642
Krupnov, A.F.	Th2.7	502
Krupnov, A. F.	M1.1	1
Kulik, V.V.	T5.2	136
Kuranov, U.V.	W4.4	308
Kushta, T.M.	W5.8	335
Kutuzov, V.V.	T6.4	152
Kuzmitchiev, I.K.	W8.8	440
Lai, P.	W4.2	301
Lebedev, S.P.	W3.5	274
Lebedev, S.P.	W3.9	280
Lebedev, S.P.	W3.10	294
Lees, R.M.	W3.4	270
Lees, R.M.	Th8.4	679
Lees, R.M.	Th7.6	654
Lees, R.M.	W3.2	263
Lees, R.M.	Th8.2	672
Lei, L.-M.	W5.2	317
Levchenko, I.V.	W4.4	308
Levin, G. Ya.	Th6.3	610
Lewis-Bevan, W.	Th7.6	654
Li, H.	W2.3	243
Li, X.	Th2.4	491
Li, S.-z.	T8.2	198
Li, D.	Th1.8	471
Li, Y.	T6.6	158
Li, C.	T6.6	158
Li, D.	T6.5	154
Li, Y.	Th8.1	668
Li, B.	W7.2	391
Li, F.	W6.3	359
Li, G.	Th5.7	595
Li, I.	Th3.7	534
Li, S-F.	T4.6	116
Li, S-F.	T4.7	120
Li, H.-Z.	W5.2	317
Li, J.	Th6.2	606
Li, Z.	Th5.4	584
Liang, Z.	Th6.2	606
Liao, F. J.	M1.4	13
Lin, Y.	Th8.1	668
Lin, X.W.	Th3.5	527
Lin, J.	W4.2	301
Lin, Y.	Th8.3	677
Litkina, T.A.	T3.4	94
Liu, C.	W6.7	376
Liu, D.	W6.6	372
Liu, D.	T6.1	140
Liu, J.Y.	Th4.5	552
Liu, S.	T3.5	95
Liu, S.	Th6.2	606
Liu, Z.	T3.5	95
Liu, T.-J.	W8.5	429
Liu, X.	W8.1	413
Liu, S.	T3.6	97
Liu, S.	Th6.1	603
Liu, Y.	W5.2	317
Liu, G. Y.	M2.1	17
Lomakin, A.M.	W1.2	217
Lothar, T.	M2.3	26
Lu, W.	Th7.8	662
Lu, W.	M2.5	34
Lu, X.	Th5.4	584
Lu, Z.-Z.	Th4.6	555
Lukin, K.A.	T1.6	57
Lukin, K.A.	T5.2	136
Luo, X.	Th8.3	676
Luther, S.	Th7.8	662
Ma, H.	T8.6	210
Ma, J.	Th4.6	555
Ma, W.	Th6.2	606
Malakhovsky, O. Yu.	W1.6	230
Manuilov, V.N.	W2.2	240
Mao, F.	Th1.7	467
Matov, O.R.	Th6.5	618
Mazur, Yu. I.	Th7.2	638
Mazur, Yu. I.	Th7.3	642
McMillan, R. W.	M1.4	13
Medvid', A.	W4.5	312
Minin, I.V.	W5.10	343
Minin, I.V.	W5.11	347
Minin, O.V.	W5.10	343
Minin, O.V.	W5.11	347
Misevichus, G.N.	W1.6	230
Mityagin, Ya. A.	W8.4	425
Miura, N.	W7.5	401
Molevich, N.E.	W7.7	409
Morozhenko, V.A.	W3.7	282
Mukhin, A.A.	W3.5	274
Mukhopadhyay, I.	Th7.6	654
Mukhopadhyay, I.	W3.4	270
Mukhopadhyay, I.	Th8.2	672
Murzin, V.N.	W8.4	425
Myasin, Ye. A.	T3.4	94
Nagatsu, M.	T5.1	132
Nakata, H.	Th7.7	658
Nanba, T.	Th7.1	634
Nosich, A.I.	W5.1	316
Nowak, H.	Th1.3	451
Nutovich, L.M.	T3.4	94

Index to Authors

Author	Session	Page
Ogarev, s.A.	T7.4	178
Ogrins, M.	W4.5	312
Oguzer, T.	W6.2	355
Ohyama, T.	M2.2	22
Ohyana, T.	Th7.7	658
Oppliger	W1.4	223
Ortenberg, M. von	M2.5	34
Ortenberg, M. von	Th7.9	663
Ortenberg, M. von	Th7.8	662
Pan, C.	W6.6	372
Pashkevich, Yu. G.	W7.6	405
Pavlichenko, O.S.	T1.6	57
Pavlichenko, R.O.	T1.6	57
Pavlovsky, O.P.	Th2.7	502
Peng, S.	T1.3	46
Pichko, V.V.	W7.6	405
Pogrebnyak, V.A.	W1.7	234
Polishchuk, O.V.	Th6.5	618
Popov, V.V.	Th6.5	618
Potter, K.A.	W4.3	304
Prasad, R.	W3.4	270
Prokhorov, A.S.	W3.5	274
Prokopenko, G.	T1.2	43
Puritis, T.	W4.5	312
Qi, L.	T8.6	210
Qi, Z.	W1.1	214
Qiao, L	Th5.2	576
Qin, J.Z.	Th4.5	552
Qin, H.	W8.7	437
Qiu, S.B.	Th3.5	527
Qiu, R.	W6.7	376
Qiu, B.	W6.7	376
Rakityansky, V.A.	T5.2	136
Rakityansky, V.A.	T1.6	57
Ramakrishna, P.V.	Th4.2	542
Renard, J.P.	Th7.8	662
Revin, I.D.	Th6.7	626
Rodionova, E.V.	W4.4	308
Romantsov, Y.A.	Th6.6	622
Roters, F.	Th7.9	663
Rothermel, H.	T1.1	35
Rutledge, D.B.	W4.3	304
Sadwick, L.P.	W5.3	321
Safonova, L.	W3.8	286
Sal'kov, E.A.	W3.6	278
Sasaki, K.	T5.1	132
Sazonov, V.P.	W5.9	339
Schenker, G.	T1.4	50
Shakhov, V.V.	W7.6	405
Shchitov,A.M.	W1.2	217
Shen, Z.	T1.5	53
Shen, Z.	W6.8	380
Shen, S. C.	M2.5	34
Shen, H.	T7.5	182
Shengang, L.	M2.3	26
Shepelsky, G.A.	W3.6	278
Shestopalov, V.P.	T6.8	163
Shestopalov, V.P.	T1.6	57
Shestopalov, V.P.	W8.8	440
Shestopalov, V.P.	W5.6	331
Shevchenko, N.V.	Th7.2	638
Shevchenko, N.V.	Th7.3	642
Shi, C.	Th5.7	595
Shitov, S.	T1.2	43
Shun, X.-W.	Th1.6	463
Shvetsov, A.A.	T7.8	192
Sinis, V.P.	Th7.5	650
Soln, J.	W2.4	247
Solovjov, A.N.	T3.4	94
Song, B.	W6.1	351
Song, B.	Th4.1	538
Song, S.	T6.1	140
Song, B.	T4.9	128
Sstroganov, V.V.	T2.2	66
Stark, R.A.	Th2.1	479
Starodubrovsky, R.K.	Th4.4	548
Stepanov, O.N.	W8.4	425
Stoklitsky, S.A.	W8.4	425
Su, S.	Th4.9	568
Su, K.-q.	Th5.5	588
Suchalkin, S.D.	W2.5	249
Sudhakaran, G.R.	W3.4	270
Sultan, N.	W8.2	417
Sun, L.	T4.3	104
Sun, J.	Th6.2	606
Sun, M.	Th2.4	491
Sverdlov, B.A.	T2.4	72
Takahashi, K.	T5.1	132
Tan, Y.,	T7.7	188
Tang, B.	W8.7	437
Tang, X.	W8.5	429
Tarapov, S.I.	T6.2	144
Tarasov, M.	T1.2	43
Tarasov, G.G.	Th7.3	642
Tarasov, G.G.	Th7.2	638
Tastogi, A.K.	T4.2	103
Tchigarev, S.G.	T3.4	94
Tiwari, A.K.	T4.2	103
Trent'ev, Ya. V.	W1.5	227
Tseytlin, M.B.	T3.4	94

Index to Authors

Author	Session	Page
Tsitson, I.I.	T3.4	94
Tsukishima, T.	T5.1	132
Tuchendler, J.	Th7.8	662
Turygin, S.	T1.2	43
Tzuang, C.-K.	Th4.9	568
Usikov, A. Ya.	Th6.3	610
Vasilyev, Yu. B.	W2.5	249
Vasjukov, V.D.	W4.4	308
Vasker, A.I.	W1.3	221
Vavriv, D.M.	Th6.4	614
Vertiy, A.A.	T6.2	144
Vinogradov, e.A.	W3.1	261
Volkov, A.A.	W3.9	290
Volkov, S.P.	W3.10	294
Vystavkin, A.	T1.2	43
Wang, M.	W4.2	301
Wang, F.X.	T7.3	173
Wang, Y.	Th1.9	475
Wang, X.	W2.1	236
Wang, D.	Th1.8	471
Wang, Y.P.	Th3.2	515
Wang, Q.-M.	W5.2	317
Wang, D.	T6.5	154
Wang, B.	W4.1	297
Wang, L.	W6.9	384
Wilke, I.	W1.4	223
Witters, J.	Th7.10	664
Wu, Z.	Th3.4	523
Wu, J.-G.	Th1.6	463
Wu, H.	W6.6	372
Wu, X.	T4.5	112
Wu, Z.	T7.7	188
Wu, Z.	W8.5	429
Wu, X.	Th4.7	559
Wu, J.	Th6.2	606
Xiao, L.-L.	Th4.8	563
Xiong, C.	T3.6	97
Xiong, C.	T3.5	95
Xu, L.H.	Th8.4	679
Xu, F.	W6.3	359
Xu, G.J.	Th2.6	498
Xu, P.	T7.5	182
Xu, L.-G.	Th2.2	483
Xu, L.-H.	W3.2	263
Xu, S.	T4.3	104
Xu, X.	Th4.7	559
Xu, S.	T4.5	112
Xue, C.-T.	W5.2	317
Xy, Z.	T1.3	46
Yakavenko, V.M.	Th2.8	506
Yakimchiyk, U.V.	T6.8	163
Yakimchiyk, U.V.	W8.8	440
Yakimchuk, U.B.	W5.6	331
Yakovenko, V.M.	W1.7	234
Yan, Y.	Th3.4	523
Yan, Y.	T2.3	68
Yan, Y.	Th5.2	576
Yang, X.	Th4.3	546
Yang, Z.	Th6.2	606
Yang, H.-S.	Th4.6	555
Yang, X.	Th2.3	487
Yang, Q.-R.	W5.4	325
Yang, Y.	W6.5	367
Yeremenko, Z. Ye.	W6.4	363
Yeremka, V.D.	W2.6	253
Yeremka, V.D.	W2.7	257
Yi, Q.	Th1.5	459
Yin, Y.	T3.1	82
Yin, Y.	T3.2	86
Yoroshetsky, I.E.	W1.5	227
Yu, Y.	Th5.8	599
Yu, Y.	Th1.4	455
Yurchenko, L.V.	Th8.5	683
Zaitsev, J.S.	W1.2	217
Zeng, Z.	Th5.7	595
Zhang, H.-W.	W5.2	317
Zhang, M. G.	M1.2	2
Zhang, W.	Th1.2	447
Zhang, Z.	Th3.3	519
Zhang, J.L.	Th2.6	498
Zhang, G.-J.	Th1.6	463
Zhang, W.-X.	Th4.8	563
Zhang, D.	Th5.2	576
Zhang, B.	Th6.2	606
Zhang, D.G.	T8.3	202
Zhang, L.-q.	Th5.5	588
Zhao, S.	Th7.6	654
Zhao, Y.G.	T7.3	173
Zhao, D.	W8.7	437
Zhao, K.	W6.3	359
Zhao, Z.	T7.6	184
Zhao, E.	T1.5	53
Zheng, D.	W6.9	384
Zheng, G.	T4.8	124
Zhong, J.	W8.3	421
Zhou, X.	Th6.2	606
Zhou, B.	W4.1	297
Zhou, H.	W2.1	236
Zhou, Z.	Th2.5	495
Zhou, C.	W6.9	384

Index to Authors

Author	Session	Page
Zhu, Y.-M.	Th2.2	483
Zhu, L.	Th4.8	563
Zhu, M.	T6.5	206
Zhurakhovskiy, V.A.	W2.7	257
Zvyagin, S.A.	W7.6	405

SUB-MILLIMETER MICROWAVE SPECTROSCOPY WITH PRIMARY RADIATION SOURCES

Andrei F. Krupnov
Radiophysical Research Institute
Institute of Applied Physics
Russian Academy of Sciences
Nizhny Novgorod, 603600, Russia

ABSTRACT

In this paper we present spectroscopic results obtained with radiation sources operating at fundamental frequencies up to greater than one terahertz. These sources are powerful, tunable over broad bandwidths, and have excellent spectral qualities. Absorption spectra of several molecular species measured with these oscillators are presented and discussed.

M1.2

RESEARCHES OF MM WAVE PROPAGATION IN CHINA

M. G. Zhang
(China Research Institute of Radiowave Propagation)

ABSTRACT

Researches in China are outlined of mm wave propagation, including the main research units and the main measurements and studies of rain attenuation, rain caused depolarization and rainfall characteristics.

1. INTRODUCTION

Researches of mm wave propagation began in China in the late seventies. The measurements were made previously at frequencies between 10 and 40 GHz, and now are made at frequencies up to about 100 GHz. The main items are rain attenuation, rain caused depolarization and rainfall characteristics. The effects of atmospheric gases, clouds, sand and dust-storms and scintillation are measured as well.

2. RESEARCH UNITS

The main research units are China Research Institute of Radiowave Propagation (CRIRP), Xidian University (XIDIAN) and Wunan University (WUDA).

CRIRP has a research center special for mm wave propagation- Qingdao Research Center. The Center has a terrestrial path system operating at 12, 25, 33, 72 and 94 GHz, an Earth-space system consisting of an Earth station for Satellite BS-2 and a 35 GHz radiometer, and a meteorological system consisting of a rain radar, a rain gauge network and a particle measuring system. Figure 1 is the illustration of it. The Center organizes some measurements also outside Qingdao for other items, e. g. sand and dust-storms. At the main body of CRIRP, multiple frequency measurements of rain attenuation were made also on a terrestrial path for several years, and absorption and radiation of atmospheric gases and cloud attenuation have been measured in the last years. Typical measurements and statistical analyses of rain intensity have been made for the whole country.

Department of Physics of XIDIAN has made measurements of rain attenuation and rain caused depolarization at 35 GHz with relevant rainfall measure-

ments on a terrestrial path in Xian, and now installed a 94 GHz system. More theoretical studies were made there.

Department of Space Physics of WUDA measured rain attenuation on a slant path using a 35 GHz radiometer in Wuhan, and statistically analysed rain intensity data for the whole country.

In addition, some other units are involved in measurements of atmospheric gases effects.

3. MEASUREMENTS AND STUDIES OF RAIN ATTENUATION

Rain attenuation has been measured on terrestrial paths in Xinxiang, Qingdao and Xian and on slant paths in Beijing, Qingdao, Wuhan, Taibei and Hong Kong, Rain intensity being measured simultaneously.

The examples of long-term statistics of rain attenuation and relevant rain intensity for terrestrial paths are given in Table 1 for Xinxiang[1] and in Figure 2 for Qingdao[2].

The long-term statistics of rain attenuation and relevant rain intensity for slant paths are given in Table 2.

Relevant studies have been done for the prediction models of rain attenuation by CRIRP[3], XIDIAN[4] and WUDA[5], and the existing typical models tested against the Chinese data. As seen from Figure 2, the model in CCIR Report 338-6 is in reasonable agreement with the measured results in Qingdao. Using the testing variable presented in CCIR Report AA/S, with the Chinese data for slant paths, the mean error and the standard deviation of the model in CCIR Report 564-4 are found to be 7% and 36%, respectively. for 0.01% of time.

4. STUDIES OF RAIN CAUSED DEPOLARIZATION

Rain caused depolarization has been studied by XIDIAN and CRIRP. On a 2.2 km path in Xian, measurements have been made at 35 GHz with a linear polarization of 45°, relevant meteorological factors being measured or collected for Xian. Using the first order scattering approximation, the rain intensity data of ten years and the measurement result of rain drop canting angles, the statistics of cross polarization discrimination (XPD) caused by rain for Xian has been estimated as shown in Figure 3[6].

Further estimations are made recently for 94 GHz, taking into account the effects of incoherent and multiple scattering[7,8].

5. MEASUREMENTS AND ANALYSES OF RAINFALL

In addition to the simultaneous measurements of rain intensity with propagation experiments, analyses of the statistics of rain intensity have been made by CRIRP and WUDA based on the data from the conventional meteorological stations all over the county. The statistics of rain intensity for several tens of points, the contours of rain intensity for 0.1% and 0.01% of time and twelve rain climatic zones in China have been drawn.

Figure 4 shows the contours of rain intensity for 0.01% of time[9].

Additional measurements have also been made in Xinxiang, Nanjing and Guangzhou for the conversion of rain intensity data with different integration time. According to CCIR Report 563-4, the conversion factor of the statistics from 10 minutes to 1 minute can be written as

$$\rho_{1'}(P) = aP^{b} \qquad (0.001\% \leq P \leq 0.03\%)$$

where P is the percentage of time for which the rain intensity is exceeded, a and b are found as listed in Table 3

An analysis based on data from over twenty typical points shows that the relationship between the worst month and the annual statistics of rain intensity in China is

$$P = 0.22P_w^{1.16}$$

where P and P_w are the time percentage for annual and worst month statistics, respectively.

REFERENCES

1. D. Z. Hu et al. [1988] Measurements of rain attenuation at frequencies 10 - 40 GHz in middle region of China. International Symposium on Radio Propagation, Beijing.
2. D. Z. Hu et al. [1991] Measurements of rain attenuation at frequencies 10 - 80 GHz in Qingdao region. 4th National Symposium on Radio Propagation, Wuhan.
3. Y. Z. Fu [1985] An empirical prediction model of rain attenuation. '85'

ICAP.

4. J. M. Xiao et al. [1991] Prediction of rain attenuation for mm wave on Earth - space paths. 4th National Symposium on Radio Propagation, Wuhan.
5. H. J. Li et al. [1987] An improved model for the prediction of rain attenuation statistics. 87' ICAP.
6. Y. P. Wang et al. [1988] A study of the statistics of XPD and CPA in the K - band induced by rain. International Symposium on Radio Propagation, Beijing.
7. G. Y. Ma et al. [1991] Effects of incoherent scattering of rain medium. 4th National Symposium on Radio Propagation, Wuhan.
8. Y. Yan [1991] Effects of the depolarization due to rain on mm and sub - mm waves. 5th National Symposium on mm and sub - mm wave Technology, Qingdao.
9. CCIR Documents [1986 - 1990]: Doc. 5/305 (China), Development of a climatical map of rainfall intensity for China.
10. S. B. Qiu [1991] Conversion of rainfall rates from 10 minutes to 1 minute for some regions in China. 5th National Symposium on mm and sub - mm Wave Technology, Qingdao.

Table 1 Long-term statistics of rain attenuation and relevant rain intensity in Xinxiang
path length: 2.5km pol.: horizontal

Freq. (GHz)	Period	Rain attenuation in dB (rain intensity in mm/h) exceeded for percentages of time (%)								
		0.001	0.002	0.003	0.006	0.01	0.02	0.03	0.06	0.1
12.1	80-84	6.3	5.8	5.2	4.0	3.5	2.6	2.4	1.9	0.9
25.3	84	14.8	12.7	11.5	8.8	7.6	5.7	4.9	3.0	1.5
35.5	80-84	30.0	26.6	24.8	20.5	16.5	11.0	9.4	6.8	4.8
		(98)	(82)	(71)	(51)	(42)	(26)	(21)	(14)	(9)

Table 2 Long-term statistics of rain attenuation and relevant rain intensity for slant paths

1 station	Lat.	long.	height	Sat.	freq.	elev.	pol	years
Beijing	40°N	116°E	0.05km	SIRIO	11.5GHz	20.5°	C	2
time %	7E-3	1E-2	2E-2	4E-2	7E-2	1E-1	2E-1	4E-1
A (dB)	24.0	22.8	19.9	14.6	9.0	6.0	3.2	
R (mm/h)	87.0	80.7	63.0	40.5	23.6	15.0	6.0	2.3

2 station	lat.	long.	height	Sat.	freq.	elev.	pol.	years
Qingdao	36°N	120°E	0.10km	BS-2	12.0GHz	46.7°	C	2
time %	1E-2		1E-1					1E0
A (dB)	13.0		10.4					3.8
R (mm/h)	68		13					

3 station	lat.	long.	height	Sat.	freq.	elev.	pol.	years
Wuhan	30.5°N	114.4°E	0.08km	RAD	35.3GHz	50.0°	V	1
time %	1E-2		1E-1		3E-1			1E0
A (dB)					10.6			5.4
R (mm/h)	78		21.0		7.5			2.9

4 station	lat.	long.	height	Sat.	freq.	elev.	pol.	years
Taibei	25.1°N	121.6°E	0.00km	RAD	11.6Ghz	20.0°	H	1
time %	1E-2		1E-1	2E-1	4E-1	7E-1		1E0
A (dB)			8.5	5.7	3.8	2.7		2.2
R (mm/h)	80.0		43.0	34.6	26.1	19.3		15.0

5 station	lat.	long.	height	Sat.	freq.	elev.	pol.	years		
Hong Kong	22.2°N	114.2°E	0.00km	RAD	11.6Ghz	20.0°	H	1		
time %	1E-2	2E-2	4E-2	7E-2	1E-1	2E-1	4E-1	7E-1		1E0
A (dB)	12.0	8.1	5.5	4.0	3.3	2.0	1.2	0.8		0.6
R (mm/h)	88.0	64.9	47.9	37.4	31.6	15.7	7.7	4.3		3.0

Table 3 Conversion parameters

	a	b
Xinxiang	1.0357	-3.54E-2
Nanjing	1.1006	-3.52E-2
Guangzhou	1.0496	-5.87E-2

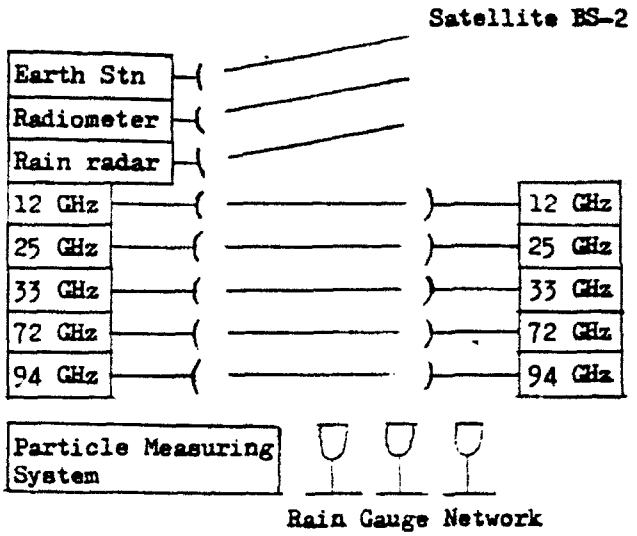

Figure 1 MM Wave Measuring System of Qingdao Research Center

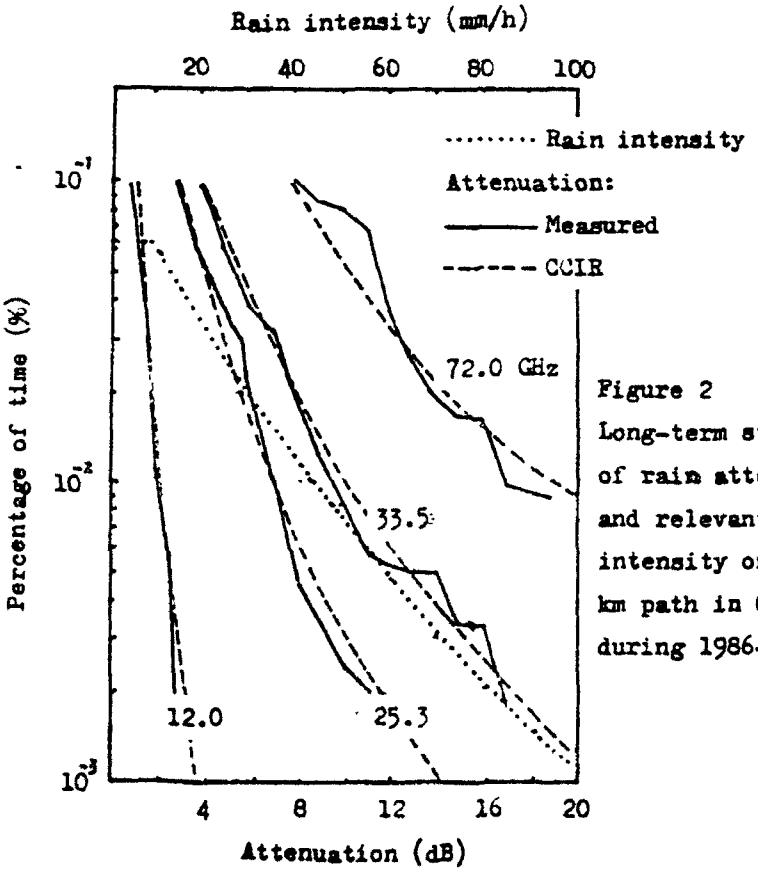

Figure 2 Long-term statistics of rain attenuation and relevant rain intensity on a 1.26 km path in Qingdao during 1986-1989

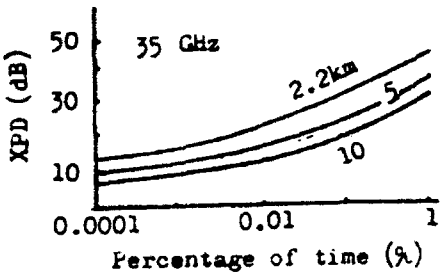

Figure 3 XPD estimated for Xian

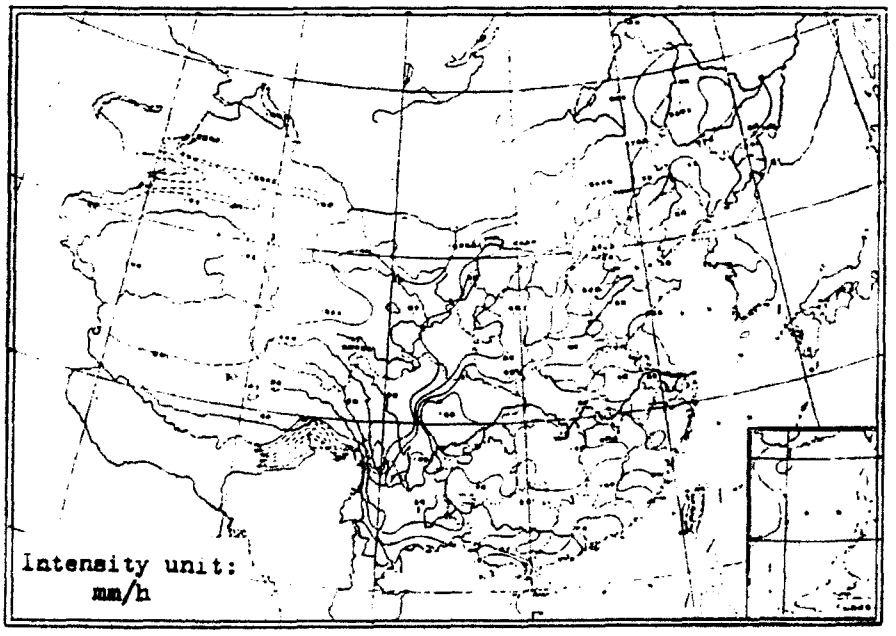

Figure 4 Contours of rain intensity for 0.01% of time

COPY AVAILABLE TO DTIC DOES NOT PERMIT FULLY LEGIBLE REPRODUCTION

NOVEL STRANGE AND ULTRASHORT-PULSE MID- AND FAR-INFRARED LASERS AND THEIR APPLICATIONS

Fritz K. Kneubühl

Infrared Physics Laboratory
Swiss Federal Institute of Technology (ETH), CH-8093 Zurich, Switzerland
Tel. (1) 377 23 40 Fax (1) 371 59 89

The realization of powerful **50ns- pulse TEA** [1] **and hybrid** [2] **10 μm CO_2 lasers** [3] and **far-infrared gas lasers pumped by CO_2 lasers** [4, 5] in the early seventies gave a drastic impetus to the further development of mid-and far-infrared lasers. In the meanwhile these lasers have found wide applications in basic and applied research. Thus, these lasers helped to study and to understand new basic laser priniciples as well as to develop **ultrashort-pulse mid- and far-infrared laser systems** with pulse durations in the pico- and femtosecond range. The following reviews the recent development in these fields of research as well as applications.

The broadband optical feedback by standard laser mirrors does not provide longitudinal mode-selectivity [e.g.6]. Longitudinal mode selection is achieved e.g. by axially periodic laser structures called **distributed -feedback (DFB) lasers** [6, 7]. In these lasers which were introduced in 1971 [7, 8], a frequency-dependent feedback distributed over the laser axis and originating in the Bragg effect replaces the feedback by resonator mirrors. Today, DFB is widely used in dye [7, 8] and semiconductor [9] lasers. After many attempts DFB was also realized in gas lasers [10, 11], i.e. in optically pumped far-infrared gas lasers with periodically corrugated waveguides. These lasers permit to test DFB theories [12, 13] and remarkable DFB phenomena, e.g. nonlinear phenomena and in-gap modes in DFB lasers with interrupted periodic refractive index modulations [6,14] which are now of interest in semiconductor lasers [15].

A **strange modification** of DFB lasers are the **helical-feedback (HFB) lasers** [6, 16-19] which exhibit an axially **helical structure** instead of the axially periodic structure of DFB lasers. As demonstrated by group theory [16-18] the feedback in HFB lasers represents a quasi-Bragg effect. The first proper HFB lasers in operation were optically pumped gas lasers with helical oversized metallic waveguides]16-19]. Another kind of DFB laser consists of mixture of a laser dye with a cholesteric liquid crystal [6, 13, 20] which in the laser-wavelength scale exhibits the symmetry of the continous symmetric double helix [17, 18]. HFB represents a rather sophisticated optical feedback in lasers.

A successful scheme to generate **single intense picosecond 10 μm pulses** represent the "Optical-Free-Induction-Decay" or **OFID-10 μm CO_2 laser systems** first realized in 1974 [21, 22]. These systems consist usually of a hybrid or TEA CO_2 laser, a laser-triggered plasma shutter, and a cell of hot CO_2 gas acting as OFID spectral filter. The plasma shutter first truncates the 50 to 100 ns pulse. The subsequent hot CO_2 cell transforms the truncated pulse into a ps pulse by OFID. Hitherto, the OFID systems suffered from the unreliable performance of the plasma shutter which drastically reduced their range of application. In the meanwhile, new designs of plasma shutters improved performance and reliability considerably [23-25]. As a result the new OFID laser systems generate reproducible single, intense laser pulses of 30 to 300 ps as well as 50 to 100 ns pulses truncated without jitter within 10 ps. Just recently [26], a **new type of 10 μm OFID-CO_2 laser system** was discovered which uses far-infrared laser gases, e.g. CH_3F, as OFID spectral filter instead of hot CO_2 gas. This very promising new laser scheme is now under investigation.

Verification and evaluation of single 10 μm pulses shorter than 0.5 ns requires an **autocorrelation measurement**, e.g. with a Michelson interferometer followed by a nonlinear material for 2nd-harmonic generation. Hitherto, single crystals of GaAs or Te served as nonlinear material. Recently, it was demonstrated that polycristalline GaAs, ZnSe, CdTe work as well in pulse-autocorrelation measurements with less optical adjustment [27, 28].

The single 30 ps to 300 ps 10 μm OFID-CO_2-laser pulses are predistinated for **testing so-called fast mid-infrared detectors**. Consequently, a comparative test with these pulses on pyroelectric detectors, non-resonant p-Ge Detectors and resonant photon-drag detectors made from $Al_x\ Ga_{1-x}$ As/GaAs multi-quantum-well systems was performed to examine the present detector theories [29].

The reproducible single 30 ps to 300 ps 10 μm OFID pulses as well as as the 10 ps-truncated 50 ns to 100 ns pulses of 10 μm wavelength open **new aspects on optical pumping of far-infrared - laser gases.** Besides the generation of ultrashort subnanosecond far-infrared superradiant emissions [30] they also permit the observation of two-photon noise-initiated fluctuations of Dicke's far-infrared superradiance [31] and other exciting phenomena.

Finally, the single ultrashort far-infrared pulses are presently **applied to high-T_c superconductors** to gain further information on their exciting and complicated features and to test their potential as far-infrared detectors.

References

[1] Beaulieu, A.J. (1970), Appl. Phys. Lett. **16**, 504

[2] Gondhalekar, A. Holzhauer, E. Heckenberg N.R. (1973), Phys. Lett. **46 A**, 229

[3] Witteman, W.J. (1987): The CO_2 Laser, Springer, Berlin, FRG

[4] Chang, T.Y., Bridges T.J. (1971) Proc. P.I.B. Symposium on Submum Waves, 93, Polytechnic Press, N.Y. USA

[5] Button, K.J., Inguscio M. Strumia F. (1984) Rev. of Infrared & mm Waves **2**, Plenum Press, London, UK

[6] Kneubühl, F.K., Sigrist M.W. (1991): Laser, 3rd ed., Teubner, Stuttgart, FRG

[7] Kogelnik, H., Shank, C.V., (1971), Appl. Phys. Lett. **18**, 152

[8] Shank, C.V., Borkholm, J.E., Kogelnik, H: (1971), Appl. Phys. Lett. **18**, 395

[9] Nakamura, M., Yariv, Y., Yen H.W., Somekh, S., Garvin, H.L. (1973) Appl. Phys. Lett. **22**, 515

[10] Affolter, E., Kneubühl, F.K. (1979), Physics Lett. **74 A**, 407; (1982), IEEE J. Quantum Electron. **QE-17**, 115

[11] Kneubühl, F.K., Affolter, E. (1980) J Opt. (Paris) **11**, 449; (1982) in "Infrared & mm Waves", Acad. Press. N.Y. US[illegible] **5** ch.6, 303

[12] Gnepf, S., Kneubühl, F.K. (1984) Int. J. Infrared & mm Waves, **5**, 667; (1986) in "Infrared & mm Waves" Acad. Press, N.Y. USA, vol. **16**, ch. 2, 35

[13] Kneubühl, F.K. (1992): Theory on DFB Lasers. Harwood, Chur, Switzerland, in preparation

[14] Wildmann, D., Gnepf, S., Kneubühl, F.K. (1987) Appl. Phys. **B42**, 129

[15] Nakano, Y., Tada, K. (1988); IEEE J. Quantum Electron. **QE24**, 2013

[16] Preiswerk, H.P., Küttel, G., Kneubühl, F.K. (1982) Physics Lett. **93A**, 15

[17] Preiswerk, H.P., Lubanski, M., Gnepf, S., Kneubühl, F.K. (1983), IEEE J. Quantum Electron. **QE-19**, 1452

[18] Preiswerk, H.P., Lubanski, M., Kneubühl, F.K. (1984) Appl. Phys. **B33**, 115

[19] Arnesson, J., Cui, D., Gnepf, S., Kneubühl, F.K. (1989) Appl. Phys. **B49**, 1

[20] Kneubühl, F.K. (1983) Infrared Physics **23**, 115

[21] Yablonovitch, E. and Goldhar (1974) Appl. Phys. Lett. **25**, 580

[22] Kwok, H.S. (1985) Infrared Physics 25, 53

[23] Kälin, A.W., Kopiczynski, T.L., Kesselring, R., Schötzau, H.J., Kneubühl, F.K. (1990), Digest 15th Int. Conf. Infrared & mm Waves, Orlando, 655

[24] Kälin, A.W. (1991) Ph.D. thesis ETH Zurich

[25] Kälin, A.W., Kesselring, R., Cao, H., Kneubühl, F.K. (1992) Infrared Physics, in print

[26] Scherrer, D.P., Kneubühl, F.K. (1992) Infrared Physics, in print

[27] Kesselring, R., Kälin, A.W., Kneubühl, F.K. (1990) Digest 15th Int. Conf. Infrared & mm Waves, Orlando, 475

[28] Kesselring, R. (1992) Ph.D. thesis ETH Zurich

[29] Kesselring, R., Kälin, A.W., Sigg, H., Kneubühl, F.K. (1992) Rev. Sci. Instr., in print

[30] Scherrer, D.P., Kälin, A.W., Kesselring, R., Kneubühl, F.K. (1991) Appl. Phys. **B53**; (1992) Optics Comm., in print

[31] Bakos, J.S., Scherrer, D.P., Kneubühl, F.K. (1992) Phys. Rev., in print

M1.4

OPTICAL PHASE AND FREQUENCY CONTROL OF FET OSCILLATOR

Liao, Fu Jiang
Beijing Vacaum Electronics Research Institute,
P.O.Box 749, Beijing, 100016, P.R. China.
R.W. McMillan
Physical Science Laboratory,Georgia Tech Research Institute,
Georgia Institute of Technology, Atlanta, GA 30332, USA.

ABSTRACT

This paper gives a method to use the optical fiber network to control the phase and frequency of FET oscillator independently.In the phased array antenna,there are thousands of MIMIC transmit/receive(T/R) modules.This technique can be used to synchronize the frequencies for all the modules and to adjust their signal phase individually to make the beam forming and steering easy.

I Introduction

The new generation of phase array antennas are very important to the airbone and space-based communication and radar systems.This new generation of antenna systems operating at mm-wave frequencies (20 GHz and above) will be composed of independent and spatially distributed MIMIC T/R modules[1].One of the fomidable challenges in the phased array antennas is the frequency synchronization of the individual T/R modules using the optical fiber networks.Recent years,an increasing interesting has been paid to the light effects to control the various functions of the FET's,which includes frequency,phase and amplifier gain controls[3-9].Optical control not only proides the light coupling medium,but also allows the control signal to be distributed using optical fiber network.This offers advantages,especially where electrical isolation and immunity from electromagnetic interference are important requirements.There are three methods for the optical frequency and phase control of FET oscillators, i.e. the direct injection locking,indirect injection locking and phase locking.

In the direct optical injection locking,the reference signal is distributed through the optical fiber network, the modulated optical signal which carries the RF reference is used to shine on the active area of FET.Because the nonlinearity limitation of the optical fiber network,the transmitted RF signal is weak and not enough to make FET oscillation stable,therefore the indirect injection locking can be used. In the indirect injection locking,the transmitted optical signal will return to RF signal first,then is amplified to some higher signal level and used to electrically injection locking the FET oscillators[8] or use an injection locked oscillator to serve as an interface between the optical feed and the T/R module[11].

Optical injection locking of oscillator in principle is almost identical to electrical injection locking.From small signal electrical theory,the locking range Δf_m can be related to the injected power P_{inj} , the oscillator output power P_{opr} and the oscillator external Q_{ext} by [12,13]

$$f = \frac{f_{opr}}{Q_{ext}} \sqrt{P_{inj}/P_{opr}} \qquad \cdots\cdots\cdots\cdots\cdots\cdots \quad (1)$$

here the optically shifted unlocked operating frequency of the oscillator, f_{opr}

corresponds to the natural frequency of the illuminmated oscillator. P_{inj} is the equivalent electrical power generated by the absorbed optical signal.

There is a phase angle between the oscillator signal and the injected signal.Under the locked codition,$d\theta/dt=0$ and

$$\theta = \arcsin(2\Delta f/\Delta f_m) \qquad \text{.....} \qquad (2)$$

where $\Delta f=f_{opr}-f_{inj}$ is the optically controlled difference frequency between the operating frequency f_{opr} and the injected frequency f_{inj} .This phase difference can vary widly between oscillators due to manufacturing tolerances.In the phased array antenna applications,it is necessary to lock the phases of a large number of oscillators to a single reference.Therefor,the phase locking technique must be used to make the phase synchronization.The beam forming for the phased array antenna requires adjustment of both amplitude taper and phase taper[14].

The optical phase locking method and test result will be described in following section. The phase adjustment method is also given to meet the beam forming and steering requirement.

II Optical control of frequency and phase for MW/MMW FET Oscillator

Fig.1 shows the linear phase locking loop and phase adjustment diagram.The reference signal is transmitted by the fiber optical link system to the phase detector and compared the phase with that of FET oscillator signal. The pnase error signal will pass through the filter and feed back to the FET oscillator.When the frequency and phase of the FET output signal is exactly equal to the frequency and phase of referece signal, the FET oscillation is locked to the reference signgl.If the phase of referece signal is changed, the phase of the FET oscillation must follow this change.This is the way to control the phase of the FET oscillation.In this test, a stretch line is used to as the phase shifter and inserted between the reference signal generator and electro-optic modulator (EOM). This arrangement means the phase control component can be put on the control board and seperated with the antenna array board. A phase detector is used to checkthe phase change of the FET oscillation when the length of the stretch line is changed. Fig. 2 shows the optical phase locked FET oscillation output signal spectrum.When the length of the stretch line is changed,the FET oscillation frequency is not changed.So the phase and frequency of FET oscillation can be controlled indepently.Fig.3 shows the measured result for the FET oscillation phase change when the length of the stretch line is changed. The stretch line can be changed to move the straight line on the oscilloscope to its highest position, it is the start position for the master signal phase change.Then the stretch line can be continuously lengthened or shortened,the straight line on the oscilloscope will move down until to its lowest position if the length change of the stretch line is half of wavelength. The upper straight line on the oscilloscope is for 0° phase shift of the reference locking signal. The lower line is for 180° phase shift.

III Discussion and Conclusions

The beam forming and steering technique is the key point for the phased array antenna application. The optical beam forming generally can fall into one of the two areas:fiber optic beam forming networks (BFNs) and optical processed BFNs[15].In the fiber optic beam forming networks,the variable phase shifters and variable power amplifiers must be inserted to create an array aperture with the approperiate phase and amplitude distribution.A programmable optical fiber delay line or other phase shifters can be used in the fiber optic beam forming networks.Most phased array antenna architectures studied so far put the phase shifter on the antenna board,therefore the light weight and easy operation are required for the phase shifter.The optical phase locking of FET oscillator technique described in this paper not only makes the frequency and phase synchronization for all the T/R modules,but also can separate the phase shifter from the T/R module.The phased array antenna board can be simplified.

Acknowledgment

This study was part of a project supported by Westinghouse and carried out in Georgia Tech.The authors gratefully acknowledge the guidance of Dr.R.A.Moore of Westinghouse and Mr.J.J.Gallagher of GTRI during this program.

References

[1] A.S.Daryoush, "Optical synchronization of Millimetr Wave Oscillators for Distributed Architectures,"IEEE Trans. on MTT, Vol.38, No.5, May 1990 , pp.467-476.

[2] P.R.Herczfeld and A.S.Daryoush, "Fibr Optic Feed Network for Large Aperture Phased Array Antennas, " Microwave J., Aug.1987,pp.160-166.

[3] R.R.Forrest and A.A.Salles,"Optics control microwaves," MSN, June 1981, pp.112-122.

[4] A.J.Seeds at al.,"New developmets in optical control techniques for phased array radar, " 1988 IEEE MTT-S Digest, pp.905-908.

[5] A.A.Salles, "Optical control of GaAs MESFET's,"IEEE Trans.on MTT, vol. MTT-31,NO.10, Oct.1983, pp.812-820.

[6] S.R.Cochran & S.Y.Wang, "Efficient optical injection locking of electronic oscillators, "Microwave J.,May 1989, pp.315-327.

[7] R.N. Simons, "Microwave performance of an optically controlled AlGaAs/GaAs high electron mobility transistor and GaAs MESFET,"IEEE Trans. On MTT, VOl. MTT-35, NO.12, Dec. 1987,pp.1444-1455.

[8] P.R.Herczfeld at al." Indirect subharmonic optical injection locking of a millimeter wave IMPATT oscillator, "IEEE Trans. on MTT, Vol.MTT-34,NO.12, Dec.1986,pp.1371-1375.

[9] D.C.Buck & M.A.Cross," Optical injection locking of FET oscillators using fiber optics, " 1986 IEEE MTT-S Digest, pp.611-613.

[10] R.D.Esman at al., "Optical phase control of optically injection-locked FET microwave oscillator, " IEEE Trans.on MTT, Vol.37, NO.37, NO.10, Oct.1988, pp.1512-1518.

[11] T.Berceli at. al., " A Double-Stage Injection-Locked Oscillator for Optically Fed Phased Array Antennas, " IEEE Trans,on MTT,Vol.39, NO.2, Feb.1991, pp.201-208.

[12] R.Adler, "A study of locking phenomena in oscillators, "PIEEE Vol.61, NO.10 ,Oct.1973, pp.1380-1385.

[13] K.D.Stephan, " Inter-injection-locked oscillators for power combining and phased arrays. " IEEE Trans. on MTT, Vol.MTT-34, NO.10, Oct.1986, pp.1017-1027.

[14] N.Jesperson at al., " Optically Controlled Beamforming for Phase array antennas, "1986 IEEE AP-S, pp.357-359.

[15] P.R. Kunath and K.B.Bhasin, "Optically controlled phased array antenna concepts using GaAs monolithic microwave integrated cirauits, " 1986 IEEE AP-S, 1986,pp.353-355.

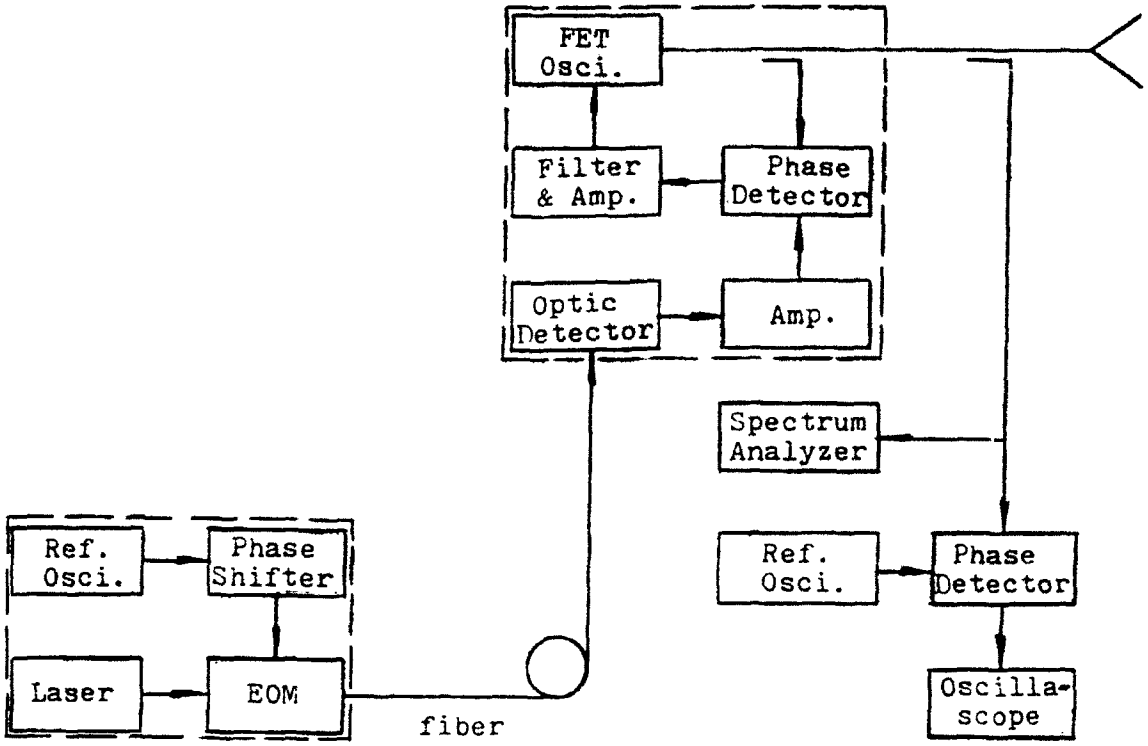

Fig.1 Linear phase locking loop and phase adjustment diagram.

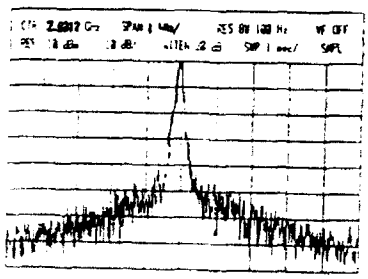

Fig.2 Phase locked FET oscillator output signal displayed on spectrum analyzer while its phase was changing.

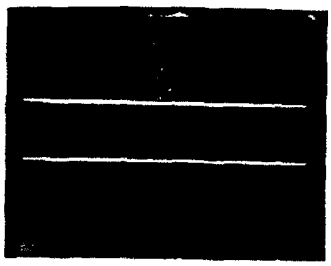

Fig.3 Phase control test for FET oscillator. Upper line is for 0° phase shift, lower line is for 180° phase shift.

M2.1

A NEW MILESTONE OF ACTIVE DEVICE—VACUUM MICR)ELECTRONICS AND ITS PRELIMINARY RESEARCH IN P. R. CHINA

Han C. Hu
(Beijing Vacuum Electronics Research Institute)
Guang Yi Liu
(Electronics Research Institute, Chinese Academy of Sciences)

HISTORY OF DEVELOPMENT OF ACTIVE DEVICES FACTORS PAVING THE WAY & FACTORS LIMITING THE DEVELOPMENT

1. Vacuum Triode

In 1906 Lee DeForest invented the electrostatically controled vacuum triode. The factor paving the way was the Edison Effect in 1883 which discovered the source of electrons. The principle of electrostatic control has been employed for the development of receiving tubes, transmitting tubes and gas-filled tubes operating in the long wave, medium wave and short wave wavebands. The limiting factors were the transit time taking by the electron to traverse the cathode to anode space, lead inductance and interelectrode capacity. These factors become serious at a frequency of 300MHZ(λ=1m).

2. Microwave Tubes

In 1939 the Varian brothers developed the klystron and in 1940 Rardall & Boot developed the multicavity magnetron. The factors paving the way were research in 1930s on studies of waveguide transmission, electron motion in crossed electric and magnetic fields, velocity modulation and electron bunching, incorporation of the resonant cavity into the tube. The new principles circumvented the limitation imposed by transit time, lead inductance and interelectrode capacity, thereby providing the means of generation and amplification in decimeter and centimeter wavebands. Microwave tubes encountered limitation in millimeter waveband owing to the small size of the structure being of the same order as the wavelength. The consequences of small size were difficulty in power dissipation and difficulty in fabrication.

3. Semiconductor Devices.

1948 was the year of the advent of semiconductor. The factors paving the way was the employment of diode crystal detector in radar during second world war and its study in depth after the war with the measurement of surface potential distribution. The current control effect was discovered when the measuring probe was very near to the p-n junction lead serving as the emitter. Semiconductor promoted the miniaturization of electronic equipment, however, it was limited by being unable to withstand high temperature and strong radiation.

4. Laser Devices

1960 was the year of the advent of ruby solid state laser and He—Ne gas laser. The factor paving the way was the study of Maser (Microwave Amplification By Stimulated Emission of Radiation) in the 1950s. Maser employed a microwave resonant cavity to support energy level transition in microwave waveband. Similarly laser employed an optical cavity to support energy level transition in visible light waveband. Laser was limited by the fixed frequency determined by energy difference in a transition.

5. Integrated Circuit

1960s were the years of advent of integrated circuit which made use of thin film technology to integrate semiconductor and L,C,R into a circuit. IC developed rapidly through the stages SSI,MSI,LSI,VLSI,VHSIC continually advancing in the scale of miniaturization.

6. Cyclotron Resonance Maser(CRM)

1970s were the years of advent of CRM which was a device in which electrons interacted with fast wave using the relativistic change of mass with velocity to achieve phase bunching. This principle circumvented the limitation of structural size being of the same order as wavelength, thereby providing high power in millimeter and submillimeter wavebands.

7. Free Electron Laser(FEL)

1970s were the years of advent of FEL. A pumping electromagnetic wave is scattered by a relativistic electron beam traveling in the opposite direction. The wavelength of the scattered wave depends on the wavelength of the pumping wave and energy of the e-beam. Thus FEL provides high power in submillimeter waveband and its frequency is tunable.

8. Vacuum Microelectronics(VME)

In 1988 at Williamsburg, 1st Vacuum Microelectronics Conference heralded the advent of VME. The factors paving the way were study of field emission in the research of vacuum breakdown, microfabrication technology in developing microelectronics and observation of micrometer dimensions with electron microscope[1]. This new device circumvents the previous limitations with potentiality of miniaturization to nanoelectronics as well as capable of withstanding high temperature and strong radiation.

THE PRINCIPAL FACTOR IN THE MINIATURIZATION OF ACTIVE DEVICE—CURRENT DENSITY OF ELECTRON SOURCE[2]

The size of active device is related to the current density of its electron source. This can be seen from the following relation $Ps = Po/\eta$ where Ps is the supplied power, Po is the output power and η is the efficiency. $Ps = VI$ where V and I are voltage and current respectively. $I = JA$ where J is current density and A is the area of electron source, hence the greater J has, the smaller A is, it means the device could be made smaller.

The renowned researchers in the field of vacuum microelectronics, Henry F. Gray and Charles A. Spindt remarked in the foreword of Proc. Ist International Vacuum Microeletronics Conference, June 1988 "Since the invention of the transistor some 40 years ago, research and development in the field of solid state electronics has dwarfed that of vacuum electronics. It is generally accepted that the transition from vacuum tubes to solid state transistors was due primarily to the fact that one could obtain a far greater current density in a transistor compared to that available from a vacuum tube's thermionic cathode. This greater current density allowed the electronic devices based on solid state transistors to be orders of magnitude smaller than their vacuum tube counterparts. However semiconductor is not a panacea, the optical and acoustic mode scattering limits the saturation drift velocity to about 3×10^7cm/s. With the successful demonstration of both a high current density metal field emitter array (FEA) and a silicon planar vacuum transistor based on FEA's, a new vacuum microelectronics has emerged".

In order to get a clearer understanding of the relation between current density and device miniaturization, table 1. will list the current density capabilities of various electron sources for comparison.

Table 1. Current density, working condition and device size of various electron sources.

Electron Source	Current Density J	Working Cond.	Device size
Oxide Cathode	200ma/cm² cw	1100°K	mm~cm, 10^{-3}m~10^{-2}m
Ba—W Cathode	3~5A/cm² cw	1300°K	mm~cm, 10^{-3}m~10^{-2}m
P,N Current Camier	No published data	300°K	0.1μm~μm, 10^{-7}m~10^{-6}m
FEA Field Emitter Array[3]	>1000A/cm² in array, >10^7A/cm² single field emitter, MTBF) 80,000hrs.Medium J data(SR1)	300°K	nm~μm, 10^{-9}m~10^{-6}m

An article in IEEE publication "The institute" June 1989[4] issue expressed the viewpoint that vacuum microelectronics also named nanoelectronics will play a major role in the last decade of this century i. e. 1990～2000 on the emerging electronic technology stage. The basis of this prospect is that in the miniaturization from microelectronics to nanoelectronics, the 10^{-6}m feature is reduced to 10^{-9}m in so doing J will be increased by three orders of magnitude, FEA is expected to have such capability based upon its demonstrated performance.

THE PRINCIPAL PERFORMANCE OF VACUUM MICROELECTRONICS DEVICE

The two principal disadvantages of vacuum tube i. e. thermionic cathode requiring a heater and fabrication involving mechanical machining can be circumvented by employing vacuum microelectronics technology.

1. Performance of Field Emitter Array.

A. No need of heating, it can work at room temperature.

B. The current density of FEA is higher than that of thermionic cathode by several orders of magnitude, thus enabling the vacuum tube to miniaturize from mil—scale (mil is 1×10^{-3}inch or 2.54×10^{-5}m) to submicron scale 10^{-7}m. Such small size can be fabricated by using solid state device fabrication technology and silicon integrated circuit technology. i. e. using the integral microgrid or gate to implement low voltage modulation. Fig. 1 shows the high current density integral grid field emitter array experimented by Stanford Research Institute for application in high definition flat panel display.

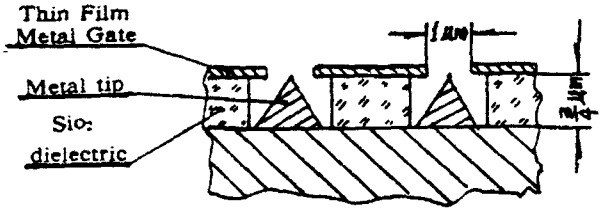

Fig. 1 Schematic diagram showing integral grid field emitter array

2. Performance of Vacuum Microelectronics Device(VMD)

A. It possesses the merits of vacuum tube, high temperature resistant)775°K[5] and radiation resistant)10^{17} neutrons/cm^2, for comparison, the capability of solid state device is respectively 600°K and 10^{13} neutrons/cm^2.

1. In this device the electron motion is entirely ballistic, hence its drift velocity is higher than that in solid state device 3×10^7cm/s limited by scattering. The velocity of electron in vacuum approaches the velocity of light, hence vacuum microelectronics can achieve higher switching speed or higher operating frequency.

3. The Operation of Vacuum Microtriode Requires Only Low Vacuum.

In order to avoid the occurence of ionization when the electron traverses the path from cathode to anode, the mean free path λe of the electron in the residual gas must be much greater than the cathode to anode distance d, i. e. $\lambda e \gg d$. For air the mean free path[6] is given by a simple expression $\lambda(mm)=6.6/p$ where λ is in millimeter and p is the pressure in pascal . The mean free path of electron in gas $\lambda e = 4\sqrt{2}\,\lambda gas = 5.66\lambda gas$. In vacuum microtriode d can be as small as 1 μm, $\lambda e \gg d$ can be fulfilled with $\lambda=10^3\mu m$ or $\lambda=1mm$. The required vacuum is therefore $p=6.6$ pascal or $6.6/133=.05$ Torr.

4. The transit time in Vacuum Microtriode.

In GaAs, InP and Si semiconductor materials the peak electron drift velocity approaches 2×10^7cm/s, the

time required to traverse 0. 5μm channel is 2.5×10^{-12}sec[7]. The transit time of electron in the uniform electric field of vacuum microtriode is $t=[2d^2m/ve]^{1/2}$, for $d=0.5\mu m$, $v=20$volts, $t=3.8\times10^{-13}$s, when $t=T/10$ where T is period of high frequency signal, transit time effect is not serious, $T=10t=3.8\times10^{-12}$s, $f=1/T=2.64\times10^{11}$Hz or 2 64GHz.

5. Vacuum Microelectronics Technology Can Be Employed For The Fabrication Of Submillimeter Devices

USSR and USA have done research on planar BWO (Backward Wave Oscillator). U. S. Scientists fabricated thin film interdigital slow wave structure on single crystal quartz and diamond substrate with a pitch of 18μw, this BWO can operate at 1000GHz with a maximum output of 100μw. The microwave tube structure with a period of 18μm is a minute dimension which can not be fabricated by mechanical machining technique.

OVERVIEW OF VACUUM MICROELECTRONICS PRELIMINARY RESEARCH PROJECTS IN P. R. CHINA.

For more than thirty years Chinese scientists have been continually paying attention to the advances of vacuum microelectronics. As early as 1976, Electronics Research Institute, the Chinese Academy of Sciences (ERI-CAS) fabricated miniature planar thermionic cathode triode with dimensions of the order of millimeter and submillimeter. In 1978 the group of cathode specialists led by Prof. P. Bian led the way with research and development on TFFEC (Thin Film Field Emission Cathode)[8]. The experimentation on the scheme and flow chart of TFFEC processing[11] obtained support from many industrial institutions such as Nanjing Semiconductor Research Institute, Beijing Electron Tube plant and 14th Radio Plant of Shanghai. The group solved successively the processing of hole punching, tip growing and packaging. Through using the measures of wide channel dielectric surface isolation[9], interval scribing[10] and beam type lead-out etc, the group solved the difficult problems of capability to withstand the voltage across the spacing[10] of the order of micrometer and three dimensional packaging. These efforts had the aim to lay the foundation to implement TFFEC research with the relatively poor integrated circuit processing facilities in P. R. China. In 1986 the project obtained the support of National Natural Sciences Foundation of China (NNSFC) which promoted the union of research resources in P. R. China. The union of research resounces in the initial stage was a research group formed by researchers from ERI-CAS, Xi Dian Univercity (XDU) and Li—shan Microelectronics Institute (LSMI). LSMI with its relatively strong integrated circuit processing facility served as the processing base for the group, they were concentrated to fabricate the sandwich type molybdenum cone field emission cathode(see Fig. 2)[11], when the joint testing group formed by ERI-CAS, XDU and Scientific Instrument Plant, the Chinese Academy of Sciences (SIP-CAS) tested the cathode, 100 micro amperes of emission was obtained(under a vacuum of 2×10^{-6}pa).

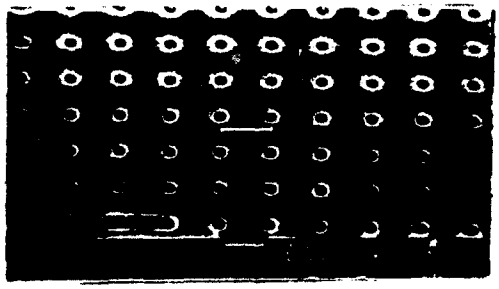

Fig. 2 A SEM micrograph of TFFEC fabricated by LSMI (Nov. 1987)

The research on TFFEC in P. R. China was not limited in following the processing developed by SRI, during the period 1986～1987 with the support of NSFC, LSMI and ERI—CAS have done experiment in the entire processing with the facilities in their laboratories. These researches have displayed some creativity[11]. Besides fabrication processing, some subprojects related to TFFEC had successively achieved progress with distingushing features. For instance, during this period, the following progresses were achieved, development of a special purpose imitating SRI design all solid state digital pulse generator; free of metal gasket and oil, fast loading

and unloading ultra high vacuum system; potential distribution and electric field simulator for the space of the order of micrometer; measurement of distributed parameter and graphic design of TFFEC; three dimensional packaging of TFFEC etc. These achievements were partially reflected in the proceedings of 1st, 2nd and 3rd Chinese Field Emission Symposium. In 1990 XDU began the research on the application of TFFEC, they initiated the research on the flat panel display device using TFFEC.

In late 1980s, the preliminary TFFEC research in P. R. China obtained the recognition of International Field Emission Symposium (IFES) and International Vacuum Microelectronics Conference (IVMC). The paper submitted by researchers of P. R. China was accepted as early as 1988 on 1st IVMC and was given special invitation[9]. In 1989 for the first time P. R. China sent a delegate to attend the 2nd IVMC. In this conference the formuld[11] for the calculation of tip electric field derived by Prof. EnZe Luo of XDU obtained favorable appraisal by conference experts. Prof. Luo was elected to be the standing member[12] of the program committee by the conference. From that time, the research on TFFEC and Vacuum Microelectronics began the movement toward high tide. In 1990, 3rd Chinese Field Emission Symposium marked the beginning of gaining momentum. In this symposium, both the topics involved in the fields of the subject and representative figure of the attendance at this conference bore a resemblance to the conference held abroad. Presently, the vacuum microelectronics technology in P. R. China is moving with great strides toward the prosperous future.

REFERENCES

1. Ivor Brodie, IEEE Trans. on Electron Devices 36(11)(1989)2637
2. Henry F. Gray, Charles A. Spindt, IEEE Trans. on Electron Devices 36(11)(1989)2635
3. Richard F. Greene, Henry F. Gray, Charles A. Spindt, Intenational Electron Devices Meeting, IEDM89 (1989)15
4. Nanoelectronics and Vacuum Electronics May Play Larger Role in the 1990s, The Institute, 13(6)(1989)8
5. Z. A. Peng, J. L. Chen, H. C. Hu, Thin Film Science and Technology(In Chinese)4(3)(1991)1
6. John F O'Hanlon, A User's Guide to Vacuum Technology, John Wiley & Sons, (1980)9
7. F. J. Liao, Acta Electronica Sinica (In Chinese)19(3)(1991)89
8. Guang-Yi Liu, 34th International Field Emission Symposium, Prog. & Abst., July (1987)8
9. Guang-Yi Liu, Jing-Hua Liu, 1st International Vacuum Microelectronics Conference, Tech. Prog., Williamsburg, June (1988), 8-7
10. Guang-Yi Liu, Xie-Qiao Liu etc, 38th International Field Emission Symposium, Prog. & Abst., August (1991), p2-39
11. Chun-Heng Wei, 2nd Chinese Field Emission Symposium, Shen Zheng, Dec. (1987)
    Xian Qing Shi, 2nd Chinese Field Emission Symposium, Shen Zheng, Dec. (1987)
12. En-Ze Luo etc, Proc. of 1st, 2nd and 3rd Chinese Field Emission Symposium. (1986)(1987)(1990)
13. En-Ze Luo, Prof. of 2nd International Vacuum Microelectronics Conference, Bath, (1989)95

Study of the Dynamical Properties of EL2 centers in GaAs by Infrared and Millimeter Wave Measurements

Tyuzi Ohyama

Department of Physics, College of General Education, Osaka University, Toyonaka, Osaka 560, Japan

In this work we report on the far-infrared laser cyclotron resonance absorption by conduction electrons as well as Zeeman absorption by shallow donors in semi-insulating GaAs. Combining with results obtained from the microwave photoconductivity measurements over the temperature range of 4.2 - 250 K, various new features for EL2 centers in semi-insulating GaAs are clarified under photoexcitation conditions.

I. Introduction

The EL2 center is the dominant mid-gap state in LEC-grown GaAs crystals, which is known as a deep donor.[1] This deep level makes it possible to obtain semi-insulating undoped crystals, on which high quality GaAs single crystals are epitaxially grown. The origin and nature of the EL2 center has been subject of controversy since its first observation. Besides its importance for semiconductor technology, EL2 itself is a basically interesting object for basic research. The main probe for investigating the characteristics of that deep center has so far been restricted to photoluminescence[2], photocapacitance measurements[1] and Deep Level Transient Spectroscopy (DLTS)[3]. Both FIR-magneto-absorption[4] and microwave photoconductivity measurements enable us to get an experimental novel insight into the dynamical behaviour and the electronic properties of the EL2 center.

II. Samples and Experimental Procedures

Experiments are performed on two LEC-grown semi-insulating GaAs crystals, one of which is an as-grown sample (GaAs-LEC-2) and the other was annealed in a nitrogen atmosphere at 800 ℃ for thirty minutes (GaAs-LEC-1). As the far-infrared source, wavelength of 119 and 220 μm were obtained from an H_2O laser, and 84 and 172μm from a D_2O laser, all of which are operated in the pulsed mode at the repetition of 30 Hz in synchronized combination with the photoexcitation light pulses at 15 Hz. The excitation light is provided by a xenon flash lamp with a pulse width of 1 μs. The absorption spectra are obtained as $\ln (I_O/I_E)$ by a two-channel boxcar averager with an aperture of 0.5 μs. Here I_E and I_O are the transmitted beam intersities of the pulsed FIR laser with and without the photoexcitation.

The microwave set-up, on the other hand, was a nonresonant reflection-type wave guide system working at 35 GHz. In order to obtain the decay profile of the microwave photoconductivity, we employed a wave-memory system. It should be noted that, when recording the decay profile after the photo-pulse excitation at a fixed temperature, the sampling time was much too short to produce any noticeable photo-quenching effect, which is a characteristic nature of the EL2 center. On this account, the wave-memory system was very useful.

In order to make selective excitation, we employed two kinds of filters: one to cut off wavelength shorter than 0.9 μm (1.38 eV), hereafter called IR filter and the BBG (Below Band Gap) excitation, and the other to cut off wavelengths longer than 0.75 μm (1.65 eV), IRC filter and the ABG (Above Band Gap) excitation. By making use of the IR filter, we could suppress the band-gap excitation, so that

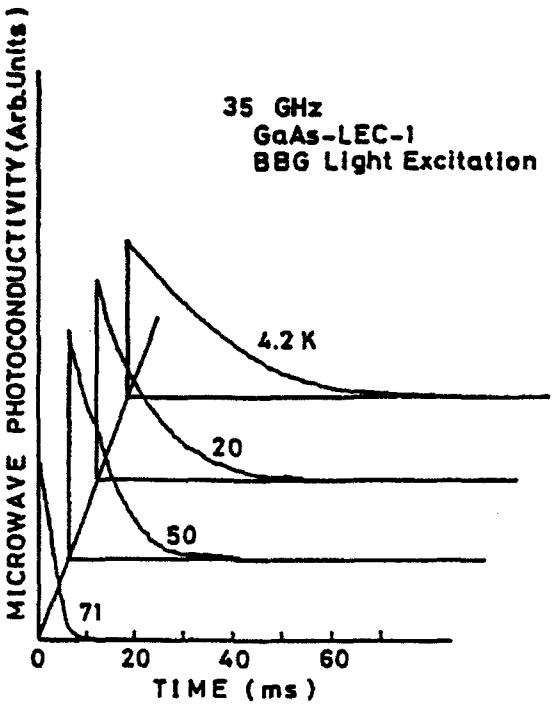

[Fig. 1] Temperature dependence of decay profiles of microwave photoconductivity with IR filter.

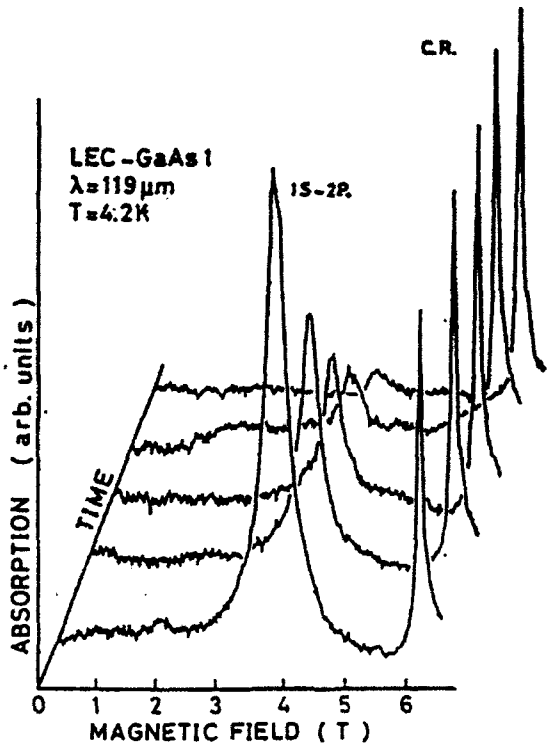

[Fig. 2] Time-resolved cyclotron resonance (CR) and impurity Zeeman absorption signals with IRC filter at the wavelength of 119 μm. Each trace is taken after exposure of the sample to the BBG light.

electrons could be excited only from the mid-gap states. With the aid of the IRC filter, on the other hand, electrons could be excited mainly from the valence band. We are thus able to make experiments under the condition of selective excitation.

III. Experimental Results

a) Microwave Photoconductivity

The time-resolved microwave photoconductivity measurement is a powerful aid to understand the capture mechanism of photoexcited carriers as well as electronic properties of the EL2 center. The method is particularly successful for high resistive semi-insulating GaAs, since no electrode contact problem arises.

Figure 1 shows decay profiles of the microwave photoconductivity obtained at various temperatures and with IR filter. All the quantities decay very nearly exponentially. It is clearly demonstrated that the electron lifetime strongly depends on temperature above 50 K under the BBG excitation condition. The lifetime becomes shorter as the temperature is raised above 50 K. The photoconductivity signal obtained with the IR filter decreases rapidly in intensity as the time proceeds. The diminished signal never recovers its original strength below 140 K. This feature must be connected with the "photo-quenching effect", which is a characteristic behaviour of EL2 centers in LEC-grown semi-insulating GaAs.

If we use the IRC filter in place of the IR filter, it is found that the lifetime is 10 μs in the order of magnitude and almost temperature independent. Though the photoconductivity signal decays after each photo-pulse, we can obtain the same signal intensity for any length of time.

b) Far-infrared Magnetoabsorption

A fully compensated sample as semi-insulating GaAs contains very few neutral shallow impurities and a great deal of ionized impurities at low temperature equilibrium. It is practically impossible to get proper information of semi-insulating GaAs which contains very few neutral shallow impurities and conduction electrons without photoexcitation, because only shallow neutral donors and conduction electrons can absorb photons in the FIR region.

Suppose that the semi-insulating GaAs is illuminated by ABG or BBG light. Most of electrons excited from the valence band or from the mid-gap states are instantly captured by shallow impurities which are neutralized as a consequence. In this way we can investigate even the character of semi-insulating GaAs through the FIR magneto-optical absorption of photo-neutralized impurities and short-lived conduction electrons.

A series of time dependent traces under photoexcitation with the IRC filter is shown in Fig.2. The signal showing up at 3.8 T arises from the $1s \rightarrow 2p_{+1}$ Zeeman transition of typical shallow donor electrons. The cyclotron resonance of conduction electrons, on the other hand, is observed at 6.2 T. In this case, electrons involved in both resonances are mainly excited from the valence band and not from the mid-gap states. Signals are obtained with the wavelength of 119 μm and at various steps during the photo-quenching by the BBG excitation. It is demonstrated that the donor Zeeman absorption signal gradually dies away, as the photo-quenching proceeds. The cyclotron resonance absorption of conduction electrons, on the other hand, scarcely undergoes a change. This fact suggests that the photo-quenching effect of EL2 centers is closely related with shallow impurities. Similar results are obtained for experiments with different wavelength.

IV. Discussions

For understanding all the observations, we propose a model of the metastable state for the EL2 center after photo-quenching. The ground state of the EL2 center will be composed of an As_{Ga} antisite and a shallow impurity that is in the vicinity and coupled very weakly. Provided that the stable configuration of the EL2 center is strongly charge-state-dependent, continuous release and capture of an electron by the center through the BBG excitation will raise a migration or a transition to a metastable atomic configuration. As a result a complex center consisting of an As_{Ga} antisite strongly coupled with a shallow impurity is built up, and the EL2 center is translated to its metastable state. To be more precise, both the shallow impurity which serves the Zeeman absorption and As_{Ga} antisite are raised to their metastable state. If the EL2 center turns into its metastable state by the BBG light excitation without forming a complex center, the ionized shallow donor is still neutralized by an electron excited from the valence band by the ABG light excitation and should be able to contribute to the Zeeman absorption. Our experimental result, however contradicts this assumption.

The time variation of the photoexcited conduction electron density derived from the microwave photoconductivity measurements is given by the simple relation:

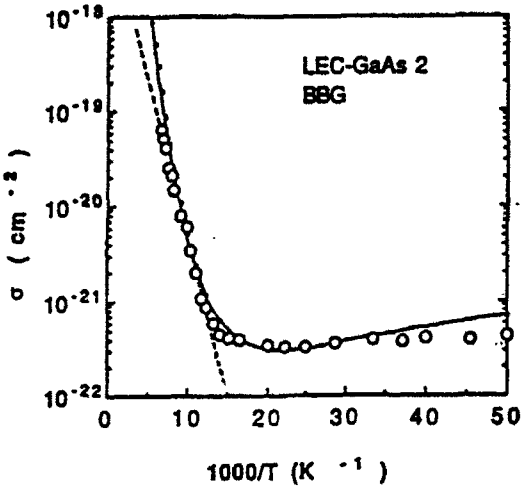

[Fig. 3] Temperature dependence of the electron capture cross-section σ by the EL2 center. Open circles represent the results obtained from the microwave photoconductivity. The dotted straight line yields the value of the activation energy E_A=70 meV.

$$n_e(t) = n_0 e^{-t/\tau}$$

where n_0 is the density of initially created electrons and τ the lifetime of electrons given by $1/\tau=N^+<v\sigma>$. Here N^+ is the density of the ionized EL2 center, <v> the mean square thermal velocity of electrons and σ the electron capture cross-section. Figure 3 shows the dependence of the electron capture cross-section σ on the reciprocal temperature. At higher temperature (T>80 K), we can deduce for the electron capture cross-section:

$$\sigma = \sigma_\infty \exp(-E_A/k_B T)$$

where E_A is a characteristic activation energy, k_B the Boltzmann constant and σ_∞ the capture cross-section for T= ∞. The dotted line in Fig.3 yields E_A=70 meV. E_A may originate from a barrier in the conduction band related to the Franck-Condon shift of the EL2 center.

In summary, various new features of electronic and defect properties for the EL2 center in semi-insulating GaAs have been observed by infrared laser magnetooptical absorption as well as microwave photoconductivity measurements.

This work has been partially supported by Casio Science Promotion Foundation.

References

1) For a review and list of early references, J.S. Blakemore and S. Rahimi: Semiconductors and Semimetals, ed. R.K. Willardson and Albert C. Beer (Academic Press, Inc., London, 1984) Vol.20, chap.4, P.234.

2) M. Tajima: Jpn. J. Appl. Phys., 23 (1984) L690.

3) D.V. Lang: J. Appl. Phys., 45 (1974) 3023.

4) T. Ohyama, H. Nakata and E. Otsuka: Jpn. J. Appl. Phys., 24 (1985) L641.

WHISPERING GALLERY MODE IN DIELECTRIC WAVEGUIDE AND DIELECTRIC RESONATORS *

Liu Shenggang

(*University of Electronic Science and Technology of China, Chengdu, Sichuan* 610054, *P. R. China*)

Trinogga Lothar

(*Faculty of Information and Engineering Systems, Leeds Polytechnic, Leeds LS*6 3*QS, UK*)

ABSTRACT

A systematic study of the whispering gallery mode (WGM) in cylindrical dielectric waveguide and resonators is presented in this paper. The general dispersion equations and the behaviour of the waves in a dielectric waveguide are given. The resonance frequencies, unloaded quality factors of the dielectric resonators have also been obtained. Furthermore, the planar whispering gallery (WG) solid dielectric resonators and hollow dielectric resonators have been studied as well. The coupling and possible applications of WGM of the dielectric resonator (DR) are discussed and the general equations concerning the coupling of a WGM DR with two microstrips are given in this paper.

INTRODUCTION

The study of dielectric waveguides and resonators has a long history. Owing to the development of optical fibres, wave propagation along dielectric waveguides becomes an attractive subject in the engineering field. Additionally, DR' s have also been widely used in conjunction with microstrips for filter and oscillator applications. As the frequency increases the dimensions of the micrwave components decrease and introduce new problems. Using the WGM, larger sized DR's can be used in mm-wave applicatons. A number of papers [1~7] have been published and this work builds on these studies.

It is well kown that the modified Bessel function $K_n(x)$ represents a decaying (evanescent) field whilst the Hankel functions of the second kind $H_n^{(2)}(x)$ are usually used to represent the outgoing propagating wave. In the case of the WGM there are different cases as shown in Table 1. For the case $k_1 > \beta > k_z$ there is no wave propagation in the radial direction and it would be better to use the modified Bessel function $K_n(x)$

* The work is supported by the Royal Society of UK

rather than the Hankel function $H_n^{(2)}(x)$. As is the case for $\beta<k_1<k_2$ and the case where $\beta\to 0$, it is felt that it would be better to use the Hankel function $H_n^{(2)}(x)$ since there is some leakage from the wave travelling in the radial diraction. It thus seems reasonable or appropriate to use different radial variation functions for different cases as shown in Table 1.

The paper is structured as follows:

1. Systematic study of the waves propagating in a dielectric waveguide and resonator.
2. Dispersion equations of WGM of a DR.
3. Analytical formulas for unloaded Q.
4. Hollow DR WGM.
5. General coupling formulas.

GENELAL ANALYSIS

In this section, a general analysis of a dielectric waveguide is taken out. From Mexwell' s equation and boundary conditions, the field components and dispersion equation are obtained. A detail discussion is also carried out.

WHISPERING GALLERY MODE

A detail analysis of the features of whispering gallery modes is taken here. In the case of the WGM the coupling term is negligible and the TE and TM modes are independent from each other. The field components are given and the dispersion equations of WG modes in many cases are obtainad. The resonance frequency, storage energy and unloaded quality factor in a dielectric resonator are also given and studied in detail.

WGM IN A HOLLOW DIELECTRIC WAVEGUIDE AND DR

The properties of electromagnetic field of the WGM in a hollow dielectric waveguide and is studied in this section. By applying the boundary conditions, the WGM field components and dispersion equations are studied, the stored energy and unloaded Q—value are obtained by applying the methods simlliar to that of the above section. Considering the properties of the WGM, a general coupling equation of the WGM in a DR with two microstrips are studied. In special cases, the equatioons for directional power combiners and filters are also obtained.

CONCLUSIONS

A systematic theorectical study of the whispering gallery mode in a cylindrical waveguide and resonator has been presented. When $\beta\neq 0$, the general dispersion equations have been given with the consideration that the proper radial variation functions should be used in accordance with the value of β, and the dispersion equations give the relationship between β and ω with n, the azimuthal variation number, specified. When $\beta\to 0$, the dispersion equations give the relationship between n and ω in this case, the dispersion equations for TE and TM can be simplified. In the case $\beta>k_1>k_2$ there is radiation loss and the unloaded Q may be calculated.

Since in the WGM the field is concentrated in the vicinity of the dielectric boundary, there is almost no field in the central region, thus we can visualise that the hole in the guide structure will have an insignigicat effect on the wave propagating along the guide boundary. Hollow dielectric waveguide and hollow dielectric resonator have also been studied in the paper. One of the important features of the WGM in a DR is the analogy with a travelling wave ring resonator. The coupling approach and [illegible] coupling equations of the WGM of the DR with two microstrips are discussed as well here.

REFERENCES

1. Lord Rayleigh, Finite applications of Bessel functions of higher order to the whispering gallery and allied problems, Phil. Mag., 27, (1914)100
2. Wait, J. R., Electromagnetic whispering gallery modes in a dielectric rod, Radio Science, 2, (9) (1967) 1005
3. Arnoud, J., Note on the use of whispering gallery modes in communication, Bell Labs., Memorandum, 1971
4. Vedreme, C. and Arnaud, J., Whispering gallery modes of dielectric resonators, Transact. ??? IEE, Pt. H, (1982) 183
5. Jiao, X. H., Guillon P., Auxemeny P. and Cross D., Whispering gallery modes of dielectric structures. Applications to wave bandstop filters, Transact. IEEE, Mtt—S, Int. Symp. Digest (1987) 367
6. Cross, D. and Guillon, P., Whispering gallery dielectric resonator modes for w-band devices, Trnsact. IEEE, MTT 37 (1980) 1667
7. Jiao, X. H., Guillon P., Auxemeny P. and Cross D., Dielectric resonator suitable for use in planar integrated circuits at short mm-wavelength, Transact. IEEE,MTT-27 (2) (1988) 432—437
8. Kajfez D. and Guillon P. ,Dielectric resonators, Artech House Inc., 1986

Correct radial variation functions	
$r < a$	$r > a$
$Z_n(k_{c1}r) = I_n(k_{c1}r)$ $k_{c1} = \lvert k_{c1} \rvert$	$X_n(k_{c2}r) = K_n(k_{c2}r)$ $k_{c2} = \lvert k_{c2} \rvert$
$Z_n(k_{c1}r) = J_n(k_{c1}r)$	$X_n(k_{c2}r) = K_n(k_{c2}r)$ $k_{c2} = \lvert k_{c2} \rvert$
$Z_n(k_{c1}r) = J_n(k_{c1}r)$	$X_n(k_{c2}r) = N_n(k_{c2}r)$ or $X_n(k_{c2}r) = H_n^{(1)}(k_{c2}r)$
$Z_n(k_{c1}r) = J_n(k_{c1}r)$ $k_{c1} = k_1$	$X_n(k_{c2}r) = H_n^{(2)}(k_{c2}r)$ $k_{c2} = k_2$

Value of β, k_{c1}, k_{c2}	Feature of waves
1. $\beta > k_1 > k_2$ $k_{c1}^2 < 0$, k_{c1} imaginary $k_{c2}^2 < 0$, k_{c2} imaginary	slow waves $v_p = (C/\sqrt{\varepsilon_1}) < C$
2. $k_1 > \beta > k_2$ $k_{c1}^2 > 0$, k_{c1} real $k_{c2}^2 > 0$, k_{c2} imaginary	slow waves $v_p > (C/\sqrt{\varepsilon_1})$ $v_p < C$
3. $k_1 > k_2 > \beta$ $k_{c1}^2 > 0$, k_{c1} real $k_{c2}^2 > 0$, k_{c2} real	fast waves $v_p > C > (C/\sqrt{\varepsilon_1})$
4. $\beta \to 0$ $k_{c1}^2 = k_1^2 > 0$, k_{c1} real $k_{c2}^2 = k_2^2 > 0$, k_{c2} real	azimuthally travelling waves $v_\theta = w/n$ $v_p \to \infty$

Millimeter-Wave Quasi-Optical Rectifying Antennas for Power Transmission Applications (Invited Paper)

Kai Chang
Department of Electrical Engineering
Texas A & M University
College Station, Texas 77843-3128
USA

Abstract

Recent developments in 35 GHz rectifying antenna (rectennas) have made millimeter-wave power transmission possible. This paper summarizes the recent results and predicts the future developments.

Introduction

Microwave or millimeter-wave power transmission is a viable means to deliver power from space to ground [1], ground to ground, ground to space and space to space [2]. In all these systems, the DC power is first converted to RF power using tubes or solid-state devices, the RF power is then radiated into the free space and received by an array of rectifying antenna (rectenna). The RF power is then converted back into DC power by the rectenna. Figure 1 shows the system block diagram.

Microwave power transmission systems at 2.45 GHz have been extensively studied and components have been developed [1]. Operating at millimeter-wave frequencies has the advantage of smaller antennas allowing transmissions over longer distances. The efficiencies of rectenna and generator are lower at millimeter-wave frequencies, but the overall system efficiency could be higher at millimeter-wave frequency than 2.45 GHz for long distance transmission using the same size of antenna and rectenna.

35 GHz Rectennas

A 35 GHz quasi-optical integrated circuit rectenna has been recently developed at Texas A & M University with 39% RF to DC conversion efficiency. The circuit uses a microstrip dipole antenna, and a commercially available beamlead mixer diode [3]. It (Figure 2) consists of a dipole antenna, a lowpass filter, a diode, and a DC pass filter. The circuit was built on Duriod 5880 substrate with a thickness of 0.25 mm. The length and the width of the dipole were designed to be 0.46 λ_0 and 0.02 λ_0. Figure 3 shows the performance of conversion efficiency as a function of input power. It can be seen that 39% efficiency was achieved at 60 mW input power with a load of 400 ohms. The measured results agree well with the theoretical analysis using nonlinear circuit modeling. The measurements were done using a waveguide simulator in an arrangement shown in Figure 4.

The diode used was not optimized for power conversion application. Higher efficiencies of 60 to 70% could be possible if special devices are designed for this application.

System Assessment

The candidates for microwave/millimeter-wave generators are gyrotrons, klystrons, and magnetrons. At millimeter-wave frequencies (35 GHz, for example), high efficiency gyrotrons are viable sources. With the availability of rectennas and gyrotrons, 35 GHz transmission systems are feasible in the near future.

Acknowledgments

This work was supported in part by the NASA Center for Space Power. The constant encouragement of Dr. A.D. Patton is acknowledged. The author would also like to thank J.C. McCleary and M.A. Pollock for the system study, and T. Yoo and J. McSpadden for the rectenna development.

References

1. W.C. Brown, "The History of Power Transmission by Radio Waves," *IEEE Trans. on Microwave Theory and Tech.*, Vol. 32, pp. 1230-1242, September 1984.

2. K. Chang, J.C. McCleary and M.A. Pollock, "Feasibility Study of 35 GHz Microwave Power Transmission in Space," *Space Power*, Vol. 8, pp. 365-370, June 1989.

3. T. Yoo and K. Chang, "A 35 GHz Integrated Circuit Rectifying Antenna With 33 Percent Efficiency," *Electronics Letters*, Vol. 27, No. 23, p. 2117, November 7, 1991.

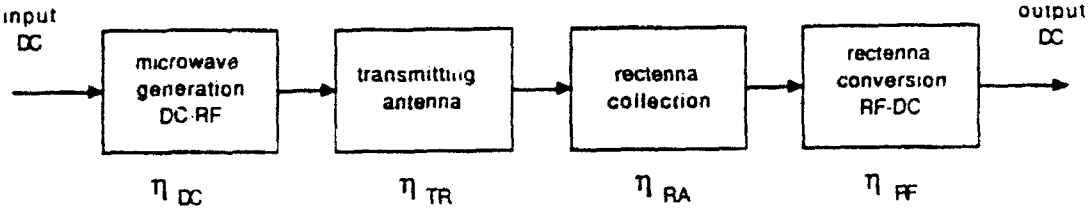

$$\eta = \eta_{DC}\,\eta_{TR}\,\eta_{RA}\,\eta_{RF}$$

Fig 1 System diagram for microwave/millimeter-wave power transmission.

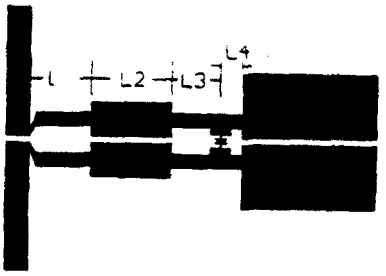

Fig 2 35 GHz rectenna circuit layout. $L1 = 0.92$ mm, $L2 = 1.19$ mm, $L3 = 0.58$ mm, and $L4 = 0.18$ mm.

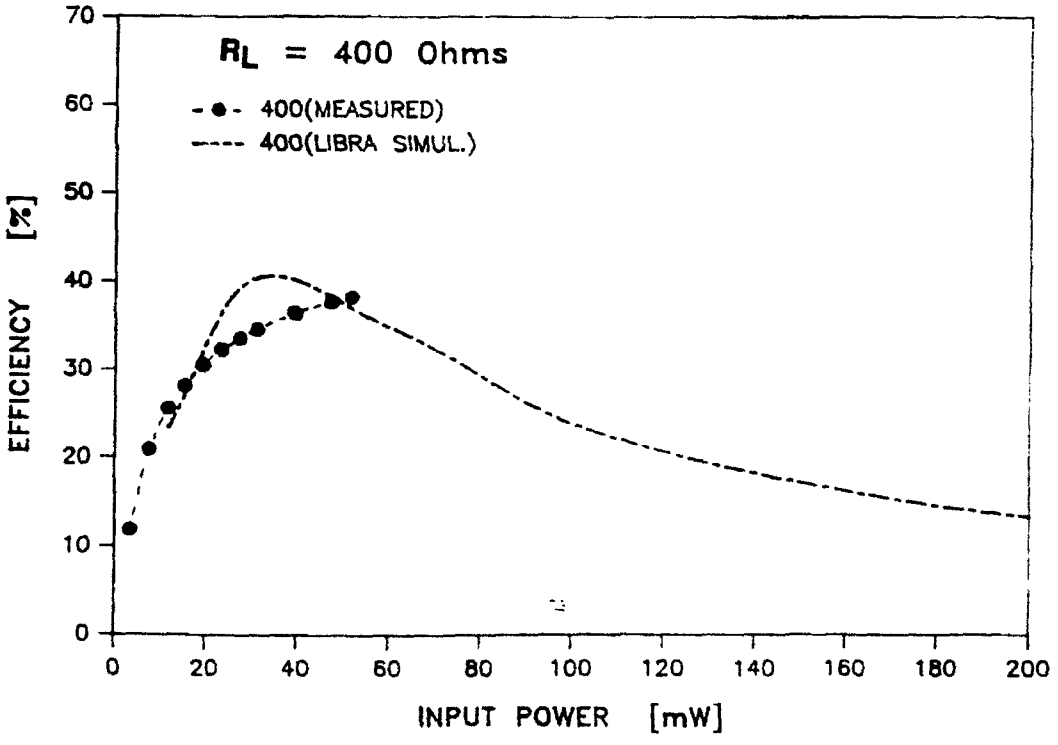

Fig 3 Measured conversion efficiency for 35 GHz rectenna.

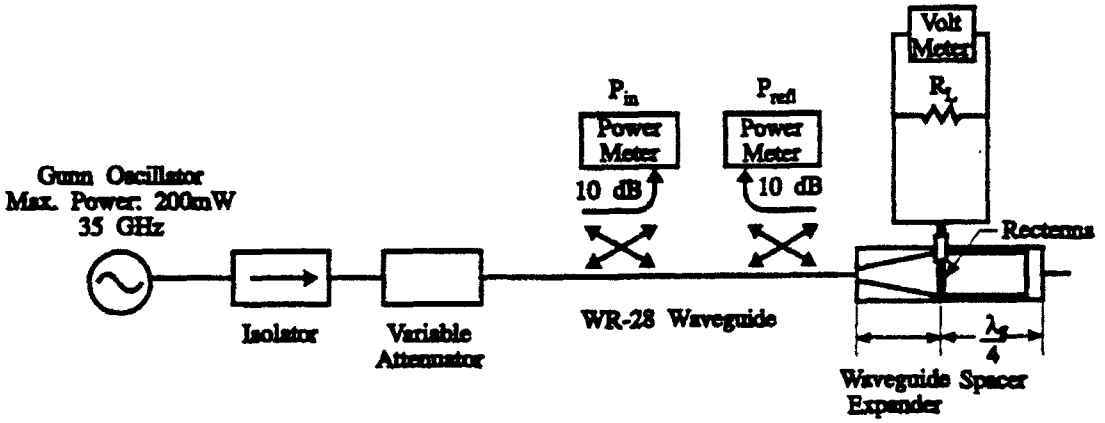

Fig 4 Conversion efficiency measurement setup.

M2.5

INTERBAND TRANSITION MODULATED CYCLOTRON RESONANCE IN SEMICONDUCTORS

S. C. Shen and W. Lu
National Laboratory for Infrared Physics
Academia Sinica
Shanghai 200083, China

and

Michael von Ortenberg
Institute fur Halbleiterphysik und Optik
Technische Universitat Brunschweig
D-3300 Braunschweig, Germany

Abstract

An interband transition modulated cyclotron resonance (CR) technique has been developed to study the CR in intrinsic wide gap semiconductors. The differential change of the FIR transmission induced by the extra monochromatic excitation light is recorded in this technique. The sensitivity of this technique is at least 10 times higher than that of conventional methods. The new technique is used to study the intraband transition and impurity transition in II-VI and III-V group semiconductors. The pronounced CR transition and impurity transition signal have been observed in the sample of CdTe and $In_{0.52}Ga_{0.48}As$/InP MQWs which could not be observed in conventional techniques. A strong resonant excitation effect has been observed. For the first time, both the spin-flip transition and CR have been observed in semimagnetic semiconductor CdMnTe. The strong exchange interaction effect has been observed. Moreover, the CR in MQWs CdTe/$Cd_{0.8}Mn_{0.2}Te$ has also been observed for the first time. Comparing to the peak position of bulk CdTe, the Cr of MQWs CdTe/$Cd_{0.8}Mn_{0.2}Te$ has a shift to lower magnetic field. It may indicate the influence of Mn in barriers.

A 345 GHz Open Structure SIS Receiver at the IRAM 30-M Telescope

H. Rothermel
MPI f. extraterrestrische Physik, 8460 Garching, Germany
K.H. Gundlach, B. Lazareff
IRAM, 38406 Saint Martin D'Heres, France

1 Introduction

Superconductor-insulator-superconductor (SIS) mixers in open structure technique have been studied in the last 10 years for application in the submilimeter wavelength range. They can be built at much lower costs than waveguide mixers and may have better transmission especially below 0.5 mm wavelength. This advantage is easily lost if the mainbeam efficiency of an open structure system falls short in comparison to a competing waveguide system. This may be the reason why open structure SIS systems have not yet been installed at radiotelescopes. We report about a system which not only has very low receiver noise but also accomplished unsurpassed sensitivity after installation at the to date largest radiotelescope precise enough for submillimeter observations.

2 Description of the receiver

The receiver consists of an open structure SIS mixer in a liquid Helium bath dewar, a Gunn-oscillator with frequency-tripler, and a beam combiner.

The open structure mixer [1-3] is based on an aspheric immersion lens of 1 cm diameter, made from crystal quartz, and a 0.5× 5 mm fused quartz substrate which carries the SIS junctions (fig 1). A movable backplane behind the substrate is used to peak the mixer gain at a given frequency. As its tuning characteristic is soft and much wider than the sideband distance (2.7 GHz), we conclude that this receiver sees a continuum source with equal sensitivity in both sidebands. The mixer element, produced in the IRAM junction laboratory [4] consists of a series array of two Nb-Aloxide-Nb junctions of 2 μm^2 each. The junction array has a total capacitance of 60 fF ($\pm$ 50%) which is sufficient to short the feed antenna almost perfectly. Very little signal could reach the mixer unless the junction capacitance was compensated by a resonant circuit. An inductance in shunt connection would be the best method but, in order to allow for DC biasing of the junction, a large capacitance has to be connected in series with it. The deposition of a sufficient large capacitance without parasitic resonance, is a technological problem. On the other hand, an inductance in a series resonance transforms the normal resistance of the junction of roughly 50 Ω down to a few ohms. With a quarterwave transmission line this small impedance has to be transformed back into its orginal value or larger, to match the antenna. We have chosen this compensation method implementing the small series inductance by chosing the transmision line the right amount longer than 1/4 wavelength. With different characteristic impedance of the transmission line both the junction capacitance can be removed and the normal resistance can be transformed to any desired value. Most important this compensation method can handle the large tolerances in junction capacitance inherent in the production method (fig.2) Superconducting coils on both sides of the mixer block produce a field of 100 Gauss in order to suppress the Josephson effect. The mixer output is connected to low noise amplifiers on the 4.2 K and 77K stage of the dewar which have an overall gain of 50 dB and a bandwidth of 1000 to 1800 MHz. Mixer

and preamplifiers are integrated into a commercial (Infrared Laboratories) 3-liter lHe bath dewar which has a quiescent hold time of 3 days.

The local oscillator [5] consists of a Gunn oscillator followed by a frequency tripler. The InP Gunn oscillator covers a frequency range of 110−120 GHz, with an output power of more than 10 mW, and a maximum power of 38 mW at 115 GHz. The tripler output is injected into the signal path by various Mylar and Polypropylene foils providing coupling ratios between 1.5 and 4 % depending on LO power available at various frequencies. The Gunn-oscillator was phaselocked to the 10th harmonic of a commercial synthesized frequency generator (HP 8671) using a harmonic mixer, a diplexer and a commercial (STS) lock-box (fig. 3). Frequency tracking in both the LSR and heliocentric reference system was accompished under the control of the telescope computer.

The amplified IF signal from the dewar is connected to a third low-noise amplifier of 40dB gain and afterwards (fig. 2) converted to the frequency range of the IRAM filter spectrometer (512 1MHz filters centered at 342 MHz), using a 1700 MHz second LO which is hand-set.

3 Measurements

The receiver optics must be matched to the telescope optics. The effective focal ratio of the Nasmyth focus is : $f_e/D = 9.73$. Aiming at a -14 dB taper at the edge of the secondary mirror, the receiver should have a beam radius $w_0 = 6.2mm$ at the waist.

The beam of the receiver was measured using a rotary table and a chopped cold load with a 30 mm aperture at a distance of 600 mm. Reading the beamwidths in the E and H cuts at the 8.6 dB threshold, waists where derived asuming two Gaussian profiles. These two waists served as a basis for the design of the optics necessary to adapt the receiver to the telescope. Although the measured beam profiles are not Gaussian, it is not wrong to design an optical system by first adjusting a Gaussian profile to the measured beam and calculating secondary waist sizes and positions using formulae for the 1st order Gaussian mode. The only additional requirement is to make the aperture large enough that higher order modes are transmitted without diffraction. A grooved Polyethylene lens with 100 mm focal length was designed which has a diameter of 50 mm corresponding to 2 w. The secondary waist is in a distance of 200 mm from primary waist. It is elongated now in the H-plane (table below).

	w_{01}	w_{02}
E-plane mm	3.67	7.46
H-plane mm	2.32	11.8

With a 11.8 mm waist in the H-plane the telescope was underilluminated leading to the elongated beam profile observed when scanning the planet Mercury (fig. 4). This shortcoming can be corrected in future by e.g adding a prism.

The receiver noise is 116K at 345 GHz if measured in the laboratory without matching optics at the 1st IF in 50 MHz bandwidth and a bath temperature of 3.8K, corresponding to 3000m altitude (fig. 5). Values below 100K have been reached at 340 GHz and a bath temperature of 1.5K. The average noise temperature over the full bandwidth of 512 the MHz IRAM filter spectrometer is ~20K higher. Some noise is added by (i) the grooved lens necessary to match beams of receiver and telescope, (ii) the 2nd IF conversion (fig. 3), (iii) 50 m cable, equalizers

and other backend components. The overall noise temperature recorded by the telescope computer during the observing period (table below) is 50K higher than laboratory results and degrades towards the edges of the tuning range. The gain was stable to better than 1% for integration times in excess of 5 hours.

LO Freq. GHz	U bias mV	I bias μA	Noise T.[50MHz] K (DSB)	Noise T.[500MHz] K(DSB)
330	3.8	7.5	157	170
333	3.8	7.5	135	155
336	3.8	13	151	208
339	3.8	13	149	160
342	3.8	13	152	160
345	3.8	13	173	180
348	3.8	13	170	216
351	3.8	13	226	242
354	3.8	13	235	270
357	3.8	8	264	310
360	3.8	8	330	

From pointing cross-scans on the planets we derive the following antenna temperatures and corressponding mainbeam and aperture efficiencies for the antenna:

Object	Diam. arc sec	Br. Temp. K	Elevation degree	Scan Width arc sec	Mainbeam arcsec	T_a K	η_b	η_a
Mercury	4.8	518	28	9x12.5	9.3	18.2	0.14	0.072
Venus	12.2	203	32	12x15		45	0.14	
Mars	4.2	215	31	9.5x12.5	10	6.0	0.14	0.072
Jupiter	42.7	165	56	44		75		
Saturn	14.5	150	30	16.5x17.5		2	0.14	
Uranus	3.44	95	30	8x10		1.6		
Neptun	2.6	90	31			0.4		

To show the capability of the system we give two examples of galactic spectra. The first (fig. 6), is the circumstellar envelope of a carbon-rich star measured at the ^{12}CO (3-2) transition at 345.8 GHz. The next (fig. 7) the same transition from the rare isotope ^{13}CO observed in a molecular cloud complex. The last spectrum (fig. 8) is from an external galaxy. NGC 891 is a ordinary galaxy similar to the Milky Way which is seen almost perfectly edge on. Apart from its great scientific interest this object was chosen, because it is about a factor of 20 weaker than radiogalaxies which have been studied so far at these frequencies at competing telescopes. At an absorption constant $\tau = .22$ towards zenit and a system noise temperture of 1242K this spectrum was recorded in 30 minutes. The RMS noise on the baseline is ~0.02K in a 4 MHz channel and the line emission (0.12 K antenna temperature) is measured with reasonable quality. The large width of the emission line in comparison to the previous spectra is due to a large number of objects at different radial velocities seen in this distant galaxy with a 10" antenna beam. 12 spectra of comparable quality have been taken from different regions of

this source in 7 hours of observing time. In combination with spectra taken lower transitions of CO taken previously with the same antenna these data will be used to derive excitation temperatures.

4 Conclusions

To our knowledge this is the first open structure system of its kind which was installed at a large radiotelescope for scheduled observations by observers not engaged in this project. In a 2.5 weeks observing period at 24 hours operation per day and roughly 50 frequency changes the system proved to be extremely stable, reliable and convenient to handle. Its high sensitivity combined with an angular resolution of ~10"and ~ 70 m^2 of effective area of this telescope at 0.86 mm wavelength allows for investigations at extragalactic objects not possible with competing telescopes.

References

[1] Rothermel, H., Eckart, A., Gundlach, K.H., Lucius, M.,"Open Structure SIS Receiver for Submillimeter Radioastronomy between 350 and 700 GHz" Int. Conf. on Millimeter Wave and Far Infrared Technology, Beijing, June 1990 Suppl. Conf. Dig. p.4

[2] Rothermel, H., Billon-Pierron, D., Gundlach, K.H.,"An Open Structure SIS Mixer for 345 GHz", Proceedings of Sixteenth International Conference on Infrared and Millimeter Waves, p.135, Lausanne, 1991.

[3] Wengler, M.J., Woody, D., Miller, R.E., and Phillips, T.G., International Journal of Infrared and Millimeter Waves, 6, 697, 1985.

[4] Gundlach, K.H., "Fabrication of Nb-Al/Alox-Nb Tunnel Junctions and First Mixer Experiments in the 100 GHz Frequency Range", Iram Working Report #203, 1990.

[5] Rothermel, H.,"Solid State Oscillators for Selected Frequencies between 100 and 700 GHz", Proceedings of Sixteenth International Conference on Infrared and Millimeter Waves, Lausanne, p.69, 1991.

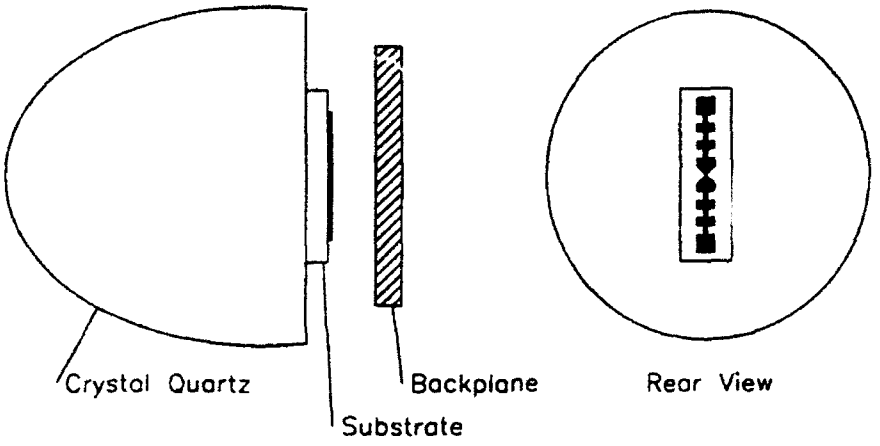

fig. 1

Schematic of the open structure SIS mixer.

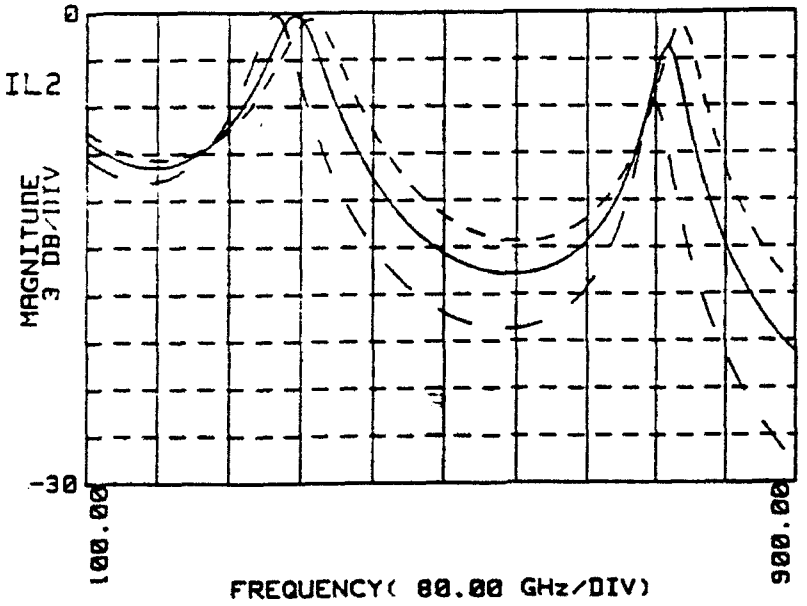

fig. 2

Frequency response of a 2-junction array with 45 to 90 fF total capacitance compensated by a 5 ohm transmission line.

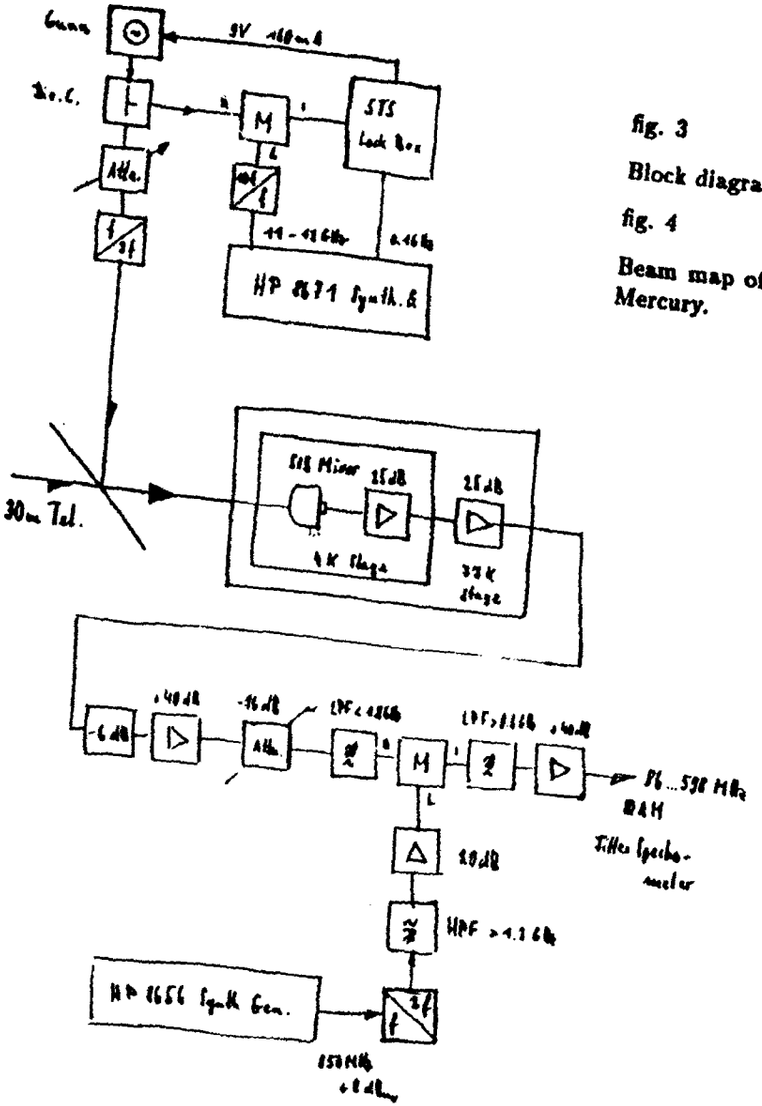

fig. 3

Block diagram of the 350 GHz SIS receiver installed at the 30-M telescope.

fig. 4

Beam map of the receiver at the 30m telescope, measured at the sky observing the planet Mercury.

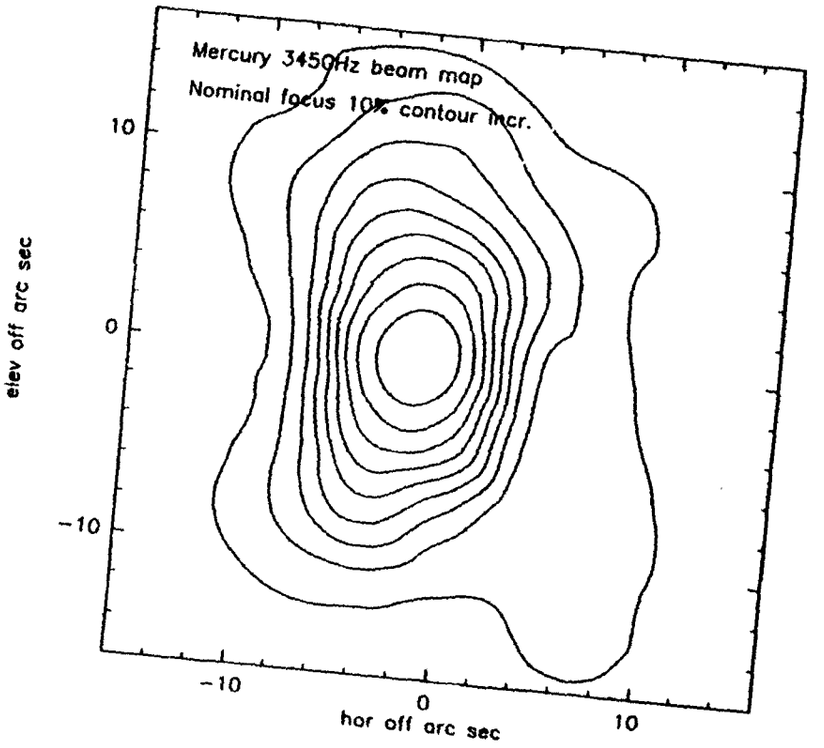

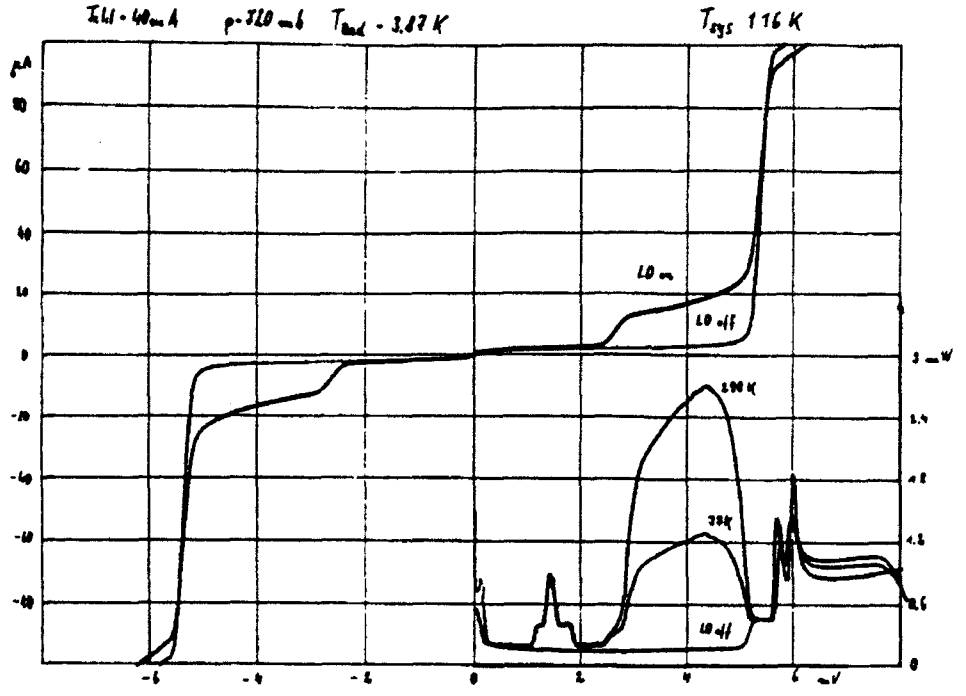

fig. 5

Calibration curve for the receiver noise temperature measured in the laboratory at 345.8 GHz.

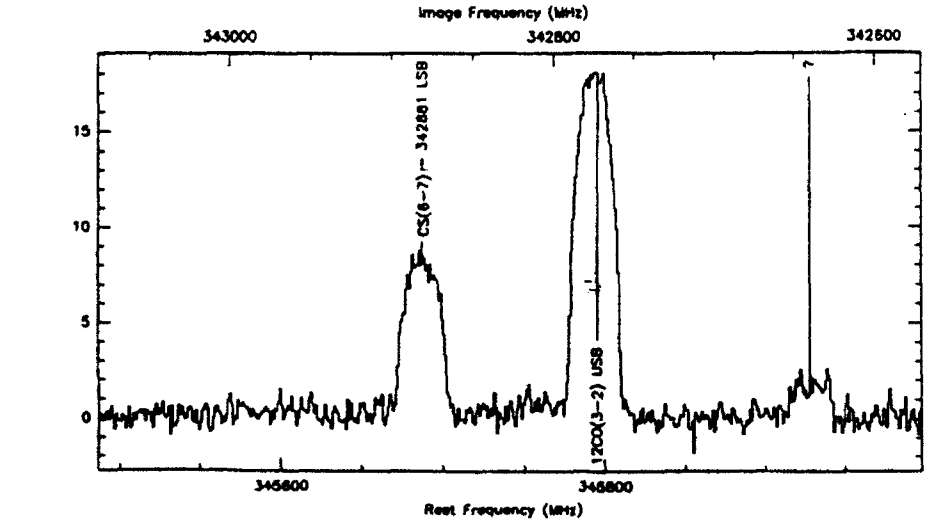

fig. 6

Molecular line emission (345.8 GHz) from ^{12}CO (3-2) measured at the source IRC+10216.

188; 1 CALORIIRC2 13CO(3-2) IRAM-30M-B30 O: 13-FEB-1992 R: 13-FEB-1992
RA: 5:32:47.001 DEC: -5:24:24.00 (1950.0) Offs: 0.0 0.0 Eq
Unknown Tau: 0.5584 Tsys: 2410. Time: 2.000 El: 43.62
N: 512 I0: 256.5 V0: 8.000 Dv: 0.9068 LSR
F0: 330587.957 Df: -1.000 Fi: 333304.405
B ef: 0.7800 F ef: 0.7800 G im: 1.000
9893

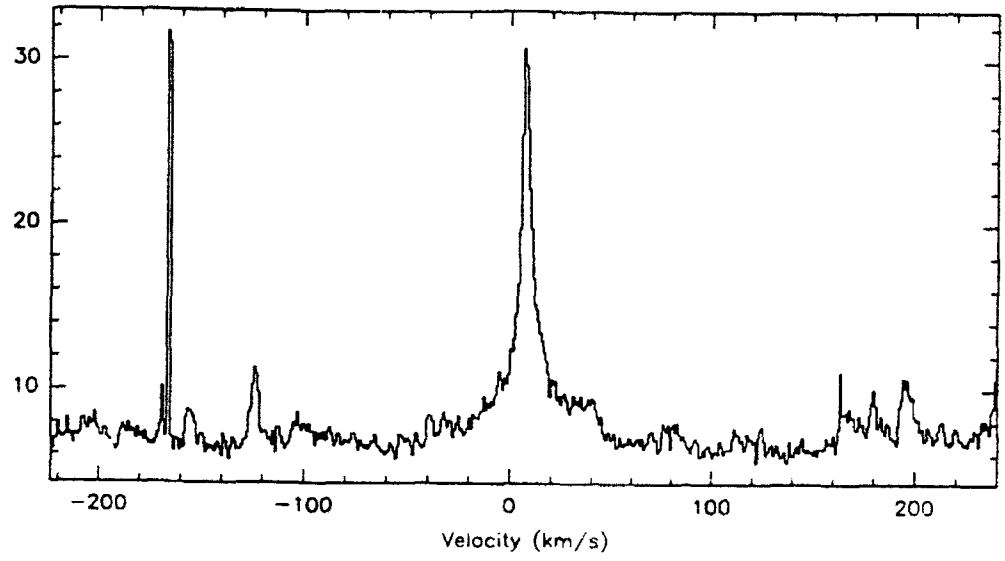

fig. 7

Isotopic line emission (330.6 GHz) from ^{13}CO (3-2) measured at the source OR IRC2.

28; 1 N891A CO(3-2) IRAM-30M-B70 O: 28-MAR-1992 R: 28-MAR-1992
RA: 2:19:24.300 DEC: 42:07:16.99 (1950.0) Offs: -20. -50. Eq
Unknown Tau: 0.2227 Tsys: 1242. Time: 15.00 El: 73.05
N: 127 I0: 64.13 V0: 700.0 Dv: 3.468 Hel.
F0: 345795.975 Df: -4.000 Fi: 343073.456
B ef: 0.6800 F ef: 0.6800 G im: 1.000
7162, 7173- 7174,

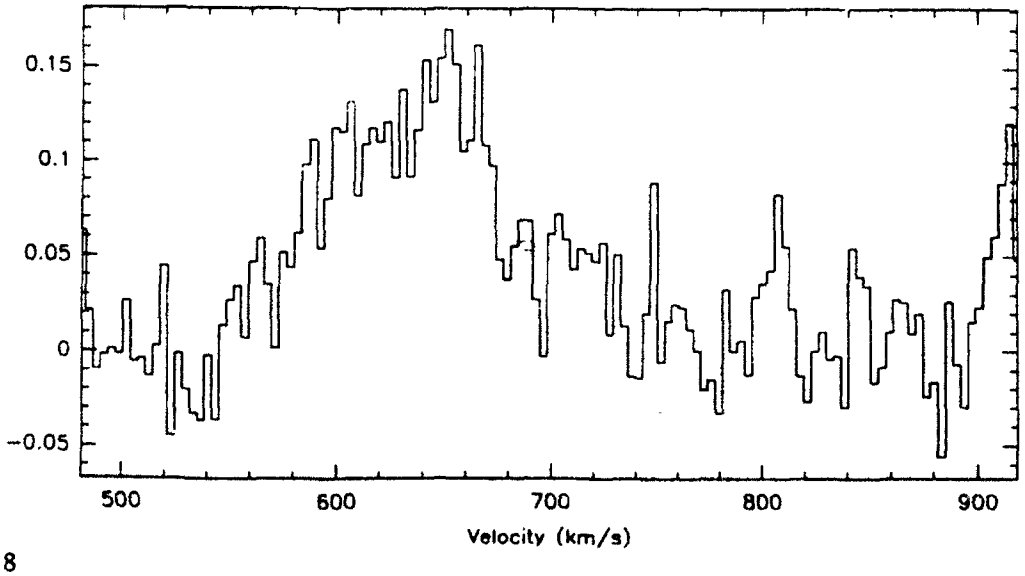

fig. 8

Molecular line emission (345.8 GHz) measured at the external galaxy NGC 891.

T1.2

SIS JUNCTION MM WAVE RECEIVERS

A.Vystavkin, M.Tarasov, V.Koshelets, S.Shitov, V.Belitsky,
S.Kovtonjuk, O.Kaplunenko, G.Prokopenko, L.Filippenko,
V.Kaplunenko, M.Khabipov, S.Turygin
Institute for Radio Engineering and Electronics, Russian Academy of Sciences, Mochovaya str, 18, Moscow, 103907, Russia
tel. (7095)2032784, telex 411429 IRESC, fax (7095)2038414

1. Introduction.

Development of low noise receivers of mm and sub mm wave bands is stimulated mainly by radioastronomy requirements for measurements, for example, of cosmic background noise with temperature of the order of 3 K, thermal radiation of interstellar dust, synchrotron radiation from ionized cosmic regions, molecular lines radiation with temperature 10 – 100 K. Achievements in sensitivity of such receivers increase leads to the possibility of application in passive and active radar, communications technique, studies of materials and biological systems, etc. The best sensitivity in the band 0,6 – 3 mm is achieved by receivers with superconductor–insulator–superconductor (SIS) junctions. In SIS mixers noise temperatures ~10 K which is close to quantum limit and conversion gain close and even higher unity were achieved at frequencies of the order of 100 GHz. The best attained results for SIS mixers and receivers obtained by different authors are presented in table

frequency, GHz	100	250	350	500
T_{dsb}^{M}, K (mixer)	6	40	–	240
T_{dsb}^{R}, K (receiver)	20	60	150	420

The upper limit of SIS mixer signal frequency may be estimated by expression: $F_{max}=2\Delta/h$ where 2Δ – the sum energy gap of superconductors, h – Planc's constant. For the most common junctions of structure Nb–AlO_x–Nb this relation gives F_{max}=750 GHz.

Input beam of SIS mixer in radioastronomic observations is an output beam of parabolic antenna, converted by quasioptic methods with lenses and mirrors into Gaussian beam which is fed into cryostat. For SIS mixer matching with such beam two methods are using: one of waveguide type with scalar horn and placed in waveguide SIS junction with IF/RF filters and another of quasioptic or opend type with planar antenna which directly transforms Gaussian beam energy to current via SIS junction integrated in such planar antenna structure.

2. SIS series–parallel arrays.

The traditional series SIS–arrays have some disadvantages the noticeable influence of difference in the junction's normal state resistance and significant mismatch at IF output. To overcome these drawbacks of the traditional series arrays we have proposed and developed a new concept of parallel biased SIS arrays. The parallel connection on dc and IF is provided by specially designed superconducting circuits which maintain the same low frequency voltages across any junction in the array. At the same time SIS junctions are connected in series for rf signals because of high impedance of biasing circuits.

The most evident advantage of parallel biased SIS arrays is the equality of dc voltages even at significantly spreading of the

junction normal state resistances. The variation of the local oscillator (LO) power for different junctions due to the difference of the normal state resistances does not result in noticeable deteriorations of the mixer performance. Another preference of the parallel biased SIS arrays is decreasing of the IF output impedance. It gives a possibility to provide the matching of high efficiency mixer (where individual junctions have very large output dynamic resistance) with standard 50 Ohm IF amplifier.

High quality Nb–AlO_x–Nb tunnel junctions were employed as the elements of the parallel biased arrays. The optimized preparation conditions were used to avoid intrinsic stress in the junction electrodes. As a result the SIS junctions with R_j/R_n ratio about 50 and the gap smearing $\delta V_g \simeq 100$ μV have been realized for the junction areas 3÷5 μ^2 at ambient temperature 4.2 K. For 100 GHz microwave experiments the ten or eleven 2.5 μ^2 junction arrays were designed and fabricated on crystalline or amorphous quartz substrates (0.09 ÷ 0.2 mm thick) The array normal state resistances were 17 ÷ 20 Ω; for the case of maximum conversion gain ($\alpha \approx 1$) at $f_{lo} \approx 100$ GHz. The values of the rf input impedances were 700÷800 Ω, the output differential resistances – about 45 Ω.

The lowest receiver noise temperature $T_r^{dsb}=19.5\pm2$ K has been achieved for small LO power with $G_m \simeq -2$dB. Mixer with one tuning (non–contacting backshort placed at 5/4 λ from SIS array) was used for SSB measurements, the receiver noise temperature T_r^{ssb} as low as 40 K has been realized. The estimated mixer noise temperature $T_m^{ssb} \simeq 6\pm3$ K This value is very close to the quantum limit $hf/k \simeq 5$ K. The measured receiver noise temperature was determined mainly by the input circuits rather than the mixer and IF amplifier noise contribution. Preliminary experiments with over mode waveguide input system have demonstrated even lower T_r values.

3. Integrated quasioptic mixer chip.

Another solution of matching problem may be demonstrated by the example of integrated quasioptic structure for SIS mixers and direct detectors. In this structure spiral antenna parameters allows to transform impedance of free space 120π Ω to 50 Ω and further matching of SIS $R_n \simeq 8$ Ω is realized by microstrip impedance transformer that allows not only to tune out stray capacitance, but also to transform the real part of impedance to antenna output resistance value.

The mixer noise temperature as low as 8±6 K at the hot input for 109.8 GHz LO frequency was measured in such quasioptic mixer at the second quasiparticle step.

4. DC SQUID RF amplifier.

One of the most promising types of IF amplifiers are DC SQUID RF amplifiers (SQA) which have noise temperatures lower 0.5 K at frequencies up to 500 MHz. The nearest competitor of SQA are cooled HEMT amplifiers which have $T_N \sim (1–3)$ K at $f \sim (1–3)$ GHz, but have rather high power dissipation and nearly achieved their ultimate parameters. SQA has more than one order reserve in the limit of gain, noise temperature and signal frequency even on the basis of the present technology The advantages of SQA are extremely low power dissipation of several picowatt, small size (~1 mm^2) and full electrical and temperature

compatibility with superconducting sensitive devices such as Josephson and SIS mixers.

To increase the input signal frequency and bandwidth of SQA we designed a four-loop dc SQUID with an integrated input coil in the form of rectangular turns inside the loops. Our measurements of noise temperature has shown T_N=0.4 K that is only twice higher above the calculated quantum limit. Taking the limiting value of Josephson frequency in SQUID loop corresponding to Nb energy gap one can in principle achieve gain of 20 dB at signal frequency almost 10 GHz.

5. Superconducting LO source.

Superconducting mm and sub mm local oscillator may have many advantages for SIS receivers in comparison with BWO or Gunn diod oscillators. Temperature and technological compatibility of such oscillator with SIS junction allows to integrate it at the same substrate. Extremely low necessary LO power level of several nanowatt and small dissipation in superconducting high Q-factor resonators allow to utilize several types of superconducting oscillators.

The most natural type seems to be Josephson oscillators based on small single junctions. Another one is one or two dimensional arrays of small single junctions, large (also called continuous or distributed) Josephson junctions. In distributed junctions oscillations frequency may be determined either by length of junction in which fluxons oscillations occur or by voltage and magnetic field in flux flow mode.

It is possible to construct a non-Josephson oscillator, for example by means of regenerating external resonator by negative dynamic resistance at IV curve of superconductor-insulator-normal metal-superconductor (SINS) junction over the energy gap voltage. Junction with SINS structure may have large region of negative dynamic resistance. Such junction may be connected to microstrip resonator which is easily compatible to SINS junction. We have designed and tested integrated circuit with SINS oscillator junction, microstrip resonator, microstrip transformers and additional SIS junction microwave detector.

6. Digitizing of output signal.

At the output of integrated superconducting receiving chip may be applied a superconducting ADC for conversion of IF signal in digital signal for further computer processing and displaying. Such ADC can be based on rapid single flux quantum (RSFQ) logic. We designed and tested experimentally all necessary elements of such ADC made on the base of niobium. A technology was developed for this. It was shown that logic elements using RSFQ-logic have switching frequencies up to 100 GHz and more. Experimental prototype of such 8-bit ADC was designed and manufactured. The working ability of elements of this ADC was demonstrated. Successful operation of whole two-bit ADC of such type was also demonstrated.

7. Conclusion. On the way to integrated superconducting receiver.

Our results in development of superconducting SIS mixers, IF SQUID amplifiers, superconducting LO and ADC makes possible to design and create integrated superconducting single-chip receiver. Before such chip cooled ferrite modulator-phase-shifter may be placed. We have designed and produced such device for SIS radioastronomic receiver placed in vacuum cryostat.

Full text of this paper will be spread at the Conference or send on the request.

T1.3

FIVE mm MICROWAVE RADIOMETER RECEIVER

Xu Zhicai
(Purple Mountain Obervatory Academia Sinica,Najing,China)
Peng Shusheng
(Xian Space Radio Technology institute , Xian,China)

ABSTRACT

The paper presents the principle of 5mm microwave radiometer receivers, which include four frequencies:50.30GHz,53.74GHz,54.96GHz and 57.95GHz, and the test results. AS usual, the receiver is Dicke-type so as to eliminate the gain vibration of the receiver system, but its sensitivity is less than that of a total-power type. In 5mm receivers,a total-power receiver is used to get higher sensitivities and periodic calibration is adopted to reduce the gain shift of the receiver system.This receiver is called Total-power-Switch receiver,TS receiver for short.From the test results,a conclusion can be got that TS receivers are feasible and has a large extent of development, especially in remote sensing on satllites.

Key words: total-power receiver, TS receiver, sensitivity, gain shift, periodic calibration

Instroduction

A microwave radiometer is a useful tool in remote sensing, because microwave can penetrate the content of the atmosphere, such as cloud, rain and haze,and has the all-weather ability.In China,radiometers have only been used on the ground to measure the water vapor and rain of the atmospere. The wave lengths used in the radiometer usually are 8mm and 13.5mm,these radiometers are Dicke receivers. Now 5mm radiometer receivers are developed in total-power type for a satellite remote sensing.A periodic calibration technology is adopted to eliminite the gain shift of the system in receivers.We call this receiver a total-power-Switch receiver, TS receiver for short. The principle of a 5mm TS receiver is described in the sencod part, the theoretical measurement sensitivity is presented in the third part and the test results are given in the fourth part.At last the conclusion and acknowledgments are given.

Foundamental principle of TS radiometer

The Dicke switch used in Dicke radiometers has an important function to eliminate the gain shift of the receiver system by alteratively inputing the antenna temperature signal and the calibrating signal with a high freqency in the integration time. This technology results in that the sensitivity of a Dicke radiometer is just as half times as that of a total-power radiometer.If the gain shift is little enough as the performance of devices has been greatly developed, it is not necessary to input the calibration signal just following the antenna signal.The calibration signal can be put off for an interval. AS a result, a total--power radiometer is adopted to improve the sensitivity. In satellite remote sensing, the antenna of a radiometer must be cyclely scanned in

order to attain a wide scanning belt on the earth. In cycle scanning, the radiometer gets several instaneous fields of view (IFOV) and two calibration fields of view, one for cold sky and another for warm temperature blackbody, which are used to calibrate IFOV's temperatures. This technology is called periodic calibration. It has been used to control the system gain and calibrate the IFOV's temperatures in 5 mm TS radiometers. In figure 1 is shown the sketch of a 5 mm TS radiometer. The system includes a reflecter, a feed horn, a mixer, a local oscillator, an IF amplifier, a square-law detector, a LF amlifier, an integrator, A/D and D/A tranfers as well as a microprocessor. In the measurement at the laboratory, a chopping-wave wheel, which is shown in figure 2, is used instead for a reflector to get cold and warm temperatures. A personal computer is used to store and process the output data from the microprocessor. The motor is controlled by the microprocessor and drives the chopping-wave wheel. A/D transfer puts the output of the integrator into digital data and the output of the D/A transfer control the gain of IF amplifier. Here it must be mentioned that an ideal integrator has been used in the TS radiometer.

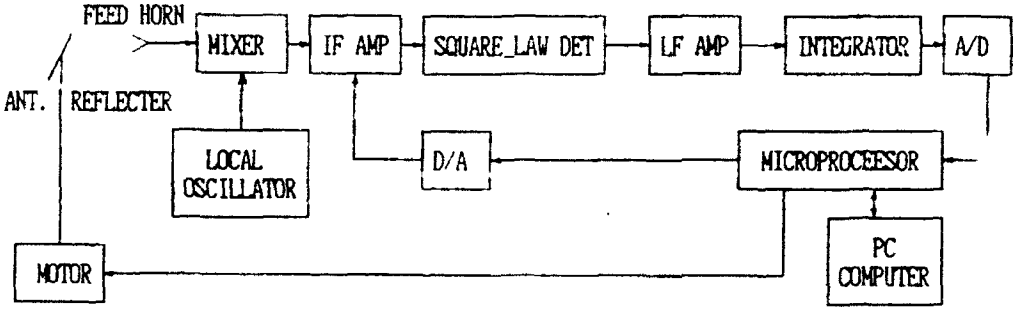

Fig.1 A 5mm TS radiometer

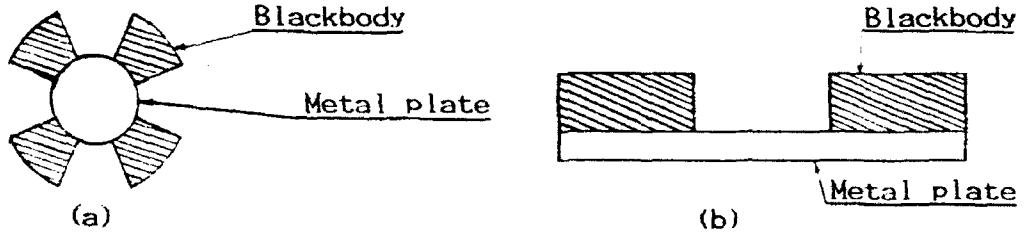

Fig.2 A chopping-wave wheel

The period of the system is 25.6 seconds. In the laboratory measurement, there are eight fields of view, two of which are calibration fields of view, in one period. The integration time is 1.8 seconds. The motor runs an angle, 45° , at a time so that the cold and warm temperature signals reach the horn in turn. Take the seventh (cold) and the eighth (warm) field of view as calibration fields of view and the temperatures of other six fields of view can be deducted by calibration. When the horn looks at the eighth field of view, the output of the receiver is the reference voltage to control the system gain. The time series are shown in figure 3.

Theoretical measurement sensitivity

As a total-power radiometer, its sensitivity is given in theory by:

$$\triangle Tmin = Tsys \sqrt{[1/B\tau + (\triangle G/G)^2]} \qquad (1)$$

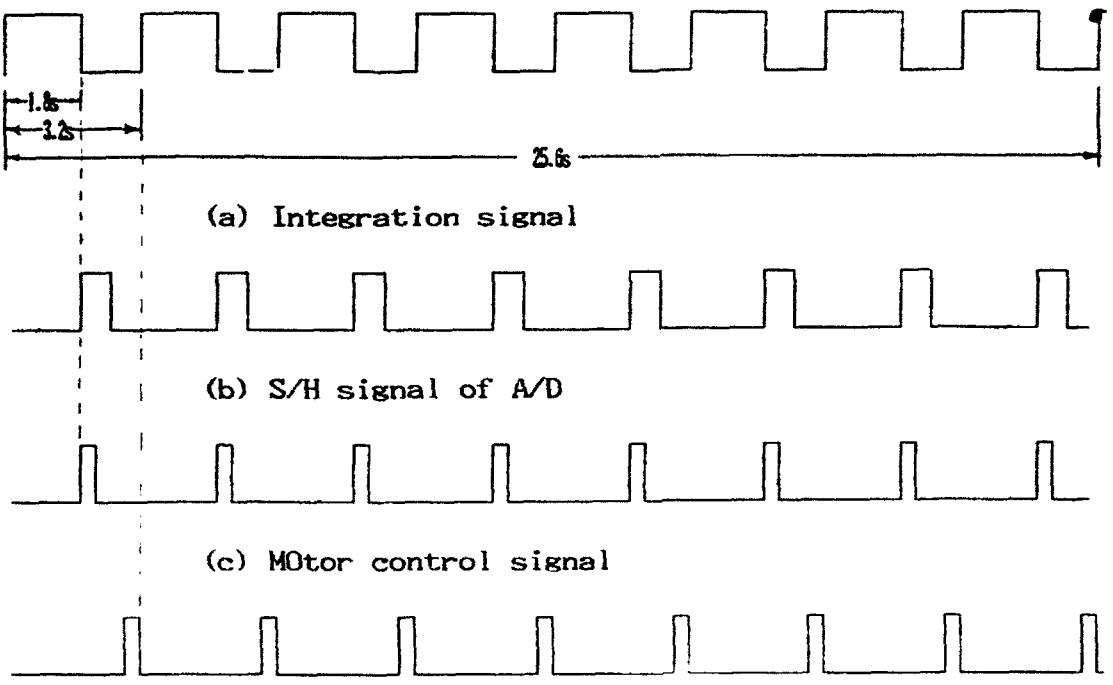

Fig.3 Time series

where Tsys is the system noise effective temperature, in k; ß is the band width of the receiver, in Hz; τ is the integration time, in s; and (△G/G) is the relative gain shift in τ seconds.
Just as describling above, the seventh and the eighth fields of view are calibration fields of view in TS radiometers. The temperatures of other six fields of view are given as follows:

$$Ti = T8 + \frac{Vi-V8}{V8-V7}(T8-T7) \qquad (2a)$$

or

$$Ti = T7 + \frac{Vi-V7}{V8-V7}(T8-T7) \qquad (2b)$$

(i =1,2,3,4,5,6,7,8)

where Vi is the receiver output when the horn observes the ith field of view. T7 and T8 are the temperatures of the cold and warm calibration blackbodies, respectively. From equation (2a) or (2b), get

$$\Delta Tmeas(i)=\sqrt{[(\Delta Ti)^2+(\frac{Vi-V8}{V8-V7})^2(\Delta T7)^2+(\frac{Vi-V7}{V8-V7})^2(\Delta T8)^2]} \qquad (3)$$

(i = 1,2,3,4,5,6)

where △Ti, △T7 and △T8 are defined by equation (1), △Tmeas(i) is the measurement sensitivity of the ith field of view in a TS radiometer. To take the gain shift into account, equation (3) must be altered by

$$\Delta Tmeas(i)=\sqrt{[(\Delta Ti)^2+(\frac{Vi-V8}{V8-V7})^2(\Delta T7)^2+(\frac{Vi-V7}{V8-V7})^2(\Delta T8)^2+(\Delta Gi/G)^2Tsys^2]} \qquad (4)$$

where ($\triangle Gi/G$) is the relative gain shift of the receiver system between the ith field of view and the calibration field of view.

Test results

In laboratory measurement, two fields of view are adopted, one is 102k and another 290k, and the calibration temperatures are the same, e.g. T7=102k and T8=290k. When i=1,3,5,7, the horn looks at the cold blackbody, e.g. Ti=102k (i=1,3,5,7); when i=2,4,6,8, the horn looks at the warm blackbody, e.g. Ti= 290k (i=2,4,6,8). Under these conditions, we have

$$\triangle T_{meas}(i)=\sqrt{[(\triangle Ti)^2+(\triangle T7)^2+(\triangle Gi/G)^2 Tsys^2]} \quad (i=1,3,5) \qquad (5a)$$

and

$$\triangle T_{meas}(i)=\sqrt{[(\triangle Ti)^2+(\triangle T8)^2+(\triangle Gi/G)^2 Tsys^2]} \quad (i=2,4,6) \qquad (5b)$$

The test results of 50.30GHz, 53.74GHz, 54.96GHz and 57.95GHz four channels are shown in Table 1. From the results, we know the relative gain shift of the receiver system in one period is very little enough not to affect the receiver sensitivity and the measurement sensitivities are very high.

Table 1 The characteristics of 5mm TS radiometers

f(GHz)	measuerment sensitivities(k)		$\triangle Gp/G$[c]
	cold[a]	warm[b]	
50.30	0.181	0.238	5.46E-6
53.74	0.277	0.305	3.45E-5
54.96	0.280	0.326	2.18E-5
57.95	0.296	0.331	1.80E-5

a) The horn looks at the cold blackbody, T=102k
b) The horn looks at the warm blackbody, T=290k
c) $\triangle Gp/G$ is the relative gain shift of the receiver in one period (25.6s)

Conclusion and acknowledgment

Four-channel 5mm TS radiometers have been designed and will be applied to remote sense the atompheric vertical temperature distribution on satellits. From the test results the TS radiometer is realistic and can be used in any other microwave radiometers.

The authers are very thinkful to Mr. Sheng Yijian, Mrs. Liming, Mr. Rong Yahe and Mr. Lao Xuangao who have attended the work.

FAR-INFRARED BALLOON-BORNE IMAGING OF THE CYGNUS REGION

A.P. Holenstein, G. Schenker, St. Clerc, D. Huguenin* and F.K. Kneubühl

Infrared Physics Laboratory
Swiss Federal Institute of Technology (ETH), CH-8093 Zurich, Switzerland
Tel. (1) 377 23 40 Fax (1) 371 59 89

* Geneva Observatory, CH-1290 Sauverny, Switzerland

Since the terrestrial atmosphere exhibits poor transmission for far-infrared and submillimeter radiation, relatively few observations of astronomical objects exist in this wavelength range. Reliable observations have to be performed from satellites, rockets, stratospheric balloon gondolas or aircraft. Far-infrared astronomy provides important information on star formation in molecular clouds. During the contraction of a protostellar cloud into a massive main-sequence star most of the energy is emitted in the far-infrared wavelength range. For the observation of the galactic Cygnus-X region, which contains many active star-forming clouds, a 60 cm diameter far-infrared balloon-borne telescope (Fig. 1) has been developed at ETH Zurich in collaboration with the Geneva Observatory [1-3]. Its design is based on similar balloon-borne telescopes built by the authors for successful far-infrared solar spectroscopy [4] and imaging [5]. The Cassegrain-type telescope is equipped with secondary-mirror chopping and an attached photometer including a liquid helium cooled silicon bolometer with an NEP of $1.3 \cdot 10^{-14}$ W/Hz$^{1/2}$ and three mesh bandpass filters. The latter are centered at the wavelengths 80 μm, 130 μm and 310 μm with bandwidths of only ± 3 μm, ± 3 μm and ± 15 μm, respectively. These bandwidths are the smallest ever used in flown astrophysical photometers. For comparison we show in Fig. 2 the spectral transmissions of these 3 filters with those used by the Infrared Astronomical Satellite (IRAS) [6] which performed a complete far-infrared survey of the sky in 1983. The pointing accuracy of the stabilized telescope is ± 17 arcsec with a stability of typically 3 arcsec RMS.

Observations have been performed during 5 hours on the occasion of a flight with a 380'000 m^3 stratospheric balloon at a height of 39 km at Aire/Adour, France, on September 26/27, 1990. Successful measurements have been made on the dust emission of the molecular could complexes DR21/W75N and S106 at 80 μm and 130 μm wavelength as well as on Mars at all wavelengths mentioned above [1-3]. Because of the considerably smaller bandwidths of our filters our measured intensity contour maps are of higher quality than those performed by the IRAS satellite in spite of the fact that the 60 cm IRAS telescope was operated at a temperature of 3 K in comparison to 250 K of our telescope. An example of such a spectral intensity map is shown in Fig. 3. On the basis of the 80 μm and 130 μm data dust colour temperatures of 36 ±2K for DR21, 34±4K for W75N and 45±6K for S106 have been calculated. Furthermore, peak-intensities and total luminosities for the different sources have been determined and compared with the results of other authors.

The next flight of our telescope for far-infrared imaging of the Cygnus region should take place in April 1992 with a new broadband filter which has a bandpass between 225 μm and 295 μm wavelength.

References:

[1] A. Holenstein, G. Schenker, F.K. Kneubühl, Intern. J. of Infrared & mm Waves, **11** (1), 55 (1990)
[2] A. Holenstein, Ph.D. thesis No 9570, (1991), ETH Zurich, Switzerland
[3] A. Holenstein, G. Schenker, D. Huguenin, F.K. Kneubühl, Astron. & Astrophysics, submitted for publication
[4] J. Rast, F.K. Kneubühl, E.A. Müller, Astron. & Astrophyiscs. **68** 229 (1978)
[5] C.G. Degiacomi, F.K. Kneubühl, D. Huguenin, Astrophys. J. **298**, 918 (1985)
[6] G. Neugebauer et al. (27 authors), Astrophys. J. **278**, L1-L6 (1984)

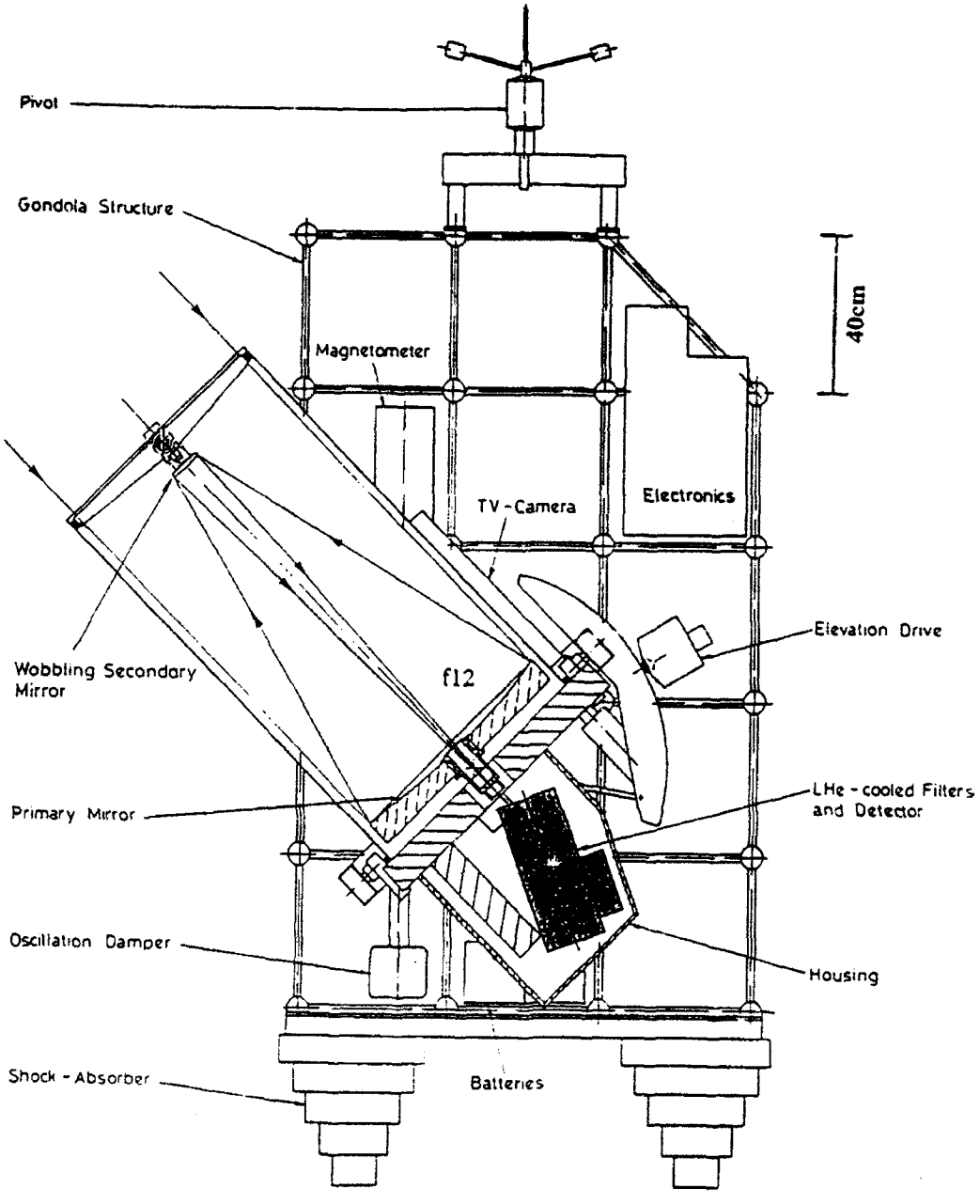

Fig. 1 The balloon-borne far-infrared telescope of ETH Zurich and Geneva Observatory flown on September 26/27, 1990 at Aire/Adour, France

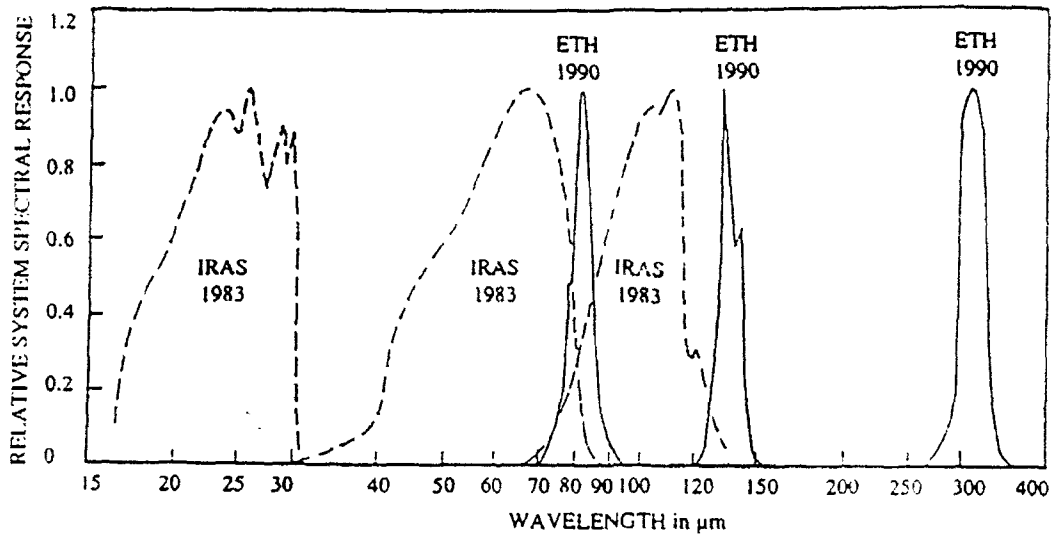

Fig.2 Comparison of spectral filters used by the IRAS satellite [6] and by the ETH Zurich / Geneva Observatory balloon-borne telescope [1-3]

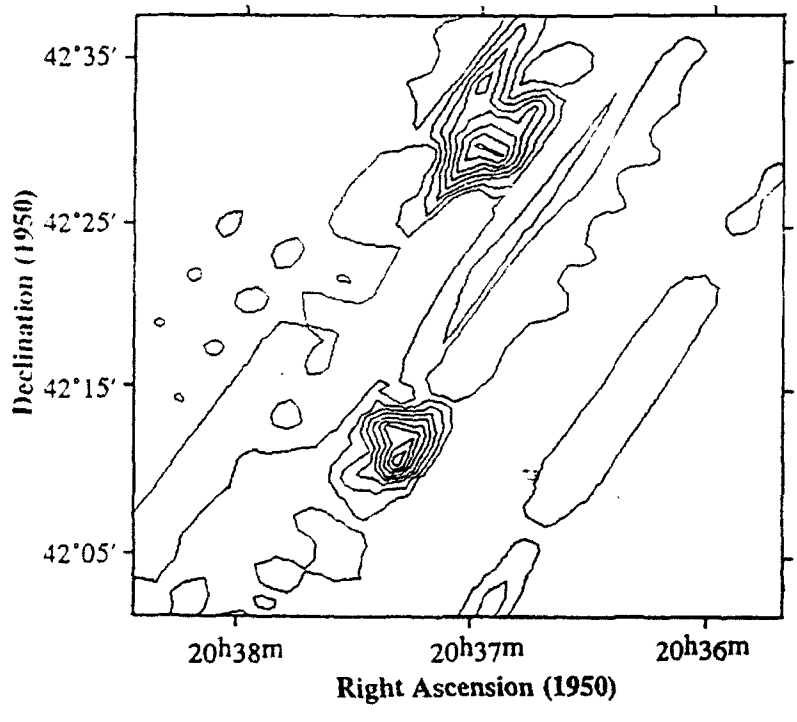

Fig. 3 130 μm image of Cygnus DR21/W75N taken by ETH Zurich / Geneva Observatory balloon-borne telescope on Sept. 26/27, 1990

T1.5

5mm MICROWAVE RADIOMETER SCANNING ANTENNA

Shen Zongzheng and Zhao Enhui
(Xi'an institute of Space Radio Technology, Xi'an, China)

ABSTRACT

The paper presents the design and the test results of 5mm offset paraboloidal scanning antenna for spaceborne microwave radiometer,which includes four frequencies: 50.3GHz,53.74GHz,54.96GHz,and 57.95GHz.A 90° offset paraboloidal reflector fed by corrugated conical horn is used to get 360° circular scanning and high beam efficiency. The test main beam efficiencies are approximately 97 percent.The antenna is feasible, especially in spaceborne remote sensing .

INTRODUCTION

The 5mm spaceborne microwave radiometer is an useful instrument in remote sensing to measure profile of the atmospheric temperature, using in the oxygen resonance band(50-60GHz) .It has the all-weather ability. An antenna is required with multi-frequency, dual (linear)Polarization, high beam efficiency and fast scanning. A 90° offset paraboloidal scanning antenna fed by corrugated conical horn with a orthogonal-mode coupler is developed. That antenna system has advantages: simple, lightweight. It has no high frequency rotating joint. Thus the fine electrical performances are easy ot access.

THE GENERAL PRINCIPLE

The configuration of the antenna is shown in Fig. 1. That includes a offset paraboloidal reflector, a corrugated conical horn feed, a orthogonal-mode coupler and a scanner. The 90° offset reflector is used to avoid deterioration of sidelobe level and VSWR, and to achieve scannig . The corrugated conical horn is used to improve antenna beam efficiency and to reduce spillover. The orthogonal-mode coupler is used to separat two orthogonal-components received by the antenna, and to couple them into one of receivers respectively. A mechanical scanning device is used .The feed horn is fixed on the inner circle of a bearing and the reflector is fixed on the outer lane of the bearing. The inner circle is fixed and the outer lane is rotated round axis of the horn by a motor.In the spaceborne remote sensing,the 360° cyclical scanning of the antenna beam is in the perpendicular plane to the spaceborne velocity vector.In the each scannig periodic, the radiometer gets several instaneous fields of view (IFOV) and two calibration fields of view, one for cold sky and the other for warm blackbody.

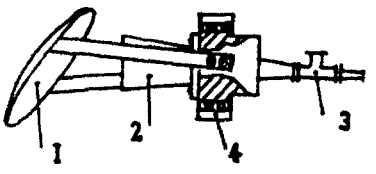

1. offset reflector 2.corrugated horn
3. orthogonal-mode coupler 4.scanner

Fig.1 The configuration of the antenna

THE MAIN POINTS OF DESIGN

1. The Design of Offset-Parabolic Reflector

The geometry of the single-offset-parabolic is shown in Fig. 2. The basic parameters of the reflector are obtained by the simple geometry relationship[1], the focal length F of the paraboloid:

$$F = \frac{d\ (\mathrm{Cos}\,\theta_e + \mathrm{Cos}\,\theta^*)}{4\,\mathrm{Sin}\,\theta^*} \qquad (1)$$

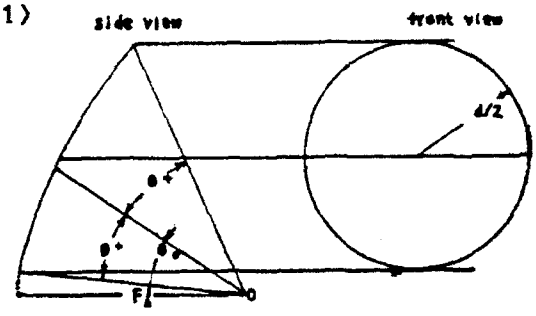

Fig.2 Geometry of the reflector

where

θ_e ——the offset angle

θ^*——the half angle subtended at the focus by feed on the reflector rim

d ——the diameter of the projected aperture of the offset reflector. It can be gaven as follows:

$$d = B\,\frac{\lambda}{\theta_{-3dB}} \qquad (2)$$

where

λ ——the oprating wavelength

θ_{-3dB}——the half power beamwidth

B ——the parameter on field distribution of the antenna aperture.

The half power beamwidth is determinded by the desirable resolution at nadir. The cross-polarization is increased with the offset angle. Usally the large offset angle is not used. However becuse of the particular scanning requirement, the 90° offset angle have to be used. To reduce the cross-polarization, a small illuminate half angle θ^* is used and a suitable taper level at the edge of the reflector is used.

2. The Design of The Corrugated Conical Horn

The radiation pattern characteristics of a corrugated conical horn can be normalized conveniently by using the dimensionless parameter Δ in wavelengths[1](Fig.3):

$$\Delta = a\,\tan\left(\frac{\theta_f}{2}\right) \qquad (3)$$

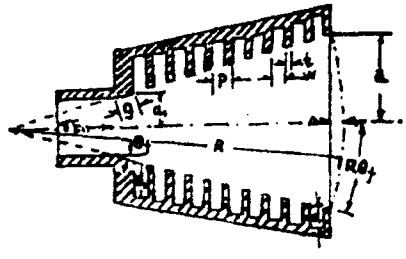

Fig.3 Geometry of the corrugated horn

In this design, the small flage-angle horn is used. It is desirable for the radiometer antenna applications to have $\Delta \leqslant 0.2$ to obtained high beam efficiencies. If a higher beam efficiency is required , Δ must be reduced, which requires the horn half flage-angle to be reduced and the horn length to be increased by a corresponding amount.

3. The Main Beam Efficiency

The main beam efficiency, described by α_m, is defined as the ratio of the radiating power in the main beam Ω_m to the total radiating power. α_m is given as following:

$$\alpha_m = \frac{\int_{\Omega_e} P(\Omega)\,d\Omega}{\int_{4\pi} P(\Omega)\,d\Omega} \qquad (4)$$

The main beam efficiency means that when the Ω_m is constant, the larger

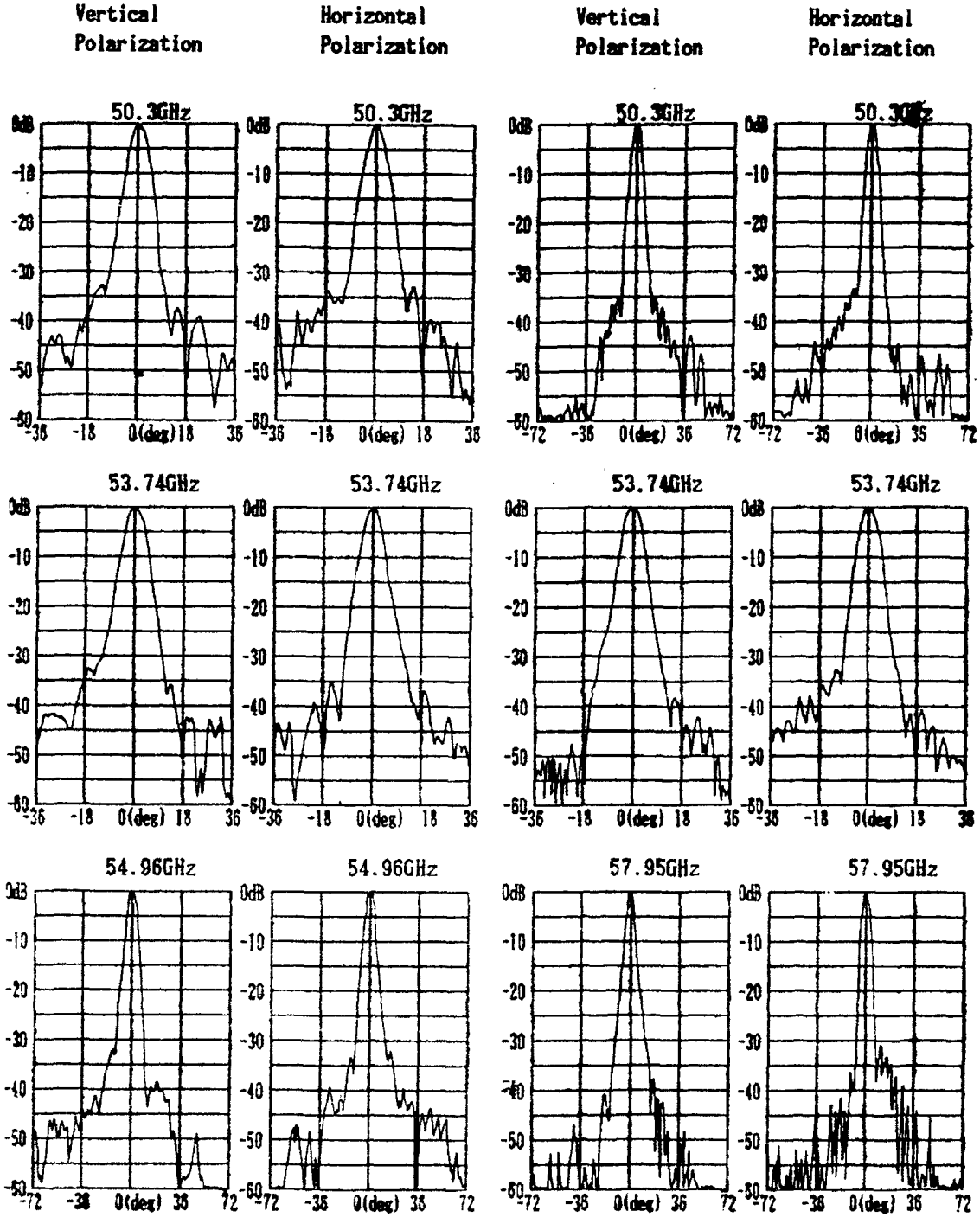

a.Elevation plane patterns.

b.Azimuth plane patterns.

Fig.5 Test radiation patterns at 50.3, 53.74, 54.96 and 57.95GHz for offset reflector with corrugated horn feed.

the α_m is, the more concentrated the antenna energy is and the lower the sidelobe level is, or, the lower the noise temperature is . The measurement main beam efficiency is given by integrating of the antenna pattern data got in measurement.

THE DESIGN EXAMPLE AND THE TEST RESULTS

The 5mm microwave radiometer scanning antenna is developed. The offset parabolic reflector has a diameter D of 72mm and a offset angle θ_e of 90°. The feed horn has a semi-flage angle of 4.7°, covered four frequencies(50.3GHz,53.74GHz,54.96GHz,57.95GHz).The feed horn provides a taper of approximately 20 dB at the edge of the reflector and has low sidelobes, low spillover,high beam efficiencies,and similar patterns of the E- and H- plane (shown in Fig.4).

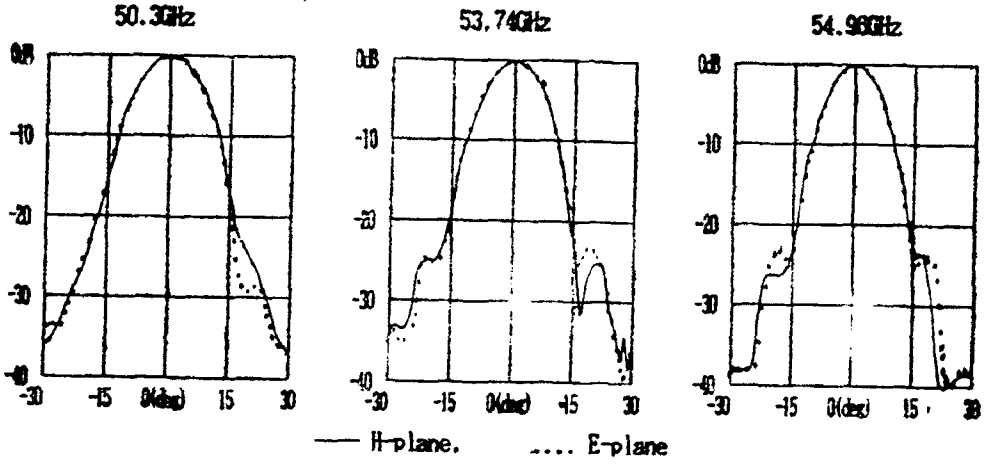

Fig. 4 Test radiation pattens for corrugated conical horn.

A good impedance match at the throat is obtaind when two tapers are made between the input waveguide and the corrugated horn aperture : One is a smooth taper and the second is the slot depth taper . The antenna combination gives a VSWR of less than 1.15 at four frequencies.The test second radiation patterns for both vertical and horizontal polarization shown in Fig. 5. These patterns shown: The patterns at four frequencies are very similar.The all of patterns beamwidths are approximately 6.0°. Nearly all sidelobe level are more than 30 dB below the peak. The main beam efficiency at each frequency is about 97 percent.

CONCLUSION AND ACKNOWLEDGMENT

5mm offset reflector scannig antenna has been designed, the test result is satisfactory. It will be applied to spaceborne microwave radiometer, also can be used in other similar remote senser.

The authers are very thankful to Prof. Lu Mingr, Prof. Wang Yifei,Mr. Zhang Shichang, Mr. Gao Xuanzheng, Mr.Zhong ying and the members of the task who have attended the work.

REFERENCES

1. A.W.Rudge, K.Milne, A.D.Olver and P.Knight, The Handbook of Antenna Design, Vol.1, Peter Peregrinus Ltd., London, UK(1982), 205,219,360 and 367.

CORRELATION REFLECTOMETRY VIA STOCHASTIC NOISE SIGNALS.

V.S.Korostelјov, K.A.Lukin, O.S Pavlichenko,
R.O.Pavlichenko, V.A.Rakityansky, V.P.Shestopalov.

Institute of Physics and Technology
Institute of Radiophysics and Electronics
of Ukrainian Academy of Science, Kharkov, Ukraine

1.Introduction

Main problems of microwave reflectometry using measurement of phase delay of reflected wave - density fluctuations and trapped modes in the oversized waveguide transmission systems - still need solution. An alternative approach which is discussed now - to use the pulse radar reflectometry and time of flight measurement [1]. The difficulty of this approach - the need of ultra short (<1ns) microwave pulses - was successfully overcome [2].

In this report we discuss a new approach [3] to reflectometry technique - use of stationary wide-band noise microwave signals and correlation technique for measurements of plasma cut-off layer position. The key components of this scheme are the microwave oscillator producing wide-band stochastic noise signal (F=35GHz, F≤1GHz, P≥1W) [4,5] and controlled PIN-diode delay line. The necessary calculations were done for the upper X-mode reflectometry for two devices: "Uragan-2M" torsatron (Kharkov Institute of Physics and Technology) and ITER. The principal layout and parameters of the noise correlation reflectometer (NCR) which is being developed for U-2M torsatron in the Institute of Radiophysics and Electronics of the Ukrainian Academy of Science (Kharkov,IRE) are described.

2. Auto- and cross-correlation functions of stochastic microwave signals reflected in a plasma.

Stochastic microwave signal propagation in a plasma was modeled by means of a numerical code NOISIM. The input block of code was generating a stationary random function describing a time behavior of stochastic microwave signal amplitude. Second block was producing a random function with the frequency band corresponding to that of the NOISE BWO developed in IRE and described a time behavior of probing microwave signal amplitude. Then for each Fourier component of microwave signal with a frequency corresponding to that of the upper X-mode the phase delay was calculated and reflected signal time behavior was obtained by means of inverse FFT. Finally auto- and cross- correlation functions of input and output signals were calculated.

Plasma parameters needed for microwave propagation studies (electron density and magnetic field) were calculated by means of numerical codes

describing 2D plasma equilibrium for tokamak with a double-null diverter (EQUT) and stellarator (EQUS). The calculations were done for ITER Standard Case (B=4.85T, J=22kA, $n(0)=1*10^{14}cm^{-3}$, $\beta_j=0.6$, $l_i=0.65$) and U-2M Standard Case (B=2.4T, $n(0)=1*10^{13}cm^{-3}$, $\angle(0)=0.24$, $\angle(a)=0.47$).

The analysis of the auto-correlation functions for input and output signals and cross-correlation one for input and output signals for "U-2M" UX-mode reflectometry shows that the auto-correlations functions of input and output signals are similar and their half width is equal to 2.5 ns (inverse of frequency band width). The cross-correlation function demonstrates clearly the time lag of the noise signal in a plasma. The time lag for signals, which are reflected at the same distance from the plasma edge (40 cm) for two devices with a different plasma radius (ITER- 2.15 cm, U-2M- 0.3 m) is shown on Fig.1. The analysis of the time lag versus the cut-off layer distance for both experiments which was obtained by the probing frequency variation shows a strong diminution of average velocity $\bar{v}_n$ of noise signal propagation in a plasma ($\bar{v}_{n(ITER)} \approx 0.1c$, $\bar{v}_{n(U-2M)} \approx 0.03c$). This give grounds for nontrivial and encouraging conclusion about comparatively larger slowing-down of noise microwave signal in devices of lesser size. Reason of this phenomenon is a considerable decrease of a wave group velocity only in a region adjacent to cut-off layer. Numeric calculations using code NOISIM allowed to evaluate the integration time which is necessary for obtaining of acceptable signal-to-noise ratio. From such calculations one can make a conclusion that for noise oscillator with a noise frequency band $\Delta F \approx 0.5$ GHz the acceptable integration time is of order of 10 μs. Of course the correlation technique can be used in a pulse radar reflectometry. Unquestionable advantage of the noise oscillator is much larger (factor of 30-50) output detector signal at equal radar oscillator power and correlator detector integration time (fig.2).

3. Noise correlation reflectometer for "Uragan-2M" torsatron

The noise correlation reflectometer is developed now in IRE for UX-mode reflectometry on the "Uragan-2M" torsatron . Basically the layout of the reflectometer repeats the homodyne reflectometer one; main differences are the noise oscillator and controlled delay line. Delay line with fixed delay time will be used for a time lag compensation in waveguides between oscillator and antenna. The controlled delay line have to provide a variable time lag corresponding to that in "Uragan-2M" plasma.

The noise oscillator is a source of stationary random signals of middle power (2-10 W) in the K_a-band. Operating principle of oscillator

is based on the effect of dynamical stochastisation of O-type backward wave tube oscillations due to nonlinear interaction between electron beam and longitudinal electric field of an intensive surface EM wave field of slow-wave structure. Stable generation and electron retuning of carrying frequency of stochastic oscillation spectrum is provided by use of wide band weakly resonant oscillatory system. Such generators allow to obtain stochastic signals in the frequency range of 30-100 GHz with the noise band 0.3-1.5 GHz and power of 10-0.5 W. Now the noise generators in the frequency band of 34-64 GHz with the noise band of 0.3-1 GHz and output power of 5-1 W are manufactured in the IRE.

The microwave controlled delay line consists of a set of short single-mode waveguides connected to each other via PIN-diode switches providing step-wise change of time lag during a time less then 10 ns. In the delay line which is being developed now the time lag step is chosen to be equal of 0.1 ns which corresponds for U-2M reflectometry the cut-off distance shift of order of 1 mm.

4.Conclusion.

We have shown that the stochastic microwave signals can be used in reflectometry for fusion plasma. Estimates of time lag ranges for UX-mode reflectometry for the "Uragan-2M" torsatron and experimental tokamak-reactor ITER are made. It is shown that the noise radar and pulse radar can be used for measurement of cut-off layer position even in a magnetic traps with plasma radius of 20-30 cm. The accuracy of cut-off layer position measurement is increasing in a large tokamaks. We hope that the proof-of principle experiment which is planned now for the U-2M torsatron will reveal a possible difficulties which are not seen usually for a new approach.

References

1. O.S.Pavlichenko, A.I.Skibenko, I.V.Jasin, ITER Diagnostic Workshop, Garshing, Germany, ITER-PH-07-0-15,Feb.12-23(1990).
2. S.H.Heijnen, C.A.Hugenholtz, P.Pavlo, 18 European Conference on Controlled Fusion and Plasma Physics, Berlin, Pt.4 (1991),309.
3. V.S.Korosteljov,K.A.Lukin,O.S.Pavlichenko,R.O.Pavlichenko, V.A.Rakitjansky,V.P.Shestopalov. Proc. of the IAEA Tech. Meeting on Microwave Reflectometry for Fusion Plasma, Abingdon, England, 4-6 March 1992.
4. B.G.Efimov, K.A.Lukin, V.A.Rakityansky, JPT,58,#12 (1988), 2398, (in Russian).
5. K.A.Lukin, V.A.Rakityansky, V.P.Shestopalov. Proceedings of All-Union School-Seminar "Microwave Physics and Applications" Moscow State University, Part 1, (1991),115,(in Russian).

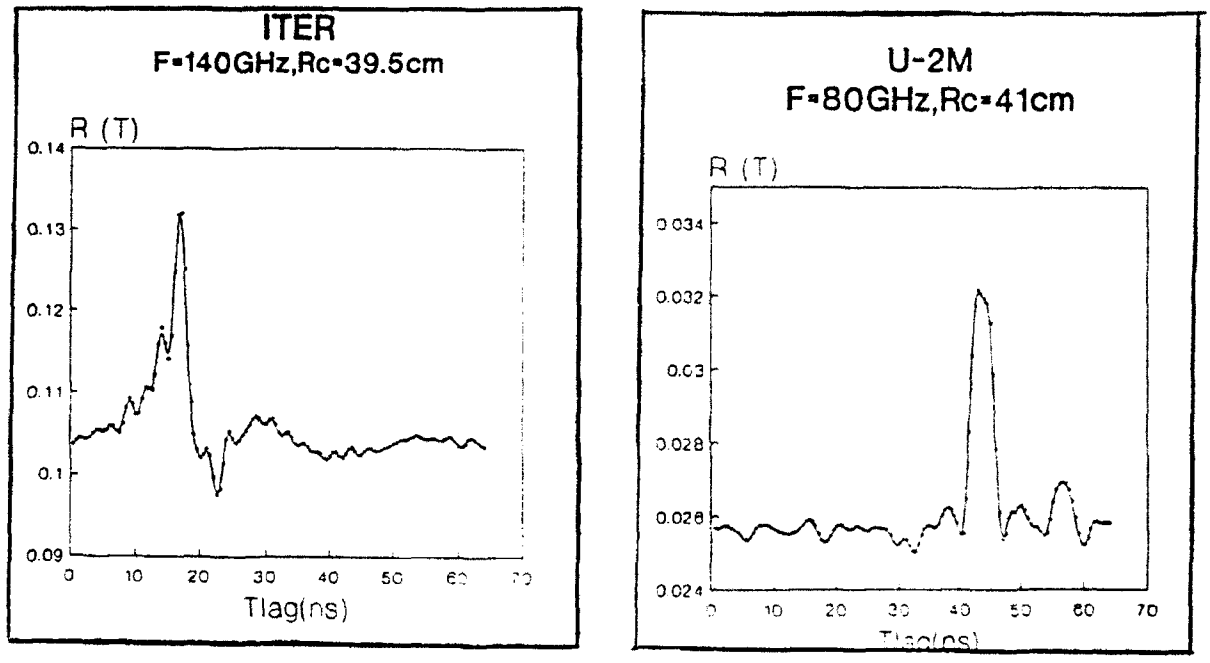

The time lag of reflected signals for ITER and U-2M

Figure 1.

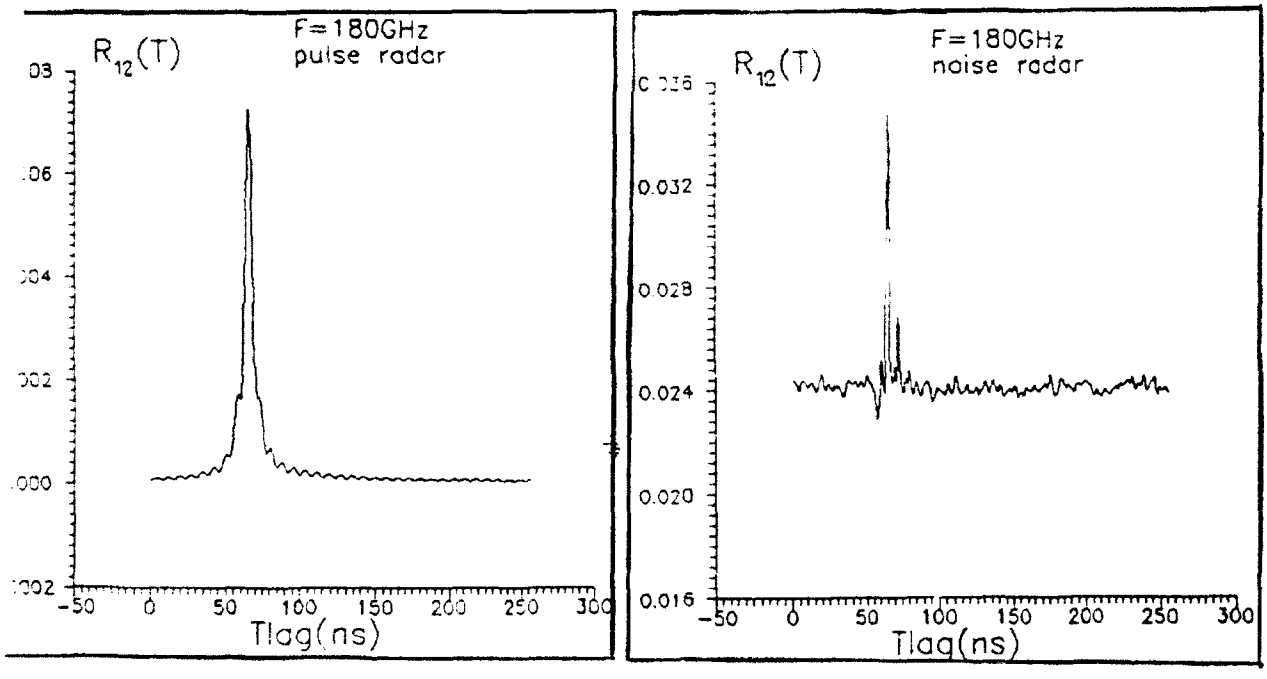

Pulse and noise propagation for ITER

Figure 2

T2.1

INVERSION OF RAIN DISTRIBUTION ALONG EARTH-SPACE PATH BY METEOROLOGIC RADAR AND SATELLITE

Hu Da-Zhang

Qingdao Research Center of CRIRP
33 Fu Long Shan, Qingdao, China (266003).

Abstract: A new method on inversion of rain distribution along Earth-Space path by meteorologic radar and satellite is given in this paper. A inversed recurrent formula of specific attenuation of rain is derived from radar equation and a assume of exponent relation between specific attenuation of rain K and radar reflectivity Z, K=cZ**d. Anoptimum solution of parameter c and d is given by computer . Tne combined system of 713 meteorologic radar at frequency 5.4 GHz and BS-2B satellite receiver at frequency 12 GHz are described. Data of experiment and results of rain intensity distribution along Earth-Space path are also presented. This method may be applied to improvement for recent meteorologic redar with one frequency.

1. Introduction.

There are considerable error by conventional meteorologic radar, because they need to employ data of radar echo to determine two parameters of radar reflectivity and specific attenuation of rain. In order to reduce the error, a double frequency meteorologic radar [2] or double polarization meteorologic radar [3] are refered. Other method of radar-radiometer is presented by lu-lin [1], but the method is not right in begger rain, because radiometer have not high distinguish at bigger rain. Here a new method of radar-satellite is presented and its employment is not restricd by case of begger rain. for used when begger rain.

2. Principle of inversion of rain distribution by radar-satellite.

In the method of radar-satellite, both antenna of radar and satellite receiver all point to direction of satellite BS-2B (see Fig.(1)). The radar echo and satellite signal are received, simultaneously.

In general, the radar echo P(r) is given by following radar equation :

$$P(r)=\frac{Ca}{r^2}Z(r)\exp\left(-2\int_0^r K(r')dr'\right) \tag{1}$$

which

$$C_a=\frac{\pi^3}{1024\,Ln2}\cdot\frac{P\,hG\theta\varphi}{\lambda^2}\cdot\frac{(m^2-1)^2}{(m^2+2)^2} \tag{2}$$

where r is a distance between radar and atmospheric precipitation (such as rain, cloud, snow and and fog and so on); Z(r) are radar reflectivity from atmospheric precipitation; K(r) are specific attenuation of rain; P is peak power of transmit; h is a special length of transmit pulse; G is antenna gain; θ , φ are half-power-bean width of radar antenna at vertical and horizon plane, respectively. The parameter of m is complex index of refractivity of rain water. In equation (1), the radar echo intensity depend on both radar reflectivity and the specific attenuation of rain along Earth-Space path. Because both radar reflectivity and specific attenuation of rain are determined by raindrop size distribution and rain type, they have some inner re-

lation. In order to simplity problem, a exponent relation between radar reflectivity and specific attenuation of rain is assumed as :

$$K = cZ^{d} \tag{3}$$

where coefficient of c and d are determined by experiment.

The space distribution of rainfall intensity are assumed form r1 to rn+1 (see Fig.1). In the range form ri to ri+1 the rainfall intensity is Ri. Substituted eq.(3) into eq.(1), the specific attenuation of rain K is represented by measured value of radar echo P(r), i=1,2,...,n and value of paraments c and d as the following recurrent equational set:

$$K1 = c\left[\frac{P(r1)r1^{2}}{Ca}\right]^{d}$$

$$K2 = c\left[\frac{P(r2)r2^{2}}{Ca}\, e^{2K1(r2-r1)}\right]^{d}$$

.....

$$Kn = c\left[\frac{P(rn)rn^{2}}{Ca}\, e^{2\sum_{i=1}^{n-1} K(ri+1-ri)}\right]^{d} \tag{4}$$

Because both antennas of radar and satellite receiver all point to same direction, the satellite attenuation of rain can wrote as

$$A(dB) = \sum_{i=1}^{n} Ki(r_{i+1}-r_i) \tag{5}$$

The equations of (4) and (5) are a contradictory equation set, which have n+1 equations and have n+2 unknown numbels (They are the parameters of c, d and Ki, i=1,2,... ,n). In order to solute the contradictory equations, a optimum solution method is presented below section. After soluting the specific attenuation of rain K , the rain intensity can be soluted by Olsen formula [4] as:

$$K = aR^{b} \tag{6}$$

where coefficients a and b are depended by the operate frequency and raindrop size distribution. For famous M-P model of raindrop size distribution, a=0.00213 and b=1.209 at frequency of 5.4 GHz. If both radar frequency f1 and satellite frequency f2 is not same, a formula of scala frequency can be used by CCIR [5] as:

$$A2 = A1*G(f2)/G(f1) \tag{7}$$

where

$$G(f) = f^{1.72}/(1+3*10^{-7}\, f^{3.44})$$

where A1 and A2 are specific attenuation of rain at frequencies f1 and f2, respectively.

3. Optimum solution of parameters c and d

Based on empirical relation between radar reflectivity Z and rain intensity R, Z=200R**(1.6) and Olsen formula eq.(6), the typical value of parameters c and d is as c=0.00004 and d=0.75, the range of parameter c is from 10**(-7) to 10**(-4) and the range of parameter d is from 0.6 to 1.2. In order to find the optimum solution of parameters c and d, a objective function is introduced as:

$$Q = [A - \sum_{i=1}^{n} Ki(r_{i+1} - r_i)]^2 \qquad (8)$$

where A is measured attenuation of rain by satellite receiver. If both frequency of radar and frequency of satellite are not same, the value of rain attenuation of radar is scaled by equation (7). Under sum sign the term of $Ki(r_{i+1} - r_i)$ is represent as the predictive value of rain attenuation.

A program figure of the optimum solution of rain intensity distribution is shown in the Fig.(2). There are two compared ring to approach true value of parameters c and d. One ring is used to find the optimum parament of d with step length Δd, when fixed parameter of c (c=10**(-4)), where d=10**(-J), the range of(-J) from (-1) to (-4) (corre- sponding to accuracy with 10**(-4)). Other ring is used to find the optimum parameter of c whth step Δ c, when the parameter of d is fixed as optimum value soluted by above ring, where c=10**(-m), the range of (-m) from (-7) to (-11) (corresponding to accuracy with 10**(-12)). Each ring includes a lot of compare process, which found two values of Q (corresponding to parameters c and d) and Q'(corresponding to parameters of c' and d') by equation (8), then compared two Q and Q', the smaller value of Q (or Q') is as new initial value of Q. Similizing above process, chose a new parameter of c' (or d'), with some step length of c (or d), uptil to find the optimum value of c (or d), which corresponding to a minimum value of Q. Based on this optimum parameters of c and d, the value of specific attenuation of rain K by equation (3) are found. Finally, The rain intensity distribution are soluted by optimum value of K by formula (6).

4 . Experimental system

The experimental system is shown in the Fig.1. Both antennas of radar and satellite are co-sited and pointed to direction of satellite BS-2B. After the data of radar and satellite receiver are collected, they are passed a conversion A/D and entered into a computer of IBM-PC/XT. The equipment is established in Qingdao of China, where longitude is E 120°19', the latitude is N 34°4' high of sea level is 114 m, the azimuth is 179°52' and elevation is 46°44'. The parameters of radar and satellite are shown in the Table 1. Substitute radar parameters into eq. (2) , the parameter of Ca=1.91*10**(-11) (mw $km^2 m^3/mm^6$).

Table 1. The paraments of radar and satellite.

Radar	Satellite
Frequency f=5.4 GHz	Frequency f=12 GHz
Peak transmit power P=260KW	Transmit power P=100W
Pulse duration h=1s	Longitude of BS-2B
Antenna size D=3.8m	E 110
Antenna gain G=38dB	Antenna Gain
Bean width = =1.2	G=53dB
Min. detectable -107mw	Antenna size D=5 m

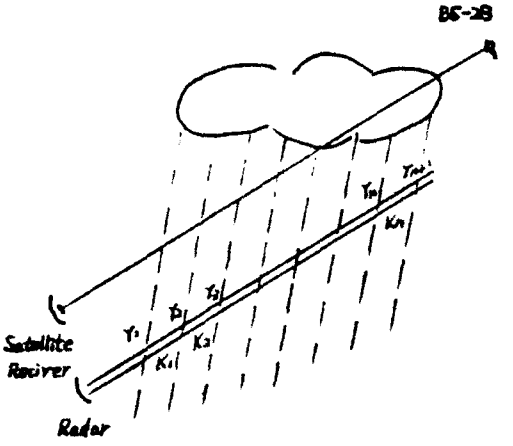

Fig. 1 Experimental system.

5. Data and results

Typical data of radar echo and satellite attenuation of rain at July 31, 1986 in Qingdao are shown in table 2 and Fig. 3. There are data of three sets , which repre-

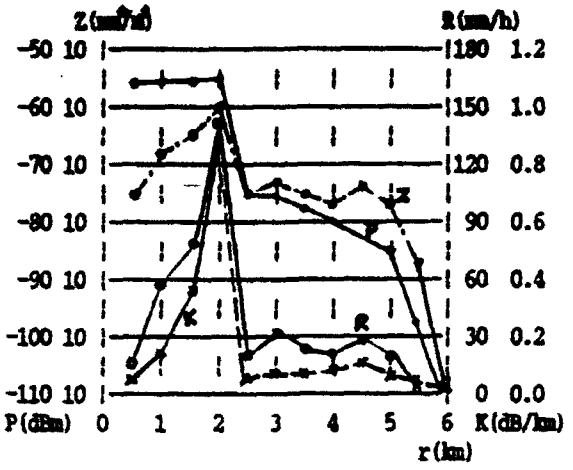

(a). Haevy rain

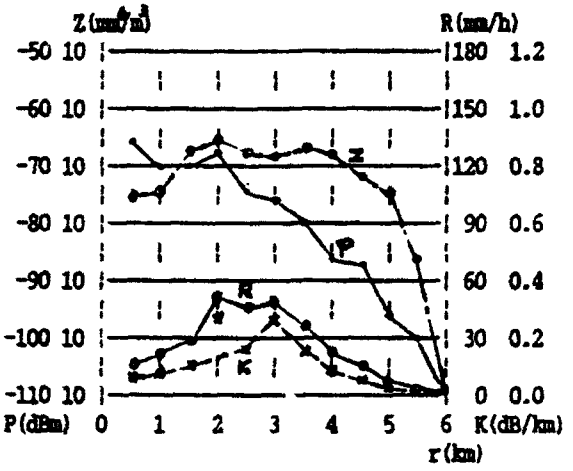

(b). Middle rain

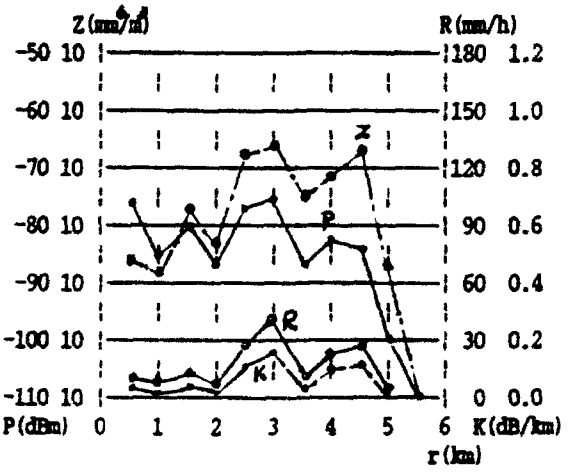

(c). Small rain

Fig.3 Inversed results of rain intensity R, redar reflectivity Z, special attenuation of rain Ki on Earth-Space path at July 30 , 1986 in Qingdao, China.
Time (a). 22:36 (b). 22:42 (c). 22:52

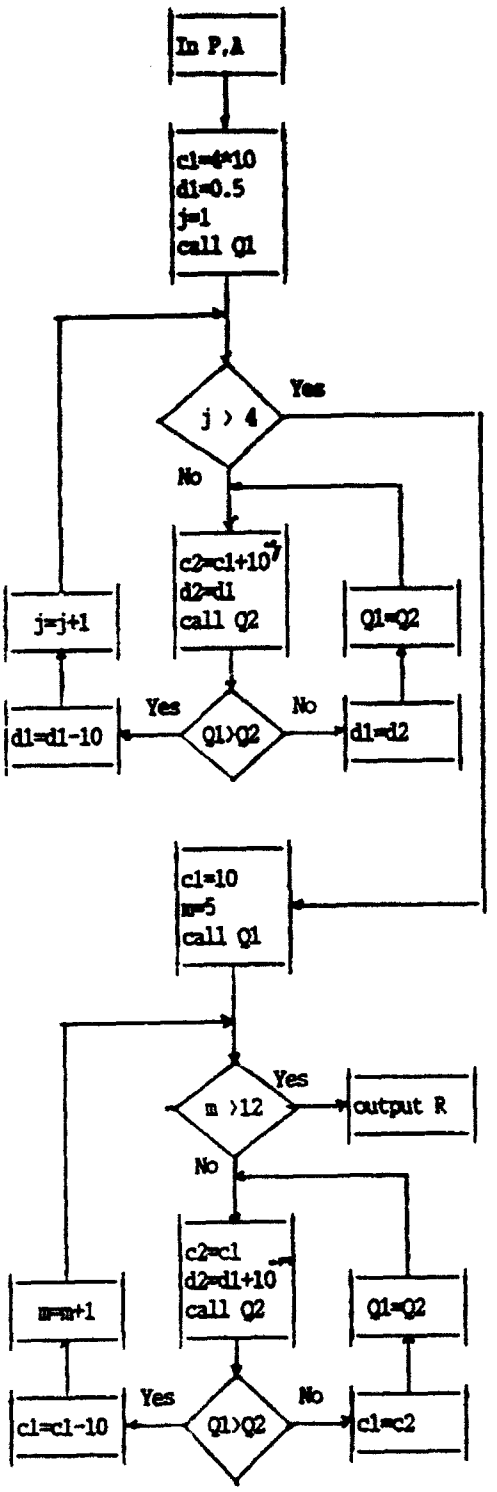

Fig. 2. The program of optimum solution of rain distuibution by radar-satellite.

sented three kind of rain: begger, middle and small rainfall. The results of parameters of sec, d and Q are listed in the Table 2. The results of rain intensity distribution R(r), radar reflectivity distribution Z(r), specific attenuation of rain K(r) and radar echo P(r) are shown in the Fig. 3. The paraments of c and d are very close value given by Joss, where c=3.15*10**(-4) and d=0.732 [6]. Results of mean square error Q are smaller than 0.1 dB from Tab. 2, it is shown that the method of radar-satellite is available.

Table 2. Typical rain

Time	Kind of Rainfall	A(dB)	Results of inversion		
			c	d	Q
22:36	Heavy Rain	5.0	7.90*10**(-5)	0.791	.0966
22:43	Mid. Rain	3.0	1.79*10**(-4)	0.691	.00738
22:52	Small Rain	1.3	1.79*10**(-4)	0.691	.00028

6. Conclusions

This paper has present a new method for measured rainfall intensity along Earth-Space path. In improving measured method by single frequency radar,it has three areas:

(1). It can determines the radar refrectivity, the specific attenuation of rain and rainfall intensity on Earth-Space path, It has the problem of measured principle by single frequency radar, which need assume the factor of specific attenuation of rain are very smaller and neglectful .

(2). It is not necessary to measure the radar parameters of Ca, which includes the radar transmit power, antenna gain, been width, because a new parameter c/Ca represe-ntes the paraments of Ca in the eq(4) , here the paraments c/Ca is found by optimum method.

(3). The radar-satellite method is available for any kind of rain, because the rain is heavy, distinguish of measured attenuation is good, but the radar-radiometer method is not available when heavy rain, because distinguish of measured temparetrue by radiometer is not high when heavy rain.

Reference:

1. Lu D. R. and Lin H., Comparisons and combined uses of radar and radiometer in the remote sensing of rainfall distribution, Scientia Atmospherica Sinica, Vol.4, No. 1, 1980, p30-39.
2. Yamada M, A. Ogawa, O. Faruma and M. Yokoi, Measurement of rain attenuation by dual-frequency radar, 1987 ISAP (Japan), P468-472.
3. McCormich, G. C. and A. Hendry, Principles for radar determination of the polarization properties of precipitation, Radio Science, Vol. 10, No. 4, p421-434, April 1975.
4. Olsen, R. L., D. V. Rogers and D. B. Hodge, The aR**b relation in the calculation of rain attenuation, IEEE Trans. Vol. AP-26 ,No. 2, p318-329.
5. CCIR Report 338, 1984.
6. Goldhirsh J., Prediction method for rain attenuation statistic at variable path angle and frequency between 13 to 100 GHz, IEEE Trans. Ant. Pro. Vol. AP-23(6), 780, 1975.

T2.2

CORRELATION OF CLOUDINESS AND RAIN COMPONENTS OF MILLIMETER RADIO WAVE ATTENUATION IN HYDROMETEOROLOGICAL FORMATIONS IN THE TROPOSPHERE

V. V. Stroganov
Radiophysical Research Institute
Nizhny Novgorod 603600, Russia

Measurements by the method of remote radio sounding in the spaced points of zenith attenuation at 4,8,13.5 and 30 mm wavelengths in the troposphere with clouds and rain show that times and distances of correlations of these attenuations are in the 3-35 minute intervals and 2-20 km, respectively, independently on the rain intensity.

Measurements show that cloudiness and rain components of attenuation are badly correlated between each other. If falling rains are strictly connected with regions of cloudiness, the rain drops on the zenith path appeared to be fallen from different regions of a moving cloud that makes the rain structure the oblique-stratified character. Taking into account that velocities of the drops falling differ on the average by a number of two for mizzly rains and pouring ones, it should be expected that the time of attenuation correlation in mizzly rain will exceed that of a strong pouring rain (with similar wind velocity).

The role of rain in the attenuation of millimeter waves increases relative to the cloud with an increase of the wavelength in strong pouring rains but drops in mizzly rains. This is confirmed by the correlation of the rain intensity with attenuation at different wavelengths. For mizzly rains, the coefficient of the intensity correlation with attenuation increases with decrease of the wavelength. The inverse is observed in a strong pouring rain (30 + 70 mm/hr.); the coefficient of the intensity correlation with attenuation drops with the wavelength decrease. Here, the time of correlation is changed that testifies to the fact that times of attenuation correlation of millimeter wavelengths in the rain and cloudiness parts are different.

For a pouring rain (Fig. 1), the autocorrelation functions of the rain intensity and 30 mm wavelength attenuation (curves 4 and 3, respectively) coincide. This is explained by the fact that a contribution of a cloud into the 30 mm wave attenuation in strong pouring rains is small in comparison to that of the rain.

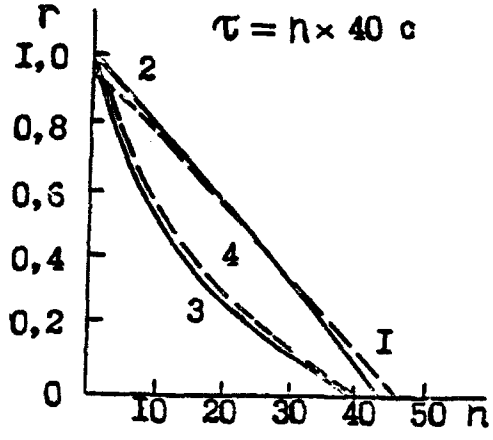

Fig.1

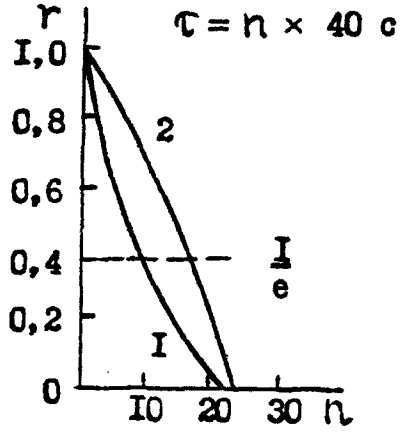

Fig.2

It is evident that time of correlation found over these two curves are due to the rain and can be considered the time of correlation of the rain component of millimeter wave attenuation.

Curves in Figure 1 (1 and 2) are the correlation of 4 and 8 mm wave attenuation and the autocorrelation of one of them. Curves are also practically coincided, but the time of correlation found exceeds twice the time of correlation found from the first two curves. It can be explained by the role of cloudiness only. Time of correlation of millimeter radio wave attenuation in cloudiness part in case of a strong pouring rain is larger (in the given case by two times) than the time of correlation of attenuations in the rain part.

It is on the contrary for mizzly rain (Fig. 2). The time of correlation of 4 mm wave two times smaller than that of the rain intensity of autocorrelation (curves 1,2, respectively). From here it follows that the time of correlation in millimeter radio wave attenuation in mizzly rain is twice as large as the time of correlation in the cloudiness part of the cloud-rain system. In particular, it explains the observed double saturation of the structural functions of millimeter wave attenuation in clouds with mizzly rains (the first saturation is due to cloudiness, the second is due to rain. The time of saturation is two to three times larger). The differences of corralation times for millimeter radio wave attenuation in the rain and cloudiness components of hydrometeorological formations for pouring and mizzly rains denote that the mean dimensions of inhomogeneities of strong rain (horizontal) are smaller than that of the cloudiness, while dimensions of inhomogeneities of mizzly rain exceed that of the cloudiness.

T2.3

RAIN INDUCED DEPOLARIZATION AT MILLIMETRE AND SUB–MILLIMETRE WAVES IN A XI'AN ENVIRONMENT

Y.Yan
(Xidian University, Xi'an, 710071, China)

ABSTRACT

The rainfall rate accumulative distribution, raindrop size distribution and raindrop canting angle distribution in Xi'an have been obtained using the least square method from the data measured over a long period of time.The rain induced depolarization in this environment has been studied.The cross polarization distrimination, XPD, was computed over a frequency range of 30 GHz to 400 GHz for non–spherical drops.The variations of XPD with frequency, rainfall rate and copolar attenuation, CPA, were investigated.A mathematicl relationship was established between the XPD and CPA, raindrop canting angle.The results obtained using the Xi'an raindrop size distribution have been compared with those assuming the Laws and Parsons (L–P) distribution.The role of multiple scattering also has been discussed, it is shown that the multiple scattering play an important part in short millimetre and sub–millimetre waves.

INTRODUCTION

The ever increasing demand for high capacity radio channels has led to the use of orthogonal polarization and higher frequency range in order to increase channel capacity without the attendant increase in bandwidth.Rainfall is a major impairment to radio wave propagation at millimetre and sub–millimetre waves.This had lead to the interest of many workers in the study of rain induced attenuation and depolarization on terrestrial and earth–space communication links.In the system using orthogonal polarizations, it becomes necessary to model the true shape of the raindrop as closely as possible in order to fully study the effect of rainfall on the electromagnetic wave propagation.Consequently, the spheroidal drop shape and in recent times the Pruppacher–Pitter drop shape have been assumed for scattering purposes.The non–spherial shape results in differential attenuation and differential phase shift of the orthogonal polarizations, thus leading to further signal degradation in the form of depolarization.

Understanding depolarization properties of the transmission medium is of crucial importance in planing frequency reuse by employing orthogonal polarization in a radio communication system.The rain induced depolarization, which concurs with heavy rain attenuation, is determined by locally rainfall, raindrop size distribution and raindrop canting angle distribution.In this paper, rain induced depolarization has been studied using the Xi'an raindrop size distribution and raindrop canting angle distribution.The purpose of this paper is to assess our current considering of the rain induced depolarization at millimetre and sub–millimetre waves and to discuss the relationship between the XPD and CPA and the role of multiple scattering.

RAIN MEDIUM PARAMETER IN XI'AN ENVIRONMENT

In order to study rain induced depolarization at millimetre and sub–millimetre waves, it is necessary investigating rainfall rate, raindrop size and canting angle distribution.

1. Rainfall Rate Accumulation Distribution

The equation of rainfall rate accumulative distribution is obtained using the least square method from the 5–minute data measured in Xi'an over a long period of time(eleven years).

$$p(x \geqslant R) = 0.001694e^{-0.106R} \tag{1}$$

where, R is the 5–minute rainfall rate (mm / hr), p(x ⩾ R) is the probability exceeded the mean year time of arising rainfall rate R.

2. Raindrop Size Distribution

In the Xi'an area, the raindrop data have been measured with different method, in different time, different climate condition.Then, the equation of raindrop size distribution has been obtained using the least square method,

$$n(D) = 5612.29exp(-3.74R^{-0.21D}) \tag{2}$$

where, D is the diameter of raindrop (mm), n(D) is the function of raindrop size distribution.The data were measrued in the condition: rainfall rate is smaller than 20 mm / hr.

3. Raindrop Canting Angle Distribution

The equation calculating raindrop canting angle distribution has been obtained using the least square method from the data measrued with different method,

$$p(\theta) = \frac{1}{\sqrt{2\pi}s} e^{-(\theta-u)^2/2s^2} \tag{3}$$

where, θ is the raindrop canting angle, u is the average value of raindrop canting angle which has Gaussian statistical distribution, s is the standard deviation, p(θ) is the distribution function of raindrop canting angle.The data were measrued in the condition: rainfall rate is smaller than 40 mm / hr.

CALCULATION OF RAIN INDUCED POLARIZATION

In frequency reuse system employing orthogonal polarization, the interfering crosstalk between the two channels through depolarization caused by raindrops can severely restrict the utility of such system. The degree of depolarization may be represented by the ratio of cross–polarized to copolarized signals at the receiver.

The depolarization effect can be evaluated in terms of the cross–polarization discrimination XPDH, XPDV, where H, V refer to horizontal and vertical polarizations, respectively.In the condition of single scattering, the cross polarization discrimination is given by (reference 1),

$$XPDH = 20lg\frac{(v+h)-(v-h)\cos 2ue^{-2s^2}}{(v-h)\sin 2ue^{-2s^2}} \tag{4}$$

$$XPDV = 20lg\frac{(v+h)+(v-h)\cos 2ue^{-2s^2}}{(v-h)\sin 2ue^{-2s^2}} \tag{5}$$

where, $v = e^{-jkvl}$, $h = e^{-jkhl}$, kv and kh are propagation constants of two characteristic

polarization of waves without depolarizations, repectively.L is the effective distance across the flat rain region.

The variation of XPD with rainfall rate at 35GHz and 300GHz is illustrated in figure 1 for a terrestrial links.Figure 2 show the variation of XPD with frequency from 30GHz to 400GHz.

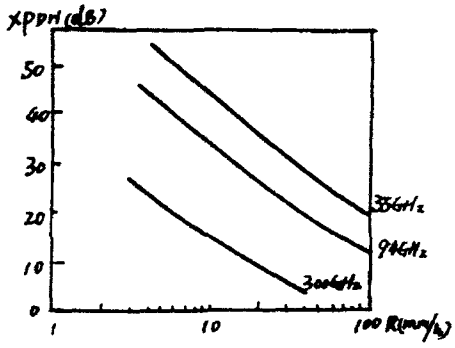

Fig. 1 Variation of XPD with rainfall rate.

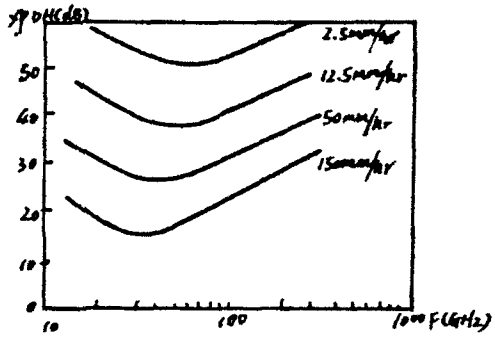

Fig. 2 Variation of XPD with frequency.

VARIATION OF XPD WITH COPOLAR ATTENUATION

Measurement of copolar attenuation and rainfall rate are easier than that of cross polarization discrimination.Therefore, it is interesting to have a formula to infer XPD with the peior given value of CPA.Froming the equation (1), a formula of computing XPD in terms of CPA can be represented as,

$$XPD = CPA - 20lg(e^{CPAV/20} - e^{CPAH/20}) - 20lg(\mathrm{tg}2u) \tag{6}$$

Figure 3 shows the variation of XPD with CPA at 34.8Ghz, comparing with the formula to compute XPD in terms of CPA suggested by CCIR (reference 2).It can be seen that the result of equation (6) is more in agreement with the measured values than that of equation suggested by CCIR.

THE ROLE OF MULTIPLE SCATTERING

As the operating frequencies of communication systems more higher into the millimetre wave region, the effect of multiple scattering in precipitation media become more significant.Considering the effect of multiple scattering, the rain induced cross polarization discrimination can be given by (reference 3),

$$XPDH = 20lg\frac{1 - \frac{2\pi}{K_0}L\int[(1-F_0)f_h + \frac{1}{2}F(f_h + f_v) + \frac{1}{2}F(f_h - f_v)\cos 2ue^{-2s^2}]nda}{\frac{2\pi}{K_0}L \cdot \frac{1}{2}\sin 2ue^{-2s^2}\int(f_h - f_v)nda} \tag{7}$$

$$XPDV = 20lg\frac{1 - \frac{2\pi}{K_0}L\int[(1-F_0)f_v + \frac{1}{2}F(f_h + f_v) - \frac{1}{2}F(f_h - f_v)\cos 2ue^{-2s^2}]nda}{\frac{2\pi}{K_0}L \cdot \frac{1}{2}\sin 2ue^{-2s^2}\int(f_h - f_v)nda} \tag{8}$$

where, k_0 is the wave number in free space, F_0 is the ratio of spherial shape to total, F is that of the non-spherial shape, fhand fv is the forward scattering coefficient of non-spherial shape raindrop to horizontal and vertical polarizations, respertively, a is the radius of raindrop.

Figure 4 shows the comparison of multiple scattering and single scattering at frequencies of 34.8GHz, 94GHz and 400Ghz, respectively.It can be seen that the role of multiple scattering in short millimetre and sub-millimetre band become more significant.

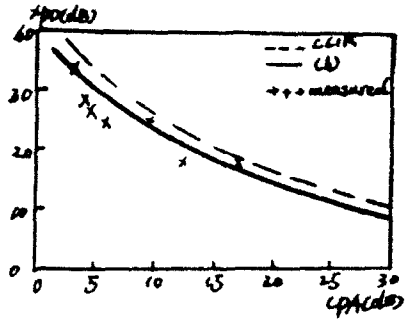

Fig 3 Variation of XPD with CPA at 34.8Ghz.

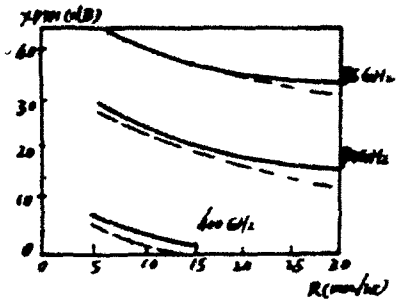

Fig 4 Comparison of multiple and single scattering.

CONCLUSION

The rain induced depolarization in a Xi'an environment has been studied over a frequency range of 30GHz to 400GHz in terms of cross polarization discrimination, using a Xi'an raindrop size distribution and raindrop canting angle distribution measured with different method. A theoretical relationship of computing cross polarization discrimination in terms of copolar attenuation and average canting angle of the raindrops has been developed for terrestrial links in millimetre wave band.It is more convenient than the formula to compute XPD in terms of CPA suggested by CCIR.The role of multiple scattering has been discussed.It is shows that the effect of multiple scattering play an important part in short millimetre and sub-millimetre band.

REFERENCES

1. YanYi, Journal of Northwest Telecommunication Engineering Institute. 14(4)(1987), 92.
2. CCIR, Rep.721-1, 5(1982), 185.
3. YanYi, Chinese Journal of Radio Science, 3(3-4)(1988), 29.

T2.4

MEASUREMENTS OF ATMOSPHERIC ATTENUATION IN THE REGION OF 300 GHz

N. I. Furashov, V. Yu. Katkov and B. A. Sverdlov
Radiophysical Research Institute
Lyadov Street 25/14
Nishniy Novgorod 603600, Russia

An experimental range has been designed to study interaction of millimeter and submillimeter wavelength radiation with the near-ground atmospheric layer. The range consists of a transmitter, a receiver, and a 1-km maximum path length one-way transmission link equipped with meteorological instrumentation. The transmitter and receiver antennas comprise 920-mm diameter mirrors. Backward wave oscillators are used as sources of radiation in the frequency range up to to 1000 GHz. The transmitted and received signals are recorded by pneumatic or crystal detectors.

This paper presents experimental results obtained to date on molecular absorption by water vapor at 260 and 340 GHz as well as on attenuation by hydrometers at 260 GHz. Measurements were carried out at the 1-km path length. Stability of the radio system gain estimated by analyzing the scatter of molecular absorption data and their reproducibility in the similar clear air conditions were no worse than ± 0.2 dB at 260 GHz and ± 0.3 dB at 340 GHz, during a few months. The rapid fluctuations in the received signals caused by atmospheric turbulence had the rms amplitudes of 1-5% and the spectral widths (at half maximum) of 0.3 - 5 Hz.

Molecular absorption by water vapor. By processing jointly new experimental material and the data obtained by us earlier in laboratory and field measurements, a semi-empirical formula has been derived for the atmospheric absorption coefficient Γ (in dB/km) at 340 GHz:

$$\Gamma = (0.107 \pm 0.008)\ 10^{-2}\ e\ P\ (306/T)^{3.3}$$
$$+ (0.012 \pm 0.002)\ e^2\ (306/T)^{12 \pm 5},$$

where e and P are partial water vapor pressure and dry air pressure, respectively, in Torrs; T is air temperature in deg. k, e = 3-25 Torr, T = 269-306 K. This result was one of those used to calibrate an algorithm for computing microwave absorption by water vapor [1]. The absorption coefficient values of 0.7 to 4.4 dB/km measured at 260 GHz in the ranges T = 260-283K, e = 1.3-8.8 Torr (relative humidity up to 100%) coincide with those predicted by the method [1] within the experimental uncertainties. Nearly the same absorptions at 260 and 340 GHz are given by the model

[2] that predicts essentially different (lower) absorption levels than the method [1] does only at frequencies below approximately 50 GHz.

No anomalies of the kind [3-5] (extremely high temperature dependence of the absorption coefficient, effect of sunlight on the absorption) were observed at the measurement frequencies.

Attenuation by rain. To accurately measure the water equivalent precipitation rate R, a high sensitivity precipitation gauge of the weighting type has been constructed. The gauge has a resolution of 0.03 to 0.3 mm/h and a precipitation accumulation time of 60 to 10s.

The measured dependencies of the attenuation coefficient Γ on the rain rate were compared with those calculated for various raindrop size distributions in [6]. As waited, the comparison shows significant variability of size distribution. For example, during a 2.5-h moderate rain accompanied by thunder ($R \leq 20$ mm/h) the averaged experimental dependence $\Gamma(R)$ corresponds to the LP distribution. At the same time, for a 1.5-h period ($R \leq 8$ mm/h) the experimental points were grouped almost continuously in time around a curve calculated for the J-T distribution. The J-d distribution was found to be most appropriate for the prediction of attenuation by a typical autumn light rain ($R \leq 1$ mm/h).

Attenuation by snowfall. On the whole, nine snowfall events have been studied. In four cases, falling show was classified as wet, the others as moist. The average values of specific attenuation were 2.3 dB/km / mm/h for moist snow ($R \leq 1.3$ mm/h, T = -12 - +0.3 C) and 6 dB/km / mm/h for wet snow ($R \leq 0.8$ mm/h, T = +0.3 - +1.6 C). The maximum scatter of the data was about 50%.

Attenuation by fog. A regression relationship between the attenuation coefficient Γ and the visibility V was found to be $\Gamma = 120/V$ (V = 50 - 1000 m, T = +3C). To investigate deeply attenuation by fog, now we are working at the construction of a fog liquid water content meter.

REFERENCES

1. V. Yu. Katkov, "A method for the semi-empirical prediction of microwave absorption by water vapor," Proc. of the 3rd All-Union School on Millimeter nd Submillimeter Wave Propagation in the Atmosphere, Charkov, IRE AN USSR, 1989, pp. 28-29).

2. H. J. Liebs, "MPM - an atmospheric millimeter wave propagation model," Int. J. IR and MM Waves, 1989, vol. 10, no. 6, pp. 631-650.

3. G. A. Tanton, S. S. Mitra, J. D. Stettler, R. L. Morgan, J. F. Osmundsen, and J. G. Castle, "Near-ground atmospheric

attenuation of 0.89 mm radiation," Fourth Int. Conf. on IR and MM Waves, Dec. 10-15, 1979, The Americana of Bal Harbour, Miami Beach, Florida, Post-Deadline digest contributions nd program additions and changes, p. 27.

4. G G. Gimmestad and H. A. Gebbie, "Measurements of near millimeter wave atmospheric attenuation in the temperature range 259 to 282K," Int. J. IR and MM Waves, 1992, vol. 3, no. 1, pp. 77-82.

5. J. M. Galm, F. L. Merat and P. C. Claspy, "Estimates of atmospheric attenuation sensitivity with respect to absolute humidity at 337 GHz," IEEE Trans. Ant. Propag., 1990, vol. 38, no. 7, pp. 982-986.

6. R. L. Olsen, D. V. Rogers and D. B. Hodge, "The aR relation in the calculation of rain attenuation," IEEE Trans. Ant. Propagation., 1978, vol. AP-26, no. 2, pp. 318-329.

T2.5

THE INTEGRATION TIMES AND THE RAINFALL CLIMATIC CLASSIFICATION IN CHINA

Dong Qingsheng
(Qingdao Research Center of CRIRP, Qingdao, China)

ABSTRACT

The statistical characteristics of rainfall intensity observed at a given point will depend on the integration time of the rain gauge. According to the analyses of the experimental data, the conversions between five (ten) minutes and one minute rain rate distributions are discussed in this paper. The one minute rain rate cumulative distributions and the rainfall climatic classifications of the typical regions in china are given too.

INTRODUCTION

The rainfall can cause the serious attenuation and depolarization in MM wave band. It is important to research the statistical characteristics of rainfall intensity. Because of the rapid varying nature of the rain rate at a given point the cumulative rain rate distribution observed will depend on the integration time of the rain gauge and the different integration times of the gauge will result in the different statistical characteristics of rain rate. The rainfall with high intensity, rain storm or heavy rain, tends to be concentrate in a short period of time, typically a few minutes. A short integration time of one minute will be appropriate for the purposes of the rain attenuation prediction and of the rainfall climatic classifications because longer integration time will smooth the peak value of the rainfall intensity. The long_term rain rate distributions with five or ten minutes integration time are readily available in the radio meteorological services in China. It is urgent need that these data are converted to equivalent one minute rain rate distributions in order to complete the rainfall climatic classification in China. According to the analyses of the experimental data the conversions between one minute and five(ten) minutes rain rate distributions are discussed in this paper. The equivalent cumulative distributions of the one minute rain rate and the rainfall climatic classifications of the tpical regions in China are given.

THE DISCUSSIONS FOR APPROXIMATE CONVERSION FORMULA

Resent analyses suggest that the rain rate distribution is better described by a model[1], i.e.

$$P(R>r) = a\cdot\exp(-ur)/r^{b} \quad (1)$$

where

$$b=8.22\cdot R_{0.01}^{-0.584} \quad (2)$$

$$a= 0.0001\cdot R_{0.01}^{b}\exp(uR_{0.01}) \quad (3)$$

$$u=0.015_0.045 \quad (4)$$

The accurate value of u not only depend on the geographical features of a region but also depend to the integration time of the rain gauge.[2] Let $P_1(R_1)$ and $P_t(R_t)$ be the rain rate distributions with one minute and t minutes (five minutes or ten minutes) integration time at a given point respectively. Then,

$$P_1(R_1) = a_1 \exp(-u_1 R_1)/R_1^{b_1} \quad (5)$$

$$P_t(R_t) = a_t \exp(-u_t R_t)/R_t^{b_t} \quad (6)$$

Let $R_1=R_t=R$, i.e. corresponding to the same rain intensity, and $u_1 \doteq u_t$ where this is a approximation between one minute integration time and five(ten) minutes integration times, a approximate conversion formula can be obtained:

$$P_1(R)/P_t(R) \doteq (a_1/a_t)R^{b_t-b_1} \doteq A \cdot R^B \quad (7)$$

The formula (7) is used to provide the conversion between the rain rate distributions with integration times of five (or ten) minutes and one minute. The coefficients A and B will be determined by the regressive analyses of the experimental data.

THE REGRESSIVE ANALYSES OF THE EXPERIMENTAL DATA

In order to determine the coefficients A and B, the rain rate is measured on the different integration times, one minute, five and ten minutes, at Xingming, Henan(1981_1983, with tipping_bucket rain gauge), Qingdao, Shandong(1986_1988, with the tipping_bucket rain gauge) and Guangzhou, Guangdong(1989_1990, with photoelectric gauge) respectively. Because the influence of integration time is most evident in the heavy rain and the rainstorm, the rain rate data of 960 minutes and 1030 minutes are collected from 16 heavy rain or rainstorm in 1981_1983 at Xingxiang and from 28 heave rain or rainstorm in 1986_1988 at Qingdao respectively. The coefficients A and B are determined by the logarithm regression of the experimental data:

$$P_1(R)=0.0030\,R^{1.076}\ P_5(R) \quad \text{at Qingdao} \quad (R>30\ \text{mm/h}) \quad (8)$$

$$P_1(R)=0.001\,R^{1.817}\ P_{10}(R) \quad \text{at Qingdao} \quad (R>30\ \text{mm/h}) \quad (9)$$

$$P_1(R)=0.1130\,R^{0.598}\ P_5(R) \quad \text{at Xingxiang} \quad (R>30\ \text{mm/h}) \quad (10)$$

$$P_1(R)=0.0004\,R^{1.642}\ P_{10}(R) \quad \text{at Xingxiang} \quad (R>30\ \text{mm/h}) \quad (11)$$

$$P_1(R)=0.0150\,R^{1.190}\ P_{10}(R) \quad \text{at Guangzhou} \quad (R>30\ \text{mm/h}) \quad (12)$$

where $P_1(R)$, $P_5(R)$ and $P_{10}(R)$ is the probability of rain rate R with one minute, five minutes and ten minutes respectively. The comparisons of the conversion values obtained from eqs. (8)~(12) and the measuremental values indicate that the conversion formula can well describe the conversion relationship between the rain rate cumulative distributions with different integration time. The error is less than 7% and 10% when $P_1(R)$ is obtained from $P_5(R)$ and $P_{10}(R)$ respectively.

The rainstorm data collected at Qingdao, Xingxiang and Guangzhou belong to the I, II and III zone in CCIR rain climatic classification respectively. In order to examine the validity of the conversion formula, the long_term cumulative distribution values of rain rate from Ottawa, Canada[5](H zone) and Finland[4](E zone) are regressed. As same as above, we can obtain:

COPY AVAILABLE TO DTIC DOES NOT PERMIT FULLY LEGIBLE REPRODUCTION

$$P_1(R)=0.1020\ R^{0.670}\ P_5(R) \quad \text{at Ottawa} \quad (R>20\ mm/h) \quad (13)$$

$$P_1(R)=0.0500\ R^{0.806}\ P_{10}(R) \quad \text{at Ottawa} \quad (R>20\ mm/h) \quad (14)$$

$$P_1(R)=0.4900\ R^{0.280}\ P_5(R) \quad \text{at Finland} \quad (R>15\ mm/h) \quad (15)$$

$$P_1(R)=0.1320\ R^{0.780}\ P_{10}(R) \quad \text{at Finland} \quad (R>15\ mm/h) \quad (16)$$

The error analyses shown that the conversion error is less than 10% at Ottawa and 5% at Finland.

RAINFALL CLIMATIC CLASSIFICATION OF THE TYPICAL REGIONS IN CHINA

Because of the lack of the rain rate data with one minute integration time, the rainfall climatic classification in China is very rough in CCIR Report 563. It may be believed that there are same conversion relationship between rain rate distributions with different integration time in the same rainfall climatic zone. Therefor by means of the above conversion formula (8)_(16) (corresponding to L, M, N, K and E zone respectively) and the long_term rain rate cumulative distributions (>10 years) with five or ten minutes integration time[3-7], the equivalent one minute rain rate cumulative distributions and the rainfall climatic classification at the typical regions of China are shown at Tab.1.

Table 1 Equivalent one minute rain rate cumulative distribution (mm/h)

Region	Location	Time probability % 0.03	0.01	0.003	0.001	Rain climatic zone
Beijing	39°48′N 116°28′E	40	56	84	117	M
Zhenzhou	34°43′N 113°39′E	42	58	82	114	M
Jinan	36°41′N 116°59′E	41	71	112	152	L
Qingdao	36°04′N 120°19′E	27	58	107	158	L
Nanjing	32°19′N 118°48′E	37	65	105	146	L
Nanchang	28°40′N 115°58′E	46	74	107	144	L
Taiyuen	37°47′N 112°33′E	17	32	61	98	K
Nanzhou	36°03′N 103°53′E	16	26	45	65	E
Yinchuan	38°24′N 106°13′E	11	22	44	65	E
Nanning	22°49′N 108°21′E	78	114	155	195	N
Guangzhou	23°08′N 113°19′E	81	116	159	198	N

REFERENCES

1. CCIR Document 5/377_E 1986_1990.
2. Dong, Q.S., Proceeding of 5th NC MMW_SUBMMW 169_173, 1991.
3. Segel, B., Ann des Telecommunic. 35 434_438, 1980.
4. Project COST 205, Alta Frequenza vol.LIV 3 116_132, 1985.
5. Dong, Q.S. and Wu, Z.Z., Report for MMWP Workshop, France, 1990.
6. CCIR Document 5/305_E 1989.
7. Chou, S.B. et al., Report of CRIRP, 1989.

T2.6

MM WAVE PROPAGATION EXPERIMENT IN SAND DUST STORM AND SMOKE

Dong Qingsheng
(Qingdao Resrarch Center of CRIRP, Qingdao, China)

ABSTRACT

The situation of the MM wave propagation experiment in the sand dust storm and smoke at Jinan, Shangdong, China are introduced and the attenuation by the sand_dust storm and smoke are discussed.

INTRODUCTION

The absorption and the scattering of flying dust particle and smoke can cause the extinction of signal energy. The attenuation depends on the physical characteristics of the dust particles and smoke, for exemplar the shape, the size distribution and the permittivity. Because of the lack of knowledge of the physical characteristics, it is very difficult for the calculation and the model analyse of the attenuation due to the sand_dust storm and the smoke in MM wave band. The direct propagation measurements are desired. A MM wave propagation experiment in sand-dust storm and smoke is completed by Qingdao Research Center of CRIRP at Jinan(36°41′N,116°59′E), China in Apr. 1991. The frequencies of MM wave propagation path are 35 GHz, 72 GHz and 93 GHz. The length of the path is 770 m and 130 m respectively. At first, the 770 m experiment path is seted up at the large sandhill area closed to Yellow River to measure the attenuation due to flying sand-dust particles by wind and due to smoke. At second, the 130 m experiment path is seted up at a sandy road to measure the signal attenuation due to the sand-dust storms by high speed travel of a vehicle. The measurement systems of the experiment path are made up of the MM wave measurement system, the visibility instrument, the precipitation integration instrument and meteorological instruments as shown as Fig.1. The performences of MM wave measurement system are indicated at Tab.1. In the following sections the experiment data about the physical characteristics of sand-dust particles and the attenuation due to sand-dust storms and smoke are discussed.

Tab.1 The Performence of MM Wave Measurement Systems

		Transmitter			Receiver		
Frequency	GHz	35	72	93	35	72	93
Antenna		Cassegrain			Horn	Cassegrain	
Aperture	CM	60	50	50	4.5	50	50
Gain	dB	45	50	53		50	53
Dynamic range	dB				45	45	45
Discriminability	dB				0.1	0.1	0.1

MM WAVE PROPAGATION IN THE SAND-DUST STORMS

2.1. The Physical Characteristics Of The Sand Dust Particles.

COPY AVAILABLE TO DTIC DOES NOT PERMIT FULLY LEGIBLE REPRODUCTION

The sand-dust particles can cause the absorb and the scattering of MM wave signal. Assume the shape of the particle is sphere, we can obtain the attenuation by the Rayleigh approximation:

$$A = 1.029*10^{6}\cdot \varepsilon''/(\lambda((\varepsilon'+2)^{2}+\varepsilon''^{2}))\int_{0}^{\infty} r^{3}N(r)\,dr \quad dB/km \qquad (1)$$

where $\varepsilon=\varepsilon'-j\varepsilon''$ is the permittivity of the sand-dust particle. Therefore the attenuation due to the sand-dust storm will depent on the particle shape, the particle size distribution and the permittivity.

(1). The Particle Size Distribution.

The measurement results of the six samples of the flying sand-dust particle in the experiments are shown in Tab.2. It is evident that the particles with size range 0.04-0.15 mm are about 80% of total number.

Tab.2 The Size Distribution Of The Sand-Dust Particles

	Probability %					
Diameter mm	Sample 1	2	3	4	5	6	Mean
0.30>D>0.15	25	5	20	10	0	0	10
0.15>D>0.10	20	20	20	35	5	10	18
0.10>D>0.05	30	60	45	50	65	60	52
0.05>D>0.04	15	5	10	3	20	25	13
0.04>D>0.02	5	5	5	2	10	5	5.3
0.02>D	5	5	0	0	0	0	1.7

(2). Particle Shape.

The particle shape is very irregular. The shape analyses of two typical samples are shown in Tab.3. It is clear that the shape of most particles is non-spheric.

Tab.3 The Shape Of The Sand-Dust Particles

	Sphere		Spheroid		Edge type	
Diameter mm	Sample 1	Sample 2	1	2	1	2
0.30>D>0.15	20	0	20	0	60	100
0.15>D>0.10	25	15	25	10	50	75
0.10>D>0.05	16	34	34	16	50	50
0.05>D>0.04	30	40	30	0	40	60
0.04>D>0.02	40	40	0	0	60	60
0.02>D	0	0	40	0	60	0

(3). Complex Permittivity.

The permittivity of the sand-dust particle will depends on the moisture content. The measurement data of the permittivity are vsry scarce in MM wave band. The measurement values of the permittivity of the sandy soil collected in the experiment at 33.5 GHz are shown in Tab.4.

Tab.4 The Permittivity Of The Sand-Dust[5,7]

Frequency	Soil Type	Moisture Content %	Permittivity
33.5 GHz	Sandy soil	0	2.51-j0.0343
		1	3.11-j0.1240
		2	3.34-j0.2880

2.2. The Attenuation Of Flying Sand-Dust By Wind.

At the first, the experimental instruments shown in Fig.1 are installed at a 770 m propagation path. The maximum wind speed is about 8 m/s in the experimental period. The flying particles of the sand-dust can be observed at the altitude above 1 m corresponding to the visibility is

less than 2 km. There is only a smaller change of the signal level, ± 0.2 dB/km, at 93 GHz and non change is observed at 35 GHz and 72 GHz.

2.3. The Attenuation Due To The High Speed Travel Of The Vehicle.
As the second, the measuremental instruments are installed at a 130 m sandy road. The altitudes of the transmissive and the receive antennas are all about 2 m. The dense dry sand-dust storm due to the high speed travel of a truck can be maintained about 10 seconds above the path. The visibility is less than 2 m at the storm. The attenuation of the signal is recorded at the same time. The eight valid data are shown at Tab.5. The maximum attenuation is about 0.75 dB/km at 93 GHz and there are not level changes at 35 and 72 GHz. To take an average, the dense dry sand-dust storm with the length of 90 m only causes the attenuation of 0.6 dB/km at 93 GHz. Therefore, the influence of the dry sand-dust storm should be negligible when the frequency is less than 100 GHz.

Tab.5 The Attenuations Due To The Sand-Dust Storm By The Vehicle
(Frequency: 93 GHz)

Sample	1	2	3	4	5	6	7	8	Mean
Storm Length m	40	70	80	80	110	110	120	110	90
Attenuation dB/km	0.75	0.43	0.60	0.60	0.70	0.50	0.70	0.50	0.60

THE ATTENUATION DUE TO SMOKE

The smoke by the explosion or the burn can cause the attenuation of MM wave. The research of the attenuation by smoke will mainly depend on the direct experiment measurement because of the uncertainty of the permittivity of smoke. The propagation experiment in smoke is completed at a 770 m path on a non-wind day. The burn of the firewood and the grass poured by the engine oil can produce dense smoke with the length of 100 m along the path. The typical measurements of the attenuation and visibility are shown at Fig.2. The data are discussed for the "burn period" and the "smoking period" respectively. In the "burn period", the flame rise to the sky but the smoke is weaker and the visibility is greater, the strong fluctuates of the signal level with the amplitude variances of ±7 dB/km and ±2 dB/km are observed at 93 GHz and 72 GHz, respectively. The frequency ranges of the scintillation are about 0.5~2 Hz at 93 GHz. In the "smoking period", the burn is near stop and the smoke reach the most dense situation with the least visibility, the small variances of the signal level with the amplitude of ±1 dB/km are observed at 93 GHz and non changes of the signal level are observed at 35 GHz and 72 GHz. It is evident from above discussions that the dense smoke can only cause very small variance of the signal level, typically ±1 dB/km at 93 GHz, but the strong fluctuate of the signal level, typically ±7 dB/km at 93 GHz and ±2 dB/km at 72 GHz, can be observed in the "burn period". The main reason caused above phenomenon is probably from the fact that the notable variance of water vapour in the "burn period" will result in the notable variance of the imaginary part of the permittivity of the smoke particles and the strong fluctuate of the signal level will be caused.

CONCLUSIONS

According to above discussions of the experimental results, some interested conclusions can be obtained:
1). The very small attenuation are caused by the dense sand-dust storm, with the visibility of a few meters, composed of the flying particles of the dry sand-dust due to the high speed travel of the vehicle at the frequency range below 100 GHz, typically 1 dB/km at 93 GHz.

2). The dense smoke due to the burn of the firewood and grass poured by engine oil can only cause very small variances of the signal level typically ±1 dB/km at 93 GHz, in the "smoking period". But the strong fluctuate of the signal level, typically ±7 dB/km at 93 GHz and ±2 dB/km at 72 GHz, are caused in the "burn period". The reasonable explain is possibly that the notable variances of the water vapour in the "burn period" will result in the notable variances of the imaginary part of the permittivity of the smoke particles and then the strong fluctuate of the signal level will be caused.

3). The shape of most of the sand-dust particles is non-spheric and the maximum equivalent diameter is less than 0.3 mm. The particles with the diameter 0.04-0.15 mm will be greater than 80% of the total number.

ACKNOWLEDGMENT

Many thanks to D.Z. Hu, J.Q. Zhao, J. Huang, Z.W. Zhao, H.J. Chong Z.C. Wu and S.P. Wang for their contributions to this experiment and the helpful discussions.

REFERENCES

1. Zhao, Z.W., Report of CRIRP, 1991.

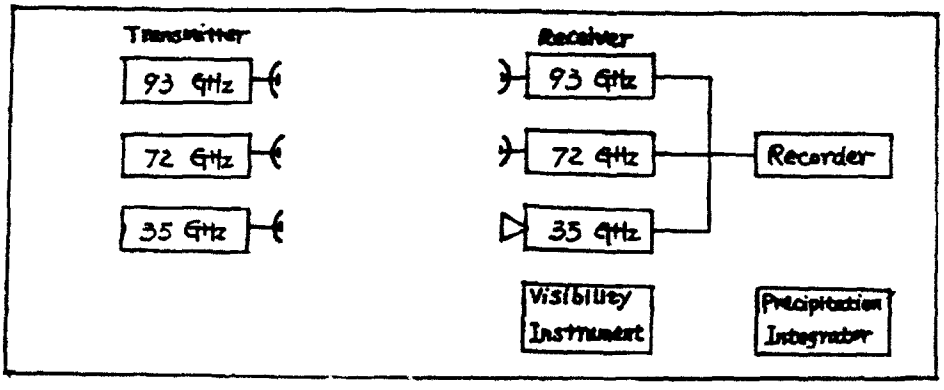

Fig.1. The measurement systems

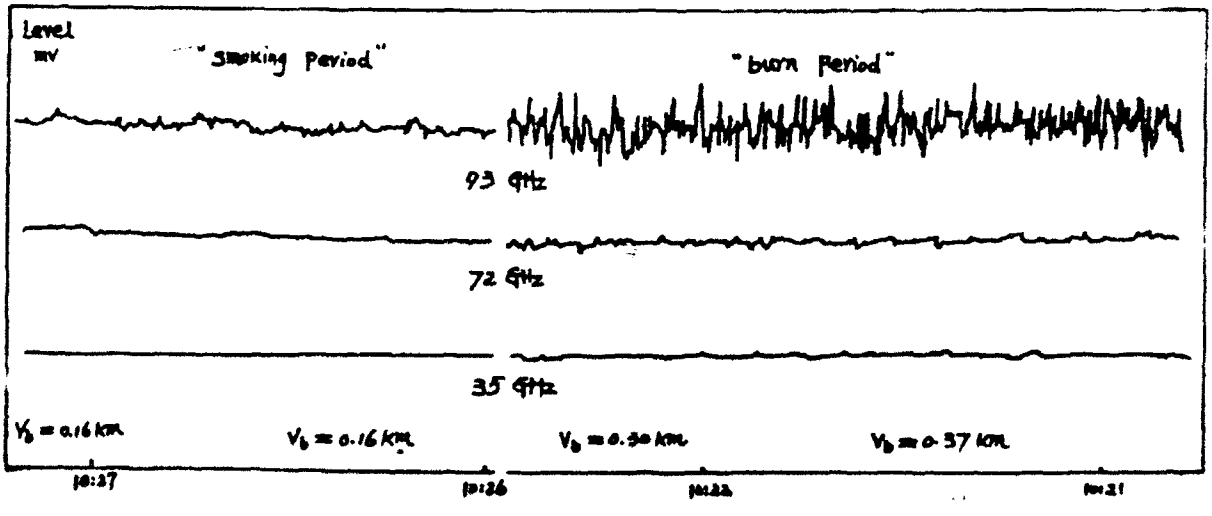

Fig.2. Attenuation due to smoke

T3.1

COMPARISON BETWEEN THE FEL READIATION AND CYCLOTRON RADIATION

Yin Yuanzhao
(Institute of Electronics, Academia Sinica, Beijing, China)

ABSTRACT

In FEL, there are two kinds of radiations: the free electron laser radiation (FELR) and the cyclotron radiation (CR). This paper has theoretically pointed out that if the initial transverse velocity of the electron beam is large and the parameters of FEL are not suitable, CR will dominate, especially when the energy of electron beam is low. But CR do not have double Doppler frequency upshift and with the limitaion of the guide magnetic field, its radiation frequency is much smaller than FELR. Therefore, it is very important to distinglish these two radiations and to suppress CR.

INTRODUCTION

In FEL, under the action of the guide magnetic field, the beam will do cyclotron motion. This cyclotron motion can interact with the electromagnetic wave and produce a coherent stimulated radiation, that is, the cyclotron radiation (CR). At the same time, under the action of the wiggler, the beam will do periodic movement which interacts with the electromagnetic wave too and produce another coherent stimulated radiation, that is the free electron laser radiation (FELR). Therefore, in FEL the two mechanisms for both FELR and CR exist. This paper shows when the beam energy is high and its initial transverse velocity is small, the frequency and growth rate of FELR is much larger than CR, so CR do not play any significant role. But on the contrary, the frequency of CR will be close to FELR and CR growth rate will become large, CR can not be neglected.

THE DISPERSION RELATIONS

We assume the static magnetic field is composed of the bifilar helical wiggler and the guide magnetic field:

$$\overline{B}_0 = B_w[cos(k_w z)\hat{e}_x - sin(k_w z)\hat{e}_y] + B_{//}\hat{e}_z$$

where B_w and $B_{//}$ is the wigger and guide magnetic fields, $k_w = 2\pi / \lambda_w$ and λ_w are the

wavenumber and wavelength of the wigger. The electromagnetic wave is a plannar wave, $\bar{E} = E_x \hat{e}_x$, $\bar{B} = B_y \hat{e}_y$. Take the electron motion in the static magnetic fields as the zero order, solve the equation of electron motion

$$d\bar{v}/dt = -e/(m_0\gamma)[\bar{E} + \bar{v} \times (\bar{B} + \bar{B}_0)/c - \bar{v}(\bar{v} \cdot \bar{E})/c^2]$$

the equation of continuity

$$\nabla \cdot (N\bar{v}) + \partial N/\partial t = 0$$

and the wave equation

$$\nabla \times (\nabla \times \bar{E}) + (1/c^2)\partial^2 \bar{E}/\partial t^2 = -(4\pi/c^2)\partial \bar{j}/\partial t$$

together, by making use of the Maxwell equation

$$\nabla \times \bar{E} = -(1/c)\partial \bar{B}/\partial t$$

and the rf current dencity

$$\bar{j} = -eN\bar{v}$$

after some tedious algebra, we obtain the dipersion relations: for FEL mode

$$[\omega^2 - c^2k^2 - \omega_p^2(\omega - kv_{\parallel})^2/((\omega - kv_{\parallel})^2 - \Omega_{\parallel}^2)][\omega - (k + k_w)v_{\parallel}]^2$$
$$= (\omega_p^2/4)v_w(k + k_w)[v_w(ck - \beta_{\parallel}\omega) - \Omega_w(\omega - kv_{\parallel})/(\omega - kv_{\parallel} - \Omega_{\parallel})] \quad (1)$$

for CR mode

$$(\omega^2 - c^2k^2)(\omega - kv_{\parallel} - \Omega_{\parallel})^2$$
$$= (\omega_p^2/4)v_{\perp}^2(ck - \beta_{\parallel}\omega)(k + \Omega_{\parallel}/v_{\parallel})/c \quad (2)$$

where $\omega_p = (4\pi e^2 n_0/(m_0\gamma_0))^{1/2}$ is the plasma frequency, $\Omega_{\parallel} = eB_{\parallel}/(\gamma_0 m_0 c)$ and $\Omega_w = eB_w/(\gamma_0 m_0 c)$ are the cyclotron frequecies in the guide and wigger magnetic fields, $v_{\parallel}$ and $v_{\perp}$ are the initial axial and transverse velocities of electron, respectively. $v_w = \Omega_w v_{\parallel}/(\Omega_{\parallel} - k_w v_{\parallel})$ is the transverse velocity of electron caused by the wiggler.

RESULTS AND DISCUSSION

From the dispersion relations (1) and (2), we can obtain the radiation frequencies ω_{rFEL} and ω_{rC} and the growth rates ω_{iFEL} and ω_{iC} for the FEL mode and CR mode, respectively, as follows:

$$\omega_{rFEL} = (1+\beta_{\parallel})\gamma_{\parallel}^{2} v_{\parallel} k_{w} \tag{3}$$

$$\omega_{rC} = (1+\beta_{\parallel})\gamma_{\parallel}^{2} \Omega_{\parallel} \tag{4}$$

and

$$\omega_{iFEL} = (\sqrt{3}/4)\omega_{p0}^{2/3}[\beta_{w}^{2}(1+\beta_{\parallel})ck_{w}/(\beta_{\parallel}\gamma_{0})]^{1/3} \tag{5}$$

$$\omega_{iC} = (\sqrt{3}/4)\omega_{p0}^{2/3}[\beta_{\perp}^{2}\Omega_{\parallel 0}/\beta_{\parallel}\gamma_{0}^{2})]^{1/3} \tag{6}$$

where $\Omega_{\parallel 0} = eB_{\parallel}/(m_0 c)$ is the nonrelativistic cyclotron frequency in the guide field, $\omega_{p0} = \omega_{p}\gamma_{0}^{1/2}$, $\beta_{\parallel} = v/c$, $\beta_{\perp} = v_{\perp}/c$, $\beta_{w} = v_{w}/c$, $\gamma_{0} = (1-\beta_{\parallel}^{2}-\beta_{\perp}^{2})^{-1/2}$, $\gamma_{\parallel} = (1-\beta_{\parallel}^{2})^{-1/2}$.

The radiation frequencies and growth rates for the FEL mode and CR mode as a function of the electron beam energy E, the guide magnetic field $B_{\parallel}$ and the initial transverse velocity $\beta_{\perp}$ of the electron beam have shown in Figs.1,2 and 3, respectively. From these figures, we can see FEL mode has the resonance property, the resonance condition is $\Omega_{\parallel} - \beta_{\parallel} ck_{w} = 0$, according to Eqs. (3) and (4), this is just the same condition for $\omega_{rFEL} = \omega_{rC}$. This condition has been expressed by a dot–and–dash line in Figs.1 and 2. Obviously, in experiments we should avoid the resonance, but we can properly approach it to increase the FELR growth rate. The CR mode does not have the resonance property. The FELR growth rate increases when the wiggler field increases. The CR growth rate increases when the guide magnetic field and initial transverse velocity of electron increase. Because the guide magnetic field must strong enough, the best way to suppress CR is to reduce the initial transverse velocity of the electron beam as low as possible. Generally, the initial transverse velocity of electrons has little influnce on the frequencis of FELR and CR and the FELR growth rate. The FELR has the double Doppler frequency upshift property, its frequency is approximately propotional to the electron energy square. But the CR do not have the double Doppler frequency upshift property, its frequency is approximately propotional to the electron energy and axial magnetic field. Obviousely, the most effective way to increase the FEL frequency is to increase the electron energy. Under the certain condition, it will make the FELR growth rate smaller than CR.So it becomes more important to reduce the initial transverse velocity of electron beam in order reduce the CR growth rate in free electron lasers.

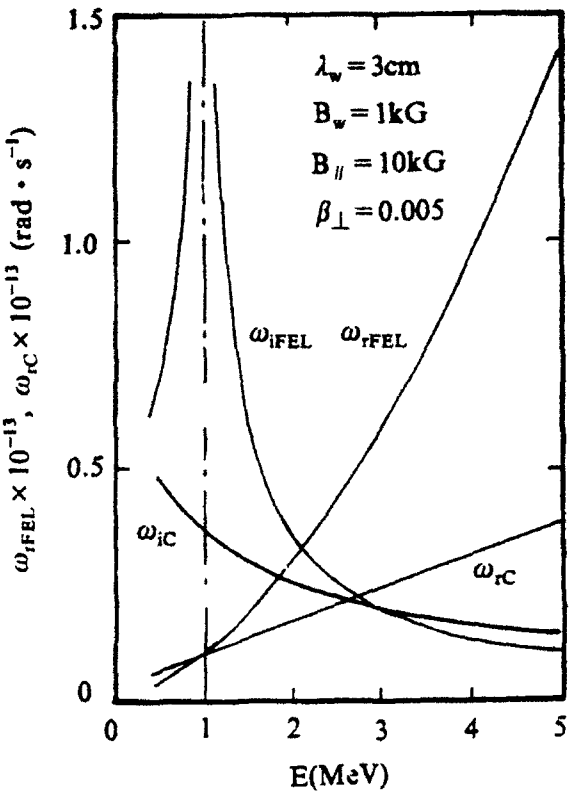

Fig.1

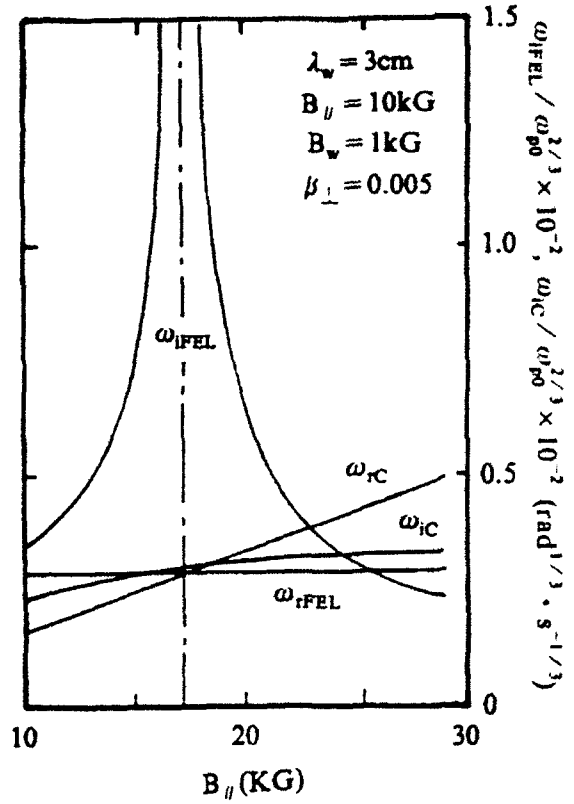

Fig.2

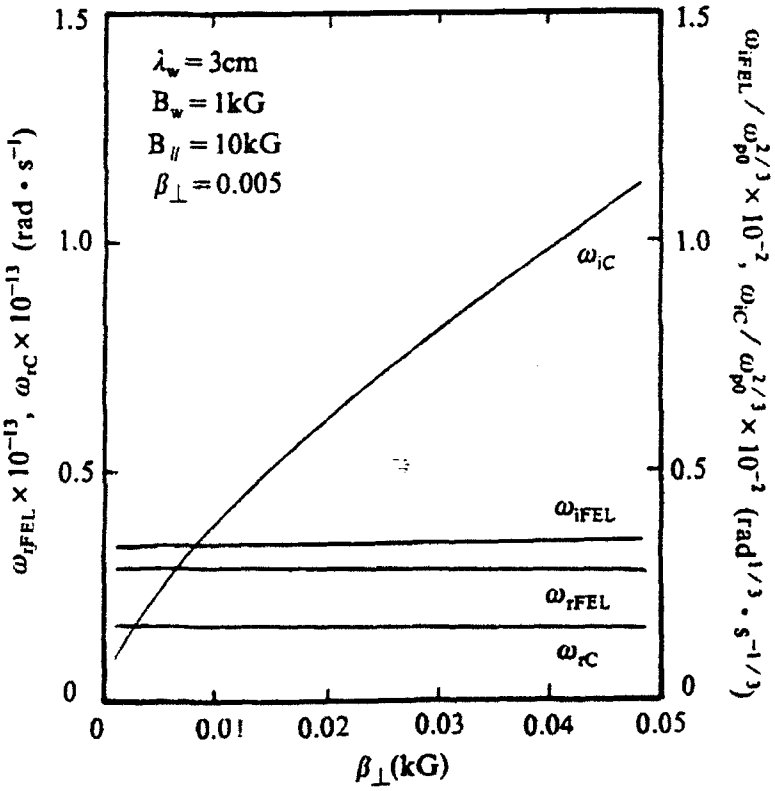

Fig.3

T3.2

FREE ELECTRON LASER WITH ELECTRON RING AND ELECTROMAGNETIC PUMPING WAVE

Yin Yuanzhao
Institute of Electronics, Academia Sinica, Beijing, China)

ABSTRACT

A free electron laser with electron ring and electromagnetic pumping wave is studied. The drifting and rotating electron ring of large radius goes through a cylindrical waveguide and interacts with its TE mode. By making use of the Vlasov distribution theory and three dimensional wave equation, the dispersion relation of the scattered wave in the Compton region has been deduced. According to the numerical analysis, the growth rate and radiation frequency of the scattered wave as a function of the guide magnetic field, electron beam energy, electron rotating ratio and radial position of electron ring have been discussed.

INTRODUCTION

The free electron lasers can produce coherent radiation from millimeter and submillimeter to optical range and as tunnable high power lasers are rapidly developing in the recent two decades. In most FEL researches, the static magnetic wiggler is used. In this paper the traveling electromagnetic wave as a wiggler (EM wiggler) is studied, that is, the electromagnetic wave propagating in the direction against the electron beam motion acts as a pumping wave and is scattered by the electron beam. In comparison with the static magnetic wiggler, this kind of EM wiggler has very short wavelength and can be used in the two–stage FEL.

THE DISPERSION RELATION

The relativistic motion equation of electron in the guide magnetic field is

$$d\bar{v}/dt = -e/(\gamma m_0)[\bar{E} + \bar{v} \times (\bar{B} + \bar{B}_{//})/c - \bar{v}(\bar{v} \cdot \bar{E})/c^2] \qquad (1)$$

where $\bar{B} = B_{//}\hat{e}_z$ is the guide magnetic field. $\bar{E} = \bar{E}_1 + \bar{E}_2$, $\bar{B} = \bar{B}_1 + \bar{B}_2$, $\bar{E}_1$, $\bar{B}_1$ and $\bar{E}_2$, $\bar{B}_2$ are the electric and magnetic fields of the pumpimng wave and scattered wave, respectively. For the TE modes of cylinderical waveguide, their z–components are

$$B_{z1} = \frac{1}{2} A_1 J_{l1}(k_{c1} r) exp[-i(k_1 z + l_1 \theta + \omega_1 t)] + c.c., \quad E_{z1} = 0$$

and

$$B_{z2} = \frac{1}{2} A_2 J_{l2}(k_{c2} r) exp[i(k_2 z + l_2 \theta - \omega_2 t)] + c.c., \quad E_{z2} = 0$$

The other components can be obtained by making use of the Maxwell equations.
The longitudinal wave equation of the scattered wave is

$$[\nabla^2 - (1/c^2)\partial^2/\partial t^2] B_{z2} = -4\pi(\nabla \times \bar{j})_z / c \tag{2}$$

The pertubated current dencity $\bar{j}$ can be obtained from the pertubated velocity and distribution function.
Under the action of the guide magnetic field, the pumping and scattered wave, the discribution function of the relativistic electron ring is determined by the following Vlasov equation:

$$\partial f(\bar{p},\bar{r},t)/\partial t + \bar{v}(\bar{r},t) \cdot \partial f(\bar{p},\bar{r},t)/\partial \bar{r} - e\{\bar{E}(\bar{r},t) + \bar{v}(\bar{r},t) \times [\bar{B}(\bar{r},t) + \bar{B}_{\parallel}]/c\} \cdot \partial f(\bar{p},\bar{r},t)/\partial \bar{p} = 0 \tag{3}$$

We choose the equilibrium distribution according to the properties of electron beam as follows:

$$f^{(0)}(p_\theta, p_Z, P_\theta) = n_0 R_0 \oplus [\triangle^2 - (p_\theta - \hat{p})^2] \delta(P_\theta - P_0) \delta(p_Z - \gamma_0 m_0 v_{\parallel})$$

where n_0 and R_0 is the equiliblium density and radius of the beam, $\hat{p}$ is the average azimuthal momentum, $\triangle$ is the momentum spread, $P_\theta = r(p_\theta - eB_{\parallel} r/(2c))$ is the canonical azimuthal momentum, $\oplus$ is the Heaviside step function and $P_0 = eB_{\parallel}(R_0^2 + a_0^2)/(2c)$. The equilibrrium velocity $\bar{v}_0 = v_{\theta 0}\hat{e}_\theta + v_{\parallel}\hat{e}_z$. Expand the velocity and distribution function of the electron ring:

$$\bar{v} = \bar{v}_0 + \bar{v}^{(1)}, \quad f = f^{(0)} + f^{(1)} + f^{(2)}$$

and solve Eq. (1), (2) and (3) together, only keep the beat terms of the pumping wave and scattered wave, which satisfy the following relations:

$$\omega = \omega_2 - \omega_1, \quad k = k_1 + k_2, \quad l = l_1 + l_2$$

we get the dispersion relation:

$$(\omega_2^2 - c^2 k_2^2 - c^2 k_{c2}^2)(\omega - v_{\parallel} k - l\Omega_{\parallel})^2 = \omega_p^2 C^3 \tilde{A}_1^2 F J_{l2}(k_{c2} R_0)(Q - l_2 S_5) S_6 / (8\gamma_0^2 R_0^3 D_{l2} \Omega_{l1}^2 \Omega_{l2})$$

THE NUMERICAL ANALYSIS AND DISCUSSION

The growth rate ω_i as a function of the azimuthal mode number l_2 is shown in Fig.1. the maxium growth rate ω_{imax} in Fig.1, its corresponding frequency ω_2, azimuthal mode number l_2 and electron rotating ratio α as a function of the radial position R_0 of electron ring are shown in Fig.2. Here the electron rotating ratio $\alpha = v_{\theta 0} / v_{//}$ is defined as the ratio between the azimuthal and axial components of electron velocity in equilibrium. From Figs.1 and 2, we can see when R_0 increases and is close to the waveguide wall, ω_{imax} increases and moves to larger l_2. At the same time, ω_2 and α increase. This is a very interesting result. It means in practice the electron ring should be close to the waveguide wall. In order to show the working property of low energy electron ring, as a example, Fig.3 is presented.

As a conclusion, we point out that in the electromagnetic wave pumping case, the rotating electron ring provides saveral advantages: frist, by suitablely choosing parameters, we can increase the electron rotating ratio to make the growth rate increase. Terefore, it meams the guide magnetic field not only focuses the electron beam and prevents it from divergence but also makes the beam rotate with large radius, increases the effective distance of interaction between the electrons and the elctromagnetic waves, so that the growth rate will inhance and the device can be very compact. Second, when the electron ring is close to the waveguide, both the growth rate and radiation frequency will increase. This is useful to get higher frequecy with a electron beam of lower energy. Third, by shoosing parameters properly, it is possible to make the electron ring to produce high frequency radiation for which generally a high energy beam is needed. Fourth, We can use this electron ring to make a two-stage FEL. In the first stage, this ring produces the CARM radiation. Then this powerful radiation propagates through the second stage FEL interaction region as a traveling wave in the same waveguide where the interaction happens as described in this paper. We hope by adjusting α we will be able to made the whole device shorter and get higher output power.

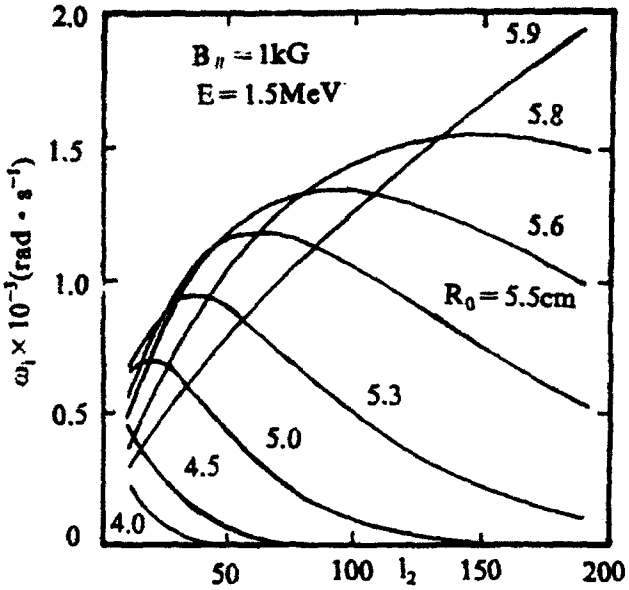

Fig.1

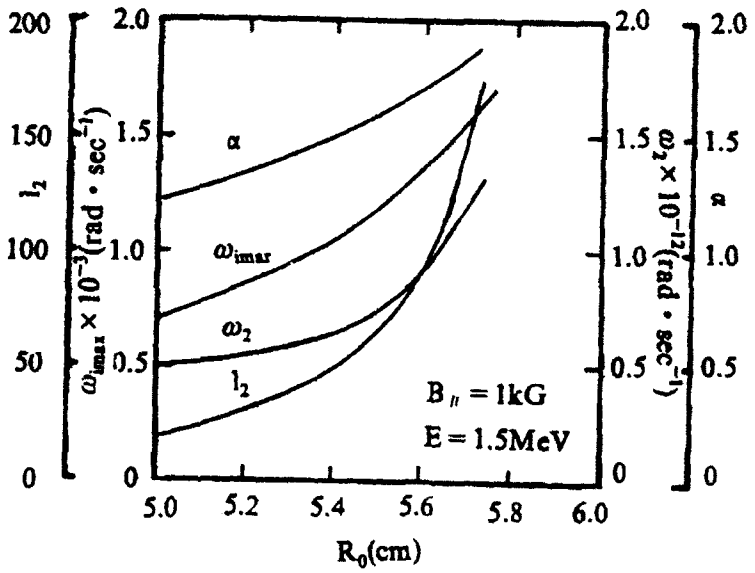

Fig.2

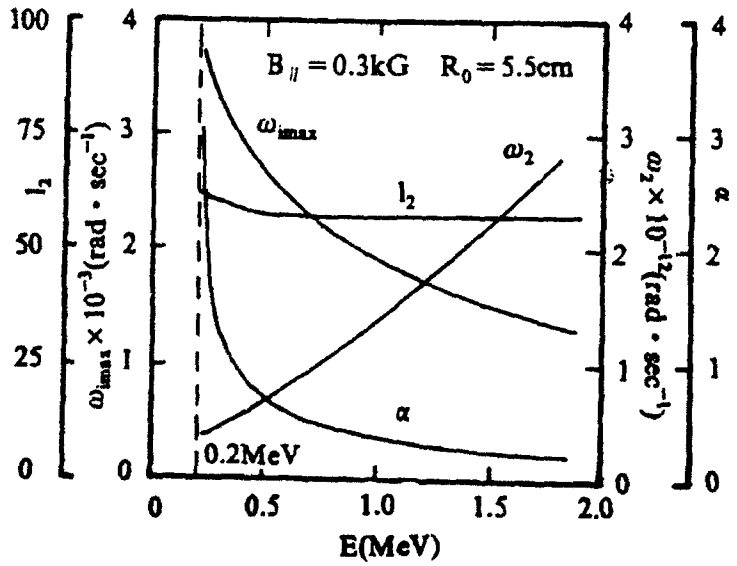

Fig.3

T3.3

SIMULATION OF FEL PUMPED BY ELECTROMAGNETIC WAVE IN THE RELATIVISTIC BACKWARD WAVE OSCILLATOR

Tianquan Deng

(*Institute of High Energy Electronics, University of Electronic Science and Technology of China, Chengdu* 610054, *P. R. China*)

ABSTRACT

The theory of stimulated scattering of electromagnetic waves by high-current relativisitic electron beams is devoleped with the transverse inhomogeneity of incident and scattered waves, and the presence of a magnetic field of 20 kG focusing the particles taken into account. The nonlinear results including the coupling coefficient versus the longitudinal magnetic field and the radius of electron beam, the excitation curves, powers and efficiency etc. are obtained on a set of input parameters of our recently established accelerator and FEL system with an electron energy of 600 keV and a current of 3 kA. It is shown that the electrodynamic system of backward wave oscillator (BWO) in the form of a cylindrical waveguide with a periodically corrugated wall can have a high Q-factor for oscillations at wavelenghts much shorter than the corrugation period of 1. 95 cm and the wavelengths of incident pump waves. The relativistic 3. 2 cm backward wave oscillator provided powerful scattered radiation at 3—8 mm with integral power of 30 MW and efficiency up to 13%

INTRODUCTION

Free electron lasers (FEL' s) have the potential of providing very high-power, continuously tunable, coherent radiation over an extensive range of wavelengths, many applications in military, industrial, agricultural, medical and biological areas etc. and are currently the subject of an intensive research effort[1]. More attention has been paid to the electromagnetically pumped free electron laser (EM—FEL) in recent years because EM—FEL enables significant increases in the radiation frequency ($\lambda \approx \lambda_w/4\gamma^2$) for the same beam parameters (as compared to the magnetostatic wiggler-driven FEL, $\lambda \approx \lambda_w/2\gamma^2$) and continuous tunability by changing the electromagnetic pump frequency.[2,3] In the EM—FEL, the generation of the pump wave and it's scattering can be accomplished by the same electron beam, even directly in the same interaction space, this is called two-stage FEL[4,5] (Fig. 1 shown). Many radiation sources that induce a

transverse electron oscillation would, in principle, function as a pump field. Generating radiation of 200 MW of power and 3. 2 cm of wavelength by the relativistic backward wave oscillatior is thought to function as the pump wave in the present study. A practical EM—EFL electrodynamic system is simulated using the complete equations of EM — FEL by Bratman et al.[6], to obtain the coupling coefficient versus the longitudinal magnetic field and the radius of electron beam, the excitation curves, powers versus the focusing magnetic field, frequency and efficiency. All the computing results can direct our experiment of free electron laser pumped by electromagnetic waves which is in progress in University of Electronic Science and Technology of China.[7]

THEORETICAL BACKGROUND

In the case of scattering by a beam of electrons moving with a translational velocity $v_{//}$, the incident wave (pump) $\bar{A}_i$ and the scattered wave (signal) $\bar{A}_s$ can be expressed as:

$$\bar{A}_{i,s} = C_{i,s}(z,t)\hat{A}_{i,s}(\bar{r}_\perp)exp[i(\omega_{i,s}t - k_{i,s}z)]$$

When stimulated scattering can occur in the pump generator (Fig. 1) with consideration of HF—LF wave interaction in relativistic backward wave oscillator, the complete equations of particle motion and resonator excitation have the form[6]:

$$\left.\begin{aligned}
&\frac{dw}{dZ} = Im[\bar{\omega}_i F_i a_i exp(i\theta_i) + \bar{\omega}_s F_s a_s exp(i\theta_s) + Ga_s a_i^* exp(i(\theta_s - \theta_i))] \\
&\frac{d\theta_{i,s}}{dZ} = -\delta_{i,s} + \mu_{i,s} w \\
&\frac{da_i}{dt} + \frac{\omega_i}{2Q_i} = iM_i\omega_i \int_0^{Z_m}(F_i\rho_{1,0} + Ga_s\rho_{1,-1})dZ \\
&\frac{da_s}{dt} + \frac{\omega_s}{2Q_s}a_s = iM_s\omega_s \int_0^{Z_m}(F_s\rho_{0,1} + G^* a_i\rho_{-1,1})dZ
\end{aligned}\right\}$$

RESULTS AND DISCUSSIONS

Fig. 2 shows the wave coupling coefficient G versus the radius of electron beam; Fig. 3 shows G versus the magnitude of the longitudinal magnetic field, when the E_{01} wave scatters to the H_{11}, E_{01}, E_{11}, H_{01}, and H_{21}. Fig. 3 shows that when B≈12kG, the coupling coefficient G→∞.

The growth of the scattered wave power is restricted by: depletion of the pump wave and lockout of the electrons losing energy from synchronism with the combination wave(the shift of bunches from deceleration to acceleration wave phases). Fig. 4 shows that, after starting oscillation, when time t≈15ns, the pump waves get to the power saturation of 200 MW; when time t≈19ns, the scattered waves to the power saturation of 30 MW.

Non-monotonic dependence of the BWO radiation $P_i(B)$ is explained by cyclotron absorption of the fundamental harmonic of the counter-running wave by the linear electron beam at resonant magnetic fields: $\omega_i + |h_i| v_{//} \approx \omega_H$, just shown in Fig. 3, B≈12 kG is satisfied this condition. However, it is found that the pumping of transverse electron oscillations results in the enhancement of coupling between the beam and the HF(scattered) wave. This fact explaines the increase in the power of scattered radiation $P_s(B)$ near the edges of the cyclotron absorption line in spite of the decrease in the power of pump wave. These are shown in Fig. 5.

CONCLUSION

Numerical study shows that it is possible to realize a two-stage FEL where great Doppler frequency up-conversion occurs twice, and where short wave radiation using stimulated wave scattering by high-current relativistic electron beam can be obtained drectly in the interaction space of the pump wave generator. It is showing that both the pump as well as the FEL interaction are strongly affected by the guide magnetic field. And the process from the start of oscillation to the end of saturation is clearly demonstrated by the curves of powers of incident and scattered waves. The theory and the numerical results are very useful to our undertaking experiment of EM-FEL, and agreeable with our initial experimental results.

REFERENCES

1. T. C. Marshall, *Free Electron Lasers*, New York, Macmillan, 1985.
2. R. A. Kehs et al., "Free electron laser pumped by a powerful traveling electromagnetic wave," IEEE Trans. Plasma Science, vol. 18, No. 3, June 1990.
3. Yoonho Seo, "The nonlinear evolution of a free electron laser with electromagnetic wigglers," Phys. Flunids B 3 (3), March 1991.
4. Y. Carmel et al., "Demonstration of a two-stage backward-wave-oscillator free-electron laser," Phys. Rev. Lett., vol. 51, No. 7, Aug. 1983.
5. G. G. Denisov et al., "Powerful electromagetic millimeter-wave oscillations produced by stimulated scattering of microwave radiation by relativistic electron beams," Int. J. Infrared millimeter waves, vol. 5, 1984.
6. V. L. Bratman et al., "Stimulated scattering of waves in microwave generators with high-current relativistic electron beams: simulation of two-stage free electron laser," Int. J. Electron., vol. 59, No. 3, 1985.
7. Jianqiang Wu, Tianquan Deng, Zheng Liang et al., "Experimental investigation of electromagnetically pumped free-electron-laser," 16th Int. Conference on IR and MM waves, Switzerland, Aug. 1991.

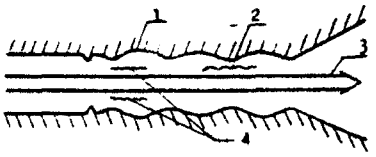

Figure 1. Stimulated wave scattering by a high—current relativistic electron beam in the interaction space of pump wave generator.
1: BWO pump wave generator; 2: pump wave;
3: relativistic electron beam; 4: scattered wave.

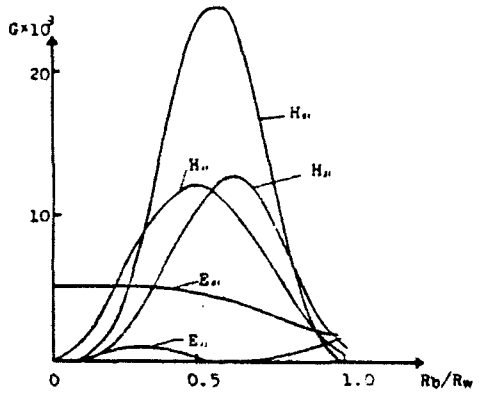

Figure 2. The wave coupling coefficient G versus the radius of electron beam injection for scattering of the E_{θ} wave.

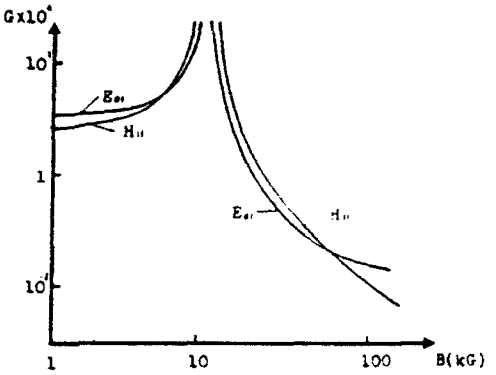

Figure 3. The wave coupling coefficient G versus the guide magnetic field for scattering of the E_{θ} wave

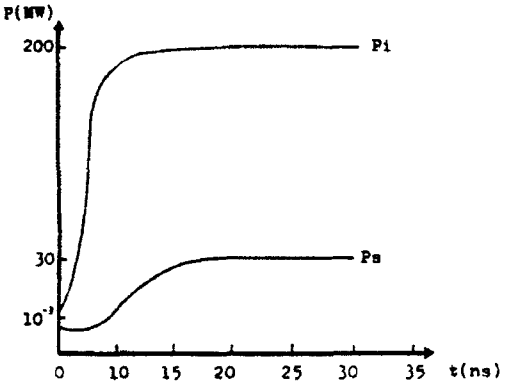

Figure 4. Characteristics of FEL to start oscillation.

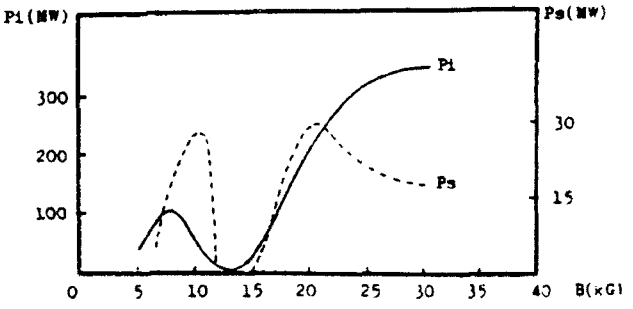

Figure 5. The power of a LF pump wave and a HF scattered wave versus the guide magnetic field.

STUDY OF CENTIMETER AND MILLIMETER WAVE RANGE POWERFUL OROTRONS'EFFICIENT REGINES AT THE IRE OF THE ACADEMY OF SCIENCES OF THE USSR

Ye. A. Myasin, M.B. Tseytlin, G. A. Bernachevsky, B. A. Belavsky, V. V. Evdokimov, V. D. Kotov, A. N. Solovjov, S. G. Tchigarev, L. M. Nutovich I. I. Tsitson, U.V. Andreev, T. A. Litkina, Inst. of Radioengineering and Electronics, Russian Academy of Sciences, 141120 Friasino, Moscow, Russia

ABSTRACT

The orotron was proposed in the USSR by F. S. Rusin and G. D. Bogomolov in 1966. Its function has been studied for several years by different research groups in the USSR (V. P. Shestopalov, et al.) and abroad (D. E. Wortman, R. P Leavit, et al.). By this time, the opinion derived from these investigations is that the orotron is a small power millimeter wave range harmonic oscillations generator (whose efficiency is consequently low) of pulse or continuous action.

The research of which the results will be exposed in the current report were mainly axed on the goal of investigation of the possibility of creating powerful and efficient centimeter and millimeter wave range orotrons with an output power of unities to hundreds kW. These investigations at the IRE of the Academy of Sciences of the USSR started sixteen years ago as an initiative of Dr. Z. S. Chernov. At this time, they are practically completed.

In the report we will be considering the problems of theoretical analysis of the electron wave interaction in the orotron under a substantially nonlinear regime. His parameters optimization methods, in particular, the methods of efficiency increase, will be discussed, and the excitation theory results for higher parasitic types of oscillations will be reported.

We will also be considering the device basic constructions' peculiarities adequate to the theoretical models conceived. Last, we will be discussing the results of experimental studies, most of which are scheduled in the table.

Results of experiments in pulse regime (τ_p < 5mks. T/τ_p - 10^3)

f(GHz)	P(kW)	η%	Q_1*0^3	U(kV)	1(A)	j(A/cm^2)
10	53	35	0.8	13	11.6	50
37.5	40	17	2	19	12	
90	1.2	6	5	20	1	100

Here, η_p is the pulse duration, T is the duration between two neighboring pulses, f is frequency, P is the pulse output power, η is efficiency in percent, and Q_1 is the quality factor.

T3.5

THE SPACE CHARGE EFFECTS IN ORBITRON AND EECRM MASER*

Liu Zhiqing

(*Institute of Electronic Product Reliability and Environmental Testing of China*, *P. O. Box* 1501—658, *Guangzhu* 510610, *P. R. China*)

Xiong Caidong and Liu Shenggang

(*Institute of High Energy Electronics, University of Electronic Science and Technology of China, Chengdu* 610054, *Sichuan, P. R. China*)

INTRODUCTION

There is more interest in electrostatic electron cyclotron resonance maser (EECRM), which is similar to Orbitron, because of its attractive advantages to gyrotron[1—4], e. g., it may be voltage tunable, it may operate at high cyclotron harmonic and nonrelativistic case, it requires no magnetostatic field. By now, most articles for EECRM and Orbitron dealed with an ideal model, i. e., the space charge effects were neglected. Whereas, one can see from the results given below that the space charge effects play a important role in EECRM, and may change some EECRM characteristics.

THE AFFECTION OF SPACE CHARGE FIELDS IN EECRM SYSTEM

In the cylindrical coordinate (R, φ, z), we can get the ac space charge fields at the beam position as[3] $E_\varphi = jH_1R_1 + H_2R_0\varphi_1$, $E_R = jH_4R_0\varphi_1 + H_3R_1$, and the dc component is $(E_R)_0 = \rho_0(R_0)\tau/2\varepsilon$, and coefficients are

$$H_1 = \frac{m\rho_0\tau}{2\varepsilon}R_0^{-2m-1}\frac{(R_c^{2m} + R_a^m R_b^m)(R_a^m R_b^m - R_0^{2m})}{R_b^{2m} - R_a^{2m}} \tag{1}$$

$$H_2 = -\frac{m\rho_0\tau}{2\varepsilon}R_0^{-2m-1}\frac{(R_c^{2m} - R_a^{2m})(R_b^{2m} - R_0^{2m})}{R_b^{2m} - R_a^{2m}} \tag{2}$$

$$H_3 = -\frac{\rho_0\tau}{2\varepsilon R_0} + \frac{m\rho_0\tau}{2\varepsilon}R_0^{-2m-1}\frac{(R_0^{2m} + R_b^{2m})(R_0^{2m} + R_a^{2m})}{R_b^{2m} - R_a^{2m}} \tag{3}$$

$$H_4 = \frac{m\rho_0\tau}{2\varepsilon}R_0^{-2m-1}\frac{(R_0^{2m} - R_a^m R_b^m)(R_0^{2m} + R_a^m R_b^m)}{R_b^{2m} - R_a^{2m}} \tag{4}$$

where m, R_0, R_a, R_b, τ, are the number of azimuthal harmonics, the average equilibrium radius of the electron beam, inner and outer radii of conductors and the radial thickess of electron beam, respectively. Starting from relativistic equation of electron in the coaxial cavity with the voltage between the inner and outer conductors U_0, We can get the perturbation of electron motion perturbation: $R_1 = (R_1)_{max}\sin\Omega_c t$, $R_0\varphi_1 = (2 - \beta_{0\varphi}^2)^{1/2}(R_1)_{max}\cos\Omega_c t$, $z_1 = -\beta_{0\varphi}\beta_{0z}(2 - \beta_{0\varphi}^2)^{-1/2}(R_1)_{max}\cos\Omega_c t$, where $\Omega_c = (2 - \beta_{0\varphi}^2)^{1/2}\omega_0$, $\beta_{0\varphi} = v_{0\varphi}/c$, $\beta_{0z} = v_{0z}/c$. In the cases of $v_{0z} = 0$ and $v_{0\varphi} = 0$, one can see that the tranverse oscillation still exists. It is obvious that this is the inherent oscillation in EECRM system.

* The project supported by National Natural Science Foundation of China No. 6861040

Consider the dc space charge effect, electron motion equation changes, and the angular frequency must satisfy

$$\omega_0^2 = |e|U_0/\gamma_0 m_0 R_0 ln\frac{R_b}{R_a} + |e|\tau\rho_0(R_0)/2\varepsilon\gamma_0 m_0 R_0 \tag{5}$$

in order to sustain the circular orbit motion. We find from equation (5) that $\Omega_r = (2-\beta_{0z}^2)^{1/2}\omega_0$ increases, which shows that dc space charge effect make the inherent oscillation frequency shift up, as well as the operating frequency when the inherent oscillation mode couples with the electron cyclotron mode.

THE INSTABILITY ANALYSIS OF DISPERSION EQUATION IN EECRM SYSTEM

The general dispersion equation of TE_{mn} mode is worked out as[4]

$$\frac{\omega^2}{c^2} - k^2 - k_c^2 = \frac{\omega_p^2}{c^2}\frac{1}{N_0\Omega_t^4}(\Delta_1\Omega^4 + \Delta_2\Omega^3 + \Delta_3\Omega^2 + \Delta_4\Omega + \Delta_5 + \Delta_6\Omega^{-1} + \Delta_7\Omega^{-2}) \tag{6}$$

where coefficients $\Delta_{1\sim7}$ include the influence of both the high frequency fields and space charge effects[5]. N_0 is a constant of integration, ω_p is the plasma frequency of the beam. And $\Omega = \omega - kv_{0z} - m\omega_0$, $\Omega_t^4 = \Omega^2\Omega_r^2 - \Omega_m^4$, $\Omega_r^2 = \Omega_c^2 - \Omega^2$, $\Omega_m^4 = M_1\Omega^2 + M_2\Omega + M_3$, $M_{1\sim3}$ are modified coefficients which include the space charge effects[5]. It is possible for the vacuum wave—guide mode ($\omega^2 - c^2k^2 - c^2k_c^2 = 0$) couples with the electron cyclotron mode ($\omega - kv_{0z} - m\omega_0 = 0$) only when $U_0 \geqslant (U_0)_{cr} = \gamma_0 m_0 R_0^2 k_c^2 ln\frac{R_b}{R_a}/|e|m^2\gamma_{0z}^2 - \tau R_0\rho_0(R_0)ln\frac{R_b}{R_a}/2\varepsilon$ which shows that the dc space charge effect may reduce the electrostatic focusing voltage U_0, and is conducive to the synchronous cyclotron instability. This property is not mentioned before. In fact, the space charge effects here promote the loss of potential energy of electrons, then are conducive to both the stimulation of wave fields and the occurrence of instability. The singularity $\Omega_t^4 = 0$ stands for the tranverse oscillation instability which due to the coupling between the inherent oscillation and the electron cyclotron mode. The approximate growth rate of this instability have been driven out as[6]: $I_m(\delta\omega) = \left(\frac{|D_1|}{4(2-\beta_{0z}^2)^{1/2}\omega_0\omega_c}\right)^{1/2}$. Notice that plasma frequency $\omega_p^2 = \frac{e^2N_e}{\gamma_0 m_0\varepsilon_0} = \frac{|e|I}{\gamma_0 m_0\varepsilon_0 v_{0z}} \propto I$, where I is the current of electron beam, we can get that $I_m(\delta\omega) \propto I^{1/3}$ for the synchronous cyclotron instability, and $I_m(\delta\omega) \propto I^{1/2}$ for the inherent oscillation instability. When the beam current I is larger than 1 ampere, we get $I^{1/2} > I^{1/3}$, which due to the contribution of space charge effects to this tranverse oscillation instability. The results above have no difference with the description of the negative-mass instability[7], and are also similar to that space charge effects can increase the small signal gain in the cross-field devices.

CONCLUSION

The space charge effect may make the frequency of the inherent oscillation upshift; it is condunive to the synchronous instability and it increases the growth rate of instability. There are similar results to the TM_{mn} modes[8].

REFERENCES

1. Liu Shenggang, et al, J. App. Phys., 59(11) (1986), 3621.
2. Alexeff, I. and Dyer, F., Phys. Rev. Lett., 45(5) (1980), 351.
3. Pantell, R, H., IRE. Trans. on ED., 7(1) (1960), 22.
4. Liu Shenggang, Scientia Sinica A., 22(8) (1979), 901.
5. Xiong Caidong and Liu Shenggang, J. Systems Engineering and Electronics, 12(11) (1990), 26, in Chinese.
6. Xiong Caidong, Journal of Postgraduates, University of Electronic Science and Technology of China (UESTC), 7(1) (1990), 65, in Chinese.
7. Lau, Y. Y., IEEE. Trans. on ED., 31(3) (1984), 329.
8. Xiong Caidong, Master's thesis, Institute of High Energy Electronics, UESTC., 1988, in Chinese.

T3.6

ANALYSIS OF INSTABILITY IN EECRM SYSTEM*

Caidong Xiong and Shenggang Liu

(Institute of High Energy Electronics, University of Electronic Science and Technology of China, Chengdu 610054, Sichuan, P. R. China)

INTRODUCTION

The concept of electrostatic electron cyclotron resonance maser (EECRM) was proposed in 1984[1]. Its mechanism is that: injecting a relativistic or nonrelativistic cyclotron electron beam into the coaxial waveguide system (see Fig. 1), a radial electrostatic field between the inner and outer conductors is used to restrict the electron cyclotron motion, while electrons interact synchronously with coaxial high frequency fields (TE, TM or TEM modes), resulting in coherent radiation. So it is necessary to give a detailed analysis to the electron motion in the EECRM system.

THE STEADY STATE MOTION OF ELECTRONS IN EECRM SYSTEM

Neglecting the space charge forces and the high frequency field forces in the coaxial cavity, the steady state circular orbit equation of electron motion may be written as

$$\gamma_0 m_0(-R_0\omega_0^2) = eU_0/R_0 ln\frac{R_b}{R_a} \tag{1}$$

where R_0 is the average equilibrium radius of electron beam. Supposing there are perturbation $(R_1, R_0\varphi_1, z_1)$ of electron motion, we can get that

$$R_1 = (R_1)_{max}\sin\Omega_c t \tag{2}$$

$$R_0\varphi_1 = \sqrt{2-\beta_{0\varphi}^2}(R_1)_{max}\cos\Omega_c t \tag{3}$$

$$z_1 = \frac{-\beta_{0\varphi}\beta_{0z}}{\sqrt{2-\beta_{0\varphi}^2}}(R_1)_{max}\cos\Omega_c t \tag{4}$$

* The project supported by National Natural Science Foundation of China No. 6861040

where $\Omega_e = \sqrt{2 - \beta_{0\varphi}^2}\omega_0$, $\beta_{0\varphi} = v_{0\varphi}/c$, $\beta_{0z} = v_{0z}/c$, when $v_{0z} = 0$ (i. e. , no longitudinal motion), the transverse motion exists. In the nonrelativistic case, $\beta_{0\varphi} = 0$, $\Omega_e = \sqrt{2}\omega_0$, the transverse oscillation still exists. It is obvious that this is the inherent oscillation in EECRM system. Therefore it is possible for this inherent oscillation couples with the electron cyclotron mode, resulting in instability. Consider the dc space charge effect, electron motion equation changes and the angular frequency must satisfy $\omega_0^2 = |e|U_0/\gamma_0 m_0 R_0 ln(\frac{R_b}{R_e}) + |e|\tau\rho_0(R_0)/2\varepsilon\gamma_0 m_0 R_0$ in order to sustain the circular orbit motion of electrons. This requires that electrons should have more initial kinetic energy ($\frac{1}{2}m_0 R^2\omega_0^2$) to overcome the defocussing effect of space charge, and to achive the steady electron beam equilibrium.

THE INHERENT OSCILLATION INSTABILITY IN EECRM SYSTEM

The general dispersion equation of TE_{mn} mode in EECRM system was dervied out as[2]

$$\frac{\omega^2}{c^2} - k^2 - k_c^2 = \frac{\omega_p^2}{c^2}\frac{1}{N_0\Omega_t^4}(\Delta_1\Omega^4 + \Delta_2\Omega^3 + \Delta_3\Omega^2 + \Delta_4\Omega + \Delta_5 + \Delta_6\Omega^{-1} + \Delta_7\Omega^{-2}) \quad (5)$$

where coefficients $\Delta_{1\sim7}$ include the influence of both the high frequency fields and space charge effects[2]. N_0 is a constant of integration, ω_p is the plasma frequency of electron beam. And $\Omega = \omega - kv_{0z} - m\omega_0$, $\Omega_t^4 = \Omega^2\Omega_e^2 - \Omega_m^4$, $\Omega_e^2 = \Omega_e^2 - \Omega^2$, $\Omega_m^4 = M_1\Omega^2 + M_2\Omega + M_3$, where $M_{1\sim3}$ are modified coefficients which include the space charge effects. Equation (5) includes two kinds of instabilities represented by two singularities: $\Omega = 0$ and $\Omega_t^4 = 0$. The former, $\Omega = 0$, has been investigated in detail by Liu[1]. So, we will focus on the $\Omega_t^4 = 0$. Neglecting the space charge effects, we get that $\Omega_e^2 = \Omega_e^2 - \Omega^2 = 0$, i. e. , there exists the inherent oscillation with the eigenfrequency $\Omega_e = \sqrt{2 - \beta_{0\varphi}^2}\omega_0$, and this oscillation may couple with the electron cyclotron mode ($\Omega = \omega - kv_{0z} - m\omega_0$) results in transverse oscillation instability, which becomes more complex when the space charge effects are included.

Let' s apply diagram to analyse the $\Omega_t^4 = \Omega^2\Omega_e^2 - \Omega_m^4 = 0$. Defining $f_1(\Omega) = \Omega^2\Omega_e^2 = -\Omega^4 + A_0^2\omega_0^2\Omega^2$, and $f_2(\Omega) = \Omega_m^4 = M_1\Omega^2 + M_2\Omega + M_3$, we get the curves of $f_1(\Omega) \sim \Omega$ and $f_2(\Omega) \sim \Omega$, as shown in Fig. 2. The intersection problem of curve $f_1(\Omega)$ and curve $f_2(\Omega)$ is discussed by Xiong and Liu[2], which shows that curve $f_1(\Omega)$ may intersect curve $f_2(\Omega)$ when the vlotage U_0 is larger than the following cirtical value $(U_0)_{crit.1}$

$$(U_0)_{crit.1} = R_0 ln\frac{R_e}{R_b}\left\{\left[\frac{m\rho_0\tau(1-\beta_{0\varphi}^2)}{2\gamma_0^5\varepsilon(1-\beta_0^2)(2-\beta_{0\varphi}^2)}\right]^2\frac{R_0^{2m}(R_t^{2m} - R_e^{2m})}{(R_t^{2m} - R_e^{2m})(R_t^{2m} - R_b^{2m})} - \frac{\rho_0\tau}{2\varepsilon}\right\} \quad (6)$$

where τ is the radial thickness of beam, m is the number of azimuthal harmonics. As a rough estimation, $(U_0)_{crit.1}$ is the order of hundreds of volts, so we obtain $U_0 > (U_0)_{crit.1}$ in the general case, and there are two points of intersection (Ω_{e1}, Ω_{e2}) for $f_1(\Omega)$ and $f_2(\Omega)$. Then there exixts an inherent oscillation in EECRM system, and it is possible for coupling between

this inherent oscillation and the cyclotron mode, resulting in the transverse instability. The approximate growth rate of this instability has been worked out as [3]

$$I_m(\delta\omega) = \left(\frac{|B_1|}{4\sqrt{2-\beta_{0\varphi}{}^2\omega_0\omega_r}}\right)^{1/2} \tag{7}$$

where ω_r is the operating frequency. we also find that the space charge effects can increase the growth rate[3].

CONCLUSION

There exists a critical value for the electrostatic potential U_0 which affects the inherent oscillation in the EECRM system. The instability $\Omega_i^4 = 0$ may still exist in the nonrelativistic case. It is necessary to have more initial kinetic energy of electron beam in order to overcome the defocussing effect of spece charge and to sustain the circular orbit motion of electrons.

REFERENCES

1. Liu Shenggang, Scientia Sinica A., 29(6) (1986),657.
2. Xiong Caidong and Liu Shenggang, J. Systems Engineering and Electronics, 12(11) (1990),26, in Chinese.
3. Xiong Caidong, Liu Zhiqing, Yu Shanfu and Liu Shenggang, 16th Int. Conf. IR/MM Waves, Lausanne, Switzerland, Aug. 26—30,1991.

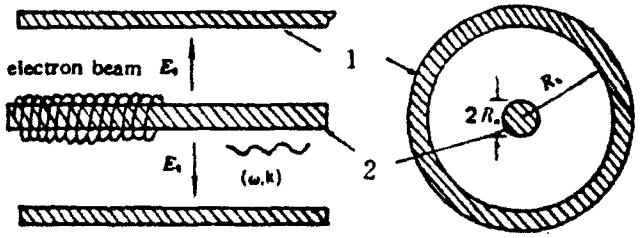

1. outer conductor; 2. inner conductor

Fig. 1 Schematic diagram of EECRM system

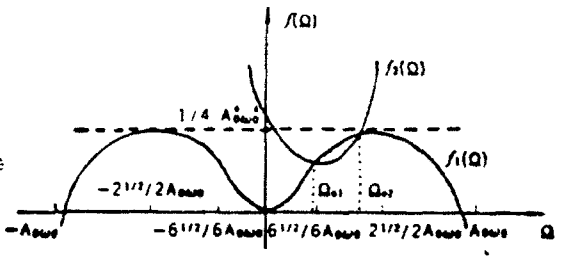

Fig. 2 The graph of $\Omega_i^4 = 0$

T4.1

RESEARCH ON THE MMW RADOME

Gong Cheng, Chen Ke-qin
(Shanghai Research Institute of Microwave Technology, China)

ABSTRACT

A MMW radome with the good experimental results was developed. Some engineering problems to design a high performance MMW radome are discussed.

1. INTRODUCTION

The radome is an extremely important component in an airborne radar system. As we know, there are many typical design programs and products for CMW radome. However, it seems difficult to design a high quality MMW radome which demands not only higher transmission coefficient but also lighter weight and higher strength. Especially, the radome material loss will be obvious with the increasing frequency. We have to pay attention to choose the proper material for the radome in MMW band besides design the radome shape, profile and thickness.

2. BASIC PRINCIPLE

As shown in Fig.(1), a radome is used to design in the single solid dielectric wall. When the thickness d satisfies the following formula

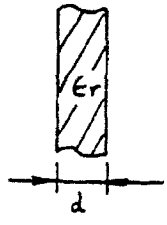

Fig.(1)

$$d = \frac{n \cdot \lambda}{2\sqrt{\epsilon_r - \sin\theta}}$$

the transmission coefficient of the radome will be maxium, where θ the angle of incidence, λ the wavelength, d the thickness, ϵ_r the relative dielectric constant and n the integer. From the above formula, it is clear that the thickness d is directly proportional to the wavelength λ, so that the wall thickness for a MMW radome will be more thinner than CMW one's. As a result, the radome strength cann't fulfil the engineering requirement.

Some parameters of the practical radome candidate materials are given in Table (1).

	Alumina 99%	PTFE	PI	Resin-glass Laminate
ϵ_r	9.6	2.2	3.4	4.14
$tg\delta$	10^{-4}	3×10^{-4}	10^{-3}	2.6×10^{-2}

Table (1)

Using the above formula and parameters in Table (1), we can list the numerical

results of thickness d in Table (2) with $n = 1, \theta = 0$, $\lambda = 8.6$mm and 32mm.

λ (mm) \ d(mm)	Alumina 99%	PTFE	PI	Resin-glass Laminate
8.6	1.39	2.90	2.33	2.11
32	5.16	10.71	8.68	7.86

Table (2)

Considering the electrical, mechanical and enviromental properties, the MMW radome made of inorganic material with the thickness d = 1.39 is not reasonable. On the other hand, the MMW radomes made of organic materials or composite materials are suitable. It is necessary to choose a proper organic or composite material for the MMW radome.

3. CHOICE OF MATERIAL

In general, the lower loss tangent, higher strength and good heat resistance are criteria for choice of radome wall material. Comparing the organic and composite materials listed in Table (1), we have to know the merits and demerits each and every. In the MMW radome design, the loss tangent of the resin-glass laminate is too high to use and the PTFE is better than PI. However the strength of PTFE is lower than that of PI. When the MMW radome is set on the missile or vehicle, the heat-resistance of material will be important. The limited temperature of PTFE is 250°C, PI 316°C even more. But the PTFE seems flexible. For our practical purpose, we have developed a new type composite material which consists of PTFE as the base and glass fibre as the reinforcement. In the MMW band, the dielectric constant $\epsilon_r = 2.8$, loss tangent $tg\delta = 10^{-3}$. The strength of the MMW radome has been also improved greatly.

4. EXPERIMENTAL RESULTS

Three radome in MMW band were developed. They are
(1) a half-wave single wall radome with PTFE,
(2) a half-wave single wall radome with the new composite material,
(3) a half-wave single wall radome with the resin-glass laminate.
The transmission coefficients of these radomes were measured. The results are listed in Table (3).

θ° \ T%	(1)	(2)	(3)
0	98.2	96.6	87.1
30	97.7	94.6	71.2

Table (3)

It is clear that, in the MMW band the new composite material reinforced with glass fibre laminate can be used for the radome wall. A practical MMW streamline radome of full-wave length (n = 2) is made of this new reinforced material in our laboratory. The transmission coefficient t = 80% and press-resistance P = 6 Kg/cm^2. By the way, we have to mention that this new reinforced material is cheap and flexible. In the MMW band, this reinforced material will open up broad prospects for engineering applications.

REFERENCES

1. Benjamin Rult, Microwave J., 28(1)(1985), 145.
2. Benjamin Rult, ibid., 28(5)(1985), 265.
3. Gong Cheng and Chen Ke-qin, Microwave and Communication, (1)(1991), 8.

T4.2

SHIELDED SUSPENDED COUPLED DIELECTRIC GUIDE AND DIRECTIONAL COUPLER

Alok Kumar Rastogi
Department of Physics, MVAM
Bhopal (M.P.), India

and

A. K. Tiwari
Dept. of Electronics Engineering, MACT
Bhopal (M.P.), India

Abstract

A shielded suspended coupled dielectric guide was analyzed using the effective dielectric constant method. The dispersion characteristics of shielded suspended coupled dielectric guides have been plotted for various dimensional parameters. From the dispersion characteristics the wave impedances have also been derived. By computing the even and odd mode propagation constants, various directional couplers have been obtained.

T4.3

A SIMPLE AND ACCURATE METHOD FOR ANALYSIS OF DIELECTRIC PERIODIC STRUCTURES*

Xu Shanjia
Department of Radio and Electronics
University of Science and Technology of China
Hefei, Anhui, 230026, P.R.China

Sun Liguo
Institute of Remote Sensing Applications
Beijing, 100101, P.R.China

ABSTRACT

A simple and accurate approach for analysis of dielectric periodic structures is proposed in this paper. The method combines the coupled-mode theory with Floquet theory and joins the eigenmode expansion with the space harmonic expansion properly. As a result, the whole analysis procedure is significantly simplifid. Numerical results for the filter characteristics of some dielectric periodic strctures show that the present method is effective, accurate and useful.

INTRODUCTION

Dielectric periodic structures have been of increasing importance in optical and millimeter wave applications. In nearly every application, the most significant quantities describing the behaviour of the periodic structures are the dispersion curves. Therefore, the dispersion analysis of these structures is of essential significance. There are a lot of methods used to analyze the dispersion characteristics of the dielectric periodic structures; two representitives of them are coupled-mode approach[1] and Floquet-Bloch expansion method.[2] The former expands fields in the periodic structures in terms of eigenmodes in unperturbed waveguide and offers relatively simpler analysis procedure with an assumpsion that the periodic layer act as only a small perturbation in a planar multilayered medium. This approximation yields good results only if the periodic change is sufficiently small, so that its use may produce erroneous results in many practical cases. The latter uses an expansion of the fields in terms of Floquet space harmonics and the propagation of EM waves along periodic dielectric structures is formulated as a rigorous boundary value problem. The rigorous treatment gives very accurate results. However, it is rather complex and requires time consuming and elaborate high precision computer program to yield accurate quantitative results, it is not economic from viewpoint of engineering.Besides, the Floquet method is not so convenient to use in analyzing the periodic structures in which the groove profile is not in exactly rectangular form.

In this paper, we propose a simple but accurate approach for analysis of the dielectric periodic structures. The approach combines the coupled mode theory with Floquet theory and joins the eigenmode expansion with the space harmoinc expansion properly. As a result, the whole analysis procedure is significantly simlified. Numerical examples show that the present method is effective, accurate and useful.

THEORY

* Supported by The National Natural Science Foundation of China and The Foundation of State Educational Commission.

The dielectric periodic structures considered here are depicted in the insect of Fig.1 and Fig.2. The former is the grating medium with periodic modulation of its permittivity, and the latter is the grating layer with rectanguler corrugations. In the present analysis the transversal fields in the dielectric periodic structures are expanded by the eigenmodes of the unperturbed waveguide as:

$$\begin{aligned} \mathbf{E}_t(x,y,z) &= \sum_\mu (a_\mu(z) + b_\mu(z))\mathbf{e}_t^\mu \\ \mathbf{H}_t(x,y,z) &= \sum_\mu (a_\mu(z) - b_\mu(z))\mathbf{h}_t^\mu \end{aligned} \tag{1}$$

where $\mathbf{e}_t^\mu, \mathbf{h}_t^\mu$ are the eigenmode functions; and $a_\mu(z), b_\mu(z)$ are respectively, the model applitudes of the forward and the backward travel waves along the z axis. By substituting the model expansions into Maxwell's equations, a set of coupled differential equations for amplitude of each mode is obtained:

$$\begin{aligned} da_\mu(z)/dz + j\beta_{z\mu}a_\mu(z) &= -j\sum_\nu (K_{\mu\nu}^{(+)}a_\nu(z) + K_{\mu\nu}^{(-)}b_\nu(z)) \\ db_\mu(z)/dz - j\beta_{z\mu}b_\mu(z) &= j\sum_\nu (K_{\mu\nu}^{(-)}a_\nu(z) + K_{\mu\nu}^{(+)}b_\nu(z)) \end{aligned} \tag{2}$$

where $\beta_{z\mu}$ is z component of β_μ, the propagation constant of the eigenmode in the unperturbed waveguide, which can be obtained with transverse resonance technique. The coupling coefficient $K_{\mu\nu}^{\pm}$ in Eq. (2) are given by:

$$K_{\mu\nu}^{\pm} = \omega\varepsilon_0 \int_{-\infty}^{+\infty} \Delta n^2(x,z)(\mathbf{e}_t^\mu \mathbf{e}_t^{\nu *} + e_z^\mu e_z^{\nu *})dx \tag{3}$$

Because the refraction $\Delta n^2(x,z)$ is a periodic function of z, it may be expanded in terms of Fourier series such that:

$$\Delta n^2(x,z) = \sum_l c_l(x)exp(-jl2\pi z/d) \tag{4}$$

where d is the periodicity of the structure.

When the surface waves propagate in the direction normal to the grating, the resulting two-dimensional boundary value problem is scalar and the TE and the TM modes remain independent from each other. For TE_0 mode, the Eq.(2) reduces to following equations:

$$\begin{aligned} da_\mu(z)/dz + j\beta_\mu a_\mu(z) &= -jK_{TE}(a_\mu(z) + b_\mu(z)) \\ db_\mu(z)/dz - j\beta_\mu b_\mu(z) &= jK_{TE}(a_\mu(z) + b_\mu(z)) \end{aligned} \tag{5}$$

where

$$\begin{aligned} K_{TE} &= \sum_l K_{te}^l \exp(-jl2\pi z/d) \\ K_{te}^l &= \omega\varepsilon_0 \int_{p_1}^{p_2} c_l(x) e_y^{\mu 2} dx \end{aligned} \tag{6}$$

From Eq.(5), we obtain the following equation:

$$d^2a_\mu/dz^2 + \beta_\mu^2 a_\mu + 2\beta_\mu K_{TE}a_\mu - (dK_{TE}/dz)/K_{TE}(da_\mu/dz + j\beta_\mu a_\mu) = 0 \tag{7}$$

If the term $(dK_{TE}/dz)/K_{TE}$ in (7) is negligible, which corresponds to the case of gradual variation of the coupling coefficient along the periodic direction, Eq.(7) becomes the following simpler form:

$$d^2a_\mu/dz^2 + \beta_\mu^2 a_\mu + 2\beta_\mu K_{TE} a_\mu = 0 \tag{8}$$

Eq.(7) and (8) are the second-order ordinary linear differertial equations with periodic coefficients. According to Floquet's theorem, the amplitude $a_\mu(z)$ may be expanded in terms of space harmonic wave as:

$$a_\mu(z) = \sum_n A_n^\mu \exp(-jk_n^\mu z) \tag{9}$$

where $K_n^\mu = k_{z0}^\mu + 2\pi n/d$ and k_{z0}^μ is the propagation constant of the foundamental mode in dielectric periodic structure. Substituing (9) into (7) or (8), we get following system of linear homogenous equations:

$$\sum_l K_{te}^l((\beta_\mu^2 - k_{n-l}^{\mu 2} + (2\pi l/d)(\beta_\mu^2 - k_{n-l}^{\mu 2}))A_{n-l}^\mu + 2\beta_\mu \sum_p K_{te}^p A_{n-l-p}^\mu) = 0 \tag{10}$$

or

$$(\beta_\mu^2 - k_n^{\mu 2})A_n^\mu + 2\beta_\mu \sum_l K_{te}^l A_{n-l}^\mu = 0 \tag{11}$$

Eq.(10) and (11) can be written in a matrix form:

$$\overline{\overline{S}}\mathbf{A} = 0 \tag{12}$$

A nontrivial solution for **A** exists only if the following determinant equation holds:

$$\det(\overline{\overline{S}}) = 0 \tag{13}$$

The dispersion characteristics of the periodic structure is given by seeking the root of the dispersion equation (13) numerically.

NUMERICAL EXAMPLES

To verify the validity of the present approach, two dielectric periodic structures show in the inset of Fig.1 and Fig.2 are considered, which are of current practical interest.

Fig.1 gives the stopband characteristics of the sinusoidally modulated periodic structure. The curve shows both Re $(k_{z0}^\mu d)$ and Im $(k_{z0}^\mu d)$ around Re $(k_{z0}^\mu d)$ =3.14159, where the Bragg condition is satisfied. A comparison between the results obtained by different methods is also given, very good agreement has been found. Since Floquet method is recognized as rigorous and accurate one, the effectiveness and the accuracy of the present approach is thus justified.

Fig.2 shows the dispersion curve for TE mode along a rectangular profile grating in immediate vicinity of the stopband. The results obtained by coupled-mode approach is also given, it can be found from the curves that the stopband position calculated by the present method is at Re $(k_{z0}^\mu d) = 3.1415$,as it should be according to the Bragg condition, whereas at Re $(k_{z0}^\mu d) = 3.15$ calculated by the couple-mode approach, therefore the accuracy of the present method is further justified from the other side. Besides, there are some difference of the center frequences and bandwidth of the stopband between different methods. It's believed that the present approach should be more accurate.

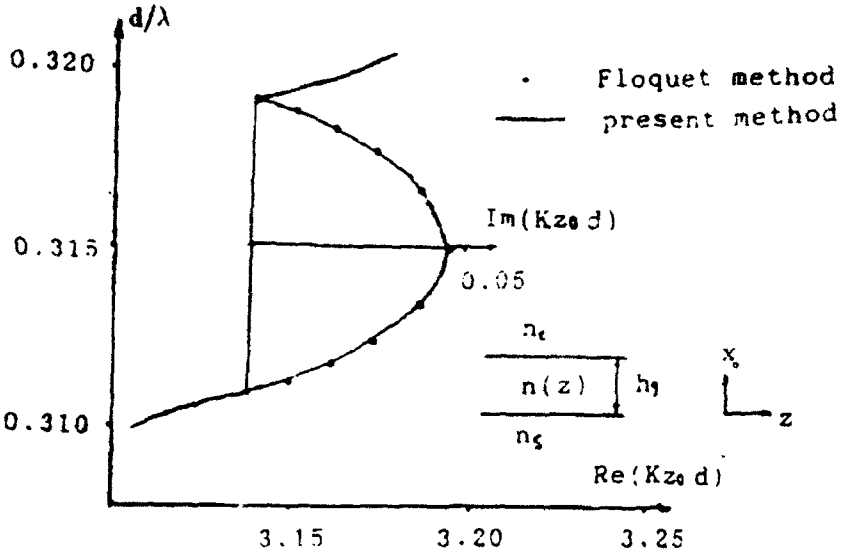

Fig. 1 Variation of $k_{z0}d$ with d/λ for the sinusoidally modulated medium

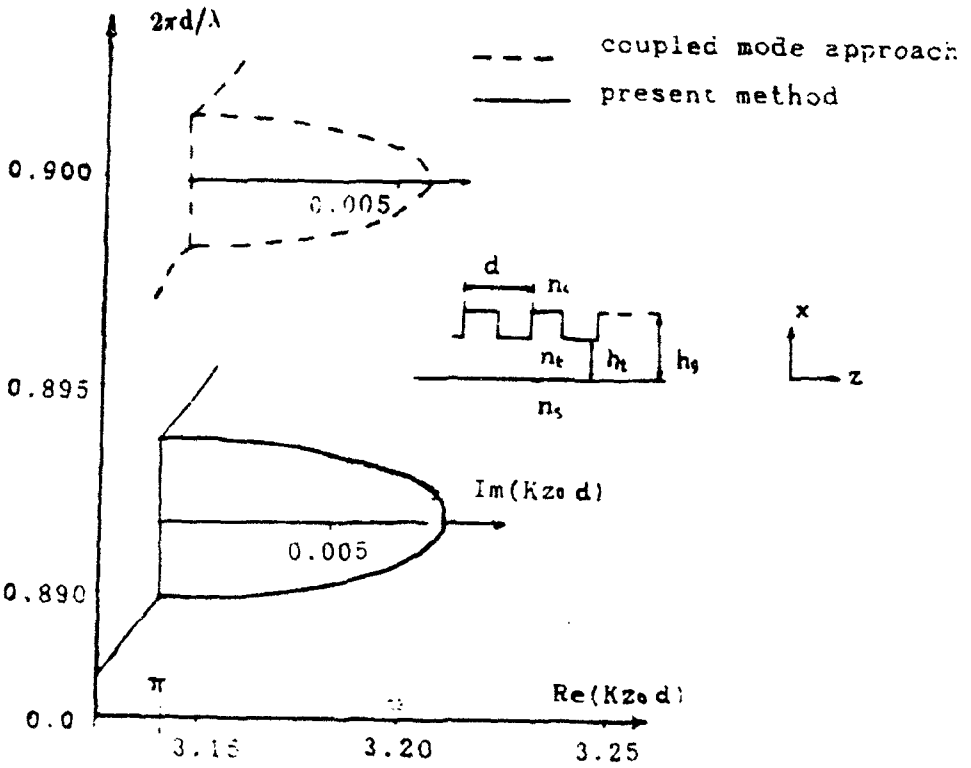

Fig. 2 The dispersion characteristics of rectangular-profile grating

REFFERENCES

1. A.Yariv et al, IEEE Trans. QE-13, No.4, pp.233-252, 1977.
2. S.T.Peng et al, IEEE Trans. MTT-23, No.1, pp.123-133, 1975.

T4.4

Characteristic Impedance of Waveguides and a Design Method for Two-section Quarter-wave Transformers

Junichiro HASHIMOTO+ and Fujio ISHIHARA+

+Faculty of Engineering, Tamagawa University, Machida, Japan

By using the correct rectangular waveguide impedance, the design of high performance quarter-wave transformers is made possible. This paper presents an improved design method for two-section maximally flat transformers, which makes better use of waveguide impedance peculiarities.

Each pair of standard rectangular waveguides is analyzed (twenty kinds of waveguides connections, corresponding to 1.7-140.0 GHz). The results show that our designs provide more than a 40-dB return loss (VSWR 1.02) for almost all pairs of waveguides, in both overlap and wide bandwidths.

1. Characteristic Impedance of Rectangular Waveguides

Obtaining a reflection coefficient at a point where waveguides connect, requires the use of the correct characteristic impedance of waveguides. The correct impedance of rectangular waveguides is listed below. This impedance has been theoretically obtained.[1]

$$Z_G = \frac{b}{b_k} \frac{K_w}{\sqrt{1-\left(\frac{\lambda}{\lambda_c}\right)^2}} \qquad \cdots(1)$$

Kw: vacuum impedance, bk: arbitrary constant,

λc: cut-off wavelength, λ: wavelength in vacuum. (Fig. 1)

There are two methods for analyzing waveguide electric-magnetic characteristics. One is to directly solve the characteristic differential equations resulting from Maxwell's equations. This method is especially useful for tapered waveguides. The other is to calculate transfer T-matrixes, which is useful for multisection flat waveguides. Each method

obtains the same results both theoretically and numerically. When applying the T-matrix method to multisection quarter-wave transformers (Fig. 2), the composed T-matrix is

$$[T_t]=[T_1][T_2]\cdots[T_i]\cdots[T_n][T_{n+1}] \quad \cdots(2)$$

$$[T_i]=\frac{1}{2\sqrt{Z_iZ_{i-1}}}\begin{bmatrix}(Z_i+Z_{i-1})\exp(-j\theta_i) & (Z_i-Z_{i-1})\exp(+j\theta_i)\\ (Z_i-Z_{i-1})\exp(-j\theta_i) & (Z_i+Z_{i-1})\exp(+j\theta_i)\end{bmatrix} \quad \cdots(3)$$

$$\Theta_{n+1}=0 \quad \cdots(4)$$

Additionally, the composed reflection coefficient is

$$\Gamma=T_{12}/T_{22} \quad \cdots(5).$$

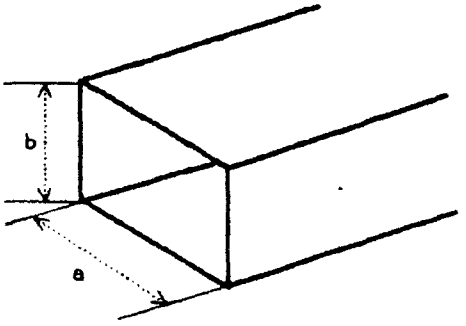

Fig.1 Rectangular waveguide

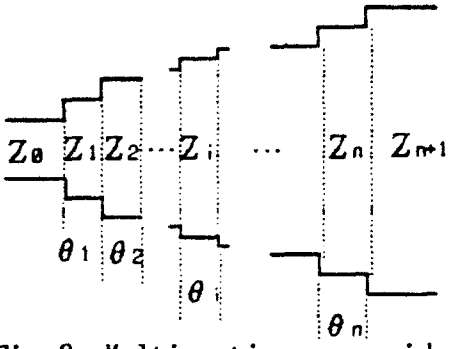

Fig.2 Multisection waveguide

2. Theoretical Design Method for Maximally Flat Transformers

By using the correct characteristic impedance (1), it is possible to design multisection quarter-wave transformers that exhibit excellent performance. Our results show that if only the TE10 mode exists, one- or two-section transformers can obtain a return loss of almost more than 40 dB in both overlap and wide bandwidths. Here, we present the two-section maximally flat transformers (Fig.3). The conditions to maximize return loss at a frequency fs are as follows:[2] [3]

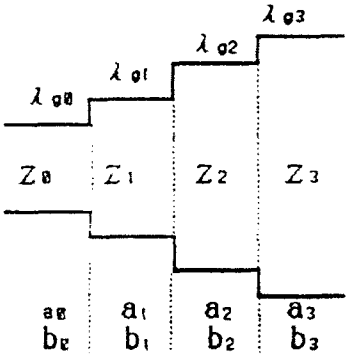

Fig.3 Two-section quarter-wave Transformer

$$(Z_2/Z_1)^2=Z_3/Z_0 \quad \cdots(6)$$

$$\lambda_{g2}^2-\lambda_{g1}^2=\frac{1}{2}(\lambda_{g3}^2-\lambda_{g0}^2) \quad (\lambda g\text{: wavelength in waveguide}) \quad \cdots(7)$$

$$(Z_1/Z_0)^2=\frac{\lambda_{g1}^2+\lambda_{g2}^2\sqrt{Z_3/Z_0}}{\lambda_{g1}^2+\lambda_{g2}^2/\sqrt{Z_3/Z_0}} \qquad \cdots(8)$$

3. A New Design Method Based on Maximally Flat Transformers

Conditions (6)-(8) result in a very effective transformers. However they do not take into account waveguide peculiarities. One peculiarity is that both input and output waveguides have a common frequency fp where the impedance of the two waveguides matches. If each section of a quarter-transformer has the same impedance as the input and output waveguides at fp, all impedance is perfectly matched at the frequency fp. The conditions for this are as follows:

$$\frac{b_1}{\sqrt{1-\left(\frac{c}{2a_1\,fp}\right)^2}}=\frac{b_0}{\sqrt{1-\left(\frac{c}{2a_0\,fp}\right)^2}} \qquad \cdots(9)$$

$$\frac{b_2}{\sqrt{1-\left(\frac{c}{2a_2\,fp}\right)^2}}=\frac{b_0}{\sqrt{1-\left(\frac{c}{2a_0\,fp}\right)^2}} \qquad \cdots(10)$$

The design of two-section quarter transformers has four free parameters, a1, a2, b1 and b2 (the length of the transformer depends on the wavelength in the waveguide, which is determined by a1 or a2). That means four conditions play a part in the shape of a two-section transformer. Condition (8) is relatively less effective than (6) and (7). Therefore, by choosing conditions (9) and (10) instead of (8), it is possible to design a system that takes advantage of both the maximally flat method and the fp peculiarity. When a wide bandwidth is used, in which both fs and fp are included, the new design method will possibly get better results than the ordinary maximally flat method.

4. Numerical and Experimental Results

One result is shown in Fig.4. The input waveguide has a=22.900 mm, b=10.200 mm and the output waveguide has a=28.500 mm, b=12.600 mm.

When a bandwidth is between 8.2 GHz and 12.4 GHz, the new design method results in a minimax return loss of 45.35 dB, while the

maximally flat method results in one of 43.18 dB. Which method gets better results depends on where the frequency fp exists. In actual application, higher modes should be considered. In that case the two methods get almost the same results, and our experimental data closely coincide the theoretical results.

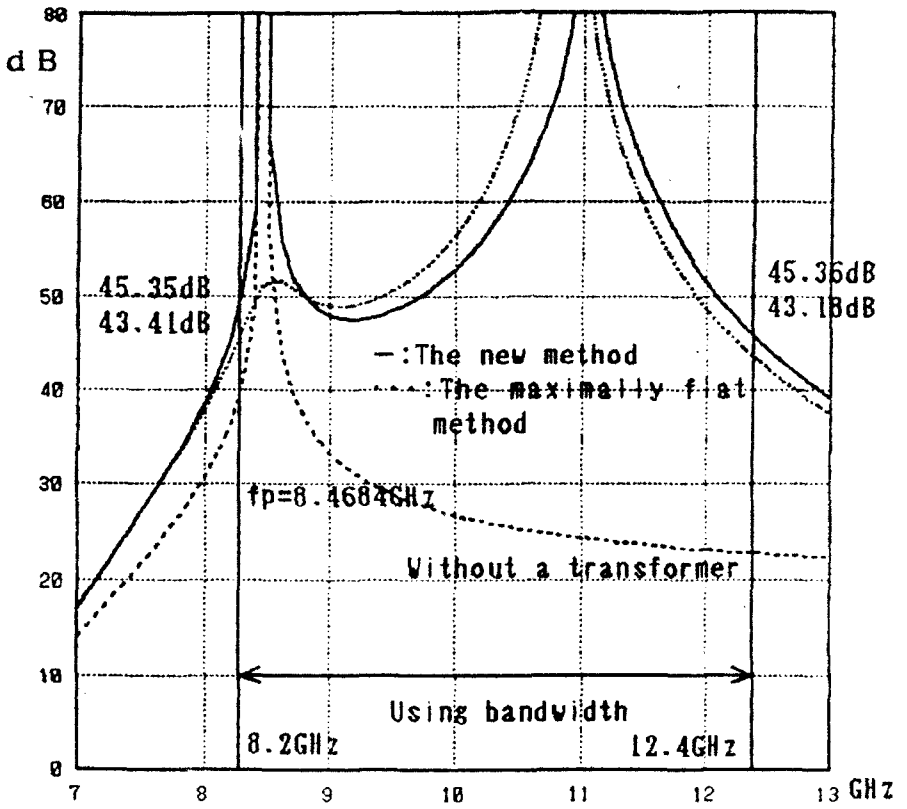

Fig.4 A result comparing the maximally flat method and the new method

5. References

(1)Ishihara F. and Iiguchi S.:"Equivalent Characteristic Impedance Formula of Waveguide and Its Applications", Trans. IEICE, J75-C-I, pp.52-60 (1992).

(2)Matthaei G.L., Young L. and Jones E.M.T.:"Microwave Filters, Impedanse-Matching Networks,andCoupling Structures", McGraw-Hill Book Company Inc. (1964).

(3)Young L.:"Inhomogeneous Quarter-Wave Transformers of Two Sections", RE Trans. Microwave Theory & Tech., MTT-8, pp.645-650 (1960).

DISPERSION CHARACTERISTICS OF A CIRCULAR CYLINDRICAL DIELECTRIC WAVEGUIDE WITH PERIODIC METALLIC STRIPS*

Xu Shanjia and Wu Xinzhang
Department of Radio and Electronics
University of Science and Technology of China
Hefei, Anhui, 230026, P.R.China

ABSTRACT

Dispersion characteristics of a circular cylindrical dielectric waveguide with periodic metallic strips are analyzed by a rigorous formulation. The filter property of the metallic strip loaded structure is carefully investigated for both TE and TM modes. On the basis of the analysis, some usefull guidelines for the design of the filter are thereby suggested.

INTRODUCTION

The millimeter-wave region is increasingly utilized for various systems. It has generated a need for developing new types of filters and antennas to suit the various constraints imposed by these systems. In 1986, a new type of circular cylindrical dielectric periodic structures were proposed.[1] It is a circular cylindrical dielectric waveguide with corrugations which is used as an omni-directional leaky wave antenna and has been investigated theoreticaly and experimently.[2] [3] In this paper, a circular cylindrical dielectric waveguide with periodic metallic strips is analyzed by a rigorous formulation. Since the radiation properties of the periodic structure can be analysed in a similar way, only the filter propertis are carefully studied for both TE_{01} and TM_{01} modes here. The theoretical analysis is essentially the same as the spectral domain approach, [5] which is a powerful tool for the analysis of the striplines. In this paper, the brillioum diagrams for TE_{01} and TM_{01} modes are given. On the basis of the analysis, some useful guidelines for the design of the filters are thereby suggested.

ANALYSIS

Fig.1 shows the geometry structure of the cylindrical dielectric waveguide with periodic metallic strips and the coordinate system for the present analysis. We assume that the fields are invariant in the ϕ direction, so that TE and TM modes can be considered respectively. Since both TE and TM modes can be analyzed in a similar way, we will consider only the TE modes for simplicity. From Maxwell's Equations, the electromagnetic fields for TE modes can be expressed in different region as follows:

In Region I $\quad 0 \leq r \leq a$

$$E_{\phi 1}(r,z) = \sum_{n=-\infty}^{\infty} A_{1n} \frac{-j\omega\mu_0 J_1(k_{rn}^{(1)} r)}{k_{rn}^{(1)} r} \exp(-jk_{zn} z) \qquad (1)$$

* Supported by the National Natural Science Foundation of China and the Foundation of State Educational Commission.

$$H_{z1}(r,z) = \sum_{n=-\infty}^{\infty} A_{1n} J_0(k_{rn}^{(1)} r) \exp(-jk_{zn} z) \tag{2}$$

In Region II $r \geq a$

$$E_{\phi 2}(r,z) = \sum_{n=-\infty}^{\infty} A_{2n} \frac{-j\omega\mu_0 H_1^{(2)}(k_{rn}^{(2)} r)}{k_{rn}^{(2)} r} \exp(-jk_{zn} z) \tag{3}$$

$$H_{z2}(r,z) = \sum_{n=-\infty}^{\infty} A_{2n} H_0^{(2)}(k_{rn}^{(2)} r) \exp(-jk_{zn} z) \tag{4}$$

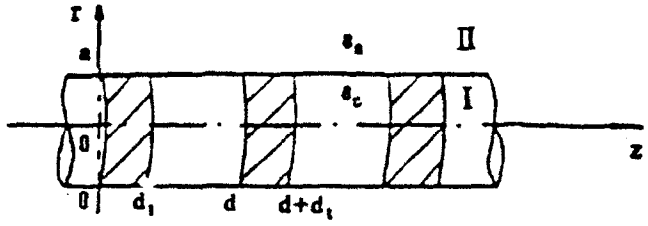

Fig.1 Configuration of circular cylindrical dielectric waveguide with periodic metallic strips.

where

$$k_{rn}^{(1)2} = k^2 \varepsilon_c - k_{zn}^2 \tag{5}$$

$$k_{rn}^{(2)2} = k^2 \varepsilon_a - k_{zn}^2 \tag{6}$$

$$k_{zn} = k_{z0} + \frac{2n\pi}{d} \tag{7}$$

The boundary conditions at r=a are given by:

$$E_{\phi 1}(a,z) = E_{\phi 2}(a,z) = \begin{cases} 0 \text{ on metallic strips } (0 \leq z \leq d_1) \\ E_\phi(z) \text{ otherwise} (d_1 \leq z \leq d) \end{cases} \tag{8}$$

$$H_{z1}(a,z) - H_{z2}(a,z) = \begin{cases} J_\phi(z) \text{ on metallic strips } (0 \leq z \leq d_1) \\ 0 \text{ otherwise } (d_1 \leq z \leq d) \end{cases} \tag{9}$$

where $E_\phi(z)$ and $J_\phi(z)$ are respectively, the unknown electric fields in the slot and the unknown surface current density in the metallic strip. From Floquet theory, we can expand them as follows:

$$E_\phi(z) = \sum_{n=-\infty}^{\infty} \tilde{E}_{\phi n} \exp(-jk_{zn} z) \tag{10}$$

$$J_\phi(z) = \sum_{n=-\infty}^{\infty} \tilde{J}_{\phi n} \exp(-jk_{zn} z) \tag{11}$$

From Eq.(1) – (11), we have:

$$\tilde{E}_{\phi n} = \frac{-j\omega\mu_0}{a} \frac{1}{T_n} \tilde{J}_{\phi n} \tag{12}$$

where:

$$T_n = \frac{k_{rn}^{(1)} J_0(k_{rn}^{(1)} a)}{J_1(k_{rn}^{(1)} a)} - \frac{k_{rn}^{(2)} H_0^{(2)}(k_{rn}^{(2)} a)}{H_1^{(2)}(k_{rn}^{(2)} a)} \tag{13}$$

On the other hand, we can expand the unknown surface current $J_\phi(z)$ in terms of known basis functions $\eta_i(z)$, and $\eta_i(z)$ must satisfy Floquet theory, i.e.

$$J_\phi(z) = \sum_{i=1}^{\infty} c_i \eta_i(z)$$

$$= \sum_{n=-\infty}^{\infty} \sum_{i=1}^{\infty} c_i \tilde{\eta}_{in} \exp(-jk_{zn} z) \tag{14}$$

Comparing (14) with (11), we get:

$$\tilde{J}_{\phi n} = \sum_{i=1}^{\infty} c_i \tilde{\eta}_{in} \tag{15}$$

Inserting (15) into (12), we obtain:

$$\frac{-j\omega\mu_0}{a}\frac{1}{T_n}\sum_{i=1}^{\infty} c_i \tilde{\eta}_{in} = \tilde{E}_{\phi n} \tag{16}$$

Multiplying (16) by $\tilde{\eta}^*_{pn}$ and sum over all n from $-\infty$ to $+\infty$, we obtain the following matrix equations:

$$\begin{aligned}\frac{-j\omega\mu_0}{a}\sum_{i=1}^{\infty}\sum_{n=-\infty}^{\infty}\frac{\tilde{\eta}_{in}\tilde{\eta}^*_{pn}}{T_n}c_i &= \sum_{n=-\infty}^{\infty}\tilde{E}_{\phi n}\tilde{\eta}^*_{pn} \\ &= \frac{1}{d}\int_0^d E_\phi \eta^*_p dz \qquad \text{(Parseval Equation)} \\ &= 0\end{aligned} \tag{17}$$

that is:

$$\mathbf{R}\mathbf{c} = 0 \tag{18}$$

where :

$$R_{ip} = \sum_{n=-\infty}^{\infty}\frac{\tilde{\eta}_{in}\tilde{\eta}^*_{pn}}{T_n} \tag{19}$$

A notrival solution for (18) exsits only if the following determinal equation holds:

$$\det\mathbf{R} = 0 \tag{20}$$

The equation (20) is the general form of the dispersion relation of the circular cylindrical dielectric waveguide with periodic metallic strips. It though simple in form, involves matrix of infinite order which must be truncated. The accurate depends on the order of the truncated matrix or the number of the terms of the basis function and the number of Floquet modes retained in the analysis.

NUMERICAL RESULTS

The solution accuracy of the present analysis is influenced by the choice of basis functions. If the exact current distribution on the metallic strip is given, the solutions becomes exact. In the present paper, the following forms have been chosen:

$$\eta_i(z) = \begin{cases} \cos\left((i-1)\pi z/d_1\right) & 0 \le z \le d_1 \\ 0 & d_1 \le z \le d \end{cases} \qquad \text{for TE modes} \tag{21}$$

$$\xi_i(z) = \begin{cases} \sin\left(i\pi z/d_1\right) & 0 \le z \le d_1 \\ 0 & d_1 \le z \le d \end{cases} \qquad \text{for TM modes} \tag{22}$$

Aithough the current in the circular direction tends to concentrate at the edges of the metallic strip, this effect is approximately taken into account.

Fig.2 and Fig.3 show the typical dispertion diagram for TE_{01} and TM_{01} modes respectively. The enlarge dispersion curve at vicinity of stopband is also shown in the inset of Fig.2 and Fig.3. As expected, the Bragg reflection occurs at $\beta d = \pi$. For frequencies in this region, $k_z = \beta - j\alpha$ is complex. This stopband results from the coupling between $n = 0$ space harmonic of forward waves and $n = -1$ space harmonic of backward waves. This phenomenon can be applied to bandreject filters. In a forbidden region above the two lines

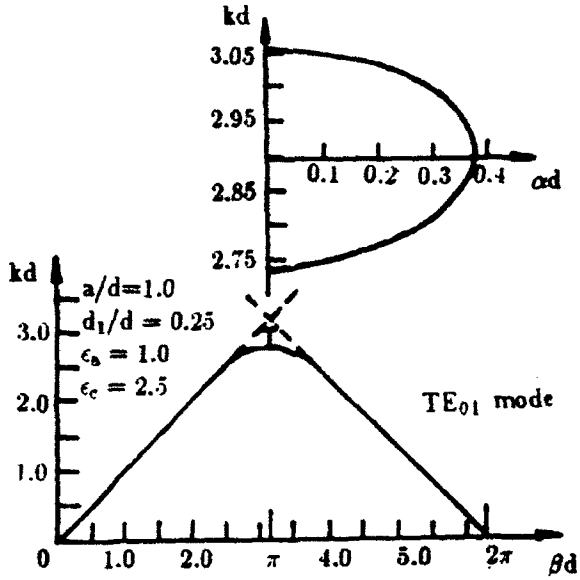

Fig.2 Dispersion diagram for TE_{01} mode

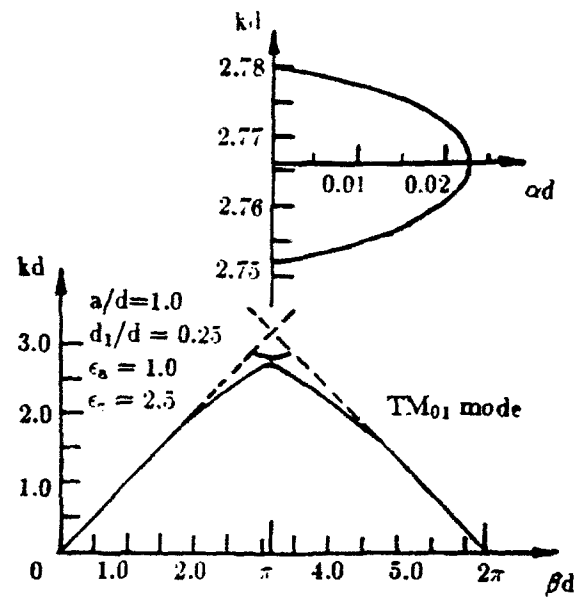

Fig.3 Dispersion diagram for TM_{01} mode

$kd = \beta d$ and $kd = 2\pi - \beta d$, the surface wave couples to a leaky wave that radiates outgoing beams. Here considerations is given to the guiding rather than scattering properties.

REFFERENCE

1. S.T.Peng, Xu Shanjia and F.K.Schwering. 1986 IEEE-APS Digest. pp.697-700.
2. Xu Shanjia, Min Jianhua. S.T.Peng and F.K.Shwering, 1989 IEEE-APS Digest.
3. Xu Shanjia, International Journal of Infrared and Millimeter Waves, pp.405-417, 1989.
4. K.Ogusu, IEEE Trans on MTT, Vol.MTT-29, pp.16-21, 1981.
5. L.Schmidt and T.Itoh, IEEE Trans on MTT, Vol.MTT-28, pp.981-985, 1981.

T4.6

ANALYSIS OF A PLANAR TRANSMISSION LINE WITH DISCONTINUITY USING THE NEW TIME-DOMAIN METHOD OF LINES

Ling Chen Si-Fan Li
Department of Radio Engineering, Southeast University
Nanjing, 210018, P.R.China

ABSTRACT

In this paper, the new technique of time-domain analysis of discontinuities in a planar transmission line is presented. In the process of time-domain analysis, the analysis model of system and the concept of transfer function are employed and the frequency-domain method of lines and the technique of the fast Fourier transform are used. The result shows this method is very simple and calculating time can be greatly reduced.

INTRODUCTION

In recent years, using the method of lines to analyse the characteristics of a planar transmission line has been developed. But, the application of the time-domain method of lines began just now. In 1989, S.Nam and H.Ling first proposed the time-domain analysis method of lines of a planar transmmision line. But, using that method, when the number of time-points is large, the calculating time will be very long. Using the method presented in this paper, the calculating time can be greatly reduced becuase of employing the technique of the fast Fourier transform(FFT). Specially, when the number of time-points is very large, its advantages will be more clear.

THEORY ANALYSIS

Because the relation between a field distribution and an input signal is linear in a planar transmission line, the planar transmission line can be analysed as a linear network. The analysis model of the linear system and the concept of transfer function can be employed. The analysis model is shown in Fig.1.

Fig.1 the analysis model of linear system

In time-domain, the relation between the input signal and the output response is expressed in equation(1).

$$y(t)=h(t)*x(t) \tag{1}$$

To transfer to frequency-domain:

$$Y(\omega)=H(\omega)\times X(\omega) \tag{2}$$

where $Y(\omega)$, $H(\omega)$ and $X(\omega)$ are Fourier transform expressions of $y(t)$, $h(t)$ and $x(t)$, respectively. When the input signal is an ideal pulse, there are:

$$x(t)=\delta(t) \quad \text{and} \quad X(\omega)=1 \tag{3}$$

From equations(1) and (2), we can obtain:

$$y(t)=h(t) \tag{4}$$

$$Y(\omega)=H(\omega) \tag{5}$$

Equations(4) and (5) indicate the transfer function h(t) of system is equal to the impulse response of system. If the transfer function has been solved, the output response can been easily obtained for any definite input signal.

According to the above principle, to solve the field distribution of a planar transmission line for a definite input signal equates to solve the output response of system. The analysis method of system can be employed.

FORMULATION AND PROCEDURE OF THE METHOD

Let us consider a planar transmission line with discontinuity shown in Fig.2. It is assumed that the structure has spatial sysmmetry in x direction, so that the problem can be reduced by factor 2.

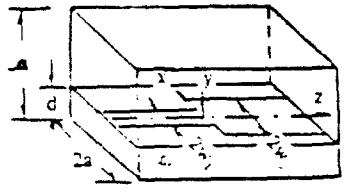

Fig.2 a step microstrip line

A.the Fourier transform of the input signal

First, the input signal is transfered to freguency-domain with the Fourier transform. Supposing $x(t)$ donates the input signal, its frequency-domain expression $X(\omega)$ can be found by

$$X(\omega)=\int_0^{\infty} x(t)e^{-j\omega t}dt \tag{6}$$

Secondly, the operating frequency band is discretized. Because the planar transmission line has band pass characteristic, for using the technique of FFT, it is necessary to expand periodically and to discretize in frequency-domain. In order to regain the continuous Fourier transform waveform by the sample values of discretized points, expaning and discretizing in frequency-domain must satisfy the frequency-domain sampling theorem and the time-domain sampling theorem respectively. Thus, the discretized frequency

-points and the sample values of the input signal at these points are defined.

B.full-wave analysis of a planar transmission line using the method of frequency-domain lines:

For the structure of planar transmission line with discontinuity shown in fig.2, we apply the hybrid homogeneous boundary conditions to solve the field distribution in the discontinuity region with ψ^e and ψ^h being discretized only in and near the discontinuity region. This approach avoids solving the eigenvalue equation and simplifies the calculation[3]:

$$\bar{E}=\nabla\times\nabla\times(\psi^e\hat{z})/(j\omega\varepsilon)-\nabla\times(\psi^h\hat{z}) \tag{7}$$

$$\bar{H}=\nabla\times(\psi^e\hat{z})+\nabla\times\nabla\times(\psi^h\hat{z})/(j\omega\mu) \tag{8}$$

Functions ψ^e and ψ^h are discretized in x and z directions with unequidistant, then they will be denoted by matrices $[\psi^e]$ and $[\psi^h]$, respectively.

We take the incident wave as the impressed wave, denoted by $\psi_I^{e,h}$, and the reflected wave as the excited wave, denoted by $\psi_E^{e,h}$. According to the transmission line theory, in the homogeneous regions, there are:

$$\psi_I^{e,h}=C_I^{e,h}(x,y)e^{-j\beta z} \tag{9}$$

$$\psi_E^{e,h}=C_E^{e,h}(x,y)e^{+j\beta z} \tag{10}$$

in region 1, $\beta=\beta_1$; in region 2, $\beta=\beta_2$.

At $z=0$ and $z=l+\alpha_2$, $\psi_I^{e,h}$ and $\psi_E^{e,h}$ satisfy the hybrid homogeneous boundary conditions:

$$\left.\frac{\partial\psi_{I,E}}{\partial Z}\right|_{z=0}=\mp j\beta_1 C_{I,E}=\mp j\beta_1 e^{\pm j\beta_1\alpha_1}\psi_{I,E}\Big|_{z=\alpha_1}=A^{\pm}\psi_{I,E}\Big|_{z=\alpha_1} \tag{11}$$

$$\left.\frac{\partial\psi_{I,E}}{\partial Z}\right|_{z=l+\alpha_2}=-j\beta_2 C_{I,E}=-j\beta_2 e^{-j\beta_2\alpha_2}\psi_{I,E}\Big|_{z=l}=-B^{-}\psi_{I,E}\Big|_{z=l} \tag{12}$$

With the method proposed by *Worm et al.*[2], we can obtain

$$\left[Z^{I,E}\right]_{red}\begin{bmatrix}\bar{J}_z^{I,E}\\ \bar{J}_x^{I,E}\end{bmatrix}_{strip}=\begin{bmatrix}\bar{E}_z^{I,E}\\ \bar{E}_x^{I,E}\end{bmatrix}_{strip} \tag{13}$$

for strip structures

For the strip structure shown in Fig.2, the strip region is split up into two parts, i.e. transmission line region A and discontinuity region B. The sum of the number of ψ^e and ψ^h lines in region A should be larger than that in region B. By rearranging the rows and columns of matrix $[Z^{I,E}]$, we obtain

$$\begin{bmatrix}\left[Z_{11}^{I,E}\right] & \left[Z_{12}^{I,E}\right]\\ \left[Z_{21}^{I,E}\right] & \left[Z_{22}^{I,E}\right]\end{bmatrix}\begin{bmatrix}J_A^{I,E}\\ J_B^{I,E}\end{bmatrix}=\begin{bmatrix}E_A^{I,E}\\ E_B^{I,E}\end{bmatrix} \tag{14}$$

The superposition of the impressed field and the excited field must satisfy the tangential condition for the conductor surface

$$\begin{cases} E_A = E_A^I + E_A^E = 0 & (15) \\ E_B = E_B^I + E_B^E = 0 & (16) \end{cases}$$

In region A, the field distribution is homogeneous in Z direction, J_A^I can be solved by 2-D analysis of the transmission line at port 1. J_A^E has the relation with J_B^E as follows

$$J_A^E = [P] J_B^E \qquad (17)$$

where matrix [P] can be determined easily.

So J_B^I, J_B^E and J_A^E can be solved from equations(14)-(17) and the S parameter of the discintinuity region can be calculated.

C.the inverse Fourier transform

If the field distribution at every frequency-point has been solved, the time-domain field distribution can be solved easily with FFT. From the feature of the Fourier transform: the magnitude spectrum is an odd function of frequency and the phase spectrum is an even function of frequency, we can obtain:

$$YR(k+1) = YR(N-k+1) \qquad (18)$$

$$YI(k+1) = -YI(N-k+1) \qquad (19)$$

$(k = 1, 2, \cdots\cdots, N/2)$

where YR(k) is the real part of Y(k) and YI(k) is the imaginary part of Y(k), N is the number of sampling points in a sample period. In general, $N=2^m$, m=1,2,——. According to this, if the field distribution at N/2 frequency-points has been solved, the field distribution at N time-points can be solved with the technique of FFT.

CONCLUSION

Appling the approach described above, we have developed a computer program for analysing the characteristics of a planar transmission line with step discontinuity shown in Fig.2 in time-domain. The calculating results show this method is available in time-domain analysis. The calculating process is simple and clear and the calculating time can be reduced greatly comparaed with the other methods. This approch can be applied to various planar structures.

REFERENCES

[1] H.Diestel and S.B.Worm, IEEE Trans. Vol.MTT-32 PP.633-638, 1984

[2] S.B.Worm and R.Pregla, IEEE Trans. Vol.MTT-32 PP.191-196, 1984

[3] Z.Q.Chen and B.X.Gao, IEEE Trans. Vol.MTT-37 PP.606-611, 1989

[4] S.Nam and H.Ling, IEEE Trans. Vol.MTT-37 PP.2051-2057, 1989

THE NEW APPROACH OF FULL-WAVE ANALYSIS OF DISCONTINUITIES IN A PLANAR TRANSMISSION LINE

Ling Chen Si-Fan Li
DEPARTMENT OF RADIO ENGINEER, SOUTHEAST UNIVERSITY
NANJING, 210018, P.R.CHINA

ABSTRACT

In this paper, the new approach of full-wave analysis of discontinuities in a planar transmission line is presented. In using the method of lines, by introducing the hybrid homogeneous boundary conditions, the field distribution and various parameters of the inhomogeneous region are solved according to the field distribution of the homogeneous region with the transmission relation of wave in both regions. Comparing with other methods of analysis of discontinuities, this approach is more simple and more accurate

INTRODUCTION

In recent years, some methods of analysis of planar transmission lines have been developed. At higher operating frequencies, full-wave analysis is more accurate than quasi-static analysis. The method of lines is a semianalytic and semidiscrete full-wave analysis method. It avoids the choice of basic functions and the relative convergence problem. This method not only has been applied to analyse discontinuity problems on the Dirichlet and the Neumann homogeneous boundary conditions, but also on the hybrid homogeneous boundary conditions [2], [3]. But, in applying to the hybrid homogeneous boundary conditions to analyse the field distribution in discontinuity regions[3], the authors considered the reflected wave existing only in the discontinuity regions. We consider it can be transmitted to the homogeneous regions as a new "exciting source". According to this, the new approach of full-wave analysis of discontinuities is presented. In this paper, this method is introduced in detail and an illustrative example of a planar transmission line with step discontinuity is given. The result shows this approach has higher accuraty and reliability.

FORMULATION

Let us consider the planar transmission line with discontinuity shown in

Fig.1. We apply the hybrid homogeneous boundary conditions to solve the field distribution in the discontinuity region with ψ^e and ψ^h being discretized only in and near the discontinuity region. This approach avoids solving the eigenvalue equation and simplifies the calculation[3]:

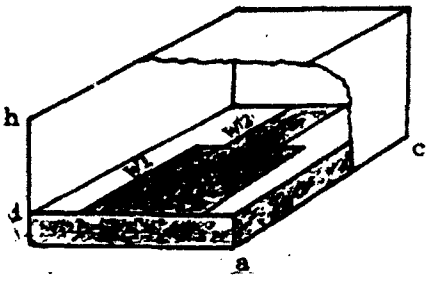

Fig.1 a step microstrip line

$$\bar{E}=\nabla\times\nabla\times(\psi^e\hat{z})/(j\omega\varepsilon)-\nabla\times(\psi^h\hat{z}) \tag{1}$$

$$\bar{H}=\nabla\times(\psi^e\hat{z})+\nabla\times\nabla\times(\psi^h\hat{z})/(j\omega\mu) \tag{2}$$

Functions ψ^e and ψ^h are discretized in x and z directions with unequidistant, then they will be denoted by matrices $[\psi^e]$ and $[\psi^h]$ respectively.

We take the incident wave as the impressed wave, denoted by $\psi_I^{e,h}$, and the reflected wave as the excited wave, denoted by $\psi_E^{e,h}$. According to the transmission line theory, in the homogeneous regions, there are:

$$\psi_I^{e,h}=C_I^{e,h}(x,y)e^{-j\beta z} \tag{3}$$

$$\psi_E^{e,h}=C_E^{e,h}(x,y)e^{+j\beta z} \tag{4}$$

in region 1, $\beta=\beta_1$; in region 2, $\beta=\beta_2$.

As z=0 and $z=l+\alpha_2$, $\psi_I^{e,h}$ and $\psi_E^{e,h}$ satisfy the hybrid homogeneous boundary conditions:

$$\left.\frac{\partial\psi_{I,E}}{\partial Z}\right|_{z=0}=\mp j\beta_1 C_{I,E}=\mp j\beta_1 e^{\pm j\beta_1\alpha_1}\psi_{I,E}\Big|_{z=\alpha_1}=A^{\pm}\psi_{I,E}\Big|_{z=\alpha_1} \tag{5}$$

$$\left.\frac{\partial\psi_{I,E}}{\partial Z}\right|_{z=l+\alpha_2}=-j\beta_2 C_{I,E}=-j\beta_2 e^{-j\beta_2\alpha_2}\psi_{I,E}\Big|_{z=l}=-B^{-}\psi_{I,E}\Big|_{z=l} \tag{6}$$

With the method proposed by *Worm et al.*[2], we can obtain

$$\left[Z^{I,E}\right]_{red}\begin{bmatrix}\bar{J}_z^{I,E}\\ \bar{J}_x^{I,E}\end{bmatrix}_{strip}=\begin{bmatrix}\bar{E}_z^{I,E}\\ \bar{E}_x^{I,E}\end{bmatrix}_{strip} \tag{7}$$

For the strip structure shown in Fig.1, the strip region is split up into two parts, i.e. transmission line region A and discontinuity region B. The sum of the number of ψ^e and ψ^h lines in region A should be larger than that in region B. By rearranging the rows and columns of matrix $[Z^{I,E}]$, we obtain

$$\begin{bmatrix}[Z_{11}^{I,E}] & [Z_{12}^{I,E}]\\ [Z_{21}^{I,E}] & [Z_{22}^{I,E}]\end{bmatrix}\begin{bmatrix}J_A^{I,E}\\ J_B^{I,E}\end{bmatrix}=\begin{bmatrix}E_A^{I,E}\\ E_B^{I,E}\end{bmatrix} \tag{8}$$

The superposition of the impressed field and the excited field must satisfy

the tangential condition of the conductor surface

$$\begin{cases} E_A = E_A^I + E_A^E = 0 \\ E_B = E_B^I + E_B^E = 0 \end{cases} \tag{9}$$

In region A, the field distribution is homogeneous in Z direction, J_A^I can be determined by

$$J_{Aij}^I = (J_A^I\big|_{z=0})_i e^{-j\beta_1 \sum_{k=1}^{j} e_{zk}} \tag{10}$$

$$(i=1, 2, \cdots\cdots, N_{ex};\ j=1, 2, \cdots\cdots, N1_{ez})$$

where $J_A^I\big|_{z=0}$ and β_1 can be solved by 2-D analysis of the transmission line at port 1. J_A^E has the relation with J_B^E as follows

$$J_{Aij}^E = J_{Bi1}^E e^{-j\beta_1 \sum_{k=j+1}^{N1_{ez}+1} e_{zk}} \tag{11}$$

$$(i=1, 2, \cdots\cdots, N_{ex};\ j=1, 2, \cdots\cdots, N1_{ez})$$

So we have

$$J_A^E = [P] J_B^E \tag{12}$$

where matrix [P] can be determined by equation(11). Taking equations(8) and (12) into (9), we can obtain

$$[Z_{12}^I] J_B^I + \{[Z_{11}^E][P] + [Z_{12}^E]\} J_B^E = -[Z_{11}^I] J_A^I \tag{13}$$

$$[Z_{22}^I] J_B^I + \{[Z_{21}^E][P] + [Z_{22}^E]\} J_B^E = -[Z_{21}^I] J_A^I \tag{14}$$

From equations(13) and (14), J_B^I and J_B^E can be solved and then J_A^E can be determined by equation(12). The S parameter of the discintinuity region can be calculted.

CONCLUSION

Appling the approach described above, we have developed a computer program for full-wave analysing the characteristics of a planar transmission line with step discontinuity shown in Fig.1 in frequency-domain. The results are shown in Fig.2 and Fig.3. The calculating results show this method is accurate and available. The calculating process is simple and clear and it avoids solving the eigenvalue equation. This approch can be applied to various planar structures.

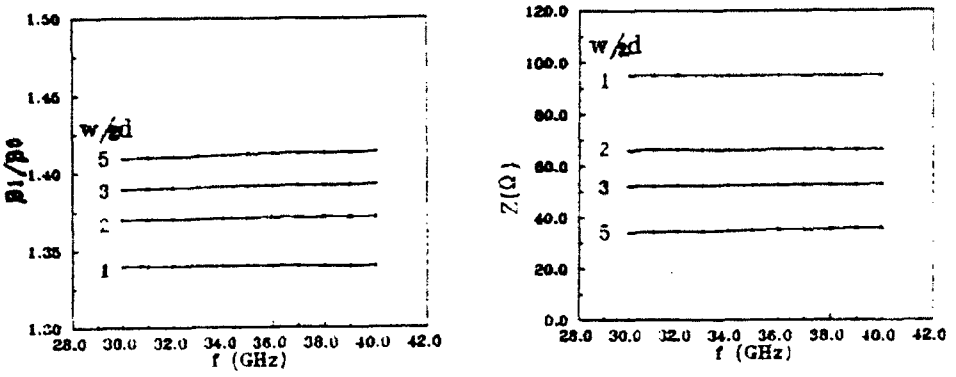

(ε_r=2.22, d=0.254mm, a=8mm, b=5mm)

(a) (b)

Fig.2 Dispersion characteristics for shielded microstrip lines

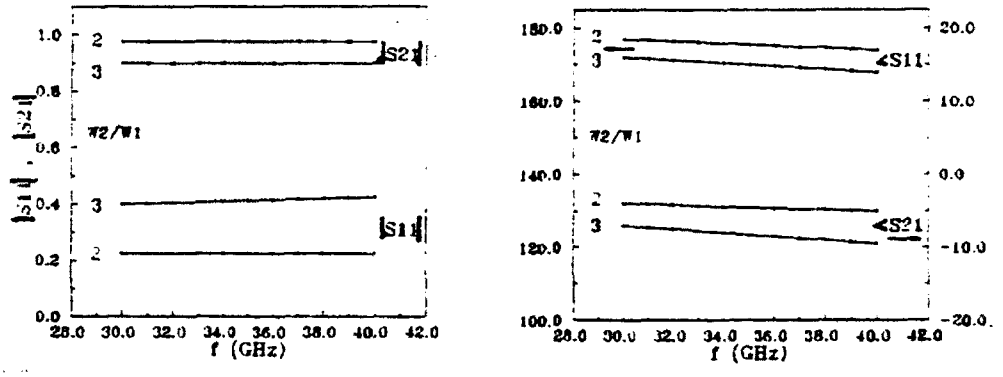

(ε_r=2.22, d=0.254mm, a=8mm, b=5mm, w1/d=3)

(a) (b)

Fig.3 the S parameters of a microstrip step discontinuity

REFERENCES

[1] H.Diestel and S.B.Worm, Analysis of hybrid field problems by the method of lines with nonequidistant discretization, IEEE Trans. *Microwave Theory and Tech.* Vol.MTT-32 PP.633-638, 1984

[2] S.B.Worm and R.Pregla, Hybrid-mode analysis of arbitrarily shaped planar microwave structures by the method of lines, IEEE Trans. *Microwave Theory and Tech.* Vol.MTT-32 PP.191-196, 1984

[3] Z.Q.Chen and B.X.Gao, Deterministic approch to full-wave analysis of discontinuities in MIC's using the method of lines, IEEE Trans. *microwave Theory and Tech.* Vol.MTT-37 PP.606-611, 1989

T4.8

TRANSIENT ANALYSIS OF MICROSTRIP STEP DISCONTINUITIES ON ANISOTROPIC SUBSTRATE HAVING A TILTED OPTICAL AXIS

GUOWU ZHENG and KANGSHENG CHEN
ZHEJIANG UNIVERSITY, HANGZHOU 310008, P. R. CHINA

ABSTRACT

In this paper, we present the numerical simulation of transient response of short pulse propagating through a microstrip step junction on anisotropic substrate having a tilted optical axis. In the simulation, the FD-TD method is extended to treat the cases having tilted optical axis expressed by a permittivity tensor with off-diagonal elements. The results show that the dispersion of transient signal caused by microstrip step discontinuities is quite significant and the dependence of transient characteristics of microstrip lines on the tilted angle of optical axis for anisotropic substrate can not be neglected.

INTRODUCTION

With the development of MIC and MMIC the transient analysis of microstrip lines with anisotropic substrates has attracted considerable attention[1-2]. Transient analysis of electromagnetic field is useful not only in clarifying the field response but also in providing information on the mechanism by which the distribution of the electromagnetic field in the stationary state is brought about. In general, anisotropic substrates demand an exact three dimensional treatment using all electromagnetic field components. Furthermore, the analysis of propagation of short pulse wave requires computation in the time domain. As a time domain vector analysis method for a three dimensional electromagnetic field, the FD-TD method [3] and the TLM method[4] are used. For the problems involving anisotropic medium, the FD-TD method developed so far is difficult to formulate the cases having tilted optical axis expressed by a permitivity tensor $\bar{\bar{\varepsilon}}$ with off-diagonal elements. Koike et al[1] have extended TLM method to transient analysis of microstrip lines on anisotropic substrate having tilted optical axis, but the effects of microstrip step discontinuities on transient response have not been included in their analysis. In this paper, we extended the FD-TD method to the three-dimensional vector analysis in the time domain for dielectric material with a tensor involving off-diagonal elements. In contrast to the traditional FD-TD method, The field components $\vec{E}$, $\vec{D}$, $\vec{H}$ are involved in the set of difference forms of maxwell's equations. In the simulation procedure, $\vec{D}$ is first simulated in time domain, $\vec{E}$ is then obtained by the constitutive relation $\vec{D} = \bar{\bar{\varepsilon}}\vec{E}$. In comparison with the method developed by [1], less memory is needed in the extended FD-TD method proposed in the paper.

With this extended FD-TD method, the transient response of short pulse propagating through a microstrip step junction on anisotropic substrate having a tilted optical axis is numerically simulated in detail. It is shown that the transient dispersion caused by microstrip

step discontinuities is quite significant and the dependence of transient characteristics of microstrip lines on the tilted angle of optical axis for anisotropic substrate can not be neglected. The results so obtained are valuable for understanding the anisotropic substrate orientation effects on transient response of microstrip and the design of MIC and MMIC.

FORMULATION FOR THE EXTENDED FD-TD METHOD

The structural model of microstrip lines in the analysis is shown in Fig. 1. Both conductor and dielectric are assumed to be lossless. The anisotropy of substrate is represented by the following dielectric tensor when the structure coordinate(x,y) is in coincidence with the principal optical axes(ξ,η)

$$\bar{\bar{\varepsilon}} = \varepsilon_0 \begin{bmatrix} \varepsilon_\xi & 0 & 0 \\ 0 & \varepsilon_\eta & 0 \\ 0 & 0 & \varepsilon_z \end{bmatrix} \tag{1}$$

where $\varepsilon_0$is the permittivity in free space. If the ξ, η coordinate system is tilted with respect to the xy coordinate system by an angle θ, as shown in Fig.1. The permittivity tensor $\bar{\bar{\varepsilon}}$ in the xyz coordinate system is given by

$$\bar{\bar{\varepsilon}} = \varepsilon_0 \begin{bmatrix} \varepsilon_{xx} & \varepsilon_{xy} & 0 \\ \varepsilon_{yx} & \varepsilon_{yy} & 0 \\ 0 & 0 & \varepsilon_z \end{bmatrix} \tag{2}$$

where
$$\varepsilon_{xx} = \varepsilon_\xi \cos^2\theta + \varepsilon_\eta \sin^2\theta$$
$$\varepsilon_{yx} = \varepsilon_{xy} = (\varepsilon_\eta - \varepsilon_\xi)\sin\theta\cos\theta \tag{3}$$
$$\varepsilon_{yy} = \varepsilon_\xi \sin^2\theta + \varepsilon_\eta \cos^2\theta$$

In contrast with the conventional FD-TD method. the maxwell's equations are written as

$$\nabla \times \vec{E} = \frac{1}{\mu}\frac{\partial \vec{H}}{\partial t} \qquad \nabla \times \vec{H} = \frac{\partial \vec{D}}{\partial t} \tag{4}$$

Where
$$\vec{D} = \bar{\bar{\varepsilon}}\,\vec{E} \tag{5}$$

Following Yee's procedure[3], we first place the field components on the mesh as depicted in Fig.2. It sould be pointed out that the components of $\vec{D}$ are placed in the same position as ones of $\vec{E}$. Using Yee's notation, the difference forms of Maxwell's equations (4) can be constructured. The equation for Dx component can be written as:

$$D_x^{n+1}(i,j,k) = D_x^n(i,j,k) + \Delta t\left[\frac{H_z^{n+1/2}(i,j+1,k) - H_z^{n+1/2}(i,j,k)}{\Delta y} - \frac{H_y^{n+1/2}(i,j,k+1) - H_y^{n+1/2}(i,j,k)}{\Delta z}\right] \tag{6}$$

Where Δx, Δy, Δz are the space discretization units in x, y, z direction, respectively, and Δt is the time increment interval.

For computational stability, the relation among Δx, Δy, Δz and Δt must satisfy:

$$V_{max} \Delta t \le \left[\sqrt{\frac{1}{\Delta x^2} + \frac{1}{\Delta y^2} + \frac{1}{\Delta z^2}}\right]^{-1} \tag{7}$$

where V_{max} is the maximum phase velocity in the configuration being

analyzed. The treatment of boundary condition on the metal wall and interface of dielectric is similar to our previous work[2]. J. Fang's model[5-6] to deal with the absorbing boundary condition at the end is utilized in the analysis.

NUMERICAL SIMULATION AND RESULTS

For the numerical simulation by the extended FD-TD method, Gaussion short pulse is to be chosen because of its smooth property in time

$$g(t) = \exp\left[-\frac{(t-to)^2}{T^2}\right] \qquad (8)$$

At the initial excitation instant, the spatial distribution of electronmagnetic field is supposed to be uniform in the exciting plane and under the metal strip only the normal field components are considered.

The parameters of the model to be analyzed, as shown in Fig.1, are as follows. The elements of dielectric tensor are ε_ξ=11.6, ε_η=9.4, ε_z=13, the width of metal strip N_{w1}=N_{w2}=6(for uniform microstrip), N_{w2}=9(for microstrip step discontinuity), the dimension of microstrip lines N_x=15 N_h=8 N_y=28 N_{zs}=65 N_z=120, and $\Delta x=\Delta y=\Delta z$, $C\Delta t/\Delta x$= .515, for the initial Gaussion pulse T=140Δt, t_0=300Δt.

The typical effects of step discontinuity on the dispersion of Gaussion short pulse wave propagating along uniform and step discontinuity microstrip lines in which the tilt angle θ of the optical axis is equal to zero are shown in Fig.3. We can find that the amplitude of pulse after step junction is smaller than that propating along uniform microstrip at the same position. Comparing the wave amplitudes just before the step junction, the signal for the case of step discontinuity is smaller than that for the uniform case, which can be explained by the reflection from the step junction.

Fig.4 demonstrates the effects of tilt angle θ on the distortion of the Gaussion short pulse wave scattered by microstrip step junction. It is evident that the transient response of microstrip is obviously affected by the change of θ, the Gaussion pulse at θ=0 is lead to those at $\theta=\pi/3$. The results is coincident with [2], qualitatively.

REFERENCES

1. S. Koike, et al,"Transient analysis of microstrip line on anisotropic substrate in three-dimensional space," IEEE Trans. MTT, Vol.36, No.1, Jan. 1988, pp34-43
2. Guowu Zheng & Kangsheng Chen,"Effects of substrate anisotropy on the dispersion of transient signals in microstrip lines," Int. J. of Infrared & Millimeter waves, Vol.11, No.4, 1990
3. k. S. Yee,"Numerical solution of initial boundary value problems involving maxwell's equation in isotropic media," IEEE Trans. Ap, Vol.14, No.3, May 1966, pp302-307
4. S. Akhtarzad and P. B. Johns,"Solution of Maxwell's equations and time by the t.l.m. method of numerical analysis ," Proc. IEE, Vol.122, No.12, Dec. 1975, pp1344-1348.
5. J. Fang & K. K. Mei,"A super-absorbing boundary algorithum for solving electromagnetic problems by time-domain finite-difference method," In 1988 IEEE AP-S Int. Symp. Dig., June 1988, pp472-475
6. X. Zhang, et al,"Time-domain finite difference approch for calculating discontinuities and termination effects," IEEE Trans. MTT, Vol.35, Dec. 1988, pp1775-1787

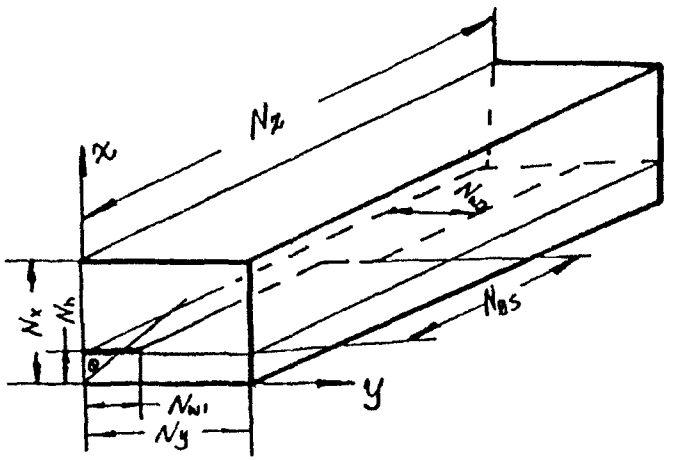

Fig.1 the microstrip structure with anisotropic substrate

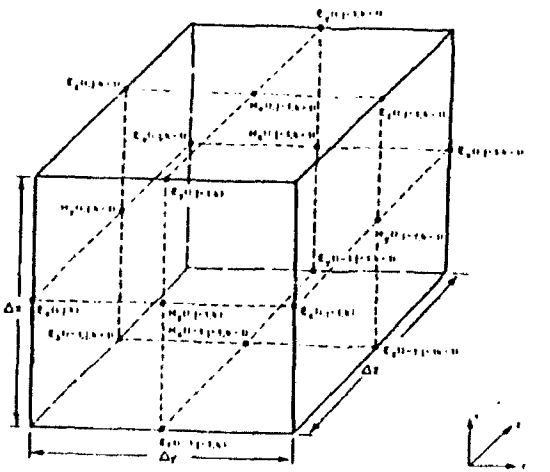

Fig.2 the position of field components in difference mesh

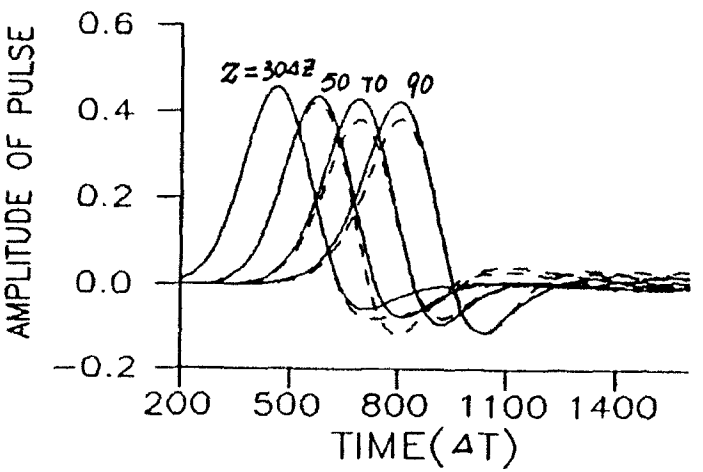

Fig.3 The shapes of Gaussion pulse propagating along microstrip at the same tilt angle of optical axis(θ=0)

—— uniform microstrip

---- step discontinuity microstrip

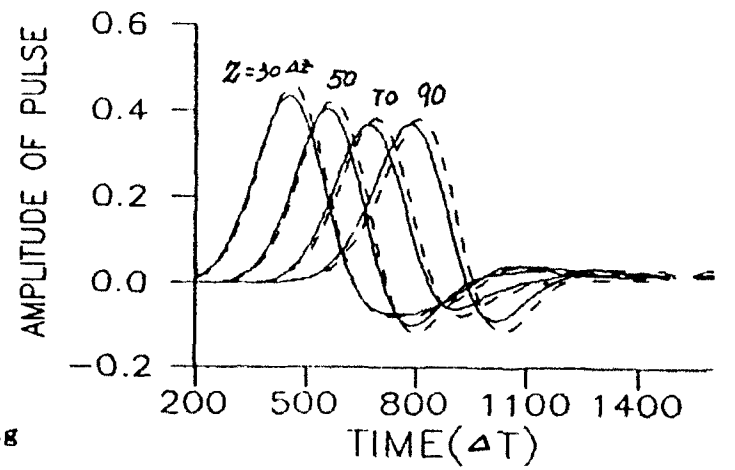

Fig.4 The shapes of Gaussion puse propagating along step discontinuity microstrip with different tilted angle of optical axis

---- θ=0 —— θ=π/3

T4.9

EFFICIENT ANALYSIS OF FINLINE STRUCTURES BY THE BOUNDARY-ELEMENT METHOD

Bin Song , Junmei Fu
(Xi'an Jiaotong University, Xi'an, P.R.China)

ABSTRACT

A boundary-element method is presented for the rigorous investigation of a generalized finline configuration. The method is accurate and covers the metallization thickness, mounting grooves, and arbitrary cross sections. By this approach, calculations can be performed using far fewer nodes than by the finite-element method. To show the efficiency of this approach, two examples are given.

INTRODUCTION

A variety of planar transmission lines are used in newly developed millimeter-wave circuits. Among these, finlines are widely employed, allowing high flexibility in circuit realization. Up to now, many papers have been published describing experimental and theoretical investigation of finlines. However, most of the methods either have restricted application or require a large computer memory and long computing time, e.g., the modified mode-matching technique[1] and the transverse resonance method[2] can only study structures of regular cross sections , and the finite-element method(FEM) may handle arbitrary cross-sectional geometries[3], but the number of nodal points divided is very large, so the CPU time required is considerable. The purpose of this study is to develop a very general boundary-element procedure which can analyze generalized finline configurations of arbitrary cross sections , including finite metallization thickness, substrated mounting grooves, asymmetric structures, and more than one dielectric region. The boundary-element method(BEM) proposed in this paper has a few merits, i.e., the required size of the computer memory being small, the computation time being short and the results obtained having fairly good accuracy.

THEORY

Consider a waveguide of arbitrary shape which is uniform in the Z direction and which consists of isotropic, lossless dielectric media. The cross section can be divided into several subregions homogeneously filled with a dielectric material. Assumed that the electromagnetic wave propagates along the Z direction of the form, and in a typical subregion, the longitudinal field components satisfy the Helmholtz's equation

$$\nabla_t^2 Ez + (ki^2 - \beta^2)Ez = 0 \tag{1a}$$

$$\nabla_t^2 Hz + (ki^2 - \beta^2)Hz = 0 \tag{1b}$$

where ∇_t^2 is the transverse Laplacian operator, and ki is the wavenumber in the subregion.

Using the method of weighted residuals[4], from (1) the following equations can be obtained.

$$Ez(ri) + \int_L \frac{\partial G(r_i, r_j)}{\partial n} Ez(rj)dl = \int_L G(ri, rj) \frac{\partial E_z(r_j)}{\partial n} dl \tag{2a}$$

$$Hz(ri) + \int_L \frac{\partial G(\gamma_i,\gamma_j)}{\partial n} Hz(rj)dl = \int_L G(ri,rj) \frac{\partial H_z(\gamma_j)}{\partial n} dl \qquad (2b)$$

here G(ri,rj) is Green's function in two-dimensional free-space. The position of a node inside subregion is represented by the vector ri , and that on boundary L is denoted by the vector rj . $\hat{n}$ and $\hat{t}$ refer to the outward unit normal vector and the tangential unit normal vector, respectively, as shown in Fig.1.

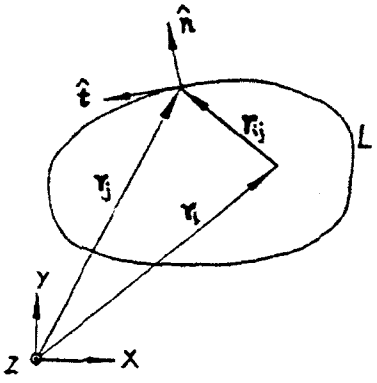

Fig. 1 Two-dimension region surrounded by boundary L.

Considering Gauss' principle, (2) can be rewritten as

$$Ez(ri) = -\int_L \frac{\partial G(\gamma_i,\gamma_j)}{\partial n} Ez(rj)dl + \int_L G(ri,rj) \left[\frac{\partial E_z(\gamma_j)}{\partial n} + \frac{\beta}{\omega\varepsilon_i}\cdot\frac{\partial H_z(\gamma_j)}{\partial t}\right]dl + \frac{\beta}{\omega\varepsilon_i}\int_L \frac{\partial G(\gamma_i,\gamma_j)}{\partial t} Hz(rj)dl \qquad (3a)$$

$$Hz(ri) = -\int_L \frac{\partial G(\gamma_i,\gamma_j)}{\partial n} Hz(rj)dl + \int_L G(ri,rj) \left[\frac{\partial H_z(\gamma_j)}{\partial n} - \frac{\beta}{\omega\mu}\cdot\frac{\partial E_z(\gamma_j)}{\partial t}\right]dl - \frac{\beta}{\omega\mu}\int_L \frac{\partial G(\gamma_i,\gamma_j)}{\partial t} Ez(rj)dl \qquad (3b)$$

Assumed that the boundary L is smooth, letting ri approaches it and considering Cauchy's principal value of integration, and using the following equations

$$Et = \frac{j\omega\mu}{k_i^2-\beta^2}\left(\frac{\partial H_z}{\partial n} - \frac{\beta}{\omega\mu}\cdot\frac{\partial E_z}{\partial t}\right)$$
$$Ht = -\frac{j\omega\varepsilon_i}{k_i^2-\beta^2}\left(\frac{\partial E_z}{\partial n} + \frac{\beta}{\omega\varepsilon_i}\cdot\frac{\partial H_z}{\partial t}\right) \qquad (4)$$

the next equations is derived as follows,

$$(1/2)Ez(ri) + \int_L \frac{\partial G(\gamma_i,\gamma_j)}{\partial n} Ez(rj)dl = \int_L G(ri,rj)\left[-\frac{k_i^2-\beta^2}{j\omega\varepsilon_i} Ht(rj)\right]dl + \frac{\beta}{\omega\varepsilon_i}\int_L \frac{\partial G(\gamma_i,\gamma_j)}{\partial t} Hz(rj)dl \qquad (5a)$$

$$(1/2)Hz(ri) + \int_L \frac{\partial G(\gamma_i,\gamma_j)}{\partial n} hz(rj)dl = \int_L G(ri,rj)\left[\frac{k_i^2-\beta^2}{j\omega\mu} Et(rj)\right]dl - \frac{\beta}{\omega\mu}\int_L \frac{\partial G(\gamma_i,\gamma_j)}{\partial t} Ez(rj)dl \qquad (5b)$$

Dividing the boundary L into N constant elements, and equation (5a) and (5b) are then discretized as,

$$(1/2)Ezi + \sum_{j=1}^{N}\left(\int_{Lj}\frac{\partial G(\vec{r}_i,\vec{r}_j)}{\partial n}dl\right)Ezj = \sum_{j=1}^{N}\left(\int_{Lj}G(ri,rj)dl\right)\left[-\frac{k_i^2-\beta^2}{j\omega\varepsilon_i}Htj\right] + \frac{\beta}{\omega\varepsilon_i}\sum_{j=1}^{N}\left(\int_{Lj}\frac{\partial G(\vec{r}_i,\vec{r}_j)}{\partial t}dl\right)Hzj \quad (6a)$$

$$(1/2)Hzi + \sum_{j=1}^{N}\left(\int_{Lj}\frac{\partial G(\vec{r}_i,\vec{r}_j)}{\partial n}dl\right)Hzj = \sum_{j=1}^{N}\left(\int_{Lj}G(ri,rj)dl\right)\left[\frac{k_i^2-\beta^2}{j\omega\mu}Etj\right] - \frac{\beta}{\omega\mu}\sum_{j=1}^{N}\left(\int_{Lj}\frac{\partial G(\vec{r}_i,\vec{r}_j)}{\partial t}dl\right)Ezj \quad (6b)$$

(6) can be represented in the following matrix form:

$$[A][Ez] + \frac{k_i^2-\beta^2}{j\omega\varepsilon_i}[B][Ht] - \frac{\beta}{\omega\varepsilon_i}[C][Hz] = 0$$
$$[A][Hz] - \frac{k_i^2-\beta^2}{j\omega\mu}[B][Et] + \frac{\beta}{\omega\mu}[C][Ez] = 0 \quad (7)$$

where [Ezj], [Hz], [Et], [Ht] are N×1 column matrices, and the elements of them represent the field values at nodal points on the boundary; [A], [B], [C] are N×N coefficient matrices.

In the same way, to subregion Sj, the boundary matrix equation like (7) can be formed. Considering the continuity of the tangential electric and magnetic fields along the common interface between contiguous subregions(say the ith and jth), the following equations are required.

$$\overset{(i)}{Ez} = \overset{(j)}{Ez} \quad ; \quad \overset{(i)}{Hz} = \overset{(j)}{Hz} \quad ; \quad \overset{(i)}{Et} = \overset{(j)}{Et} \quad ; \quad \overset{(i)}{Ht} = \overset{(j)}{Ht} \quad (8)$$

So the final boundary matrix equation of the whole region can be obtained, and can be written as a *homogeneous* equations set in the form

$$[U][X] = 0 \quad (9)$$

where the elements of matrix [U] are all the functions of propagation constant.

Considering the condition that makes (9) exist nonzero solutions, namely,

$$|U| = 0 \quad (10)$$

the propagation constant β can be obtained.

In our approach, Hankel function, which satisfies radiation condition, is employed as Green's function, so no spurious solutions appear.

RESULTS

First of all, the asymmetrical bilateral finline treated in [1] is calculated with our method, and Fig.2 shows its dispersion behavior. Our results agree roughly with those in [1] except that the propagation constant of HE2 mode is higher than that of HE1 mode for frequencies beyond 19.6 GHz instead of 20 GHz reported in [1].

In order to show the flexibility of this method, we study a bilateral finline in circular waveguide housing which cannot be handled with the modified mode-matching technique[1] or the transverse resonance method[2]. Calculated results for the dispersion characteristics are shown in Fig.3. The obtained results for zero grooves depth and zero metallization thickness are in agreement with data obtained via the FEM[3]. For a finite grooves depth and finite metallization thickness, the propagation constant of HE1 mode slightly increases, while those of the higher order modes increase remarkably. The above BEM calculations are performed with 126 nodes, while the corresponding FEM calculations need at least 400 nodes.

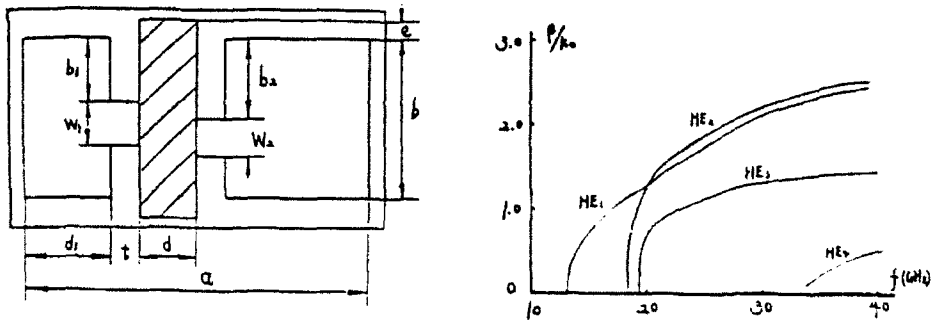

Fig. 2 Normalized propagation constant as a function of frequency for the asymmetrical bilateral finline.
(a=2b=7.112mm ; a1=2.2606mm ; b1=1.201mm ; w1=2.5mm ; b2=2.156mm ; w2=1.5mm ; e=0.7mm ; d=0.254mm ; t=0.07mm ; εr=9.6)

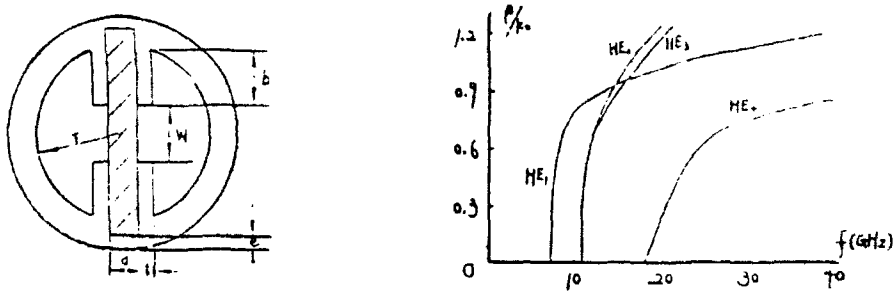

Fig. 3 Dispersion characteristics of the bilateral finline in circular waveguide housing.
(r=4.165mm ; d=0.254mm ; w=0.3mm ; e=0.35mm ; t=0.005mm ; εr=2.2)

CONCLUSIONS

In this paper, a boundary-element procedure for the rigorous investigation of generalized finline structures is proposed. The method has a few merits, i.e., it can handle generalized finline configuration which includes finite strip thickness, substrate mounting grooves, more than one dielectric region and arbitrary cross-sectional geometries, and it only requires a small computer memory and short computation time. Moreover, the results obtained have fairly good accuracy. In addition, this approach can be applied to the full-wave analysis of various microwave and millimeter-wave transmission lines with arbitrary cross-sectional geometries.

REFERENCES

1. R.Vahldieck and J.Bornemann, IEEE Trans., MTT-33, 7(1985), 916.
2. J.Bornemann and F.Arndt, IEEE Trans., MTT-21, 1(1986), 85.
3. Eswarappa and G.Costache, IEEE Trans., MTT-37, 2(1989), 299.
4. C.A.Brebbia, Boundary element techniques in engineering, Butterworth, London, 1980.

Development of a High-Power, Power-Modulated TEA CO_2 Laser System as a Driving Source of Electrostatic Plasma Waves

K. Sasaki, K. Takahashi, T. Fujii, M. Nagatsu and T. Tsukishima

Department of Electrical Engineering, Nagoya University, Nagoya 464-01, Japan

ABSTRACT

A high-power, power-modulated TEA CO_2 laser system is developed with the intention of applying it to high-temperature plasmas for diagnostic purpose. Two-mode pulse injection locking is adopted to obtain the required output pulses of the TEA CO_2 laser. Together with the power modulation, the gain-switched spike of the output pulses are also suppressed by the adopted method, resulting in elongation of pulse duration. Two feedback loops are incorporated for reliable power modulation. The power-modulated output so obtained is used to excite electrostatic plasma waves in laboratory plasmas.

1. INTRODUCTION

We have proposed the driven scattering method as a novel diagnostic scheme for high-temperature plasmas.[1] In driven scattering, electrostatic plasma waves are excited by the ponderomotive force of an externally injected power-modulated laser beam. Certain plasma parameters such as ion temperature can be derived from the dispersion relation of the excited electrostatic wave. The dispersion relation can be measured by FIR laser scattering. The main advantage of the driven scattering method over the conventional ion Thomson scattering is that the incident laser power for scattering measurement can be considerably lower than that for the conventional case, because the scattering cross section is much larger for the super-thermal density fluctuations (electrostatic waves) than for thermal fluctuations.

A high-power, power-modulated laser source with long pulse duration (1μs) is indispensable for the driven scattering plasma diagnostics. The long pulse duration is needed to measure the dispersion relation of the excited waves with high signal-to-noise ratio. In this paper, we present a TEA CO_2 laser system which can yield a high-power, power-modulated output with long pulse duration. The two-mode pulse injection locking scheme is adopted to modulate and elongate the output pulse of the TEA CO_2 laser. Two feedback loops are incorporated in the present system to achieve reliable power modulation.

2. LASER SYSTEM

The two-mode pulse injection-locked TEA CO_2 laser system including feedback stabilization loops is schematically shown in Fig.1. The system consists of a hybrid TEA CO_2 laser as the injection source and a main TEA CO_2 laser.

The hybrid TEA CO_2 laser is composed of a TEA section and a cw section. The 4.9m-long cavity resonator consists of a spherical partial mirror M1 mounted on a piezoelectric transducer PZT1 and a gold-coated plane mirror M2. The active length of the cw section is 60cm, which is designed to realize both the above and below threshold operation in the range of the discharge current obtainable with our power source. The main TEA CO_2 laser is a Lumonics 601 with an unstable resonator consisting of a

convex mirror M9 and a concave mirror M10. The spherical radii of M9 and M10 are 2.5m and 10m, respectively. The cavity length is 5.2m which is close to the cavity length of the hybrid laser. The convex mirror M9 is mounted on PZT2.

In the present system, two-mode pulsed field of the hybrid TEA CO_2 laser is injected into the cavity of the main TEA CO_2 laser through the coupling hole (5mm diameter) bored at the center of M10. The injected two-mode field is obtainable with the cw section in the below threshold state.[2] When the frequencies of the injected two modes coincide with the two respective adjacent longitudinal modes of the main TEA CO_2 laser, the two modes of the main laser are allowed to oscillate exclusively, and the output pulse of the main laser is power-modulated with the beat frequency between the two modes. In this power modulation scheme, therefore, the modulation frequency is equal to the longitudinal mode spacing of the cavity, $c/2L$, where c is the speed of light and L is the cavity length of the main TEA CO_2 laser.

Two feedback loops are incorporated for stabilized operation of the system. The first feedback loop (loop 1) is for stabilization of the two-mode injection pulse, and it consists of a pyroelectric detector PYRO1, the lock-in stabilizer 1 and PZT1. The second feedback loop (loop 2) is for adjusting the cavity length of the main laser, and it consists of a pyroelectric detector PYRO2, the lock-in stabilizer 2 and PZT2.

Operation of the laser system is divided into two parts: "stand-by period" and "on period". In the stand-by period, the cw section of the hybrid laser is in the above threshold state and yields an output of about 2W. The cw radiation is utilized to feedback-stabilize the cavity lengths. If we stabilize the cavity length of the hybrid laser by loop 1 so that the minimum cw output is obtained at PYRO1, two longitudinal modes of the hybrid laser are located symmetrically with respect to the line center of the gain

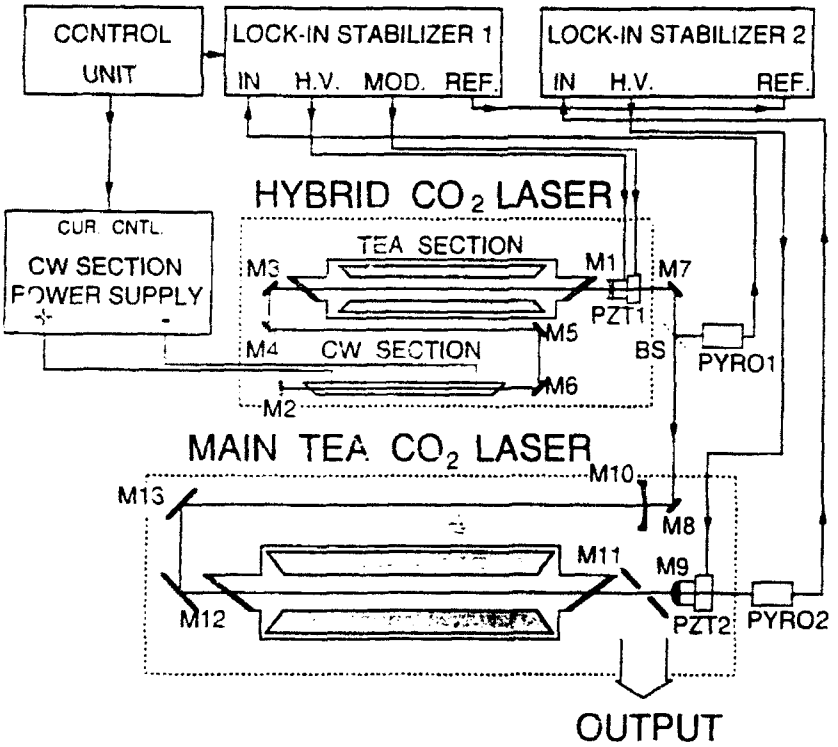

Fig.1 Schematic of the present laser system: M, BS, PYRO, and PZT stand for mirror, beam splitter, pyroelectric detector, and piezoelectric transducer, respectively.

profile for the cw section. In spite of the symmetrical distribution, we seldom observe simultaneous two-mode oscillation for the cw section due to a strong competitive relation between the two modes; we usually have a single-mode output.[2] The single-mode cw radiation is injected into the cavity resonator of the main laser. Against this injected field, the cavity of the main laser acts as a sort of Fabry-Perot interferometer.[3] Hence, if the cavity length of the main laser is tuned by loop 2 so that the intensity of the transmitted cw beam becomes maximum, the frequency of the injection field coincides with one of the longitudinal modes of the main laser. The transmitted beam is monitored by PYRO2 through a small hole (1mm diameter) bored at the center of M9. In this way, the cavity lengths of the hybrid and main lasers are maintained at their optimum values during the stand-by period.

As described in the previous letter,[2] with the cw section in the above threshold sate, we did not obtain the desired two-mode pulsed output from the hybrid laser. In the present system, we increase the discharge current of the cw section and bring it into the below threshold state[4] to obtain two-mode pulse, about 100ms before we fire the TEA section and the main TEA CO_2 laser. With the cw section in the below threshold state, two longitudinal modes (which are located symmetrically with respect to the line center) are allowed to oscillate simultaneously. At the on period, two-mode pulsed field thus generated is injected into the main TEA CO_2 laser. The frequencies of the injected two modes coincide with two respective longitudinal modes of the main laser. This is because the cavity lengths of the hybrid and main TEA CO_2 lasers are set almost equal to each other and we have already matched one of the injected modes with one longitudinal mode of the main laser in the stand-by period. If the time delay between the initiation of the discharge of the main laser and the injection time of the two-mode pulse of the hybrid laser is properly chosen, two longitudinal modes of the main laser are injection-locked, so that a high-power, power modulated output is obtained as a result of beat note between the two modes.

3. RESULTS AND DISCUSSION

Figure 2(a) shows a multimode output pulse from the main TEA CO_2 laser which was observed for the case with no injection field. The output energy was over 6J. When the two-mode pulsed field of the hybrid TEA CO_2 laser was injected with a proper timing after the initiation of the discharge of the main TEA CO_2 laser, a power-modulated output such as shown in Fig.2(b) was obtained. The modulation frequency in Fig.2(b) is 29MHz, which agrees with the longitudinal mode spacing of the main laser, not with the beat frequency of the injection pulse. The gain-

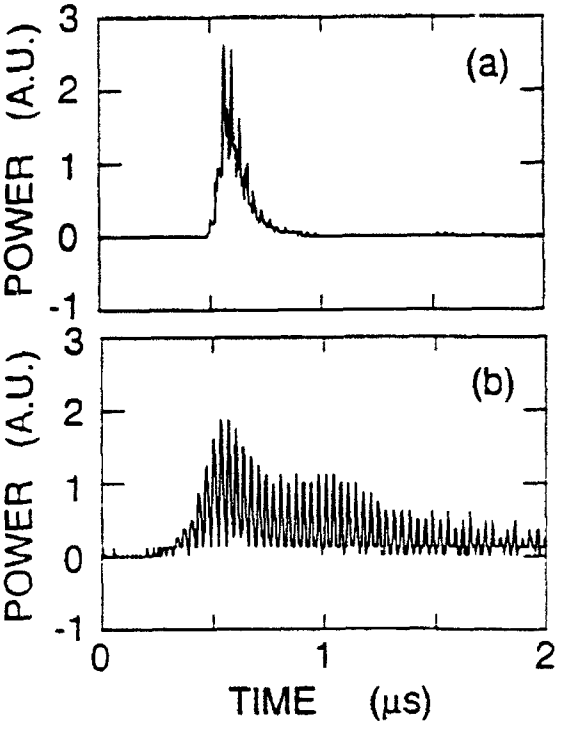

Fig.2 Examples of the output waveform of the main TEA CO_2 laser. (a) Multimode output pulse observed for the case with no injection field. (b) Power-modulated long-pulse output obtained when the two-mode pulsed field of the hybrid laser is injected with proper timing.

switched spike of the waveform in Fig.2(b) is well suppressed, so that the pulse duration is elongated to about 800ns in full width at half the maximum. The pulse duration of 800ns is about five times as long as that of the the multimode pulse shown in Fig.2(a).

Figure 3(a) summarizes the relative appearance frequency or distribution of the power-modulated outputs of the main TEA CO_2 laser as a function of modulation depth. The modulation depth is defined by $m=\{(P_{max}-P_{min})/(P_{max}+P_{min})\}\times 100$ (%), where P_{max} and P_{min} are the maximum and minimum values of the oscillatory waveform within one period. Each power-modulated output pulse shown in Fig.3(a) was obtained with feedback loops 1 and 2, switched on. Although the modulation depth varied from shot to shot. 76 percent of the total shots had a modulation depth larger than 70%. Hence sufficient stability was achieved for practical use.

For the sake of reference, experiments were repeated for the free-running case with feedback loops disconnected. The results for the free-running case are shown in Fig.3(b). It is seen that the average modulation depth is about 35%, and the distribution is also broad compared with the case with the feedback loops on. Eight percent of the outputs for the free-running case were multimode and are ranked in the group $m=0$.

In summary, we have developed a high-power TEA CO_2 laser system which can yield a power-modulated long-pulse output. By incorporating the feedback control loops in the laser system, we have obtained the power-modulated outputs with sufficient stability for practical use. The present laser system can be applied to the diagnostics of large tokamak plasmas, provided that some increase in the output power is made. We expect to have an output power of more than 150MW by amplifying the output pulse of the present laser system, using a large CO_2 laser device such as a Lumonics 620 with a triple-pass configuration. This work is supported by a Grant-in-Aid for Scientific Research from the Ministry of Education, Science and Culture of Japan.

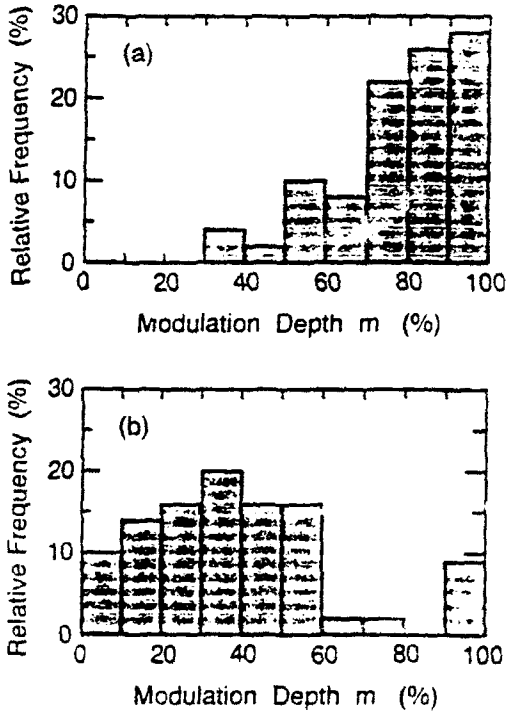

Fig.3 Relative appearance frequency of the power-modulated output as a function of their modulation depth: (a) for the case with the feedback loop active, (b) for the case of free running, that is, with the feedback loop off.

REFERENCES

[1] M. Nagatsu and T. Tsukishima, Jpn. J. Appl. Phys. **20**, 2155 (1981).

[2] K. Sasaki, H. Ohno, T. Fujii, and T. Tsukishima, Jpn. J. Appl. Phys. **29**, L2226 (1990).

[3] K. Sasaki, M. Yoshioka, and T. Tsukishima, Rev. Laser Eng. **16**, 681 (1988) [in Japanese].

[4] G. Scott and A. L. S. Smith, Opt. Commun. 50, 325 (1984).

NON-COHERENT REFLECTOMETRY METHOD FOR MEASUREMENT OF PLASMA CUT-OFF LAYER POSITION

V.V.Kulik, K.A.Lukin, V.A.Rakityansky

Institute of Radiophysics and Electronics, Ukrainian Academy of Sciences, 12, Acad. Proskura str., 310085, Kharkov, Ukraine

ABSTRACT

The paper describes the method called a non-coherent reflectometry technique. Using this method we can be able to provide a high precision of the measurement of the fusion plasma cut-off layer position and its microfluctuations simultaneously.The method is based on the application of the millimeter wave narrow-band noise signal and its spectral processing. Two modification of the method are discussed, and one of them uses an autodyne regime of the noise signal oscillator.

I .INTRODUCTION

The coherent length l_c is the one of the main characteristics of the noise signals. Its value is

$$l_c = v/\Delta f$$

where v is a propagation velocity of the signal and Δf is its power spectrum width. The value of l_c defines a distance where a conerency property of the signal is saved. It is known that the power spectrum of the sum of the radiated and reflected signals obtains a periodic modulation at condition if the propagation distance between the reference and reflected signals exceeds sufficiently the coherent length of radiation signal [1]. In this case, the modulation period is connected with v and L as follow $T_\omega = v/2L$. The physical nature of this effect is reduced to an ordinary monochromatic interference of Fourier components of noise signal. Hence, we can estimate the distance to reflector measuring a period of modulation and knowing v. The distance measurement with help of such method is described in [2] where the author proposed a noise radar system with a double spectral processing of sum signal. A high precision and resolution of the method take place in the case when $2L >> l_c$.The absence of controlled delay line in the reference signal circuit is a great advantage of the method described.

II. NON COHERENT-REFLECTOMETRY

The design of sources of steady-state intencive noise signals of mm wave band with sufficiently wide and homogenious power spectrum of

frequencies is an important problem for the development of non-coherent reflectometers. As an source of noise signal is used a weak-resonant backward wave oscillator (WBWO) of mm wave band [3] that generates chaotic oscillations. The excitation of chaotic oscillations beromes possible due to the chaotization of WBWO oscillations under interaction of electron beam with intensive field of weak-resonant oscillation system [4,5]. The packaged chaotic oscillators of mm wave band are developed in IRE AS of Ukraine and they provide the power spectrum width of radiation oscillations over 300MHz and integral power of some watts.

II.1. NON-COHERENT REFLECTOMETER

Fig.1 shows an experimental set-up of non-coherent reflectometer. The reflected signal is added with a reference one and sum signal passes to spektrum analyzer. The frequency band of the spectrum analyzer have to be sufficient for observation of noise signal power spectrum with the width above 300MHz. The output modulated signal from spectrum analyzer is converted to digital form and is wrote to the memory of computer. The time of one measurement is defined with a sweep velocity and this time can be very small (t 2ms). The set of measurements is carried out during an existence time of the plasma. The results of them are processed with computer. Fig.2 shows the power spectrum both of the radiated chaotic signal and the sum signal. The non-coherent reflectometry allows to observe two different space scales

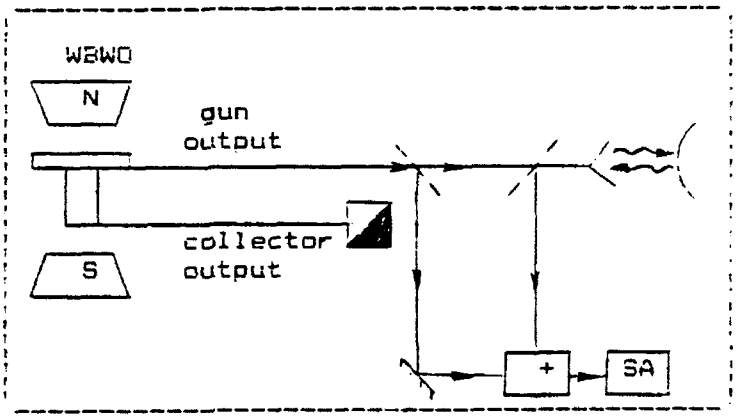

Figure 1.

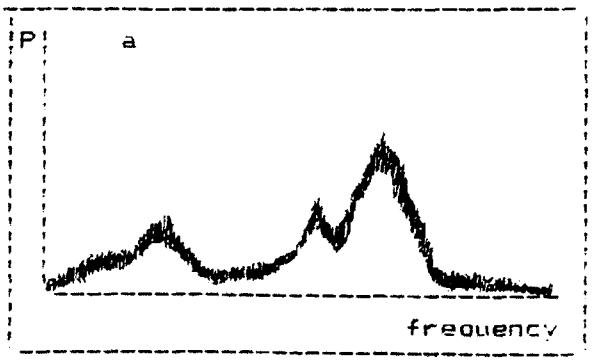

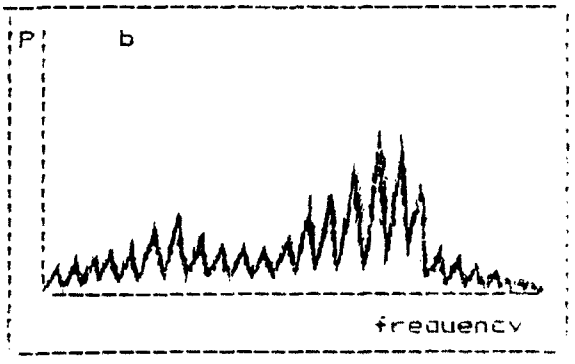

Figure 2.

of distance change L: mean wavelength of noise signal λ and coherent length l_c. The change of the L within the limits λ causes a change of phase shift between the reference and reflected signals. The result is a shift of interference figure without a significant change of modulation period ΔT_ω. The observation evolution of absolute frequency value f_m of one of the minimums allows to record a small scale shift of cut-off layer position. In particularly, the distance change equal to $\Delta L=\lambda/2$ corresponds to the frequency shift $\Delta f_m=T_\omega$. This method is like to that which uses a fixed frequency monochromatic signal and allows to measure fluctuations having ΔL=1mm. The measurement of value T_ω is for more large distance.

The processing of sum signal is effective for L just above l_c too. For higher precision we have to provide conditions for taking larger values dT_ω/dL. Fig.3 shows the measured relations $T_\omega(L)$ and N(L), where $N(L)=\Delta f/T_\omega$ is a number of variations which are observed on spectrum analyzer for a sum signal. The most values of dT_ω/dL are observed for small values of L, and the optimum conditions for measurement take place for N(L)=3-4. In this case, the minimum position is recorded with sufficient accuracy and dT_ω/dL is about 0.2MHz/cm.

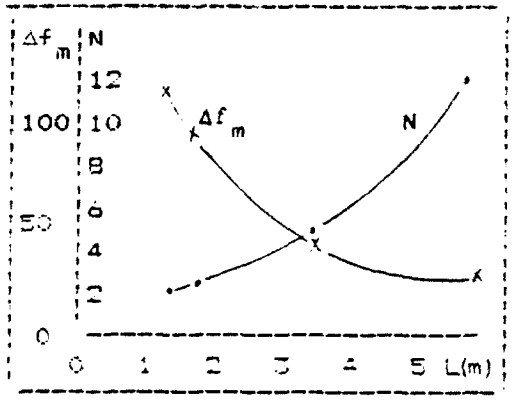

Figure 3.

II.2. AUTODYNE REGIME OF THE CHAOTIC OSCILLATOR OPERATING

Fig.4a shows an illustration diagram of non-coherent reflectometer using an autodyne regime of the chaotic oscillator [6]. The presence of

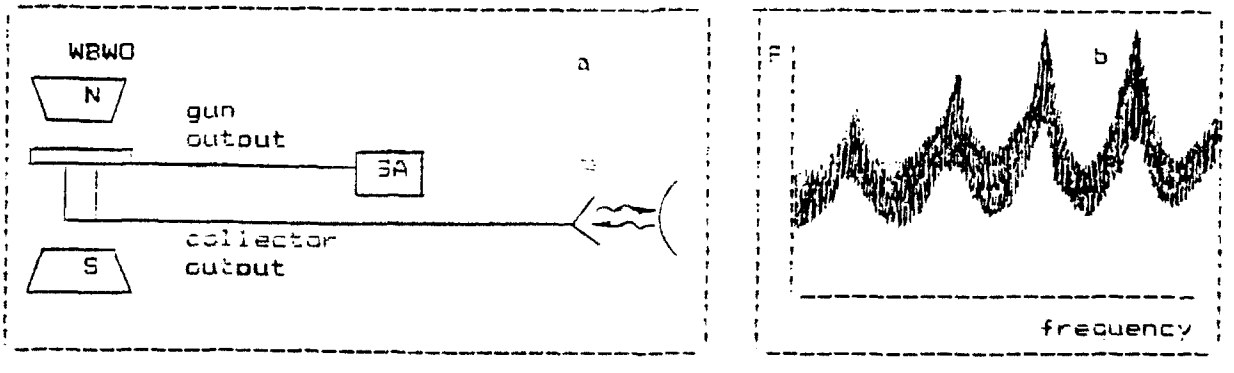

Figure 4.

power output from both the collector end and the gun one is a feature of the WBWO. It allows to use the collector output to radiate and to receive a noise signals while the gun output is used for recording of

the spectrum modulation. The reflected signal with a small amplitude and delay 2L is amplified with an active element of the oscillator and one interacts with oscillations in system.The result is a periodical modulation of spectrum (fig.4b). In this case, the amplitudes of the interacted signals are essentially different, that is why, the observed modulation depth is more less of said case. A sufficiently high sensibility for autodyne effect is provided with the linear amplification of the reflected signal in the WBWO. The spectrum characteristics (fig.4b) given for the reflected signal level of 20 dB with respect to radiated signal. It should be noted, the scheme of non-coherent reflectometer using an autodyne behavior of the WBWO is more simple because, in this case, the oscillator is used not only as a transmitter but as a sensitive receiver, an amplifier and a mixer too.

III.CONCLUSION

The application of the non-coherent reflectometry method allows to measure a plasma cut-off layer position with error of 2cm and it allows to define a small fluctuation of a position about 1mm. The time of the measurements can be decreased if to use a spectrum analyzer with a parallel processing of noise signal. The application of the autodyne regime of the chaotic oscillator operating allows to sufficiently simplify the scheme of reflectometer, and it saves the main advantages of the method. The method suggested has no sensibility to hindered influence of other signals, and its using is reasonable for development of systems for the precision measurement of distance to objects and for the definition of its displacement characteristics.

REFERENCES

1. V.S.Troitsky, Journal of Technical Physics, Vol.25, No8, August, 1955, p.p.1426-1435, (in Russian).
2. J.L.Poirier, Radio Science, Vol.3, No.9, September, 1968, p.p.881-886.
3. K.A.Lukin, V.A.Rakityansky, V.P.Shestopalov, Proceedings of All-Union School-Seminar "Microwave Physics and Applications". Moscow State University, Part 1, (1991)115
4. B.P.Bezruchko, L.V.Bulgacova, S.P.Kuznetsov, D.I.Trubetskov, Radiotechnic and Electronics,Vol.28,No.6,June, 1983,p.p.1136-1139 (in Russian)
5. B.P.Efimov, K.A.Lukin, V.A.Rakityansky, V.P.Shestopalov, Journal of Technical Physics Letter,Vol.15,No.18,1989,p.p.9-12,(in Russian)
6. B.P.Efimov, K.A.Lukin, V.A.Rakityansky, Journgal of Technical Physics. Vol.58,No.12,December,1988,p.p.2398,2400,(in Russian).

T6.1

DUAL-BAND MILLIMETER WAVE OSCILLATORS FOR MEDICAL USE

Song Shuxian Liu Dongcheng Deng Ciping
(Beijing Institute of Technology,Beijing,China)

ABSTRACT

Some millimeter wave oscillators produced in the requirements of a long range coherent oscillation(LRCO)[1] will be given in this paper.These oscillators have some advantages over others used before for their suitable power output(enough to trigger LRCO to occur) , wide band (dual-band design) , and simple structures then low cost, etc. . These oscillators are available and fit for use in LRCO research or clinic treatments. Some apparatuses were also produced, one of which will be shown at the end of this paper.

INTRODUCTION

Microwave/millimeter-wave has a very good perspective in biological and medical applications.But therapies by thermal-effects have some disadvantages in practice,for it must be carried out by a very high power radiation which needs complicated and expensive equipments, and also may cause some heavy damages to human bodies. So recently, the applications of nonthermal-effects have got more and more attention.

REQUIREMENTS OF MILLIMETER WAVE OSCILLATORS FOR MEDICAL USE

Our millimeter wave oscillators for medical use are on the basis of the nonthermal effects between microwave and biological bodies. The mechanism of nonthermal effects can be expounded by a coherent oscilation model produced by H. Frohlich [1, 2],which mainly include following parts:

(I) a long range coherent oscilation(LRCO) exists between electromagnetic wave and biological tissues(cells, giant molecules, polar molecules,etc.)which make essential role in growing and reproducting of these tissues;

(II) LRCO is a nonlinear reacction which can be triggered by only a little microwave energy from outside of human body,and the energy needed in the reaction is supplied by human body itself,not from outside;

(III) LRCO exists on a band of frequencies which mainly near the high part of microwave frequencies,i.e.millimeter wave,and far-infared.

After H. Frolich,S.T.Webb and some other researchers[3] verified the existence of LRCO by experiments. Then the model of LRCO became a radical theory and principle in this research area, i.e. the area of nonthermal reaction between microwave (especially millimeter wave)and biological bodies and also its applications in medical clinics.

From above theory we know that our oscillators for medical use must meet some requirements which include:

a.suitible power output,which is enough to trigger the LRCO to happen, but far less than that needed to cause damage on human bodies.

b. wide spectrum of frequencies, which come from the special design of dual-band or harmonic oscillation with all the frequencies produced mainly in or near millimeter wave band.

c. simple structure, which is composed of solid millimeter wave devices and can be manufactured easily,and in that can soon get a much extensive medical applications.

DUAL-BAND MILLIMETER WAVE OSCILLATORS PRODUCED

According to the requirements we have made several millimeter wave oscillators shown as Fig.1,(a)--(h),which include following sorts:

(1) structures made of combination of cavity and waveguide. Fig. 1(a) is a dual band oscillator that consists of one 8mm cylindrical cavity oscillator and one 2cm waveguide oscillator. The dual-band wave is got out from the waveguide in a cross polarized structure, and the cavity is used to obtain a stable oscillation which may cause some difficulties in fabrication.The maximum output of the oscillators is about 50~70mW for 2cm oscillator and 20 ~30mW for 8mm oscillator.

(2) structure made of combination of two waveguides. Fig.1(c) is a dual-band oscillator consist of two simillar waveguides (shown as Fig. 1(b)) , one of which is 2cm waveguide and another 8mm waveguide. This structure needs no complicated fabrication and more can produce more frequencies though it may not be so stable. The maximum power output is 50~70mW for 2cm and 20~30mW for 8mm.

(3) structure made of microstrip. This structure comes from a recently developed antenna, active antenna of microstrip[4,5],where the oscillator and antenna for radiation are made in one subatrate. This cause the structure very simple and easy to produce or fabricate in a conformal surface with biological body and then makes it very convenient in practiccal use. Fig.1(d) and Fig.1(e) are the basic forms of the oscillator,and Fig.1(f)is the section view. We have got some oscillators of 8mm, 5mm, and 4mm band and the main problem is the too lower power output. The oscillators shown in Fig. 1(d) and Fig.1(e) can only get a output of 1~2mW. But this problem can be solved by contacting the oscillator and antenna with the surface of biological bodies .Then the power will be enough to excite the coherent oscillation in human bodies. Fig.1(g) and Fig.1(h)are two transforms of Fig.1(d) and Fig.1(e),where Fig.1(g) is a structure of two or more oscilllators using power combination in radiation,and Fig.1(h) is a structure which can produce harmonic oscillation for getting wider specctrum.

DISCUSSION

Because the LRCO happen in a wide band,not on only one single frequency, the requirements for stable and pure frequency is not imperative. This character will make the last two sort oscillators introduced above have better perspective in medical application, especially the third which is obviously easy to be put in practical use of clinics. Some apparatus, one of which is shown in Fig. 2, have been made using above oscillators and now are being used in hospitals.

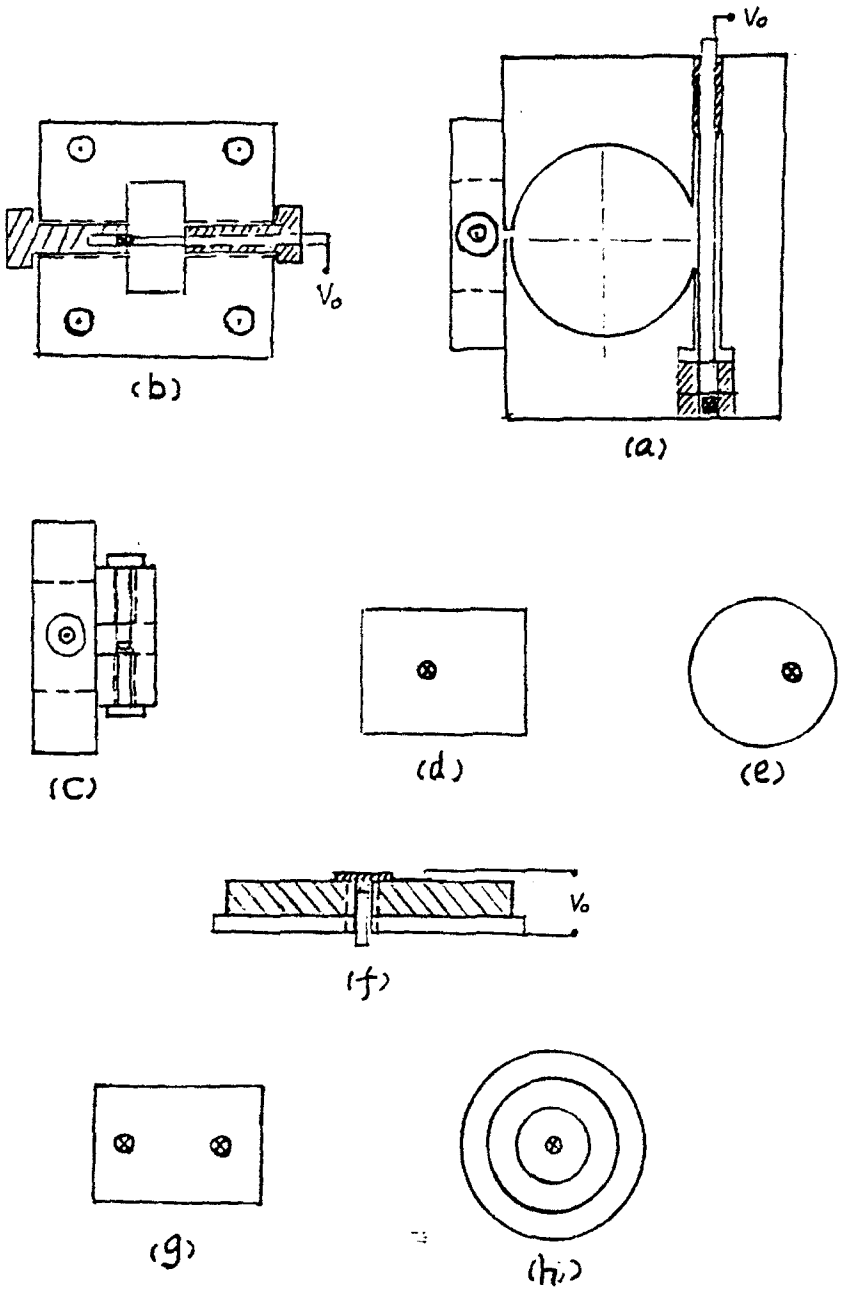

Fig.1 structures of some dual-band oscillators

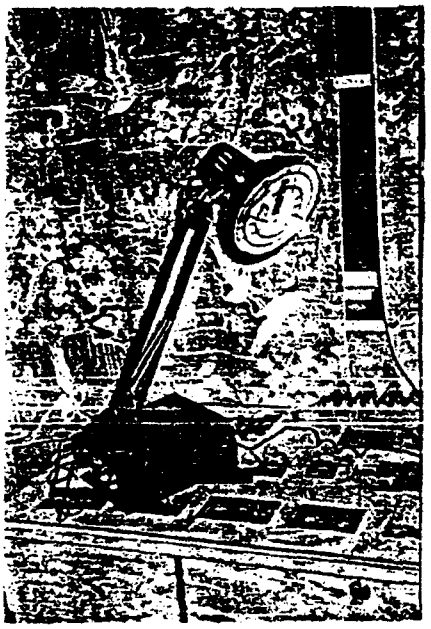

Fig.2 medical apparatus using dual-band oscillator

REFERENCES

[1] H. Frohlich, "Long-Range Coherence and Energy Storage in Biological Systems" International Journal of Quantum Chemistry, Vol.II, 1968, pp.641-649.

[2] H. Frohlich, "Coherent Electric Vibrations in Biological Systems and the Cancer Problem", IEEE MTT-26,No.8,Aug. 1978,pp.613-617.

[3] S.J. Webb,et al,"Resonances between 10 and 10 Hz in active bacterial cells as seen by Laser Raman spectroscopy", Phys. lett., 60, 1977, pp.267-268.

[4] T.O. Perkins, "Active Circular Patch Antenna", Microwave Journal, Mar. 1987,PP.109-117.

[5] Kai Chang, "Millimeter-wave Spacial and Quasi-optical Power Combining Techniques", International Conference on Millimeter-wave and Far-infared technology, ICMWFT'89, June 19-23,1989, Beijing.

T6.2

QUASIOPTICAL TRANSISTOR ON RUBY

Vertiy A.A., Gavrilov S.P., Tarapov S.I.

Institute of Radiophysics and Electronics, Academy of Sciences of the Ukraine, 12 Acad. Proskura st., 310085 Kharkov, the Ukraine

The device described in the paper belongs to the field of the transistor technique of the millimeter and infrared wavelength range (10^{11}Hz^2 < ν < 10^{15}Hz). It may be used in communication lines, data handling devices, radiometer systems.

Usually, in modern communication lines of optic, submillimeter and millimeter wavelength ranges the most effective transmission of is realized by wave beams which propagate in the waveguides adequate to the frequency range. At present there exists a problem of data handling. So the use of ordinary solid state transistor devices /1/ in these ranges faces essential difficulties which manifest themselves in the impossibility to decrease their constructive capacity and inductance.

It is known now transistor devices operating in the optic frequency range in which a highfrequency energy flow or pulse controls a similar object. The physical principle on which the device's operation is based involves a phenomenon of nonlinear absorption of electromagnetic energy by a substance in the presence of a set of discrete energetic levels. Due to the distances between these levels being lied in the range 1 ÷ 10 eV such devices can operate only in the optic frequency range.

A shortcoming of the optical transistor is also the fact that it may operate only in several narrow bands of frequencies the mean values of which correspond to energy levels of the working substance. An attempt to expand the frequency range by resonator retuning leads to falling of the amplification coefficient of the transistor, a growth of nonlinear distortions, deterioration of stabilization conditions of the transistor. Besides, one may change the discrete spectrum of operating frequencies only by replacement of the working substance of the transistor.

This problem may be solved if the transistor consisting of the Fabry-Perot resonator, working substance placed in it will be supplied by a source of the regulated magnetic field and magnetic used as a working substance.

The device described (Fig.1) includes copper mirrors 1,2 which form the Fabri-Perot resonator. The working substance 3 (ruby cylinder) is placed between mirrors. The channel 4 of excitation and saturation presented as a waveguide which connected with the resonator by the coupling element 5. The information channel 6 (waveguide) is connected with the mirror 1 by its own coupling element 7. The channel 8 (waveguide) is connected with the mirror 2 by a coupling element 9. The source 10 of the regulated magnetic field (solenoid) is placed outside the resonator. Here vector $\vec{B}_0$ of the static magnetic field of the high homogeneity is perpendicular to the vector $\vec{B}_1$ of the magnetic component of the electromagnetic field in the resonator.

Let us consider the operation of such quasioptical transistor. The magnetic field B_0 removes the degeneration of energy levels of magnetic atoms of the working substance 3, here the distance between the levels depends on $\vec{B}_0$. Thus, the system of energy levels is

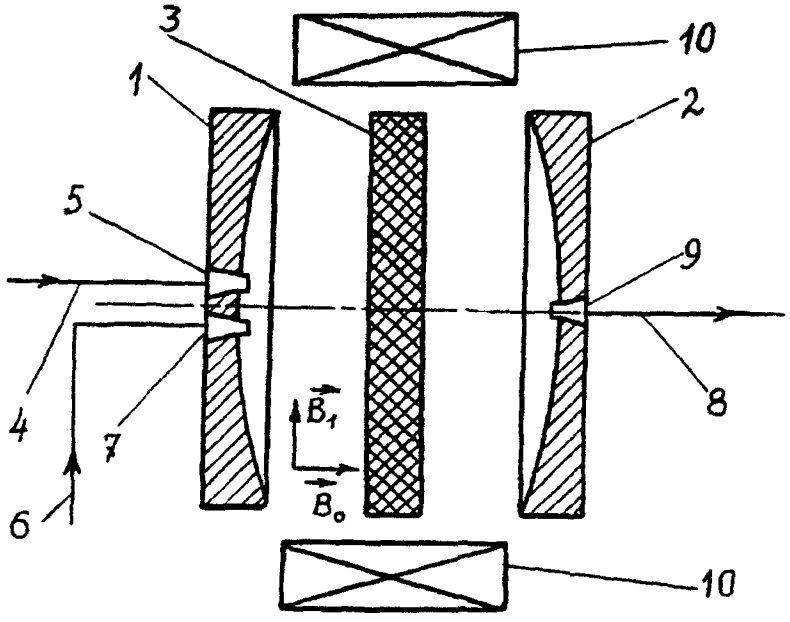

Fig. 1

formed in the working substance 3. The frequencies of quantum transitions lie in the range from the shortwave part of the mm range and higher at the value $B_o \gtrsim 3$ T.

In the resonator tuned in the frequency ν of the signal coming from channels 1 and 2 the condition of the magnetic resonance

$$h\nu = W_M - W_{M-1}, \text{ where}$$

W_M, W_{M-1} are the values of energies of stationary states of a magnetic in the static magnetic field; M,M-1 are the natural values of the operator S_{Bo} of the effective magnetic spin projection on the direction of the static magnetic field $\vec{B}_o$; $\omega = 2\pi\nu$ is the circular frequency of the exciting SHF-field; h is the Planck's constant is being kept. Here the magnetic dipole transitions arise with absorption of energy of the electromagnetic field. The value of the absorbed energy depends nonlinearly on the the value $|\vec{B}_1|$. When the codition of saturation is not observed ($|\vec{B}_1| \ll \gamma\sqrt{T_1 T_2}$) the absorption in the magnetic is large, the resonator is practically does not transmit the electromagnetic energy and, therefore, the signal in the receiving channel is practically equal to zero (i.e. the transmission coefficient of the resonator $\mathcal{T} \ll 1$, Fig.2). In the fully saturated substance ($|\vec{B}_1| \gg \gamma\sqrt{T_1, T_2}$) the absorption is practically absent and the resonator has the maximum possible transmission coefficient $\mathcal{T}$.

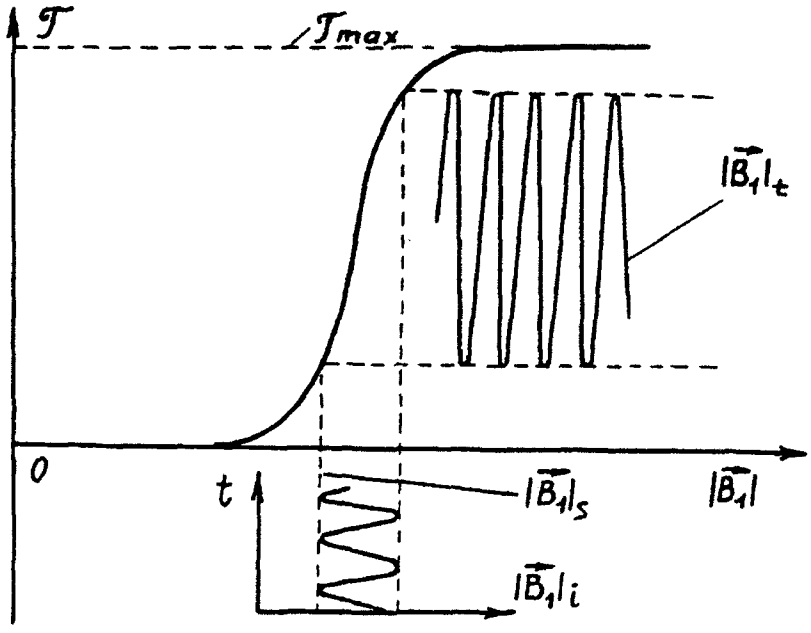

Fig. 2

The character $\mathcal{T} = \mathcal{T}(|\vec{B}_1|)$ calculated in /4/ has been used for realization of regime of transistor functioning. By changing the signal amplitude in the channel 4 of saturation and excitation the value $|\vec{B}_{1S}|$ is chosed corresponding to the "working point" of the transistor. The information signal comes to the resonator through the information channel 6. As a result a processed (amplificated) information signal comes to the receiving channel 8.

The retuning of the working frequency is realized by changing the value of the static magnetic field $|\vec{B}_0|$ and tuning of the resonator according to the condition of the magnetic resonance.

The regulation of the steepness of the device characteristic is realized by changing only the field $|\vec{B}_0|$ within the working frequency band of the resonator. Her an important positive moment is the fact that the retuning of the working frequency is realized in the continuous frequency range, and the regulation of steepness of the device characteristic is realized without changing the frequency of the working generator and resonator geometry. Besides, many of magnetics may work at room temperatures that allows to create small-size devices of data processing at SHF.

Positive properties achieved allow to use effectively the quasi-optical transistor in the communication systems, computer devices where information beams are treated and switched with supervelocities. Besides abovementioned properties assume the succesful application in other fields of science and technique, for example, in medicine and biology when modeling neurostructures for the purpose of study and diagnostics of brain work.

Experimental test of the transistor operation on the radiophysical complex "BURAN" /5/showed a good agreement of the calculated

characteristics and real ones. There was also observed inversionless amplification of the information signal and bistability of working characteristics of the quasioptical resonator.

At present the experimental and theoretical works concerning the use of the given device in the information systems at SHF have being carried out.

References

1. Andrushko L.M., Fedorov N.D. Electron and Quantum SHF Devices. M.: Radio i svyaz', 1981, 189p. (in Russian).
2. Monosov S.P. Nonlinear Ferromagnetic Resonance. M.: Nauka, 1971, 231p. (in Russian).
3. Gibbs H. Optic Bistability. M.: Mir, 1988, 615p. (in Russian).
4. Vertiy A.A., Gavrilov S.P., Tarapov S.I., Shestopalov V.P. Observation of the bistability phenomenon in ESR-conditions on millimeter waves. DAN SSSR, 1990, V.313, No.4, p.849-853.
5. Vertiy A.A., Ivanchenko I.V., Popenko N.A., Tarapov S.I., Shestopalov V.P. A millimeter wave radiospectrometer for material analysis below T 10. Int. Journ. of Infr. and Mill. Waves, 1989, v.10, No.3, p.395-404.

T6.3

W-BAND HARMONIC MODE GaAs GUNN DIODES

Deng Yanmao
(Nanjing Electronic Devices Institute, Nanjing, China)

ABSTRACT

Fabrication and performances of the second-harmonic mode W-band GaAs Gunn diodes are briefly presented. By means of researched interrelation between DC I/V curves, fundamental and harmonic performances of the devices , some criteria of designning and selecting devices suitable to harmonic mode operation are provided. Harmonic output power of 40mW at 95 GHz with a conversion efficiency of 1.36 percent and output power greater than 10mW over all of the W-band have been achieved.

INTRODUCTION

Though three-terminal solid-state devices, such as FET, HEMT, HBT, have established their place in the millimeter-wave range. Gunn and IMPATT diodes still maintain their superriority above 30GHz. GaAs and InP Gunn diodes as one of the important millimeter-wave solid-state devices are widely used in local oscillators, injection-locked oscillators and amplifiers.

Although we have obtained over 20mW of output power at 90GHz with fundamental mode GaAs Gunn diode[1], physical constraints of the W-band fundamental mode devices become critical, as the operation frequency is increased. These devices are not only hard to be reproduced, but also hard to be applied since their operation temperature and voltage range are very narrow. Consequently for the frequency higher than about 65GHz. GaAs Gunn harmonic oscillators are generally used at present. Its advantages are apparent. First, since the harmonic mode devices may somewhat mitigate the contradiction between frequency and power, compared with fundamental mode devices at the same operating frequency, chip dimension can be larger, and fabrication process tends to be easier. Next, the processing of GaAs material and devices are more mature than that of InP. So GaAs devices have lower cost and better reliability. Theory and technique for the harmonic extract are being upgraded. The best harmonic performance reported so far is output power of 96mW at 94GHz with a conversion efficiency of 2.7 percent[2].

However, it has experimentally been found that Q-band(33-50GHz) fundamental devices are not suitable for W-band (75-110GHz) harmonic mode operation. This paper will mainly present interrelation between DC , fundamental and harmonic performances from devices respect, so that some criteria of designning and selecting devices suitable for harmonic mode operation may be obtained. The performance of W-band harmonic mode GaAs Gunn diodes will be reported. These devices have successfully been applied in some W-band Gunn harmonic oscillators. Output power of 40mW at 95GHz with a conversion efficiency of 1.36 percent and output power greater than 10mW over all of the W-band have been achieved.

DEVICE FABRICATION

The design of W-band harmonic mode GaAs Gunn diodes is basically similar to that of Q-band fundamental mode ones.
The n+-n-n+ GaAs structures were grown on low resistivity n+ substrates using VPE method. The doping concentration of the active layers ranged from 7×10^{15} to $1.5\times10^{16}cm^{-3}$. The thicknesses of the active layers were in the range of 2.0 to 2.7 μm. The carrier concentrations and the thicknesses of the highly doped n+-buffer and n+-contact layers were about 1×10^{18} cm^{-3}, 2 μm and 1 μm, respectively.
The ohmic contacts on both sides on the wafer were formed with alloyed AuGeNi/Au metallizations. Conventional electroplated heat sink structures were used. Mesa diameters of fabricated diodes chips were 60-80 μm. Individual chips were thermal-compressionally bonded into gold-plated copper stud packages. Cross-like gold ribbons were then bended. Chips were finally hemetically sealed within the packages (package model NEDI T085).

PERFORMANCE AND RESULTS

It has experimently been found that all Q-band fundamental devices are not suitable for W-band harmonic mode operation. We researched interrelation between normalized DC I/V curve, fundamental and harmonic performances for different batches of the devices.
Q-band RF performances of these devices were measured in a standard reduced height post-coupled waveguide oscillator. Their W-band RF performances were measured in a full-height waveguide cap cavity. Fig. 1 shows several typical normalized DC I/V curves (Vt and It are threshold voltage and current, respectively).

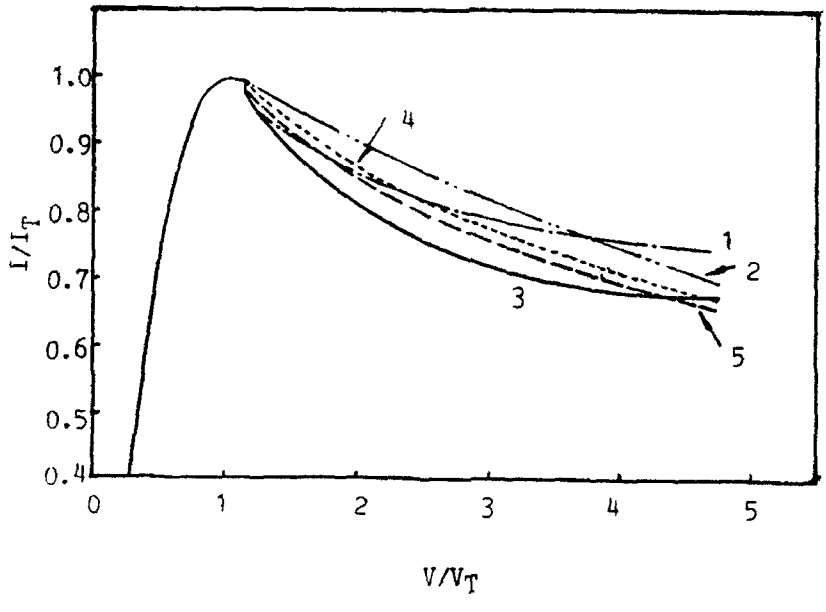

Fig. 1 Several typical normalized DC I/V curves

The characteristic data of typical DC performance as well as fundamental and harmonic performances for different batch of the devices are listed in table 1.
From the DC and RF test results presented above, following laws can be obtained:

A. For those batches which have almost the same fundamental output power, its harmonic output power may be very different.
B. For larger current peak-valley ratio (represented by I/It value at V/Vt=3.5), harmonic performance is not necessarily satisfactory, while abrupt current drop-back at the threshold point (represented by ΔI) is desirable for good harmonic performance.

Table 1 DC, fundamental and harmonic perfomances for different batch of the devices

batch No.	DC				fundamental		harmonic	
	Fig. 1 curves No.	Δ I (mA)	It/I (V/Vt =3.5)	Vt (V)	f1 (GHz)	P1 (mW)	f2 (GHz)	P2 (mW)
14-1	3	60	1.43	1.32	45.8	95	94	33
18-6	5	50	1.39	1.28	47.2	95	94	35
24-6	1	40	1.28	1.24	47.6	105	90	20
35-3	4	10	1.32	1.25	47.4	94	93.5	6
10-4	2	0	1.30	1.10	50.5	92		little

C. Measured threshold voltage are all lower, ranged from 1.10 to 1.35V.
D. For the devices having larger fundamental output power, the operation current is generally greater than 1A, while for the devices having larger harmonic output power and higher conversion efficiency, the operation current is all less than about 0.9A, corresponding to DC power consumption of about 2.5-4 W.
Obtained best experimental results for W-band harmonic mode GaAs Gunn diodes are summarized in table 2.
Using these Gunn diodes, University of Electronic Science and technology (Chengdu) has developed a wideband mechanically tunable harmonic oscillator, which can deliver output power greater than 10 mW over all of the W-band[3].

Table 2 Obtained best performance for W-band harmonic mode GaAs Gunn diodes

batch No.	Vo (V)	Io (mA)	f (GHz)	P (mW)	η (%)
14-1	3.9	900	90	41	1.17
14-1	3.8	730	100	27	0.91
18-6	4.32	680	95	40	1.36
18-6	3.75	700	100	25	0.95

According to above experimental results, some criteria of designning and selecting the devices, which are suitable for harmonic mode operation, can be summarized as following:

A. Usually have greater fundamental output power and higher conversion efficiency.
B. Have as large abrupt current drop-back as possible at the threshold point.
C. Correspondent DC power consumption is from 2. 5 to 4 W.
It has experimentally been demonstrated that above criteria are valid for designning and selecting harmonic mode devices.

DISCUSSIONS

For increasing harmonic extract efficiency and harmonic output power, it is necessary to exert every effort in all respects of material, devices and circuit. Larger abrupt current drop-back at the threshold point is related to higher low-field mobility of the active layer. RF current generated by the domain transit in the active layer contains certain harmonic current components. Obviously, in order to produce rich harmonic components, the harmonic mode devices require abrupt concentration changes between both boundaries of the active layer. MBE is beneficial to grow hyperabrupt doping concentration. In addition, for certain nL product, less mesa diameters, corresponding to lower operation current, may decrease temperature rise and maintain certain terminal impedance of the diodes. Therefore, the harmonic mode devices possess lower current characteristic compared with fundamental ones. At certain DC power consumption, exchanging low current for high voltage is also beneficial to increase conversion efficiency.

CONCLUSION

By means of researched relation between DC I/V curves, fundamental and harmonic performances of the second-harmonic mode W-band GaAs Gunn diodes. Some criteria of designning and selecting devices suitable for harmonic mode operation have been provided. The devices must have larger abrupt current drop-back at the threshold point and relatively lower DC power consumption.

ACKNOWLEDGMENT

The author would like to thank Zhang Dehong and Zhou Biru for providing GaAs epitaxial material, Cao Kangbai and Li Xizhi etc. for contribution some of the harmonic test results.

REFERENCES

1. Zuo Qinghua and Zhu Shinian, Proceeding of 2nd International Symposium on Recent Advances in Microwave Technology, (1989), 506.
2. S. J. J. Teng and R. E. Goldwasser , IEEE Elect. Dev. Lett., 10 (9) (1989), 412.
3. Cao Kangbai et al., 5th National mm & Smm Waves Symposium, (1991), 475.

T6.4

THE EXPERIMENTAL INVESTIGATION OF THE SUPER-SLOW ELECTROMAGNETIC WAVES IN THE PERIODIC SEMICONDUCTOR STRUCTURE

A.A.Bulgakov, S.K.Kondrashin, V.V.Kutuzov

Institute of Radiophysics and Electronics,
Acad. of Science of Ukraine, 12 Proscura st.,
310085 Kharkov , Ukraine

It was predicted in the works [1] the possibility of the superslow magnetic waves existence in the periodic structures formed by the semiconductor-dielectric layers. The theoretical estimation for modern semiconductor materials shows that the accessible electromagnetic wave slowing-down value is equal to $10^4..3x10^4$. Such a great slowing-down is conditioned by both the structure periodicity and the specific distribution of the electromagnetic field in the structure layers.

In order to verify this supposition the authors carried out the experimental investigation of the periodic structure wave properties. This structure consists five InSb-sitall layer pairs. The thickness of every layers is 0.25 mm (InSb) and 0.35 mm (sitall). InSb has such parameters: concentration - 10^{15} cm^{-3}, mobility - $5x10^5$ $cm^2V^{-1}s^{-1}$. The dielectric constant of the sitall is equal to 13.2. The structure dimension is $3.5x6.5$ mm^2. It is placed in the rectangle waveguide in a such way that layers plane is parallel to the waveguide big wall. Such an experimental configuration is connected with the magnetic field unsusceptibility of the structure own oscillations when it is placed parallel to small wall. The external magnetic field controls effectively such structure parameters as the frequency gap zone disposition and the wave attenuation.

It is important to mention the peculiarity of the waveguide used. The waveguide transversal wave number is defined by the big wall dimension and dielectric filling. The corresponding structure wave number depends upon big wall structure dimension, the relation between layers thicknesses and their numbers, the constant magnetic field amplitude. Therefore when waveguide is completely filled along big wall, the wave type of interest cannot be activated. In order to avoid such situation one used partial waveguide filling - the structure dimension in cross-section along big wall is equal to 3.5 mm. The big wall dimension of the waveguide measuring section is equal to 7.2 mm. In such configuration it is possible to some extent the change of the periodic medium wave number by structure shifting along

big wall. The cryogenic device includes the measuring section and is placed between the magnet poles in such way that strength lines of the magnetic field are directed parallel to the structure layers.

Experimental investigations consist of the varying investigation of the amplitude-frequency characteristics of the measuring section and electromagnetic wave velocity vs external magnetic field value. Experiments were carried out for the following wavelength ranges: 6 mm, 8 mm, 15 mm and temperatures: 300 K, 78 K. The magnetic field was changed from 0 to 7 kE. During experiment authors observed in some frequency bands both monotonous and nonmonotonous dependence of the electromagnetic power attenuation coefficient of the measuring section upon the magnetic field value. The local effects of the same sign are in the range 1..4 GH.The power attenuation decrease reaches 13 dB in above mentioned range of the magnetic field.

The authors suppose the following results explanations. When own oscillations are activated, electromagnetic energy in the structure is absorbed partially by it. This leads to attenuation coefficient increasing. The external magnetic field changes the dielectric constant tensor components. As a result the energy redistributed between the layers of semiconductor and dielectric. The dielectric energy losses are much greater than the semiconductors ones. If the magnetic field is applied, the main part of the own oscillations energy is concentrated in dielectric, that results attenuation coefficient decreasing. This effect has been observed in experiment.

The electromagnetic wave velocity has a value of 33±9 in the frequency bands where it was observed the essential decrease of electromagnetic power attenuation. It should be noted that the theoretical estimation the slowed-down velocity for the similar but infinite structure has a value 25 [1].

1. Bass F.G., Bulgakov A.A., Tetervov A.P. *Visokochastotnie svoistva poluprovodnikov so sverhreshetkami*, Moscow, Nauka, 1989.

T6.5

MM-Wave Bi-Turning VCO

Wang Dongjin and Li Dunfu
(Univ. of Science and Tech. of China, Hefei, China)

INTRODUCTION

Owing to the progressing of MM-wave semiconduct devices,various kinds of MM-wave systems have been created that deal with different work fields. The simplified principle of a MM-wave pulse doppler system can be seen from fig.1. There, the function of MM-wave phase locked loop is that the recevied signal can pass through the crystal filter . Thus a double turning VCO would be required in the system, and the fine turning direction could be changed.

As we know, only the positive turning direction can exist using ordinary principle, the new bi-turning VCO must be searching for a new structure and working modle.

ANALYSIS AND DESIGNING

The new structure of the bi-turning VCO is shown in fig.2. The varactor1$^{\#}$composition with Gunn diode in the main cavity works with the ordinary principle,so that the varactor can be omitted in the equivalent circuit analysis. The another varactor 2$^{\#}$is located in the frequency turning cavity behide the high-Q cavity,and the VCO can be represented in a simplified equivalent circuit fig.3. As seen in the reference place a-a to the right, there is:

$$Y_a = G' + j\left[\omega(c' + c_v') - \frac{1}{\omega L'} - Y_0 ctg\left(\frac{2\pi}{\lambda_g} l\right)\right] = g_a + jb_a \tag{1}$$

By putting $b_a = 0$, the oscillation frequency ω is determined as:

$$\omega' = \frac{1}{2(C' + C_v')}\left[Y_0 ctg\left(\frac{2\pi}{\lambda_g} l\right) + \sqrt{Y_0^2 ctg^2\left(\frac{2\pi}{\lambda_g} l\right) + \frac{4(c' + C_v')}{L'}}\right] \tag{2}$$

Thinking about the characteristics of the varactor, two kinds of conclusions can be deduced from eq .):

1) If $ctg\left(\frac{2\pi}{\lambda_g} l\right) \geqslant 0$,

the frequency ω' increases when the turning voltage increases also, ie. positive turning.

2) If $ctg\left(\frac{2\pi}{\lambda_g} l\right) < 0$, the eq.(2) rewrites as:

$$\omega' = \sqrt{\left\{\frac{Y_0 ctg\left(\frac{2\pi}{\lambda_g} l\right)}{[2(C' + C'_v)]}\right\}^2 + \frac{1}{L'(C' + C'_v)}} - \left|\frac{Y_0 ctg\left(\frac{2\pi}{\lambda_g} l\right)}{2(C' + C'_v)}\right|$$
$$= \sqrt{A^2 + \omega_0'^2} - |A| \tag{3}$$

It is clearly seen that when the turn voltage increases, the capacitance of the varactor C'_vdecreases, then the frequency ω' decreases also. In other words, as $l \to 0.5\lambda_g$, the negative turn can be completed . Thus the method of changing turn direction by varying the place of shorting plate has shown a useful and easy way for VCO designers to work out this problem . The adimitance seen to right from point c—c as:

$$Z_c = R_0 + G' + j\left[\omega(L_1 + L_2)\frac{\omega^2 - \omega_0^2}{\omega^2} + \omega^2 M_2^2 L' L_2 Y_a\right]$$
$$= R_c + jX_c \tag{4}$$

where

$$\omega_0^2 = \frac{1}{[C_0(L_1 + L_2)]}$$

putting $X_c = 0$ will detemine the oscillation frequency of the high—Q cavity containing the varactor. As we see, the value of $M_2$is not only a function of the diameter of the coupling hole between high—Q cavity and the frequency turning cavity, but also it depends upon the value of $\omega_0 - \omega'$. So, $\omega_0 = \omega'$represents the maximum coupling condition, and the high—Q cavity is strongly disturbed by the varactor , the frequency turning band will be wide; otherwise , the band narrow. This way, the turning band can be controlled easily ; wide or narrow according to what usage is necessary .

In the same way, the adimitance at point e—e is:

$$Y_e = G + j\omega C + Y_l + \frac{1}{Z_d} = g_e + jb_e$$

where

$$Z_d = j\omega L + \omega^2 M_1^2 L_1 L_2 / Z_c, \quad M_1 = k_1 / \sqrt{L_1 L}$$

$M_1$is the coupling factor between the main cavity and the high—Q cavity.

Putting $b_e = 0$, the solution is the oscillation frequency of the VCO. The analysis above gives a brief view of the advantages of the bi—turning VCO, but the phase noise is another important characteristics of a signal source especially in a doppler system. It is a common knowledge that to reduce the phase noise of phase locked source, the phase noise of VCO must be lower, especially in the Fourier frequency far from the carrier. Phase noise of a cavity stabilizied Gunn oscillator states as:

$$L(f_m) = \frac{FKT}{8Q_l^2 P_0}\left(\frac{f_0^2}{f_m}\right) \tag{6}$$

$$Q_l = \frac{1}{2g_e}\left(-\frac{b_e}{\omega}\right) \tag{7}$$

Where F, P_0, $f_0$and $f_m$are noise figure of Gunn diode , carrier power, carrier frequency and Fourier frequency away from the carrier, respectively. It is a efficient way to reduce the oscillator's phase noise by increasing the value of Q_l. So, raising the Q factor of high–Q cavity and expanding the value of $\omega_m - \omega_0'$as large as possible. These are the key factors in considering a low phase noise oscillators design, where $\omega_m$and $\omega_0$are the frequencies of main oscillator and high–Q cavity containing the varactor, respectively. But increasing the value of $Q_l$would make the frequency tunning band narrow. It can be seen from this that there have contradictary requirements between low phase noise and the wide frequency turning band , the VCO might choose a suitable value for both phase noise and the frequency turning band of the VCO.

EXPERIMEN RESULTS AND CONCLUSIONS

Based upon the above analysis and after careful design, careful examination of the device and fine adjusting, the desirable bi–turning VCO has been made at last. The main characteristics of the VCO that have been tested by the Meterology Station of Ministry of Spaceflight and Aviation are:

output power: 17～20 db mw
rough turning: (10～20) Mhz / (0～15)V
fine turning: (± 1～± 5)Mhz / (0～15)V
phase noise: $-60dB_c$ / Hz (f_m = 1 KHz)
$-93dB_c$ / hz (f_m = 50 kHz)

Inserting the bi–turning VCO to the phase locked loop, the phase noise spectrum of the phase locked source is the same as that of a standard source——the LO osillator; and the receiving singal containing the doppler frequency of a moving target smoothly passes the crystal filter to the back–end of the system. The matter shows that the VCO is satisfactory for the doppler system.

Generally speaking,the Gunn osillator stabilized by a high–Q cavity containing varactor is a efficient method to make a high quality VCO.

The authors thank senior engineer Shen Yijian and Mr. Xiong Huapin for their help in experimenting and discussions.

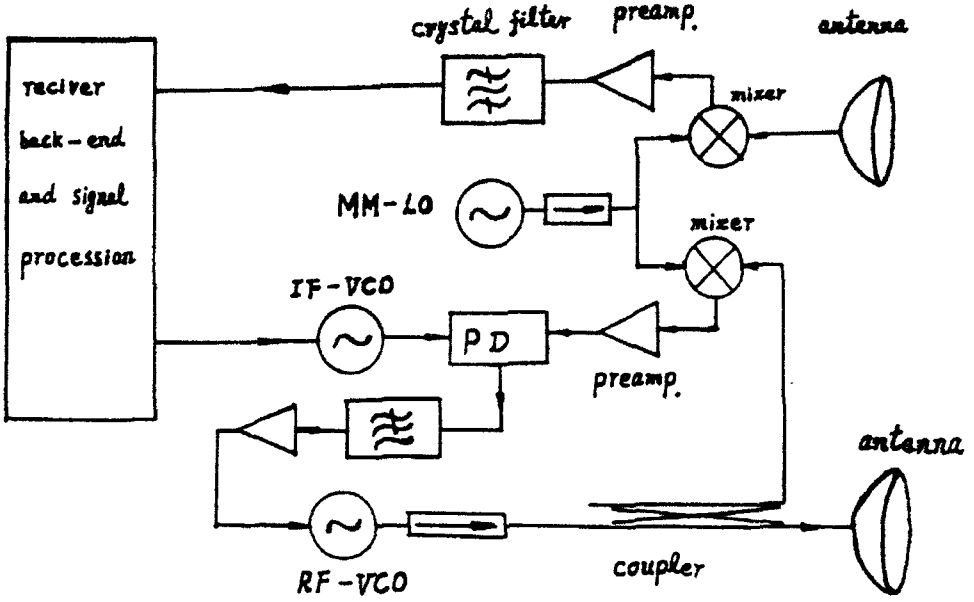

Fig. 1. Sketch of working principle of pulse doppler system.

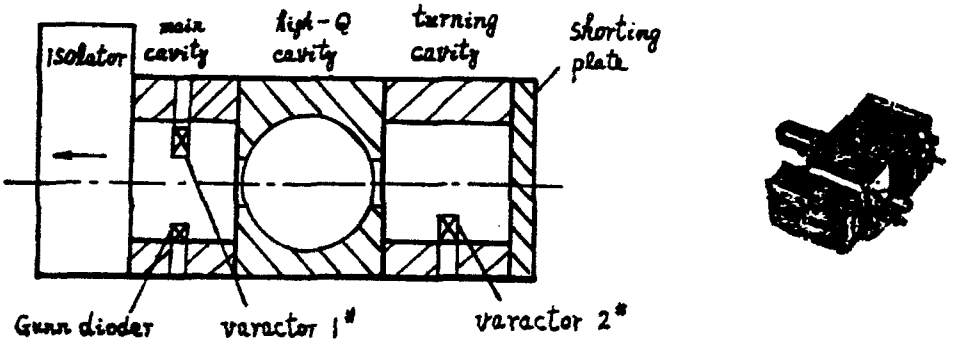

Fig. 2. A cross-section view of bi-turning VCO and its photo.

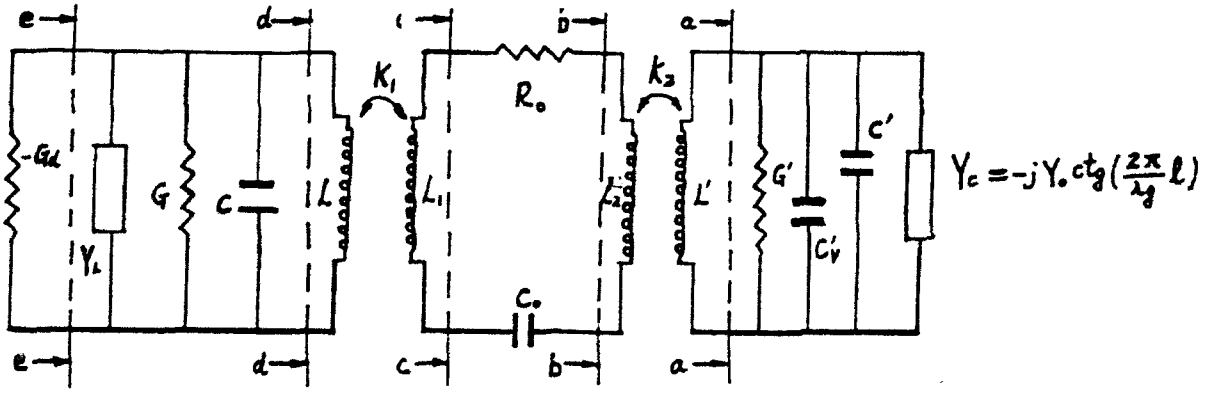

Fig. 3. Simplified equivalent circuit of bi-turning VCO

T6.6

KA-BAND GUNN VCO'S

Li Chengxi
(The Institute of Electronic Engineering of PLA)
Li Yong
(NO. 16 Institute, the Ministry of Machine-Building and Electronics Industries of China)

ABSTRACT

This paper describes the design and fabrication method of Gunn. VCO's at ka-band, and which have achieved broadband performances, centre frequency in (31-39) GHz, electronic tunninge range $\triangle$Fmax>1.4GHz. The Gunn. VCO's possesses practical usage value.

INTRODUCTION

For millimeter systems application the broadband electronic tunning range of oscillator is particalar significance. It can be used as local oscillator in millimeter wave systems or rader systems. This paper detailed describes the design and fabrication method of Gunn. VCO'S at Ka-band, centre frequency in 31-39 GHz, compares the tuning performance of the full-

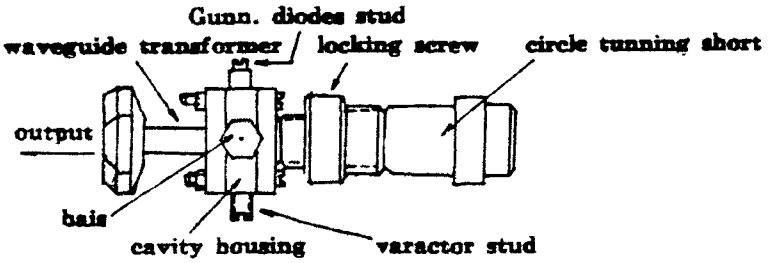

(a). Full-height waveguide resonator

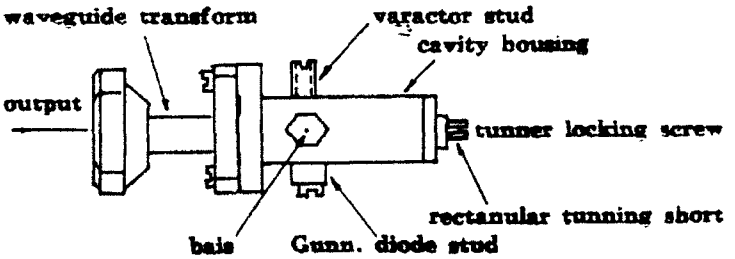

(b). Reduced-height waveguide resonator

Fig. 1 Gunn. VCo configuration

height waveguide resonator with the reduced-height waveguide resonator. Fig. 1 (a) (b) show the structure of full-height and reduced-height waveguide resonator.

8mm RANGE RECTANGULAR RESONATOR

The lowest-order propagating mode in rectangular waveguide is TE10, also called the dominant mode. To prevent other mode, usually select $1.05a < \lambda < 1.60a$, where a is wide-side in rectangular waveguide. In Ka-band waveguide BJ-320, a= 7.112mm, b=3.556mm, select length of cavity housing $l=0.5\lambda g=4.838$mm. In term of field distribution of TE101 mode in a rectangular waveguide resonator, Gunn diodes and varactor are installed at middle resonator. The length of restonator can be tunned by back-short, so the centre frequency of VCO can be set up.

THEROY OF EXTENDING ELECTRONIC TUNNING RANGE

In term of perturbation law:

$$\triangle\omega/\omega=(\triangle Wm-\triangle We)/(Wm+We) \qquad (1)$$

where the $\triangle We$ and $\triangle Wm$ are variations of electronic and magnetic energies, the We and Wm are electronic and magnetic energies in resonator. $\triangle\omega/\omega$ is frequency relatative variation. when resonating, We=Wm, so:

$$We+Wm=2We=2(W0+Wv) \qquad (2)$$

where the W0 is electronic energies in resonator (no contained varactor), the Wv is electronic energies in varactor.

$$Wv=CvVV*/4 \qquad (3)$$

$$\gamma=(Cmax-Cmin)/2(Cmax+Cmin) \qquad (4)$$

so $$\triangle\omega/\omega=\pm\gamma Wv/(W0+Wv) \qquad (5)$$

From (5) in order to extend tunning range:
(a). select varactor with big γ and high Q.
(b). request tight couple for varactor and Gunn diode.
(c). request small W0 and low Q1 resonator
When the package factor is consided, the tunning range can be shown:

$$\triangle F=Fc0*(C0-Cv)*Pv/(2Q1*Cv*P1) \qquad (6)$$

Where the Fc0 is varactor cutoff frequency in zero bais, the Q1 is Q factor assoicated with the load varactor, the Pv is power dissipated in varactor, the P1 is power delivered to the load. In order to further extend tunning range, we modified the structure of the resonator, used the reduced- height resonator, lowered Q1 of the osillator, achieved our aim. The dimension parameter of the resonator are: a=7.112mm, b=3.200mm, l=4.838mm, $\triangle$b=0.356mm.

RESULTS OF THE EXPERIMENT

The equivlent circuit for analys is shows in Fig. 2. Taking into account of package of Gunn diodes and varactor. We used the small resistor's Gunn

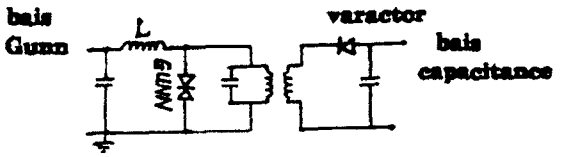

(a) bais circuit

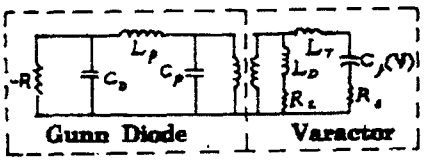

(b) equivlent of Gunn.VCO

Fig. 2 The bais and equivlent of electronic Gunn. oscillator

diodes produced by 55th insititute and big Y varactor produced by changchun semi- conductor factory. Fig. 3-5 shows tunning curves of diffient centre frequency in full- height resnator. Fig. 6-7 shows tunning curves of diffient centre frequency in reduced-height resnator. Tab. 1 shows the tunning range of reduced-height is wider than that of full-height resonator.

Tab. 1 Comparison of tunning range of full-height waveguide with reduced-height waveguide.

centre frequency (GHz)	tunning range △F (GHz)	output power P0 (mw)	type
35.37 35.53	1.25 1.41	23 36	reduced-height resonator
34.722 35.243 35.580	0.13 0.22 0.38	21 27 23	full-height resonator

ACKNOWLEDGMENT

The authors are very grateful to students Li Yingshen, Jiang Yuntai and teachers Wang Zijun, Gao Weidong.

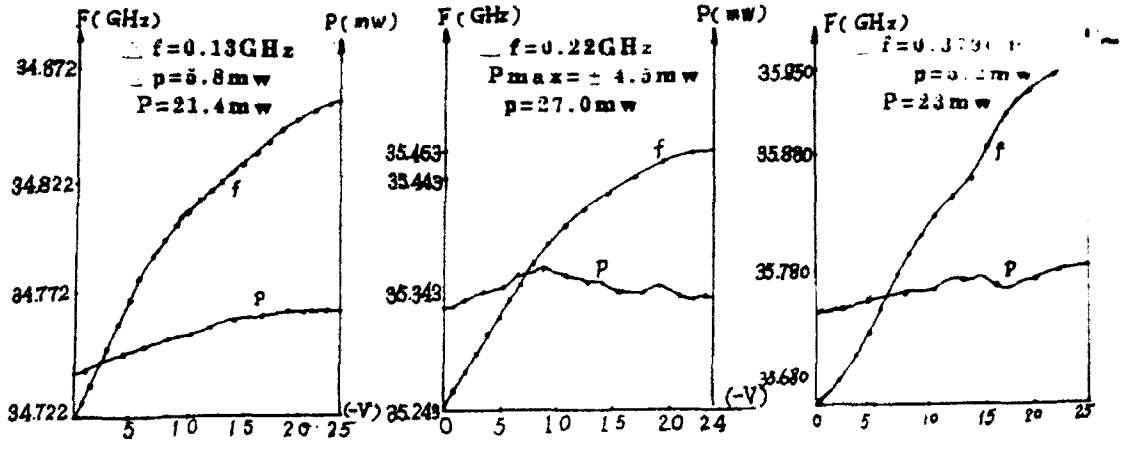

Fig. 3-5 f=34.722 (f=35.243 f=35.580) GHz
in full-height resonator

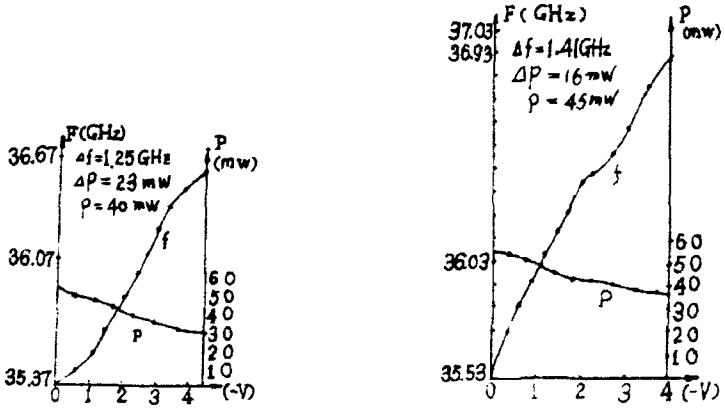

Fig. 6-7 f=35.370 (f=35.530) GHz in reduced-height resonator

REFERENCE

1. Leonard D ' Varactor Tuned Gunn Oscillators with Wide Tunning Rang
The 25GHz Frequency Band' IEEE MTT-S 1979 PP. 177
2. 'Lumped-Element Design Improves 40GHz VCO. 'Miccrowaves NO. 9 1979
3. Dowing. B and Meyers. F 'Q-Band (38GHz) Varactor-Tuned Gunn Oscillat
Electronic Leters, vol 9 NO. 11, PP244-245. 1973.
4. Rubin. D 'Varactor Tuned Millimeter Wave MIC Oscillator'. IEEE Tran
pp866～867 NO. 11 1976
5. 李成蹊'转移电子振荡器电子调频'1985. 《固体电子学研究与进展》

T6.7

NEW WAVE PROCESSES IN THE INHOMOGENEOUS SEMICONDUCTORS AND SUPERLATTICES

F.G.Bass, A.A.Bulgakov, S.I.Khankina

Institute of Radiophysics and Electronics,
Acad. of Science of Ukraine, 12 Proscura st.,
310085 Kharkov , Ukraine

The new types of waves have been theoretically predicted and investigated, the formation of which is conditioned by the inhomogeneity of semiconductor structure. It is shown that in the classical superlattice formed by periodically recapitulating semiconductor and dielectric layers, the propagation of surface electromagnetic waves with phase velocities of the order of 10^7 cm/s is possible. The spectrum of these oscillations depends considerably upon the physical parameters of the semiconductor and structure geometry and the wave decrement is determined mainly by dissipative processes in the dielectric. Namely this fact leads to a considerable deceleration of electromagnetic wave in comparison with the deceleration in an inhomogeneous semiconductor.

The waves in an inhomogeneous semiconductor have been also investigated for the case whenthe concentration of charge carriers in semiconductor and plasma frequency ω_p are the function of the coordinate z. If the constant electric field is applied in the direction of concentration variation, then the propagation of inhomogeneous waves of the concentration is possible under an angle to this direction. Their existence is conditioned both by longitudinal oscillations of carrier with plasma frequency ω_p and transversal oscillations with the frequency $\omega_N = (q|e\,E_0|/m)^{1/2}$ where q is the impurity gradient, ω_N is the electrical analog of the internal hydrodynamical waves frequency. The amplitude of such wave has its maximum value near the layer in which the plasma frequency is close to the wave frequency. Thus, in different layers being perpendicular to concentration variation direction, the waves with different frequencies propagates. While the external electrical field is absence, the inhomogeneous concentration waves have an interesting peculiarity: the wave number component in the plane z=const is proportional with ql, where l is a natural number. Hence the characteristic linear dimension of concentration variation q^{-1} determines imambiguously the periodicity of the field in perpendicular plane.

T6.8

CONTINUOUS RADIATION GENERATORS' UTILIZATION IN COHERENT MILLIMETER RADARS. RADIATION PROPERTIES, CONSTRACTION SCHEMES, RESULTS OF EXPERIMENTS

Alexey A. KOSTENKO, Grigoriy I. Khlopov, Victor P. Shestopalov, Uriy V. Yakimchiyk

Institute of Radiophisics & Electronics Academy of Sciences of the Ukraine
12, Acad. Proskura st., Kharkov, 310085, Ukraine

The constraction scheme of coherent radars with continuous radiation is in accord with the general idea of a classical interferometer, the arms of which are represented by the tracks of reflected and reference signals. The presence of frequency fluctiations of the ge - nerator leads to a shift in phase estimation of the reflected signal and this phase's derivative. Basides, in millimeter band it is characteriistic that the role of technical fluctuations increases, which have got non-stationary nature, which in its turn doesn't allow to use spectral-correlation theory [1] while examining generator parameters applied to the concrete working conditions.

In this article we provide an analysis of the effect which substantionally non-stationary frequency fluctiations produce on the work of coherent radars and we suggest a new criteria for estimating radiation quality of the transmitting devices. Basides, we have developed a method of taking measurements and have stadied experimentally different vacuum and solid-state generators of millimeter band.

Examining the signal at the input of linear part of the reciver of the coherent radar, it has been shown that with the change of velocity of the object being stadies, mean-square error is determined by the following expression

$$\sigma_v = C/V_0 * \sqrt{d_\nu(T,\tau)} \quad , \qquad (1)$$

where C-is velocity of light in vacuum, V_0-velocity of object's movement, $d_\nu(T,\tau)$-modified structural function for relative fluctuations of generator frequency, T-time of observations, τ-time of signal propagation to the object and backwards, d -represents mean-square dif - ference of generator frequency, averaged in iterval T and measured at the time moments, which differ by the interval τ

$$d_\nu(T,\tau) = 1/2 * \langle [\bar{\nu}(t+\tau) - \bar{\nu}(t)]^2 \rangle \quad , \qquad (2)$$

$$\bar{\nu} = 1/T * \int_t^{t+T} \Delta\omega(t')/\omega_0 * dt' \quad , \qquad (3)$$

where ω_0- carrier frequency of emitted oscillations, $\Delta\omega(t) = \omega(t) - \omega_0$- random frequency fluctiations. Thuse from the phisical point of view the value $\sqrt{d_\nu}$ corresponds to the short-term nonstability of genera - tor frequency. As the measurement error σ_v is inversely proportional to velocity V_0 and is proportional to time τ, then, as the numerical analysis show, when the distances tc the object are small (<1 km) the generators even with noticable frequency fluctuations ($\sqrt{d_\nu} \sim 10^{-8}$) allow to provide for coherent signal processing reflected from trans- portation vehicles, moving with velocities approximateli 100 km/hour. At the same time while locating objects moving at small velocities (V_0 <10 km/hour) and at great distance from the radar (>3 km), the

the requirements to the radiation qnality become very strict ($\sqrt{d_y} < 10^{-10}$).

The scheme of measuring test bed for examining of radiation properties in accordance with a suggested criteria of radiation quality is shown in Fig. 1. The spectrum of a radiation of the tested gene - rator 1 is transfered into radio-frequency range by means of a shift with the oscilations of the frequency standart assembly 2. Frequency difference voltage from the output of mixer 3 arrives at two digetal frequency meters 4,5 the control of which is provided by the generator of trigger pulses 6. It should be noted that frequency meter 4 is actuated directly and frequency meter 5 is actuated after interval τ, which is determined by the delay line 7. The time of observation T and interval τ are established in accordance with the suggested mode of radar, and generators being investigated should be of the same type and be in the same conditions in order to provide for the equality of dispersions of their friquencies' fluctuations. Difference frequency measurement error limits the estimate of maximum small values of short-term non-stability by the value $\sqrt{d_y} \sim 10$.

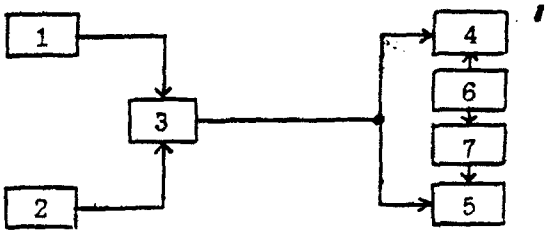

Fig. 1.

The results of investigations of vacuum and solid-state generators of fourmillimeter range are shown in Fig.2 (1-IMPATT-diode with stabilizing resonator, 2-diffraction radiation generator, 3-TWT, 4-IMPATT diode without stabilization reso - nator, 5-klistron). Between not-powrful devices the least unstable frequency ($\sqrt{d_y} \sim 10^{-10}$) is characteristic of IMPATT-diode with high Q-factor ($Q \sim 7000$) stabilizing resonator (curve 1), in which effective suppression of quick frequency fluctuations of radiated os - cillations is achieved. For powerful generator devices the best characteristics may be attributed to the diffraction radiation generator [2], for which high quality of radiation (curve 2) is provided owing to the high Q-factor ($Q \sim 3000$) resonance system and isolated spase of in - teraction and energy output.

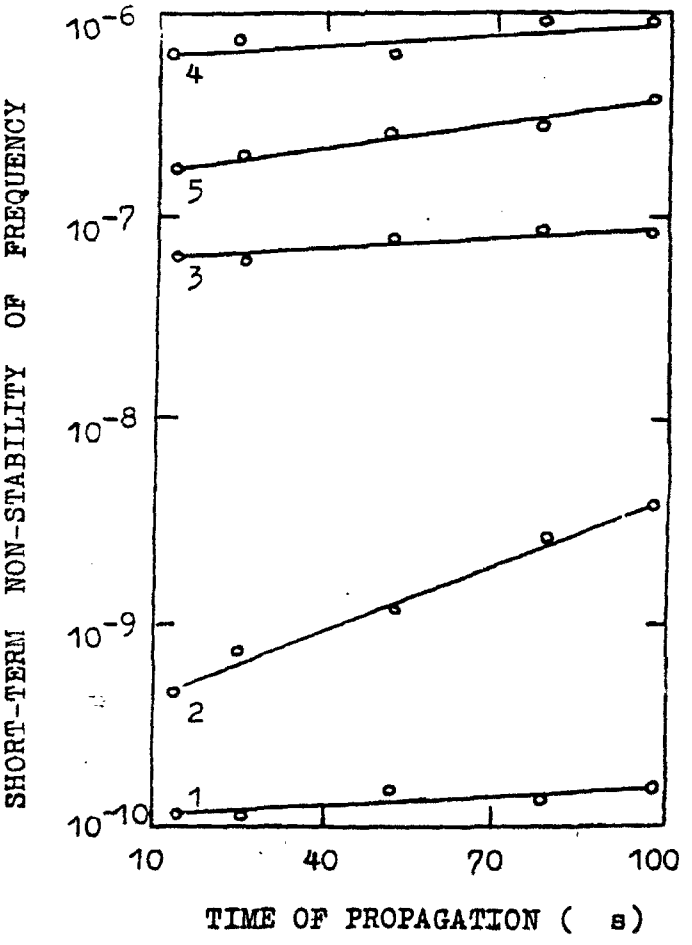

Fig. 2.

At the same time, for TWT (curve 3) and klystron (curve 4) it is characteristic to have higher value of electronic shift of frequency and lower Q-factor resonance system, in connection with which the influence of technical unstabilities is much higher. Juxtaposed characte - ristics may be attributed to IMPATT-diode with low Q-factor resonance sistem (curve 5).

Taking into consideration the experiments, which have been carried out on the basis of IMPATT-diode and diffraction radiation generator there has been created a series of coherent technological ra - dars, designed for velocity measurement of the railway vehicles, sea ships as well as for learning the characteristics of propagation of coherent radiation of twomillimeter range in next to the earth layer of the atmosphere. Among the peculiarities of receiver-transmitter schemes of such radars we can name utilization of the principle of "floating intermediate frequency" [3], which allows to practically achieve, using simple means, the coherent accumulation of a signal and to increase significantly the range. In the papers there can be found the schemes of radar construction, their characteristics and the results of research in natural conditions.

REFERENCES

[1] G.Kadel, "Einfluss der Oszillator-Kurzzeit-Stabilitat auf die Me genauigkeitvon CW-Dopplerradargeraten", Frequenz, 1988, vol. 42, 1, pp 21-23.

[2] V.P.Shestopalov et. al., " Difraction Radiation Generators", Kiev, 1991 (in Russian).

[3] M.I. Skolnic, "Radar Handbook", McGraw-Hill Book Company, New-York, 1971.

The Attenuation of Electromagnetic Waves Due to Fog

Professor D J Harris, University of Wales College of Cardiff, Cardiff, UK

The operation of optical, infrared and millimetric systems using propagation through the atmosphere may be affected by fog. An overview of the situation is given from the standpoint of a potential user.

Wavelength limitations due to molecular absorption. Radiation may be attenuated by molecular absorption, and this is shown in fig.1. For wavelengths $< 1\mu m$ or $> 10mm$, this attenuation will be small. In the approximate range 30 to $600\mu m$ the attenuation is greater than 50dB/km and applications will be limited to short ranges. Across the remaining part of the spectrum the wavelength must be chosen to avoid excessive attenuation.

Attenuation due to fog. Two approaches to the determination of attenuation can be taken, (i) computational predictions based on fog parameters and (ii) predictions based on experimental measurements of fog attenuation and parameters.

Analytical approach. Fog can be characterised by water content(g/m^3), droplet size distribution, and temperature. Energy may be lost by scattering and absorption. Fog droplets are approximated as dielectric spheres with a complex refractive index. Loss characteristics then depend on the dimension of the spheres relative to the wavelength. The temperature may affect the refractive index. A practical fog consists of water spheres with a drop size distribution , and the effect of the drops must be summed over a unit volume.

The basic theory of scattering and absorption by spherical dielectrics of refractive index $m = n - jn'$ was established by Mie[1]. The power loss due to a single object is given by the scattering, absorption and extinction cross-sections C_{sca}, C_{abs} and C_{ext}, where $C_{ext}=C_{sca}+C_{abs}$. They can be normalised to give $Q_{ext}=C_{ext}/\pi r^2$ etc, where r is the sphere radius. The full analysis involves an infinite summation of complex expressions, but some limitations can be applied.

The complex refractive index of water is tabulated[2,3], and shown in figs.2a & b. Sample values for m are:-

$\lambda = 0.65\mu m$	$m = 1.33 - j1.64\ 10^{-8}$	$\lambda = 3mm$	$m = 2.77 - j1.32$
$\lambda = 10.6\mu m$	$m = 1.18 - j0.08$	$\lambda = 10mm$	$m = 4.3 - j2.6$

Using the Mie expressions, the value of Q_{ext} can be computed, as illustrated in fig.3 for $\lambda = 3.5\mu m$. Three regions can be classified:- region A, the Rayleigh approximation for $2\pi r/\lambda < 1$; region B where the Mie approach or its approximation must be used, and region C where the drop radius $\gg \lambda$, when $Q_{ext} \to 2$.

Rayleigh scattering-region A. If $2\pi r/\lambda < 1$, Q_{ext} can be approximated by:-

$$Q_{ext} = Q_{sca} + Q_{abs} = \frac{8}{3}\left(\frac{2\pi r}{\lambda}\right)^4 |K|^2 + 4\left(\frac{2\pi r}{\lambda}\right) I_m(-K) \quad \text{where } K = \frac{m^2 - 1}{m^2 + 1}$$

Absorption predominates except where $I_m(-K)$ is very small.

At millimetric wavelengths $Q_{ext} \approx Q_{abs}$, and the attenuation in dB/km $= 8.2(M/\lambda)I_m(-K)$, where λ is in mm and M is the water content (g/m^3). This loss is shown in fig.4 for a water content of $1g/m^3$. The loss is proportional to water content.

Mie scattering-region B. The power loss in this region is sensitive to drop-size distribution, which is needed for the summation. The Mie approach is lengthy and complex, but an alternative approximation is available[4] within limits. The drop size distribution and water content depend on fog type and density, but the distribution expression $n(r) = ar^{\alpha}\exp(-br)$ has been used to model fogs and clouds. Typical values:-

Fog type	α	$r_m\mu m$	$N(cm^{-3})$	a	b	$M(g/m^3)$
1. Advection fog	3	10	20	0.027	0.3	0.37
2. Advection fog	3	8	20	0.066	0.38	0.19
3. Radiative fog	6	4	100	2.37	1.5	0.063
4. Radiative fog	6	2	200	607	3.0	0.016

N is the total drop number, r_m is the peak distribution radius and M is the water content. These are shown in fig.5. Recent measurements with better resolution show that large populations of sub-micron drops can exist, and that distributions can be bimodal. These can lead to increased attenuation at the shorter wavelengths.

Calculated attenuation of EM radiation through fog

The variation of attenuation with wavelength, obtained by summing the Mie extinction across the fog droplet distributions of the table, are shown in fig.6. This shows the low attenuations at millimetric wavelengths, and the way in which the smaller droplet size distributions increase the relative attenuations at the very short wavelengths. Many publications give computed attenuations based on particular dropsize distributions. Pinnick et al[5] determined attenuations using 341 measured distributions to determine extinction coefficients (attenuation in dB = 4.3 x ext. coef.) as a function of fog water content at several wavelengths. Two are shown in figs. 7 (a) and (b) for 0.55 and 11μm. The lines correspond to linear relationships. For fog with 0.2g/m^3 water content, these give attenuations of 200 and 80 dB/km at 0.55 and 11μm respectively.

Measured attenuation due to fog.

Values have been reported for the overall attenuation along a given transmission path in fog, but they vary widely, and quantifying values for fog conditions are rarely given. To enable comparisons to be made, simultaneous measurements are needed of attenuation, water content and droplet size distributions. This is not easy, and conditions vary along the path.

Since attenuation is not sensitive to fog drop size at millimetric wavelengths, predictions and measurement should give good agreement, and this has been shown experimentally. Millimetric attenuation measurements can therefore be used to determine water content. Early measurements[6] used a 3mm radar and lasers at 0.63, 3.5 and 10.6μm along the same path. Attenuations greater than 50dB over a 2.6km path at 0.63μm were obtained with a mean water content along the path of about 0.1g/m^3, but a mismatch of sensitivities made a wider correlation difficult to obtain. Measurements using an open-resonator[7] at 3mm wavelength with an axial laser beam at 0.63μm for artificial fogs gave the results shown in fig.8.There is considerable scatter of results, but for very dense fogs of 0.8g/m^3 an attenuation of nearly 2000dB/km is indicated. This is considerably in excess of predictions from figs 6 and 7, but more in line with the linear extrapolation of 7(a). This difference may be due to the presence of submicron drops in the fog.Measurements have also been carried out on extinction coefficient and water content for laboratory fogs at about 10μm wavelength. Fig.9 shows the results of one such measurement[8] at 10.59μm.At this wavelength a linear relationship has been found, giving extinct. coeff.≈ 150km^{-1} per g/m^3.

There seems to be a dearth of simultaneous measurements on attenuation and water content for natural fogs in the open literature.The use of millimetric open-resonators, or 10μm laser attenuation measurements, might allow water content to be determined.

Conclusions

At millimetric wavelengths the attenuation closely follows the Rayleigh predictions, being insensitive to droplet size distributions, giving 3dB/km for 1g/m^3 at 3mm. For the range 30-600μm the Rayleigh approximation may still be used, but molecular absorption > 50dB/km limits applications to very short ranges.

For the range 0.5-30μm predictions are less clear. At about 10μm ,attenuation is given by ≈ 630M dB/km, where M is in g/m^3. Theoretical predictions are available, but for wavelengths below 10μm they are drop size distribution dependent. Confirmation experimental results seem to be few and show discrepancies with predictions, and further experimental work would seem to be called for.

References

1. MIE G. Ann. Physik, 25, pp377-445 1908
2. HALE G. and QUERRY H, App. Optics, 12, pp555-563 1973
3. RAY P, App. Optics, 11,8 pp1836-1844 1972
4. VAN DER HULST H, Light Scattering by Small Particles, Dover 1981
5. PINNICK R, et al, Jnl. Atmos. Sciences, 36,8 pp1577-1586 1979
6. CHU T. and HOGG D, Bell Syst. Tech. Jnl. pp723-759 1968
7. HARRIS D. and PICKARD S, Proc. URSI Symp. ESA SP-194, pp201-205 1983
8. NOLAN P. and JENNINGS S. Jnl. Atmos. and Oceanic Tech. 4,3, pp391-400 1987

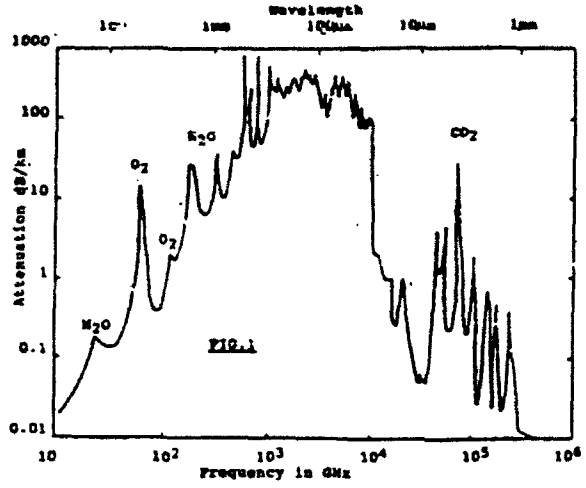

FIG.1

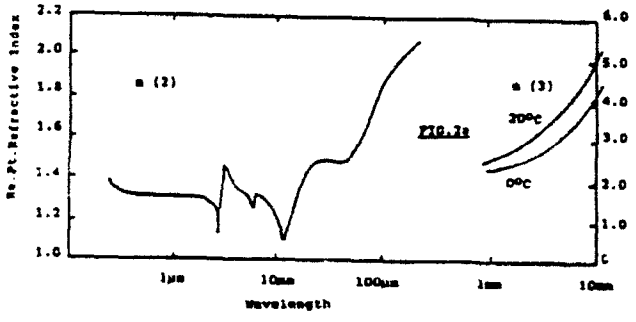

FIG.2a

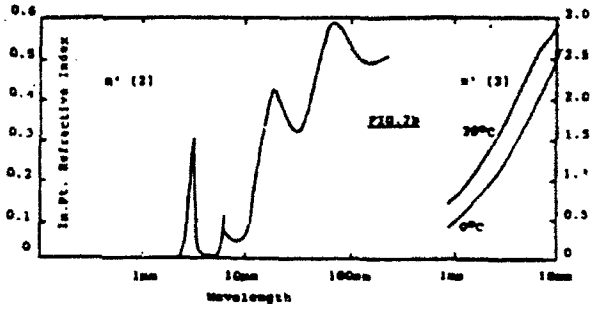

FIG.2b

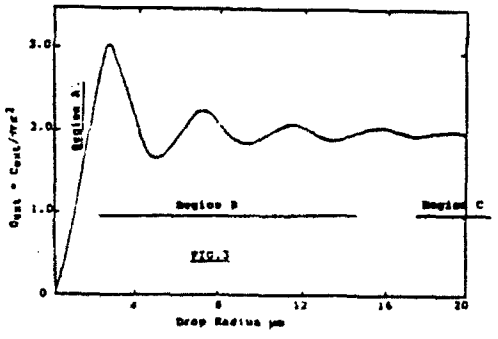

FIG.3

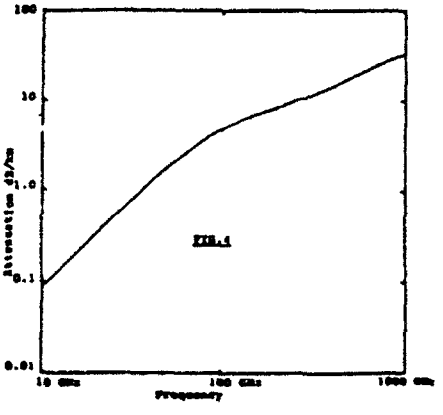

FIG.4

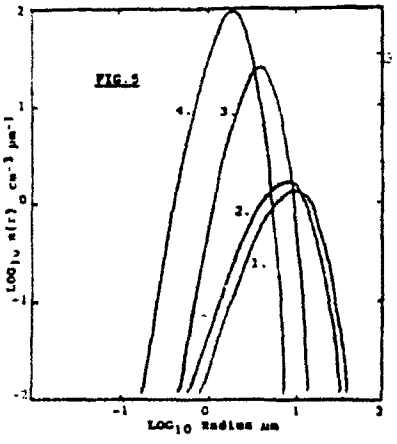

FIG.5

COPY AVAILABLE TO DTIC DOES NOT PERMIT FULLY LEGIBLE REPRODUCTION

T7.2

A NEW MODEL OF FREQUENCY SCALING OF RAIN ATTENUATION

Huang Jie and Hu Dazhang

Qingdao Research Center of
China Research Institute of Radiowave propagation
33 Fu Long Shan, Qingdao, China (266003)

Abstract: A new empirical model for frequency scaling of rain attenuation on terrestrial path is proposed. This model based on the experimental data of rain attenuation from different region in the world, such as the China, Japan,UK,Sweden, FRG and Italy. Comparison with the current models of frequency scaling of rain attenuation is made. Because a region factor o.ol is included in the our model, thus predict precision is improved and is good than the other model. This model applies to a range of frequency of 10-80 GHz.

(1).Introduction:

Frequency scaling method, which the rain attenuation at one frequency is predictor by the rain attenuation measured at other frequency , is very importance as to design of radio system at frequency above 10 GHz. In recent years a number of scientists have investigating on the frequency scaling of rain attenuation [1], [2], [3], [4], hh[5]. Reviewing the current models of frequency scaling of rain attenuation, we need to do following three improvements on the frequency scaling of rain attenuation:

(a). to add some data of rain attenuation from China in the model of frequency caling;
(b). to extend the range of frequency region to 80 GHz;
(c). to add a region factor of Ro.ol in the model of frequency scaling of rain attenuation.

(2). Data of rain attenuations

In order to offer a new model of frequency scaling of rain attenuation, we had made an experiments of rain attenuation at frequencies of 12, 25.3. 33.5 and 72.0 GHz on a terrestrial path with 1.26 KM in Qingdao during 1986-1988 [6] and had also made an experiment of rain attenuation at frequencies of 12, 25.3 and 33.5 GHz on a terrestrial path with 2.5 KM in Xinxiang during 1981-1985 [7]. In order to add the suitable region of the frequency scaling of rain attenuation,we had also collected some data of rain attenuations from UK, Sweden, FRG, Italy and Japan [8]. These data, which are a statistic value of cumulation distribution of rain attenuation above one year are listed on the Tab. 1. The parameters of frequency, polarization, length of path, easured period, during and cumulation distribution of rain intensity are also liste in the Tab. 1.

Tab. 1. Long-term distribution of rain attenuation at frequencies above 10GHz

Location (Nation)	Frequency GHz	Polar.	length (km)	period	years	Rain attenuation in dB and rainfall intensity in mm/h exceeded for various percentages of time (%)								
						0.001	0.002	0.003	0.006	0.01	0.02	0.03	0.06	0.1
Qingdao (China)	12.0	V	1.26	86-89	4	3.1	2.8	2.6	2.3	1.9	1.7	1.4	1.1	0.7
	25.3	V	1.26	86-89	4	-	10.7	9.3	7.7	7.2	6.1	5.4	3.7	3.0
	33.5	V	1.26	88-89	4	-	17.0	16.4	10.6	9.5	7.9	7.0	5.0	3.9
	72.0	V	1.26	88-89	2	-	-	-	-	17.0	13.8	12.6	11.2	7.9
	*					(110)	(85)	(74)	(52)	(45)	(31)	(24)	(12)	(10)

Xinxiang	12.0	H	2.5	80-84	5	6.3	5.8	8.2	4.0	3.5	2.6	2.4	1.9	0.9
	25.3	H	2.5	80-84	5	14.8	12.7	11.5	8.8	7.6	5.7	4.9	3.0	1.5
(China)	33.5	H	2.5	80-84	5	30.0	26.6	24.8	20.5	16.5	11.0	9.4	6.8	4.8
	*					(98)	(82)	(71)	(51)	(42)	(26)	(21)	(14)	(3)
Meidle-	19.4	V	7.4	73-75	3	18.6	14.7	12.9	9.9	8.1	6.0	5.2	4.2	3.2
sham	36.1	V	7.4	73-75	3	-	32.2	31.0	27.0	22.7	18.6	15.7	13.3	11.9
(U.K)						(50)	(39)	(32)	(23)	(18)	(13)	(10)	(6)	(4.5)
Stockho-	10.8	H	15.0	76-77	2	15.2	12.0	10.4	9.1	8.4	6.8	-	-	-
lm	17.9	H	15.0	76-77	2	-	30.0	27.2	22.8	19.2	14.0	12.2	10.0	9.0
(Sweden)	36.0	H	15.0	76-77	2	-	-	-	56.0	47.0	35.0	30.0	24.0	21.0
	*					(70)	(52)	(43)	(30)	(23)	(17)	(14)	(9)	(6)
Darmsta-	12.4	H	20.0	76	1	19.6	16.8	14.8	11.6	9.2	6.8	5.4	3.7	2.8
dt	15.0	H	20.0	76	1	28.4	23.0	20.9	16.8	14.1	10.4	9.0	5.6	4.6
	29.0	H	20.0	76	1	-	-	-	46.0	39.0	32.0	27.4	22.0	18.0
(FRG)	39.0	H	20.0	76	1	-	-	-	-	-	-	-	36.0	27.5
	*					(50)	(43)	(38)	(28)	(22)	(16)	(12)	(8)	(5.5)
Fucino	11.0	V	9.5	75-77	2	16.0	14.0	12.7	9.2	7.6	6.0	4.8	4.1	3.0
	17.8	V	9.5	75-77	2	29.8	25.6	23.3	19.1	15.6	12.1	10.7	8.1	6.3
(Italy)	*					(100)	(75)	(64)	(47)	(35)	(25)	(20)	(14)	(9)
Tokyo	11.5	C	1.3	79-80	1	6.3	5.5	5.0	3.4	3.1	1.8	1.3	0.9	0.8
	34.5	C	1.3	79-80	1	-	-	-	19.3	16.3	11.3	9.9	6.6	5.0
(Japan)	81.8	C	1.3	79.80	1	-	-	-	33.8	29.3	24.5	21.7	17.4	14.6
	*					(109)	(98)	(94)	(83)	(66)	(42)	(33)	(22)	(17)

* Value in parenthesis is represented rainfall intensity.

(3) Model of frequency scaling

From Table 1 we chose rain attenuation exceed 0.01% of time to represent the measured value of rain attenuations for each path. There are pair of rain attenuations (f2>f1) of 20 sets, which get data with same frequency, same polarization and same path from in the Table 1. Besed on the data of 20 sets, a empirical model of frequency scaling of rain attenuation is derived. The value of A2, which is the rain attenuation at frequency of f2, may be expressed by the value of A1, which is the rain attenuation at frequency of f1, as follows:

$$A2 = A1 \left(\frac{f2}{f1}\right)^{H}$$

where H is a empirical coefficients, which is a function of the frequencies of f1, f2 ; rain attenuation A1 and rainfall intensity for 0.01% of the time Ro.01, as follows

$$H = 2.2154+0.0039f1-0.0129f2-0.0191A1-0.0044Ro.01$$

where f1 and f2 are in GHz; A1 is in dB and Ro.01 is in mm/h.

Assuming f1 = 10 GHz and A1 = 2 dB, a relation between the parameter A2/A1 and frequency for two rainfall intensity Ro.01 = 40 mm/h, which represented as temperature , region, and Ro.01 = 80 GHz, which is represented as the tropical and subtropical region. The relation between values of A2/A1 and frequency are shown in the Fig.1. A predictive results of rain attenuation using the model of exponential model (CCIR) is also shown in this figure.

For P % of the time of the rain at- tenuation A(P%) is by CCIR [10]

$$A(P\%) = 0.12\ A(0.01\%)\ P^{-(0.546+0.043\lg P)}$$

where A(0.01%) is the rain attenuation for 0.01% of the time by the formula of frequency scaling.

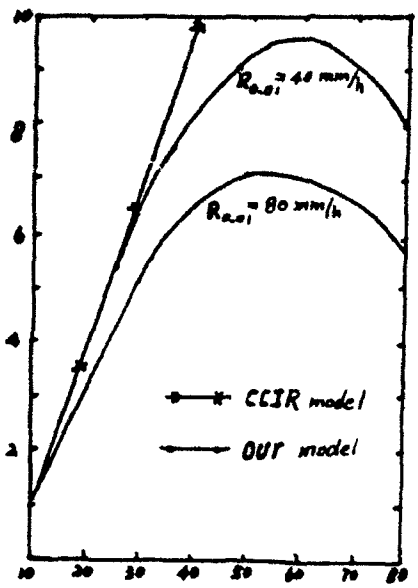

Fig. 1. The relation between predicted rain attenuation and frequency using CCIR model and our model(A1=2dB, f1=10 GHz)

(4). Comparison with other models

Review on aspects of the frequency scaling of rain attenuation, there are five models with typical meaning : Linear model, Exponential model [2], Hodge model [3], Boithias model [1], Modified model [11]. In order to estimate the precision for various models of frequency scaling of rain attenuation, a parameter of S, which is mean square error of predictive value of rain attenuation, is defined as:

$$S = \sqrt{\frac{1}{n}\sum_{i=1}^{n}(A2i-A2i')^2}$$

where A2i and A2i' are noted as measured and predictive value of rain attenuation for ith set. Based on rain attenuation data , the results of mean square error are listed in Table 2 for several models. From Tab. 2 we show that the range of mean square errors are from 3.9 to 7.7dB for our model. The minimum of mean square error is 3.98 dB for our model, next one is 4.36 dB for the modified linear model, next are exponential model (CCIR), Hodge model and Boithias model. In our model, the precision of prediction is higher than order moder. The applicational range of frequency is from 10 GHz to 80 GHz.

Table 2. Precision of arin attenuation for several models

No	models	formula	fre. range	mean squire error
1	Linear model	A1=A2*(f2-6)/(f1-6)	10-25GHz	5.65
2	Exponential model	$A1=A2*g(f2)/g(f1)$ $g(f)=f^{1.72}/(1+3*10^{-7}f^{3.34})$	7-50GHz	6.52

3	Hodge model	$A2=(A1/a1)^{b2/b1} * (b1/b2)^{0.5(1-b2/b1)} * a2^{\pi b2/b1}$		6.53
4	Boithias model	$A2=A1*(g(f2)/g(f1))^{1-H}$ $g(f)=f^2/(1+10^{-4}f^2)$ $H=1.12*10^{-3}((g(f2)/g(f1))^{0.55}*(A1*g(f1)))^{1/2}$		7.64
5	Modified model	$A2=A1(f2-6)^{(1.1+1/(f2-f1))}/(f1-6)$	10-80GHz	6.36
6	Our model	$A2=A1*(f2/f1)^{H}$ $H=2.2154+0.0039f1-0.0129f2-0.0191A1-0.0044Ro.01$	10-80GHz	3.98

References

(1). Boithias L. [1989], Frequency scaling for rain attenuation , Ann, des Telecomm, Vol. 44, 5-6,186-189.

(2). CCIR Report 721-2[1989], Attenuation by hydrometeors, in particular precitation, and other atmospheric particles,

(3). Hodge D.B. [1977] , Frequency Scaling of Rain Attenuation , IEEE Trans. Antenna and propagation, vol. AP-25, 3, 446-447.

(4). Furuhawa Y. and T.Ihara , [1981], Remote sensing of Path-averaged raindrop size distribution from microwave scattering measurement , IEEE Trans. Antenna and propagation, Vol. AP-29, 2 ,275-281.

(5). Hu Dazhang and Huang Jie [1988], Inversion of path raindrop size distribution, Chinese Journal of Radio Science, Vol. 3, 1, 1-9.

(6). Hu Dazhang , Zhang Zhenwai and Huang Jie [1991], Measurement of rain attenuation at frequencies 10-80 GHz in Qingdao, 4th Chinese Conference on Radiowave Propagation (Wuhan), p227.

(7). Hu Dazhang, Don Qingshen and Su Jinmin [1988], Measurement of rain attenuation at frequencies 10-40 GHz in middle region of China , 1988 International symposium on Radio propagation [ISRP'88, Beijing] , 243-246.

(8). CCIR Document 5/378 [1988], Data Banks used for testing prediction method in sections E, F, and G of volume V.

(9). CCIR Report 563-2 [1982] , Radio meteorological Data.

(10). CCIR Report 338-5 [1989], Propagation Data and Prediction methods required for Line-of-sight radio-relay system.

(11) Huang Jie [1990], A modified Linear model for frequency scaling , no publish.

EXPERIMENTAL INVESTIGATION ON ATMOSPHERIC GAS & CLOUD ABSORPTION AT MILLIMETER WAVEBAND

Ja Ri Jin, Wang Feng Xia, Zhao Yi Guang
(China Reseach Institute of Radio Wave Propergation)

EQUIPMENT AND PRINCIPLE

A dual-frequency radio telescope used here can work at the frequency of 9.375 GHz or at 22.23 GHz. Its antenna uses a five-horn Cassegrain feed system, and has two mutually perpendicular difference patterns and a summation pattern. The antenna is fixed on the support which is suited to the equatorial coordinates, and each of its difference pattern is at an angle of 45° to the celestial declination. The output ports are respectively connected with three Dicke receivers (two for difference and one for sum).
'Difference-lobe-maximum method' is introduced in this paper. Based on the flat-earth approximation, the sun radiating temperture observed by the radio telescope is given by

$$T = (2T_B \Omega / \Omega_A) \exp(-\tau_0 \sec\theta) \qquad (1)$$

The output voltage of the receiver is

$$V(\theta) = (2T_B \Omega G / \Omega_A) \exp(-\tau_0 \sec\theta) \qquad (2)$$

where T is the brightness temperature of the sun, Ω_B is solid angle of the sun, Ω_A is solid angle stretched by the antenna, G is the gain of the receiver, θ is zenith angle, τ_0 is total zenith absorption. Taking the logarithm of (2) yields

$$\ln V(\theta) = \ln (2T_B \Omega G / \Omega_A) - \tau_0 \sec\theta \qquad (3)$$

thus, measuring θ and $V(\theta)$, one can evaluate τ_0. Meteorological parameters should be obtained (with the radiosonde) while measuring in order to compare the experimental values with theoretic ones.

MEASUREMENT RESULT

1. Relation between absorption and zenith angle

The data in table 1, measured in various weather condition during the spring and summer in 1990, illustrate the variation of radiation strength of the sun with zenith angle. Dividing them into three segments by zenith angle, and evaluating the zenith absorption at each segment, we obtain table 2

Table 1 radiation strength of the sun versus zenith angle, in mV units

sthength	fine			overcast			cloudy		
θ °	Vc	Vs	ΔV	Vc	Vs	ΔV	Vc	Vs	ΔV
87	52.0	26.6	25.4	51.0	20.7	30.3	52.8	23.2	29.6
85	63.0	43.8	19.2	58.6	36.9	27.7	62.4	40.3	22.1
83	66.0	54.3	11.7	62.1	47.3	14.8	65.2	51.0	14.2
80	69.6	63.9	5.7	65.4	57.0	8.4	68.1	60.8	7.3
76	73.0	71.0	2.0	68.3	64.5	3.8	71.1	68.3	2.8
70	77.0	77.0	0.0	70.7	70.7	0.0	74.2	74.2	0.0
65	79.8	79.9	-0.1	73.6	73.8	-0.2	75.2	75.1	0.1
55	82.6	83.0	-0.4	77.3	77.3	0.0	80.0	80.1	-0.1

Table 2 τ_o(dB) measured at different zenith angles

θ °	weather	fine	overcast	cloudy
θ ≥ 80	τ_{oc} (dB)	0.069	0.078	0.074
	τ_{oo} (dB)	0.075	0.081	0.078
80 ≥ θ >72	τ_{oc} (dB)	0.075	0.080	0.076
	τ_{oo} (dB)	0.075	0.081	0.078
72 ≥ θ >55	τ_{oc} (dB)	0.076	0.081	0.078
	τ_{oo} (dB)	0.076	0.081	0.078

2. Relation between absorption and absolute humidity

It is assumed that linear correlation exists between zenith atmospheric gas and cloud absorption and the density of surface water vapor, or $\tau_o = a+b\rho$. Make regressions in various weather conditions, the results are shown in table 3.

3. Relation between zenith absorption and frequency

Average value of zenith gas and cloud absorption measured contemporaneously at 9.375 GHz and 22.23 GHz in the summer in 1990 is shown in table 4.

Table 3 Relation between surface water vapor density ρ and τ_o

weather parameter	fine (n=56)			overcast (n=52)			cloudy (n=37)		
waveband	a	b	r	a	b	r	a	b	r
3.2 cm	.054	.0012	.883	.0557	.0016	.896	.054	.0012	.797
1.25cm	.096	.055	.841	.110	.078	.911	.107	.066	.776

Table 4 Average value of zenith gas and cloud absorption in the summer

τ_o (dB) f (GHz)	τ_o, fine	τ_o, overcast	τ_o, cloudy
9.375	0.075	0.083	0.077
22.23	1.175	1.678	1.428
$\tau_{9.375}/\tau_{22.23}$	0.064	0.023	0.054

ANALYSIS

1. Mathematical model of the absorption's variation with zenith angle at low elevation angles

With the table 1 and table 2, the atmospheric absorption at high elevation angles (low zenith angles in other words) can be evaluated by

$$\tau = \tau_o \sec\theta \tag{5}$$

Unfortunately it will result in a considerable error using (5) at low elevation angles, since that the flat-earth approximation will be not valid at that time.

Atmospheric absorption shoud be a function of $D(\theta)$, distance through the absorbing atmosphere, in fact, it is assumed that the absorption is proportional to $D(\theta)$, thus

$$\tau = b_0 + b_1 D(\theta) \tag{6}$$

where

$$D(\theta) = [(a_e+h_e)^2 - a_e^2 \sin^2\theta]^{1/2} - a_e\cos\theta \tag{7}$$

$$a_e = K \cdot a \tag{8}$$

$$K = 1/(1+a \cdot \Delta N \sin\theta) \tag{9}$$

$$-\Delta N = 7.32\exp(-0.005577N_s) \tag{10}$$

$$N_s = (77.6/T)(P+4810 \cdot e/T) \tag{11}$$

where N_s is surface refraction index , T is atmospheric temperature, P is atmospheric pressure, e is atmospheric absolute humidity, h_s is effective height of the absorbing atmosphere.
Relation between h_s and ρ is given by

$$h_s = 5.97 - 0.06\rho \quad \text{(for 9.375 GHz)} \tag{12}$$
$$h_s = 6.28 - 0.703\rho \quad \text{(for 22.23 GHz)} \tag{13}$$

2. Relation between zenith absorption and surface absolute humidity
The plots of the experimental determined zenith absorptions τ_o versus the surface water vapor density ρ are show in Fig. 1 and Fig. 2)

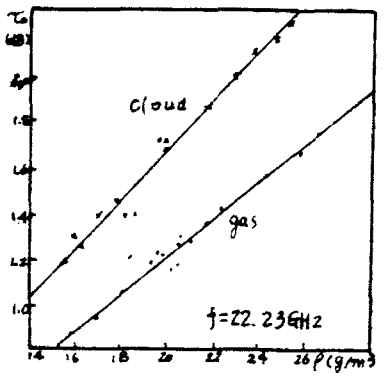

Fig. 1 τ_o versus ρ (f=22.23GHz)

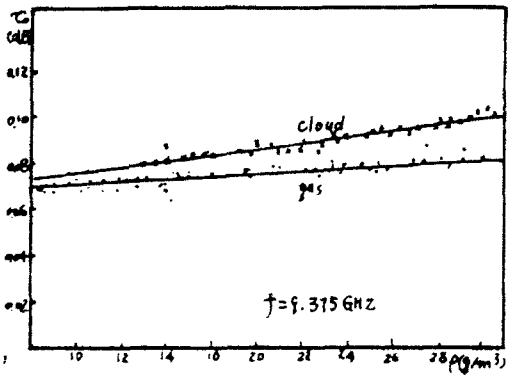

Fig. 2 τ_o versus ρ (f=9.375GHz)

From Fig. 1 and Fig. 2, we can conclude that τ_o is indeed proportional to ρ when $\rho < 24 g/m^3$. However, the measured values are less than calculated ones when $\rho > 24 g/m^3$. The regressive results are shown in table 3, from which the following linear equations can be produced.
for f=9.375 GHz

$$\tau_o gas = 0.054 + 0.0012\rho \tag{14}$$

$$\tau_o cloud = 0.057 + 0.0016\rho \tag{15}$$

for f=22.23 GHz

$$\tau_o gas = 0.096 + 0.055\rho \tag{16}$$

$$\tau_o cloud = 0.011 + 0.078\rho \tag{17}$$

3. Relation between the absorption and frequency
It is assumed that the gas absorption and cloud absorption is proportional to frequency at the wavebands of 9.375 GHz and 22.23 GHz. According to table 4, the equations expressing the relation between absorption and frequency will be simulated as following

$$\tau_o gas = [0.054 - 0.00326(f_1 - f_2)] + [0.0012 - 0.00419(f_1 - f_2)]\rho \tag{18}$$

$$\tau_{o\,cloud} = [0.057-0.00412(f_1 - f_2)] + [0.0016-0.0059(f_1 - f_2)]\rho \quad (19)$$

where f1=9.375GHz, 10GHz$<$f2$<$22.23GHz.
The following equations express the general relation of atmospheric gas absorption and cloud absorption with zenith angle, surface absolute humidity and frequency

$$\tau_{gas}=[(0.053+0.00132\rho)(f_1 - f_2)^2]D(\theta) \quad (20)$$

$$\tau_{cloud}=\{[0.057-0.00412\cdot(f_1 - f_2)] + [0.0016-0.0059(f_1-f_2)]\rho\}D(\theta) \quad (21)$$

$D(\theta)$ equates to $\sec\theta$ for $\theta<70^\circ$, and is determined by (7) for $\theta>70^\circ$.

CONCLUSSION

The following conclussions can be obviously drawed from all of the above:
1. The flat-earth approximation is only used for elevation angles above 16°. Otherwise the effect of curved earth must be considered.
2. Equation (1) through (3) are not valid when considerably large water drips are consisted of in the cloud.
3. Though it is reluctant that deriving the relationship between absorption and frequency from the data of these two wavebands, the experimental values τ_o using equation (18) and (19) are in good agreement with the theoretical ones at the waveband of 12 and 22.23 GHz.

T7.4

FLUCTUATIONS OF MMW PROPAGATING IN LAYERED INHOMOGENEOUS TURBULENT THICKNESS

G.A. Andreyev, and S.A. Ogarev

Institute of Radioengineering & Electr., Russian Academy of Sciences
18 Marx Avenue, GSP-3, Moscow 103907, Russia

Fluctuations of millimeter waves (MMW) on atmospheric radiochannel output cause the coherence losses of a signal. decrease the trustworthiness of transmitting data, and resolving power of angular detective systems. To solve the statistical problems of data receiving in satellite and terrestrial radiocommunication systems, radiocontrolling, and in remote sensing of atmosphere, terrestrial covers and other objects, it's necessary to compute structural and correlation functions of wave's level and phase. The adoption of voluminous quantity of publications concerning propagation of optical and infrared waves in turbulent atmosphere is not ever possible due to pecularities of MM wave band: the greater wavelengths in comparison with optical wavelengths led to the mostly manifesting of wave properties of MM beam wave - divergence while propagating. The interdependence between spatial ρ and temporal τ arguments of correlation functions must differ from the usually implied as $\rho = V_{\perp}\tau$ for a plane wave. The exceeding of the first Fresnel radius $\sqrt{\lambda L}$ over the outer turbulent scale L_0 causes the usage of biparametrical spectral density $G_n(\varkappa)$ of air index of refraction pulsations [1].

The aim of the paper was: - to derive the parametrical dependences of spatial-temporal correlation and structural functions of fluctuations of amplitude level, phase and phase difference (angle of arrival or direction of propagation) of Gaussian MMW beam on atmospheric radiochannel output (as a layered inhomogeneous atmosphere thickness); - to approximate the correlation functions, spectra, and mean-square dependences of fluctuations of amplitude level, phase and phase difference (angle of arrival) of MM beam - on the parameters: propagation path geometry, position of receiving points, intensity of turbulent pulsations of index of refraction.

The real atmosphere represents a complicated layered structure, which is mostly manifest itself at low elevation angles of slanted satellite-Earth paths. It was supposed that structural characteristic C_n^2 smoothly changes in a layer Δz. For the height dependence $C_n^2(z)$ the experimental profiles [2] were used, approximated by the following dependence:

$$C_n^2(z) = C_{n0}^2 \cdot (z/z_0)^{-2/3} \cdot \exp[-z/z_n] , \qquad (1)$$

where C_{n0}^2 - the terrestrial value of structural characteristic, z_0 and z_n - the numerical coefficients, derived at the approximation of the experimental profiles. While entering into the Earth's atmosphere a radiowave, which source is a satellite, may be taken into account as a plane wave. Then the formula of mean-square of level fluctuations $\chi = \ln\{A/A_0\}$ becomes as follows:

$$\tilde{\sigma}_\chi^2 = 0.306 \cdot \pi L_*^{5/6} \cdot C_{n0}^2 \cdot (\sin\vartheta)^{-2/3} \cdot k^{7/6} \cdot z_n^{11/6} \cdot (z_n/z_0)^{-2/3} \cdot$$

$$\cdot \int_0^{L_{*\infty}} \int_0^{\infty} \varkappa_*^{-5/3} \cdot \xi^{-2/3} \cdot e^{-\xi \sin\vartheta} \cdot \left[1 - \cos\left[\left(\frac{\xi}{L_*} - \frac{z}{L_*}\right) \cdot \varkappa_*^2\right]\right] \cdot d\varkappa_* d\xi , \qquad (2)$$

where $L_* = L/z_n$, and $\xi = l/z_n$ - dimensionless variable along the integration path. In the supposition of "frozen" homogeneous turbulence (C_n = const), and the Kolmogorov spectral density of media refractive index pulsations, the evaluation of the effective turbulent thickness L_T follows from the comparison of (2) with the well-known expression of level fluctuations $\sigma_\chi^2 = 0.307\, C_n^2\, k^{7/6}\, L_T^{11/6}$ of a plane wave:

$$\frac{\tilde{\sigma}_\chi^2}{\sigma_\chi^2} = C_\chi^2(\vartheta, L_*, l_0) \cdot (z_n/L)^{11/6} \cdot (z_n/z_0)^{-2/3} \equiv 1 ; \qquad (3)$$

$$L_T = \left(C_\chi^2(\vartheta, L_*, L_0)\right)^{12/11} \cdot z_0^{4/11} \cdot z_n^{7/11} , \qquad (4)$$

where the numerical parameter $C_\chi^2(\vartheta, L_*, L_0)$ (which is defined by the value of integral in expression (2) and dependent upon the shape of phase front, atmospheric turbulence and diffractional divergence of a beam) is shown in Fig.1 in 3-dimensional way. The estimation of the effective turbulent thickness L_T was made as a result of numerical integration of expression of mean-square log-amplitude fluctuations σ_χ^2 of MMW, taking into account the height dependence $C_n^2(z)$, the biparametrical turbulent spectrum, parameters $z_0 = 3.15 \cdot 10^3$ (m) and $z_n = 2.27 \cdot 10^3$ (m), and propagation path elevation angle $\vartheta = 30^\circ$. The value of equivalent turbulent thickness L_T appeared to be ≈ 2.56 km. With due regard for beam parameters the expressions (2-4) become more complicated by analogy with [2,3].

The temporal, spatial, and mutual (time-spatial) structure

functions of log-amplitude fluctuations of a MM beam wave are plotted in Fig.2, normalized by doubled dispersion $2\sigma_\chi^2$ of a plane wave fluctuations. The computations were set forth by numerical technique on a mini-super computer MicroVAX (VAX-11/780), and a personal computer IBM PC-AT/286 with usage of programs of adaptive two-dimensional integration taking into account biparametrical turbulent spectrum, height dependence $C_n^2 = C_n^2(z)$ of cloudless atmosphere. Computations were made with the following parameters: L = 5000 m, λ = 8.3 mm, waveparameter $P = L/k\rho_0^2 \approx 168$, L_0 = 10 m, $l_0 \approx 10^{-3}$ m. As it follows from the computing, in MMW-band there is the interdependence $\rho_e = C_\rho \cdot V_\perp \tau_e$ (where $V_\perp$ - cross drift velocity of atmospheric permittivity inhomogeneities) between spatial ρ_e and temporal τ_e correlation intervals of level and phase fluctuations, that differs from usually implied (see (*)). The coefficient of proportionality C_ρ depends upon the value of waveparameter P and equals ≈ 2.

Fig.3 shows the parametrical family of temporal structural functions of MMW-beam phase, which proves the necessity of regard for outer turbulent scale in description of the second statistical moments of MM beam-wave fluctuations (curves (1) and (3)).

As follows from computations, the characteristics of MM beam wave in line-of-sight paths with usage of transmitting antennae of apertures about 1 meter, correspond more to propagation characteristics of a spherical than a plane wave. In case of usage of antenna with aperture $2\rho_0 \approx (0.6...1)$ m, forming a beam, the interval of waveparameters for path distances $L \approx 10^4$ m corresponds more closely to the area of spherical wave ($P \to \infty$). By the values of outer scale $L_0 \approx 10$ m, there is the strong dependence of asymptotical values of structural functions upon P .

There were calculated the normalized energy (frequency) spectra $G(\Omega_*) = \tau_0 G_*(\Omega_*)$ of level and phase using the Fourier transform from approximated ACF, as a function of normalized argument $\Omega_* = \tau_0 \Omega$, where for level $\tau_0 = \frac{1}{V_\perp}\sqrt{\frac{L}{2\pi}}$, and for phase $\tau_0 = \frac{1}{V_\perp}\frac{L_0}{2\pi}$. The spectra that were computed with the approximate formulas, are in good coincidence with ones derived from theoretical ACF with the usage of FFT technique [3]. As it follows from the results of computation, taking into account the turbulency of cloudless atmosphere, the fluctuation log-amplitude and phase spectra are low-frequency. The level spectrum max lies within the values $\Omega_{0*} = 3...4$; and phase - is near $\Omega_{0*} = 4$. For instance, if $V_\perp$ = ...2 mps, so Ω_0 = 0...1.4 Hz. The amplitude spectra width is $\Delta\Omega_\chi$ = ...5.4 Hz, and phase - $\Delta\Omega_\varphi \approx 1.4$ Hz.

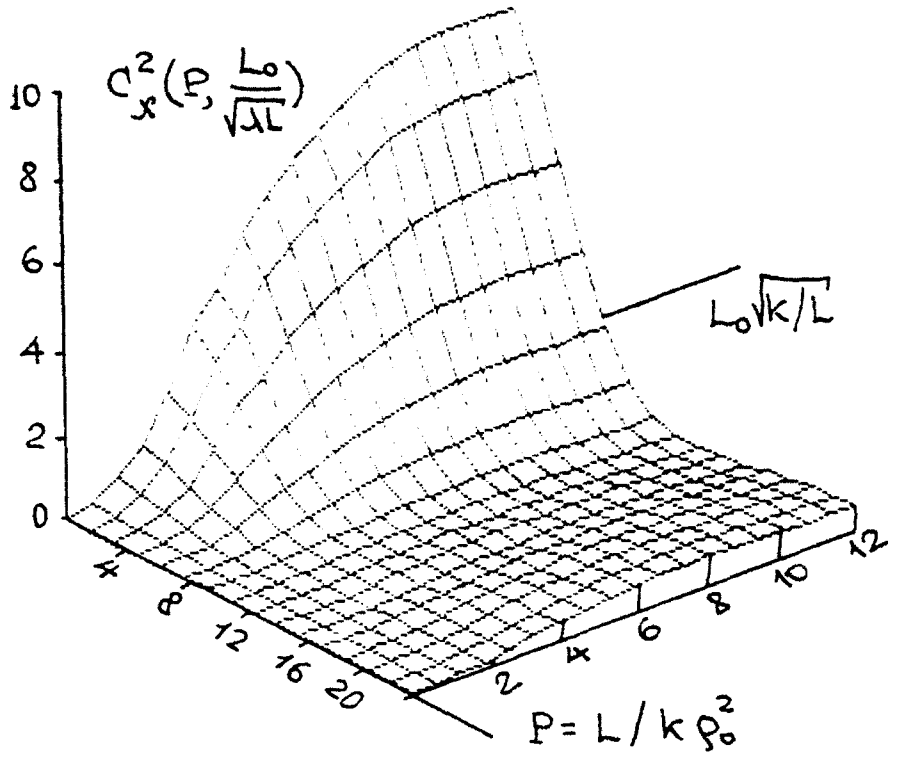

Fig. 1

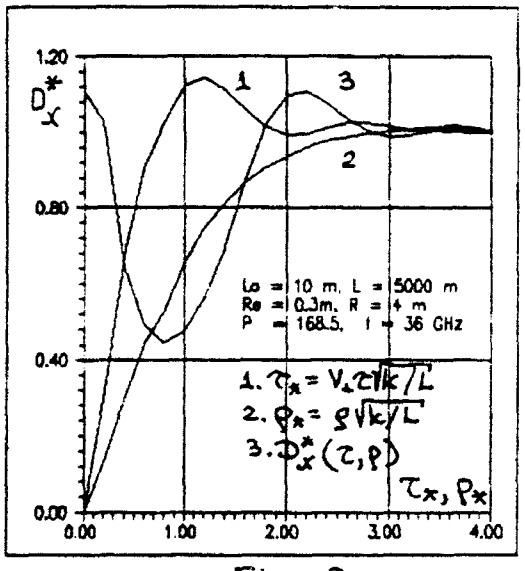

Fig. 2

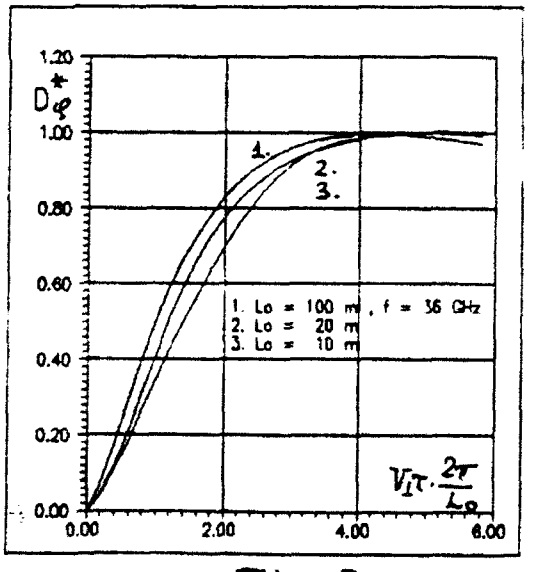

Fig. 3

References

1. Andreyev G.A. //Izv. VUZov SSSR. ser. Radiofizika, 1964, v.7,No 6.
2. Andreyev G.A., Ogarev S.A. //Radiotekchnika, 1988, No 11, pp. 45-47.
3. Andreyev G.A., Ogarev S.A. The coherence losses of MMW-field in turbulent atmosphere. Dig. of 1989 Internat.Symposium on EMC'89. Nagoya, Japan, 1989, vol.1, pp. 58-63.

SCANNING RADIOMETER AND ATMOSPHERIC ATTENUATION AT 3 MM WAVE BAND

Xu Peiyuan* Cao Yiting# Shen Huibo# Cao Yinlong*
(* Institute of Electron Physics, Shanghai University of Science and Technology, Shanghai, China 201800)
(# Purple Mountain Observatory, Academia Sinica, Nanjing, China 210008)

ABSTRACT

A scanning radiometer at 3 mm wave band is developed. A 90° offset parabolic reflector antenna system is mounted on an elevation-over-azimuth mounting to steer the antenna beam. The receiver is a total power type radiometer. This scanning radiometer is composed of all Chinese production. The solid state diode noise source as second calibration source is primarily calibrated by the cold and hot microwave absorbers at the feed horn aperature. The primary result of the atmospheric zenith total attenuation at 3 mm wave band is reported.

INTRODUCTION

In the early eighties a 3 mm wave band radiometer[1] with an 1.2 m equatorial mounting cassegrain antenna was developed as a small radiotelescope in China. But in its receiver some devices, such as the mixer, ferrite isolator and switcher were imported. In the early ninties, a scanning radiometer at 3 mm wave band is developed with all Chinese production for remote sensing application.

ANTENNA SYSTEM

A 90° offset parabolic reflector and a conical corrugated feed horn compose a scanning antenna system[2]. Its sidelobes are lower than -25 dB, its beam efficiencies are higher than 94% and its standing wave ratios are less than 1.22 at 90-100 GHz band. The receiver cabin which is rigidly connected with the feed horn and the reflector are set on an elevation- over-azimuth mounting. Because the offset angle is 90°, the elevation axis conincides with the axis of the feed horn. When the beam is steered in elevation, the feed horn and the receiver cabin have not to rotate along with. So this scanning antenna system has very good mechanical stability. The space for steering the beam elevation, just the rotating space of the 90° offset reflector itself, is more compact and the rotated load is more light than non-90° offset reflector antenna system. These distinguished performance are very important in some cases, such as airborne and space-borne.

RECEIVER SYSTEM

In the later half eighties a series of 3 mm wave band devices, such as GaAs Schottky diode mixer, Gunn oscillator, solid state diode noise source, ferrite isolator,circulator and switcher have been developed in China. As a first step a total power type radiometer receiver system has been developed with all Chinese production. A GaAs Schottky diode mixer, an adjustable local Gunn oscillator and an IF FET amplifier with 700 MHz bandwidth compose the front end of this receiver. The system noise figure is lower than 10 dB.

RECORD AND CALIBRATION

The radiometer output data are recorded on a strip chart recorder. A solid state diode noise source is used as second calibration source, which noise is coupled into the mixer by a directional coupler in LO waveguide branch. The noise temperature of this source is primarily calibrated at the feed horn aperture using the cold (liquid Nitrogen) and hot (environment) microwave absorbers. Then this calbrated noise source is as second calibration source to calibrate the antenna temperature of the observed object.

PRIMARY OBSERVATION OF ATMOSPHERIC ATTENUATION

Atmospheric remote sensing is one of the application of this scanning radiometer. The primary observation was carried on the flat roof of the Institute of Electron Physics in the night of Oct. 14, 1991. It was a clear night and the sky was free from cloud. After the calibration by the cold and hot microwave absorbers, the antenna beam was steered from the zenith to the horizon by each 10° step in elevation and the atmospheric brightness temperature was measured. The zenith atmospheric total attenuation τ(dB) is calculated by the following formula[3]:

$$\tau(\mathrm{dB}) = 4.343\ \mathrm{Ln}\left(\frac{T_m - T_b}{T_m - T_z}\right),$$

in which T_b is the cosmic background brightness temperature i.e. 2.7 K, T_m is the atmospheric mean radiating temperature. We calculated the T_m using Liebe's atmospheric absorption model[4] and the radiosonde data of the Shanghai Meteorological Observatory. The results show an usable relation

$$T_m(\mathrm{K}) = T_g - 12,$$

when the surface temperature is near 280 K. The measured zenith brightness temperature T_z was 66.4 K and the zenith atmospheric total attenuationwas 1.13 dB at that night.

REFERENCES

1. Huang Fuquan, 3rd National MM & SUBMM Wave Sym. Papers & Digests, p. 291, Shanghai, China, March 1986.
2. Xu Peiyuan et. al., Fifth National MM & SUBMM Wave Sym. Papers & Digests, p. 81, Qing Dao, China, May 1991.
3. Westwater E.R. et. al., IEEE Trans. AP-38(1990), 1569.
4. Liebe H.J., Int. J. of Infrared & Millimeter Waves 10(1989) 631.

T7.6

INVESTIGATION OF RAIN-INDUCED XPD BY USING DIFFERENTIAL ATTENUATION AT 30-100 GHz

Zhao, Zhenwei
(China Research Institute of Radiowave Propagation,
No.33 Fulongshan, Qingdao, China)

ABSTRACT

It is proved that the rain-induced differential attenuation (ΔA) is the dominating cause of rain-induced XPD at 30-100 GHz. The approximate relations of XPD to the differential attenuation are presented. The XPD values calculated by measured ΔA are compared to the values predicted by theoretical models, a high agreement is obtained.

1. INTRODUCTION

In order to make the frequency reuse system operate reliably, an adequate cross-polarization isolation between the orthogonally polarized channels must be maintained. So it is very important to research the rain-induced XPD and a lot of work in this respect has been done by many scholars.[2][3][4][5]

Based on rain-induced XPD theory, the relationship of XPD to the differential attenuation(ΔA) and differential phase shift($\Delta\phi$) are derived. The influence of $\Delta\phi$ to XPD value are examined, which demonstrate that ignoring the influence of $\Delta\phi$ in investigation of rain-induced XPD at 30-100 GHz is reasonable, thus, XPD can be determined by diferential attenuation and mean canting-angle of rain drops. Especiallly for circular polarization, XPD can just be determined by ΔA.

2. RAIN-INDUCED XPD OF HORIZONTAL AND VERTICAL POLARIZATION WAVE

Consider a linearly polarized plane wave incident in direction Z on a slab region of rain media as shown in Fig.1. a differential equation governing the variation of electric field Eh and Ev along propagation direction Z is written as [1]

$$d\vec{E}/dz=M\vec{E} \qquad (1)$$

the solution of (1) is

$$\vec{Er}=T\vec{Eo} \qquad (2)$$

Where E is a column vector with elements Eh and Ev, the elements of T are given by [1]

$$T11=\cos^2\phi\exp(\lambda_1 L)(1+G\tan^2\phi)$$

$$T12=T21=\cos^2\phi\exp(\lambda_1 L)(1-G)\tan\phi \qquad (3)$$

$$T22=\cos^2\phi\exp(\lambda_1 L)(G+\tan^2\phi)$$

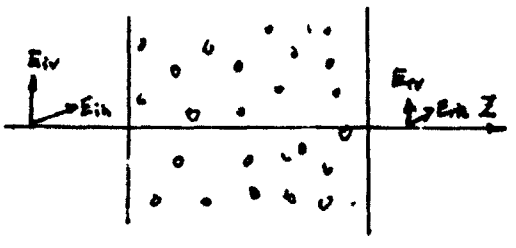

Fig.1 Geometry for Transmission through a Rain Media

and where

$$G=\exp(\lambda_2-\lambda_1)L \qquad (4)$$

Here λ_1 and λ_2 are eigenvalues of the matrix [M] and ϕ represents

$$XPD=-20\lg\left|\frac{\{1-\exp[j(k_1-k_2)L]\}\sin 2(\theta_0-\tau)\cos(\theta_0-\tau)}{\cos^2(\theta_0-\tau)+\exp[j(k_1-k_2)L]\sin^2(\theta_0-\tau)}\right| \quad (18)$$

where $j(K1-K2)L=jm(Kx-Ky)L=m\cos 2\tau(\Delta\psi+j\Delta\beta)$ (19)

Substituting (17) and (19) in (18), we get

$$XPD\doteq-20\lg\left|\left[(1-10^{\frac{\Delta A}{20}}e^{j\Delta\phi})tg(\theta_0-\tau)\right]/\left[(1+10^{\frac{\Delta A}{20}}e^{j\Delta\phi}tg^2(\theta_0-\tau)\right]\right| \quad (20)$$

For circular polarization, $\theta_0-\tau=45^\circ$, the rain-induced XPD is

$$XRDc\doteq 20\lg\left|(1+10^{\frac{\Delta A}{20}}e^{j\Delta\phi})/(1-10^{\frac{\Delta A}{20}}e^{j\Delta\phi})\right| \quad (21)$$

For horizontal and vertical polarization, based on $tg^2\theta_0 \ll 1$, (20) reduce to

$$XPDh=-10\lg\left|(1-10^{\frac{\Delta A}{20}})^2+4\cdot 10^{\frac{\Delta A}{20}}\cdot\sin^2\frac{\Delta\phi}{2}\right|\cdot tg^2\theta_0$$

$$XPDv=A+XPDh \quad (22)$$

Because $tg2\theta_0\doteq 2tg\theta_0/(1-tg^2\theta_0)\doteq 2tg\theta_0$ (23)
(23) and (10) are identical

4. THE CALCULATION OF RAIN-INDUCED XPD AT 30-100GHz

XPD are determined by ΔA and $\Delta\phi$. Reference [4] point out presumably that ΔA is dominating cause of rain-induced XPD above 30 GHz. In order to examine the influence of $\Delta\phi$ to XPD, ignoring $\Delta\phi$, the XPD errors (ΔXPD) of horizontal or vertical polarization is assumed as

$$\Delta XPD=\left|XPD_{h,v}(\Delta A,\Delta\phi)-XPD_{h,v}(\Delta A,\Delta\phi)|_{\Delta\phi=0}\right| \quad (24)$$

The rain attenuations and phase shift of horizontal and vertical polarization wave were calculated by Maggriori[5] in the 1-400 GHz for ellipsoidal rain drops, L-P rain drop size distribution, water temperature 20°C and constant rain drop canting-angle. Using Maggriori's results and based on (17), the eq(24) is calculated for 1.0 Km path length of uniform rain. The calculated ΔXPD is shown in Fig 2 (The calculations show that the values of σ and path length L have negligible influence to ΔXPD).

In most interesting rainfall range 12.5-50 mm/h, just as shown in Fig 2, ΔXPD is within 3 dB in 30-100 GHz ignoring differential phase shift, so it is reasonable to ignore rain-induced differential phase shift in investigation of rain-induced XPD at 30-100 GHz. In this case, eq(10), (20) and (30) are proximately

$$XPDh=-20\lg\left|(1-10^{\frac{\Delta A}{20}})tg2\theta_0/2\right| \quad (25)$$

$$XPDv=A+XPDh \quad (26)$$

$$XPD=-20\lg\left|\frac{(1-10^{\frac{\Delta A}{20}})tg(\theta_0-\tau)}{(1+10^{\frac{\Delta A}{20}}tg^2(\theta_0-\tau))}\right| \quad (27)$$

$$XPDc=20\lg\left|(1+10^{\frac{\Delta A}{20}})/(1-10^{\frac{\Delta A}{20}})\right| \quad (28)$$

where ΔA in dB.

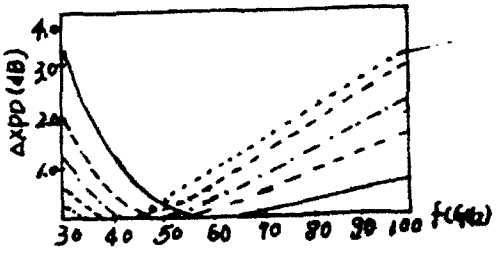

Fig 2 the ΔXPD induced by ignoring $\Delta\phi$

5. COMPARISIONS OF XPD VALUES CALCULATED BY MEASURED DIFFERENTIAL ATTENUATION DATA AND PREDICTED BY THEORETICAL MODELS

The measured differential attenuation data given by reference [6] at 30.9GHz is shown in Fig 3 where the sum attenuation is the attenuation of sum signal of horizontal and vertical, the points shown as crosses are averaged differential attenuation.

an effective canting-angle.

For the Gaussian canting-angle distribution of rain drops, there is [3][4]

$$\lambda_2-\lambda_1=-j(Kx-Ky)\exp(-2\sigma^2)\cos\xi=-j(Kx-Ky)m\cos\xi \tag{5}$$

where σ is the effective standard deviation of the canting-angle distribution, Kx and Ky are the propagation constants along the principle planes of the constant canting-angle model, ξ is the path elevation angle, for Gaussian canting-angle distribution of rain drops with mean θ_0, the effective canting-angle $\phi=\theta_0$.

Make $\phi=\theta_0$, we can get from (3)

$$T12=T21=(T11-T12)\,tg2\theta_0/2 \tag{6}$$

Assume that rain attenuation of horizontal and vertical polarization are Ah and Av respectively, then

$$T11=10^{-\frac{Ah}{20}}\exp(-j\phi_h) \tag{7}$$

$$T22=10^{-\frac{Av}{20}}\exp(-j\phi_v) \tag{8}$$

where ϕ_h and ϕ_v are phase shift of horizontal and vertical polarization through rain media. Rain-induced XPD of horizontal and vertical polarization can be obtained

$$XPDh=20\lg|T11/T12|=-20\lg|(1-T22/T11)tg2\theta_0/2|$$

$$XPDv=20\lg|T22/T21|=-20\lg|(1-T11/T22)tg2\theta_0/2| \tag{9}$$

Substituting (8) in (9), we can get

$$XPDh=-10\lg\left|\left[\left(1-10^{\frac{\Delta A}{20}}\right)+4\cdot10^{\frac{\Delta A}{20}}\cdot\sin^2\frac{\Delta\phi}{2}\right]tg^2 2\theta_0/4\right|$$

$$XPDv=A+XPDh \tag{10}$$

Where the differential attenuation $\Delta A=Ah-Av$

the differential phase shift $\Delta\phi=\phi_h-\phi_v$

3. RAIN-INDUCED XPD OF AN ARBITRARY POLARIZATION WAVE

(3) and (8) reduce to

$$10^{\frac{\Delta A}{20}}\exp(j\Delta\phi)=T22/T11=(G+tg^2\theta_0)/(1+Gtg^2\theta_0) \tag{11}$$

where

$$G=\exp(\lambda_2-\lambda_1)L=\exp[(\Delta\alpha+j\Delta\beta)m\cos\xi] \tag{12}$$

$$\Delta\alpha=-Im(Kx-Ky)L$$

$$\Delta\beta=Re(Kx-Ky)L \tag{13}$$

Thus

$$T22/T11=\frac{\exp[(\Delta\alpha+j\Delta\beta)m\cos^2\xi]+tg^2\theta_0}{1+\exp[(\Delta\alpha+j\Delta\beta)m\cos^2\xi]tg^2\theta_0} \tag{14}$$

Because $\Delta\alpha$ and $\Delta\beta$ are small arguments, G≈1, in general mean θ_0 is only a value of several degree i.e

$$tg^2\theta_0<<1 \tag{15}$$

then

$$10^{\frac{\Delta A}{20}}\exp(j\Delta\phi)\approx T22/T11\doteq\exp[(\Delta\alpha+j\Delta\beta)m\cos\ ] \tag{16}$$

thus

$$\Delta A\doteq20m\cos^2\xi\,\Delta\alpha\,tge$$

$$\Delta\phi=\Delta\beta\,m\cos \tag{17}$$

For a linearly polarization wave with polarization tilt angle τ ($\tau=0$ for horizontal polarization, $\pi/2$ for vertical polarization), the XFD is [3]

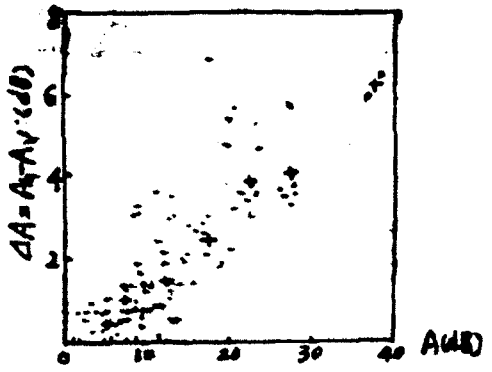

Fig 3 Measured differential attenuation to sum attenuation(A)

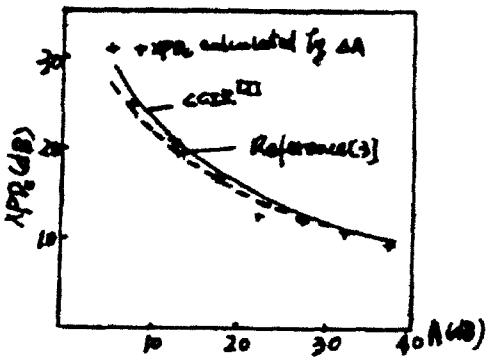

Fig 4 the XPD values calculated by measured ΔA and predicted by theoretical models

Using the measured averaged ΔA,based on eq(28) ,the calculated XPDc values and XPDc values predicted by CCIR model and model of reference[3] are shown in Fig 4. As shown inFig 4, the XPD values calculated by measured differential attenuation and by theoretical models have a good agreement.

6. CONCLUSION

The relationship of XPD to differential attenuation is derived approximately at 30-100 GHz. If the differential attenuation was measured, the XPDc would be determined. If differential attenuation and XPD for a certain polarization were measured,the mean canting angle would be derived and XPD values for any polarization would be calculated.so it is convenient for investigation of rain-induced XPD.

REFERENCE

[1] T.Oguchi,"Scattering properties of P-P form raindrops and cross-polarization due to rain calculation at 11,13,19.3 and 34.8GHz" Radio Sci Vol-12 No.1 1977 pp41-51

[2] R.L.olsen,"Cross polarization during precipitation on terrestrial links:A review " Radio Sci Vol-16 No.5 1981 pp760-779

[3] Zhao,zhenwei,"The two-order small argument approximation of rain-induced XPD theory and XPD prediction" Chinese J of radio sci Vol.5 No.3 1990 pp52-58 (in chinese)

[4] J.A.Morrison M.J.Cross and T.S.Chu,"Rain-induced differential attenuation and differential phase shift at microwave frequencies" B.S.T.J Vol-52 No.4 1973 pp599-640

[5] D.Maggiori,"Computed transmission through rain in the 1-400 GHz frequency range for spherical and elliptial drops and any polarization " Alta frequenza

[6] R.A.Semplak, "Effect of oblate raindrops on attenuation at 30.9 GHz" Radi Sci 5 March 1970 pp559-564

[7] CCIR, "Cross-polarization due to atmosphere" CCIR study Group Rep 722 XVth Plenary Assembly Vol v pp185-193 Int Telecommu Union, Geneva

T7.7

MEASUREMENT OF MILLIMETER WAVE SCINTILLATION ON A TERRESTRIAL PATH

Wu Zhizhuang ,Tan Yaqing
Qingdao Research Center Of China Research Institute Of Radiowave Propagation

ABSTRACT

In this paper, we introduce the experiment of measuring MMW scintillation on a terrestrial path in Qingdao from May to October, 1989. Under different weather conditions, the scintillation intensities and power spectra of three frequencies have been calculated . The calculation results have been discussed.

1.INTRODUCTION:

The atmosphere is turbulent medium. When millimeter wave propagate in the atmosphere, its amplitude and phase would fluctuate randomly. This is the scintillation phenomenon. Measuring and analysis the scintillation data may give a criterion for estimating the limit accuracy of the measuring system. On the other hand, as the scintillation was caused by the turbulence of atmosphere, it may set up some relations between the MMW scintillation and the atmosphere turbulence, and reverse the turbulent parameters of the atmosphere along the traveling path. In this paper,We introduce the experiment of measuring MMW scintillation on a multiple-frequency terrestrial path in Qingdao from May to October, 1989. Under different weather conditions, the scintillation intensities and power spectra of three frequencies have been calculated. The calculation results have been discussed.

2.MEASURING EQUIPMENTS AND DATA PROCESSING METHOD

The experiment of measuring MMW scintillation was completed on a terrestrial path with four frequencies ----12.0, 25.3, 33.5 and 72.0GHz. This system was established for the purpose of measuring the rain attenuation. The system characteristics can be seen in table 1. The transmitters are installed on Little-fish Mountain and the receivers are set on the top of Fulong Mountain. The lenth of the path is 1.26Km.

Table 1. Measuring system characteristics

frequency(GHz)	12.0	25.3	33.5	72.0
polarization	h	h	h	h
transmitting power(mW)	100	80	50	20
transmitter antenna gain(dB)	11.9	21.3	45.0	49.1
receiver antenna gain(dB)	40.5	49.1	19.1	49.1
fine day receiving power(dBm)	-81.5	-71.2	-82.1	-50.3
minimum receiving power(dBm)	-126.5	-125.0	-116.0	-107.0

When it's raining, the scintillation effect was drowned out by rain

attenuation, because the MMW signal aviation caused by scintillation is much smaller than by rain, so we did not measure scintillation in raining day. From May to October in 1989, we measured the scintillation 46 days, including fine days, cloudy days and foggy days. The measurement began at 8:30 and ended at 9:00 each day. The meteorological data on the ground were recorded at the same time.

The receiving signals were send to a computer through an A/D conversion interface and stored. The integrating time of the receivers are about 10ms. The computer sampling interval for store and record is 0.1s. When processing the data, we selected 0.2s as the sampling interval. Taking FFT method to calculated the power spectrum of the measuring data. Using 1024 points for each sample. The sample length is 204.8s.

The scintillation intensity was described by the logarithmic mean square error, σ^2_{lnI} ,it is defined by

$$\sigma^2_{lnI} = \langle (\ln I - \ln \langle I \rangle) \rangle$$

where I is instantaneous measuring data, $\langle \quad \rangle$ indicated to take the mean-value of time. The unit of measuring data is mV.

3. CALCULATION RESULT AND DISCUSSION

As 25.3GHz equipment got into trouble, it's measuring result could not analysis. So we only calculated the measuring data of 12, 33.5 and 72GHz. Select typical results of 3 days for discussion, they can represent basically the scintillation of find day, cloudy day and foggy day. Their meteorological data can be seen in table 2.

Table 2.Meteorological data on the ground

date (1989)	weather	P(mb)	T(c)	H(%)	Vw(m/s)	wind direction
July 31,08:31	fine	998.0	26.5	77	1.0	SE
Sep.24, 08:30	cloudy	1002.5	23.5	85	1.4	SE
Aug.11, 08:30	foggy	992.0	26.5	95	3.7	S

Figure 1 is the scintillation power spectrum measured in find day. It could be seen that MMW scintillation power spectrum is similar to the spectrum function of the atmosphere turbulence. With the assumption of homogeneous and isotropic, Kolmogrov gave the turbulence spectrum in inertial area as

$$\Phi_n(K) = 0.33 C_n^2 K^{-11/3} \qquad 2\pi/L_o < K < 2\pi/l_o$$

where $K=2\pi/l$ is the number of waves, l is the scale of turbulence, L_o and l_o is the outer and inner scale of turbulence respectively. C_n^2 is the structure constant of refractivity.

Assume that the MMW scintillation spectra can be approximate by a function as $Cf^{\quad}$, where f is scintillation frequency, C is a constant. It can be seen in figure 1 that the index n is became small as the signal frequency increase. That is, the higher the signal frequency is, the more important the high-frequency scintillation portion would be.

The scintillation intensity is indicated by the logarithmic mean square error . In figure 1 it can be seen that if the signal frequency is higher, its scintillation intensity is larger.

Figure 2 is the measuring results of cloudy day. It can come to a conclusion just as the same as find day, That is, if the signal frequency is higher, the high-frequency scintillation portion is more

important and the scintillation intensity is larger.

Compare figure 1 and figure 2, it could be seen that the index n is almost the same for a certain signal(for example 12GHz), but the scintillation intensity are different. The scintillation intensity in fine day is greater than in cloudy day. That could be explained by the layer structure stability of the atmosphere. Because the layer structure of atmosphere in the cloudy day is more stable than in fine day, the atmosphere turbulence in fine day is more intense than in cloudy day, accordingly, the MMW scintillation in fine day is more intense than in cloudy day.

Figure 3 is the measuring result in foggy day. It is obvious that the index n in figure 3 is greater than in figure 1 and 2. The scintillation intensity is also large. That could not explain by the stability of atmosphere. Because the layer structure of atmosphere is very stable in foggy day, otherwise it is impossible to form the fog. The recording of wind velocity is 3.7m/s. There are some inhomogeneous fog masses, their scales arrange from several meters to several hundred meters. They passed through the detecting path and made the water vapor distribution along the path changed continuously. This caused the measuring data flutter. As the fog massed passed through the path, it is slow change of the water vapor distribution, so the low-frequency scintillation in foggy day is important. The signal amplitude variation is quite large, it is contributed by the water vapor attenuation to the MMW. It's not merely the effect of the atmosphere turbulence.

REFERENCES

1.E.Vilar and J.Haddon " Measurement and Modeling of Scintillation Intensity to Estimate Turbulence Parameters on an Earth-space Path ",IEEE Trans.AP,Vol.AP-32 No.4 Apr.1984.

2.Huang Jie, " An Automatic Data Processing System For MMW Measurement ".Qingdao research center of China research institute of radiowave propagation.

3.Tan Yaqing," THe Power Spectrum Calculation of MMW Scintillation in Clear Sky " . Qingdao research center of China research institute of radiowave propagation.

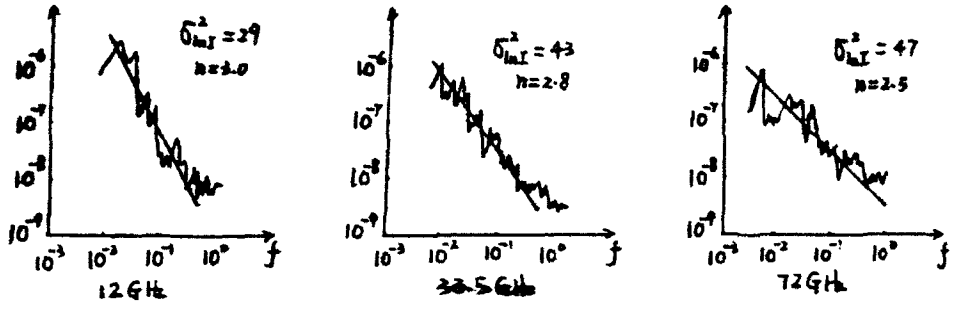

Fig. 1 Measuring result on July 31, 1989.

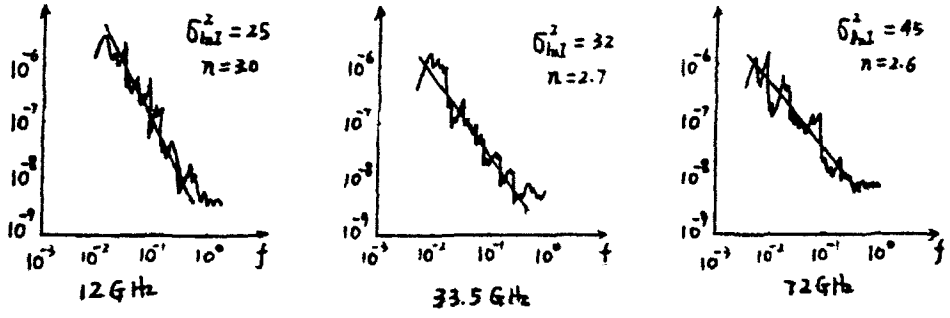

Fig. 2 Measuring result on Sep. 24, 1989.

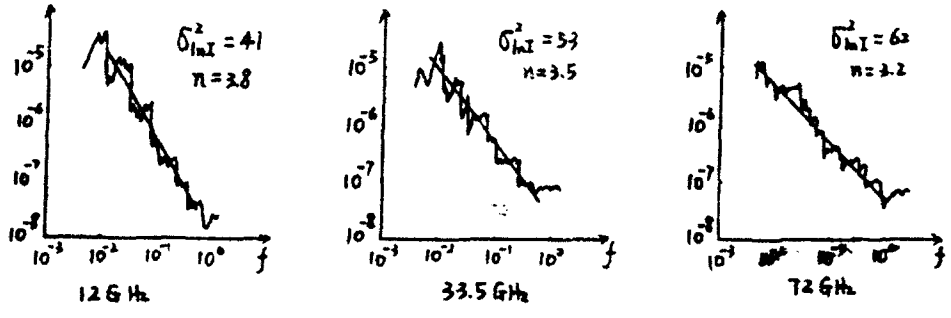

Fig. 3 Measuring result on Aug. 11, 1989.

T7.8

THE USE OF ATMOSPHERIC MOLECULAR EMISSION LINES FOR PASSIVE REMOTE SENSING OF THE EARTH SURFACE

A.A. Shvetsov

Institute of Applied Physics, Russian Academy of Science,
46, Uljanov Street, 603600, Nizhny Novgorod, Russia

Abstract

A novel method using atmospheric molecular line emission for millimeter and submillimeter wave remote sensing of terrain is developed. This method enables one to estimate emissivity and thermodynamic temperature of terrain by measuring brightness temperature of the earth at two frequencies belonging to an atmospheric line, and improve recognition of earth cover.

Brightness temperature is measured directly value by passive remote sensing. It is the result of adding the directly emitted radiation and scattered by rough surface atmospheric emission.

Brightness temperature of terrain in Rayleigh-Jeans approximation at the frequency ν can be written as

$$T_b(\nu,\vartheta,\phi)=\varepsilon(\nu,\vartheta,\phi)T_c+[1-\varepsilon(\nu,\vartheta,\phi)]\bar{T}(\nu,\vartheta,\phi), \qquad (1)$$

where ϑ and ϕ are zenith and azimuth view angles, respectively, T_c is thermodynamic temperature of emission layer of cover,

$$\bar{T}(\nu,\vartheta,\phi)=[1-\varepsilon(\nu,\vartheta,\phi)]^{-1}\int_0^{2\pi}d\phi'\int_0^{\pi/2}T_a(\nu,\vartheta',\phi')\rho(\nu,\vartheta,\phi,\vartheta',\phi')\cos\vartheta'\sin\vartheta'\,d\vartheta', \qquad (2)$$

-mean atmospheric brightness temperature averaged over scattering indicatrix, ϑ' and ϕ' - zenith and azimuth incident angles, respectively, $T_a(\nu,\vartheta',\phi')$ - the atmospheric brightness temperature, $\rho(\nu,\vartheta,\phi,\vartheta',\phi')$ - bidirectional spectral reflectivity of terrain.

There exists the following relationship between emissivity and bidirectional spectral reflectivity:

$$\varepsilon(\nu,\vartheta,\phi)=1-\int_0^{2\pi}d\phi'\int_0^{\pi/2}\rho(\nu,\vartheta',\phi',\vartheta,\phi)\cos\vartheta'\sin\vartheta'\,d\vartheta'. \qquad (3)$$

Integration in (2) and (3) is made along upper hemisphere. In

general case, $\varepsilon(\nu,\vartheta,\phi)$, $\rho(\nu,\vartheta,\phi,\vartheta',\phi')$ and $T_b(\nu,\vartheta,\phi)$ depend on polarization.

The value $T_b(\nu,\vartheta,\phi)$ is not a stable characteristic of cover in millimeter and submillimeter ranges owing to strong changeability of thermodynamic temperature of thin cover emission layer and to fluctuation of the atmospheric brightness temperature caused primarily by variations of cloud and atmospheric moisture content.

Moreover, a great deal of natural earth covers have emissivity close to unity, therefore variations of T_c and $\bar{T}(\nu,\vartheta,\phi)$ make approximately equal contribution to variability of $T_b(\nu,\vartheta,\phi)$.

Emissivity is a more stable cover characteristic in comparison with brightness temperature and can be used for classification of the cover. This value can be obtained solving equation (1), if $\bar{T}(\nu,\vartheta,\phi)$ and T_c are known. However, thermodynamic temperature value of terrain is usually unavailable by remote sensing. It leads to essential errors at estimation of terrain emissivity and to mistakes in recognition of different kinds of cover.

To overcome this difficulty, the dual-frequency measurement of terrain brightness temperature can be used.

There is a unique possibility to fulfil these measurements in the millimeter and submillimeter wave regions. There are many strong atmospheric emission lines of such molecules as H_2O, CO, O_2, O_3 et al. in the range of interest.

Moreover, most of covers have constant emissivity within the frequency range belonging to the same emission line. Hence, solving a set of two equations similar to (1) for the two experimental value $T_b(\nu_1,\vartheta,\phi)$, $T_b(\nu_2,\vartheta,\phi)$ and the corresponding values $\bar{T}(\nu_1,\vartheta,\phi)$, $\bar{T}(\nu_2,\vartheta,\phi)$, and $\varepsilon(\nu,\vartheta,\phi)=\varepsilon(\vartheta,\phi)$, one can obtain

$$\varepsilon(\vartheta,\phi) = 1 - \frac{T_b(\nu_1,\vartheta,\phi)-T_b(\nu_2,\vartheta,\phi)}{\bar{T}(\nu_1,\vartheta,\phi)-\bar{T}(\nu_2,\vartheta,\phi)} . \qquad (4)$$

$$T_c = \frac{T_b(\nu_1,\vartheta,\phi)\bar{T}(\nu_2,\vartheta,\phi)-T_b(\nu_2,\vartheta,\phi)\bar{T}(\nu_1,\vartheta,\phi)}{T_b(\nu_1,\vartheta,\phi)-T_b(\nu_2,\vartheta,\phi)-\bar{T}(\nu_1,\vartheta,\phi)+\bar{T}(\nu_2,\vartheta,\phi)} , \qquad (5)$$

Thus, such a remote sensing method make it possible to measure not only emissivity, but also the thermodynamic temperature of the emission layer, the latter being an important characteristic of earth cover too.

The values of $\bar{T}(\nu_1,\vartheta,\phi)$ and $\bar{T}(\nu_2,\vartheta,\phi)$ can be estimated from the formula (2) employing experimental or theoretical values of $T_a(\nu_1,\vartheta',\phi')$ and $T_a(\nu_2,\vartheta',\phi')$.

Fortunately, most of covers are diffuse scattering in millimeter and submillimeter wave bands, therefore the angular dependence of $\rho(\nu,\vartheta,\phi,\vartheta',\phi')$ can often be neglected. In this limit case of Lambert's cosine law the dependence $\bar{T}(\nu)$ calculated in the approximation of the plane-parallel isothermal atmosphere model can be expressed as [1]

$$\bar{T}(\nu) = T_o\{[1-2E_3[\tau(\nu)]] , \qquad (6)$$

where T_o - thermodynamic temperature of atmosphere, $\tau(\nu)$-zenith optical depth, and $E_3[\tau(\nu)]$ - integral exponential function.

In another extreme case of smooth surface when the reflection is specular $\bar{T}(\nu,\vartheta,\phi)=T_a(\nu,\vartheta,\phi+\pi)$.

However, information of the atmospheric brightness temperature is not necessary, if there is a reference surface, whose indicatrix is similar to that of the surface under investigation, and the emissivity $\varepsilon_o(\vartheta,\phi)$ is known and not equal to unity. In such a case the emissivity of the investigated surface can be estimated from the equation

$$\frac{1-\varepsilon(\vartheta,\phi)}{1-\varepsilon_o(\vartheta,\phi)} = \frac{T_b(\nu_1,\vartheta,\phi)-T_b(\nu_2,\vartheta,\phi)}{T_b^o(\nu_1,\vartheta,\phi)-T_b^o(\nu_2,\vartheta,\phi)} , \qquad (7)$$

where $T_b^o(\nu_1,\vartheta,\phi)$ and $T_b^o(\nu_2,\vartheta,\phi)$ - brightness temperatures of the reference surface at frequencies ν_1 and ν_2, respectively, measured under the same conditions as $T_b(\nu_1,\vartheta,\phi)$ and $T_b(\nu_2,\vartheta,\phi)$.

If the thermodynamic temperature of the reference surface T_c is also available, then as a result of brightness temperatures measurement, one can obtain

$$T_c = \frac{T_b(\nu_1,\vartheta,\phi)}{\varepsilon(\vartheta,\phi)} - \frac{[1-\varepsilon(\vartheta,\phi)][T_b^o(\nu_1,\vartheta,\phi)-T_b^o(\nu_2,\vartheta,\phi)]}{[1-\varepsilon_o(\vartheta,\phi)]\varepsilon(\vartheta,\phi)} , \qquad (8)$$

where $\varepsilon(\vartheta,\phi)$ has been obtained from the equation (7).

To estimate $\varepsilon(\vartheta,\phi)$ and T_c, most accurately it is necessary to choose the cover with large possible albedo $a(\vartheta,\phi)= 1-\varepsilon(\vartheta,\phi)$, as a reference surface. For this purpose can be used either an earth surface covered of deep snow layer, dry sand, vegetation, or water

surface.

To solve remote sensing problems which not require the absolute measurement of emissivity, but need only discrimination of different kinds of coves, one can use the difference $T_b(\nu_1,\vartheta,\phi)-T_b(\nu_2,\vartheta,\phi)$, independent of the thermodynamic temperature.

The above mentioned method can be used both in ground-based as well as by low altitude airborne investigations of raditiometric characteristics of terrain, if ground-airplane path attenuation is negligible.This method can be generalized to measurements through the atmospheric layer. However, in this case attenuation and emission of lower atmospheric layers have to be taken into account.

References

1.Паршин В.В.,Рыбушкин С.О.,Швецов А.А. О возможностях дистанционных измерений излучательной способности и термодинамической температуры земных покровов по их радиотепловому излучению в миллиметровом диапазоне. Межведомственное научно-техническое совещание "Статистические методы и системы обработки данных дистанционного зондирования окружающей среды". Тезисы докладов. 1989, Минск, стр.108.

2.Федосеев Л.И., Швецов А.А. К описанию радиотепловых контрастов.2-й Всесоюзный симпозиум по миллиметровым волнам. Тезисы докладов,1978, Харьков, ИРЭ АН УССР, т.2, стр.170.

T8.1

SOLITON SOLUTIONS OF PERIODIC AND NONPERIODIC INHOMOGENEOUS NONLINEAR KLEIN-GORDON EQUATIONS

F.K. Kneubühl and J. Feng
Infrared Physics Laboratory
Swiss Federal Institute of Technology (ETH), CH-8093 Zurich, Switzerland
Tel. (1) 377 23 40, Fax: (1) 377 59 89

Solitary waves and solitons represent an important stable state of nonlinear systems in many fields of applied mathematics and physics such as fluid dynamics, elementary particle physics and laser science. In laser physics solitons are studied and applied mainly in infrared optical fibres and waveguides. The soliton regime of pulse transmission in single-mode optical fibres permits drastic improvement of data transmission over large distances. Research on solitons is concentrated on solitons and solitary waves in homogeneous media whilst the study of solitons in periodic or otherwise inhomogeneous media started only recently. This already resulted in remarkable results, e.g. in the phenomenon of in-gap solitons [1]. Our interest in solitons in periodic or otherwise inhomogenous media is related to applications in fibre optics as well as to the theory of pulsed distributed-feedback (DFB) and distributed-Bragg-reflector (DBR) lasers.

In this study we focus our attention to the solitons and solitary-wave solutions of periodic or otherwise inhomogeneous nonlinear modifications of the well-known one-dimensional Klein-Gordon equation which have been rarely investigated [2]. These modified Klein-Gordon equations can be represented by

$$u_{xx} - n(x)^2 c^{-2} u_{tt} = k_c^2 \mu(x) \cdot \frac{d\Phi(u)}{du} \qquad (1)$$

where k_c indicates the Compton circular wavenumber, c the velocity of light in vacuum, n(x) the spatially varying refractive index and

$$\Phi = \Phi(u, x) = \mu(x)\, \Phi(u) \qquad (2)$$

the potential. The factor $\mu(x)$ defines its spatial variation. The standard Klein-Gordon equation is given by the conditions

$$n(x) = \mu(x) = 1; \qquad \Phi(u) = \frac{1}{2} u^2 \tag{3}$$

Up to the present we have found a number of analytical soliton and solitary-wave solutions for typical modulations of $n(x)$ and $\Phi(x, u)$, including linear, almost quadratic, hyperbolic and periodic refractive index modulations as well as sech - square and periodic modulations $\mu(x)$ of non-quadratic potentials $\Phi(u)$. Among the results we find kink solitons, kink-antikink solitons, solitary waves, quasi-Floquet solutions, perturbations over classical solutions, as well as relations to in-gap and out-gap solitons.

References:

[1] W.Chen and D.L. Mills:
Phys. Rev. Lett. 58, 160 (1987)

[2] e.g. F.K. Kneubühl and J. Feng:
Chinese Journal of Infrared Research (10th anniversary, invited paper),
in Chinese and in English, (1992), in print

T8.2

COMPLEX PERMITIVITY(ε) AND PERMEABILITY(μ) MEASUREMENTS AT MILLIMETER WAVELENGTHS

Jian kun-hua Chen zhong Li shi-zhi
(Beijing Institute of Technolongy)

ABSTRACT

A Complex Permitivity and Permeability measurement system is discussed in this paper. Free space wave method has been used to measure the parameters (ε μ) of loss dielectric and magnetic materials at millimeter wavelength. POWELL method and penalty function are used to solve the mutiple value problems. Testing results of some typical materials and testing accuracy of the system are shown in this paper.

INTRODUCTION

1.Measurement method of 8 mm wave band absorb material parameters.
A Free space wave method (FSWM) has been used to measure the absorb material parameters at millimeter wavelengths in this paper. Many new technical ways have been derived in this measurement system. For exanple, terminal short circuit method; Double-short end method, etc. A absorb material plate is fixed in the free space, its thickness is d, as shown in Fig 1. The reflect coefficient and transmit coefficient shown as follows.

$$R_o = \frac{R_{12}-R_{23}e^{-j2\psi}}{1+R_{12}R_{23}e^{-j2\psi}} \qquad (1)$$

$$T = \frac{(1-R_{12}^2)e^{-j\psi}}{1-R_{12}^2e^{-j\psi}} \qquad (2)$$

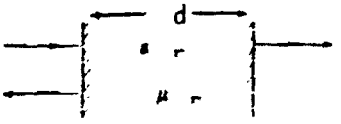

Fig 1

where $R_{12}=\frac{\sqrt{\mu_r/\varepsilon_r}-1}{\sqrt{\mu_r/\varepsilon_r}+1}=-R_{23}$

$\psi = 2\pi d\sqrt{\mu_r\varepsilon_r}/\lambda_0$

If we use metallic plate of short circuit instead of the third region in Fig 1. We get:

$$Rc=\frac{R_{12}-e^{-j2\psi}}{1-R_{21}^2e^{-j2\psi}} \qquad (3)$$

We can derive several equations to calculate ε_r and μ_r from Eq. (1) and (3), For example, By short-open end method we derived formula as follows:

$$C_1=\sqrt{\mu_r/\varepsilon_r}=\pm\left[\frac{RcRo+Rc+Ro+1}{RcRo-3Ro+1}\right]^{1/2} \qquad (4)$$

$$C_2=\sqrt{\mu_r\varepsilon_r}=-[-(y-2n\pi)+j\ln A]+\frac{\lambda_0}{4\pi d} \qquad (5)$$

where $Y=\arg\left(\frac{R_{12}-Rc}{1-R_{12}Rc}\right)$; $A=\left|\frac{R_{12}-Rc}{R_{12}Rc}\right|$

from Eq. (4) and (5), we get

$$\mu_r=C_1 C_2 \quad ; \qquad \varepsilon_r=C_2 / C_1 \tag{6}$$

where C_1 is taken plus or minus sign from $|R_{12}|<1$

In Eq. (5), becuase n can take arbitrary integer values, it makes $\sqrt{\mu_r \varepsilon_r}$ multiple roots. we can use the thinner sheet to increase the distance of the roots.

a.a. Measurement of the dielectric material

For $\mu_r=1$ dielectric material the above computation is still effective, and only one test is needed for ε_r, from (3) we get:

$$\sqrt{\varepsilon_r}=-j\frac{\lambda_o}{2\pi d}T e^{-j\tau} \tag{7}$$

Where, T and τ are solution of equation

$$-j\frac{1+Rc}{1-Rc}\cdot\frac{\lambda_o}{2\pi d}=\frac{th(T e^{j\tau})}{T e^{j\tau}} \tag{8}$$

It is called terminal short circuit end method.

b. Measurement of the plastic model and rubber type magnetic material. We can use double short-circuit end method to measure this kinds of materials. We measure one kind of material which has different thickness, the reflective coefficients of two diffrent tests are:

$$R_{1a}=\frac{R_{121}-e^{-j\psi_1}}{1-R_{121}e^{-j2\psi_1}} \tag{9}$$

$$R_{2a}=\frac{R_{122}-e^{-j\psi_2}}{1-R_{122}e^{-j2\psi_2}} \tag{10}$$

where, $\psi_1=2\pi d_1\sqrt{\varepsilon_r\mu_r}/\lambda_o$, $\psi_2=2\pi d_2\sqrt{\mu_r\varepsilon_r}/\lambda_o$

Eq. (9) and (10) can be considered as the transcendental equation of complex variable quantities. We take the POWELL method of multiple variable (optimizing) numerical solution and adopte penalty function method and transform correlated optimizum problem to uncorrelated one to solve limited problem, the process is shown as follows:

a) To establish target function

$$f(x)=\sum_{i=1}^{n}[fi(x)]^2 \tag{11}$$

where $f(x)=Re[Rj-Rm]$, or $Im[Rj-Rm]$.

$j=1,2$, x is self variable vector.

$x=\{\varepsilon_r', \varepsilon_r'', \mu_r', \mu_r''\}$

b) Penalty function.

$$T(x, m)=f(x)+M\sum_{k=1}^{n}\{\min[0, gk(x)]\}^2 \tag{12}$$

where gk (x) is ε_r, μ_r and R_{12} physical correlated condition or subband bound correlated condition. For instance, $\varepsilon_r''>0$, $1<\varepsilon_r'<5$, etc, M is penalty factor, it's selected in tested program, for example. M=5 or M=10 etc.

c) POWELL method is used to solve uncorrelated limitation value problem:

$$\min_{x \in R^n} T(x, M) \tag{13}$$

It is the optimum solution for ε_r and μ_r values.

2. The measurement system is shown in Fig 2. It can carry out the dot frequency test of the material's complex ε and μ and the reflective coefficient at (26.5~40) GHz.

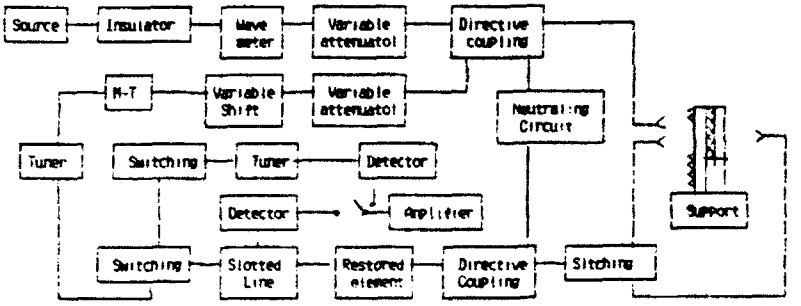

Fig 2

a. Principle of this system.

High freguency instead method is used in the balancing bridge system. The reflection and transmition coefficient of the measured material sheet can be achived according to the following equations:

$$R=\exp\left[-\frac{A_1-A_1'}{8.686}j(180^\circ+\varphi_1-\varphi_1')\right] \tag{14}$$

$$T=\exp\left[-\frac{A_2-A_2'}{8.686}j(180^\circ+\varphi_1-\varphi_2')\right] \tag{15}$$

where, A_i, φ_i (i=1.2) are amplitude and phase datas of metallic sheet; A_i', φ_i' (i=1, 2) are material sheet datas when the system is in the balance situation.

b. Four steps are used to increase the accuracy of this system.

(1)High stability signal source and high accuracy restored elements are used in this system.

(2)Equal-armed bridge is used to decrease phase error which caused by frequency moving of signal source. System's phase error $\Delta\varphi < 0.3^\circ$.

(3)Neutraling circuit is adopted to reduce the effect of antenna coupling and background scattering. Interference level can be reduced to -50 dB below comparing with metallic sheet.

(4)Window specimen support is used ,high quality absorbing material is used to reduce the edge diffraction effect of specimen.

It shows that the testing accuracy is greatly increased when all of the steps are taken.

RESULTS AND ANALYSIS

A lot of tests and analyses have been done in this system. Some datas of testing results were shown in table 1. It shows that it has good agreement between testing results and typeical material datas.

Higher testing accuracy of mesuring middle or large loss absorber has achieved by using this method. The accuracy of this system are shown as follows:

$$(\Delta\varepsilon_r', \Delta\varepsilon_r'') < \varepsilon_r' \times 10\%$$

$$(\Delta\mu_r', \Delta\mu_r'') < \mu_r' \times 10\%$$

Tabel 1.

f(GHz)	27	33	39
Teflon	ε_r=2.079-j0.0171	ε_r=2.091-j0.015	ε_r=2.066-j0.0058
Polystyrene	ε_r=2.573-j0.013	ε_r=2.596-j0.017	ε_r=2.592-j0.019
Brackrubber	ε_r=8.338-j0.637	ε_r=8.400-j0.660	ε_r=8.342-j0.594
Absorber	ε_r=29.60-j25.53	ε_r=27.34-j25.27	ε_r=25.29-j24.06
Magnetic material	ε_r=6.669-j1.316 μ_r=0.813-j0.168	ε_r=6.714-j1.328 μ_r=0.798-j0.024	ε_r=6.267-j1.426 μ_r=0.828-j0.011
Magnetic rubber	ε_r=14.97-j1.427 μ_r=0.828-j0.393	ε_r=14.47-j0.646 μ_r=0.801-j0.346	ε_r=14.70-j0.281 μ_r=0.769-j0.272

REFERENCES

1. C.k.Campdell, Senior Member, Free-Space permittivity Measurements on Dielectric Materials at Millimeter Wavelengths, IEEE TRANSACTIONS ON INSTRUMENTATION AND MEASUREMENT. VOL. IM-27, NO.1, MARCH 1978.
2. John C. Joseth,Multiple Angle of Incidence Measurement Technique for the Permittivity and Permeablility of Lossy Materials at Millimetter Wavelengths, USAF, AFIT/GE/ENG/86D-58.

T8.3

INTERNAL MATCHING BROADBAND METHOD OF MILLIMETER WAVEGUIDE CIRCULATOR

Zhang Deng guo
(Southwest Jiaotong University,
Chengdu, Sichuan, P.R.China)

ABSTRACT

The internal matching broadband method of millimeter waveguide circulator is presented in this short paper, which have explained the bandbroadening attempts in literatures and also directed our successful developments of MMW waveguide circulator.

INTRODUCTION

In order to obtain broadband circulator, a quarterwave step transformer is often used in the waveguide junction. That is the well known external matching broadband method of waveguide circulator, the transformer can be a circular (triangular, hexagonal, Y-shape and so on) pedestal, or even a dielectric sleeve.

The internal matching broadband method is not the one based on a quarterwave step transformer. There are many means of so called internal matching broadband method, such as the lowest mode & shortest path length and the optimum height of the junction & place of the ferrite.

THE LOWEST MODE AND SHORTEST PATH LENGTH

It is known from the general theory of the scattering matrix that the bandwidth of a circulator is based on the identity of the rate of change of phase of the three eigen-values with frequency. Employing the lowest possible mode and shortest associated path length implies broadband. The exact operation modes of partial height ferrite H-plane waveguide circulator are HE_{11n+q} (n=0,1,2,...; q≠1/2) hybrid modes [1], and the height of the ferrite cylinder h is in proportion to n + q. Both of the 8-mm and 3-mm waveguide circulator [2] [3] in the lowest modes HE_{11q} have the most broad bandwidth.

THE OPTIMUM HEIGHT OF THE JUNCTION & PLACE OF THE FERRITE

The ferrite of the E-plane waveguide Y-junction circulator is a circular disk. The equivalent circuit of the resonance frequency splits for the rotational phase eigen-excitations is shown in Fig.1, thus

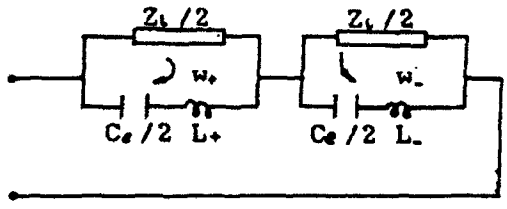

Fig.1 Equivalent circuit of the E-plane waveguide circulator

$$\frac{1}{w_-^2} - \frac{1}{w_+^2} = \frac{2\sqrt{3}\, C_e Z_t}{w_0} \qquad (1)$$

where $w_0 = (w_+ + w_-)/2$

$L_\pm = (u \mp k) L$

It is clear from (1) that in order to increase the bandwidth of the circulator, either the line impedances Z_t of the waveguide arms must be increased, i.e., the width of the waveguide must be decreased [4] [5] ; or the impedance slope parameter of the resonant circuit must be decreased, i.e., the coupling of waveguide and resonator fields , represented by C_e , must be increased [4] [6] .

REFERENCES

[1] Dengguo Zhang, Zhengde Wu, "New investigation of operation modes of H-plane waveguide circulator", Proceeding of the second Asia-Pacific M. C, pp.550, Oct. 1988.

[2] Dengguo Zhang, Zhengde Wu, "Development of a broadband 3-mm PHF H-plane waveguide circulator",The 13th Int. J. of In/MMW,Hawaii, U.S.A, Dec. 1988.

[3] Piotroski W. S, "Low loss broadband EHF circulator", IEEE Trans. MTT-26, pp.863-866, Nov. 1976.

[4] Solbach K., "E-plane circulator aid mm-wave design", Microwave & RF, pp.73-78, Dec 1983.

[5] Geobel U., et al., "Broadband fin-line circulators", 1982 IEEE MTT-S Digest, pp.249-252.

[6] Solbach K., "Equivalent circuit representation for the E-plane circulator", IEEE Trans. MTT-32, pp.806-809, May,1982.

T8.4

SOLITONS IN PERIODIC STRUCTURES WITH KERR-NONLINEARITY

J. Feng and F. K. Kneubühl

Infrared Physics Laboratory
Swiss Federal Institute of Technology (ETH), CH-8093 Zurich, Switzerland
Tel. (1) 377 23 40 Fax (1) 371 59 89

A Kerr medium embedded in a periodic structure exhibits a large variety of interesting features, such as bistability, self-pulsing and chaos, gap solitons and solitary waves. It was found recently, that an intense optical trains can penetrate undistorted through a distributed feedback reflection filter, in spite of the fact that their carrier frequency lies well within a forbidden band of the periodic structure [1-4]. In this work we extend the discussion of such "in-gap" solitary waves to the solitary waves whose carrier frequency of the optical waves may lies far outside the forbidden frequency gap.

The one-dimensional periodic medium under study has the linear refractive index

$$n_{lin}(z) = n_0 + n_1 \cos(2k_B z) \quad (0 < n_1 << n_0)$$

and the nonlinear susceptibility

$$\chi_{nonlin} = n_0 n_2 |E|^2 \ .$$

Our study bases on the nonlinear coupled-mode equation

$$\begin{cases} \frac{\partial E_f}{\partial z} + \frac{n_0}{c}\frac{\partial E_f}{\partial t} = i\Delta k E_f + i\kappa E_b + i\alpha\left(|E_f|^2 + 2|E_b|^2\right) E_f \\ \frac{\partial E_b}{\partial z} - \frac{n_0}{c}\frac{\partial E_b}{\partial t} = -i\Delta k E_b - i\kappa E_f - i\alpha\left(2|E_f|^2 + |E_b|^2\right) E_b \end{cases}$$

where $E_{f,b}$ are components of the total field

$$E(z,t) = E_f(z,t)\exp[-i\omega t + ik_B z] + E_b(z,t)\exp[-i\omega t - ik_B z] \ ,$$

$\kappa \approx \frac{1}{2}k_0 n_1/n_2 > 0$ is the coupling constant, $\Delta k \approx (\omega - \omega_B) n_0/c$

describes the frequency detuning in units of wave vector, $\alpha \approx \frac{1}{2}k_0 n_2/n_0$ is a measure for the nonlinearity.

The usual "in-gap" soliton can be found using the boundary condition $\lim_{\substack{z\to\infty \\ t \text{ fixed}}} E_{f,b}(z,t)=0$.

However a wave with carrier frequency outside forbidden frequency gap in general does not satisfy this boundary condition. We have shown that under the boundary condition

$$\lim_{\substack{z\to\infty \\ t \text{ fixed}}} |E_b(z,t)| = \text{const} \neq 0 \ , \quad \lim_{\substack{z\to\infty \\ t \text{ fixed}}} \frac{d|E_b(z,t)|}{dz} = 0 \ ,$$

solitary solutions exist.

In contrast to the known "in-gap solitons", the new solitary solutions have their carrier frequency mainly outside the frequency gap of the periodic structure, so we refer them as "out-gap soliton".

They possess some interesting properties: two solitary solutions, the "bright soliton" and the "dark soliton", may exist for the same boundary conditions; for the same "forward" background field intensities $\lim_{z\to\infty}|E_f(z,t)|^2$ and same other parameters, two "backward" intensities $\lim_{z\to\infty}|E_b(z,t)|^2$, which allow solitary solutions, may exist; solitary waves with velocity larger than the speed of light also exist, at least mathematically.

[1] W.Chen, D.L.Mills:
Phys.Rev.Lett.58, 160-163 (1987)

[2] D.N.Christodoulides, R.I.Joseph:
Phys.Rev.Lett. 62, 1746-1749 (1989)

[3] A.B.Aceves, S.Wabnitz:
Phys.Lett. A 141, 37-42 (1989)

[4] J.E.Sipe, H.G.Winful:
Opt.Lett. 13, 132-133 (1988)

T8.5

Ka-BAND NRD GUIDE POWER DIVIDER

Mingli Zhu
(Huazhong University of Science and Technology
Wuhan, 430074, Hubei, China)

ABSTRACT

In this paper, the characteristic of the coupling NRD guide is analysed, and a kind of NRD guide power divider in coupler style is designed in Ka band. The power divider is made up with a nonsymmetric NRD guide coupler which the transiter of the isolation port is cut off and a model matching load is sticken on the end dielectric strip of the isolation port. Because it possesses simple structure, small size and good performance, it would have great use value.

INTRODUCTION

Generally, the nonradiative dielectric waveguide (NRD guide) power divider can be constituted with Y-style junctor and branch line. But the performance of the isolation between two output ports in Y junction power divider is very poor, it usually be lower than 10 dB. After absorbing materials being sticken on the suitable places of the output ports, the isolating degree would be increased, but the insertion loss would also be greatly increased simultaneously. Although the performance of isolating of the branch line divider is relatively good, the bandwidth is very narrow. Its bandwidth could be increased by using multi-order division, but the total size would be very large. In this paper, a kind of NRD guide power divider in coupler style is designed on the base of analysing the characteristic of coupling NRD guides, it could utilize the good performance of a coupler and a satisfied result would be obtained.

ANALYSIS OF THE COUPLING NRD GUIDE

The structure of coupling NRD guides is shown in Fig. 1. The coupling between two dielectric waveguides occurs through vanishing fields. Its characteristic equations can be easily obtained by the even-odd mode method because of the symmetric structure about the YOZ plane as

$$\frac{\varepsilon_r \alpha_1^o}{\alpha_2^o}\left[1-\frac{\varepsilon_r \alpha_3^o}{\alpha_2^o}\,tg(\alpha_2^o a)\right]th(\alpha_1^o \frac{d}{2})+\left[\frac{\varepsilon_r \alpha_3^o}{\alpha_2^o}-tg(\alpha_2^o a)\right]=0$$

$$\frac{\varepsilon_r \alpha_1^e}{\alpha_2^e}\left[1-\frac{\varepsilon_r \alpha_3^e}{\alpha_2^e}\,tg(\alpha_2^e a)\right]cth(\alpha_1^e \frac{d}{2})+\left[\frac{\varepsilon_r \alpha_1^e}{\alpha_2^e}-tg(\alpha_2^e a)\right]=0 \qquad (1)$$

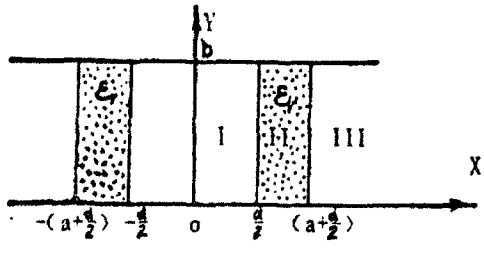

Fig. 1 The coupling NRD guide

The propagating constants are determained by

$$\beta^e = [\varepsilon_r k_0^2 - (\alpha_1^e)^2 - (\pi/b)^2]^{\frac{1}{2}}$$
$$\beta^o = [\varepsilon_r k_0^2 - (\alpha_1^o)^2 - (\pi/b)^2]^{\frac{1}{2}} \quad (2)$$

where α_i is the wavenumber along the x direction in the region of i. $k_0^2 = \omega^2 \varepsilon_0 \mu_0$. The coupling coefficient of the coupler is

$$K = \frac{1}{2}(\beta^o - \beta^e) \quad (3)$$

The coupling degree of the symmetric directional coupler shown in Fig.2 is obtained by the network method as

$$C = -10 \lg|(\sin K l_e)| \quad (4)$$

where l_e is the equivalent coupling length.

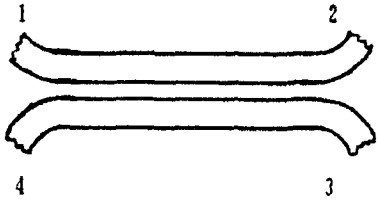

Fig. 2 The symmetric NRD guide directional coupler

The NRD guide power divider is made up with a directional coupler which the transiter of the isolating port is cut off and the absorbing material is sticken on its end dielectric strip. The methods of analysis and computation of a coupler can apply to the divider after the coupling length being revised.

Because of the same propagating constants in the two dielectric guides, power can be transfered from one waveguide to the another if the coupling length is long enough when the structure is completely symmetric. The coupling length greatly depends upon the operating frequency, and modes possess dispersion characteristic, so the bandwidth is very narrow. But the bandwidth could be increased by using nonsymmetric structure because of the different propagating constants of the two dielectric waveguides. The coupling characteristic of the nonsymmetric coupling slab guide is shown in Fig. 3. It can be found that the maximum coupling power decreases and the

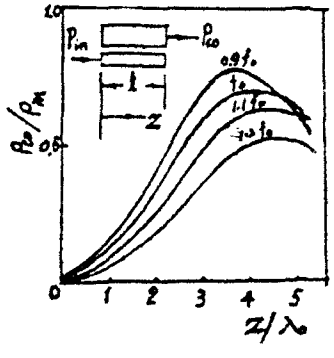

Fig. 3 The characteristics of the nonsymmetric coupling slab-guide

maximum coupling point moves to the end of the coupler while the frequency ascending.

These usually limit the bandwidth of the coupler. It is notable that the coupling power would be returned to the first one while the coupling length adding after the maximum power transfersion occuring. So we can utilize the effect to increasing the bandwidth of the coupler.

DESIGN AND MEASUREMENT OF THE POWER DIVIDER

The practical structure of the power divider is shown in Fig.4. According to the transimission characteristic of NRD guide, the single mode operating bandwidth would be relatively broad if the ratio of the dielectric strip's width and heigth a/b is 1. In Ka band, we can use Teflon (ε_r =2.05) and make a = b =4.0 mm. In order to

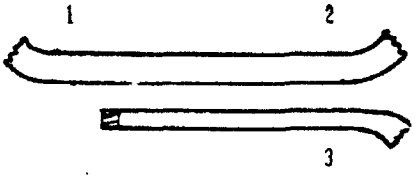

Fig. 4 The NRD guide power divider

obtain broad bandwidth of the power divider, the widths of the two dielectric waveguides should be different. First of all, more than half of the power is coupled into the second waveguide from the first one at the lower frequency by choosing the suitable waveguide dimensions and the coupling distance. Then, adjust the coupling length to return the overdose coupled power to the first one. So the coupling degree could be reduced to 3 dB at higher frequency. The measured results show that the relative bandwidth would be more than 3% while the value of a is in the region of 3.58 mm to 3.74mm. The high impedance of the absorbing material which is sticken on the end dielectric strip must match with the characteristic impedance of the dielectric waveguide to obtain great isolation of the two isolating ports. The measured results are shown in Fig. 5. The

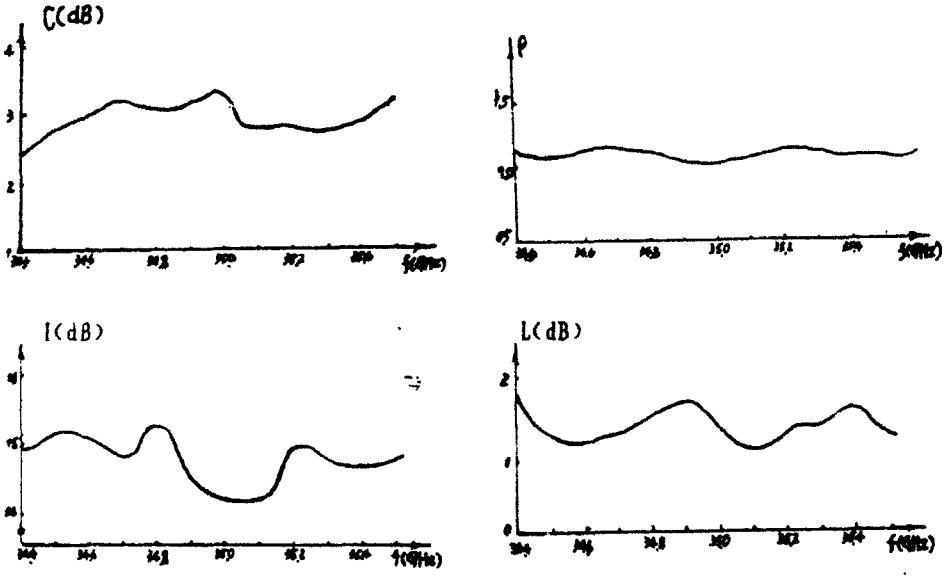

Fig. 5 The characteristics of the NRD guide power divider

performance of the divider within the 3% relative bandwidth are

power division: $C = 10 \lg (P_2 + P_3) / P_1 = 3 + 0.4$ (dB)

inserting loss: $L = 10 \lg P_1 / (P_2 + P_3) < 1.9$ (dB)

isolating degree: $I = 10 \lg P_2 / P_3 > 14$ (dB)

VSWR.: $\rho < 1.3$

REFERENCES:

1. T. Yoneyama et al., IEEE Trans., MTT-29, Nov., 1981.
2. T. Yoneyama et al., IEEE Trans., MTT-31, Aug., 1983.
3. P. K. Ikalainen et al., IEEE Trans., MTT-35, No.7, 1987.

T8.6

NRD WAVEGUIDE LSE MODE EXCITER

Hong Ma, Lanfen Qi
(Huazhong University of Science and Technology
Wuhan, 430074, Hubei, China)

ABSTRACT

In this paper, the operating principle of a LSE_{11}^{e} mode exciter from LSM_{11}^{e} mode in nonradiative dielectric waveguide (NRD guide) is analysed. Then the LSM_{11}^{e} -LSE_{11}^{e} mode converter has been designed and fabricated in Ka band. The calculated and measured results all show that the converter possesses the advantages of high convertion efficiency and broad bandwidth. It would be very useful to NRD guide balanced mixer and the integrated front ends.

INTRODUCTION

Because nonradiative dielectric waveguide (NRD guide) possesses the characteristics of almost completely suppressing radiation at bends and discontinuities and conduction loss decreasing when operating frequency increasing within a given range of frequency, it is suitable for being used as transimission line to compose millimeter-wave integrated front ends. Previously, a 3 dB NRD guide directional coupler had been used in the balanced mixer of the front-end circuits [1]. But the size of the 3 dB NRD guide coupler is quitely large , the output symmetry and the bandwidth characteristic are not easy to be obtained. These factors directly limit the improvement of the performance of the mixer. If the LSM_{11}^{e}-LSE_{11}^{e} mode converter presented in this paper and the crossbar structure are adopted in the balanced mixer, the design and adjustment would be simplified and the structure of the mixer would be compacted. The performance of the NRD guide circuits will be improved.

ANALYSIS OF THE LSE_{11}^{e} MODES EXCITER

All kinds of transimission modes in NRD guide can be classified as two types, longitudinal-section magnetic modes (LSM modes) and longitudinal-section electric modes (LSE modes). The field lines of some lower order modes in NRD guide are shown in Fig. 1. The dispersion characteristics of TE_{10}^{e}, LSE_{11}^{e} and LSM_{11}^{e} modes are shown in Fig. 2. Generally , LSM_{11}^{e} mode, the lowest LSM mode, is chosen as the operating mode in NRD guide because of its low transimission loss. But TE_{10}^{e} mode and LSE_{11}^{e} mode can also be propagated in the condition of same structure parameters of the NRD guide. When the exciting electric field possesses the components along the x- and y- direction, LSM and LSE modes will be excited out respectively.

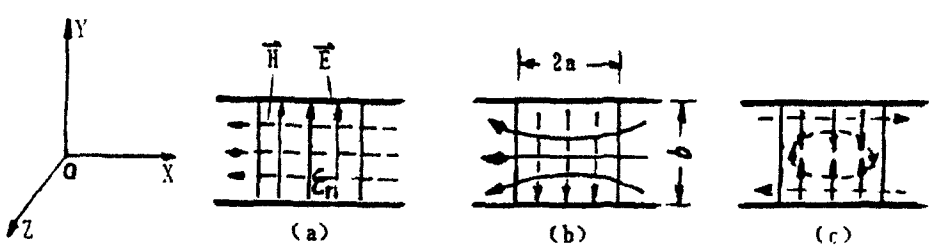

Fig.1 The fields lines of NRD guide, (a)TE_{10}^{e} ,(b)LSM_{11}^{e},(c)LSE_{11}^{e}

If a thin metal probe is inserted in the dielectric strip of the NRD guide along the x- direction, as shown in Fig. 3, the incident power of the LSM_{11}^{0} mode will be partially converted into the power of the LSE_{11}^{0} mode. Assuming the x- direction component of the field for the LSM_{11}^{0} mode as

$$E_x^i = (k^2 - k_{x1}^2) \cos(k_{x1}x) \cos(\frac{\pi}{b}y) e^{-j\beta_1 z} \quad (1)$$

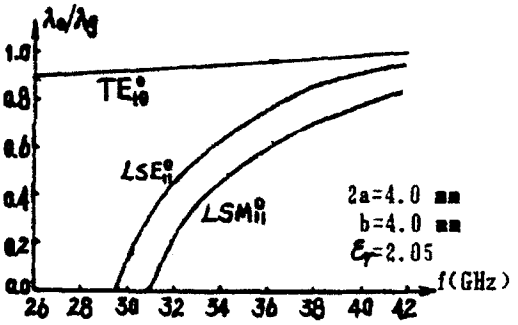

Fig. 2 The dispersion characteristics of NRD guide

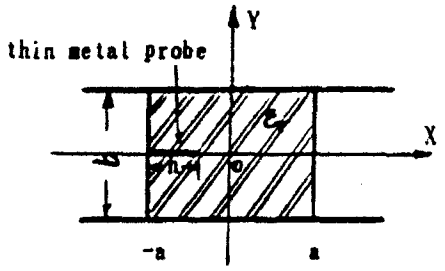

Fig. 3 The NRD guide modes converter

where $k^2 = \omega^2 \mu_0 \varepsilon_0 \varepsilon_r$, k_{x1} and β_1 are the wavenumbers of LSM_{11}^{0} mode along the x- and z- directions respectively, the induced current by E_x^i on the thin metal probe is given by

$$I_x = \sum_{n=1}^{N} I_n \sin[\frac{n\pi}{h}(x_0 + a)], \quad (-a \le x \le -a+h) \quad (2)$$

Here the magnetic vector potential $\vec{A}$ only possesses the x- direction component, $\vec{A} = \vec{a}_x A_x$, which is determined by the relation

$$\nabla^2 A_x + k^2 A_x = -\mu_0 J_x \quad (3)$$

Because the excited electric fields should possess the characteristic of symmetry for x- axis, and higher order modes should be cut-off, there are only LSM_{11}^{0} and LSE_{11}^{0} modes excited out by Ax.
The Green's function [2] in equation (3) is

$$G = A_1 \cos(k_{x1}x) \cos(\frac{\pi}{b}y) e^{\mp j\beta_1 z} + A_2 \sin(k_{x2}x) \cos(\frac{\pi}{b}y) e^{\mp j\beta_2 z} \quad (4)$$

where

$$A_1 = \frac{\cos(k_{x1}x_0)}{jb\beta_1(d + \frac{1}{2k_{x1}}\sin 2k_{x1}d)} \quad (5)$$

$$A_2 = \frac{\sin(k_{x2}x_0)}{jb\beta_2(d - \frac{1}{2k_{x2}}\sin 2k_{x2}d)} \quad (6)$$

where k_{x2} and β_2 are the wavenumbers of LSE_{11}^{0} mode along the x- and z- directions respectively.
Therefore Ax can be obtained as

$$A_x = \iiint \mu_0 J_x G \, dv_0 = \sum_{n=1}^{N} \mu_0 I_n [B_{1n} \cos(k_{x1}x) e^{\mp j\beta_1 z} - B_{2n} \sin(k_{x2}x) e^{\mp j\beta_2 z}] \cos(\frac{n\pi}{b}y) \quad (7)$$

where

$$B_{1n} = \frac{n\pi h[(-1)^n \cos k_{x1}(h-a) - \cos(k_{x1}a)]}{jb\beta_1(a + \frac{1}{2k_{x1}}\sin 2k_{x1}a)(h^2k_{x1}^2 - n^2\pi^2)} \tag{8}$$

$$B_{2n} = \frac{n\pi h[(-1)^n \sin k_{x2}(h-a) - \sin(k_{x2}a)]}{jb\beta_2(a + \frac{1}{2k_{x2}}\sin 2k_{x2}a)(h^2k_{x2}^2 - n^2\pi^2)} \tag{9}$$

And the excited electric field is

$$E_x = -\frac{1}{j\omega\varepsilon_0\varepsilon_r}\sum_{n=1}^{N} I_n[B_{1n}k_{x1}^2\cos(k_{x1}x)\, e^{\mp j\beta_1 z} + B_{2n}k_{x2}^2\sin(k_{x2}x)\, e^{\mp j\beta_2 z}]\cos(\frac{n}{b}y)$$
$$- j\omega\mu_0\sum_{n=1}^{N} I_n[B_{1n}\cos(k_{x1}x)\, e^{\mp j\beta_1 z} + B_{2n}\sin(k_{x2}x)\, e^{\mp j\beta_2 z}]\cos(\frac{n}{b}y) \tag{10}$$

The boundary condition on the surface of the metal probe is

$$Ex + E\dot{x}^{i} = 0, \quad (y = z = 0) \tag{11}$$

Substituting Eq.(1) and Eq.(10) into Eq.(11), we can obtain the N-dimension linear equations as

$$[C_{mn}]\,[I_n] = [D_m], \quad (m, n = 1, 2, \ldots, N) \tag{12}$$

where

$$C_{mn} = (\frac{k_{x1}^2}{j\omega\varepsilon_0\varepsilon_r} + j\omega\mu_0)\, B_{1n}\cos[k_{x1}(-a + \frac{m}{N}h)]$$
$$+(\frac{k_{x2}^2}{j\omega\varepsilon_0\varepsilon_r} + j\omega\mu_0)\, B_{2n}\sin[k_{x2}(-a + \frac{m}{N}h)] \tag{13}$$

$$D_{mn} = (k^2 - k_{x1}^2)\cos[k_{x1}(-a + \frac{m}{N}h)] \tag{14}$$

We define the ratio of the $|Ex|$ of the excited LSE_{11}^{0} mode and $|E\dot{x}^{i}|$ of the incident LSM_{11}^{0} mode, η, as the convertion efficiency of the LSM - LSE mode converter, which can be written out as

$$\eta = \frac{\pi k_{x2}\left|\sum_{n=1}^{N} I_n B_{2n}\right|}{b\omega\varepsilon_0\varepsilon_r(k^2 - k_{x1}^2)} \tag{15}$$

According to the equation (15), the computation results of η are shown in Fig. 4 and Fig. 5. It is obvious that the mode convertion caused by the single metal probe is relatively strong within a very broad bandwidth. If the length of the metal probe is increased, the convertion efficiency will be notably improved. But, when $h \geq 2a$, Eq. (15) will not be used because of the influence of the higher order modes.

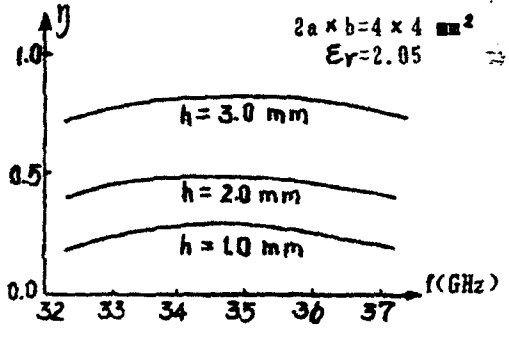

Fig. 4 The convertion efficiency vs. frequency

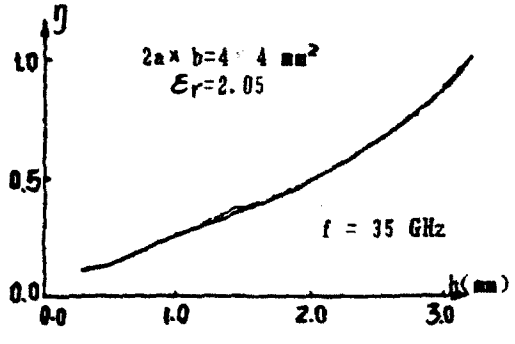

Fig.5 The convertion efficiency vs. the length of probe

MEASUREMENT OF LSM^{0}_{11} /LSE^{0}_{11} MODES CONVERTER

In order to measure the output power of LSE^{0}_{11} mode of the LSM^{0}_{11}-LSE^{0}_{11} mode converter, it is necessary to re-converted the LSE^{0}_{11} mode into LSM^{0}_{11} mode to couple it into a rectangle metal waveguide [3]. This kind of measurement method is shown in Fig.6. The measured insertion loss of the converter is shown in Fig. 7.

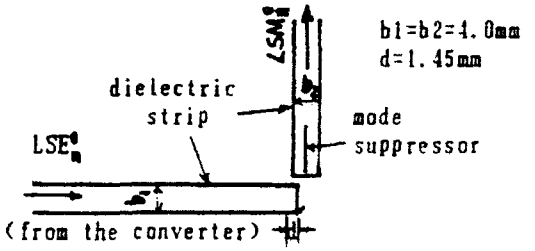

Fig.6 Measurement method of LSE^{0}_{11} mode

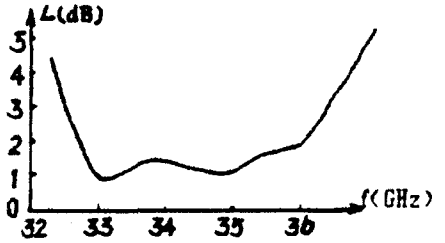

Fig.7 The insertion loss of LSM-LSE modes converter

In addition, we can adopt multi-metal probes to improve the convertion efficiency. The distance between two metal probes should be the times of the wavelength of the LSE^{0}_{11} mode.

CONCLUSION

A kind of LSE mode exciter in NRD guide has been analysed, and the LSM-LSE mode converter of NRD guide has been designed and fabricated. It was found that the characteristic of insertion loss and bandwidth of the converter are quite good. It can be applied to the NRD guide balanced mixers and the front ends to improve the performance of the circuits.

REFERENCES

1. T.Yoneyama, 1989 IEEE MTT-S Digest, 1083-1086.
2. R.E.Collin, " Field Theory of Guided Waves", Mc Graw-Hill, New York, 1960.
3. F.Kuroki, T.Yoneyama, the 3rd. APMC'90, Tokyo, Japan, 7-10.

W1.1

WIDEBAND 8mm-WAVE MIXER WITH HIGH IF

Zhou Qi
(NO. 16 Institute, the Ministry of Machine-Building
and Electronics Industries of China)

ABSTRACT

Broadband 8mm-wave balanced mixer has been developed in waveguide, finline, microstripline and packaged Si-diodes. A noise figure (DSB) of less than 7dB was achieved over the 4GHz (from 4 to 8GHz) instantaneous IF frequency band with the RF swept from 34 to 38GHz and the LO at 30GHz. Similar results were obtained with another mixer when the RF was swept from 30 to 34GHz and the LO at 38GHz. The mixers utilize native devices and materials. The performance of the mixers is stable and reliable.

INTRODUCTION

In parallel with the development of millimeterwave radar weapon and communication systems, a need for millimeter-wave surveillance receivers have been increasing. In order to meet this requirement, a mixer with broadband coverage must be developed. This requires broadband width capabilities at both RF and IF bands. Consequently, high performance mixer diodes, wide instantaneous bandwidth mixer circuits and low noise IF amplifiers are needed. Mixer noise figure is a strong function of the quality of the diodes and its associated parasitic elements. In order to ensure satisfactory performance, the two diodes must be very closely matched. Recently, the mixer with the full waveguide band from 26.5 to 40GHz had been developed using GaAs beam lead Schottky barrier diodes. However, the development of the broadband mixers using native packaged Si-diodes and materials was needed in practical applications.

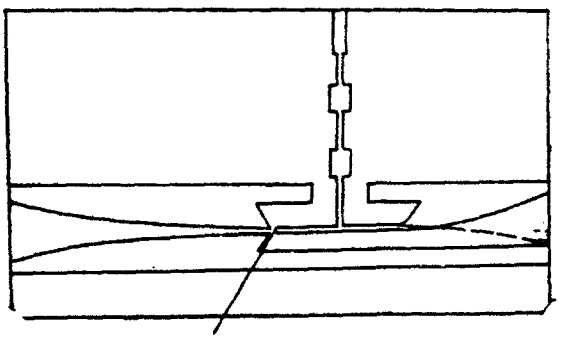

Fig. 1 Integrated circuit of the mixer

This paper describes the design and performance of a broadband balanced mixer using packaged diodes at millimeter-wave frequencies. Specifically covered are diode characteristics, circuit design considerations, and performance measurements. A design was selected that utilizes two

orthogonal transmission lines. The RF input uses a waveguide to finline transition and the LO is transitioned from waveguide to microstripline. The IF signal is extracted by means of a Chebyshev low pass filter designed in microstripline. The packaged diode pair is conveniently mounted at the junction of the finline and the microstripline. Fig. 1 shows the layout of the integrated circuit for the mixer. Integrated circuit technologies provied the advantages of low cost, light weight and small size.

DESIGN CONSIDERATIONS

The RF input port is required to provied wider bandwidth, lessreflection and matching. A waveguide to finline transition was selected. Waveguide-finline transition yields a wideband balanced line transformer which is terminated by a matched diode pair. To achieve good RF matching, a exponential taper finline transition was incorporated into the design. The gap size between the tapered finlinees is varied to achieve the optimum impedance match to the mixer diodes. A length of the tapered finline is 1.5-2 λg at the center frequency of the RF. The finline ended-impedance was chosen to be 150-170ohms which is consistent with two diodes in series. The converting diodes are mounted as close to the RF port as possible so as to minimize path losses which add directly to noise figure.

The LO input is injected into the diode pair using a single- ended transmission line. The waveguide to microstripline transition uses two overlapping sine-exponential tapers by way of two-sided substrate etching. The circuit provides a simple technique for converting to the microstrip propagation mode and is very broadband. The diodes are in parallel with respect to the LO signal. The problem here is to provied a good LO return so that the diodes are well matched. This is accomplished by adding open shut stubs at on the balanced input side. The lengths of the stubs may be trimmed to optimize the LO match. In addition the LO is also matched to the diodes by matching sections between the filter and the diodes.

In the designed finline balanced mixer, good isolation between the LO and RF port is achieved because the electric fields of the finline and microstripline are perpendicular to each other. More than 20dB isolation was observed between the LO and RF.

The design of the IF network matching circuit is very important. The diodes are in parallel with respect to the IF circuit. The IF frequency is extracted via a five-section low -pass filter designed in microstripline. The low-pass filter is required to pass the IF frequency and reject the LO and RF signals. Distributed lines were used to approximate lumped elements. First element of the filter is high impedance line (110ohms). This filter has a nominal passband from dc to 10GHz and cutoff frequency is chosen to provide attenuation greater than 20dB at the RF and LO frequencies. The location of the filter was designed as possible as far from the diodes.

MEASUREMENT RESULTS

The noise figure of the mixer was measured for RF coverage from 34 to 38GHz at a fixed LO of 30GHz. LO drive was +13dBm. The IF band was evaluated from 4 to 8 GHz. Measured results are presented in Figure 2(a). The noise figures of the mixer ranged from 3.5dB to 6.6dB over the 4GHz IF bandwidth. Also shown are the noise figures of another mixer in Fig. 2(b). The LO drive of this mixer was +13dBm with LO frequency at 38 GHz, while the RF signal was swept from 30 to 34GHz.

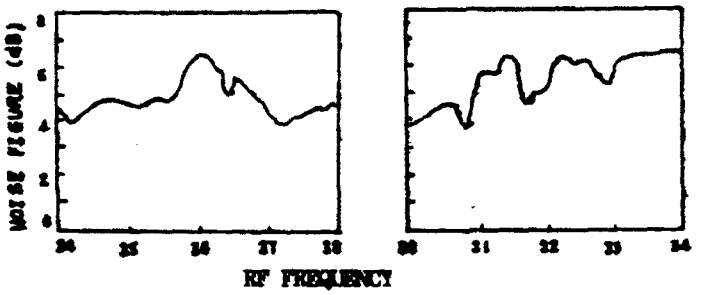

(a) LO at 30GHz (b) LO at 38GHz

Fig. 2 Noise figure of the mixers

CONCLUSION

The mixer described in this paper demonstrated that using packaged diodes and planar technology can also achieve wider bandwidth at the RF and IF port. A few key technologies are the designs and the fabrications of the waveguide-finline transition and the waveguide-microstripline transition. Although the specifications of the mixer are not as good as those usually obtained in mixer utilized GaAs beam lead Schottky barrier diodes. However, a major result of the mixer development is that cost savings are incurred by using native devices and materials so that it is available. The mixer has been applied in millimeter- wave surveillance receivers.

REFERENCES

1. R. S. Tahim, T. Pham, and K. Chang "MM- Wave Integrated Circuit Wide- band Downconverters "Microwave Journal 1985, pp131
2. Chandra Gupta and John Del Conte " Trends in MM-Wave Mixer Designs" Microwave Journal April 1984, pp83
3. D. W. Ball and L. Q. Bui " Wideband mm-Wave Mixers For EW Applications" Microwave Journal July 1982, pp65

DC-to-120 GHz HARMONIC MIXERS for MILLIMETER-WAVE INSTRUMENTATION

A. M. Shchitov, J. S. Zaitsev, A. M. Lomakin

Institute of Eiectronic Measurements "KVARZ"
176 Prospekt Gagarina
Nizhni Novgorod 603009 Russia

Abstract

A set of harmonic mixers is designed for use with mm-wave radio measuring equipment. Four types of waveguide mixers cover frequency range from 26 to 120 GHz. The mixer of coaxial type covers frequency range 0-40 GHz.

Introduction

Harmonic mixers of antiparrallel-pair diode configuration are usually used for downconverting signal frequency of mm-wave band [1]. In design process of mm-wave harmonic mixers the sampling technique of frequency conversion and thin-film hybrid technology are used. All this, along with the development of a monolithic GaAs pair of mixing diodes with low parasitics and a step recovery diode (SRD) with extremely short transition time (less 25 ps) allowed to have:

- comparatively low conversion loss (30-35 dB, up to 78 GHz and 50-55 dB, up to 120 GHz) for a large number of LO harmonic measurements (20 and more);
- high isolation of mixer LO and signal inputs (40-50 dB);
- low sensitivity of conversion loss to LO power level variation;
- low phase noise level.

Design

Harmonic waveguide mixer design, based on a sampler [2], is shown in Fig. 1 and includes: a mixing assembly, a gate pulse shaping circuit (or LO harmonic generating circuit), broadband waveguide-microstrip transition and output signal generating circuit.

Key problems in designing a wideband sampling converter

are connected with input signal path matching and with providing a uniform gate pulse harmonic spectrum in operating frequency range. Besides, in mm-wave range the elimination of parasitic emission, caused by circuit components with sizes of wavelenth order, is of great importance.

Taking all this into account, the input signal path is formed by a wideband waveguide-microstrip transition made as a seven-step Chebyshev transformer from rectangular waveguide section to the П-form section, and also by 50 Ohm microstrip line, made for loss minimization thin (0.3 mm) quartz substrate.

Mixing node base is a monolithic diode pair, practically noninductively connected to the combination of slot and microstrip lines not coupled with each other. GaAs beam lead diode pair [3] has two seriesly connected stripline Schottky barriers 1x12 μm, thoroughly matched in electric and geometric parameters. Surface bridging of stripline barrier provides better isolation between the diodes.

Diode parameters are given in Fig.1. Direct voltage drop of the diodes differs in 3% (I = 1 mA). Short gate pulses formed by a slotline cavity are applied to the diodes through the storage capacitors. The pulses periodically open the diodes for a short period of time with LO frequency.

To cover the frequency range up to 120 GHz it is necessary to generate a gate puls of not more than 5 ps duration with effective voltage amplitude at 0.3-0.5 V diode. For this reason a special small-size Si SRD, made by bipolar technology with active mesa-structure forming at a copper heat-sinker, was constructed. Mesa-structure diameter $\sim$ 15 μm provides small parasitic cavity $C_o \sim 0.15$ pF. Vacuum submicron epitaxy provides high quality semiconductor structure with thin base and sharp p-n junction. This structure defines SRD specifications: transition time $\lesssim$ 25 ps, breakdown voltage > 10 V, effective minority carrier lifetime $\sim$ 0.5 ns, series resistance $\sim$ 1.5 Ohm. To minimize the required LO power (to 100 mW and less) and to provide wide and uniform frequency band at LO input (1 - 12 GHz) and IF output up to 1 GHz, slotline parameters (l,W) are optimized, value of C is selected about 0.5-1 pF, storage capacitors 0.5 pF.

Large value (40 - 50 dB) of signal - local oscillator (RF-LO) inputs isolation is provided by mixer construction-field orthogonality in slotline and waveguide, and also by high identity of mixer diode parameters.

The mixers are mounted in miniature packages. Coaxial connectors of SMA(f) type are used for LO and IF tracts. Cross-sections of 26-118 GHz waveguide channals meet the requirements, adopted in Russia. Several types of cross-sections are developed to meet the international standard (WR-28, WR-22, WR-19, WR-15, WR-10). Besides, models of one- and two-channel harmonic mixers with coaxial connectors of OS-50 type in 0-40 GHz frequency range are developed.

Experimental results

Typical characteristics of coaxial and waveguide mixers, and conditions of their measurement at 25° C are given in Fig. 2,3.

The mixers keep high-level parameters under severe service conditions: within tamperature range from -40°C up to +70°C, relative humidity 98%. Maximum input power of RF signal is not less than 10 mW, and of LO signal - 200 mW.

Conclusion

The abovementioned harmonic mixers are successfully used in frequency stabilization and synchronization systems, designed for mm-wave frequency synthesizers [4], and are used nowdays for development of state-of-the-art oscilloscopes, frequency counters, network analyzers, etc.

References

1. R.Matreci,"Unbiased Subharmonic Mixers for Millimeter-Wave Spectrum Analyzers", Hewlett-Packard Journal, November, 1986.

2. I.Merkelo,R.Hall,"Broad-Band Thin-Film Signal Sampler",IEEE Journal, of Solid-State Circuits, vol.sc-7,no.1,February, 1972.

3. В.Зайцев, Н.Огаркова, В.Соколов, А.Витов,"Монолитные диодные пары с барьером Шотки на GaAs для преобразователей частоты мм-го диапазона", Передовой опыт, N3, 1990

4. G.Altshuller, O.Anikin, O.Pavlovsky,"Millimeter-wave synthesizers" (in this book)

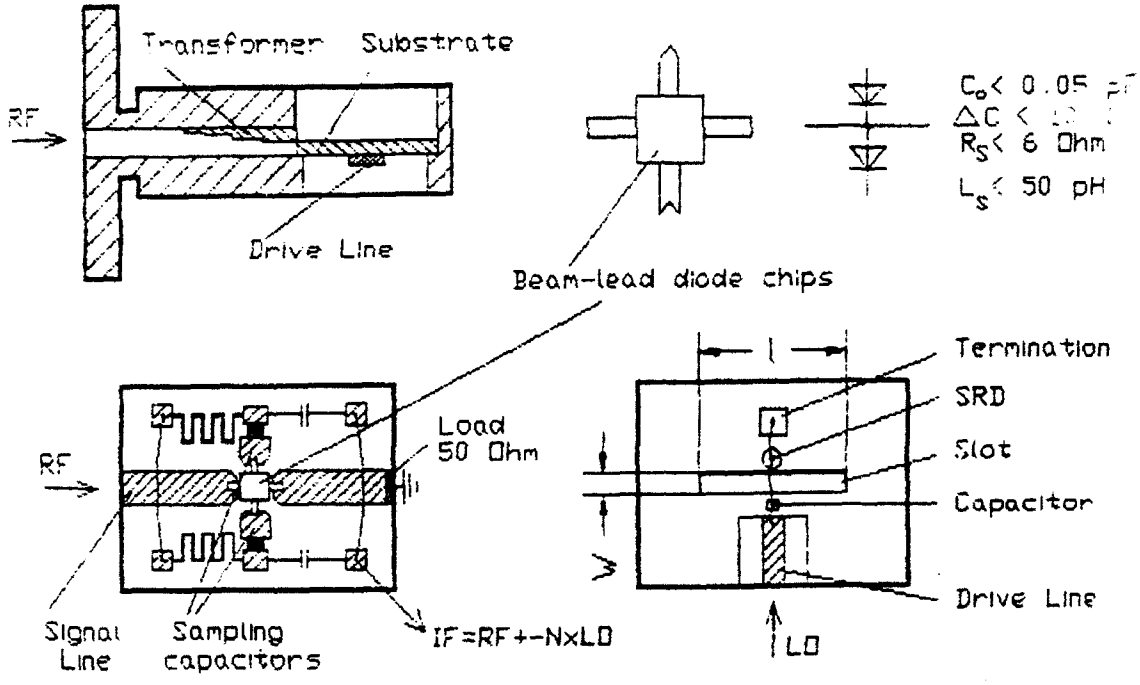

Fig.1. Sampler Design

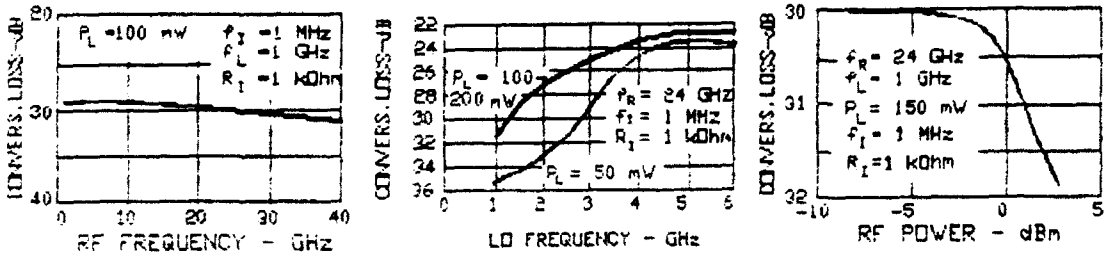

Fig.2. Coaxial Sampler Typical Performance

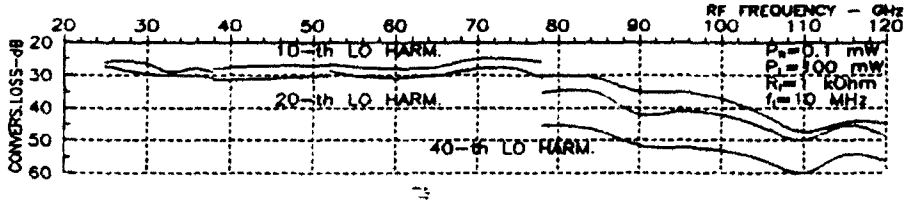

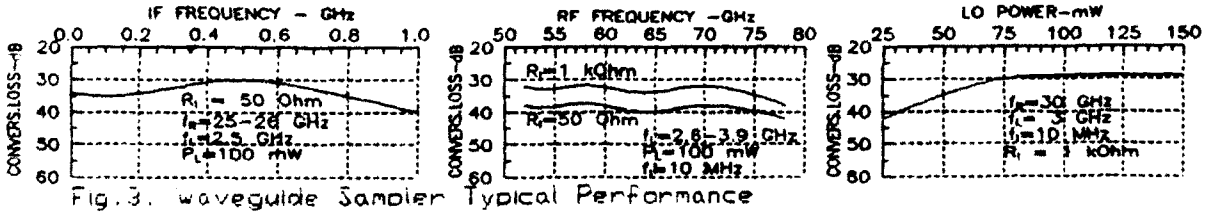

Fig.3. Waveguide Sampler Typical Performance

W1.3

DETECTOR OF MILLIMETER WAVES BASED ON INHOMOGENEOUS ELECTRON HEATING

A.I. Vakser

Institute of Radiophysics and Electronics,
Academy of Sciences of the Ukraine, 12 Academic.
Proscura Str., 310085, Kharkov, Ukraine

It is well known that super high frequency (SHF) waves whose amplitude exceeds the value of plasma field E_{pl} ($E_{pl} \simeq 10^{-2} \div 10^{-1}$ V/cm for the temperature of external thermostat T_o = = 4.2 K, $E_{pl} \simeq 10^{-1} \div 10$ V/cm for T_o = 77K ÷ 300 K) can heat electron gas: electron temperature T_e becomes more than T_o [1,2]. Hereat if the volume and surface thermal conductivity are great enough the temperature of crystal lattice T_p is equal to T_o. This is the situation when a volume thermostat is available [1-3]. Due to the attenuation of SHF-waves a gradient of T_e arises and appropriate thermo-e.m.f. V_T occurs.

In the absence of external constant magnetic field $\vec{H}$ the V_T mentioned arises in the direction of wave propagation $\vec{k}$ ($\vec{k}$ is a wave vector) [2]. If magnetic field $\vec{H}$ is available and $\vec{H} \perp \vec{k}$ additional thermo-e.m.f. V_{TH} arises in the direction which is perpendicular to $\vec{H}$ and $\vec{k}$ [3] (Fig. 1). This is a hot electron Nernst-Ettingshausen effect [3]. The latter used to be as a basis for millimeter detector [3]. Such operating devices have volt-watt sensitivity $\gamma = V_{TH}/P$, where P is power of falling radiation, γ = 500 V/W for $10^{10} \div 10^{11}$ Hz range [3].

Here in this paper different physical phenomena and proper modifications of the devices are suggested with the purpose of increase in detector sensitivity γ. It is shown that each of proposed physical reasons may result in the increase in sensitivity of semiconductor detector.

I. Lattice heating.

A propagation of SHF-waves in massive semiconductors with bounded thermal conductivity may be accompanied by lattice heating: $T_p > T_o$ (Fig.2). In this case due to the fact that $\gamma \sim V_{TH}$ and in its turn $V_{TH} \sim \Delta T$, where ΔT is a temperature difference between receiving and dark faces of the sample, the

increase in ΔT leads to the increase in γ .

2. Form effect.

If the sensitive element has a tapered form and a receiving sample face is a wide face and dark (narrow) end is cooling up to the T_o (see Fig. I,2), the temperature difference ΔT as well as sensitivity γ increase in comparison with a rectangular sensitive element [4].

3. Electron-phonon thermodrag.

As it was shown in [5] this cause at certain conditions can increase grad T_e. For this reason selecting high purity semiconductor elements containing large cross thermoconductivity one can achieve the increase in ΔT and γ .

Comparative characteristics of the parameters of various devices containing semiconductor sensitive elements made of InSb, GaAs, Si and Ge are adduced. Strict calculations show that simultaneous presence of these three factors allow to increase γ really at least by an order of magnitude greater.

References

[1] E.M.Conwell. High Field Transport in Semiconductors (Acad. Press, N.Y. & London, 1967).

[2] S.Asmontas. Electrogradient Phenomena in Semiconductors (Mokslas, Vilnius, 1984).

[3] A.N.Vystavkin et al. Radiotekn. i Electron. 8 (1963), 994; 17 (1972), 1273.

[4] F.G.Bass, A.I.Vakser. Phys. Letters A 159 (1991), 284.

[5] Yu.G.Gurevich, O.L.Mashkevich. Phys. Rep. 181 (1989),327.

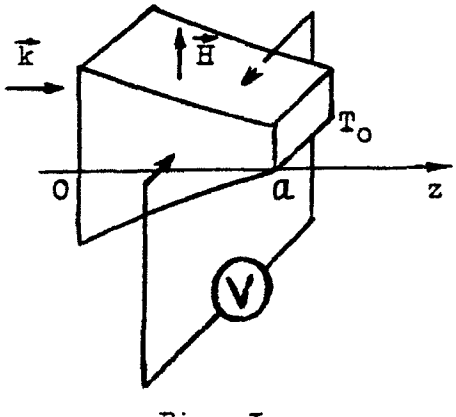

Fig. 1

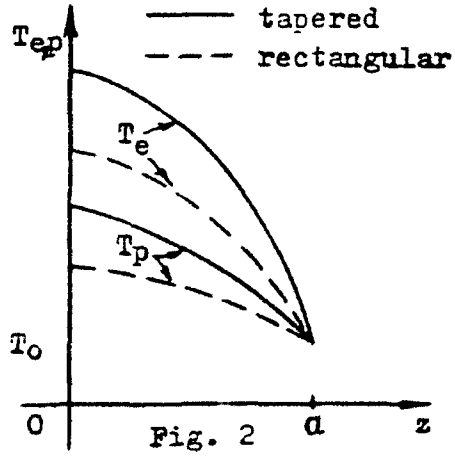

Fig. 2

A THIN-FILM ANTENNA-COUPLED MOM DETECTOR OF IR RADIATION

I. Wilke, Y. Oppliger*, K.Gilles, W. Herrmann and F.K. Kneubühl
Infrared Physics Laboratory
Swiss Federal Institute of Technology (ETH), CH-8093 Zürich, Switzerland
Tel. (1) 3772340 Fax (1) 3715989
*CSEM, CH-2007 Neuchâtel

We report on the design, fabrication and performance of an infrared detector which consists of a thin-film metal-metaloxide-metal (MOM) diode integrated with a microstrip antenna. This antenna-coupled diode is used for the detection of cw 10 μm CO_2- laser radiation.

Since the late sixties point-contact MOM-diodes with a response time shorter than 10^{-14} s have been the fastest available detectors[1] and mixers[2] of infrared laser radiation. Nevertheless, their use was hitherto restricted to laboratory applications. One of their major disadvantages is the low mechanical stability of the point-contact MOM-diode. In addition, the sensitivity and the response time of the MOM-diode, which strongly depend on the size of the contact area and the thickness of the metaloxide layer, vary as a result of the inherent difficulties in the fabrication process and consequently lead to nonidentical devices.
Present microlithography techniques enable the fabrication of microstructures with a minimum linewidth of less than 0.1 μm. This permits the production of shock-proof, well-defined thin-film MOM diodes with response times comparable to that of the point-contact configuration.
Our thin-film Ni-NiO-Ni microstructures are fabricated with the aid of electron-beam lithography in cooperation with the Centre Suisse d'Electronique et de Microtechnique (CSEM) Neuchâtel. The thickness of the Ni films is 0.22 μm, that of the NiO approximately 5 nm. The layers are deposited by plasma sputtering and a conventional lift-off process. Our MOM-diodes with a contact area of 0.25 μm * 0.25 μm (Fig.1) are the smallest compared to those investigated by other authors[3-7]. Furthermore, they are as small as the edge-MOM's[8] fabricated in a more complicated process.
Each MOM diode is integrated with a microstrip dipole antenna which collects the energy of the incident ir radiation field. Subsequently, it applies the collected energy in form of an ir-frequency ac voltage to the MOM diode. This type of a thin-film antenna works less efficient than e.g. the whisker of a point-contact MOM diode because the microstrip lies on a dielectric substrate whilst the whisker is embedded in air. In our case the substrate consists of 370 μm Si covered with a thin insulating layer of SiO_2. The antenna with the MOM contact at its center is formed by two metal strips, which are 0.25 μm wide and between 5.4 μm and 22 μm long (Fig.2) . In order to improve the efficiency of the thin-film antenna, the substrate is etched to reduce the thickness to 3 μm. While integrated-circuit antennas are well established in the mm-wave region[9] and prototypes have been developed for the submillimeter range[10], there have been no such antennas for ir radiation with a wavelength of 10 μm up to the present.

We investigated the performance of our MOM-diodes with respect to laser power, bias voltage, chopper frequency, temperature, polarisation of the incident laser radiation, contact area, substrate thickness and different antenna designs.

As reported previously[11] the recorded voltage consists of a polarisation-independent part and a polarisation-dependent part which exhibits a $\cos^2\Theta$- dependence for a variation of the angle Θ between the plane of polarisation of the linearly polarized laser-light and the antenna axis. This observation agrees well with theory[12] which predicts that the rectified dc part of the laser-induced ac voltage is proportional to the square of the component of the laser field parallel to the antenna. Moreover, this result is in accordance with the measurements performed with point-contact diodes which also demonstrated that the response of the diode is mainly due to the component of the laser field parallel to the whisker[2,13].

Our first experiments performed with MOM diodes of three different antenna lengths (5.4 μm, 16 μm, 22 μm) revealed that the polarisation-independent part exhibits no significant change with antenna length whilst the polarisation-dependent part increases for shorter antennas. This property can be explained by damping of the laser-induced antenna currents in this frequency range[14,15,16].

Measurements with respect to the size of the contact area, which determines the RC time constant of the device, showed that the polarisation-dependent part of the signal nearly disappears for a contact size larger than 1 μm^2. MOM-diodes with a contact area of this size are obviously too slow to rectify the ir-frequency voltage supplied by the antenna.

If the MOM-diodes are cooled, either by liquid nitrogen or increasing the chopper frequency, we observe for some of them a decrease of the polarisation-independent part of the signal while the polarisation-related part remained unchanged.

From all these data we conclude that the polarisation-dependent part of the MOM diode's response is due to antenna coupling. Part of the polarisation-independent signal is caused by thermal heating. In order to verify that this thermal component of the signal is not related to the polarisation we have measured the absorption of a pure Si-wafer and a SiO_2 coated wafer for the 10 μm CO_2-laser radiation. These experiments demonstrated that the heating is mainly caused by absorption of the radiation in the SiO_2 layer. Since the area of the laser spot on the surface of the Si chip is large compared to the dimensions of the MOM diode and antenna, this region is heated isotropically and, therefore, the thermal fraction of the voltage does not depend on the polarisation of the laser radiation.

In order to improve the antenna coupling we are actually fabricating antennas which are shorter than 5.4 μm. In the future we intend to use the diodes for mixing in the infrared.

References

1. S.M. Faris, T.K.Gustafson, J.C. Wiesner, IEEE J. Quant. Electron. QE9(7), 1973, p.737.
2. L.O. Hocker, D.R. Sokoloff, V. Daneu, A. Szoke, A. Javan, Appl. Phys. Lett.12(2), 1968, p.401.
3. J.G. Small, G.M. Elchinger, A. Javan, A. Sanchez, F.J. Bachner, D.L. Smythe, Appl. Phys. Lett. 24(6), 1974, p.275 .
4. G.M. Elchinger, A. Sanchez, C.F. Davis, A. Javan, J. Appl. Phys. 47(2), 1976, p.591.
5. S.Y. Wang, T. Izawa, T.K. Gustafson, Appl. Phys. Lett. 27(9), 1975, p.481.
6. E. Wiesendanger, F.K. Kneubühl, Appl. Phys. 13, 1977, p.343.
7. A.B. Hoofring, V.J. Kapoor,W. Krawczonek, J. Appl. Phys. 66(1), 1989, p.430.
8. M.Heiblum,S.Y.Wang,J.R.Whinnery, T.K.Gustafson,IEEE J.Quant.Electron. QE14(3), 1978, p.159.
9. D.B. Rutlege, D.P. Neikirk,D.P. Kasilingam, Infrared & Millimeter Waves 10,1983, p.1.
10. G.M. Rebeiz, W.G. Regehr, D.B. Rutledge, R.L. Savage, N.C. Luhmann Jr., Int. J. Infrared & Millimeter Waves, 8(10), 1987, p.1249.
11. I.Wilke, W.Herrmann, F.K. Kneubühl, Digest of the 15th Conference on Infrared and Millimeter Waves, Orlando, December 1991.
12. H.C. Torrey, C.A. Whitmer, "Crystal Rectifiers", Radiation Lab Series 15, McGrawHill, New York 1948.
13. B.I. Twu, S.E. Schwarz, Appl.Phys. Lett. 25(10), 1974, p.595.
14. J.A. Marsh, PH.D. thesis, Ohio State University, 1949, p.48.
15. B.L. Coleman, Pil. Mag. 41, 1950, p.276.
16. D.B. Rutledge, S.E. Schwarz, A.T. Adams, Infrared Physics 18, 1978, p.713.

Acknowledgements

This study is supported by ETH Zürich, GRD/EMD Bern and CSEM Neuchâtel. We wish to thank J. M. Stauffer, CSEM Neuchâtel, for active help as well as Prof. Dr. H. Melchior, ETH Zürich, Prof. Dr. N. de Rooij, University Neuchâtel, and Dr.H. Luginbühl, CSEM Neuchâtel, for advice and support.

Figure 1: Ni-NiO-Ni diode with a contact area of 0.25 μm * 0.25 μm

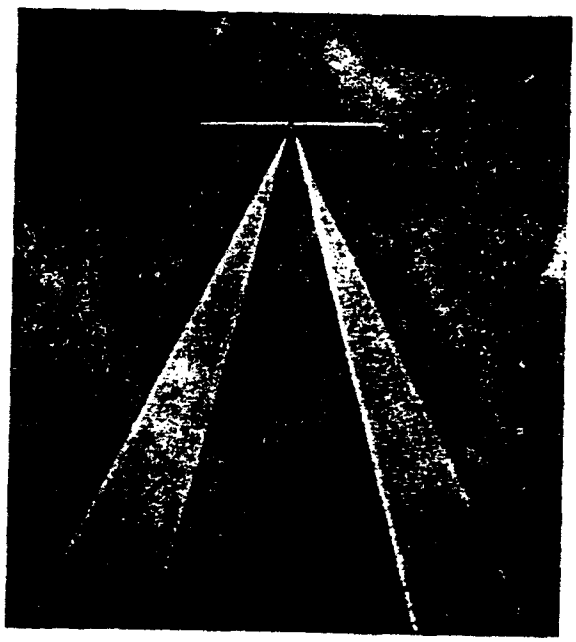

Figure 2: Thin-film dipole antenna with electrical leads

W1.5

A NOVEL ROOM TEMPERATURE OPERATED FAST-RESPONSE FIR DETECTOR

A.P.Dmitriev, S.A.Emelyanov*), S.V.Ivanov,
P.S.Kop'ev, Ya.V.Terent'ev, I.D.Yaroshetsky

A.F.Ioffe Institute, 194021, St.Petersburg, Russia

A novel room temperature operated fast-response FIR detector has been proposed. The detection idea is based on the effect recently discovered of fast-response photocurrent origination under the FIR excitation /1/. The sensitivity of the detector has been found for two typical FIR wavelengths together with the linearity range. The detector response time has been estisated. The ways to improve the detector parameters are discussed.

In present paper we propose to apply for the FIR light detection the recently discovered effect of fast-response current origination in semiconductor 2D-structures under the FIR excitation.

1. The GaSb/InAs/GaSb single quantum well structure grown by MBE on semiinsulated GaAs substrate in 100 direction has been used as a detector active element. The thickness of the GaSb buffer layer, the InAs quantum well, and the GaSb cap layer were 1000 nm, 20 nm, and 20 nm, respectively ($n_s = 1.1 \cdot 10^{12}$ cm^{-2} and $\mu = 5 \cdot 10^4$ cm^2/(V·s) at T = 77 K). The samples were 5 mm in lenght and 3 mm in widht. The measurments were performed on NH_3 and D_2O pulsed FIR lasers optically pumped by CO_2 laser. The wavelenght of the former λ = 90.6 μm, pulse duration 40 ns, maximum intensity on the sample I_{max} = 8 kW/cm^2. The wavelenght of the latter λ = 385 μm, pulse duration 80 ns, maximum intensity I_{max} = 250 W/cm^2 (for more details of our laser system see /2/). The laser pulse structure allowed us to measure detector response time with the accuracy better than 10 ns. For comparison, the laser pulse was also recorded by photon-drag detector /3/. The sample was placed between the poles of a constant magnet at T = 300 K so that the magnetic field was parallel to the sample surface. The FIR light was normal to the surface. The photocurrent duplicated laser pulse structure and flowed along the 2D layer perpendicular to the magnetic field was recorded.

Figs. 1 and 2 show the current density into the well vs magnetic field for both wavelenghts at $I = I_{max}$ (a and b show two opposit signes of the magnetic field). The current are seen to be approximately proportional to the magnetic field . At B = 2 T it reaches the value of 200 A/cm^2 on λ = 90.6 μm and 100 A/cm^2 on λ = 385 μm**).

Fig.3 shows the current density vs FIR light intensity for both wavelenghts at B = 1.6 T. It is seen, that the current is linear on B up to 80 W/cm^2 on λ = 385 μm and up to 3 kW/cm^2 on λ = 90.6 μm. Also, the current decreases rapidly with increasing FIR radiation frequency.

2. We advance the following physical model of the detection. As a rule, in GaSb/InAs/GaSb single quantum well structures there is a strong built-in electric field (up to 100 kV/cm) inside the well. In particular, this field

---

*) Contact author

**) The current density at T = 4.2 K is two order higher than that at T = 300 K but here the current is not linear even at relatively low I .

may be due to the difference between the number of the donors on the interfaces /4/. In our structure the existence of this field was shown experimentally /5/. In such a system there is a so-called "loop of extrema" in the electron energy spectrum /5/: $\mathcal{E}^{\pm}(k) = \frac{\hbar^2 k^2}{2m^*} \pm \alpha k$, where α - spin-orbit coupling constant (fig.4a).

If we apply an external magnetic field along the sample surface (OX direction) the electron gas become strongly asymmetrical in OY direction of k-space: $\mathcal{E}^{\pm}(k_y) = \frac{\hbar^2 k_y^2}{2m^*} \pm \left(\alpha k_y + \frac{1}{2} g \mu_B B\right)$. Of course, in the velocity space the energy spectrum remain symmetrical ($v = \frac{1}{\hbar} \cdot \frac{\partial \mathcal{E}}{\partial k}$). The FIR light induces the optical transitions between two spin subbands. Probability of such transition is not too small owing to the linear on k term in Hamiltonian. In k-space the transitions are vertical but in v-space they are tilted. The strong difference between the populations of the initial states 1 and 1′ due to the spectrum asymmetry gives rise to the photocurrent. The photocurrent increases with increasing B because of increasing of the state 1 population. Since in our structure d_z = 20 nm the Fermi level is lied close to the second quantum-size level /6/ so the transitions within this level are supposed to be responsible for the photocurrent.

Thus, the basic idea of the detection is a high asymmetry in k-space of the electron gas induced by relatively low magnetic field and, consequently, high asymmetry of the optical transitions in compair with the known high-speed effects (photon-drag etc.). For example, fig 4b shows the optical transitions on λ = 385 μm at B = 4.6 T calculated using the parameters of our structure. The optical transition initial states 1 and 1′ are seen to be shifted from each other on the energy scale on the value of the order of 10 meV.

3. If we use the above structure as a detector it yields the following parameters. In linear regime the sensitivity on the 50 Ω load (sample resistence 200 Ω) is 20 and 0.2 (mV·cm^2)/(T·kW) for λ = 385 μm and λ_2 = 90.6 μm, respectively. The linearity range is up to 80 W/cm^2 and 3 kW/cm^2, respectively. The response time is better than 10 ns.

Of course, the above parameters can be considerably improved. For instance, one can modify the parameters of the GaSb/InAs/GaSb structure or utilize the structures based on the other narrow gap materials. Also, it may be promising to use the multiple quantum well structures or superlattices. Finally, it is possible to design a matrix detector to record the space distribution of the laser beam intensity.

REFERENCES:

1. A.P.Dmitriev, S.A.Emelyanov, S.V.Ivanov, P.S.Kop'ev, Ya.V.Terent'ev, I.D.Yaroshetsky - JETP Lett., 54, 273 (1991).
2. S.D.Ganichev, S.A.Emelyanov, I.D.Yaroshetsky -JETP Lett., 35, 368 (1982).
3. M.F.Kimmitt - Infrared Phys., 17, 459 (1977).
4. J.Luo, H.Munekata, F.F.Fang, P.J.Stiles - Phys.Rev.B, 38, 10142 (1988).
5. Yu.A.Bychkov, E.I.Rashba - JETP Lett., 39, 78 (1984).
6. M.Altarelli, J.C.Maan, L.L.Chang, L.Esaki - Phys.Rev.B, 35, 9867 (1987).

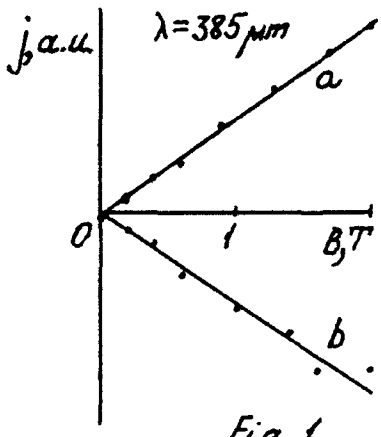

Fig. 1

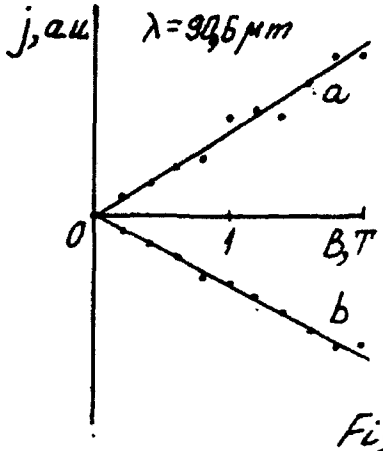

Fig. 2

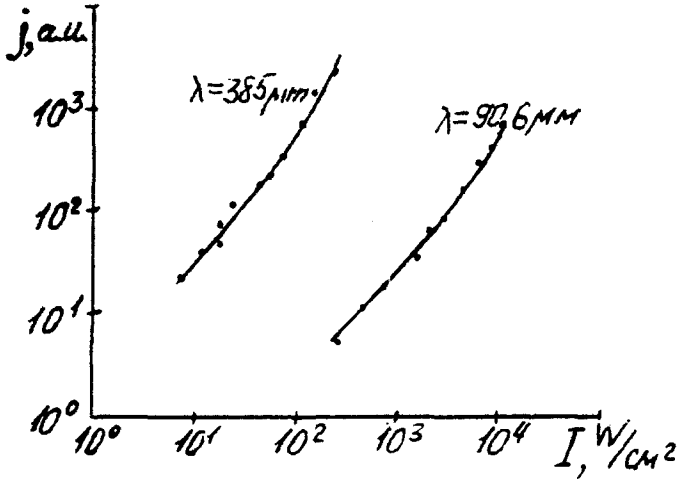

Fig. 3

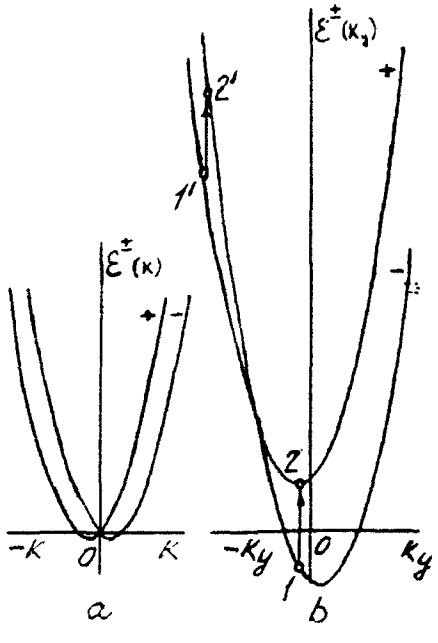

Fig. 4

W1.6

Mm-wave InP beam-lead Schottky diodes

V.G.Bozhkov, O.Yu.Malakhovsky, T.N.Korablyova, G.N.Misevichus

(Research Institute of Semiconductor Devices, Tomsk, Russia,)

The main advantage of InP Schottky barrier diodes (SBD) as compared to GaAs ones is a lower barrier height. It allows us to hope, that these diodes are capable to work at lower heterodyne power, when being used as mixer ones and without bias when being used in detector circuits. Recent attempts to realise this advantage of InP SDB are described in papers [1,2]. The results obtained demonstrate electrical (microwave) parameters of SBD are high enough to confirm investigators' expectations. At the same time there are still problems related to material, technology and diodes' design, which require solution. In particular, Au and Au-Ni are used as Schottky barrier metallization in [1,2], but their reliability is not high enough for practical applications. Properties of semi-insulating InP, used as substrate material in [1] are considerably worse than those of semi-insulating GaAs. The honey-comb design of InP SBD using high doped substrate [2] is inconvenient for promising hybrid-integrated and monolithic circuits in mm-wave range.

The attempts to fabricate the InP SBD with low barrier height were being carried out in our laboratory during last period of time. The great progress in improving the stability and reproduceability of diodes' parameters was reached when sufficiently perfect epitaxial layers of InP on semi-insulating and high-doped GaAs substrates were grown and used.

In this paper the results of fabrication and examination of InP SBDs, using GaAs substrate material are presented. Two types of diodes were fabricated. The first type diodes, using high-doped substrate material, were mounted in small-size metal-ceramic cases (diameter 0.6 mm). The second type diodes, using semi-insulating substrate material, were fabricated as beam-lead diodes. It schoud be said that LF- and HF - parameters of these two types of diodes are quite similar. So in the following we are limit ourselves by discussing of the results for beam-lead diodes, as being of greatest interest for the fabrication of hybrid-integrated and monolithic circuits.

The parameters of semiconductor material used are the following:

the thickness and the impurity concentration for high-doped n^+-InP layer are 1-2 um and 10^{19} cm^{-3},respectively; analogous values for n - InP layer are 0.15-0.3 um and $3*10^{16}$-10^{17} cm^{-3}. Transition layer of variable composition (InGaAsP) was grown between semi-insulating GaAs substrate and n^+-InP layer. All layers are VPE-grown.

The BLD fabrication process inclu .s the SiO_2 layer deposition on InP. The layer thickness is 0.5 um, the deposition method is pirolithical oxidation at T=250 C. The windows with a 3 um diameter are opened by photolitographic techniques. Schottky barriers are formed by galvanic deposition of two-layer metal..zation Rh-Pt into windows with following thermal evaporation of Ti and Au layers. Beam leads are formed by galvanic deposition of a 6 um -thick Au film. Construction of so fabricated InP beam-lead diode is similar completely to that of GaAs commercial one of AA138 type (fig.1).

The I-V characteristics of such BLD are quite perfect: n (ideality factor) < 1.2, R_s=10-25 Ohm, $V_r(I_r$=10 uA) > 3V. The barrier height according to our estimations is 0.4-0.45 V. The parasitic (constructive) capacitance of the diode was decreased to values of 0.01 - 0.015 pF by etching of surface (air) channel between anode contact finger and underlying substrate.

Such diodes quite successfully operate as mixer ones and really require less heterodyne power (as compared to GaAs diodes) for reaching optimum values of conversion loss. Results for 8- and 3- mm-wave regions are demonstrated in fig.2. But their sensitivity as detector diodes operating without bias (zero-bias detectors) is rather low. After some investigations with thermal treatments and variation of diode material parameters we achieved rather stable and reproducible reduction of barrier height. The I-V characteristics are shown in fig.3. There are three types of diodes. They may be conveniently characterized by the value of forward voltage at the current of 100 uA: 1 - V_f=300 mV (without thermal treatment); 2 - V_f= 200 mV; 3 - V_f=150 mV. About the characteristics of first type diode there was told above. The 2 and 3 type diodes, which corresponds to different thermal treatments, show much worse characteristics as mixer ones. The conversion loss increases to values of 9-10 dB, apparently because of degradation of n and Vr parameters. But as detector diodes they demonstrate high sensitivity at low microwave power levels (fig.4.). Preliminary measurements of tangential sensitivity give values from 40 to 47 dBmW at bandwidth of

videoamplifier from 1kHz to 2 MHz.

Less investigations were carried out at 3-mm wave region. The 2 type diodes show values of current sensitivity (B_i) to be > 1 A/W at R_l=100 Ohm and power levels from 10 to 1000 uW. Values of B_i are situated in limits 300-600 V/W at R_l=1 kOhm and power levels from 20 to 1000 uW. Note that all measurements of microwave parameters of beam-lead diodes were carried out after mounting them in small-sized metal-ceramic cases, for which optimum measuring diode chambers were designed.

References

[1] R.E.Neidert and S.C.Binari. Millimeter-wave planar InP Schottky diodes and their small-signal equivalent circuit. IEEE Trans. Microwave Theory Theoh., V.37, p.1694-1698, Nov.1989.

[2] A.P.Kryukov et all. Low-freqency noise and sensitivity of 3-mm range amplitude fluctuation GaAs- and InP-detectors. Electron. Teoh., ser.1, Microwave electronics, iss.1 (435), p.23, 1991

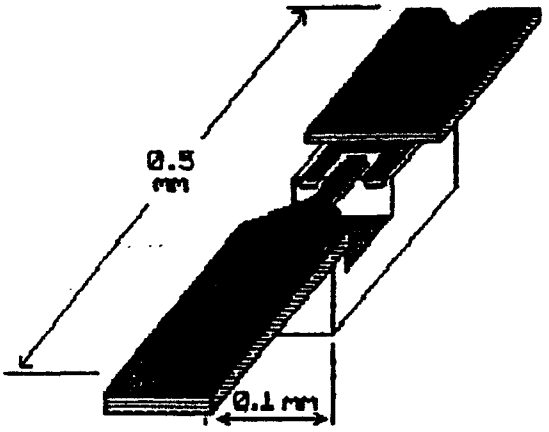

Fig.1.

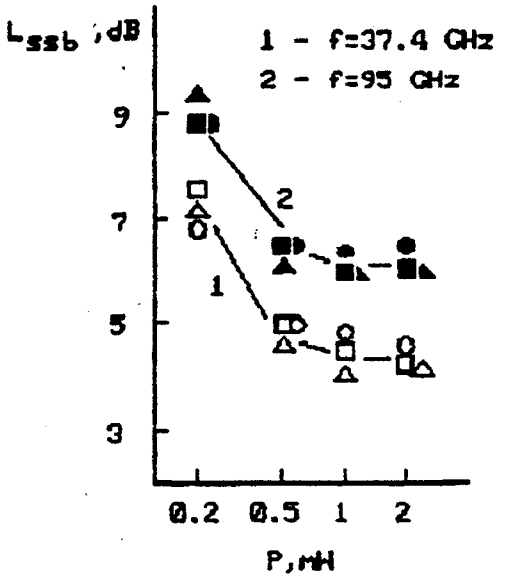

Fig.2.

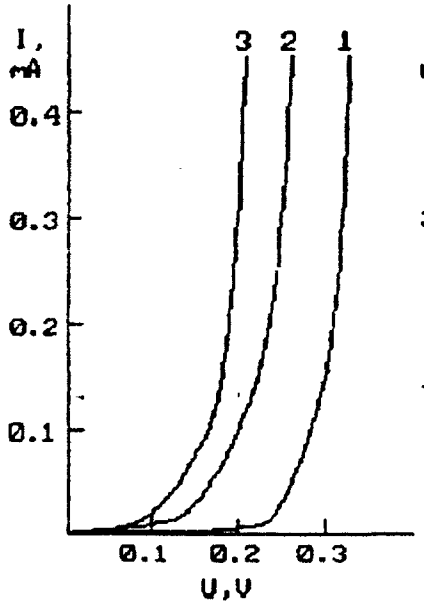

Fig.3

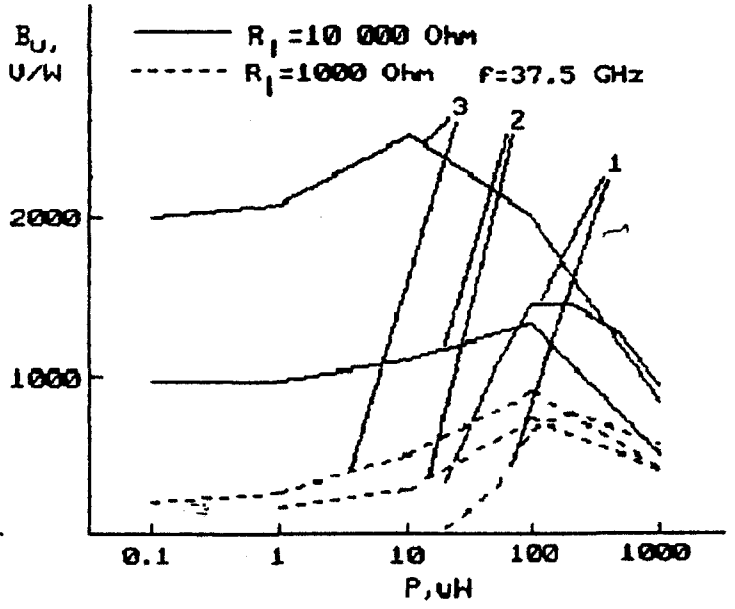

Fig.4.

W1.7

2D ELECTRON GAS AS A FAR-INFRARED AND MILLIMETER-WAVE DETECTOR

V.A.Pogrebnyak, D.D.Khalameida, V.M.Yakovenko
Institute of Radiophysics and Electronics, Ukrainian Academy of Sciences, Kharkov 3I0085 Ukraine

In this paper we present the results of detector effect studies in 2D electron gas. The physical principle of operation of the detector is shown in Fig.I. Far-infrared or millimeter-wave radiation falls on the left side of a two-dimentional n-type sample. Electromagnetic waves attenuate exponentially along 2D sample. On account of wave attenuation the electron temperature gradient ∇T_e arises in the gas. We consider such waves which weakly heat the electron gas: $T_e - T/T \ll 1$, where T_e is electron temperature, T lattice temperature. If we apply magnetic field $\vec{H}$ perpendicular to the electron temperature gradient, then the thermomagnetic electromotive force V arises in the direction, which is perpendicular to ∇T_e and magnetic field $\vec{H}$.

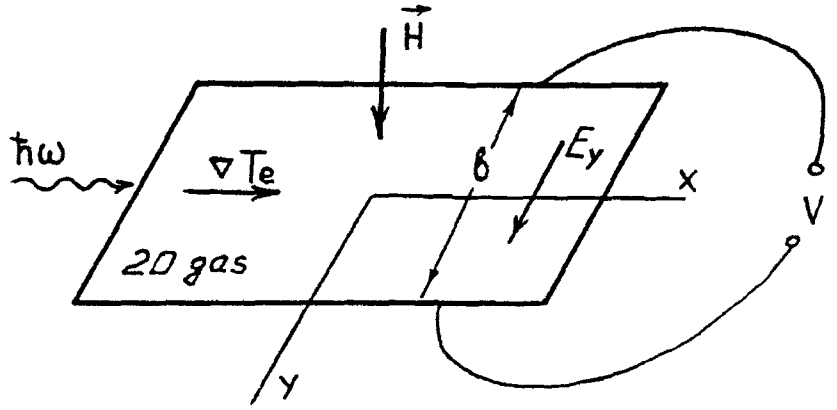

It is the hot electron Nernst effect and accordingly the Nernst electromotive force in 2D electron gas. This phenomenon underlies also the principle of operation of the millimeter-wave bulk semiconductor detector . Theoretical and experimental investigation of this phenomenon in 2D electron gas have been done in the domain of quantum magnatic oscillation of V(H) at Helium temperature.

The Nernst field E_y can be found from the system of such equations and boundary conditions

$$j_i = \sigma_{ik} E_k + \beta_{ik} \nabla_k T_e ,$$
$$j_x = j_y = 0 , \quad \nabla_y T_e = 0, \qquad (I)$$

where j is the current density, σ_{ik} is the conductivity, β_{ik} is the thermodiffusion coefficient. From the equations and boundary conditions one can obtain expression for Nernst field E_y

$$E_y = -\phi \nabla T_e , \quad \phi = -\frac{\sigma_{11}\beta_{12} - \sigma_{12}\beta_{11}}{\sigma_{11}^2 + \sigma_{12}^2} , \qquad (2)$$

where ϕ is the differential Nernst coefficient. All kinetic coefficients are concerned two-dimensional gas, and they are calculated on the basis of quantum transport theory for 2D systems. In the case of strong magnetic field, $\sigma_{12}^2 \gg \sigma_{11}^2$, we obtain

$$E_y = -\frac{2\pi^2 T}{3\sigma_{12}} g(\varepsilon_F) \frac{\partial g}{\partial \varepsilon_F} W(\varepsilon_F) \nabla T_e , \quad V = E_y \cdot b , \qquad (3)$$

where $g(\varepsilon_F)$ is the density of electron states in two-dimensional case, ε_F is Fermi energy, $W(\varepsilon_F)$ is the smooth function, describing quantum diffusion of an electron orbit in the transverse magnetic field. The formula explains the experimental magnetic field dependence of photothermomagnetic voltage in 2D gas at Helium temperature, shown in Fig.2

The experiments were carried out with 2D electron gas which exists at interfaces of blocks boundaries in $Hg_{0.8}Cd_{0.2}Te$ crystal . Equation (3) gives relatinship between the experimental data and physical phenomenon for the case of electromagnetic wave interaction with 2D electron gas. It is seen from Fig.2 that V(H) has alternating sign character in accordance with Eq.(3), because $\partial g/\partial \varepsilon_F \sim A \cos\left(\hbar\omega_H / 2\pi\varepsilon_F\right)$ where $\omega_H = eH/mc$ and $A \gg I$. Such behaviour of V(H) permits to raise the sensitivity of the detector device.

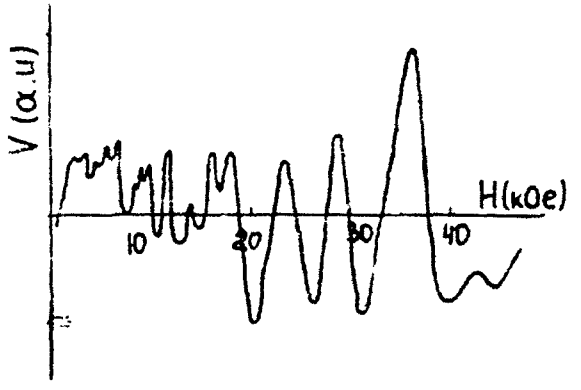

On the basis of these studies it is shown that 2D electron photothermomagnetic effect is a very sensitive method of detection of far-infrared and millimeter-wave radiation.

W2.1

NUMERICAL SIMULATIONS OF OPERATIONAL CHARACTERISTICS OF CUSPTRON TUBE WITH AN ANTI-COAXIAL-MAGNETRON-TYPE WAVEGUIDE CIRCUIT

XIAOMIN WANG, HONG ZHOU, and KANGSHENG CHEN
(Institute of Electrophysics, Zhejiang Uni. Hangzhou, China)

ABSTRACT

A new kind of mm-wave cusptron tube with anti-coaxial-magnetron-type wall structure is proposed. The dispersion equation of its RF circuit and the coupled resonant interaction equations of electrons with the waveguide mode fields are derived. A numerical simulation of the non-linear process is carried out. It is found that in the cusptron tube proposed here, there may exists a new energy conversion mechanism with higher efficiency than that of conventional cusptron. Numerical results also show that the saturation efficiency for this mechanism is not sensitive to the applied dc magnetic field Bo. The saturation efficiency as the function of operation parameters, such as Bo and V, and the geometry of waveguide circuit is numerically illustrated. From that, the optimized design parameters for anti-coaxial-magnetron-type cusptron can be determined.

INTRODUCTION

The cusptron tube is a promising device for efficient operation at higher cyclotron harmonic mode [1]. So far, it has not been well studied to operate the device at millimeter-wave band. The aim of this paper is to extend its operating frequency to millimeter-wave range. Instead of scaling the conventional magnetron-type cusptron (CMT cusptron) down to millimeter-wave band , we propose here a new kind of cusptron tube with slotted coaxial cylindrical waveguide circuit, similar to the anode blocks of anti-coaxial-magnetron, and call it as anti-coaxial-magnetron-type cuptron (ACMT cusptron). Fig.1 shows the cross section of the new waveguide circuit, which can be divided into three regions. Radiation is produced in the outer coaxial cylindrical waveguide region by the negative-mass instability at a high harmonic of the electron cyclotron frequency, using very low applied magnetic field. The electromagnetic power is extracted out axially from the inner cylindrical waveguide cavity which is coupled to the N-slotted resonator. Since the slots are introduced on the outer surface of inner conductor, the maching of this new waveguide circuit seems to be easy.

In this article the non-linear evolution of radiation fields of ACMT cusptron is studied by particle simulation approach [2]. The results show that there may exists a new mechanism for energy conversion by which the ACMT cusptron can provide higher efficiency than CMT cusptron. The functional dependence of the saturation efficiency η on the operation parameters, such as V and Bo, and the geometry of waveguide circuit are numerically illustrated. The results are valuable for determining the optimized design parameters of ACMT cusptron.

CHARACTERISTIC EQUATIONS

The transverse wave number k of the TE mode fields in a N slots' coaxial waveguide is given by :

$$\frac{N\vartheta_o}{\pi}\sum_{n=-\infty}^{\infty}\left(\frac{\sin\Gamma\vartheta_o}{\Gamma\vartheta_o}\right)^2\frac{F_\Gamma(ka)}{F'_\Gamma(ka)} = \frac{J_0(kr)\,Y_0'(kb) - J_0'(kb)\,Y_0(kr)}{J_0'(ka)\,Y_0'(kb) - J_0'(kb)\,Y_0'(ka)} \qquad (1)$$

where the cutoff condition kz=0 is assumed; $\Gamma=m+nN$; m is the mode index; m=0 for 2π mode and m=n/2 for π mode.

$$F_\Gamma(kr) = J_\Gamma(kr) - \frac{J'_\Gamma(kd)}{Y'_\Gamma(kd)}\,Y_\Gamma(kr) \qquad (2)$$

Suppose only the resonant component of the total force is included in the interaction between an axis-encircling electron beam and the mode fields of a slotted cylindrical waveguide, the set of self-consistent characteristic equations for the resonant trajectory of electrons can be derived as :

$$\frac{d\alpha}{dt} = -\frac{\omega E}{c B_o}\,a_{N_o}\,F'_{N_o}(\alpha)\cos(\Phi) \qquad (3)$$

$$\frac{d\Phi}{dt} = -\Delta\omega + \frac{\omega E}{c B_o}\,a_{N_o}\,F_{N_o}(\alpha)\sin(\Phi)\left(\frac{N_o^2}{\alpha^2} + \frac{\Delta\omega}{\omega} - 1\right) \qquad (4)$$

$$\frac{d\gamma}{dt} = -\frac{\omega E}{c B_o}\left(\frac{\Omega_o}{\omega}\right)^2 a_{N_o}\,\frac{\alpha}{\gamma}\,F'_{N_o}(\alpha)\cos\Phi \qquad (5)$$

where N_o is the resonant harmonic number; ω is the eigenfrequency of the empty waveguide; $\alpha=kr$; $a_{N_o}=\sin N_o\vartheta_o/[N_o\vartheta_o F_{N_o}(ka)]$; $\Delta\omega = \omega - N_o\Omega = \Delta\omega_0 + \omega(\gamma-\gamma_0)/\gamma$, and $\Omega=\Omega_o/\gamma=eB_o/mc\gamma$ is the relativistic cyclotron resonance, for N_o-th resonance, $\Omega=\omega/N_o$; Φ is the phase shift between the electrons and the wave fields. (3) and (5) are essentially equivalent due to the relation $\gamma^2=1+(\Omega_o\alpha/\omega)^2$.

To determine the field amplitude E_o self-consistently, (3) and (4) should be coupled to the energy conservation equation, which is given by :

$$n_L\,m\,c^2\,\frac{d\langle\gamma\rangle}{dt} + \frac{1}{2}\,\varepsilon_0\,\varepsilon'\,\frac{d\,E^2}{dt} = 0 \qquad (6)$$

where $\langle\rangle$ stands for an average over the initial random phase distribution of electrons; n_L is the electron density per unit length; ε' is the effective dielectric constant of the waveguide for TE mode which is given by :

$$\varepsilon = \pi\sum_\Gamma\left(\frac{\sin\Gamma\vartheta_o}{\Gamma\vartheta_o}\right)^2\left\{d^2\,\mathcal{F}_\Gamma^{\,2}(kd) - a^2\,\mathcal{F}_\Gamma(ka) - a^2\left(1+\frac{\mathcal{F}_\Gamma(ka)}{ka}\right)\right.$$
$$\left. - \frac{\Gamma^2}{k^2}\left[\mathcal{F}_\Gamma^{\,2}(kd) - \mathcal{F}_\Gamma^{\,2}(ka)\right]\right\}$$
$$+ \frac{\pi^2}{N\vartheta_o}\left[a^2\,\mathcal{G}^2(ka) - b^2\,\mathcal{G}^2(kb) + a^2\left(1+\frac{\mathcal{G}(ka)}{ka}\right)\right] \qquad (7)$$

where

$$\mathcal{F}_\Gamma(kr) = \frac{J_\Gamma(kr)\,Y'_\Gamma(kd) - J'_\Gamma(kd)\,Y_\Gamma(kr)}{J'_\Gamma(ka)\,Y'_\Gamma(kd) - J'_\Gamma(kd)\,Y'_\Gamma(ka)} \qquad (8)$$

$$\mathcal{G}(kr) = \frac{J_1(kr)\,Y'_1(kb) - J'_1(kb)\,Y_1(kr)}{J'_1(ka)\,Y'_1(kb) - J'_1(kb)\,Y'_1(ka)} \qquad (9)$$

The saturation conversion efficiency of the device is given by :

$$\eta = \frac{\varepsilon_0\,\varepsilon'\left(E_{max}^2 - E_{initial}^2\right)}{2\,n_L\,m\,c^2\,(\gamma_0-1)} \qquad (10)$$

where γ_o is the initial relativistic factor of electrons.

Equations (3) and (4) describe the motion of a single electron in the wave fields, and (6) describes the evolution of the self-consistent field driven by the collective response of the electrons. In order to couple them together, a phase average over the single electron motion is necessary. This will be done numerically in the next section, by solving the trajectories of a large number of electrons with random initial phase distribution.

PARTICLE SIMULATION AND NUMERICAL RESULTS

Initially, the actual randomly distributed electrons in the ideal E-layer is assumed to be unperturbed, that is, the electrons are set to be positioned symmetrically about the axis of the waveduide structure, and the energy of each electron is given by a predetermined value resulting from the cathode voltage. With time increment the perturbation in each electron's position is computed by equations (3) and (4), from which the energy for each electron can also be determined. Then the energy, transferred from electrons to the field, can be evaluated through (6) by comparing the resulting average energy with initial average energy of electrons. Next time increment repeats the above procedure.

In the numerical simulation of the operational characteristic of cusptron devices, an ideal E-layer having a constant line density of the typical value $n_L=\pi a^2 n_0=1.6\times10^{10}$ cm^{-1} as the radiation source is used. Three parameters, the ratio a/b of outer radius a to the inner radius b for the N-slotted resonator, the aplied magnetic field Bo and the initial relativistic factor of the electrons, γ_o , will be varied for parameteric study.

Presented in Fig.2 is the functional dependence of the conversion efficiency η on the ratio a/b for both π mode and 2π mode. The results determine the range of a/b value in which the optimized output efficiency can be obtained. It is expected that the output efficiency of the π mode is more than double than that of the 2π mode. And it is of considerable advantages for ACMT cusptron that the efficiency is roughly twice as high as that of the CMT cusptron.

From the polar plot of particle positions and phases at various time step (Not given here for saving space) it shows that there exists another energy conversion machanism in ACMT cusptron, which is not inherent in CMT cusptron. Those electrons located in the retarding field region will lose energy, cycle in smaller radius and meet much stronger retarding field, thus more and more energy could be radiated. While those electrons located in accelerating field region will absorb energy, cycle in larger radius and experience weaker and weaker accelerating field. So only smaller amount of field energy is absorbed. If the operational parameters such as Bo are properly adjusted , those "useless electrons" will finally drift to the retarding region. This effect leads to a more efficient operation.

Unlike the CMT cusptron , Fig.3 shows that the saturation efficiency is not sensitive to the applied magnetic field for ACMT cusptron if Bo exceeds a value which depends on the number of slot cavities N and the ratio a/b. Optimum initial beam energy γ_o, determined by cathode voltage, as a function of the ratio a/b is illustrated in Fig.4. It is found that the optimum voltages for the ACMT cusptron is higher than that in CMT cusptron.

Fig.2-4 are useful for the optimization of design of ACMT cusptron operating at 8mm wave band.

REFERENCE

1. W.Namkung, J.Y.Choe, H.S.Uhm, and V.Avres,Int.J.Electronics, 1988, Vol.65, No.3, 381
2. S.P.Kuo ,K.K.Tiong and P.E.Miller,Phys.Fluids, Vol.31, No.6, 1821, 1988.

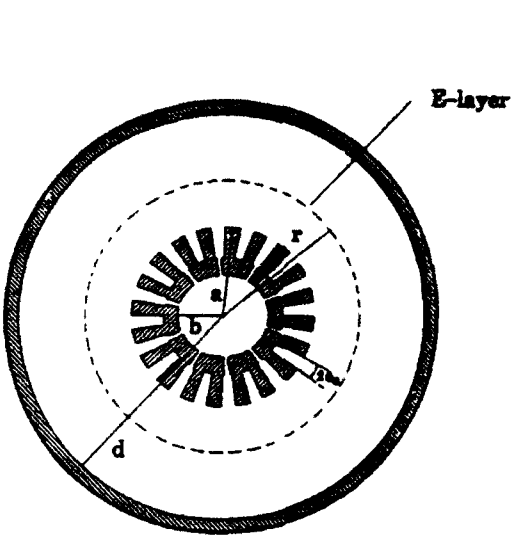

Fig.1 The cross section of the wall configuration for ACMT cusptron

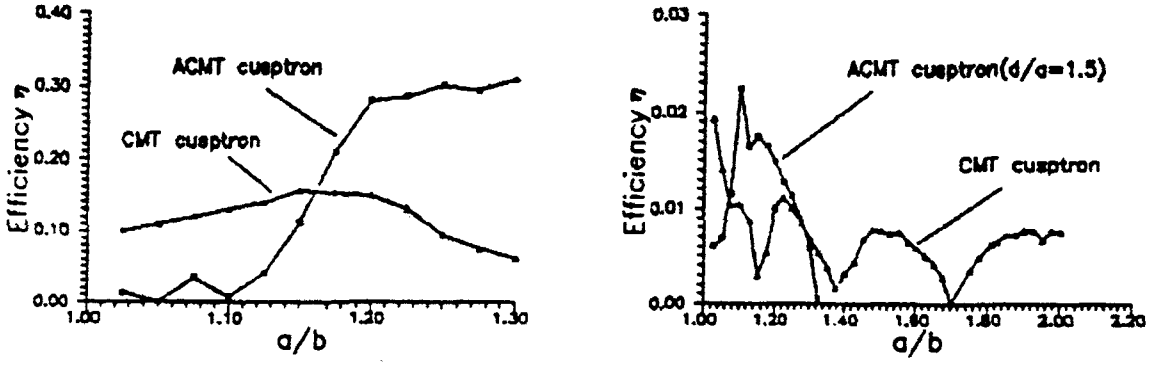

(a) π mode (b) 2π mode

Fig.2 The functional dependence of conversion efficiency η on the ratio a/b (N=20 , λ=8 mm)

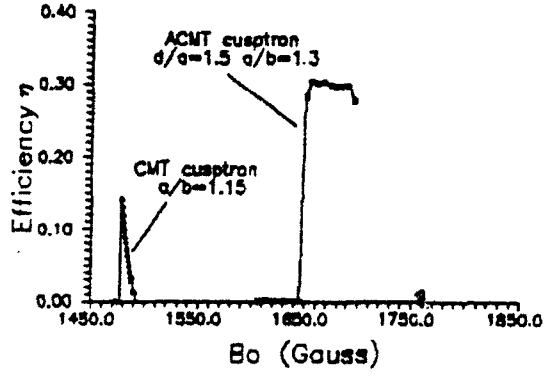

Fig.3 The conversion efficiency η versus applied magnetic field (N=20 π mode λ=8mm)

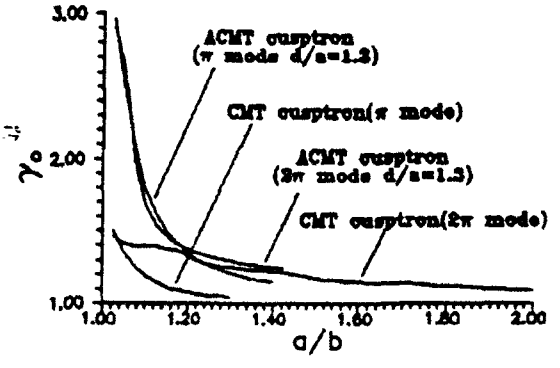

Fig.4 The relativistic factor γ in optimum operation as the function of the ratio a/b (for N=20 λ=8mm)

SIMULATION OF NON-ADIABATIC COLLECTOR FOR GYROTRONS

A.L.Goldenberg, V.N.Manuilov
Institute of Applied Physics of Academy of Sciences
Nizhny Novgorod, Russia

Introduction

Modern nuclear fusion installations need long-pulsed or CW near 1 MW gyrotrons for heating of plasma at electron - cyclotron resonanse frequensies over 100 GHz. One of problems of these tubes is to provide admissible thermal regime of their collectors, that is a sufficient operation surface for a powerful electron beam. Traditional ways of increase in a collector's surfase by means of either increase in its radius or decrease in an angle between its surfase and magnetic field line are associated with the higher requirements for accuracy of mechanical and magnetic axial symmetry, the larger collector's surface is needed .

Principles

Hereinafter a new way of increase in the operation collector's surface is given.It is based on the perturbation of the magnetic field so that on a part of electron trajectories the following condition opposite to the adiabatic one is valid

$$\varepsilon = \frac{h}{d} >> 1 \qquad (1)$$

where h is the electron trajectory pitch ,d - the scale of the magnetic field perturbation. This perturbation can lead to dramatic increase in velocities of cyclotron oscilations in an electron beam up to 10 times or more and to consequent larger length of its sinking in a collector.

Example

Let us consider the collector of a gyrotron at 140 GHz frequency with electron beam voltage 70 kV and its power 1.4 MW.Cavity beam parameters are as follows : pitch-factor g=1.3,beam radius R_0=7.68 mm ,beam width ΔR_0=0.14 mm,current

I=20 A.Magnetic field in the cavity B_0 =5.68 T. The internal radius of a cilindrical collector is chosen 110 mm.The calculated length of the operation area of the collector using the single main coil is about 2 cm at which thermal load of the collector is near 20 kW/cm^2,that is approximately an order over an acceptable value for CW regime.

Magnetic System

According to the idea of considerable increase in gyration velocities of electrons the magnetic field along electron tragectories must contain the region of fast (in scale of an electron trajectory pitch) variation of the angle between a magnetic field line and the axis.This case analogous to the injection of electrons across magnetic field where they obtain some occilation velocities .

The desired magnetic field in a collector region can be formed by means of at least 2 additional coils with opposite partial fields comparable by values with the magnetic field of the main coil in the collector region (Fig 1).

Calculation Results

Providing the condition (1) is valid, the trajectory analysis [1] shows considerable increase in gyration velocities of electrons after the non-adiabatic region (Fig 1).The increase can be so large that some electrons do not reach the collector surfase,being reflected due to the adiabatic increase of obtained gyration velocities .The reflected electrons can not get the cavity as well and undergo several reflections before to get the collector surface .

The increase in gyration velocities does not surely provide sufficient increase in the length of electron's sinking in a collector , L .The reason of this is that after the non-adiabatic region the initial gyration phases of all electrones are close to each other (Fig. 1).In order to increase L ,it is necesary to mix the phases.This can be achieved on rather long electron paths owing to a spread in new obtaned gyration velocities of electrons and corresponding spread of their longitudinal velocities .To provide the phase mixing it is expedient to include into the gyrotron magnet system a third additional

coil forming rather smooth decrease in the magnetic field after the non-adiabatic region (Fig. 2).The optimised by sizes,currents and positions of 3 additional coils,the operation collector length L=23.8 cm.So the found magnetic field distribution allows to increase the collector length L more than 10 times and have the mean collector power load 1.5 kW/cm^2 admissible for CW regime.

REFERENCES

1.A.L.Goldenberg, V.K.Lygin, V.N.Manuilov and oth., "Cyrotron", Gorky, USSR, Inst. Appl. Phys. , 1981, pp. 86-106.

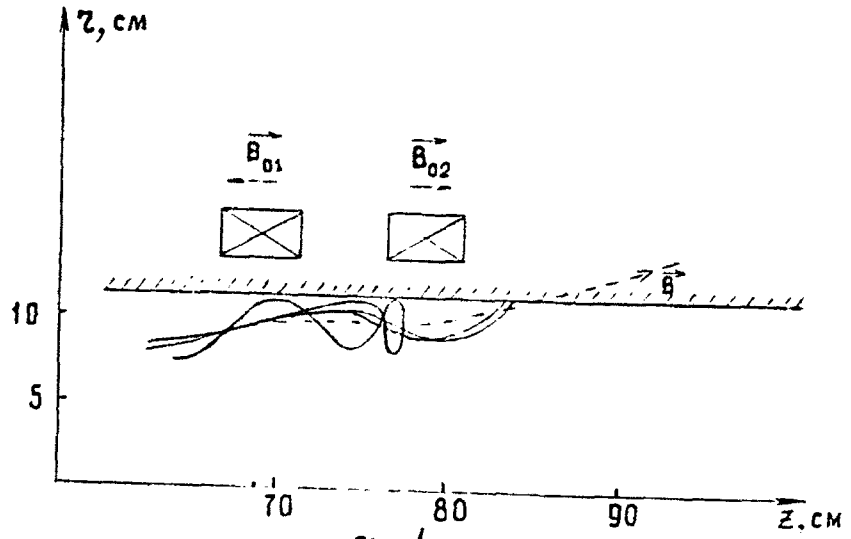

Fig. 1

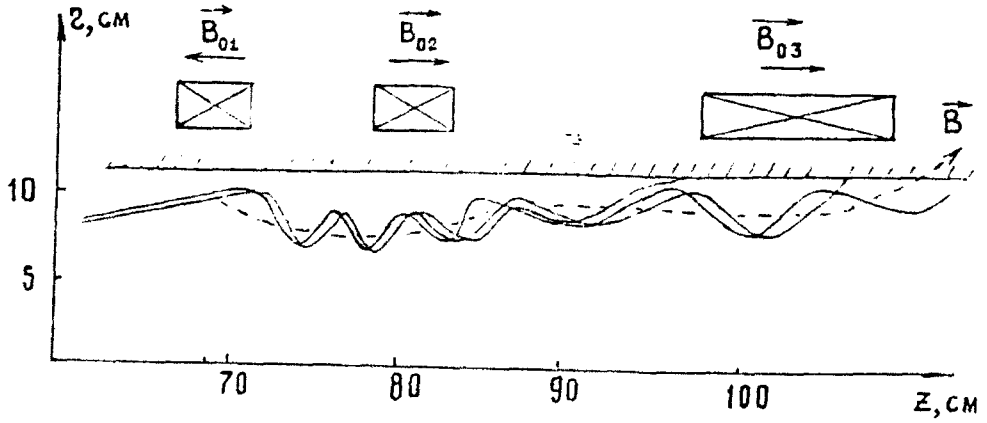

Fig. 2

W2.3

A STUDY OF HARMONIC GYROTRONS WITH TWO STRUCTURES

Li Hongfu, Du Piazhong and Hu JianKai

(Research Institute of High Energy and Microwave Electronics, University of Electronic Science and Technology of China, Chengdu, Sichuan 610054, P. R. China)

ABSTRACT

The interaction between electron beam and RF field in the inner and outer slotted coaxial waveguides is studied on the basis of a study of the multi-conductor structure in this paper. The electron efficiency is calculated numerically at eight harmonic of the electron cyclotron frequency in these structures at f_c=35GHz. The influence of electron velocity distribution in the beam is taken into consideration in numerical calculatron. The results show that the inner slotted structure is good for an increase in the interaction efficiency.

INTRODUCTION

Considerable progress has been made in the last decade in research on and development of gyrotron oscillators. The gyrotyons have been shown to be capable of producing high power millimeter wave radiation with high efficiency. High-power gyrotron oscillators have been used very successfully for plasma start-up and subsequent electron cyclotron resonance heating of tokamak plasmas. However, high-frequency gyrotrons generally require large magnetic fields if they are to operate at the fundamental cyclotron mode. If instead they are operated at harmonic frequencies, the magnetic field can be reduced in inverse proportion to the number of the harmonic. However, when gyrotyon is operating in higher harmonic modes, the electron efficiency decreases with increasing harmonic number, but it increases with increasing beam energy. The demand for high-power high-frequency sources motivates the search for many other novel ways of improving the operation of high farmonic gyrotrons. Further ,it is also desirable that the gyrotrons should be reasonably compact for some applications. In 1981, Destler et al. [1-2] reported the generation of a high-power microwave radiation at the twelfth harmonic by a higy-energy (2Mev) rotating electron beam. This experment featured an innovation interaction structure: a waveguide with a magnetron-type slotted boundary, which was clearly identified as the reason for effective harmonic interaction and good mode selectivity. Further experimental investigations at the University of Maryland have shown that the cusp-injected axis-rotating electron beam in a lower energy regime can also produce microwave radiation efficiently in a magnetron-type structure[3,4]. Both theoretical and experimental works on this type of device have been pursued since that time[5-8]. This device has been called cusptron oscillator.

In this paper, The electron interaction with RF field in the inner and outer slotted coaxial waveguides is investigated at eighth harmonic of the electron cyclotron frequency on the basis of a study of the multi-conductor structure[9-11]. The influence of electron velocity distribution in the cusp-injected axis-rotating beam is taken into consideration . The results show that the inner slotted coaxil structure is of great advantage for electron interaction with RF field, as pointed out in reference 11.

FIELD EQUATION

1 Field Equations in Magnetron-type Structure

The cross section of slotted-wall magnetron cavity and circulating electron beam is shown in Fig1. This structure is cusptron one, it may be considered as a special example of a multi-conductor[19]. The field distributions in region $0 \leqslant r \leqslant r_1$ are given by

$$H_r = \sum_{m=-\infty}^{\infty} E_m \frac{k_r}{\omega\mu_0} \cdot f(\theta_m) \cdot \frac{J_m}{J_{m1}} Sin(\omega t - m\theta) Sin\beta z \tag{1}$$

$$H_\theta = \sum_{m=-\infty}^{\infty} E_m \frac{\beta}{\omega\mu_0} \cdot f(\theta_m) \cdot \frac{J_m'}{J_{m1}'} Sin(\omega t - m\theta) Cos\beta z \tag{2}$$

$$H_z = -\sum_{m=-\infty}^{\infty} E_m \frac{\beta}{\omega\mu_0} \cdot f(\theta_m) \cdot \frac{m}{k_r r} \frac{J_m}{J_{m1}} Cos(\omega t - m\theta) Cos\beta z \tag{3}$$

$$E_r = -\sum_{m=-\infty}^{\infty} E_m f(\theta_m) \cdot \frac{m}{k_r r} \frac{J_m}{J_{m1}} Sin(\omega t - m\theta) Sin\beta z \tag{4}$$

$$E_\theta = \sum_{m=-\infty}^{\infty} E_m f(\theta_m) \frac{J_m'}{J_{m1}'} Cos(\omega t - m\theta) Sin\beta z \tag{5}$$

$$E_z = 0 \tag{6}$$

where

$$J_m = J_m(k_r r), J_{m1} = J_m(k_r r_1)$$

$$f(\theta_m) = \frac{2n\theta_m}{\pi} \cdot \frac{Sin(m\theta_m)}{m\theta_m}$$

$$m = N + 2np \qquad (p = 0, \pm 1, \pm 2\cdots)$$

The characteristic equation is

$$\frac{2n\theta_m}{\pi} \sum_m \frac{J_{m1}}{J_{m1}'} \left(\frac{Sinm\theta_m}{m\theta_m}\right)^2 = \frac{J_{m1}Y_{m2} - J_{m2}Y_{m1}}{J_{m1}'Y_{m2} - J_{m2}'Y_{m1}} \tag{7}$$

where $2\theta_m$ is the angle subtended by each slot, $2n$ is number of slots. N is integer.

2 Field Equations in the Inner Slotted Structure

The cross section of this structure is shown in Fig. 2. Its field distributions are given by

$$H_r = \sum_{m=-\infty}^{\infty} E_m \frac{k_r}{\omega\mu_0} \cdot f(\theta_m) \cdot F(k_r r) Sin(\omega t - m\theta) Sin\beta z \tag{8}$$

$$H_\theta = \sum_{m=-\infty}^{\infty} E_m \frac{\beta}{\omega\mu_0} \cdot f(\theta_m) \cdot F'(k_r r) Sin(\omega t - m\theta) Cos\beta z \tag{9}$$

$$H_z = -\sum_{m=-\infty}^{\infty} E_m \frac{\beta}{\omega\mu_0} \frac{m}{k_r r} \cdot f(\theta_m) \cdot F(k_r r) Cos(\omega t - m\theta) Cos\beta z \tag{10}$$

$$E_r = -\sum_{m=-\infty}^{\infty} E_m \frac{m}{k_r r} \cdot f(\theta_m) \cdot F(k_r r) Sin(\omega t - m\theta) Sin\beta z \tag{11}$$

$$E_\theta = \sum_{m=-\infty}^{\infty} E_m f(\theta_m) \cdot F'(k_r r) Cos(\omega t - m\theta) Sin\beta z \tag{12}$$

$$E_z = 0 \tag{13}$$

where

$$F(k_r r) = \frac{J_m Y_{m2} - J_{m2} Y_m}{J_{m2} Y_{m3} - J_{m3} Y_{m2}}$$

$$F'(k_r r) = \frac{J_m' Y_{m2} - J_{m2}' Y_m}{J_{m2}' Y_{m3} - J_{m3}' Y_{m2}}$$

The characteristic equation is

$$\frac{m\theta_m}{\pi} \sum_m F(k_r r_2) \left(\frac{Sinm\theta_m}{m\theta_m}\right)^2 = \frac{J_{m1}Y_{m2} - J_{m2}Y_{m1}}{J_{m1}'Y_{m2} - J_{m2}'Y_{m1}} \tag{14}$$

CALCULATION RESULTS

At first, let us discuss the electron motion in cusp—injected system. The transition width of magnetic cusp is neglected. The

ideal step—function cusp transition at $z=0$ is shown in Fig. 3. The electron motion in region $z<0$ and $z\geqslant 0$ satisfies:

$z<0$:

$$\beta_{\perp} = 0 \tag{15}$$

$$\beta_{11} = (1-\frac{1}{\gamma_0^2})^{1/2}$$

$z\geqslant 0$:

$$\beta_{\perp 0} = \frac{\eta B_0}{\gamma_0 C} r_0 \tag{16}$$

$$\beta_{110} = \{1-\frac{1}{\gamma_0^2}[1+r_0^2 B_0^2 (\frac{\eta}{C})^2]\}^{1/2} \tag{17}$$

$$\alpha = \frac{r_0 B_0 (\frac{\eta}{C})}{\{\gamma_0^2 - [1+r_0^2 B_0^2 (\frac{\eta}{C})^2]\}^{1/2}} \tag{18}$$

Here, $\beta_{\perp 0}=v_{\perp 0}/C$, $\beta_{110}=v_{110}/C$, $\alpha=\beta_{\perp 0}/\beta_{110}$. Equations (16)—(18) show that $\beta_{\perp 0}$, β_{110} and α are functions of injection radii of electrons in beam.

The electron dynamics are governed by the Lorentz force equation

$$\frac{dP}{dt} = -e[E+V\times(B_0+B)] \tag{19}$$

Equation (19) and field equations (1)—(6) or (8)—(13) are solved numerically to obtain electron interaction efficiency. The electron beam is divided into five layers from inner to outer surface of beam . Every E-layer has its injected radius r_0 and initial α . we calculate arerage efficiency of every E-layer. Finally, overall average efficiency of the electron beam may be evaluated . The numerical results are given in Table 1.

Table 1

	magnetron cavity	inner slotted coaxial cavity
electron beam voltage	50Kv	60Kv
outer E-layer initial r_0	4.37mm	4.77mm
inner E-layer initial r_0	3.77mm	4.37mm
α of outer E-layer	3.1	4.116
α of inner E-layer	1.44	1.95
η_h of outer E-layer	10%	9.0%
η_h of inner E-layer	0.74%	10.3%
overall electron efficiency	6.3%	8.6%
mode of cavity	TE_{811}	TE_{811}
harmonic number	8	8
length of cavity	10λ	10λ

The calculation results show that the inner slotted structure is good for an increase in the electron interaction efficiency η_h. when the electrons lose energy, the Larmor radius will reduce . In a outer slotted structure , the electrons will be further and further away from the slotted boundary, but in an inner slotted structure the electrons will be closer and closer to the slotted boundary, therefore , the electrons will experience a stronger and stronger RF field. There is initial distribution of

α of electrons in the beam. In the magnetron structure the α of outer E-layer is higher than one of inner E-layer, and the RF field experienced by outer electrons is stronger than the field experienced by inner ones, so the efficiency of the outer E-layer is much higher than the inner one. In a inner slotted structure, the α of the outer E-layer is higher than one of the inner E-layer, but the RF field experienced by outer electrons is lower than inner one, Therefore, the efficiency difference between the outer and inner E-layers is not great.

REFERENCES

1 Destler, W. W. et al., Appl. Phys. Lett. 38(1981),570.

2 Destler. W. W. et al, J. A. P., 52(1981),2740.

3 Namkung, w., Phys. Fluids, 27(1984), 329.

4 Chojnacki, E., et al., J. A. P. 61(1987)268.

5 Chu, K. R. et al., Int. J. of IR/MM Waves, 5(1984), 37.

6 Namkung, W. et al., Int. J. of Electronics. 66(1986), 381.

7 Tiong, K. K., Kuo, S. P., Int. J. of Electronics, 65 (1988), 397.

8 Tiong, K. K., Kuo, S. P., Int. J. of Electronics, 70 (1991), 815.

9 Li Hongfu, Liu Shenggang, J. of Chengdu Institute of Radio Engineering, 16(1987), 357.

10 Li Hongfu, Xu Fengling, Liu Shenggang, Int. J of Electronics. 65(1988), 409.

11 Li Hongfu, Li Xiang, Int. J. of Electronics, 70(1991), 213

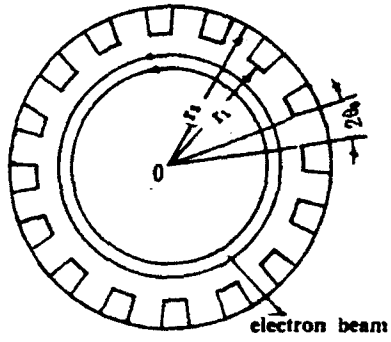

Fig. 1 the cross section of magnetron-type structure

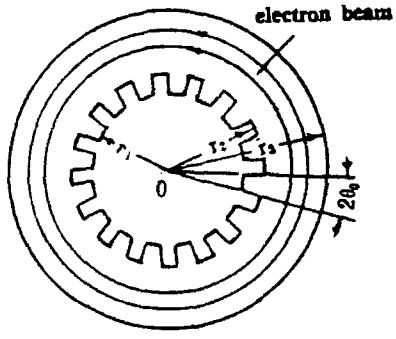

Fig. 2 the cross section of inner slotted structure

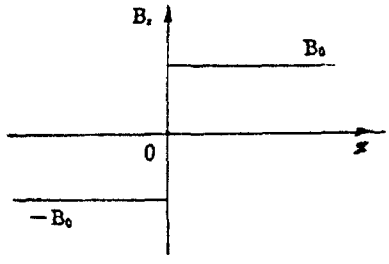

Fig. 3 the distribution of magnetic cusp system

W2.4

The Helical Čerenkov Effect and Harmonic Emission in a Medium

Josip Šoln

Harry Diamond Laboratories
2800 Powder Mill Road
Adelphi, Maryland 20783
USA

Summary

The S matrix, in which the photon propagator incorporates index of refraction n (which may depend on the radiation frequency), is used to describe the spontaneous emission in a uniform magnetic field with a dielectric medium. The important ingredient in the S matrix is the Fourier transform of the electron current density which, in turn, is determined by the electron helical trajectory in a uniform magnetic field (in a dielectric medium). Regardless of what the dependence of n is on the radiation frequency, one can, by utilizing the customary definition of Bessel functions, expand the Fourier transform of the electron current density into a Fourier-like series in which there formally to each term corresponds a harmonic index, m. For sufficiently long interaction time T (or interaction length L) one finds that the expression for the angular-spectral energy distribution can be written as a sum over the harmonic angular-spectral energy distributions (each being associated with harmonic index m).

The actual spontaneous emission can be split into two "branches": a vacuum branch and a Čerenkov branch. These are distinguished by $nv_o < 1$ and $nv_o > 1$, respectively. Here, v_o and $v_\perp$ are parallel and perpendicular components of the electron velocity with respect to the uniform magnetic field, respectively. The vacuum branch is associated with harmonic indices satisfying $m \geq 1$ (the backward Čerenkov branch) and $m \leq o$ (the forward Čerenkov branch). The $m = o$ term in the expression of the angular-spectral energy distribution corresponds to the new effect: a helical Čerenkov effect.

The helical Čerenkov effect, unlike the usual Čerenkov effect, depends on the radius of curvature of the electron trajectory which is measured in the plane perpendicular to the direction of the electron guiding center. For rather energetic electrons, 1 MeV and above, this effect is the strongest when the radius of curvature is comparable to the radiation wavelength in the medium. The longer the radiation wavelength is, the easier it is to observe the helical Čerenkov effect with higher energy electrons. Specifically, in water and in the visible spectrum (n = 1.33) the magnetic fields of the order of 30 T would be needed to observe this effect. However, in the microwave end of the spectrum and in the medium with n = 1.5, this effect is observable with magnetic fields of only about 1 T. As to the lower energy electrons, say below 0.5 MeV, we argue that the effect should be observable in water in the visible spectrum with magnetic fields of about 4.5T.

Finally, we find that as long as index of refraction n is a slowly varying function of the radiation frequency (in some range of frequencies), the spontaneous emission may go into a large number of harmonics for either of the two branches. Specifically, for given radiation angle θ, measured with respect to the direction of the uniform magnetic field, to each harmonic index there corresponds a radiation frequency with the harmonic angular energy distribution. The sum of harmonic angular energy distributions gives the desired (total) angular energy distribution. Choosing the magnetic field of 4 T, an interaction length of 100 cm, $\theta = 0.1$ rad, $v_o = 0.63$, $v_\perp = 0.6$, and $n = 1.4$, we find that there are 37 significantly different from zero angular energy distributions for the spontaneous emission into the fundamental and harmonic frequencies (all occurring in the vacuum branch); the total angular energy distribution is 4.16 eV in this case. If the spontaneous emission is occurring in a vacuum ($n = 1$) instead of a dielectric, we determine that the total angular energy distribution is just 0.03 eV. We see that the presence of the dielectric medium increased the energy of the spontaneous emission at $\theta = 0.1$ rad by more than 138 times.

SUBMILLIMETER CYCLOTRON RESONANCE LASERS AND THEIR APPLICATIONS

Yu.B.Vasilyev, Yu.L.Ivanov, S.D.Suchalkin
AF Ioffe Institute, Academy of Sciences, 194021, St.Petersburg, Russia

1. Cyclotron resonance lasers.

The tunable cyclotron resonance (CR) lasers that have been made recently are perspective devices for submillimeter spectroscopy [1-3]. The lasers are single germanium crystals in the form of parallepipeds with a typical size of 4x5x20 mm^3 supplied with ommic contacts and provided by an outer Fabri-Perot cavity. All the system is maintained in a superconducting solenoid at liquid helium temperature. The laser operation is based on the property of a hot hole system in germanium to produce the population inversion of light hole Landau levels in strong crossed electric and magnetic fields. The emission spectrum has a single line of 0.2cm^{-1} wide, which can be continuously tuned in the range from 110 to 360 μm (frequency from 28 to 91 cm^{-1}). The radiation power of the pulse is 0.5 - 1.0 W and the pulse duration is 0.1-0.5 μs. The laser is small enough to be placed in a standard helium transport cryostat which permits CR laser application outside the laboratory, for example, in a vehicle. Continuously tuning in a wide frequency range provides a unique possibility for laser application in atmospheric monitoring, quality tests of semiconductor materials, in research, etc. In this paper we demonstrate a possibility of using CR lasers for solid state spectroscopy.

2. Shallow impurity spectroscopy.

In this section we present CR laser applications to shallow impurity investigation with references to n-GaAs and p-Ge. Photothermal ionization spectra were obtained by sweeping the laser frequency. Figure 1 shows the photoconductivity spectrum of p-type Ge with the carrier concentration of $N_a - N_d = 1.5 \times 10^{11}$ cm^{-3} at 7.3 K. Identification of impurities in Ge was made by comparising the peak frequency in the spectrum with the catalogue data. Note that the laser emission was weakened by 2 orders to avoid the spectrum distortion. The signal/noise ratio was more than 100. The spectra of high purity epitaxial GaAs with a residual impurity concentration of $N_d - N_a = 10^{12} cm^{-3}$ at 4.2 K are shown in figure 2 without (1) and with (2,3)

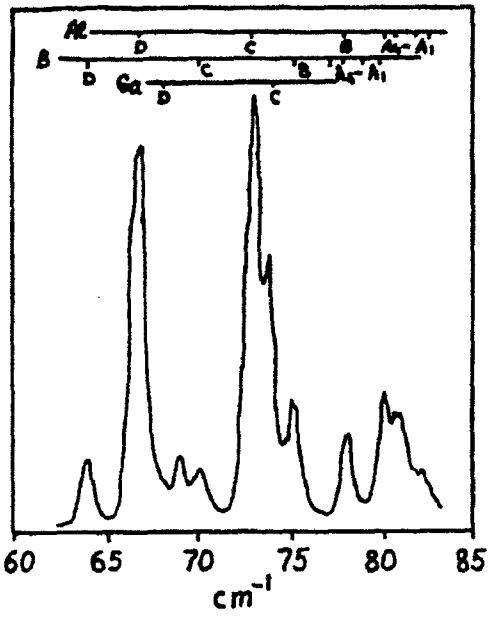

Fig.1. Photoconductivity spectrum of p-Ge at 7.3 K.

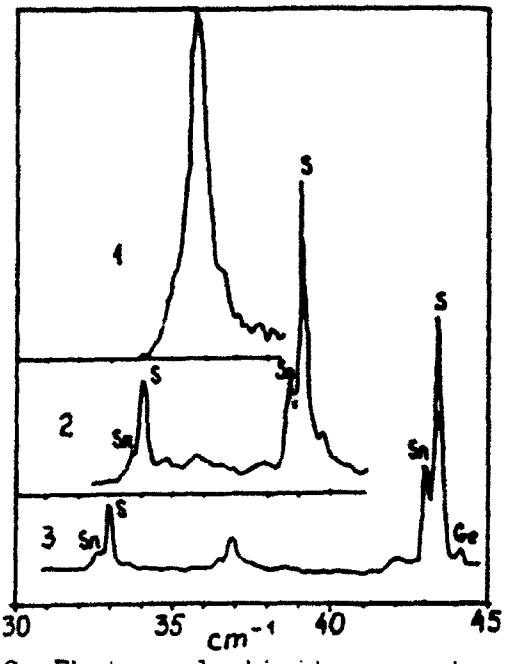

Fig.2. Photoconductivity spectrum of high purity n-GaAs at different magnetic fields: 1.B=0, 2.B=0.33T, 3.B=0.67T

magnetic field. All the curves for n-GaAs were obtained at additional intrisic illumination. The impurities were identified from the position of the photoconductivity peaks associated with the 1s -2p_ transitions. The impurity species responsible for these peaks are indicated in figure 2.

3. Hot hole cyclotron resonance in germanium.

Spectra of the cyclotron absorption and amplification in the germanium light hole subband in strong crossed electric and magnetic fields are shown in figure3. The experiment was performed at fixed laser frequency with the sample magnetic field sweeping at different values of the sample electric field. The absorption line has a clearly pronounced structure associated with transitions between the nonequidistant Landau levels. Four well-defined peaks can be identified at the laser frequencies more than 75 cm^{-1}. As the electric field increases, the absorption peaks shift up the magnetic field axis and their intensities change. Besides, the first absorption peak is replaced by an

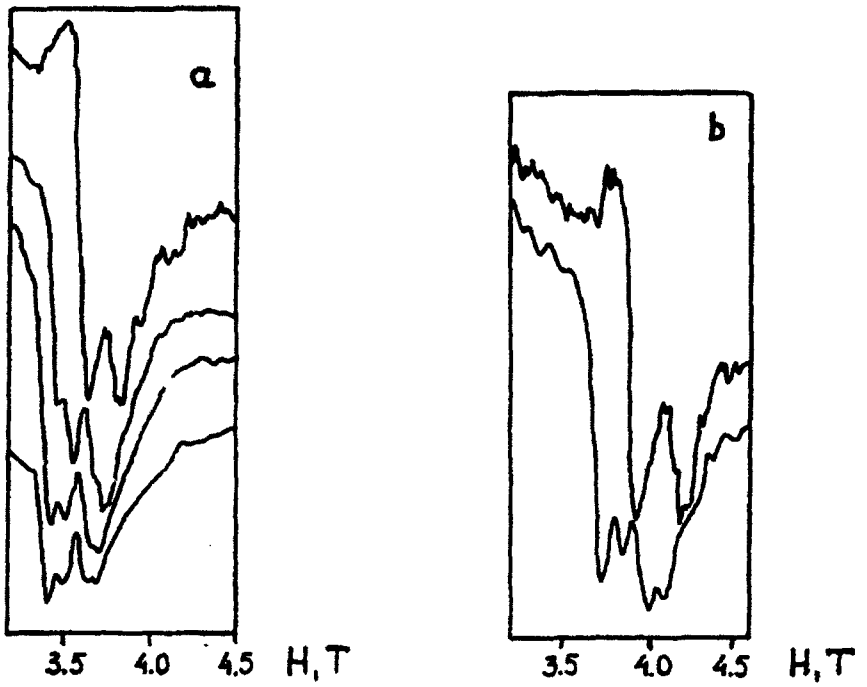

Fig.3. Transmission of the 71.1 cm^{-1} (a) and 77.2 cm^{-1} (b) lines of CR lasers at different electric fields, kV/cm: a) 1-0.7, 2-1.2, 3-2.4, 4-5.0, b) 1-1.08, 2-5.0

amplification peak.The strong shifting of the absorption peaks with the electric field is connected with different values of the Stark-effect for each low Landau level of the light holes. We can conclude from these data that the inversion in germanium occurs only within one Landau level pair which has the highest separation at a given magnetic field. Since at weak electric field the absorption maximum refers to the first peak, we may suggest that it is due to the transitions between the first and the second Landau levels. At a high electric field there is an amplification between the same levels. Note that several absorption peaks due to the cyclotron transition of the light holes have been resolved for the first time.

4. 2D semiconductor structure studies.

Submillimeter cyclotron lasers can be used for cyclotron absoption studies of 2D semiconductor structures. Measurements were made at a fixed laser frequency by tuning the sample magnetic field. Wedged samples were used to avoid lineshape distortion due to multiple reflection. The samples studied were high mobility GaAs - AlGaAs

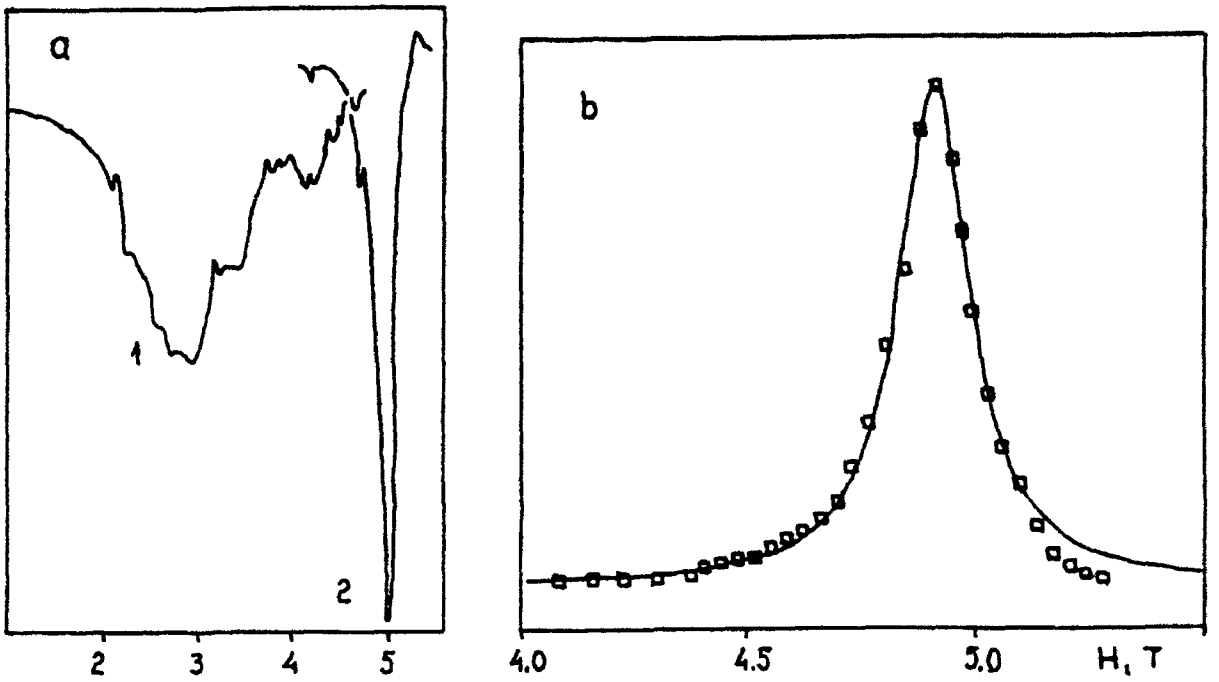

Fig.4. a) Transmission of 148 μm line in a 2D GaSb-InAs-GaSb system (1) and GaAs-AlGaAs heterostructure (2)
b) Cyclotron absorption in a GaAs-AlGaAs heterostructure: squares - experiment, solid - Drude model with the fitting parameters $\tau = 10^{-11}$s, $m/m_0 = 0.067$

heterostructures and single 100 A GaSb-InAs-GaSb quantum wells, with electron densities 4.0×10^{11} cm^{-2} and 9.6×10^{11} cm^{-2}, respectively. Typical magnetotransmission spectra for a 2D electron gas in a GaAs-AlGaAs heterojunction and semimetallic GaSb-InAs-GaSb layer are shown in Figure 4. The spectra reveal the specific features of 2D absorption, such as a shift of the line position in a tilted magnetic field and quantum oscillations. The data allow one to define, with high accuracy, the effective mass and relaxation time by means of computer fitting based on the Drude model.

REFERENCES

1) Vasilyev Yu.B., Yu.L.Ivanov: Proc. the 18th ICSP, 1986, p.1659.
2) Unterrainer K., et al.: Solid-State Elec.,1989, vol.32, 1527.
3) Ivanov Yu.L., et al.: JETP Lett., 1991, vol.53, 493.

W2.6

PRODUCTION AND STUDY OF AXIS-CIRCLING ELECTRON BEAMS FOR PENIOTRONS

V.D.Yeremka
Institute of Radiophysics and Electronics
Academy of Sciences of Ukraine
12, Acad.Proskura st., Kharkov 85, 310085, Ukraine
I.I.Golenitskiy, B.C.Djubua, O.W.Evtushenko, V.P.Sazonov
R & P Corp. Istok, Fryazino, Moscow region, 141120, Russia

The gyrodevices with peniotron mechanism of interaction are well-known /1-3/. In last years the results of the theoretical study of peniomagnetrons with throghout gyroresonance /4/, autoresonant peniotron generators and amplifiers of MM and subMM wavelengths at the harmonics of cyclotron frequencies /5-8/ have published. Power performancies of peniotrons to a large degree depend on parameters of electron-optical system /3/. Systems with partial shielding and compression of the beam in a region of the gun are the most economical and effective. Diode and triode constructions of such guns were originally described in /9,10/ and then in /3/.

In this paper the results of computer simulations of the triode gun /9/ forming the mono-pipe electron flow for the amplifier peniotron at the higher harmonics of cyclotron frequency working in the autoresonant regime at the frequency of 50 GHz are cited /4/ (Fig.1).

According to Bush' theorem $\theta = (1-\psi_c/\psi)\omega_c/2$ the encircling of mono-pipe flow around the axis of system with cyclotron frequency $\omega_c = \eta B$ is provided at the flows of magnetic field induction ψ_c at the cathode and the one in the opposite direction. If radial components of velocity is neglected ($V_r=0$) and taking into account that in this case the angular electron velocity equals to $V_\varphi=\omega_c D/2$, correlation $D_c^2 = 4{,}55\ 10^{-11} UW_\varphi/|BB_c|$ connecting the middle diameter of the flow in the interaction space (D), magnetic field induction at the cathode (B_c) and the one in the interaction space (B), interaction space potential (U) and relative value of rotative energy of the flow $W_\varphi = V_\varphi^2/(V_z^2+V_\varphi^2)$, follow from the low of conservation energy. The middle

equilibrium diameter of flow in the interaction space at the presence of intensive field at the cathode defined by the known correlation $D = D_c(B_c/B)^{1/2}$. In order to provide small spreads of rotative energy of electrons and required current density at the cathode, the width of annular emitter must be far less the middle cathode diameter ($\Delta/D_c << 1$).

Cited analytical correlation are basis criterions for a choice of the parameters of triode gun, forming large-orbit mono-pipe electron flow with desired level of rotative energy. Realization of these criterions is archieved by the following computer calculations of the gun and magnetic system, matching of the gun with the magnetic field in interaction space on perpose to decreasing of radial pulse of the flow.

According to the findings of computer calculations the gun forms the beam with small spreads of rotative velocity and power of electrons (2% and 6% correspondently) at the next parameters and basis geometrical dimentions of the constractions (Fig.2):

accelerating voltage	6 kV
first anode potential	2,4 kV
beam current	260 mA
beam microperveance	0,588$\mu A/V^{3/2}$
middle diameter of electron flow	1,4 mm
electron flow thickness	0,4 mm
diameter of floating-drift channell	2,6 mm
middle diameter emitter	5,2 mm
emitter width	0,2 mm
middle current density on the cathode	10 A/cm^2
transversal velocity to longitudinal velocity ratio	1,6
relative power of flow rotation with the cyclotron frequency	0.7

Desired parameters of the emitter are realised in spetially designed construction of metal-porous cathode with the longevity which is not less 1000 hours at the permissible current density which is not more 30 A/cm^2. In order to create required distribution of magnetic field induction at the axis of system, providing the throughout gyroresonanse condition, magnetic system of alloy of samarium and cobalt is used. Experimental curve of

distribution of longitudinal component of magnetic field at the axis of system is shown in Fig.3. Value of beam transmission to the collector which was measured is 67%, approximately corresponds to the level of beam transmission in a diode gun. Reasons of the decreasing of beam transmission were determined.

REFERENCES

1. Gaponov A.V., Yulpatov V.K. Interaction of closed electron beams with electromagnetic field in empty resonators//Radio Enginering and Electronic Physics.-1962.-N.2>-PP.631-642.
2. Yamanouchi K., Ono S., Shibata Y. Cyclotron fast wave tube. The double ridges travelling wave peniotron //Microwave Tubes.Proc.of the 5th Int.Congr./Paris, Sept.,1964/New York and London:Acad.Press.,1964.-PP.96-102.
3. Dohler G. Gallagher D., Scafuri F., Moats R. Peniotrons of mm wave frequencies//XII International Conference on Infrared and Millimeter waves.Lake Buena Vista (Orlando), Flo, Dec.14-18, 1987. Conf.Dig. New York, N.Y.-1987.-PP.242-243.
4. Yeremka V.D.,Zhurachovskiy V.A.,Shestopalov V.P. Large-orbit peniotron with the throughout gyroresonance//Radio Enginering and Electron Physics.-1989.-v.34.N.9.-PP.1900-1907.
5. Baird I.M., Barnett L., Grow R., Preudenberg R., 1987. Harmonic Auto-Resonant Peniotron Interaction//I.E.D.M. Technical Digest, Washington, D.C., PP.913-916.
6. Yokoo K., Sato N., Ono Sh. Auto-resonant peniotron oscillator (ARPO) for generation of millimetre and submillimetre waves// Int.J.Electronics.1990.Vol.68.N.3.PP.461-470.
7. Yeremka V.D.,Zhurachovskiy V.A., Kovalenko A.M. Nonlinear analytic theory of auto-resonance peniomagnetron//I.C.M.F.I.90 Supplementary Conference Digest, Beijing, China, PP.60-63.
8. Yeremka V.D., Zhurakhovskiy V.A., Kovalenko A.M. Autoresonance peniomagnetron with spreads and unhomogeneities//I.C.M.W.F.I. 90.-Supplementary Conference Digest,Beijing,China.PP.52-55.
9. Golenitskiy I.I., Develeva A.P., Sazonov V.P., Anur'ev V.S., Evtushenko O.V. Electron gun for RF devices. Pat.N 1029783 (USSR) H01J 23/06, 1981.

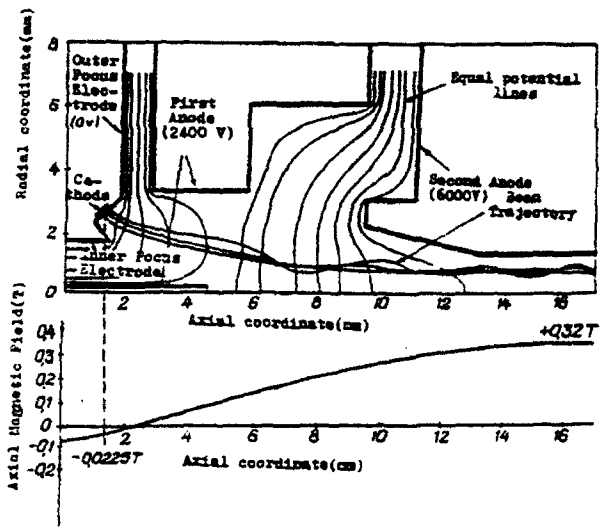

Figure 1.Geometrical arrangement of the triode gun with electron trajectories potential lines and the axial magnetic field

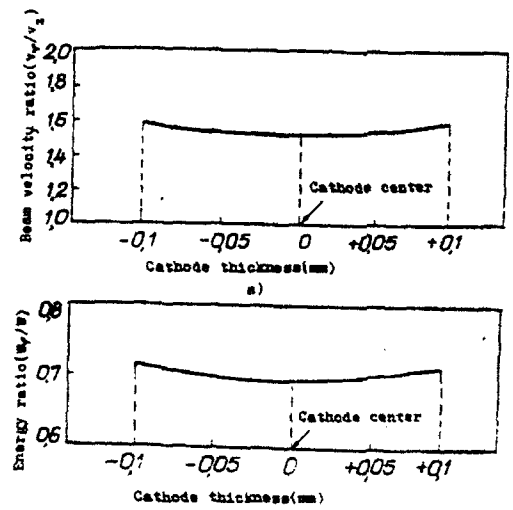

Figure 2.The dependence of the beam velocity ratio:a) and the energy ratio(b) on the cathode thickness

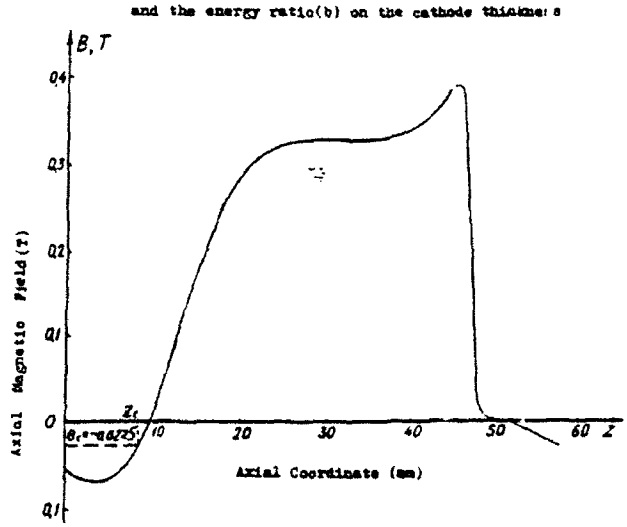

Figure 3. Axial distribution magnetic field

W2.7

POWER AND BAND CHARACTERISTICS OF AUTORESONANT AMPLIFIER-PENIOTRON

V.D.Yeremka,V.A.Zhurakhovskiy,
Institute of Radiophysics and Electronics
Academy of Sciences of Ukraine
12, Acad.Proskura st., Kharkov 85, 310085, Ukraine

Domination of peniotron mechanism of electron-wave interaction, which is always present in gyrodevices, can be provided by corresponding choice of initial condition /1/. In the case of ideal mono-pipe beam peniotron mechanism of interaction in comparison with gyrotron mechanism is characterized by the absence of electrons with "bad" phases, less influence of spreads of guiding centers, axial velocities of electrons on power characteristics of device at higher harmonics of the cyclotron frequency.

Autoresonant peniomagnetron in which mono-pipe beam interacts in homogeneous magnetic field with the electromagnetic wave, propagating with the phase velocity $V_{ph}=C$ (C is the light velocity in vacuum) in electrodynamic system, demonstrates high efficiency of power exchange in the regime of throughout cyclotron gyroresonance /2/. It is stipulated by the power equivalence of nonsinchronism of rotation of the working wave and beam, when the phase of field in the frame of moving electrons takes succesion of values from 0 to 2π excepting in this way the influence of initial phases of particles on power characteristics of interaction.

In that work in the assumption of the absence of spreads of coordinates and velocities of electrons, the influence of space charge and dispersion of electrodynamic system nonlinear self-consistent theory of autoresonant amplifier peniomagnetron in the band of near-resonant frequencies defined by the parameter

$$\mu = \left(\frac{\omega}{\omega_e}\right) - 1 \qquad (1)$$

where ω is circular frequency of the field, ω_e is "sinchronous" frequency connected with beam parameter by the gyroresonance condition

$$\omega_e = - \frac{n\,\Omega}{\gamma(1-\beta_z)}\,, \quad n = 1,2... \qquad (2)$$

is deduced . In correlation (2) γ is the relativistic factor, $(-\Omega)$ is cyclotron frequency, β_z is longitudinal electron velocity rated to C.

Self-consistent motion of magnetoguided electron rotating with cyclotron frequency in the field of going one's way T-wave is described by the next system of equations:

$$\frac{dR}{dt} = \frac{e\,A\,s\,(r/a)^n}{m\,\Omega}\sin\psi \qquad (3)$$

$$\frac{dr}{dt} = - \frac{e\,A\,s\,(r/a)^n}{m_e\,\Omega}\left(\frac{nR}{r}\right)\sin\psi \qquad (4)$$

$$\frac{d\gamma}{dt} = \frac{e\,A\,s\,(r/a)^n\,R\,\omega_e}{m_e\,c^2}\sin\chi \qquad (5)$$

$$\frac{d\mathcal{R}}{dt} = \mu\omega_e s - \frac{e\,A\,s(r/a)^n R}{m_e\,\Omega}\left[\left(\frac{n^2}{r^2}-\frac{1}{R^2}\right)+\frac{U\omega_e\Omega}{2c^2\gamma\,(1+U(1-\gamma/\gamma))}\right]\cos\chi \qquad (6)$$

where $s = (1-\beta_z)$, $U = P_o/Q_o$, $\chi = p-n\alpha-\phi+D$ is effective phase of forces of RF-field, $p = \omega(t-z/c)$, $A = \mathrm{mod}(E)$, $D=\arg(E)$, E is slowly changing complex amlitude E_φ of strength of azimuthal component of electric field at arbitrary radius by formula

$$E_M = |E|\left(\frac{\rho}{a}\right)^n$$

where (R,Φ) are polar coordinates of the guiding center of electron orbit, (r,α) are polar coordinates of electron in the frame connected with the guiding center (Fig.1); e, m_e are charge and rest mass of electron, consequently, P is power of the beam of particles accounting rest energy transferring by them, Q is power of the working wave; o is index of initial values.

The system of differential equations (3)-(6) has three integrals of motion:

$$r^2 + nR^2 = \mathrm{const} \qquad (9)$$

$$r^2 + \left[\frac{2nc^2}{\Omega\,\omega_z}\right]\gamma = \mathrm{const} \qquad (10)$$

$$\frac{e}{m_e\,\Omega}\,A\cos\psi\;nR\left(\frac{r}{a}\right)^n - \frac{\mu\omega_e r^2}{\alpha} = \mathrm{const} \qquad (11)$$

It follows from correlation (11) that in the case of beam coaxial electrodynamic system ($R_o=0$), when

$$\cos\psi = \frac{\mu\omega_e m_e\,\Omega(r^2-r_o^2)}{2eAnR(r/a)^n} \qquad (12)$$

interaction of electron with electromagnetic wave doesn't depend on its initial phase and is defined only by the field characteristics.

In the gyroresonance regime ($\mu=0$) effective phase of forces of electromagnetic wave remains the same in the process all over the motion of particle, leading in the final to its full transversal braking. In the case of realization of initial condition $\gamma_o s_o = 1$ owing to formula (7) simultaneous full longitudinal braking of particle also realized. Maximum electron efficiency in the gyroresonance regime is defined from the integral of motion (10)

$$\mathcal{E}_m = \frac{r_o^2\,\Omega^2}{2\gamma_o s_o(\gamma_o-1)} \qquad (13)$$

Tuning out from the resonance regime ($\mu \neq 0$) leads to slow change of value ψ and particle leaving of braking phase of field forces in which it was initially according to formula (12). Maximum of transferring of electron power to RF field is achieved now in the point, where $\sin\psi = 0$, after that the particle begins to accelerate increasing its energy of electromagnetic field.

In Fig.2 maximum electron efficiency versus the frequency parameter μ/M at $A_0 = 1{,}5\times10^4$ V/m, $\gamma_0=1{,}02$, $U = 10^5 \times M^2$, $n = 10$, $\beta_{z0} = 0{,}096$ is shown. As it follows from the graph in Fig.2 increasing of the band of maximum electron efficiency in M times requires increasing of device current is proportionate to excitation parameter U at the constant value of initial wave amplitude A in M^2 times.

$$\left(\frac{dy}{dt}\right)^2 = \frac{(1-hy^2)^r(1+\delta y^2)-by^2}{\nu - \Omega^2}$$

$$y = \sqrt{x}\,,\quad x = -z\frac{eA_0(r_0/a)^n\sqrt{n\gamma_0 s_0}}{m_e\sqrt{2}\,c^2(\gamma_0-1)^{3/2}}\,,\quad h = \frac{2n^2(\gamma_0-1)c^2}{\omega^2 r_0^2\,\gamma_0 s_0}\,, \qquad (14)$$

$$\nu = \frac{\gamma_0\beta_{z0}}{\gamma_0 - 1}\,,\quad \delta = \frac{\gamma_0 - 1}{\gamma_0}\,,\quad b = \frac{\mu^2\omega_e^2\,\Omega\,c^2 m_e}{2e^2A_0^2\,(r_0/a)^{2n}}\,(\gamma - 1)$$

In the gyroresonance regime at the condition $\gamma_0 s_0 = 1$, when equation is success to solve analitically for some values n. In particular (figure indexes correspond to number of the cyclotron harmonic

$$x_1 = \frac{\sqrt{1+\delta}}{\delta}\left[F(\zeta,V)-E(\zeta,V)\right] + \sqrt{x}\sqrt{\frac{1-x}{1+\delta x}}$$

$$x_2 = \delta^{-1}\mathrm{sh}^2 x\sqrt{\delta}\,,\quad x_3 = \frac{1}{1+\delta}\,\frac{\mathrm{sn}^2(x\sqrt{1+\delta},V)}{\mathrm{dn}^2(x\sqrt{1+\delta},V)} \qquad (15)$$

$$x_4 = \frac{\mathrm{th}^2 x\sqrt{1+\delta}}{1+\delta(1-\mathrm{th}^2 x\sqrt{1+\delta})}\,.\quad x_5 = \frac{1}{\sqrt{1+\delta}}\left[F(\zeta,V)-E(\zeta,V)\right] + \sqrt{\frac{x}{(1+\delta x)(1-x)}}$$

where $\zeta = \arcsin\sqrt{\frac{x(1+\delta)}{(\delta x+1)}}$, $V = \sqrt{\frac{1}{1+\delta}}$, $F(\zeta,V)$, $E(\zeta,V)$ are elliptical integrals of the first-kind and second kind, respectively

Investigation of band characteristics of autoresonant peniotron carries out by the means of the numerical solution of equation (14). In Fig.3 electron efficiency versus the frequency parameter μ/m is shown for the same values that in Fig.2. Sinchronous efficiency was 40%. Half-power band width is $\approx 0{,}2M\%$ and is defined, analogously to the case of maximum efficiency, by beam current. Decreasing of the band at the decreasing of beam current is explained by the increasing of the number of electron turns N, which are necessary to achieve "sinchronous" value of electron efficiency (Fig.4) because of that the resonant characteristics of examined gyrodevice shown more sharply.

In the conclusion we give summary data of the example of cal-

culations of nonrelativistic autoresonant peniotron-amplifier at the 10th cyclotron harmonic. The beam is electron mono-pipe, gun voltage is 10 kV (γ_0=1,02), initial pitch-angle is 60°, current I = 0,3A, initial radius is 1 mm, number of electron turns N = 5. Working wave is T-wave. "Sinchronous" frequency of electromagnetic field is 95 GHz, physical length of interaction space L = 20,5 mm, input power Q_0 = 0.1 W, sinchronous amplification σ_e=40eV, output power Q=1 kW. Regime is continuous [illegible] one, order of gyroresonance n = 10, "sinchronous" electron efficiency $\varkappa_e$=33%, half-power band width is 2%, introduction of magnetostatic field B is 0,3 T.

REFERENCES

1. Gaponov A.V.,Yulpatov V.K. Interaction of the closed electron beams with the electromagnetic field in empty resonators//Radio Enginering and Electronic Physics.-1962.-V.7,N.4.-PP.631-642.
2. Yeremka V.D.,Kovalenko A.M.,Zhurachovskiy V.A. Nonlinear analytic theory of the autoresonance peniomagnetron//I.C.M.F.T.90. Supplementary Conference Digest, Beijing China.-PP.60-63.

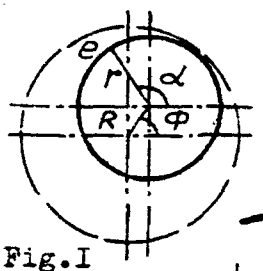

Fig.I Cross-sect. view of the interaction space of autoresonant peniotron

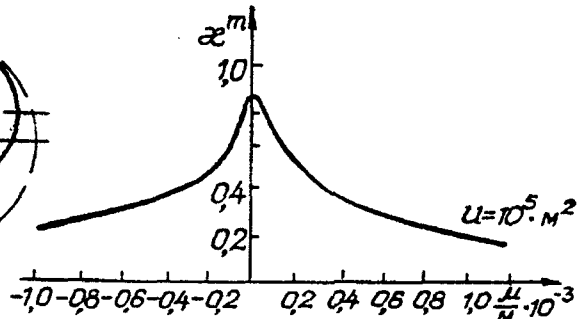

Fig.2. Maximum electron efficiency versus the frequency parameter (A_0=I,5xI0^4 V/m, U=I0^{5}xM^2, n=I0)

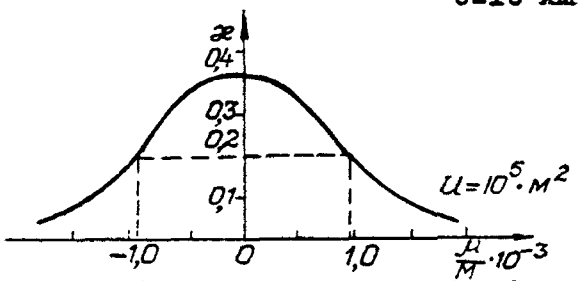

Fig.3. Electron efficiency versus the frequency parameter (A_0=I,5xI0^4 V/m, U=I0^{5}xM^2, n=I0)

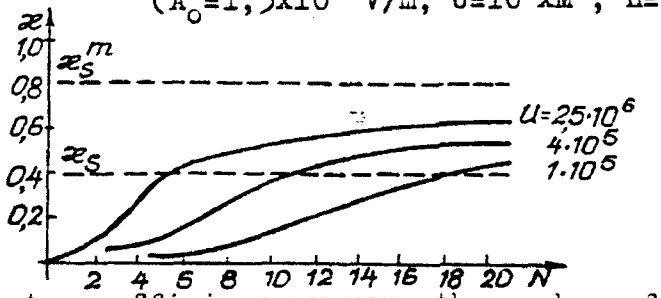

Fig.4. Electron efficiency versus the number of electron turns for three values of exitation parameter (U=I0^5, 4xI0^5, 2,5xI0^5, A_0=I,5xI0^4 V/m, n=I0)

W3.1

THE CONCEPT AND PERFORMANCE OF A CONTINUOUS SUBMILLIMETER WAVE SPECTROMETER IN THE RANGE OF 250 mkm TO 7.5 mm WAVELENGTH

E. A. Vinogradov
General Physics Institute
Russian Academy of Science
Moscow 117942, Russia

ABSTRACT

The conventional FIR spectroscopy has recently managed to go down to wavelength 3 mm (30 cm^{-1}). However, the usage of non-monochromatic sources which deliver very low power levels in mm-wave band results in the need of He-cooled detectors, acquisition times of hours, and yet numerous sharp spectral lines in gases and solids are not resolved. A radio frequency sweep generator approach to spectrum acquisition was implemented in MASS4 submillimeter spectrometer, which covers the wavelength range of 8-0.2 mm (1.3-50 cm^{-1}) with a set of monochromatic CW tunable vacuum backward wave oscillators (BWO). The powerful sources permit the use of room-temperature opto-acoustic, pyroelectric and diode detectors as well as cooled ones when low non-disturbing power levels are necessary, and to reduce acquisition time to a few seconds and minutes.

MASS4 uses quasi-optic elements to shape the beam and has a complete kit of lens, wire grid elements, and mirrors which may be arranged into different configurations to form interferometers and other schemes. The optimized wire grids enable us to perform measurements within the entire submillimeter waveband without significant change in parameters and the need of mechanical adjustment.

Either amplitude, phase and polarization spectra can be measured in transmitted and reflected radiation. The combination of BWO power of 10 mW typ. and Golay cell NEP of 10^{-10} $W/Hz^{1/2}$ results in dynamic range of ordinary power loss measurements of 10^{-4} - 10^{-5}, while elaborate heterodyne-based methods can extend this value to theoretical limits of 10^{-8}.

A single-mode quasioptic beam results in enhanced accuracy of measurement. The comparison of the results obtained by different independent methods implemented on MASS4 proves the accuracy of refractive index measurements better than 0.2%.

An adaptive dual-channel registration unit performs both detector data acquisition and software power instability correction which yields in the spectrum reproduceability within 0.3% (1-2% in worst cases). This feature results in the possibility of precision complex refractive index measurements based on vector spectrum acquisition with Single-Sideband and Double-Sideband modulation, and mathematical post-processing. The accuracy of the extracted phase spectrum is about 0.3 - 0.6 degrees for transparent samples. The resolution of the spectrometer reaches 30000, and for special applications may even be increased with the help of a phase-locked loop.

MASS4 is a reconfigurable multipurpose instrument which can be effectively used in material science, physics, chemistry and biology. The use of the instrument is illustrated by practical research results. The water quantities as low as $3*10^{-5}$ in pure cyclohexan may be inspected. Cyclotron resonance and mobility in semiconductors were measured. The spatial distribution of mobility and losses in GaAs epitaxial wafers were observed. Ferromagnetic resonance, magnetic field-induced dichroism and Faraday rotation in magnetic semiconductors, magnetic fluids and X-band ferrites were measured. The spectral characteristics of the reflection by human skin and its variation caused by dimethylsulfoxide was investigated.

The spectrometer and its sub-assemblies are currently available on the market.

Torsion-Rotation FIR Spectrum of $^{13}CD_3OH$

Li-Hong Xu[a], R.M. Lees[a] and J.W.C. Johns[b]

[a] CEMAID and Department of Physics, University of New Brunswick, Fredericton, N.B., Canada E3B 5A3

[b] Herzberg Institute of Astrophysics, National Research Council of Canada, Ottawa, Canada K1A 0R6

Abstract

The Fourier transform far-infrared (FIR) spectrum of $^{13}CD_3OH$ has been investigated from 15 to 240 cm^{-1} at 0.002 cm^{-1} resolution. About 100 *b*-type transition branch systems have been assigned, giving a map of the torsion-rotation energy level manifold with links among torsional states for n=0-3 and a K range of K=0-14. The branch origins have been fitted to a complete set of J-independent molecular constants for the vibrational ground state.

Introduction

A thorough understanding of the torsion-rotation energy level structure of the vibrational ground state of $^{13}CD_3OH$ is an essential foundation for further vibrational spectroscopy of the molecule. Analysis of infrared (IR) fundamental vibrational bands rests on a knowledge of ground-state combination differences. Therefore, in order to establish precise energy level positions in the ground state energy manifold, the study of the FIR spectrum is a necessary first step in an investigation of the IR vibrational spectrum. The IR region around 10 μm is of particular interest in the latter, of course, in connection with the optical pumping of FIR laser lines of $^{13}CD_3OH$ with CO_2 lasers [1-3].

The ground state of $^{13}CD_3OH$ was investigated initially in the microwave region by Sastry et al. [4], and results were obtained for low torsional states at low K and J rotational quantum numbers (n_{max}=2, K_{max}=2, J_{max}=5). In this work, we have explored a much wider range of states in a high-resolution Fourier transform spectroscopic study in the 15-240 cm^{-1} range. We now have an extensive map of the energy level structure for n=0-3, K=0-14 and J=0~35, which has also permitted determination of a complete set of ground state molecular constants. In addition, the ground state transition frequencies have been applied in constructing closed IR/FIR frequency combination loops to determine and confirm FIR laser transition identifications and to predict potential new FIR laser lines [1-3].

FIR Spectrum and Analysis

The FIR spectrum of $^{13}CD_3OH$ was recorded from 15-240 cm^{-1} on the modified DA3.002 Bomem spectrometer in Ottawa at a resolution of 0.002 cm^{-1}. This instrument is a Michelson interferometer, in which a folded optical path using a rooftop mirror in the moving arm gives a path difference of 5 m for the maximum mirror travel of 1.25 m. Dynamic alignment of the optics is maintained by actively stabilizing a fixed reflector in the moving arm through feedback signals derived from triple He-Ne laser beams simultaneously sent through the system. The FIR source was a high-pressure mercury lamp, the interferometer beamsplitter was a thin mylar sheet, and the germanium detector was cooled by liquid helium pumped down below the lambda point to about 1.2K. The absorption cell was a multipass White cell set to a total pathlength of 2.0 m, with the sample maintained at room temperature and a pressure of 200 mTorr.

At the low end of the spectrum, compact $\Delta K=0$ *a*-type multiplets can still be seen at high J, but at higher wave number the principal structure consists of $\Delta K=\pm 1$ *b*-type branch systems. These are scattered more or less randomly throughout the entire spectral range due to the irregular variation of torsion-rotation energy with quantum numbers n, τ and K. In this paper, we will use n to label the torsional state, τ to indicate the torsional symmetry, and K to denote the projection of the total rotational angular momentum J along the molecular near-symmetry *a*-axis [5].

In assigning the *b*-type Q-branches, we first calculated the branch origin frequencies and approximate intensities using the reported parameters [1,4], and arranged the origins in ascending wavenumber order for convenient comparison with the spectrum. When a Q branch ($\Delta J=0$) was thought to be recognized in the spectrum near the calculated origin position, we then looked for the corresponding R ($\Delta J=+1$) and P ($\Delta J=-1$) branches using calculated *a*-type frequencies in the following relations

$$R(J) - Q(J+1) = Q(J) - P(J+1) = \nu_a(J+1 \leftarrow J)$$
$$R(J) - P(J+2) = \nu_a(J+2 \leftarrow J+1) + \nu_a(J+1 \leftarrow J)$$

With this technique, we were able to assign 100 FIR branch systems, comprising nearly 6000 individual absorption lines. These transitions link the torsional states n from 0 to 3, K values from 0 to 14 and J values typically up to 35 for each of the A, E_1 and E_2 torsional symmetries. A schematic view of the ground state torsion-rotation map, showing the specific state-to-state transition linkages achieved, is given in Fig. 1.

Ground-State J-Independent Parameters

In order to model the J-dependence of the branch lines and extrapolate to the J-independent origins, we fitted the branch frequencies by least squares to an expression involving a Taylor series energy level expansion of the form

$$E(n\tau K,J) = W(n\tau K) + B(n\tau K)\,J(J+1) - D(n\tau K)\,J^2(J+1)^2 + \ldots$$

For a *b*-type $(n'\tau'K') \leftarrow (n''\tau''K'')$ transition, in which $K'=K''\pm 1$, the series origin is given by $\nu_0 = W(n'\tau'K') - W(n''\tau''K'')$, where $W(n\tau K)$ is the J-independent part of the energy. Our fits yielded branch origins with standard deviations of the order of ± 0.005 cm^{-1}, while the overall Taylor series expansions generally reproduced the observed frequencies to close to the estimated measurement accuracy of ± 0.0005 cm^{-1} for unblended lines.

With the neglect of very small terms due to molecular asymmetry shifts, $W(n\tau K)$ can be expressed in first order as a sum of products of fundamental molecular constants with expectation values of the corresponding torsion-rotation operators in the Kivelson-Kirtman formulation [5]:

$$\begin{aligned} W(n\tau K) = {} & V_3 \langle 1-\cos 3\gamma\rangle/2 + F\langle P_\gamma^2\rangle + [A - (B+C)/2]\,K^2 + V_6\langle 1-\cos 6\gamma\rangle/2 \\ & - D_{KK}\,K^4 + k_1\,K^3\langle P_\gamma\rangle + k_2\,K^2\langle P_\gamma^2\rangle + k_3\,K\langle P_\gamma^3\rangle + k_4\langle P_\gamma^4\rangle \\ & + k_5\,K^2\langle 1-\cos 3\gamma\rangle + k_6\,K\langle P_\gamma(1-\cos 3\gamma)\rangle + k_7\langle P_\gamma^2(1-\cos 3\gamma)\rangle \end{aligned}$$

Here, γ and P_γ are the torsional angle and angular momentum, respectively; V_3 and V_6 are the first two coefficients in the Fourier expansion of the threefold torsional barrier potential; F is the reduced internal rotation constant; A, B and C are the effective rotational constants; and D_{KK} and k_1 to k_7 are terms describing rotational and torsional centrifugal distortion and their effects on the barrier. A linear dependence is known to exist among several of the matrix elements [5], and means that one parameter must be constrained in fitting the branch origins. This is conveniently done by setting either k_7, k_6 or V_6 to zero. With each of these constraints, a weighted non-linear least squares fit was then carried out to the ν_0

origins, fitting the axial moments of inertia I_{a1} and I_{a2} directly rather than the related F and A constants derived from them. The results are given in Table 1 for the three fits, showing the behaviour of the parameters with the change in constraint. The sets of J-independent parameters reproduce the observed branch origins with similar overall weighted standard deviations from 7.2-8.1, meaning that on average the model fits each data point to within about 8X its standard deviation, or about ±0.005 cm^{-1}. In a given fit, the constrained parameter, which would in fact be expected to have a non-zero value, has been absorbed into effective values of the other parameters in the I_{a1}, I_{a2}, V_3, V_6, k_6 and k_7 group due to the linear dependence, hence the values of these constants are somewhat contaminated through the constraint. From qualitative physical arguments, one would expect centrifugal distortion with increasing torsional angular momentum to open up the CD_3 umbrella slightly and bring the D atoms and the H atom closer together, thus raising the barrier. Alternatively, one could argue that the force due to a repulsive barrier would tend to close down the CD_3 umbrella at the top of the barrier potential, thus decreasing I_{a2} and increasing F. Both of these effects should lead to a positive k_7 term, hence would imply that the true situation for the molecular parameters lies somewhere between Fit I and Fit III. This would then imply in turn that the V_6 term affecting the barrier shape is quite small and negative, between 0 and -1.65 cm^{-1}.

Acknowledgements

This work was made possible in part by a grant to the Centres of Excellence in Molecular and Interfacial Dynamics (CEMAID), funded by the Network of Centres of Excellence Programme in association with the Natural Sciences and Engineering Research Council of Canada. One of us (R.M.L.) also gratefully acknowledges operating support from NSERC and the University of New Brunswick Research Fund. We thank Mario Noël of the Herzberg Institute of Astrophysics for skillful technical assistance in operating the Bomem spectrometer, and Dr. Giovanni Moruzzi of the University of Pisa for stimulating conversations and the use of his general microcomputer analysis program in preparing Figure 1.

References

1. I. Mukhopadhyay, R.M. Lees and W. Lewis-Bevan, "Identification of the High Efficiency 127 μm FIR Laser Line of $^{13}CD_3OH$," *Int. J. Infrared and Millimeter Waves* **9**, 545-553 (1988).
2. Li-Hong Xu, R.M. Lees, I. Mukhopadhyay, and J.W.C. Johns, "Fourier Transform Spectroscopy of $^{13}CD_3OH$: Assignment of Far-Infrared Laser Lines," J. Mol. Spectrosc. **153** (Oka issue), in press.
3. Li-Hong Xu, R.M. Lees and J.W.C. Johns, "FIR Laser Assignments and Predicted Frequencies for Optically Pumped $^{13}CD_3OH$," this conference.
4. K.V.L.N. Sastry, I. Mukhopadhyay, R.M. Lees, J. Vanderlinde and D.P. Donovan, "Microwave and Millimeter Wave Spectra of $^{13}CD_3OH$," *13th Int. Conf. IR and MM Waves*, Honolulu, Hawaii, (ed. R.J. Temkin), *Proc. SPIE* **1039**, 416-417 (1988).
5. R.M Lees and J.G. Baker, "Torsion-Vibration-Rotation Interactions in Methanol. I. Millimeter Wave Spectrum," *J. Chem. Phys.* **48**, 5299-5318 (1968).

A symmetry:

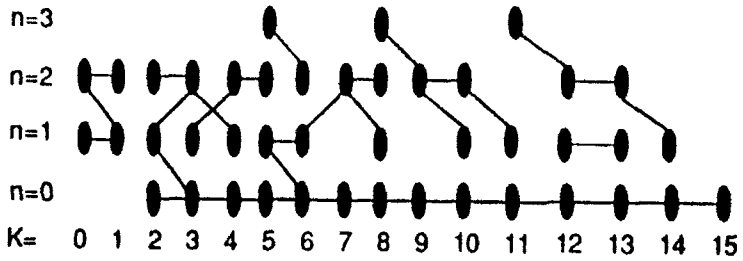

E1 symmetry:

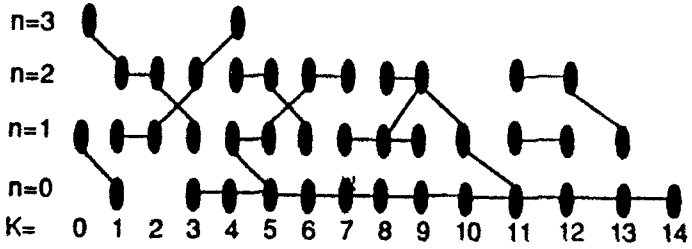

E2 symmetry:

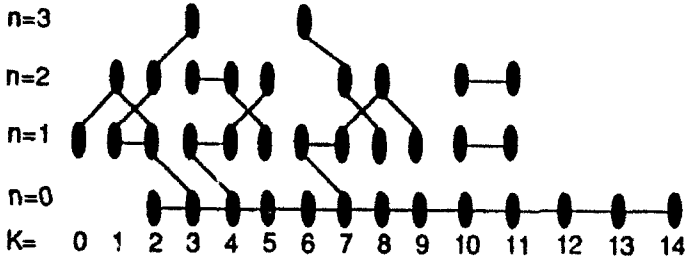

Fig. 1 The investigated FIR transitions within the ground vibrational state for each symmetry. Each filled ellipse represents a set of energy levels sharing all the quantum numbers but J. Lines represent the investigated line series.

Table 1. $^{13}CD_3OH$ ground state J-independent parameters.

Parameter	Matrix element	Fit I	Fit II	Fit III
I_{a1} (amu Å^2)		0.754633(56)	0.753937(180)	0.770094(127)
I_{a2} (amu Å^2)		6.38727(205)	6.38821(175)	6.37273(219)
V_3 (cm^{-1})	$\langle 1-\cos 3\gamma\rangle/2$	370.211(15)	370.302(39)	368.226(22)
V_6 (cm^{-1})	$\langle 1-\cos 6\gamma\rangle/2$	-1.646(11)	-1.726(22)	0(fixed)
D_{kk} (MHz)	$-K^4$	0.471(95)	0.463(88)	0.541(107)
k_1 (MHz)	$K^3\langle P_\gamma\rangle$	1.359(369)	1.340(344)	1.751(416)
k_2 (MHz)	$K^2\langle P_\gamma^2\rangle$	-16.01(57)	-16.02(53)	-17.86(61)
k_3 (MHz)	$K\langle P_\gamma^3\rangle$	-85.5(9)	-85.8(8)	-89.7(9)
k_4 (MHz)	$\langle P_\gamma^4\rangle$	-285.22(157)	-285.21(146)	-283.85(166)
k_5 (MHz)	$K^2\langle 1-\cos 3\gamma\rangle$	165.53(757)	166.69(709)	195.70(786)
k_6 (MHz)	$K\langle P_\gamma\rangle$	144.7(474)	0(fixed)	3379.6(466)
k_7 (MHz)	$\langle P_\gamma^2(1-\cos 3\gamma)\rangle$	0(fixed)	-610.1(1850)	13254.5(913)
S.D.[a]		7.69	7.19	8.11

Conversion factors used: 505376 amu Å^2 · MHz
1 cm^{-1} = 29979.2458 MHz

[a] Standard deviation of the fit, in weighted cm^{-1}.

W3.3

MICROWAVE ABSORPTION AND COMPLEX FORMATION IN SOME DONOR - ACCEPTOR MIXTURES

K.N.ABD EL NOUR, M.Z. EL SABEE & S.L.ABD EL MESSIEH
Microwave Physics Dept. National Research Centre Dokki, Cairo- Egypt .
* Chemistry Dept. Faculty of Science Cairo University. Egypt

Dielectric relaxation behaviour of polar molecules in non-polar solvents using microwave absorption methods have been frequently studied. Such studies using binary mixtures in non-polar solvents, however, are limited. The work reported here is an investigation of the dielectric relaxation behaviour of mixtures containing complexes formed between either polar or non-polar donors (methyl methacrylate MMA and styrene St) and two polar acceptors (N.phenyl maleimide NPMI and octadecyl maleimide ODMI) in non -polar solvents (carbon tetrachloride and benzene). The measurements were carried out on dilute solutions (not more than 1 mole%) of mixtures of donor and acceptor with different compositions, namely 1:3, 1:1 and 3:1 respectively in carbon tetrachloride and benzene at tempertures of 20.30 and 40 c.

The dielectric loss ϵ'' was measured in the frequency range 0.2 - 18 GHz using a sweep - frequency spectro-photometer from HP, U.S.A.described earlier. The accuracy of the measurements was $\pm$ 3% The static dielectric constant was measusred at 2 MHz by the dipolmeter, type DM01 from WTW, Germany to an accuracy of $\pm$ 1% An Abbé refractometer from Carl Zeiss Jena, Germany was used to measure the refractive index n_D of the Na D line for the investigated solutions to an accuracy of $\pm 1 \times 10^{-4}$.

The results obtained for the dielectric loss $\Delta\epsilon''/\chi$ at the different frequencies (ω) are analysed by the sum of Debye terms using the equation,

$$\Delta\epsilon'' = (\Delta\epsilon_0 - \Delta n_D^2) \sum G_i \frac{\omega\tau_i}{1+\omega^2\tau_i^2} \quad , \quad \sum G_i = 1$$

X is the concentration in mole fraction and Δ means the difference between the solution and solvent . Fitting of data was done by computer program. An example of the analyses is given in fig. (1) for ODMI and MMA and the mixture of two components with composition 1:3 ,1:1 and 3:1 in carbon tetrachloride at 20 c. From this figure it is seen that the first absorption region describing both molecules is represented by one Debye term. Any deviation from the experimental points being comparable with the error limits. This is not surprising in view of the fact that separate loss maxima are likely to appear only for mixtures in which the two components (A and B) have very different relaxation times τ_A and τ_B with the ratio $\tau_A / \tau_B > 6$ for the observable reso'ution (1). This is the case of MMA with both acceptors. The use of styrene in the mixture is also acceptable. because it is a non-polar material.

The presence of the second high - frequency absorption region (about 100 GHz) could be assigned to the segmental rotations i.e. the internal

mobility either in the donor or in the acceptor or both . A large part of this region lies outside the capability of the available measuring equipment which may lead to less accurate results.

The measured values of the relaxation times associated with the first absorption region are compared with those calculated either from the sum of the two components of the intensities $X_D\tau_D$ and $X_A\tau_A$, where the X's are the mole fractions and τ's are the measured relaxation times of the individual components (donor and acceptor respectively), or from the emperical relation proposed by Madan (2) taken into consideration the molecular environments.

It is of great interest to notice that the values of τ_{expal} are higher than the calculated ones τ calcd. This could be attributed to the polar complexes formed by the interaction between donors and acceptors which increases the molecular volume and consequently the relaxation time. In order to find an expression describes the complex formation, the relative increase in relaxation time

$$\frac{\tau_{expal} - \tau_{calcd}}{\tau_{calcd}} = \frac{\Delta\tau}{\tau_{calcd}}$$

is calculated. It is interest to find that the relative change increases with increasing the donor concentration leading to an increase in the complex formation. This result is supported by the increase in the apparent activation energy ΔH.

From the values of $\frac{\Delta\tau}{\tau_{calcd}}$ It is also found that the complex formation decreases with increasing temperature which is the case of association in alcohols. These complexes are expected to vanish at a temperature not too far from 40 c. Also it is reasonable to expect that the complex formation between the donor and acceptor in the inert solvent (carbon tetrachloride) is higher than that in active solvent i.e. benzene.

On the other hand. the data of $\frac{\Delta\tau}{\tau_{calcd}}$ indicated that the complex formation is greater in case of using styrene as a non-polar donor. rather than using the polar donor (methyl methacrylate) while the complexes formed by ODMI is greater than that formed by NPMI.

The interaction between the donors and acceptors which is described by the relative increase in the relaxation time is also investigated by means of dielectric polarization measurements (2). Despite of the higher values of the equilibrium constant (K) obtained here compared with those found spectrophotometrically, the dielectric method is considered to be a good indication for complex formation.

References :

(1) M.P. Madan. Can . J. Phys. 65 (1987) 1573.
(2) M.G. Mikhael. S.M.Mokhtar. G.R. Saad and M.M. Naoum. J.Polym Sci. 27 (1989) 185.

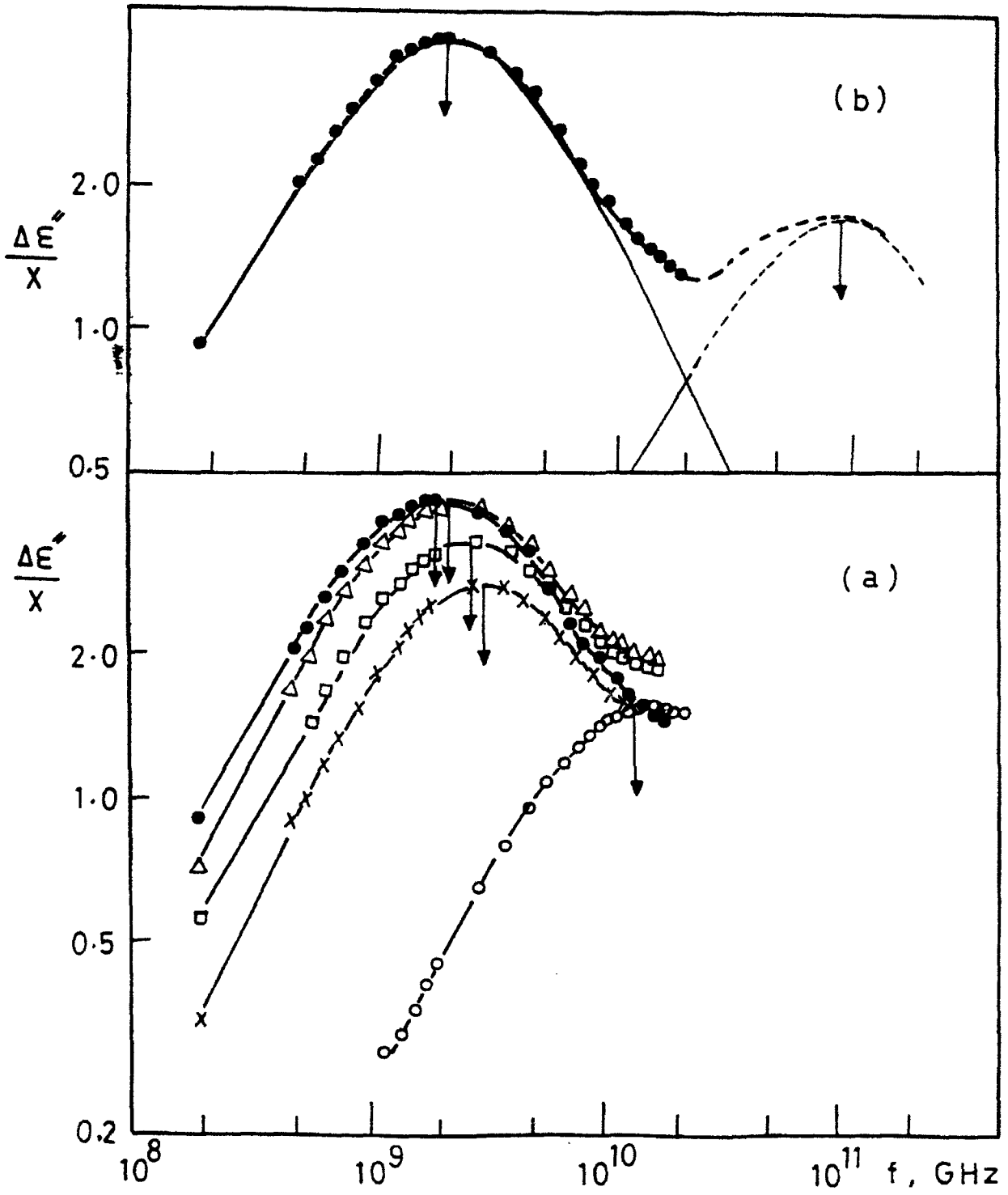

Fig (1) a_ Absorption curves of • ODMI and o MMA and the mixture of two components with composition △ 3:1, □ 1:1 and x 1:3 in CCl_4 at 20°C.

b_ Fitting the data of ODMI by the sum of two Debye terms.

FAR INFRARED LASER STARK SPECTROSCOPY OF O-18 METHANOL : DETERMINATION OF ELECTRIC DIPOLE MOMENT*

G.R.Sudhakaran
Department of Physics
State University of New York
Oswego, NY 13126
U.S.A.

R.Gopalsamy*, I.Mukhopadhyay, P.K.Gupta
and R.Prasad*
Laser Programme
Centre for Advanced Technology
Government of India
Department of Atomic Energy
Indore 452 013, M.P.
INDIA

R.M.Lees
Centre of Excellence in Molecular and
Interfacial Dynamics (CEMAID)
Department of Physics
University of New Brunswick
Fredericton, N.B.
E3B 5A3, CANADA

and

R.R.J.Goulding
Department of Physics
Memorial University of New Foundland
St., Johns, N.F.
A1B 3XY, CANADA

* Also with the Department of Chemistry, Devi Ahilya Vishwavidyalaya Indore 452 001, M.P., India

* This paper is dedicated to the memory of our colleague late Dr.R.L.Bhattacharjee of the University of Rochester, New York, who contributed a lot in the field of FIR laser Stark spectroscopy. His untimely demise mourn us all and his absence will be felt by all of us for a long time to come.

A B S T R A C T

In this paper, the laser Stark spectrum of oxygen-18 substituted methyl alcohol has been studied with the HCN laser operating at 337 μm, upto a d.c. electric field of about 41 KV/cm. The spectrum has been assigned to the $J_K = 9_8 \leftarrow 10_5$ transition for E_2 - species in the torsional vibrational ground state. The frequency for this transition as obtained from combination relations of observed absorption peaks in a recently recorded Fourier transform far-infrared (FIR) spectrum, is 310 MHz above the 337 μm laser line frequency. From the analysis of the Stark spectrum at low electric fields, the parallel component of the electric dipole moment is obtained as 0.898 (2) Debye which is very close to the value reported for the parent CH_3OH species.

Far Infrared Fourier transform and laser Stark spectra

In the last few years there has been a significant interest in the spectroscopy of O-18 substituted methanol, mainly because of the use of this species as an efficient optically pumped FIR laser active medium [1-2]. There is a need for precise value of the electric dipole moment in order to calculate the relative strength of FIR laser lines and to calculate the Stark tuning of the frequency of the laser emission lines.

In this work, the laser Stark spectra of $CH_3{}^{18}OH$ have been recorded using the 337 μm laser line of the HCN laser, upto a maximum d.c. electric field of about 41 KV/cm for both parallel and perpendicular polarizations. The experimental details can be found in Ref. (3).

The family of transitions is assigned to the ground state transition $J_K = 9_8 \leftarrow 10_5$ E_2 n = Ø, in $CH_3{}^{18}OH$, whose zero field frequency is obtained from combination relations of measured FIR absorption spectrum, as 29.7126(5) cm^{-1}. The FIR abosrption spectra were recorded in the range 30-220 cm^{-1} by using a BOMEM Fourier transform spectrometer at the Herzberg Institute of Astrophysics in Ottawa, at a resolution of Ø.ØØ4 cm^{-1}. A sample of 97.8% enrichment in O-18 was used and was supplied by MSD isotopes of Canada. The sample cell was 15 cm long and was fitted with high density polyethylene windows. The detector was a liquid helium cooled germanium bolometer. The spectrum was calibrated by means of water vapor absorption lines present as contaminants. The spectrum was recorded at room temperature at a pressure of about 2 torr. The uncertainty in the frequency of unblended lines is estimated to be on the order of ± Ø.ØØØ5 cm^{-1}.

The assignment of various Stark components are presented in Table 1. The Stark shift for E-species in methanol type molecule can be expressed as [4-7]:

$$W_{stark} = (A + BM^2)\,E^2 - CME$$

Where E is the d.c. electric field, C is the first order Stark co-efficient given approximately by $\mu_a K/J(J+1)$ with μ_a as the component of the electric dipole moment along the near symmetric axis of the molecule and the second order coefficients A and B are related to the matrix elements of the direction cosines in a complicated way.

At low electric fields the Stark effect is essentially first order in nature. From the observations at low fields the parallel component of the electric dipole moment is obtained as μ_a = Ø.898 (2) Debye. This value is very close to the value obtained for normal $^{12}CH_3OH$ [3,6,7]. This value also compares very well to the values obtained by J.C.Petersen and S.E.Choi recently by means of double resonance technique [8]. The perpendicular component of the dipole moment can be obtained from the observation at high electric fields and this work is in progress.

ACKNOWLEDGEMENT

We are grateful to Dr.J.W.C.Johns for the use of BOMEM Fourier transform spectrometer at the Herzberg Institute of Astrophysics in Ottawa.

Table - 1

ΔM = Ø		ΔM = + 1			ΔM = - 1		
M	E (KV/cm)	M'	M"	E (KV/cm)	M'	M"	E
- 9	3.65963	- 9	- 1Ø	4.8342Ø	- 4	- 3	5.28Ø73
- 8	4.115Ø7	- 8	- 9	5.669Ø2	- 3	- 2	6.29999
- 7	4.6983Ø	- 7	- 8	6.8533Ø	- 2	- 1	7.824Ø3
- 6	5.47488	- 6	- 7	8.7Ø738	- 1	Ø	1Ø.32849
- 5	6.59121	- 5	- 6	11.92Ø48	Ø	+ 1	15.25977
- 4	8.26Ø85	- 4	- 5	19.12324			
- 3	11.Ø8566						
- 2	16.99736						
- 1	41.17Ø7						

REFERENCES

[1] N.Ioli, A.Moretti, D.Pereira, F.Strumia and G.Carelli, Appl.Phys. B48, 299-304 (1989).

[2] R.R.J.Goulding, C.Young, R.M.Lees, W.Lewis-Bevan and J.W.C.Johns, Infrared Phys. 28, 297-306 (1988).

[3] L.H.Johnston, R.P.Srivastava and R.M.Lees, J.Mol.Spectrosc. 84, 1-40 (1980).

[4] J.O.Henningsen, J.Mol. Spectrosc. 83, 70-93 (1980).

[5] M.Inguscio, A.Moretti, G.Moruzzi and F.Strumia, Int. J.IR and MM waves, 2, 943, 986 (1981).

[6] K.V.L.N.Sastry, R.M.Lees and J.Van der Linde, J.Mol.Spectrosc. 88, 228-230 (1981).

[7] T.Amano, J.Mol. spectrosc. 88, 194-206 (1981).

[8] J.C.Petersen and S.E.Choi, J.Opt.Soc. Am. B3, 2256-2259 (1991).

SUBMILLIMETER MAGNETIC AND DIELECTRIC PROPERTIES OF THE RARE-EARTH ORTHOFERRITES

AnzinV.B., Kozlov G.V., LebedevS.P.,Mukhin A.A., Prokhorov A.S.
Institute of General Physics of Russia Acad. Sci., 38 VavilovSt.,117942Moscow,Russia

The rare-earth orthoferrites ($RFeO_3$, where R is a rare-earth ion or yttrium) have proved to be an interesting class of weak ferromagnets (D_{2h}^{16}-Pbnm spase group) for applicatons and investigations of various types of magnetic interactions, spin-reorientation phase transitions and high-frequency phenomena [1-4].

We have investigated magnetic and dielectric properties of the orthoferrites $RFeO_3$ (R=Y, Tm, Dy, Gd, Ho, Er, Tb) at submillimeter (SBMM) wavelengths (ν=100-1000 GHz). The single crystals of $RFeO_3$ were grown by float zoning with radiative heating. Transmission $T(\nu)$ and phase shift $\Phi(\nu)$ spectra of the a-, b-, c-cut plane-parallel plates of the orthoferrites were measured by the submillimeter *"Epsilon"* BWT spectrometer[5]. The antiferromagnetic resonance (AFMR) modes (quasiferromagnetic (F) and quasiantiferromagnetic (AF)) were observered in all orthoferrites investigated .

Figure 1 presents the transmission spectra of the yttrium orthoferrite as an example. The common feature of such spectra is the presence of periodic oscillations, resulting in the interference of waves inside the plane-parallel plates Besides the interference oscillations, the spectra $T(\nu)$ contain sufficiently narrow absorption lines, which correspond to quasi-ferromegnetic and quasi-antiferromagnetic AFMR modes according to the excitation conditions.

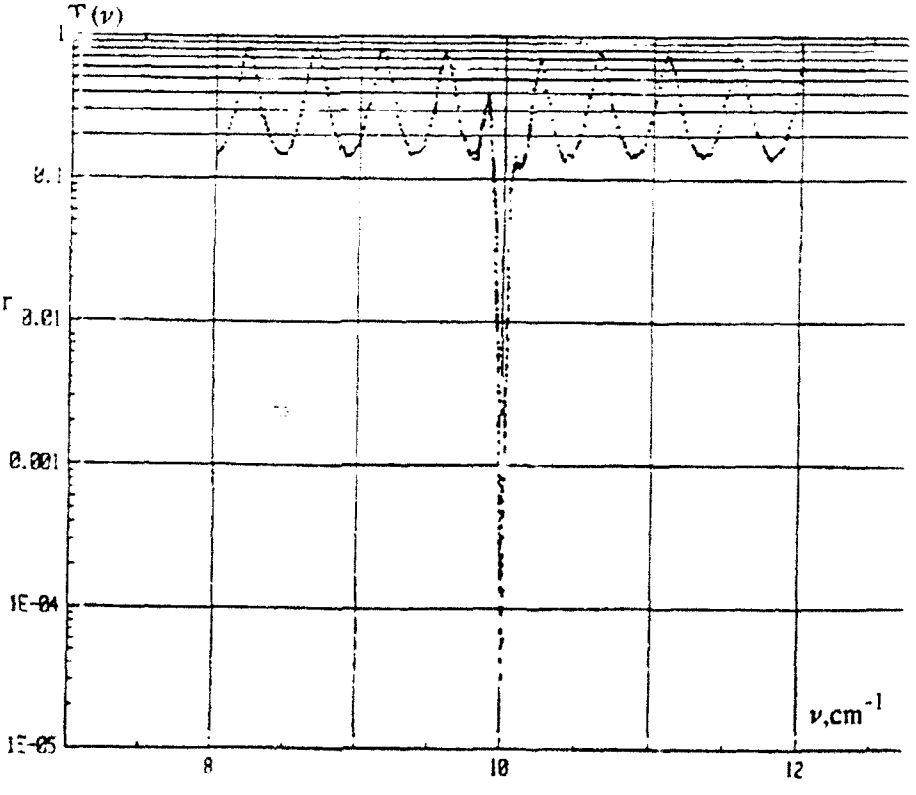

Fig.1 Transmission spectrum of $YFeO_3$ plate (d=2.05mm) at 300K near F mode.

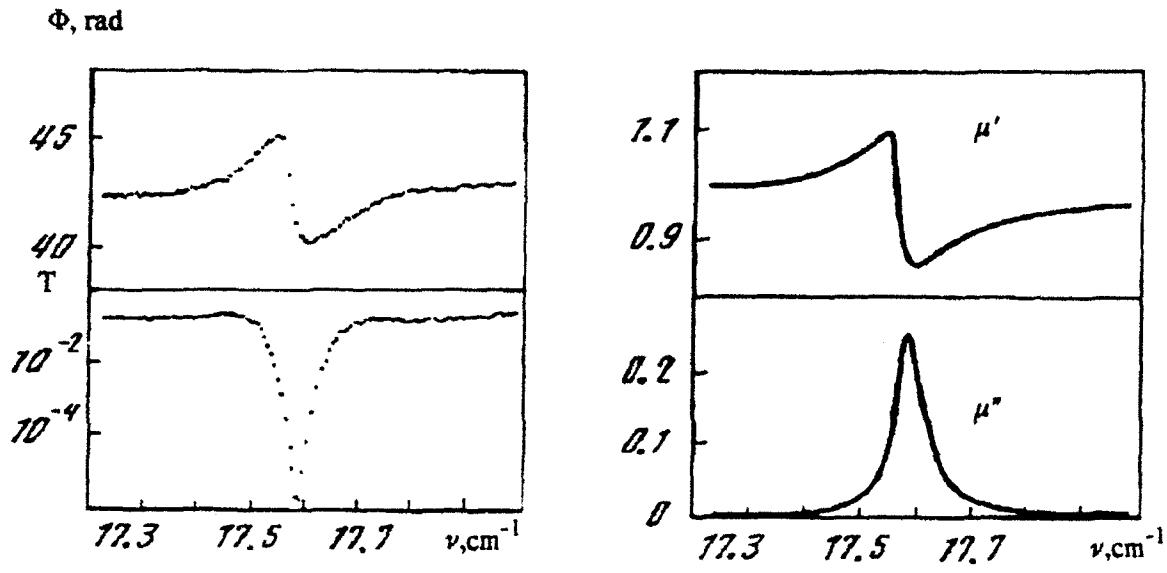

Fig.2. Magnetic spectra of $YFeO_3$ plate (d=0.818 mm) at 300K near AF mode

Using experimental dependences $T(\nu),\Phi(\nu)$ the spectra of the permeability $\mu=\mu'+i\mu''$ are calculated according to the well-known formulae for a plane-parallel plate .The dependences $\varepsilon'(\nu)$ and $\varepsilon''(\nu)$ were obtained using the oscillating $T(\nu)$ curves beyond the absorption lines. These dependences given in the form of polynomials were next interpolated into the resonance region. The typical results of such measurements are shown in Fig. 2.

The magnetic spectra of measured orthoferrites are well described within the accuracy of the experiment by the harmonic oscillator model for a permeability dispersion :

$$\mu_k = 1 + \Delta\mu_k \nu_0^2 / (\nu^2 - \nu_0^2 + i\nu\Gamma), \qquad (1)$$

where ν_0 is the resonance frequency, Γ is the linewidth, $\Delta\mu_k$ is the mode contribution to the static permeability, k=x,y,z. As a result, for determining the parameters of the AFMR modes we usually measured the transmission spectra only and then fitted them by least squares, using a simple model of a damped harmonic oscillator (1).

Fig.3 Transmission spectra of $TmFeO_3$ plate (d=2.7 mm) at 300 K near F mode in the magnetic field H⊥c–axis.

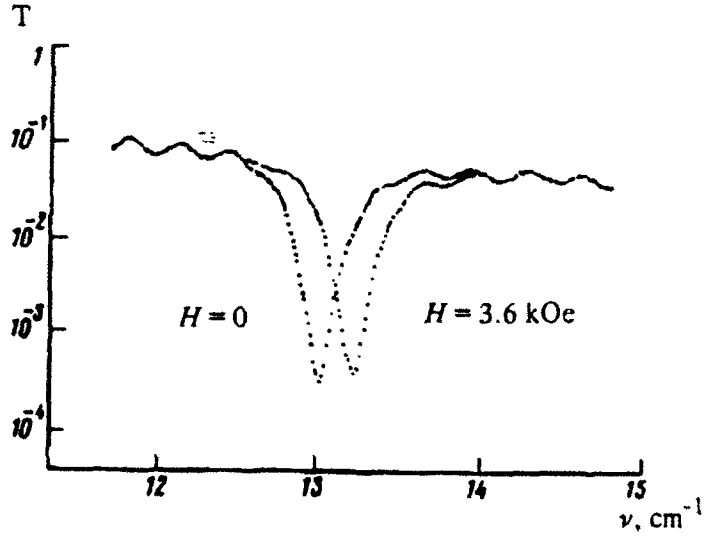

At room temperature for all orthoferrites studied by us at SBMM wavelengths $\varepsilon'(\nu)$=const and $\varepsilon''(\nu)$ is a linear function of frequency.Tables 1 and 2 present the values of some dielectric parameters of the orthoferrites at AFMR frequencies and parameters of the AFMR-modes.

We have also studied the AFMR-mode behaviour in the magnetic field H⊥m⊥c-axis. Fig.3 shows the resonanse frequency increase in the magnetic field for $TmFeO_3$.

Thus, the orthoferrites are the materials possessing in the SBMM range very high-quality magnetic and dielectric parameters. As the dielectric materials they are weakly absorbing at SBMM wavelengths (small angular dielectric loss tangent), having high refractive indices and birefringence. As the magnetic materials rare-earth orthoferrites possess narrow high-quality resonance lines and high linear coupling coefficients between the AFMR frequencies and the external magnetic field.

Table 1. Dielectric parameters of the orthoferrites at *300K* near AFMR frequencies

Crystals	*F*-mode AFMR				AF-mode AFMR			
	ε_z'	ε_z''	n_z	$tg\delta_z$	ε_y'	ε_y''	n_y	$tg\delta_y$
$YFeO_3$	25.4	0.04	5.04	0.0016	21.9	0.09	4.68	0.004
$TmFeO_3$	27.8	0.50	5.27	0.018	22.2	0.26	4.71	0.012
$DyFeO_3$	26.2	0.26	5.12	0.010	24.0	0.20	4.90	0.008
$GdFeO_3$	24.7	0.13	4.97	0.005	23.5	0.12	4.85	0.005
$HoFeO_3$	26.2	0.23	5.12	0.009	22.8	0.17	4.78	0.007
$ErFeO_3$	26.2	0.14	5.12	0.005	23.3	0.14	4.83	0.005
$TbFeO_3$	26.0	0.25	5.10	0.01	24.0	0.26	4.90	0.01

Table 2. AFMR-mode parameters of the orthoferrites at *300K*.

Crystals	F-mode AFMR				AF-mode AFMR			
	ν_0, GHz	Γ, GHz	$\Delta\mu_y$ $\times 10^4$	$\mu_y''(\nu_0)$	ν_0, GHz	Γ, GHz	$\Delta\mu_z$ $\times 10^4$	$\mu_z''(\nu_0)$
$YFeO_3$	299.4	0.9	8	0.27	526.8	2.1	7.5	0.19
$TmFeO_3$	402	7.5	8.5	0.04	698	8.4	9.0	0.075
$DyFeO_3$	379.5	10.5	9	0.03	510	10.5	7.0	0.034
$GdFeO_3$	305	12	8	0.02	605.7	12.9	8.0	0.037
$HoFeO_3$	378	15	8	0.02	597	9.0	7.5	0.051
$ErFeO_3$	377	8	8	0.04	673	7.0	8.0	0.077
$TbFeO_3$	322	20	8	0.013	537	15.	6.5	0.023

Thus, the orthoferrites are the materials possessing in the SBMM range very high-quality magnetic and dielectric parameters. As the dielectric materials they are weakly absorbing at SBMM wavelengths (small angular dielectric loss tangent), having high refractive indices and birefringence. As the magnetic materials rare-earth orthoferrites possess narrow high-quality resonance lines and high linear coupling coefficients between the AFMR frequencies and the external magnetic field.

We have also investigated $RFeO_3$ (R=Y,Tm, Dy, Ho, Er) in the wide temperature range $T = 4.2\text{-}300K$. At low T we revealed in $TmFeO_3$, $HoFeO_3$ and $ErFeO_3$ orthoferrites not only two narrow AFMR modes of the Fe-subsystem but also several wide absorpsion lines identified as the rare-earth modes which are caused by electronic transitions inside the Tm^{3+}, Er^{3+}, Ho^{3+} ion ground multiplets. We have found, that among these transitions not only magnetodipolar, but also the electrodipolar ones take place for $TmFeO_3$ [2]. The temperature dependences of the resonance frequencies, linewidths and mode contributions to the static permeability and permittivity were derived.An increase (up to 30%) in the quasistatic dielectric permittivity along c-axis ε_z in $TmFeO_3$ was observed at low T, resulting from an appreciable contribution of the electrodipolar rare-earth modes in Tm^{3+}.

Unusual and complicated behaviour of the magnon modes were found in $TmFeO_3$, $ErFeO_3$, $DyFeO_3$, $HoFeO_3$, which manifested near spin-reorientation phase transitions in softening of the AFMR modes and interaction with the rare-earth modes.

We have developed a theory describing all variety of dynamical properties observed in the orthoferrites with various rare-earth ions.The theory is based on a use of a general linear response of the R-subsystem with respect to a high-frequency external magnetic field and anisotropic exchange fields of the Fe-subsystem.

As a result, the dynamics and static magnetic properties of the orthoferrites investigated (for example, the presence SRPTs and resonance mode behaviour were consistently described. We have obtained a good agreement between the experimental and calculated temperature dependences of the resonance frequencies and other mode parameters of the orthoferrites investigated.

References

1. R. L. White, J. Appl. Phys. 40 (1968) 1061

2. K. P. Belov, A. K. Zvezdin, A. M. Kadomtseva, R. Z. Levitin, Orientational phase transitions in the rare-earth magnets (Nauka, Moscow, 1979)

3. Balbashov A.M., Kozlov G.V., Lebedev S.P.,Mukhin A.A., Pronin A.Yu., Prokhorov A.S., Sov. Phys. JETP, 1989, v.68, N3, p.629.

4. Mukhin A.A., Pronin A.Yu., Prokhorov A.S., Kozlov G.V., Zelezny V., Petzelt J., Physics Letters A, 1991, v.153, N8,9, p.499.

5. Volkov A.A., Goncharov Yu.G., Kozlov G.V., Lebedev S.P., Prokhorov A.M., Infrared Phys., 1985, v.25, p.369.

W3.6

THE MICROWAVE PHOTOCONDUCTIVITY OF A GAPLESS SEMICONDUCTORS PRODUCED AS A RESULT OF FORMATION OF AN ENERGY GAP

S.G.Gasan-zade, E.A.Sal`kov and G.A.Shepelsky

Iustitute of Semiconductors of Ukraine,
Kiev, 252650, Ukraine.

In gapless semiconductors (GS) the bottom of the conduction band touches the top of the valence band and the impurity states inevitably land in an energy spectral region that corresponds to allowed energy states of perfect crystal. The band structure of GS of the type of the $Hg_{1-x}Cd_xTe$ was explained in terms of the inverse band model. The degeneracy of the bands Γ_8 is connected with crystal symmetry and extremum of the Γ_8- term may be located below the Γ_8 for $x < x_c=0.16$ (T=4.2K). Application of external perturbation (magnetic field, strain etc.) leads to creation of an energy gap in point Γ_8 (k = 0) and changes physical characteristics of GS. In this paper we consider the photoconductivity (PC) of gapless $Hg_{1-x}Cd_xTe$ which in far-infrared up to millimeter range arising as a result of opening of an energy gap by magnetic field or uniaxial stress.

Quantization of the electron spectrum in a magnetic field gives rise to Landau subbands of electrons and holes. In the case GS $Hg_{1-x}Cd_xTe$ energies of Landau subbands increase linearly with magnetic field and energy gap between conduction band and valence band is created. The expression for the gap in magnetic field $\delta(H)$ may be written as

$$\delta(H) = \frac{1}{4}\hbar\frac{eH}{m_nc}$$

Thus the gap $\delta(H)$ is determined by the displacement of the lower electron subband only. A simplified scheme describing the variation of the electron spectrum in a magnetic field with allowance acceptor state ε_A in conduction band is given in fig.1. The field H_c is deformined by the equality $\delta(H)=\varepsilon_A$ i.e. when $H>H_c$ the resonance acceptor level enters into the magnetic field induced gap. In the gapless state (H=0) interband PC is negligible due to the high recombination rate. The opening of an energy gap must lead to the appearence of interband PC in wide spectral range as a function of magnetic field. We have previously reported the results of study of interband PC in

infrared range [1]. Here we have considered PC in millimeter wave range, when photosignal is a result of transition of electrons on acceptor states.

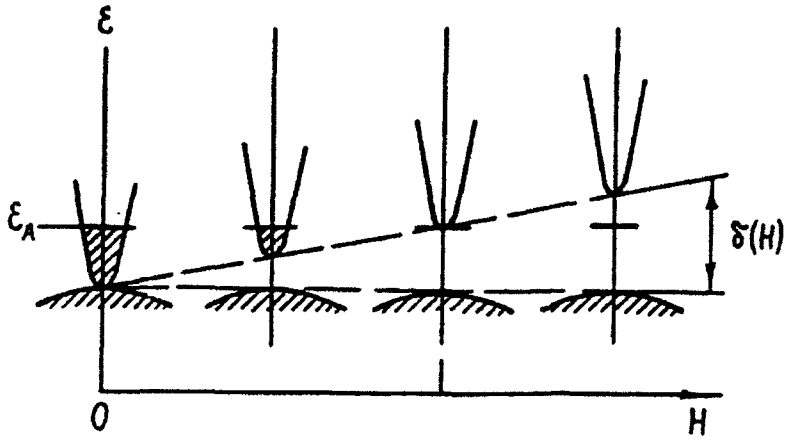

Fig.1 Transformation of the band structure for gapless $Hg_{1-x}Cd_xTe$ in a magnetic field.

In normal semiconductors microwave PC is determined by the free electrons' heating (μ-PC). Conductivity of gapless $Hg_{1-x}Cd_xTe$ changes as result electron heating (changes of mobility) and as result of change of electron concentration:

$$\Delta\sigma = e\left(n\frac{\partial\mu}{\partial T_e} + \mu\frac{\partial n}{\partial T_e}\right)\Delta T_e$$

In absence H the second component is negligible and PC is μ-PC. When magnetic field readjust the magnitude of $H_r = 2mc(3\pi n)^{2/3}/e$ and the last Landau level approachs to Fermi level, the conductivity is determined by the freez-out of electrons on the acceptor states. In this case concentration member is dominant in microwave PC. It is evident from fig.2 experimental field dependence of PC in millimeter wave range have a high maximum at the $H=H_r$. The results of the experiments with uniaxial stress are interpreted in terms of the formation of an energy gap due to the lifting of the degeneracy of the Γ_8 band by lowering the symmetry of the crystal lattice. We have studied the compaund $Hg_{1-x}Cd_xTe$ with x=0,155 (ε_g = -13±5 meV) under a uniaxial compression up to P = 3,5 kbar in the temperature range 1,7 - 77 K. Deformation dependence of the Hall coefficient R_h and resistivity ρ has some peculiar features. Reversal of the sign of $R_h(P)$ indicates that in the region of maximum strain the conductivity is determined by the free holes whose mobility and hence the effective mass approximaly equal to electron masses (when P = 0 one usually

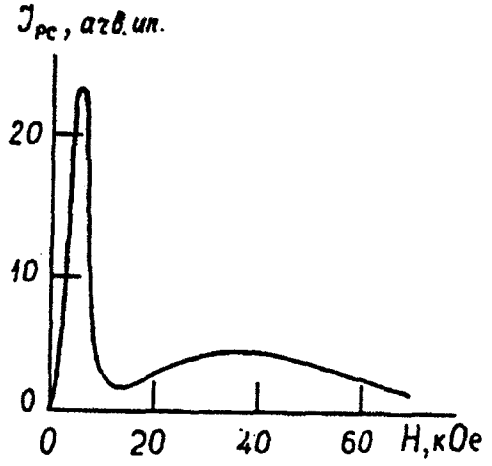

Fig.2 Magnetic field dependence of the microwave PC of $Hg_{1-x}Cd_xTe$ ($x \simeq 0,158$). λ = 8 mm. T=4,2K.

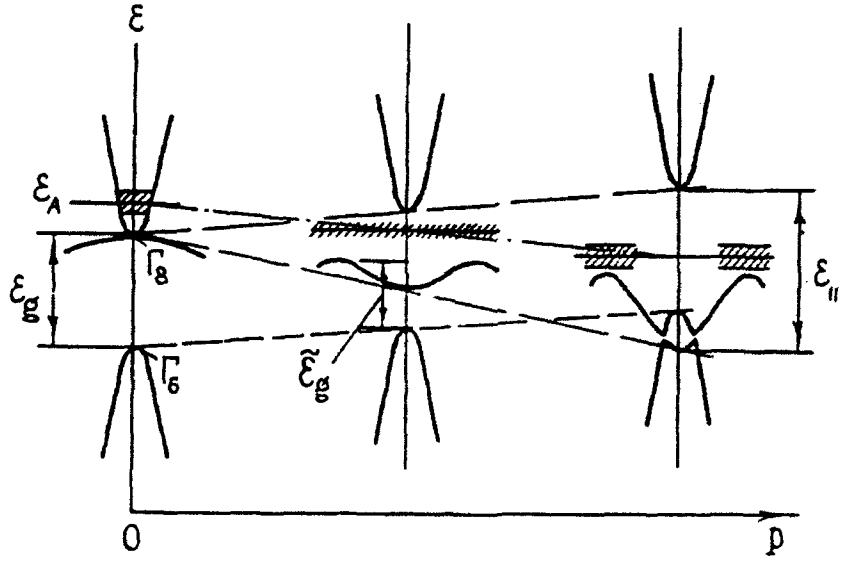

Fig.3 Band structure of GS $Hg_{1-x}Cd_xTe$ as a function of uniaxial deformation.

has $\mu_n/\mu_p \sim 10^2$). Scheme of a structural change in the energy band of a gapless semiconductor caused by a uniaxial stress shows in fig.3. In the absence of strain the conductivity is determined by the free electrons (even when $N_A >> N_D$, N_A and N_D are concentrations of acceptors and donors respectively).

When $P > P_c$ the acceptor states enter the pressure - induced energy gap and make the electrons to be frozen-out. Highly strained crystal has the conductivity which determined by the free holes with small

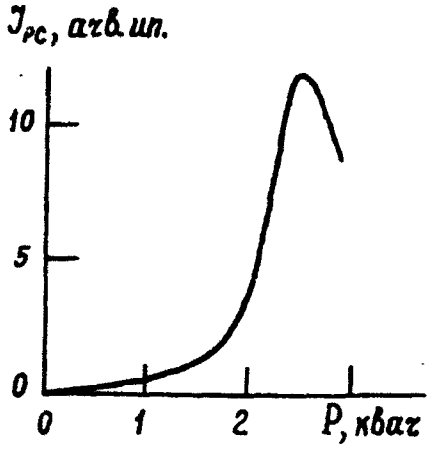

Fig.4 Microwave PC of $Hg_{1-x}Cd_xTe$ ($x \simeq 0,155$) with uniaxial deformation. λ =8 mm. T=4.2K

effective masses. The formation of an energy gap under action uniaxial stress leads to the appearence of microwave PC.

Notice that curve of deformation dependence of PC have the maximum (fig.4), when $P=P_o$ and Fermi level coincide with the bottom of the conduction band.

---

1. S.G.Gasan-zade, V.A.Romaka, E.A.Sal'kov and G.A.Shepelsky - Pis'ma Zh.Eksp.Teor.Fiz., v.39, No.12, p.553-556 (1984).

W3.7

EFFECT OF THE MAGNETIC FIELD ON THE POLARIZATION OF THERMAL EMISSION FROM AN ISOTROPIC SEMICONDUCTORS

A.G.Kollyukh and V.A.Morozhenko

Institute of semiconductors, Ukrainian Academy of Sciences, Kiev

Studies of thermal emission that enable one to obtain an information about the properties of semiconductors are carried out extensively in the last few years [1].

In the present work an effect of the magnetic field on polarization characteristics of thermal emission from an isotropic semiconductors is first investigated.

Consider a thermal emission from the heated semiconductor platelet with a thickness d. As well known, if an angle of incidence φ is different from the right angel, the reflection coefficients of emission polarized in parallel (p) and transversely (s) to the plane of incidence, are different. As a result, the non-polarized beam of thermal emission, that interacts with a semiconductor surface, is divided into two partially polarized beams, those are: the outgoing thermal emission with a dominating p-component of polarization and the internal emission with a dominanting s-component (see an insert in Fig.1). It may be supposed that,at sufficiently weak absorption, a field of wave with a dominating s-polarization exists in platelet. If the magnetic field B is applied collinearly to propagation

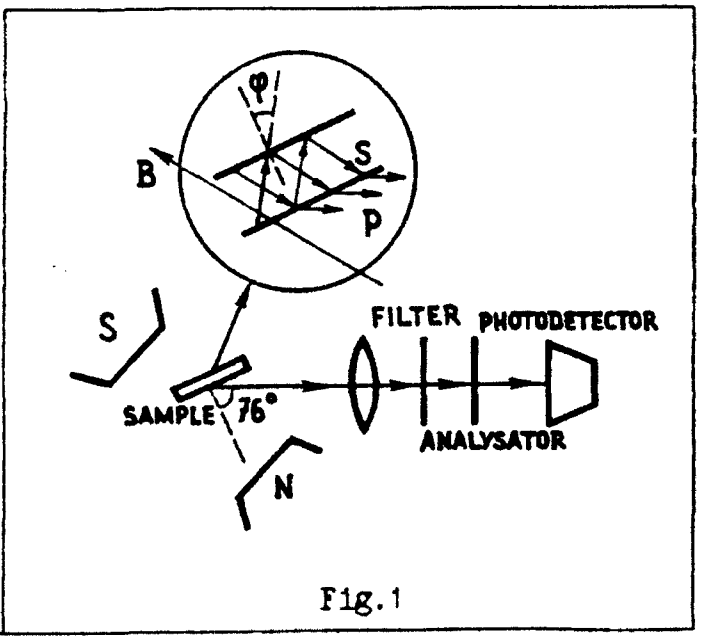

Fig.1

direction of reflected waves inside of the crystal, the polarization plane of these waves will be rotated through an angle β (Faraday effect). This effect is described by the following relation [2]

$$\beta = \frac{Ne\ Bd\lambda}{8\pi^2 c^3 \varepsilon_o n(m^*)^2}$$

where N and m^* are the density and effective mass of free charge carrier ers respectively, λ is the wavelength of radiation observed, n is refractive index.

Under these conditions, the s-polarized waves interact with a semiconductor surface at changed intensities of s- and p-components of emission which intensities are determined by the angle β (see (1)). Thus, a redistribution of intensities of reflected and refracted emission occurs and this redistribution shows up as the change in the degree of polarization of the emission observed. Taking into account one event of reflection, the intensity of outgoing emission may be presented as

$$I_{s,p} = Q(1-R_{s,p})(R_{s,p}\exp(-kd)\cos^2(\beta)+R_{p,s}\exp(-kd)\sin^2(\beta)+1) \qquad (2)$$

where $R_{s,p}$ is the reflectivity, k is the absorptic coefficient, Q is the Plank function.

It follows from (2) that the degree of polarization of outgoing beam, determined as $D=(I_p-I_s)/(I_p+I_s)$, has an oscillating character under the magnetic field.

Fig.2 presents the numerically calculated degree of polarization as a function of the magnetic field for a n-InSb crystal. The multiplied reflection have been taken into account. Dispersion of absorption is considered according to [3]. It is found that the maximal change of D(B) occurs at the Brewster angle for the s-polarized beam. Because of this, all calculations are made just for this angle.

Curves 1,2 show the plots D(B) for a monochromatic emission with a wavelength 7,11 and 16μm, respectively. Curve 4 presents the value of D(B) for the integral thermal emission over the band from 7 to 11μm. As seen, these dependences are of a nonmonotonic type. Dependences D(B) for a narrow spectral bands are oscillating. In this case the maxima of the degree of polarization correspond to rotation of polarization plane through an angle $i\pi/2$ where i=1,3,5..., and the period of oscillations is determined by the spectral dependence of radiation absorbtion in the crystal. However, the oscillations disappear in D(B) for the case of integral thermal emission (curve 4). This may be understood taking into account not only the dependences of β and of absorption coefficient on λ but also the dependence of Plank function on λ. Indeed, the rising region of the D(B)-dependence is dominating at small B and then, with increasing B, the contribution of different dependences D(B) with a phase mismatch are mixed and, as a result, the degree of polarization becomes independent of the magnetic field.

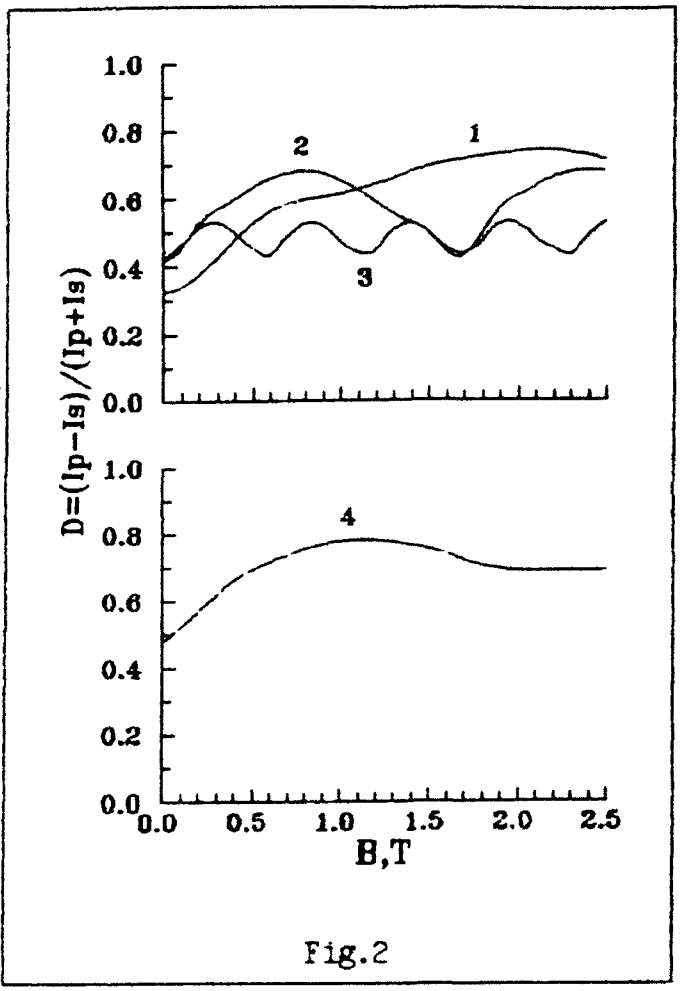

Fig.2

We have studied experimentally the non-oriented plane-parallel polished n-InSb platelets, 0,5x1,6x0,017cm in size, with a density of noncompensated impurity $n=1,5.10^{18}cm^{-3}$. The angle between the normal to

a wide surface (that emitted radiation) and the magnetic field direction was 14° (a Brewster angle) and we observed emission at the angle of 76°.The sample temperature 310K was held. Non-cooled pyroelectric photodetector was used.

Fig.3 shows experimentally obtained degree of polarization of thermal emission as a function of the magnetic field. Curve 1 demonstrates this dependence observed over a narrow spectral band $16\pm0,3\mu m$ while curve 2 shows such a dependence for an integral emission measured in a region from 7 to 11μm.

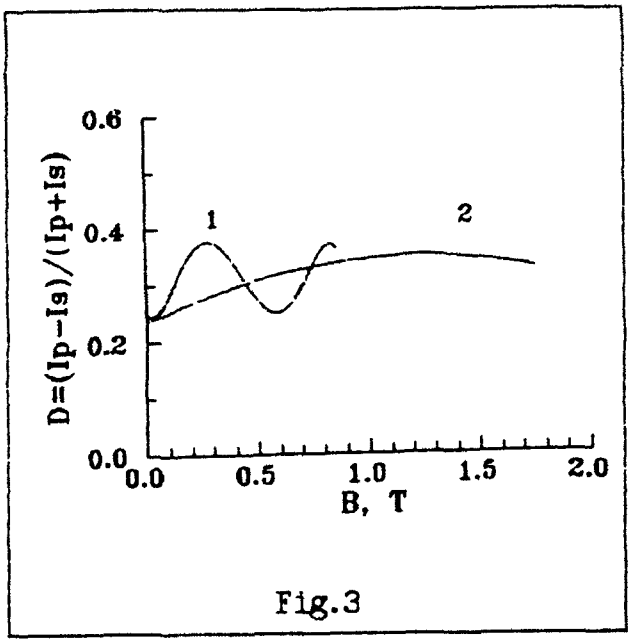

Fig.3

As could be expected, these dependences are non-monotonic and their agreement with calculated one is rather good. The fact that experimentally obtained values are lower than the predicted values may be connected with a finite angular aperture under measurement conditions. From the analysis of calculated and experimental data the electron effective mass $m^*=0,031m$ is obtained. This value check well with those obtained previously by the other methods.

1. V.K.Malyutenko, Infrared Phys. v.32, 291, 1991.
2. T.S.Moss, G.J.Burrell, B.Ellis, Semiconductor Opto-Electronics, Butterworth & Co. Ltd. 1973.
3. W.G.Spitzer, H.Y.Fan, Phys. Rev. v.106, 882, 1957.

TRANSMISSION, REFLECTION AND ABSORPTION IN TRUNCATED SUPERLATTICE

R.Brazis and L.Safonova

Institute of Semiconductor Physics, Gostauto 11,
2055 Vilnius, Lithuania

Introduction

Periodic layered structures are known to support a variety of electromagnetic modes [1,2]. Some of them are encountered in separate single layers, whereas the other are characteristic of periodic structures, e.g., the bulk modes [3] which are describable in terms of dielectric function of an effective homogeneous polarizable medium. However, the effective medium model is expected to fail when the superlattice spatial period is comparable with the wavelength, and/or the number of periods is small.

This work is aimed to show that, besides the above modes, truncated superlattices exhibit a non-reciprocity in reflection and absorption. Magnetic field induces additional non-reciprocity effects, which are comparable to those arising due to the finite size of the structure.

Model description

Let us consider p-polarized electromagnetic wave incident on a multilayer structure consisting of alternating semiconductor and insulator layers in d.c. magnetic field which is parallel to the layers, and normal to the plane of incidence. Suppose that the interfaces are flat, with the step-like carrier density profile. Seeking for the transmission, reflection and absorption coefficients we will use two approximations.

(*i*) Transmitted and reflected electric and magnetic fields of the wave in each layer obey the conditions of tangential component continuity at each interface, and resulting fields are calculated including a layer-by-layer computing algorithm;

(*ii*) The truncated periodic structure is thought as a single homogeneous anisotropic layer, and the transmission, reflection and absorption coefficients are calculated using an effective dielectric tensor of the structure.

In both cases a recurrent formulas for the complex reflection and transmission coefficients are used.

In the case (*i*) the dielectric functions are

$$\varepsilon_{xx} = \varepsilon_{yy} = \varepsilon_L(1-\omega_p^2/(\omega^2-\omega_c^2)),\ \varepsilon_{xy} = -\varepsilon_{yx} = i\varepsilon_L\omega_p^2\omega_c/\omega(\omega^2-\omega_c^2),\ \varepsilon_2=\text{const.},$$

where ω_p is the free carrier plasma frequency, ω_c is the cyclotron frequency in d.c.magnetic field B_o, ε_L is the semiconductor dielectric constant.

In the case (*ii*) the dielectric functions are [3]

$$\tilde{\varepsilon}_{xx} = \varepsilon_{xx}\varepsilon_2 d/\Delta,\ \tilde{\varepsilon}_{xy} = -\tilde{\varepsilon}_{yx} = \varepsilon_{xy}\varepsilon_2 d_1/\Delta,\ \tilde{\varepsilon}_{yy} = \varepsilon_{xx}d_2\delta + \varepsilon_2 d_1\delta_x/d\Delta,$$

where $\Delta = \varepsilon_{xx}d_2 + \varepsilon_2 d_1$, $\delta = \varepsilon_1 d_1 + \varepsilon_2 d_2$, $\delta_x = \varepsilon_{xx}d_1 + \varepsilon_2 d_2$, $d = d_1 + d_2$ is the period of the structure.

As a result, the effects of structure truncation, and the validity of an effective medium model are to be determined. The effective medium approximation is to be applied to the cases when the first, layer-by-layer, calculation technique is not applicable.

Results

Let us consider first the case of normal incidence on a finite periodic structure employing detailed layer-by-layer calculation, as defined in Section (*i*).

It is noticeable that the transmission coefficient T does not depend on the direction of incident wave (Fig.1). The reflection R and absorption A coefficients differ considerably for the cases of forward (1) and backward (2) incidence (Fig.1,a). The non-reciprocity of reflection and absorption is enhanced or suppressed depending on the magnitude of applied magnetic field. Non-monotonous behaviour of $R(B_o)$ and $A(B_o)$ is caused by superposition of several factors, like magnetoplasma cut-off, and the Fabry-Perot resonances of the extraordinary Voigt mode, or the stop- and pass- bands of superlattice.

Let us consider now the same structure using the effective medium model. The structure is thought now as a homogeneous slab characterized by the dielectric constant $\tilde{\varepsilon}$. This approach does not account for the structure asymmetry failing to show, therefore, the non-reciprocity of reflection and absorption (Fig.1, dashed lines). In spite of proper description of general features, this model does not predict some important peculiarities of reflection, transmission and absorption in magnetic fields. The predictions of the effective medium model are seen to improve for wavelengths significantly exceeding the spatial period of superlattice (Fig.1,b). Note that now both the layer-by-layer and the effective medium appoximations predict the same cut-off and resonance positions. The non-reciprocity effects are seen to cease.

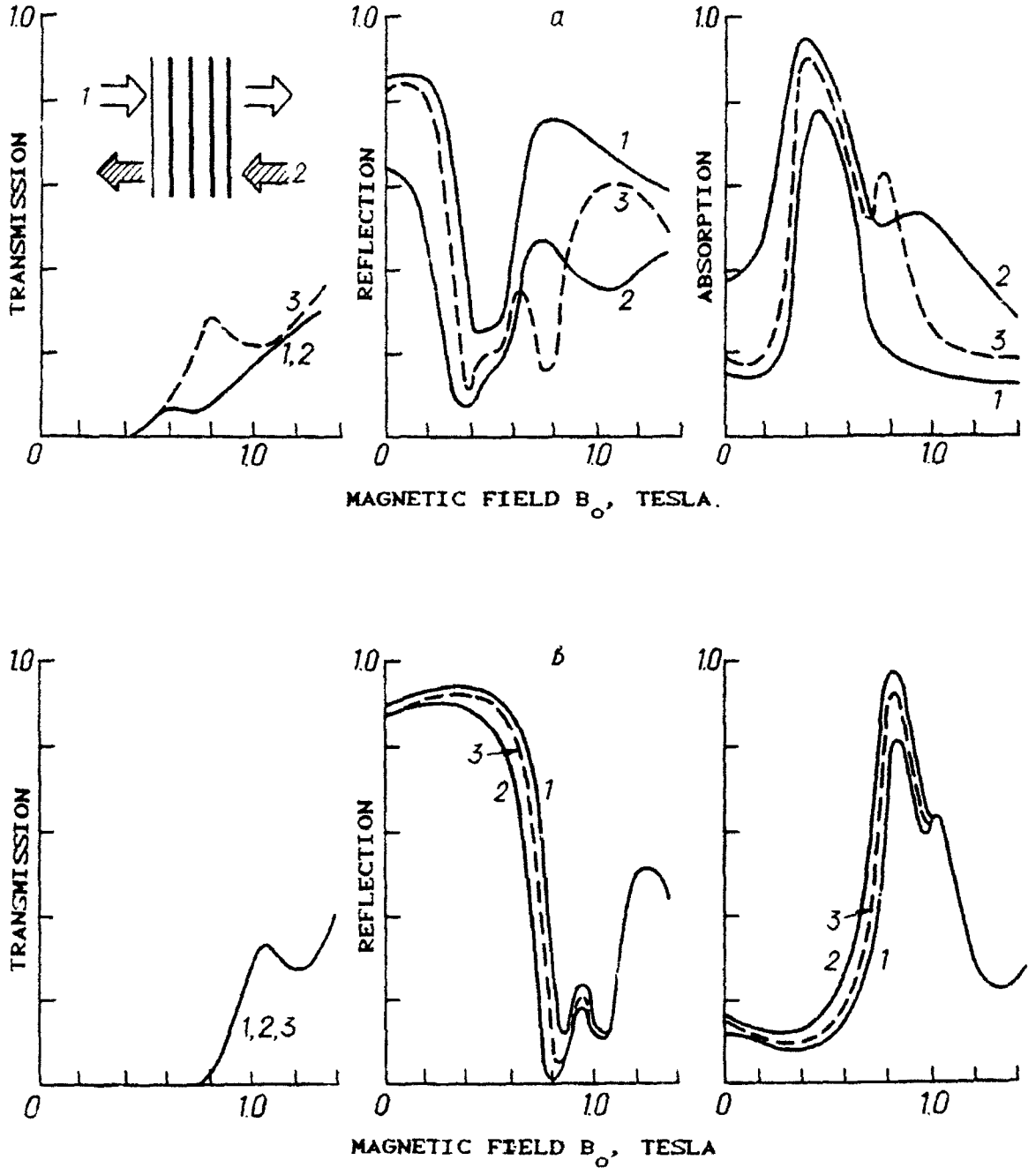

Fig.1. Transmission, reflection and absorption coefficients vs B_o for the structure containing 8 periods. d_1 = 400 μm (InSb, $n = 2 \cdot 10^{14}$ cm^{-3}), d_2=200 μm (Al_2O_3); 1- incidence on InSb layer, 2- incidence on Al_2O_3 layer, 3 - effective medium approximation; incident wave frequency f= 75 GHz(a), and 37,5 GHz(b).

As far as the applicability of the effective medium model is justified, it is of interest to use it in configurations which are difficult to treat exactly. Let us consider the structure with the layers oriented at the angle of $\pi/4$ (Fig.2). Wave transmission through

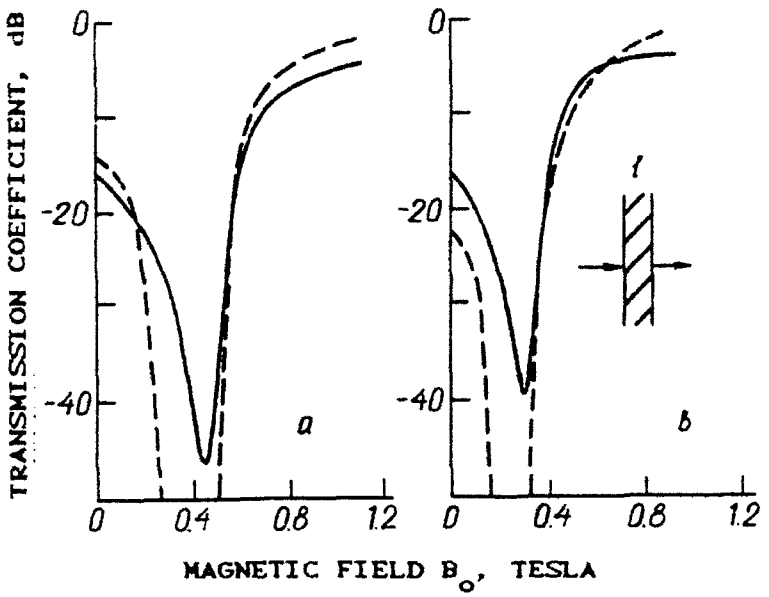

Fig.2. Magnetic-field dependence of transmission. ℓ=3,85 mm, d_1= 200 μm (InSb, $n=2\cdot10^{14}cm^{-3}$), d_2=500 μm (Al_2O_3), f=37,5 GHz (a), 50 GHz (b).

the structure is calculated using Fresnel formulas with the dielectric tensor $\tilde{\varepsilon}$ transformed according to the angle of layer inclination. The calculated $T(B_o)$ dependence (Fig.2, dashed lines) exhibits a pronounced minimum related to the excitation of bulk modes [3]. Experiments on the structure (Fig.2, solid lines) confirm the existence of the resonance, although the experimental minimum is shallow compared to the calculated one

Conclusions

Electromagnetic response of truncated periodic structures exhibit non-reciprocity effects, as well as magnetically controlled resonances, which are observable in reflection, absorption, and transmission. These effects may arise both in millimeter wave region and in the far infrared device structures.

References

1. P.Yeh, Optical Waves in Layered Media, J.Wiley and Sons, N.-Y.,1989.
2. R.Brazis, L.Safonova, Proc. SPIE, 1988, vol.1029, p.74.
3. R.Brazis, L.Safonova, Int.J. IR and MM Waves, 1987, vol.8(5). p.449.

DIELECTRIC CHARACTERIZATION OF MATERIALS AT SUBMILLIMETER WAVELENGTHS USING BWO SPECTROMETERS

Anzin V. B., Goncharov Yu. G., Gorshunov B. P., Kozlov G. V., Lebedev S. P. Volkov A. A.
Institute of General Physics, Russian Academy of Sciences, Vavilov str. 38, 117942, Moscow, Russia

Just as the visible light, radio waves or microwaves, the submillimeter (SBMM) radiation ($\lambda = 0.3 \div 3$ mm, $\nu = 3 \div 33$ cm^{-1}) has its own important areas of industrial, scientific and medical applications. At present, however, the majority of these are practically virgin, because of the absence of the available SBMM radiation.

Owing to the development in Russia of special sources of the SBMM radiation, the miniaturized backward-wave oscillators (BWO), it has become possible to build a unique SBMM BWO-spectrometers, which combine the most significant merits of both infrared spectroscopy and microwave technique [1]. Like lasers, the SBMM BWOs produce beams of polarized monochromatic radiation of high spectral intensity, whose operating frequency, in addition, is continuously tunable in a broad range. It is due to the BWO-spectrometers that the direct wide-band measurements of dielectric and magnetic spectra of substances became possible for the first time at the SBMM waves. As a result, various substances and physical phenomena are now accessible for fundamental and applied research in the SBMM wavelength range [1, 2].

In this report we outline the abilities of the SBMM BWO-spectroscopy in the material science.

The idea of the measurements and its realization in quasioptical spectrometer «Epsilon» are shown in Fig.1. In general, the SBMM properties of different materials are dependent stromgly on

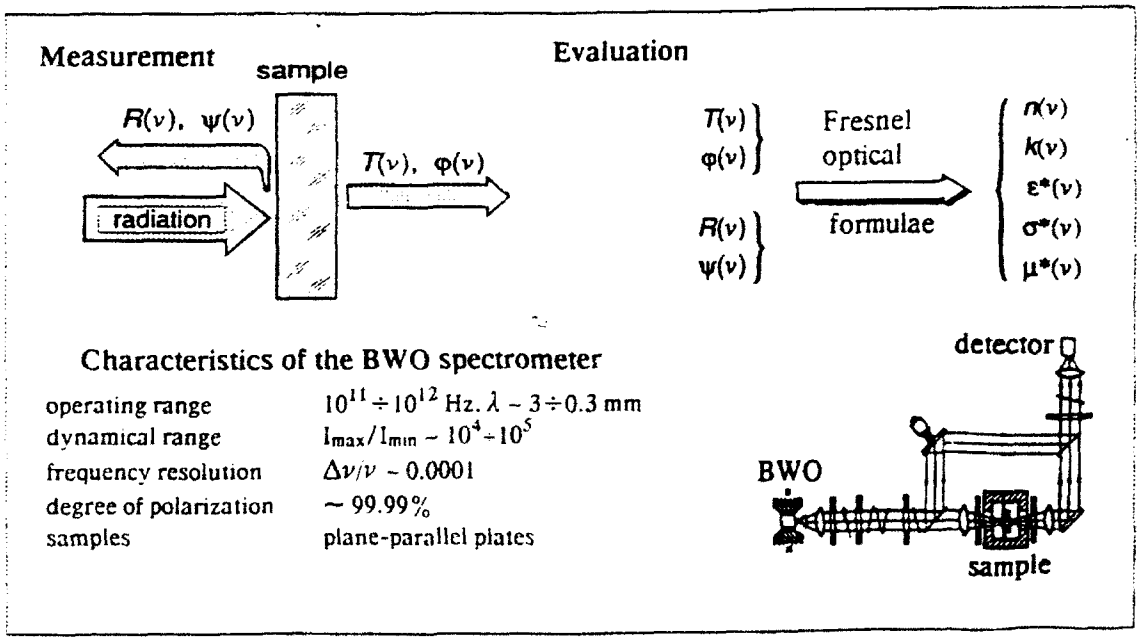

Fig.1. Characterization of the dielectric measurements by quasioptic BWO spectroscopy.

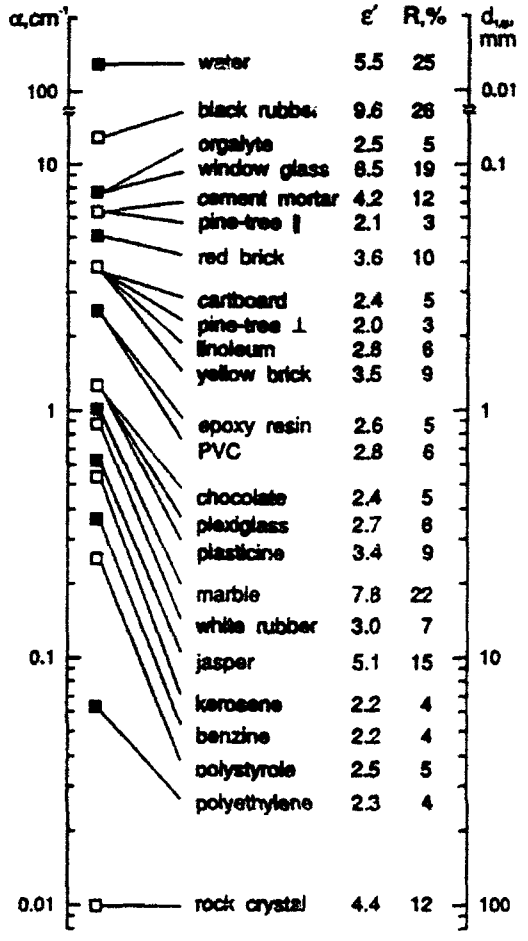

Fig. 2 Dielectric properties of usual materials at frequency 300 GHz (λ = 1 mm, room temperature).
α — absorption coefficient;
ε' – dielectric permittivity;

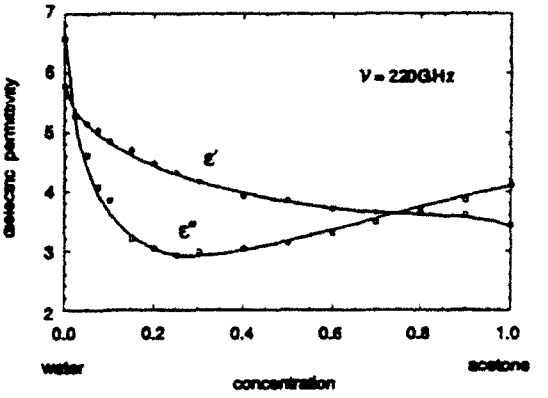

Fig. 3 Variation of the SBMM dielectric properties of the water–acetone mixture in dependence of composition

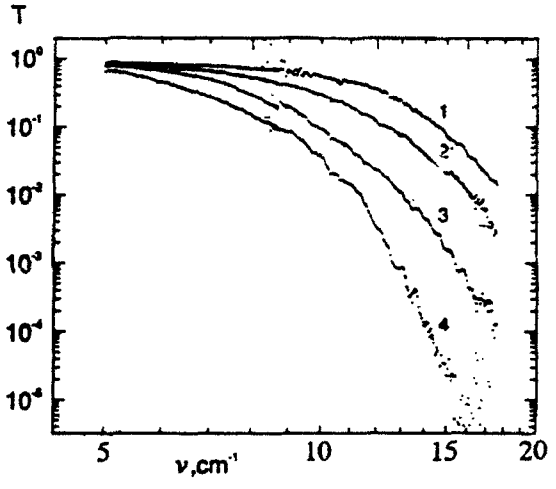

Fig. 4 Transmittivity of chemically identical porous ceramics (curves 1 – 4) with different size of pores (0.5 ÷ 0.8 mm,

their chemical composition, aggregate state, micro- and mesostructure, symmetry, topology, etc. Fig.2 shows how broad the range of these properties is. In most cases the SBMM radiation easily penetrates through the samples of thickness of 1 ÷ 5 mm, convenient for handling.

Fig. 3 presents the explicit dielectric «passport» of the water-acetone mixture. One can clearly see the pronounced dependence of the SBMM dielectric properties of the mixture on its composition. This correlation offers a method of contactless characterization of water solutions.

Figs. 4 and 5 demonstrate the sensitivity of the SBMM radiation to the internal structure of materials. The figures refer to two substances, a commercial porous ceramics and SiO_2 (quartz) samples in three different modifications. In both cases the SBMM radiation evidently distinguishes identical in outward appearence samples, revealing substantially different values of transmittivity

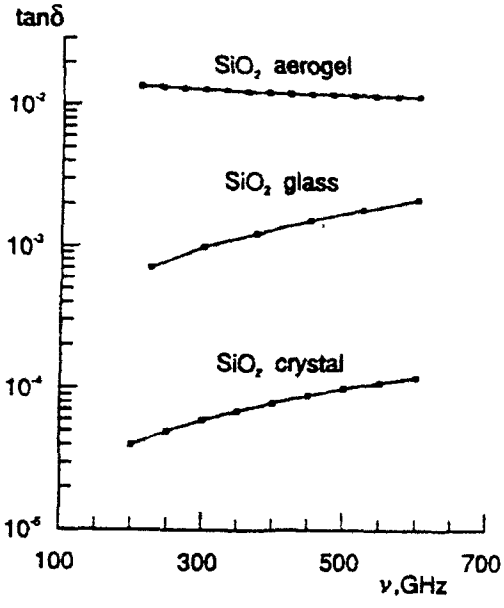

Fig. 5 SBMM absorption of quartz in three different states — single crystal, glass and aerogel.

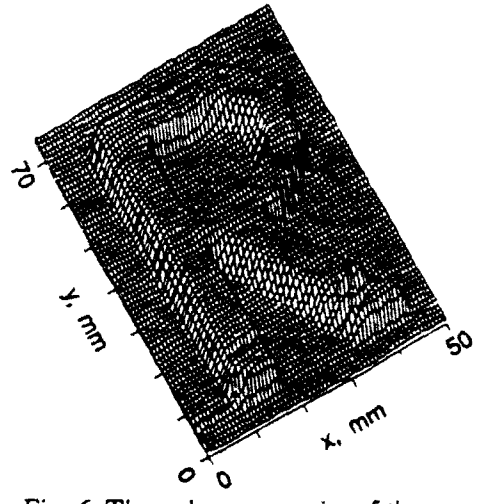

Fig. 6 The «phase portrait» of the paper letter «R» registered by radiation with $\lambda = 1.5$ mm.

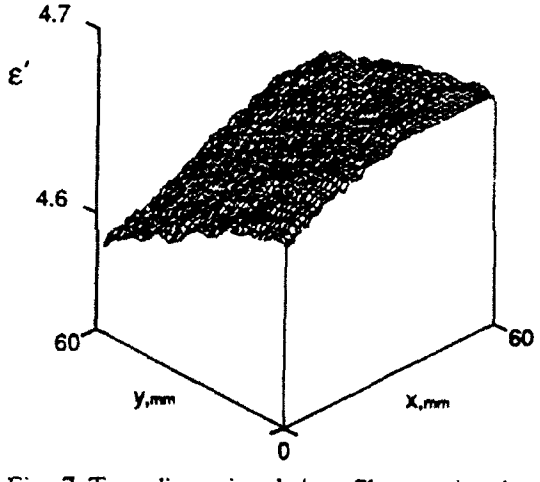

Fig. 7 Two-dimensional ε' profile over the plane of the boron nitride industrial plate.

and absorptivity. The abrupt decrease of transmittivities in Fig.4 is due to SBMM-radiation scattering by pores of different sizes. Much more profound is the changing of the SBMM absorption in quartz: crystal, glass and aerogel (Fig.5). Low density SiO_2 (aerogel), which is only 5% as dense as the bulk crystal or glass, reveals a giant absorption compared with that of crystalline or glass SiO_2. This phenomenon is not yet fully understood. Nevertheless, the general result (the smallest density of the sample corresponds to the highest the SBMM absorptivity) is highly striking and promising for application.

Having shorter wavelength compared with radio and microwaves, the SBMM radiation has a great advantage for introscopy. SBMM spectrometers allow to perform local (in plane of the sample, which can be either a plane parallel plate or a film on the substrate) measurements, mapping the dielectric parameters with a spatial resolution of about 1 mm (Figs. 6 and 7). The sensitivity of the BWO interferometric methods is high enough to detect the inhomogeneity of the optical thickness down to 10 μm.

The following examples (Figs. 8 and 9) are devoted to the problem of the SBMM characterization of the materials used in radioelectronic industry. Fig.8 demonstrates a method for distinguishing between fundamental and technological absorption mechanisms in the high Q-factor

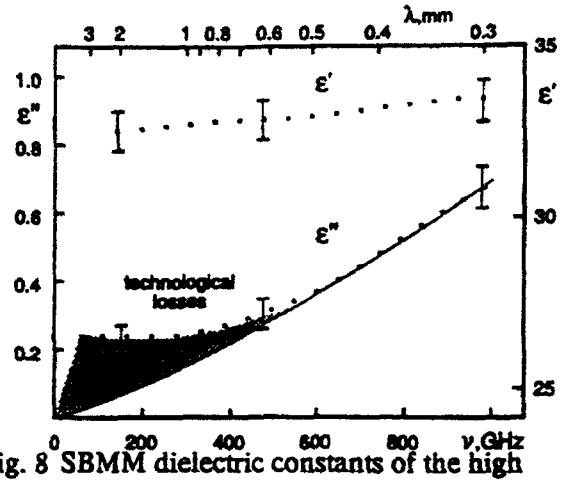

Fig. 8 SBMM dielectric constants of the high Q-factor industrial microwave ceramic.

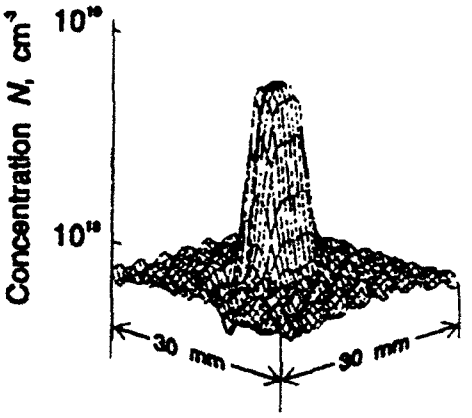

Fig. 9 Density of free carriers distribution in semiconductor plate of Si used in microelectronics (registered at $\lambda = 1.5$ mm).

microwave ceramics. In this case the SBMM dielectric constants measured by BWO-spectrometers are of great importance, setting the level of fundamental losses for the microwave region.

When testing semiconductors the SBMM approach is a local, contactless and nondestructive one in contrast to conventional methods, based on Hall effect, four-probe technique, etc. Fig.9 shows the two-dimensional pattern of the distribution of the charge carrier density in commercially produced silicon plate. The panorama is calculated on the basis of the SBMM local transmission and phase spectra.

In summary, by a few selected examples we have demonstrated the abilities of the submillimeter BWO spectrometers in materials characterization. The spectrometers allow measurements of dielectric and magnetic parameters of practically any kind of material at frequencies $3 \div 33$ cm^{-1} in the temperature interval $5 \div 1000$ K as well as local sensing with spatial resolution of about 1 mm.

References

1. *A.A.Volkov, Yu.G.Goncharov, G.V.Kozlov, S.P.Lebedev, A.M.Prokhorov.*
Dielectric measurements in the submillimeter wavelength region.
Infrared Physics, vol. 25, № 1/2, p.369, 1985.

2. *A.A.Volkov, G.V.Kozlov, A.M.Prokhorov.*
Progress in submillimeter spectroscopy of solid state.
Infrared Physics, vol. 29, № 2-4, p. 747, 1989.

CHARACTERIZATION OF MILLIMETER-SUBMILLIMETER FILTERS BY USE OF BWO SPECTROMETERS

Anzin V.B., Goncharov Yu.G., Gorshunov B.P., Kozlov G.V., Lebedev S.P., Volkov A.A.
Institute of General Physics, Russian Academy of Sciences, Vavilov Str. 38, 117942, Moscow, Russia

Along with the mastering of millimeter (MM) and submillimeter (SBMM) spectral ranges for the purposes of spectroscopy, the problem of construction of different filtering systems is becoming increasingly important. By analogy to optical units, various MM–SBMM high-, low- and band-pass filters can be developed using metallic grids, meshes or dielectric layers as elements. However, the characterization of these constructions by measuring their electrodynamic properties is not so easy and trivial for conventional spectroscopic techniques.

In this report we discuss the abilities of Backward-Wave-Oscillator spectrometers [1], developed in the Institute of General Physics of the Russian Academy of Sciences, for studying the electrodynamic properties of the SBMM filters. (Some details of the method of BWO-spectroscopy and related references see in the report of Anzin V.B. *et al.*, contributed to this Conference).

BWO-spectroscopy is a nonconventional technique of far-infrared spectroscopy, which employs a radiation «of high quality» — intensive, monochromatic, polarized and frequency tunable. The working frequency range of the technique is $10^{11} \div 10^{12}$ Hz. In this spectral range the BWO-spectroscopy is nearly the only one, giving the possibility of reliable and detailed investigation of the characteristics of the filters. Figs. 1 – 4 present a few typical examples of the

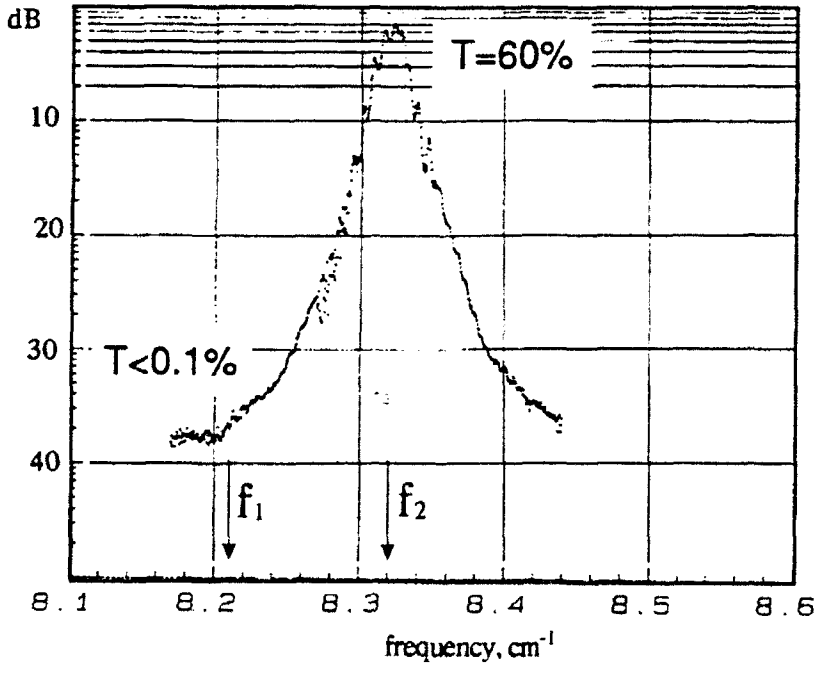

Fig.1. Transmittivity *vs* frequency of the tandem of two wire-grid Fabry-Perot interferometers (high-contrast band-pass filter). The filter separates two closely situated SBMM laser lines of frequencies $f_1 = 8.21$ cm^{-1} and $f_2 = 8.32$ cm^{-1}.

BWO-characterization of the filters. We note that in two cases (Figs. 1 and 4) the filters were developed in our laboratory for special purposes:

1) Separation of the two closely situated SBMM laser lines;
2) Express measurement of the wavelength of the SBMM radiation (filter–λ-meter).

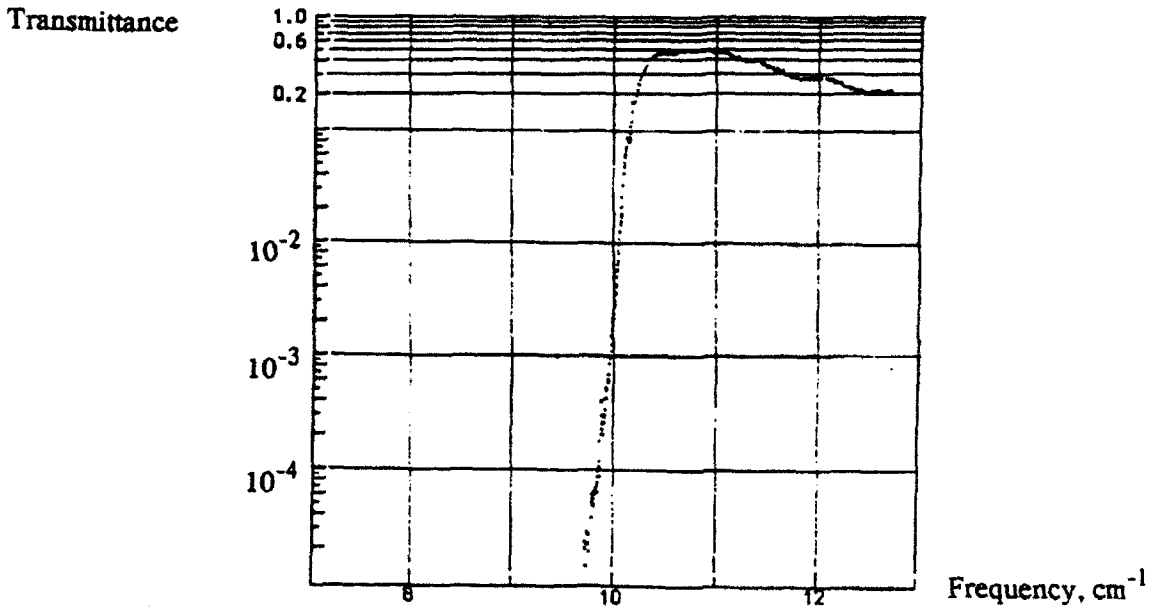

Fig.2. Transmittivity *vs* frequency of the perforated metallic cutoff filter.

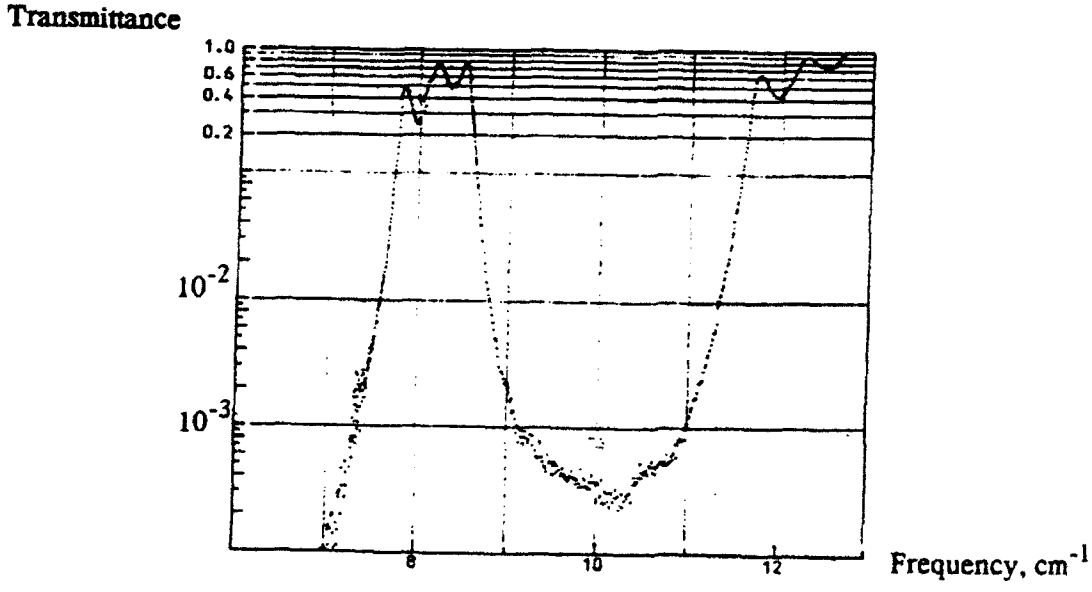

Fig.3. Transmittivity *vs* frequency of the band-pass mesh filter.

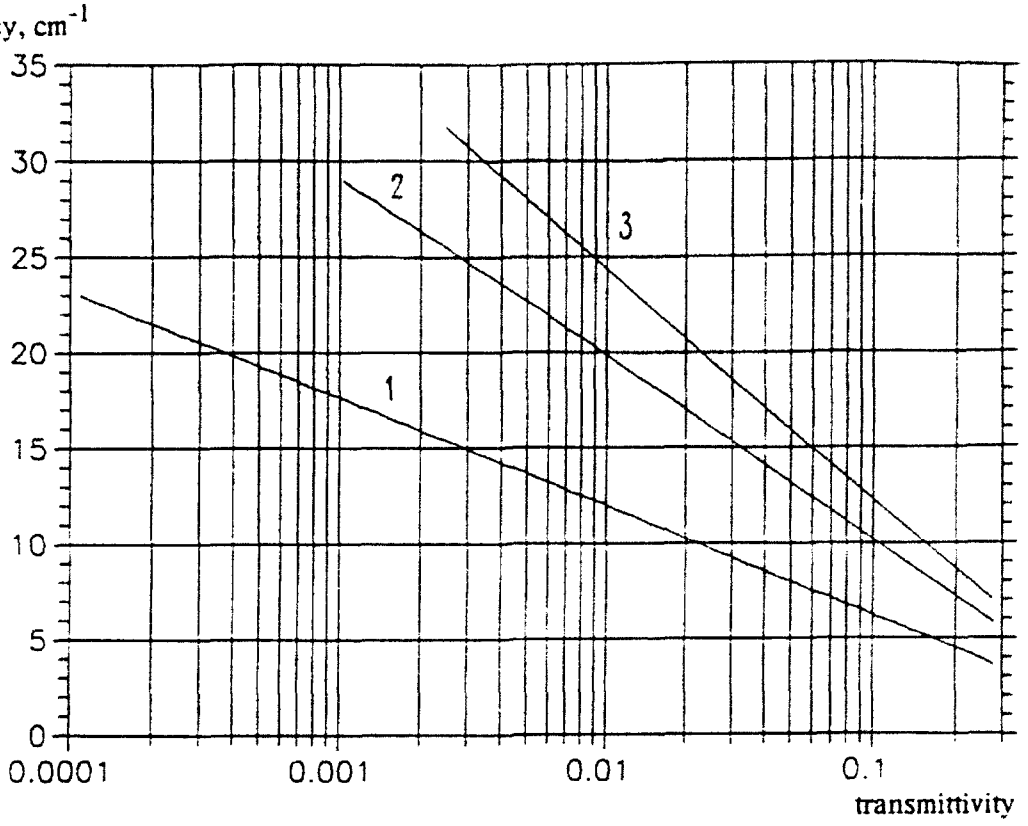

Fig.4. Transmittivity *vs* frequency of the plane-parallel plates made of a dielectric with low reflectivity, R = 7% and absorption coefficient $\alpha = 4\pi k/\lambda$ propotional to frequency, where k = const ≈ 0.05. Due to the single-valued relation between transmittivity and wavelength the filter is used as λ-meter.

Acknowledgement

We are grateful to Dr. F. Keilmann from Max Plank Institute, Stutgart, for stimulating this work, fruitful discussions and collaboration.

Reference

1. *A.A. Volkov, Yu.G. Goncharov, G.V. Kozlov, S.P. Lebedev, A.M. Prokhorov.*
Dielectric measurements in the submillimeter wavelength region.
Infrared Physics, vol. 25, № 1/2, p.369, 1985.

DESIGN AND PERFORMANCE OF Ka-BAND INTEGRATED CIRCUIT MIXER

Wang Biao, Zhou Baoqing, Bei Linxie
(Institute of Technical Physics Academia,
Shanghai, China)

ABSTRACT

Integrated circuit mixer using a crossbar suspended stripline configuration was developed with GaAs beam lead diodes made in home.Together with an IF amplifier,the system exhibits a 3.1-3.7dB double sideband(DSB) noise figure over 50-550 MHz IF bandpass with the LO at 33-38 GHz.Integrated circuit building blocks, such as filter, electric probe type transition and matching circuits,were also developed.

INTRODUCTION

The rapid acceleration of millimeter-wave activities has led to a strong demand for low-noise integrated mixers for both civil and military applications.Prior to this,fabricating mixers for this portion of spectrum required the use of packaged schotty diodes or whisker-contected diode array.Because of the drawbacks in realibity and repeatability,they don't get general high volume use.The integrated circuit technologies,on the other hand, share none of the abovementioned drawbacks because of the absence of good beam lead diode,and provide the advantages of low noise temperature,low cost,light weight and small size.These also have the potential of direct translation into monolithic circuits and even large-scal integration.

we have developed a ka-band crossbar suspended stripline integrated circuit mixer with the beam lead diodes made in home.together with an IF amplifier,the receiver front-end exhibits a 3.1- 3.7dB double sideband noise figure over 50-550 MHz IF bandpass with LO at 33-38 GHz.The LO/RF isolation was achieved larger than 20 dB.

To facilitate the mixer development,filter,electric probe type transition,matching circuits,were developed in integrated circuit to form with low insertion loss.The performance of these components will be discussed.

CROSSBAR STRIPLINE BALANCED MIXER

The circuit configuration of our crossbar stripline mixer is shown in Fig.1.The RF signal is applied to mixer diodes from a waveguide perpendicular to the circuit board.The crossbar configuration is formed by two mixer diodes with opposite polarity connected in series across the broadwall of the waveguide.The diodes are thus in series with respect to the RF signal and in parallel with respect to the IF and LO signals.The IF signal is extracted via a low-pass filter and the LO signal is injected from the other side through an electric

probe type transition.

1.Electric Probe Type Transition

The waveguide to suspended stripline transition is the important part of the mixer.An electric probe type transition was investigated,as shown in Fig.2. It consists of an electric probe inserted into waveguide formed by an extension of the suspended stripline.This idea is very similar to the conventional waveguide to coaxial line transition.By optimizing the probe shape theoretically,broad bandwidth has been accomplished with low insertion loss,and the maximum of insertion loss is less than 0.7dB as the LO is swept from 30 GHz to 38 GHz.The dimensions of the transition were determined as shown in Fig. 2,where a=7.112mm, b=3.556mm, 2w=0.374mm, x1=1.800mm, d2=0.254mm, d3=3.630mm, Er=2.22mm, z1=2.1mm.

2.Filter Design

To pass the IF frequency with a low insertion loss and reject the LO and RF signals,a low-pass filter is required.In this mixer,the Chebyshev IF filter with a 0.1dB ripple are computed.The filter performance is optimized through the COMPACT computer program,as shown in Fig.3 and Fig.4.The output and input impedances are both 50 ohm.

3.Mixer Design Considerations

To guarantee the cutoff frequency of the dominant waveguide mode(LSM11) of suspended stripline much larger than the frequency band of interest,a cross section of 3.00x1.60mm^2, a Duroid substracte thickness of 0.254mm were selected.The cutoff frequency of LSM11 mode is 47.8 GHz.

In mixer design,the performance parameters of primary concern are the operating bandwidth,the conversion loss and the noise temperature. The equivalent circuit model of the crossbar suspended stripline integrated circuit mixer is shown in Fig.5.To treat this analytilly,a special program has been developed for nonlinear and linear analyses of the balanced mixer.The nonlinear analysis is based on multi reflection techniques.Using this program,we can predict the conversion loss,noise temperature,IF and RF impedance for design.

The beam lead diodes we used were provided by the Institute of Metallurgy, Shanghai, China,and the parameters are listed in table 1.

Table 1. Parameters of the diode

Para.	Rs(ohm)	Cp(pf)	Cj0(pf)	Vb(v)	Is0(pA)	Ø(v)	n
vol.	5/7	0.06/0.09	0.05/0.07	6.0	~1	1.0	1.3

It shows that under fully turned-on conditions,the IF output impedance is about 50 ohm and the RF input impedance is about 100ohm,while the reactance part being tuned out by sliding short. Waveguide impedance is in the range of 400 to 600 ohm and can be matched to the RF signal input impedance by a reduced-height taper transformer.

4.Mixer Performance

Together with an IF amplifier,a 3.1-3.7dB double sideband noise figure was achieved over 50-550 MHz IF bandpass with the LO at 33-38 GHz,and the noise figure of IF amplifier is less than 1.5dB. Fig.6 shows the performance of the integrated circuit mixer.

The LO and RF ports are isolated each other because of the the perpendicularity, and the LO/RF isolation was achieved larger than 20dB.

CONCLUSIONS

The integrated circuit exhibits a state-of-the-art performance for narrow-band operation at ka-band.Because of the lack of broad-band IF amplifier,the performance for wide-band operation has not been achieved,but it is significant to carry it.

REFERENCE

1.U.H.Gysel, proc. 5th European Microwave conf.,sept,1975. page491-495

2.A.G.Cardiasmenos and P.T.Parrish, IEEE MTT-S Int. Microwave symp. dig. Apr.30-May.2,1979,page22-24.

3.K.Louie,IEEE MTT-S Int. Microwave Symp. 1982,page 369-371

4.RAGHBIR.S.TAHIM,GEORGE M.HAYASHIBARA,KAI CHANG, IEEE Trans. Microwave theory tech.,VOL.MTT-31,March 1983,page 277-283.

5.B.Glance and R. Tramarulo,IEEE Trans. Microwave Theory Tech.,VOL. MTT-21,Feb. 1973,page117-118.

6.A.R.Kerr,IEEE Trans.,Microwave Theory Tech.,VOL. MTT-23,Oct.1975.

7.Daniel N. and A.R.Kerr,IEEE Trans. Microwave Theory Tech.,VOL.MTT-26,1978.

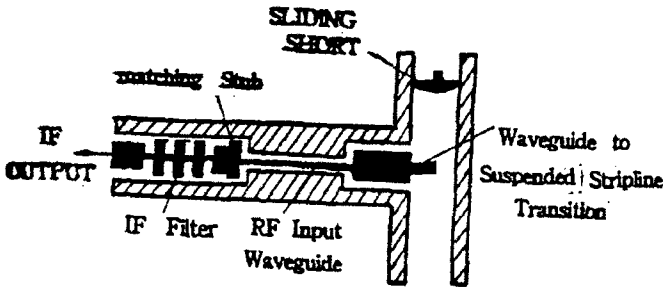

Fig.1 Crossbar stripline mixer

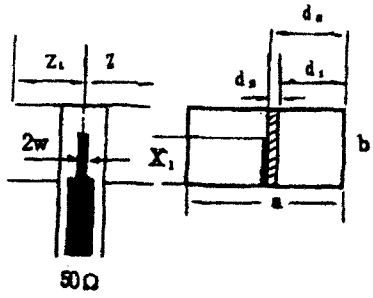

Fig.2 Waveguide to suspended stripline transition

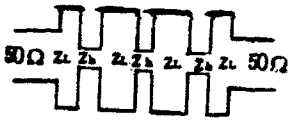

Fig.3 Low-pass filter CirCuit Lagout and Z_L=32Ω, Z_h=160Ω

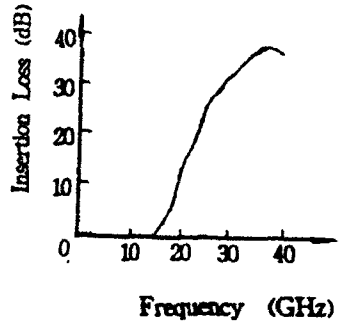

Fig.4 Predicted Performance of a Low-Pass filter

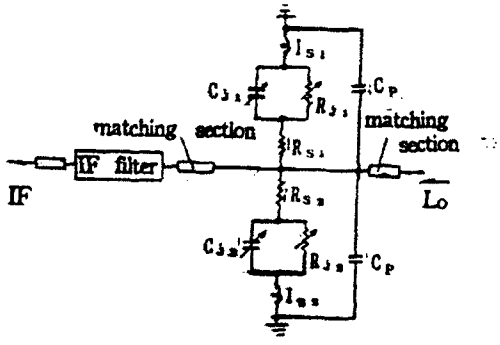

Fig.5 Crossbar stripline mixer equivalent Circuit

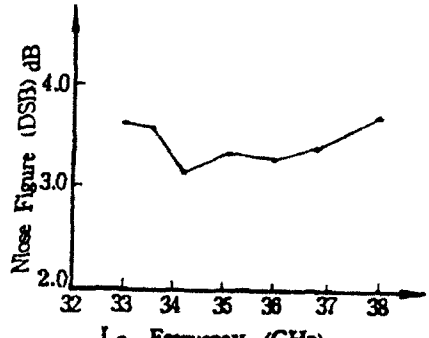

Fig.6 DSB noise figure for mixer

W4.2

Ka-BAND GaAs GUNN MMIC VCO

LaiPing,WangMaosen,LinJinting
(Nanjing Electronic Devices Institute,Nanjing,China)

ABSTRACT

A full monolithic GaAs Gunn VCO is presented in this paper.The designed VCO incorporates a Gunn diode,a Schottky diode,matching network and bias circuit on a 5mmX3mm chip.The Gunn oscillator delivers 2.5mW at 38GHz with the maximum of 3mW at 34.6GHz and the tuning bandwidth of 90GHz.A further improvement may be attained by better process control.This is the first report of a Ka-band MMIC VCO and millimeter wave MMIC at home.

INTRODUCTION

Monolithic microwave integrated circuits fabricated on GaAs substrates have shown several attractive advantages over hybrid technology in the area of cost,size,weight and some RF performance.As the frequency increases to the millimeter-wave range,monolithic technology becomes more attractive because of the smaller size of both lumped and distributed circuit elements.The design,fabrication and RF measurement of a full monolithic millimeter-wave VCO based on a Gunn diode are presented in this paper.

DEVICES

As compared with MMIC using GaAs MESFET,the MMIC based on Gunn device has less requirements for material and the process is much easier.The Gunn structure material used in this MMIC VCO is grown by vaper phase epitaxy on semi-insulating substrate,and a Schottky diode used as tuning element is also fabricated compatibly.Both diodes are circular with diameter about 30 microns and 50 microns,respectively.The concentration (n) width (L) product (nL) is in the range of 3.0 to $3.4X10^{12}$ /cm^2 .The area of Gunn diode is determined by the maximum safe temperature rise for the Gunn diode's active area and the calculated thermal resistance of the GaAs substrate with the thickness of 80 microns.The diameter of varactor is determined by the zero bias capacitance,which should be chosen to meet provides the maximum tuning bandwidth for the VCO.The cathode connection to two diodes is accomplished using airbridge technology.These bridges are plated to approximately 6 to 8 microns thick to enhance heat sinking.

CIRCUIT DESIGN

The circuit design is accomplished by using of the TOUCHSTONE CAD program.In this simulation,the Gunn diode,airbridge,pad and via hole are defined as a single negative resistance device in the oscillator circuit.The impedance of circuit added to the impedance of the defined negative resistance device must be zero to meet the oscillation condition. The optimization routine is used to determine the size of

microstrip circuit which meets the oscillation condition and optimum impedance match at desired frequency.Figure 1 shows the performance predicted by the computer simulation.The varactor capacitance can be chosen for maximum tuning bandwidth as predicated by the computer simulation.Its bandwidth is 400MHz.So far,a full monolithic millimeter-wave VCO can be fabricated as the circuit layout.Figure 2 shows the final layout of the MMIC.Ground returns for both Gunn and varactor diodes are provided by airbridges,ground pads and via holes.The microstrip line couples the Schottky tuning varactor to the circuit.Varactor and Gunn diode bias voltages are applied through single section RF chokes with cutoff frequency of 20GHz.An inter-finger microstrip capacitance is used as DC block at the output terminal.

FABRICATION

The circuits were fabricated from epitaxial GaAs n+/n/n+ layers deposited by VPE onto undoped semi-insulating liquid encapsulated (LEC) grown substrate.Main fabrication processes of this VCO are introduced as follows:

A. Forming a via hole with 80 microns in depth by PDE.
B. Making the Gunn cathode.
C. Chemical etching unwanted top n+ and part of n layer.
D. Defining the diode geometry and struture by mesa etching away unwanted n layer and bottom n+ layer,selectively.
E. Forming anodes and the microstrip circuit.
F. Making Schottky contact for varactor diode.
G. Making airbridges with high spans.
H. Thinning the substrate to 80 microns and electroplating a 50 microns thick gold layer to form heatsink.
I. Seperating the wafer to single chips and mounting.

MEASUREMENT AND PERFORMANCE

The monolithic VCO chips were mounted in appropriate test fixtures for DC and RF measurement.The DC and RF characteristic have been measuremented.A typical DC characteristic of a monolithic Gunn diode is shown in Figure 3.
There are two testing structures used for RF measurement of the monolithic VCO chip,one is the microstrip probe structure,another is the metal probe structure.For both of the two testing structures,the key point is to reduce the transition loss to minimum.The measurement result shows that,when the varactor at zero bias,an output power of 2.5mW at 38GHz and 3.0mW at 34.6GHz are achieved.The maximum tuning bandwidth 90GHz is gained with minimum output power 0.6mW.Frequency spectra of MMIC Ka-band VCO is show in Figure 4.

CONCLUSION

A full monolithic GaAs Gunn VCO is described in detail,including design,fabrication and test.The Gunn VCO delivers 2.5mW at 38GHz with the maximum of 3mW at 34.6GHz and the tuning bandwidth of 90GHz.A further improvement may be attained by better process control.Further work is continuing.

ACKNOWLEDGMENTS

The authors would like to thank Cheng Yan,Xie Zhonghua,Zhao Dade and He Jufen for their great support and useful help.

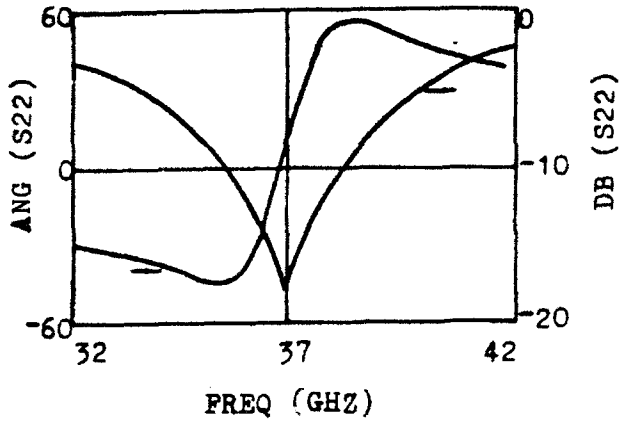

Fig.1 Computer Model Result (S22)

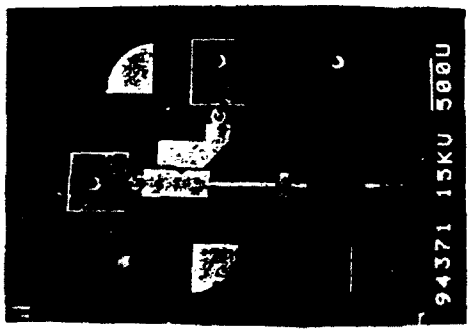

Fig.2 Gunn VCO Circuit Layout

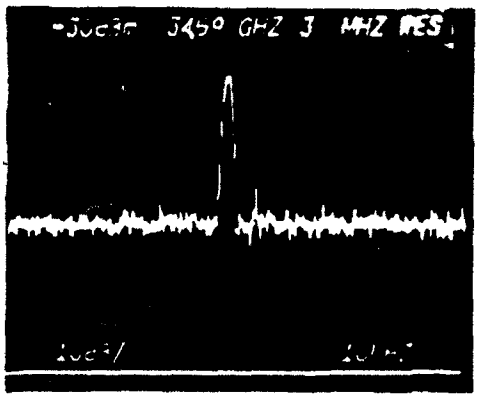

Fig.4 Frequency Spectra of MMIC VCO

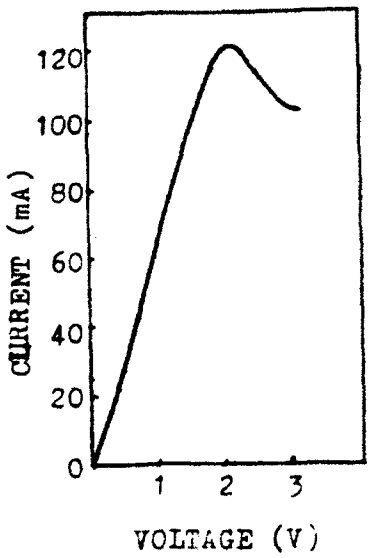

Fig.3 A Typical I-V Characteristic of Gunn Diode

Progress in Millimeter-Wave Integrated-Circuit Horn Antennas

Yong Guo
Department of Electrical and Computer Engineering
College of Engineering, Clemson University
Clemson, SC 29634

Jung-Chih Chiao, Kent A. Potter, David B. Rutledge
Division of Engineering and Applied Science
California Institute of Technology
Pasadena, CA 91125

Abstract — **Integrated-circuit probe-excited horn-antenna arrays etched in silicon are well developed. They are a very promising class of antenna arrays for millimeter and submillimeter applications. Further development of this technology involves integrating mixers and amplifiers into the antenna arrays. In an effort to develop an antenna-mixer array based on the existing technology, horn structure and various antenna probes inside the pyramidal horns have been examined on scaled model-horns at the microwave frequencies. In this paper, modeling results of horn structure and design principles of these antenna probes have been presented, which include the resonant impedance, the operating frequency, and the bandwidth of the horn antennas. The horn structure design illustrates a new approach in developing quasi-optical antenna-mixer array. These probe measurement results provide a guideline in designing horn probes for millimeter/submillimeter-wave integrated-circuit horn-antenna-mixer arrays.**

I. Introduction

In millimeter/submillimeter-wave systems, because of their shorter wavelengths compared with microwave systems, the waveguide circuits become much smaller, which makes them very difficult and expensive to build. However, quasi-optical components provide a solution to this problem. Millimeter-wave integrated-circuit horn-antennas combine antennas and mixer circuits into a single entity. The design is based on an exiting technology by which dipole excited integrated-circuit horn antennas are made in silicon [1]. The horn antennas consist of probes suspended on a thin oxynitride membrane inside pyramidal horns which are chemically etched in silicon. The antennas are free of dielectric losses and have plenty of space for electronic interconnections between the probes. The aperture efficiency of these etched horn antennas has been improved to 72% [2]. Recent research shows that the experimental results agree well with the theoretical analysis, including radiation patterns and resonant dipole impedances [3]. These types of circuits could be mass produced by standard integrated-circuit technology and will find applications in millimeter-wave imaging systems, remote-sensing, radio astronomy, and communication systems.

The horn-antenna-mixer design requires consideration of horn structure, impedance matching, conversion loss and frequency response of the antenna-mixer circuit. Antenna probes are required not only to couple the free-space wave energy to the mixer circuit but also to provide a suitable impedance, the embedding impedance, to the mixer diodes. This impedance over a wide frequency range is also important for mixer performance because various frequency components exist in the mixer circuits. In order to achieve an impedance-matched antenna-mixer array, the characteristics of the antenna probes inside the horns must be investigated.

II. Horn Structure Design

In order to avoid the difficulty to supply an LO power at a frequency close to RF, a subharmonically-pumped antenna-mixer array is designed which is pumped by an LO at only half of the RF frequency. Since the RF and the LO frequencies differ by approximately a factor of two, in

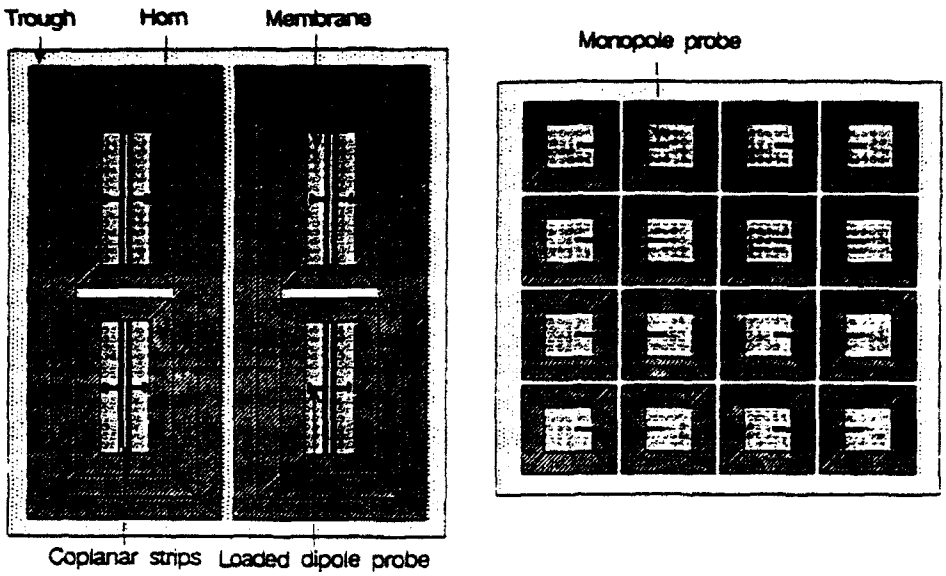

Figure 1 The horn structure of the subharmonically-pumped mixer design, one LO horn corresponding to four RF horns; (a) LO horns, the trough made of two silicon wafers is put on the top of the horns. (b) RF horns, monopoles are used for the RF reception.

principle, it is easier to realize the isolation between the RF and the LO. Furthermore, spurious responses associated with the odd harmonics of the LO can be rejected by using an antiparallel diode pair. The subharmonically-pumped horn-antenna-mixer array is shown in Figure 1. It consists of a set of forward- and backward-looking horns facing back to each other made silicon wafers. Every four RF horns are provided with one LO horn which is a rectangular-shaped horn. The spacing between RF horns is 1λ. Four RF horns, as a sub-array, together with one LO horn, form a unit cell. This design will keep the best symmetry, and the beam patterns of the sub-array will be improved by a factor of 4 compared with that of the single RF horn. Since the size of the LO horns should be twice that of the RF horns, the area between the LO horns is covered by a structure with long trough on each row of the LO horns so as to fill up the space between the LO horns and converge the incoming energy into the LO horns. Every monopole from each of the four RF horns will couple the RF signal down to the LO horn through a coplanar-strip transmission line. A dipole probe is employed to receive the LO. The mixer diodes are located in the center of the LO membrane, and the IF is led out from the ends of the LO horn.

III. Probe Modeling

The impedances of various probes were measured in low-frequency model-horns, which were made of two different types. One type was a 3×3 array made of aluminum, and the other type was a half horn made of copper sheet sitting on a big copper-clad circuit board that was used as an image plane. These two types of modeled horns were used alternatively, depending on the feed location of the probe inside the horn. The modeled design frequency is 5 GHz. The horn opening is 1λ, and the probe is placed inside the horn about 0.37λ away from the apex. Measurements were made on an HP 8510 Network Analyzer. The probe configurations are shown in Figure 2 and the measured probe impedance plotted on the Smith chart are illustrated in Figure 3.

Frequency Tuning — Figure 2(a) shows a monopole in a full horn. The impedance is plotted as a function of the monopole length on the Smith chart (Figure 3(a)). The resonant resistance of 16 Ω

is achieved at the monopole length of 0.22 λ. In comparison, the resonant resistance of a lossless monopole on a ground plane in free space is 25 Ω for a monopole length of 0.25 λ. Figure 2(c) shows a half dipole in a half horn. The impedance is plotted as a function of the half-dipole length (Figure 3(c)). The resonant resistance is 25 Ω at the half-dipole length of 0.20 λ. Since the voltage across the half dipole in the half horn is half that in a full horn, the measured impedances are only *half* of the actual impedances; therefore, for a dipole in a full horn, the resonant resistance is 50 Ω at the full-dipole length of 0.40 λ. This result was verified by millimeter-wave measurements [2] and theory [3]. This dipole probe also provides a very good matching impedance for the mixer diode pair.

Impedance Tuning — Figure 2(b) shows a folded monopole in a full horn. The impedance is plotted as a function of the monopole-probe length (Figure 3(b)). A resonant resistance of 50 Ω is obtained for a monopole length of 0.19 λ. This resistance matches the impedance of two mixer diodes connected in antiparallel. Hence, this folded monopole is suitable for LO reception in a fundamentally-pumped antenna-mixer-array. Figure 2(d) shows a half folded-dipole in a half horn. The impedance is plotted as a function of the half-dipole length (Figure 3(d)) . The resonant resistance of 68 Ω is obtained at the half-dipole-probe length of 0.18 λ. For the same reason stated above, the resonant resistance of a full folded-dipole in a full horn would be 136 Ω at the full-folded-dipole length of 0.36 λ, compared with 200 Ω for a lossless folded dipole in the free space. This folded-dipole impedance needs to be transformed to be about 200 Ω to be used as an RF reception element in a balanced fundamentally-pumped antenna-mixer-array design.

Broad Bandwidth — Figure 2(e) shows a fan-probe in a full horn, which is designed as a broadband probe-excited horn-antenna. By tuning the flare angle and width of the fan, a resonant resistance of 65 Ω has been obtained at the design frequency of 5 GHz. The return loss is better than 10 dB over a frequency range of 2 GHz. Figure 3(e) shows the impedance plotted as a function of frequency.

Probe Loading — Figure 2(f) shows a half loaded-dipole in a half rectangular-horn, to be used potentially for LO reception in the subharmonically-pumped antenna-mixer. The dipole probe was loaded with a short stub on the end near the horn sidewall to compensate for the capacitive

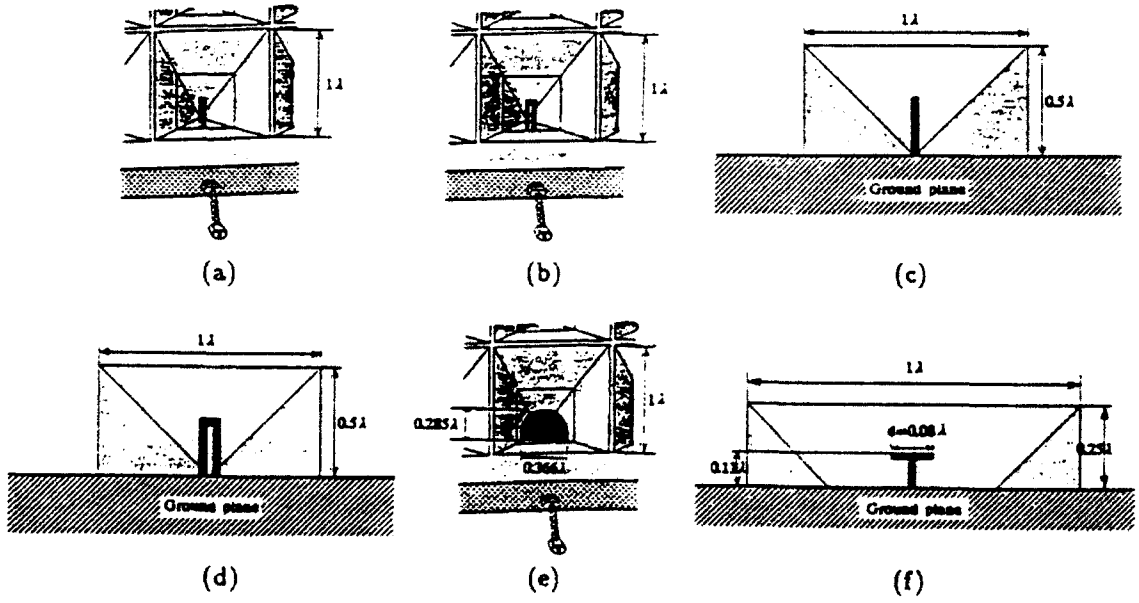

Figure 2 Probes inside pyramidal horns; (a) monopole, (b) folded-monopole, (c) half dipole, (d) half folded-dipole, (e) fan-probe, (f) half loaded-dipole inside a rectangular horn.

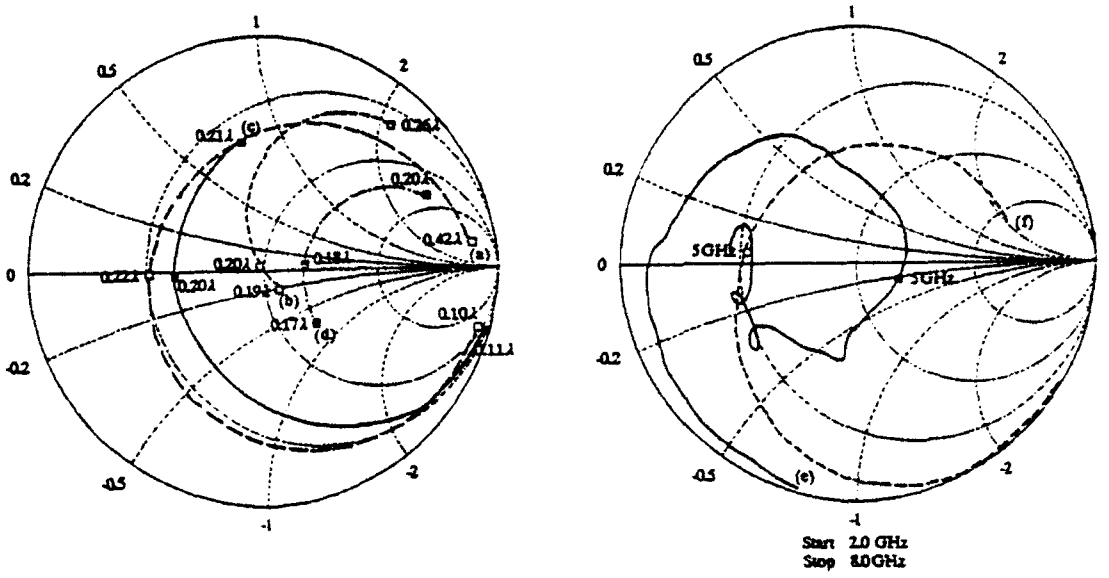

Figure 3 The probe impedance plotted on the Smith chart. (a) monopole, (b) folded-monopole, (c) half dipole, (d) half folded-dipole, (e) fan-probe, (f) half loaded-dipole inside a rectangular horn.

impedance of the relatively shorter dipole-probe. Figure 3(f) shows the impedance plotted as a function of frequency. The resonant resistance of 18 Ω is achieved at the loading-stub length of 0.08 λ, which corresponds to 36 Ω for a full loaded-dipole in a full horn. This loaded-dipole can be used to match the impedance of two mixer diodes connected in antiparallel. A half loaded-folded-dipole in a half rectangular-horn was also tested. The resonant resistance of 54 Ω, or 108 Ω for a full loaded-folded-dipole, was obtained at the loading-stub length of 0.12 λ. This probe could provide a suitable matching impedance for single-diode mixers.

IV. Conclusion

All these impedance measurements indicate that the presence of the horn increases the effective length of the probe element, which agreed well with the millimeter-wave aperture efficiency measurements [2] and the theoretical analysis [3], in which a dipole probe was used as an antenna element. They also indicate that the resonant frequencies can be controlled by changing the length of the probes or loading the probes, and that resonant resistances can be increased to a reasonable matching range by folding the probes. The fan-probe design indicates that the bandwidth can be increased by changing the probe width. These modeling measurements illustrate the probe design principles in an extended frequency range and provide very useful options in choosing probe elements in integrated-circuit horn-antenna-mixer arrays.

V. Acknowledgements

We appreciate the support of Aerojet ElectroSystems Co., Azusa, CA. and the Army Research Office through the Jet Propulsion Laboratory.

VI. References

[1] G. M. Rebeiz, D. P. Kasilingam, Y. Guo, P. A. Stimson, D. B. Rutledge, "Monolithic Millimeter-Wave Two-Dimensional Horn Imaging Arrays," *IEEE Transactions on Antennas and Propagation*, September, 1990.

[2] Y. Guo, K. Lee, P. Stimson, K. Potter, and D. Rutledge, "Aperture Efficiency of Integrated-Circuit Horn Antennas," *Microwave and Optical Technology Letters*, January, 1991.

[3] G. V. Eleftheriades, W. Y. Ali-Ahmad, L. P. Katehi, G. M. Rebeiz, " Millimeter-Wave Integrated-Horn Antennas: Part I-Theory, Part II-Experiment " *IEEE Transactions on Antennas and Propagation*, November, 1991.

MILLIMETER WAVE INTEGRATED CIRCUITS BASED ON A DIELECTRIC SLOTTED WAVEGUIDE

Bankov S.E., Vasjukov V.D., Duplenkova M.D., Kalinichev V.I.,
Kozin V.N., Kuranov U.V., Levchenko I.V., Rodionova E.V
The Moscow Power Engineering Institute
Krasnokazarmennaja 14, Moscow, E-250, Russia, 105835

ABSTRACT

Parameters, capabilities and possible technical applications of millimeter-wave integrated circuits based on a dielectric slotted waveguide are discussed.

INTRODUCTION

In this work we employ the sputtering technique for fabrication of integrated circuits at millimeter wave band. The main characteristic feature of the proposed circuits as compared with the known variants is application of a dielectric slotted waveguide (DSW) as a base transmission line (fig.1).

At first the various elements based on the DSW have been suggested and investigated. These elements have been successfully used for designing and fabrication of a broad class of millimeter-wave integrated devices including passive and quasi-optical elements, semiconductor diodes, ferrites, radiators, etc. In particular the sputtering technique is very attractive for fabrication of the antennas and beam shaping networks.

Due to ease of fabrication the devices such as the transmitters and receivers have comparatively low cost and at the same time posses the quite acceptable technical capabilities at millimeter wave band. Besides they have sufficiently low weight and small dimensions.

That is why the devices based on the DSW are very promising in those applications when the cost, weight and dimensions are the most desirable capabilities while the magnitude of the received signal is large enough. Various types of meters such as velocity-, distance-, displacement-, vibration-, humidity meters, etc. are most suitable to satisfy this requirement.

Some first variants of the detector receiver, homodine transmitter-receiver and humidity meter have been already tested by experience. The obtained results obviously show that at millimeter waves the proposed integrated devices can successfully compete with analogous devices based on microstrips, fin-line and metal waveguide.

ELEMENTS AND THEIR CAPABILITIES AT F = 30-70 GHz

Passive Elements

A waveguide (fig.1):	
-transmisson loss	8-10 dB/m, ε=9.6, λ=8.0 mm
(λ is the free-space	20-25 dB/m, ε=9.6, λ=4.0 mm
wavelength)	4-5 dB/m, ε=3.84, λ=8.0 mm
	10-12 dB/m, ε=3.84, λ=4.0 mm
A directional coupler (fig.2):	
-directivity	40 dB
-longitudinal dimension	1.5λ
-operating frequency band f_{max}/f_{min}	$\leq$ 3.0

A rectangular waveguide adapter(fig.3):	wide-band	narrow-band
-operating frequency band $\Delta f/f_o$	0.4-0.5	0.1
-input VSWR	$\leq$ 1.3	$\leq$ 1.2
-insertion loss	0.5 dB	0.5 dB
-dimensions	(1.5-2)λ	0.5 λ

fig.1

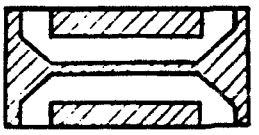

fig.2

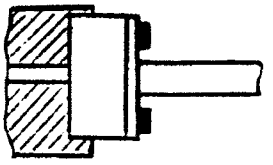

fig.3

A ferrite resonance isolator (fig.4):

-insertion loss	(0.7-1.5) dB
-reverse loss	$\geq$ 30 dB
-operating frequency band $\Delta f/f_o$	0.05
-longitudinal size	1.5λ

Resonators (fig.5):

-Q-factor	3000
-characteristic size	(1-1.5)λ

Auxiliary elements of the channel are Y,T joints, stepped and tapered impedance transformers, short-circuited stub, turning, matched load, etc.

Elements with Semiconductor Diodes

A detector section based on the Shottky diodes (fig.6):

-VSWR	(1,2 - 1.3)
-volt-watt sensitivity	10^3 V/W
-operating frequency band $\Delta f/f_o$	0.2
-equivalent noise power	10^{-10} W/Hz

The IMPATT oscillator based on a metal waveguide with output to DSW produces the power about 150 mW.

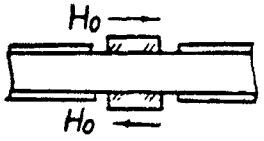

fig.4

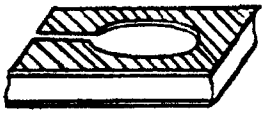

fig.5

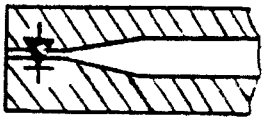

fig.6

Antennas and Beam-Shaping Networks

A multichannel divider of lens type:

-loss	(0.5 -1.0) dB
-number of channels	10 - 16

A fan-shaped antenna:

-efficiency	0.9-0.95
-antenna aperture efficiency	0.8
-dimensions of radiating curtain	(48x0.5) mm
-beam width	$(7x60)^\circ$

A narrow-beam antenna:

-efficiency	0.85-0.9
-antenna aperture efficiency	(0.6-0.7)
-dimensions of radiating curtain	(48x120) mm
-beam width	$(2.8x7)^\circ$
-gain	22.5 dB at f=62 GHz

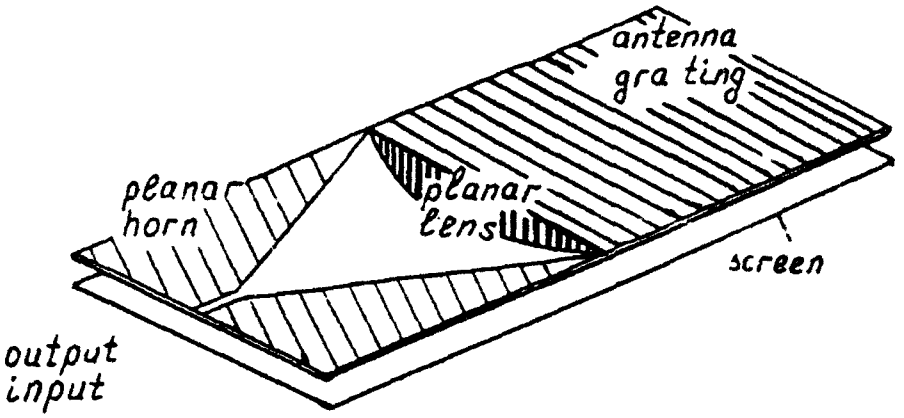

fig.7

INTEGRATED DEVICES

Velocity Meter.

Dimensions of the microwave block are 220x70x15 mm. A range of measu-red velocities is from 5 to 300 km/hour. Distance to the object: 300-500 m.Resolution (0.1-5.0)km/hour.There is digital output or autonomous indication This meter may be used for measurement of motor transport velocity.

The velocity meters (fig.8) include an IMPATT oscillator of the continuous signal (O) with the output power about 100 mW, balancing mixer (diodes D1, D2), circuit of signal distribution (double directional coupler (DDC)), shorts (S1, S2), beam-shaping network and high-directional antenna (A). The operating frequency is 60 GHz.

The velocity meter represents a homodine transmitter-receiver including the antenna with the beam width of $(7x3)^{\circ}$. The frequency of the alternating voltage on the diodes D1, D2 is equal to the Doppler shift of the radiated signal. Measuring this frequency one can determine the velocity of the moving object.

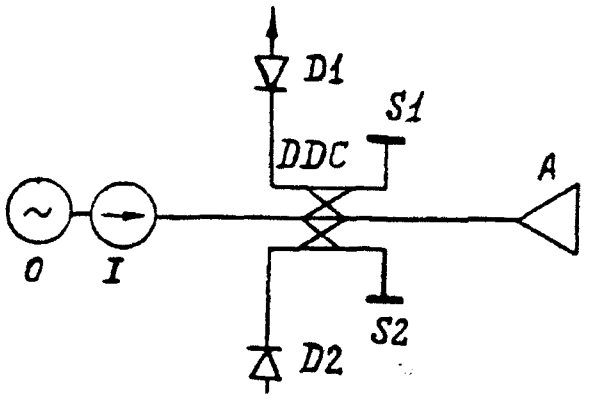

fig.8

Humidity Meter

Dimensions of the microwave block including an oscillator and immersed to liquid sensing unit are 80x24x20 mm. A range of measured humidity is (0 - 20)%. Resolution is (0.02-0.1%). There is autonomous indication of humidity. It is possible to place an analogy to digital converter and pass information to a computer.

The humidity meter (fig.9) includes a microwave oscillator (O), detectors (D1, D2), isolator (I), sensing element (SE), matched load (M) and directional coupler (DC). All the devices except of the oscillator are simply fabricated on the base of ceramic layer (ε=9.6) with the dimensions

of (24x60x0.5 mm). The central operating frequency is 60 GHz.

The meter measures electromagnetic wave attenuation in the SE. attenuation depends on the humidity of the liquid. Thus measuring the vo on the diodes D1 and D2 it is possible to determine the liquid humidity

Superior requirements to the frequency and power stability of oscillator are unnecessary. So it allows to decrease the cost of the devi using such simple oscillators. Measurement results do not almost depend chemical composition of the liquid. The meter can be used for humid measurement of various liquids such as oil, spirits and so on.

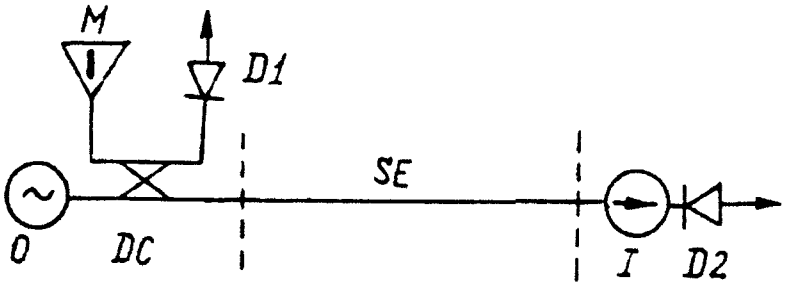

fig.9

Double Channel Speed Meter.

Dimensions of the microwave block are 120x30x50 mm. A range o measured velocities is from 3 to 150 km/hour. Resolution is not more ther (1-3)%. There is a digital output.

This meter may be used for exact measurement of motor transpor velocity.

The speed meter (fig.10) includes an IMPATT oscillator of the continuous signal (O) with the output power about 20 mW, two directional couplers (DC), two-input fan-shaped antenna (5x15)° (A), two diodes (D1,D2), Y-divider (Y) and shorts (S1, S2). The operating frequency is 61.25 GHz.

Application of the double-channel scheme of the speed meter permits to decrease the measurement error caused by displacement of the means of transport in the plane that is perpendicular to the direction of their motion.

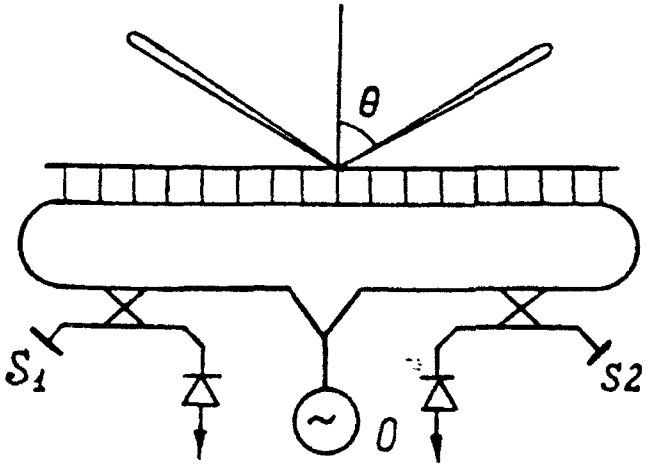

fig.10

CONCLUSION

Thus the parameters and capabilities of some elements and devices ir integrated performance at millimeter waves are presented in this paper. The elaborated electrodynamic models and computer programs allow to analyze and design the various structures based on the DSW using the scattering matrices technique. The calculated and experimental results obtained in the work stimulate further researches in this field.

APPLICATION OF CO_2 LASER TO FORMATION OF SILICION COBALT RESISTIVE FILMS

A.Medvid', T.Puritis, J.Kaupužs, M.Ogriņš, A.Kalnača

Thermal treatment is used in microelectronics technology to stabilize electric parameters of the resistive films [I] , however, too high temperature, destructive for other integrated circuit elements is necessary to optimize the resistive films.

The destruction can be avoided by the local selective laser heating due to large difference in the absorptance and reflectance of an integrated circuit elements (metallic paths, p-n junctions, resistive films etc.) as well as their strong wavelenght and intensity dependence.

Some results of experimental and theoretical investigation of laser heating of the silicon cobalt films are reported there.

The silicide films just after sputtering are amorphus ones. The temperature resistance coefficient (TRC) of these films is negative and resistance themselves is rather temporaly instable. Crystallization of the silicide films into highest cobalt silicide $CoSi_2$ improves the parameters of films. The resistance of films is reduced by factor of 5 to 6 and TRC passes through zero value.

Experiments were carried out on films prepared by ion plasma sputtering in argon atmosphere from alloy containing 27% Co and 73% Si (atoms). This composition after laser treatment transforms into $CoSi_2$ with addittional I9% Si. Such deviation from the stoichiometry gives resistive layer with TRC near to zero (TRC of $CoSi_2$ is positive).

Experimental samples were prepared on 400 μm Si substrata. The 0.6 μm SiO_2 thermal oxidate was formed on the substratum. The resistive layer of thickness 0.0I - I μm, mostly 0.08 μm was sputtered on the SiO_2 layer and coated by second SiO_2 layer of thickness 0.6 μm. The samples represented rectangles (3 x 9 mm) with vacuum - - deposited Al contacts on the ends for resistance measurements.

The most suitable radiation for given structure was concluded from calculations to be that of Q - switched CO_2 laser, since at first 99.8% of radiation is absorbed in the SiO_2-Co+Si-SiO_2 layers while only 0.2% in the silicon what must protect p-n junctions on the same silicon substratum; secondly the temperature field over

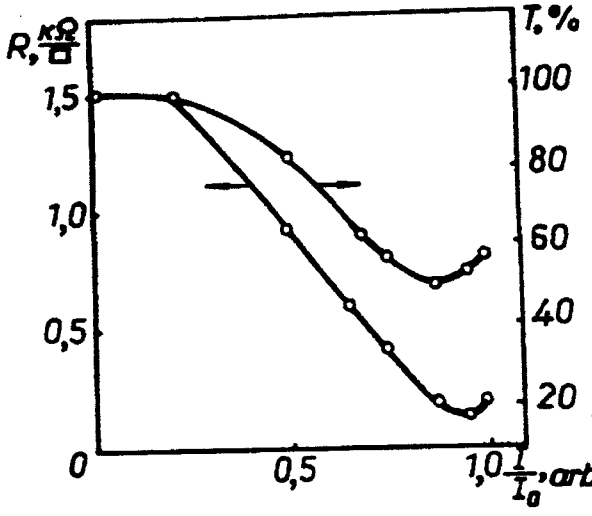

Fig. I

heated layers is nearly uniform just after laser pulse and that excludes fast cooling of the structure and amorphism of resistive films. Therefore the Q - switched CO_2 laser with wavelenght I0.6 μm was used.

Laser treatment causes decrease in the reflectance as well as increase in absorptivity of the resistive film [2]. The resistance of film reduces, but TRC changes from negative of about - IC^{-3} I/K to positive one less than IC^{-5} I/K. The surface resistance (curve I) and transmittance (curve 2) are plotted vs intensity of incident laser radiation (λ = I0.6 μm, pulse duration I50 ns, peak power I MW) in figure I. Both the surface resistance and transmittance of resistive layer reduces monotonously with intensity of radiation up to 9 MW/cm^2. The reflectance also reduces from 40% to 30% while absorptivity increases by factor of I.5, but TRC becomes positive ($< IC^{-5}$ I/K) at that intensity. Both curves in figure I tend upwards at sufficiently high intensity. It can be related to the destruction of the resistive film.

It is seen that the optical checking and control of the process (curve 2) is more sensitive than electrical one, (curve I) because significant change occur at smaller intensity.

The electron photoemission studies showed that the electron exit work reduces by factor of 2 after laser treatment. It confirms the chemical combination is formed.

The temperature field dynamics of the four layer structure SiO_2-Co+Si-SiO_2-Si was studied theoretically in dependence of laser pulse energy and intensity, absorptance and thickness of each layer. The heat conduction equation

$$C(T)\,\gamma(T)\,\frac{\partial T}{\partial t} = \lambda(T)\,\frac{\partial^2 T}{\partial x^2} + We^{-\kappa x}$$

where C is the heat capacity, γ is the density, λ is the heat -

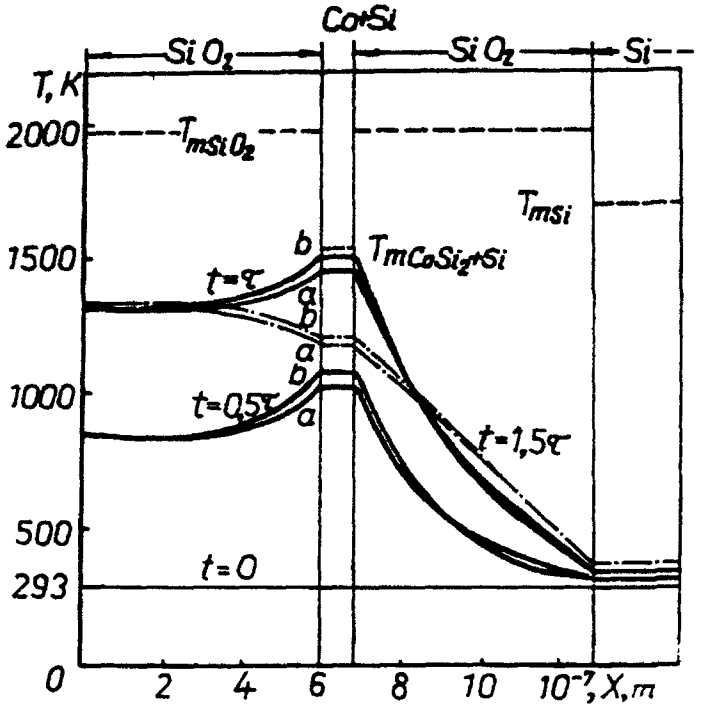

Fig.2.

conductivity, and K is the absorptivity, was solved for given four-layer structure with layer thicknesses S_I, S_2, S_3 and S_4. Numerical solution of the equation was obtained neglecting heat exchange to environment as well as reflection of radiation on the interfaces. Two extremes were considered to estimate possible variation of temperature field due to variation of parameters of Co+Si layer during laser pulse: I) the structure of Co+Si layer is the same as the initial one during laser pulse , 2) chemical reaction happens just at the begining of a laser pulse so that radiation is absorbed in the layer of the final structure. Besides, it was assumed that $S_2 \ll S_I + S_3$ and $S_2 \ll \ell$, where $\ell = \sqrt{(\lambda\tau)/(c\rho)}$ is the distance of heat propogation in the Co+Si medium during laser pulse.

The absorptivity was found experimentally for either extreme to be 2 x 10^7 I/m and 3 x 10^7 I/m respectively. Other parameters are not critical. They were accepted to be those of final structure and estimated considering the excess silicon to be concentrated in cube like inclusions uniformely distributed over $CoSi_2$ layer.

The temperature field for both first (a) and second (b) extremes at various times t is sketched in figure 2. The fusion temperatures for each layer (dashed lines) are indicated in the figure. It was taken for calculations: $S_I = S_3 = 600$ nm, $S_2 = 80$ nm, $\tau = 150$ ns, intensity of radiation 1.75 x 10^{10} W/m^2. The intensity of radiation was taken to reach temperature in the Co+Si near to fusion temperature of $CoSi_2$ - Si eutectic.

It was obtained from calculations: I) the temperature fields differ very slightly for both extremes; 2) the maximum temperature occurs in the Co+Si layer while silicon substratum is heated up

insignificantly during laser treatment.

Conclusions:

I) Absorption in a Co-Si layer is not resonance absorption;

2) Fusion and successive destruction of the resistive layer happens at energy above optimum for treatment;

3) Laser treatment is cumulative one: the same effect can be reached by repeated treatment with less intensity, however, the threshold intensity must be exceeded;

4) Since at least one SiO_2 layer is necessary, it indicates that the thermal effect is important, although resistive layer isn't melted out. On the other hand, thermal treatment takes much more time as laser treatment. So it is reasonable that a photo-thermochemical reaction is involved.

5) The optical methods, i.e. measurement of either reflected or transmitted radiation, are most convenient to check the procedure of chemical reaction in the resistive film.

I. Murarka G.P. Silicides for VLSJ applications. Academic Press, New-York, London, I983.

2. Gavars P., Medvid' A., Puritis T. Izv.AN LatvSSR, Ser.fiz. i tehn.nauk, N6, 75(I989).

ACCURATE ELECTROMAGNETIC SIMULATION OF OPEN RESONATORS LOADED WITH DIELECTRIC SLABS AND PERIODIC GRATINGS

Alexander I. Nosich

Bilkent University, 06533 Ankara, Turkey
(on leave from the Institute of Radiophysics and Electronics,
Ukrainian Academy of Sciences, Kharkov, Ukraine)

The paper deals with theoretical investigation of wave scattering and diffraction from combined two-dimentional scatterers such as finite collection of nonclosed metal circular cylindrical screens placed into a plate-parallel dielectric medium or containing a periodic diffraction grating. These scattering problems are simulating the electromagnetic behaviour of various active and passive devices based on inhomogeneous open resonators. From somewhat different point of view the same structures serve as models of open waveguides like dielectric slab containing metal scatterers purposed to forming certain special features of radiation pattern or mode conversion coefficients.

Geometry of considered problems is clear from Figures 1 and 2. A material slab has a sandwich-like structure and house a finite number of screen-shaped scatterers both inside and outside the slab. Each screen is assumed to be perfectly conducting and zero-thickness, of arbitrary width, radius and orientation, and does not intersect the boundaries of layers. Some particular scattering geometries of this kind represent an open two-mirror resonator with a dielectric slab, reflector antenna with point-source excitation near a plane dielectric interface, and finite-element grating coupler in a dielectric waveguide. These structures are analysed in detail, and the results cover characteristics of mode conversion and scattering, radiation patterns, etc., for H-polarized excitation.

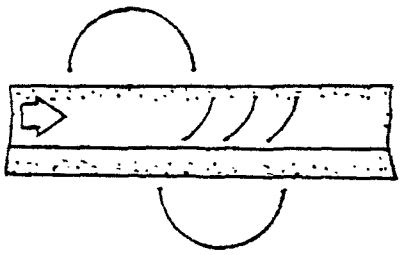

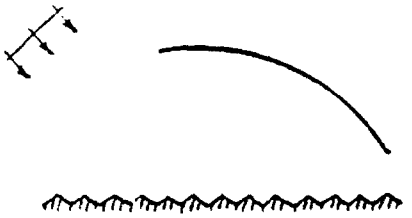

Solution is obtained by a numerical-analytical approach combining Green's function technique with that of dual series equations for screen surface current functions. Inverting a part of initial operator leads to regularized algebraic equations solvable numerically with any desired accuracy.

Another relative class of scattering problems is formed by screen-shaped scatterers near a periodic grating modelling cavities of millimeter wave oscillators such as orotrons. Green's functions of various gratings are available numerically, and this gives an opportunity to apply a modified approach to account properly the effect of grating.

OPTIMIZATION DESIGN AND EXPERIMENT FOR 3MM QUASI-OPTICAL POWER COMBINER OF SOLID-STATE SOURCES

Cheng-tian Xue, Qiao-min Wang*
Li-ming Lei, Hui-zhen Li, Hai-wen Zhang, Ying Liu

Dept.of Electronics Science,Nankai Univ. Tianjin 300071
* Computer Center, Tianjin Univ. Tianjin 300072,P.R.China

ABSTRACT

It is described that a novel and compact combiner with quasioptical open resonators in this paper.The combiner combines effectively output power of active solid state devices to produce a RF single frequency and strong power signal. Phase coupling has been accomlished and RF power exceeded the sum of the individual diode outputs. This paper lays stress on explaining the theory and method of optimal design for the key assembly,source-array of the combiner.

INTRODUCTION

As operating frequency increasing into the millimeter and submillimeter range,the mode density of closed cavity increases,mode separation decreases,and excitation of single frequency oscillation in the cavity becomes increasingly more difficult.However,quasioptical combining techniques offer an effectual way to overcome the limitations. Many plans may be adopted for the quasioptical power combiner. A novel and compact power combiner is shown in Fig.1. It consists of a concave spherical reflector with a diameter for aperture of 10.6 cm, a radius of curvature of 21.2cm and a hybrid concave reflector with spacing L.

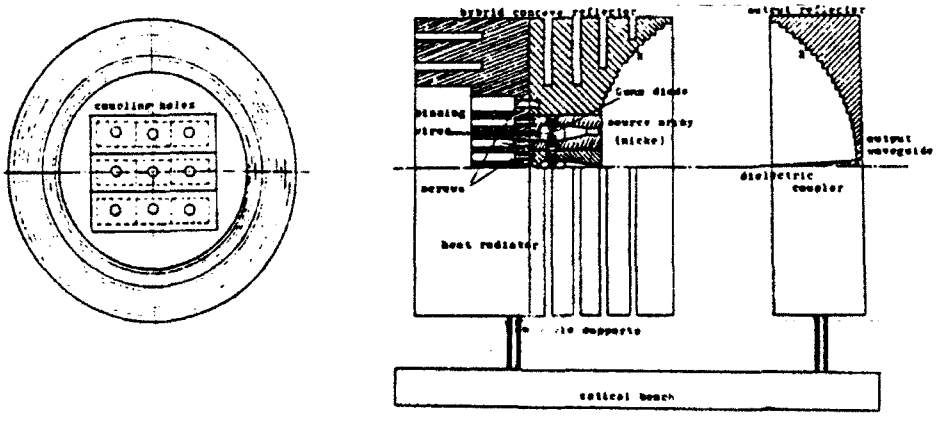

Fig.1 structure of a novel quasioptical power combiner

The latter (by the name of input reflector) includes a circular plane with diameter of 5.0cm and a concave spherical reflector with a diameter for aperture of 10.6 cm, a radius of curvature of 21.2cm. Gunn diodes are fixed in niches of the inner surface of the input reflector.A well-designed for source-array(niche)not only can gain higher output power of desired mode and larger fractional power,but also can make the combiner arrangement more compact and practical.(The fundamental power is denoted by P, and the fractional power is denoted by F.The fractional power of the combiner is defined as the power ratio of the fundamental mode to all of the modes.)

THEORY AND METHOD OF DESIGN

The combiner gets the optimum combining results ,only when the following problems are solved well. 1). A suitable impedance transformation set should be adopted to make active devices creating high RF energy as possible in the cavity. For the packed diodes,the more they create RF energy to approach their normal value,the better.

2). the field in the cavity must be satisfied optimum phase coupling relation. The stable and strong fundamental mode oscillation may be set up in the cavity,only when the RF signals stimulated by every active devices in the cavity have fit phase distribution to superpose effectively the power of the fundamental modes and cancel the power of other modes each other.

3). On the hand,the active devices radiate RF signals in the cavity respectively, on the other hand,are acted by the strong RF field in the cavity at the same time.Only when this action(named as the activation) is proper, every active devices can radiate the strongest RF signals and can't be hurt or destroyed by the RF field.

Next, it is done to realize impedance matching between the quasioptical cavity and the load.

We start with fluctuant equations,using the concrete boundary conditions in the cavity, and look for the basic design formulas for the combiner from the point of combination between electromagnetic field and equivalent circuit. Then we adopt the "global" optimization design method to compile many kinds of practical computing programs in Fortran language for NxN,Nx(2N)source arraies of the combiner (to see appendix A please). The sizes for the cavity are determined using following formulas(1)

$$\frac{r}{W_m}=\sqrt{N\pi}\left[\frac{R^2}{(2R-L)L}\right]^{-1/4} \qquad 0\leq\left|1-\frac{L}{R}\right|\leq 1 \qquad L=\frac{\lambda}{2}q$$

$$P_{m,n,q}=\left\{q+(m+n+1)\frac{\cos^{-1}\pm(1-L/R)}{\pi}\right\}\frac{c}{2L}$$

The design for the source-array has accomplished using following following formulas according to the "global" optimization rule(to see references 2)

$$P=\left\{\sum_{p}^{NxN}H_m(2x_p)\,H_n(2Y_p)\,\cos B_{mn}\exp\left[-(x_p^2+y_p^2)\right]\Big/\sum_{p}^{NxN}\cos B_{mn}\right\}^2$$

$$F=\left[\sum_{p}^{NxN}R'_{oo}\cos B_{mn}\right]^2\Big/\sum_{mn}^{2Q}\left(\sum_{p}^{NxN}R_{mn}\cos B_{mn}\right)^2 \qquad \eta=P/(NxN)x10$$

$$B_{mn}=kz_p+V(x_p^2+y_p^2)-(m+n+1)t_g^{-1}V \qquad B'_{mn}=kz_p-(m+n+1)t_g^{-1}V$$

$$R_{mn}=\sqrt{\frac{2}{m!n!\pi}}\,\frac{1}{W}H_m(2x_p)H_n(2y_p)\exp\left[-(x_p^2+y_p^2)\right]$$

$$W^2=W_o^2(1+V^2) \qquad R'_{oo}=\sqrt{\frac{2}{\pi}}\,\frac{1}{W}$$

EXPERIMENT

We have repeatly done the experimental exploration for eight kinds of the structure of the combiner source-array, and realized successfully phase couple.The measuring circuit for characteristics of the combiner is shown in Fig.2.

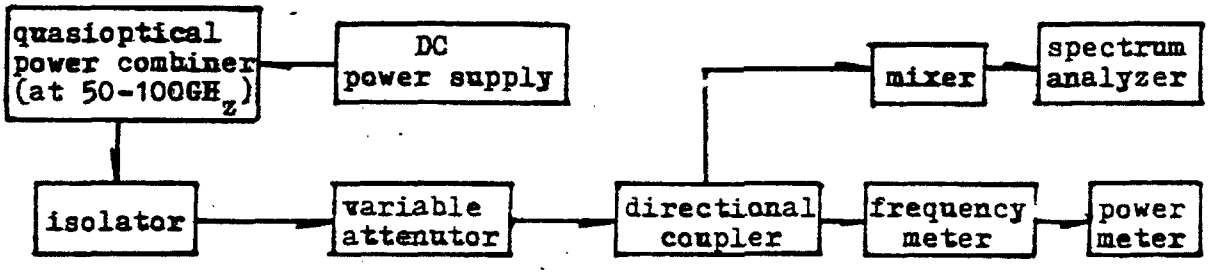

Fig.2 The measuring circuit for characteristics of the combiner

CONCLUSION

The output power of the combiner exceeded the sum of individual diode outputs. Although,the matching problems between the niches and the cavity haven't been fully solved,the results of this work show that the combiner described above has potential and stupendous merits.

ACKNOWLEDGEMENT

This work was supported by NSFC and M-EIM of P.R.China.

APPENDIXES

A). The flowchart for optimization design of the array of the combiner is shown in Fig.3.

B)The specificity of the combiner is shown in Table(1).

C)Fig.4 illustrates the fractional power coupled into the fundamental mode for three different source-array configurations containing 3x3,5x5,and7x7 active devices in regular rectangular arrays by Gaussian weight sources.

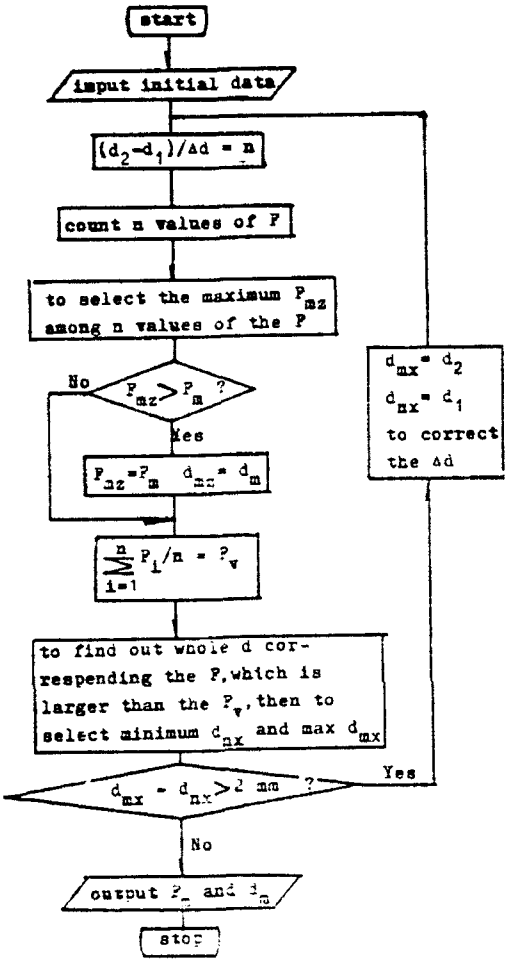

Fig.3 The flowchart for the source-array of the combiner.

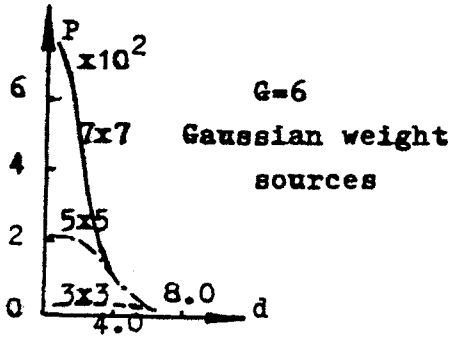

Fig.4 The fractional power of the combiner

Fig.4 shows the increase of power as the number of sources increases.

G	NxN	d_{op}	P_{max}	P	η
2	3x3	4.1	0.48	9.4	0.3
	5x5	2.9	0.51	43	0.6
	7x7	2.1	0.52	154	1.0
4	3x3	4.9	0.83	21.2	0.7
	5x5	2.9	0.86	155	2.0
	7x7	2.1	0.86	600	3.8
6	3x3	4.5	0.91	30.2	0.6
	5x5	2.9	0.93	204	1.4
	7x7	2.1	0.93	760	2.6

Table1.The specificity of the combiner

Note: Here η is different from the combining efficiency of conventional waveguide cavity power combiner.

REFERENCES

(1).Cheng-tian Xue etc. "Millimeter-Wave Quasioptical Power Combining Techniques",Int.J.Infrared and Millimeter Waves,Vol.9, No.4, pp395-404,1988.

(2).Qiao-min Wang etc."Optimization Design of Quasioptical Source-array of Solid State Source Power Combiner at Frequency 100 GHz",Int.J. Infrared and Millimeter Waves,Vol.11, No.11,pp1269-1283,1990.

(3).Jun-xiang Ge etc. "Millimeter Wave Quasioptical Power Combiner", Dept.of Radio Engineering Southeast Univ.Nanjing 210018,1991,China.

(4).M.Nakayama etc."Millimeter and Submillimeter Wave Quasi-optical Oscillator with Multi-Elements",IEEE MTT-S Digest,pp1209-1212,1990.

DESIGN CRITERIA OF THE NEAR-MILLIMETER WAVE QUASI-OPTICAL MONOLITHIC DIODE-GRID FREQUENCY MULTIPLIER ARRAY

R. J. Hwu and L. P. Sadwick
Department of Electrical Engineering
University of Utah

Introduction

Increased interest in the near-millimeter region, defined as wavelengths from 3 mm to 300 μm, has stimulated the development of sensitive heterodyne receiver for a wide range of applications in radio astronomy, plasma physics, radar and satellite-based radiometry. The heterodyne receiver requires a moderate power level from its local oscillator system. The power requirement is too high for a single diode multiplier combined with a low frequency source. To overcome the power limitations of a single-diode multiplier, spatial power combining [1,2] of the outputs of large planar arrays of nonlinear frequency multiplication devices has been implemented by the design of a diode grid [3,4]. Thousands of diodes were integrated with a periodic grid in this approach to investigate the possibility of producing watt-level CW output power in the near-millimeter wave region. This is an attractive approach-combining the power of each distributed device using monolithic integrated circuit techniques, thereby resulting in potentially low-cost fabrication and small-size realization. Ideally, this approach should provide inexpensive, watt-level CW output power, solid-state sources in the near-millimeter wave region. Low-loss quasi-optical structures are used for filtering, matching, and terminating the multiplier circuit [3,4], because waveguide, stripline or coaxial structure become lossy and extremely expensive to fabricate as the frequency is increased beyond 100 GHz. The quasi-optical structures are eminently suited to LO applications in near-millimeter systems in which quasi-optical diplexing structures are commonly employed.

The efforts on the development of monolithic diode-grid frequency multiplier arrays can be divided into two major areas [5]. The first area is in the improvement of the device structure of the individual frequency multiplication element, the second area is in the development of the diode-grid array design. In the improvement of the device structure, the barrier varactor structure was proposed to replace the hyper-abrupt Schottky diode structure due to its stronger C-V nonlinearity, and the possibility of providing back-to-back operation for the higher harmonic (odd-harmonic) generation. Two types of barrier varactors have been studied. One is the Barrier-Intrinsic-N^+ (BIN) diode which is a transit-time-limited device [4,5]. The other is the modified BIN diode with a doped epilayer replacing the intrinsic epilayer of the BIN structure, which is a dielectric-relaxation-time-limited device [6]. In the development of the diode-grid design, a full 2-inch wafer, instead of part of a wafer, was used to fabricate the diode-grid [4,5]. The diode-grid design with a back-to-back configuration which does not require dc biasing lines was also implemented [4,5]. Only one metal contact was, therefore, needed in the fabrication process. In this paper, the limitations and optimum designs related to these two aspects of the development of the monolithic diode-grid frequency multiplier array will be discussed. Potential problems related to these two aspects of the development of diode-grid frequency multiplier arrays along with the associated device physics will be presented in this paper.

Device Concept

The Barrier-Intrinsic-N^+ (BIN) diode incorporates a thin undoped semiconductor layer (I) on a heavily doped layer (N) serving as a back contact. On top of the undoped layer, there is an ultrathin electron-blocking barrier layer (B) in contact with a metal top layer [7-9]. With the low doping region, the action of the device depends upon the charge which is injected from the substrate into the epitaxial layer under forward bias. The device can be switched rapidly between two capacitance states which correspond to accumulation of electrons at the barrier and depletion of the intrinsic layer, respectively, by the applied bias. This results in a highly nonlinear capacitance-voltage characteristic which is needed for efficient harmonic generation.

Back-to-Back Diode Configuration

1. Capacitance-Voltage Characteristic

Due to the blocking barrier of the BIN structure, two diodes should be able to operate back-to-back generating a symmetrical capacitance-voltage curve. The sharp spike in the capacitance-voltage curve eliminates even harmonics and thus favors tripling operation. In addition, the height and width of this capacitance-voltage curve can, in principle, be adjusted by doping control alone. This arrangement needs no external ohmic contact, thereby making a highly efficient frequency tripler in which the efficiency should not degrade with high fundamental power. Only one metal layer is required which greatly simplifies the fabrication task [4,5]. In addition, no idler is needed in the circuit design, again making the circuit construction much simpler [4,5]. This back-to-back configuration is considered to be a very important feature of the BIN diode-grid frequency tripler array. The back-to-back diode configuration results in a much smaller ratio of C_{max}/C_{min} (a factor of 2) and smoother (i.e., lower gradient slope) C-V characteristic which, therefore, reduces the nonlinearity which is utilized to generate harmonics.

2. Cut-Off Frequency

The operation of one single diode is very different from that of two back-to-back connected diodes [5]. To determine this effective series resistance, a series of high-frequency impedance measurements were performed on one single diode, as well as on two back-to-back diodes. The high-frequency impedance measurements were performed employing an impedance analyzer. The value of the effective series resistance is determined to be between $1.5R_S$ and $2R_S$.

Frequency Limitations

1. GaAs Barrier-Intrinsic-N$^+$ Diode (Transient-Time-Limited Device)

The basic action of the BIN diode varactor is the movement of mobile space charge into the epilayer under forward bias conditions and out of it under reverse bias conditions [5]. The maximum cut-off frequency of the BIN diode is determined by the time it takes electrons to cross the epitaxial layer (i.e., $v_d/\pi d_{epi}$). It is then clear that the maximum cut-off frequency of a BIN diode is strongly dependent on the epilayer thickness and saturation drift velocity [5].

In the GaAs BIN diode structure, a Mott barrier is formed by a thin intrinsic layer sandwiched between the metal contact and a charge sheet created by selective doping [8,9]. The original structure proposed for the BIN diode tripler [5] has an aluminum metal gate in intimate contact with a layered GaAs structure consisting of a 300 Å thick undoped GaAs, a 100 Å thick $2x10^{18}$ cm^{-3} heavily doped n$^+$ layer, another 1500 Å thick undoped layer, and a thick heavily doped n$^+$ region grown on top of a semi-insulating GaAs substrate. The electric field distributions of this structure under different bias conditions have been studied [5]. From the device simulation results, the electric fields in the epitaxial layer is fairly high. Due to the symmetrical nature of the back-to-back BIN structure; when one diode is reversed biased, the other diode will be forward biased. Assuming the pertinent fields being those in the transition region between accumulation of electrons at the barrier and full depletion of the epilayer, an average electric field value of ≈ 50 kV/cm was determined. The corresponding drift velocity value of ≈ $1x10^7$ cm/sec for a GaAs BIN diode with an epilayer thickness of 1500 Å was then used. The drift velocity value was taken from the Monte Carlo simulation results of Iafrate et al. [10].

The intrinsic cut-off frequency and series resistance of the back-to-back connected GaAs BIN diode with the original structure are close to 100 GHz and 200 Ω (an average drift velocity of $1x10^7$ cm/sec is used), respectively. Therefore, it is very unlikely that the back-to-back GaAs BIN diode will be useful as a highly efficient near-millimeter wave frequency tripler [5].

2. GaAs Modified Barrier-Intrinsic-N$^+$ Diode (Relaxation-Time-Limited Device)

The transition from a transit-time-limited device to a dielectric-relaxation-time-limited device occurs when the Debye length becomes less than the epilayer thickness of the BIN diode structure. The modified BIN (MBIN) structure (with a doping level higher than $1x10^{16}$ cm^{-3} in the epitaxial layer of the BIN structure) is no longer a transit-time-limited device and actually behaves in a similar fashion to a Schottky diode (a dielectric-relaxation-time-limited device) [6]. The GaAs MBIN diode structure discussed here has a sheet charge doping of $2x10^{18}$ cm^{-3} which is the same as that of the original GaAs BIN diode structure. The GaAs MBIN structure with an undoped barrier region thicknesses of 400 Å

and an epitaxial layer thicknesses of four times of the undoped barrier region thicknesses (1600 Å) (needed to gain a reasonable capacitance ratio for the back-to-back operation) has been studied. The GaAs MBIN diode structures have weaker C-V nonlinearities than the original GaAs BIN diode structure. As mentioned before, the MBIN diode is a dielectric-relaxation-time-limited device. The mobility decreases and, thus, the resistivity and relaxation time increase when the field in the epilayer region is higher than the critical field. Therefore, the electric field in the epilayer needs to be kept smaller than the critical field to avoid the degradation of the speed and device performance during the operation of the MBIN diode frequency tripler. Due to this consideration, the operation of these MBIN diodes are limited to low pump amplitudes. The optimum operating power level is determined with an epilayer electric field in the MBIN structures being less than the critical field. It should be pointed out that the low pump amplitude here corresponds to an input power per diode possibly higher than that for an individual GaAs BIN diode due to the small input impedance of the MBIN structure. The intrinsic cut-off frequency of the back-to-back GaAs MBIN diode designs under a back-to-back configuration at low pump amplitude operation is ≈ 3.4 THz.

Monolithic Diode-Grid Frequency Multiplier Array Design

The general feeling about the development of monolithic diode-grid frequency multiplier arrays is that the larger the wafer size is (the larger total number of diodes) that one can use to fabricate the diode grid, the higher is the total output power one would obtain. In this section, the temperature distribution on the diode-grid substrate is studied to determine the possibility of increasing the total output power by increasing the wafer area (i.e., increasing the total number of diodes).

In the monolithic diode-grid frequency multiplier array approach, a metal grid is utilized to integrate output power of a large number of solid state devices. The problem of solving the temperature distribution on the grid is similar to the problem of finding the steady-state temperature distribution on a conduction cross section heated by a Joule heat source [11]. The temperature distribution on a diode-grid substrate has been analyzed under the assumption that there is perfect heat sinking at the four edges of the substrate. From the simulation results, the temperature distribution on the substrate is proportional to the input power.

1. Monolithic Back-to-Back GaAs BIN Diode-Grid Frequency Tripler Array

In the last two years, fifteen GaAs BIN diode-grid frequency tripler arrays have been fabricated with high-frequency measurements performed on each wafer. The highest tripling efficiency obtained was 8.5% at an output frequency of 100 GHz [12]. This wafer was destroyed shortly thereafter by pumping it with too much power. While efforts have been devoted to repeat this result with additional samples, it has not been possible to reproduce the results of this measurement; in fact, no output power has been detected at a frequency of 100 GHz from any of the other wafers. Through this study, however, it was noticed that power could be obtained at the output port (W-band detector) before the detector was shielded from the input source radiation. It was further observed that once the detector was completely enclosed and sealed by absorbers the detected power disappeared. At least part of the results obtained from this particular sample are therefore believed to be due to scattered source power (third harmonic) sensed by the diode detector since no effort had been taken to shield the detector from random radiation at that time. It should be noted that the cut-off frequency and series resistance of these GaAs BIN diodes were determined to be 600 GHz and 33 Ω, respectively, assuming an average drift velocity of 3×10^7 cm/sec [8,9]. A maximum tripling efficiency of 24% at an output frequency of 100 GHz was therefore predicted for these GaAs BIN diode-grid tripler arrays [12].

This section intends to explain the experimental observation that little or no output power was observed from the above GaAs BIN diode-grid tripler arrays. The average drift velocity decreases dramatically with increasing temperature. This has been investigated experimentally by Windhorn et. al. using the microwave-time-of-flight technique [13]. Based upon the temperature distribution simulation, the peak temperature on a diode-grid substrate is determined to be higher than 200 °C if the input power is 30 W on an area of 15 cm^2 which are close to the amount of input power and the area of the GaAs BIN diode-grid design on a 2-inch wafer used in the above frequency tripling experiments, respectively. It should be pointed out that the reason of using such a high total input power in the original GaAs BIN diode-grid tripler array experiment is due to the use of optimistic drift velocity value of 3×10^7 cm/sec proposed originally [8,9] to estimate the device series resistance and cut-off frequency. From the

temperature distribution results, the temperature distribution on the GaAs BIN diode grid is very high and the drift velocity is further reduced. Based upon the result of Windhorn et. al. [13], the value of $6x10^6$ cm/sec should be used to calculate the intrinsic cut-off frequency and series resistance of the GaAs BIN diode-grid frequency tripler array. The calculated series resistance (using a saturation velocity value of $6x10^6$ cm/sec) have been shown to be more in agreement with the high-frequency impedance measurement results performed [5]. The calculated intrinsic cut-off frequency also agrees well with the GaAs BIN diode-grid frequency tripling experimental results. The intrinsic cut-off frequency and series resistance of the GaAs BIN diode-grid tripler array used in the previous experiments are close to 60 GHz and 330 Ω (an average drift velocity of $6x10^6$ cm/sec is used), respectively.

2. Monolithic Back-to-Back GaAs MBIN Diode-Grid Frequency Tripler Array

It should be pointed out that due to the relatively low input impedance of the device, the optimum pumping power is high for each diode. It is impossible to fabricate a diode grid on a full 2-inch wafer due to the lack of an available power source and the extremely high temperature distribution on the diode grid. The GaAs BIN diode structure does allow larger wafer area integration (larger number of diodes integrated) compared to the MBIN diode structures due to the small pumping power required. However, due to the relative low intrinsic cut-off frequency, the high frequency performance of the GaAs BIN diode is poor in comparison to that of the MBIN diode.

ACKNOWLEDGEMENT: The authors wish to acknowledge the support of the Air Force Engineering Research Initiation Grant RI-B-91-12.

[1] J. W. Mink, "Quasi-Optical Power Combining of Solid-State Millimeter-Wave Sources," IEEE Trans. Microwave Theory and Tech., **MTT-34**, No. 2, pp. 273-279, 1986.
[2] D. B. Rutledge and S. E. Schwarz, "Planar Multimode Detector Arrays for Infrared and Millimeter-Wave Applications," IEEE J. Quantum Electronics, **QE-17**, P. 407, 1981.
[3] C. F. Jou, W. W. Lam, H. Chen, K. Stolt, N. C. Luhmann, Jr., and D. B. Rutledge, "Millimeter-Wave Monolithic Schottky Diode-Grid Frequency Doubler," IEEE Trans. Microwave Theory and Tech., **MTT-36**, No. 11, pp. 1507-1514, 1988.
[4] R. J. Hwu, C. F. Jou, W. W. Lam, U. Lieneweg, N. C. Luhmann, Jr., and D. B. Rutledge, "Millimeter-Wave Monolithic Diode-Grid Frequency Multipliers," 1988 IEEE MTT-S Digest, pp. 533-536, 1988.
[5] R. J. Hwu, "Quasi-Optical Monolithic Planar Solid-State Diode-Grid Frequency Multipliers at Millimeter-Wave Region with Watt-Level Output Power," Ph. D. dissertation, UCLA, 1991.
[6] R. J. Hwu and S. C. Kao, "Design Consideration of Monolithic Millimeter-Wave Diode-Grid Frequency Tripler Arrays," International Symposium on Recent Advances in Microwave Technology (ISRAMT'91), Reno, Nevada, August 18-21, 1991.
[7] U. Lieneweg and J. Maserjian, "Harmonic Generation in the Near-Millimeter-Wave Range by Thin MOS Structures," 6th Intl. Conf. and Millimeter Waves, Tech. Dig., P. F-5-6, 1981.
[8] J. Maserjian and U. Lieneweg, "BIN Diode Harmonic Multiplier," A Concept Proposal at JPL/Cal. Tech., 1987.
[9] U. Lieneweg, B. R. Hancock, and J. Maserjian, "Barrier-Intrinsic-N^+ (BIN) Diodes for Near-Millimeter Wave Generation," 12th Intl. Conf. Infrared and Millimeter Waves, Tech. Dig., pp. 6-7, 1987.
[10] D. K. Ferry, editor-in-Chief, "Gallium Arsenide Technology," pp. 443-448, Howard W. Sams & Co., Inc., 1985.
[11] R. J. Hwu, L. P. Sadwick, N. C. Luhmann, Jr., and D. B. Rutledge, "DC and Millimeter-Wave Performance of Watt-Level Barrier-Intrinsic-N^+ Diode-Grid Frequency Multipliers Fabricated on III-V Compound Semiconductors," 1988 IEDM, Tech. Dig., pp. 191-194, 1988.
[12] M. Jakob, Heat Transfer, **Vol. 1**, pp. 167-169, John Wiley and Son, Inc., 1949.
[13] T. H. Windhorn, T. J. Roth, L. M. Zinkiewicz, O. L. Gaddy, and G. E. Stillman, Appl. Phys. Lett., **Vol. 40**, P. 513, 1982.

A NEW KIND OF COMPOUND MICROSTRIP QUASI-OPTICAL POWER COMBINER

Yi-Jun He and Quan-Rang Yang

Research Inst. of EMF & Microwaves

Department of Radio Engineering

Southeast University , Nanjing, 210018

P.R. China

ABSTRACT

In this paper, A new kind of compound microstrip quasi-optical power combiner, which is that the radiant power of many two-device microstrip oscillators is combined in the quasi-optical resonator, is proposed. Experiments indicate that output power and resonant frequency have relation to the size of each two-device microstrip oscillator and the place of devices. The combining powers are 250(mw) using four Gunn devices and a combining efficiency of about 60% has been achieved at X-band.

I. INTRODUCTION

Conventional waveguide power combiners are limited in power output ,efficiency and number of soures that may be combined in the millimeter-wave region. In order to obtain High-power, solid-state sources must use large numbers of devices. On the other hand, quasi-optical resonators have linear dimension large compared to wavelength and they offer an attractive approach to overcome these limitations. Several different approaches to quasi-optical power combining have been develped by researchers during the last one decade[1]-[3]. More recently a planar quasi-optical approach has been suggested for combining the output powers of millimeter wave device[4]. Two types of quasi-optical arrays have been reported to date[5]. One uses a distributed oscillator approach in which the devices are mounted in a periodic grid structure [6] and placed in an open quasi-optical cavity. A second approach involves arrays of coupled individual oscillator elements[7]. In this paper, we present for the first time a new kind of compound microstrip quasi-optical power combining structure, which uses many two-device microstrip oscillators. We report the results of experiments with an X-band model consisting of four Gunn diodes.

II. COMBINER CONFIGURATION

To investigate the feasibility of our approach, the configuration of the X-band resonator is shown in fig. 1. The resonator consists of two surfaces which are large in terms of the operating waveleth. one surface is a perfect planar reflector, the other reflector is an opposing concave spherical mirror. Fig. 2 shows the structure of the planar reflector. there is a dielectric medium which high is 1(mm) and relative permittivity is 2.8 on the planar reflector and there are two microstrip patches on the dielectric. The size of the microstrip patch is a × b. The output power is extracted by a waveguide at the center of the pherical mirror.

The device operation principle can be more closely described by a simple equivalent circuit(fig.3). N,L,C and R are the four parameters of the equivalent circuit of quasi-optical resonator. $-R_d$ and C_d are the parameters of the equivalent circuit of each Gunn device. The oscillation frequency was calculated using the equivalent circuit shown in fig.3.

The resonator proposed here has the following advantages:a large number of devices can be mounted, it has a large heat dissipation capacity and has a simple biasing circuit and construction.

III. EXPERIMENT

Following table 1 shows the combining power and frequency with the different size of microstrip patch and the place of each device using two X-band Gunn diodes. We obtain that the size of each two-device microstrip oscillator and the place of each device have a large effect on the output power and resonant frequency. The same time (see table 2), we have succeeded in power combining for up to 4 diodes (2 X 2) , obtaining an output power is 250(mw) at 10.755 Ghz and a combining efficiency of about 60% (combining efficiency=output power/the sum of power of each device in normal waveguide resontor).

IV. CONCLUSION

A new kind of compound microstrip quasi-optical power combining oscillator is presented. A simple equivalent circuit was used to predict the oscillation frequency of devices with an acceptable degree of accuracy. It is expected that the monolithic quasi-optical technology will be an important tool in achieving reproducible low-cost, high-performance devices operating at millimeter wave and even higher millimeter-wave frequencies.

REFERENCES

[1]. L.Wandinger and V. Nalbandian "Millimeter-wave power combining using quasi-optical techniques" IEEE Trans. VOL.MTT-31 NO. 2 Feb. 1983 pp189-193.

[2]. M. Nakayama, M.Hieda, T.Tanaka, K. Mizar "Millimeter wave quasi-optical oscillator with multi-elements" The 3rd APMC Tokyo, 1990. pp977-980.

[3]. Song-Lin Young, Karl. D. Stephan "Stabilization and power combining of planar micriwave oscillators with an open resonator" IEEE MTT-S Digest 1987 pp185-188.

[4]. J.W.Mink "Quasi-optical power combining of solid-state millimeter wave soures" IEEE Trans. VOL. MTT-34 Feb. 1986 pp273-279.

[5]. D.B.Rutledge etal. "Quasi-optical power combining arrays" IEEE MTT-S Digest 1990

[6]. Z.B.Popovic, R.M.Weikle, M.Kim, K.A.Potterand D.B.Rutledge "Bar-grid oscillators" IEEE Trans. VOL MTT-38 Mar. 1990 pp225-230

[7]. Robert A.Vork and Richard C.Compton "Quasi-optical power combining using mutually synchronized oscillator arrays" IEEE Trans. VOL. MTT-39 NO.6 June 1991 pp1000-1009.

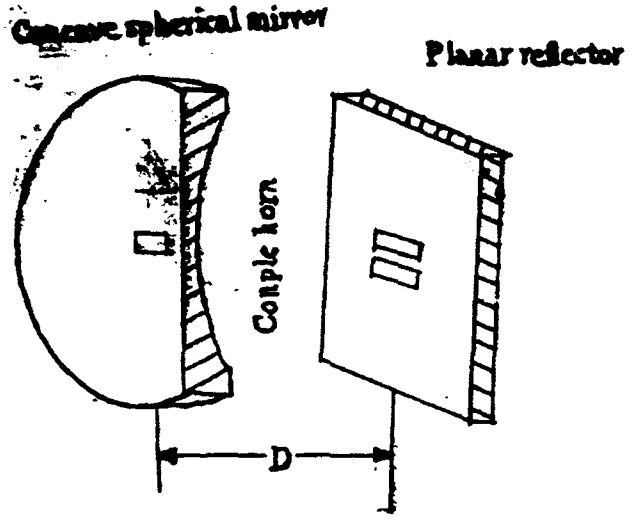

Fig. 1. The resonator configuration

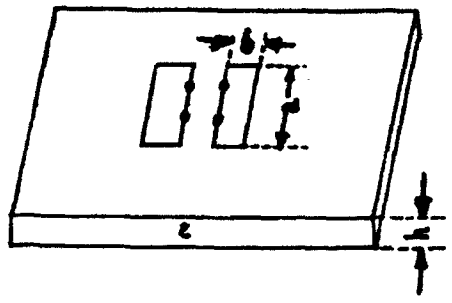

Fig.2 The structure of the planar refector

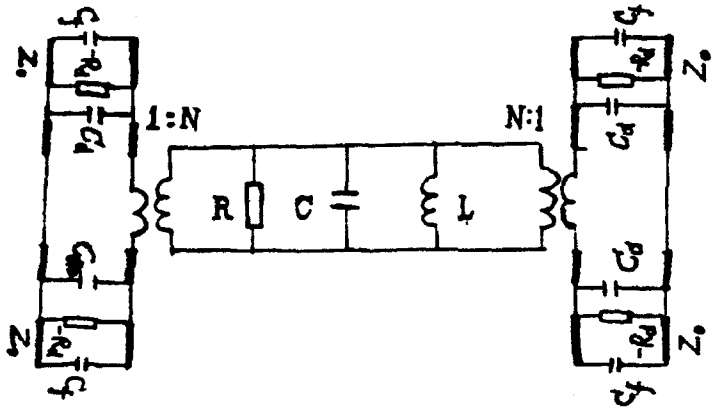

Fig.3 The equivalent circuit

TABLE I

power(mw)	frequency(GHz)	effiency	a × b(mm)	V(v)	d(mm)
30	8.785	57%	14 × 9	10	14
32	10.515	58%	14 × 6.5	9.2	14
30	12.4	57%	16 × 9.2	10	14
152	11.15	69%	14.2 × 10	10	10

TABLE II

power(mw)	frequency(GHz)	effiency	a × b(mm)	V(v)	d(mm)
250	10.755	60%	22 × 11	10	10

A SOLID-STATE GENERATOR WITH A QUASIOPTICAL DIELECTRIC RESONATOR

S.N.Kharkovsky and A.Ya.Kirichenko

Institute of Radiophysics and Electronics, Academy of Sciences of the Ukraine, 310085 Kharkov, the Ukraine

Dielectric resonator (DR) with lowest modes finds many applications in oscillator designs at microwave frequencies due to the temperature -stable, high permittivity materials, availability of low-cost /1/. However the most DR applications are in the range of 2 to 20 GHz. The degradation of Q-factor, decrease of the DR dimensions with increase in operating frequency limits the use of DRs with lowest modes for mm wave range.

In this work we present a new mm-wave range solid state generator which appeared as a result of the purposeful research of oscillating systems adequate to this range and effectively conjugated with semiconductor diodes.

In our generator electromagnetic oscillations are realized by Gunn diodes or IMPATT-diodes. Resonance conditions are provided by a quasi--optical dielectric resonator (QDR) in a form of dielectric semidisks with a metal mirror. In a two-diode module (Fig.1) diodes 1,2 are positioned in separate rectangular grooves in the mirror 3 and they excite in a semidisk 4 poor dissipated azimuthal modes of the high order (for example, the distribution of the electric field of the mode with the azimuthal wave number $n = 9$ is shown by dash lines in Fig. 1). These modes are of the "whispering gallery" type. Since modes are formed by the "sliding" traveling waves inside the dielectric corresponding to small incidence angles their reflection factor practically equals to 1. That is why these fields are localized in the vicinity of the resonator side surface and the resonator has a high value of Q-factor. The output of the energy is carried out by means of the dielectric waveguide (DW).

One may assemble a multidiode generator from one- or two-diode modules by means of distributed electromagnetic coupling between semidisks mounted on a general mirror. It provides generation of high--stable electromagnetic oscillations with a frequency of the range 10-150 GHz and summarization of powers of a great number of Gunn diodes or IMPATT-diodes.

The experimental investigations are carried out in the 8 mm wave band. The QDR dimensions are as follows: the radius - $R \sim 5\lambda$, the height -

- $H \leq \lambda$ (λ is the length of the wave in the resonator).

Fig.2 shows electronic tuning frequency Δf and output power p of EH oscillation of the two-diode Gunn generator (curves 1). Operating frequency is approximately 40.02 GHz, maximum output power is 150 mW. These characteristics are compared with measured frequency and output power versus voltage V of one diode in the reduced-height rectangular waveguide (curves 2) and of the one-diode module with QDR (curves 3). As the Figure shows output powers of one-diode generators (dashed curves 2 and 3) differed slightly. In the case of two diodes summation of their powers and stabilization of the operating frequency are observed.

A mechanical tuning of frequencies of the generator with QDR is accomplished by several methods. For example, the DR can be used in the form of two dielectric semidisks on a general mirror (Fig.3). The resonance frequencies of the odd (even) type oscillations are monotonically increased (decreased) with the decrease of the distance d between the semidisks (dashed curves in Fig.4 for the mode with the azimuthal wave number n = 41). The tuning of the generation frequency (approximately 2%) is accomplished in the generator with diodes displaced in the middle of the QDR system (continuous curve f). The output power change is shown in Fig.4 (continuous curvep).

Conclusion. A possibility of designing a solid-state generator on the basis of semidisk quasioptic dielectric resonator has been shown in the mm-wave range. It is a new class of the solid-state generators which have a good perspective at short mm-wave range. The device can be designed by means of hybrid-integral technology and conjugates effectively with integrated circuits of the mm-wave range.

References.

1. H.Bierman. DROs Meet EW and Countermeasure System Needs. Microwave J., vol. 30 , N 10 (October 1987), pp.44,46,48,52-54,56,60, 64,66.

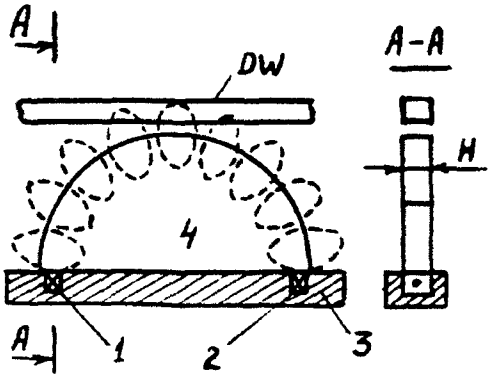

Fig.1

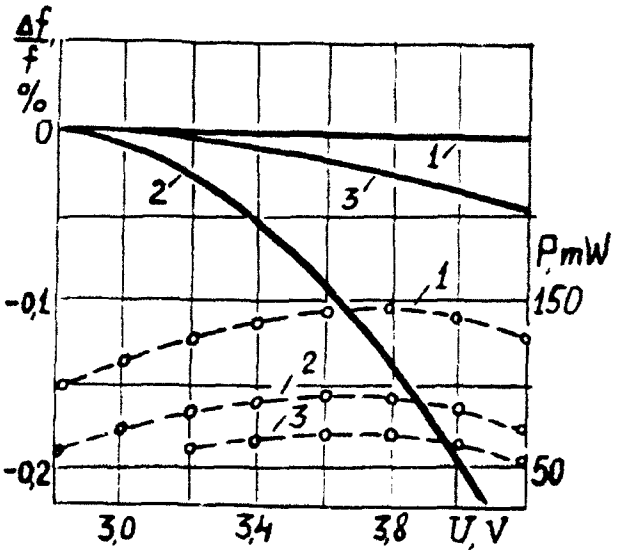

Fig.2

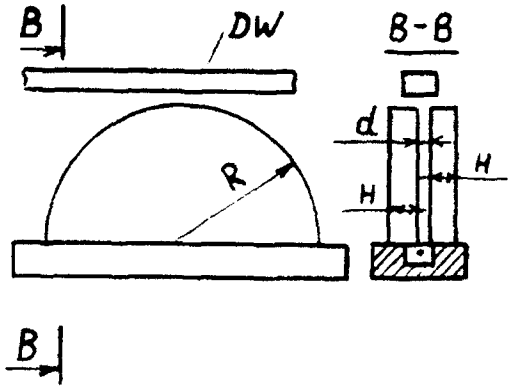

Fig.3

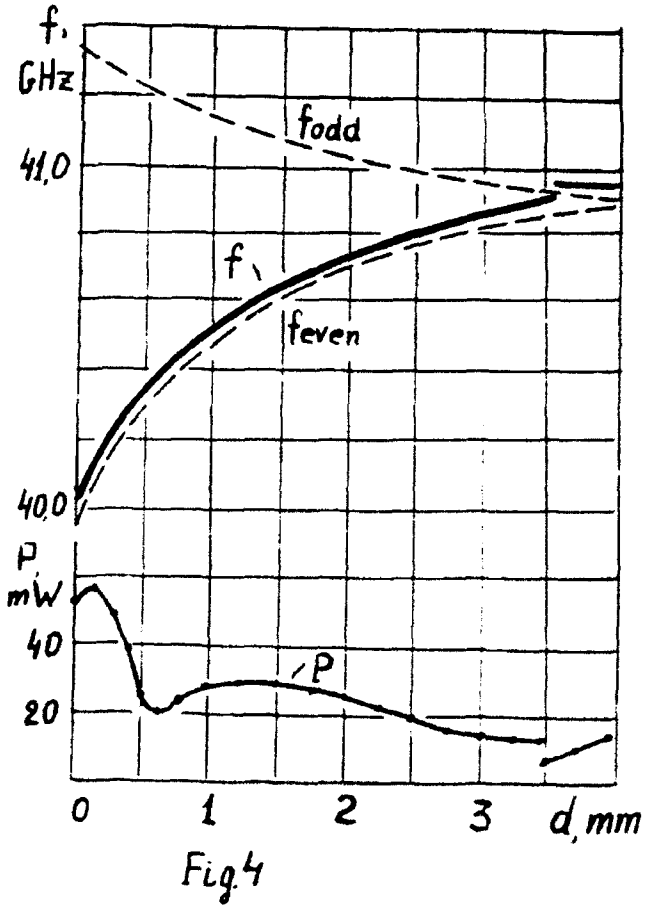

Fig.4

FERRITE AND SEMICONDUCTOR QUASIOPTICAL DEVICES OF MILLIMETRIC AND SUBMILLIMETRIC WAVE BAND ISOLATORS, CIRCULATORS, SWITCHES

Alexey A. Kostenko, Grigoriy I. Khlopov, Victor P. Shestopalov, Uriy B. Yakimchuk

Inst. of Radiophysics & Electronics Acad. of Sciences of the Ukraine
12, Acad. Proskura st., Kharkov, 310085, Ukraine

Ferrite and semiconductor devices of quasioptical type constraction has it's specificity which is connected with the transformation of working type of modes into highest ones. That is why it is necessary to provide for the regularity of active element switching on in the cross-section of the quasioptical line. In other words the ferrite and semiconductor element must be excuted in the form of a flat-parallel structure, which completely overlaps the cross-section of a transmission line.

In this connection it is preferable to use Faraday rotator of plane of polarization combined with the polarization divider in form of a cruciform ramification of the quasioptical line of transmission with small-mesh diffraction grating in diagonal cross-section [1], which allows to realize a wide set of functional devices of different tipe. In these conditions a polarization plane turning angle $\alpha=45^\circ$ is characteristic for nonreciprocal circulator (Fig. 1a) and isolator (Fig. 1b), and at $\alpha=90^\circ$ there are properties of reciprocal cwitch (Fig. 1c, 1d). The parameters of similar devices are determined by attenuation in the line of transmission, polarization divider, material, by the losses in the process of transformation into the highest modes as well as by the presence of reflections from the ferrite element. And it should be mentioned that the last factor is of particular importance, while the contribution of other components may be minimized. Girotropic character of the magnetized ferrite leads to the difference in wave resistances of medium for the polarized in cirle weves of the right and left directions of polarization plane rotation, in connection with the matching of the ferrite element in quasioptical transmission line represents a nontrivial task.

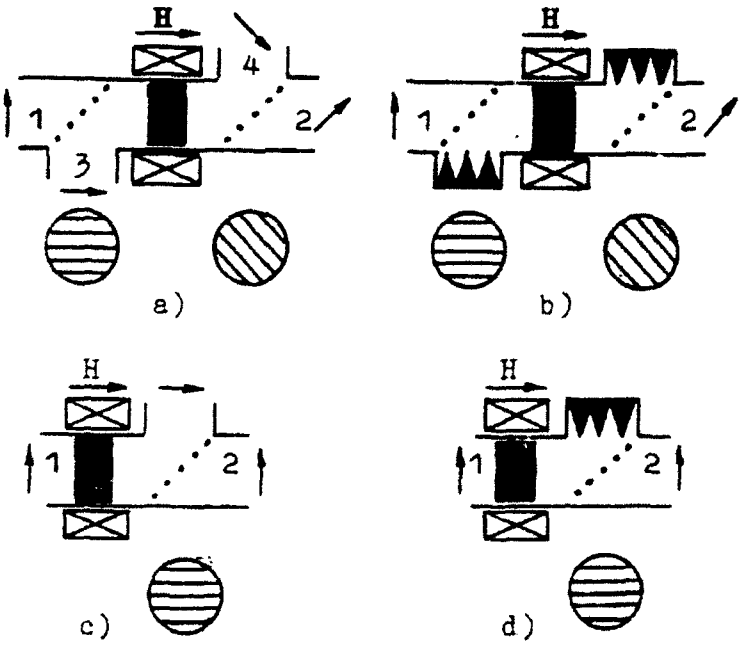

Fig. 1.

We have suggested a matching method [2], based on utilization as a ferrite element of multilayer structures in the form of gyrotropic resonators Fabri-Pero, which can be independently adjusted for each of the orthogonal field components.

Based on such structures, in the frequency band 140 GHz there have been developed a quasioptical circulator, isolator and channel selector switch for oversize waveguide with a round cross-section of 10λ diameter with the mode H_{11} [3]. The ferrite element, exercised in a form of a sistem of four yttrium ferrite disks with the summed up thickness of $\sim 6\lambda$, provided for the polarization plane turning angle $\alpha = 45^{\circ}$ at outer mugnetic field strength H=8000 A/m, introducing losses into the line, which are no more then 0,3 dB.

For circulator (Fig. 1a) summed up losses in the device in frequency band 0,5% are 1 dB (Fig. 2, curve 1), and here the channel discrimination (curve 2) is no more than 22 dB. The similar parameters are characteristic of isolator (Fig. 1b) and switch (Fig. 1c). In the latter case the switching of working regimes is exercised during the switching of the outer magnetic field. In order to eliminate the shunting effect of short-circuiting turn, formed by the walls of the waveguide, the latter is made of dielectric with a thin conducting cover ($\sim 2*10^{-4}$ mm) on the interior surfase. The time of switching in such a device was 10^{-5} s.

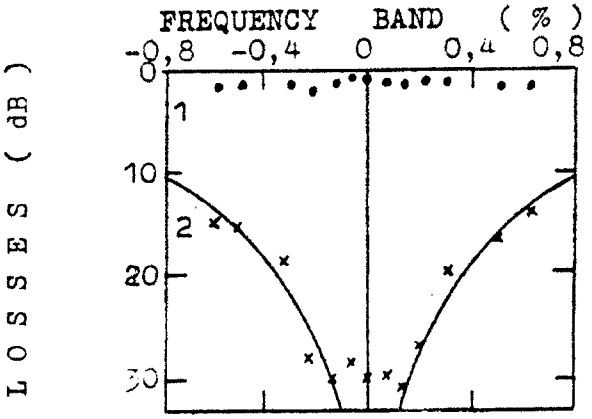

Fig. 2.

Another class of switching devices of quasioptical type is based on utilization of the photoconductivity in semiconductors. In this case a semiconductor plate is installed in the diagonal cross-section of the cruciform ramification of a quasioptical transmission line. In absence of optical pumping, the electromagnetic wave from the input arm passes with small losses semiconductor plate, the thickness of which is chosen to be equal to the half of wavelength in the material, and then it arrives at the direct output arm. Optical radiation is proided through side arm, as a resalt of which the concentration of non-equilibrium curriers in the semiconductor increases and the wave is reflected from the plate into the side output arm. Electrodinamic characteristics of a similar device have been studies in the frequency band 140 GHz, and the semiconductor plate was made of Ge ($\varepsilon = 15,7$; $\rho = 45\ \Omega*cm$) and Si ($\varepsilon = 11,5$; $\rho = 150\ \Omega*cm$). In absence of optical pumping and in case of ramification in H-plane, the losses in electromagnetic energy transmission from input arm into direct output arm were 0,3 dB (for Ge) and 0,8 dB (for Si) and bandwidth in this case was equal to 12% and 20% accordingly. In case of optical pumping the losses electromagnetic energy transmission from input arm into side output arm are determined by a density of radiating power, and their

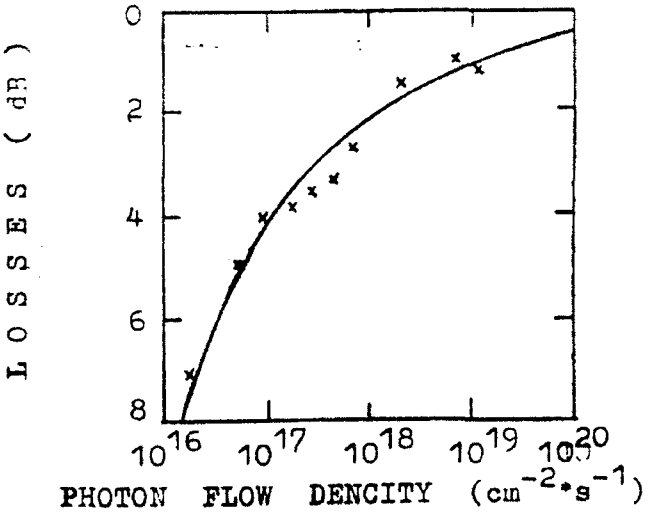

Fig. 3.

dependance on the flow of photon power is shown in Fig. 3 (smooth-curve-calculation, dots-resalt of experiments). As can be seen, in order to make losses less then 1 dB, the dencity of photon flow must be more than 10^{19} $cm^{-2}*s^{-1}$, which corresponds to power ~ 1 W

In case of impuls optical pumping it is necessary to take into consideration the velocity of non-equilibrium carrier generation, which at small periods of time of the optical radiation action, leads to encreasing of the necessary value of intensity. Numerical solution of continuity equation for this case for impulse duration $\tau = 10^{-7}$ s allows to determine the distribution of non-equilibrium carrier concentration and, by holding reflectivity factor $\sim$1 dB to determine the necessary photon flow density, which should be not less 10^{-20} $cm^{-2}*s^{-1}$, which excesses by an order of magnetude the corresponding intensity value in case of stationar optical pumping. For the chosen parameters the necessary power of optical pumping source $\sim$300 W.

Such a device has been experimentally made in frequency band 140 GHz based on oversize waveguide with round cross-section of 10λ diameter with the mode H_{11}, and as a source of optical pumping there was used a semiconductor injection laser GaAs, maximum radiation for which corresponds to the wavelength $\lambda = 0{,}9\ \mu m$ which well agrees with the spectra of photoconductivity of Ge and Si. Recovery time in such a device at the level 10 dB is $(1\text{-}5)*10^{-6}$ s and losses are no more than 1 dB.

The date provided in the paper confirm the good prospects for the use of Fraday effect in ferrite and for the use of the mechanism of photoconductivity in semicnductors while creating quasioptical ferrite and semiconductor devices of millimeter and submillimeter wavelength band.

REFERENCES

[1] H.J. Hindin, J.J.Taub, "Faraday Rotation in Oversize Waveguide at Two and One Millimeter Wevelengths", Pros. IEEE, 1966, vol. 54, 7, pp 988-989

[2] A.A. Kostenko, "Matching of Ferrite Elements of Nonreciprocal Quasioptical Devices", Radiotekhnika i Elektronika, 1981, vol 26, 10, pp 2044-2052.

[3] A.A. Kostenko, G.I. Khlopov, "Quasioptical Ferrite Devices", Izvestiya Vuzov, Radiofizika, 1989, vol 32, 4, pp 502-509.

W5.7

STUDY ON QUASI-OPTICAL SPHERECORNERECHELETTE OPEN RESONATOR SOLID-STATE OSCILLATOR

O.I.BELOUS, A.I.FISUN, A.M.FURSOV, A.A.KIRILENKO

The solving of some problems of radiophysics and millimeter and submillimeter wave techniques put forward higer requirements to the sources of electromagnetic radiation. On the first place it concerns the spectrum characters. The high stability of frequancy oscillation can be reached with the help of outer sinhronization of the frequency by frequency standard. The other way of achievement of the high stability frequency of signal is the rising unloaded Q-factor of oscillating system of generator. This way allows to solve several problems at the some time. In particular high Q of oscillating contour decreases the level of frequency noise near from the carrier frequency. The short-term and long-term stability of the frequency is defined with the stability of geometry dimensions of the resonator and the value unloaded Q. Hermetisation and termostabilisation decrease assentially the influence of the outer destability factors on the long time stability.

The results of the analysis characters of the solid-state generators with quasi-optical oscillation system are considered in this paper. The resonator of the generator consists of a smooth spherical mirror and mirror that is made up of two echelettes at angles 45 to the resonator axis. It is the spherecornerechelette open resonator(1). The calculations of the amplitude and phase of electromagnetic field in this resonator are discribed in this report. This calculation shows that the allocation of the electromagnetic field in the aperture of the slot depends on the coupling factor (the size of the slot) in the case of the excitation of the resonator on the resonance frequency. The mechanism of the excitation of oscillations in this resonator with the help of Gunn-diode or IMPATT-diode was examined. It has been allowed to solve the optimisation problem of the internal active element placement in the dispersion open resonator with the grating.

1. A.V.Archipov, O.I.Belous, B.M.Bulgakov and other. Millimeter Wave Stable Solid-State Sources With Srhereechelette Open Oscillating System. Int. Conf. on Millimeter Wave and Far-Infrared Technology. China. 1990. p.539-540.

W5.8

The Calculation of the Transitions between the Quasi-Optical Waveguides

Vladimir K. Kiselyev, Taras M. Kushta
Institute of Radiophysics and Electronics

Ukrainian Academy of Sciences
12 Acad. Proskura st.,Kharkov, Ukraine

The quasi-optical waveguides of the class of "hollow dielectric channel" (DC-waveguide) [1], namely the hollow dielectric waveguide (HDW) [2], the metal dielectric waveguide (MDV) [1,3] ets., are widely used for the transmission of the electromagnetic waves of mm and submm ranges. Many devices are created on the base of such transmission lines and an actual task is the conjugation of the quasi-optical lines, in particular ones, which are fulfiled on the DC-waveguides of the same type having the different sizes of the transversal section.

The main task of this work is to apply the well-known method of the examination of the non-regular transmission lines [4], to the DC-waveguides of the variable section.

According to the paper [4], the amplitudes of the spurious waves, which arise in the result of the scattering of the operating mode with the index m by the final part of the waveguide of variable section, are defined by

$$P_j = \pm \left[\frac{h_m(0)}{h_j(l)} \right]^{1/2} \exp(-i\gamma_j(l)) \int_0^l S_{mj} \left[\frac{h_j}{h_m} \right]^{1/2} \exp(i(\gamma_j - \gamma_m))dz \qquad (1)$$

where $h_k(z)$ is the propagating constant of the mode of the number

k, l-is the transition length, $\gamma_k = \int_0^z h_k \, dz$.

The coordinate axis z - is the axis of regular waveguides connected by the transition. Its origin coincides with the beginning of the non-regular region. The formula (1) with the supper sign leads to $P_j(l)$ at $j>0$, $j\neq m$ and it leads to $P_j(0)$ at $j<0$ with the down sign. Now it necessary to calculate the coupling coefficients S_{mj} in the limits of non-regular region. Let us take the expression for the coupling coefficient of the waves in the waveguide, that filled by piecewise homogeneous medium, as the initial formula [3]

$$S_{mj} = \frac{1}{2h_j(h_j - h_m)} \oint_C \nu \left[(\varepsilon-1)(E_s^m E_s^j - E_z^m E_z^j) + \frac{\varepsilon-1}{\varepsilon} E_n^m E_n^j \right] ds \quad (2)$$

Here E_s^k, E_z^k, E_n^k - is the values of the $\vec{E}$-field component of the mode of index k at the interior bondary of the channel of the regular waveguides, $\nu(z)$ - is the tangent of the angle between z-axis and the tangent to the bondary surface, that is perpendicular to the cross-section circuit, ε - is the permittivity, z, n, s - are local transverse coordinates along the medium bondary on the circuit C.

The boundary condition of the impedance type, which for the normal component of $\vec{E}$-field at n=o have the next form [3]:

$$\frac{\partial E_n}{\partial n} = \begin{cases} ik \dfrac{(\varepsilon-1)^{1/2}}{\varepsilon} E_n & \text{for HDW} \quad (3a) \\ -k \dfrac{(\varepsilon-1)^{1/2}}{\varepsilon} \operatorname{tg}(kd(\varepsilon-1)^{1/2}) E_n & \text{for MDW}, \quad (3b) \end{cases}$$

where $k=2\pi/\lambda$. λ - is the wavelength, d - is the non-resonant dielectric layer thickness in MDW, ε - is the permittivity, of the channel wall of DC-waveguide.

Taking into account that the condition $h_m/k \approx 1$ is subisfied in DC-waveguide, let us introduce, analogously to the work [5], in which the problem of the propagating of the electromagnetic

waves along the Earth was considered, the parameter ε_{eff}, t means of which the bondary conditions for DC-waveguide will be written in the next general form :

$$\frac{\partial E_n}{\partial n} = \frac{ik}{(\varepsilon_{eff})^{1/2}} E_n \quad . \qquad (4$$

From here, in particular for the above-mentioned bondar structures taking into account (3a, b) it is easy to receive the next evident expressions for ε_{eff} :

$$\varepsilon_{eff} = \begin{cases} \varepsilon^2/(\varepsilon-1) & \text{for HDW} \\ -\varepsilon^2 ctg^2(kd(\varepsilon-1)^{1/2})/(\varepsilon-1) & \text{for MDW.} \end{cases}$$

Substituting into (2) the values of $\vec{E}$-field component and ε_{eff} for ε, we find the coupling coefficients S_{mj}, and so the amplitudes of spurious waves P_j .

As an example the circular tapered transition ($\nu(s)=(a_2-a_1)/l$, where a_1 and a_2 - are the radii of the interior channels of DC-waveguides, that are conjugated), in which EH_{1m}-modes of DC-waveguide propagate [1], was considered.

In Fig. 1a,b the concrete examples of the calculating of the amplitude of the sporous waves for the dominant EH_{11}-mode versus the length of the round tapered transition with the parameters $2a_1=12mm$, $2a_2=20mm$, are presented. Fig. 1a corresponds to HDW with $\varepsilon=2.3$, $tg\delta=0.05$ (carbolite), fig. 1b corresponds to MDW with $\varepsilon=3.03$, $tg\delta=0.01$ (mylar). The calculations hawe been done for $\lambda=1mm$ and antiresonant dielectric layer thickness ($2kd(\varepsilon-1)^{1/2}=\pi/2$).

Formulas, have been recieved by us, allow to do the calculations of the transitions with another forms of the transverse section and to examinate the possibility of the optimization of the transition about the minimum of the loss to transformation of operating modes into the spurious ones.

REFERENCES

[1] Yu. N. Kazantsev, "Circular waveguides of the class o "hollow dielectic channel," Radiotechnics and Electronics

vol.29, no. 8, pp.1441-1450, 1984.

[2] "Electronics and radiophysics of millimeter and submillimeter radiowaves," under red. A. Ya. Usikov, I. D. Truten et al. Kiyev, Nauk. Dumka, 1986.

[3] Yu. N. Kazantsev, "Electrodinamic of wide gas-dielectic and metal-dielectic waveguides," Dis. of dr. phys.-math. sc., Moskow, 1973.

[4] P. Z. Katsenelenboum, "The theory of the non-regular waveguides with the slow-changing parameters," Moskow, Ac. of Sci. of USSR, 1961.

[5] E. L. Feinberg, "The propagating of the radiowaves along the Earth surface," Moskow, Ac. of Sci. of USSR, 1961.

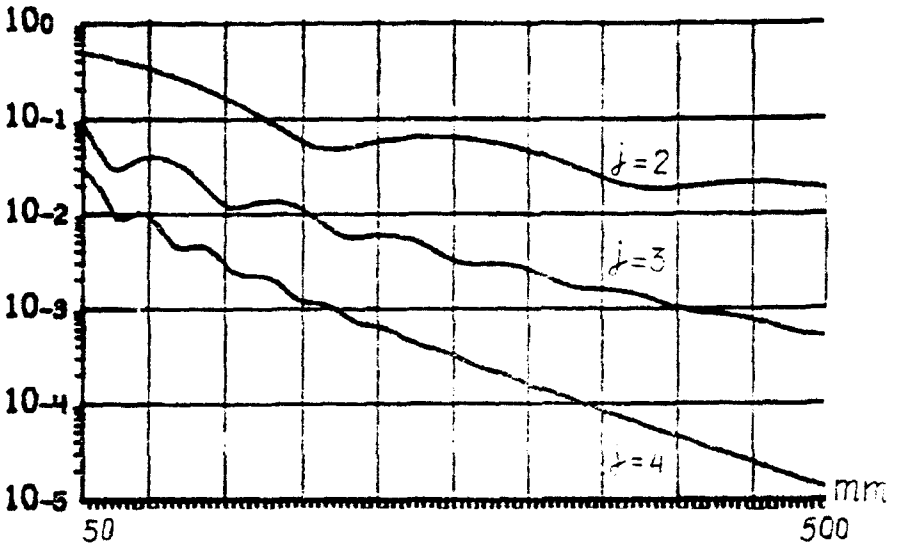

Fig. 1a

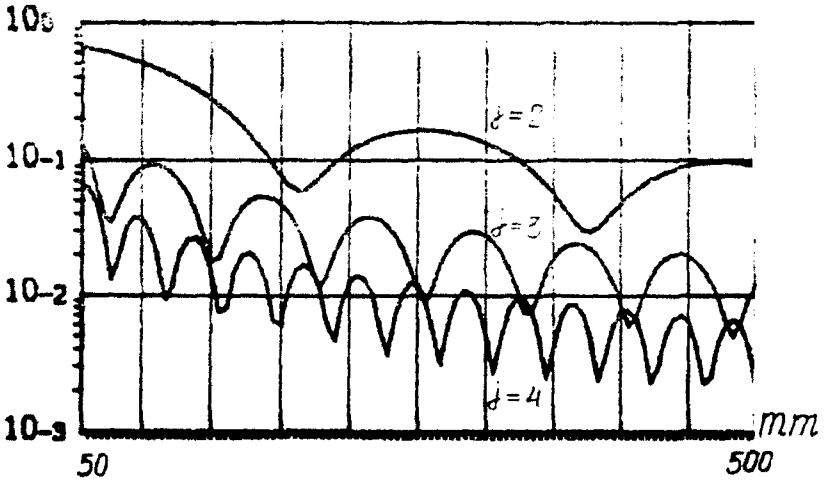

Fig. 1b

A NEW TYPE OF AN OPEN RESONATOR FOR MM- AND SUB-MM-WAVELENGTH RANGE ELECTRON DEVICES

V.P. SAZONOV

Research and Production Corporation "Istok"
Fryazino, Moscow region, 141120

1. INTRODUCTION

Open resonators made as two flat and parallel to each other mirrors were for the first time employed in 1958 in designing sub-mm-wavelength range molecular amplifier and oscillator [1]. Following application of open resonators were in gyrotrons [2] and orotrons [3]. These devices feature a principle of protracted interaction of electrons with microwave field. Microwave electronics also widely employs a principle of short-term interaction of electrons with microwave field as well, for instance in the klystron-type electron devices. Well-known types of open resonators, however, do not permit to use them in electron devices featuring short-term interaction of electrons with microwave field. Therefore the task of this paper comprises the insight into this problem and the seeking of its suitable solving.

2. THE PRINCIPLES OF DESIGNING FOCUSING OPEN RESONATORS (FORs)

An analysis of various types of open resonators has shown the possibility to attain a suitable solution to the above-mentioned problem using the focusing of an electromagnetic field. Following this process, the necessity to maintain an electromagnetic field arises for the possibility to its subsequent application in effecting its short-term interaction with an electron stream. To secure a focally-converged field a horn can be used, and to effect the electron interaction with a field there can be employed, for instance a closed waveguide's section connected to a horn through holes in its walls. Applications of the mentioned techniques result in a structure of a focusing open resonator (FOR) shown in Fig.1.

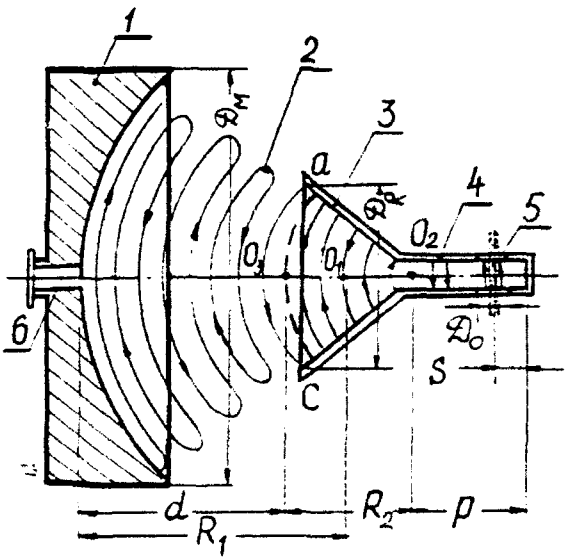

Fig.1. Focusing open resonator.

1. A concave mirror. 2. An electric field.
3. A horn. 4. A waveguide's section.
5. A hole for the electron to pass.
6. Microwave power input (output).

The question naturally comes,

whether the generation of stable oscillation in the offered resonator is possible. The answer to this question follows based on the possible application of the theory of open resonators [4]. Assume the appearance of a standing wave in the offered resonators. Then in the opening of a horn, in the cross-section aO_3c (Fig.1), for instance, there may appear an electric node. Theoretical substitution of a spherical surface for this cross-section will result in a system comprising two mirrors - a concave one with a curvature rading - R_1, and a convex one with a curvature radius - R_2, and with interval between them - d (Fig.1). The theory of open resonators says that this system sees the generation of stable oscillations, if the relationships are met: $d < R_1 < d + R_2$, i.e. in this system comprising a spherical concave mirror and a horn with a section of a short-circuited waveguide, oscillations will be stable, if the center of a curvature radius of a spherical mirror (point O_1) is located on the axis inside a horn, i.e. in the interval between a neck which is a center of a wavefront's curvature in a horn (point O_2), and a center of a horn opening (point O_3).

An approximate analysis of the properties of an offered FOR has shown that the diameter D_R of a horn and the diameter D_M of a mirror have to be connected through the relationship: $D_M D_R \geq 4 d \lambda_p$, where λ_p is a resonance wavelength. It approximately follows that $n\lambda_p/2 = d + R_2 + p$, where n is an integer. Q - factor of a resonator comprises about: $Q \approx 2\pi(d + R_2 + p)$, where δ is a summed relative loss for a single pass of a wave from a mirror to a short-circuit in a waveguide.

3. THE RESULTS OF EXPERIMENTAL STUDIES OF A FOCUSING OPEN RESONATOR

To experimentally study a FOR, a special mock-up has been designed and produced. A resonator's prototype features following basic dimensions. The length of a conical horn - 27 mm. An angle of a horn opening 30°. The length of a waveguide connected to a horn - 3 mm. Waveguide dimensions - 2.4 x 1.2 mm. The diameter of a horn's outlet - 15.5 mm. Mirror's radii of curvature - 50 - 100 mm. A spherical mirror's diameters - 65 - 100 mm.

An excitation of a resonator has been effected through a waveguide's section connected to a horn. This connection has been adjusted by a diaphragm D, having a hole. This diaphragm is 0.05 mm in thickness, and a hole has a diameter 0.8 mm. Fig.2 shows the results of experimental studies at the 3.2 mm - wavelength. Dashed vertical lines indicate critical locations of a mirror's curvature center.

The left line shows the coincidence between the centers of a mirror's curvature and of a horn's wavefront. The right line shows the location of a mirror's center of curvature in the center of a wavefront at a horn's outlet. As the limits of existence of stable oscillations are being approached step by step, Q-factor drops, and the resonance oscillations do not occur at these limits. The insertion between a horn and a mirror of a cardboard cone (Fig.2), coated with a conducting layer with a surface resistance 300 - 400

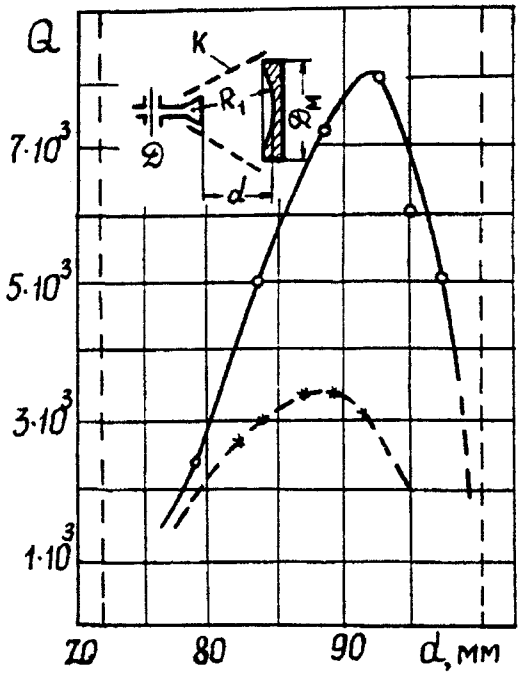

Fig.2. FOR's Q-factor dependence on the interval between a horn and a mirror - d .

•o• a mirror's diameter D=100 mm

•∆• a mirror's diameter D=65 mm.

Ohms, did not affect a resonator's properties. Measurements of a characteristic wave impedance ρ in the gap using a method of disturbances gave ρ = 5 Ohms, and this value is not far from estimations. Shunt-impedance for an optimum structure comprises about 40 kOms.

4. FOR - BASED ELECTRON DEVICES.

Based on a FOR there can be designed a number of the Foro klystron type devices [6]. Fig.3 shows a multicavity Foro klystron with FORs located along a spiral, not interfering with each other. Changing form of a space housing an interaction of an electron stream with microwave field, can give various device combinations. Foro

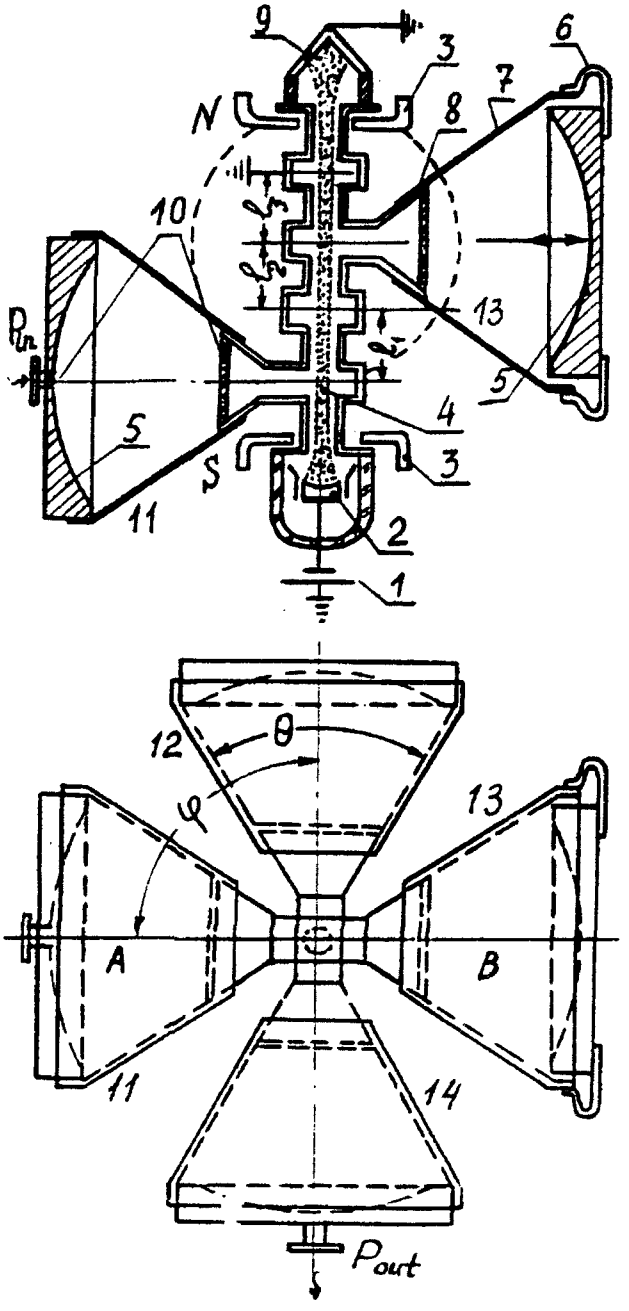

Fig.3. Quadricavity amplifier Foro klystron

1. A power source. 2. An electron gun.

3. A magnetic pole piece.

4. An electron stream. 5. A mirror.

6. Bellows. 7. An absorbing screen.

8. A horn. 9. A collector.

10. A vacuum seal.

11,12,13,14. Focusing resonators.

twistron [7], for instance. Applications of an elliptic mirror with two horns locxated in the focus of an ellipsoid can result in the production of a FOR - based Foro oscillator [8]. See Fig. 4.

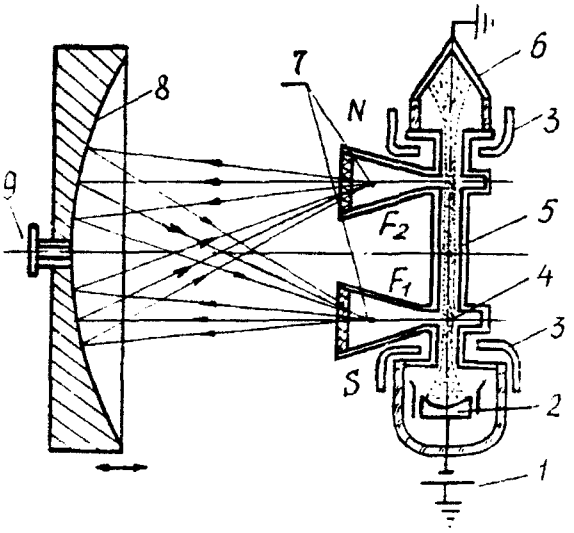

Fig.4. An oscillator with a two-horn elliptic mirror.

1. A power source. 2. An electron gun.
3. A magnetic pole piece. 4. An electron stream.
5. A drift tube. 6. A collector.
7. Two horn in the focuses of an elliptic mirror - 8.
9. Energy output.

5. ACKNOWLEDTHISMENTS

The author of paper would very much like to thank U.S. Shatilov for corresponding measurement realization, and A.V. Myshletsov for designing an experimental installation.

6. REFERENCES

1. A.M. Prohorov; On sub-mm-wave molecular amplifier and oscillator, ЖЭТФ, vol.34, p.1658, 1959.
2. A.V. Gaponov et al.; Induced synchronous radiation by electrons in hollow resonators, Letters to ЖЭТФ, vol.29, p.430, 1965.
3. F.S. Rusin, G.D. Bogomolov; An electron device for the generation and amplification of mm- and sub-mm-wavelength range oscillations, An author's certificate, USSR, №195557, dated November 16, 1965.
4. L.A. Weinshtein; Open resonators and open waveguides, Moscow, Publishers Soviet Radio, 1966.
5. V.P. Sazonov; An open resontor, An author's certificate, USSR, №982479, dated February 26, 1981.
6. V.P. Sazonov; Sub-mm- and mm-wavelength range amplifier multiresonator klystron, An author's certificate, USSR, №982482, dated May 6, 1981.
7. V.P. Sazonov; An "O" type microwave device of mm- and sub-mm-wavelength range, An author's certificate, USSR, №982481, dated May 13, 1981.
8. V.P. Sazonov; V.S. Shatilov; An open resonator, An author's certificate, USSR, №1243550A dated February 24, 1983.

ELEMENTS OF THE DIFFRACTION QUASIOPTICS. PART 1: THE MAIN PROPERTIES

Minin I.V. and Minin O.V.
Institute of Applied Physics, Novosibirsk, 630117, USSR

The elements of the diffraction quasioptics (EDQ) [1] are intended for transformation of incident wave fronts into the required ones. The EDQ operation principle is based on creation of specifically chosen discrete phase delays over the wave front. There are three main types of EDQ (by the principle of disposition with respect to the propagation direction of the electromagnetic wave) [1]: transverse (made mainly on a flat surface), longitudinal-transverse (made on an arbitrary curvilinear surface) and longitudinal (representing a system of screens located along the direction of the electromagnetic wave propagation). The EDQ can operate both in the "transmission regime" and the "reflection regime". According to the application the EDQ can be of amplitude (binary) and phase inversion type.

The main physical properties of the EDQ, development at our Institute, are briefly surveyed in the present work.

The principle of the EDQ construction is founded mainly on the laws of geometric optics and is described in literature [2,3,4] rather in detail. It should be noted that the problem of restoration of the EDQ phase profile by the preset focusing properties refers to the class of incorrect problems and it has no single solution even in the simpliest cases [5]. For mathematical modeling of the EDQ physical properties and carrying out of numerical experiments in order to find out the main laws of diffraction of the EDQ electromagnetic waves a scalar approximation is used. The structure of the field formed by the high-transmission EDQ in the region of observation is defined on the basis of strict calculation of Fresnel-Kirchhoff diffraction integral by a special algorithm the essence of which is considered in [6] as an example of the wave diffraction on the flat axisymmetric EDQ. In some cases for the fast modeling of

frequency-forming EDQ properties (mainly for the analysis of their aberration characteristics) a geometric theory of diffraction is used [7]. The problems of the numerical experiment technology and the structure of the computer complex are represented in [8].

Let's consider some general properties of the EDQ. The characteristic features of the EDQ are the following: a low inherent thickness of a phase profile (making the value in the order of the radiation wavelength), a low weight, low absorption losses of microwave power in the EDQ material, the possibility of the large-sized EDQ construction (up to several meters), lower required precision of the phase profile creation in comparison with mirrors, the possibility of the EDQ construction on the surface of the arbitrary shape, high electromagnetic compatibility of different EDQ, their noise immunity and so on. As the transformation of the wave front incident on the EDQ takes plase only due to piece-constsnt or piece-continuous phase modulation this causes the appearance of frequency properties, that is the dependence of the space position and the shape of the focusing region on the wavelength of radiation incident on the EDQ [9]. This fact is especially important in the range of mm-waves where monochromatic radiation sources are usually used. Moreover, the frequency properties of such elements can be controlled by selecting the method of synthesizing of the EDQ phase profile [4], changing the EDQ surface shape, the values of this surface sagging deflection and its orientation in space; it's possible both to enhance them and to create super wideband systems. We should note that the value of the EDQ spectral resolution at a great number of Fresnel zones on its aperture is defined by the formula of the diffraction grating.

Another inportant property of the EDQ, constructed on the curvilinear surface is the dependence of the longitudinal resolution on the value of the sagging deflection and space orientation of this surface [9]. As far as the transverse resolution (with respect to the optical axis) is concerned, these EDQ are the diffraction-limited elements and their resolution is characterized by the diffraction limit [6] It should be mentioned that at a low number of Fresnel zones the EDQ resolution is even

better than the Airy's formula yields.

The possibility the EDQ construction without axial symmetry allows to realize focusing systems with space-frequency depeeeendence of the focusing region position [10]. Besides the EDQ are not obligatory analogous to microwave lenses and mirrors (that is, they are used not only to focus the radiation into the point of diffraction-limited sizes but to provide the focusung of the incident radiation into 3D region of arbitrary shape [3]). As the EDQ are capable to operate both in near- and far-field zones the mentioned property allows to create systems of forming of the radiation pattern of rather exotic shape.

One more characteristic feature of the EDQ is the dependence of their diffraction effectiveness on the number of the phase quantization levels of the incident wave front. This allows not only to choose the complexity of the EDQ construction depending on their specific application but to redistribute the energy by different diffraction orders. Besides, the selection of the mentioned parameter and the selective properties of the EDQ at the operation with the radiation including several multiple harmonics [11] can be controlled. It is possible to use one and the same EDQ for operation with the radiation of several multiple wavelength, to mix them in one and the same focusing region and so on.

The EDQ capability to combine properties of several different focusing systems is one more important feature. For example, it's possible to create a dynamically changeable shape of the focusing region by combining two 1D EDQ [12], to realize polarization-sensitive mm-optics [13], to construct EDQ operating simultaneously in IR- and mm-ranges and so on.

REFERENCES

1. Minin I.V. and Minin O.V. (1989) Diffraction optics. Achievements and prospects. Theses of the Proc. of All-Union Semonar on processing technique of 2D signals (Moscow, Part 2) 10-11.

2. Minin I.V. and Minin O.V. (1989) The focusing elements of diffraction quasioptics and their application. Theses of the Proc.

of the 3 All-Union School on propagation of mm- and submm waves in atmosphere (Harkov) 251-252.

3. Minin I.V. and Minin O.V. (1991) The construction prinsiple of elements of diffraction quasioptics for focusing of coherent radiation into the arbitrary space configuration. Theses of the Proc. of the 1 Ukranian Symp. "Physics and Techn. of mm- and submm radiowaves" (Harkov, Part 1) 14-15.

4. Minin I.V. and Minin O.V. (1990) Control of focusing properties of diffraction elements. Sov. J. Quantum Electron. 20 (2), 198-199.

5. Minin I.V. and Minin O.V. (1989) Optimization of focusing properties of diffraction elements. Sov. Letters to the J. Tech. Phys. 15, 23, 29-33.

6. Baibulatov F.X., Minin I.V. and Minin O.V. (1985) Investigation of the focusing properties of the Fresnel zonel plate. Radiotechnika and Electronica, 30, 9, 1034-1039.

7. Minin I.V, Minin O.V. and Zherebin V.V. (1989) The system of geometrical simulation of diffraction optics. Theses of the Proc. of the 5 All-Union Conf. on Computer graphics (Novosibirsk) 87.

8. Minin I.V. and Minin O.V. (1990) The integrated system of the computer-aided designing of elements of diffraction quasioptics. Computer optics, 7, 89-96.

9. Minin I.V. and Minin O.V. (1989) Invariant properties of elements of diffraction quasioptics. Computer optics, 6, 89-97.

10. Minin I.V. and Minin O.V. (1987) Diffraction radiooptical systems of microwave range. Theses of the Proc. of the 6 All-Union Conf. "Methods and means of measuring of electromagnetic characteristics of materials in HF- and SHF-ranges (Novosibirsk) 15-16.

11. Minin I.V. and Minin O.V. (1989) Selection of harmonics of coherent radiation by means of computer optics. Theses of the Proc. of the All-Union seminar on the processing techniques of 2D signals (Moskow, Part 2) 29-30.

12. Minin I.V. and Minin O.V. (1989) A new type of computer optics elements. Ibid, 31-32.

13. Certificate of authorship 1617398 (USSR, 1990).

ELEMENTS OF THE DIFFRACTION QUASIOPTICS. PART 2: THE MAIN APPLICATIONS

Minin I.V. and Minin O.V.
Institute of Applied Physics, Novosibirsk, 630117, USSR

Let's consider some classes of typical mm-systems based on certain physical properties of the EDQ.

Systems of plasma diagnostics. A diagnostics system on the basis of the off-axis EDQ [1] is rather effective for investigation of plasma formations, for example, in problems connected with the controlled thermonuclear synthesis, of operation of magnetic hydrodynamic generators and so on [2]. In such a system the angular separation of probing trajectories, the plasma diagnostics in a local region simultaneously at several close wavelength through one and the same antenna are fulfilled due to the usage of space-spectral-focussing properties of the EDQ with off-axis position of the focusing region [3]. This allows to carry out experiments on the backward and bistatic scattering, to obtain the information on space and energetic properties of plasma, its dynamics and so on. Besides, when necessary the EDQ can be used simultaneously as a focusing device and a special packer investigations in reacting media, on ballistic tubes [2] and so on.

Another type of millimeter and submillimeter systems is based on the EDQ capability to provide the radiation focusing in the arbitrary space configuration. This allows to create systems of microwave retaining of plasma in the arbitrary region, devices for obtaining microwave-discharges of complicated 3D configuration and some others [4].

Systems of quasioptical radiovision. Mm-systems of direct quasioptical radiovision are based on the high-effective diffraction radiolenses, the requirements to the radiolense are started in work [5]. The combination of the focusing and frequency EDQ properties [6] allows to realize the construction system of radioimages of 3D objects in real time [7]: a vertical

image scanning is carried out, for example, by electronic polling of the receiver arrays and a horizontal image scanning is carried out by moving the object; and a look by depth of scene essentially exceeding the depth of the radiolens sharpness is carried out by frequency scanning (by deviating the wavelength of the radiation sources).

Antenna systems. The EDQ are capable to form the antenna pattern of arbitrary shape. In such antennas the pattern scanning can be provided in the range not less than $\pm 20^{\circ}$ due to the shifting of the eadiation receiver position, and antenna amplification changes not more than by 1.5 dB and the level of the side lobes changes insignificantly [8]. The advantages of antennas on the EDQ basis are the absence of the aperture blockage (as in systems of Cassegrain antenna type), the simplicity of their manufacturing. Frequency properties of the EDQ which considerably increase the noise immunity of antenna systems, allows to control their frequency selectivity, noise characteristics and so on are of importance. Besides as the EDQ can work in the "transmission regime" they can be used as a radio-transparent cap for protection of a relevant equipment against the environment action: that is, it's possible to escape the direct action of this environment on the radiation receiver (or radiation source), to reduce requirements to the conditions of their maintanance. As the EDQ can be constructed on the surface of the arbitrary shape such antennas combine their properties with the properties of the radome. This is important in particular for a considerable reduction of the wind loads on the large sized antennas, for a distortion reduction of the antenna pattern caused by a special radome and so on. The possibility of construction of such nonmetal antennas of different designs plays a great role. For example, it makes possible to manufacture antennas for automobile radars to be used in fogs, rains and so on. The aerodynamic properties and design of the antenna are defined by the application and the shape of the automobile.

Such antenna can be widely used in communication systems of different application, in radio transmitting systems (as wave front correctors as well), in report television systems, systems

of duplex communication and other fields of national economy. Satellite TV is one of the promising fields of application of antenna systems on the EDQ basis using practically all above mentioned characteristic features. A variety of antenna shapes, their aesthetical and structural accordance with the interior of flats, private cottage and different buildings, rather high technical parameters allow to realize a great number of antenna systems for reception of the satellite TV programs not only of classical microwave range but of mm-range as well [8].

Mm-systems for scientific investigations. The range of millimeter and submillimeter waves is characterized, in particular, by the fact that the EDQ diameter-to-the radiation wavelength ratio is the same as that of integral optics elements. This allows, for example, to carry out the development and simulation of properties of the relevant optical system as their manufacturing is considerably simpler in mm-range than in IR- and optical ranges. Thus on the basis of the EDQ it's possible to construct a set of planar optical logic elements for optical polychromatic computers [9] to optimize optical elements of integrated optics, devices of radiation input/output and so on.

Besides simulation the EDQ have one more important property. For example, they can be used for construction of a great number of optics of millimeter and submillimeter lasers of different applications, both for focusing of their radiation into the arbitrary region and for prescribed transducing of the wave front.

There is a number of other possible fields of EDQ application. So, on the basis of development of construction principles and studying of EDQ properties in microwave range we managed to show possibility of shock wave focusing in nonlinear regime in principle [10], that is very important both from point of view of physics and that of applied sciences, for example, for medicine.

REFERENCES

1. Certificate of authorship 1347690 (USSR, 1988).

2. Minin I.V. and Minin O.V. (1991) Application of elements of diffraction quasioptics for microwave diagnostics of plasma. Theses of the Proc. of the 1 Ukranian Symp. "Physics and Techn. of mm- and submm radiowaves (Harkov, Part 2) 11-12.

3. Minin I.V. and Minin O.V. (1987) Diffraction radiooptical systems of microwave range. Theses of the Proc. of the 6 All-Union Conf. "Methods and means of measuring of electromagnetic characteristics of materials in HF- and SHF-ranges (Novosibirsk) 15-16.

4. Minin I.V. and Minin O.V. (1990) Diffraction optics in physics of the high densities of energy. Collection of works: "Waves and diffraction-90" (Moskow, Physical Society), 3, 187-189.

5. Minin I.V. and Minin O.V. (1986) A wide-angular multicomponent diffraction microwaves lens. Radiotechnique and electronics, 31, 4, 800-806.

6. Minin I.V. and Minin O.V. (1988) Diffraction lenses on parabolic surfaces. Computer optics, 3, 21-29.

7. Minin I.V. and Minin O.V. (1988) Microwave flaw detectors on the basis of diffraction quasioptics. Theses of the Proc. of the All-Union Conf. "Optical radiowave and thermal techniques of non-destructive testing" (Mogilyov, Part 1) 40-41.

8. Minin I.V. and Minin O.V. (1991) Diffraction antennas of mm-range. Theses of the Proc. of the 1 Ukranian Symp. "Physics and Techn. of mm- and submm radiowaves" (Harkov, Part 1) 356-357.

9. Minin I.V. and Minin O.V. (1989) Elements of the optical computer on the basis of the diffraction quasioptics. Theses of the Proc. of the All-Union Seminar on processing techn. of 2D signals (Moskow, Part 2) 33-34.

10. Minin V.F., Minin I.V. and Minin O.V. (1991) The dynamics of shock wave focusing with the elements of diffraction quasioptics. Book of abstracts the 18 Int. Symp. on Shock Waves (Sendai) 39-40.

CALCULATION OF S-PARAMETERS OF PLANAR JUNCTIONS BY BOUNDARY-ELEMENT METHOD

Bin Song , Junmei Fu
(Xi'an Jiaotong University, Xi'an, P.R.of China)

ABSTRACT

A method , which is a combination of the equivalent waveguide model and the boundary-element technique, is described for calculating the frequencies-dependent scattering parameters of planar junctions. This approach has a few merits, e.g., simple deducing, short computation time and considerable flexibility.

INTRODUCTION

Open planar multiport junctions are found in practical applications, particularly in the spectral range from microwave to short millimeter-wave frequencies, in the integrated circuits. Up to now, several approaches have been presented for the analysis of such structures. However, these methods all have a few restricted applications, for example, only regular-shape planar junctions may be studied, and some approximation are employed, so there exist considerable discrepancies between the published results. In our investigation, a boundary-element method using Green's function and a planar waveguide model are employed to compute the frequency-dependent scattering parameters of arbitrary-shape planar junctions.

THEORY

The waveguide model as shown in Fig.1 has been introduced for a microstrip line. It consist of electrical walls at the top and the bottom of the line, and magnetic walls at the sides. The effective width Weff of the model as well as the effective dielectric constant ε_{eff} are frequency-dependent model parameters [1]. Through the above-mentioned equivalence, a planar multiport junction can be changed into a H-plane multiport waveguide junction.

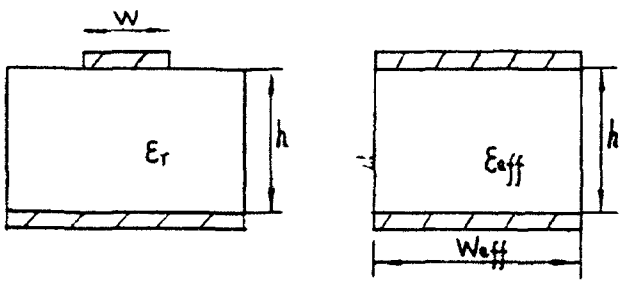

Fig. 1 Open microstrip line and its waveguide model.

A waveguide junction as shown in Fig.2 is considered. Assuming the height of the waveguide model is much less than the wavelength (in order to ensure that higher-order modes which vary in the Z-direction are suppressed), only the Ez, Hx, Hy field components exist. The Ez field in this junction satisfies Helmholtz's equation :

$$\nabla^2 Ez + k^2 Ez = 0 \tag{1}$$

Considering the region surrounded by the boundary L as shown in Fig.3 and using the fundamental solution [2] and Green's formula, from (1) we obtain the following equation :

$$ui + \int_L u\, q^* dl = \int_L u^* q\, dl \tag{2}$$

where

$$u^* = (1/4j) H_0^{(2)}(kr) \tag{3}$$

$$q^* = (jk/4) H_1^{(2)}(kr)\cos\alpha \tag{4}$$

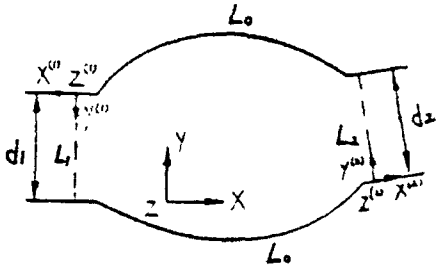

Fig. 2 A mutiport waveguide junction.

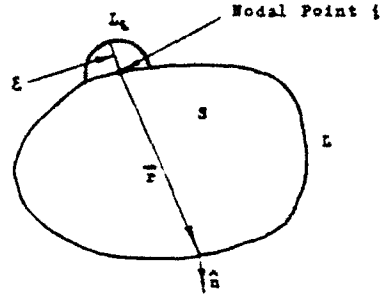

Fig. 3 Two-dimension region surrounded by L.

Here u_i is the value at the node i, q and q^* are the outward normal derivatives of u and u^*, respectively, $H_0^{(2)}$ and $H_1^{(2)}$ are the zeroth- and first-order Hankel functions of the second kind, respectively, and α is the angle between the vector $\vec{r}$ and the outward unit normal vector $\hat{n}$.

Noting that the node i is placed on the boundary L and considering the integration path L_ε going around the node i as shown in Fig.3, and using the Cauchy's principal value of integration, we obtain

$$Ci\, ui + \int_L u\, q^* dl = \int_L u^* q\, dl \tag{5}$$

where $Ci = 1 - (\theta/2\pi)$, to a smooth boundary, $Ci = 1/2$.

Dividing the boundary L into quadratic line element, then (5) can be discretized and is rewritten as

$$Ci\, ui + \sum_{e=1}^{N} [\, hi\ h2\ h3\,]e \begin{bmatrix} u1 \\ u2 \\ u3 \end{bmatrix} = \sum_{e=1}^{N} [\, g1\ g2\ g3\,]e \begin{bmatrix} q1 \\ q2 \\ q3 \end{bmatrix} \tag{6}$$

In the matrix notation, (6) can be rewritten as follows :

$$[\,H\,][\,U\,] = [\,G\,][\,Q\,] \tag{7}$$

From (7), the following equation is obtained for the waveguide junction in Fig.2 :

$$[\ [H]_0\ [H]_1\ [H]_2\ ] \begin{bmatrix} [U]_0 \\ [U]_1 \\ [U]_2 \end{bmatrix} = [\ [G]_0\ [G]_1\ [G]_2\ ] \begin{bmatrix} [Q]_0 \\ [Q]_1 \\ [Q]_2 \end{bmatrix} \tag{8}$$

where the subscripts 0, 1 and 2 denote the quantities corresponding to the boundaries L_0, L_1 and L_2 in Fig.2, respectively.

The u on $L_i (i=1,2)$ may be expressed analytically as

$$u(x^{(j)}=0, y^{(j)}) = 2\delta_{ij} f_{j1}(y^{(j)}) - \sum_{m} (1/j\beta_{im}) \int_0^{d_i} f_{im}(y_0^{(i)}) f_{im}(y_0^{(i)}) \cdot g(x^{(i)}=0, y^{(i)}) dy_0 \quad (9)$$

where

$$f_{im}(y^{(j)}) = \sqrt{2/a_i} \sin m\pi y^{(i)}/a_i \ , \quad m=1, 2, 3, \ldots$$

$$\beta_{im} = \sqrt{k_0^2 \varepsilon_{ri} - (m\pi/a_i)^2}, \quad m=1, 2, 3, \ldots$$

Discretizing (9), and considering (8), then the values of u at nodes on Li can be obtained by using an interpolating function. Therefore, the solutions on Li allow the determination of the scattering parameters Sij as follows :

$$S_{jj} = \int_0^{d_j} u(x^{(j)}=0, y^{(j)}) f_{j1}(y^{(j)}) dy^{(j)} - 1$$

$$S_{ij} = \sqrt{\beta_{i1}/\beta_{j1}} \int_0^{d_i} u(x^{(i)}=0, y^{(i)}) f_{i1}(y^{(i)}) dy^{(i)} \ , \quad i \neq j \quad (10)$$

The presented approach can be applied easily to the analysis of planar multiport junctions.

RESULTS

The first example is a dual port junction as shown in Fig.4 , and its dimensions are : w1=w2=0.608mm, h=0.65mm, θ =60, εr=10.1. Computed results for the S-parameters as a function of frequencies are shown in Fig.4, and are compared with the numerical results obtained via the field-matching method [3]. It can be found that our

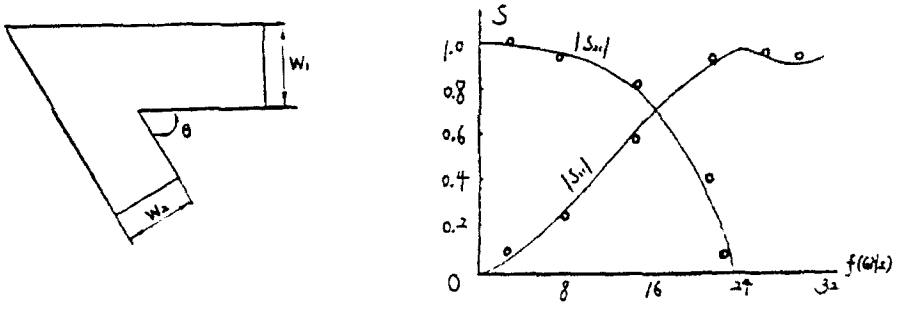

Fig. 4 Reflection coefficients and transmission coefficients of the dominant mode of a dual port planar junction.
(——— this method ; o o o [3])

results are in good agreement with data in [3]. However, our approach has more flexibility , e.g., it can study generalized-shape planar multiport junction, while the field-matching method only can analyze regular-shape ones.

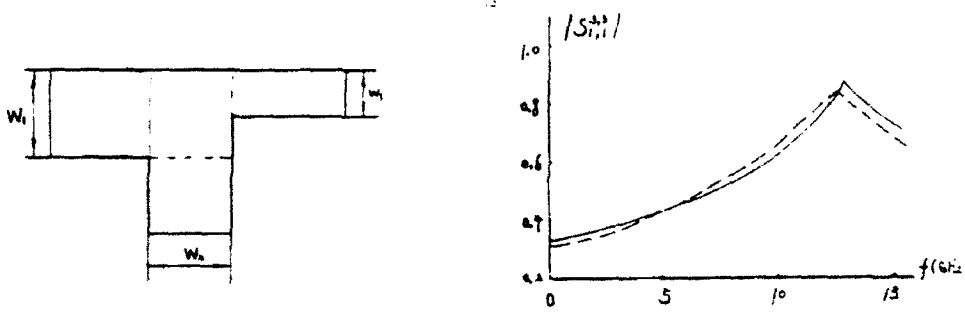

Fig.5 Reflection coefficients of the dominant mode at the third port of a triport planar junction.
(——— this method ; - - - experimental results[1])

The second example is a triport junction as shown in Fig.5 , and its dimensions are : W1=0.977cm, W2=W3=0.780cm, h=0.158cm, ε_r=2.32. Fig.5 shows its transmission coefficients and reflection coefficients , which are all compared with experimental data in [1].

CONCLUSIONS

In this paper, the waveguide model concept and the boundary-element technique are employed to investigate the planar multiport integrated circuits, and the s-parameters of such structures are calculated. Two examples are given, and the comparison of the obtained results with data available in literature shows good agreement. in addition, this method has more flexibility, it can analyze arbitrary-shape planar multiport configurations.

REFERENCES

1. W.Menzei and I.Wolff, IEEE Trans., MTT-25, 2(1977), 107.
2. C.A.Brebbia, The boundary Element Techniques in Engineering, Butterworth, London, 1980.
3. R.Mehran, IEEE Trans., MTT-26, 3(1978), 400.

W6.2

ON THE ELIMINATION OF INFINITIES IN THE PO COMPONENT OF EQUIVALENT EDGE CURRENTS

Taner Oguzer , Ayhan Altıntaş and O. Merih Büyükdura*
Department of Electrical and Electronics Eng., Bilkent University
06533 Bilkent, ANKARA, TURKEY
* Department of Electrical and Electronics Eng., Middle East Technical University
06531, ANKARA, TURKEY

January 9, 1992

Abstract: Equivalent edge currents for the Physical Optics (PO) contribution to the edge diffraction are derived by choosing a proper coordinate system for a half plane. It is seen that these expressions for the PO component are free from singularities except at shadow and reflection boundaries on the Keller Cone. To find the total diffracted field, the expressions for the fringe contribution given earlier by Michaeli should be used along with the PO contribution obtained here. The procedure is applied to the problem of backscattering from square and triangular plates. Higher order diffractions are also accounted for by combining the equivalent currents with the Uniform Theory of Diffraction (UTD). The results obtained are compared with previous solutions and measured data.

1 Introduction

It is known that the Geometrical Theory of Diffraction (GTD) [1] and its uniform versions (UTD and UAT) fail in the vicinity of diffracted ray caustics. To overcome this difficulty , an equivalent current method (ECM) has been suggested by Ryan and Peters[2]. In this method, equivalent electric and magnetic currents which are considered to radiate in free space are introduced in the place of the diffracting edge. Since these equivalent currents are derived from the GTD fields; strictly speaking, they are valid for observation directions only on the Keller Cone of diffraction. More rigorous asymptotic expressions for equivalent currents for arbitrary directions of observation has been achieved independently by Mitzner [3] and Michaeli [4] based on identifying the equivalent current line integral with the asymptotic edge contribution to the radiation integral of the physical surface current density on a conducting half-plane. Unfortunately, these expressions for the equivalent currents become infinite at various aspects of observation. In a subsequent paper [5], Michaeli considered these currents as arising separately from physical optics (PO) and fringe components and showed that for the fringe component the infinities can be eliminated by choosing a proper skew coordinate system for the asymptotic integration. However, it was asserted by the same author[6] that the infinities in the PO component cannot be eliminated in a similar way.

In the present paper, equivalent edge currents for the PO contribution are derived by choosing a proper coordinate system for a half plane in a manner similar to the treatment in [5]. It is seen that these expressions for the PO component are free from singularities except at shadow and reflection boundaries on the Keller Cone.

2 Equivalent Edge Currents For Far Zone Scattering

Consider a perfectly conducting flat surface S on the xy-plane with an edge C. At any point on the edge, the unit vector $\hat{t}$ is tangent to the edge, $\hat{n}$ is normal to the surface, and the unit binormal vector is given by

$$\hat{b} = \hat{n} \times \hat{t}. \tag{1}$$

The scattered far field from this structure is given by the following radiation integral

$$\hat{\mathbf{E}}^s = \frac{jkZ}{4\pi}\frac{e^{-jkR}}{R}\hat{s} \times \hat{s} \times \int\int_S \hat{J}_T(x,y)e^{j(k_x x + k_y y)}ds, \tag{2}$$

where Z is the intrinsic impedance, k is the wavenumber, and $\hat{J}_T(x,y)$ is the total induced current on the surface. R is the distance to the observation point measured from the origin at the coordinate system. $\hat{s}'$ and $\hat{s}$ are the unit vectors for incident and observation directions. In addition, k_x and k_y are given by

$$k_x = k\ \hat{s} \cdot \hat{x}, \tag{3}$$

$$k_y = k\ \hat{s} \cdot \hat{y}. \tag{4}$$

By using the asymptotic evaluation approach in [4], the edge diffracted part of the total scattered far field written in the (t,b) coordinate system is given by

$$\hat{E}^d = \frac{jkZ}{4\pi}\frac{e^{-jkR}}{R}\hat{s} \times \hat{s} \times \int_C\int_o \hat{J}_T(t,b)e^{jk(b\hat{b}\cdot\hat{s}+t\hat{t}\cdot\hat{s})}db\ dt, \tag{5}$$

where "o" denotes the asymptotic end-point contribution at b=0. Let

$$\vec{K}(t) = \int_o \hat{J}_T(t,b)e^{jkb\hat{b}\cdot\hat{s}}db, \tag{6}$$

then,

$$\hat{E}^d = \frac{jkZ}{4\pi}\frac{e^{-jkR}}{R}\hat{s} \times \hat{s} \times \int_C \vec{K}(t)e^{jkt\hat{t}\cdot\hat{s}}dt. \tag{7}$$

The edge diffracted field can also be expressed as due to the equivalent edge currents along the edge:

$$\hat{E}^d = \frac{jkZ}{4\pi}\frac{e^{-jkR}}{R}\int_C [\hat{s} \times \hat{s} \times \hat{t}\mathbf{I} + Y\hat{s} \times \hat{t}\mathbf{M}]e^{jkt\hat{t}\cdot\hat{s}}dt. \tag{8}$$

Equating the two integrands, we have

$$\mathbf{I} = K_t - K_b \cot\beta \cos\phi, \tag{9}$$

$$\mathbf{M} = -Z\frac{\sin\phi}{\sin\beta}K_b, \tag{10}$$

where K_t and K_b are the tangential and binormal components of the vector $\vec{K}$.

3 PO Component Of Equivalent Edge Currents

The determination of PO component of equivalent edge currents requires the asymptotic evaluation of the following integral:

$$\vec{K}^{PO}(z) = \int_o \vec{J}^{GO}(x,z)e^{jkx\hat{x}\cdot\hat{s}}dx. \tag{11}$$

Here, the phase of $\vec{J}^{GO}(x,z)$ is $-kx\hat{x}\cdot\hat{s}'$. Hence, the integral becomes singular when:

$$\hat{x}\cdot\hat{s}=\hat{x}\cdot\hat{s}'. \tag{12}$$

The singularities of a similar integral for the fringe component of the equivalent currents are reduced to a single direction by choosing a proper skew coordinate system for the integration [5]. However, the equivalent approach which corresponds to the replacement of the $\hat{x}$ direction by the $\hat{\sigma}$ direction for the integration does not have similar effect on the PO components. Because, as mentioned in [5], such a step "merely replaces the previovus cone of singular $\hat{s}$-directions, by another cone, defined by $\hat{s}\cdot\hat{\sigma}=\hat{s}'\cdot\hat{\sigma}$, and only for glancing incidence. $\hat{\sigma}=\hat{s}'$, does the latter collapse into a single direction, $\hat{s}=\hat{\sigma}$". The above argument assumes a skew coordinate direction fixed by the incidence angle for all observation directions. In fact, for equivalent currents, there is no need for such a restriction: the skew coordinate direction may be determined by both the incident and observation directions ($\hat{s}'$ and $\hat{s}$). After all, the expressions for the equivalent edge currents are always functions of observation aspect. So for each observation direction, the skew coordinate direction on the surface of the half plane is determined separately. To apply this approach, we will again use the skew coordinate system (σ,z) with an arbitrary skewness angle γ as follows:

$$x=\sigma\sin\gamma, \tag{13}$$

$$z=z+\sigma\cos\gamma. \tag{14}$$

Then, the end-point contribution from the integral

$$\vec{K}^{PO}(z)=\sin\gamma\int_{o}\vec{J}_{GO}(\sigma\sin\gamma,z+\sigma\cos\gamma)e^{jk\sigma\hat{\sigma}\cdot\hat{s}}d\sigma, \tag{15}$$

is evaluated to obtain the PO equivalent edge currents as:

$$\begin{aligned}\mathrm{I}^{PO} &= -\frac{2Y}{jk}E_z^i\frac{\sin\phi'\sin\gamma}{\sin\beta'[(\sin\beta'\cos\phi'+\sin\beta\cos\phi)\sin\gamma+\cos\gamma(\cos\beta-\cos\beta')]}\\ &+ \frac{2}{jk}H_z^i\sin\gamma\frac{\cot\beta'\cos\phi'+\cot\beta\cos\phi}{[(\sin\beta'\cos\phi'+\sin\beta\cos\phi)\sin\gamma+\cos\gamma(\cos\beta-\cos\beta')]},\end{aligned} \tag{16}$$

$$\mathrm{M}^{PO}=\frac{2Z}{jk}H_z^i\frac{\sin\phi\sin\gamma}{\sin\beta[(\sin\beta'\cos\phi'+\sin\beta\cos\phi)\sin\gamma+\cos\gamma(\cos\beta-\cos\beta')]}. \tag{17}$$

It is seen that, these expressions are functions of the skewness angle γ. If we let γ be

$$\cot\gamma=\frac{\cos\beta-\cos\beta'}{\sin\beta'\cos\phi'+\sin\beta\cos\phi} \tag{18}$$

the PO equivalent currents become as follows:

$$\begin{aligned}\mathrm{I}^{PO} &= -\frac{2Y}{jk}E_z^i\frac{\sin\phi'(\sin\beta\cos\phi+\sin\beta'\cos\phi')}{\sin\beta'[(\cos\beta-\cos\beta')^2+(\sin\beta\cos\phi+\sin\beta'\cos\phi')^2]}\\ &+ \frac{2}{jk}H_z^i\frac{\sin\phi(\sin\beta\cos\phi+\sin\beta'\cos\phi')}{[(\cos\beta-\cos\beta')^2+(\sin\beta\cos\phi+\sin\beta'\cos\phi')^2]}\end{aligned} \tag{19}$$

$$\mathrm{M}^{PO}=\frac{2Z}{jk}H_z^i\frac{\sin\phi(\sin\beta\cos\phi+\sin\beta'\cos\phi')}{[(\cos\beta-\cos\beta')^2+(\sin\beta\cos\phi+\sin\beta'\cos\phi')^2]} \tag{20}$$

The only singularities of these expressions occur at the incidence and reflection boundaries on the Keller Cone. Physically, the direction of the skew coordinate $\hat{\sigma}$ in this case is the direction of the projection of $(\hat{s}-\hat{s}')$ vector onto the half plane. It is a function of both $\hat{s}'$ and $\hat{s}$, as described earlier. The natural question to ask at this point is what happens when $(\hat{s}-\hat{s}')$ vector has zero projection on the half plane;

in other words, when $(\hat{s} - \hat{s}')$ has only a normal component to the surface of the half plane. In this case, the above definition of $\hat{\sigma}$ fails. However, a close examination reveals that when $(\hat{s} - \hat{s}')$ vector has only a normal component to the half plane, the observation direction is either on the incident or on the reflection shadow boundary on the Keller Cone. Both of these cases correspond to directions for which the field is not ray-optical and the equivalent current concept is not valid.

It is also noted that the equivalent current expressions given in (19) and (20) are the same as those in [7,8] where they are determined for a finite size plate by an application of Stokes' Theorem.

4 Conclusions

In this paper, we obtained PO equivalent currents in the same way as fringe equivalent currents by choosing an proper oblique direction for the asymptotic integration. This work therefore complements the work of Michaeli [5]. The PO and fringe equivalent currents are valid for arbitrary directions of observation, so they are more general than the GTD equivalent currents. The numerical accuracy of these equivalent currents have been established on two examples of backscattering from square and triangular plates.

References

[1] J.B. Keller, "Geometrical theory of diffraction," J. Opt. Soc. Am., Vol. 52, pp. 116-130, 1962.

[2] C.E. Ryan and L. Peters, "Evaluation of edge diffracted fields including equivalent currents for the caustic regions," IEEE Trans. Antennas and Propagation, Vol. AP-17, pp. 292-299, May 1960.

[3] K.M. Mitzner, "Incremental length diffraction coefficients," Aircraft Divison, Northrop Corp., Tech. Rep. AFAL-TR-73-296, April.1974.

[4] A. Michaeli, "Equivalent edge currents for arbitrary aspects of observation," IEEE Trans. Antennas and Propagation, Vol. AP-32, No.3, March 1984.

[5] A. Michaeli, "Elimination of infinities in equivalent edge currents. Part I: Fringe current components," IEEE Trans. Antennas and Propagation, Vol. AP-34, No.7, July 1986.

[6] A. Michaeli, "Elimination of Infinities in equivalent edge currents, Part II: Physical optics component," IEEE Trans. Antennas and Propagation, Vol. AP-34, No.8, August 1986.

[7] R.J. Marhefka, O.M. Buyukdura and W. Ebihara, "Radar Cross Section Studies, Phase III," Tech. Rep. 716621-1, The Ohio State University, ElectroScience Laboratory, Columbus, Ohio, April 1986.

[8] M. Ando, T. Murasaki and T. Kinoshita, "Elimination of False Singularities in GTD Equivalent Edge Currents," IEE Proc., Part. H, to be published.

W6.3

ANALYSIS OF TRANSMISSION CHARACTERISTICS OF INHOMOGENEOUS PLANAR DIELECTRIC WAVEGUIDES USING METHOD OF TRANSFER MATRIX

Xu Fuyong , Zhao Keyu , Yang Zhongying and Li Feng
(Lanzhou University , Lanzhou , China)

ABSTRACT

The transmission characteristics of inhomogeneous planar dielectric waveguides are calculated by solving the transfer matrix equations which are obtained by separating the waveguide into n layers. This method is of universality for analysing the waveguides with arbitrary distributions of dielectric constants .

INTRODUCTION

Inhomogeneous planar dielectric waveguides have important applications in millimeter waves and optical integrated circuits. Those methods for analysing this kind of waveguides, which have been reported, include the methods of the contrast, the finite element , the boundary element and the network analysis. [1] But their eigenfunctions are complex and the solving requires a large amount of work. furthermore they are only suitable for waveguides with specific structures. As discussed in this paper , the waveguide is divided into n layers and each layer is considered homogeneous because of its extreme thinness. Based on the longitudinal field method and the boundary conditions of fields, [2] some simple equations of the transfer matrixes of the eigenvalues are obtained , which require less computing time. Therefore , this method may be used to analyse inhomogeneous planar dielectric waveguides with general structures .

THEORETICAL ANALYSIS

An inhomogeneous planar dielectric waveguide is divided into n layers along the y-direction as shown in Fig. 1. The dielectric of each layer is assumed as homogeneous and its relative dielectric constant $\varepsilon_r(y)$ is only the function of the coordinate variable y . Suppose the eigen waves transmit along the z-direction and the field components have no variations in the x-direction , then the expressions of the field components for TM modes and TE modes of the eigen waves in the i-th dielectric layer respectively are

TM modes

$$\left.\begin{aligned} E_{zi} &= \Phi_i(y)\, e^{-jkz} \\ E_{yi} &= -\frac{K}{K_{ci}^2}\frac{\partial E_{zi}}{\partial y} \\ H_{zi} &= \frac{j\omega\varepsilon_0\varepsilon_{ri}}{K_{ci}^2}\frac{\partial E_{zi}}{\partial y} \\ E_{xi} &= H_{yi} = H_{zi} = 0 \end{aligned}\right\} \quad (1)$$

TE modes

$$\left.\begin{aligned} H_{zi} &= \Psi_i(y)\, e^{-jkz} \\ H_{yi} &= -\frac{K}{K_{ci}^2}\frac{\partial H_{zi}}{\partial y} \\ E_{xi} &= \frac{j\omega\mu_0}{K_{ci}^2}\frac{\partial H_{zi}}{\partial y} \\ H_{xi} &= E_{yi} = E_{zi} = 0 \end{aligned}\right\} \quad (2)$$

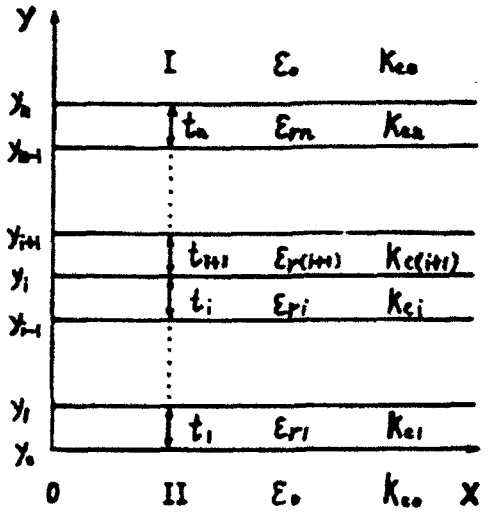

Fig. 1 A planar dielectric waveguide separated into n layers

Where $\Phi_i(y)$ and $\Psi_i(y)$ are both the transverse transmission functions, k is the wave number of the eigen waves, and $k_{ci}^2 = k_i^2 - k^2 = k_0^2\,\varepsilon_{ri} - \beta^2$ is the cut-off wave number of the equivalent transmission line in the i-th dielectric layer. The wave equations of the longitudinal field components are

$$\left.\begin{aligned} &\Delta_T E_{zi} + K_{ci}^2 E_{zi} = 0 \\ \text{and}\quad &\Delta_T H_{zi} + K_{ci}^2 H_{zi} = 0 \end{aligned}\right\} \quad (3)$$

Hence

$$\frac{d^2\Phi_i(y)}{dy^2} + K_{ci}^2\Phi_i(y) = 0 \quad (4)$$

The solution of eqn. (4) is given by the following matrix

$$\begin{bmatrix} \Phi_i(y) \\ \Phi_i'(y) \end{bmatrix} = \begin{bmatrix} \cos k_{ci}y & \sin k_{ci}y \\ -k_{ci}\sin k_{ci}y & k_{ci}\cos k_{ci}y \end{bmatrix} \cdot \begin{bmatrix} A_i \\ B_i \end{bmatrix} \qquad (y_{i-1} < y < y_i) \quad (5)$$

By substituting y_i and y_{i-1} respectively for y into eqn. (5), using the recursion method and the continuous boundary conditions of the tangential field components E_x and H_z (TE modes) or H_x and E_z (TM modes) on the $y=y_i$ dielectric interface, we get the expressions of the transfer matrixes for TM modes and TE modes

TM modes

$$\begin{bmatrix} \Phi_n(y_n) \\ \Phi'_n(y_n) \end{bmatrix} = \begin{bmatrix} M_{11} & M_{12} \\ M_{21} & M_{22} \end{bmatrix} \cdot \begin{bmatrix} \Phi_o(y_o) \\ \Phi'_o(y_o) \end{bmatrix} \tag{6}$$

TE modes

$$\begin{bmatrix} \Psi_n(y_n) \\ \Psi'_n(y_n) \end{bmatrix} = \begin{bmatrix} N_{11} & N_{12} \\ N_{21} & N_{22} \end{bmatrix} \cdot \begin{bmatrix} \Psi_o(y_o) \\ \Psi'_o(y_o) \end{bmatrix} \tag{7}$$

Whence

$$\begin{bmatrix} M_{11} & M_{12} \\ M_{21} & M_{22} \end{bmatrix} = \prod_{i=1}^{n} \begin{bmatrix} \cos k_{xi}y_i & \sin k_{xi}y_i \\ -k_{xi}\sin k_{xi}y_i & k_{xi}\cos k_{xi}y_i \end{bmatrix} \cdot \begin{bmatrix} \cos k_{xi}y_{i-1} & \sin k_{xi}y_{i-1} \\ k_{xi}\sin k_{xi}y_{i-1} & k_{xi}\cos k_{xi}y_{i-1} \end{bmatrix}^{-1} \cdot \begin{bmatrix} 1 & 0 \\ 0 & \varepsilon_{r(i-1)}k_{xi}^2/\varepsilon_{ri}k_{x(i-1)}^2 \end{bmatrix} \tag{8}$$

$$\begin{bmatrix} N_{11} & N_{12} \\ N_{21} & N_{22} \end{bmatrix} = \prod_{i=1}^{n} \begin{bmatrix} \cos k_{xi}y_i & \sin k_{xi}y_i \\ -k_{xi}\sin k_{xi}y_i & k_{xi}\cos k_{xi}y_i \end{bmatrix} \cdot \begin{bmatrix} \cos k_{xi}y_{i-1} & \sin k_{xi}y_{i-1} \\ -k_{xi}\sin k_{xi}y_{i-1} & k_{xi}\cos k_{xi}y_{i-1} \end{bmatrix}^{-1} \cdot \begin{bmatrix} 1 & 0 \\ 0 & k_{xi}^2/k_{x(i-1)}^2 \end{bmatrix} \tag{9}$$

The surface waves only propagate perpendicularly to the planar dielectric waveguide in I-region and II-region outside the waveguide, thus they attenuate exponentially:

$$\left.\begin{aligned} E_{xI} &= E_{oI}\, e^{-jk_x}\, e^{-\beta_1(y-y_n)} \quad , \quad y>y_n \\ E_{xII} &= E_{oII}\, e^{-jk_x}\, e^{\beta_1 y} \quad , \quad y<y_o \end{aligned}\right\} \tag{10}$$

Based on the boundary conditions of the fields on the interfaces $y=y_n$ and $y=y_o$ as well as the transmission condition $k_{xo}^2 < 0$ for the surface waves, the equations of the transfer matrixes of the inhomogeneous planar dielectric waveguide are obtained

TM modes

$$\begin{bmatrix} E_{oI} \\ -\beta_1 E_{oI} \end{bmatrix} = \begin{bmatrix} 1 & 0 \\ 0 & \varepsilon_{rn}k_{xo}^2/k_{xn}^2 \end{bmatrix} \cdot \begin{bmatrix} M_{11} & M_{12} \\ M_{21} & M_{22} \end{bmatrix} \cdot \begin{bmatrix} E_{oII} \\ \beta_1 E_{oII} \end{bmatrix} \tag{11}$$

TE modes

$$\begin{bmatrix} H_{01} \\ -\beta_1 H_{01} \end{bmatrix} = \begin{bmatrix} 1 & 0 \\ 0 & k_{c0}^2/k_{cn}^2 \end{bmatrix} \cdot \begin{bmatrix} N_{11} & N_{12} \\ N_{21} & N_{22} \end{bmatrix} \cdot \begin{bmatrix} H_{01}' \\ -\beta_1 H_{01}' \end{bmatrix} \tag{12}$$

Where k_{c0} is the cut-off wave number in the air , $\beta_1^2 = k^2 - k_0^2$.

RESULTS AND DISCUSSIONS

The computing programs of the FORTRAN language based on the above formulas give results correspondent with literature. If n=1, the results also conform satisfactorily with the results of the single-layer dielectric waveguide.
The dispersive characteristics of the dielectrics with continuous linear and parabolic distributions have been computed . The acquired dispersive curves are shown as Fig. 2 and Fig. 3. In these figures the correspondent k value in case of $\beta/k=1$ is exactly the cut-off wave number k_c .

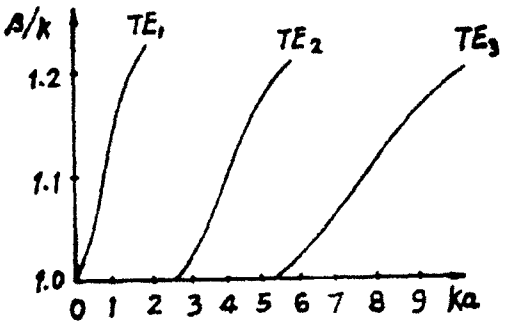

Fig. 2 A dispersive curve according to the linear distribution

CONCLUSIONS

The advantages of the method discussed in this paper are:
A. The universality for analysing inhomogeneous planar dielectric waveguides with arbitrary distributions of dielectric constants;
3. No limitation of the conditions of the regions outside the planar dielectric waveguides;
C. Less computing time.
Therefore , this method has certain practicability in engineering designs.

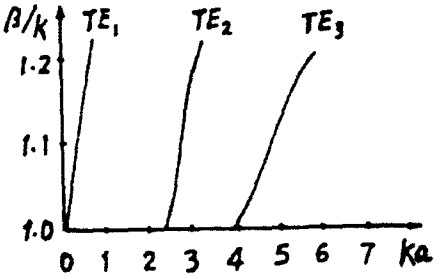

Fig. 3 A dispersive curve according to the parabolic distribution

REFERENCES

1. Xu Shanjia. Journal of Electronics, 10 (1) (1988). 17.
2. Chen Mengyao, Xu Fuyong and Zhao Keyu, Electromagnetic Fields and Microwave Techniques, Higher Education Press, Beijing (1989), 262.

W6.4

ELECTROMAGNETIC WHISPERING GALLERY MODES IN A RADIAL LAYER DIELECTRIC RESONATOR

Yu.F. Filippov, S.N. Kharkovsky, Z.Ye. Yeremenko

Institute of Radiophysics and Electronics Academy of Sciences of Ukraine,310085,Kharkov

Axially homogeneous azimuthal oscillations ($\partial/\partial z=0$) of the highest order of the "whispering gallery" type ($n \gg 1$ where n is the azimuthal index) are studied in the radially layer dielectric resonator (Fig.1). Such structures were studied [1] on the lowest types of oscillations.

The dispersion equation was obtained from the solutions of the Maxwell ones satisfying the conditions of radiation at infinity and by continuity of tangential components of electromagnetic fields at the boundary of adjacent regions:

$$A\,B = C, \qquad (1)$$

$$A = \beta_{21} - \alpha_{11}.B = \delta_{32}(\alpha_{22} - \alpha_{32}) - \delta_{33}\xi(\alpha_{22} - \beta_{32}),$$

$$C = \delta_{21}(\alpha_{21} - \alpha_{11})[\alpha_{22}/\gamma_{22}(\delta_{32} - \delta_{33}\xi) - \alpha_{32}/\gamma_{32}(\gamma_{32} - \delta_{33}\xi)],$$

$$\alpha_{ij} = 1/\sqrt{\varepsilon_i}\ (J_n'(\varkappa_{ij})/\ J_n(\varkappa_{ij})),\quad \beta_{ij} = 1/\sqrt{\varepsilon_i}\ (N_n'(\varkappa_{ij})/\ N_n(\varkappa_{ij})),$$

$$\delta_{ij} = J_n(\varkappa_{ij})/\ N_n(\varkappa_{ij}),\quad \gamma_{ij} = J_n'(\varkappa_{ij})/\ N_n'(\varkappa_{ij}),$$

$$\varkappa_{ij} = \sqrt{\varepsilon_i}\ k\ r_j,\quad \xi = (\alpha_{33} - \gamma_0)/(\beta_{33} - \gamma_0)\ ,$$

$$\gamma_0 = 1/\sqrt{\varepsilon_4}\ (H_n^{(1)'}(\varkappa_{43})/\ H_n^{(1)}(\varkappa_{43})).$$

Here ε_i, r_j are the permittivity and radius of corresponding layers, $k = 2\pi f/c$, $f = f' + if''$ - complex frequency, $J_n(\varkappa)$,

$N_n(x)$, $H_n^{(1)}(x)$ the Bessel, Neuman and Hankel functions (the prime designates differentiation by the argument).

The left-hand side of Eq.(1) determines the resonance frequency of the independent partial modes of the disc H^d_{nmo} ($A = 0$, $r < r_1$) and ring H^r_{nmo} ($B = 0$, $r_2 < r < r_3$) resonators without coupling between them ($C = 0$). This coupling is determined by the clearance value $h = r_2 - r_1$.

Fig.1 illustrates dependences of the radiation Q-factors $Q = f'/2f''$ and the adjusted resonance frequencies $2r_3 f'$ on the parameter $h' = h/\lambda_0$ ($\lambda_0 = \lambda_k\sqrt{\varepsilon_3}$, λ_k is the wavelength of the intrinsic oscillation $H^r_{40.1.0}$ in the ring without correllation with the disc).

The numerical study of Eq. (1) was done at $n = 40$, radial index $m = 1$ (curve 1), $m = 2$ (curve 2) for $\varepsilon_1 = \varepsilon_3 = 2.04$ (fluoroplastic-4), $\varepsilon_2 = \varepsilon_4 = 1$, $r_3 = 5.3$ cm, $L = (r_3 - r_2)/\lambda_k = 0.53$ where $(r_3 - r_2)$ is the thickness of the ring. The dashed curves ($C = 0$) correspond to spectral characteristics of partial modes of the disc (curve 6) and of the ring of a fixed thickness (the horisontal straight line 7) by changing r_1. There is a defined point of intersection of the spectral curves (the frequency degeneracy). Q-factors of these intrinsic oscillations do not depend on r_1.

The independent partial oscillations H^o_{nmo} with different radial indices m exist in a homogeneous disc resonator (n is fixed). The approqch of the spectral curves and intersection of their radiation Q-factors with $m = 1$, $m = 2$ is observed with the appearrance of clearance (a decrease of r_1) between disc and ring for the above parameters . An increase of h leads to pushing apart (by frequency) these partial oscillations. The oscillation $H^o_{40.1.o}$ corresponds to the lowest one $H^r_{40.1.o}$ of the ring and $H^o_{40.2.o}$ - to the lowest oscillation $H^d_{40.1.o}$ of the disc when the clearance is rather large ($h > \lambda_0$). Their Q-factors become constant.

The point of degeneracy of the undisturbed oscillations shifts towards lesser clearances in comparison with the point of equal Q-factors. It may be explained by the presence of both the interaction and transformation of the oscillations $H^o_{40.1.o}$ and $H^o_{40.2.o}$ to these ones of ring and disc. The minimum of radiation Q-factor $H^o_{40.2.o}$ corresponds to the clearance $\sim \lambda_k/4$; the equality of $H^o_{40.1.o}$, $H^o_{40.2.o}$ corresponds to the clearance $\sim \lambda_0/4$.

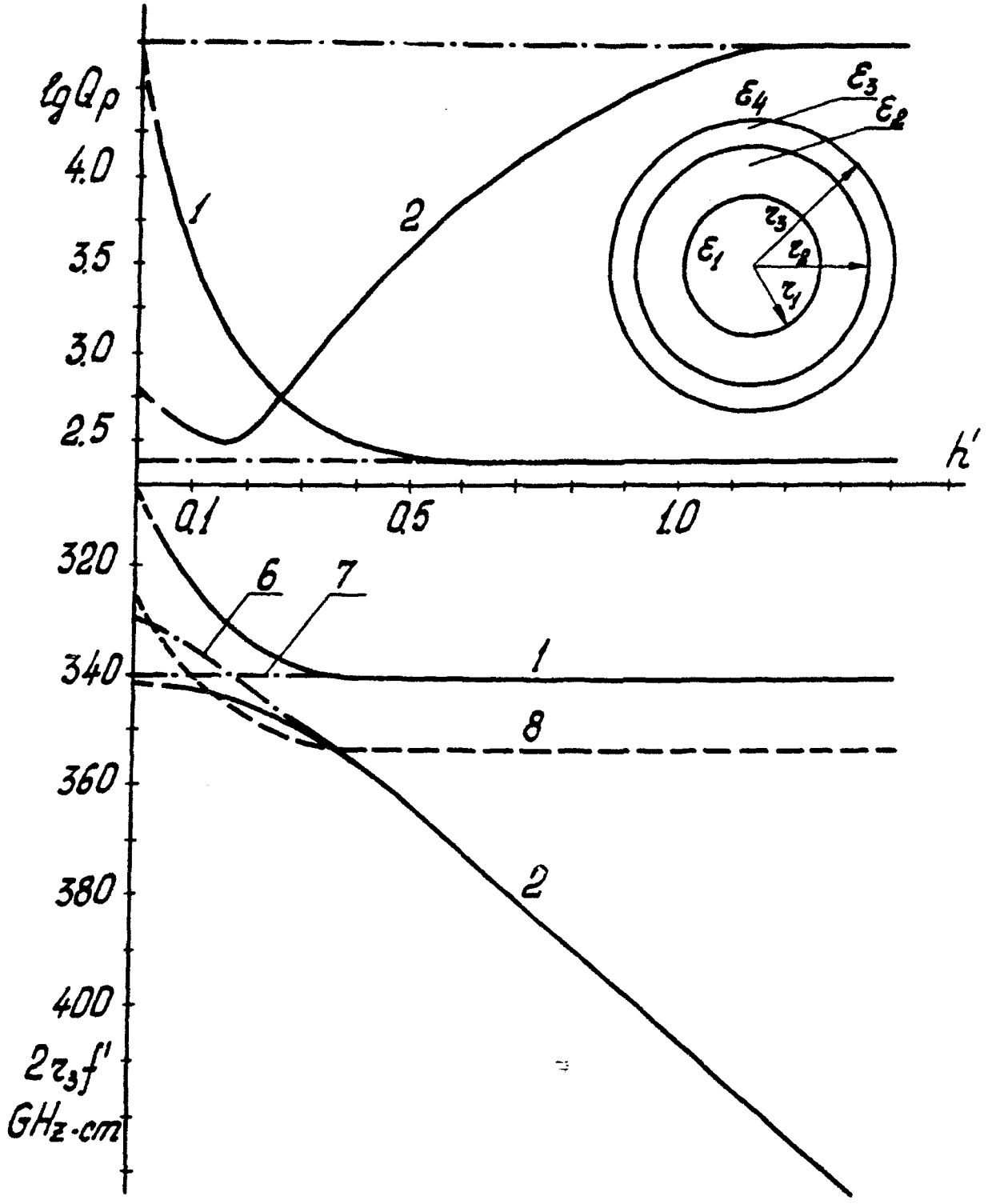

Fig.1 Dependences of the radiation Q-factors and the adjusted resonance frequencies $2r_3f'$ on the relative clearance value h'.

The field distribution in radius of component H_z confirms the considered processes.

The interaction between oscillations with different azimuthaly indices n in the homogeneous resonator is not observed. In particular, it is absent between partial oscillations $H^{o}_{40.1.0}$ (curve 2) and $H^{o}_{42.1.0}$ (curve 8) in Fig.1. Such interaction appears with the azimuthal inhomogeneity .

It can be shown that an increase of permittivity of the internal disc ε_1 leads to the interaction region shifting towards larger clearances and the appearance of the interaction between high radial oscillations (m = 3,4...). If the permittivity of layers $\varepsilon_{1,3}$ increases the region of interaction of the oscillations with azimuthal indices m = 1,2 narrows and dispersion curves steepness increases. However, the clearance value corresponding to the equality of Q-factors is still $\sim \lambda_0/4$. If L increases the region of interaction shifts towards lesser clearances. The oscillations with m = 3,4... appear in the ring when L > 1. If L < 0.5 then the interaction between different radial types of oscillations manifests itself stronger in comparison with the case considered above.

Intrinsic resonance frequencies can be shifted by filling different materials in the clearance. Such shift is more prominent in the region of interaction.

CONCLUSION

The paper is concerned with the theoretical analysis of the radial layer dielectric resonator with azimuthal oscillations of the highest order .It was shown that in the case of the 4-layer resonator partial oscillations of the disc and ring with equal azimuthal but with different radial indices interact. These oscillations form the normal modes of azimuthal oscillations of a layer resonator. The interaction between oscillations with different azimuthal indices n in the homogeneous resonator is not observed.

The considered resonator can be used as the flowing cuvette for measuring in the millimeter range of the complex permittivity of substances (including chemicaly active ones) which are located in the clearance between layers.

REFERENCE

[1] Zaki K.A., Chen C., IEEE Trans. Microwave Theory Tech., vol. MTT - 33, pp. 1448 - 1452, Dec. 1985.

W6.5

DIMENSIONS OPTIMIZATION OF CORRUGATED RECTANGULAR FLEXIBLE WAVEGUIDES IN MILLIMETER BAND

Chin, Yao Kun He, Hua Yao and Yang, Yixin
(Shanghai Transmission Lines Research Institute, China)

ABSTRACT

A corrugated rectangular flexible waveguide was considered as a periodical structure. It was analyzed and synthesized on the cascade two-port network theory. The discontinuity of the joint between the standard metal waveguide and the flexible waveguide was also took into account. A corrugated rectangular flexible waveguide in Ka-band has been optimally designed and tested; the results of the experiments meet the theory well.

I. INTRODUCTION

The rectangular corrugated flexible waveguides are widely used in microwave and millimeter wave bands. If the equivalent network method was used to analyse the waveguides, they can be considered as periodical structures. The analysis and synthesis becomes easier, especially when the computer is used in calculation. It's known that the lumped parameter equivalent circuit was deduced by quasi-electrostatic method in the case that the dimensions of the discontinuities of the waveguides are much smaller than the wavelength and the distances between discontinuities are large enough, but the comparisons of experimental results and the theoretical calculations show that the equivalent circuit is also effective in the corrugated rectangular waveguide if there are more than four corrugations in every unit length of the dimension of wavelength.

On the viewpoint of equivalent circuit, a single mode corrugated waveguide was composed of a cascade of many separate circuits with same equivalent parameters. It's a cascade of two-port networks, thus the transmission matrix(T matrix) or the chain matrix can be used, when the T matrix of a single separate circuit T_1 was obtained, the T matrix of the whole waveguide can be obtained by calculating the mth power of the T_1 (m is the number of the corrugations of the waveguide)

It is necessary to notice that whether the corrugated waveguides are used as main feed line or expedient linking components, corrugated waveguides are always connected with the flanges of standard rectangular waveguides or the waveguide components. Those discontinuities ought to be considered in calculating the transmission matrix T.

When the transmission matrix of the whole corrugated waveguide obtained, the functional relationship between the voltage standing wave ratio (VSWR) and the dimensions of the cross section and the corrugation is also found, the optimal design and the tolerance analysis of the parameters of the waveguide can be carried out by using a computer. In millimeter band, the dimensions and the tolerance of the waveguides is very small. It is very important to select those dimensions parameters optimally.

In this paper ,as an example, a rectangular corrugated waveguide of Ka band was optimally designed ,and some samples ware manufactured by the precise electroplating method.Experiments show that the theoretical model we put forward is successful, and the technology of making the waveguide is also effective.

II. THEORY

Fig.1 shows the cross section (without sleeve) of a corrugated rectangular flexible waveguide.The periodic cells of the corrugated structure can be divided in several ways, which one is the most reasonable depends on the experiments[1].

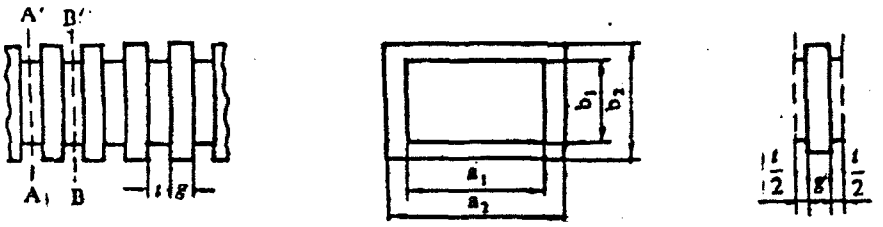

(a) (b)

Fig.1 Cross section and unit cell of a corrugated rectangular waveguide

(a) Cross section. (b) Unit cell

In this paper, the unit cell in Fig. 1b was chose with tries and compressions.The segment between AA'and BB' was cut as an unit cell. It's equivalent circuit can be considered as a cascade of three uniform single mode waveguide.The first one has the parameters $a_1$and b_1, the width and height of the middle part are $a_2$and b_2 , and the parameters of the third part possesses the same sizes as the first one. The width of the slot and ridge are t and g,respectively. In this unit, there are two step discontinuities at the joint points of first waveguide with the second one and the second one with the third one. The lumped equivalent circuit model can be used to deal with the discontinuities because it's dimensions are much smaller than the wavelength. With strict consideration ,the higher modes will couple to each other because of the close discontinuities, but in fact, the coupling may be negligible for it is very week in both experimental and theoretical calculations.The transmission matrices of the three segments of uniform waveguide ware described as t_1,t_2 and t_3, ($t_1 = t_3$)respectively, t_4,t_5 and t_6 represent the transmission matrices induced by the resistance discontinuity , inductive and capacitive susceptances of the joint of the first and second waveguide respectively. t_7,t_8 and $t_9$represent the homologues transmission matrices of the joint of the second and third waveguide respectively ($t_7 = t_4$, $t_8 = t_5$, $t_9 = t_6$) ,in summing, the transmission matrix of this unit cell is

$$[T_i] = \left[\prod_{i=1}^{9}(t_i)\right] \tag{1}$$

The transmission matrix of a resistance discontinuity had been calculated by R.N.Ghose [2], The matrices of inductive and capacitive susceptances had been obtained by R.E.Collin[3] and N.Macuvitz[4]. Notice that the transmission matrices are obviously in accord with the reciprocity and symmetry rule, from formula (1),we have

$$[T_i] = \begin{bmatrix} u + jv & jw \\ -jw & u - jv \end{bmatrix} \tag{2}$$

$$u = [\cos\theta_2 - (B_C - B_L)\sin\theta_2]\cos\theta_1 - \left(\frac{Z_1(B_C - B_L)}{Z_2}\cos\theta_L + \frac{Z_2^2 - Z_1^2(B_C - B_L)^2 + Z_1^2}{2Z_1Z_2}\sin\theta_2\right)\sin\theta_1 \tag{3}$$

$$w=\left(\frac{Z_1(B_C-B_L)}{Z_2}\cos\theta_2+\frac{Z_1^2-Z_1^2(B_C-B_L)^2-Z_2^2}{2Z_1Z_2}\sin\theta_2\right) \tag{5}$$

Here $\theta_1=\frac{2\pi}{\lambda_{g_1}}t$, $\theta_2=\frac{2\pi}{\lambda_{g_2}}g$, $\lambda_{g_1}=\lambda/\sqrt{1-\left(\frac{\lambda}{2a_1}\right)^2}$, *and* $\lambda_{g_2}=\lambda/\sqrt{1-\left(\frac{\lambda}{2a_2}\right)^2}$

,in which Z_1, Z_2 are the wave resistances of the first and second segment of waveguides respectively. B_C and B_L are the inductive and capacitive susceptances of the step discotinuities.

If the corrugated rectangular flexible waveguide is composed of n parts of corrugations, the main transmission matrix is the product of the matrices of every unit cell, i.e.

$$[T_i]=\left[\prod_{i=1}^{n}(T_i)\right]=[(T_i)^n] \tag{6}$$

we obtain

$$[T]=\begin{bmatrix} chmr+jv\frac{shmr}{shr} & jw\frac{shmr}{shr} \\ -jw\frac{shmr}{shr} & chmr-jv\frac{shmr}{shr} \end{bmatrix} \tag{7}$$

where

$$r=Arch\ u \tag{8}$$

so the voltage reflect ratio of the corrugateg rectangular waveguide will be:

$$\Gamma=S_{11}=\frac{T_{21}}{T_{11}} \tag{9}$$

the standing wave ratio of input voltage is :

$$\rho=\frac{1+|\Gamma|}{1-|\Gamma|}=\frac{1+\left|\frac{T_{21}}{T_{11}}\right|}{1-\left|\frac{T_{21}}{T_{11}}\right|}$$

$$=\frac{1+\left(w\frac{Shmr}{shr}\right)^2}{(chmr)^2-\left(v\frac{shmr}{shr}\right)^2}+\frac{chmr\left[\left(v\frac{shmr}{shr}\right)^2-\left(w\frac{shmr}{shr}\right)^2\right]}{\left[(chmr)^2-\left(v\frac{shmr}{shr}\right)^2\right]} \tag{10}$$

this formula shows that the VSWR of the corrugated rectangular flexible waveguide is a complex.With given dimensions of the corrugations , this complex has complicated relation with the friquency.When in following case:

$$(chmr)^2-\left(v\frac{Shmr}{Shr}\right)^2=0$$

when $\rho\to\infty$, the resonance occurs, It's the worst case for transmission. The resonance must be avoided in designing the waveguide for the working band.

Considering the discontinuities of the joints of the flexible waveguide and standard waveguide. The main transmission matrix will be multiplied by resistance , capacitance and inductitity matrices of the discontinuities at the joints in both left and right hand .

Based on above network analysis, the optimization of parameters of the waveguide can be carried out on the computer, the optimization here means to get the smallest VSWR for millimeter band by choosing most suitable parameters of the corrugated waveguide.

the parameters to be optimized are sizes of the cross section and the depth of the corrugation. The target function to be optimized can be chose in this way, in Ka band , for different frequency f_i, to compute function $|\Gamma(f_i)|$, find the biggest value, $|\Gamma_{max}(f_i)|$, then change the sizes of cross section to different combinations, $|\Gamma_{max}(f_i)|$ also will change, there is one combination that reduce the $|\Gamma_{max}(f_i)|$ to smallest, that combination of parameters is the optimal values, i.e.

$$|\Gamma| = \min_{i=1,6} [\max |\Gamma(x_i, f_i)|] \tag{11}$$

with the restriction of flexibility and single-mode condition

$$0.05 \leq \frac{a_1}{a_2} \leq 0.1; \qquad 0.05 \leq \frac{b_1}{b_2} \leq 0.1$$

III. EXPERIMENTS AND RESULTS

According to the theoretical analysis , a general program for optimization and tolerance analysis of the corrugated rectangular flexible waveguides was made in Fortran 77 language, it runs well on a 80386 computer. for Ka-band, the results are: $a_1 = 6.60$, $a_2 = 7.6$, $b_1 = 3.0$, $b_2 = 4.0$, $t = 0.5$, $g = 0.66$ (in mm). The tolerance of broad and narrow side are ± 0.03 mm and ± 0.02 mm, respectively, a sample was manufactured by the precise electroplating method. It's standing wave ratio and attenuation characteristic ware tested on the Marconi 6600 sweep oscilloscope. The experimental results are shown in Fig.2 and Fig.3. Fig.2 shows both theoretical and experimental results which agree with each other for the tested frequency range of 32 ~ 37.5 GHz , VSWR and attenuation not exceed 1.18 and 1.8 dB / m, respectively.

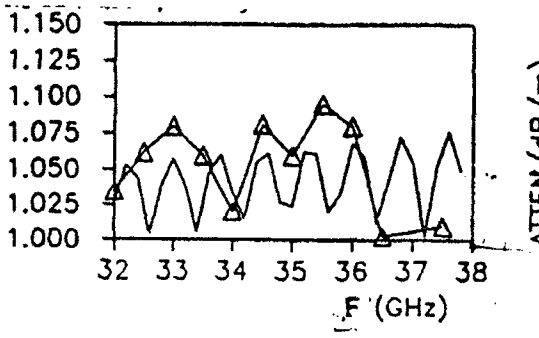

Fig.2. VSWR characteristics of corrugated rectangular waveguide

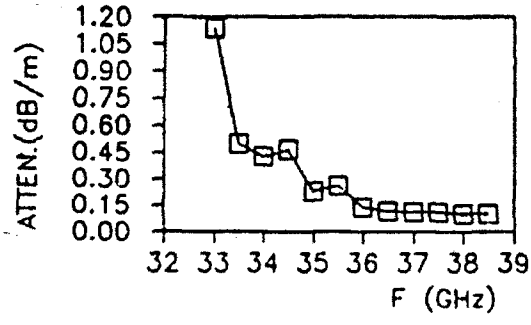

Fig.3. experimental results of Attenuation characteristics

IV. DISCUSSIONS

Using lumped parameter equivalent network to analyze the corrugated rectangular flexible waveguide is an effective means, results of experiments support the theory . The analysis method and the manufacturing process of the corrugated rectangular flexible waveguide presented in this paper is useful for both microwave and millimeter wave bands. Especially of importance for the shorter millimeter band as W-band, the small dimensions of waveguide require the strict tolerance, without optimization, it would be impossible to design a satisfactory waveguide. In order to enlarge the manufacturing tolerance , we are new working on the corrugated waveguide which has transform parts. Achievements will be published soon.

V. ACKNOWLEDGMENT

The authors are deeply grateful to Mrs.Wang, zheng qin of the Technical Physics Institute, Academia Sinica, for his cooperation in making the sample of corrugated waveguide.

REFERENCES :

[1] M.A.R. Gunston, A simplified analysis of corrugated waveguide structures, the Marconi Rev. Vol.33. No.178, Third Quarter 1970, pp260-266.

[2] N.Ghose, 'microwave circuit theory analysis' New York, McGraw-Hill, 1963.

[3] N. Macavitz, 'Microwave Handbook', MTT, Radiation Lab. Series, Vol.10, New York, McGraw Hill,1983.

[4] R.E. COllin, 'Foundations for microwave engineering', McGraw-Hill, 1966.

W6.6

A NEW CALIBRATION METHOD FOR THE FOUR-PORT REFLECTOMETER

Wu Hongxiong, Liu Daquan and Pan Chuhua
(Zhongshan University, Guangzhou, China)

ABSTRACT

A new calibration method for the four-port reflectometer is presented and has been applied to Ka-band measurements. The results show that the reported method is simplicity and rapidity for calibration procedure and has the same measurement accuracy as the one in 1.

INTRODUCTION

The four-port reflectometer(Fig.1)presented in 2,compared with the six-port systems[3], is structurally very simple. Then, it is specially ideal for millimetre-wave frequencies.This paper presents a new method for calibrating the reflectometer. It only employs a sliding short, and its calibration procedures are only a half of the one in 1, too. The method has been applied to a Ka-band four-port system. Experimental results are given and compared with the values obtained by means of the method in 1.

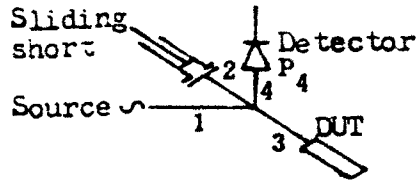

Fig.1 The four-port reflectometer

THE PRINCIPLE OF THE NEW CALIBRATION METHOD

For a 4-port reflectometer shown in Fig.1, if Γ_1-Γ_4 are the reflection coefficients of the loads connected at the four ports,respectively, the power reading P_4 at port 4 can be expressed as follows :[4]

$$P_4 = \left| \frac{K_1\Gamma_2\Gamma_3+K_2\Gamma_2+K_3\Gamma_3+K_4}{K_5\Gamma_2\Gamma_3+K_6\Gamma_2+K_7\Gamma_3+1} \right|^2 \qquad (1)$$

where K_1-K_7 are the system parameters and can be determined by calibration procedure directly. On the other hand, one of port 2 and port 3 is always terminated with a sliding short in the calibration and the measurement procedures. If Γ_2 (or Γ_3)$=\Gamma e^{j\alpha}$, (1) can also be written as

$$P_4(\alpha) = K\left| \frac{1+ae^{j\alpha}}{1+be^{j\alpha}} \right|^2 \quad \text{or} \quad K\left| \frac{1+ae^{-j\alpha}}{1+be^{j\alpha}} \right|^2 \qquad (2)$$

where K is a real parameter while a and b are complex parameters.
To calibrate this reflectometer, the method presented in this paper is that the following three reference loads are used in the four different procedures:

A sliding short, $\Gamma=\Gamma e^{j\alpha}$ $(1-|\Gamma| \ll 1)$

B matched load, $\Gamma=\varepsilon$ $(|\varepsilon| \ll 1)$

C metal plate, $\Gamma=-1$

while the four different procedures are as follows:

Procedure I: A attached port 2, B attached port 3

Procedure II: A attached port 3, B attached port 2

Procedure III: A attached port 2, C attached port 3

Procedure IV: A attached port 3, C attached port 2

And then, in every procedure, the sliding short is moved to N positions in a equal steplength over a half waveguide wavelength and the $P_4(\alpha)$ at each position is collected. Finally, using the similar method in 1, we define the following integrals:

$$C_n=\frac{1}{2\pi}\int_0^{2\pi} P_4(\alpha)e^{-jn\alpha}d\alpha$$

$$=\frac{1}{2\pi}\int_0^{2\pi} K\left|\frac{1+ae^{j\alpha}}{1+be^{j\alpha}}\right|^2 e^{-jn\alpha}d\alpha \quad n=0,1,2 \tag{3}$$

Computing these integrals by a summation of the detected power readings for N short positions, the values of C_n can be determined. On the other hand, from the analytic expressions on the right side of (3), using the complex variable function theory leads to

$$C_0=K[-ab^*-(1+|a|^2)-a^*b]/(1-|b|^2)$$

$$C_1=K[a-(1+|a|^2)b+a^*b^2]/(1-|b|^2) \tag{4}$$

$$C_2=K[-ab+(1+|a|^2)b^2-a^*b^3]/(1-|b|^2)$$

where * denoted the complex conjugate. Soving the simultaneous Eqs (4) yields

$$b=-C_2/C_1$$

$$a=Q^*(1\mp\sqrt{1-4/|Q|^2})/\,2 \tag{5}$$

$$K=2|C_1+C_0b|/[|Q|(1\mp\sqrt{1-4/|Q|^2})]$$

where

$$Q=[C_0(1+|b|^2)+2Re(C_1b^*)]/(1+C_0b)$$

Now, using the values for K, a and b and noting that K_I, a_I, b_I — K_{IV}, a_{IV}, b_{IV} in the four procedures are related to K, a, and b in (5)

$$a_I=a^*,\quad b_I=b,\quad K_I=K\ ;\quad a_{II}=a^*,\quad b_{II}=b,\quad K_{II}=K$$
$$a_{III}=a,\quad b_{III}=b,\quad K_{III}=K\ ;\quad a_{IV}=a,\quad b_{IV}=b,\quad K_{IV}=K\ . \tag{6}$$

After related calculations, the following iterative formulas for calculating the system parameters can be given as follows:

$$(F_1)_{n+1}=\frac{1-(K_1/K_2)_n\,[1+(K_3/K_2)_n^{-1}]+(K_1/K_2)_n^2(K_3/K_2)_n^{-1}}{1-(K_4/K_2)_n[1+(K_3/K_2)_n^{-1}]+(K_4/K_2)_n^2(K_3/K_2)_n^{-1}} \tag{7}$$

$$(F_2)_{n+1}=\frac{1-[(\frac{K_1}{K_2})_n+(\frac{K_4}{K_2})_n](\frac{K_3}{K_2})_n^{-1}+(\frac{K_1}{K_2})_n(\frac{K_4}{K_2})_n(\frac{K_3}{K_2})_n^{-2}}{1-[(K_1/K_2)_n+(K_4/K_2)_n]+(K_1/K_2)_n(K_4/K_2)_n} \tag{8}$$

$$(\Gamma)_{n+1}=\pm\sqrt{a_{III}a_{IV}/(F_1)_{n+1}}=(\Gamma)_0\Big/\sqrt{(F_1)_{n+1}} \tag{9}$$

$$(\frac{K_3}{K_2})_{n+1}=\pm\sqrt{\frac{a_{III}/b_{IV}}{(F_2)_{n+1}}}=(\frac{K_3}{K_2})_0\Big/\sqrt{(F_2)_{n+1}} \tag{10}$$

$$(K_6)_{n+1}=b_I[1+\varepsilon_n(K_7)_n]/(\Gamma)_{n+1}-\varepsilon_n(K_5)_n \tag{11}$$

$$(K_7)_{n+1}=b_{II}[1+\varepsilon_n(K_6)_n]/(\Gamma)_{n+1}-\varepsilon_n(K_5)_n \tag{12}$$

$$(K_4/K_2)_{n+1}=a_I[1+\varepsilon_n(K_1/K_2)_n](\Gamma)_{n+1}-\varepsilon_n(K_3/K_2)_{n+1} \tag{13}$$

$$(\varepsilon)_{n+1}=\frac{a_I-(K_4/K_2)_{n+1}(\Gamma)_{n+1}^{-1}}{(K_3/K_2)_{n+1}(\Gamma)_{n+1}^{-1}-a_I(K_1/K_2)_n} \tag{14}$$

$$(K_1/K_2)_{n+1}=1+a_{III}[(K_3/K_2)_{n+1}-(K_4/K_2)_{n+1}]/(\Gamma)_{n+1} \tag{15}$$

$$(K_5)_{n+1}=(K_6)_{n+1}-b_{III}[1-(K_7)_{n+1}]/(\Gamma)_{n+1} \tag{16}$$

$$|K_2|_{n+1}=\frac{\sqrt{K_I}\ |1+\varepsilon_{n+1}(K_7)_{n+1}|}{|\Gamma|_{n+1}|1+\varepsilon_{n+1}(K_1/K_2)_{n+1}|} \tag{17}$$

Letting $K_1=0$, $K_4=0$ and $\varepsilon=0$ in (7)-(17),the iterative intial values can be obtained.

EXPERIMENTAL RESULTS

To verify the new method,a Ka-band four-port reflectometer has been set up, as shown in Fig.2.All system is controlled by IBM microcomputer via a interface circuit. P at port 4 is measured by a low-barrier Schottky diode detector whose deviation from square law is calibrated in terms of

the method proposed in 5. The sliding short is drived by the stepmotor. The reflectometer is calibrated by using the method in 1 and the one in in this paper for comparison. As for the calibration time,the former is about 16 min, and the latter is only a half of it. Experimental results at a frequence of 36GHz are shown in Table 1,in which $\Gamma'$is the reflection coefficient of another sliding short. It can be seen from Table 1 that two sets of the system parameters obtained by using two methods agree very well each other.

To examine the reliability for above calibration results, the reflection coefficient from the polished metal plate having ideal $\Gamma''=1\angle 180^{\circ}$is measured ten times.The results obtained by means of two groups of the system parameters are exactly the same and are listed in Table 1,too. (For simplicity, only a set of the measured data is given.)On measurement errors of the method reported, please refer to 2.

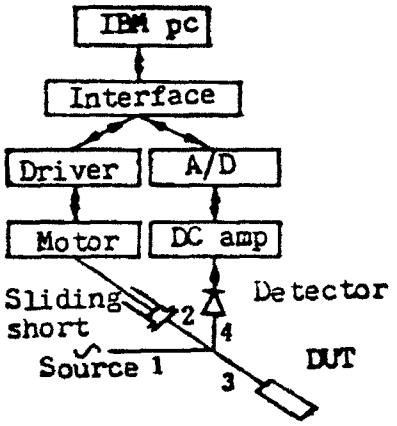

Fig. 2 An experimental 4-port working in a Ka-band

Table 1 measured values of system parameters and ref. coef.

	Method in 1	Present method	Measured Γ''	Ideal Γ''
K_1	$0.0618\angle 51.23^{\circ}$	$0.0608\angle 49.78^{\circ}$	$0.9986\angle 180.11^{\circ}$	
K_2	$1.5389\angle 0^{\circ}$	$1.5388\angle 0^{\circ}$	$0.9998\angle 180.23^{\circ}$	
K_3	$1.4107\angle 182.53^{\circ}$	$1.4101\angle 182.60^{\circ}$	$1.0003\angle 180.09^{\circ}$	
K_4	$0.0556\angle 232.31^{\circ}$	$0.0557\angle 232.38^{\circ}$	$1.0002\angle 180.16^{\circ}$	
K_5	$0.0128\angle 223.86^{\circ}$	$0.0128\angle 223.86^{\circ}$	$1.0022\angle 180.05^{\circ}$	$1\angle 180^{\circ}$
K_6	$0.0877\angle 321.51^{\circ}$	$0.0877\angle 321.51^{\circ}$	$1.0020\angle 180.09^{\circ}$	
K_7	$0.1217\angle 321.90^{\circ}$	$0.1217\angle 321.90^{\circ}$	$1.0005\angle 180.11^{\circ}$	
ε	$0.0135\angle 99.53^{\circ}$	$0.0134\angle 99.57^{\circ}$	$0.9976\angle 180.16^{\circ}$	
Γ	$0.9954\angle 178.75^{\circ}$	$0.9954\angle 178.75^{\circ}$	$1.0023\angle 180.10^{\circ}$	
Γ'	$0.9888\angle 177.14^{\circ}$	———	$1.0016\angle 180.00^{\circ}$	

CONCLUSIONS

From all mentioned above and Table 1, the following conclusions can be drawn: The reported method can cut calibration time down to half of one required in 1, only requires a sliding short and has the same accuracy as the one in 1.These features make this new method especially suitable to calibrate a practical engineering four-port reflectometer.

REFERENCES

1. K. Brantervik, IEEE Trans. Microwave Theory Tech.,33(7)(1985),569.
2. K. Brantervik and E. Kollberg, IEEE Trans. Microwave Tteory tech., 33 (7)(1985),563.
3. G. F. Engen, IEEE Trans. Microwave Theory Tech., 25(12)(1977),1075.
4. T. Nemoto and D. F. Wait, IEEE Trans. Microwave TheoryTech.,16(10) (1968),866.
5. C.A.Hoer,K.C.Roe,and C.M.Allred,IEEE Trans.Instru.Meas.,25(4)(1976), 324

AUTOMATIC MEASUREMENT FOR DIELECTRIC PROPERTIES OF SOLID MATERIAL AT 890GHz*

Qiu Bingsheng,Liu Chengjia,Huang Jiangjun and Qiu Ruman
(Zhongshan University,Guangzhou,China.)

ABSTRACT

An automatic measurement system has been used to measure the complex dielectric constant of solid materials at 890GHz.This instrument can be used as a two-beam interferometer for determining the refractive index or as a transmitter for measuring the absorption coefficient of dielectric materials at FIR and SMMW frequency. The results for seven low-loss solid materials and the accuracy of the measurement are presented.

INTRODUCTION

There is a growing interest in potential applications for the sub-millimeter wave(SMMW) spectral region. This interest is not liminted to fundamental studies,such as spectroscopy,plasma diagnostics and optical frequency measurement,but includes increasing military and civilian requirements. The development of functional systems in SMMW region is dependent on the development of sources, detectors, mixers and quasi-optical components.However,the development of quasi-optical components, including windows,attenuators,isolator,modulators and power couplers, etc,requires accurate data on the dielectric properties of materials in this spectral region. A survey of the literature[1] has revealed a serious shortage of data in this region, beoause measurements are extremely difficult to carry out accurately.We select typical frequency of SMMW(890GHz) to build a measuring system of dielectric properties of materials.The capability of this system to provide accurate values for the refractive index and absorption coefficient at 890GHz has been demonstrated for the solid materials,including TPX,quartz,teflon,poly-ethylene and polpropylene,etc.

EXPERIMENTAL SET-UP

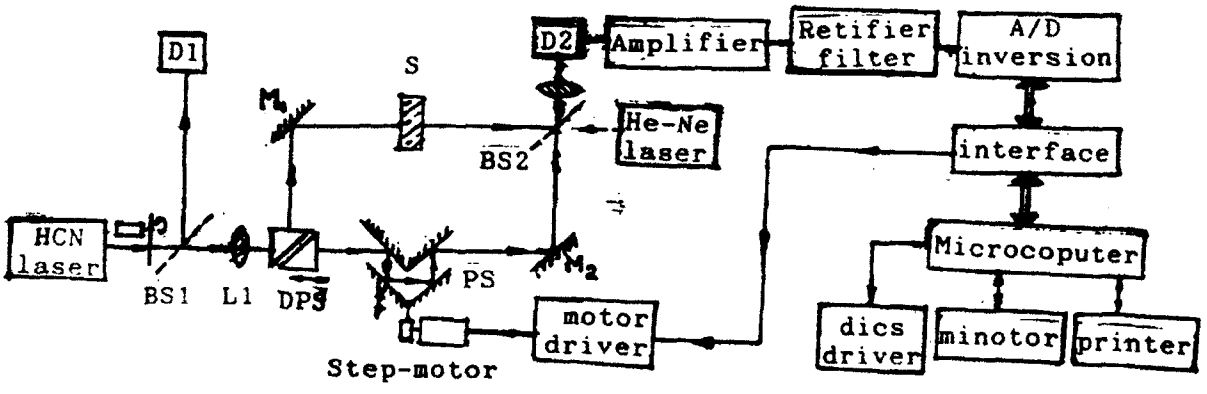

Fig.1 Block diagram of automatic measurement system for dielectric properties

* Project supported by the Fund of the Natural Sciences of P.R.C.

Fig.1 shows the block diagram of the auto-measurement system for SMMW dielectric properties measurement at the frequency of 890GHz using two-beam interferometer. A HCN laser is as the source having output power of 4mw with power stability of about 5% and operating frequency of 890,760+0.1MHz with frequency stability of 2*10-7[2].The laser output is a stable,linearly-polarized,Gaussian beam which is well suited to the measurement of dielectric properties, and the beam waist radius is 2.2mm at output window.The quasi-optical components in this system are designed and made by our laboratory.The double-prism couple (DPC, i.e, variable power divider) is made of two right angle prisms, which is composed of clear-glass-like TPX,and makes the component ideally suited for alignment of the apparatus.When the gap between the two prisms is varied,the ratio of two beam powers changes a range about 14db.The variable phase-shifter(PS) is composed of two right angle reflectors and used for measurement of the phase shift, where one reflector is fixed and the other one is driven by a set of stepping-motor and gears.L1 and L2 are TPX lenses,the BS1 is a mylar- film beam splitter and BS2 is fused quartz beam splitter.

The output of HCN laser beam ,which is modulated by a chopper for pyro-electric detector ,is divided into two part by BS1. A small portion of the beam is picked up for monitoring by the detector D1.The primary beam passes through a 15cm focal-length lens L1 and then is divided two beam by the DPC.The transmitted beam passes through machanical phase shifter,while the reflected beam reflected by reflector M1 and comes to focus at the sample S. The beam waist at the sample has a radius w0=0.4cm. They are combined by a splitter BS2. The combined beams are then focus onto a pyroelectric detector D2. The detector signal is sent to a amplifier and electronic circuit, the signal can be displayed on a chart recorder. A He-Ne laser in the other arm of the interferometer is used to align the optical system and used to orient the sample. The sample mount provides for adjusting in horizontal and vertical planes. While the automatic measuring system is operating, the microcomputer gives an output signal to drive stepping motor, each time the stepping motor turns a small angle, the PS gives an increment value of phase shift. The output signal of D2 via amplifying and processing is delivered to a computer for sampling and the sampling value is stored in the register. After the entire scanning process is finished, the microcomputer begins data processing, and then displays and prints out the measuring result curve.

MEASUREMENT OF DIELECTRIC PROPERTIES OF SOLID MATERIALS

A. Refractive index.

The measuring system can be used for the measurement of the refractive index. The first stage of the measurement procedure is to insert the solid sample in the sample mount, adjusts the DPC to equalize the two beam intensities at detector D2, and adjusts the PS at start position. By using computer to drive the stepping motor scanning, an interfero-

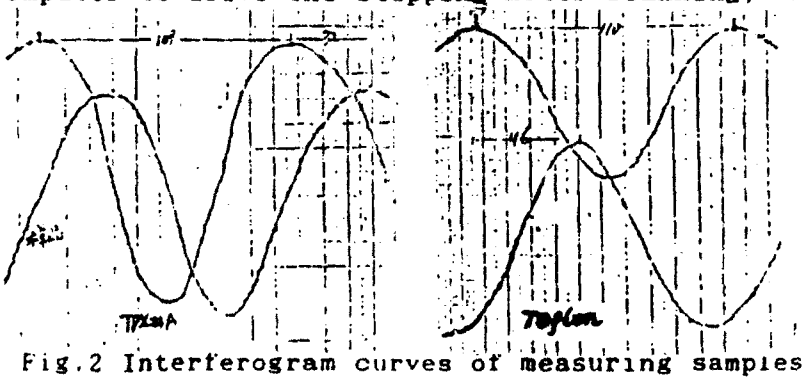

Fig.2 Interferogram curves of measuring samples

gram curve including the information of the sample phase shift is obtained. The sample is then removed and repeats scanning, another interferogram curve with no sample phase shift is also obtained. Fig.2 shows the two of these interferogram curves. By comparing the two curves, the net path change produced by the phase shifter to restore the null condition is equal to L. The refractive index n of the sample calculation formula is given as follows[3]:

$$n = 1 + \frac{N\lambda + L}{d} - \frac{\delta\lambda}{2\pi d} \qquad (1)$$

where λ is the wavelength in air, d the sample thickness, N an integer and δ is a phase shift which arises from the effect of multiple reflections in the sample, and this term is usually quite small. N can be computed as an approximate value of the index is available,otherwise, measurements on at least two different sample thichness are required to determine N.

B. Absorption coefficient

For the case of radiation normally incident on a phane of the sample, parallel plate of thickness d, the transmission T related to the refractive index n and absorption coefficint α is [3]

$$T = \frac{\rho(1-R)^2 R}{1+\rho^2-2\rho\cos\varphi} \qquad (2)\ ; \qquad \alpha = -\frac{1}{d}\ln(\rho/R) \qquad (3)$$

where $$\rho = Re^{-\alpha d}\ , \qquad R = \left(\frac{n-1}{n+1}\right)^2\ , \qquad \varphi = \frac{2\pi}{\lambda} nd \qquad (4)$$

Measurement of the sample transmission T for determining the absortion coefficient α is accomplished with minor modification of the instrument described above. The beam of the reflected by M1 is used and the other one is absorbed.Detector D1 is used for monitoring the output power of the laser, and D2 is used for measuring T while the sample is inserted and removed from the sample mount. Assuming the pyroelectric detector and amplifier have linear response. The ratio T1/T2 of the measurement with two times is transmission T of the sample.

Usually, the accuracy of the absorption coefficient measurement is more than 10% causing the unstable of laser output power.In order to improve the measurement accuracy, we use an electronic circuit and digittal voltmeter for measuring the D1 and D2 output signal. The accuracy of transmission measurement within 0.5% is obtained. Block diagram of the electronic circuit is shown in Fig.3.

Fig.3 Block diagram of electronic circuit for measuring transmission

RESULTS AND DISCUSSION

The values of refractive index and absorption coefficient which we have obtained for a number of solid materials at room temperature are presented in Tabble I. Some results obtained by literatures are shown for comparison.

The main sources of error in the measuring index n are the uncertainty in the measurement of sample thichness d and the net path change L. It can be expressed as

$$\Delta n = \frac{1}{d}\left[(\Delta L)^2 + (n-1)^2 (\Delta d)^2\right]^{1/2} \qquad (5)$$

Representive standard errors for sample thickness and net path change, such as TPX sample, are ±0.004mm and±0.002mm, respectively. From the formula(5), the standard error in the index of TPX is ±0.0001. The results of standard errors in the sample's index values are shown in Table I.

The error in the measurement of absorption coefficient mainly depends upon the uncertainty in the measurement of transmission, index and sample thichness. It can be expressed as

$$\left(\frac{\Delta\alpha}{\alpha}\right)_{Tot}=\left[\left(\frac{\Delta\alpha}{\alpha}\right)_T^2+\left(\frac{\Delta\alpha}{\alpha}\right)_n^2+\left(\frac{\Delta\alpha}{\alpha}\right)_d^2\right]^{1/2} \qquad (6)$$

This computation is rather involved. We found that the standard error of absorption coefficient depends strongly upon the uncertainty in the measurement of transmission T, for example, the uncertainty of T is 1.5% for the sample of Quartz at T=0.65, it will result in standard error of absorption coefficient of 7.6%. So a special electronic circuit was added to improve the accuracy of transmission measurement as mentioned above. By using holding circuit and digital voltmeter, the influence of output power fluctuation can be decreased and the accuracy of measured transmission T is better than 0.5%. So the measuring errors of the absorption coefficient α are typically about 3 percent.

TABLE I. EXPERIMENTAL RESULTS

Material	THIS WORK AT 890GHZ					Literalure	
	Thickness* (mm)	L (μm)	n±Δn	T	α (cm^{-1})	n	α (cm^{-1})
Crystalline Quartz	10.984±.003	119.1	2.1133±.0004	0.674	0.098	2.114	0.1 [4]
Crystalline Gernanium	15.100±.003	80.4	3.9904±.0006	0.0807	1.073	4.006	0.76 [5]
ZnSe	2.857±.003	15.2	3.1246±.002	0.304	1.931	3.124	[6]
Tefion	14.200±.004	97.9	1.4333±.0003	0.593	0.351	1.391	0.39 [7]
TPX(A)**	15.674±.004	118.8	1.4583±.0002	0.611	0.292	1.457	0.31 [4]
TPX(B)	15.662±.004	117.7	1.4585±.0002	0.602	0. 38		
Polyethylene High Density	15.040±.005	20.7	1.4711±.0003	0.595	0.266	1.463	0.272 [5]
Polypropylene (Sintered)	12.731±.008	150.5	1.4875±.0004	0.313	0.836	1.499	0.27 [4]

* The meassurements of sample thickness are carried out by the Institute of Guangdong Metrological Science.
** The material of TPX has been stored for more then 10 year.

The data given here are measured at a single frequency, it can provide guidance at higher or lower frequency as well. The measuring system can also be used to measure the dielectric properties of liquid materials.

REFERENCES

1. G.J.Simonis,Int.J. IR and MM Waves, vol.3.439(1982)
2. Qiu Bingsheng, et al.,Int.J. IR and MM Waves,Vol.9, 923(1989)
3. J.M.Dutta,et al.,IEEE Trans.MTT-34, 932(1986)
4. J.Chamberlain,et al., Infrared Phys.Vol.11,74(1971)
5. P.F.Goldsmith. Infrared and MM Waves,Ed.by K.J.Button, Vol.6,335 (1982)
6. T.Hottric,et al.,Opt.Commum.Vol.7 229(1973)
7. D..Bicanic and A.Dymanus, Infrared Phys.Vol.14,153(1974)

HIGHER-ORDER MODES IN COAXIAL CHIROWAVEGUIDES

Shen Zhongxiang
(Nanjing Aeronautical Institute, 210016, China)

ABSTRACT

The propagation characteristics of higher-order modes in coaxial chirowaveguides, which consist of coaxial transmission lines filled with chiral materials, are investigated in this paper. The analysis is based on analytic formulation of electromagnetic field components and application of boundary conditions. Numerical results are presented for the variation of the propagation constants with frequency and the radius ratio of inner and outer conductors

INTRODUCTION

Chiral media have long been known in optics under the more common name of optically active materials. Such materials are characterized by an intrinsic left- or right-handedness at optical frequencies, due to a helical natural structure. Renewed, recent interest in chiral media stems primarily from the possibility that, through advances in polymer science, or through the manufacturing of artificial dielectrics [1,2], substances possessing a rotatory power at microwave or millimeter-wave bands might be produced.

Recently a new type of guided-wave structure, named chirowaveguide, was suggested by Engheta et al. [3]. The chirowaveguides consist of cylindrical waveguides filled with homogeneous isotropic chiral materials. Due to the electromagnetic chirality of the material inside the waveguide, several important features are associated with this type of guided-wave structure. Such waveguides will have a variaty of potential applications in integrated optics, electronic devices, and optical communications systems as well as in their millimeter-wave and microwave counterparts.

In this paper, we analyze the propagation characteristics of higher-order modes in coaxial waveguides filled with homogeneous isotropic chiral media. The expressions for the electromagnetic fields inside the coaxial chirowaveguide are given, and the boundary conditions are used to derive the characteristic equations for the higher order modes.

FORMULATION

It has been shown that in the case of a chiral medium made of randomly oriented and uniformly distributed lossless, short, wire helices, the set of constitutive relations for time-harmonic fields ($\exp(-j\omega t)$) has the form

$$\vec{D} = \varepsilon \vec{E} + j\xi \vec{H} \qquad (1)$$

$$\hat{H} = j\xi_c \hat{E} + \hat{B}/\mu \qquad (2)$$

where ϵ, μ, ξ_c represent the dielectric constant, permeability, and chirality admittance of the chiral medium, respectively.

In the chirowaveguide, the direction of propagation is along the z axis. Considering the z-dependence $\exp(j\beta z)$ for the field components inside the guide and using chiral constitutive relations (1) and (2) and the source-free Maxwell equations, the transverse components of electric and magnetic fields inside the chirowaveguide can be expressed in terms of the longitudinal components of $\hat{E}_t$ and $\hat{H}_t$

$$E_t = ja\,\nabla_t E_z + jb\,\vec{a}_z \times \nabla_t H_z + c\,\nabla_t H_z + d\,\vec{a}_z \times \nabla_t E_z \qquad (3)$$

$$H_t = ja\,\nabla_t H_z - j(b/\eta_c^2)\,\vec{a}_z \times \nabla_t E_z - c(\eta_c^2)\,\nabla_t E_z + d\,\vec{a}_z \times \nabla_t H_z \qquad (4)$$

where

$$a = \beta\left[\tfrac{1}{2}(k_+^2 + k_-^2) - \beta^2\right]/h_1$$

$$b = \omega\mu(\beta^2 - k^2)/h_1$$

$$c = 2\omega^2\mu^2\xi_c\beta/h_1$$

$$d = \omega\mu\xi_c(\beta^2 + k^2)/h_1$$

$$h_1 = (k_+^2 - \beta^2)(k_-^2 - \beta^2)$$

$$K_\pm = \pm\omega\mu\xi_c + \sqrt{k^2 + (\omega\mu\xi_c)^2}$$

and $\eta_c = \eta/\sqrt{1+(\eta\xi_c)^2}$, with $\eta = \sqrt{\mu/\epsilon}$, $\nabla_t = \nabla - \frac{\partial}{\partial z}\vec{a}_z$ and $k = \omega\sqrt{\mu\epsilon}$ with ω being the radian frequency of the time-harmonic fields.

The longitudinal components E and H can be expressed in terms of functions U_+ and U_- according to

$$E_z = P_+ U_+ + P_- U_- \qquad (5)$$

$$H_z = q_+ U_+ + q_- U_- \qquad (6)$$

with

$$\nabla_t^2 U_+ + P_+ U_+ = 0 \qquad (7)$$

$$\nabla_t^2 U_- + P_- U_- = 0 \qquad (8)$$

and

$$P_+ = k_+^2 - \beta^2$$

$$P_- = k_-^2 - \beta^2$$

$$q_+ = (k_+^2 - k_-^2)P_+/(4j\omega^2\mu^2\xi_c)$$

$$q_- = -(k_+^2 - k_-^2)P_-/(4j\omega^2\mu^2\xi_c)$$

For the coaxial chirowaveguide whose inner and outer conductors are at radii R_2 and R_1, respectively, the use of a polar coordinate $r\phi z$ system yields the following solutions for U_+ and U_- in the range $R_2 < r < R_1$.

$$U_+(r) = [A_1 J_n(\sqrt{P_+}\cdot r) + B_1 Y_n(\sqrt{P_+}\cdot r)]\exp(jn\phi) \qquad (9)$$

$$U_-(r) = [A_2 J_n(\sqrt{P_-}\cdot r) + B_2 Y_n(\sqrt{P_-}\cdot r)]\exp(jn\phi) \qquad (10)$$

where A_1, B_1, A_2, and B_2 are constants to be determined. Here Jn and Yn are the Bessel functions of order n of the first kind and the second kind, respectively.

Enforcing the boundary condition that the tangential components of electric field equal to zero at $r=R_1$ and $r=R_2$ and using the equations (3) and (4) to yield

$$\begin{bmatrix} P_+ J_n(\sqrt{P_+}R_1) & P_+ Y_n(\sqrt{P_+}R_1) & P_- J_n(\sqrt{P_-}R_1) & P_- Y_n(\sqrt{P_-}R_1) \\ P_+ J_n(\sqrt{P_+}R_2) & P_+ Y_n(\sqrt{P_+}R_2) & P_- J_n(\sqrt{P_-}R_2) & P_- Y_n(\sqrt{P_-}R_2) \\ SS1(R_1) & SS2(R_1) & SS3(R_1) & SS4(R_1) \\ SS1(R_2) & SS2(R_2) & SS3(R_2) & SS4(R_2) \end{bmatrix} \begin{bmatrix} A_1 \\ B_1 \\ A_2 \\ B_2 \end{bmatrix} = 0 \qquad (11)$$

where

$$SS1(R) = T_1 J_n(\sqrt{P_+}R)/R + T_3\sqrt{P_+}J_n'(\sqrt{P_+}R)$$

$$SS2(R) = T_1 Y_n(\sqrt{P_+}R)/R + T_3\sqrt{P_+}Y_n'(\sqrt{P_+}R)$$

$$SS3(R) = T_2 J_n(\sqrt{P_-}R)/R + T_4\sqrt{P_-}J_n'(\sqrt{P_-}R)$$

$$SS4(R) = T_2 Y_n(\sqrt{P_-}R)/R + T_4\sqrt{P_-}Y_n'(\sqrt{P_-}R)$$

and $T_1 = n(jcq_+ - aP_+)$, $T_2 = n(jcq_- - aP_-)$, $T_3 = dP_+ + jbq_+$, and $T_4 = dP_- + jbq_-$. In order to accomplish a nontrivial solution of (11), we must require the determinant of the coefficient matrix in (11) equals to zero, that is

$$\text{Det}\ [\ H\ (\beta)\ ]_{4\times4} = 0 \qquad (12)$$

where the expressions for the elements of the matrix $[\ H(\beta)\ ]$ can be obtained from equation (11) straightly. The propagation constant β can be found by solving the resulting characteristic equation (12).

NUMERICAL RESULTS

In this section we present calculated results for the propagation constants of higher-order modes in coaxial chirowaveguide. The example consists of a coaxial line homogeneously filled with a chiral medium of relative scalar permittivity $\varepsilon_r = 1$, relative scalar permeability $\mu_r = 1$ and chiral admittance $\xi_c = 1$ mS. The descriptor EHmn used in [6] is adopted here for chiral modes. The resulting propagation diagram is given in Fig.2. The results for $R_2 = 0$ (that is circular metal chirowaveguide) are in agreement with the data in [6]. The variation of the propagation constants for HE_{11} and HE_{-11} with the ratio R_2/R_1 is shown in Fig.3.

REFERENCES

1 Jaggard DL et al., Appl. Phys., Vol.18, 1979, pp.211-216.
2 Engheta N et al., IEEE Trans., Vol. AP-30, No.12, 1982, pp.1213-6.
3 Engheta N, and P.Pelet, Optics Letters, Vol.14, No.11, 1989, pp.593-595.
4 Pelet P et al., IEEE Trans., Vol.AP-38, No.1, 1990, pp.90-97.
5 Eftimice C et al., Radio Science, Vol.24, No.3, 1989, pp.351-359.
6 Svedin JAM, IEEE Trans. Vol.MTT-38, No.10, 1990, pp.1488-1496.
7 Cory H et al., IEE Proc. pt-H,, Vol.138, No.1, 1991, pp.51-54.
8 N.Marcuwitz, Waveguide Handbook, New York: McGraw-Hill, 1951.

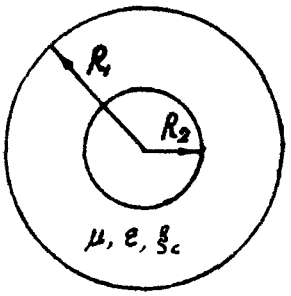

Fig.1 Cross section of coaxial chirowaveguide.

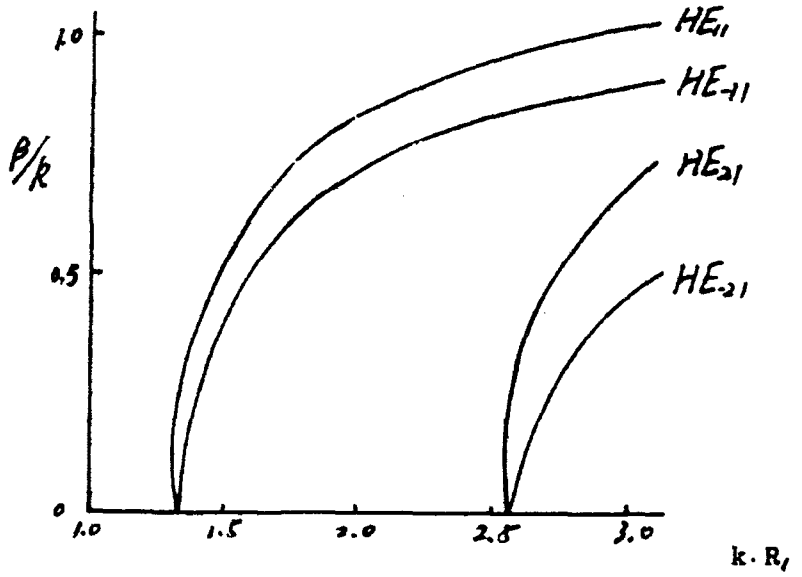

Fig.2 Dispersion relations for the higher order modes in coaxial chirowaveguide. ($R_2 = \frac{1}{2} R_1$)

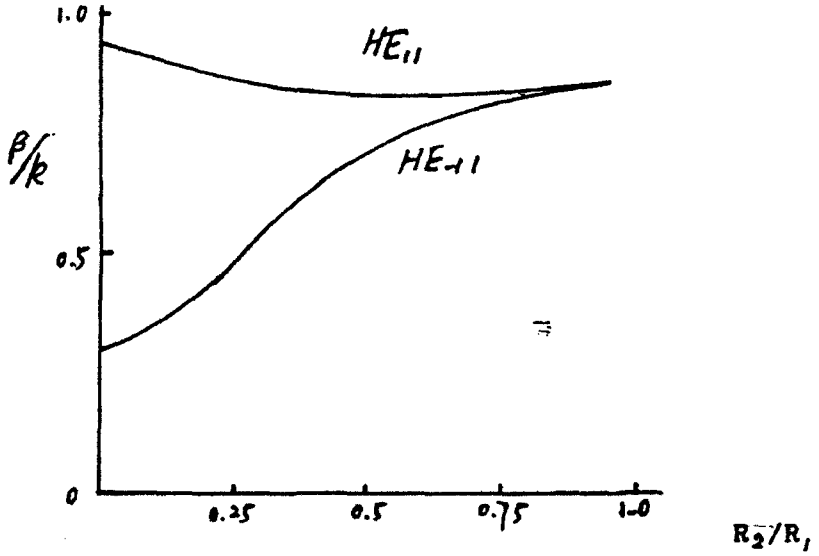

Fig.3 Variation of the normalized propagation constants with the ratio R_2/R_1. ($kR_1 = 2.0$)

W6.9

RESEARCH ON IMPROVING ISOLATION OF 8mm PIN SWITCH

Zhou Chun, Fang Yu, Fang Puming, Wang Liangchen,
Wang Li, Zheng Dong
(Institute of Semiconductor, Academia SINICA)

ABSTRACT

The planar structure PIN fin-line switch has been done successfully in our grope in 1989. Tpical performances of the device are shown bellow: the operation frequency 33-35GHz, the insertion loss I 1.odB, standing wave coefficienct s 1.2, switching time 80ns, power standing P 1w, and rather good reliability.

Isolation is one of the important characteristics of a switch. How to increase the isolation of the switch will be presented in this paper. what steps should we take to improve this parameter while keeping insertion loss and other parameters nearly constant? It is just the goal of this experimental research. The initial results of 25dB increament is obtained, with nearly same insertion loss.

RESTRICTING THE TRANSMISSION OF PARASITIC MODE

Because of the discontinuity between the waveguide and fin-line, a parasitic mode will be raised at the junction. This mode is not under control of PIN diodes, because it passes through the upper-side of the finline resulting of the limitation of the switch isolation. In this work, remarking improvments of isolation are archieved by means of restricting the leaking power under the condition of using PIN switch with higher isolation.

Therefore it is very important to find useful methodes to destroy parasitic transmission line in order to lower leaking power. One of the method is to use a piece of film with absoring electromagnetic wave and electronic isolation functions. This method has been proved to be availale.

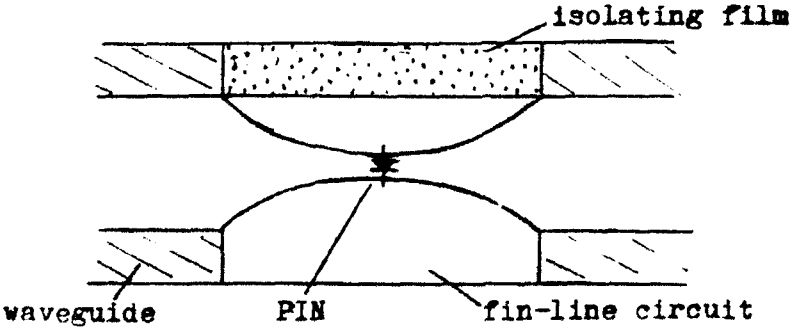

Fig. 1

PROCESS OF MAKING ISOLATION FILMS

In the experiment, three kinds of thin films are choosen. 1. plastic film. serving as a standard for the comparision with other films. 2. alloy film. 3. absorbing-wave film.

1. Alloy Film

On the thin mica film, after evaporating metals of In and Sn, a kind of alloy film is obtained. Through changing the fractions of every kind of metals. the different magnitude of surface resistance R of the film can be achieved. Better results have been when using this film. But some shortcomings exist in the alloy films too. The adhesion of metal to mica is weak; this fault get rise to the poor mechanical performence and low realiability rate.

Another kind of alloy film is gotten in the case of using Al and Ni. Like InSn alloy film, it also has good results in the improving isolation measurement.

2. Absorbing-wave film

This kind of film has better mechanical performance and good results.

RESULT AND CONCLUSION

The measurement of isolation is made under the condition of f=35GHZ, and input power P=700-800mW. The Fig. 2 shows the diagram of measurement system.

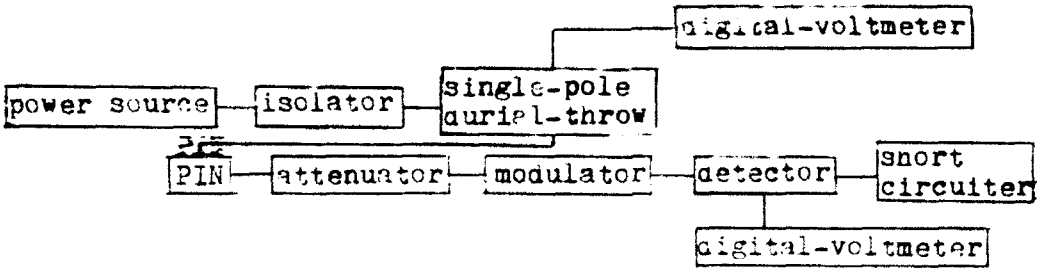

Fig. 2

Comparing to the plastic film, isolation improvments of resulting fromusing using other films are displayed on Table I. Two different methods are used in the experiment: a. Only one film is used. b. Two films are taken. The structure charts are shown bellow respectively

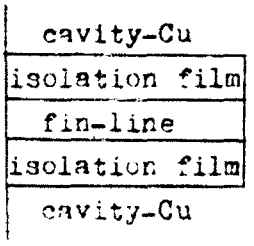

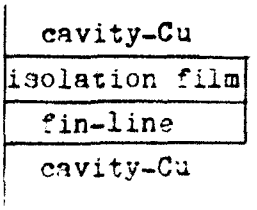

CONCLUSION:

1.The parasitic mode exists certainly in the fin-line switch. It takes the upper-fin strip as its transmission line. In the switch, parasitic mode contribute to the leak power without being controlled by PIN diode. Bellow,representing several typical results in our experiment.

2.To restrict parasitic mode,the method discussed above is very useful but it is not the only one must be taken to reach the object. In principle,other methods can also be taken to destroy parasitic transmission line,such as making filter circuit on upper-line metal.

3.In the experiment,a phenomenon is found that only at the time original isolation(while plastic film is taken) are high enough,the advantage of changing film is obvious.So that a conclusion can be obtained: the magnitude of parastic mode is rather small, and it can contribute the influence to isolation only when output power of switch in isolating situation reach the same value order as the parasitic mode.

film(one)	plastic film	InSn alloy film	ΔI
isolation	35 dB	52 dB	17 dB
film(one)	plastic film	absorbing film	ΔI
isolation	33.1 dB	43.9 dB	10.8 dB
film(two)	plastic film	absorbing film	ΔI
isolation	37.5 dB	62.5 dB	25 dB

Table.1

REFERENCE

Peng ChuanCai and Jin ZhaoTing, Science and Technology of Solid Film, 2(1989), 69.

W7.1

FAR-INFRARED SPECTRAL EMISSION FROM SIMPLE IONIC FILMS

Kunao HISANO

Department of Mathematics & Physics
The National Defense Academy,
Yokosuka 239, Japan

Introduction

It is obvious that the frequency dependent dielectric properties of substances are responsible to the optical properties. The long wavelength lattice vibrations reflect the infrared dielectric properties of ionic crystals. The lattice vibrations are based on the potential energy between atoms in which both harmonic and anharmonic (damping) terms are included. Transverse optical phonons in polar crystals interact strongly with electromagnetic wave when the retardation of the Coulomb interaction between ions is included[1]. This results in a mixed excitation of the crystal as one of the normal modes called polaritons[2]. Therefore,the far-infrared spectroscopy has been one of the powerful means to discuss lattice dynamical properties of ionic crystals. Since the infrared emissivity is equal to the absorptance in a thermally balanced system according to the Kirchhoff's law[3],the emission spectroscopy has been also a powerful means particularly for its temperature dependence because of ease of its measurement. In this report, present author will review his own work on the temperature dependence of phonon modes in some cubic ionic crystals obtained by means of far-infrared spectral emission spectroscopy.Measurements are made on metal-backed films at an oblique emission angle. The spectral analysis is performed for the observed spectra using a theory of virtual modes for slabs derived from the polariton modes [5,6]. The estimated temperature dependence is discussed in terms of a theory of phonon anharmonicity.

Infrared Dielectric Response

The dielectric function $\epsilon(\omega)$ of a cubic polar crystal such as alkali-halides is given by the following relation within the harmonic approximation of lattice vibrations:

$$\epsilon(\omega) = \epsilon_\infty \frac{\omega_L^2 - \omega^2}{\omega_T^2 - \omega^2} , \qquad (1)$$

where ϵ_∞ is the high frequency dielectric constant. ω_T and ω_L are, respectively, the transverse optical (TO) and the longitudinal optical (LO) frequencies of long wavelengt' lattice vibrations. Therefore, the static dielectric constant ϵ_0 is given as

$$\epsilon(0) = \epsilon_\infty \frac{\omega_L^2}{\omega_T^2} . \qquad (2)$$

The classical description for the dielectric function, including dampings caused by the lattice anharmonicity, is written as

$$\epsilon(\omega) = \epsilon_\infty \frac{\omega_L^2 - \omega^2 - i\gamma\omega}{\omega_T^2 - \omega^2 - i\gamma\omega} . \qquad (3)$$

The thermodynamical Green function technique for many body problems predicts the dielectric function as [4]

$$\frac{\varepsilon(\omega)}{\varepsilon_\infty} = \frac{\omega_L^2 - \omega^2 + 2\omega_T(\Delta_1(\omega) - i\Gamma(\omega))}{\omega_T^2 - \omega^2 + 2\omega_T(\Delta_1(\omega) - i\Gamma(\omega))} , \qquad (4)$$

where ω_T and ω_L are, respectively, the quasi-harmonic TO and LO mode frequencies incorporating the effects of thermal expansion. $\Gamma(\omega)$ is the imaginary part of the phonon self-energy describing the frequency dependent damping mainly reflecting the two-phonon density of state. $\Delta_1(\omega)$ is the real part of the self-energy describing the frequency shift.

Virtual Modes

A detailed theory has been given on the optical properties of an ionic slab by Fuchs and Kliewer [5,6]. In a thin slab, the finite thickness of crystal and the coupling between phonons and photons cause an alteration of polariton dispersion curves and the appearance of many virtual modes which have incoming or outgoing waves outside the slab (radiative modes).

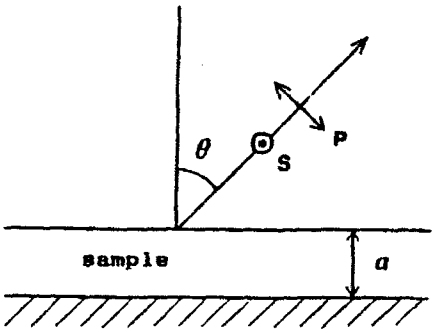

Fig.1.Diagram giving definitions of emission angle θ, film thickness a and radiation polarizations p and s.

Based on the diagram shown in Fig.1, the infrared properties of metal-backed ionic slabs can be determined from the following equations: These are, for p- and s-polarization,

$$L_p = 1 - [i\beta/\beta_0\epsilon(\omega)]\tan\beta a$$
$$L_s = 1 + (i\beta/\beta_0)\tan\beta a, \qquad (5)$$

where

$$\beta_0=\sqrt{(\omega/c)^2-k_x^2} \qquad \beta=\sqrt{\epsilon(\omega/c)^2-k_x^2}, \qquad (6)$$

where k_x is the wave vector of the field of radiation in direction of x. Writing

$$P_p = (2 - L_p)/L_p$$
$$P_s = (2 - L_s)/L_s, \qquad (7)$$

the emissivity E(ω) are then

$$E_p = (1 - |P_p|^2)$$
$$E_s = (1 - |P_s|^2), \qquad (8)$$

for p- and s-polarization, respectively. Using the relation $k_x=(\omega/c)\sin\theta$ and the dielectric function given by equation(3) a typical example of the p-polarized spectrum of NaCl slab caiculated basing on equation (8) is shown in Fig.2, together with absolute value of the dielectric function. No emission peak around the LO mode frequency is predicted for s-polarization spectrum.

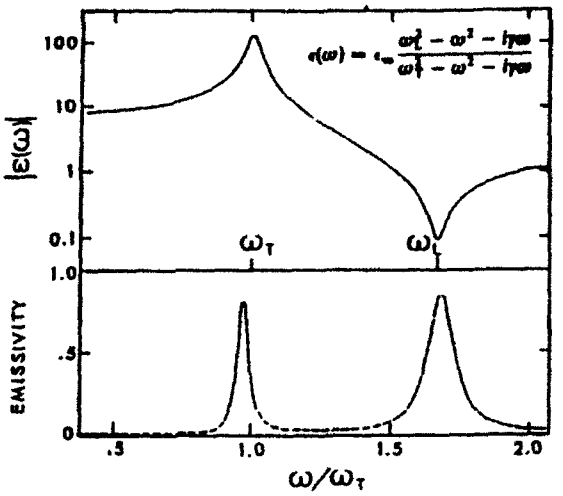

Fig.2.Dielectric dispersion and p-polarized emission spectrum for 2μm NaCl film with emission angle of 45°.

Experimental

Metal-backed polycrystalline films of cubic ionic crystals have been prepared by vacuum evaporation onto platinum plates. Emission spectra at an oblique emission angle have been measured using either Fourier transformed (FTIR) or grating infrared spectrometers [8-10]. Fig.3 shows a schematic drawing for the laboratory equipped FTIR spectrometer.

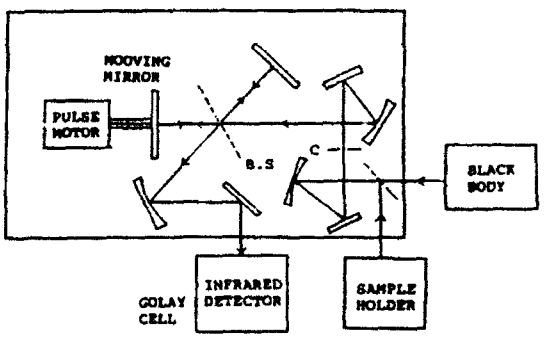

Fig.3.Schematic drawing of laboratory equipped FTIR spectrometer.

A mylar sheet beam splitter and a Golay cell radiation detector were used in this spectrometer. The whole optical system was enclosed in a housing and flushed with a stream of dry nitrogen gas to remove the effect of atmospheric absorption. Fig.4 shows a sample heater

set at a part of light source of a Brucker IFS113v vacuum FTIR spectrometer together with a blackbody radiator. A wire grid polarizer was used for the polarization measurments. The spectral radiation intensity from a sample was normalized to that from a black body radiator to estimate the emissivity

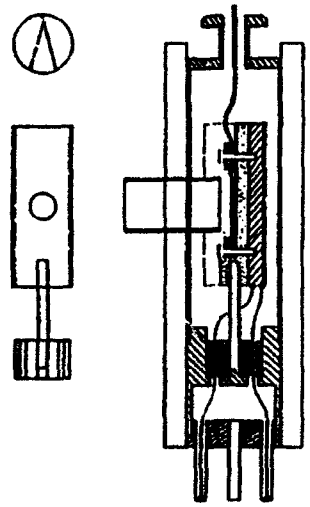

Fig.4.Sample heater(b) and balck body radiator (a) for a Brucker IFS 113v spectrometer.

Results and Discussion

As typical examples, Figs.5 and 6 show the temperature dependene of p-polarized spectra of NaCl film having 1.7μm thickness and CaF_2 films having 1.4μm thickness, respectively [8,12]. It is clear from Fig.5 that the spectra for NaCl show anomalous emission peaks around the LO mode frequency unlike the calculated results shown in Fig.2. These anomalies have been also observed for KBr and KCl films but not for fluorides such as BaF_2 and CaF_2 [9,10,13]. The anomalous fine structures have been caused by the considerable structure in the self-energy of the TO phonons around the LO mode frequency [14].

In order to derive the frequency dependence of the self-energy as well as phonon modes at various temperatures, the

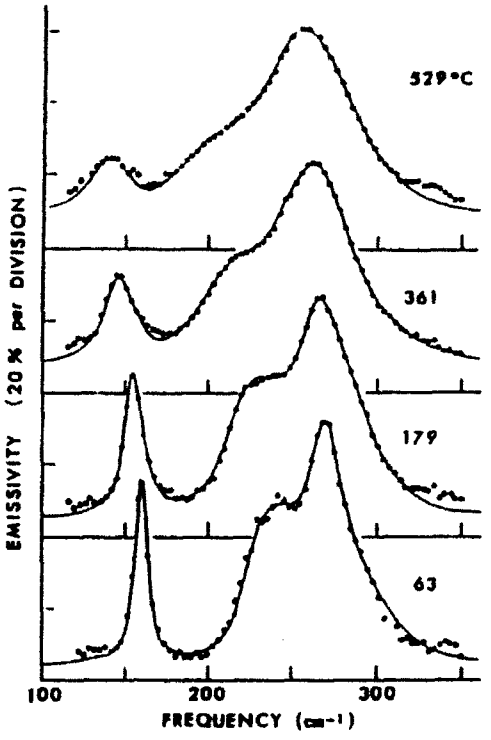

Fig.5.p-polarized spectra for the 1.7μm NaCl film at various temperatures measured at 45° emission angle.

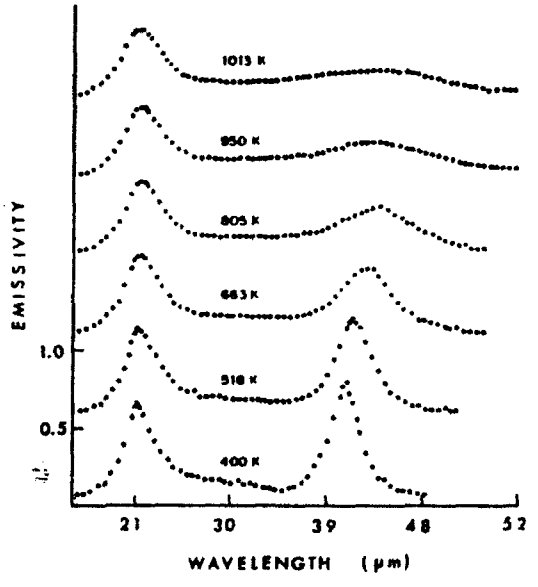

Fig.6.p-polarized spectra for the 2.0 μm CaF_2 film at various temperatures measured at 45° emission angle.

lineshape analysis has been performed for NaCl and KCl using equation (8) and the following empirical form for the

self-enrgy: That is

$$\Delta_2(\omega) - i\Gamma(\omega) = \sum_{j=1}^{5} \frac{\omega_j^2 p_j}{\omega^2 - \omega_j^2 + i\omega\gamma_j} \qquad (9)$$

The above empirical form with five Lorenzian shapes is based on the room temperature self-energy obtained theoretically [14]. The solid line in Fig.5 shows the results obtained from lineshape analysis for NaCl. Fig.7 shows the self-energy at various temperatures.

The self-energy and its temperature dependence are caused by various multiple phonon interactions through the non-linear terms of lattice potential. These multiple phonon interactions have been discussed in detail by previous authors including temperature dependence

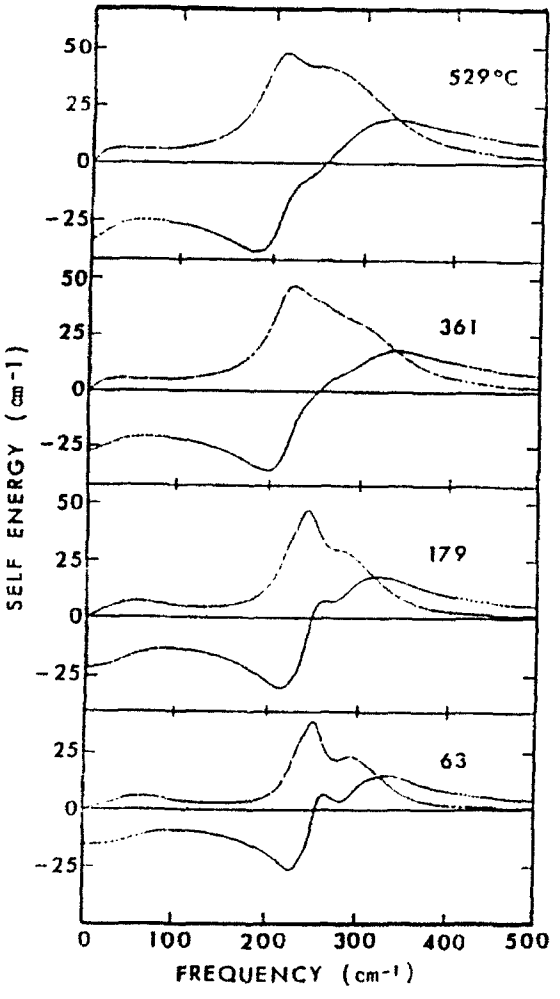

Fig.7.Self energy function for NaCl at various temperatures.
----, $\Gamma(\omega)$; ——, $\Delta_2(\omega)$

[15,16]. The large peak in $\Gamma(\omega)$ is mainly caused by two phonon interaction which reflects two phonon density of state.The two phonon interaction gives a sub-linear temperature dependence, while the other higher order interactions give a super-linear dependence. Fig.8 plots the temperature dependence of the scaling factor for the self-energy indicating linear increase with temperature, which has not yet been clearly understood theoretically.

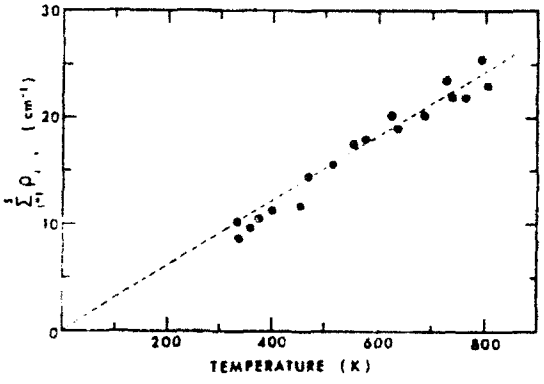

Fig.8.Temperature dependence of scaling factor for NaCl. ●,1.7μm; ◎,2.5μm

REFERENCES

[1] M Born & K Huang:Dynamical Theory of Crystal Lattice.(Oxford University Press,London,1954) p.82
[2] C H Henry & J J Hopfield: Phys.Rev. Lett.,15(1965)964
[3] T O McMahon:J.Opt.Soc.Amer.,40(1950) 276
[4] R A Cowley: Adv.Phys.,12(1963)42
[5] K L Kliewer & R Fuchs: Phys.Rev. 150 (1966)573
[6] R Fuchs,K L Kliewer & W J Pardee: Phys.Rev., 150(1966)589
[7] K Hisano:J.Phys.C:Solid St. Phys.,13 (1980)5823
[8] K Hisano & H Tanaka: Proc. 9th Japan Symp. Thermophysical Properties, Nagaoka,(1988),p.247
[9] K Hisano & H Tanaka: J.Phys.C:Solid St.Phys.,19(1986)6311
[10] H Tanaka & K Hisano: J.Phys.C: Condens.Matter, 1(1989)9539
[11] A Aoki, H Tanaka & K Hisano: Proc. 12th Japan Symp. Thermophysical Properties, Kyoto,(1991) p.9
[12] K Hisano: Infrared Phys.25(1985)415
[13] K Hisano & H Tanaka: J.Phys.C:Solid St.Phys.,19(1986)1509
[14] K Hisano,F Placido,A D Bruce & G D Holah: J.Phys.C:Solid St. Phys., 5(1972)2511
[15] A D Bruce: J.Phys.C:Solid St.Phys., 6(1973)174
[16] J E Eldridge & P R Staal: Phys.Rev. B13(1977)4608

W7.2

INTERACTIONS BETWEEN MILLIMETER WAVE AND POLAR AND NONPOLAR MOLECULES

Chen Jianbo and Li Binhong
(Shanghai Jiao Tong Univesity)

INTRODUCTION

The spectrum of interaction between millimeter wave and molecule can lie in three bands: 1. electron spectrum in ultraviolet and visible lightbands; 2. molecule vibration spectrum within near infrared and medial infrared bands; 3. molecule rotation spectrum covering the infared, millimeterwave and microwave bands. Neglecting the coupling between the vibration and rotation of the molecule, the interaction between millimeterwave and molecule corresponds to the transition between two rotation energylevels of molecule.

There are polar and nonpolar molecules. Both principles and analytical methods of their interaction with millimeter wave are different. The intrinsic electric dipole moment of a polar molecule can directly couple with EM wave, and molecule state can transit between its rotational energy levels. Since the nonpolar molecule does not have intrinsic electric dipole moment, it can not couple with EM wave directly and its state can not transit between rotational energy levels. However, when there exists a nonpaired electron in nonpolar molecule, its uncancelled self-spin magnetic moment will precess under the applied magnetic field, and the quantization of the precession will split each rotational level into several sublevels. The transition of the molecule state between any two sublevels well also correspond to millimeter wave frequency.

In this paper, we present the theoretical computation of the interaction of millimeter wave with two kinds of molecules by using quantum mechanics. From the computation results of the typical polar molecule H_2O and nonpolar molecule O_2, their peaks of absorption coincide with those of measured atmospheric attenuation curve very well. Therefore, this analytical and computing method will also be suitable for other substance molecules.

ANALYSIS OF INTERACTION BETWEEN MILLIMETER WAVE AND POLAR MOLECULE H_2O

1. Basic Principle

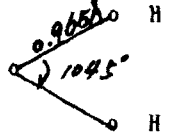

Fig.1 Scheme of structure of water molecule

Fig.1 shows the structure of H_2O, since its positive and negative change centers do not coincide, it has a intrinsic electric dipole moment and is called a polar molecule. Let us find out its rotational energy levels by using quantum mechanics, and estmate its absorption spectrum.

The molecule consists of nucleuses and electrons. neglecting the coupling between electronic self-spin magnetic moment and orbital magnetic moment, the molecule Hamiltonian operator can be written as

$$H=-\frac{h^2}{2M_c}\sum\Delta_i^2-\sum_a\frac{h^2}{2M_a}\Delta_a^2-\sum_{i,a}\frac{Z_a e^2}{4\pi\epsilon_0 r_{ai}}+\sum_{a,b}\frac{Z_a Z_b e^2}{4\pi\epsilon_0 R_{ab}}$$

$$+\sum_{i>j}\frac{e^2}{4\pi\epsilon_0 r_{ij}}=T_E+T_N+V_{NE}+V_{NN}+V_{EE} \tag{1}$$

Where i stands for the ith electron having mass of Me;
α stands for the a nucleus having atomic order of Z_α and mass of M_α;
T_E and T_N are kinetic energy operators of electron and nuleus respectively;
V_{NE}, V_{NN}, V_{EE} are static electrical interactional energies between a electron and nucleus, a nucleus and another and a electron and another respectively.

The Schrödinger equation of the molecule is

$$\hat{H}\psi(\vec{R}_\alpha,\vec{r}_i)=E\psi(\vec{R}_\alpha,\vec{r}_i) \tag{2}$$

Where E stands for the total energy of the molecule, ψ stands for the whole wavefuntion of the molecule, while depends on all the positions of nuclei and electrons. when all the nulei are fixed, the Schrödinger equation for electron motion becomes:

$$\hat{H}_e\psi_e(R_\alpha,r_i)=E_e(R_\alpha)\psi_e(R_\alpha,r_i), \tag{3}$$

Where $\hat{H}_e=T_E+V_{NE}+V_{EE}$, $E_e(R_\alpha)=E-V_{NN}(R_\alpha)$

We obtain results for Ee and ψe under special positions Ra fixed by solving(3), but they are what we are not interested in here.

What are emphasized are the motions of nuclei. Therefore, we first write down the whole wavefuntion as a product of electron wave function and nucleus wavefuntion:

$$\psi(R_\alpha,r_i)=\psi_e(R_\alpha,r_i)\psi_N(R_\alpha) \tag{4}$$

substituting (4) into (2), thinking of $T_N\psi_e\psi_N\approx\psi_eT_N\psi_N$, and taking (3) into account.

We have $$\hat{H}_N\psi_N(R_\alpha)=E\psi_N(R_\alpha) \tag{5}$$

Where $$\hat{H}_N=T_N+V(R_\alpha)=T_N+E_e(R_\alpha)+V_{NN}(R_\alpha) \tag{6}$$

and E stands for total energy of the moleczule system. The above two equations tell us that nuclei are in motion in a potential field $V(R_\alpha)$. Solving (5) will give us the eigen value E and eigen function $\psi_N(R_\alpha)$.
Neglect the coupling kinetic energy between vibration and rotation and translational motion energy, We have

$$H_N=T_N+V(R_\alpha)=Tr+[T_V+V(R_\alpha)]=Hrot+Hvib \tag{7}$$

substituting (7) into (5), let $\psi_N=\psi_{rot}*\psi_{vib}$, $E=E_{rot}+E_{vib}$, we have

$$H_{rot}*\psi_{rot}=E_{rot}*\psi_{rot} \tag{8}$$
$$H_{vib}*\psi_{vib}=E_{vib}*\psi_{vib} \tag{9}$$

In millimeter wave band, we only need to solve (8).

From the reciprocity of operator, we first find out the eigen function Urot.sym. =Ujkm for symmetric gyro molecule according to the relations of matrix and quantum mechanics:

$$\det[(\ _n|Hrot|\ _n-Erot)\delta_{nn}=0 \tag{10}$$

According to the orthogonality, the inner products have only k possible values. Therefore (10) can be simplified to a finite rank determinant.

$$dit(H_{k'k''}-E_{rot}\delta_{k'k''})=0,\quad k'k''\in[-J,J] \tag{11}$$

Where
$$H_{k'k''}=\int\Phi^*_{JKM}{}'H_{rot}\Phi_{JKM}{}''d\tau$$

$$= \delta_{x}'_{x}''(h/2)\,[(2C-A-B)(K')^{2}+(A+B)J(J+1)]+\delta_{x}''_{x}'_{+2}(h/4)(B-A)[J(J+1)-K'(K'+1)]^{1/2}[J(J+1)-(K'+1)(K'+2)]^{1/2}+\delta_{x}''_{x}'_{-2}(4/h)(B-A)[J(J+1)-K'(K'-1)]^{1/2}[J(J+1)-(K'-1)(K'-2)]^{1/2} \quad (12)$$

and A,B and C are constants depending on moments of inertia about three main axes. Eigen value E_{rot} can be obtained by solving (10).

2.Numerical solution and coparision with measured result.
there are many techniques to solve (11), we use QR technique here. For H_2O molecule, we have

A=80888.48 MHz, B=43066.19 MHz, C=28103.30 MHz

Input them into the computer, we obtain 2J+1 values for each J. After comparing and selecting among these valuesm, the following transitions within millimeter waveband can be found:

J from 5_{-1} to 6_{-5}, $v1=0.76\ cm^{-1}$, $\lambda=13.575$ mm
J from 3_{-2} to 2_{+2}, $v2=6.07\ cm^{-1}$, $\lambda=1.647$ mm
J from 5_{-4} to 4_{0}, $v3=10.83 cm^{-1}$, $\lambda=0.923$ mm

These frequencies have a good agreement with the absorption peaks of measured atmosphere attenuation curve of H_2O molecule. This shows that the physical model and computing method used here are correct and can be used to other kinds of polar molecules.

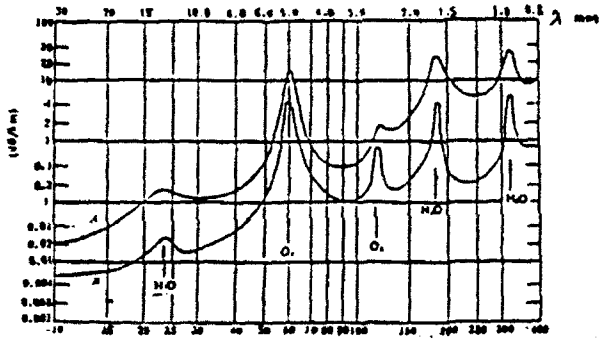

Fig.2, atmosphere attanuation curve: A. sea lever, temperature t=20℃, atmospheric presure P=101325 Pa, water vapour density $\rho=0.075 Kg/m^3$, B. 4Km altitude sky, t=0℃, $\rho=0.001 Kg/m^3$.

ANALYSIS OF INTERACTION BETWEEN MILLIMETER WAVE AND NONPLOAR MOLECULE O_2

1. Basic principle
Fig.3 shows the structure of O_2 molecule. Since its positive and negative charge centers coincide with each other, there is no intrinsic electric dipole moment. EM wave can not cause transition between retational energy levels of the whole molecule. However in the O_2 molecule there are two unpaired electrons located in $1\pi g^*(2P_x)$ and $1\pi g^*(2P_y)$ orbits respectively. Because their self-spins are in the same direction, there exists a intrinsic megnetic moment. This magnetic moment precesses around the applied magnetic field (such as the orbit magnetic field), and the precessions will be quantized. This quantization is so called reorientating quantizion of self-spin.

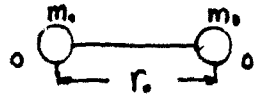

Fig.3 structural scheme of O_2 molecule

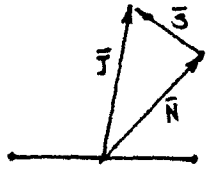

Fig.4 vector scheme of electronic total moment of O_2 molecule

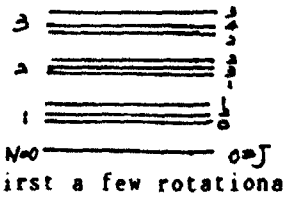

Fig.5 first a few rotational energy levels of 3Σ state

As shown in Fig.4, the electronic total moment of moment of the molecule J is the vectorial summation of its total orbital moment of momentum N and total self-spin moment of momentum S. According to the vectorial summaton principle in quantum mechanics, J=N+S, N+S-1, ……, N-S. Because each unpaired electron has self-spin quantum number S1=S2=1/2, the two electrons spinning in the same dirction have quantum member of total self-spin moment of momentum S=S1+S2=1, therefore J=N+1, N, N-1. That means that each given energy level N will split into three sublevels as shown in Fig.5. Their spectum terms are as follows:

$$F_1(N)=BN(N+1)+(2N+3)B-\lambda-[(2N+3)^2B^2+\lambda^2-2\lambda B]^{1/2}+\gamma(N+1) \quad (13)$$
$$F_2(N)=BN(N+1) \quad (14)$$
$$F_3(N)=BN(N+1)-(2N-1)B-\lambda-[(2N+1)^2B^2+\lambda^2-2\lambda B]^{1/2}-\gamma N \quad (15)$$

Where both λ and γ are conatants, $\lambda=1985$ cm, $\gamma=-0.008$ cm, $B=h/(8I)$, and stands for the moment of inertia.

Let $\Delta J=\pm 1$, $\Delta N=0$, we get two series of absorption spectrum lines:

$$\nu_+(N)=F_2-F_1=-(2N+3)B+\lambda-\gamma(N+1)+[(2N+3)^2B^2+\lambda^2-2\lambda B]^{1/2} \quad (16)$$
$$\nu_-(N)=F_3-F_2=(2N-1)B+\lambda+\gamma N-[(2N-1)^2B^2+\lambda^2-2\lambda B]^{1/2} \quad (17)$$

When these transitions occur, the rotational states and vibrational states do not change, so these spectrum lines can only called as electron self-spin reorientation spectrum lines.Besides, according to spectrum theory and symmetry of rotational energy levels, it can be proved that the O_2 molecule has only energy levels whose N=odd number.

2. Numerical solution and comparision with measured result.

From structral and physical parameters of molecule, we have B=1.43777 cm. Besed on (15)and (16), the computer provides the following:

N	$\nu_-(N)$	$\nu_+(N)$
1	2.8671	1.8767
3	2.3672	1.9490
5	2.1643	1.9870
7	1.9726	2.0150
9	1.9446	2.0386
11	1.920	2.060
13	1.900	2.080
15	1.880	2.099
17	1.860	2.118
19	1.842	2.137

Fig.6 N dependences of $\nu_-(N)$ and $\nu_+(N)$

Observation of the numerical solution shows that both two spectrum lines lies around wavelength $\lambda=1/\nu=5$ mm. That indicates that this wavelength should be a absorption peak. This peak almost is the same as that in measured atmospheric attenuation curve of O_2 (see Fig.2). Therefore, it can be expected that the physical model and analytical method used here are suitable for other kinds of nonpolar molecules.

(This project was supported by Natural Scientific Fund of China)

W7.3

Far IR transmission spectra of $YBa_2Cu_3O_{7-\delta}$ thin films

A. HADNI, X. GERBAUX,

Laboratoire Infrarouge Lointain, Laboratoire de Minéralogie, Cristallographie et Physique Infrarouge, URA CNRS 809, Université de Nancy I B.P. 239 F-54506 Vandoeuvre-les-Nancy, France.

It is shown that transmission measurements of the normal phase in the Far IR (FIR), (i.e. $\nu < 120$ cm^{-1}), lead directly to plasma frequency ν_p if d.c. conductivities measurements are available. It is found that ν_p is a constant in the normal phase to within experimental errors, and since d.c. resistivity appears as a linear function of temperature, collision frequency ν_c is also a linear function. For one sample (3), $\nu_p = 4300$ cm^{-1} and $\nu_c = 1.07\ T + 27$ cm^{-1}, with $\nu_p^2 = \dfrac{N_0 e^2}{m\ \epsilon_0\ \epsilon_\infty\ (2\pi c)^2}$.

At higher frequencies, i.e. beyond 120 cm^{-1} and still in the normal phase , transmission decreases, while it should increase with frequency in the assumption of a simple Drude model. To explain that decrease, and also the small value observed for the transmission in the near IR (e.g. 10% at 4000 cm^{-1} for the MgO plate coated with a 1000 Å YBaCuO film), a strong highly damped oscillator has to be assumed in the Mid IR. The most simple model is made of one overdamped oscillator centered at $\nu_o = 360$ cm^{-1} where neutrons diffraction (14) has reve-

aled a broad peak in the phonons density of state. The quite unusual strength and damping necessary to fit the experimental data is not yet understood but should come from the high density of carriers in the ab plane.

For the superconductive phase at 7 K, the FIR transmission data (e.g. 1% transmission at $\nu = 20$ cm^{-1} for the MgO plate coated with one superconductive film, increasing with frequency), can be roughly retrieved by keeping the same plasma frequency found in the normal state (e.g. $\nu_p = 4300$ cm^{-1}), and putting $\nu_c = 0$. In fact, the observed transmission is higher than calculated, depends on the quality of the sample, and suggests a two-phases composition.

Some of these conclusions (2, 3) are close to those of Fiory et al obtained by a quite different method (14).

References

1 - X. GERBAUX, A. HADNI, M. TAZAWA and J. HUBSCH, Phase Trans. 30, 173 (1991)

2 - X. GERBAUX, M. TAZAWA, A. HADNI and J. HUBSCH, SPIE 1341, IR Technology, 239-243 (1990)

3 - X. GERBAUX, M. TAZAWA, A. HADNI, J. HUBSCH and A. KITADE, Infrared Phys. 31, 517-526 (1991)

4 - W. HO, P.J. WOOD, W.F. HALL, P. KOBRIN, A.B. HARKER and R.E. DE WAMES, Phys. Rev. B. 38, 7029 (1989)

5 - P.G. QUINCEY, P.B. WHIBBERLEY and J.R. BIRCH, Solide State Comm. 76 (1990)

6 - K.F. RENK, H. ESCHRIG, U. HOFMANN, J. KELLER, J. SCHUTZMANN and W. OSE, Physica C, 165 1 (1990)

7 - G.P. WILLIAMS, R.C. BUDHANI, C.J. HIRSCHMUGL, G.L. CARR, S. PERKOWITZ, B. LOU and T.R. YANG, Phys. Rev. B, 41, 4752 (1990)

8 - M.K.CRAWFORD, G. BURNS and F. HOLTZBERG, Solid State Comm. 70, 557 (1989)

9 - D.R. TILLEY and J. TILLEY, "Superfluidity and superconductivity" - Adam Hilger (1990), 3rd Edition

10 - L. GENZEL, A. WITTLIN, M. BAUER, M. CARDONA, E. SCHONHERR and A. SIMON, Phys. Rev. B, 40, 2170 (1989)

11 - A. HADNI and X. GERBAUX, Infrared Phys., 30, 465 (1990)

12 - M. TINKHAM, "Far Infrared Properties of Solids", Ed. S.S. MITRA et S. NUDELMAN, Plenum Press New York, p. 223 (1970)

13 - T. TIMUSK, Phys. Rev. Lett., 66, 663-666 (1991)

14 - A.T. FIORY, A.F. HEBARD, R.H. EICK, P.M. MANKIEWICH, R.E. HOWARD and O; MALLEY, Phys. Rev. Lett., 65, 3441-3444 (1990)

15 - B. RENKER, F. GOMPF, E. GERLING, D. EWERT, H. RIETSHEL and A. DIANOUX, Z. Phys. B, 73, 309 (1988)

16 - R. FEILE, U. SCHMITT, P. LEIDERER, J. SCHUBERT and U. POPPE, Physica C, 152, 494 (1988)

17 - R. FEILE, Physica C, 159, 1-32 (1989)

18 - D.J. FRANK and M. TINKHAM, Phys. Rev. Lett., 50, 1611 (1983)

19 - K. KAMARAS et al, Phys. Rev. Lett., 64, 84 (1990)

20 - K.F. RENK et al, Physica B, 165 et 166, 1253-1254 (1990)

21 - VAN DER MAREL, BAUER et al, Phys. Rev. B, 43, 8606-8609 (1991)

W7.4

ABSORPTION PROPERTIES OF PURE WATER VAPOR AT 297, 343, 412 AND 460 GHz

N. I. Furashov and V. Yu. Katkov
Radiophysical Research Institute
Lyadov Str. 25/14, Nizhny Novgorod, Russia

The nature of the infrared and microwave absorption by water vapor in the transparency windows remains still not clearly understood. Partially, this is due to the lack of experimental information needed. As for the existing experimental data on pure water vapor absorption properties in the near millimeter wave region, they are incomplete and contradictory (see, for example [2].

In the present study, the dependence of the pure water vapor absorption coefficient on the pressure and temperature has been determined at frequencies of 297, 343, 412 and 460 GHz, which corresponds to the window regions. The experiments were performed using a multitransverse absorption cell of 2.5 - m base length, a backward wave oscillator and pneumatic detector of the Golay type. In measurements, the path length of the cell was 140 m, the cell temperature and pressure were varied from 285 to 350K and from 0 to 30 Torr (r.h. $\leq$ 90%), respectively.

In agreement with the theory of H_2O spectral line broadening, the absorption measured with an accuracy of $\pm$ 0.1 to $\pm$ 0.3 dB km^{-1} is proportional to the pressure squared. At the same time, the normalized absorption coefficients γ (in dB $km^{-1}Torr^{-2}$) deduced from the pressure dependencies with rms errors of 6,4,5 and 3% at 297, 343, 412 and 460 GHz, respectively, are significantly higher (up to 7 times at 297 GHz) than those predicted by the kinetic line shape. Besides, the absorption decreases more rapidly with the increase in temperature T than the theory predicts. In addition, its temperature dependence differs noticeably from the power law and can be reproduced within the above uncertainties by a sum of two power-law functions:

$$\gamma = \gamma_1(300/T)^{n_1} + \gamma_2(300/T)^{n_2} .$$

Since this relationship is not pronounced so that all four of its parameters could be determined independently, the experimental data fit is made under the assumption that the parameter n_1 has the theoretical value. By assuming this, we suppose that any rate the wings of the nearest H_2O lines depend on the temperature in approximate accordance with the prediction. The results obtained from the least-squares fit to the data are given in the Table as compared with the theory.

Frequency		297	343	412	460
Theory	γ_1	0.0025	0.0054	0.0108	0.0305
	n_1	3.7	3.5	3.6	3.3
Experiment	γ_1	0.0065	0.0077	0.0164	0.0310
	γ_2	0.00645	0.0121	0.0133	0.0224
	n_2	14.1	10.9	11.6	10.2

It is seen from the Table that the experimental values of γ_1 are systematically higher than the calculated ones. Therefore, apart from the nature of a strong temperature dependent absorption term, the kinetic line shape is not correct. In this connection it should be noted that in spite of the generally accepted standpoint the quadratic over humidity components of the atmospheric absorption coefficients at 343 and 412 GHz obtained by us earlier at 306K [2] are not equal to the normalized pure water vapor absorption coefficients corresponding to the same frequencies and temperature; the former are about 1.5 times less than the latter. Moreover, preliminary results of another study indicated that the wings of the 380 GHz pure water vapor line are not described by the kinetic line-shape (as well as by Lorentz and Van Vleck-Weisskopf formulas) indeed.

Thus, some disparities have been found between the classical theory of molecular absorption by water vapor and the experiments which are unambiguously associated with inaccuracies of classical

line shapes beyond the line core. However, the principal question of a strong temperature dependent absorption term attributed to the far H_2O line wings or not cannot be yet answered.

REFERENCES

1. Atmospheric Water Vapor, Ed. A. Deepak, T. D. Wilkerson, and L. H. Ruhnke, Academic Press, 1980.

2. N. I. Furashov and V. Yu. Kathov, Int. J. IR and MM Waves, 1985, vol. 6, No. 8, pp. 751-764.

W7.5

APPLICATION OF IR AND FIR RADIATION IN HIGH MAGNETIC FIELD SPECTROSCOPY

N. Miura

Institute for Solid State Physics, University of Tokyo,
Roppongi, Minato-ku, Tokyo 106, Japan

The IR and FIR laser magnetospectroscopy in high magnetic fields is a powerful means for solid state physics. Tuning the magnetic energy levels in substances by magnetic fields with the incident photon energy, we can observe resonant structures in the spectra arising from electronic transitions such as cyclotron resonance or impurity transitions. In high magnetic fields, the energy of the cyclotron motion, $\hbar\omega_c = \hbar eB/m^*$ (B is the magnetic flux density, and m^* is the effective mass) becomes very large, and hence high resolution measurements become possible. The cyclotron resonance becomes observable even in very low mobility semiconductors, since the condition $\omega_c\tau > 1$ is easily satisfied. Moreover, as $\hbar\omega_c$ exceeds various excitation energies in solids, a variety of new phenomena are expected to occur in very high magnetic fields. On the other hand, the radius of the cyclotron orbit, $l = \sqrt{\hbar/eB}$ becomes very small with increasing fields, and it can be reduced to a size even comparable with the lattice constant in sufficiently high magnetic fields. We can expect that the effect of the reduction of the wavefunction extension also gives rise to new phenomena.

The recent progress of pulse magnet technology has enabled us to measure the infrared magneto-optical spectra up to very high magnetic fields. At ISSP, we have developed several techniques for generating ultra-high magnetic fields. We can generate ultra-high fields up to 450T by the electromagnetic flux-compression technique, up to about 200T without destroying samples by the single-turn coil technique, and long non-destructive pulse fields up to about 50T by the conventional type of solenoid pulse mangets[1]. These magnetic fields have been successfully employed for investigating cyclotron resonance and impurity spectroscopy in semiconductors, high field spectroscopy of high T_c superconductors, *etc.* by combining the fields with molecular gas lasers at infrared and far-infrared wavelength range. In this paper, we report the latest results on the cyclotron resonance in low mobility semiconductors, such as diamond, SiC and AlAs, as well as the anomalous temperature dependence of the effective mass and the new type of combined resonance in Pb-compounds.

Figure 1 shows a typical example of the experimental traces of the magnetic field pulse and the cyclotron resonance signals in n-type 3C-SiC at a wavelength of 119μm from an H_2O laser. The magnetic field produced by the single-turn coil technique reaches 150T at its maximum, and has the same magnitude twice on the

increasing and decreasing slopes. For $B//< 100 >$ axis, two resonance peaks are observed on both the slopes, corresponding to the light mass and heavy mass valleys at the X-points. Although the duration of the field pulse is very short, of the order of $5\mu s$, we can obtain accurate absorption curves by using a very fast detector of doped Ge cooled to liquid He temperatures. For the shorter wavelengths from a CO_2 laser and a CO laser, a photovoltaic HgCdTe detector was employed. Investigating the resonance fields at various wavelengths as shown in Fig. 2, we found that the conduction band of 3C-SiC is very parabolic up to 53.8meV showing no sign of the camel's back structure which has been observed in GaP. A number of impurity transitions were also observed at low temperatures below 100K for different wavelengths. We found that the lines are from three different kinds of donor levels which have different binding energies. In p-type SiC, cyclotron resonance was observed corresponding to the effective mass of $0.45m_0$.

Semiconducting diamond as well as SiC has been considered to be a promising material for future devices operating at rather high temperatures. In IIb-diamond, classical cyclotron resonance abosorption peaks were observed corresponding to the heavy hole(m_h^*), light hole(m_l^*) and the spin-orbit-split-off(m_{so}^*) bands for the field directions parallel to the $< 100 >$, $< 110 >$, and $< 111 >$ axes, for the wavelengths between $28\mu m$ and $119\mu m$. It should be noted that the hole resonance in the split off band is observed with a comparable intensity in the high energy range due to the very small spin-orbit splitting (~6meV). Figure 3(a) shows the cyclotron resonance for three different field directions at λ=$119\mu m$, and Fig. 3(b) shows the resonance for three different wavelengths. The resonances of thermally excited carriers were observed only at relatively high temperatures above about 280K. Owing to the high magnetic fields, well-defined peaks were obtained in spite of low mobilities at high temperatures. Some of the peaks were observed in the electron-active circular polarization indicating negative masses of holes. We found that the effective masses were very different from those obtained by Rauch[2] at lower magnetic fields and low temperatures. The γ-parameters were determined analyzing the data on the basis of a set of the 3×3 Luttinger-Kohn Hamiltonian. We found that the effective mass of light holes and heavy holes are negative in some directions. This arises from the strong mixture of the heavy and light hole bands with the split-off hole band which is located very close to the two bands. It is interesting to note that the Landau level structure of the valence band in diamond is very different from those of Ge and Si which are well known, due to the very small spin-orbit splitting.

AlAs is an important material as barrier layers for GaAs-AlAs quantum wells or superlattices, but the details of the band structure has not been well known because of its low mobility. In n-type AlAs, the cyclotron resonance was observed corresponding to the effective mass of $0.47m_0$ at a photon energy of 10.4meV[3]. No resonance peak was observed at a field corresponding to the mass of about $1.1m_0$ which has been observed in 2D samples at lower fields. This suggests the existence of the camel's back structure near the X-point. However, there is also a possibility

that the observed mass of $0.47m_0$ corresponds to the heavy mass.

Pb-chalchogenides have been known to be narrow gap semiconductors, and to have large temperature dependence of the band gap. They are of interest from a viewpoint of the structural phase transition, since PbGeTe or PbSnTe solid solutions show a transition from the cubic to the rhombohedral phase at some temperatures. In sufficiently high magnetic fields we can expect to observe the phase transition in PbTe which does not show any phase transition at finite temperatures. In PbSe and PbTe, anomalously large change of the effective mass with temperature has been observed by measurements in a wide temperature range. The large change cannot be explained by simply taking account of the temperature change of the band gap within the framework of the $k \cdot p$ theory. This suggests that there are some factors other than the band gap which determines the temperature dependence of the effective mass[4]. This was examined also by a comparison between PbTe and PbSe and by a measurement in Mn-doped PbSe samples in which the band gap can be varied by the Mn concentration. Figure 4 shows typical examples of the cyclotron resonance curves in p-type PbTe samples at CO_2 laser wavelengths. An anomalous absorption peak (indicated by 'X' in the figure) was observed, and this peak was found to change the relative intensity to the heavy mass peak (denoted as 'H') with changing wavelength and temperature. The anomalous peak was assigned as the combined resonance involving the spin-flip. This combined resonance becomes allowed due to the large inter-spin level matrix elements in the $k \cdot p$ Hamiltonian, and the crossing of the two Landau levels with opposite spins. It is the first combined resonance which has ever been observed in the Faraday configuration.

References

[1] N. Miura, T. Goto, K. Nakao, S. Takeyama, T. Sakakibara, T. Haruyama and T. Kikuchi: Physica B **155** (1989) 23.

[2] C. J. Rauch: Phys. Rev. Lett. **7** (1961) 83.

[3] N. Miura, H. Yokoi, J. Kono and S. Sasaki: Solid State Commun. **79** (1991) 1039.

[4] H. Yokoi, S. Takeyama, N. Miura, and G. Bauer: Phys. Rev. B **44** (1991) 6519.

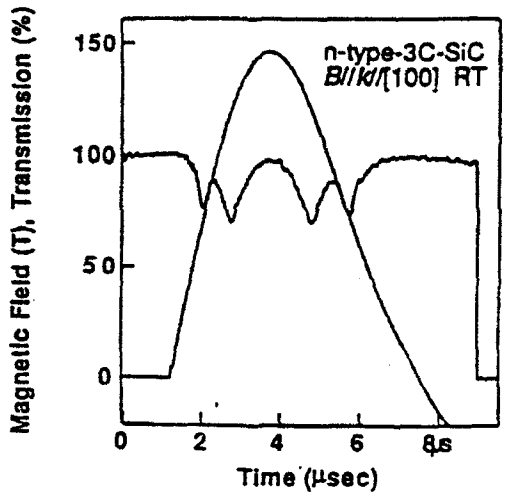

Fig. 1 Recorder traces of the magnetic field pulse produced by the single-turn coil technique and the cyclotron resonance in n-type 3C-SiC at a wavelength of 119μm.

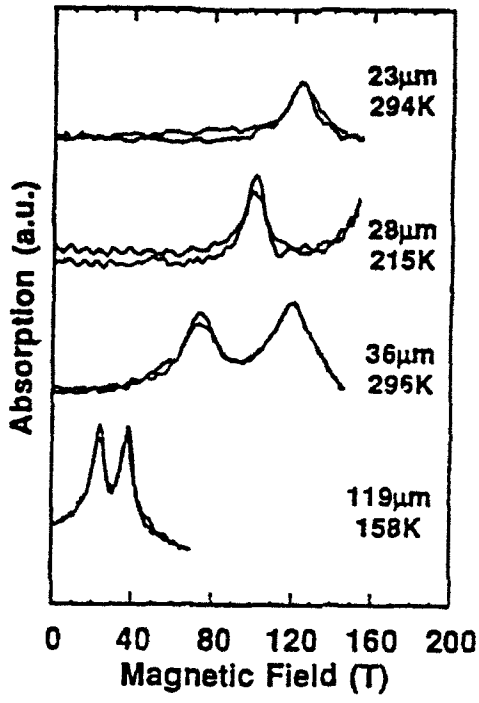

Fig. 2 Cyclotron resonance curves in n-type 3C-SiC for different wavelengths.

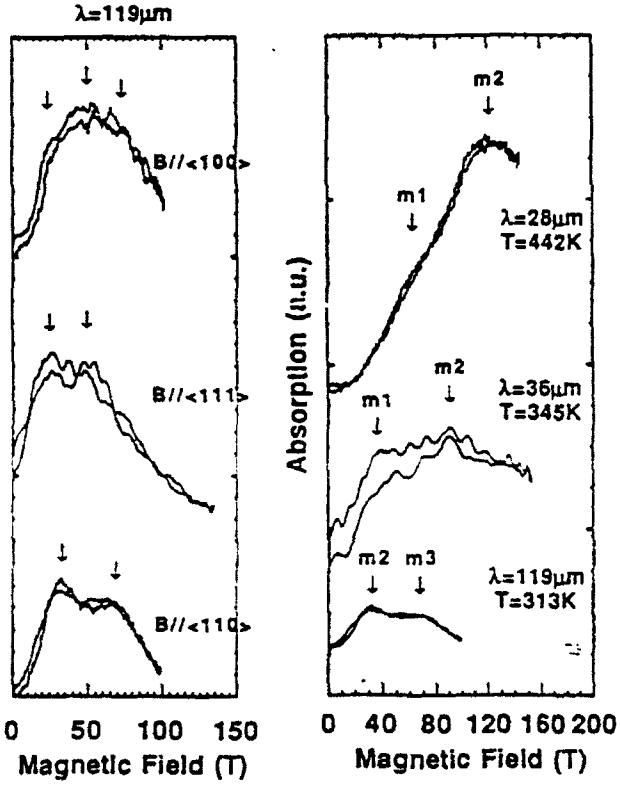

Fig. 3 (a)(left) Cyclotron resonance curves in p-type diamond at 119μm for three different field directions. (b)(right) Cyclotron resonance at various wavelengths.

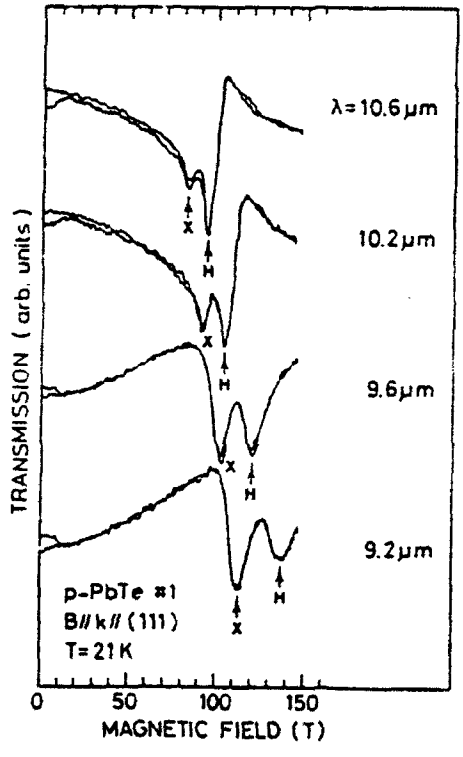

Fig. 4 Cyclotron resonance in p-type PbTe at different wavelengths.

EXPERIMENTAL STUDY OF FOUR-SUBLATTICE ANTIFERROMAGNET $CuCl_2 \cdot 2H_2O$ RESONANCE PROPERTIES

V. V. Eremenko, S. A. Zvyagin, V. V. Pishko, Yu. G. Pashkevich, V. V. Shakhov

In the present paper antiferromagnetic resonance (AFMR) in four-sublattice rhombic antiferromagnet $CuCl_2 \cdot 2H_2O$ for different orientations of an external magnetic field is studied experimentally. The comparison of experimental results with calculations of dynamic susceptibility for different magnetically ordered phases as well as studying the exchange mode (EM) and acoustic mode (AM) interactions are perfomed.

Measurements were performed using a submillimeter transmitting radiospectrometer. The spectrum was scanned by a pulsed magnetic field. Backward-wave tubes served as microwave sources and a n-InSb crystal cooled up to the liquid helium temperature served as a detector. The experimental temperature was 1.8 K.

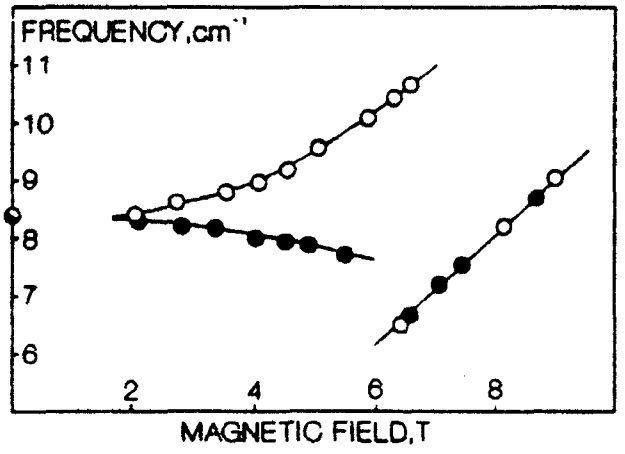

Fig. 1

1. To align an external magnetic field parallel to the crystal b-axis, the field-frequency dependence (FFD) of AM and EM ω_{2387} (see notations in ref.[1]) absoption is presented in Fig.1 by white dots. Theory [1] predicted EM ω_{1388} aproaching to AM with magnetic field rising. Experimentally that mode was not observed. For interpretation of the experimental result, let us estimate high-frequency (HF) susceptibility of four-sublattice rhombic $CuCl_2 \cdot 2H_2O$ and apply the method described in [1,2]. For the Γ_{3e}

phase the high-frequency susceptibility as a frequency (ω) function can be defined as follows

$$\chi_{xx}(\omega) \simeq (4S_0)\frac{(g\mu_b)^2}{\hbar V_0}\frac{\omega_{eM}^{2467}}{\omega^2-(\omega_{eM}^{2467})^2}\left(\frac{D}{E_2}\right)^2\sqrt{\frac{E_2+E_0\beta^2}{E_2}},$$

$$\chi_{yy}(\omega) \simeq \frac{\omega_{eM}^{1388}}{\omega^2-(\omega_{eM}^{1388})^2}(1-\beta^2)\left(\frac{D}{E_2}\right)^4\frac{D^2}{(E_2+E_0\beta^2)E_2^{1/2}(E_2-E_0\beta^2)^{1/2}}\beta^2\frac{(g\mu_b)^2}{\hbar V_0},$$

$$\chi_{zz}(\omega) \simeq (4S_0)\frac{(g\mu_b)^2}{\hbar V_0}\frac{\omega_{eM}^{2467}}{\omega^2-(\omega_{eM}^{2467})^2}\left(\frac{D}{E_2}\right)^2\sqrt{\frac{E_2}{E_2+E_0\beta^2}},$$

where S_0 - is the ion spin, E_2 - the intralayer ferromagnetic exchange, E_0 - the interlayer antiferromagnetic exchange, D - the Dzyaloshinsky-Moriya interaction constant, μ_b - the Bohr magneton, g - the g-factor, $E_2=E_0+E_2$, V_0 - the unit cell volume, $\beta=H_y/E_0$, H_y - the external magnetic field parallel to the y-axis. For χ_{yy} the residue is seen to be anomalously small in the entire field H_y region. Therefore the EM absorption intensity with ω_{1388} is low everywhere. For EM ω_{2467} $\chi_{zz} \ll \chi_{xx}$ which defines the experimental polarization of that mode : the magnetic microwave field component $h_\omega \| a$.

2. Fifure 1 gives also the field-frequency AFMR dependence (dark dots) of $CuCl_2*2H_2O$ in a magnetic field applied in the ab-plane at the angle $\beta=40°$ to the a-axis. It should be noted that in this case the absorption line intensity is comparable with that of ω_{2467} at H||b.

3. If an external magnetic field is oriented parallel to the crystal c-axis, the magnetically ordered phase Γ_{4e} with ω_{2388} and ω_{1467} exchange modes is realized. We have calculated high-frequency susceptibility of those modes. For ω_{1467} χ_{zz} is small for the whole field H_z region and the EM absorption intensity with ω_{1467} is extremely small.

For ω_{2388} at $H_z \ll H_m=(E_0*E_2)^{1/2}$ where H_m is the field of intersection of EM and AM FFD, $\chi_{xx} \gg \chi_{yy}$, so that the excitation of EM ω_{2388} should be observed at $h_\omega \| a$.

At $H_z \approx H_m$ HF susceptibility can be written down as

$$\chi_{xx}(\omega) \simeq \chi_{yy}(\omega) \simeq \frac{1}{2}(4S_o)\ \frac{(g\mu_b)^2}{\hbar V_o}\ \frac{\omega_{eM}^{2zee}}{\omega^2-(\omega_{eM}^{2zee})^2}\ \frac{\omega_{eM}^{2zee}}{E_o}\ .$$

The above calculation of EM ω_{2zee} showed only a slight slope of its FFD (the resonance frequency softening is 0.4 cm^{-1} in a magnetic field of 5 T). It makes impossible to observe the EM ω_{2zee} corresponding absorption line while scanning the spectrum by a magnetic field. That result is confirmed by the absence of sample "bleaching" at 8.4 cm^{-1} for EM ω_{2zee}.

The symmetry analysis gives evidence about the interaction between ω_{2zee} EM and AM which can occur and should be accompanied with an intensity rising of EM while approaching AM (as well as at H||a) and deformation of AM FFD. We have studied in detail the assumed interaction region, however, the above features have not been detected.

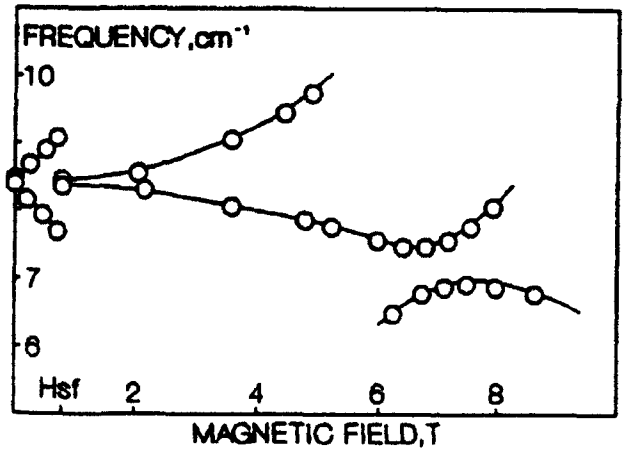

Fig.2

4. Figure 2 presents AFMR FFD in $CuCl_2 \cdot 2H_2O$ for an external magnetic field H||a. An accuracy of the sample orientation in a magnetic field is ±3′. The absorption spectrogram at 9.1 cm^{-1} is shown in Fig.3. Peculiarities of an absorption signal in the intermediate state are described in detail elsewhere [3].

In the zero field resonance frequencies for the upper and lower EM proved to be equal to 8.45 cm^{-1} and 8.4 cm^{-1},

respectively. The absorption contour along the frequency axis was restored using sample "bleaching" in an external magnetic field near 8.4 cm^{-1} with the step of 0.03 cm^{-1}.

In a magnetic field of about 7 T the interaction between EM

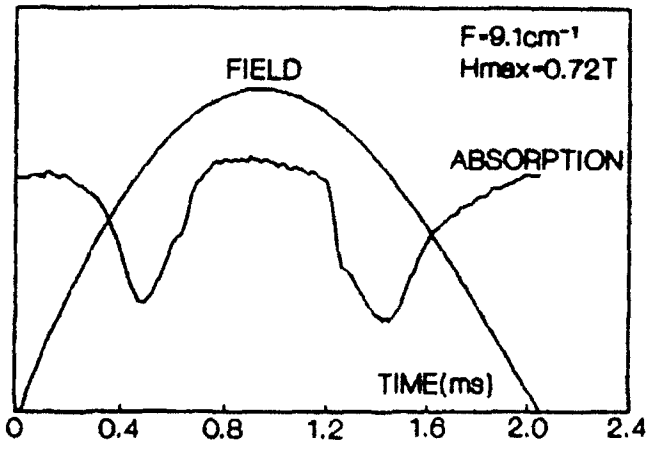

Fig.3

and AM was observed upon their approaching each other accompanied with the typical intensity transfer from a stronger AM to a weaker EM and their FFD splitting.

The anisotropic exchange interaction constant D, being the "coupling parameter" of EM and AM, was obtained from the least difference of interaction mode frequencies in the vicinity of the interaction field. As a result, the tangent of sublattice magnetization canting angle in the zero field was defined to be $tg\alpha=0.07$. The α angle value is in a good agreement with the data obtained in [4] by nuclear magnetic resonance.

[1] Pashkevich Yu.G.,Sobolev V.L.,Shahov V.V., Sov. J. of Low Temp. Phys., 1986, v.12, N-9, p.545

[2] Bar'yakhtar V.G.,Eremenko V.V.,Naumenko V.M.,Pashkevich Yu.G., Pishko V.V.,Sobolev V.L., JETP (Russ.), 1985, v.88, N-4, p.1382

[3] Eremenko V.V.,Klochko A.V., Naumenko V.M., Pishko V.V., Sov. J. of Low Temp. Phys., 1985, v.11,N-3, p.179

[4] Kubo T.,Yamahaku H.,Phys.Rev.B, 1985, v.32,N-3, p.1831

W7.7

E-BEAM IONIZER-SUSTAINER LASER ON ROTATIONAL TRANSITIONS OF MOLECULES

E.Ya.Kogan, N.E.Molevich

Pedagogical Institute, Samara, Russia

Pure rotational lasers can work in IR and FIR spectral range. To create the power pure rotational laser it is necessary to overcome the rapid rotational relaxation (RRT). In [1] it has been suggested to use for the pumping of the rotational laser the excitation of vibrational levels and the intramolecular vibration to rotational (VRT) energy transfer. For the diatomic molecule the last mechanism of vibrational ralaxation has been in detail discussed in review [2]. The peculiarity of VRT-relaxation as compared with VT-relaxation is the resonant transfer of the molecular vibrational energy to its high excited rotational states and only then to translation energy by RRT-channel. Such way of the relaxation is possible for the hydrogenous diatomic molecules, e.g., hydrogen halides and for the certain polyatomic molecules. In molecule HF at VRT-relaxation of level with vibration quantum number V=1 can be excited rotational levels with quantum number $J \geq 13$, at relaxation of V=5 - level can be excited even rotations with $J \geq 30$. Taking into account the comparatively slow rate of high rotational states relaxation, under the certain conditions such excitation made "over" can lead to the appearance of the rotational population inversion. The similar effect has been observed during the chemical reactions with the creation of the high vibration excited HF-, OH-, OD-, NH-molecules [3,4] and their generation on pure rotational transitions.

In [5] the high power pure rotational gasdynamic laser due to vibrational excitation of HF-H_2 mixture has been investigated. In [6] we suggested to use the vibrational excitation of molecules in e-beam ionizer-sustainer discharge for the generation in FIR

spectral range. In the present work we in detail investigate the similar discharge in a HF-H_2-Ar mixture.

The important peculiarity of HF-discharge is the different ranges of the effective vibrational excitation of HF by the electron-molecule collision (electron energy U~1V) and electron attachment (U>2,5V). Therefore it is possible to use the mixtures with the relatively great fraction of HF-molecules (1%) and to inject a large power in the internal molecular states by the e-beam discharge.

The stability of such discharge in mixtures HF-H_2-Ar (pressure P≥1atm) has been experimentally verified in [7,8], where the e-beam ionized-sustainer laser on the vibrationally rotational transitions of HF was investigated at constant electric field $E/N \sim 10^{-17} - 10^{-16}$ V cm^2. The generation in the range λ=2,7-3 μm has been obtained. But the windows were not transparent for the radiation with λ >9 μm. Thus it was not investigated the possibility of the longwave radiation from pure rotational transitions. However in [7] the laser worked on many lines of each vibrational band (V=1-3) simultaneously and it indirectly testified the rotational non-equalibrium of HF. Energy output of laser [8] was less than 50 μJ (impulse duration τ=2,5 μs). In the reported spectrum range the more power laser already existed and such e-beam laser on the vibration-rotation transitions of HF did not pay attention. The possibility to obtain the more longwave generation in this mixture seems be more attractive.

We has been conducted the numerical modeling of the discharge in HF-H_2-Ar mixtures. The kinetic model describes the evolution of the 25 rotational levels (J=0-24) at the 4 vibrational states (V=0-3) of HF and the 4 vibrational states of H_2 (without rotational structure). This model includes VRT-, VT-, VV- and RRT-relaxation, the vibrational pumping by the electron-molecule collisions, which

is averaged with the help of the electron energy distribution f(U). It includes also the equation for the gas temperature and Boltzmann non-stationary equation to define f(U). The last equation takes into account the influence of the constant electric field, ionization, electron attachment, elastic and inelastic electron-neutral collisions. The electron energy loss at the rotational excitation of the molecules is described in diffusion approximation. The electron density n_e can be obtained by equation

$$\frac{dn_e}{dt} = Q - K_r n_e^2 - K_a n_e n_{HF},$$

where Q is the rate of electron-ion pairs creation by e-beam, K_r, K_a are constants of the recombination and attachment averaged with f(U), respectively.

This model permits to define the optimum discharge parameters and the laser characteristics. In the mixture $Ar:H_2:HF=100:10:0,5$ (P=1at), ionized by a beam of the high energy electrons (U≈200kV, I≈0,1A/cm) at the optimum constant electric field the maximum inversion of population has been obtained on the transition J=14 → J=13 ($\Delta N \gtrsim 10^{15}$ cm^{-3}). It is known, that the cross section for the stimulated retational emission of HF is about two orders of magnetude larger than for the vibrational emission: $\sigma \gtrsim 2\ 10^{-13}$ cm^2. Hence, such population inversion results in a high gain of the active medium ($\alpha \gtrsim 10$ cm^{-1}). The partial inversion of the vibrational levels is not exceeded 10^{13}-10^{14} cm^3. Thus gain, corresponding the emission with $\lambda \approx 2,7\text{-}3\ \mu m$ is in the thousand times smaller than in the longwave range ($\lambda \approx 10\text{-}20\ \mu m$). The estimated power of the such rotational laser is P ~ kW/cm^3 in 20 μ s-impulse. The experimental investigation of the gain on the rotational transitions can confirm the efficiency of VRT relaxation channel.

1. V.I.Igoshin, N.E.Molevich, A.N.Oraevski. Sov.Kvantovaya Electronica, 1984, V.11, P.1515.
2. V.I.Igoshin, N.E.Molevich, A.N.Oraevski. Sov.Himiya Vysokih Energi, 1987, V.20, P.3.
3. R.L.Wilkins. J.Chem.Phys., 1977, V.67, P.5838.
4. E.R.Sirkin, G.C.Pimentel. J.Chem.Phys., 1981, V.75, P.604.
5. V.I.Igoshin, N.E.Molevich, A.N.Oraevski. Int.J.Infr. and Millim. Waves, 1984, V.5, P.403.
6. E.Ya.Kogan, N.E.Molevich, A.N.Oraevski, A.M..Soroka, V.A.Sheglov. Sov.Himicheskya Physica, 1987, V.6, P.41.
7. S.R.Byron, L.Y.Nelson, G.J.Mullaney. Appl.Phys.Lett., 1973, V.23, P.565.
8. R.M.Osgood, D.L.Mooney. Appl.Phys.Lett., 1975, V.26, P.201.

W8.1

STUDY OF A GUNN OSCILLATOR WORKABLE IN DUAL BANDS

Liu Xinghua
Dep. of Information and Electronics, Zhejiang University

Abstract

An oscillator workable in both Ku- and Ka-band whichconsists of only a single Gunn diode is described in this paper.The oscillator's outout power is greater than 15mw in the fundamental frequency range from 17-20 GHz(Ku-band), and exceeds 3mw in the second harmonic frequency range from 34-40 GHz(Ka-band).

INTRODUCTION

The Gunn oscillator is one of the most important solid-state millimeter-wave source.It possesses such advantages as low FM noise and a wide operating frequency range, and is, therefore, extensively used in millimeter-wave systems as a local oscillator. Useful output powers from Gunn diodes have been observed in the 95-GHz range, as early as 1975(1). Since then, a lot of work has been done in theories and experiments to extract the output power as large as possible at the harmonic from Gunn diodes. In 1985, John E. Carlstrom, Richard L. Plambeck and D. D. Thornton reported an encouraging experimental result that for the second harmonic Gunn oscillator with a continuous tuning range from 65-115 GHz which is based on a disk and post resonator with a mechanically adjustable post length, its output power is greater than 2mw, and exceeds 10mw from 80-102 GHz. Of late years, a good many research works for this field have also been made, and a howling success has already been had in China.

In this paper, a Gunn oscillator workable in both Ku- and Ka-band, in which the Ku-band is correspoding to the fundamental mode and the Ka-band corresponding to the second harmonic, is described. This type of oscillator has the advantages of making full use of its frequecy spectrum resources and being able to work in the desired higher band without the traditional frequency multiplier circuit.

DESIGN AND ANALYSIS OF CIRCUIT

An equivalent circuit of the oscillator is shown in Fig.1. The basic theorem of this oscillator is such that the output power for fundamental frequency is directly coupled out from the fundamental cavity resonator known as a master resonator, and the output power for the second harmonic, which is generated inside the master cavity due to the nonsinusoidal characteristic of the current flowing through the diode, can be coupled out through a particular type of coupling assembly. Such an assembly must simultaneously have the two functions as follows: 1. it can completely trap the fundamental energy within the master cavity. 2. the second harmonic in the cavity can be easily coupled out through it. The simplest method to accomplish the two

functions is to use a section of waveguide through which the fundamental mode can not propagate but the second harmonic can. This is the way usually adopted to extract the harmonic power from the Gunn diode oscillator.

From the above theorem, it follows that the master cavity is crucial for this type of oscillator. Whether its design is reasonable or not directly determines the performance3 of the oscillator. In addition, the following must be considered in design:

1. When the fundamental and the second harmonic energy are coupled out from the master cavity, a coupling coefficient should be selected to be such a value that the output power may be coupled out at suitable level, whereas the coupling should bot be made so tight that the Q value of master cavity heavily decays, resulting in an unstable operation.
2. Gunn diode is a low-impedance one, so that reduced-height waveguide mounts have to be used in order to achieve a better impedance match to the low-impedance diode.
3. The bias choke in this oscillator should work normally over both the fundamental and harmonic frequency bands simultaneously. Any RF signal leakage from the oscillator bias choke shouldn't apear in both frequency bands.
4. The mechanical tuning must be continuous without any frequency and power jumps in both frequency bands.

Based on the above considerations, many experiments on the fundamental cavity have been carried out first, and the experimental results are illustrated in Fig.2. This clearly indicates that resonance frequencies for full height waveguide cavity are almost independent of the plunger positions. This is due to the effect of the coaxial mode with the mounting post as the center conductor and the top and bottom waveguide walls as end planes rather than that of the waveguide mode designed primarily, so that its resonance frequency is mainly determined by the waveguide height and is independent of the length of the waveguide cavity. At first the oscillator frequency increases as waveguide height is reduced, but when the height is reduced to some level, the tuning plunger starts to play an important role, or the frequency of oscillation could vary with different positions of the plunger. At this time the coaxial oscillating mode is replaced by the waveguide oscillating mode in the resonator. Also, it has been found from our experiments that as the waveguide height is continuously reduced, the range of tuning frequency will be gradually expanded, but a further reduction of height will not result in an evident expasion of the frequency range. According to these experimental results obtained above, we choose h=b/2=4mm as the height of fundamental cavity so that the oscillator has a wider frequency range of mechanical tuning and could porvide a better impedance-match to Gunn diode.

After the fundamental resonator is determined, the next step is how to take out the fundamentall and second harmonic from it separately, and meanwhile, the fundamental mode in master cavity will not be disturbed in the one hand and there is not any coupling between them at the output in other hand.In our practically used circuits, in order to make the configuration of oscillator not so complicated to machine, we made use of two mutually perpendicular sections of tapered waveguides to connect them to Ku-and Ka-band standard waveguides and to output the fundmental and second harmonic powers, respectively. The bias choke circuit in (2) by a increased scale is transplanted in our

oscillator. The configuration of experimental circuit is shown in Fig.3, where 1-fundamental cavity, 2-Gunn diode, 3-fundamental tapered waveguide section, 4-second harmonic tapered waveguide section, 5-frequency tuning plunger.

THE RESULTS OF EXPERIMENTS

The results of experiments for the Gunn oscillator are shown in Fig. The oscillator's output power is greater than 15mw in the fundamental frequency range from 17-20 GHz,and exceeds 3mw in the second harmonic frequency range from 34-40 GHz.

When requiring a purer frequency spectrum, We can insert two bandpass filters corresponding to the above described frequency bands at the places A and B of the Gunn oscillator in Fig.3 so as to suppress those higher harmonic frequencies, and this can also improve the isolation one port from the other.

THE PROSPECT OF APPLICATIONS

Although our present oscillator circuit is used for the purpose of experiment, it may be exhibited from the experimental results that the oscillator frequency spectrum resources could be exploited as fully an effectively as possible by this type cf one diode-multiband oscillator circuit. And we might predict that it would, perhaps, provide a wide prospect of applications in future in the following fields:

1. This type of oscillator circuit is, surely, an effective way of expanding the bandwith of RF source without much additional cost. When applying it to an instrument, PIN modulation circuits can be placed in waveduide 3 and 4 to apply modulation signals.
2. If a varactor is mounted neer the Gunn diode in the fundamental cavity, an electrical tuning oscillator is formed which can meed the needs of the applications for communications and electronic warfare.
3. A high stability oscillator can be constructed by putting a dielectric resonator into the fundamental cavity, or by placing a high Qinvar cavity near the fundamental cavity,so that some kind of mode in invar cavity may be coupled to the fundamental cavity so that some kind of mode in invar caviuty may be coupled to the fundamental cavily through an aperture.

The author believes that this type of oscillator would, of course, be applicable to many other fields besides those as already mentioned above.

REFERENCES

(1).T. G. Ruttan, "Gunn-diode osillator at 95GHz, "Electron. Lett.,VOL. 11, PP.293-294, July 1975.
(2).John E. Carlstrom, Richard L. Plambeck, and D. D.Thornton,"A continuously tunable 65-115-GHz Gunn oscillator, "IEEE Trans. Microwave Theory Tech., vol. MTT-33, PP.610-619, July 1985.

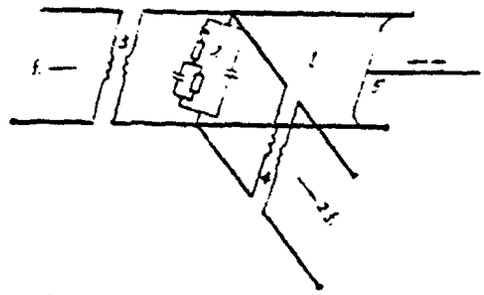

Fig.1. Equivalent circuit of the Gunn oscillator.

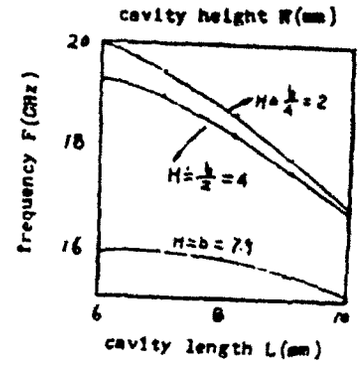

Fig.2. Tuning curves for the fundamental cavities of various heights H.

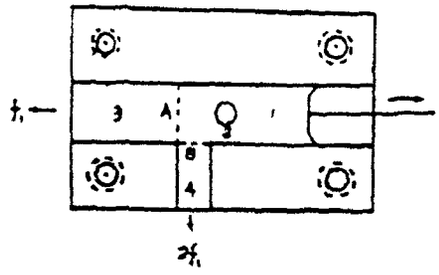

Fig.3. Bottom view of the Gunn oscillator.

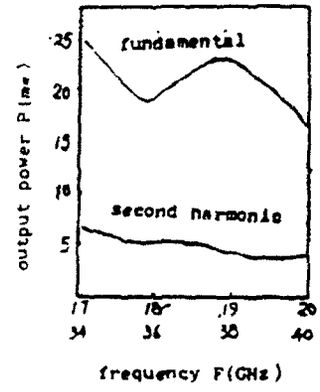

Fig.4. Output powers versus fundamental and second harmonic frequencies.

TUNING PERFORMANCE OF Ka-BAND RADIAL LINE VARACTOR CONTROLLED OSCILLATORS

Nizar Sultan

President, Canadian Space & Telecom Inc.- CSAT
Orleans, Ontario, Canada

ABSTRACT

A Gunn-varactor Voltage Controlled Oscillator, VCO, proposed earlier by Ondria, using cap or disc structures separating the diodes across the narrow wall of a waveguide, is analyzed theoretically and experimentally at Ka-band. Almost any desired bandwidth, centre frequency and oscillation power can be tailored to the requirements.

Comparison of the experimental results to the theory shows excellent correlation. This provides a design tool for such a cost effective millimeter wave VCO in which a single cavity with replaceable discs and diodes can provide a whole range of VCO's.

1. INTRODUCTION

Some satellite and electronic warfare applications at Ka-band, 26 to 40 GHz, require solid-state oscillators that are rugged, cost effective and fast electronically tunable over the maximum possible tuning bandwidth possible.

An oscillator mechanically tunable with a cap or disc structure across a waveguide was first proposed by Misawa (ref. 1) using an IMPATT diode. Later on, Ondria achieved oscillations with a similar structure but with a Gunn diode as the source (ref. 2). He then added a varactor diode on the other side of the disc across the narrow wall of the waveguide, as in fig.1, to obtain the fast wideband electronically tunable Voltage Controlled Oscillator, VCO.

Both Ondria and Solbach et al. achieved oscillations experimentally at the fundamental and harmonic frequencies respectively, (refs. 3-5). Later on, Sultan developed a new and complete equivalent circuit and software that can theoretically predict the complex structure VCO tuning characteristics to high accuracy. This paper outlines the novel concept of "double radial line" introduced in the theory and provides typical experimental results and some comparison with the theory.

2. CAVITY DESCRIPTION

Fig. 2 below shows the details of the cavity structure. The key issue that made the theoretical analysis possible is the realization that such a complex microwave waveguide structure contains two sets of interdependant "double radial transmission lines".

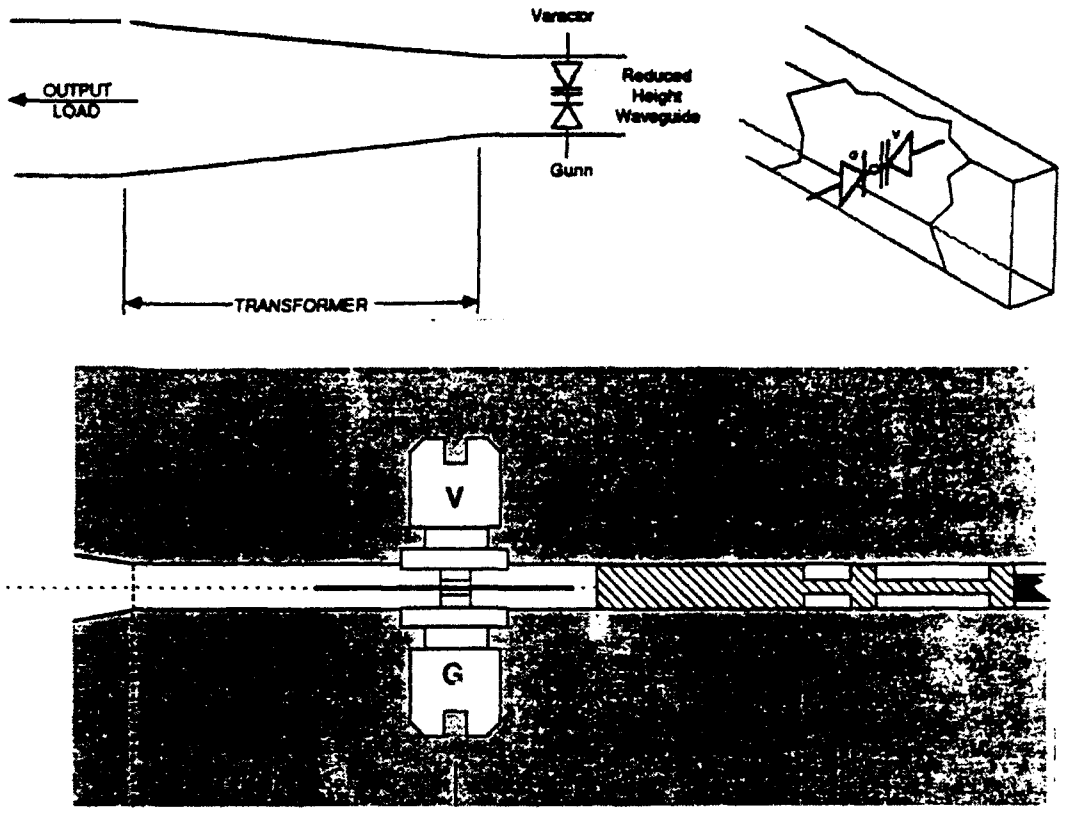

Fig. 1- Varactor Controlled Gunn Oscillator using two radial line discs separating the two diodes in series.

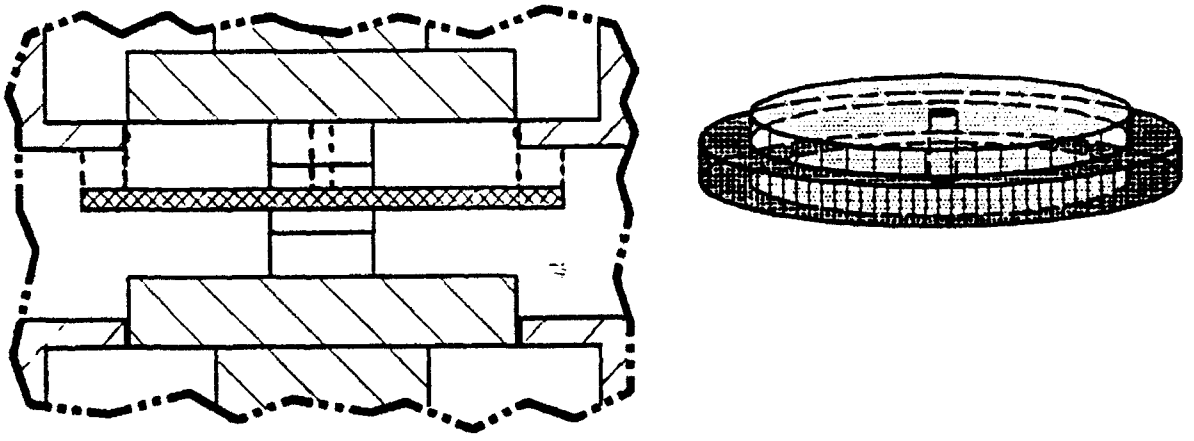

Fig. 2- Radial lines structures used to derive the theoretical analysis.

3. PARAMETRIC ANALYSIS

The theoretical and experimental analysis investigated the VCO tuning characteristics: tuning range, power and centre frequency. These are functionsof many parameters such as:

varactor bias, varactor characteristics, Gunn bias, Gunn caracteristics, each radial line disc diameter, each radial line disc position, the sliding short circuit distance, etc.

4. SELECTED RESULTS

Typical tuning response of such a VCO is shown in fig. 3a. Tuning ranges of 3.7 GHz and powers as high as 60 mw were achieved at Ka-band. The theoretical predictions of the experimental results were demonstrated, as shown in fig.3b. In some cases, the effect of a disc displacement by a few mils only can be predicted with sufficient accuracy and was found to have a critical effect on the tuning characteristics of the VCO. Fig. 3c displays the effect of the waveguide cavity sliding short on the electronic tuning range.

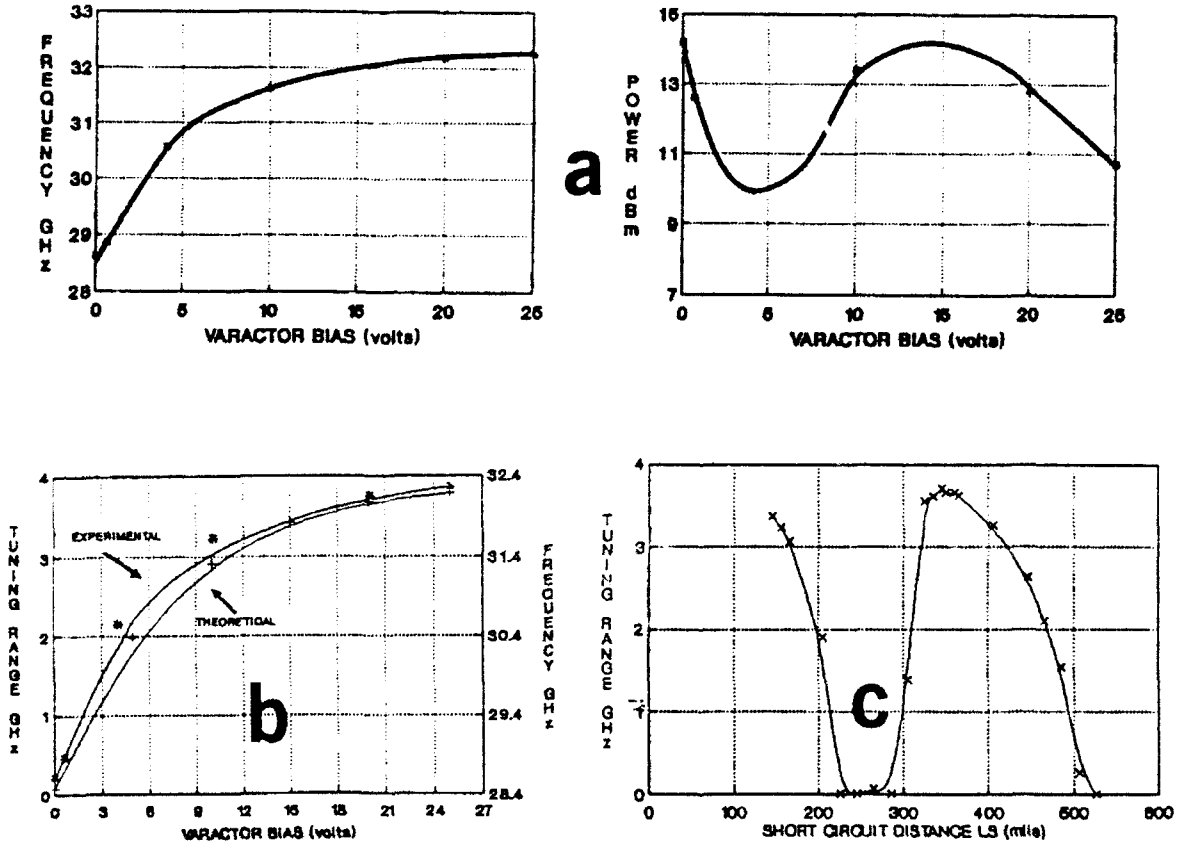

Fig. 3 VCO Tuning performance: a- Typical experimental results, b- Comparison of theory to experiments, c- Electronic tuning range dependance on short position.

5. CONCLUSION

The recognition that such a VCO structure contains double radial lines is the key issue to resolving theorically the analysis of this waveguide VCO. Almost any desired bandwidth, centre frequency and oscillation power can be tailored to the requirements. Comparison of the experimental results to the theory shows excellent correlation. This provides a design tool for such a cost effective millimeter wave VCO in which a single cavity with replaceable discs and diodes can provide a whole range of VCO's.

6. ACKNOWLEDGMENTS

This work was sponsored by the Defence Research Establishment Ottawa DREO, Canada and performed in part while at Canadian Astronautics Limited, Ottawa, Canada. Special acknowledgments are due to Dr F. Palmer and Messrs. A. Sewards, L. Rowlandson and P. Yansouni for their continued support at DREO. The author is grateful to Mr. R. Meierer for his valuable contribution to the software development. He is also grateful to all involved at Canadian Astronautics Limited, particularly Mr. M. Gale for initiating the Millimeter work at CAL, Mr. G. Koutsavakis for project management support and Mr. T. Mascioli for his assistance in project support.

7. REFERENCES

1 -T. Misawa, "An Oscillator Circuit With Cap Structures For Millimeter Wave IMPATT Diodes" IEEE Vol. MTT-18. 1970.

2 -J. Ondria, "Wide-band mechanically tunable and dual in-line radial mode W-band cw Gunn diode oscillators" 7th Biannual Conf. Active Microwave Semiconductor Devices and Circuits, Cornell Univ., N.Y., 1979.

3 -J. Ondria, "Partially integrated electronically tuned millimeter-wave (35-75 GHz) Gunn oscillators", 11th E M C, 1981.

4 -J. Ondria, "Novel approaches to wide electronic tuning bandwidth in solid-state millimeter sources", SPIE, 1982.

5 -K. Solbach, F. Sickling & H. Barth, "Harmonic Gunn oscillators allow frequency growth", Microwaves & RF, 1983.

6 -N. Sultan, "Theoretical Analysis & Experimental Verification of Wideband Tunable Radial Line Millimeter Waveguide Voltage Controlled Oscillators", 15th International Conference on Infra-Red and Millimeter Waves, Dec. 10-14, 1990.

7 -N. Marcuvitz, "Waveguide Handbook", New York Dover Publications, 1965.

8 -N. Sultan & G.T. Wright, "Electronic tuning of the Punch-Through transit-time (PITT) microwave oscillator", IEEE Vol. MTT-20, No. 11, 1972

W8.3

U—BAND HIGH STABILIZED GUNN OSCILLATOR

Cao Jihua and Zhong Jinming
(University of Science and Technology of China, Hefei, China)

ABSTRACT

A series of millimeter—wave high stabilized Gunn oscillators has been developed using the construction of transverse rod circuit proper to this laboratory. This paper takes the U—band for an example and analyzes the frequency locked principle of this kind of the cavity—stabilized oscillators by the numerical method of computer. Using this construction we have developed several U—band high stabilized Gunn oscillators (UHGO's) which frequency is 50.30, 53.74, 54.96, 57.95 and 58.65 GHz, respectively. When the embient temperature changes in the range from $-5°$ to $+45°$, the temperature coefficient of these UHGO's is in the range of 10^{-6}— $10^{-7}/℃$. This paper also shows the several elements which cause the mode of UHGO to jump and how these mode jumps are avoided.

I. INTRODUCTION

UHGO is used to make high sensitivity receiver in regions of secret communication, meteorological satellite, interstellar communication, etc.. It's a important device. It is used as a local oscillator in front end of the high sensitivity receiver. Hence, it's quite necessity to investigate the kind of applicable and key devices. Up to the present, many papers reported the analysis of the principle of the cavity—stabilized Gunn oscillator and the experimental results[1-6]. Several oscillating circuits of those Gunn oscillators are all the longitudinal rod circuits, but yet this laboratory used own proper circuit, i.e. transverse rod circuit. The advantages of the transverse rod ciruit are being tuned easily, decreasing the machine damage and possessing good stabilization, etc.. Of course, the design of this kind of cavity—stabilized oscillators must conforms locked principle. It has been confirmed by numerical calculations (see Section Ⅱ).
The measured results are given in Section Ⅲ. The difficult problem about the mode jump of UHGO will be mentioned in Section Ⅳ.

Ⅱ. STRUCTURE DESIGN

UHGO consists of main cavity, stabilizing invar cavity and isolator (see Fig. 1). The equivalent circuit is shown in Fig. 2. Notice, the distance l between the Gunn diode and the coupling operature of the stabilizing cavity is about $\lambda_g/4$ in Fig. 1. But the l of the longitudinal rod osicillator[4] is about $\lambda_g/2$.
From the plane A—A to the left, the input admittance of the stabilizing cavity is given by

$$Y'_e = \frac{\left[G_e - j\left(\omega C_e - \frac{1}{\omega L_e}\right)\right]Y_0^2}{G_e^2 + \left(\omega C_e - \frac{1}{\omega L_e}\right)^2} = G'_e + jB'_e$$

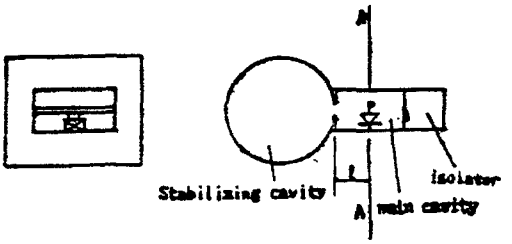

Fig. 1 UHGO configuration

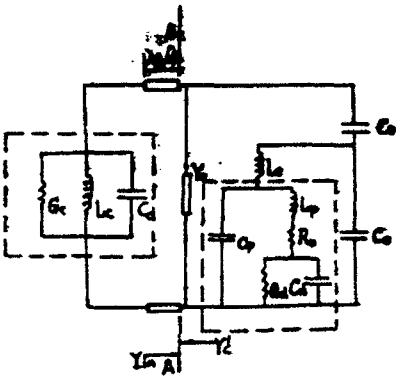

Fig. 2 Equivalent circuit of UHGO

Its response curve $B_c' \sim f$ is shown in Fig. 3. Hence, it is necessary to satisfy

$$\begin{aligned} B_{in} &< 0 \quad \text{for } f > f_0 \\ B_{in} &= 0 \quad \text{for } f = f_0 \quad \text{Condition I} \\ B_{in} &> 0 \quad \text{for } f < f_0 \end{aligned}$$

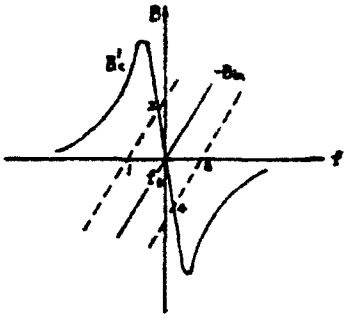

Fig. 3 Diagram of locked principle

The B_{in} changes with the time and the temperature. So that the oscillating frequency f of the Gunn oscillator drifts. For example, when the f drifts to the point 1 (or 3), the frequency of the oscillator is pulled by the stabilizing cavity to the point 2 (or 4). This is just locked principle.

The following calculation will confirm that the transverse rod oscillator satifies Condition I.

See Fig. 2. Form the plane A—A to the right, the input admittance is obtained

$$Y_{in} = \{(j\omega C_e)^{-1} + [j\omega C_c + (j\omega L_c + Y_1^{-1})^{-1}]^{-1}\}^{-1} + Y_0 \qquad (1)$$

where

$$Y_1 = j\omega C_p + [j\omega L_p + R_0 + (G_d + j\omega C_d)^{-1}]^{-1}$$

We separate the imaginary part from Expression (1) to obtain Expression of B_{in}. Substituting the element values into Expression of B_{in} and using the CAD, we obtain a set of numerical results for the frequency and B_{in} (see Table I).

Above element values:

Gunn diode parameters $G_d = -0.03\upsilon$,

$C_d = 0.09$pF, $L_p = 0.1$nH, $R_0 = 0.5\ \Omega$,

$C_p = 0.1$ pF.

Circuit parameters $C_e = 0.02$pF, $L_c = 0.301$nH.

If we take the f = 50.4 GHz as the center frequency, the data (see Table I) satify Condition I. Hence the quenction is confirmed.

Table I: f and B_{in}

f=49.8 GHz	B_{in}= .00019
f=50.0 GHz	B_{in}= .00012
f=50.2 GHz	B_{in}= .00005
f=50.4 GHz	B_{in}= −.00000
f=50.6 GHz	B_{in}= −.00005
f=50.8 GHz	B_{in}= −.00009
f=51.0 GHz	B_{in}= −.00013

Ⅲ. EXPERIMENTAL RESULTS

Table Ⅰ shows the characteristics for several typical UHGO's. These UHGO's have examined through long time. We can see the compensated action of the stabilizing cavity from Table Ⅰ. At room temperature, the frequency essentially return to the prime frequency after forty minutes. When the ambient temperature changes from $-5℃$ to $+45℃$, the temperature coefficient is in the range of $10^{-6}-10^{-7}/℃$.

Table Ⅰ: Characteristics of Seceral UHGO's

No.	f(GHz)	Δf_{max}(MHz) in range of $0''-40'$ at room tenperature	Δf(MHz) between points $0''$ and $40'$ at room temparature	temperature coefficient ($-5°+45°$) (/℃)	Power (mW)
05—28	50.30	2.08	2.01	5.3×10^{-7}	37
09—28	53.74	0.61	0.12	6.0×10^{-7}	54
07—25	54.96	2.20	0.92	7.4×10^{-7}	27
10—30	57.95	1.01	0.03	7.1×10^{-7}	18
15—28	58.65	3.44	2.19	4.4×10^{-7} ($0°-+40℃$)	8

Fig. 4 shows the spectrum photograph of UHGO NO. 10—30. It is observed by a sweep generator. It is can be seen that the oscillator's spectrum is very pure.

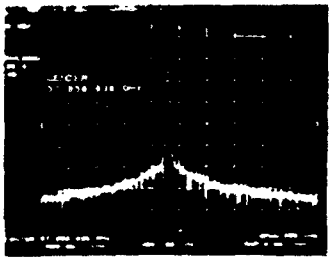

Fig. 4 Spectrum of UHGO No. 10—30

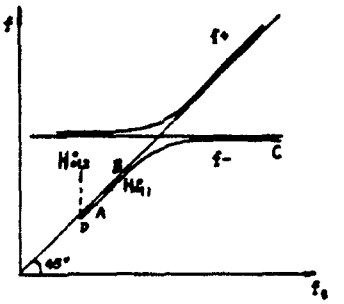

f_0—inherent oscillating frequency of H°_{011} cavity
f —scillating frequency of high stabilized oscillator

Fig. 5 Performance of high stabilized oscillator

Ⅳ. MODE JUMP

1. The Choice of Performance Curve of the High Stabilized Oscillator

The length ot the H°_{011} cavity is tuned by a plunger, the pe-formance curve of UHGO is shown as the f_- — curve in Fig. 5. It only has a single curve. But the longitudinal oscillator has two curves, i.e. the f_+ — curve and the f_- —curve from points B to C[5]. Therefore UHGO has not the mode jump between curves f_+ and f_-.

When UHGO oscillates in the range from A to B, the oscillating frequency can be locked by the high Q cavity and there is no mode jumps.

2. Temperature Effect

The parameter values of some Gunn diodes obvionaly change with ambient temperature, then the performance curves transform, which can also cause mode jump. Therefore, it is necessary that we should do a lot of temperature tests in processes of research and manufacture.

3. Isolator Problem

Generally, the narrow band ($\pm$500 MHz) junction isolator is used in UHGO, because it possesses the advantages of small insertion loss, small volume, low price, etc.. When the reflection coefficient of output load is at a certain value, the equivalent circuit maybe satisfy oscillating condition again at a certain frequency which is beyond the bandwidth of the isolator. This is just mode jump.

Usually UHGO is used as a local oscillator. Only the local oscillator (UHGO) matches completely with the load (mixer), the kind of mode jumps can be vanished.

4. If the Q value of the stabilizing cavity is smaller, the mode jumps as indicated above may occur easily.

5. When the bias voltage at Gunn diode terminals is not suitable, the mode jump may also occur.

REFERENCES

1. Bernard F., IEEE Trans. Microwave Theory Tech., 25(1977) 318.
2. S. Nagano and S. Ohnaka, IEEE Trans. Microwave Theory Tech., 22(1974),1152.
3. I. Goldstein, IRE Trans. Microwave Theory Tech., 5(1957),57.
4. Y. Ito, H. Komizo and S. Sasagawa, IEEE Trans. Microwave Theory Tech., 18(1970),890.
5. S. Nagano and S. Ohnaka, IEEE Trans. Microwave Theory Tech., 20(1972),174.
6. T. Cutsinger, MSN & Communications Technology, 17(13)(1987).

WIDE RANGE TUNABLE SUBMILLIMETER CYCLOTRON RESONANCE GERMANIUM LASER: SPECTRAL CHARACTERISTICS AND APPLICATIONS.

Ya.A.Mityagin, V.N.Murzin, S.A.Stoklitsky, O.N.Stepanov
P.N.Lebedev Physical Institute, Leninsky prosp.53, Moscow,
117924 Russia.

1. Landau levels population inversion in hot carriers system in E and H fields.

The recent investigations of hot charge carriers in semiconductors in strong electric and magnetic fields resulted in the creation of a new class of coherent radiation in the submillimeter wave range – hot carrier p–Ge lasers [1]. The processes of stimulated light emission in hot carrier system can be considered as the transitions between different Landau Levels (LL) of holes in degenerated valence band of germanium. The most interesting lasing process is concerned with cyclotron resonance (CR) type transitions between neighboring light hole LL[2,3]. This type of emission processes attracted much attention due to its narrowband gain spectrum,(see Fig.1) and possibility to continuously tune the emission frequency in considerably wide range by changing of applied magnetic field. In this paper the results of experimental spectroscopic studies of this emission mechanism in p–Ge and quantum model calculation of hole dynamics and LL population in strong $E \perp H$ fields are summarized and possible ways to expand the tuning range of CR lasers are discussed.

The mechanism of LL inversion population, according to our experimental studies and theoretical calculations[4] is related to quantum mixing of light and heavy holes LL in degenerated valence band of Ge in crossed $E \perp H$ fields. As a result of mixing the scattering lifetimes of light holes in LL are strongly influenced by the lifetimes of heavy holes. Since the heavy holes lifetimes(which are involved in streaming motion) are very short, the admixing of heavy hole state to the light hole state substantially reduced the light hole lifetime. The mixing of states decreases with LL number, therefore the light holes in the high levels have a longer lifetimes than in the low LL and a population inversion can arise.

2. Stimulated cyclotron resonance emission p–Ge crystals.

In previous experiments two regions of CR laser emission in p–Ge crystals were found[2,3]. In crystals with acceptor impurity concentration $N_A < 10^{13}$ cm^{-3} CR emission was observed in spectral interval $\nu = 25 - 50$ cm^{-1}($\lambda = 200 - 400$ μm)[4], while in more doped samples ($N_A > 5\ 10^{13}$ cm^{-3}) it was observed in spectral range

$\nu = 70 - 90$ cm^{-1}($\lambda = 110 - 160$ μm)[3]. Our investigation showed that there are two ways to expand the tuning range of CR lasers. Firstly, this kind of emission was found to be very sensitive to E,H fields orientation with respect to crystallographic axes of the sample[5],because of the strong anisotropy of heavy hole subband in Ge. Choosing the proper orientation of E,H fields (namely, H $\parallel$ [110], E at the angle $\varphi = 60 - 70^{\circ}$ to the [110]axis),one can obtain the stimulated CR emission in a range $\nu. = 40 - 95$ cm^{-1}($\lambda = 105 - 250$ μm)[5]. So, in a device with two laser samples made of p–Ge with different doping level it is possible to realize a continuous tuning of the emission frequency over a strikingly wide spectral range $\nu = 25 - 95$ cm^{-1}($\lambda = 105 - 400$ μm)(Fig.2), with the emission linewidth less than 0.2 cm^{-1}[5].

The second way to expand the tuning range of CR laser is to apply a uniaxial stress to p–Ge crystal. Since uniaxial deformation lifts the valence band degeneracy in Ge, it significantly changes the degree of light and heavy hole states mixing, the lifetimes of light holes and the population inversion between the light hole LL. Experimentally a considerable expansion of CR emission range to lower H (and, correspondingly, to the low frequency region) in uniaxially stressed p–Ge was found(Fig.3) [6,7]. The use of a stress allows to obtain in a single properly oriented p–Ge crystal the CR emission frequency tuning in the range $\nu = 30 - 95$ cm^{-1}($\lambda = 105 - 330$ μm). However, it should be noted that CR emission spectrum in a stressed crystal becomes more complicated that in unstressed one. As our calculations show[7] in stressed Ge a population inversion for several pairs of light hole LL can be simultaneously achieved, so the transitions between different pairs of LL may contribute to lasing. This will lead to the splitting of CR emission line, as is observed in an experiment[7,8].

3. Future prospects and applications.

CR germanium lasers are the unique widely tunable sources of coherent radiation which cover a spectral range $\nu = 25$ cm^{-1}– 95 cm^{-1} ($\lambda = 105 - 400$ μm), the pulse emission power being rather high (10 – 100 mW). The linewidth of CR lasers in usual conditions is found to be about 0.1–0.2 cm^{-1} [5]. Subsequent development of CR lasers as monochromatic sources is possible by means of creation of a perfect resonator and magnetic systems.

Undoubtedly, the tunable submillimeter CR germanium lasers can be effectively used in a wide variety of applications: in molecular and cryogenic spectroscopy, in radioastronomy (as a heterodyne source), in nonlinear spectroscopy. Just now the CR lasers are successfully used in solid state physics: in the analysis of shallow impurities in GaAs[9] in the studies of the two dimensional electron gas in GaAs/AlGaAs heterostructures [10].

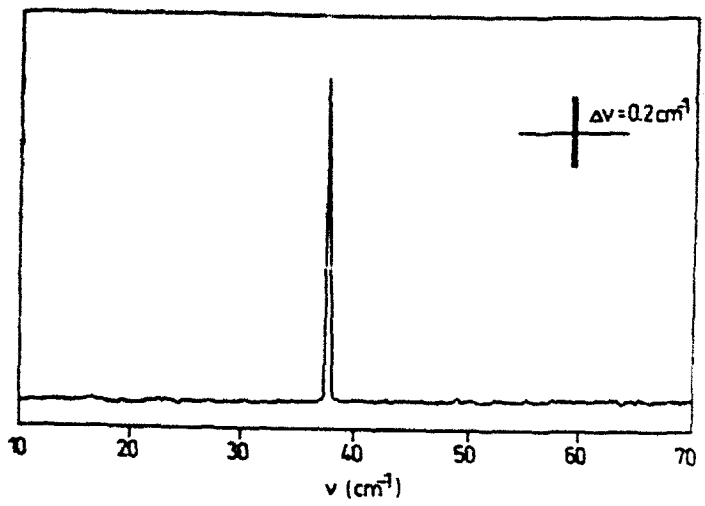

Fig.1 Spectrum of cyclotron type laser emission in p–Ge (N_A = 6 10^{12} cm^{-3}) in E ⊥ H fields (H = 17.3 kOe, E = 1.9 kV/cm).

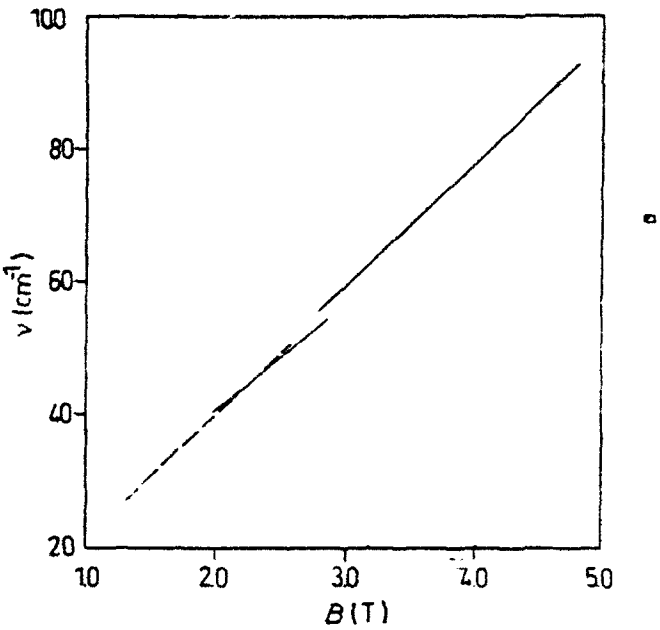

Fig.2 The cyclotron emission frequency versus magnetic field.
(_____) – sample with N_A = 7 10^{13} cm^{-3};
(– – – –) – sample with N_A = 6 10^{12} cm^{-3}; H ∥ [110].

In our experiments we have used the CR germanium laser for the intra–cavity spectroscopy of superconductors in the vicinity of superconducting gap. Attaching the Nb_3Ge film (T_c = 18K) to the waveguide CR laser the noticeable changes of the output lasing intensity were observed . This method can be used for the measurements of impedance and weak absorption in the metals and superconductors in the important frequency range ν = 30–100 cm^{-1}.

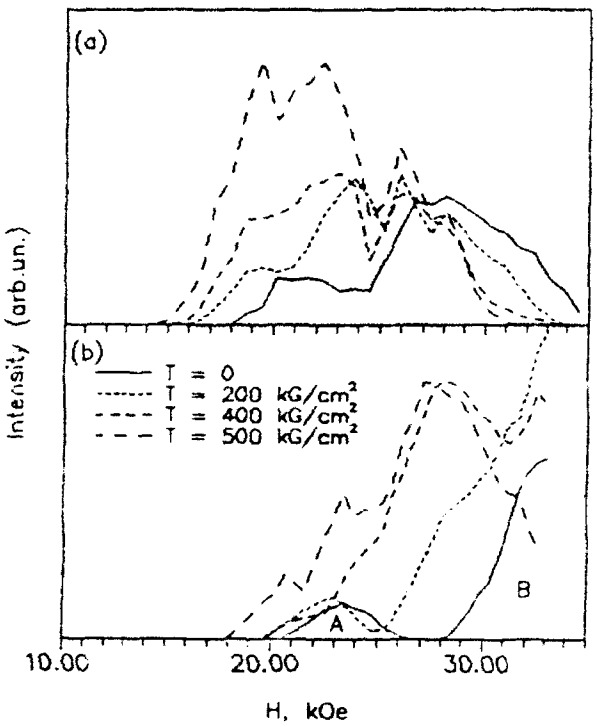

Fig.3 The cyclotron stimulated emission intensity in stressed p–Ge vs. magnetic field
H ∥ [110]
(a) – $\varphi = 60^\circ$ (b) $\varphi = 70^\circ$

References:

1. For a latest review, see the collection of papers *Far–Infrared Semiconductor Lasers* (eds.E.Gornik,A.A.Andronov and A.Miller) published in a special issue of Opt.Quantum Electron. 23(1991).
2. Yu.L.Ivanov,Yu.B.Vasil'ev Sov.Tech.Phys.Lett.,10,398(1984)
3. Yu.A.Mityagin,V.N.Murzin,S.A.Stoklitsky,I.E.Trofimov Sov.Phys. – JETP Lett. 46,144(1987)
4. Yu.A.Mityagin,V.N.Murzin,S.A.Stoklitsky Opt.Quantum Electron.,23, S287(1991)
5. Yu.A.Mityagin,V.N.Murzin,S.A.Stoklitsky,A.P.Chebotarev,I.M.Mel'nichuk Opt.Quantum Electron.,23, S301(1991)
6. V.I.Gavrilenko,V.V.Nikonorov Opt.Quantum Electron.,23, S217(1991)
7. Yu.A.Mityagin,V.N.Murzin,S.A.Stoklitsky,O.N.Stepanov Semicond.Sci.Technol.,1992,(in press)
8. E.Gornik,K.Unterrainer,C.Kremser,Yu.I.Ivanov Proc 20th Int.Conf.Phys.Semicond. Thessaloniki, Greese, p.2467
9. Yu.L.Ivanov Opt.Quantum Electron.,23, S253(1991)
10. E.Gornik,K.Unterrainer,C.Kremser Opt.Quantum Electron.,23, S267(1991)

W9.5

VARACTOR TUNING FOR 3MM HARMONIC OSCILLATORS

Taijun Liu
(Chongqing Institute of Posts and Telecommunications, Chongqing, P.R. of China)
Zhengde Wu, Xiaohong Tang
(University of Electronic Science and Technology of China, Chengdu, P.R. of China)

ABSTRACT

According to the circuit properties of a harmonic oscillator, we present a new idea that is varactor tuning at the fundamental frequency(VTFF) and extracting power from the harmonic frequency(EPHF) for electronic tuning of harmonic oscillators.Then we adopt the idea to design oscillator circuits. Finally, we developed successfully the first 3mm electronically tuned harmonic oscillator in our country in 1988, using a varactor diode made in China which is suitable for a parameter amplifier as an electronic tuning device. The most electronically tuned bandwidth (ETB) of the oscillator is more than 4 GHz. When the ETB is equal to ±100MHz, the output power is larger than 10mW. When the ETB is equal to ±500MHz, the output power is larger than 5mW.

INTRODUCTION

A 3mm electronically tuned oscillator is a key part of a 3mm phaselocked system and a frequency modulation continuous wave system. Because a 3mm electronic tuning varactor diode cannot be made in China and it is impossible to get it from other countries, the only way in which a 3mm electronically tuned oscillator can be researched is to find potentialities of the devices that now we have. Then according to the nonlinear analytic results that we had gotten from a harmonic oscillator,we presented a new idea that is VTFF and EPHF ,and studied possibilities using a varactor diode made in China that is suitable for a parameter amplifier as an electronic tuning varactor diode. On the basis of these we successfully developed the first 3mm electronically tuned harmonic oscillator in our country. Some typical experimental results are given in this paper.

THE NEW IDEA FOR VARACTOR TUNING

A circuit model of a harmonic oscillator is shown in Fig.1,where N1 and Nm indicate describing functions of a dynamic Van der pol model of a Gunn diode.[1] The fundamental frequency loop is on the left,and the harmonic frequency loop is on the right. We define tuning sensitivities as

$$S_i = |\Delta\omega_1|/|\Delta B_i| \qquad (i=1,2)$$

It stands for the fundamental frequency variation in different harmonic loops which are produced by reactance variation per unit. According to calculation , S1 is far larger than S2, that is, the

tuning ranges which are produced by the reactance variation of the fundamental frequency loop are far wider than those which are produced by reactance variation of the 2nd harmonic frequency loop. If a variable reactor is introduced into the fundamental frequency loop to change the fundamental frequency and the 2nd harmonic powers are extracted from the 2nd harmonic frequency loop, we can realize electronic tuning for the 2nd harmonic frequency indirectly. That is our new idea, e.g. varactor tuning at a fundamental frequency(VTFF) and extracting power from the harmonic frequency(EPHF).

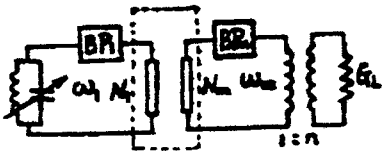

Fig.1 A circuit modle of a harmonic oscilltor

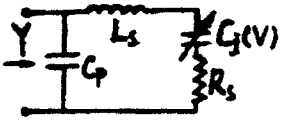

Fig.2 An equivalent circuit of a varactor diode

THE POSSIBILITY ANALYSIS FOR USING A NATIVE VARACTOR DIODE

An equivalent circuit of a varactor diode is shown in Fig.2. Input admittance for a varactor diode is

$$Y = G + jB$$

where

$$G=\frac{\omega^2 R_s C_j^2}{(1-\omega^2 L_s C_j)^2+\omega^2 R_s^2 C_j^2}$$

$$B=\omega C_p\left[1+\frac{C_j}{C_p}\ \frac{1-\omega^2 L_s C_j}{(1-\omega^2 L_s C_j)^2+\omega^2 R_s^2 C_j^2}\right]$$

We chose a varactor diode made in China which is suitable for a parameter amplifier, its parameters are: Ls=0.11nH, Rs=2.448Ω, Cp=0.135pF, Cj(0)=0.216pF,Cj(-4)=0.114pF. According to calculations, when the biased voltage applied to a varactor diode changes from 0V t -4V, the ratio of the relative variation of the equivalent susceptanc at the fundamental frequency (f1=47.2GHz) to that of the equivalent susceptance at the 2nd harmonic frequency is about 213. Hence, the variation of junction capacitance of a varactor diode has far stronger influence upon the susceptance of fundamental frequency loop than upon that of the 2nd harmonic frequency loop. Then if we use the method which is VTFF and EPHF and introduce this kind of varactor diode into the fundamental frequency loop of a harmonic oscillator when we design a electronically tuned oscillator, it is possible to obtain some satisfactory results.

DESIGNING OF THE OSCILLATOR CIRCUITS

There are two essential conditions for a varactor tuning oscillator which are: 1. the energy produced by a active device must effectively couple to a varactor diode; 2. the junction capacitance variation of a varactor diode must cause the variation of susceptance in the external network which we look out from the place where a active device is. According to the two essential conditions, we have carried out computer simulated research on the fundamental frequency equivalent circuit of the oscillator and determined the key elements which affect the performance of the oscillator. Accordingly, we designed a 3mm electronically tuned harmonic

oscillator in which it is easy to debug and control its tuning characteristics.as shown in Fig.3.[2]

EXPERIMENTAL ILLUSTRATION FOR VTFF AND EPHF

There are three structures of the electronically tuned oscillators which are different in output coupling ways, as shown in Fig.4. Fig.4(a) shows a simple structure of an electronically tuned fundamental frequency oscillator. Fig.4(c) shows a structure of an electronically tuned harmonic oscillator. Fig.4(b) shows a special structure in which there is a piece of short standard 3mm waveguide between the harmonic oscillator and the output fundamental frequency waveguide. Because the fundamental frequency is cut off in the standard 3mm waveguide,it can only be coupled to a fundamental frequency load in the form of a fade mode. Fig.5 shows the output characteristics, namely the output frequency as a function of varactor biased voltage for a same electronically tuned harmonic oscillator in which the output coupling structure is respectively one of the three structures described above. From Fig.5 we can see that curve (b) coincides with curve (c) very well except very small deviation. The deviation comes by two reasons. One is that the former has a small load at the fundamental frequency while the later doesn't have loads at the fundamental frequency,and the other is that there are different errors between the measurment syste at the two wavebands and parallaxes caused by the operators. Curve (a) in Fig.5 indicates that the oscillating state of the oscillator has obviously changed and the oscillator has a strong load at the fundamental frequency. So large frequency deviation was caused and the mode jump variation occurred midway. Hence, the fact was proved that the electronically tuned oscillator really operated in the form of VTFF and EPHF.[3]

TYPICAL EXPERIMENTAL RESULTS

Using a 6mm GaAs Gunn diode and a varactor diode which is suitable for a parameter amplifier, we developed successfully the first 3mm electronically tuned harmonic oscillator in our country in 1988, which is shown in Fig.6. Fig.7 shows typical characteristic curves of the oscillators, namely frequency and power as a function of the biased voltage which is applied to varactor diode. According to the curves in Fig.7, we know that the most ETB of the oscillator is more than 4GHz. When the ETB is equal to ±100MHz, the output power is larger than 10mW. When the ETB is equal to ±500MHz,the output power is larger than 5mW. Moreover, the frequency stability is about 10^{-5} after the oscillator being tuning on for half of an hour. The average temperature frequency stability is better than -5MHz/°C within a range of temperature from -50°C to +50°C.

CONCLUSION

Although the junction capacitance variation of a varactor diode which is suitable for a parameter amplifier is nonlinear and the ratio of the junction capacitance variation is very small, we still got some satisfactory results because we made use of the method: VTFF and EPHF.

ACKNOWLEDGMENT

The authors are thankful to prof. Weigan Lin for his constant encouragement during the course of this work.

REFERENCES

1. Zhengde Wu, Electronics Journal, 13(No.4)(1985).36.
2. Taijun Liu, M. E. Degree Thesis, University of Electronic Science and Technology of China, December, 1988.
3. Xiaohong Tang, Dr.E. Degree Dissertation, University of Electronic Science and Technology of China, July,1989.

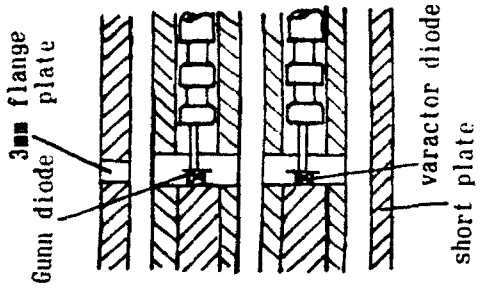

Fig.3 The structure decomposition diagram of a 3mm electronically tuned harmonic oscillator

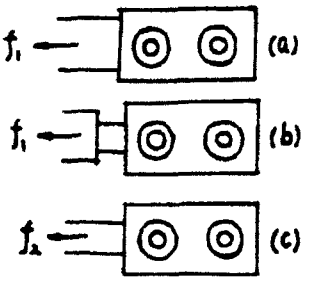

Fig.4 Three structures of the electronically tuned oscillators for illustrating the idea which is VTFF and EPHF

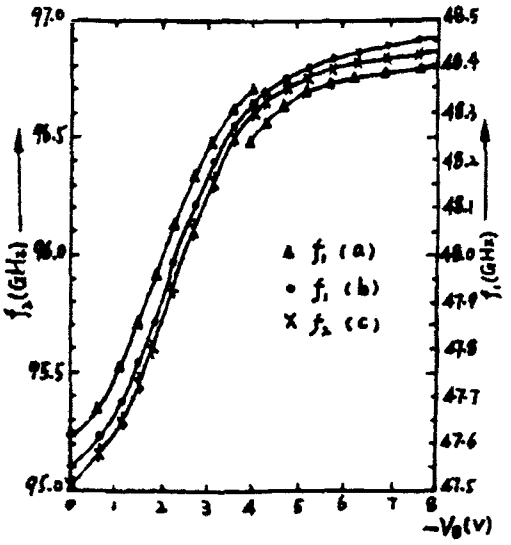

Fig.5 The tuning characteristics of the three structures

Fig.6 A 3mm electronicly tuned harmonic oscillator

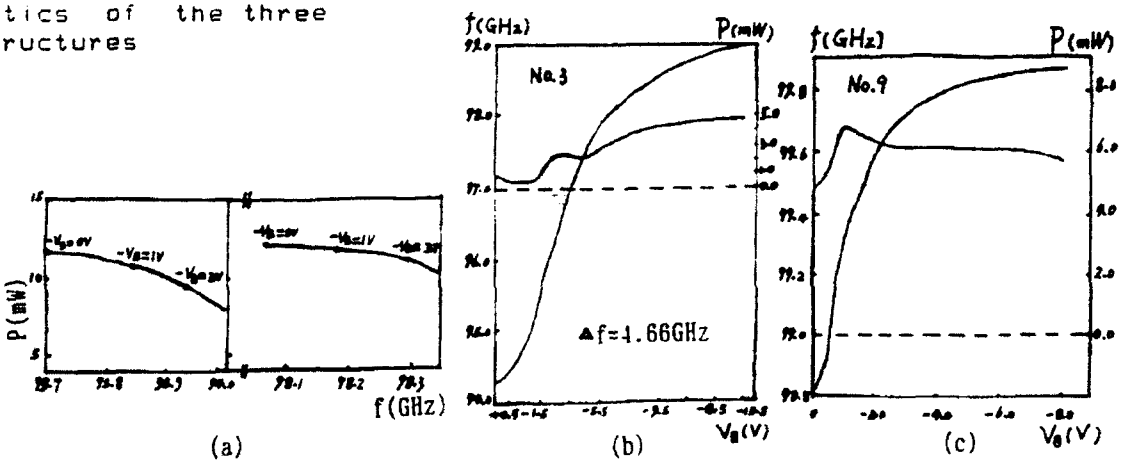

Fig.7 Some typical characteristic curves of the 3mm electronically tuned harmonic oscillators

W8.6

SUPERSLOW WAVES IN PERIODIC STRUCTURES

A.A.Bulgakov and V.D.Korolev

Institute of Radiophysics and Electronics,
Acad. of Science of Ukraine, 12 Proscura st.,
310085 Kharkov , Ukraine

It is known that developing of millimeter and submillimeter (MSM) wavebands is impossible without active elements. Up to date the devices using quantum superlattices and ballistic motion of carriers in submicrone structures are of first rate importance.

In this report we should like to attract attention on a possibility of the creation of semiconductor elements of MSM bands without complicated submicron technology. Distributed interaction of drift carriers in a semiconductor with slow electromagnetic waves is the mechanism which put into effect an instability of electromagnetic waves similar to that one in a travelling-wave tube or back-wave tube. In order to put into operation such interaction it is necessary to provide an equality of velocity of semiconductor drift carriers and propagation wave velocity. It is known that drift velocity is a less than heat velocity, i.e. it has an order of 10^7-10^8 cm/s. In addition, on electromagnetic wave in a solid state propagates with velocity $c/\sqrt{\varepsilon}$ ($c = 3\times10^{10}$ cm/s is the vacuum light velocity, ε is the dielectric permeability), i.e. approximately is equal to 10^9 cm/s. Velocities of surface plasmons and magnetic plasmons also considerably exceed drift velocities [1]. Thus, it is necessary to increase carrier velocities by two or three orders or slow down an electromagnetic wave in order to obtain this synchronism. For increasing velocities it is possible to use ballistic motion of carriers in submicrone structures. In another case we propose to make use the layer-periodical structures consisting of semiconductor and dielectric layers [2].

In vacuum electronics comb-periodic structures became common use to obtain delay. The mechanism of delay in such structures is possible to consider as follows. A period of the structure is a resonator for the electromagnetic wave. The difference of oscillation phases between different resonators leads to propagation of a slow wave along the periodic structure. That velocity of propagation seems as low as we want in the case of almost zero phase difference between adjacent resonators, but it is difficult to realize this situation on account of wave damping calling into action phase erosion. Usually in the

periodic structures delay is of the order of 100.

There are some "resonant" types of waves in semiconductors: surface and volume plasmons and magnetic plasmons. Without damping velocities of these waves can be very low, but in practice damping is relatively high even in pure semiconductors. Therefore velocities of "resonant" waves differ slightly from the light velocity in vacuum. Another situation can be realized in the layer-periodic structure including the layers of a semiconductor ($\varepsilon_1 = \varepsilon_{01}\left[1 - \frac{\omega_p^2}{\omega(\omega + i\nu)}\right]$, where ε_{01} is the dielectric permeability of the lattice, ω_p is the plasmon frequency, ν is the effective frequency of collisions; d_1 is the thickness of the layer) and dielectric (ε_2, d_2). In Fig.1 dispersion curves for non-damping structures are shown

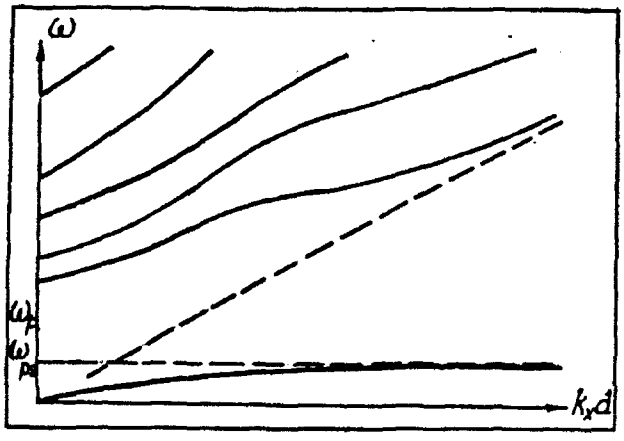

Fig.1.

(k_x is the component of the wave vector directed along layers, $d = d_1 + d_2$ is a period of the structure). It is shown that the lower curve asymptotically tends to the frequency of the surface plasmons $\omega_{ps} = \omega_0 / \sqrt{\varepsilon_{01} + \varepsilon_2}$ (ω_0 is lengmur frequency) propagating along boundaries of the dielectric and semiconductor. Another dispersion curves correspond to the frequency higher than ω_p. In this region the layer-periodic structure behaves like the dielectric lattice. The field structure of the lowest dispersion curve is schematically introduced in Fig.2a for volume and Fig.2b for the surface waves.

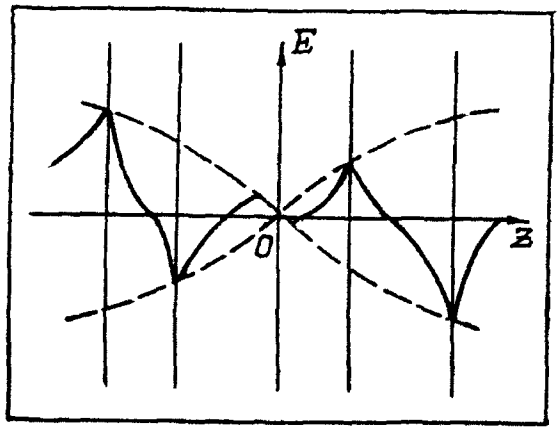

Fig.2a.

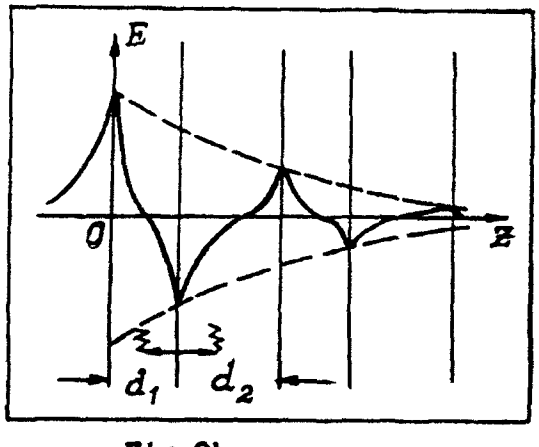

Fig.2b.

Dashed curves are envelopes for the field distributions inside the layers. It is shown from figures that in the infinite structure the field has a periodical character although inside a layer it decreases exponentially from the boundary. In the finite lattice the field decreases exponentially deep into the structure.

The dispersion curve changes its form if we take into account damping in semiconductor layers [3,4] (Fig.3). The longitudinal wave number can be written in form $k_x = k'_x + ik''_x$ and we find that

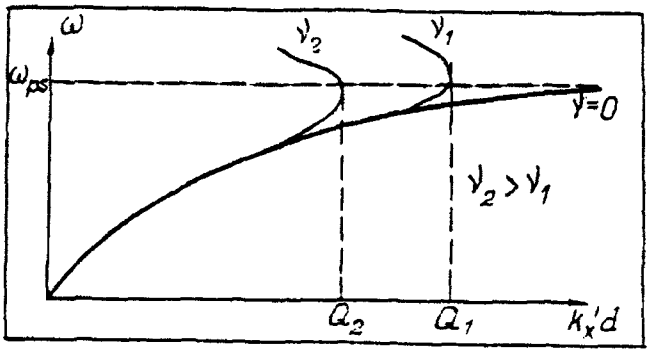

Fig.3.

$$k'_x d \simeq -\ln\left[\frac{\nu}{\omega_{ps}}\,\frac{\varepsilon_{o1}+\varepsilon_2}{\varepsilon_2}\right], \qquad (*)$$

$$k''_x d \simeq -\operatorname{arctg}\left[\frac{\omega_{ps}}{\nu}\right].$$

If frequency of collision $\nu \to 0$, than $k'_x d \to \infty$ and $k''_x d \to -\pi/2$. It is impossible that the value of $k'_x d$ is grater than the value given by formula (*). Let $(k'_x d)_{max} = Q$. The value of Q have been calculated for different structures with InSb as a semiconductor ($\varepsilon_{o1} = 16.7$, $\nu \simeq 10^{11}$ s^{-1}, $\omega_p \simeq 10^{12}$ s^{-1}) and dielectric layers ($\varepsilon_2 = 5$). We have obtained $Q = 2..4$ for the infinite structure, with the magnetic field $Q = 10..15$; for a surface wave in the semi-infinite structure $Q \simeq 50$; in the structure in a metal substrate $Q \simeq 50..70$.

Let us estimate the minimum phase velocity by the formula

$$v_{ph\ min} = \frac{\omega_{ps} d}{Q}.$$

The value of the structure period d is restricted by the formula application of the dielectric permeability. Therefore we have assumed $d \simeq 3..10$ μm for the estimations. In this case phase velocity $v_{phmin} \simeq 10^6..10^8$ cm/s with $\omega_{ps} \simeq 10^{12}$ s^{-1}. The great decay is obtained due to the fact that the investigated wave attenuation is less than in a homogeneous semiconductor since the wave energy concentrated in general in the low losses dielectric layers. In fact, the field in the semiconductor is proportional to $\exp(-\zeta\sqrt{k_x^2 + |\varepsilon_1|\omega^2/c^2})$ and in the dielectric $\sim \exp(-\zeta\sqrt{k_x^2 - \varepsilon_2\omega^2/c^2})$, where ζ is the coordinate counted from the boundary between the semiconductor and dielectric (see Fig.2). Thus, semiconductor layers define dispersion properties of the structure, and dielectric layers define wave

damping. As a result, the low damping electromagnetic wave propagation with the low phase velocity is possible.

1. Kaner E.A.,Yakovenko V.M. *Gidrodinamicheskie neustoichivosty v tverdotel'noy plasme*, Usp.Fis.Nauk , 1975, v.115, p.1,p.41.
2. Bass F.G.,Bulgakov A.A., and Tetervov A.P. *Visokochastotnie svoystva poluprovodnikov so sverhreshetkamy* , Moscow , Nauka, 1989, 288 p.
3. Alfano R.R. Damping effects on the polariton and plasmariton dispersion curves in *n*-GaAs, J.Opt.Soc. of Amer., 1970, v.60, N 1, p.66.
4. Covner G.S.,Alexander R.W., Bail R.G. and Jr.J. Surface electromagnetic waves with damping, Phys.Rev.B, 1976, v.14, N 4, p.1458.

W8.7

HIGHLY STABLE KA-BAND GAAS GUNN MICROSTRIP OSCILLATOR

Zhao Dade, Deng Yanmao, Qin Honggui, Tang Binqian,
Xiang Jialing, Sun Xiaopeng and Shao kai
(Nanjing Electronic Devices Institute, Nanjing, China)

ABSTRACT

A high performance and stabilized Ka-Band GaAs Gunn Full microstrip oscillator has been developed. It is stabilized using a dielectric resontor in a unique hybrid configuration. The oscillator provide 170mw of cw output power at 33GHz,and frequency stability of 9.7ppm/℃.

INTRODUCTION

It is acknowledged that the millimeter-wave microstrip oscillators have the advantages of small size,light weight,and low cost as well as ease of integration. Therefore, the millimeter-wave full microstrip GaAs Gunn oscillator is still the priority for most practical application purposes of fully integrated millimeter-wave receivers.

A number of authors have developed a variety of configurations of millimeter-wave microstrip oscillator,however,all these configurations should be trimming carefully to ensure the "best match".[1,2] This paper describes a novel and very simple Ka-Band full microstrip GaAs Gunn oscillator stabilized with a dielectric resonator. A design of the oscillator has been achieved by considering the package transformed impedance and the impedance of a GaAs Gunn device. By comparison between the computed and experimental results of the microstrip oscillator at Ka band, the availability of this method has been completely verified. This method can be also used in V-band and W-band with simple modification. A very high output power is easily obtained in this microstrip oscillator configuration without any trimming microstrips,showing experimentally the "best match" condition.The matching method described above is superior to that reported before, because it can be practiced for high output power in the circuit layout without an additional timming limit.An 170mW output power at 33GHz and frequency stability of 9.7ppm/℃ represent the state-of-the-art performance using the Ka-band microstrip Gunn oscillator with a dielectric resonator.

OSCILLATOR DESIGN

Fig1. shows the layout of highly stable Ka-band full microstrip GaAs Gunn Oscillator consisting of a packaged GaAs Gunn diode, a dielectric resonator and a microstrip circuit fabricated on a Duroid substrate.The thicknesses of the Duriod,rolled copper and gold film are 0.254mm,14um and 0.7um, respectively.The circuit board is enclosed in a sufficiently small rectangular channel to suppress propagation of higher order modes and guarantee a single quasi-TEM mode at Ka-band.[3] The GaAs Gunn device on a cylindrical stud is inserted into one sidewall of the channel. This structure minimizes parasitic reactance of the device.The Gunn diode made by Nanjing Electronic Devices Institute has 7 ohm

negative resistance in small-signal model, however, it may have a higher negative resistance when the oscillator reaches a steady state.The output matching network consisting of package and microstrip circuit should be able to transfer the negative resistance of Gunn diode to the optimum load. The dielectric resonator has a ε_r=30 and a Tcf=2ppm/℃. The unloaded Q of the resonator is approximately 2000 at 35GHz. The operating frequency of the oscillator is changed readily by the variation of length of the resonator.

OSCILLATOR PERFORMANCE

For testing purposes,the microstrip-to-waveguide transitions consisting of a microstrip probe through a slot in the broad wall of the waveguide are used.These can be eliminated when the oscillator is to be interfaced with other integrated circuit components. Fig.2 provides a photograph of the experimental Ka-band microstrip oscillator. Fig.3 shows the measured output power and frequency , at the waveguide output flange of the microstrip oscillator as a function of bias voltage. The maximum output power measured is 170mw at 33GHz with a DC to RF efficiency of 2.9%.As yet, the microstrip-to-waveguide transition has not been optimised. The discrete GaAs Gunn diode used above is measured to be 210mw(f=33.1GHz) in a waveguide cavity. This clearly shows that the microstrip circuit extracted 80% of the maximum available diode power.It corresponds to the total circuit loss,including the transitions,is estimated to be 0.8dB.The bias tunning bandwidth is 320MHz with power variation of 3dB in the bias rang of 3.6volt to 5.6volt. The temperature stability of the oscillator with a high Q dielectric resonator is illustrated in Fig.4, the total temperature variation over 26℃ to 80℃ is 18.1MHz ,which corresponds to an oscillator frequency temperature coefficient of 9.7ppm/℃. It is also found from some experiments that a 2.2GHz of variation has been easily obtained by trimming the length of the resonator for a same output power.

CONCLUSION

A 35GHz dielectric resonator stabilized Gunn full microstrip oscillator was developed.Output powers of 170mw was obtained from a 210mw diode, the bias tuning bandwidth was 320MHz with power variation of 3dB.Frequency temperature coefficient of 9.7ppm/℃ is also obtained. This oscillator with a dielectric resonator has good performances suitable for some systems applications such as communication,and radar as a local oscillator and can offer many advantages of light weight,low cost,compact rugged structure,simple technology and easy tuning as well as its potential for high-volume,repeatable manufacturing.It can be easily integrated with other microstrip circuits to form a fully integrated mm-wave receiver front-end.Finally,the novel microstrip configuration can be easily modified to form VCO and power combiner.

ACKNOWLEDGEMENTS

The authors wish to thank Prof. Lin Jinting, Guo Changning, Mao Kunchun and Wang lieqiang for their encouragement and helpful discussions.

REFERENCES

1 DAVID RUBIN,IEEE Trans.MTT-24,(1976)11,866.
2 A.S. Dasyoush,IEEE MTT-S,(1986),109.
3 P.Yen,IEEE MTT-S(1983),139.

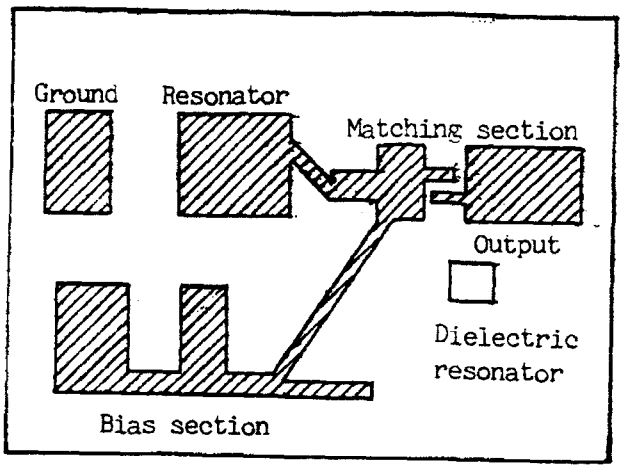

Fig. 1 35GHz full microstrip oscillator circuit layout

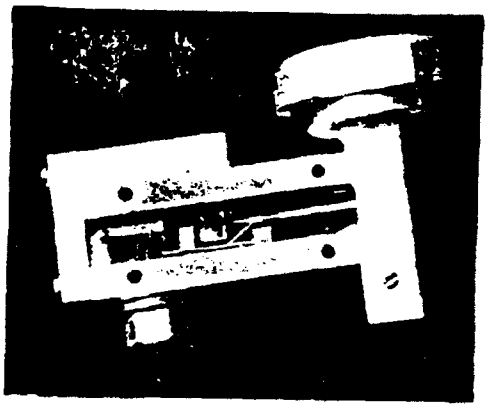

Fig. 2. Complete 35 GHz full microstrip oscillator in test housing.

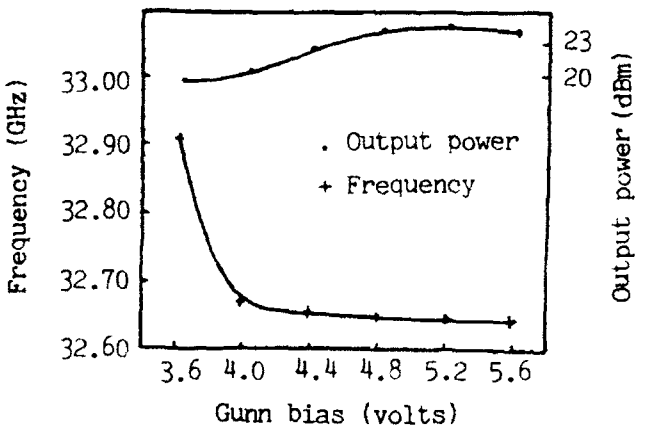

Fig. 3 Bias characteristics of output power and frequency of full microstrip oscillator

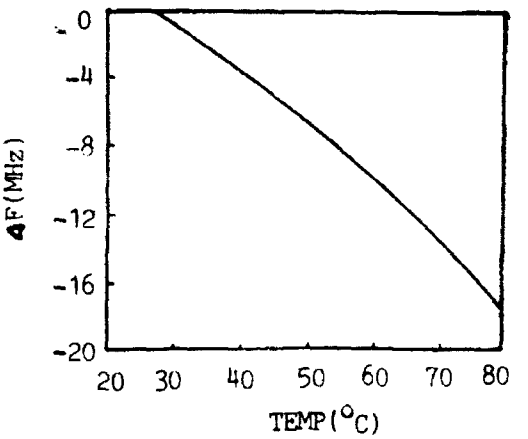

Fig. 4 Oscillator temperature performance

OPEN RESONATORS WITH MATCHING EXCITATION.

Igor K.Kuzmitchiev, Alexey A.Kostenko, Grigoriy I.Khlopov,
Victor P.Shestopalov, Uriy V.Yakimchiyk

Institute of Radiophysics and Electronics
Ukrainian Academy of Sciences

12, Acad. Proskura st., Kharkov, 310085, Ukraina

At present open resonators which are estimated as highquality resonant system, are widely used in millimeter and submillimeter wavelength bands. Characteristics of open resonators are determined by energy losses which are traditionally formed by ohmic and diffraction losses, communication losses as well as losses caused by not matching excitation caused by the difference in structures of the exciting E_e and working E_w fields. Taking all this into consideration it is evident from the physical point of view that the above-mentioned type of losses is accompanied by the following phenomena. First, there is field emission from the open resonator owing to the "overflow" of power of the exciting communication opening beyond the edges of one of the resonator mirrors. Second, there is a difference between directional (radiation) pattern of the exciting opening and working field oscillation structure, which is equivalent to power "pumping over" (transfer) of the exciting field in highest modes, for many of which the resonance condition may not be valid.

In particular, we have measured experimentally field sections in planes E and H (Fig. 1, curves 1 and 2, accordingly) for widely used element of communication of an open resonator with the load in the form of a narrow opening in the centre of the flat mirror with the diameter 15λ (λ - wavelength). The field of TEM_{00q} mode, which is well described by Gaussian distribution, is calculated for the plane, being measured, and is shown in Fig. 1 (curve 3). As it is seen from the figure, some part of radiator power is being lost because of its "overflow" beyond the edge of the mirror, and field structure, which is intercepted by the mirror (Fig. 1, hatched domain) differs greatly from the structure of the mode field of the open resonator. These differences are related with diffraction peculiarities of radiation field on a thin opening with flange and they can't be eliminated for the given type of communication element. For all this, not all the power, radiated into the volume of an open resonator, will be transformed into working mode.

Let us examine a problem, concerning excitation of semisymmetric open resonator with Gaussian distribution of the field by rectangular waveguide, situated in the centre of a flat mirror, in which wave H_{10} is propagated and its component E_y has the form [1]

$$\dot{E}_y = -j\,\frac{\omega \mu_a a}{\pi}\cdot H_{oz}\cdot \cos\frac{\pi x}{a}\cdot e^{-j\beta z}\,. \qquad (1)$$

Let's introduce excitation efficiency of the open resonator in the form [2]

$$\eta = \frac{\left|\int_S E_e E_w\, dS\right|^2}{\int_S |E_e|^2 dS \cdot \int_S |E_w|^2 dS}\,, \qquad (2)$$

where integration is exercised in an infinite plane S near one of the mirrors. Putting (1) into (2) we shall give an expression for resonator excitation efficiency

$$\eta = \frac{4\pi}{\tilde{a}\tilde{b}} \cdot \Phi^2\left(\frac{\tilde{b}}{2}\right) \cdot \left\{ e^{-\left(\frac{\pi}{2\tilde{a}}\right)^2} + j\,\frac{e^{-\left(\frac{\tilde{\pi}}{2}\right)^2}}{2} \cdot \left[\overline{W(z)} - W(z)\right] \right\}, \qquad (3)$$

where $z = (\pi/2\tilde{a}) + j(\tilde{a}/2)$; $\Phi(\tilde{b}/2)$ - probability integral; $W(z)$ - probability integral of complex argument (the line stands for complex-conjugated function) ; $\tilde{b} = b/\omega_0$ and $\tilde{a} = a/\omega_0$ - normalized dimentions of communication element ; ω_0 - radius of field spot on the flat mirror of the open resonator.

The results of calculations, shown in Fig. 2, where there are lines of permanent level η , demonstrate, that the right choice of communication opening allows to substantially increase the effectiveness of excitation of the open resonator of the above-mentioned geometry up to the value $\eta = 0{,}88$ with the opening dimentions of $\tilde{a} = 2{,}91$ and $\tilde{b} = 1{,}98$.

It is necessary to mention that the absolute dimentions of the communication opening amount to several wavelengths and this leads to strong shunting (by-passing) of the resonator by the load from the side of the feeding line. That is why it is necessary to control separately the field of excitation and communication of the open resonator with the waveguide transmission line, using thin semitransparent screens, situated in front of the horn aerial aperture in the centre of the flat mirror and not distorting its directivity diagram. Specifically we used one-dimentional E-polarized diffraction gratings, choosing different parameters of which it is possible to provide for the given magnitude of communication of the resonator with the load.

We have made all the necessary calculations and produced a semisymmetric open resonator for fourmillimeter wavelength band, the dimentions of which were chosen in such a way that it was possible to obtain an optimal value of loaded Q-factor Q_1 [3]. Mirrors' apertures and radius of curvature of spherical reflector are equal to $5{,}5\lambda$, and as an exciting device horn antenna is used, which is situated in the centre of a flat mirror. The dimentions of horn opening were determined considering the condition of field matching (Fig. 2, $a = 3{,}3\lambda$, $b = 2{,}3\lambda$, and horn length was 10λ , phase error in aperture $< 9°$).

We can see in Fig. 3 field sections in E and H planes (curves 1 and 2, accordingly) of the suggested exciting device, which are measured in the plane of a spherical mirror. In the same Fig. 3 (curve 3) there is shown distribution of field TEM_{00q} mode of the resonator, which is calculated in the plane being measured. As it is seen, the communication element provides for the axissymmetrical directional pattern, which coincides with the field spot dimention on level e^{-2} (-8,68 dB) with accuracy $\leq 5\%$. In order to control communication of the open resonator with the feeding line, the opening (aperture) of the horn aerial was closed by means of E-polarized belt diffraction grating with the period $\ell = 0{,}2\lambda$ and an opening $d = 0{,}1\lambda$.

In Fig. 4a there is a spectrum region of the open resonator when matching excitation is utilized. This spectrum region is photographed at distances L/R, which correspond to the optimal Q-factor of the resonator. As can be seen, in this case only TEM_{00q} mode is excited in the resonator as the exciting field practically coincides with the field of working mode (Fig..3). Owing to this such an open resonator

posseses a unimodal resonance curve in the interval of re-tuning of wavelength order, which is important in the process of creating selective oscillation chains of millimeter and submillimeter wavelength bands.

At the same time the spectrum picture qualitatively changes for the resonator with the slot type of excitation as it is shown in Fig. 4b, where there is a spectrum region, photographed at the same distances between the mirrors L/R. In such an open resonator parallel with the TEM_{00q} mode there are being excited two highest TEM_{10q} and TEM_{20q} modes, which are explained namely by the difference between the exciting field E_e and working field E_w according to Fig. 1.

The measurement of losses accounting for not matching excitation has shown that when matching way of energizing is used, these losses are 19%, which corresponds adequately with the above-given theoretical estimates and when slot excitation method is used, the losses increase up to 50%.

Thus we can say that the experiments made confirm the advantages of the suggested method of matching excitation of open resonator and prove that it is possible to gain practically unimodal frequency characteristic in multimode oscillation systems of the high-frequency band region of millimeter and submillimeter wavelength bands.

REFERENCE

[1] V.I. Volman, U.V. Pimenov: "Technical electrodynamics", (1971, in Russian).

[2] "Microwave scanning antennas", edited by R.C. Hansen, vol. 1: Apertures, Academic Press, New York and London, 1964.

[3] R.F. Soohoo: "Nonconfocal multimode resonators for masers", Proc. IEEE, vol. 51, pp. 70-75, Jan. 1963.

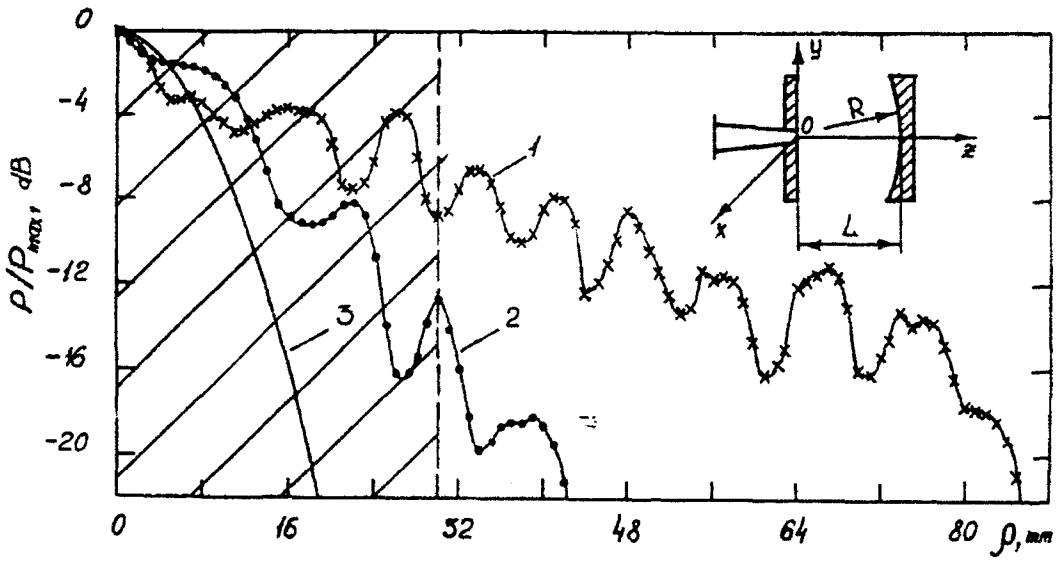

Fig. 1. Field distribution from the slot (opening) communication element in the centre of the flat mirror of the open resonator.

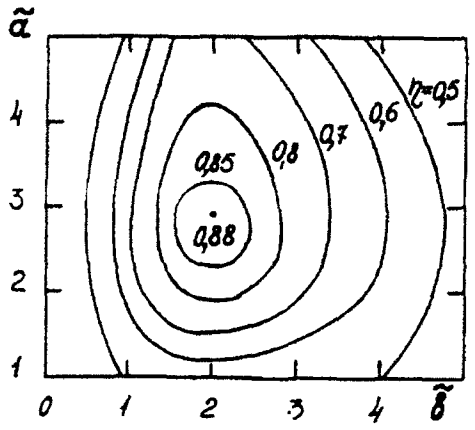

Fig. 2. Excitation efficiency of the open resonator depending on the dimensions of the exciting communication element.

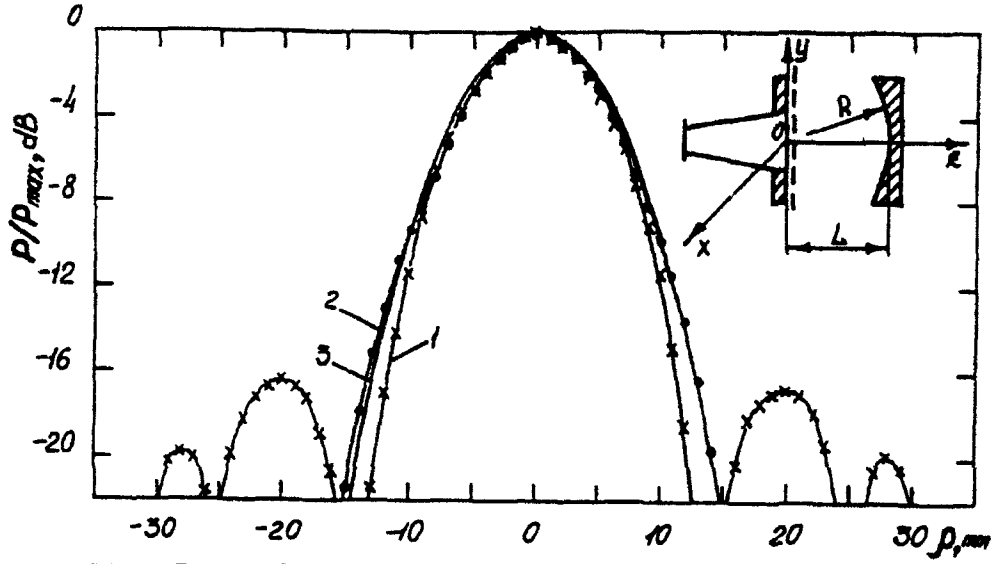

Fig. 3. Field distribution from the aperture communication element in the centre of the flat mirror of the open resonator.

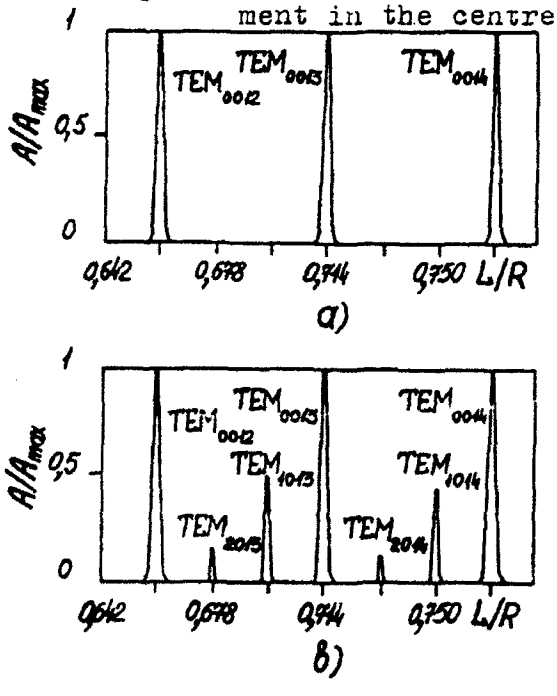

Fig. 4. Vibration spectrum of the open resonator:
a - excitation by aperture communication element;
b - excitation by slot (opening) communication element.

ANTENNA ELEMENTS AND ARCHITECTURES FOR WIDE-BAND MULTIFUNCTION ACTIVE PHASED ARRAYS

N Fourikis

Microwave Radar Division
Defence Science and Technology Organisation
PO Box 1500 Salisbury, South Australia 5108

ABSTRACT

Wide-band multifunction active phased arrays WMAPA, have several attractive characteristics. The requirements for the realisation of WMAPAs are outlined and several realisation options for antenna elements and array architectures have been explored. Promising research areas are outlined.

1. INTRODUCTION

One phased array operating over a wide bandwidth at cm/mm wavelengths has the following attractive characteristics:

(a) it can perform radar functions such as surveillance and target acquisition at two different bands eg. L- and X-band respectively;
(b) has excellent ECCM (Electronic Counter Counter Measures) and LPI (Low Probability of Interception) characteristics;
(c) it can perform spectrum surveillance and EW (Electronic Warfare) functions; and
(d) it can perform high sensitivity radiometric imaging functions. It is recalled here that the minimum detectable signal of a radiometer is inversely proportional to $B^{1/2}$ where B is the system bandwidth.

The realisation of WMAPAs is reaching the realms of possibility because:

(i) wide-band T/R (Transmit/Receive) modules have been realised [1]; and
(ii) narrow-band phase shifters operating at RF have been substituted by wide-band delay lines operating at optical wavelengths [2].

Costs limit the widespread use of active phased arrays, at present.
In this paper we shall focus attention on the requirements for the realisation of WMAPAs in section 2 while wide-band antenna elements and appropriate array architectures are considered in sections 3 and 4 respectively.

2. THE REQUIREMENTS

The wide-band requirement should be clarified; one can for instance have a WMAPA operating at two or more bands centred at frequencies within the L-, S-, C- of X-bands. The useable bandwidth can be 10% of the centre frequency; let us call this application one. Alternatively one can have a spread-spectrum WMAPA, where the usable band is 2-3 octaves; let us call this application two. In either case wide-band antenna elements are required.

Canonical phased arrays are arrays where the spacing between elements is constant and equal to $\lambda/2$ where λ is the wavelength of operation; furthermore amplitude tapering is used to obtain the required sidelobe level and beamshape. These arrays cannot support wide-band operation and other antenna arrangements or architectures should to be considered.

Polarisation information is desirable for it holds the promise of considerable benefits. The use of circular polarisation decreases rain induced clutter by about 10dB [3]. Similarly the use of the V and H polarisations and appropriate signal processing algorithms decrease sea clutter [4]. Polarisation agility and frequency diversity are required before these benefits can be attained. The doubling of the number of T/R modules required to accommodate two principal polarisations is at present prohibitively expensive; this is because the cost of T/R modules is high. When costs decrease by the use of a matured MIMIC technology, polarimetric WMAPAs can be contemplated. It is however important that the polarisation isolation required should be greater than 25-30dB [5]; additionally the beamwidths of polarimetric WMAPAs in the E- and H- plane radiation patterns should to be equal.

3. ANTENNA ELEMENTS

Printed circuit microstrip patch antennas or dipoles have a maximum bandwidth of say 10% to 15% of the centre frequency of operation. One can propose the tuning of such elements for application one. The tuning of dipoles/monopoles at UHF has been reported [6]; more explicitly a monopole was tuned from 30-90 MHz with the aid of high Q passive circuits which were inserted, under a microprocessor control, between the antenna and the front-end of the receiver. With this arrangement the SNR of the system remained approximately constant in the band of operation. More importantly however, a band-pass filtering (BPF) function was afforded by the antenna; in a multi-source environment such a BPF is often required to excise jammers operating outside the band-pass of the receiver. The tuning of narrow-band antenna elements operating at microwaves is a promising area for research.

Printed circuit tapered slot antennas (TSAs) [7&8] offer wide-band performance, have low profile and are inexpensive to fabricate. TSAs can have acceptable input VSWRs and a gain of about 6dB over 2-3 octaves; additionally their E- and H-plane radiation patterns can be approximately equal. The E-, H, and D- plane maximum cross polarisation radiation was about -11dB with respect to the maximum co-polarisation radiation for the antipodal TSAs considered in reference [9]; by contrast the E- and H- plane maximum cross polarisation level was about -27dB for the planar TSAs while their D-plane maximum cross polarisation level was about -11dB [9]. Here the D-plane is the diagonal plane with respect to the antenna plane. It is clear that some work is required to decrease the maximum cross polarisation level in the D-plane before planar TSAs are used for polarimetric WMAPAs.

4. ARRAY ARCHITECTURES

While canonical phased arrays are not suitable for wide band operation these arrays have one desirable quality: graceful degradation. More explicitly if 5% or 10% of the elements fail, the array sidelobe does not substantially deteriorate. While phased arrays having a random spacing or minimum redundancy [10] have been considered these arrays do not offer graceful degradation. Controlled redundancy arrays [11] have a random spacing between antenna elements and redundancy which can be controlled. The spacing between elements is such that the effects of mutual coupling can be ignored at the lowest frequency of operation. Additionally space tapering is used.

5. CONCLUDING REMARKS

WMAPAs have several attractive characteristics; the requirements for the realisation of these arrays have been outlined and the importance of polarisation information emphasised. Specific areas considered were: wide band antenna elements, and suitable array architectures. The concept of wide band operation has been clarified and two applications outlined; in the first

application narrow-band tunable antennas are tuned across a wide band, while in the latter application the instantaneous bandwidth is 2-3 octaves wide. For application one, tuned dipoles/monopoles/patches can be contemplated for use, while for application two, TSAs are promising candidates for antenna elements of WMAPAs; here again some work is required before planar TSAs can be considered for polarmetric WMAPAs. Controlled redundancy phased arrays are more suitable for wide-band operations than canonical phased arrays.

Costs limit the widespread use of active phased arrays; when these costs decrease by the use of a mature MIMIC technology, active phased arrays and WMAPAs which can take advantage of information afforded by polarisation will come of age.

6. REFERENCES

[1] M Priolo, G St. Onge, W Coughlin, J Bugeau and D Meharry, "Transmit/Receive Modules for 6 to 18 GHz Multifunction Arrays", 1990 IEEE MTT-S Inter. Microwave Symp. Digest, Vol 3, pp 1227, 8-10 May 1990, Dallas, Texas USA.

[2] F G Sheehan and J R Forrest, "The Use of Optical Techniques for Beamforming in Phased Arrays", Proc. SPIE, Vol 477, 1984, pp82-89.

[3] W B White "Circular radar cuts rain clutter" Electr. March 1954 p 158.

[4] N C Currie and C E Brown "Principles and applications of millimetre-wave radar" Artech House 1987 p 285.

[5] A J Blanchard "Demands on polarisation purity in the measurements and imaging of distributed clutter" in Inverse Methods on Electr. Imaging W M Boerner et al Eds Hingham MA Reitel Publ. 1985 pt 2 p 721.

[6] N Fourikis, A Parfitt, T Tang and M W Gunn "Microprocessor tuned antennas" Second Australian (ATERB/CSIRO) Symp. on Antennas held on 15-16 Feb 1989 in Sydney Aust.

[7] P J Gibson "The Vivaldi aerial" Proc Ninth European Microwave Conf. Brighton UK 1979 p 101-105.

[8] S N Prased and S Mahaparta "A novel MIC slot-line antenna" ibid p 120.

[9] N Fourikis, N Lioutas and N V Shuley "A parametric study of the co- and cross-polarisation characteristics of tapered planar and antipodal slotline antennas" Paper submitted to IEE 1992.

[10] Y Lee and S V Pillai "An algorithm for optimal placement of sensor elements" 1988 Int. Conf. on Acoustics, Speech and Signal Proc. Vol 5 p 2674, 11-14 April 1988 New York NY USA.

[11] N Fourikis and N Lioutas "Novel wide-band multifunction phased arrays" 16th Int Conf. on IR and mm Waves 26-30 Aug 1991. Lausanne Switzerland.

HRR PROFILES PROCESSING TECHNIQUES FOR LFMCW MILLIMETER WAVE RADAR

He Songhua,Guo Guirong,Guo Xiuhuang,Zhang Wei
(Changsha Institute of Technology,Hunan,China,410073)

ABSTRACT

Target detection and tracking under strong land clutter background is of key importance for air-to-surface weapons. At the operating frequency of millimeter wave, radar targets can be describ- in terms of multiple scattering centers; with a modest bandwidth of transmitted signal, target high range resolution (HRR) profiles can be obtained from received data. The performance of target detection and tracking can be enhanced by using a wealth of information about target scattering centers provided by HRR profiles

INTRODUCTION

The widespread application of millimeter wave technology in military systems has become recently possible due to the rapid progress in the MMW hardware development. One typical application is millimeter wave terminal precision guidance which use wideband technology to obtain range resolution much smaller than target length. Under high range resolution circumstance, not only does the capability of traditional methods of point target detection and tracking become ambiguous, but how the data should be processed does as well. In our work summarised in this paper, we present a novel method of target detection, tracking, angle and velocity computation based on HRR profiles.

LFMCW MILLIMETER WAVE RADAR HRR PROFILES

Asumme the transmitted signal has a linear frequency sweep, t is time varaiable and t_m elapses since the start of the nth sweep, then

$$t=n*Tp+t_m \qquad (0\leq t_m < T_p, n=0,1,2,\cdots) \tag{1}$$

The transmitted signal can be expressed as

$$s_1(n,t_m)=A*\cos(2\pi*(f_0+(\Delta F/(2Tp))*t_m)*t_m+\Phi_m)$$

$$(0\leq t_m\leq Tp) \tag{2}$$

where Tp is sweep period and ΔF is sweep bandwidth. At the operating frequency of millimeter wave f_0, targets size is much larger than a wavelength. A target can be described as composed of M scattering centers, the mth scattering center has intial slant rang R_m and radial velocity V_m. Assuming that demodulation of the received signal is achived by mixing with the transmitted FMCW waveform and the observation time N* Tp is small enough, the demodulated component can be writtern as follows:

$$x(n,t_m)=\sum_{m=1}^{M} A_m \cdot \cos 2\pi \{[(\Delta F/Tp)\cdot(2R_m/C)-f_o(2V_m/C)]\cdot t_m$$

$$-f_o(2V_m/C)\cdot nTp+f_o(2R_m/C)-(2\Delta F/Tp)\cdot(R_m/C)^2\} \quad (3)$$

Over one sweep, n is constant, and generally, frequency difference caused by ΔR_m (range difference from scattering centers) is much larger than that caused by ΔV_m, $f_o(2V_m/c)$ term is omitted as a constant error, then (3) can be written as follows:

$$x(t_m)=\sum_{m=1}^{M} A_m \cdot \cos(2\pi \cdot f_m \cdot t_m+\theta_m) \quad (4)$$

$$f_m=(\Delta F/Tp)\cdot(2R_m/C) \quad (5)$$

The peaks of FFT data of sampled demodulated signal give results of range R_m and the spacial distribution of target scattering along range axis is which called range profiles. Range resolution of FFT is

$$\Delta=C/(2\Delta F) \quad (6)$$

HRR PROFILES DETECTION THEROY

High range resolution is effective solution to target detection under strong land clutter and noise background.the higher resolution, the fewer clutter and noise energy is in the resolution cell of interest. when Δ is much smaller than target length, although target energy is also dispersed in different cell, yet not uniformed dispersed. Target energy is mainly concentrated into range cells of strong scattering centers,so S/J ratio of strong scattering centers cells is further increased than the averaged S/J ratio.

Improvememt of detection performance is expected with emphasis on strong scattering centers.According to the data provided by Currie [1]and Edward[2], a S/J ratio of greater than 8 db in strong scattering centers cells will be expected for guidance application when $\Delta < 0.3$ meter.

1. m/N Detector

N is selected according to the maximum possible target length ΔR, m is selected appropriately according to the possible number of target strong scattering centers.Every spectrum line of FFT output is detected with CFAR P_f, if there are more than m alarm spectrum lines among N continuous spectrum lines,target is detected.

2. Intergrated Range Cell Detector

Series $\{y_i\}$ is constructed according to FFT output $\{X_i\}$:

$$y_i=\left(\sum_{j=i-N_1/2}^{i+N_1/2} |X_j|\right)/N_1 \quad (7)$$

N_1 is selected according to spread line number of one strong scattering centers.A CAFR detector can also be constructed based on series $\{y_i\}$.

Simulated results show that intergrated range cell detector provide better performance than single range cell detector.

3. Target Discriminator

Elimination of strong target-like clutter returns will be expected by using some spatial feature algorithm based on HRR profiles, such as spatial extent discrimination and contextual feature discrimination.

HRR PROFILES TRACKING THEORY

Target range center position R_o can be estimated from FFT spectrum peaks. R_o is used to control the local frequency of some mixer so that the center of range tracking window changes in accordance with change of R_o

Target angle is measured by means of amplitude information of HRR profiles. Assuming the receiving radar beam direction stays at A,B,C, D which has azimuth and elevation angles of $(\alpha_o-\Delta\alpha, \beta_o)$,$(\alpha_o+\Delta\alpha, \beta_o)$, $(\alpha_o, \beta_o-\Delta\beta)$, $(\alpha_o, \beta_o+\Delta\beta)$,the transmitting beam direction stays at 0 with angles α_o and β_o, then the angles between signal direction of the mth scattering centers and receiving beam axis are given by the following equation:

$$\cos\theta_{i,m}=-\sin\beta_m \cdot \sin\beta_i+\cos\beta_m \cdot \cos\beta_i \cdot \cos(\alpha_m-\alpha_i)$$

$$(i=A,B,C,D) \qquad (8)$$

where (α_i, β_i) are angles of position i.HRR profiles at A, B, C, D will give the amplitude of the mth scattering center:$u_{i,m}$,then

$$u_{i,m} \propto F(\theta_{i,m}) \qquad i=A,B,C,D \qquad (9)$$

where $F(\cdot)$ is beam pattern of receiving antenna.(9) and (8) can give solution of M scattering centers:

$$(\alpha_1, \beta_1),(\alpha_2, \beta_2), \cdots ,(\alpha_m, \beta_M)$$

The performance of angle measuring and tracking is improved due to high range resolution because (1) Target angle can be estimated by several strongest scattering centers, weak scattering cells are omitted, that decreases error caused by clutter and noise, (2) Interference among scattering centers is decreased that decreases target glint, and (3) Target angle estimation is an average of mutiple scattering centers

VELOCITY COMPUTATION BASED ON HRR PROFILES

N FMCW Sweeps give N HRR profiles$\{X(n,i),n=0,1,\cdots,N-1,i=0,1,\cdots,L-1\}$, for target range cell i,compute

$$V(k,i)=\sum_{}^{N-1} X(n,i) \cdot \exp(-j2\pi \cdot n \cdot k/N) \qquad (10)$$

From equation (8),it is easy to show that the peaks of V spectrum are near to velocity cell k_o,

$$k_o = -N \cdot f_o \cdot (2V_o/C) \cdot T_r$$

where V_o is the radial velocity of target.Furtherly,equation(10) has velocity resolution

$$\Delta v = C/(2 \cdot f_o \cdot N \cdot T_r) \qquad (11)$$

At MMW frequency, f_o is higher, for the same Δ v, the required observation time will be less. It is possible that high resolution of both range and velocity should give two dimensional image of target.

SUMMARY AND CONCLUSION

The use of wideband LFMCW millimeter wave leads to better detection and tracking performance.The key techniques involved are A) Using wideband waveform to stimulate target scattering centers information; B) Using very high speed one or two dimensional FFT processor to obtain range, angle and velocity of target scattering centers; C) Information synthesis or fusion of multiple scattering centers.

REFERENCE

1. N.C.Currie,et.al., "MmW land clutter Model update", pp217-221,1987 International radar Conference.

2. C.E.H.Edward, "Expected radar cross section of ground targets at MMW" ,HDL Report R-620-66-4, Harry Dimond Laboratories,19,July,1966

3. D.L.Mensa, High Resolution Radar Imaging, Artech House Inc., 1981.

THE LONGWAVE RADIATION AROUND BUILDINGS AT DIFFERENT ANGLES

H.Nowak[1] and K.Cena[2]

[1]Department of Building and Environmental Physics, Institute of Building Science I-2
Technical University of Wroclaw, Wyspianskiego 27, 50-370 Wroclaw, Poland
[2]Environmental Science, Murdoch University, Murdoch, WA 6150, Australia.

ABSTRACT. A model by Cole (1976) was adapted for the South-Western region of Poland (51 °N) to calculate the longwave radiation around buildings at different angles. The predictions was validated with a set of measurements performed during summer and winter on a building at four angles of surface inclination, and under overcast and clear skies.

INTRODUCTION

Various empirical models describing the longwave radiative environment around buildings have been developed for horizontal surfaces . This limitation excludes pitched roofs and walls. The existing models (Berdahl and Fromberg, 1982; Idso and Jackson, 1969; Roach, 1955; Swinbank, 1963; Unsworth and Monteith, 1971) was empirically verified mostly for clear sky conditions, rather than for cloudy skies and different levels of air pollution. Cole (1976) proposed a simple empirical model for calculation of longwave radiation incident on surfaces at all angles, from horizontal to vertical. The model was modified numerically to suit the local conditions in the South-West region of Poland. The aim of this paper is to compare measurements obtained under a range of conditions with the modified Cole's model, and to discuss it's applications.

METHODS AND RESULTS

The longwave radiation $R(\alpha)$ incident upon a surface inclined at an angle α is a sum of the atmospheric $R_A(\alpha)$ and ground radiation $R_G(\alpha)$ (Cole, 1976). The atmospheric component is given by:

$$R_A(\alpha) = R_A\, k_1 + b\, k_2\, \sigma\, T_a^4 \qquad (1)$$

where: R_A is the atmospheric radiation incident upon horizontal surface, Wm^{-2},

k_1, k_2 are coefficients dependent on inclination of the surface,

b is a coefficient representing weather conditions,

σ is Stefan-Boltzmann's constant, $5.67 * 10^{-8}$ W $m^{-2}K^{-4}$,

T_a is the air temperature, K.

The ground component is given by:

$$R_G(\alpha) = R_G \sin^2(\alpha/2) \qquad (2)$$

where R_G is the ground radiation in Wm^{-2}.

Cole (1976) published values of all coefficients for different angles of inclination. For the purpose of this study values of R_A and R_G was numerically modified. Using equations (1) and (2) with the modified coefficients the values of longwave radiation were computed for four angles and two seasons. These were compared and correlated with measurements obtained on a building in Wroclaw (51 °N). Figure 1 presents data for winter conditions when the longwave radiation was measured in the range from 180 to 340 Wm^{-2}, with the highest values for an overcast sky for all angles.

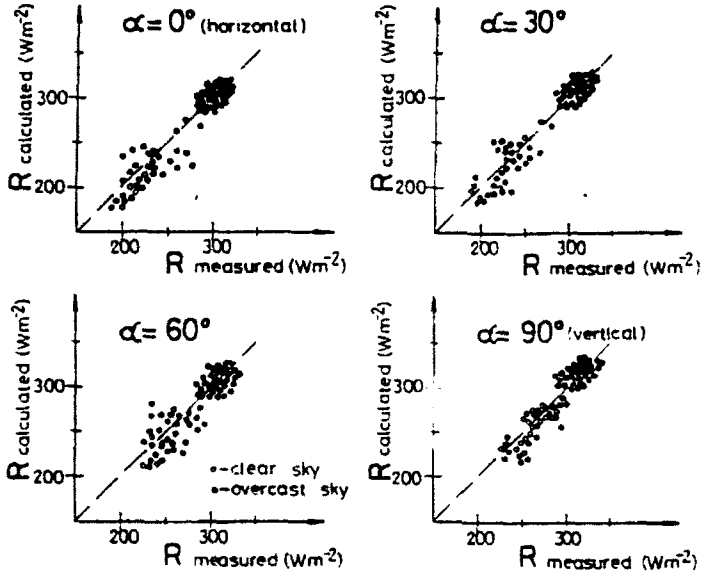

Fig.1. Comparison of longwave radiation incident upon surfaces inclined at 0° (horizontal), 30°, 60° and 90° (vertical), for winter conditions with clear and overcast skies, as calculated from the modified Cole's model and measured in Wroclaw (51 °N).

Figure 2 presents the comparison for summer conditions and a clear sky only. The values measured in summer (from 200 to 450 Wm^{-2}) were higher than in winter and were also dependent on the angle of incidence.

DISCUSSION AND CONCLUSIONS

The measured and calculated values of longwave radiation agreed for all angles of inclination and weather conditions. The best statistical correlation was found for measurements obtained under a clouded sky (Figure 1). As expected, the measurements showed that longwave radiation from an overcast sky upon surfaces at an angle is almost independent of the inclination. For clear sky conditions, the radiation will be higher at low angles of inclination. This relationship can be important for various designs of radiative cooling systems. Predictably, the highest radiation intensities for clear skies were measured for vertical surfaces.

Figure 3 compares the modified Cole's model and the present data, with models by Idso and Jackson (1969), Roach (1955), Swinbank (1963),and Unsworth and Monteith (1971) calculated for horizontal surfaces at a range of air temperatures. For clear sky conditions the highest correlation was found for the model by Idso and Jackson (1969). For winter, the agreement is not so good, particularly in reference to the most frequently cited Swinbank's model. The differences between the two models were discussed in detail by Nowak (1989).

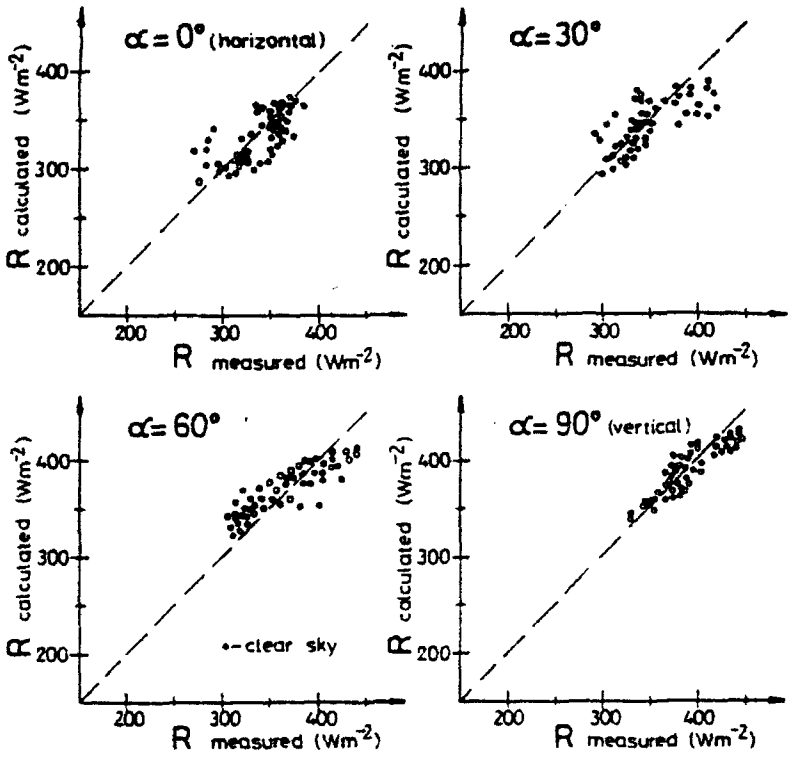

Fig.2. Comparison of longwave radiation incident upon surfaces inclined at 0° (horizontal), 30°, 60° and 90° (vertical), for summer conditions with a clear sky, as calculated from the modified Cole's model and measured in Wroclaw (51 °N).

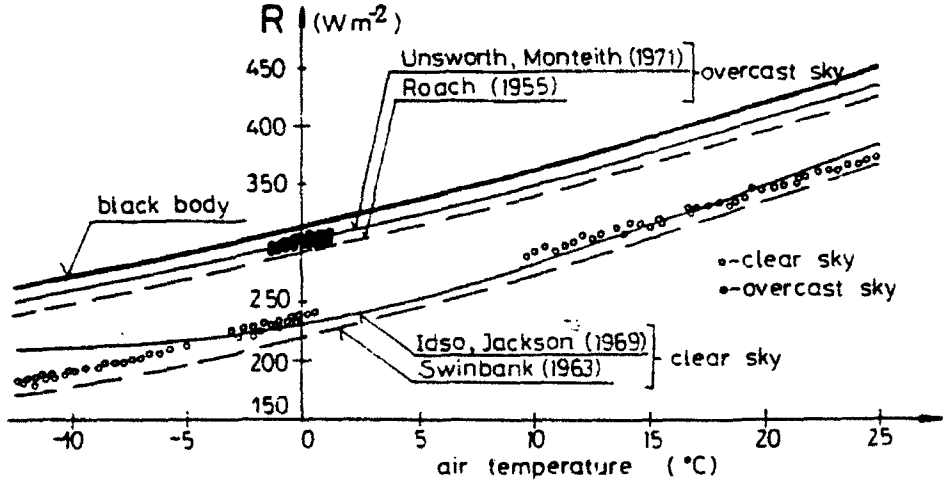

Fig.3. Comparison of longwave radiation incident on horizontal surfaces in winter and summer conditions, with clear and overcast skies, calculated from the modified Cole's model (circles) and other models (lines) for a building in Wroclaw (51 °N).

For an overcast sky, the modified Cole's model predicts values in a much closer agreement to the models by Unsworth and Monteith (1971), Roach (1955) and the theoretical relationship for the black body model. The set of available measurements for an overcast sky was, however, limited to a narrow range of air temperatures, around 0 °C, and further measurements would be helpful.

In conclusion, an encouraging agreement was found between the Cole's model adapted to the climatic conditions in the South-Western region of Poland and a set of measurements of longwave radiation incident on a surface, for different angles of inclination. It will be important to extend this validation to a much wider range of geographical regions and different levels of air pollutions in particular. A working model for calculation of the longwave radiation under various conditions is needed, among others, for modelling of various components of the heat balance of buildings (Nowak, 1991) and their dependence on the physical environment.

REFERENCES

1. Berdahl P., Fromberg R.: The thermal radiance of clear skies. Solar Energy, Vol.4, pp.299-314, 1982.

2. Cole R.J.: The longwave radiation incident upon the external surface of buildings. Building Services Engineering, Vol.44, pp.195-206, 1976.

3. Idso S.B., Jackson R.D.: Thermal radiation from the atmosphere. Journal of Geographical Research, Vol.74, pp.5397-5403, 1969.

4. Nowak H.: The influence of atmospheric radiation on the heat balance of low - -sloped roofs. Int. Conf. on Millimeter Wave and Far-Infrared Technology (1990), Eds: A.S. McMillan and G.M.Tucker. Int.Acad.Publishers, Oxford, pp.174-177, 1989.

5. Nowak H.: The longwave radiative heat transfer of the building envelopes. Infrared Physics, Vol.32, pp.357-363, 1991.

6. Roach W.T.: Measurements of atmospheric radiation and the heat balance at the ground at Kew, May 1953-May 1954. Air Ministry, Met. Society, Vol.2, 1955.

7. Swinbank W.C.: Longwave radiation from clear skies. Quarterly Journal of the Royal Meteorological Society. Vol.89, pp.339-348, 1963.

8. Unsworth M.J., Monteith J.L.: Longwave radiation at the ground (i) Angular distribution of incoming radiation. Quarterly Journal of the Royal Meteorological Society, Vol.101, pp.1-13, 1971.

ACKNOWLEDGMENT. K. Cena acknowledges a travel grant from Murdoch University.

Th1.4

ANALYSIS OF SINGULARITY OF EMP ON APERTURE WITH IOEM

Kama Huang and Yongxue Yu
(Department of Radio and Electronics of Sichuan University
Chengdu, 610064, People's Republic of China)

KEY TERMS

Integral Operator Expansion Method(IOEM), Singularity, Electromagnetic Pulse(EMP), Aperture

ABSTRACT

In this paper, the analysis of singularity of EMP on aperture with Fredholm Integral Operator Expansion Method is discussed. This method substitutes infinite field on the aperture with finite inner product to simplify the numerical calculation and secure the accuracy of the solution. It is also proved that soluting the singular diffraction promblems with IOEM is also successful.

1. FREDHOLM INTEGRAL OPERATOR EXPANSION THEORY

The key of this paper is Fredholm Intergral Operator Expansion Method-(IOEM). First, we construct an operator space using Fredholm integral operator, then we prove further that this space is a dividable Hibert Space. We define the linear calculation, inner product and norm in it. According to Fourier Expansion Theory in Hibert Space,we expand Fredholm integral operator with orthonormal sets and get Fredholm Integral Operator Expansion Theory as following: [1]

For any $x(s)$, $k(s,t)\in L(r)$, the following formula is true:

$$\Gamma x(s)=\int_{\Gamma} k(s,t)x(t)dt=\sum_{n=1}^{\infty}\int_{\Gamma}\int_{\Gamma} k(s,t)\overline{k_{on}(s,t)}dsdt\cdot\int_{\Gamma} k_{on}(s,t)x(t)dt \tag{1}$$

Here $k(s,t)$ is the integral kernul of Fredholm integral operator T and $k_{on}(s,t)$ is an orthonormal set on Γ. Gennerally, the $k_{on}(s,t)$ can be chosen as:

$$k_{on}(s,t)=k_{on1}(s)\cdot k_{on2}(t) \tag{2}$$

Eq. (1) can also be applied in two and three dimension space. By using the expansion theory,we can directly get the solution of the second type

of Fredholm integral equation.

2. SOLUTION OF EMP ON APERTURE

We discuss a typical problem to illutrate the use of the method. The problem is how to calculate the distribution of fields when EMP penetrates through aperture into a two-parallel plate region. A two-parallel conducting plane with an aperture is shown in Fig.1 when a plane wave incidents on it.

$$\vec{E}_i=(\hat{x}E^i_{ox}+\hat{y}E^i_{oy}+\hat{z}E^i_{oz})\exp(-jk(\alpha x+\beta y+\gamma z))$$

We can get the following integral equation about the field E on the aperture:

$$\iint_A \bar{M}_s(\bar{r}')g(\bar{r}'/\bar{r})ds'=\hat{z}/(jkr)\cdot\bar{E}^i_o\exp(-jk(\alpha x+\beta y))\cdot\bar{h} \qquad (3)$$

where

$$\bar{M}_s(\bar{r}')=\hat{z}\cdot\bar{E}^a$$

$$g(\bar{r}'/\bar{r})=\exp(-jk|r-r'|)$$

$$\hat{h}=h_x\hat{X}+h_y\hat{Y}$$

and

$$h_y=\pi/k\left(\begin{matrix}j\\-1\end{matrix}\right)\sum_{n=1}^{\infty}C_n j^{(n+1)}\exp(j(n+1)\phi)\cdot J_{n+1}(k\rho)$$
$$+\left\{\begin{matrix}-1\\1\end{matrix}\right\}j^{n-1}\exp(j(n-1)\phi)\cdot J_{n-1}(k\rho)$$

To solve Eq. (3) by with EEM, one often expands MS as following:

$$\bar{M}_s(\bar{r})=\sum_{m=1}^{\infty}\bar{M}_s^{(m)}(\bar{r})k^m \qquad (4)$$

And subsitutes Eq. (4) into Eq. (3) to get the coefficients Ms (m). Finally one substitutes Ms(r) into the following equation to get the distribution of field in the two-parallel plate region.

$$E^{-d}=-\iint\bar{M}_s\cdot D\cdot\bar{\bar{G}}(r'/r)ds' \qquad (5)$$

Actually sometimes $\bar{E}^a\to$ or $\bar{M}s\to\infty$ on the the edge of the aperture. Several problems are caused by it. First, whether $\bar{M}s$ in all singular integral equations can be expanded in the form of Eq.(4)? Second, whether is there

only finite number of coefficient M in Eq.(4)? Third,how can we decide the number of those coefficients? These problems make it difficult to secure the accuracy in the numerical calculation.

If we apply Fredholm Integral Operator Expansion Method, we can get the following result from the integral equation (3):

$$\iint \bar{M}_s \cdot k_{on2}(\bar{r}')ds = \langle \bar{f}, k_{on1}(r) \rangle / B_n \cdot R_n \qquad (6)$$

Where $B_n = \int_A \iint_A \int g(\bar{r}'/\bar{r}) \cdot k_{on}(\bar{r}'/\bar{r}) ds ds'$

$R_n = \langle k_{on1}(r),\ k_{on2}(r) \rangle$

$f = \bar{h} + (\hat{Z}/jkr) \times \bar{E}_0^i e^{-jk(\alpha x + \beta y)}$

Eq. (6) can be proved to be finite with singularity of on the edge.

Similarily, applying operator expansion theory in Eq. (5), we can get:

$$\bar{E}^d = -\sum_{n=1}^{\infty} \int_A \iint_A \nabla' \times \bar{\bar{G}}(r'/r) \cdot \overline{k_{on}(\bar{r}', \bar{r})} ds ds' \cdot k_{on1}(\bar{r}) \cdot \int_A \int \bar{M}_s \cdot k_{on2}(\bar{r}')ds' \qquad (7)$$

Substituting Eq. (6) into Eq. (7) we can get the distributions of field in the two parallel plate region.

The key of this method is to calculate the singularity with the finite $\int_A \int \bar{M}_s \cdot k_{on2}(\bar{r}')ds'$ instead of the infinite $\bar{M}s$ By the way we solve the singularity of $\bar{E}^a$ on the edge and secure the accuracy of the solution.

3. CONCLUSTION

It can be seen that IOEM is suitable for the calculation of the field distribution of EMP on the aperture plane. The further reaserch shows that it is also successful to treat the diffraction problems with the same singularity by using IOEM.

REFRENCE:

1 Kama Huang : " Sloution of Fredholm Integral Equation Using Expansion of Operator "

Journal of university of Electronic Science and Technology of China, Vol.20, No.2, 1991, PP. 138-144.

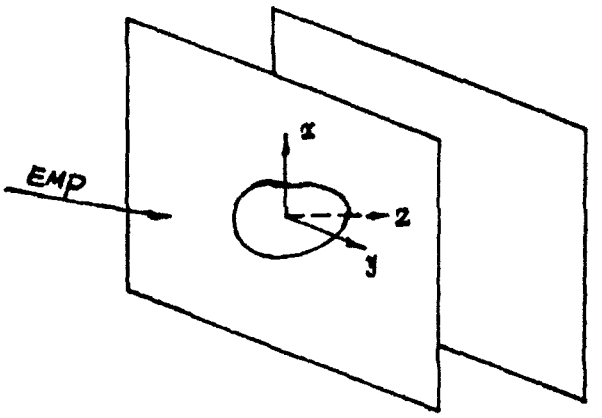

Fig.1

A function of Lateral Inhibition spectrum and Neural Networks in heat image handler

钱 毅
QIAN Yi 武汉大学空间物理系 430072
(Dept. of Space physiscs Wuhan University, Wuhan 430072, China)

ABSTRACT:

The human brain and vision systems is the most complicated intellectual information processing systems in the world that timely processes a large amount of spacial and temporal information. The knowledge of vision mechanism and its structure will be helpful for the study of image identification and image understanding, for the study of robot's vision and neural network. This article intends to improve the image formation quality of forward looking Infra-red by applying the spectrum function of lateral inhibition of the human eye to light and electricity mixture systems, so as to meet the requirement of good electromagnetic weapon system for quality.

Infrared heat image instrument is the product of the seriation to the present, called the products of the third generation. Because it is a kind of passive night vision instrument, it's working method is concealed, not easy to be detected. It can be used in all kinds of weather all time, and is able to penetrate through rain, snow, fog and haze. Besides the distance of effect is far. Being electronic waves sent out by the objects themselves, it has an outstanding merit, i.e. is can detect disguise easily. It can detect hidden tanks and cannons in disguise, engines started or not started, even being traced to heat images of planes or fighting vehicles that have just left the spots.

However, the difference of temperatures between the military target and its background and between the parts of the target is rather small, so hot images are not very clear. There is little contrast. It's hard to see the details clearly. Considering the above demerits, the anthor of the present thesis builds a mathematics mould of vision spectrum through a Fourier integral of non-circle function. The anthor points out that there is an effect of crosswise inhibition in obtaining information for the human vision, which means the greater the amount of information received, the greater the need to outstand the important parts to enlarge contrast and make the parts be memorized mord distinct. For human brain and vision system, this process is one that pre-processes information spontaneously.

The following is the limited line of sine waves consisting of 2N sine waves (N> any Rc of 0.5). For convenience, let N be positive integer;

$$f(x)=\begin{cases}0 & (x<-2Nl)\\ A\sin\frac{x\pi}{l} & (-2Nl<x<2Nl)\\ 0 & (2Nl<x)\end{cases}$$

If we change the above Space Axis X into Time Axis T, and change space periodic length 2l into time periodic T at the same time (Thus π/l is change to circular frequency ω_0), we can express it in another Fourier integral:

$$f(t)=\begin{cases}0 & (t<-N\frac{2\pi}{\omega_0})\\ A\sin\omega_0 t & (-N\frac{2\pi}{\omega_0}<t<N\frac{2\pi}{\omega_0})\\ 0 & (N\frac{2\pi}{\omega_0}<t)\end{cases}$$

To study the spectrum of this limited line of sine waves, because f(t) is odd function, it can be expressed in Fourier sine integral.

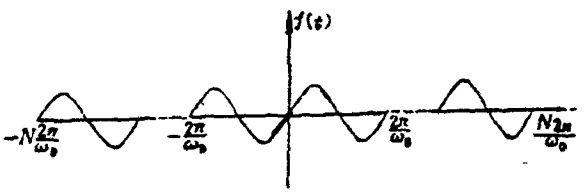

Fig. 1 Restrictable sine wave

$$f(t)=\int_0^\infty B(\omega)\sin\omega t\,d\omega$$

$$B(\omega)=\frac{2}{\pi}\int_0^\infty f(t)\sin\omega t\,dt$$

$$=\frac{2A}{\pi}\int_0^{N(2\pi/\omega_0)}\sin\omega_0 t\sin\omega t\,dt$$

$$=-\frac{A}{\pi}\int_0^{N(2\pi/\omega_0)}[\cos(\omega+\omega_0)t-\cos(\omega-\omega_0)t]\,dt$$

$$=-\frac{A}{\pi}\left[\frac{\sin(\omega+\omega_0)t}{\omega+\omega_0}-\frac{\sin(\omega-\omega_0)t}{\omega-\omega_0}\right]\Bigg|_0^{N(2\pi/\omega_0)}$$

$$=\frac{A}{\pi}\sin(\frac{\omega}{\omega_0}2N\pi)\left[-\frac{1}{\omega+\omega_0}+\frac{1}{\omega-\omega_0}\right]$$

$$=\frac{2A\omega_0}{\pi(\omega^2-\omega_0^2)}\sin(\frac{\omega}{\omega_0}2N\pi)$$

At $\omega \to \omega_0 \pm$, with the L'Hospital rule; we can get a spectrum distribution diagram of axial symmetry with ω_0 as the peak value.

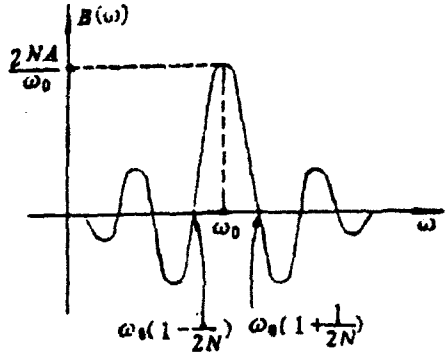

Fig. 2 A Function of Lateral Inhibition spectrum

From this spectrum mathematics mould by creation; we can conclude that in feeling and receiving outside information, human vision system is different from cameras, rather, it is a receiving process that specially designated choices between spectrum. From the mathematic mould, we can see that where the difference between the two sides is $\omega_0 / 2N$, function image dropped to zero. We can safely assume that spectrum is gathered in the scope of $\omega_0 / 2N$ around ω_0 the left and right sides. The bigger the N value, even as the greater the amount of information, the narrower the frequency band around crest ω_0. The adaptive effect of human vision system in receiving information completely suits the memory principle of human brain. To memorize a complicated image information, the human brain must first choose the main characteristics of the image to give precedence to deal with spectrum. The pre- processing connects with the neural network of the brain in the way of feedback. It is also related to the original reserved samples of "cell crowd" in the human brain. Based on this, thesis tries to realize vision neural network spectrum circuit through the exchange of discrete hartley and to apply it to the part of circuit of hot formation of image. The detecting machine turn the strong and weak signals of infrared radiation intyo corresponding electric signals, which enter the vision spectrum neural net circuit after being enlarged properly.

After the adjustment, the frequency with the highest range is takenas the spreading central frequency ω_0, which formed filtered limiter of electromagnetic wave. Scanning electric signals pass the filtered limiter to be sent to light-diode forming images after enlargement. Because the size of N value can be adjusted by the filter waves effect caused by the distance and quality of objects and bad weather and general training obtained from the wathing of objects at night. In such handled image, the "vitals" part of the objects become brighter, while the brightness gradient of the other parts attenuated quickly. The background not related to the objects can be inhibit, so that the contrast be come greater, the

objects distinctness increase and enhance the ability to distinguish the details. Because the circuit of the neural net is capable of memory, it can remember certain characteristics of the objects after the usual training with different objects. It can adjust certain vague images in bad weather. It can also be applied to improve tremulous images of the thermal imaging systems with vehicles, ships, planes trembling.

REFERENCES:

[1] Qian Yi and Li Huanju, 'A Theoretical calculation of the propagational characteristics of the mm wave in the Atmosphere,' Science Achievement Compilation of Wuhan University. 1981-1985.

[2] A. D. Culhane, M. C. Pecterar, C.R.K. Marrian, 'A neural net Approach to Discrete Hartley and Fourier Transforms,' IEEE Trans. On CAS, VOL, 36, no, 5, 1989, 695-702.

[3] J, M. Lloyd, 'Thermal Imaging Systems' plenum press 1975.

Th1.6

APPLICATION OF MILLIMETER-WAVE RADAR IN THE TRAJECTORY MEASUREMENT OF GUNS

Zhang Guang-Jin and Shun Xiang-Wen and Wu Ji-Guang
(East China Institute of Technology)

NTRODUCTION

Trajectory measurement is of great importance in the rasearch of ballistics as well as in the development and manufacture of new weapons. Tt is also indispensable for the aging test of guns and ammunitian. The goal of trajectory measurement is to obtain the motion principle of the ball. As the trajectory can be divided into two parts, that is the interior trajectory which is from the beginning point of motion to the end of the berrel, and the exterior trajectory which is out of the berrel. the trajectory measurement also inculdes interior trajectory and exterior trajectory measurement respectively. The methods of interior trajectory measurement used nowdays are rather out of date, some of them even have been used since 1960's. Among the disadvantages remain unsolved for a long time, the common problems in those methods are the poor accuracy and complicated operation.

At present, the best way for trajectory measurement is by applying radar Besides its appreciated simplicity and generality in operation, high accuracy can be provided by the method. What is more, the measurement does no harm to the gun, for there is no contact with the gun.

Presented in this paper is a millimeter-wave radar system we have developed for both interior and exterior trajectory measurement. The principle and constitution of hte system are introduced Results of practial test are given

FUNDEMENTAL PRINCIPLES

The operation of the mm-wave radar system for trajectory measurement may be oescribed with the aid of the block diagram shown in Fig.1. The mm-wave oscillation generated by the transmitter is fed through a circulator to the antenna, where it is radiated into space A portion of the transmitted signal is intercepted by to target which is the ball within the berrel and is reradiated into space. The antenna receives the returned energy and turns it to be the echo signal. Therfore, there are two signals put into the mixer through the circulator. One is the echo signal Ur and the other is the transmitted signal Ut leaked as a reference. With the motion of the ball

within the iberrl, a sequence of maximum or minmum in amplitude occurs alternatively in the output signal of the mixer. The time when the maximum or minmum occurs correspands to the ball's position where Ur travels longer than Ut at the distance n/2 or (n+1/2)/2. respectively, where n=0,1,2, .. and is the wavelength in free space.

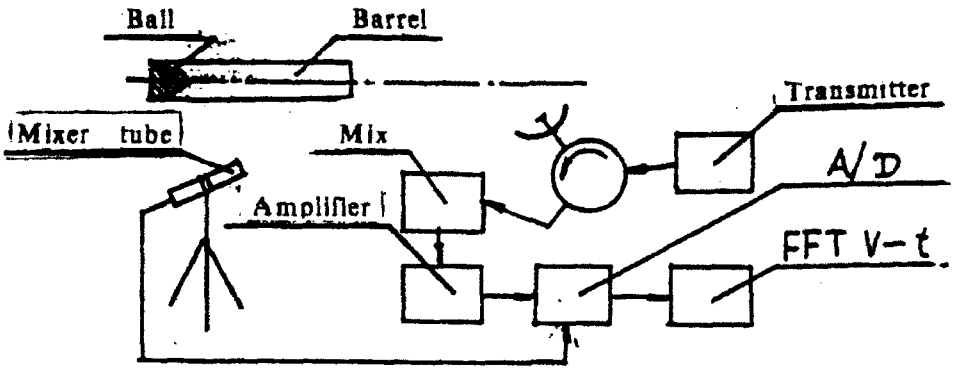

Fig.1 A block diagram radar and interior ballistics meaasurement

The output signal of the mixer is the doppler signal. The frequency of the signal is decided by the velocity of the ball. As shown in Fig.2. the typical doppler signal in interior trajectory measurement is frequency modulated Sine wave. where the variatians in the frequency embody the change in the ball's motion.

Fig.2 Wave of interior ballistics Doppler signal

The doppler signal must be processed in order to obtian the law of the ball's motion. The signal is amplified at first. and certain circuits are used to reject various interference such as the interference generated by the oscillation of the gun, the rotation of the recoil and the ball. Then the doppler signal is transformed into a numerical signal by A/D transformation and stored in computer. Finally. a FFT is applied by the computer. and the relationship between the velocity V and the time t is therefored derived. and the interior trajectory measurement is completed.

As the exterior trajectory measurement is concerned. the antenna should be turned to direct the ball's flying trace in the space. The above processing can also be applied.

The flash detector supplise acontrol signal for A/D transformor according to the flash generated at the moment when the ball bursts out of the berrel. This

signal indicates the beginning for the exterior trajectory measurement and the end for the interior trajectory measurement.

THE OPTIMAL WAVELENGTH

The berrel can be treated as a section of cylinder waveguide by its function in wave transmission. The wavelength in waveguide is given as

$$\lambda_g = \lambda / \sqrt{1 - (\lambda/\lambda_\beta)^2}$$

while λ ——— wavelength in free space

$\lambda_\beta = \pi d / J_{mn}$ ——— evanescent wavelength

d ——— diameter of the berrel

J_{mn} ——— nth root in m order Bessel function

The wave can be transmitted by the waveguide, i.e. the berrel only the condition is satisfied. The evanescent wavelength is depended on the waveguide modes as shown in Fig 3

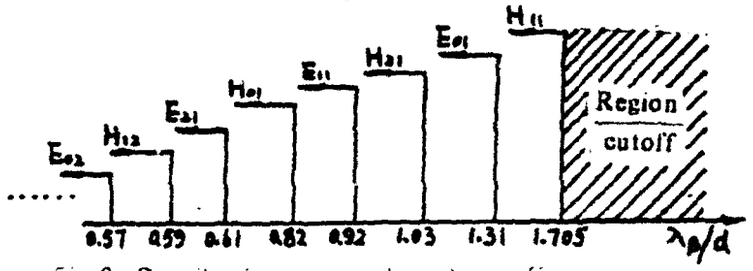

Fig.3 Distribution of wavelength cutoff

If the wavelength is chosen to meet the condition only one mode which is H11 mode here will be transmitted while other modes are evanescent. Such sigle mode transmission will lead to the best waveform and accuracy in measurement, so the wavelength which meet the above condition is defined as the optimal wavelength. The optimal wavelength corresponding to different diameter of the berrel is listed in the following table.

Calibre Ball (mm)	optimal wavelength (mm)
5.1	6.58— 8.71
7.62	9.98—12.99
12.7	16.64—21.65
14.5	19.00—24.72
20.0	25.20—31.10

For different diameter, a radar designed at the optimal wavelength must have different frequency, which will largely complicate the structure of radar. By carefully chosing the wavelength, satisfied generality has been acquired

in the sigle frequency radar system. Though the wavelength is not one of one mode is still domaint compared with other modes, under such case and the accuracy also meet the requirement with a deviation of about 0.1mm1%. For 5.1mm berrel, the wavelength of radar is 8.6mm.

TEST RESULTS

1. Interior Trajectory Measurement

Interior trajectory measurement is carried out with 5.8mm rifle, 7.62mm sub-machinegun and 14.5mm antiaircraft artillery. For every gun,15,23 and 11 balls are shot once respectively in the test. All of the measurement are completed with satisfactory results. The wave form of doppler signal stored by the oscilloscope is regular without deformity, as that shown in Fig.2. The measured curve of velocity versue time is also in agreement with the theoretical computation.

2.Exterior trajectory Measurement

The exterior trajectory measurement is carried out with 4.6mm gas gun 7.62mm rifle and 14.5mm antiaircraft artillery. The results are also satisfactory. The measured initial velocity agrees with the demarcate of the guns. The wave form stored by the oscilloscope is a regular frequency modulated sinusoid wave, signal-to-noise ratio decreases with the increase of the distance. By A/D transform and other computation, curves of exterior trajectory are acquired. According to the measured data and curves, the ratio of the radar active distance R to the diameter d of the ball can be evualated as that is the radar active distance is larger then the diamter by 9000 times.

CONCLUSION

As introduced in the above, the results of trajectory measurement we obtained by applying mm-wave radar are quite satisfactory. The data of multiple shots have good repeatability, and are in agreement with the theoretical trajectory. Meanwhile, the waveform is clear and correct as expected.

The method of trajectory measurement using mm-wave radar has many outstanding advantages superior to other methods, and is worth of much more development.

Th1.7

UNIVERSE, HUMAN BEING AND MILLIMETER WAVE

Fujian Light Industry Institute, China
Huang Wenzhou, Mao Fucheng, Hong Jinzhen

ABSTRACT

In the cosmic 2.7k background radiation field, the strongest is MMW radiation. There is also correlative discovery of the MMW energy crest in Chinese Chikung emanation. It will surely have great influence on knowledge of origin and process of life in universe.

1. Energy crest of millimeter wave found in Chikung emanation

In August 1989, Huang Wenzhou, engineer of Fujian Light Industry Institute, cooperated with research fellow, Yang Yufeng, and engineer, Zhang Huanghe, both working in Semiconductor Institute of CAS, meanwhile with Qu Daxin and Zheng Weiquan, senior engineers of No.12 Research Institute of Ministry of Machinery & Electronic Industries, P.R. of China, separately tested Chikung emanation of Lin Mengxiang, chairman of Fujian Bilinkung Research Society, and Cheng Linfeng, chairman of Beijing Huiliankung General Research Society, and his brother, to find out that there were millimeter waves fluctuating with low-frequency modulation in Chikung emanation. In other words, Chikung emanation could have an effect on MMW test instruments. Test results are as follows:

Chikung Eanation of Chikung Master Lin

	8mm Wave	4mm Wave	3mm Wave	2mm Wave
Max. indication on dynamometer (μW)	very little	4	8	0.1
Max. voltage indication on detector (mV)	0.5	2	rising to 11 after Chikung act	NM
Frequency of modulating wave measured by oscilloscope (Hz)	40—60	80—125	NM	NM

Chikung Emanation of Chikung Master Cheng

	8mm Wave	4mm Wave	3mm Wave	3cm Wave
Indication on dynamometer (μW)	1—2	NM	2—6	0.04—0.54
Indication on field strength meter (mW/cm^2)	0.4—0.7			NM
Frequency of modulating wave measured by oscilloscope (kHz)	100	NM	133	NM

In addition, energy of Chikung emanation of Chikung master Cheng brothers was measured to increase slowly along with rising of frequency by means of a 100Hz—40GHz spectrum analyzer. As spectrum of the MMW is broad, its integrad energy is high. In the meantime, very strong 3mm wave radiation was measured to exist by Xi'an Electronic Science & Technology University when a man with singular ability made tablets pass through the wall of medicine bottle, and it was stronger than the 8mm wave radiation measured at the same time. Science and technology workers in our country before had measured that in Chikung emanation there were radiations of infrasonic frequency wave, high-frequency electromagnetic wave and near infrared-ray etc., whose energy was all lower than that measured by Xi'an Electronic Science &Technology University and us. To sum up, a conclusion could be drawn that there are various radiations whose energy crest is in the MMW band. This discovery has unfolded before our eyes though it is still to be proved by more complete and comprehensive experiment.

2. Origin of human being and cosmic nonthermal background radiations at that time

We associate the discovery of mmw energy crest in human body field with the important finds on cosmic background radiation by Bell laboratory of USA in 1965, for energy crest of this famous 2.7K radiation is also in MMW band. Unless there is undiscovered cosmic radiation field of energetic neutrinos, gravitational waves or other unknown restless mass particles, the strongest in the discovered cosmic radiation field up to now is microwave radiation whose wavelength is from 1 to 10mm, as shown in following figure.

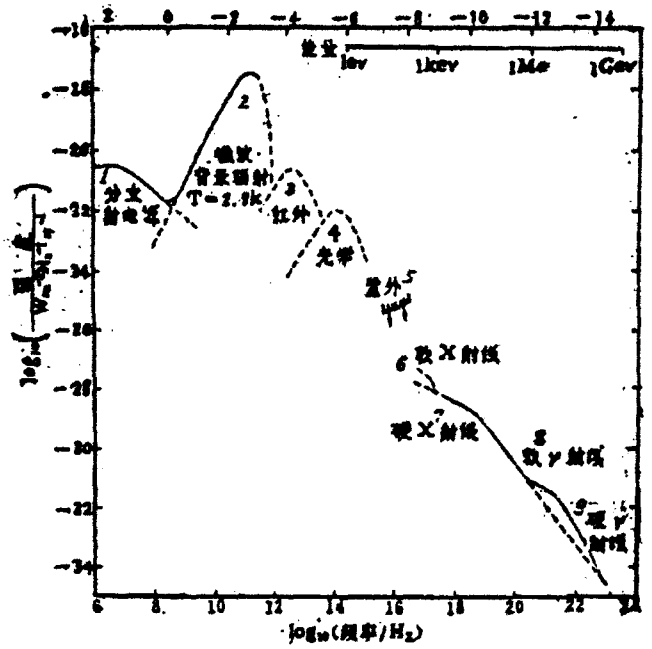

Spectrum of cosmic isotropic background radiation

The discovery of cosmic 2.7K background radiation supports the sudden expansion theory of origin of universe. Life couldn't emerge from the early hot universe. Based on Wien's blackbody radiation law, wavelength $\lambda = 0.3/T$ °K. Only when the whole cosmic background was into the submillimeter wave band, could human come into being. This puts forward a new method to determine origin time of human being. It could be said that human had made an indissoluble bond with millimeter wave at the moment of origin.

3. Status of MMW in quantum process of variation

4. Life bodies originated from different space-time fields and evolved separately

5. Regarding that life lies in oscillation from the point of view of three new theories

6. On the active treatment of disease

7. Invention of Chikung Therapeutic Apparatus Using the Millimetre Waves

8. Broad spectrum of "Chi" is holographic remains of cosmic electromagnetic phenomenon at the time of origin of human

high-ordered macrography quantum effect shown in Chikung state is the expression of natural human being. Radiations in cosmic field are of various frequency, whose energy crest is of MMW. The same is true of radiations in human body field. The extremely broad spectrum of " Chi " is exactly the holographic remains of cosmic electromagnetic phenomenon at the time of origin of human, and it shifts red gradually. From " Chi " we can see epitome of human in boundless universe and relationship between them. A wide variety of scenes in universe, such as fixed star, neutron star, planet, comet, life substance and mysterious unidentified objects, and so on, all developed from plasma cloud and were all concerned with cosmic emission. The broad spectrum radiation in " Chi " and information transmission in plama state of meriolian living thing both lively indicate that human is the epitome of universe. It wons more admiration that life bodies amazingly continue in accordance with their own genetic code. Process of universe is irreversible, So is growth of human being. Just as universe is boundless, thought of man is limitless. The reason why human and universe are alike so much is that they both came from mutation.

The important discovery of cosmic 2.7K background radiation prompts us to search for things in life similiar to quantum " remained in ancient times " so as to give informations of life bodies in earlier period. This is the basic purpose of this paper. The cosmic background radiation observed by American scientist in 1965 was awarded Nobel Price after 13 years—in 1978, then there is also correlative discovery of MMW energy crest in Chinese Chikung emanation, which will surely have great influence on knowledge of origin and process of life in universe.

Th1.8

TESTING SYSTEM FOR HIGH-ISOLATION OF MM-WAVE DARKROOM

Wang Donngjin Li Dunfu and Dou Yuanzhu

(Univ. of Science and Tech. of China. Hefei , China .)

INTRODUCTION

It is well known that MM-wave darkroom is important to study and test MM-wave system. Among the characteristics of the darkroom , isolation is one of the key factors. Thus during the period of the darkroom constructing the isolation must be measured carefully before putting the MM-wave absorber on the wall . The typical value of the isolation is about 110 d .

For measuring so higher isolation , two projects have been considered . One is using big power MM-wave transmitter and sensitive MM-wave detector ; shown in fig. 1 . Supposing that sensitivity of the detector is about -55dB and gain of the antennas 30 dB (If the gain great than 30 db , the MM-wave beam would be tco narrow to receive the signal easyly), and also let the distance between antennas be one meter, the output power of the transmitter should be several handred watts according to the calculation. It is difficulty to find such high power transmitter in the country at present; and it is impossible to use so heavy and large transmitter for measuring isolation at every place and corner of the darkroom, even if the transmitter could be found. So we have had to look for another testing system.

TESTING SYSTEM PRINCIPLE

Based upon the discussion above , it was realized that the main defect of above -cited project is the relatively low sensitivity of the MM-wave detector. As we know that the sensitivity of the receiver is much higher than the detector ; so by using MM-wave receiver to replace the detector may prove a suitable method to meet with the aim ; see fig. 2

At the measuring scene, the distance between the transmissing and receiving antennas is about to 2 meters, let it equal 2. Also let the antenna gain G be 23 db and the output power of the transmitter 19 db mw.

The transmission loss caused by passing through the space L is determined by :

$$L_1 = 20lg\left(\frac{4\pi r}{\lambda}\right) = 69.5dB$$

Assuming that the antenna effectiveness and other non-matched loss L is about 2 db together and the isolation of the darkroom L = 110 db, thus the required sensitivity of the receiver is

$$S = P_0 + 2G - L_1 - L_2 - L_3 = -116.5dBmw$$

On the other hand , the sensitivity of the receiver can be represented as:

$$S = F_{nn}KTB$$

If F_{nn}= 8 db and (this value id sufficient for effective detecting), the band width of the rece

B = 10 kkhz. Such band width is suitable for the video spectrum analyzer used as the display of the testing system. Yet, the key problem is that the if frequency must be stable enough to keep the receiving signal readable in the spectrum analyzer during the testing period,say two or three hours. According to the information of spectrum analyzer , HP 3585, spand width is about 100 kHz with analysis band 10 kHz . It means that the total frequency shift for both LO and RF source is 100 kHz . The compact phase locked source may satisfy the requeirement , but the price is high and some what heavier in weight compared with the cavity stabilized oscillator (CSO). As for econermic thinking , the designer would choose the matched CSO pair to meet with the requirments .

SYSTEM DESIGN AND MANUFACTURE RESULTS

As we know that the long term frequency stability states as:

$$\frac{\partial f}{\partial T} = \frac{\partial f_0}{\partial T} + \frac{1}{s}\frac{\partial f_1}{\partial T} \tag{4}$$

where S = 1+Q / Q is frequency stability factor , and Q and Q are the load Q factor of the stabilized cavity and unload Q factor of the main oscillator , respectively. $\partial f_0/\partial T$ and $\partial f_1/\partial T$ are the frequency variations of the stable frequency cavity and the main cavity containing Gunn dioder been influenced by temperature chang .In general ,$\partial f_1/\partial T$ is much larger than $\partial f_0/\partial T$, so the S would be as big as possible to reduce the value of $\partial f_1/\partial T$. The method is not only good for frequency shift , but beneficial in raising the short term stability of the oscillator . After fine adjusting and testing ,the characteristics of the matched CSO pair are:

transmitting source output power : 19 dBmw

phase noise −68dBc/ Hz (f_m = 1kHz)

The IF frequency shift is shown in fig. 3 . It is clear , as seen from the curves , that after half a hour of preheating the testing system would work successfully . The fin−line balanced mixer with preamplifier and the lens antenna are adopted in the system , the characteristics are:

noise figure : F_{SSB} = 4.5dB (including preamplifier)
gain of IR / RF : > 45 dB
with dynamic RF amplitude range :−45dBmw —— −110dBmw
antenna gain: 23 dB
first side lobe : <−30dB

The testing system is composed using the devices above .

TESTING STEPS AND EXPERIMENT RESULTS

A) Calibration

1) Open the door of darkroom .

2) Mount the two antennas at the distance 2 meters in the door place .

3) Using MM−wave precision attenuators in both transmission and recieving parts to replace the isolation of the darkroom .

4) Reading the total attenuation value of the two attenuators and the signal amplitude shown in the spectrum analyzer ; and marked as A_t and P_t , respectively .

B) Testing

1) Closing the door of the darkroom .

2) Moving the two parts of the system to the testing point in the same distance as the calibration condition .

3) Putting the total attenuation value to A_2

4) Reading the signal amplitude P_2 shown in the spectrum analyzer .

C) Calculation

The isolation of the darkeoom is determined by

$$L = A_1 - A_2 + P_1 - P_2 \tag{5}$$

The actual measurement results shown in fig. 4 , the isolation of the darkroom at the door is 118 dB . It is a very good result for darkroom design .

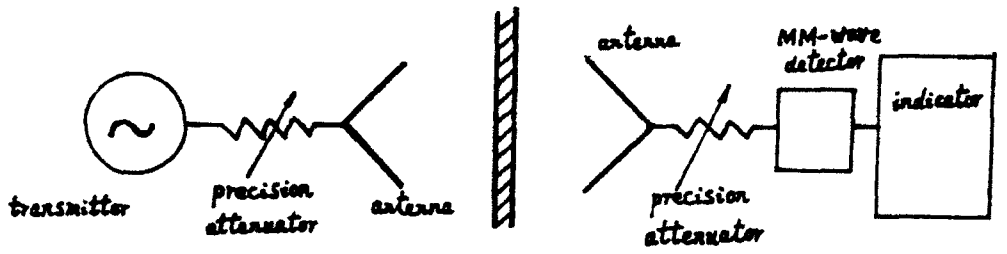

Fig. 1. Sketch of first projection

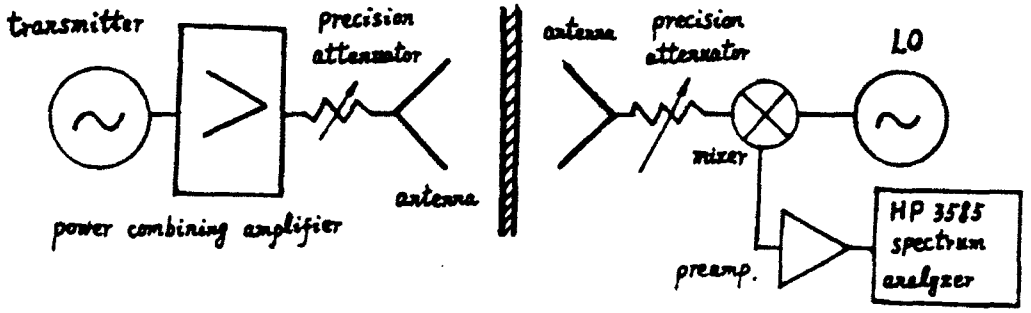

Fig. 2. Sketch of second projection .

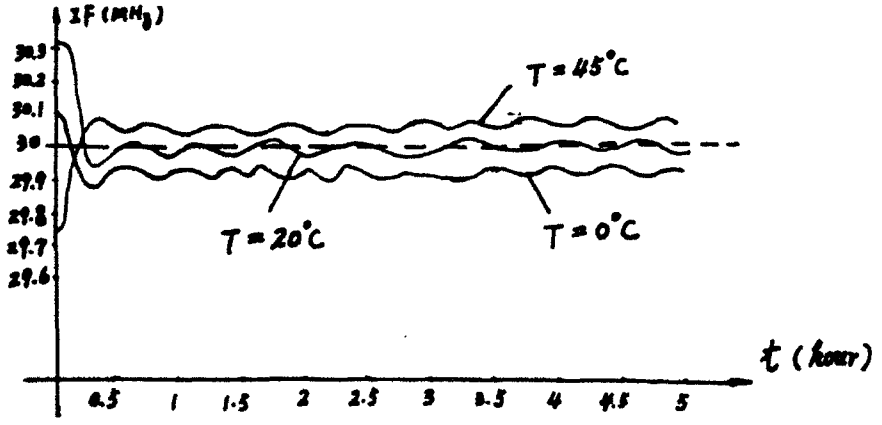

Fig. 3. IF frequency shift with temperature changing

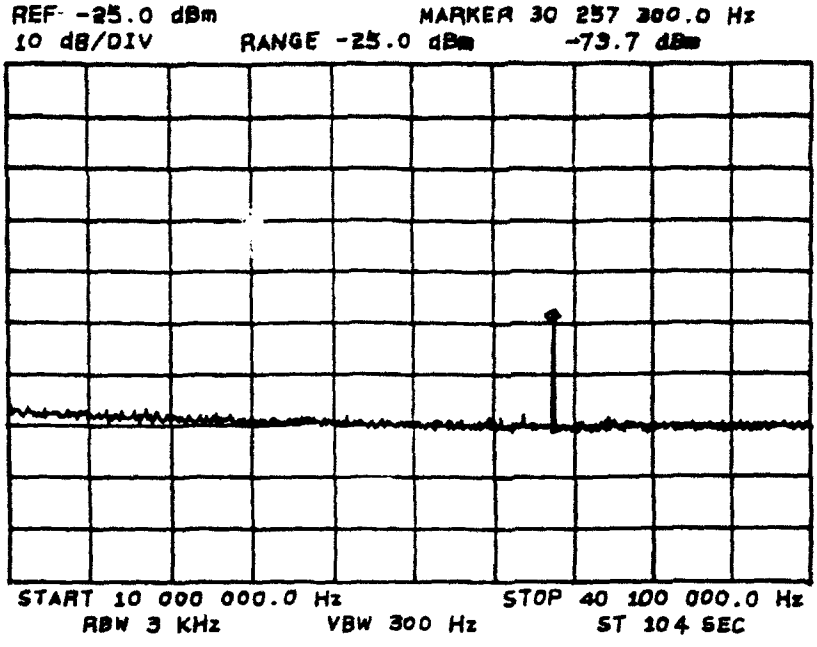

(a) calibration ($A_1 = 100\,dB$)

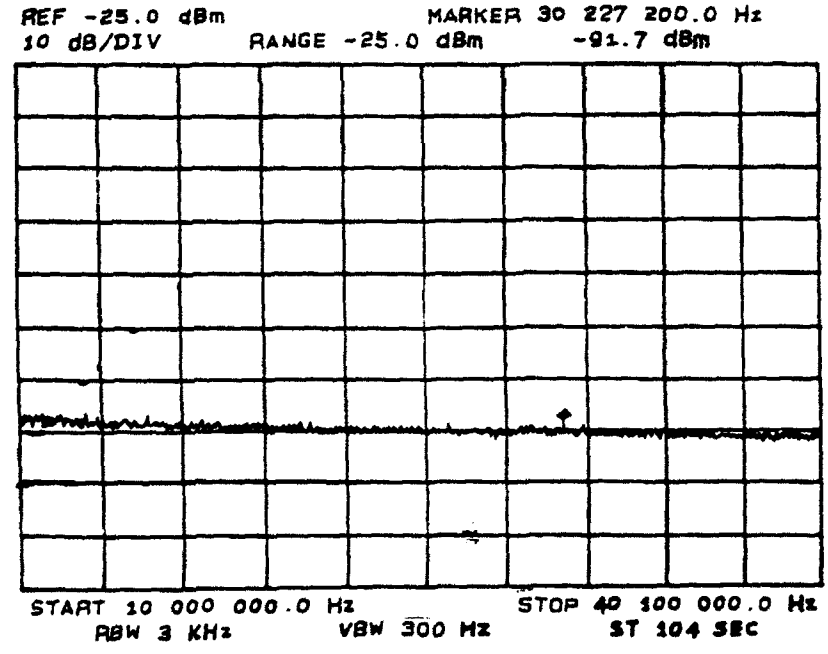

(b) testing ($A_2 = 0$)

Fig. 4. Measurement data

AN INVESTIGATION ON THE RF CHANNEL COUPLING AND THE RF SPACE COUPLING IN A MULTICHANNEL MILLIMETER-WAVE SYSTEM

Wang Yaming
(Luoyang Optoelectronic Institute, P.O. Box 030-7 Luoyang, Henan 471009, P.R. China)

Abstract

This paper describes an experimental investigation on the Ka-band RF multichannel system. It gives an experimental result of the RF channel coupling and the RF space coupling in different conditions, a measuring method , a couple of eqations that separate the RF space coupling from the RF channel coupling as well as a significant conclusion about the RF channel coupling and the RF space coupling in the millimeter-wave multi-channel system.

Introdution

In the multichannel millimeter-wave and the microwave system, the RF channel coupling and the RF space coupling have an adverse effect on the sensitivity and the precision of measurement. It is an important problem that has puzzled the engineers in microwave and system for a long time. Especially in the millimeter-wave system, this investigation has a great practical significance because the millimeter wave is shorter than the microwave wave length, the RF channel coupling and the RF space coupling are greater than that of the microwave.

Experiment

In the Ka-band, the RF channel coupling and the RF space coupling of a multichannel RF front end system are measured. The measuring block diagram is shown in Figure 1. One channel of multichannel RF front end connected to the Ka-band oscillator directly is the direct channel. The others are coupling channels. one is in opening in the RF end, the rest are connected to the matching load and the short in the RF end respectively. The RF input power in the direct channel is controlled by the attenuator. The power meter keeps watch on the RF input power in the direct channel. The IF output power in the channels is displyed by the Hp3585A spectrum. Typical coupling performance of the Ka-band

multichannel RF front end system measured is shown in table 1.

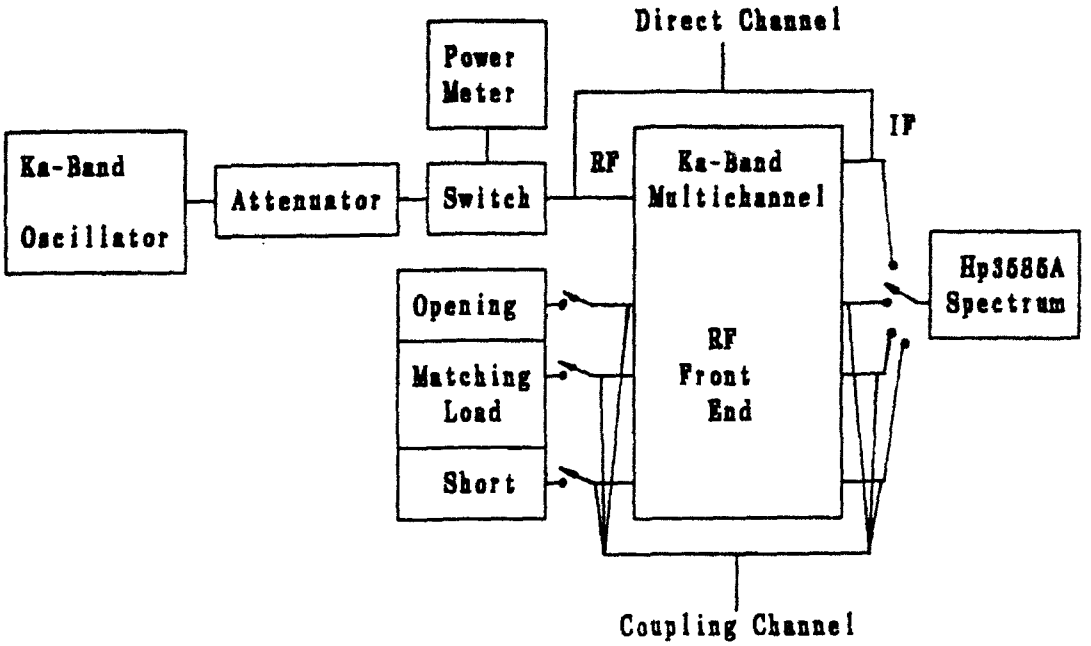

Fig. 1. Measuring diagram

Table 1. Typical coupling performance measured

A (dB)	Pin (dBm)	Pout (dBm)	Px (dBm)	Py (dBm)	Pz (dBm)
20	-20	1.9	-47.4	-72.9	-69.1
30	-30	-7.1	-47.9	-72.9	-70.2
40	-40	-17.2	-49.2	-74.4	-70.8
50	-50	-27.6	-48.7	-75.0	-71.1
60	-60	-36.8	-50.5	-74.3	-71.6
70	-70	-46.8	-50.5	-75.5	-72.1
80	-80	-56.9	-51.2	-73.9	-72.5
90	-90	-66.2	-50.2	-74.9	-71.8
100	-100	-72.5	-51.7	-74.7	-73.1
110	-110	-74.2	-50.5	-74.3	-73.3
120	-120	-74.4	-52.0	-75.1	-73.5

Where A is the attenuation in the attenuator in the measuring system. Pin is the RF input power in the direct channel. Pout is the IF output power in the direct channel. Px is the IF output power in the coupling channel that is in RF opening. Py and Pz are the IF output power in the coupling channels connected to the matching load and the short, respectively.

Discussion of the experiment result

In Table 1, for the direct channel, when Pin$\geq$ - 90 dBm, the space coupling power can not be compared with the channel coupling power in value and Pout is linear with Pin. When Pin<-90 dBm, the space coupling can compare with the channel coupling power in value. Pout is not linear with Pin. For the couplimg channel, when the RF end is in opening, the RF end is equivalent to a horn antenna. When the RF end is connected to the short, the RF channel coupling power is reflected in the RF input end. When the RF end is connected to the matching load, part of the RF channel coupling power is absorbed by matching load and the rest is reflected to the RF input end, therefore, Px>>Pz>Py.

A couple of equations that separate the RF space coupling from the RF channel coupling can be given as

$$Pa=P1+P2 \quad (1)$$

$$Pb=10^{-A}P1+P2 \quad (2)$$

Where P1 and P2 are the power of the channel coupling and the power of the space coupling respectively. A is the attenuation of the measuring system. Pa and Pb are the displayed IF power on the Hp3585A spectrum for different attenuations of the measuring system.
From (1) and (2) we have

$$P1=(Pa-Pb)/(1-10^{-A}) \quad (3)$$

$$P2=(10^{-A}Pa-Pb)/(10^{-A}-1) \quad (4)$$

The power of the RF channel coupling and the power of the RF space coupling can be given by multiplying P1 or P2 with the gain factor (or the attenuation factor) of the measuring system. It can be written as

$$Pc=K10^{-A}(Pa-Pb)/(1-10^{-A}) \quad (5)$$

$$Ps=K(10^{-A}Pa-Pb)/(10^{-A}-1) \quad (6)$$

where K is the gain factor (or the attenuation factor) of the measuring system. Pc and Ps are the power of the RF channel coupling and the power of the RF space coupling respectively. For example, in Table 1, Pa=-66.2 dBm, Pb=-72.5 dBm, A=-10 dB, K=-23 dB. From (5) and (6) , We have Pc=-100 dBm, Ps=-97.6 dBm. The RF channel coupling and RF space coupling in different conditions for the coupling channels can also be derived from (5) and (6).

The equivalent RF coupling performance measured is given by multiplying Px, Py, or Pz with K. It is shown in Table 2.

In Table 2, Pu is the RF coupling power in the coupling channel that is in RF opening. Pv and Pw are the RF coupling power in the coupling channels connected to the matching load and the short respectively

Conclusion

From the experimental investigation on RF channel coupling and the RF

space coupling in Ka-band RF front end system, we can reach the following conclusions.

Table 2. Equivalent RF coupling performance measured

A (dB)	Pin (dBm)	Pu (dBm)	Pv (dBm)	Pw (dBm)
20	-20	-69.3	-94.9	-91.0
30	-30	-70.8	-95.8	-93.1
40	-40	-72.0	-97.2	-93.6
50	-50	-71.1	-97.4	-93.5
60	-60	-73.7	-97.5	-94.8
70	-70	-73.7	98.7	-95.3
80	-80	-74.4	-97.1	-95.7
90	-90	-73.4	-98.1	-95.0
100	-100	-74.9	-97.9	-96.3
110	-110	-73.7	-97.5	-96.5
120	-120	-75.1	-98.3	-96.7

a. In the Ka-band multichannel system, for the RF opening (in coupling channel), the RF power of the space coupling is - 74.0 dBm. For the RF matching load, the RF power of the space coupling is -97.3 dBm. For the RF short, the RF power of the space coupling is -94.7 dBm.

b. For the leakproof Ka-band multichannel system and measuring system, the power of space coupling is -110 dBm.

c. In the Ka-band multichannel system, the difference between the power of the coupling channel and the power of the direct channel conforms with the isolation between the coupling channel and the direct channel.

d. The power of the space coupling is concerned with the output power of the Ka-band oscillator and the position of the measuring system.

e. The RF power of the space coupling has a value macroscopically while it is random in the microcosm. Because the random fluctuation of the space coupling changes with the environment of the electromagnetic field, therefore, when we caculate the value of the RF space coupling, we need combine Eq. (1) - (6) with mathematical statistics to process the performance measured so that we can obtain a better result.

Th2.1

A Three-Cavity Relativistic Klystron Amplifier

H. C. Chen, R. A. Stark and V. M. Ayres
Naval Surface Warfare Center
White Oak, Silver Spring, MD 20903-5000

ABSTRACT

The generation of large amplitude, monochromatic current modulation of an intense relativistic electron beam (500 KeV, 16 KA) by an external microwave source through a series of cavities has been studied via particle simulation. Various geometric configurations for cavity and gap size and cavity separation have been studied to assess feasibility and prioritized configurations for the efficient operation of relativistic klystron amplifier. A three cavity RKA was proposed for the future extra-high power microwave generation. This device could be scaled to operate in X band and below.

SUMMARY

The theory of relativistic klystron amplifier (RKA) for generating pulses of high-power rf radiation has been studied in great detail. The NRL RKA experiments have demonstrated that an annular intense relativistic electron beam (IREB) can be fully modulated by a moderate external rf source at a frequency of 1.3 GHz. Electric breakdown at the gap has been taken into account to monitor the gap length and cavity shape. Electromagnetic isolation between cavities which affects the operation of RKA has been investigated extensively. We used MAGIC, a fully electromagnetic, fully relativistic particle simulation code, to simulate IREB propagation in various RKA geometric configurations. The simulation geometry was shown in Fig. 1 where the radii of the drift tube and the IREB were r_w = 6.8 cm, r_b = 6.1 - 6.5 cm respectively, so that the annular shape beam had the thickness of Δr_b = 0.4 cm. The cylindrical cavity had radius R= 8.6 cm, the inner and outer conductors were symmetric with respect to the center of the annular beam. In the absence of an IREB, the frequency for driving the first cavity was adjusted until resonance of the second cavity occurred. The TM_{01} mode was the mode of operation and the operating frequency of 1.46 GHz was found. The beam parameters throughout the calculations were I_0 = 16 KA and Vinj = 500 KeV. An external axial magnetic field B_z = 10 Kgauss focused and guided the electron beam in drift regions. The characteristic impedance of the cavity was determined self-consistently in the simulation by the gap configuration which connected the cavity to the drift tube. The first cavity was loaded with RF energy, which generated an oscillatory gap voltage with a fixed frequency depending on the cavity size and gap shape. The second cavity was located downstream at a place for which the amplitude of current modulation was at a maximum. The important part was that the partially modulated beam by the first cavity

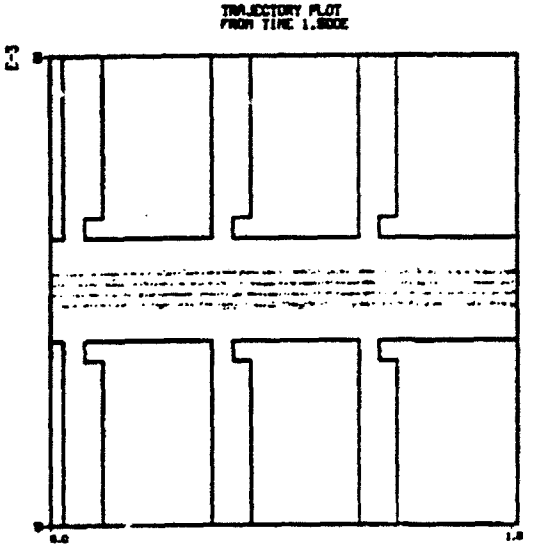

FIGURE 1 Three-cavity RKA configuration.

could energize the second cavity to generate very high gap voltage for full current modulation. Ideally, the cavities should be isolated electromagnetically from each other by requiring that the drift regions were cut off to all modes at the operating frequency. In principle, the attenuation of all modes should be optimized to prevent other modes and higher harmonics from growing and disrupting amplifier operation. Simulation parameters were Δr = 0.1cm, Δz = 0.56 cm, $\Delta t = 3 \times 10^{-12}$ sec. The simulation proceeds as follows: The first cavity was driven by an external rf source first, producing a certain oscillatory gap voltage at the resonant frequency of the cavity. After 5 nsec, the beam was injected with a current rise time of 5 nsec.

High power rf sources are in the popular demand now, especially from the accelerator community. As we know, the rf current is proportional to the rf voltage imposed on the gap. From simulation studies, we have found that the rf field that drives the gap voltage from the first cavity is not linearly proportional to the second generated gap voltage. Although we need only a moderate rf power source to generate the partially modulated IREB which in

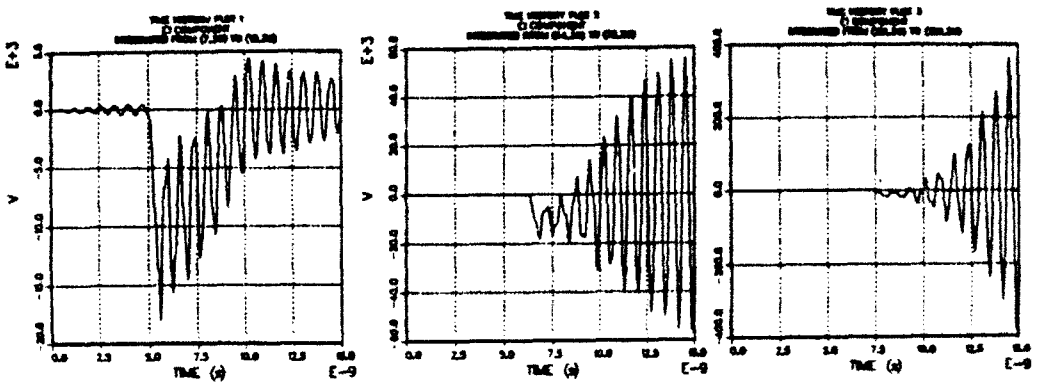

FIGURE 2 Oscillatory gap voltages of the first cavity (a), the second cavity (b) and the third cavity (c).

turn energizes a second cavity to generate a high oscillating voltage on its gap, however, there is a trend of continuous demand for a much higher power rf source, which will eventually become unavailable. In order to prevent this, we propose a three-cavity RKA which does not need a high power rf source to drive the cavity. Instead, a very weak rf source is used to prime the cavity. The magnitude of the driving rf field is no longer a factor in the operation of RKA. This concept very much resembles an auto accelerator in which the energy of the small portion of the beam is used to generate a high oscillating gap voltage to accelerate other portion of the beam. The three-cavity RKA configuration as shown in Fig. 1 is simply an extension of the two-cavity RKA. The third cavity is added further down stream with the same cavity separation. The main difference is that the first cavity will be powered by a very low power rf source which provides necessary seeding for the modulating frequency. As a matter of fact, the driving rf field is so weak that the operation of RKA becomes independent of the strength of the rf source. This gives us a lot of freedom to modulate extra high current beam without worrying about the availability of driving rf source. Simulation results of Fig 2a, 2b and 2c were the time evolution of the gap voltages of three cavities. The second cavity interacted with a weakly modulated beam and produced a moderate gap voltage which modulated the IREB partially. Finally, the third cavity was resonantly excited to produce the kind of high voltage needed to highly modulate the IREB. The current modulations after each cavity were shown in Fig 3. This configuration has the advantage of being easily scaled to a very large diameter, intense high current beam for generating extra high rf beam power. In order to have efficient operation of a RKA the cavities must remain isolated electromagnetically as far as the nonlinear beam-cavity interactions are concerned. Certain criteria for different cavity

COPY AVAILABLE TO DTIC DOES NOT PERMIT FULLY LEGIBLE REPRODUCTION

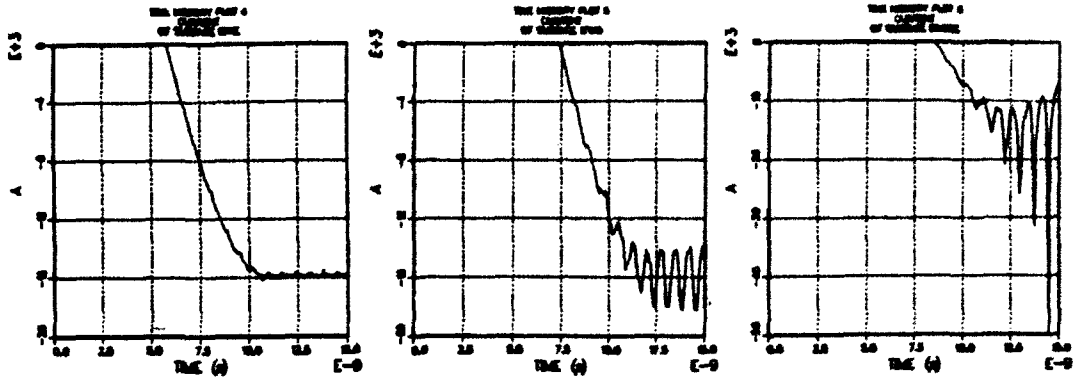

FIGURE 3 IREB current modulation at r = 0.2 cm (a), r = 0.6 cm (b) and r = 0.9 cm (c).

geometries are necessary in order to minimize gap loading effects, to avoid electrical breakdown at the gap. Once the geometric configuration is fixed, electromagnetic isolation of cavities has to be tested before injection of the IREB to optimize current modulation.

**This research was supported by the Innovative Sciences and Technology Office of SDIO, managed by Harry Diamond Laboratories.

COPY AVAILABLE TO DTIC DOES NOT PERMIT FULLY LEGIBLE REPRODUCTION

Th2.2

3 M.M. BAND (75-110 GHz.) BWO SWEEP OSCILLATOR DEVELOPMENT.

Zhu Ye-Mei; Xu Li-Gang
(Beijing Vacuum Electronic Device Research Institute.
Beijing P.R.C.)

ABSTRACT

A W-band BWO sweep oscillator has been developed. It consists of two parts, basic unit and plug-in unit. Changing the plug-in unit, other various bands in shorter millimeter wave range can be easy to get.
This instrument can be programed with a computer besides running in local state. Frequencies in both states of operation are displayed by digital panel meters. These are the main difference from traditional BWO sweep oscillators.

INTRODUCTION

Microwave sweep oscillator is the key to the automatic microwave measurement instrumentation, such as receiver, network analyzer, microwave spectrum analyzer, etc. But the function of these microwave sweep oscillators may be different in the instrumentation. For instance, in the receiver and the microwave spectrum analyzer, the microwave sweep oscillator is used as a local oscillator for realizing the heterodyne function, but in network analyzer, it is used as a transmitter which sends out linear frequency modulation signal to the device under test (the DUT). The signals reflect from and transfer through the DUT, therefore, they carry the information about the characteristics of the DUT.
Make a comparison between BWO and the solid devices in shorter millimeter wave range. BWO still has many advantages, such as RF high power output in a wide frequency range, directly creating the sweep frequency, it means that don't use the amplifying and mixing techniques, etc. It is most important that BWO oscillator can meet the request of the later function mentioned before.

PRINCIPLE AND CONSTRUCTION

An overall block diagram of the microwave sweep oscillator is shown in Fig.(1), in which a grid-levelled BWO oscillator unit is used as the shorter millimeter wave source. The frequency of the RF output is controlled by the delayline-to-cathode voltage applied to the BWO (Backward-Wave Oscillator). The amplitude of the RF output is controlled by the voltage applied between the grid and cathode of the BWO. However, shorter millimeter wave detector and directional coupler which have satisfactory frequency response in the respective band have not be developed. So, RF detector and directional coupler are not installed inside the instrument, and an external RF detector and directional coupler may be used, instead. In this mode of operation the output of the external detector is connected to the levelling amplifier input. As shown in Fig.(1), a portion of the RF output is sampled in the

directional coupler, detected and fed to the levelling amplifier. The levelling amplifier compares the amplitude of the detector output with a reference voltage and feeds a correction signal to the grid of the BWO through the grid supply so that the detector output remains proportional to the reference voltage. As the RF frequency is varied, the levelling loop operates continuously to maintain the detector output constant independent of the RF frequency. The amplitude variation of the RF at the front panel connector will therefore depend on the transfer characteristics of the directional coupler-detector combination only.

To amplitude modulate the RF output as the RF frequency is swept, a modulating signal is used in place of the reference voltage feeding to the levelling amplifier. The RF blanking during retrace, square wave , frequency marker signals, and external AM input signals are used to amplitude modulate the RF output in this manner.

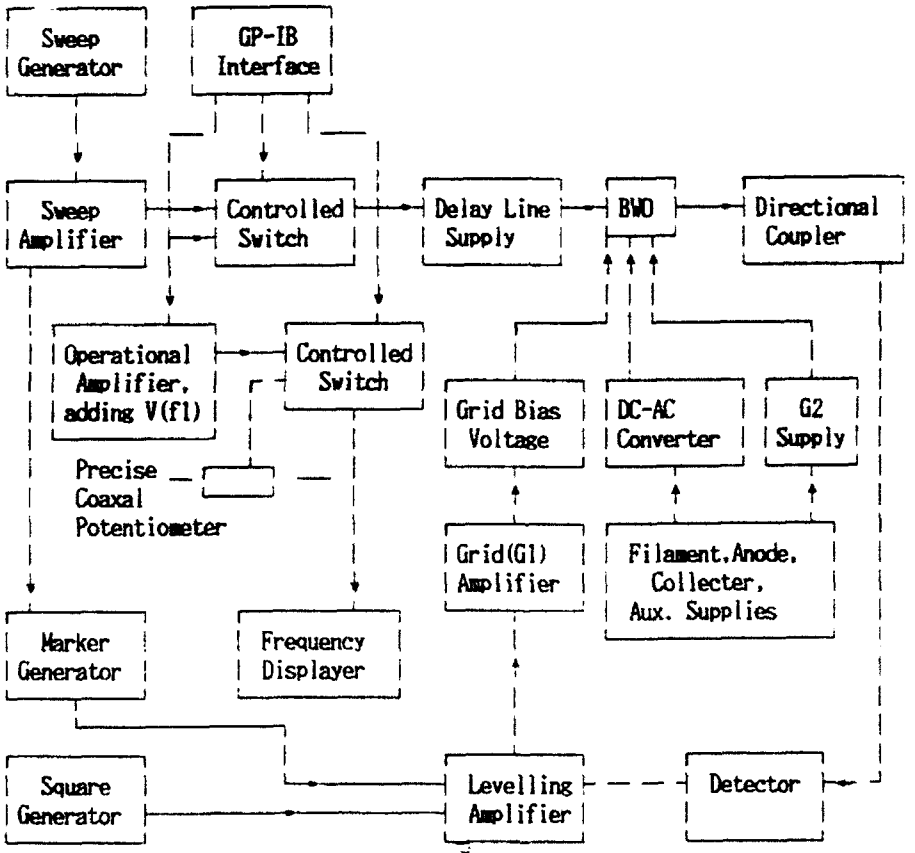

Fig.1 Overall Block Diagram

In the unlevelled mode of operation, the voltage applied to the grid of the BWO is manually set by the front panel RF level knob. Amplitude modulation of the RF output in the unlevelled mode is accomplished by feeding a modulating signal directly to the grid of the BWO.

The RF frequency range is covered by sweeping the output voltage of the delay-line supply. The sweep generator drives the delay-line supply with the required sweep voltage as determined by the settings of the front panel potentiometers. The sweep time can be divided into four steps, i.e. 0.01-0.1; 0.1 -1; 1-10; 10-100 sec. The

specific sweep time in each step range can be continuously varied with the front panel potentiometer. In addition, the sweep generator also supplies sweep voltage for synchronous output, retrace blanking and, at the slower sweep speeds, recorder pen lift during retrace.

The internally generated sweep waveform can be triggered by an external electrical trigger input or by the manual trigger switch. External control of the sweep waveform is provided by introducing an external electrical signal.

The marker generator combines the sweep signal and the voltages at the output of the marker controls to provide a marker signal when the output RF frequency corresponds to the reading of the frequency displayer.

The microwave sweep oscillator is equipped with a GP-IB interface. Therefore, it can be turned into a programmable instrument. With the GP-IB interface and GP-IB interface bus, the microwave sweep oscillator become a part of an automated instrumentation system. The GP-IB interface is made of a microcontroller (MCS-51), a D/A converter (DAC-1210), and some few chips. The function of the interface is carried out by software.

Two digital panel meters are used as the frequency displayer. The micowave sweep oscillator works under two states, the local and the remote. Under local state, the frequency displayer is feeded through controlled switch (see Fig.(1)) by a voltage from the precise coax-potentiometer which is coaxially tuned with frequency knob . Under another state, through controlled switch by a voltage from the GP-IB interface.

EXPERIMENT RESULTS

The main specifications and functions of the instrument are shown as follows.

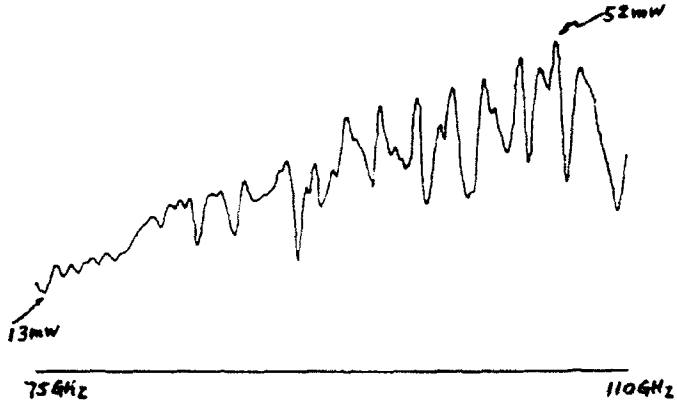

Fig.2 RF Power Output

1. Frequency range : 75--110GHz.
2. Frequency accuracy : 1%.
3. Frequency linearity : 1%.
4. Short period frequency stability : Less than $7x10^{-5}$ in ten minutes.
5. RF output power : More then 13mw, shown as Fig.(2) .
6. Sweep time : (Four steps) 0.01-0.1; 0.1-1; 1-10; 10-100sec.
   Continuous adjustment over the full range of every step.
7. Sweep output : Direct coupled, adjustable from 0-15 volts peak.
8. GP-IB interface and digital displayer .

CONCLUSION

A W-band BWO sweep oscillator has been developed, shown as Fig.(3). It is equipped with GP-IB interface. Through GP-IB bus, it can be controlled by a computer to realize programmable automatic measuring system. This instrument consist of two parts, basic unit and plug-in unit. To change the plug-in can get the other band of the shorter millimeter wave range.

Fig. 3 The outline of the microwave BWO sweep oscillator

REFERENCE

1. Automatic measuring system . (In Chinese)
   Published by Harbin Electric Instrumentation Research Institute & Electronic Science and Technology University of Chengdu.
2. Microcontroller Handbook .
   Published by Intel Corporation; Literature Department.

Th2.3

TEST OF WRC-40 (8mm) MILLIMETER-WAVE SOURCE

Yang Xiufang
(Southwest Institute of Applied Magnetics of China)

INTRODUCTION

Our institute has bought various types of millimeter-wave test instruments such as sources, measurement lines, frequency meters and waveguide accessories to meet the needs for millimeter-wave device fabrications.
Now in this country millimeter-wave measuring standards as well as millimeter-wave instrument check system and regulations have not been set up. Some institutes and factories fabricating millimeter-wave instruments have to lack some specifications. For example, the Institute of Applied Physics in the University of Electronic Science and Technology of Chengdu has lacked specification of the frequency stability.
Consequently it is necessary to investigate millimeter-wave measure and test method. By reference to the relative National Measuring and Check Regulation such as JJG 339-83, we investigated the measure and test method of millimeter-wave source and finished proof test and periodic test of XY-III (8mm) and WRC-40 (8mm) sources by means of our instruments and equipments.
This paper describes the test setup and specific test method of WRC-40 (8mm) millimeter-wave source.

TEST SETUP AND METHOD

1. Frequency range and stability test
A. Test setup
Frequency range and stabilitity test setup is shown in Fig. 1 (in the end of this paper).
B. Test method of frequency range
(a) As shown in Fig. 1, set BD-14-3-1 Variable Attenuator to maximum and FL16/3 Current Splitter to minimum range (×1).
(b) Set the 'LINE' switch of the source to 'ON' and the 'LOW VOLTAGE' switch to 'OFF'.
(c) Adjust the Oscillator's microcaliper to a desirable scale according as L-F table (see Manual).
(d) Set the 'LOW VOLTAGE' of the source to 'ON' and adjust the 'BIAS' to desirable value according as the Manual.
(e) Adjust BD-14-3-1 Variable Attenuator to make AC9/3 Galvanometer indications more than one hundred subscale.
(f) Adjust singly three Matching devices of BD- 14- 5 Detector to make AC9/3 indicate maximum .
(g) Harmonise PXZ-02 Frequency Meter to make AC9/3 indicate minimum. Read just now the frequency f'.
(h) Set the FL16/3 to maximum range (×0.0001).
(i) Decrease the attenuations of BD-14-3-1 and BD-14-3-2 until the fundmental order lamp of E3255 Automatic Microwave Frequency Transformer lights, then adjust clockwise E3255

'GAIN CONTROL' to maximum, observe the frequency displayed by the E325 Usual Frequency Counter. If the frequency is far from the frequency f', set the E3255 to 'MANUL', press the 'FUNDING ACTUATE' and readjust two variable attenuators until the E325 displays a correct frequency.

(j) Record the accurated frequency called f" by the combination of the E325/E3255 Millimeter-wave Frequency Counter.

(k) Set the 'LOW VOLTAGE' switch of the source to 'OFF' and then change the source frequency.

(l) Repeat step (a) — (k) until finishing the test of the source in whole band.

(m) Record frequency range specifications f and actully measured data f" in Table 2 (No. 901) and Table 4 (No. 907).

C. The test method of frequency stability

(a) Select a frequency (usually select centrical frequency) in whole band, according to B for measuring frequency f".

(b) After warming up the instruments for 30 minutes begin counting and record data f_i once at a minute for 90 minutes as to obtain ninety-one data, $i = 1 — 91$.

(c) Calculate the frequency stabilities as follows:

After warming up for 30 minutes:

$$\delta' = \frac{f_{i+5} - f_i}{f_i} \Big/ 5 \text{ min.}$$

After warming up for 1 hour:

$$\delta'' = \frac{f_{i+80} - f_{i+30}}{f_{i+30}} \Big/ 5 \text{ min.}$$

(d) Select $(\delta')_{max}$ and $(\delta'')_{max}$ as the test result of the frequency stability. Record them in Table 1 (No. 901) and Table 3 (No. 907).

2. CW output power

A. Test setup

Connect test setup as shown in Fig. 2 (in the end of this paper).

B. Test method

(a) Set the 'LINE' switch of the source to 'ON' and adjust the microcaliper of the Oscillator to a desirable scale.

(b) Set the 'LOW VOLTAGE' of the source to 'ON' and adjust the 'BIAS' to a specified value.

(c) Adjust BD-14-3 to zero dB and wait 2 minutes.

(d) Record the measured power p' by DC-341/ TMA-2 Millimeter-wave Dry Calorimeter. If the output of the source is over superior limit (P_{max} = 100 mW), increase the Attenuation of BD-14-3-1 to decrease input power, record just now power data P'.

(e) Set the 'LOW VOLTAGE' switch of the source to 'OFF' for changing f. Select several frequencies according to need, but must include the superior frequency limit f_H and inferior frequency limit f_L.

(f) Repeat the step (a) — (f).

(g) Record CW output power specifications P and the measured P' in Table 2 (No. 901) and Table 4 (No. 907).

SPECIFICATION AND TEST RESULT

WRC-40 is made of two instruments of No. 901 (26.5 — 35 GHz) and No. 907 (33 — 40 GHz).

1. WRC-40 (No. 901)

A. Frequency stability
The frequency stabilities are shown in Table1.

Table 1

Specification	Test Result	
Lack	Warming up for 30 minutes	$(\delta')_{max} = 8.3\times10^{-8}$/5 min
	Warming up for 1 hour	$(\delta')_{max} = 2.5\times10^{-8}$/5 min

B. Frequency range and CW output power
The frequency range and CW output power are shown in Table 2

Table 2

	Specification	Test Result
Frequency range	f = 26.5 — 35 GHz	f' = 26.42 — 35.43 GHz
CW output power	P > 20 mW	P' > 20 mW

2. WRC-40 (No. 907)
A. Frequency Stability
The frequency stabilities are shown in Table 3.

Table 3

Specification	Test Result	
Lack	Warming up for 30 minutes	$(\delta')_{max} = 4.1\times10^{-8}$/5 min
	Warming up for 1 hour	$(\delta')_{max} = 2.1\times10^{-8}$/5 min

B. Frequency range and CW output power
The frequency range and CW output power as shown in Table 4.

Table 4

	Specification	Test Result
Frequency range	f = 33 — 40 GHz	f' = 32.83 — 40.02 GHz
CW output power	P > 20 mW	P' > 20 mW

ON THE TRACK OF FREQUENCY AND POWER

In the above mentioned test setup, the frequency relative standard instrument E326 has been calibrated by the Institute of Test Technology of China and passed the test. The power relative standard instruments DC341/TMA-2 are Dry Calorimeters made in Japan and have been calibrated by the Second Research Centre of the National Defence Science Council.

RESULT

As mentioned above, WRC-40(8mm) millimeter-wave source test setup is reasonable and the

test method is feasible basically.

With the test setup and method described in this paper, the problem of the measure and test of millimeter-wave source has been solved in our institute. We provided the test data of frequency stabilities for the Institute of Applied Physics in the University of Electronic Science and Technology of Chengdu to help them to solve the problem of the specification.

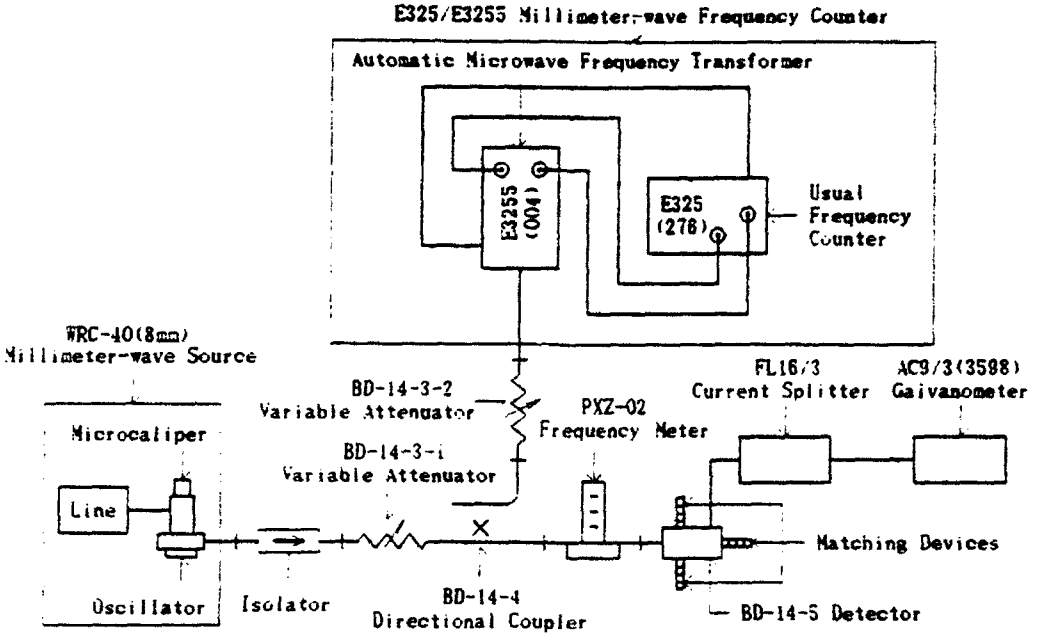

Fig. 1 Frequency range and stability test setup

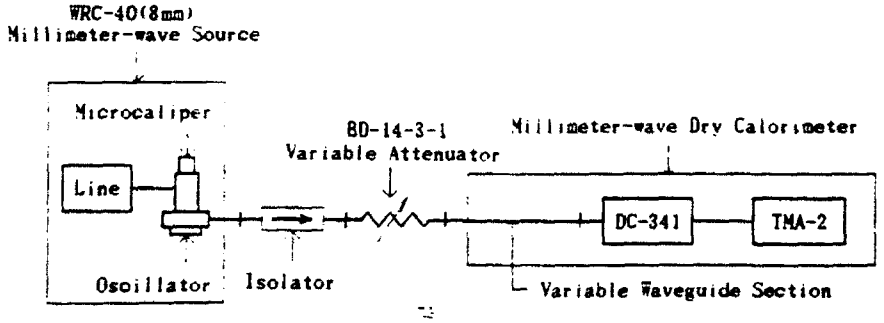

Fig. 2 Cw output power test setup

MILLIMETER WAVE INJECTED–LOCK FREQUENCY DIVIDERS

Chen Rushan, Sun Minsong and Li Xingguo
East China Institute of Technology

ABSTRACT

In this paper, the theoritical and experimental performances of a TED harmonically synchronized frequency divider are presented. The results show that such a divider has a 35.1 to 11.7 GHz division,with 25mw output power over the operating band greater than 1000MHz at 50mw input power level.

INTRODUCTION

Frequency dividers have promised many potential application in microwave / millimeter wave systems. Various analog and digital solutions have been proposed in order to realize microwave / millimeter wave frequency dividers. Among well–known analog solutions are the regenerative dividers[1]and the parameter dividers[2].Harmonic synchronization of a free–running oscillator is an alternative powrful means of performing frequency division. Small signal harmonic synchronization of nonlinear oscillators were discussed by I.Schmideg[3]. By means of TED , Upadhyaywla[4]developed a frequency divider, with dynamic frequency division up to 6 at 16GHz. The wide locking range requires the large injected harmonic signal. However,the conventional small signal analysis is no longer valid. This paper devotes itself to a more exact analysis of harmonic oscillators. A large signal nonlinear negative resistance description for the TED is adoped. The locking range of oscillators is calculated by the averaging method. The experimental results are demonstrated.

MODEL OF HARMONIC SYNCHRONIZATION DIVIDER

An efficient and pratical model is developed, which leads to a tractable description of the performance of harmonically synchronized oscillators. As shown in Fig.1, this model improves on Kurokawa's linear model[5]in that it includes inherently nonlinear effect involved in harmonic synchronization. A time–invariant linear network divides the load impedance into two parts: one is effective only for the fundamental frequency and another only for the third harmonic frequency. The active element is modeled as a real resistance, whose current–voltage dependence is described by the power series[6]

$$I = C_1 V + C_2 V^2 + C_3 V^3 \qquad (1)$$

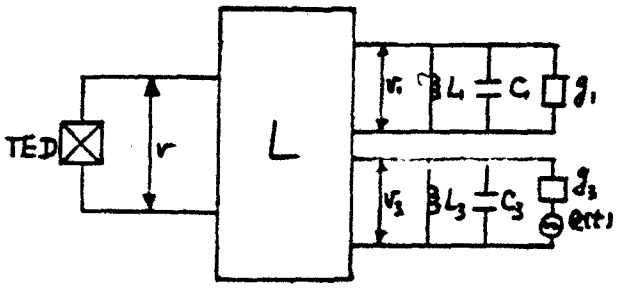

Fig.1

where $c_i = a_i$ for the fundamental frequency and $c_i = b_i$ for the third harmonic frequency ($i = 1,2,3$), the coefficient may be adjusted by an appropriate bias circuity in physical devices. It is assumed that when expanded as Fourier series, the voltage across the active element would contain only the fundamental frequency component and the third harmonic component.

Let the injected signal e(t),the fundamental frequency signal v1(t) and the third harmonic frequency signal v3(t) be as follows:

$$e(t) = V_i \cos(3wt) \quad v_1 = V_1 \cos(wt - \theta_1) \quad v_3 = V_3 \cos(3wt - \theta_3) \tag{2}$$

Substituting eqn.(2) into (1) yields

$$I_1(w) = a_1 V_1 \cos(wt - \theta_1) + \frac{3}{4} a_3 V_1^3 \cos(wt - \theta_1) + \frac{3}{2} a_3^{1/3} b_3^{1/3} V_1 V_3 \cos(wt - \theta_1)$$
$$+ \frac{3}{4} a_3^{2/3} b_3^{1/3} V_1^2 V_3 \cos(wt - \theta_3 + 2\theta_1) \tag{3}$$

$$I_2(3w) = b_1 V_3 \cos(3wt - \theta_3) + \frac{1}{4} a_3 V_1^3 \cos(3wt - 3\theta_1) + \frac{3}{4} b_3 V_3^2 \cos(3wt - \theta_3)$$
$$+ \frac{3}{2} a_3^{2/3} b_3^{1/3} V_1^2 V_3 \cos(3wt - \theta_3) \tag{4}$$

Applying Kirchhoff's voltage law to the network shown in Fig.1, one obtains

$$C_1 \frac{d^2 v_1}{dt^2} + G_1 \frac{dv_1}{dt} + \frac{1}{L_1} v_1 = -\frac{di}{dt} \tag{5}$$

$$C_3 \frac{d^2 v_3}{dt^2} + G_3 \frac{dv_3}{dt} + \frac{1}{L_3} v_3 = -\frac{di_3}{dt} + G_3 (v_3 - e(t)) \tag{6}$$

Eqns.(5) and (6) are nonlinear and homogeneous second-order differential equations. let $\tau_1 = wt$ and $\tau_3 = 3wt$. Eqns.(5) and (6) can be expressed in the following form

$$\frac{d^2 v_1}{d\tau_1^2} + v_1 = h_1 v_1 - \frac{1}{wC_1} \left[\frac{di_1}{d\tau_1} + G_1 \frac{dv_1}{d\tau_1} \right] \tag{7}$$

$$\frac{d^2 v_3}{d\tau_3^2} + v_3 = h_3 v_3 - \frac{1}{3wC_3} \left[\frac{di_3}{d\tau_3} + G_3 \frac{d(v_3 - e(t))}{d\tau_3} \right] \tag{8}$$

where $h_1 = 2(w - w_{01})/w \quad h_3 = 2(3w - w_{03})/(3w) \quad w_{01} = 1/\sqrt{L_1 C_1} \quad w_{03}$

$$= 1/\sqrt{L_3 C_3}$$

Substituting eqn.(2) into (7) and (8), one gets

$$\frac{dV_1}{d\tau_1} = -\frac{V_1}{2wC_1}\{a_1 + \frac{3}{4}a_3 V_1^2 + \frac{3}{2}a_3^{1/3}b_3^{2/3}V_3^2 + G_1 + \frac{3}{4}a_3^{2/3}b_3^{1/3}V_1 V_2 \cos(3\theta_1 - \theta_3)\} \quad (9)$$

$$\frac{d\theta_1}{d\tau_1} = \frac{1}{2}h_1 - \frac{1}{2wC_1}\frac{3}{4}a_3^{2/3}b_3^{1/3}V_1 V_3 \sin(3\theta_1 - \theta_3) \quad (10)$$

$$\frac{dV_3}{d\tau_3} = -\frac{1}{6wC_3}\{(b_1 + G_3)V_3 + \frac{1}{4}a_3 V_1^3 + \frac{3}{4}b_3 v_3^3 + \frac{3}{2}a_3^{2/3}b_3^{1/3}V_1^2 V_3 + G_3 V_1 \cos\theta_3\} \quad (11)$$

$$\frac{d\theta_3}{d\tau_3} = \frac{1}{2}h_3 - \frac{V_1 G_3}{6wC_3 V_3}\sin\theta_3 \quad (12)$$

When the free–running oscillator is synchronized, the output amplitude and phase of the frequency divider are time–independent, i.e.,

$$\frac{dV_1}{d\tau_1} = 0 \quad \frac{d\theta_1}{d\tau_1} = 0 \quad \frac{dV_3}{d\tau_3} = 0 \quad \frac{d\theta_3}{d\tau_3} = 0 \quad (13)$$

Eqns.(9)–(13) are solved for the amplitudes V_{10} and the phase θ_{10} of fundamental and V_{30}, θ_{30} for the third harmonic frequency. It should be mentioned that eqn.(13) is valid only for the case when the oscillator is locked to the injection signal, but not sufficient for evaluating the frequency division of the divider. The latter requires the stable oscillation. The remainder is to derive the stability condition. Suppose an additional small perturbation . Let us examine the circuit to see if its output will grow or die away with time.

Making use of Liapounov's method[7],one gets

$$\Delta_1 = \frac{V_{10}}{2wC_1}[\frac{3}{2}a_3 V_{10} + \frac{3}{4}a_3^{2/3}b_3^{1/3}V_{30}\cos(3\theta_{10} - \theta_{10}) + 3\cos(3\theta_{10} - \theta_{30})] \quad (14)$$

$$\Delta_2 = \frac{V_{10}}{(2wC_1)^2}[\frac{9}{2}a_3 V_{10}^2 \cos(3\theta_{10} - \theta_{30}) + \frac{9}{4}a_3^{2/3}b_3^{1/3}V_{30}V_{30}] \quad (15)$$

According to Hurwitz's theorem[7], if $\Delta_1 > 0 \qquad \Delta_2 > 0$ (16)

The frequency divider will be stable.

Substituting eqn.(14) and (15) into (16), one obtains the relative locking ranges in the fundamental frequency and in the third harmonic frequency as follows:

$$B_w = \frac{3}{4Q_1 g_1}a_3^{2/3}b_3^{1/3}V_{10}V_{30} \quad (17) \qquad B_{3w} = \frac{1}{Q_3}\sqrt{\frac{P_1}{P_{30}}} \quad (18)$$

where $Q_1 = wC_1/g_1 \qquad Q_3 = 3wC_3/g_3$

Equation (18) was derived in case of the fundamental frequency injected–lock oscillatos by Adler[8]

If $3B_w/B_{3w} > 1$, the band of the frequency division $B(w) = \frac{1}{3}B_{3w}$; otherwise, $B(w) = B_w$.

GaAs TED FREQUENCY DIVIDER CIRCUIT AND RESULTS

Fig.2 shows the 35.1 to 11.7GHz divider circuit layout implemented on a 0.25mm thick fiberglass–reinforced teflon substrate. A two–terminal TED with $N_0L > = 2 \times 10^{12} cm^{-2}$ is mounted on the microstrip line. Input and output signals are separated by using filters instead of a circulator. Initially, the TED is dc biased beyond the threshold voltage so that it oscillates in the transit time state or the circuit controlled mode.And then, the bias is reduced until the TED ceases to operate. An input signal, whose frequency is about 3 times the free–running oscillation frequency of the TED, is injected for the output to occur. As the input signal amplitude increases and bias is beyond the threshold level, an output frequency response is observed. The experiments indicate that the synchronization range depends on the drive level. This locking behavior of the divider is shown in Fig.3.It is of interest to note that the locking range of the divider is a monotonous function of the injection power. When the injection power level becomes large enough, the locking range approaches its asymptotic value. This is consistent with the prediction of the large signal model.The maximum locking range reaches 3% at 35GHz with the output power about 25mw.

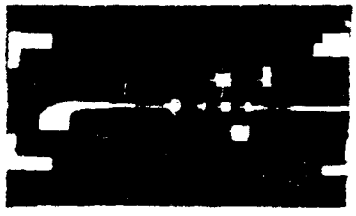

Fig.2

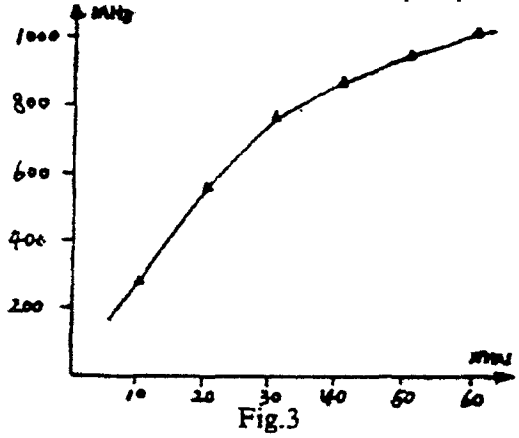

Fig.3

CONCLUSIONS

A nonlinear model has been developed. In cooperation with Van Der Pol's model for the active device, the present model is capable of calculating the locking range and the output power of harmonically synchronized oscillators. The experimental results show this model is useful for designing harmonic frequency divider circuits.

REFERENCES

1. R.L.Miller, Proc.IRE, 37(7) (1939), 446
2. R.G.Harrison, IEEE–MTT, 25(12) (1977), 1055
3. I.Schmideg, Proc.IEEE, 59(8) (1971), 1250
4. L.C.Upadhyayula, RCA Review, 34(12) 1973, 595
5. K.Kurokawa, Proc.IEEE, 61(10) 1973, 1386
6. K.Kolbach, IEEE–MTT, 30(8) 1982, 1233
7. Peter Hagedorn, Non–linear Oscillations, Oxford university Press(1981)
8. R.Adler, Proc.IRE, 44(7) 1946, 351

Th2.5

INVESTIGATION OF THE CATHODE FOR MILLIMETER WAVE TUBE

Zhou Zhizheng , Chen Aiju
(Beijing Vacuum Electronics Research Institute)

ABSTRACT

In order to satisfy the requirement of millimeter wave vacuum electron device to the cathode, a series of investigations of the cathode was done. We developed Sc_2O_3-oxide coated cathode , W-Sc_2O_3 mixed matrix cathode, improved scandate cathode, improved W matrix body and W-Mo mixed matrix scandate cathode. At the same time, many effective techniques were adopted in the last cathode fabrication process.

INTRODUCTION

With the development of millimeter wave vacuum electron device, the requirements for the cathode have become much harsher, such as low operating temperature,high emission current density, small dimension, high machining accuracy, excellent emission surface finish, long lifetime and low active material evaporation. At present, for the commercial cathode, it is impossible to meet the above requirements . In order to reach the above purposes , a series of investigations were done. We developed Sc_2O_3 - oxide coated cathode, W - Sc_2O_3 mixed matrix cathode, improved scandate cathode, improved W matrix body and W-Mo mixed matrix scandate cathode. At the same time, lots of effective techniques were introduced in the last process of cathode fabrication in order to make the cathode properties as excellent as possible.

Sc_2O_3-OXIDE COATED CATHODE

Put a little of Sc_2O_3 (1-10% by weight) powder into the coatings of general oxide coated cathode. After mixing them into uniform material, the Sc_2O_3-oxide coated cathode can be obtained according to the conventional fabrication process of oxide coated cathode. And after degassing and ageing , the emission characteristic of the cathode were measured out. The result was that the emission current density had been raised about 50% than the general oxide coated cathode at the same operating temperature. The current density drawn from the Sc_2O_3-oxide coated cathode in space-charge limited region was 1.6A/cm^2 at the operating temperature of 800°Cb. It is seen that to use this cathode for millimeter wave tube was unsatisfactory. However, it is an ideal electron source for the color display devices with high brightness, high clarity and high current density.

W-Sc_2O_3 MIXED MATRIX CATHODE

Experiments prove that after adding a little of Sc_2O_3 to the general aluminate, the emission ability of the cathode impregnated by this aluminate is much higher than that of the cathode impregnated by the general aluminate . According to this, can we make the mixed matrix by mixing a little of Sc_2O_3 powder and tungsten powder and fabricate dispenser cathode impregnated by the general aluminate? Therefore, the W-Sc_2O_3 mixed matrix cathode was developed. For fabricating this cathode, (1-10% by weight) Sc_2O_3 powder and (99-90% by weight) tungsten powder were uniformly mixed togather, and the matrix was obtained according to powder metallurgy, then the W-Sc2O3 mixed matrix cathode was fabricated by impregnating with the 5:3:2 or 4:1:1 ($BaO:CaO:Al_2O_3$)impregnant mixture. After that, the emission property can be measured in a water - cooling

anode diode . The space-charge limited current density was 6A/cm^2 at 1000 °Cb .This value is 4 times as high as that of the aluminate cathode and similar to that of Ir-coated dispenser cathode. But the emission property of W-Sc_2O_3 mixed matrix cathode was excellent at low temperature. The space-charge limited current density was 1.2-1.4A/cm^2 at 800 °Cb, which is better than that of the general oxide cathode and almost the same as that of the Sc_2O_3-oxide coated cathode.

The key process for manufacturing this mixed matrix cathode, besides the weight percent and the uniform mixing between the tungsten and Sc_2O_3 powder, were the forming pressure and the sintering temperature. As long as these factors were controlled better, an excellent cathode matrix with smooth emission surface and homogeneous porosity can be obtained. Emission of the cathode are therefore much higher. Otherwise, the emission property will become bad. Comparing this mixed matrix cathode with the scandate cathode , although emission current density was lower than the latter , the resistance to ion bombardment was indeed better. The disadvantage for this cathode was that lots of Sc_2O_3 powder was used.

IMPROVED SCANDATE CATHODE

The scandate cathode has widely used in manufacturing electron tubes today . At the 1985 Beijing International Rare-earth Scientific Conference, for this cathode mounted in water-cooling anode diode,the emission current values given in our paper were that the DC current density of deviation point was above 10A/cm^2 and the pulse emission current density was above 50A/cm^2 at the operating temperature of 1000°Cb. At 900°Cb, the DC emission current density was 5-6A/cm^2 and the pulse current density was 34A/cm^2. At present, this kind of cathode was used in millimeter wave tube . While cathode operation in electron tubes, sometimes there was the phenomenon of unsufficient emission. The reason may be caused either in tube manufacture or in cathode fabrication. As a cathode researcher, the investigation should certainly be started with the cathode fabrication . The scandate was made by co-precipitation. During preparing, it was found that for the same raw materials the emission properties of the scandate were different in each preparation, such as the normal emission current density was over 10A/cm^2 at 1000°Cb , but poorer it was 5-6A/cm^2 even much lower, only 3.1A/cm^2. The reasons were that all the concentration and temperature of every solution and velocity of the stirrer have influence on the cathode emission ability. In order to raise the cathode emission , lower the operating temperature and obtain identical emission in each preparation process, we prepared more than 10 kinds of compositions according to different combinations among the concentration, the temperature of the solution and the velocity of stirrer. Experiments gave the following conclusions: The temperature for all solution should be at room temperature. The optimum velocity of stirrer used in our experiment was 230 turns/min. The solution concentration must depend on the calculation value. As long as the above three rules were strictly obeyed while preparing, an excellent emission property can be obtained for each preparation.

IMPROVED W MATRIX BODY

The new - type cathode consists of refractory matallic matrix and active materials . When the investigation of active material reaches a definite stage, it is necessary to improve the cathode matrix in order to get excellent cathode characteristics. Such as shape of tungsten powder, size and distribution of the tungsten powder particles, spheroidization and classification of the tungsten powder and blue tungsten powder application. The purpose was to make the porosity dimension and distribution of the pore uniform and to increase the active material covering on emission surface in order to get a high and uniform emission.

A. Tungsten Powder Spheroidization Experiment

Spheroidize the general tungsten powder, then fabricate the scandate cathode according to the flow chart of general scandate cathode . The emission measurement for this cathode in water cooling anode diode gave us the following results: The DC current

density of deviation point was 7-9A/cm^2 at 900°Cb. Compared with the general scandate cathode made by unspheroidized tungsten powder, the emission current density was raised 50%. The DC current density was 4-5A/cm^2 at 800°Cb, it was much higher than the Sc_2O_3-oxide coated cathode and the W-Sc_2O_3 mixed matrix cathode. These results were satisfactory. But the disadvantage for spheroidized tungsten powder was that the forming was difficult, especially for the classified tungsten powder after spheroidized. In order to press the spheroidized and classified tungsten powder into matrix, it is necessary to mix the powder with paraffin wax. In a word, the spheroidized tungsten powder is an ideal cathode substrate material. But it is difficult to buy this kind of tungsten powder.

B. Blue Tungsten Powder Instead Of Yellow One

In the past, the tungsten matrix was fabricated by the yellow tungsten powder made by yellow WO_3 , which means particle-size is 6-7μ. Today we try to use the blue tungsten powder(mean particle-size:3-5μ) made by blue WO_{3-x} instead of yellow tungsten powder to fabricate the tungsten matrix. The cathode emission property may be obviously improved. This experiment is being done now.

C. Tungsten Powder Classification

We are going to classify the blue and yellow tungsten powder with the mean particle-size of 3μ, 5μ and 6-7μ. Remove the fine and rough powder, and fabricate cathode matrix with the medium grained tungsten powder in order to obtain an excellent emission surface with uniform porosity.

W-Mo MIXED MATRIX SCANDATE CATHODE

It is reported that the electron emission for cathodes become doubled and redoubled at the interface between tungsten and molybdenum grains. In order to get high emission current and molybdenum powder with the same particle-size should be mixed as uniform as possible according to a definite composition.

LAST CATHODE FABRICATION PROCESS

An accurate maching was needed for the cathode used for millimeter wave tube. Dimension of the cathode was small, a high maching accuracy and excellent emission surface finish must be reached. During the last cathode fabrication process, the following methods were used, such as maching, scraping, grinding with high velocity grinder and polishing with thin tungsten wire or silver sand-paper. Because the cathode is much smaller, It was difficult to grind it, maching and scraping can only be used here . Thus, it is difficult to quarantee the high accuracy and excellent finish of the emission surface. A high accuracy program-controlled lathe was therefore needed in order to meet the above requirements.

CONCLUSION

In summary, at present the scandate cathode is more satisfactory among these kinds of cathode investigated. It was this cathode that was used in electron tube. But the emission current density can not meet the requirement of electron tubes, such as a pulse emission current of 20A/cm^2 is needed for some millimeter wave tube. Experiments prove that the emission current density for the cathode in electron tube corresponds to about 1/5 of that in diode. Thus the emission current density in diode should be above 100A/cm . According to the characteristic of new type cathode, the emission current density should increase once while the operating temperature of cathode is raised about 50°Cb. If the current density is 34A/cm^2 at 900°Cb, it should be therefore 68A/cm^2 at 950°Cb, and 136A/cm^2 at 1000°Cb. In fact, it does not like this. If the progress has been extended in investigation of cathode matrix, it is possible to get the pulse space charge current density of 20A/cm^2 at 950°Cb to meet the requirement of millimeter wave tube.

Th2.6

NETWORK SYNTHESIS OF RF WINDOWS FOR MM TWTS

J.L.Zhang and G.J.Su
(Beijing Vacuum Electronics Research Institute,China)

1. ABSTRACT

A novel waveguide RF window of the MM wave TWTs is described. The design theory is presented. The results of the theory and experiment are given. The wider bandwidth or thicker window plate than old type's can be obtained.

2. INTRODUCTION

There are some common requirements which are wide bandwith, small VSWR, low loss and high power ability etc. of RF windows for TWTs. The power resistibility of low and mid-power output tubes is not serious but the wide bandwidth with a small reflection is more difficult, especially for MM TWTs, because the bandwidth rely on the thickness of the window-plate, the wave length and its dielectric coefficient Eps. Unfortunately, there are only a few choices of the dielectric materials for the window-plate, such as 99% Al2O3, quartz, sapphire and BeO etc. The dielectric coefficients Eps and strengths of the materials are quite different even for the same material which is made by different technology. In general, sapphire is more strong but its Eps is above 11, so which will limits the bandwidth of the window. BeO's Eps is about 5 to 6 but the vacuum tight and mechanical strength can not be ensured if its thickness is less than 0.5 MM. In this paper, the structure of the window with a thick plate has been discussed.

A mid-power MM wave TWT of US[1] has been using a inductance compensated waveguide window instead of Pill-box window having got a good result. VSWR is less than 1.2 in bandwidths from 6 up to 10 GHz with 1 MM thickness of the window-plate. But its frequency response was obtained by adjusting the inductance stubs on waveguide wall under cold-test. It is not easy to get predict response, however, also can no utilize theoretical optimum. Here a new structure of the inductance compensated waveguide window has been raised. The dimensions of the structure can be calculated by the microwave filter network synthesis theory to utilise the potential source of the bandwidth at the thick window plate.

3. STRUCTURE AND PHYSICAL MODLE OF THE FILTER WINDOW

The structure of the new window is shown in fig.1. There are three half wavelength cavities consisting of four pair inductant irrises on the narrow walls of the wave guide. The middle cavity is filled with dielectric plate. This is a bandpass filter. Its equivalent circuit is shown in fig.2. This filter can be designed by a standard network synthises process.

First step is to get the values of the low-pass prototype elements. For maximum flat response they are:

$$g(0)=1 \tag{1}$$

$$g(k+1)=2*\sin[(2*k-1)*pi/2], \quad k=1,2,3,\ldots,n \tag{2}$$

$$g(n+1)=1 \tag{3}$$

where

pi=3.1415926

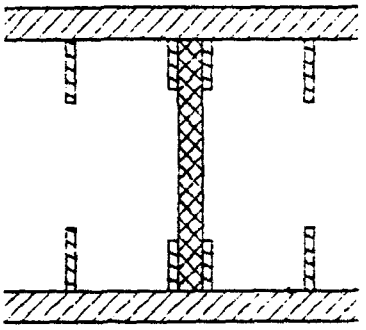

Fig 1. Structure of filter RF window

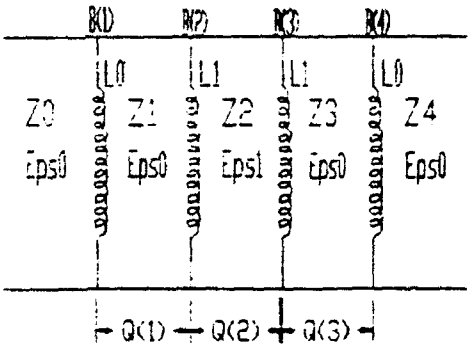

Fig 2. Equivalent circuit

If Chebyshev response is required, the ripple within pass band must be given. Then the values of prototype elements can be looked up from a table. If some other responses are interested the prototype must be given. Now the loaded susceptances of every cavity can be calculated foliowing[2]

$$B(i)=U(i)*Y(i-1) \qquad (4)$$

where

$$Y(i)=1/Z(i)$$

is the characteristic susceptances of the waveguides,

$$U(i)=sqrt([V(i)+1/V(i)]*h(i)-[1+h(i)**2]) \qquad (5)$$

In eq(5) the

$$h(i)=Y(i)/Y(i-1)$$

is the rate of the adjacent waveguides and

$$V(1)=V(n+1)=2/pi*wl'/rh*g(0)*g(1) \qquad (6)$$

$$V(i)=4/pi*wl'**2/rh**2 \quad (i.GE.2.and.i.LE.n) \qquad (7)$$

$$rh=(a1-a2)/(a1+a2) \quad (ai \text{ is the wavelength}) \qquad (8)$$

where a1 and a2 are the guided wavelength of the band sides respectively. wl' is equal to 1 in above equations.

The electric length of every cavities are:

$$Q(i)=2/pi + F(i)" + F(i+1)' \qquad (9)$$

$$F(i)'=1/2*arctg([U(i)**2+h(i)**2-1]/[2*U(i)]) \qquad (10)$$

$$F(i)"=1/2*arctg([U(i)**2+1-h(i)**2]/[2*h(i)*U(i)]) \qquad (11)$$

The dimensions of the inductant irrises can be calculated from B(i) using Marcuvitz's equations[3]. As a matter, the guide wavelengths, characteristic impedances and the electric length of the waveguides tightly relate on dielectric coefficients of the filling materials. Up to now the all dimensions of RF window can be designed.

4. RESULTS

A computer program has been created to deal with the calculation. Then the results are identified by the cold test. The typical response functions of the calculation and test are shown in fig.3 and fig.4. In same bandwidth, the thickness of the window plate of the new window increases about 2.5 times of the Pill-box window[4]. And the theory is agreed with the experiment well. Only the bandwidths of measurement are a little less than theoretical one.

5. CONCLUSION

The new filter RF window has a thicker window plate than Pill-box window[4]. It is more suitable to the MM wave TWT. The design method is convenient and accurate.

The authors are thankful to the help of computing and experiment by Mrs Y.M.Wang and Y.F.Ge.

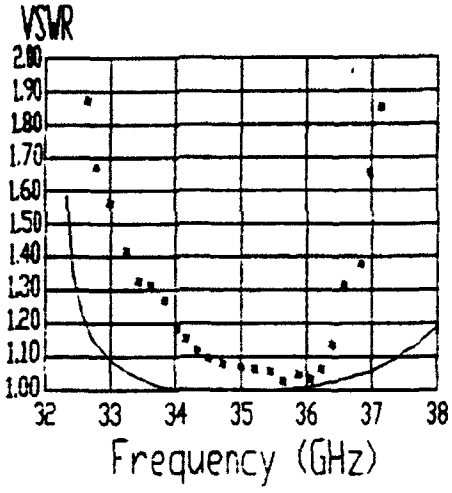

Fig 3. The responces of 95% AL2O3 ceramic window
thickness 1 mm
dielectric coefficient Eps=8.9
solid line is theoretical
stars are experimental

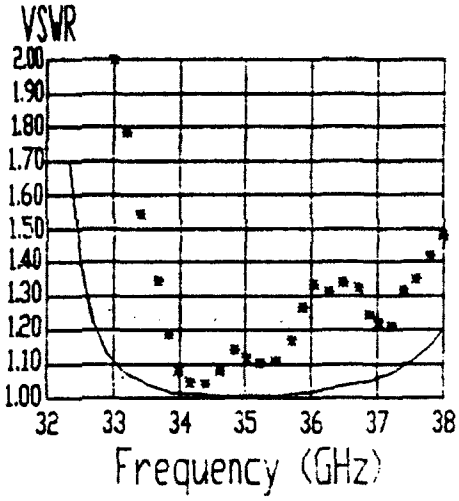

Fig 4. The responses of BeO ceramic window
thickness 1.2 mm
delectric coefficient Eps=6.5
solid line is theoretical
stars are experimental

6. REFERENCES

[1] NASA CR 134670 June 1977.
[2] G.L.Mathaei,et.al "Microwave Filters, Impedance-Matching Networks, Coupling Structures" McGraw-Hill Book Co., 1964, P528.
[3] N.Marcuvitz, "Waveguide Handbook," Peter Peregrins Ltd.,1951, P211.
[4] "Design Handbook of Low and Mid Power TWT," Defence Industry Press., Beijing, 1967.

MILLIMETER-WAVE SYNTHESIZERS

G.M.Altshuller[1], O.G.Anikin[1], O.P.Pavlovsky[1]
E.N.Karyakin[2], V.P.Kazakov[2], A.F.Krupnov[2]

[1] *IEM KVARZ*
Gagarin prospekt 176
603009 Nizhni Novgorod, Russia
[2] *IAP Russian Academy of Sciencies*
Uljanov Street 46
603600 Nizhni Novgorod, Russia

A new generation of the millimeter-wave synthesizers provide high stability and very low phase noise signal from 37.5 to 118.1 GHz. This is accomplished by phase locking mm-wave oscillator to an internal reference or external reference of 5 MHz or 10 MHz. Backward-wave oscillator (BWO) are used as a source of mm-wave signal. Each of BWO cavers the full waveguide band.

The instrument provides synthesized mm-wave signals in precise increments of 100 Hz. Maximal output power of the synthesizers varies up to 25 mW depending on waveguide band and design.

Mm-wave sygnal can be AM,FM and pulse modulated.

Combination of fast frequency switching (5-20 ms) with microprocessor control gives a wide sweep capabilities of mm-wave synthesizers.

The synthesizers consists of a main frame and mm-wave module (generator). Each of three mm-wave modules has one of bands: 37,5-53,57 GHz; 53,57-78,33 GHz; 78,33-118,1 GHz.

Figure 1 shows signal spectrum of the synthesizer at 96,02 GHz. It is taken with a spectrum analyzer at the 20 MHz IF. The vertical scale is 10 dB/div and the horizontal scale is 10 KHz/div. The resolusion bandwidth is 100 Hz.

The instruments are used as signal source for complex impedance measurements and broadband receiver testing.

Mm-wave synthesizers are used for molecular spectra measurements of OCS, N_2O, C_2D_2. A some rotational transitions were measured to test the accuracy of new synthesizers.

Figure 2 shows an absorption spectrum of OCS molecul, obtained on spectrometer with acoustic detector [1]. The signal from absorption line at FM-mode and fast frequency switching with step of 0,1 MHz is illustrated in the left part. The right part shows scan of a little part in the center of line with step of 0,0003 MHz In this case accuracy of the center line measurement is a few KHz.

Figure 3 shows absorption spectrum of J=18-17 C_2D_2 transition at frequency of 101789 MHz and at pressure of 0,5 torr in AM-mode. It was the demonstration of possibilities of the synthesizers for investigation of intermolecul interaction, in this case collisional line broadening.

The traditional videospectrometer with passing cell of one meter long and crystal detector was used for investigation of narrow line. The results show, that resolution of gas spectrometer with mm-wave synthesizer is limited by Doppler effect only($\frac{\Delta\nu}{\nu}\sim10^{-6}$).

The results of using of the instruments show high measurements precision. Furthermore a wide programmabilities does work with synthesizers extremely simple and comfortable.

Similar synthesizers up to 178 GHz are developed now. Furthermore signal on more higher frequencies can be obtained by

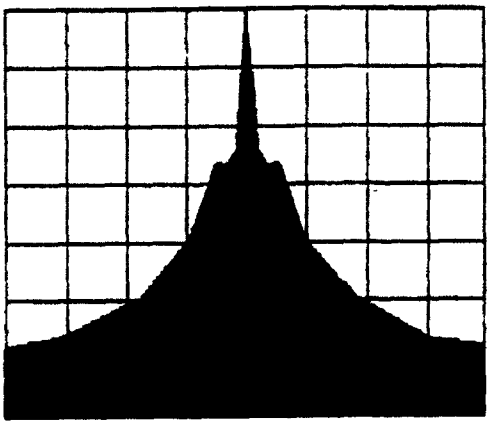

Figure 1

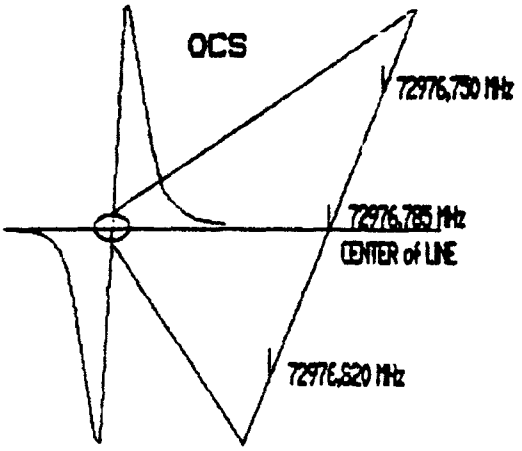

Figure 2

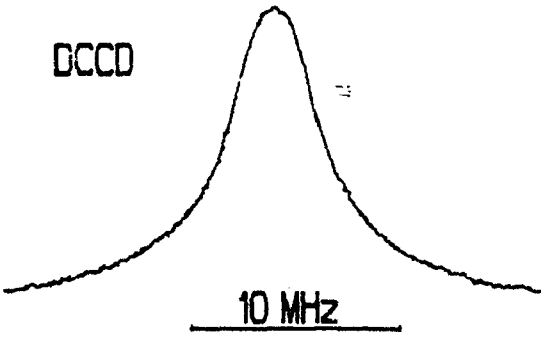

Figure 3

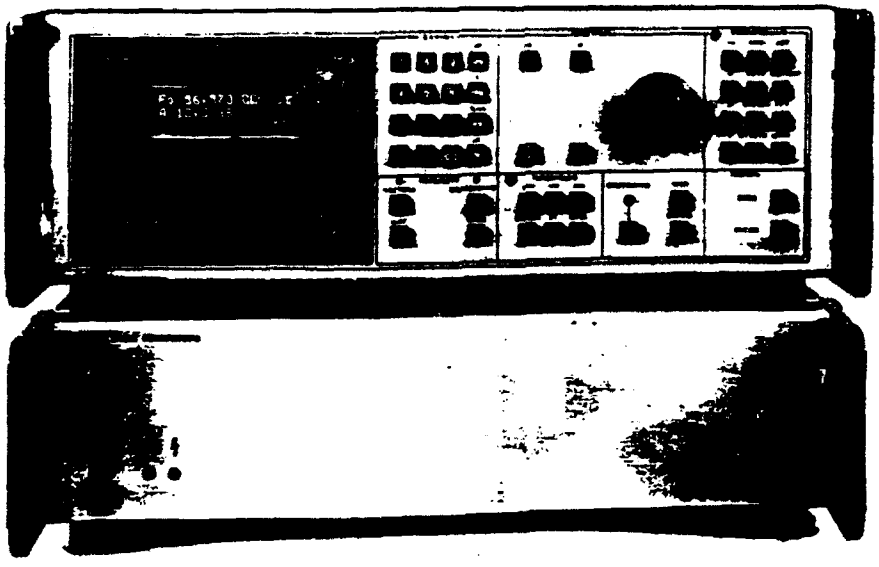

Figure 4. Mm-wave frequency synthesizer
from 53,57 to 78,33 GHz.

multiplication because of sufficient output power of the mm-wave synthesizers.

REFERENCES

[1] A.F.Krupnov, Vestnik Academy of Sciencies, USSR, 1978, N 7, pp.18-30.

Th2.8

NEGATIVE HIGH FREQUENCY CONDUCTIVITY IN SUBMICRON SEMICONDUCTOR STRUCTURES

V.M.Yakovenko

Institute of Radiophysics and Electronics,
the Ukrainian Academy of Sciences,
12, Acad. Proskura st., Kharkov, 310085, Ukraine

A modern technology allows to create semiconductor structures which possess physical peculiarities important for SHF electronics (ballistic transport, dimensional quantum effects, etc.). In particular, in such structures electromagnetic oscillations can be unstable as a result of transient radiation of the charged particle flux /1/-/2/.

In the present report a mechanism of arising of negative frequency conductivity in submicron structures has been suggested and investigated on the basis of the effect of transient radiation of particles. Such structures are as follows: well-known semiconductor structures made of galium-arsenide and aluminium-gallium arsenide (devices of the type of a tunnel amplifier with a transfer of hot electrons)/3/.

We consider a structure consisting of a semiconductor layer limited by two ideally conducting planes. Here a semiconductor occupies a space region $0 \le x < L$; a system is unlimited in the direction y,z.

A current created by an injected particle with a charge e and effective mass m, has the following form

$$j_k^{(0)} = \frac{ie\hbar}{2m}(\Psi_k^{(0)}\nabla\Psi_k^{(0)*} - \Psi_k^{(0)*}\nabla\Psi_k^{(0)}), \qquad (1)$$

where $\Psi_k^{(0)} = V^{-1/2}\exp(i\mathbf{k}\mathbf{r} - E_k\hbar^{-1}t)$ is the wave function of a free electron with the dispersion law $E_k = \hbar^2k^2/2m$, $\mathbf{k}=(k,0,0)$ is the wave vector, $\hbar$ is the Plank constant, $p=\hbar k$, $V=LS$, S is the square of the cross-section of the sample.

Further suppose that the layer is affected by a weak longitudinal homogeneous field $E = -c^{-1}\partial A(t)/\partial t$, where $A(t)=(A_x,0,0)$ is the vector-potential which is a time periodic function $A(t) = A\exp(-i\omega t) + A^*\exp(i\omega t)$. Then an addition to the stationary current of the particle may be written as

$$j_k=\frac{ieh}{2m}(\psi_k^{(1)}\nabla\psi_k^{(0)*}+\psi_k^{(0)}\nabla\psi_k^{(1)*}-\psi_k^{(1)*}\nabla\psi_k^{(0)}-\psi_k^{(0)*}\nabla\psi_k^{(1)})\frac{e^2}{mc}A(t)\psi_k^{(0)}\nabla\psi_k^{(0)*} \quad (2)$$

The whole density of the alternating current may be written as

$$J=\sum n_k j_k, \quad (3)$$

where n_k is the number of electrons in the k state.

The whole wave function of the particle $\psi_k=\psi_k^{(0)}+\psi_k^{(1)}$ satisfied the Shredinger equation

$$ih\frac{\partial\psi_k}{\partial t}=(\hat{H}_o+\hat{H}^{(1)})\psi_k, \quad (4)$$

where

$$\hat{H}_o+\hat{H}^{(1)}=\frac{1}{2m}(\hat{p}-\frac{e}{c}A(t))^2\approx\frac{\hat{p}^2}{2m}-\frac{eA(t)}{mc}\hat{p}\ ; \quad \hat{p}=-ih\frac{\partial}{\partial x}\ .$$

Having used the known method of constants variance for solving linear differential equations /4/, we find from the expression (4)

$$\psi_k^{(1)}(t)=\sum a_{k'k}(t)\psi_{k'}^{(0)}\ ;\ a_{k'k}(t)=\frac{ek[1-\exp i(k-k')L]}{mcL(k'-k)}\int_{-\infty}^{t}A(t')\exp(i\omega_{k'k}t')dt',$$

$$\omega_{k'k}=h^{-1}(E_{k'}-E_k). \quad (5)$$

Accounting for the energy of the injected particles in submicron structures to be distributed in the comparatively narrow domain near any central value of the applied intensity one may consider a distribution function to be equal to

$$n_k=(2\pi)^3 n_o\delta(k-k_o)\delta(k_y)\delta(k_z)\ ;\ hk_o=mv_o. \quad (6)$$

Substituting this value into the formula (3) and passing from summation over k and k' to integratioin we obtain the following expression for the high frequency conductivity of the semiconductor structure with allowance for poles $\omega_{k'k}+\omega=0$ and $\omega_{k'k}-\omega=0$

$$\sigma=\frac{e^2 n_o}{h\omega\tau}\left\{\frac{1}{k_-}\left[\frac{k_o-k_-}{(k_o+k_-)^2}\sin^2\frac{L}{2}(k_o+k_-)+\frac{k_o+k_-}{(k_o-k_-)^2}\sin^2\frac{L}{2}(k_o-k_-)\right]-\right.$$

$$\left.\frac{1}{k_+}\left[\frac{k_o-k_+}{(k_o+k_+)^2}\sin^2\frac{L}{2}(k_o+k_+)+\frac{k_o+k_+}{(k_o-k_+)^2}\sin^2\frac{L}{2}(k_o-k_+)\right]\right\} \quad (7)$$

where $k_\pm=\sqrt{k_o^2\pm 2m\omega/h}$, $\mathrm{Re}k_\pm>0$, $\mathrm{Im}k_\pm<0$, $\tau=L/v_o$ is the time of the electron transit through a layer, $h\omega$ is larger than the Γ width of the k_o level.

It is seen from the expression (7) that under the condition $2\hbar\omega \leq mv_o^2$ the first product specified by the processes of electron emitting of quantums of the electromagnetic field and proportional to the multiplayer k_-^{-1} exceeds the second one which, in its turn, is proportional to k_+^{-1} and specified by electron transits with quantum adsorption.

In a classic case $2\hbar\omega << mv_o^2$ from the formula (7) we arrive at

$$\sigma = -\frac{1}{2\pi} \frac{\omega_o^2}{\omega^2 \tau} \sin^2 \frac{\omega\tau}{2} . \qquad (8)$$

where $\omega_o = \left[\frac{4\pi e^2 n_o}{m}\right]^{\frac{1}{2}}$ is the plasma frequency of electrons.

Conductivity has an oscillating character specified by definite relations between the time of the electron transit trough a layer and a period of oscillations.

The absolute value of the negative conductivity reaches the most meaning at $2\hbar\omega < mv_o^2$ in the conditions of the of the resonanse: $k_o L = n\pi$, when an odd number of de Broglie semiwaves for the electrons with the energy $mv_o^2/2$ ($n=1,3,5\ldots$) falls on the sample's length

$$\sigma = -\frac{1}{2\pi} \frac{\omega_o^2}{\omega L} \sqrt{\frac{\hbar}{2m}} \sin^2 \frac{k_o L}{2} \qquad (9)$$

At $2\hbar\omega > mv_o^2$ the conductivity becomes a positive value. In the case $2\hbar\omega >> mv_o^2$ it has the following form

$$\sigma = \frac{1}{4\pi} \frac{\omega_o^2}{\omega^2 \tau} \left[\frac{mv_o^2}{2\hbar\omega}\right]^{\frac{1}{2}} \sin^2 \left[L\sqrt{\frac{m\omega}{2\hbar}}\right] . \qquad (10)$$

Under such conditions electron transits are posible only with absorption of quantums of the eletrromagnetic field.

References

1.M.V.Burtyka, O.V.Glukhov and V.M.Yakovenko. Solid State Electronics,1990,V.33,N.11,p.1339-1341.

2.M.V.Burtyka, O.V.Glukhov and V.M.Yakovenko. Solid State Electronics,1991,V.34,N.6,p.559-564.

3.V.L.Borblik and Z.C.Gribnikov. Fiz.Tech.Poluprovodn.,1988,V.22,N.9, p.1597-1605.

4.L.D.Landau and E.M.Lifshitz. Quantum mechanics. Nonrelativistic theory. Moscow, Nauka,1974 (in Russian).

Th2.9

BALLAST ELECTRON BEAMS IN O-TYPE DEVICES WITH DISTRIBUTED INTERACTION

G.A.Alexeev

Institute of Radiophysics and Electronics, Academy of Sciences of the Ukraine, 12 Acad. Proskura st., 310085 Kharkov, the Ukraine

In O-type devices with a strip electron beam an interaction channel is usually homogeneous at symmetrical placing of the beam in the channel. Here minimum of distribution of the static potential specified by the action of a static space charge is in the middle part of the beam, and ions of the residual gas considerably influence the energyexchange process. An action of such natural ion trapping may be reduced by the displacement of it from the region of effective interaction of electrons with the HF-field at the expense of asymmetric arrangement of the beam in the channel or by introducing additional ballast beams and inhomogeneities of geometry in the form of jumps of the channel's width.

On the base of analytical and numerical calculations of the potential distribution at different geometry of the channel and asymmetric placing of the electron beam the the analysis has been carried out of the influence of electrostatic fields on output characteristics of devices. It is shown that by the choice of geometric parameters of the beam (aimed distance, width, thickness) and channel (width of narrow and wide parts) one may control the absolute value of minimum of potential deflection and realise the displacement of ion trapping to the non-working region of the interaction space. The ballst part of the electron beam required for this action may amount not more than 15% of the total beams's width.

Introducing of the separate ballast beam at the definite distance from the working one allows to control more effectively the placement of the ion trapping with conservation of the total constant beams power.

It is follows from the analysis that a static space charge of the strip beam of the finite thickness influences differently on the characteristics of devices of the types: orotron, Diffraction radiation generator and resonance TWT, BWT.

STATISTICS AND VARIABILITY OF MILLIMETRE-WAVE PROPAGATION AND RELATED METEOROLOGY OVER A 500 m PATH

C. J. Gibbins

Radio Communications Research Unit
Rutherford Appleton Laboratory
Chilton, Didcot, Oxfordshire, OX11 0QX, UK

Introduction

In order to facilitate the provision of new and future communications services and to relieve spectrum congestion at lower frequencies, increasing interest is being shown in exploiting the millimetric wavebands, at frequencies above 30 GHz. At such frequencies, rain is the dominant factor in determining the reliability of communications systems. However, there is growing evidence which suggests that extrapolation into the millimetric wavebands of current prediction procedures, for example those recommended by the International Radio Consultative Committee (CCIR) [1], may not be completely reliable. Specifically, such evidence suggests that rainfall attenuation may be under-estimated at frequencies above about 40 GHz. Unfortunately, there is currently a lack of sufficient data on rain attenuation at such frequencies with which to test and improve the various prediction techniques.

To address these problems and to improve the availability of propagation data at frequencies in the millimetric wavebands, the Rutherford Appleton Laboratory operates the 500 m Millimetre-Wave Experimental Range at Chilbolton (MWERAC) in Hampshire, U.K. (latitude 57° 8'N, longitude 1° 26'W, elevation 84 m). The range is a well-instrumented open-air laboratory designed to monitor propagation in the millimetric, infra-red and optical wavebands, in conjunction with a comprehensive set of meteorological observations. Measurements from the range have been compiled into a 3-year database of propagation and related meteorology which is being used to investigate the statistics of radiowave propagation, for application to the planning and design of future communications systems, and to investigate in detail the interaction between radiowaves and the prevailing meteorology. This paper presents some of the results of the statistical analyses.

Instrumentation and the Database

The Millimetre-Wave Experimental Range at Chilbolton, which has been described in detail elsewhere [2], comprises six transmission links, 4 m above flat grassland, operating at 37, 57, 97 and 137 GHz with vertical polarization and at 10.6 and 0.63 μm with random polarization. The meteorological instruments which complement the links include three rapid-response raingauges, a rapid-response snow/hail gauge, thermometers and hygrometers at a number of locations and heights above the ground, a distrometer to measure the distribution of raindrop sizes, a microwave refractometer, barometer and an anemometer.

Data from the range, sampled at a rate of 0.1 Hz, have been calibrated and validated [3] and compiled to produce a 3-year time-series database of calibrated attenuations and related meteorology, classified according to the different kinds of events, i.e. rain, snow, fog and scintillation.

Statistical Results

Figure 1 shows the cumulative distributions of the levels of attenuation exceeded over the three-year period, for all events. As would be expected, these show that the levels of attenuation increase as a function of frequency, while the dramatic increase in the distributions for the infrared and optical systems is due to the effects of fog, the incidence of which is 2-3% of the year in southern England.

Of major importance, as noted in the Introduction, are the effects of rain on millimetre-wave propagation. The database has accordingly been analyzed in terms of rain attenuations and concurrent rainfall rates, thereby allowing a comparison with power-law relationships of the form

$$\text{Attenuation (dB/km)} = kR^{\alpha} \quad (1)$$

where R is the rainfall rate (in mm/h) and k and α are frequency-dependent coefficients. Figure 2 shows the results for 57 GHz attenuations and concurrent rainfall rates over the three-year period. The broken line is the CCIR prediction [4] based on the measured rainrate distribution. It is clear that the CCIR model underestimates rainfall frequencies at these frequencies.

Regression analyses have been carried out on the results to derive experimental values for the coefficients k and α in Eq. (1), which are listed in Table 1, together with the CCIR values for the relevant frequencies.

TABLE 1

f (GHz)	k		α	
	Present	CCIR	Present	CCIR
37	0.33	0.26	0.92	0.95
57	1.07	0.59	0.74	0.84
97	1.69	1.05	0.65	0.75
137	2.55	1.20	0.56	0.72

Overall, the CCIR model underestimates the coefficient k and overestimates the coefficient α, when compared with the results found in the present work, with the net effect of underestimating the attenuation in rain, particularly at the higher frequencies.

Long term studies of attenuation and rainfall rate, such as in Figure 2, are essential to establishing accurate and reliable models for the prediction of rain attenuation from rain rate statistics which are routinely produced by meteorological bureaux, for example. This enables system planners and designers to assess the magnitude of average fade margins to incorporate into link budgets, in order to achieve a specified level of reliability.

However, rain is a stochastic process and varies considerably both in time and space. For example, Figure 3 shows the annual cumulative distributions of rainfall rate which were exceeded over three years, as measured by the three raingauges, spaced 200 m apart, along the 500 m range. The broken line is the long-term average for the three gauges over three years. At a time percentage of 0.01% of the year, the variance in the rainfall rates which were exceeded for the nine raingauge-years in ~25%, which is typical of the expected year-to-year variability in the weather system [5].

While the statistics of propagation will vary from year to year, and must be considered in planning communications systems, there is also considerable variability within a year, and for many broadcast services, for example, an estimate of the extremes of systems performance within a year is required in the planning and design process. Such extremes are generally assessed using the concept of "worst month" [6], whereby for a given threshold (i.e. level of attention or rainfall rate), the longest time percentage of exceedance in *any* month of the year forms the basis of the resultant cumulative distribution of extreme values. Note that the worst month need not necessarily be the same month for each threshold value. From such analyses, it becomes possible to develop models to predict worst-month performance from more widely-available annual statistics.

The data from the 500 m range have accordingly been analyzed to yield monthly cumulative distributions of attenuation and rainfall rates. Figure 4 shows the time percentages which various levels of attenuation were exceeded during the worst month (for all events), compared with the annual time percentage that those levels were exceeded, for the six links, and clearly shows that a power-law relationship exists between the two quantities. It is of interest to note that the same law appears to hold for both the millimetric wavelengths, which are dominated by rainfall attenuation, and the infrared and optical wavelengths, where systems performance is influenced most by fog.

It has become customary to define a ratio Q, such that

It has become customary to define a ratio Q, such that

$$Q = P_w / P_y \qquad (2)$$

where P_w is the probability (or percentage of time) that a given threshold is exceeded in the worst month of a year and P_y is the probability that the same threshold is exceeded during the full year. Obviously, Q is also a power-law function of P_y:

$$Q = aP_y^b \qquad (3)$$

Figure 5 shows the ratio Q deduced from the attenuation data shown in Figure 4, together with the values deduced from an analogous analysis of rainfall rates, as a function of annual time percentage. While there is some scatter in the results, it is clear that approximately the same law holds for both attenuations and rainfall rates. The continuous line is the regression of all the data to Eq. (3), the resultant coefficients of which are given in Table 2, which also lists the values of a and b for separate analyses of attenuation and rain, together with the CCIR global model [7]. This latter is shown in Figure 5 as the broken line.

TABLE 2

Analysis:	a	b
Average worth month	2.25	-0.10
Annual attenuation	2.13	-0.12
Annual rain rate	2.28	-0.11
CCIR (Global)	2.85	-0.13

There are differences between the results deduced from the present work and the CCIR model. However, this is not regarded as particularly significant, since it is expected that there will be regional or climatological variations in the values of these coefficients.

Models such as these can be very useful in estimating the extremes of systems performance from widely-available long-term or annual statistics of rainfall rates, for example, and are frequently employed in the planning and design of broadcast services, which generally demand very high levels of operational reliability.

Summary

This paper has discussed some results of statistical analyses of propagation conditions in the millimetre-wave region of the electromagnetic spectrum. Such wavelengths are becoming increasingly considered and exploited in order to satisfy the demand for new communications systems and services, and to relieve spectrum congestion at lower frequencies. The results presented will be of value in the development and improvement of accurate prediction procedures required for the planning and design of such communications systems.

References

1. CCIR Report 338. "Propagation data and prediction methods required for line-of-sight radio-relay systems." *Reports of the CCIR, Annex to Vol. V*, ITU, Geneva, 1990.

2. Gibbins, C.J., Carter, D.G., Eggett, P.A., Lidiard, K.A., Pike, M.G., Tracey, M.A., White, E.H., Woodroffe, J.M. and Yilmaz, U.M. "A 500 m experimental range for propagation studies at millimetre, infrared and sptical wavelengths". *J. IERE*, 57, pp 227-234, 1987.

3. Gibbins, C.J. "Statistical studies of millimetre-wave, infrared and optical propagation over a 500 m path". Proc. VIth Int. Conf. on Antennas and Propagation, ICAP89, IEE Conf. Publ. No. 301, Pt. 1, pp 238242. 1989.

4. CCIR Report 721. "Attenuation by hydrometeors, in particular precipitation, and other atmospheric particles". *Reports of the CCIR. Annex to Vol. V*, ITU, Geneva, 1990.

5. Crane, R.K. "Rain attenuation measurement: variability and data quality assessment". *Radio Sci.*,25, pp 455-473, 1990.

6. CCIR Recommendation 581-2. "The concept of 'worst month'". *Recommendations of the CCIR, 1990*, ITU, Geneva, 1990.

7. CCIR Report 723-3. "Worst month statistics". *Reports of the CCIR, Annex to Vol. V.*, ITU, Geneva, 1990.

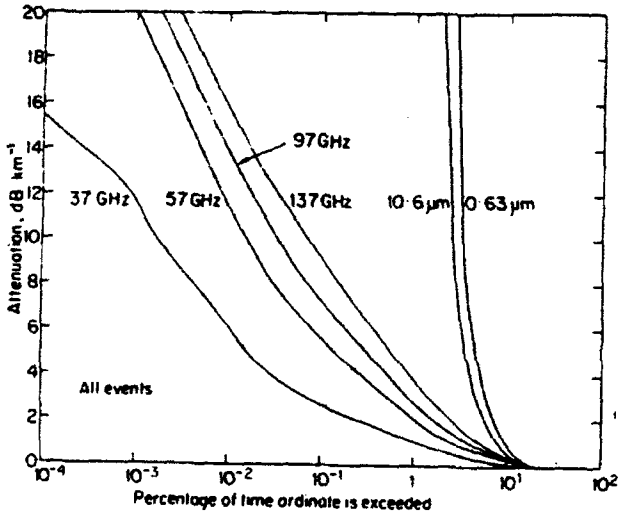

Fig. 1. Cumulative distributions of attenuations exceeded over three years for all events.

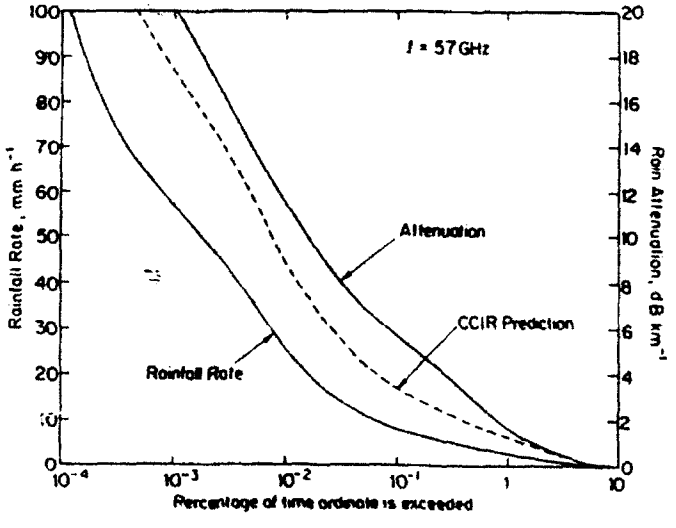

Fig. 2. Cumulative distributions of 57 GHz rain attenuations and concurrent rain rates exceeded over three years. The CCIR prediction is based on the rainrate distribution.

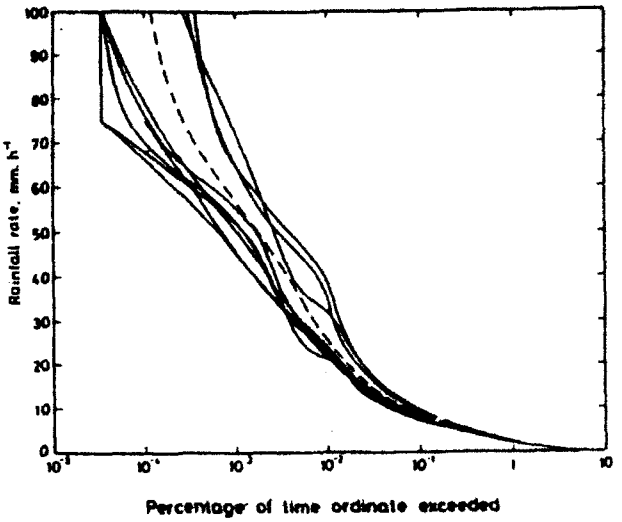

Fig. 3. Annual rainrate distributions from three spaced raingauges over three years.

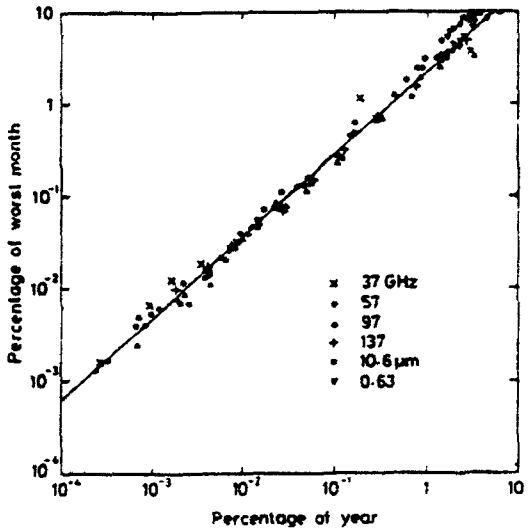

Fig. 4. Percentage of time in the worst month that various threshold attenuations were exceeded compared with annual exceedances.

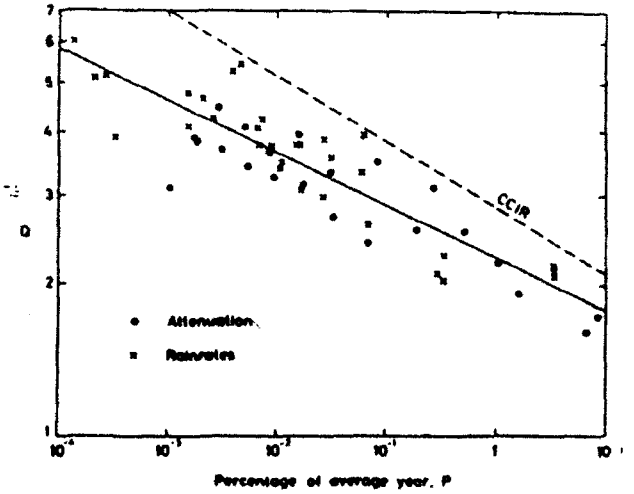

Fig. 5. Variation of the ratio a as a function of percentage of year.

ATTENUATION AND DEPOLARIZATION FOR 3MM WAVE BAND INDUCED BY RAIN

HUANG,Ji Ying and WANG,Yi Ping
(Xidian University, P.O.Box 274, 710071 Xi'an, PR CHINA)

ABSTRACT

In this article, the effects of rain induced attenuation and depolarization for mm wave have been described and discused. It is found that Weibull distribution of rain drops is in more agreement than that of L-P distribution in Xi'an area for 3 mm wave band.

INTRODUCTION

Attenuation and depolarization of radio waves through the rainy region have a strong dependence upon the size and the canting angle distributions of rain drops. Due to different climates, these effects have evidently different characters in different regions. Xi'an is located at the eastern part of Northwest China (N34°5',E108°55') has the climate of continental monsoon. Therefore, our investigation has typical significance.
It is found that in this area, Weibull distribution of raindrop sizes has better agreement with the result obtained than that of L-P distribution.

COEFFICIENTS OF ATTENUATION AND PHASE SHIFT

There are several modes of raindrop distributions such as L-P distribution, M-P distribution, A-O distribution, Weibull distribution, and log normal distribution. They all have relationships with local climates. In which the L-P distribution is used more widely. It is a discrete representation of average sizes of rain drops[1]. For 3 mm wavelength, however, in consideration of small raindrops L-P distribution usually underestimates the absorption. In this wavelength range, effects of small raindrops become more important, so that Weibull distribution will give more exact estimate.
In Weibull distribution, raindrop density spectrum n(D) as a function of the diameter D can be written as[2]

$$n(D)=n_0(c/b)(D/b)^{c-1}\,e^{-(D/b)^c} \qquad (1)$$

where $n_0=1000\ m^{-3}$, $c=0.95R^{0.14}$, $b=0.26R^{0.44}$mm, and R is the rain rate. An empirical formula based on the data in Xi'an has been expressed as

$$n(D)=n_0'e^{-\Lambda D} \qquad (2)$$

where values of $n_0'=3820\text{-}6714\ m^{-3}(mm)^{-1}$, $\Lambda=1.6\text{-}2.2\ mm^{-1}$.
The attenuation through rainy region can be calculated by[3]

$$A=4.343\int_0^{\infty} Q_{ex}(D)L_0 n(D)dD \quad \text{dB} \tag{3}$$

where L_0 is the propagation path length. $Q_{ex}(D)$ is the extinction cross section of a single drop and relates with the forward scattering coefficient by

$$Q_{ex}(D)=(\lambda^2/\pi)S(0) \tag{4}$$

For non-spherical drops, the scattering coefficient $S_{II}(0)$ in the plane formed by the symmetric axis of a rain drop and the direction of propagation is different from $S_I(0)$ which is perpendicular to the above plane. Coefficients of attenuation of dB per kilometer can be calculated with $S_{II}(0)$ and $S_I(0)$ by following formulas, respectively

$$\begin{aligned} A_2&=(\lambda^2/\pi)4.343\times10^3\int_{D_{min}}^{D_{max}} \mathrm{Re}[S_{II}(0)]\,n(D)dD \quad \text{dB/km} \\ A_1&=(\lambda^2/\pi)4.343\times10^3\int_{D_{min}}^{D_{max}} \mathrm{Re}[S_I(0)]\,n(D)dD \quad \text{dB/km} \end{aligned} \tag{5a}$$

The corresponding phase shifts can be calculated by

$$\begin{aligned} \Phi_2&=(\lambda^2/\pi^2)90\times10^3\int_{D_{min}}^{D_{max}} \mathrm{Im}[S_{II}(0)]\,n(D)dD \quad \text{deg/km} \\ \Phi_1&=(\lambda^2/\pi^2)90\times10^3\int_{D_{min}}^{D_{max}} \mathrm{Im}[S_I(0)]\,n(D)dD \quad \text{deg/km} \end{aligned} \tag{5b}$$

Substituting (1) and (2) in (5) and taking values of $S_{II}(0)$ and $S_I(0)$ from[4], for f=95GHz the attenuation and phase shift coefficients in Weibull distribution and the empirical distribution have been computed. For R=12.5mm/h, an example is

	Weibull	empirical
A_2	7.1719	8.8627
A_1	6.7794	8.3775

CALCULATION OF XPD

For calculating the coherent depolarized effect induced by non-spherical raindrops, the following formula must be used,

$$XPD_{\substack{H\\V}}=10\log\frac{D+C+C\cos4\theta_0 e^{-8\sigma^2} \mp E\cos2\theta_0 e^{-2\sigma^2}}{C-C\cos4\theta_0 e^{-\gamma\sigma^2}} \quad \text{dB} \tag{6}$$

where $\theta_0=6^\circ$, $\sigma=20.4^\circ$ (R<40mm/h), and $\theta_0=7.2^\circ$, $\sigma=33^\circ$ (R≥40mm/h) in Xi'an area. In equation (6), θ_0 is the average value of canting angles and σ is its standard deviation. Parameters C, D, and E can be obtained by

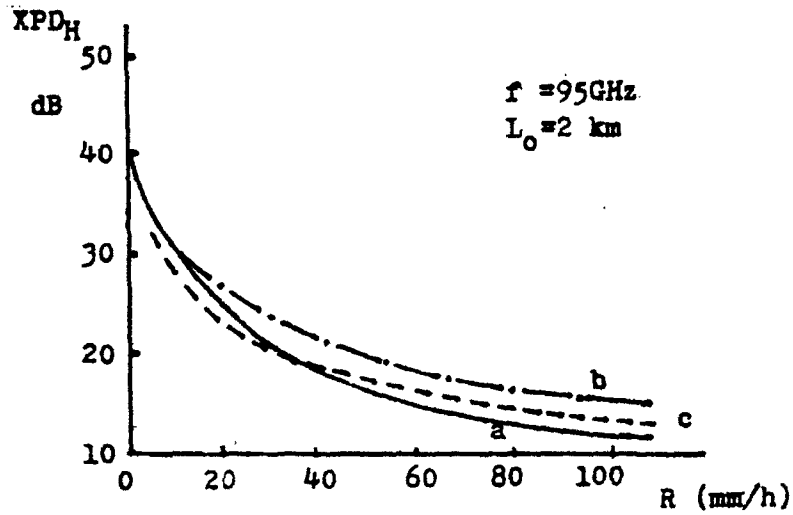

Fig.1 Variation of XPD_H with rain rate

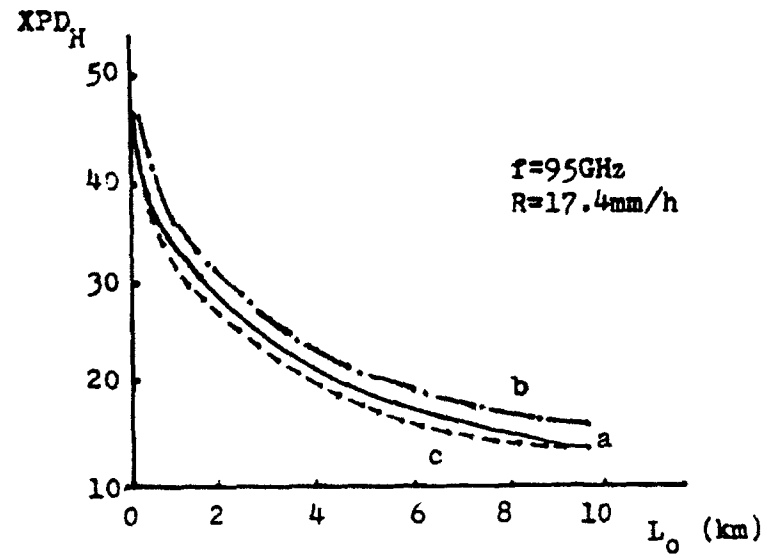

Fig.2 Variation of XPD_H with distance

formulas in[5] . The calculated attenuation and phase shift coefficients have been used to get XPD's for different paths and different rain rate. A part of results of XPD_H are shown in figures 1 and 2, respectively. Curve a is with Weibull distribution, curve b is with L-P distribution (data from [4]), and curve c is with the empirical negative exponential distribution. It is noticed that under the same condition of rain rate XPD's calculated by Weibull distribution and the empirical distribution are smaller than those by L-P distribution. This suggests that for estimating the influences of small raindrops Weibull distribution is more suitable.

STATISTICAL DISTRIBUTIONS OF XPD AND CPA

There are formulas recommended by CCIR[6] to calculate CPA for 0.01% time propability such as

$$CPA_{0.01} = aR_{0.01}^{b} L_o K_{0.01} \quad , \quad K_{0.01} = 1/[1+(L/L_o)] \qquad (7)$$

and

$$L_0=35\exp(-0.015R_{0.01})=26.96 \quad (8)$$

for R=17.4 mm/h with p=0.01%. With (7) and (8) CPA and K of other probability can be obtained by

$$CPA_p/CPA_{0.01}=0.12p^{-(0.546-0.043\log p)}=B(p)\ (0.01\le p\le 1) \quad (9)$$

and

$$K_p=B(p)(R_{0.01}/R_p)^{b}K_{0.01} \quad (10)$$

For f=95GHz and T=20°C values of a and b in different polarizations are

$a_H=1.094$ $b_H=0.7476$ (horizontal polarization)

$a_V=1.033$ $b_V=0.7483$ (vertical polarization)

These formulas have been used to obtain the statistics of XPD and CPA as shown in figure 3.

For Weibull distribution the following formula must be used [5]

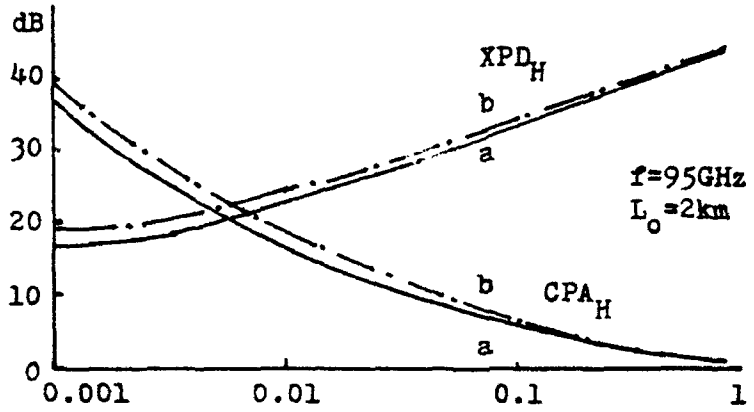

Fig.3 Percentages probability of XPD_H and CPA_H lower than ordinates

$$CPA_{H\atop V}=10\log\{\exp[-(\alpha_1-\alpha_2)L][D+C+C\cos 4\theta_0 e^{-8\sigma^2}\mp E\cos 2\theta_0 e^{-2\sigma^2}]\} \quad dB \quad (11)$$

where C, D, and E can be obtained by the same method as those in equation (6). Using attenuation and phase shift coefficients calculated by equation (5) and rainfall distribution as mentioned in above section, the statistical value of XPD and CPA can be obtained by equation (11). Results are shown in figure 3. Curve of the empirical distribution almost coincides with that of Weibull distribution. They are undistinguished from each other, so only the result of that of curve a is shown.

PRELIMINARY CONCLUSION

For the climate of internal continental area Weibull distribution of raindrops is more practical in prediction.

REFERENCES

1. Laws,J.O. and Parsons,D.A., Trans.Am.Geophysical Union 24(1943),452.
2. Sekine,M.,Chen,C.D.,and Musha,T.,IEEE Trans. AP-35(3)1987,358.
3. Huang,J.Y. and Wang,C.,Inter.J.IR and MM Waves 10(9)1989.
4. Maggiori,D., Alta Frequenza 50(5)1981.
5. Huang,J.Y. and Ma,G.Y.,J.Wuhan University(Natural Sci.) (4)1991.
6. CCIR Report 338-5, 1989.

Th3.3

3MM MICROWAVE RADIOMETER AND SKY RADIOMETRIC TEMPERATURE RESEARCH

Zhang Zuyin, DengJun
(Huazhong University of Science and Technology, Wuhan, China)

ABSTRACT

This paper describes the 3mm radiometer's structure and its property. An engineering method is given to calculate the 3mm sky temperture, and it is compared with the real measurement. We found the two results are similar.

INTRODUCTION

Because of its all-weather capability, simple configuration and good concealment, passive microwave radiometry has been utilized in more and more fields, including remote sensing, automatic guidance and so on. However, over-large antenna aperture is not suitable, so the spatial resolution of radiometry is normally not high, and this limitation has seriously effected the applications of radiometry. In order to improve the spatial resolution, radiometer is being developed to high frequency. In the early 1970s, it was reported that a 3mm imaging radiometer system was developed and a series of measurements and researches on the terrain radiometric properties was made. The research at home on this field is not still developed because of the limitation of components. Under the support of Cao Yiting, who works in ZiJin Mountain astronomical observatory, we have developed the 3mm total power radiometer and also measured the 3mm sky radiometric temperature using frequent calibration. The results obtained have shown good agreement with theoretical calculations.

3MM TOTAL POWER RADIOMETER

The parameters of the radiometer are as follows:

1. Antenna :
A. Cassegrain antenna (a) 3db beamwidth = 1.5° (b) Gain > 20db (c) First side-lobe Level < -18db
B. Horn antenna (a) 3db beamwidth = 5° (b) Gain > 20db (c) Side-lobe is not clear

2. Receiver:
Its noise figure is about 10db, IF bandwidth is 1GHZ~1.7GHZ and its Sensitivity is less than 3° k (integration time equals one second)

The radiometer block diagram is shown in Fig. 1

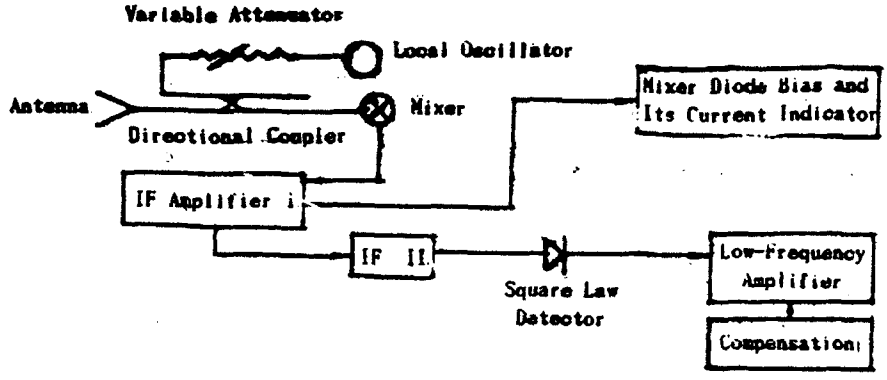

Fig. 1 Radiometer block diagram

The operation of the total power radiometer is effected by the gain fluctuations of IF amplifier, the receiver variation of temperature and the environmental interference, so the output of low-frequency amplifer drifts always and disappears unregular fluctuations. Up till now, the 3mm microwave switch for developing Dicke radiometer is unavailable at home, the only possible solution is to use total power radiometer. In this case, the frequent calibration approach must be used and the environmental interference must be avoided so that the unregular fluctuations of radiometer output did not effected the measurement.

After observing for a long time, we found that the slope-variation of the radiometer calibration curve is not clear when there is no environmental interference, but the curve intercept-variation is large because of the drift. During the period of measurements, before each sample, the radiometer antenna is illuminated with a matched local, whose temperature may be held at a constant known value, to get the intercept of the calibration curve, then we can calculate the antenna temperature according to this intercept and the calibration slope which has been got. This one point calibration method is useful to radiometer which needs frequent calibration.

3MM SKY RADIOMETRIC TEMPERATURE MEASUREMENT AND CALCULATION

Radiation brightness temperature of metal object is an important subject which needs to be solved in many fields, especially the guidance technique, and the sky radiometric temperature is the base to study metal radiometric brightness temperature. So it is very significant to measure and calculate 3mm sky radiometric brightness temperature.

The sky radiometric temperature or apparent temperature T_{SKY} usually conzists :[1,2]

$$T_{SKY} = T_{DN}(\theta) + T_{EXTAL}\, e^{-\tau \sec\theta} \quad (1)$$

$$T_{EXTAL} = T_{COS} + T_{GAL} \quad (2)$$

where τ_o is the total zenith atmospheric opacity, and T_{COS} and T_{GAL} are the cosmic and galactic brightness temperature, respectively, whose sum we call the extraterrestrial brightness temperature T_{EXTAL}. T_{COS} is independent of frequency and the zenith angle θ, which has the constant value T_{COS} =2.7k. T_{GAL} is dependent of θ and frequency. However, T_{GAL} may be neglected at 3mm wave band. Thus, $T_{SKY}=T_{DN}(\theta)$, where $T_{DN}(\theta)$ is the apparent temperature representing the downwelling atmosphere radiation. Under clear sky condition, the earth's atmosphere consists of various gas molecules, where absorptions of oxygen and water vapor play an important role. Since the atmospheric thermodynamic pressure, temperature, density and water-vapor density are a function of altitude, the absorption coefficients of atmosphere are dependent of height. To simplify, we assume that the atmosphere is stratified horizontally, shown in Fig. 2, which means the temperature and absorption coefficients are function of height only. The energy emitted at θ direction by a stratum at height z and of vertical thickness dz(thickness sec θ dz at θ direction, temperature T (z) , absorption coefficient k(z)) is k(z) T(z) sec θ dz, which, after propagation down to the surface z=0, is reduced to $k(z)\,T(z)\sec\theta\,dz\,\exp(-\int_0^z k(z)\,dz\sec\theta)$. The sum of contributions of downwelling-emitted atmospheric radiation from strata above terrain surface forms the measured sky apparent temperature T :

$$T_{SKY}=\sec\theta\int_0^{\infty} K(z)\,T(z)\exp[-\sec\theta\int_0^z k(z')\,dz']\,dz' \tag{3}$$

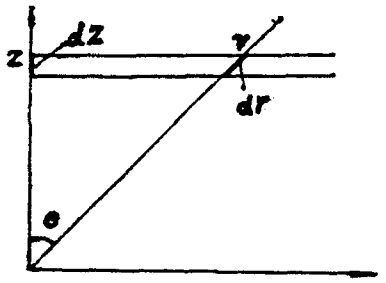

Fig. 2 A plane-stratified atmosphere radiation model

It is very difficult to calculate sky radiometric temperature using (3) directly. Not only the calculation method is complicated, but also the expressions or graphic charts of k(z) and T(z) must be got by radiosonde or other high-altitude detectors. One of the approximate methods used to calculate T_{SKY} is: [3,4,5]

$$T_{SKY}=T_M[1-a_o^{\sec\theta}] \tag{4}$$

$$a_o=\exp[-\int_0^{\infty} k(z)\,dz] \tag{5}$$

$$T_M=T_g-5.3 \tag{6}$$

$$k_{O_2}=k_{O_2}(0)\exp(-0.183z) \tag{7}$$

$$k_{WATER}=k_{WATER}(0)\exp(-0.5z) \tag{8}$$

$$k_{O_2}(0)=0.34(\nu^2/c^2)\left[\frac{\Delta V/c}{(2+V/c)^2+(\Delta V/c)^2}+\frac{\Delta V/c}{(V/c)^2+(\Delta V/c)^2}\right] \tag{9}$$

$$k_{WATER}=140.71\nu^2 p\,\rho_M\,T^{3.125}\exp(-644/T)(1-0.014\,\rho_M\,T/p)\{1/[(\nu-$$

$$22.234)^2 + \Delta\nu^2] + 1/[(\nu+22.234)^2 + \Delta\nu^2] 0.01107\ \rho_w\ \nu^2 \Delta\nu T^{-1.5} \quad (10)$$

$$\Delta\nu = 2.58 \times 10^{-3}\ p(1+0.0147\ \rho_w\ T/p)\ (T/318)^{-0.625} \quad (11)$$

According to (9), (10) and (11), we can get k_{O_2} (0) and k_{WATER} (0) substituting surface pressure p, vapor density ρ_w, temperature T, frequency ν and light velocity c. Substituting (7), (8) into (5), performing the integration, yields a_0. Substituting surface thermodynamic temperature T_g into (6) yields T_m. Then substituting T_m, a_0 into (4) yields sky radiometric temperature T_{SKY}.

The measurement and calculation results are shown in Fig. 3, there are basically the same.

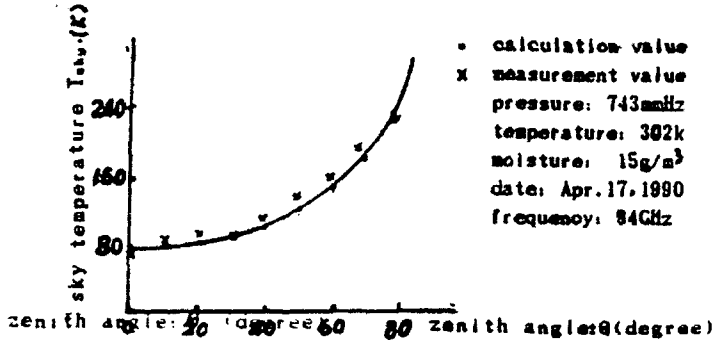

Fig. 3 3MM sky radiometric temperature

REFERECE

1. F.T.Ulaby, R.K.Moor, A.k.Fung, Microwave Remote Sensing, Volume 1, AddisonWosley Publishing Company, (1981), 191.
2. Evans, J.Ruse, H.G.Weiss, R.H.Kingston, and C.Blake, Radar Astroromy Systems, McGraw-Hill, New York, (1968), 78.
3. Jack Frederick Paris, AD 687127, Jan. (1969).
4. Paris J.F., AD 38681, May (1971).
5. Wulfsberg K.N. AD 6068;3 July (1964).

MONTE CARLO SOLUTION OF RAIN ATTENUATION FOR MILLIMETER WAVE

Wu Zhensen, Yan Yi and Chen Lihong
(Department of Physics, Xidian University, Xi'an, Shaanxi, China)

ABSTRACT

In this paper the weighted average of the scattering cross section is used to obtain the integral resultant of the transfer equation for the plane wave scattering in random medium with particle size distribution. The Monte Carlo simulation technique is done for the rain attenuation at Millimeter-wave range. The numerical simulation is in good agreement with experimental data and the multiple scattering effects must be included.

INTRODUCTION

At millimeter-wave range the multiple scattering of raindrops is becoming more and more effective with the increasing frequency. The radiative transfer theory is the major methods for solving integro-differential equations with the Monte Carlo simulation technique, in which the multiple scattering process is treated as Markov chains of collisions between photons and discrete scatterers in random medium. There is a certain probability of a photon being scattered or absorbed at each event and photon histories are traced until photon escapes from the boundaries of random medium or absorption occurs. A large of photon histories are repeated to obtain acceptable ensemble averages for the scattering power.

As any polarization is neglected, the raindrops can be simplified into equivolumic spherical particles with some size distribution. With Monte Carlo method the rain attenuation is made at millimeter-wave range for the Marshall-Palme, RRL[2] and Weibull[3] raindrop distribution. The results of numerical simulation are compared with the experimental data given by the literature[2]. It is shown that the multiple scattering effect is expected to be significant. As multiple scattering is considered, the theoretical values of rain attenuation are agreement with the measured data. However, the attenuation values for signal scattering are bigger.

MONTE CARLO TRANSFER TECHNIQUE

Let us consider a plane-parallel medium of thickness h containing randomly distributed spherical particles. A plane unpolarized wave is incident vertically in z direction. Suppose the intensity of incident wave is normalized and the effect of boundary reflection is neglected. The reduced intensity $I_{ri}(z, \mu)$ and the diffuse intensity $I_d(z, \mu)$ satisfy, respectively[5]

$$\mu \frac{dI_{ri}(z, \mu)}{dz} = -\rho < \sigma_t > I_{ri}(z, \mu) \tag{1}$$

$$\mu \frac{dI_d(z, \mu)}{dz} + \rho < \sigma_t > I_d(z, \mu) = \frac{1}{2}\int_{-1}^{1}\left[\int_0^\infty N(a)\sigma_t(a)B(\mu, \mu'; a)da\right] I(z, \mu')d\mu' \tag{2}$$

where $I(z, \mu) = I_{ri}(z, \mu) + I_d(z, \mu)$ is the total intensity, $\sigma_t(a)$ is the extinction cross section of the

particle with size parameter α and $B_0(\mu, \mu'; \alpha)$ is the phase function, which are found by the applying Mie scattering theory. $\mu = \cos\theta$, θ is the angle between the scattering direction and z axis, $N(\alpha)d\alpha$ is the number of particles per unit volume in range $d\alpha$ and ρ is the numerical density. $< \sigma_t >$ is the mean extinction cross section.

Considering raindrop size distribution, the weighted average of the scattering cross section is used to the equation (2), so that the average of phase function is written as

$$< B_0(\mu, \mu'; \alpha) > = \frac{\int_0^\infty N(\alpha)\sigma_t(\alpha)B(\mu, \mu'; \alpha)d\alpha}{\int_0^\infty N(\alpha)\sigma_t(\alpha)d\alpha} \tag{3}$$

Let optical distance $\tau = \int_0^z \rho < \sigma_t > dz$, $\tau_0 = \int_0^h \rho < \sigma_t > dz$. Then total specific intensity is given by

$$I(\tau, \mu) = \frac{1}{2}\int_0^{\tau_0} \exp[-(\bar{\tau} - \tau')/\mu] \{\int_{-1}^{1} < B_0(\mu, \mu') > I(\tau', \mu')d\mu'\} d\tau'/|\mu| + I_{in}(\tau, \mu) \tag{4}$$

where

$$\bar{\tau} = \begin{cases} \tau_0 & \mu > 0 \\ 0 & \mu \leqslant 0 \end{cases}, \qquad I_{in}(\tau, \mu) = \exp(-\tau)\delta(\mu - 1)\delta(\varphi) \tag{5}$$

and $I_{in}(0, \mu) = 0$ $(\mu < 0)$.

NUMERICAL SIMULATION

On the basis of the above discussion, we deal with the multiple scattering of raindrops for millimeter wave by the Monte Carlo method. In its simplest digital form, a Monte Carlo model is a purely stochastic construction of an ensemble of photon trajectories through the random medium. The length and direction of each trajectory segment are governed by probability density functions derived from the basic scattering and absorption properties of the medium[6].

Due to multiple scattering, the rain attenuation is estimated by Monte Carlo method. Suppose the incident wave beam is considered as a flux of photons, which contains N photons. Let $S = (\tau, \mu, \varphi)$ be phase space point, then the equation (4) can be rewritten as in the general form[7]

$$I(S) = I_{in} + \int I(S')K(S' \to S)dS' \tag{6}$$

Comparing with the equation (5), the norm of the kernel function in equation (6) $|K| < 1$, then (6) can be expanded as the Neumann series.

$$I(S) = \sum_{n=0}^{\infty} I_n(S) \tag{7}$$

where

$$I_n(S) = \int\cdots\int I_{in}(S_0)K(S_0 \to S_1)\cdots K(S_{n-1} \to S)dS_{n-1}\cdots dS_1 dS_0$$

It is easy to show that convergence of the Neumann series and existance of a solution are assured and that the intergral operator $\int K(S_{i-1} \to S_i)dS_{i-1}$ is corresponding to a transfer process of photon in a medium. A wave propagation can be regarded as a Markov chain of photon collision and scattering in the medium. So that the intensity I is corresponding to the transmitted probability P_t or the reflective probability P_r. The mean transmission T and the mean reflection R are, respectively

$$T = \sum^{N} P_t / N, \qquad R = \sum^{N} P_r / N \tag{8}$$

According to Mie theory, the extinction and scattering cross sections and the phase function are calculated for a variety of spherical raindrops and their mean values are obtained. With the statistic es-

timation and reflectance for h = 1 km at frequencies of 30.0, 33.3, 34.8, 40.0, 50.0, 60.0, 81.8, 100.0, 140.0, 245.5, 300.0 GHz.

In order to make a comparison, we also find out the rain attenuation value according to the single scattering formula[1]

$$A(db/km) = 4343\lambda^2 / \pi \int_{D_{min}}^{D_{max}} \mathrm{Re}\{S(0)\}N(D)d(D) \qquad (9)$$

where λ is incident wavelength (unit is meter), $S(0)$ is the forward scattering function of the spherical particle derived by Mie theory, and $N(D)$ is the raindrop size distribution. The formula (9), which is equivalent to the equation (1), corresponds with single scattering.

In numerical calculation MP and RRL size distributions are used. RRL model is derived by the Radio Research Laboratory of Japan from rain attenuation statistics at 11.5, 34.5 and 81.8 GHz for three years by the use of an inversion method.

RESULTS AND DISCUSSIONS

As seen in Fig.1, the multiple scattering and single scattering results are estimated by Monte Carlo method for MP size distribution, which are in good agreement with those by Dutton and Samora according to equation (9). However, the rain attenuations for single scattering are larger. Fig. 2 shows the reflectance for $h = 1km$ at same wavelength as in Fig. 1. The rain backscattering attenuations are useful for radar system.

In Fig. 3 the results of numerical simulation are compared with the experimental data given by RRL and with CCIR model[4] of rain attenuation. It is shown that the multiple scattering effect is expected to be significant. As multiple scattering is considered, good agreement is found between the measured data and RRL model calculations. There are similar results for MP size distribution. The CCIR currently adopts the relationship between the specific attenuation and the rain rate, which is obtained on the basis of the Laws and Parsons raindrop size distribution. The CCIR model calculations underestimate the measured data and our numerical results. It is found that for the same rain rate the higher the frequency, the bigger is the difference between the single scattering and multiple scattering, and that for the same frequency the higher the rain rate, the bigger is the difference, too.

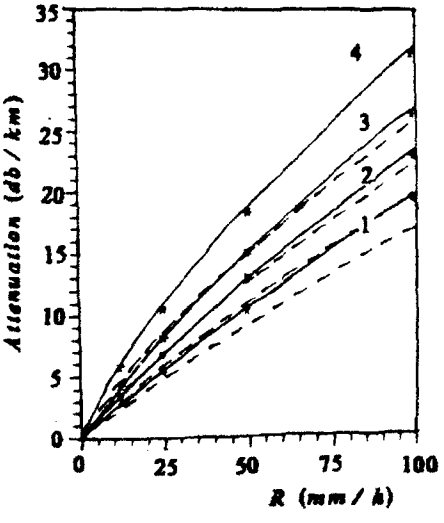

Fig.1 The rain attenuation at (1) 30.0, (2) 34.8, (3) 40.0, and (4) 50.0GHz with the MP distribution. The single scattering (— —), the multiple scattering (——), Dutton and Samora's data (* * *)[1].

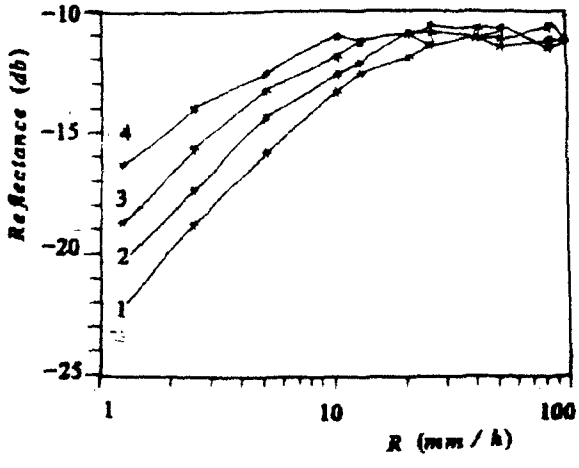

Fig.2 The reflectance for h = 1km at same wavelength as in Fig. 1.

CONCLUSION

Multiple scattering effect due to precipitate is often mentioned as a factor in the design and performance of a communications line particularly at higher radio frequencies. In order to estimate the magnitude of these effects, we have used the Monte Carlo method to study rain attenuation rather than the first order solution for milimeter wave range. It is shown that the multiple scattering effects are significant.

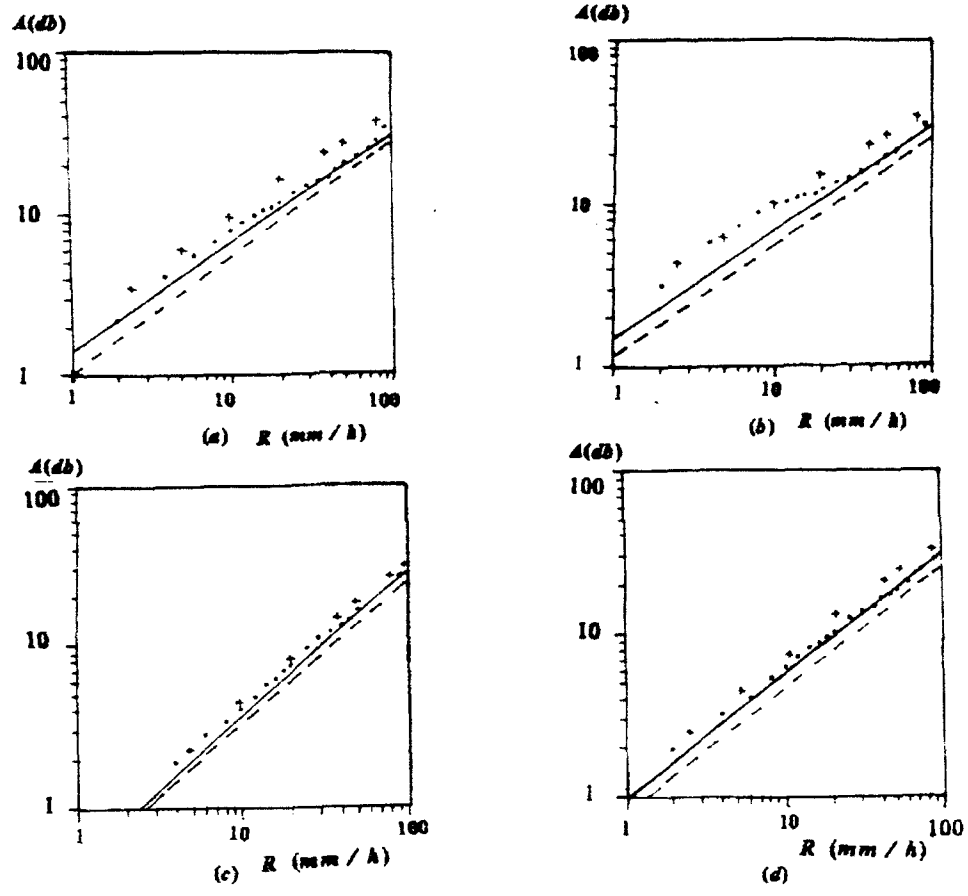

Fig.3 The rain attenuation at (a) 50.4, (b) 81.8, (c) 140.7, and (d) 245.5 GHz. The measured data (. . .), the single scattering (+ + +), RRL model (——), and the CCIR model (———).

REFERENCES

1. Dutton EJ and Samora C, NITA Report (1984), 84.
2. Manabe T . et al., IEEE Ap–35 (1987), 1326.
3. Sekine M and Lind G, Proc. 12th Europen Microwave Conf., (1982), 584.
4. CCIR, Rep. 721–1, (1982).
5. Ishimaru A, In:Wave Propagation and Scattering in Random Media, Academic Press, (1978).
6. Wang Yiping and Wu Zhensen, ACTA Opt. SINICA, 7, (1987), 458.
7. Wu Zhensen and Wang Yiping, ACTA Physica SINICA, 37, (1988) ,704.

CONVERSION OF 10-MINUTE RAINFALL RATE TO EQUIVALENT 1-MINUTE VALUE AT SOME LOCATIONS OF CHINA

Qiu Sheng Bo Lin Xiu Wan
(China Research Institute of Radiowave Propagation)

ABSTRACT

To meet the requirement of radio Communication system design at microwave and millimetre bands, conversion from 10-minute rainfall rate to its equivalent 1-minute value is set up on the basis of data from three locations: Guangzhou, Nanjing and Xinxiang in P.R. China. The conversion coefficients are given by Method of Least Square (MLS) with converting error less than 8% for the time percentage range from 0.001% to 1%.

INTRODUCTION

Almost all of the rain attenuation prediction methods available at present, require 1-minute rainfall rate data for certain time percentage (such as 0.01%) at the place concerned for calculation. However, most investigators in the world are still using tipping-bucket rain gauges or siphon rainfall recorders with integration time of more than ten minutes, with the exception of ones in Europe, Canada, Japan and China in which fast-response minute rain gauges are used. Because the long integration time may cause a large error to some thunderstorm rain measurement, it can not meet the requirement of radio communication system design. Radio engineers in every country are trying to convert 10-minute rainfall rate data to its equivalent 1-minute values. For the same purpose, we do the measurements in Guangzhou, Nanjing and Xinxiang, respectively, with JDSD-1 light-emitting raindrop minute rain gauge. The conversion methods of the two kinds of rainfall rate are presented on the basis of the data measured in this paper.

DESCRIPTION OF THE MEASUREMENT

JDSD-1 light-emitting raindrop minute rain gauge is made up of five parts: a sensor, a unit for data collecting, a unit for processing, a printer and a power. The first two parts are fixed in the open air, while the last three parts are in room. Between the first two parts and the room there is a 100-metre cable. There are three such instruments set up at 212 station for ionosphere observation in Guangzhou, the Atmosphere Seience Department Experiment Site of Nanjing University in Nanjing and China Research Institute Of Radiowave Propagation in Xinxiang, respectively, where three typical climates in China are represented.

Guangzhou is near the Tropic of Cancer, in the area of subtropical monsoon wind climatic zone with annual mean temperature of 21.8℃ and the annual total rain

amount of 1622.6mm. While the maximum rain in a day can amount to 253.8mm and there are 6.9 days[1] with rain amount of more than 50mm annually.
Nanjing is between the warm and subtropical climate zones where the annual mean temperature is 15.4℃. The total annual rain amount is 1013.4mm, the maximum one in a day amounts to 160.6mm and there are 3.3 days[1] with rain amount of more than 50mm annually.
Xinxiang lies in warm continental monsoon climatic zone with annual mean temperature and the total annual rain amount 14.0℃and 628.3mm, respectively. Rain amount in a day can be more than 50mm in 2.1 days[2] annually.
Early in July 1988, We began to work in Xinxiang, then in Nanjing and Guangzhou in July 1989. The conversion presented comes from what we have achieved at the locations mentioned above in two years.

THE CONVERSION FORMULAE

For the purpose of converting data obtained with a gauge having an integration time of τ minutes to equivalent 1-minute statistics one can define a conversion factor[3]

$$\rho_\tau(P) = R_1(P)/R_\tau(P) \tag{1}$$

where R1 and R_τ are the rainfall rates exceeded with equal probability, P, for the two integration times.
Data from 45 locations in Canada have been analyzed for τ=5 and 10 min. Results were first grouped according to the rainfall rate climatic zones and were then further merged into three distinct regions.
After further research, the power-law relations of the form:

$$\rho_\tau(P) = a \cdot P^b \tag{2}$$

were fitted over the range $0.001\% < P < 0.03\%$, where a and b can be calculated with the method of least square. Table 1 presents the results of analysis performed in this manner for τ=5 and 10 min in Canada and τ=10 min in Europe.

Table 1 Regression coefficients for rainfall rate correction factor

Region	τ = 5 min		τ = 10 min	
	a	b	a	b
Canada (zones A, B)	0.896	-3.61×10^{-2}	0.796	-7.45×10^{-2}
Canada (zones C, D, E)	0.882	-4.57×10^{-2}	0.836	-7.36×10^{-2}
Canada (zones E, K)	0.862	-5.64×10^{-2}	0.847	-8.20×10^{-2}
Europe			0.860	-7.30×10^{-2}

On the basis of these measured data, the following major conversion methods are proposed:
First, the relation between 10-minute and 1-minute rainfall rate may be expressed by the equation:

$$R_1(P) = a \cdot P^b \cdot R_{10}(P) \quad (3)$$

then $$\rho(P) = R_1(P) / R_{10}(P) = a \cdot P^b \quad (4)$$

where $R_1(p)$ is the rainfall rate exceeded with probability, P, for 1-minute integration time, while $R_{10}(P)$ is for 10-minute integration time, with the same P. Furthermore, $R_1(P)$ and $R_{10}(P)$ may be expressed directly by the equation:

$$R_1(P) = a' \cdot R_{10}^{b'}(P) \quad (5)$$

where $R_1(P)$ and $R_{10}(P)$ are the same as what have been noted above. Their coefficients a' and b' may be got from the real values of $R_1(P)$ and $R_{10}(P)$ by regression. Table 2 presents the results of analysis performed in this manner in Guangzhou, Nanjing and Xinxiang.

Table 2 Regression coefficients for rainfall rate correction factor, $\tau = 10$min

Region	a	b	$R_{1a\rho,1ap}$	a′	b′	$R_{1aR_1,1aR_{10}}$
Guangzhou	1.0496	$-6.87 \cdot 10^{-2}$	-0.98	0.838	1.1147	1
Nanjing	1.1006	$-3.52 \cdot 10^{-2}$	-0.96	1.027	1.0592	1
Xinxiang	1.0367	$-3.64 \cdot 10^{-2}$	-0.96	0.996	1.0558	1

The comparative curves between the two different rainfall rate are presented in Fig. 1, Fig. 2 and Fig. 3, where the dash and dot lines present the real-measured values of 10-minute rainfall rate, the dashed lines present the real-measured values of 1-minute rainfall rate and the real lines present the converted values by formula (3) and (5) with parameters in Table 2. From all these Figues and Tables, we can see that the converted values and the measured values are fitted very well with relative errors of less than 8% for time percentages from 0.001% to 1%.

CONCLUSION

By means of the two methods described above we can fit the converted values of 1-minute rainfall rate with the measured values very well with the relative errors of less than 8% for time percentages between 0.001% and 1%. As the 10-minute rainfall rate can be available from the meteorological information pressed by national and local meteorological service, the methods presented are of value not only for radio system designers but also for investigators in meteorological stations, they can obtain the data about 1-minute rainfall rate for little expense. However, because of the large area, the complex land shape and various climates of China, various conversion formulae should be made. So it is not enough to get data only at three stations above, more and more stations need to be set up.

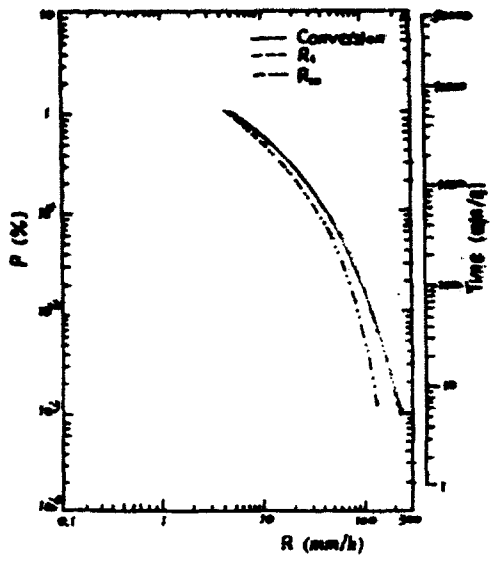

Fig. 1 1-min versus 10-min rainfall rate in Guangzhou

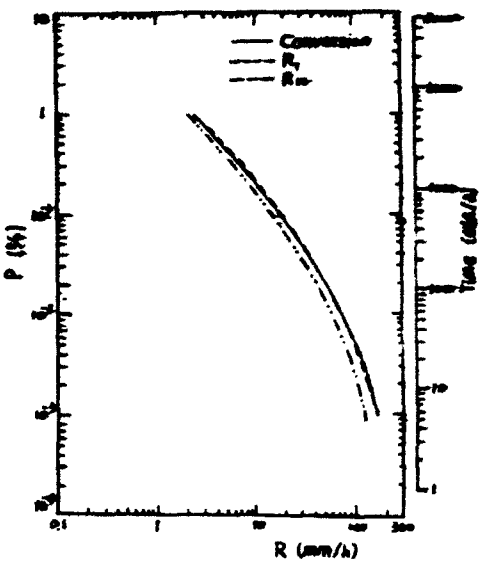

Fig. 2 1-min versus 10-min rainfall rate in Nanjing

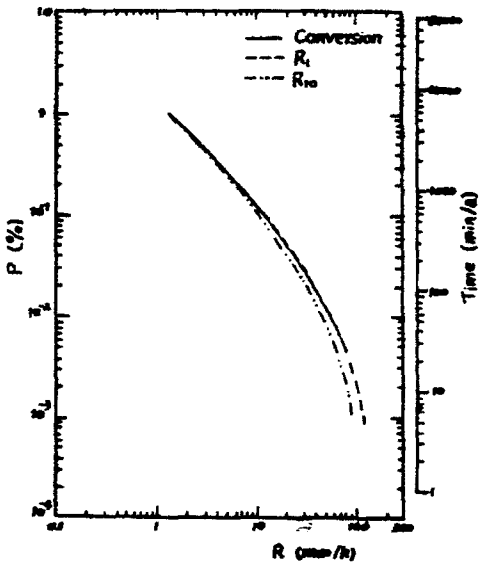

Fig. 3 1-min versus 10-min rainfall rate in Xinxiang

REFERENCES

1. 1951－1970 《China Ground Climatological Data》, National Meteorological Service of China, 1 (1976), 274.
2. Xinxiang administrative Climatography, Xinxiang Meteorological Service, 1 (1979), 112.
3. Documents CCIR Study Groups Period 1986－1990, Report (563-3), (1989), 17.

Th3.6

BACKSCATTERING CROSS-SECTION OF SAND AND SNOW SURFACES ON SHORT MILLIMETER WAVES

G.A.Andreyev, and G.I.Khokhlov

Institute of Radioengineering & Electr., Russian Academy of Sciences
18 Marx Avenue, GSP-3, Moscow 103907, Russia

In this paper the results of measurements of backscattering cross-section of sand and snow surfaces for incidence angles of 0° *(nadir)...*50° *by* 10° *steps are represented. The experiments were made during the period of 1983-1984 on the* 135 *Ghz (*2.2 *mm at wavelength) for circular polarization. In earlier papers measurements of radar backscattering from snow covers were reported for linear polarization at incidence angles of* 0° *and* 45°*. Measurements of the backscattering cross-section of sand surfaces are not known for us.*

Approximate mathematical description of millimeter waves (MMW) scattering by terrestrial covers with chaotic rough surfaces depends on root-mean-square (r.m.s.) angle of inclimation of roughness $\sqrt{\langle\gamma^2\rangle}$ and Rayleigh parameter $p = 2k\sigma_\xi\cos\theta$, where $k = 2\pi/\lambda$ is the wavenumber of incident wave, σ_ξ^2 is the variance of roughness heights, θ is the angle of incidence ($\theta = 0^\circ$ - nadir). As shown in [1,2], for surfaces with normal distribution of roughness it's convenient to divide an interval of angles from 0° to 90° in three regions:

$$1/2k\sigma_\xi \le \theta \le \pi/2; \quad 2.8\sqrt{\langle\gamma^2\rangle} \le \theta \le 1/2k\sigma_\xi; \quad \text{and} \quad \theta \le 2.8\sqrt{\langle\gamma^2\rangle}.$$

In each of these intervals scattering of MMW is described by

corresponding approximate expressions for backscattering cross-section. For large-scale ($p \gg 1$) and smooth ($\sqrt{\langle\gamma^2\rangle} < 1$) roughness of surface, at angles of incidence less than half-width of differential scattering section $\delta\theta = 2.8\sqrt{\langle\gamma^2\rangle}$ the method of tangent plane (MTP) is used [1,2]. The r.m.s. heights of roughness of sand and snow surfaces were valued by measurements of multipath interference between direct and sand- or snow-reflected rays in natural conditions [2]. They are equal to $\sigma_\xi = 2\cdot10^{-3}$m and $\sigma_{\xi\,eff} = 2.5\cdot10^{-3}$m for sand and snow surfaces, respectively. The Rayleigh parameter is $p = 2k\sigma_\xi\cos\theta \gg 1$ for $\theta \le 80^\circ$. For approach MTP backscattering cross-section may be expressed as [1]:

$$\sigma_* = \frac{|V(\theta=0)|^2}{\langle\gamma^2\rangle\cos^4\theta}\exp\left(-\frac{tg^2\theta}{2\langle\gamma^2\rangle}\right), \qquad (1)$$

where $|V(\theta=0)|$ is absolute value of Fresnel reflection coefficient. As follows from (1), one of independent parameters in backscattering cross-section expression is the variance of angles of roughness inclination $\langle\gamma^2\rangle$. It was used for estimation of $\sqrt{\langle\gamma^2\rangle}$ value by experimental dependences of $\sigma_* = \sigma_*(\theta)$.

The backscattering cross-section measurements of sand and snow surfaces were conducted in natural conditions with the usage of radar operating at 135 GHz with circular polarization and energetic potential of 140 dB for incidence angles from 0° to 50° in 10° steps. The calibration of measuring apparatus complex was made by means of comparison of signals from corner reflector with scattering signals from surfaces. The change of incidence angles of antenna beam was realised by change of position of metallic plane. For determination of $\sqrt{\langle\gamma^2\rangle}$ value the measuring backscattering cross-section of sand surfaces were presented in form of straight-line diagram, in accordance

with the dependence of $\sigma_*(\theta)$ (1), standartized by $\sigma_*(0) = |V(\theta=0)| / \langle\gamma^2\rangle$. It was got $\sqrt{\langle\gamma^2\rangle} = 0.21$ by the method of least squares. Figures 1 and 2 represent the results of mean backscattering cross-section for sand surfaces and snow covers, respectively. The solid line in Fig.1 is

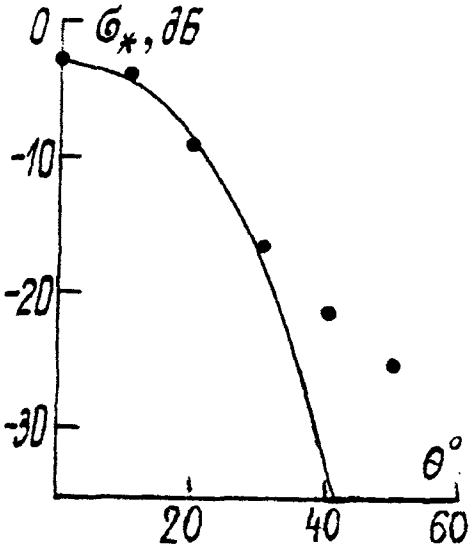

Fig.1

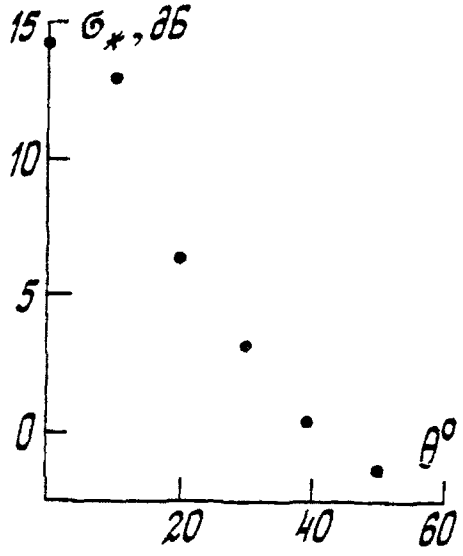

Fig.2

the dependence of $\sigma_*(\theta)$ conforming to (1) for $\sqrt{\langle\gamma^2\rangle} = 0.21$, and $|V(\theta=0)| = 0.15$. As follows from Fig.1, the experimental data confirm the dependence $\sigma_*(\theta)$, derived by MTP approximation, up to incidence angles of $\theta = 30^\circ$. This corresponds to half width of differential scattering section at $\sqrt{\langle\gamma^2\rangle} = 0.21$.

1. Andreyev G.A. // Zarubezhnaya radioelectronica. 1980, v. , No 1, pp 3-32.
2. Andreyev G.A., Chernaya L.F. // Radiotekhnica i electronica. 1981, v. 26, No 6, pp. 1198-1206.
3. Andreyev G.A., Martynova Z.A., Khokhlov G.I. // Radiotekhnica. 1979, v. 34, No 8.

EXPERIMENTAL INVESTIGATION OF THE CLOUD ATTENUATION

Li lan
(China Research Institute of Radiowave Propagation)

INTRODUCTION

Absorption and Scattering effects due to particles of cloud and fog are one of the innegligible factors to affect the performance of millimeterwave and submillimeter wave system. It is much stonger than that in clear sky conditions in addition to strong absorption band of several main gases in atmosphere. An average of 50% earth surface is covered by clouds. Heavy cloud and congested fog restrict not only the application of light wave, infared and submillimeter wave, but also restrict the application of millimeter and centimeter wave. Estmation of cloud attenuation characteristic is very difficult, because uncertainty of cloud water content and cloud extent limit the accuracy to which the attenuation can be calculated from models. However, the experimental investigation of cloud attenuation is few. Exploration of cloud attenuation was made in 1984. Measurements of the cloud attenuation were made by using sun- radio method and atmospheric radiation method on 1985 and 1990.

MEASURING PRINCIPLE AND METHOD

Cloud, which has many kinds, consists of a too much various water drip and ice crystal whose diameter is between 1 to 100um. Absorption, radiation and scattering of cloud to electromagnetic wave are sum of contribution by water drips and ice crystals. At millimeter wave band, the scattering effect can be neglected. Light temperature of observation by ground microwave radiometer is

$$Te = Te^{(o)} \exp\left[-\int_0^{\infty} \sec Z\ \alpha(h)\ dh\right] + \int_0^{\infty} T(h) \sec Z\ \alpha(h) \exp\left[-\int_0^{h} \sec Z\ \alpha(h')\ dh'\right] dh \qquad (1)$$

where $\alpha(h) = \alpha_g(h) + \alpha_c(h)$

In the right of formula (1), the first term is the radiation temperature of radio source which has been attenuated through atmosphere and cloud. $Te^{(o)}$ is the radio-source bright-temperature. The second term is the radiative temperature of atmosphere and cloud. If the measuring direction avoids the strong radio-source i.e the sun and the moon, the measuring result includes only the sum of radiation

temperature of atmosphere, cloud and universe source. The radiation of universe source is very weak, and the higher the frequency is, the weaker the radiation is. It is about 2.8° k. when frequency is higher than 1GHz. The noise temperature of universe source is less than 5 % of the atmosphere radiation temperture. Overlooking universe- source adiation, and using the intergval intermediate-value theorem, we can get:

$$Te = Tm[1-\exp(-\tau)] \tag{2}$$

where $\tau = \tau_g + \tau_c$, τ_g, τ_c are attenuations by atmosphere and cloud, respectively. Tm is average of atmosphere radiation temperature.

When we take account of the effect of ground radiation to get into antenna side-lobe, using the narrow beam antenna, apparent antenna temperature is

$$T_A = [\,1 - \exp(-\tau)\,]T_m + T_v \tag{3}$$

The noise temperature of radiometer output may be written as:

$$T_a = [\,1 - \exp(-\tau)\,]\,T_m + T_v + (1 - 1/L)\,T_o \tag{4}$$

where, L and T_o are the loss factor and physical temperature of transmission line from antenna output to radiometer- receiver input, respectively. When main beam of the antenna point at clear sky at the same elevation, the measuring radiation temperature is

$$T_a' = [1 - \exp(-\tau_g)\,T_m + T_v' + (1 - 1/L)\,T_o \tag{5}$$

According to (4) and (5), the cloud attenuation can be expressed as:

$$\tau_c = -\ln[1-(T_a-T_a'-T_v+T_v')/T_m \exp(-\tau_g))] \tag{6}$$

T_a and T_a' are measuring value, T_m and T_g are calculated from radiosonde data. T_v and T_v' can be define by more accurate calibration technique.

It is an effective method to measure atmosphere absorption using the sun as a source. Same way is took in the experiment of cloud attenuation. When cloud attenuation is measured by dual-frequency (9.375GHZ and 22.235GHZ) radio telescope the antenna is pointed at the sun orbit. A measuring curve may be obtain as the sun passes the main beam of the antenna, then we carry out regression analysis to the logrithm of the difference between the maximum and minimum of the curve with the secont of the zenith angle, so the slope of the regression line is the sum of the atmosphere and cloud attenuation in the zenith direction[2].

$$\ln R = \ln A - \tau_0 \sec Z \tag{7}$$

The advantage of sun-radio method is that the effect of side-lobe can be fully removed and measuring accuracy can be improved, but horizontally stratified atmosphere is supposed. Atmosphere radiation method can be measured various kinds of cloud attenuation, but its calibration technique and data disposal are more complex.

MEASURING RESULT AND ANALYSIS

Cloud attenuation is measured by using sun-radio method at 3.2cm and 1.35cm during spring and summer in 1984 and summer in 1990. (See table 1) Average value of cloud attenuation is 0.454dB at 22.235GHz. Typical measuring curve is shown in Fig. 1. In Fig. 2 , zenith attenuations for cloud and clear sky conditions are plotted as a function of surface absolute humidity for freqency of 9.375GHz. Measuring results show that atmosphere for uniform cloud conditions yet is seen as horizontally stratified medium. So measuring results are reasonable, attenuation is proportional to the surface absolute humidity.

Table 1 Measuring attenuation of atmosphere and cloud f= 9.375GH

Time	τ_m (dB)	τ_c (dB)	R (Relativity)
84 4 12	0.0857	0.0243	0.94
4 26	0.0870	0.0211	0.93
4 26	0.0998	0.0339	0.94
5 12	0.0890	0.0286	0.94
5 12	0.0995	0.0351	0.95
5 16	0.1015	0.0390	0.96
5 17	0.0937	0.0294	0.94
90 5 19	0.1040	0.0372	0.99
7 2	0.0900	0.0193	0.99
7 3	0.0970	0.0210	0.96
7 6	0.1120	0.0249	0.97
7 13	0.1240	0.0337	0.92

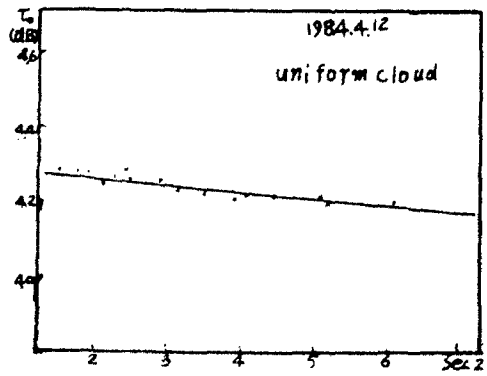

Fig.1 measuring curve for attenuation

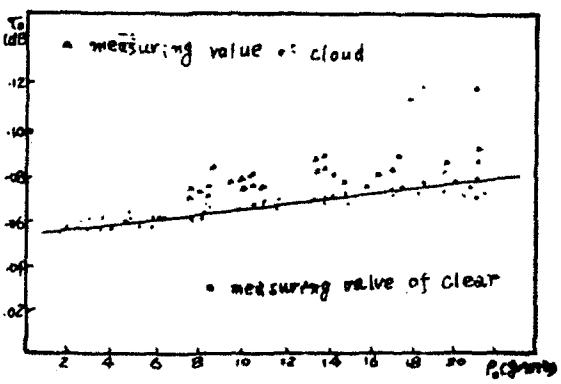

Fig.2 Atmosphere attenuation versus surface humidity

Cloud attenuation was measured with 1.26cm microwave radiometer in the end of summer, 1985. During the measurement radiosondes was set off and the height of cloud bottom was measured with the equipment of laser measurement for cloud. The theoretical value of cloud attenuation may be given by Benoit experimental formula. The theoretical value and measuring value of cloud attenuation are listed in table 2. Table 2 shows that value of theory and measurement are accorded except for few data. their correlation is better. the correlative coefficient is 0.96, where two measuring values are small. The small measuring value of attenuation is probable because that the radio rays paths didn't throughout pass the cloud layer for irregular cloud conditions. It is heavy cloud in the afternoon of the forth, september, but the cloud layer was very high. Height of cloud bottom is 6.25km measured by the equipment of laser measurment for cloud. It is clear that cloud consists of ice crystals at this height. It is well known that ice cloud absorption to electromagnetic wave are very small.

Table 2 Experimental and Theoretical Values of Cloud Attenuation
f = 23.75GHZ

Time	τ_b (dB)	τ_c (dB)	H_c (KM)	Weather
8 29	0.1934	0.1940	1.74	uniform cloud
8 31	0.6326	0.5990	2.02	heavy cloud
9 1	0.1380	0.1250	2.73	heavy cloud
9 1	0.0097	0.1200	3.65	uniform cloud
9 4	0.0689	0.0050	6.25	heavy cloud
9 5	0.3668	0.3780	3.38	heavy cloud

CONCLUSION

During the three measuring periods the cloud attenuations are measured by the sun-radio method and the atmosphere radiation method. Measuring results show that the two methods are valid. Accuracy of the sun -radio method is high, because of case that the effect of side - lobe can be fully removed, but only attenuations of uniform cloud conditions can be measured. Attenuation of various kind clouds are measured by the atmosphere radiation method.

REFERENCE

1. E.R. Westwater, Radio Scince, 13(4) (1978), 677.
2. Zhang Zhong Zhi, Li Lan, Jia Rui Jin, Chinese Journal of Radio science, 1(2) (1986), 1.

RIGOROUS NUMERICAL ANALYSIS OF QUASI-TEM TRANSMISSION LINES

Bin Song , Junmei Fu
(Xi'an Jiaotong University, Xi'an, P.R.China)

ABSTRACT

A boundary-element method is proposed for the quasi-TEM analysis of microwave and millimeter-wave transmission lines of arbitrary cross sections, including finite strip thickness, side-wall grooves, asymmetric structures and multilayered dielectric media. To show the validity and usefulness of this approach, a few interesting examples are given.

INTRODUCTION

Hitherto, various quasi-TEM transmission lines have been investigated thoroughly by many authors and many approaches to analyzing them have been devised. However, it seems that the problem has not yet been solved completely as evidenced by the considerable discrepancies between the published results remarked. In fact, most approaches of analysis either suffer from serious limitation and usually include assumptions that may lead to considerable uncertainty in the obtained results, for example, overlook the effects of side-wall grooves and the finite metallization thickness, or require a large computer memory and long computing time.

The purpose of this study is to develop a very general BEM which can handle arbitrary cross-sectional geometries, including finite strip thickness, side-wall grooves, asymmetric structures and multilayered dielectric media. The BEM proposed in this paper has a few merits, i.e., the required size of the computer memory being small, the computation time being short and the results obtained having fairly good accuracy.

The investigation is based on a quasi-TEM model which is often adequate for microwave frequencies in communication applications and for typical pulse rise times of interest in high-speed digital circuit design.

THEORY

Consider a quasi-TEM transmission line of arbitrary shape which is uniform along the Z axis direction and which consists of isotropic, lossless dielectric media. The cross section can be divided into several subregions homogeneously filled with a dielectric material. Inside a typical subregion Si, Laplace's equation

$$\nabla^2 u = 0 \tag{1}$$

holds, where u denotes the electromagnetic potential. Green's second identity over Si[1] can be expressed as

$$\iint_{S_i} [u^*(\nabla^2 u) - u(\nabla^2 u^*)]\,ds = \int_L [u^* q - u q^*]\,dl \tag{2}$$

where L is the contour of subregion Si, u^* is the fundamental solution, here we choose

$$u^* = -(1/2\pi)\ln(r) \tag{3}$$

where r is the distance between nodal point i and a certain point on the boundary L. q and q^* represent the outward normal derivative of u and u^*, respectively.

Substitute (3) into (2), and assumed that the boundary L is smooth, letting i approaches the boundary and considering the Cauchy's principal value of integration, the following boundary integral equation can be obtained

$$(1/2)\, u_i + \int_L u\, q^* dl = \int_L u^* q\, dl \qquad (4)$$

Dividing the boundary L into linear elements, (4) is discretized and can be rewritten in the following matrix notation

$$[H][U] = [G][Q] \qquad (5)$$

In the same way, to other subregions, the boundary matrix equations like (5) can be formed.

The continuity of the electric potential and the electric flux density along the common interfaces between two continuous subregions (say the mth and nth) requires that

$$u_i = u_j \qquad (6)$$

$$\frac{\partial u_i}{\partial n_i} = \frac{\partial u_j}{\partial n_j} \qquad (7)$$

Using (5)-(7), we can obtain the final matrix equation in the form

$$[A][X] = [B] \qquad (8)$$

Solving (8) for the unknown quantities, the potentials and normal derivatives at the nodal points are determined. Then, the charge density on the metal strip can be computed, therefore, the charge quantity per unit length on the inner conductor may be obtained. Once the charge distribution is known, the capacitance per unit length C is readily obtained

$$C = \frac{Q}{U} \qquad (9)$$

The characteristic impedance and the effective phase velocity are

$$Z = 1/(\, Vo\sqrt{C\, Co}\,) \qquad (10)$$

$$Ve = Vo\sqrt{Co/C} \qquad (11)$$

where Vo is the velocity of light in free space, C is the capacitance of the actual line and Co is the free-space capacitance of the line.

The expression given in (9)-(11) are for dual-conductor transmission line, however, the same procedure can be applied to find the capacitance and characteristic impedance for even and odd modes of coupled transmission lines or to find capacitance and impedance matrices for a system of n lines.

RESULTS

The first example studied is a suspended, multilayered stripline, as shown in Fig.1. Relatively high walls are treated in order to see the strong effects of side-wall grooves. The characteristic impedance Z and the wavelength reduction factor $\lambda g/\lambda o$ are computed, and the results of numerical calculation are shown in Fig.2. It can be found that the results for zero metallization thickness are in good agreement with data published by Yamashita [2] computed with the variational technique. For a

metallization thickness t/b=0.02, the characteristic impedance Z is slightly reduced and the wavelength reduction factor $\lambda g/\lambda o$ is slightly increased. When the inner

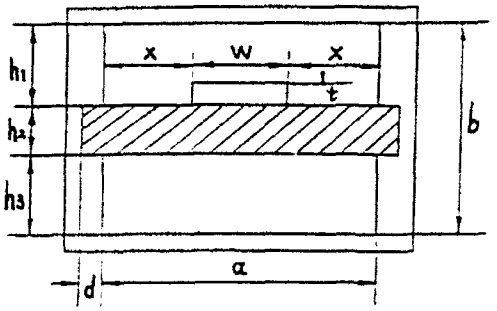

Fig. 1 Cross section of a suspanded stripline.
(a/b=1.0, h1/b=0.4, h2/b=0.2, h3/b=0.4, t/b=0.02 ;
$\varepsilon_{r1} = \varepsilon_{r3} = 1.0$, $\varepsilon_{r2} = 2.22$)

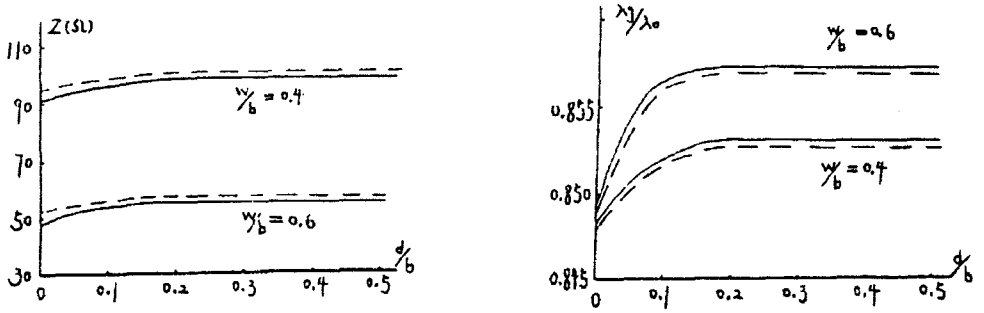

Fig. 2 *Influences* of side-wall grooves on characteristics of the suspanded stripline.
(——— this method, t/b=0.02 ; - - - - [2], t/b=0)

conductor thickness t is a small fixed value, with the increasement of the width W, the obtained results come close to those in [2]. From Fig.2, we can also found that when the depth of grooves is increased, the characteristic impedance and wavelength reduction factor are also increased rapidly but eventually no more effect are observed in the region of deep grooves. Because groove effects are significant in the range of small d, these can not be neglected when precise filters are designed. The above BEM calculations are performed with 136 nodes, while the corresponding FEM calculations need at least 360 nodes.

The next example is a broadside-coupled transmission line whose generic cross section is shown in Fig.3.

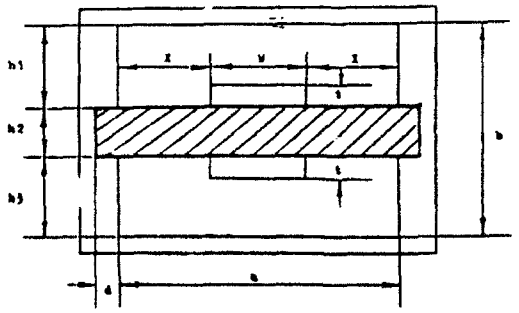

Fig. 3 Cross section of a broadside-coupled transmission line.
(a/b=2.0, h1/b=h3/b=0.4, h2/b=0.2, t/b=0.02, d/b=0.1 ;
$\varepsilon_{r1}=\varepsilon_{r3}=1.0$, $\varepsilon_{r2}=2.35$)

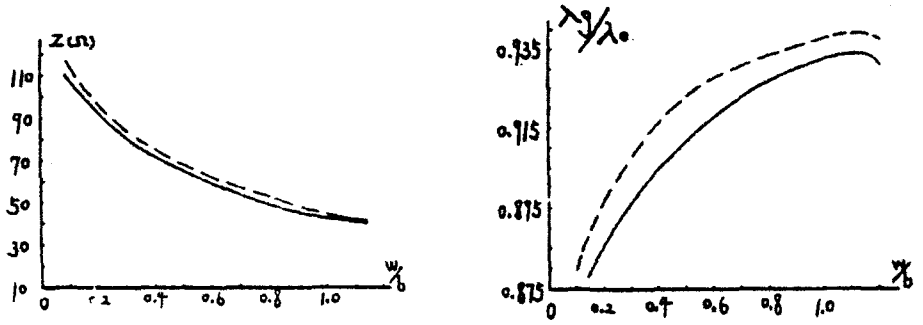

Fig. 4 Characteristic impedance and effective phase velocity of the broadside-coupled transmission line.
(———— this method ; - - - - - [3])

Computed results for the characteristic impedance Z and the effective phase velocity as a function of aspect ratio w/b, denoted by the solid line, are compared with the numerical results obtained via the variational method [3], shown by the dashed line in Fig.4. From Fig.4, it can be found that the characteristic impedance and the effective phase velocity calculated by the approach are all less than those by [3].The variational method proposed in [3] didn't consider the finite metallization thickness and the effect of side-wall grooves, while these are all thought over in this paper, so the result obtained are closer to the experimental results than those of other methods.

CONCLUSIONS

In this investigation, a boundary-element procedure for quasi-TEM analysis of microwave and millimeter-wave transmission lines with multilayered dielectric media is proposed. This approach is capable of handling various quasi-TEM transmission lines with rather arbitrary configurations, including finite strip thickness, side-wall grooves, asymmetric structures and multilayered dielectric media. The approach presented in this paper is applicable to various transmission structures involving inhomogeneous dielectric media, e.g., multiconductor transmission lines in multilayered media.

REFERENCES

1. C.A.Brebbia, Boundary Element Techniques in Engineering, Butterworth, London, 1980.
2. E.Yamashita et al., IEEE Trans., MTT-33, 12(1985), 1323.
3. D.L.Gish, IEEE Trans., MTT-19, 5(1970) 131.

EXACT SIGNULAR INTEGRAL EQUATION SOLUTION FOR THE MODE FUNCTIONS OF FINNED GUIDES

P V Ramakrishna and D Chadha, Deptt. of Electrical Engg., Indian Institute of Technology, Hauz Khas, New Delhi-110016, India

Introduction : A computationally efficient method capable of giving a large number of modes of finned guides is an important tool in the characterization of finline circuits. In [1]-[5], the TE and TM modes of finned guide have been used to characterize certain finline configurations derived from the finned guides. However, there are very few papers reported in the literature which deal with an efficient evaluation of a large number of modes of finned guides. Though the finned guide modes can be obtained as a trivial special case from the many derivations of finlines which are already available in the literature. But in terms of analytical exactness of the method (no approximations at any stage), and in terms of computational efficiency, only one other method reported in the literature [5] is equivalent to the one derived in the present paper.

In this communication we present an alternative singular Integral Equation (SIE) derivation for obtaining the TE modes of unilateral finned guides. The same derivation can be easily modified to obtain the TM modes as well and even to obtain the TE and TM modes of bilateral finned guides and these results also are reported in this communication. The present derivation is based on the method given by R.Mittra et. al. [6] for the case of microstrip line. Using the present derivation, it is found that a matrix inversion of order 3 is sufficient for obtaining upto 30 modes of the finned guide.

Derivation of TE Modes of a Unilateral Finned Guide :-

Consider the TE modes of a unilateral finned guide with its slot located symmetrically so that the structure could be reduced to the one shown Fig.1 The TE mode functions (TE to z) in the two regions could be written as,

$$\phi = \begin{cases} \sum_{n=0}^{\infty} A_n \cosh(\gamma_n(d+y))\cos(k_n X) & : \quad -d \le y \le 0 \\ \sum_{n=0}^{\infty} B_n \cosh(\gamma_n(h-y))\cos(k_n X) & : \quad 0 \le y \le h \end{cases}$$

where, $k_n = n\pi/L$, $(\gamma_n)^2 = (kn)^2 - (kc)^2$, with Kc being the cutoff wavenumber. The nature of the above expressions are such that boundary conditions on the periphery of the waveguide (except the fins) are taken care of. The expressions for Hz, Ex can be written in terms of ϕ.The boundary conditions for the fields at the fin plane are:

1) $E_{x1} = E_{x2}$ $\quad 0 \le x \le L$

2) $E_z1 = E_z2 = 0 \quad 0 \le x \le t$

3) $H_z1 = H_z2 \quad t \le x \le L$

On applying conditions 1), we can express Bn in terms of An and the resulting expression is,

$$B_n = A_n \sinh(d_n d) / \sinh(d_n h)$$

Next, denoting $A_n d_n \sinh(d_n d)$ by A_n', and applying condition 2) gives,

$$A_n' = (2/L) \int_t^L E_x(x) \cos(k_n X)\, dx \qquad --(1)$$

where, $E_z(X)$ is the tangential electric field in the fin plane.

Finally, on applying condition 3), and following the procedure similar to the one outlined in [6], one can obtain the following integral equation for $E_z(X)$:

$$(2/L) \int_t^L E_z(X') \frac{(1/2)\sin(k_1 X)\, dX'}{(\cos(k_1 X') - \cos(k_1 X))} = \sum_{n=1}^{\infty} A_n' a_n \sin(k_n X) \qquad --(2)$$

$$t \le x \le L$$

Although A_n' are as yet unknown, again following the procedure given in [6], we can write the solution of $E_z(x)$ as

$$E_z(X) = \sum_{n=1}^{\infty} A_n a_n f_n(x) + \left(\sum_{n=1}^{\infty} A_n' C_n + A_0' C_0\right) F_n(X) ; \qquad --(3)$$

$$t \le x \le L$$

Substituting for $E_z(X)$ from eqn.(3) into eqn.(1), we get the required final linear system of equations for determining A_n' as,

$$\sum_{n=1}^{\infty} (\delta_{m\,n} - (D_{m\,n} + K_m c_n) a_n) A_n' + A_0' C_0 K_m = 0 \; ; \; m=1,2,.. \qquad --(4)$$

$$\sum_{n=1}^{\infty} (-K_0 C_n) a_n A_n' + A_0' (1 - C_0 K_0) = 0 \qquad --(5)$$

The explicit expressions for a_n, C_n, $f_n(X)$, $F_n(X)$, D_{mn} and K_m are not given here for the sake of brevity, but all of them can be obtained by following same procedure used in [6]. It may be noted that all these quantities can be evaluated in closed form without resorting to any approximations whatsoever (no truncation of infinite series and no evaluation of integerals numerically). It may further be noted that, as in [6], the quantities a_n and C_n rapidly tend to zero as n increases. The zero crossing of the determinant of the system obtained from eqns.(4)-(5) would fix the cutoff frequencies k_c of the various TE modes of the finned guide. Since a_n and C_n go to zero rapidly as n increases, it is

required to invert only a small order matrix (typically 2 or 3) in order to obtain An.

Numerical Results and Discussion : Using the above derivation, the cutoff frequencies of a unilateral finned guide have been computed and are presented in Table I alongwith the results given in [7] for comparison. Following a similar procedure, one can also obtain the TM modes of a finned guide. Also, the above derivations can be applied to bilateral finned guides with certain trivial modifications. The propagation constants of a finline with low dielectric constant substrate material can thus be computed by using the Generalized telegraphists (GTE) [8] for the loaded finned guide structure. These results are given in Table II alongwith those given in [5] for comparison. Although the results of all the higher order modes presented in [5] agree equally well with those obtain using the present method, only the first ten modes are presented here for the sake of brevity. It can be seen from both Table I and Table II that the results oof the present method agree to within 1% with those obtained using other mehods. The following points are offered towards conclusion:

1) In the present method, all the elements of the final matrix can be obtained in closed from without resorting to any approximations. Also, the matrix inversion order remain extremely small (2 or 3) even for determining higher order modes. These are the two main advantages of the present method as compared to the well known Spectral Domain Method and Method of Lines.
2) As compared to the SIE formualtion of [5], the present derivation is done entirely in terms of fields and potentials without resorting to fin currents and Greens' functions. Also, in comparison to the Transverse Resonance formulation of [1], the present derivation does not resort to the Galerkin's approximation used in [1].
3) The simplicity and effectiveness of the single mode approximation formula of GTE obviates the need for going in for an elaborate hybrid mode analysis for finlines on low dielectric constant substrates. This fact has already been exploited successfully in [1].

REFERENCES

[1]. Olley C A et. al IEEE MTT-37 No.6 1989, pp 977-983.
[2]. Mazur J et al IEEE MTT-37, 1989 No.(2), pp 281-287.
[3]. P V Ramakrishna et al EL of 1989 Vol.25. No.16, pp 1399-1400.
[4]. Borneman et. al IEEE MTT-35, 1987 No.6 pp 561-567.
[5]. Omar A A et. al IEEE MTT-32, No.12, 1984, pp 1626-1632.
[6]. Mittra R et. al IEEE MTT-19, 1971 No.1, pp 47-56.
[7]. W J R Hoefer et. al IEEE MTT-30, No.12 1982, pp 2190-2194.
[8]. S A Schellkunoff et. al BSTJ, Vol.31, pp 784-804.

TABLE I

Normalized cutoff frequency ($2L/\lambda_c$) of unilateral finned guide

S.No.	(1-t/U)	Present Method	From Ref [7]
1.	2/3	0.2398	0.2379
2.	1/2	0.2249	0.2234
3.	1/3	0.2051	0.2039
4.	1/4	0.1927	0.1919
5.	1/8	0.1690	0.1690
6.	1/16	0.1518	0.1525
7.	1/32	0.1388	0.1400

Note : Refer Fig.1, d = h = 2L, λ_c = the cutoff wavelength.

TABLE II

Squares of propagation constants of the first ten modes of bilateral finliness

	Finned Guide cutoff wave number k_c (m^{-1})	β^2 (mm^{-2}) GTE Single mode	β^2 (mm^{-2}) From Ref [5]
1.	330.65	0.355	0.360
2.	1070.7	- 0.728	- 0.726
3.	1787.9	- 2.801	- 2.801
4.	1892.7	- 3.184	- 3.184
5.	1988.8	- 3.562	- 3.562
6.	2174.4	- 4.314	- 4.314
7.	2540.5	- 6.071	- 6.067
8.	2635.0	- 6.542	- 6.560
9.	2887.0	- 7.923	- 7.920
10.	3257.5	-10.250	-10.237

Note :- Finline in WR28 waveguide housing. Slot width is 1.0mm. Substrate thickness is 0.254mm. ϵ_r=2.22, Frequency is 30.0 Ghz.

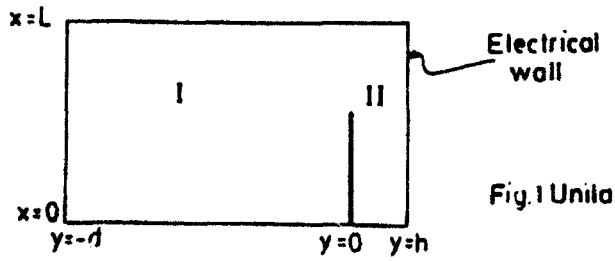

Fig.1 Unilateral finned guide : Reduced structure

Th4.3

AN EXAMPLE OF MILLIMETER-WAVE (8mm) SCALAR NETWORK MEASUREMENTS

Yang Xiufang
(Southwest Institute of Applied Magnetics of China)

INTRODUCTION

This note describes an transmission and reflection measure system by using of the HP 8757A scalar analyzer, the HP 8350B sweep oscillator, the HP 83572A RF plug-in, the HP 7470A graphics plotter and associated accessories at home and abroad.

MEASUREMENT SYSTEM

Scalar network analyzer measures the power reflected or transmitted by devices such as millimeter-wave waveguide isolators. The configuration described here is a complete scalar network measurement system as shown in Fig. 1. It consists of the source to provide stimulus to the test device, the directional couplers and waveguide detectors to sample the reflected and transmitted signals, the receiver for signal processing and display, and the plotter or printer for hardcopy output. Together, these instruments can produce fast, accurate, simultaneous swept displays of transmission loss or gain, and reflection loss or return loss as function versus frequency.

MEASUREMENT PROCEDURE

Abbrevided measurement procedure:
1. to connect measurement system as shown in Fig. 1. Press HP 8757A on PRESET. Use HP 8350B/ 83572A controls to set start/stop sweep and power level.
2. to connect HP R921D Waveguide Fixed Short to TEST PORT for making reflection calibration, then store.
3. to connect "THRU" (connect DETECTOR PORT to TEST PORT) for making transmission calibration, then store.
4. to connect Device Under Test for measuring insertion loss (dB) and return loss (dB or SWR).
5. to connect reverse Device Under Test for measuring isolation (dB).
6. to use HP 7470A for hardcopy output results tested at sweep frequence.

APPLICATION

The millimeter-wave (8mm) waveguide isolators made by our institute were measuremented with the home-made instruments (at the points of frequency), the specifications as follows:

Frequency Range: 26.5—40GHz
Bandwidth: 3GHz
SWR (Max.): 1.2
Maximum Insertion Loss: 0.5dB
Minimum Isolation: 20dB

We have imported major instrument such as HP 8757A, 8350B, 83572A, R752C, R422A, 7470A. If

buying some more accessories, we can set up above millimeter-wave (8mm) scalar network (swept frequency) measurement system. It will speed up the development of the millimeter-wave devices and improve the quality of these product with this measurement system.

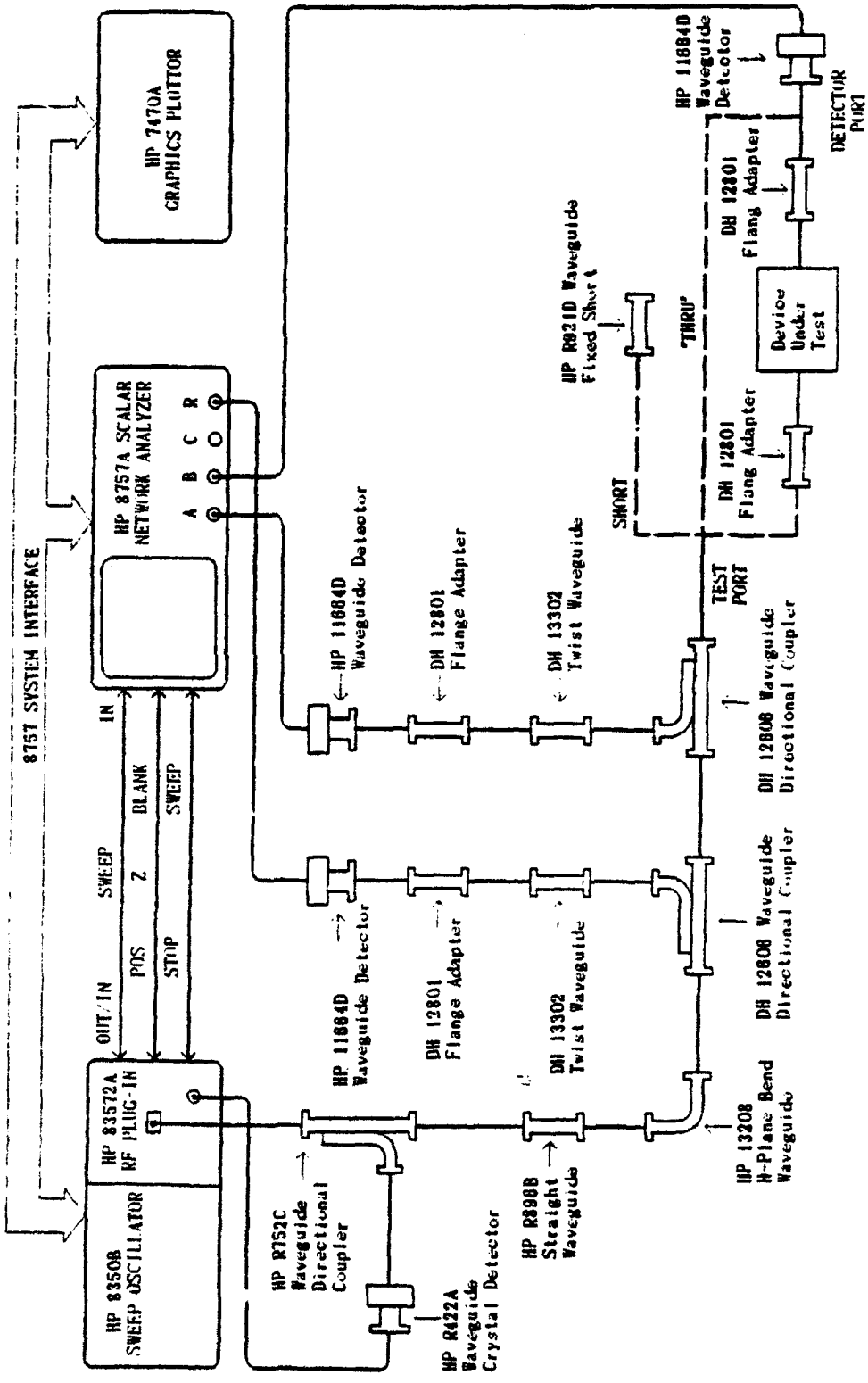

Fig. 1 Millimeter-wave (8mm) scalar network measurement system

SOME ASPECTS CONCERNING CHARACTERICTIC PARAMETER CALCULATION ALGORITHMS FOR MAIN TRANSMISSION LINES IN CM AND MM WAVE RANGE.

R. K. Starodubrovsky

Institute of Electronic Measurements "KVARZ",
176 Prospect Gagarina,
Nizhny Novgorod 603009, Russia

ABSTRACT

Modernization of the method of subareas was used for realization of improved characteristic parameter calculation algorithms of main and special transmission lines for quasi-TEM propogating waves . Results of calculations allow to receive,convenient for engineering practice,empirical expressions for wave impedance value and effective dielectric constant.

The utilization of some main and special cm and mm transmission lines (fig 1a-g) with propagating waves in quasi-TEM mode gives wide opportunity for designing of miniature ultrabroadband devices.

They are used for realization of balanced transitions and mixers (fig 1a-c), tight and supertight coupling for multisection 3db couplers (fig 1d-e), high directivity couplers (fig 1f), supporting "figured" beads (fig 1g).

The principal importance has the choice of universal and precision enough calculation method to determine characteristic parameters (wave impedance Z and effective dielectric constant) for transmission lines with different complex contours of conductors and dielectric boundaries.

Experimental results confirm the efficiency of quasi-static approximation for characteristic parameter culculation for cm and partialy for mm wave range. Some modernization of the method of subareas / 1 / is available for this problem solution. Improved calculation accuracy can be achived by

correction procedure for capacitance C per unit lenght determination. For instance, corrected capacitance per unit lenght for conductor of arbitrary contour in closed screen is

$$C_{cor} = \sum_{i=1}^{l-p} q_i / U_1 + \sum_{v=1}^{p} q_i / U_{v(av)} \qquad (1)$$

where q_i , q_v - charges on elementar segments which approximate conductor contours . Charges are determined by equation system solution:

$$\begin{cases} \sum_{j=1}^{l+m} \alpha_{1j} \cdot q_j = U_1 \\ \vdots \\ \sum_{j=1}^{l+m} \alpha_{(l+1)j} \cdot q_j = 0 \\ \vdots \end{cases} \quad \begin{matrix} \left.\vphantom{\sum}\right] \ l \text{ equations} \\ \\ \left.\vphantom{\sum}\right] \ m \text{ equations} \end{matrix} \qquad (2)$$

α_{ij} - potential coefficients

l - quantity of elementar segments on central conductor

m - quantity of segments on outer conductor (screen)

p - quantity of segments on central conductor in vicinity of conductor contour heteroqeneity(fig 2)

U_1 - potential in central points of elementar segments

Value of average potential $U_{v(av)}$ for segments in vicinity of contour heterogeneity may be determined by culculation of potentials in some points along this segments as

$$U_{v(av)} = \frac{1}{k}\left[U_v(x_1, y_1) + \ldots + U_v(x_k, y_k)\right] \qquad (3)$$

where k - the quantity of discrete points along the abovementioned segments and $U_v(x_s, y_s)$ is determined by expression :

$$U_v(x_s, y_s) = \sum_{j=1}^{l+m} \alpha_{vj}(x_s, y_s, x_j, y_j) \cdot q_j \qquad (4)$$

Values q are determined from equation system solution(2). As a rule it is enough to take quantity k equal to 3 and the mean value $U_v(x_2, y_2)$ equal to potential U_1 at the center of the segment.

Typical picture of the potential distribution at one side of conductor contour for bar conductor is illustrated in fig 3. It can be seen that substantial potential deflection along last segments in vicinity of heterogeneity takes place. Accuracy control was achieved by comparison with known precision data / 2 / for bar conductor in rectangular screen. Error decreasing is achived from (3-5)% to (0.2-0.3)% by applying formulas (1) ,(3), (4). Quantity of segments can be moderate.

The second moment of calculation method improving is to use simple but precision enough expressions for coefficients α_{ij}. For arbitrary conductor contour with good accuracy the following expression can be applied :

$$\alpha_{ii} = -2\ln\left(\frac{\ell_i}{2e}\right); \quad \alpha_{ij} = -\ln\left[e^{2(k_{ij}+a_{ij})} \cdot r_{ij(1)} \cdot r_{ij(2)}\right] \quad (5)$$

k = 0.0986	$a = -0.0531 \cdot \varphi_{ij}^2$	for j $j = i \pm 1$
0.0220	$0.0014 \cdot \varphi_{ij}^3$	$j = i \pm 2$
0.009	0.	$j = i \pm 3$
0.0	0.	$j < i-3$ and $j > i+3$

φ_{ij} - angle in radians

ℓ_i - dimension of elementar segment

The sense of values $r_{ij(1)}$, $r_{ij(2)}$, φ_{ij} is clear from fig 4. In case of inhomogeneous dielectric usage it is necessary to apply additional equations for boundary charge determination and to use condition of continuosly transition of normal vector part D through dielectric boundaries . As a rule calculation errors for inhomogeneous dielectric do not exceed (0.5-1)%. Good stability of calculation results was found for considerable segment quantity variations on conductor contours.

Results of calculations allow to receive convenient for engineering practice empirical expressions for dependence of Z and ε_{ef} on geometrical dimensions and value of ε_r. For instance, values Z and ε_{ef} of widely used microstrip line with cerntain screen conductor width may be expressed in form

$$Z = \frac{60(1+a_1)}{\sqrt{\varepsilon_{ef}}} \cdot \ln\left\{\frac{8h}{w}\cdot\frac{1}{1+a_1} + \frac{w}{4h}(1+a_1)\left[1-0.03\left(\frac{w}{h}(1+a_1)\right)^2\right]\right\} \quad w/h \le 1$$

$$Z = \frac{120\pi(1+a_2)/\sqrt{\varepsilon_{ef}}}{\frac{w}{h}(1+a_2)+2.42-0.44\frac{h}{w}\cdot\frac{1}{1+a_2}+\left\{1-\frac{h}{w}\cdot\frac{1}{1+a_2}\right\}^6} \quad (6) \quad w/h > 1$$

$$\text{where } (a_1)^{-1} = \left\{1.25\left[1+\frac{w}{h}\left(1+\frac{w}{h}(0.607^{D/w\cdot w/h})\right)\right]\right\}^{1.5[(D/w)^{4/4}-1]/[(0.5D/w)^{\frac{0.0148}{w/h}}]}$$

$$(a_2)^{-1} = \left\{1.25\left(1+\frac{w}{h}\sqrt{0.9+\frac{w}{h}}\right)\right\}^{\left[1+\frac{4.2}{1+0.3(D/w)^{0.25\,w/h}}\right]\left[(D/w)^{0.257}-1\right]}$$

$$\varepsilon_{ef} = \frac{\varepsilon_r+1}{2} + \frac{\varepsilon_r-1}{2}\left[1+\frac{10+2th(2w/h)}{w/h}\cdot\frac{1}{1+\varepsilon}\right]^{-\frac{1}{2}c} \quad (7)$$

$$\text{where } \ln(\varepsilon) = \left\{-0.1(w/h)^{1.4}\cdot(D/w-1)^{[0.7+(w/h)^{(1-w/h)}+g]}\right\};\ g = 2.25\,th^2(0.25\,w/h)$$

$$c = \left\{1-\frac{0.02}{w/h\cdot\sqrt{[1+(w/h)^{1.3}((D-D_0)/w)^2][1.6-\varepsilon_r^{-0.7}]}}\right\}^{[1-(D/w)^{-10D/w\cdot w/h}]};\ D_0/w = 1.7(w/h)^{-0.5}$$

Calculation errors of this expressions do not exceed 1%. Calculation results for configurations given in Fig 1a-g were used for microwave device engineering: hybrids, 3db couplers, precision directional couplers, reflectometers and mixers in 12-40 GHz range.

References

1. Retain D. K., Higgins J. J Accurate determination of the capacitance of a thin rectangular plate . Comm. and Electronics, 1957., 28, pp. 761-766

2. Gunston M. A. R. Microwave Transmission-Line Impedance Data . Van Nostrand Reinhold Company LTD, New York, 1972.

Figure 1. Transmission line cross sections.

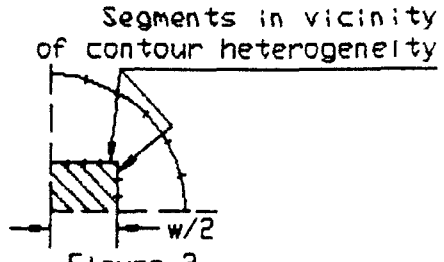

Figure 2. Elementar segments on conductor contours.

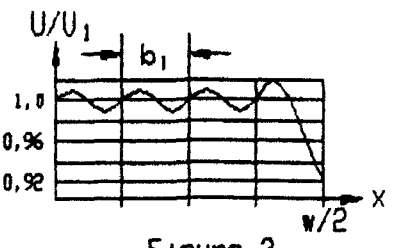

Figure 3. Potential distribution along segments.

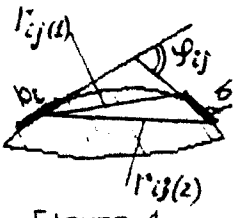

Figure 4.

Th4.5

OPTIMUM DESIGN OF WAVEGUIDE TAPER FROM RECTANGULAR TO GROOVY CROSS SECTION

Liu. Jin Ying and Qin. Jian Zhang
(Beijing Vacuum Electronics Research Institute
P. O. Box 749-34, Beijing, 100016, China)

ABSTRACT

A waveguide taper from rectangular to groovy cross section is designed using the mode coupling theory. In the frequency range of 75-110 GHz, the experimental VSWR of the taper is less than 1.04.

INTRODUCTION

Groove waveguide is found more and more applications in millimeter wave transmission system for its advantages of low attenuation, high power capability, relative large size and consequentially non-critical fabrication tolerance. The current used instruments and devices, however, are usually in rectangular waveguide for their input/output port such as the output window of the mmw sources, the input port of the powermeters, etc.. To improve the performance of the mixed system of groove and rectangular waveguides, the taper with complex transition curve, as shown in Fig.1, must take place the simple tapers, or V-type tapers. Usually it is difficult to obtain low VSWR for the later because of its straight line transition curve.

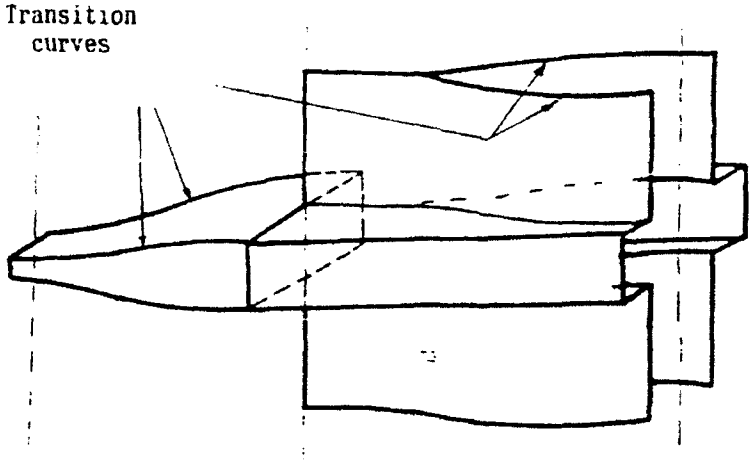

Fig.1 Waveguide taper from rectangular to groovy cross section

THEORETICAL ANALYSIS AND PROGRAM DESCRIPTION

Solymar's formulae[1] for the spurious modes in nonuniform waveguide presented the amplitutes of all transmitted and reflected waves at the input and output ports of a taper. The formulae are the solutions of the equations transformed from the solutions of Helmohotz's equations and they have been programed for the arbitrary cross section and arbitrary transition curves[2].

RESULTS AND DISCUSSION

Using the program, three tapers have been designed theoretically and the normalized amplitudes of the main spurious waves to the incident dominant mode H10 are shown in Fig.2. Curve A in Fig.3 shows the experimental VSWR of taper a and curve B is the VSWR of a taper designed using the impedance match method[3]. It is seen that the VSWR of taper a is predictively very small, and its transmission coefficient shoud be aproximate to unit because of the small amplitudes of the spurious waves at the output port.

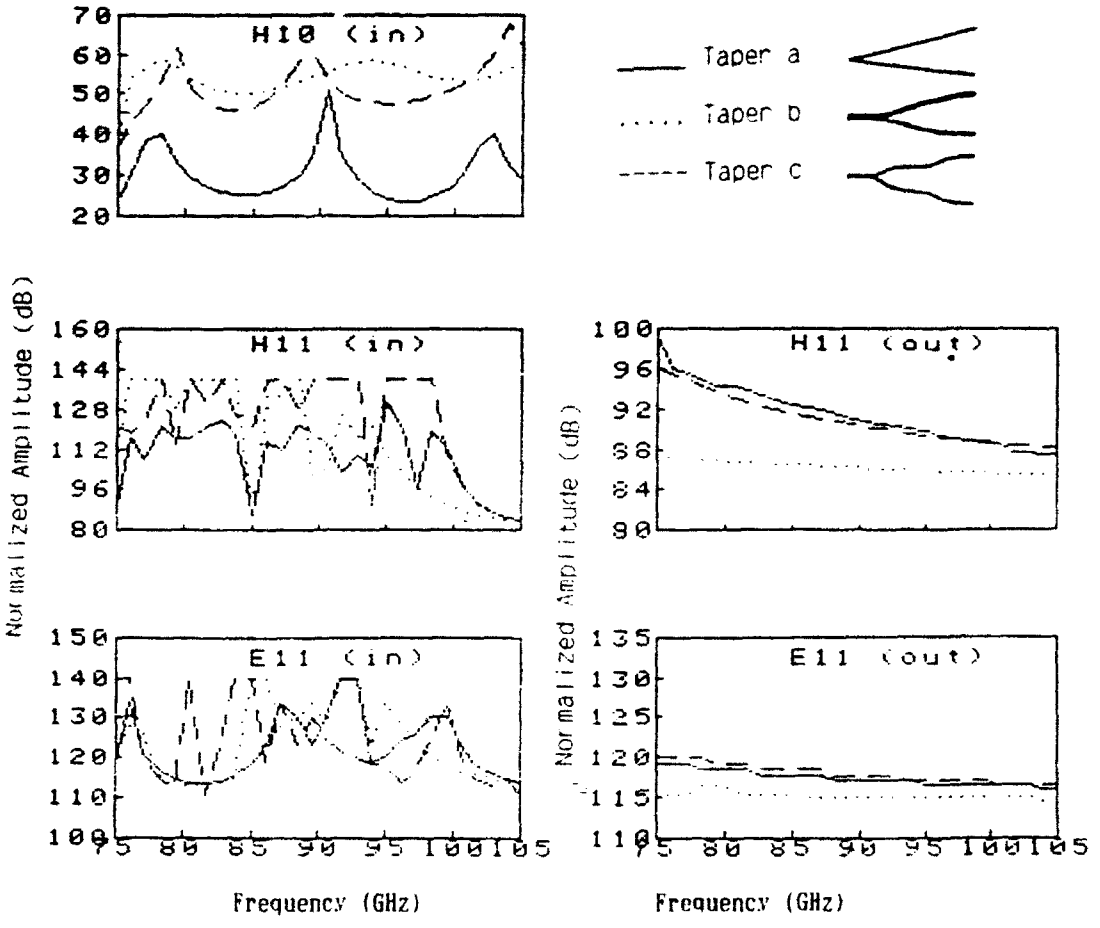

Fig.2 Normalized amplitudes of spurious waves vs frequency at input and output ports

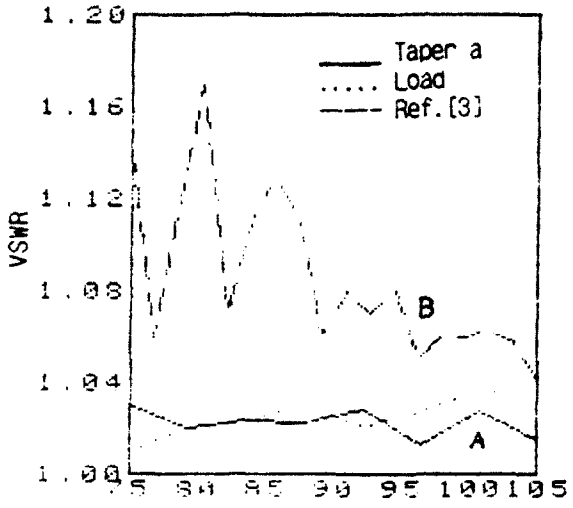

Fig.3 Experimental VSWR vs frequency

CONCLUSION

The waveguide tapers from rectangular to groovy cross section are designed using the mode coupling theory without introducing the traditional VSWR concept. The experimental results shows that this method has the advantages of directness and completeness.

REFERENCES

[1]. L. SOLYMO, " Spurious Mode Generation in Nonuniform Waveguide", I.R.E. Trans. Vol. MTT-7, July, 1959, pp.379-383.

[2]. Liu Jin Ying and Qin Jian Zhang, "CAD of Waveguide Tapers in Millimeter Wave Band Using Mode Coupling Theory". Int.Conf. on MMW and FIR Technology, Proc.Vol.2, June, 1990, pp.112-115.

[3]. J.R.Pyle. "Matched Transition Between Dissmilar Rectangular Waveguide Carrying the H10 Mode", Proc. I.R.E.(Aust.). Nov. 1961, pp.694-701.

Th4.6

THE CHARACTERISTIC EQUATION OF ASYMMETRIC DOUBLE CIRCULAR GROOVE GUIDE①

Ma Jianglei, Yang Hong-sheng, Lu Zhong-zuo
State Key Laboratory of Millimeter Wave,
Southeast University, Nanjing, 210018, P. R. China

ABSTRACT

As the development of our previous analyses on single circular groove guide and double circular groove guide with identical diameter, a theoretical investigation of the field configuration of double circular groove guide with different diameter has been made and its characteristic equation has been presented.

INTRODUCTION

Single circular groove guide is a new type of transmission medium in short millimeter wave and extra-far infrared we have presented.[1] Compared with rectangular groove guide, it is more suitable to output of high power gyrotrons. In our previous work, we have analyzed its transmission properties.[2],[3] We have discussed the field configuration, the characteristic equation and the attenuation coefficient. The results we have obtained express that as transmission waveguide, single circular groove guide shows its advantages of low loss, single mode, high power handling capacity and relatively large cross section over traditional rectangular waveguide, particularly when frequency is above 300 GHz.

Double circular groove guide can support two types of modes which have different phase velocities, that is, odd modes and even modes. Because there is coupling between the odd and even modes, the power can transfer from one groove to the other. Therefore, double circular groove configuration can be used to design a new type of coupler. On the basis of our analyses of single circular groove guide, we have studied symmetric double circular groove guide, i.e., double circular groove guide with identical diameter. It is fundamental structure of double circular groove guide. We have derived its characteristic equations and given the solutions under first-order and second-order approximation[4]. The results show that the difference between TE_{11} and TE_{12} mode is small. This will make the beat wavelength too long to be used in practice. Besides, the bandwidth of the coupler based on this structure is narrow. According to Miller's coupled wave theory and Meissner's paper[5],[6], the asymmetric structure can reduce the beat wavelength and broaden bandwidth. For this reason, we consider using the structure of double circular groove guide with different diameter to improve the properties of coupler constructed by symmetric double circular groove configuration.

① The Project Supported by National Natural Science Foundation of China

In this paper, we will analyze the construction of asymmetric double circular groove guide, give its first-order approximate characteristic equation and compare it with the situation of symmetric one.

CHARACTERISTIC EQUATION

Fig. (1) gives the cross section of asymmetric double circular groove guide investigated. The guide extends to infinite in the z-direction, the direction of wave propagation. The cross section can be devided into section A and B by central straight dotted line which can be effectively replaced by an electric or a magnetic wall corresponding to the fundamental TE odd mode (TE_{11} mode) and TE even mode (TE_{12} mode) separately. Each section consists of three parts, i.e., the arc region, the marginal exponentially evanescing region and the central parallel plane region. They are designated by (1), (2) and (3) respectively. Because of asymmetry, s_1 and s_2 are unequal and the sum of s_1 and s_2 is equal to 2s, the separation between two grooves.

Assuming the groove separation 2s meets the condition $2s > a_1(1-\cos\alpha_{01})+a_2(1-\cos\alpha_{02})$ and according to the structure illustrated in Fig. (1), we can write the boundary conditon. They are as following:

$$
\begin{aligned}
&H_{zA_1} = H_{zA_2} && (\rho=a_1,\ 0\leqslant|\alpha|\leqslant\alpha_{01})\\
&H_{zA_1} = H_{zA_3} && (\rho=a_1,\ \pi-\alpha_{01}\leqslant|\alpha|\leqslant\pi)\\
&E_{zA_1} = \begin{cases} E_{zA_2} & (\rho=a_1,\ 0\leqslant|\alpha|\leqslant\alpha_{01})\\ E_{zA_3} & (\rho=a_1,\ \pi-\alpha_{01}\leqslant|\alpha|\leqslant\pi)\\ 0 & (\rho=a_1,\ \alpha_{01}\leqslant|\alpha|\leqslant\pi-\alpha_{01}) \end{cases} && (1)\\
&H_{z'B_1} = H_{z'B_2} && (\rho'=a_2,\ \pi-\alpha_{02}\leqslant|\alpha'|\leqslant\pi)\\
&H_{z'B_1} = H_{z'B_3} && (\rho'=a_2,\ 0\leqslant|\alpha'|\leqslant\alpha_{02})\\
&E_{z'B_1} = \begin{cases} E_{z'B_2} & (\rho'=a_2,\ \pi-\alpha_{02}\leqslant|\alpha'|\leqslant\pi)\\ E_{z'B_3} & (\rho'=a_2,\ 0\leqslant|\alpha'|\leqslant\alpha_{02})\\ 0 & (\rho'=a_2,\ \alpha_{02}\leqslant|\alpha'|\leqslant\pi-\alpha_{02}) \end{cases}
\end{aligned}
$$

For convenience, we use different coordinate systems in the two sections. After analyzing the field configuration, we obtain the H_z field components under first-order approximation.

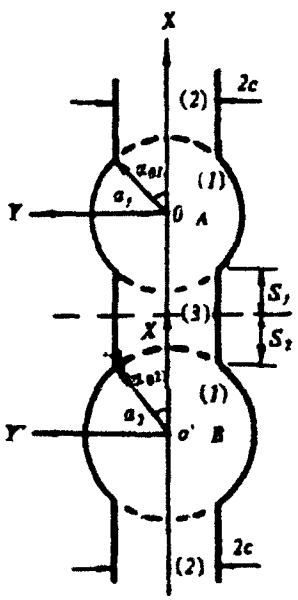

Fig. (1) The cross section of asymmetric double circular groove guide

In section A:

$$
\begin{aligned}
&H_{zA_1} = H_{A_1} J_1(k_c\rho)\sin\alpha\\
&H_{zA_2} = B_{A_1} k_c^2 \sin\left(\frac{\pi y}{2c}\right)\exp\left[-k_{xA}(x-x_{01})\right] && (2)\\
&H_{zA_3} = k_c^2 \sin\left(\frac{\pi y}{2c}\right)\left\{C_1 ch\left[k_{xA}(s+a_1\cos\alpha_{01}+x)\right]+C_1' sh\left[k_{xA}(s+a_1\cos\alpha_{01}+x)\right]\right\}
\end{aligned}
$$

and in section B:

$$
\begin{aligned}
&H_{z'B_1} = H_{B_1} J_1(k_c\rho')\sin\alpha'\\
&H_{z'B_2} = B_{B_1} k_c^2 \sin\left(\frac{\pi y'}{2c}\right)\exp\left[k_{x'B}(x'+x_{02})\right] && (3)\\
&H_{z'B_3} = k_c^2 \sin\left(\frac{\pi y'}{2c}\right)\left\{C_1 ch\left[k_{x'B}(x'-s-a_2\cos\alpha_{02})\right]+C_1' sh\left[k_{x'B}(x'-s-a_2\cos\alpha_{02})\right]\right\}
\end{aligned}
$$

Where k_c is cut-off wavenumber; H_{A_1}、H_{B_1}、B_{A_1}、B_{B_1}、C_1、C_1' are the amplitudes of field in sections A and B; x_{01} and x_{02} are the x components at arc boundaries and k_{xA}、k_{xB} are the wavenumbers in x direction in section A and B separately.

Using expressions (1)～(3) and noticing that k_{xA} is equal to $k_{x'B}$, we can derive characteristic equation. It

reads:

$$\frac{\pi u_A J_1(u_A)}{2J_1(u_A)} - \frac{A_1 P_{A_2}}{A_4} - \frac{A_1}{Q}(P_{A_1}P_{B_2} + P_{A_3}P_{B_1}) = \frac{\frac{D_1}{Q}(P_{A_4}P_{A_2} - P_{A_3}P_{A_1})}{\frac{\pi u_B J_1(u_B)}{2J_1(u_B)} - \frac{D_1 P_{B_2}}{D_4} - \frac{D_1}{Q}(P_{B_4}P_{A_2} + P_{B_3}P_{A_1})} \quad (4)$$

$$\frac{A_1}{Q}(P_{B_4}P_{B_2} - P_{B_3}P_{B_1})$$

Where $u_A = k_c a_1$; $u_B = k_c a_2$

If Let:

$$f_1(x_1, x_2) = \int_{x_1}^{x_2} \sin\alpha \sin(M\sin\alpha) d\alpha \qquad f_2(x_1, x_2) = \int_{x_1}^{x_2} \cos(M\sin\alpha)\sin^2\alpha d\alpha$$

$$f_3(x_1, x_2) = \int_{x_1}^{x_2} \sin(M\sin\alpha)\sin\alpha\cos\alpha d\alpha \qquad f_4(x_1, x_2) = \int_{x_1}^{x_2} \sin^2(M\sin\alpha) d\alpha$$

$$f_5(x_1, x_2) = \int_{x_1}^{x_2} \sin^2(M\sin\alpha)\mathrm{ch}(V\cos\alpha) d\alpha \qquad f_6(x_1, x_2) = \int_{x_1}^{x_2} \sin^2(M\sin\alpha)\mathrm{sh}(V\cos\alpha) d\alpha$$

$$f_7(x_1, x_2) = \int_{x_1}^{x_2} \cos(M\sin\alpha)\sin^2\alpha\,\mathrm{ch}(V\cos\alpha) d\alpha \qquad f_8(x_1, x_2) = \int_{x_1}^{x_2} \cos(M\sin\alpha)\sin^2\alpha\,\mathrm{sh}(V\cos\alpha) d\alpha$$

$$f_9(x_1, x_2) = \int_{x_1}^{x_2} \sin(M\sin\alpha)\sin\alpha\cos\alpha\,\mathrm{ch}(V\cos\alpha) d\alpha$$

$$f_{10}(x_1, x_2) = \int_{x_1}^{x_2} \sin(M\sin\alpha)\sin\alpha\cos\alpha\,\mathrm{sh}(V\cos\alpha) d\alpha$$

Then we have: $A_i = f_i(0, \alpha_{01})$ $\quad A_j = f_j(\pi - \alpha_{01}, \pi)$

$D_i = f_i(\pi - \alpha_{02}, \pi)$ $\quad D_j = f_j(0, \alpha_{02})$

$(i = 1 \sim 4)$ $\quad (j = 5 \sim 10)$

But it should be noticed that we must substitute V, M by V_A M_A and by V_B, M_B respectively in calculating parameters A_j and D_j. Where: $V_A = a_1 k_{zA}$ and $V_B = a_2 k_{zB}$

$$M_A = \frac{\pi a_1}{2c} \quad \text{and} \quad M_B = \frac{\pi a_2}{2c}$$

The other parameters in equation (4) are:

$$Q = P_{A_2}P_{B_1} + P_{B_2}P_{A_1}$$

$$P_{A_1} = \mathrm{ch}(y_1)A_5 + \mathrm{sh}(y_1)A_6$$

$$P_{A_2} = \mathrm{sh}(y_1)A_5 + \mathrm{ch}(y_1)A_6$$

$$P_{A_3} = M_A A_2 - V_A A_3$$

$$P_{A_4} = M_A[\mathrm{ch}(y_1)A_7 + \mathrm{sh}(y_1)A_8] + V_A[\mathrm{sh}(y_1)A_9 + \mathrm{ch}(y_1)A_{10}]$$

$$P_{A_5} = M_A[\mathrm{sh}(y_1)A_7 + \mathrm{ch}(y_1)A_8] + V_A[\mathrm{ch}(y_1)A_9 + \mathrm{sh}(y_1)A_{10}]$$

$$y_1 = V_A\left(\frac{s}{a_1} + \cos\alpha_{01}\right)$$

$$P_{B_1} = \mathrm{ch}(y_2)D_5 - \mathrm{sh}(y_2)D_6$$

$$P_{B_2} = \mathrm{sh}(y_2)D_5 - \mathrm{ch}(y_2)D_6$$

$$P_{B_3} = M_B D_2 + V_B D_3$$

$$P_{B_4} = M_B[\mathrm{ch}(y_2)D_7 - \mathrm{sh}(y_2)D_8] + V_B[\mathrm{ch}(y_2)D_{10} - \mathrm{sh}(y_2)D_9]$$

$$P_{B_5} = M_B[\mathrm{sh}(y_2)D_7 - \mathrm{ch}(y_2)D_8] + V_B[\mathrm{sh}(y_2)D_{10} - \mathrm{ch}(y_2)D_9]$$

$$y_2 = V_B\left(\frac{s}{a_2} + \cos\alpha_{02}\right)$$

The relation between u and V_A, V_B is: $u^2 = M_A^2 - V_A^2 = M_B^2 - V_B^2$ (5)

DISCUSSION

There is a series of double roots in equation (4) and the lowest pair is corresponding to fundamental TE_{11} mode and TE_{12} mode.

If a_1 and a_2 are equal, the asymmetric structure become symmetric. This condition yields:

$$M_A = M_B = M$$

$$V_A = V_B = V$$

$$u_A = u_B = u$$

$$D_i = A_i \qquad (i = 1,2,4,5,7,10)$$

$$D_j = -A_j \qquad (j = 3,6,8,9)$$

$$P_{A_i} = P_{B_i} = P_i \qquad (i = 1 \sim 5)$$

Then the characteristic equation (4) becomes:

$$\left[\frac{\pi u J_1'(u)}{2J_1(u)} - \frac{A_1 P_3}{A_4} - \frac{A_1}{Q}(P_4P_2 + P_5P_1)\right]^2 = \left[\frac{A_1}{Q}(P_4P_2 - P_5P_1)\right]^2$$

It can be separated into two expressions:

$$\frac{\pi u J_1'(u)}{2J_1(u)} = \frac{A_1 P_3}{A_4} + A_1 \frac{P_4}{P_1} \tag{6}$$

$$\frac{\pi u J_1'(u)}{2J_1(u)} = \frac{A_1 P_3}{A_4} + A_1 \frac{P_5}{P_2} \tag{7}$$

They are the same as those we have derived in the analysis of double circular groove guide with identical diameter and expressions (6) and (7) are for TE_{11} mode and TE_{12} mode separately. We have proved that when the separation between two grooves trends infinite, the characteristic equation of symmetric double circular groove guide degenerates to that of single circular groove guide. While the solution of characteristic equation of single circular groove guide has been verified by our experiment. This process indicates that the results we have get are reasonable.

REFERENCES

[1]Yang Hong-sheng, Ma Jianglei and Lu Zhong-zuo, "A New Type of Groove Guide", ISRAMT' 89, PP. 239～240

[2]Yang Hong-sheng, Ma Jianglei and Lu Zhong-zou, "The Characteristic Equation and Solution of Circular-groove Guide", International Journal of Infrared and Millimeter Waves, Vol. 12, No. 5, 1991

[3]Ma Jianglei, Yang Hong-sheng and Lu Zhong-zuo, "An Investigation of the Attenuation Characteristic of Circular-groove Guide", ISRAMT' 91

[4]Ma Jianglei, Yang Hong-sheng and Lu Zhong-zuo. "Theoretical Analysis of Double Circular Groove Guide," Submitted to International Journal of Infrared and Millimeter Waves

[5]S. E. Miller, "Coupled Wave Theory and Waveguide Applications", The Bell System Technical Journal, May, 1954, PP. 661～719

[6]J. Meissner, "Groove-guide Directional Couplers with Improved Bandwidth", Electronics Letters, Vol. 20, No. 17, 1984, PP. 701～703

SCATTERING CHARACTERISTICS OF EPITAXIAL LAYER ON LOSSY DIELECTRIC SEGMENT PARTIALLY FILLED IN WAVEGUIDE*

Xu Shanjia, Wu Xinzhang

Department of Radio and Electronics
University of Science and Technology of China
Hefei, Anhui, 230026, P.R.China

P. Greiner, C.R. Becker, R. Geick

Physikalisches Institut der Universitat
Am Hubland, 8700 Wurzburg, Germany

ABSTRACT

The scattering characteristics of II-VI-epitaxial layer on lossy dielectric substrate partially filled in rectangular waveguide are investigated by the method which combines the multimode network theory with the rigorous mode matching procedure. The experimental data verify the accuracy and the effectiveness of the present method. Extensive numerical results are given to establish useful guidelines for the contactless microwave measurement of the conductivity of the epitaxial layer.

INTRODUCTION

Recently, II-VI-semiconductor becomes more and more important in material science and engineering, because of its inherent advantages for applications in spectroscopy with optical, infrared and millimeter waves. In order to facilitate the studies of this kind of material, the measurements of its electric properties, e.g. conductivity, are of essential significance. However, conducting II-VI-semiconductors has always been a problem. In many cases, it is extremely difficult or even impossible to obtain good ohmic contacts to the sample. To solve this problem effectively, reference [1] proposed a contactless microwave bridge technique in X Band frequency range. This technique ends the conductivity measurement of the semiconductor to the transmission coefficient test of the sample which consists of the II-VI-epitaxial layer on lossy dielectric substrate segment inserted in a rectangular waveguide. In case of such a consideration, the analysis of the scattering characteristics of the semiconductor sample is of undoubtedly practical significance.

In this paper, an accurate and simple method is presented to determine the relationship theoretically between the conductivity of the semiconductor and the scattering parameters of the corresponding sample so that one can read the conductivity of the epitaxial layer from the measurement data of the S-parameters directly. In such a way, the investigation of the semiconductor pro-

* Supported by The National Natural Science Foundation of China and The Deutsche Forschungsgemeinschaft.

perties becomes more efficient and convenient. Since the present method combines the multimode network theory with the rigorous mode matching procedure and transfers the electromagnetic field boundary value problem into network analysis problem therefore, the whole calculation procedure is significantly simplified while still retaining the high accuracy of the mode matching method.

The validity of the present approach is justified by comparisons of the transmission characteristics for different samples between the experimental data and theoretical predictions. Extensive numerical results about the variations of the S-parameters with the sample parameters are given to establish useful guidelines for the contactless microwave measurement of the semiconductor sample.

BRIEF DESCRIPTION OF THE METHOD

Fig.1 shows the cross-sections of the semiconductor discontinuity structure under consideration. Here, the dielectric constants of the epitaxial layer and the substrate are complex with large real and imaginary parts. The solution procedure for this problem may be divided into two steps. First, analyze the eigenvalue problem of the empty and the sample filled waveguide respectively in the transverse cross-section. Secondly, calculate the scattering characteristics of the discontinuity in the longitudinal cross-section. The eigenvalues and eigenfunctions for the empty waveguide are well known, the key point to the eigenvalue problem in the first step is the determination of the eigenvalues and eigenfunctions in the sample filled waveguide. It is done in this paper with the microwave network method in which the electromagnetic boundary value problem is transfered to the impedance transformation in the equivalent transmission line network and the transverse resonance technique is used to determine the eigenvalues then the eigenfunctions. [2] After solving the eigenvalue problem in the transverse cross-section of two waveguides, the second step is carried out with the method described in referenc [3] in which the mode matching procedure is treated as the transformations of the impedances in two sides of the discontinuity by introducing the coupling matrix being taken into account the coupling between different modes; also the symmetrical property of the structure in longitudinal cross-section is utilized to facilatate the calculation procedure.

NUMERICAL RESULTS

Table 1 presents a comparison of the transmission characteristics for different samples between the experimental data and the theoretical predictions. It can be seen from the table that the agreement is very good for S21, the transmission coefficients of different samples. The reliability and the accuracy of the present method are thus justified.

Fig.2 shows the S-parameters versus the conductivities of the epitaxial layer. The definations of the S-parameters are as follows: $S21=|S21|\exp(j\varphi 21)$, $S11=|S11|\exp(j\varphi 11)$. The variation of the curve is as expected, because the conductivity of the epitaxial layer has a strong influence on the field distribution

in the waveguide. For instance, when the conductivity is small, say less than 15.0 (mhos/cm), the dominant mode in sample filled waveguide is a propagation mode, therefore in this region |S21| keeps flat in its maximum and reduces gradually as 6 increasing. When 6 increases from 15.0 (mhos/cm), the dominant mode suddenly becomes cutoff mode; this makes |S21| decrease rapidly with 6 increasing. As 6 is further increased the dominant mode is below cutoff deeper and deeper and finally the electromagnitc fields of the dominant mode approach to the complete standing wave distribution in the transverse cross-section which is just corresponding to the case that a perfect conductor is placed at the position where the epitaxial layer is located. In this case, |S21| reaches its minimum and is little affected as 6 increasing.

From the curves, it is found that the variations of amplitude and phase with conductivities for transmission coefficient and reflection coefficient are quite different; |S21| and φ 11 are insensitive in high conductivity region whereas either |S11| or φ 21 changes rapidly in the same region. Based on this characteristics, it may be suggested that it is better to test φ 21 or |S11| for the epitaxial layer with high conductivity; on the contrary, it is recommended to test |S21| or φ 11 for the epitaxial layer with low conductivity. More calculations were made to give the variations of S-parameters with frequency and with thickness of the epitaxial layer and substrate layer; they are omitted here because of the limited space available. All these numerical results are helpful to establish useful guidelines for the contactless microwave measurement of the conductivity of the epitaxial layer.

REFERENECES

[1] P. Greiner, L.Polignone, C.R.Becker, R. Geick, Digest of 16th IC on IR & MMW, 1991, pp.308-309.

[2] Xu Shanjia, Journal of Electronics, Vol.6,No.1,1989,pp.50-58.

[3] Xu Shanjia, S.T. Peng, F.K. Schwering, IEEE Trans. on MTT Vol.37, No.4, 1989, pp.686-690.

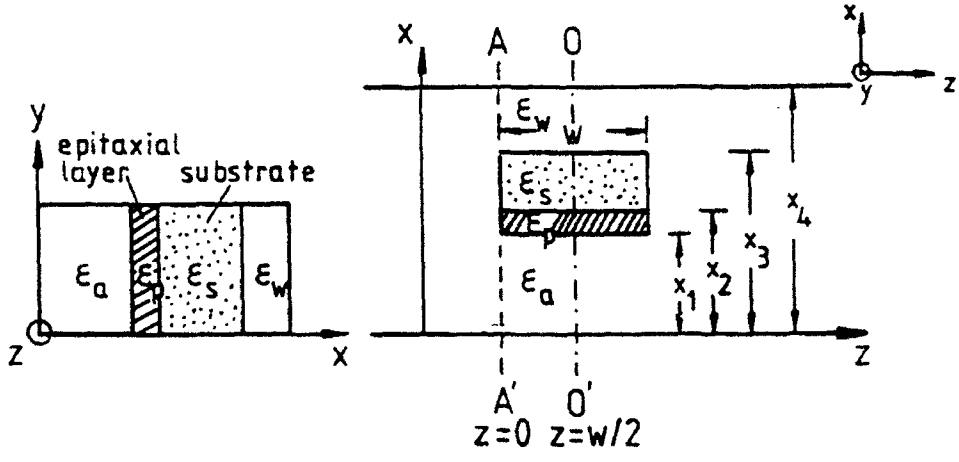

Fig.1 Cross-sections of the structure under consideration.

Table 1. Comparison of the S21 for different samples between the experimental data and the theoretical predictions σ (mhos/cm)

sample	|S21| (dB)		φ21 (degree)	
	test	theory	test	theory
CMT78(σ = 9.0)	-3.25	-3.33	-63.2	-63.75
CMT76(σ = 38.5)	-5.30	-5.19	-56.2	-55.77
Q154 (σ = 67.0)	-8.90	-9.44	-28.2	-27.41
Q114 (σ = 510.0)	-10.65	-10.28	31.7	39.22
Q107 (σ =1107.0)	-10.50	-10.47	36.8	38.74
Q105 (σ =1470.0)	-10.90	-10.32	31.8	38.32

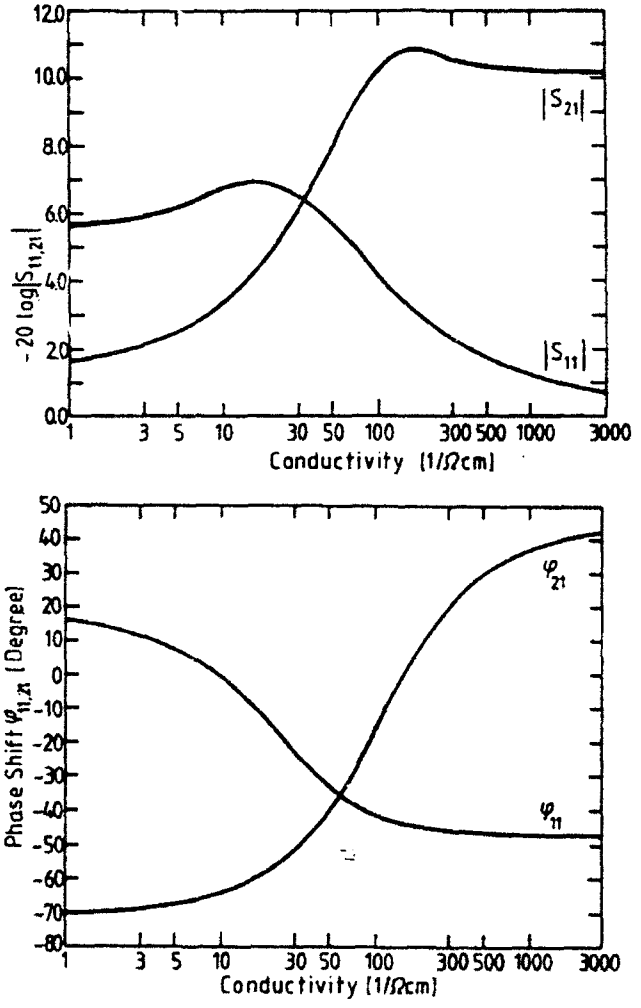

Fig.2 Variations of S21 with epitaxial layer conductivity.
S11

RESEARCH PROGRESS IN GROOVE NRD WAVEGUIDES

Wen-Xun ZHANG, Li-Ling XIAO and Lei ZHU
(State Key Lab. of MMW, Southeast University, Nanjing, CHINA)

ABSTRACT

In this paper, a brief review of the research progress in groove NRD (GNRD) waveguide is given. GNRD structure proposed by the authors is an improved one of NRD waveguide. Up to the present, the dispersion characteristics of GNRD waveguide, the coupling properties of coupled GNRD waveguides with equal or unequal groove sizes, the radiation properties of GNRD leaky-wave antenna and the reflection properties of the step discontinuity in GNRD waveguides have been studied by several methods. Some samples based on GNRD structure were constructed, calculated and tested. Their theoretical and experimental data are agreement with each other, and show an attractive prospect for application.

INTRODUCTION

In the past decade, the NonRadiative Dielectric (NRD) waveguide (Fig.1a) proposed by Yoneyama and Nishida[1] have been studied systematicallyand applied to constructing the passive components and active circuits in millimeter waves. The electromagnetic energy in the cross-section of NRD is concentrated inside and around the dielectric strip without radiation. An alternative structure of the NonRadiative Groove (NRG) waveguide (Fig.1b) had been suggested by Lampariello and Oliner[2]. However, a practical difficulty exists for assembling the NRD with precise location of strip or the NRG with accurate separation of groove plates this geometric deviation will influence sensitively to the performances of directional coupler and leaky-wave antenna.

For overcoming the assembling difficulty, a new structure of Groove NRD (GNRD) was proposed (Fig.1c) by the authors[3], which the gap between two coupled strips and the distance from the strip to leaky aperture can be fixed very precisely. Besides, both the dispersion of transmission or coupling, and the coupling or leaking coefficient are weaker than that of the conventional NRD, since the energy is more concentrated inside the dielectric region filling the grooves. Nevertheless, the GNRD, as like as the NRG, requires rigorous symmetry of the grooves cut on the plate-pair. This is trouble for fabricating an integrated circuit consisted of several GNRD components. Another new structure of Mono-Groove NRD (MGNRD) then was suggested (Fig.1d) by the authors[4], in which only one plate is cut a groove. Both the GNRD and MGNRD have been analyzed, tested and applied to the directional couplers and leaky-wave antennas in the 8mm waveband. By the comparison of major characteristics, the GNRD is better than the NRD; the MGNRD is equivalent to the GNRD, but should be taken much care in design for suppressing the spurious radiative mode due to the nonsymmetry.

ANALYSES

The transverse resonance method (TRM) based on the transverse equivalent circuits

(Fig.2) had been used for analyzing[3,4,5,6,7]:

1. The dispersion characteristic of dominant TM_{11}^z mode in the GNRD and MGNRD waveguides (Fig.3);
2. The dispersion characteristic and coupling coefficient of the coupled GNRD and MGNRD waveguides (Fig.4);
3. The dispersion characteristic and leaking coefficient of hybrid HE_{11}^z mode in the GNRD antenna (Fig.5);

The TRM is a simple and effective method, once the equivalent parameters of the steps of groove for the waveguide, or the odd-/even- mode equivalent parameters for the coupled waveguides, or the coupling between the components of hybrid mode TM_{11}^z and TE_{11}^z and the radiation immittances of these mode components at the leaky aperture for the antenna are formulated individually. But only the coupling of dominant mode between the step-pair of groove is taken into account, which results in a limitation of analysis accuracy to the engineering permission.

An exact full-wave analysis, based on the eigen-weighted boundary integral equation method (EW-BIEM) contributed by the authors too[8,9], have been applied to the GNRD waveguide, a more accurate dispersion curve and the single-mode operation bandwidth (Fig.6) of the GNRD waveguide were given [10,11]. The further application of the EW-BIEM to some distorted GNRD waveguides are just in programming.

In order to extend the bandwidth of directional coupler constructed from the GNRD waveguides, a nonsymmetric design scheme using two GNRD waveguides with different sizes was proposed, and then analyzed by means of hybrid-mode transverse resonance method[12]. The theoretical bandwidth in 8mm band excesses 4GHz (Fig.7).

For analyzing and designing a good transducer from NRD to GNRD structures, the step discontinuity met in this transducer, or served as an element of GNRD filter, should be studied and calculated. This three dimensional problem have been programming based on a combination of resonator principle with mode-matching method; it will be published later.

EXPERIMENTS

For the purpose of checking the analytical results and promoting the practical application, various experimental samples in the 8mm waveband were designed, fabricated and tested. The following characteristics and performances had been tested:

1. The dispersion curves $\beta(f)$ of GNRD and MGNRD waveguides with different groove sizes, the tested data are in good agreement with the analytical results;
2. The dispersion curves $\beta(f)$ and coupling coefficient $C(f)$ of GNRD and MGNRD directional couplers constructed from two parallel or oppositely arched waveguides, slightly narrow bandwidth of the directional couplers (Fig.8) due to the discontinuities of the junctions in waveguides;
3. The dispersion curves $\beta(f)$ of GNRD antennas, and their radiation patterns in the E-plane, a little deviation of beam direction of the antennas exists (Fig.9) due to the mismatch of termination.

CONCLUSIONS

Summarizing the results of theoretical and experimental studies, some conclusions are obvious and valuable:

1. The single-mode operation bandwidth of GNRD guide is broader than that of NRD about 6%;
2. The leaking coefficient of GNRD antenna is obviously less than that of NRD, which is of benefit to increase the aperture efficiency and to enlarge the geometric length of aperture, and finally to improve the radiation pattern; but decreases the antenna efficiency for a relatively shorter aperture with a absorbing load;
3. The weaker dispersion of GNRD antenna corresponds to a weaker sensitivity and less range of frequency-scanning;
4. The difference between odd-/even- mode phase constants of GNRD coupler is less than that of NRD coupler, so a smaller gap between the coupled strips is permissible, which can result in a strong coupling. But the coupling coefficient of GNRD is weaker and its frequency response is relatively flater than that of NRD with the same gap;
5. A constructed from two nonsymmetrical GNRD waveguides directional coupler may obviously improve the flatness of coupling.

ACKNOWLEDGMENT

This article is supported by the National Science Foundation of China.

REFERENCES

1. Yoneyama,T. & Nishida,S.(1981) IEEE Trans. MTT-29,1182-1192
2. Oliner,A.A. & Lampariello,P.(1982) Electron. Lett.,18, 1105-1106
3. Zhang,Wen-Xun & Zhu,Lei (1987) Electron. Lett.,23, 1191-1192
4. Xiao,Li-Ling; Zhu,Lei & Zhang,Wen-Xun (1989) Int.J. of Infrared and MMW, 10, 361-370
5. Zhu,Lei & Zhang,Wen-Xun (1989) J. of Southeast University (English Edition) 5-1,9-14
6. Xiao,Li-Ling; Zhu,Lei & Zhang,Wen-Xun (1988) Proc. of 2nd APMC (Beijing) 146-147
7. Xiao,Li-Ling; Zhu,Lei & Zhang,Wen-Xun (1989) J. of Microwaves (in Chinese) No.1, 1-7
8. Zhang,Wen-Xun (1988) IEEE AP-S Int.Symp. (Syracuse) 229-302
9. Zhu,Lei & Zhang,Wen-Xun (1988) IEEE AP-S Int.Symp.(Syracuse) 589-592
10. Zhu,Lei & Zhang,Wen-Xun (1989) Int.J. of Infrared and MMW, 10, 371-379
11. Zhang,Wen-Xun & Zhu,Lei (1989/1990) Proc. of the first ICMMFT (Beijing)
12. Xiao,Li-Ling & Zhang,Wen-Xun (1991) Digest of Int.Conf. on Infrared & MMW (Lausanne)

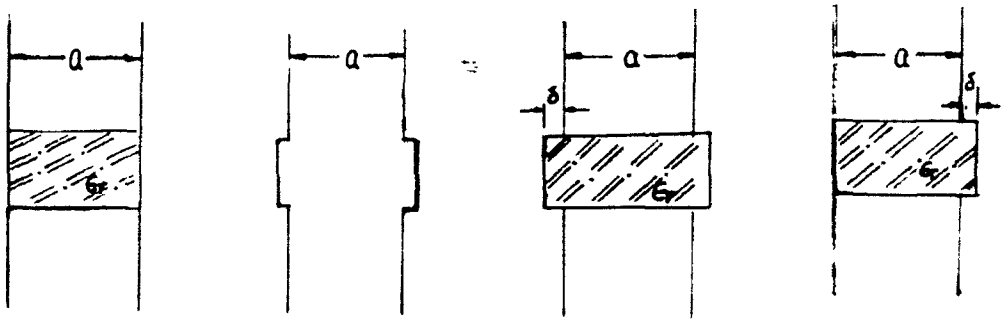

(a) NRD (b) NGD (c) GNRD (d) MGNRD

Fig.1 Cross-sections of several nonradiative open waveguides ($a < \lambda_0/2$)

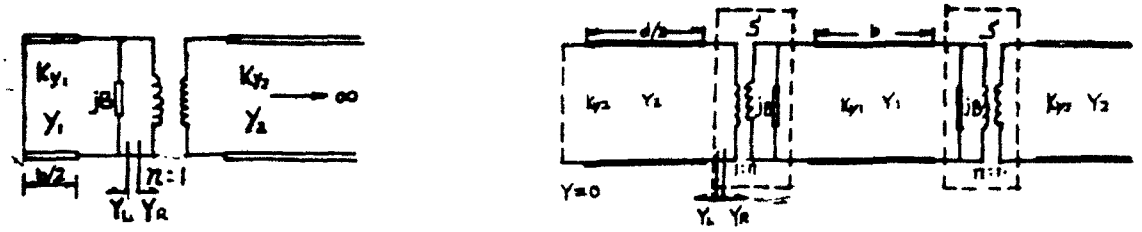

(a) GNRD waveguide

(b) Coupled GNRD waveguides

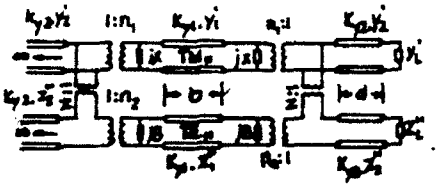

(c) GNRD leaky-wave antenna

Fig.2 Equivalent circuits of GNRD structures for transverse resonance method

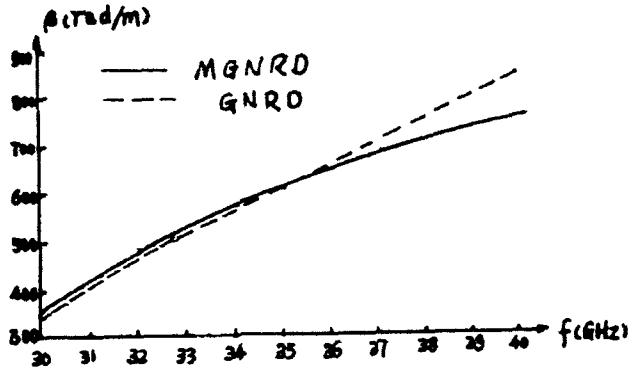

Fig.3 Dispersion characteristics of dominant mode in GNRD and MGNRD waveguides
($a_1 = 4.8mm, a_2 = 3.8mm, b = 8.56mm, \varepsilon_r = 2.05$)

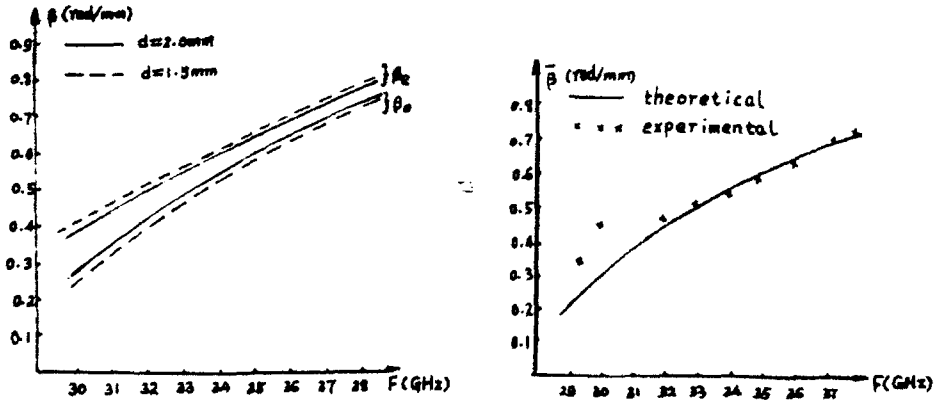

Fig.4 Dispersion characteristics and coupling coefficient of the coupled parallel GNRD waveguides
($a_1 = 4.8mm, a_2 = 3.8mm, b = 8.56mm, d = 1.5mm, \varepsilon_r = 2.05$)

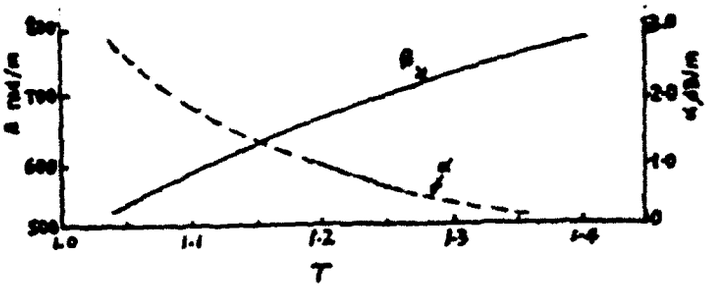

Fig.5 Phase- and leaking- coefficient of dominant mode in GNRD guide
($s_1 = 4.8mm, s_2 = 3.8mm, b = 3.56mm, d = 1.9mm, \varepsilon_r = 2.05$)

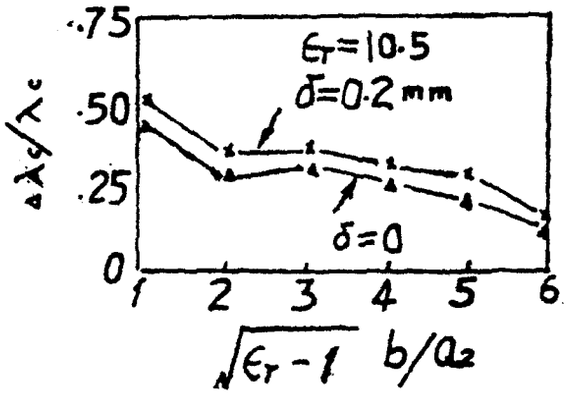

Fig.6 Single-mode operation bandwidth of GNRD waveguide
($s_1 = 4.8mm, s_2 = 3.8mm, b = 3.56mm, \varepsilon_r = 2.05$)

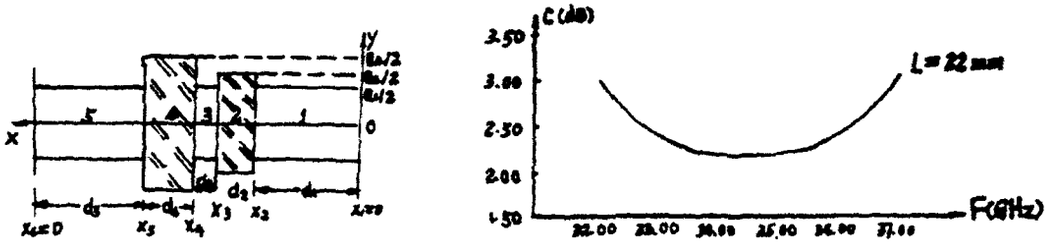

Fig.7 Coupling curve of the unsymmetric GNRD coupler
($s_1 = s_3 = s_5 = 3.8mm, s_2 = 4.6mm, s_4 = 5.0mm$,
$d_2 = d_4 = 3.56mm, d_3 = 1.0mm, \varepsilon_r = 2.05$)

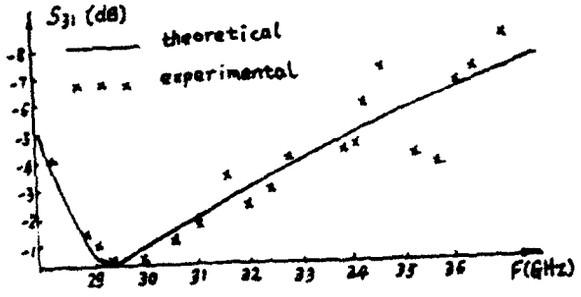

Fig.8 Coupling curve of GNRD directional coupler
($s_1 = 4.8mm, s_2 = 3.8mm, b = 3.56mm$,
$d_3 = 1.2mm, R = 40mm, \varepsilon_r = 2.05$)

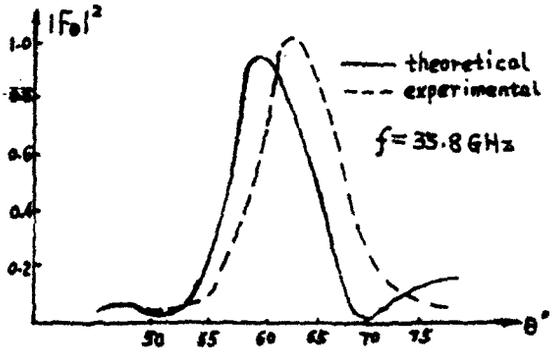

Fig.9 Radiation pattern of GNRD leaky-wave antenna
($s_1 = 4.8mm, s_2 = 3.8mm, b = 3.56mm, d = 1.9mm$,
$L = 120mm, \varepsilon_r = 2.05$)

A Millimeter-Wave Broadside Gap-Coupled Suspended Substrate Stripline Bandpass Filter

Yit-Chyun Chiang, Ching-Kuang Tzuang and Shyang Su
Institute of Communication Engineering
Microelectronic and Information Science Research Center
National Chiao Tung University
No. 1001, Ta Hsueh Road, Hsinchu, Taiwan, R. O. C.

Abstract

Design of the millimeter-wave broadside gap-coupled suspended substrate stripline (SSS) bandpass filter is presented. The filter consists of the broadside gap-coupled half-wavelength SSS resonators arranged in a non-colinear fashion. Such arrangement makes the filter more flexible to interface with other millimeter-wave circuits in a communication system. A Ka-band compressed-length seven -resonator bandpass filter is presented as an example to demonstrate the design concept. The measured characteristics of this compressed-length filter show about 1.4 dB insertion loss and greater than 10 dB return loss in the passband.

I. Introduction

Increasing progress in millimeter-wave system for communication, radar and radiometry has created the need for compact size, low-cost, high-performance filter utilizing quasi-planar printed-circuit components [1,2,3]. Fin-line and suspended substrate stripline (SSS) are the commonly used quasi-planar components for the millimeter-wave filters [1] because of their low attenuation and low dispersion in the frequency of interest. The SSS is less dispersive and can provide a stronger coupling between the resonators by using the broadside-coupling striplines than the fin-line [4], so that the SSS is more suitable than the fin-line for realizing a millimeter-wave broadband filter design.

Recently, a 19-25 GHz broadside-end-coupled SSS filter [5] is proposed for obtaining approximately 30% fractional bandwidth. The physical layout and cross-sectional view of such

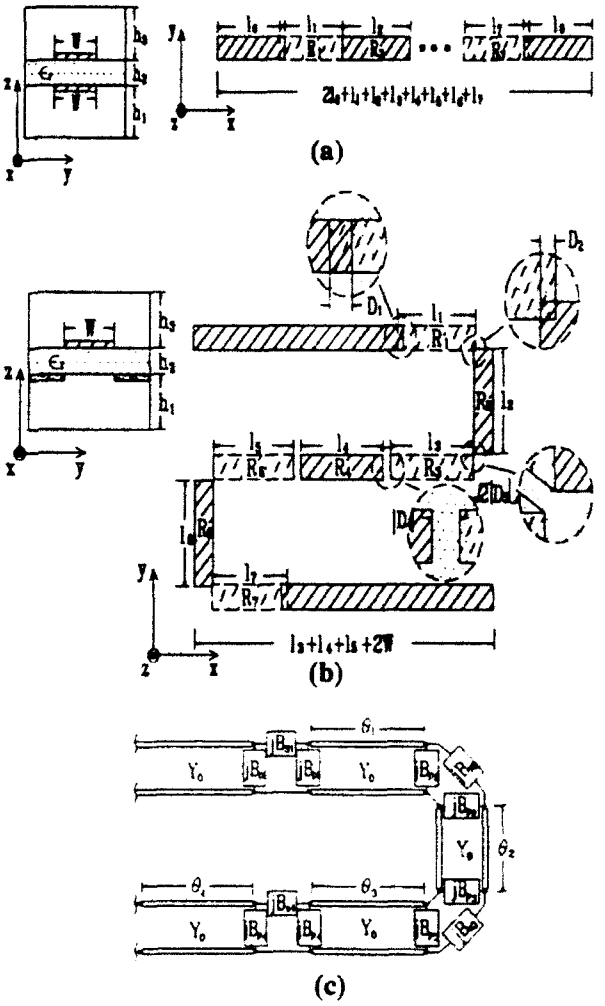

Fig. 1 (a) Physical layout and cross-sectional view of a broadside-end-coupled bandpass filter printed on a suspended substrate, Note that the resonators located at $z=h_1$ and $z=h_1+h_2$ are plotted by dashed lines and solid lines, respectively. (b) Physical layout and cross-sectional view of a compressed-length broadside-gap-coupled bandpass filter printed on both side of a suspended substrate. (c) Equivalent circuit representation of resonators R_1, R_2, R_3 and R_4 in Fig. 1 (b).

filter are shown in Fig. 1 (a). The resonators are located at both sides of the suspended substrate and arranged in a colinear configuration. In this paper, we will present a different layout techniques using the concept of the broadside gap coupling of the adjacent resonators arranged in a non-colinear fashion and demonstrate its use at the millimeter-wave frequencies. The new filter configuration makes the filter more flexible to interface with other millimeter-wave circuit in a communication system or subsystem. For example, a compressed-length construction scheme of such filter results in a reduced length of $(l_3+l_4+l_5+2W)$ between the input and output ports shown in Fig. 1 (b), which is only approximately one-third of $(2l_0+l_1+\cdots+l_7)$ for the colinear broadside-end-coupled filter shown in Fig. 1 (a). However the filter is also complicated in shape. Thus an accurate theoretic design is required to avoid the difficult task of physical fine tuning. In Section II, a discontinuity parameters de-embedding procedure based on the three-dimensional spectral-domain-approach (SDA) method is used to determine the equivalent circuit of the discontinuities associated with the filter. Once the parameters of the equivalent circuit of discontinuities are determined, the conventional filter synthesis technique [6] is invoked to determine the physical layout of the filter. The physical realization of the compressed-length filter and comparison between the theoretic and measured filter responses will be shown in Section III.

II. Description of the Ka-band compressed-length seven-resonator broadside-gap-coupled bandpass filter prototype.

A. The new filter configuration

Fig. 1 (b) shows the physical layout and the cross-sectional view of a compressed-length broadside-gap-coupled bandpass filter employing both colinear and 90°-bent broadside-gap-coupled resonators. The corresponding seven resonators are designated by R_1, R_2,---, and R_7. The resonators represented by solid and dashed lines are located at $z=h_1+h_2$ and $z=h_1$, respectively. The input SSS and resonator R_1 are placed in a colinear broadside-end-coupled configuration. Resonators R_1 (R_2) and R_2 (R_3) are arranged in a 90°-bent broadside-gap-coupled fashion. Resonators R_3 (R_4) and R_4 (R_5) are also realized by the colinear broadside gap-coupled resonators. Since the filter is a symmetrical design, resonators R_5, R_6, R_7 and the output SSS are placed in a manner same as that of the resonators R_3, R_2, R_1 and input SSS.

The equivalent circuit representation of R_1, R_2, R_3 and R_4 is shown in Fig. 1 (c). The B_{si} and B_{pi}, for i=1, 2, 3, 4, are the series and parallel susceptances of the equivalent π-circuit, which are associated with the discontinuities between resonator R_{i-1} and R_i.

B. De-embedding of the discontinuity parameters

The discontinuity parameters illustrated in Fig. 1(c) are obtained by the variational technique based on the three-dimensional quasi-TEM SDA [5]. The unknown charge distributions on the resonator are expanded by a set of two-dimensional SDA basis functions reported in [7]. The values of B_{si}/ω and B_{pi}/ω against the overlapping distance D_i of the adjacent resonators are plotted in Fig. 2 (a) and (b), respectively. The discontinuity parameters associated with the colinear broadside-end coupled and the 90°-bent broadside-gap coupled structures are represented by solid lines and dotted lines in Fig. 2, respectively. When D_i is positive, the adjacent resonators are overlapped each other as shown in Fig. 1(b). Where the overlapping region of the 90°-bent broadside-gap-coupled is assumed to be square in shape with D_i^2 in size. When D_i is negative, there is no overlapping region defined. Instead the adjacent resonators are separated each other, the shortest distance of the two resonators projected in x-y plane is $|D_i|$ and $\sqrt{2}\,|D_i|$ for the colinear and 90°-bent broadside-gap-coupled structures, respectively. The other structural parameters associated with the discontinuities are also given in Fig. 2. Although the value of B_{si}/ω and B_{pi}/ω of the broadside-gap-coupled resonators are obtained based on quasi-TEM approximation, it will be shown in the experimental result that they are insensitive to frequency variations for the given dimensions of

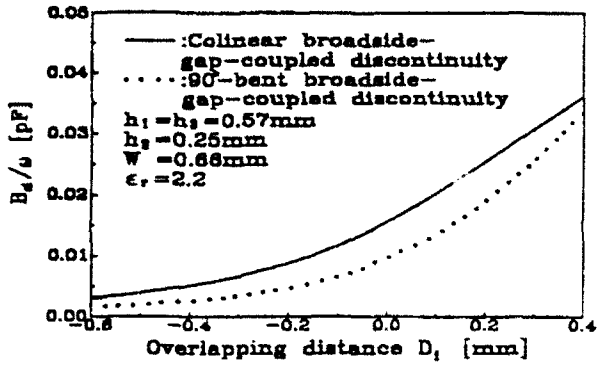

(a)

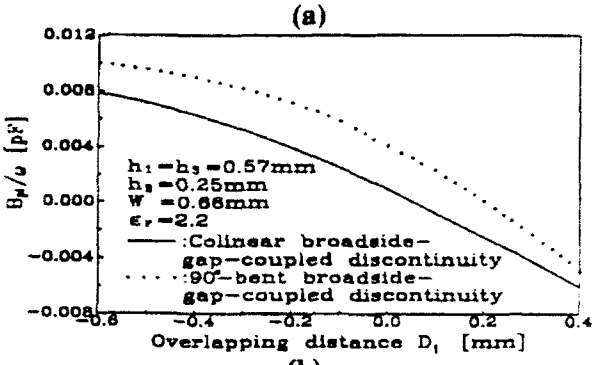

(b)

Fig. 2 (a) Series susceptances (B_s/ω) of the colinear and 90°-bent broadside-gap-coupled discontinuities as functions of the overlapping distance D_1. (b) Parallel susceptances (B_p/ω) of the colinear and 90°-bent broadside-gap-coupled discontinuities versus the overlapping distance D_1.

the broadside gap-coupled discontinuities and the midband frequency of the filter.

III. Measured and Theoretic Results

To verify the design concept, a 32-to-38 GHz compressed-length broadside-gap-coupled bandpass filter is built and tested. The photograph of the prototype is shown in Fig. 3. This prototype is printed on a 10 mils RT/5880 Duroid substrate with dielectric constant of 2.2. The structural parameters associated with filter are also given in Fig.3. Note that the prototype is fabricated without any adjustment or physical fine tuning. The well-known SSS to rectangular waveguide transitions [2] are adopted to integrate the filter with waveguide input and output.

The measured and theoretic filter responses are superimposed in Fig. 4. The theoretic filter responses are obtained by providing Touchstone™ microwave circuit simulator with

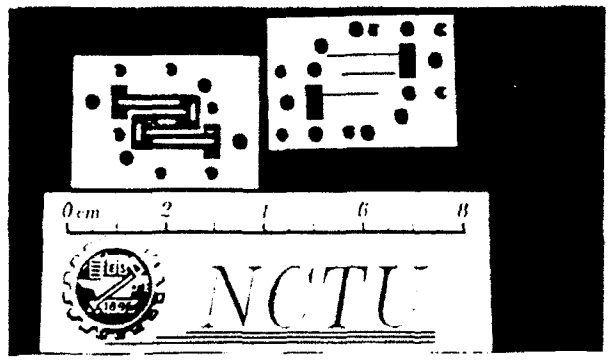

Fig. 3 Photograph of a 32-38 GHz compressed-length broadside gap-coupled bandpass filter prototype. Structural parameters associated with the prototype circuit are $h_1=h_3=0.57$mm, $h_2=0.254$mm, $\epsilon_r=2.2$, W=0.66mm, $l_1=l_7=3.03$mm, $l_2=l_6=3.17$mm, $l_3=l_5=3.21$mm, $l_4=3.23$mm, $D_1=D_8=0.27$mm, $D_2=D_7=0.06$mm, $D_3=D_6=-0.02$mm, $D_4=D_5=-0.22$mm.

the discontinuity parameters of Fig.2. the physical length of the resonators and the propagation and attenuation constants of the SSS with considering the conductor loss [7]. The theoretic filter characteristics are represented by dotted lines. The measured filter characteristics including the effect of the SSS to waveguide transitions are plotted by solid lines in Fig. 4. Due to a small shift between the front and back side circuit pattern, the first transmission zero of the filter is shifted from 32.0 GHz to 31.3 GHz and the prototype suffers approximately 5 dB ripple between 31.3 and 32.2 GHz. Nevertheless, the measured results are very close to the theoretic predictions and show about 1.4 dB insertion loss

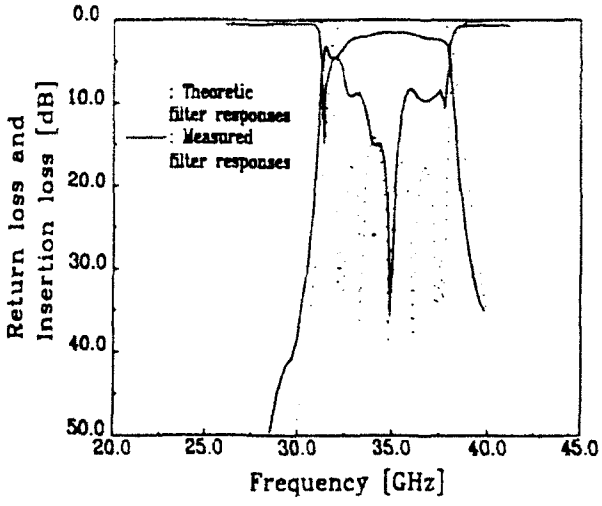

Fig.4 Theoretic characteristics and measured performance of the compressed-length bandpass filter shown in Fig. 3.

and greater than 10 dB return loss between 32.2 GHz and 38.0 GHz.

IV. Conclusions

A new technique for constructing the millimeter-wave bandpass filter based on the concept of colinear or non-colinear broadside-gap-coupling of the adjacent resonators is presented. The measured performances of a 32-38 GHz compressed-length seven-resonator bandpass filter prototype are close to the theoretic filter responses. This experimental result also indicates the validity of the quasi-TEM analysis of the broadside-gap-coupled discontinuities even for very high frequencies. The described design procedure with the aid of the rigorous field theoretic analysis is very suitable for millimeter-wave and microwave integrated circuit process.

Acknowledgement

This work was supported by the National Science Council, R. O. C., under Grand NSC81-0404-E009-119.

References

[1] R. Vahldieck," Quasi-planer filters for millimeter-wave applications," *IEEE Microwave Theory and Techniques*, Vol. MTT-37, No. 2, Feb. 1989, pp. 324-334.

[2] C. Nguyen and K. Chang," Design and performance of millimeter-wave end-coupled bandpass filters," *International Journal of Infrared and millimeter-wave*, Vol. 6, No. 7, 1985, pp. 497-509.

[3] T. N. Ton, Y. C. Shih and L. Q. Bui,"18-30 GHz broadband bandpass harmonic reject filter," *1987 IEEE MTT-S International Microwave Symposium Digest*, Session J-37, pp. 387-389.

[4] T. Itoh," Overview of quasi-planar transmission lines," *IEEE Microwave Theory and Techniques*, Vol. MTT-37, No. 2, Feb. 1989, pp. 324-334.

[5] C.-K. C. Tzuang, Y. C. Chiang and S. Su, " Design of a quasi-planar broadside end-coupled bandpass filter," *1990 IEEE MTT-S International Microwave Symposium Digest*, Session I-37, pp. 407-410.

[6] Matthaei, Young and Jones, *Microwave Filter, Impedance-Matching Networks and Coupling Structure*, New York: McGraw-Hill, 1964.

[7] Y.-C. Chiang, C.-K. C. Tzuang and S. Su, "Design of three-dimensional gap-coupled suspended substrate stripline bandpass filter," to appear on *IEE Proceedings, part H*.

Th5.1

Contemporary Millimeter Wave Radar

Stephen L. Johnston

International Radar Directory
4015 Devon Street
Huntsville, Alabama 35802
USA

Summary

This paper extends a previous ICMWFT'90 paper thru reviews of recent developments in millimeter wave radar as reflected in newly published papers on both millimeter wave surveys and millimeter wave radar applications. It is hoped this paper has chronicled progress in the developing millimeter wave radar art. Initially the very great progress was fueled by rapid advances in millimeter wave technology. Now new millimeter wave applications are being investigated and previously developed applications continue to be refined.

Introduction

For over fifteen years this author has periodically presented surveys of millimeter wave radar. A paper presented at the first International Conference on Millimeter Wave and Far-Infrared Technology (ICMWFT'90) [1] addressed many topics including millimeter wave radar frequencies, why millimeter wave radar, possible millimeter wave radar applications, and discussion of recent; i.e, up to 1989 civilian and military K_a-Band and millimeter wave radars. Its accompanying bibliography of over 100 entries presented copious references including earlier millimeter wave radar survey papers and books. In the interest of brevity new readers are encouraged to consult that reference for background information on these topics. The bibliography presented here is much shorter than that of the ICMWFT'90 paper since page limitations for this Digest generally constrain this paper to the period of 1989-1991 except in special cases. In the space available the references cited will only briefly mentioned. More extensive treatment of the references, together with further references will be given in the conference presentation. In compliance with the new definition of millimeter wave radar in the revision of IEEE STD 686, "IEEE Standard Radar Definitions" which indicates that MMW radars operate at frequencies of 30-300 GHz (wavelengths of 10-1 mm respectively), separate delineation of K_a-Band radars will not be made in this paper.

Although this paper will address millimeter wave radar systems many millimeter wave survey papers discuss both millimeter wave technology; e.g., RF sources, detectors, etc, and other millimeter wave applications, especially communications. The British authored paper by Oliver [2], the U.S. authored paper by Wiltse [4], and the Australian authored paper by Fourkis [5] are general millimeter wave survey papers while the paper by Klien [3] considered only millimeter wave radar. The three cited general millimeter wave survey papers by authors from three different countries present interesting contrasts. The radar papers cited herein will be discussed in two groups, civilian applications and military applications.

Contemporary Civilian Millimeter Wave Radar Applications

Most of the contemporary civilian millimeter wave radar activity closely follows that reported previously [1]. Detlefsen [6] discussed application of millimeter wave radar for short range civilian applications in an excellent paper presented at CICR-91 in Beijing last year. All his applications involved use of homodyne principles. Since those civilian applications are for short range systems, the resulting equipments will be very small in size. Very likely quite significant numbers of such equipments are to be anticipated. Even so, such substantial production is unlikely to have a significant impact on general millimeter wave component manufacture. Currently, automobile braking seems to be dormant in the United States.

Helicopter borne wire avoidance millimeter wave radars previously reported seem to have a mixed situation. In Beijing last year an individual from the developer of the French Romeo radar informally indicated that this W-Band radar is about thru with evaluation and should enter production shortly. In contrast, the widely described German V-Band 60 GHz wire avoidance radar has received very little publicity in the technical press recently.

Millimeter wave meteorological radars continue to be used as one-of-a-kind research tools. Survey of these special radars was presented at another conference [7]. Mead [8] reported observations of clouds and fog with a 1.4 mm MMW radar. In other civilian applications, Hadcock and Ulbay [9] described a 140 GHz scatterometer system and presented measurements of terrain. Sekine et al [10] reported observations of ground clutter with a millimeter wave radar. Hayashi et al [11] studied recognition of a vessel's shape by millimeter wave radar presumably for civilian applications. Interestingly, the paper abstract does not indicate the technique which was used for target recognition other than that a millimeter wave radar was used to observe echoes from a car carrier ship and those received from clutter. Apparently work was not done to evaluate the concept on other vessels such as tankers, freighters, etc. Military sponsored millimeter wave target recognition work will be discussed in a subsequent section of this paper. The paper by Ni Yanghua presented at CICR-91 [12] described a millimeter wave sensor at K_a-Band for airborne remote sensing.

The ICMWFT'90 paper [1] described a space borne millimeter wave debris tracking radar. Further papers by the same group have been published on their concept. In the land based civilian space area, the previously reported JPL proposed interplanetary K_a-Band gyroklystron transmitter is now joined by a study of the application of a free electron laser land based bistatic radar for imaging of a satellite in geosynchronous orbit [13]. A satellite in low earth orbit would contain the radar receiver. The receiver satellite would be tracked by an auxiliary ground based system which would also handle relay of the satellite receiver signal.

Contemporary Military Millimeter Wave Radars

Knowledge of both target radar cross section and clutter characteristics are of paramount importance in the design of military radars at any operating frequency. Extensive work on these two topics were reported in the ICMWFT'90 paper. Lawner et al [14] described a coherent FM-CW millimeter wave radar system for radar cross section measurements. Bledger et al [15] described FLASHLIGHT, a three dimensional millimeter wave imaging radar for radar cross section measurements. Robertson et al [16] described a K_a-Band instrumentation radar with a one foot resolution at NATRAD-1991. Millimeter wave tracking radars are frequently used to obtain radar cross section and clutter measurements under dynamic conditions as well as for use in millimeter wave systems.

Li Jiliang and Xie Zhang [17] described a dual band experimental radar in a new Chinese technical journal. Although dual band millimeter wave tracking radars have existed for many years, e.g., the U.S. NRL TRAKX and the Hollandse Signaalapparatan FLYCATCHER military radar [1], the Chinese radar is novel in that it operates in K_u- and K_a-Bands in contrast to the usual X and K_a band combination. Although K_u-Band is fairly close to X-Band, the latter is more established and has better performance than the former frequency. Other combinations such as X/W (i.e. 95 GHz) MMW/IR and MMW/EO have been explored as dual band millimeter wave systems. Grevins et al [18] described a millimeter wave monopulse radar for target tracking with a new antenna concept. Oderland et al [19] described the EAGLE K_a-Band tracking radar at RADAR-90. It is proposed to accomplish non cooperative target recognition (NCTR) with the high resolution mode of this radar. Archdale [20] proposed use of a millimeter wave pod mounted airborne radar operating at W-Band as a target acquisition system (TAS). It uses an Extended Interaction Amplifier (EIA) to achieve a peak power output of 1.1 kW with a duty cycle of 0.004 and a saturated gain of 45 dB.

In other contemporary military applications of millimeter wave radar, Guang Jin Zhang et al [21] at this conference describe application of millimeter wave radar for trajectory measurement of guns. This will be recognized as use of millimeter wave radar as a research

tool rather than in a military system. Here a small solid state radar is used for both interior ballistics measurements; i.e., within the gun. Measurements were made with balls in the 5.8 mm rifle, 7.62 mm sub-machine gun, and 14.5 mm antiaircraft artillery. Resulting Doppler waveforms were stored for subsequent comparison with theoretical computations. Exterior trajectory measurements were also made with a 4.5 mm gas gun, 7.62 mm rifle, and 14.5 mm antiaircraft artillery. According to measured data the ratio of radar active distance to projectile ball diameter exceeded a ratio of 9000. Unfortunately that paper has no references.

Stonier [22] proposed application of millimeter waves to the detection of Stealth aircraft, but did not present analysis to support his proposal. Clearly, further study of this concept is required. Most of the paper addressed structures and materials aspects in consonance with the author's principal field of experience. Millimeter wave radars are also being considered for several military systems; e.g., Maverick and Longbow [4,23] as examples of the MMIC (Millimeter wave Monolithic Integrated Circuit) insertion program.

As indicated above dual band/dual mode millimeter wave sensors with IR have been extensively described previously [1]. Benzer et al [24] presented their recent work on a 6 inch common aperture W-Band radar and a passive 3 to 5 um IR imager. Intended application is an air to ground missile system. The paper has extensive technical details including test results of a functional breadboard system. In a similar activity Prutzer et al [25] described a high resolution airborne multisensor system. It is an aircraft based system consisting of forward-looking and downward-looking sensor suites. Sensor suites which were evaluated include CO_2 and near IR laser radars, long wave passive IR systems extending to 12 um, and an 85.5 GHz millimeter wave radar. This is a test bed for data collection. Extensive technical data and test results were presented. It should be noted that the millimeter wave frequency used was not allocated by WARC-79 for millimeter wave radar systems [1].

In looking at all the contemporary millimeter wave radars reported herein there is an inverse relation between the extent of the work reported and the radar frequency used; viz, there is very extensive work at K_a-Band, extensive work at W-Band, a little at 140 GHz, and only one paper at 225 GHz. The paper by McMillan et al [26] described an experimental 225 GHz pulsed coherent radar. Its intended application is backscattering measurements from surfaces and materials at this frequency. This work has been reported previously [1], but it is still noteworthy since its use of optics techniques for the polarizer (beam splitter), antenna lens, and mirror scanner illustrate the transition from conventional microwave techniques to optics as the submillimeter wave region is approached. Extensive technical details of the equipment are given in the paper. It is recognized that the specific frequency used was determined by the availability of the transmitter Extended Interaction Oscillator (EIO) available, but it should be noted that this frequency was not allocated by WARC-79 for radar system application. Frequency regions of 231-235 and 238-241 GHz were allocated for SECONDARY radar use while 241-248 GHz was allocated for PRIMARY radar application.

The last contemporary millimeter wave radar topic to be discussed stems from the paper by Jin Xuan Gong at this conference [27]. The topic of millimeter wave ECM (Electronic Countermeasures) (more correctly EW; i.e., Electronic Warfare) is actually a natural progression from EW at microwave frequencies. Millimeter wave frequencies are a powerful ECCM against millimeter wave ECM. As Jin points out, ECM can be used against millimeter wave radars. Millimeter wave radar ECCM was mentioned in the ICMWFT'90 paper cited above but it only briefly mentioned increased immunity of millimeter wave radar to hostile interference with little explanation. This topic was addressed more fully in two papers [28,29] which were not cited in the ICMWFT'90 paper. Thus the Jin paper warrants further study.

Concluding Remarks

As this paper indicates, Millimeter Wave Radar is still a very active field. Although military K_a-Band radars continue to find tactical employment, current monetary constraints probably will not permit production and tactical employment of W-Band missile radars at the present time. Even so, development of such systems is expected to continue.

Bibliography

1. Johnston, S.L., "Modern K_a-Band/Millimeter Wave Radar", Internat Conf on MMW and Far-Infrared Technol" Beijing, June 1990, Conf Dig, IEEE pub cat nr 89TH0257-6, pp.481-92.
2. Olver, A.D., "Millimeterewave Systems- Past, Present, and Future", IEE Proceedings, Vol. 136, Pt. F., No. 1, February 1989, pp. 35-52.
3. Klien, S., "Millimeter Wave Radar Spawns Wide Applications", SIGNAL Magazine, Vol. 44, No. 6, February 1990, pp. 73-76.
4. Wiltse, J.C., "Status of Millimeter Wave Technology and Applications in the U.S.", Proc. 21st European Microwave Conference (EuMc), Sept 1991.
5. Fourkis, N., "Future Directions for Millimeter-Wave Systems", 16th Conf on IR and MMW, Lausanne, Switzerland, Aug 1991, SPIE Vol. 1576, pp. 424-427.
6. Detlefsen, J., "Millimeter Wave Radar Sensors for Short Range Applications to Industrial and Vehicular Traffic Environments Using the Homodyne Principle", Proc China International Conference on Radar (CICR-91) Beijing 1991, pp. 103-106.
7. Johnston, S.L., "Millimeter Wave Meteorological Radars", Conf.Digest, 15th Int. Conf on IR and MMW, 10-14 Dec. 1990, Orlando, Florida. SPIE Vol. 1514, pp. 638-640.
8 Mead, J. B., "Observations of Clouds and Fog with a 1.4 mm Wavelength Radar", Proc. ICARSS 89, Vol. 2, July 1989, pp. 521-523.
9. Hadcock, T.F., and Ulbay, F.T., "140-GHz Scatterometer System and Measurements of Terrain", IEEE Geosci and Remote Sensing Trans. Vol. 28, No. 4, July 1990, pp. 492-99.
10. Sekine, M., et al, "Observations of Ground Clutter using a Millimeter Wave Radar", Trans. Inst of Electr Inform, and Comm Engrs (Japan) Vol. E73, Feb 1990, pp. 250-254.
11. Hayashi, S, et al, "Recognition of Vessel's Shape by Means of a Millimeter Wave Radar", Jnl of Japan Institute of Navigation, Vol. 84, March 1991, pp. 131-138.
12. Ni Yanghua, "A Millimeter-Wave Radar Sensor for Airborne Remote Sensing System",Proc China International Conference on Radar (CICR-91) Beijing 1991, pp. 123-125.
13. Bruder, J.A. & Belcher, M.L., "Radar Applications of Gigawatt Sources at Millimeter Wave Frequencies", 16th Conf on IR & MMW,Lausanne, Aug 1991, SPIE 1576, pp. 432-3
14. Lawner, R.T. et al, "Coherent FM-CW Millimeter-Wave Radar Systems for Radar Cross Section Measurements", IEEE MTT Trans Vol. 39 No. 1, Feb 1990, pp. 208-211.
15. Bledger, D.J., et al, "Flashlight Radar: A Three-Dimensional Imaging Radar", MIT Lincoln Lab Report TT-74 (ESD-TR-89-167), August 1989.
16. Robertson, R.S., et al, "A K_a-Band Instrumentation Radar with One Foot Resolution", Proc 1991 IEEE National Radar Conf, Los Angeles, California, March 1991, pp. 1-5.
17. Li Jiliang & Xie Zhanao, (Beijing Inst. of Radio Meas.), "A K_u and K_a Dual Band Experimental Radar", Chinese J of Syst Engrg and Eletr, Vol.2, No. 2, July 1991, pp. 124-8.
18. Grevins et al, Millimeter Wave Monopulse Radar for Target Search and Tracking with a New Kind of Antenna Concept", Proc. 7th Radar Sym, Duesseldorf, Oct.1989, pp. 17-32.
19. Oderland, I et al, "EAGLE, A High Accuracy 35 GHz Tracking Radar", Proc. International Radar Conference (RADAR 90), Washington, DC May, 1990, pp. 461-466.
20. Archdale, A., "Millimetre Wave Radar Target Acquisition System", IEEE MTT International Symp, 1990, Vol 2, pp. 969-972.
21. Guang Jin Zhang et al, Application of Millimeter-Wave Radar in the Trajectory Measurement of Guns", this conference.
22. Stonier, R.A., "Stealth Aircraft & Technology from World War II to the Gulf-Part II: Applications and Design", SAMPE Jnl, Vol. 27, No. 5, September/October 1991, pp. 9-18.
23. Coker, N.W., Wedel, M.J., "Millimeter Wave Maverick Demonstration Program Overview", Proceedings AIAA Conference, Monterey, California, November 1990.
24. Benzer, et al, "Infrared/Millimeter Wave Common-Aperture Optics", Optical Engineering January 1989, Vol. 28, No. 1, pp. 14-19.
25. Prutzer, S., et al, "A High Resolution Airborne Multisensor System", SPIE Vol 1480, "Sensors and System Integration", 1991, pp. 46-61.
26. McMillian, R.W., et al, "An Experimental 225 GHz Pulsed Coherent Radar', IEEE MTT Trans. Vol. 39, No. 3, March 1991, pp. 555-562.
27. Jin Xuan Gong, "Millimeter Wave ECM—a New Field of Electronic Combat", this conf.
28. Johnston, S.L., "mm-Wave Radar: The New ECM/ECCM Frontier", Microwave Journal, Vol. 27, No. 5, May 1984, pp. 41-48.
29. Johnston, S.L., "MM Wave Radar Challenges and Benefits EW Applications", Microwave System News and Communications Technology, Vol 16, No.. 6, June 1986, pp. 95ff.

W BAND COMMUNICATION SYSTEM AND ELECTRICAL WAVE PROPAGATION MEASUREMENT SYSTEM

Shuyi Dong, Donggou Zhang, YiYan, LiminQiao
(Xidian University, Xi'an, China)*

ABSTRACT

In this paper, the communication system and electrical wave propagation measurement system have been researched and made at W band using direct-modulation method, which has some dirstinctive advantage, simple circuit, low cost and high reliability.It is the communication system compatible with electrical wave propagation measurement system.The measurement date are sampled by automated sampler, as measurements of propagation attenuation and cross-polarization.

INTRODUCTION

Millimeter wave communication systems involve the transfer of information between a source and a user, Modulation method has been used direct-modulation and intermediate frequency modulation by means of the mm-wave transfer of information. Usually the latter is used, but it is a complex circuit and high cost. The former is a simple circuit, but it need to solve problem of direct modulating low resistnce about mm-wave Gunn oscillator.In this pepar, the mm-wave direct-modulator of frequency has been researched and made.The W band communication system using direct frequency modulation is kind of simple circuit, low cost and high reliability.The system is compatible with electrical wave propagation measurement system.To turn modulation signal off, the intermediate frequency signal turn on field intensity indicator. The data are sampled by automated sampler, as measurements of atmospheric propagation attenuation and cross-polarization.Data are processed by microcomputer. Using curve fitting method, we can inquire into mathematical mode of molecule absorb, atmospheric curl and water coagulum versus near millimeter wave propagation to use as the design of propagation road.

BLOCK DIAGRAM OF W BAND COMMUNICATION SYSTEM AND PROPAGATION MEASUREMENT SYSTEM

Figure 1 shows the block diagram of the W band communication system and electrical wave propagation measruement system.

Main characteristics of the communication system:

(1) Work frequency band: 91-94 GHz, (2) Transmission power: > 10 mw.(3) Receiver noise figure: < 12 dB, (4) Modulating frequency departure: < 10 MHz, (5) First IF: 1-1.4 GHz,

* The project is aided financially by national natural science fund.

Second IF: 70 MHz.(6) IF band width: > 30 MHz.(7) Polarization type duplex isolation: 25dB. (8) Minimum power of receiver: < −70 dBw.(9) Video band width: > 10 MHz.(10) Magnitude–frequency characteristics of video: for 50Hz–5.5MHz, < .75dB.(11) Transmission information: duplex transmission one color TV signal & one audio (or one duty telephone), or 960 route duplex telephoneor, or 32 route duplex digital communication. (12) Audio sub–carrier: 6.5MHz(FM).

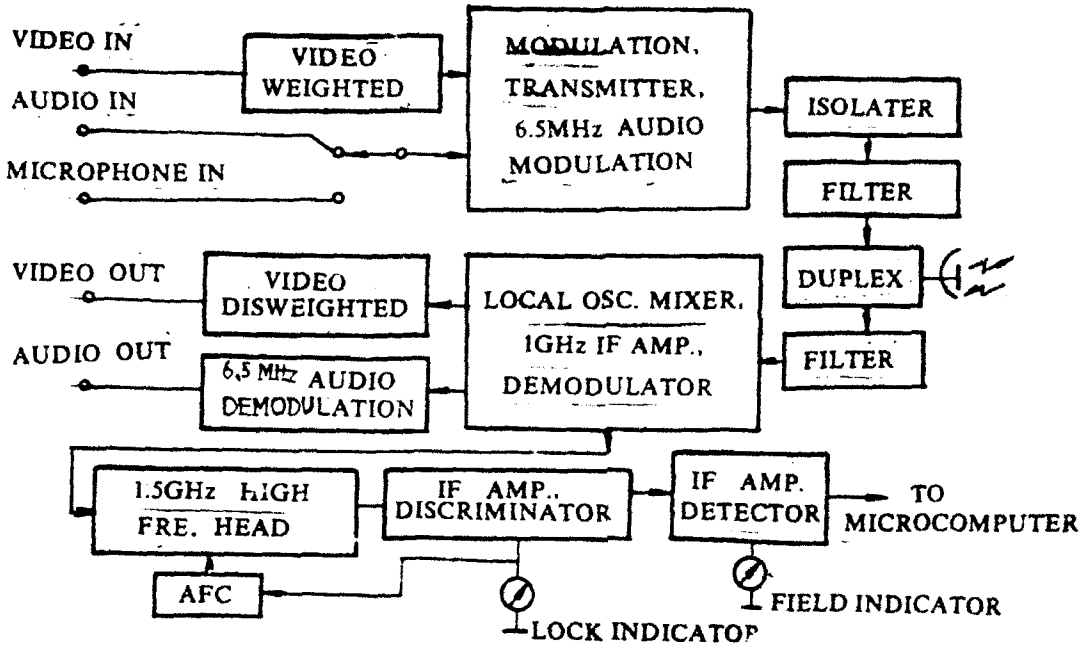

Fig.1 Block diagram of W band communication system and electrical wave measurement system

THE DIRECT–MODULATION OF GUNN OSCILLATOR AT W WAVE BAND

The direct–modulation of Gunn oscillator at w wave band(FM) shows as figure 2.

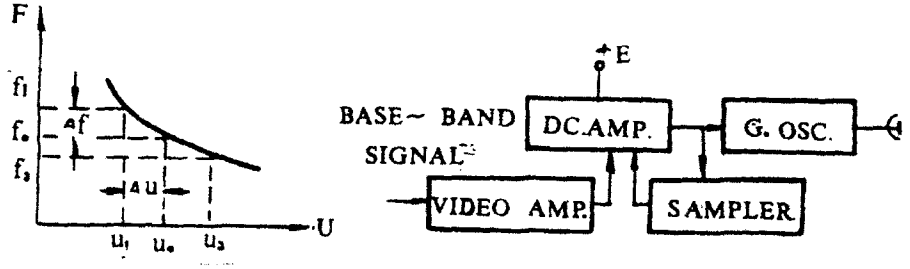

(*a*) MODULATION CHARACTERISTICS (*b*) WIDTH BAND DIRECT–FMAT W BAND OF GUNN OSCILLATOR

Fig.2 Modulation characteristics of Gunn oscillator.

DC. resistance of Gunn oscillator is about 0.5–2 Ohm, dynamic resistance is about 10–15 Ohm only, voltage is 4–5V, electric current is about 1 A. It is very hard to overcome the low resistance effect by means of convention modultaing method, because of the resistance of Gunn diode

shorted. After studying, the efective modulating was achieved.
Base-band singal can be one color TV signal plus one audio modulating frequency sub-carrier signal 6.5 MHz, or 960 / 300 route carrier telephone signals or 32 route PCM digital telephone signals. It is proved practically that the frequency modulator can work the whole millimeter wave band.Modulation band width is greater than 15 MHz and magnitude frequency characteristics less than 0.75 dB.

DISTINGUISHING FEATURE OF TESTING RECEIVER

Figure 3 shows block diagram of the testing receiver at w band.To overcome the frequency drift automatical frequency control is set up in the testing receiver. Electrical wave propagation attenuation precision is less than 1 dB. The dynamical extent of the precision attenuator is about 70 dB. The resolving power is 1 dB.The input signal of the testing receiver is from the mixer of w band receive end.Input signal frequency is 1-1.5 GHz.The local oscillator follows the tuning range 950-1450 MHz.The outputs of the field intensity are transmited into the data sampler and microcomputer.The output level of the testing receiver is in the range of TTL level to satisfy the needs of the computer.

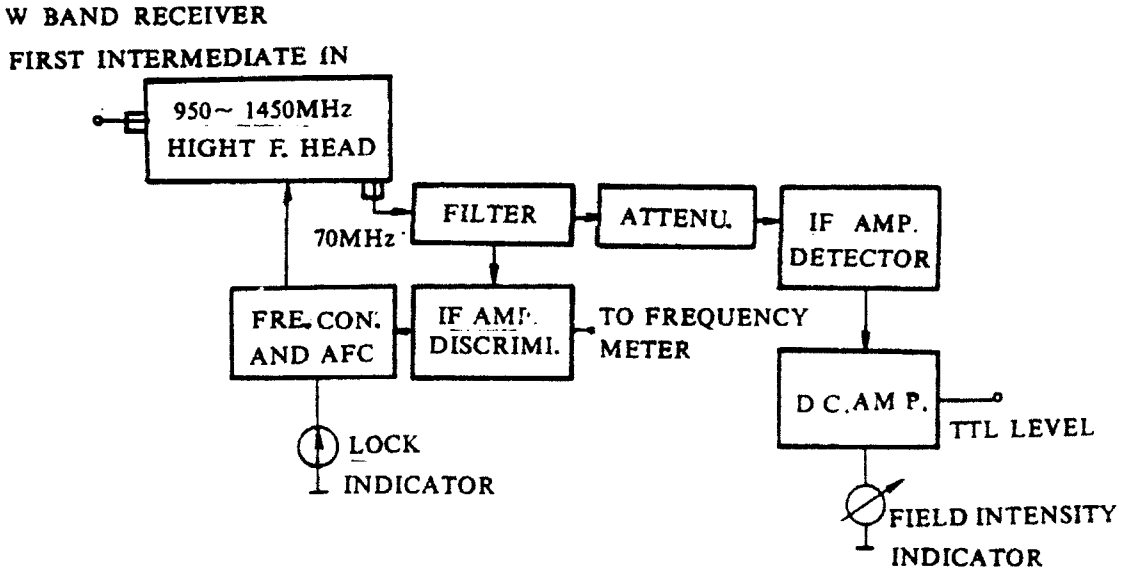

Fig.3 Block diagram of the testing receiver.

The technique index of the testing receiver as follows: (1) Frequence range: 950~ 1450 MHz.(2) Receiver sensitivity: 0.1mv. (3) Noise figure: 4dB. (4) IF: 70 MHz.(5) Dynamical range of the attenuator: 0~70dB. (6) Microcomputer interfacing level is TTL level.

MEASUREMENT OF THE CROSS-POLARIZATION

As measureing the cross-polarization of atmospheric propagation, transmitter is rotated 45 ° to product 45 ° line-polarization wave(see figrue 4).The signals received by receive antenna via the polarization separator are fallen into two route.One route is the horizontal and another is vertical polarization.The two route via the mixer are transmitted into the testing receives, respectively.They are transmitted into the microcomputer to process data sampled.The results of the

cross–polarization effect are Typed.

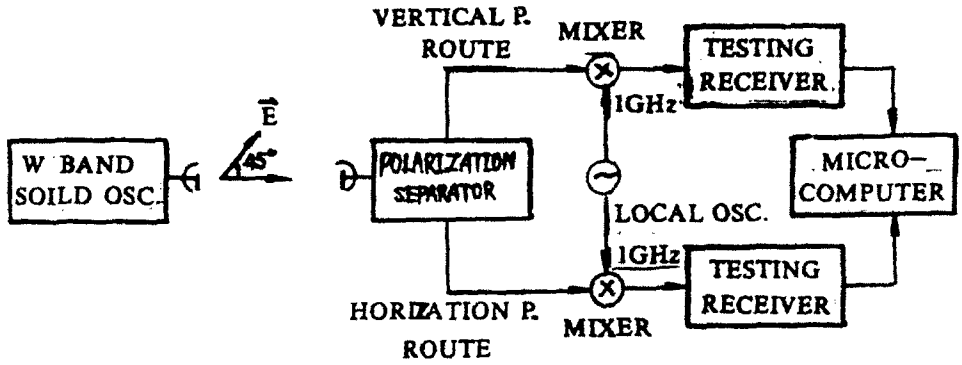

Fig.4 The cross–polarization measuring system.

The output anyone route in receive system can use as measruing atmospheric attenuation and atmosphere glimmer effcet.

CONCLUSION

It is proved practically that the communication system and electrical wave propagation feature measurement system is successful at 91 ~ 94 GHz.In the communication test the duplex information transmission has been realized.The picture of the colour TV is clear and the sound is pleasing to ear.The system are refitted as measurements of dielectric constant, RCS and others.

REFERENCES

1. Shuyi Dong, Donggou Zhang, Limin Qiao, Yi Yan, Electrical Wawe Science Journal (China), 6(1–2)(1991), 17.
2. Shuyi Dong, Yi Yan, Limin Qiao, ibid. 125.

Th5.3

APPLICATIONS OF HIGH-TEMPERATURE SUPERCONDUCTORS IN MILLIMETER-WAVE COMPONENTS

A.R.JHA,TECHNICAL DIRECTOR,JHA TECHNICAL CONSULTING SERVICES,
CERRITOS, CA 90701 (USA)

SUMMARY

This paper describes the unique properties of High-Temperature Superconducting Thin Films (HTSTF) for possible application in microwave integrated circuits. HTSTF can be characterized as Thin Film Microstrip (TFMS) lines operating at superconducting temperatures. Low insertion loss, minimum signal delay, and low power dissipation are possible with HTSTF lines compared to conventional microstrip lines. Note that conductor loss, dielectric loss, signal distortion, signal delay, and instantaneous bandwidth are dependent on the film thickness, superconducting film material, and substrate properties. Preliminary studies indicate that superconducting bulk ceramics are suitable for HTSTF lines. Thin films of Yttrium Barium Copper Oxide (YBCO) with critical temperature (T_c) of 95 K, Bismuth Strontium Calcium Copper Oxide (BSCCO) with T_c of 85 K, and Thallium Calcium Barium Copper Oxide (TCBCO) with T_c of 125 K appears to be most suitable for microwave integrated circuit applications. In addition, appropriate high temperature substrates such as MgO, Sr Tio_3 and ZrO_2 must be evaluated for optimum microwave performance. High-temperature superconducting microwave circuits can operate at liquid nitrogen temperature (77 K), which is about ten times cheaper than liquid helium. For maximum economy the refrigerant operating temperature must be close enough to the critical temperature of the materials mentioned.

Preliminary investigation seems to indicate that microwave performance of the HTSTF lines will be better than conventional gold plated copper strips if the cryogenic temperature is maintained below 40 K. However, ordinary gold plated copper microstrip loss performance appears to be better than YBCO films at 77 K above 10 GHz (Figure 1). There is a possibility to reduce the insertion loss using multiple layers of HTSTF films, but at the expense of higher cost and complexity. Regardless of the existing problems or shortcomings, implementation of HTSTF lines into microwave integrated circuits and printed circuit antennas will be found most cost-effective at microwave frequencies. Cryogenic operation will considerably reduce the insertion loss @ mm-wave frequencies (Table 1).

Preliminary calculations reveal that the insertion loss of the YBCO film of suitable thickness on the high temperature, high dielectric substrate of MgO (e_r = 10) is about 35% lower at 20 GHz compared to gold plated microstrip lines operating below 40 K temperature. Superconducting films require high dielectric substrates such as MgO, Sr Tio_3, or Zro_2 to satisfy the required microwave performance level. Two factors must be considered in selecting a suitable substrate for HTSTF lines:

a) The crystal structure of the substrate must permit formation of high quality of HTSTF films at higher sputtering temperatures necessary for higher critical temperatures.

b) The dielectric constant and loss tangent must be low enough so that the dielectric losses do not exceed the conductor losses.

Regardless of the circuit application, one must investigate the dispersion effects, conductor and dielectric losses for films and microstrips (Figure 2), and potential substrates for optimum microwave performance.

It is important to mention that the conductor loss is the most dominating performance parameter, which is proportional to the RF surface resistance R_s (Table 2). Computed values of RF surface resistance for various superconducting materials as a function of operating frequency and cryogenic temperature are shown in Figure 1. High-temperature superconducting material physics indicate that the intergranular coupling and the anisotropic property of the ceramic superconducting films can increase the conductor loss, particularly at millimeter-wave frequencies where anomalous skin resistance is more dominant. Published data indicates that the anomalous skin resistance (R_s) is greater than normal skin resistance by 1% @ 1 GHz, by 6% @ 10 GHz, and by 10% @ 20 GHz. This means that superconductor surface impedance parameter, rather than RF skin resistance (R_s), must be considered @ mm-wave frequencies to predict RF performance level with optimum accuracy.

HTSTF lines have potential applications in electronic components, microwave filters, delay lines, mm-wave printed circuit microstrip antennas, monolithic low-noise amplifiers, mm-wave phase shifters, and digital/analog signal processing integrated circuits. Implementation of HTSTF technology in microwave systems yields minimum insertion loss, ultra-fast switching capability, higher sensitivity, higher current density, lower power dissipation, higher reliability, excellent MMIC compatibility, and lower equipment cost and complexity. Computed data (Figure 1) indicates that at present YBCO lines have lower insertion losses than those for copper microstrip lines @ 77 K, but only at frequencies below 4 GHz. More research and development activities need to be undertaken in terms of equilibrium thermodynamics, kinetics, film growth temperature, oxygen pressure and surface smoothness to produce quality HTSTF films with lower insertion losses @ mm-wave frequencies. The dream of room-temperature superconductivity is now within accessible reach with rare-earth superconducting materials, if the film reproducibility and thermal stability issues are satisfactorily resolved.

TABLE 1

PROJECTED RF PERFORMANCE DATA FOR A HIGH TEMPERATURE SUPERCONDUCTING CERAMIC COMPOUND YBCA-FILM DEPOSITED ON MgO SUBSTRATE (er = 10)

T (k)	Resitivity (ohm-cm)	20 GHz Rs(ohms)	20 GHz L(dB/cm)	44 GHz Rs(ohms)	44 GHz L(dB/cm)	60 GHz Rs(ohms)	60 GHz L(dB/cm)
77	4.59×10^{-4}	0.060	1.06	0.085	1.57	0.104	1.84
65	1.63×10^{-4}	0.036	0.63	0.052	0.93	0.062	1.09
60	0.96×10^{-4}	0.028	0.52	0.042	0.77	0.048	0.90
40	0.90×10^{-4}	0.026	0.51	0.041	0.74	0.046	0.88

PARAMETERS ASSUMED:

Zo	=	50 ohms, h = 0.004"
q	=	dielectric filling factor (0.833)
e_r	=	relative dielectric constant (10)
e_{eff}	=	effective dielectric constant (8.5)
Tan δ	=	Loss Tangent (0.005 assumed)
Ld	=	0.26 db/cm (Tanδ = .005) @ 20 GHz
	=	0.52 dB/cm (Tanδ = .010) @ 20 GHz

TABLE 2

PERFORMANCE COMPARISON BETWEEN THE STANDARD MICROSTRIP LINES AND THIN FILM MICROSTRIP (TFMS) TRANSMISSION LINES

FREQUENCY (GHz)	SKIN DEPTH δ (MICRO INCHES)	SURFACE RESISTANCE RS (OHMS) STANDARD MICROSTRIP	SURFACE RESISTANCE RS (OHMS) THIN FILM MICROSTRIP (TFMS)	MICRO-STRIP WIDTH, W (INCHES)	CONDUCTOR LOSS LC (dB/cm) STANDARD MICROSTRIP	CONDUCTOR LOSS LC (dB/cm) TFMS
10	26.0	0.0260	0.0330	0.0147	0.121	0.154
20	18.4	0.0370	0.0420	0.0148	0.172	0.195
35	13.9	0.0490	0.0520	0.0148	0.226	0.240
44	12.4	0.0530	0.0550	0.0149	0.224	0.253
60	9.8	0.0640	0.0650	0.0149	0.294	0.298
70	9.1	0.0690	0.0700	0.0150	0.315	0.320
95	8.4	0.0810	0.0818	0.0150	0.355	0.359
143	6.9	0.0988	0.0990	0.0165	0.450	0.411
REMARKS:	CURRENT DENSITY IS ABOUT 37% @ SKIN DEPTH					

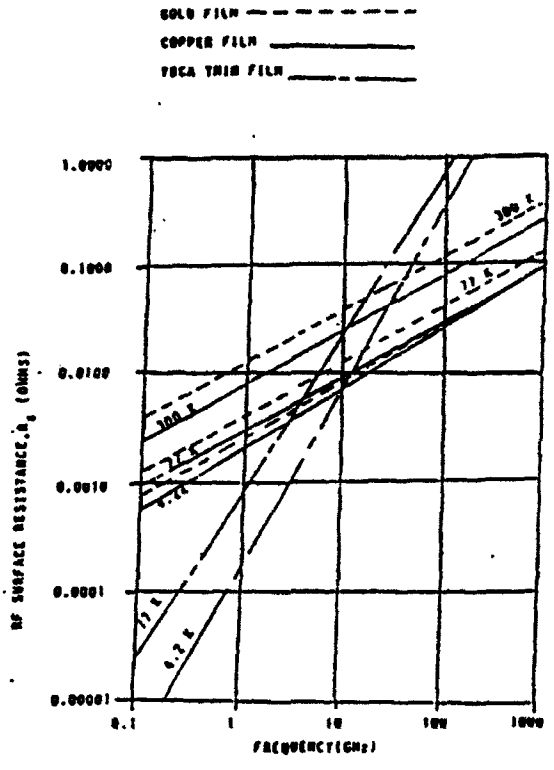

FIGURE 1. SURFACE RESISTANCE FOR VARIOUS SUPERCONDUCTING FILMS AS A FUNCTION OF TEMPERATURE AND FREQUENCY

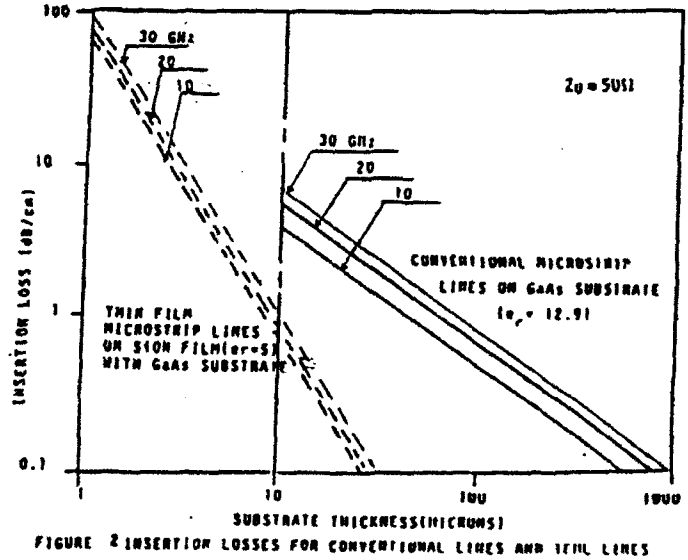

FIGURE 2 INSERTION LOSSES FOR CONVENTIONAL LINES AND THIN LINES AS A FUNCTION OF FREQUENCY AND SUBSTRATE THICKNESS

STUDY OF DUAL-BAND AND DUAL-POLARIZATION MMW ANTENNA FEEDING SYSTEM

Deng Ciping, Lu Xin, Li Zhen
Beijing Institute of Technology, P.O. Box 327,
Beijing 100081, China

ABSTRACT

The dual-band and dual-polarization (D&D) MMW antenna feeding system (AFS) presented in this paper is composed of a branching unit, in which dual-band signals are separated and isolated, and a dielectric-guide dual-reflector antenna formed by linking the dielectric filled in the branching unit and sub-reflector. This kind of AFS has a single-reflector and a common feed, so the configuration is simple and firm, meanwhile good electric properties are maintained.

Up till now, this kind of D&D MMW AFS has been used in some experimental facilities of dual-band MMW system such as radiometer, communication system, active and passive detector and so on, and the various developments are achieved.

INTRODUCTION

Compared with single-band MMW systems, dual-band MMW systems have some advantages such as antijamming and so on. In general, the AFS in dual-band is composed of a single-reflector and double feeds, but interference between the two feeds is one of the key problem to improve the system property.We have solved this problem perfectly by using a dielectric-guide dual-reflector antenna, and a branching unit in which dual-band signals are separated and isolated by means of both the high-pass property of wave-guide and the orthogonality f wave-guide modes. The antenna is formed by linking the dielectric filled in the branching unit and the sub-reflector.This kind of AFS has a single-reflector and one common feed in dual-band, so not only the configuration is simple and firm, but also the sub-reflector is fabricated to taper reflector under certain condition. Therefore the fabrication is very easy meanwhile good electric properties are maintained.

The D&D MMW AFS is used in some experimental facilities of dual-band MMW system, and the various developments are achieved. The results obtained indicate that the development of D&D MMW AFS is successful.

THEORY AND DESIGN OF D&D MMW BRANCHING UNIT

The structual drawing of D&D MMW branching unit is illustriated in Fig.1, in which the region I bounded by AA′, DD′ and EE′ is a HT-junction of wave-

guide, the region Ⅰ, DD′ and BB′, is a tapered wave-guide section, and the region Ⅱ, EE′ and CC′, is a high-reduced wave-guide with two tapered wave-guide sections. A full-high dielectric piece is symmetrically located in the wave-guide. It is convenient to link to external devices.

Both the orthogonality and the cut-off characteristic of waveguide modes are used to isolate 8mm- and 4mm-wave each other. In general, the dominant modes of 4mm- and 8mm-wave are LSM mode to the broad wall of the wave-guide and TE_{10} mode,respectively. Thus it can be seen that the electric fields of 8mm- and 4mm-wave are orthogonal in the dielectric piece, and that 8mm-wave is cut off in the region Ⅰ and 4mm-wave cut off in the region Ⅱ when b″ is less than $\lambda/2$, where λ is the wavelength of 4mm-wave in free space. So that, 8mm- and 4mm-wave are seperated with high isolation.

The impedance matching, which is very important, is performed respectively and independently in each band. For 4mm-wave it is relying upon the tapered dielectric which may not affect the transmission of 8mm-wave. For 8mm-wave, matching is done by means of a metal film located in region R on the dielectric piece, as shown in Fig.1.

THEORY AND DESIGN OF DIELECTRIC-GUIDE DUAL-REFLECTOR MMW ANTENNA

Extensing the dielectric filled in the branching unit to connect the sub-reflector,the sub-reflector can be monited by dielectric-guide instead of supportting frames. As a result, not only the configuration is compact and firm, but also the leakage and blockage are reduced and the efficiency is improved and the sidelobe level is decreased. But in this case,the variation of the optical path from the feed to the antenna aperture must be corrected. The method is by altering the shape of sub-reflector to compensate the phase difference on the main-reflector. Fig.2 illustrates the geometrical relations of electromegnetic rays in the dielectric-guide dual-reflector antenna. Considering the configuration symmetry, only half of the practical antenna is plotted in Fig.2, where F is the focal length of the main reflector, B half of the maximum dimension of the feed, L the distance between feed and apex of the main-reflector, here assuming that the distance between equivalent phase center of feed and apex of the main-reflector is L as well.

According to geometrical optics principle, it is not difficult to derive the formulation of the corrected sub-reflector.In general,the shapes of sub-reflector corrected are some complex curved surface. But in some cases,the variations of the sub-reflector diameter, d, and the dielectric constant, ε_r, not only cause angularity variation of the sub-reflector shape, but also cause the change of bending direction. Therefore the shape of the sub-reflector can be approxmated a taper cone by selecting proper ε_r and d,and the antenna properties are still maintained. Although no blokage is caused by supporting frames in the dielectric guide dual-reflector antenna, there exists blockage of dielectric-guide. In the design,both blockages of sub-reflector and dielectric-guide can get minmum values by selecting proper parameters d and L. Moreover, parameters ε_r, d and L should be considered synthesizly to ensure that antenna achieves good properties in dual-band.

It can be seen that the shape of the dielectric inserted in the feed may be selected properly to match and coincide the feed well, meanwhile the an-

tenna properties are not affected. So the configuration of AFS is compact, more stability and availibility.

EXPERIMENTAL RESULTS

The photograph of the dual-band (8mm & 4mm) and dual-polarization antenna feeding system is presented in Fig. 3. The experimental results are shown in Fig.4 to Fig.8 and presented in Table.

Although 4mm-band measurements were carried out at some frequencies, the results obtained indicate that the D&D MMW AFS is practicable. In fact, this kind of D&D MMW AFS has been used in some experimental facilities of dual-band MMW system,such as radiometer, communication system, active and passive detector, and so on. Lots of good results obtained indicate that the development of D&D MMW AFS is successful.

ACKNOWLEDGMENT

The authors are very grateful to Mr. Sun Houjun for his help.

REFERENCES

[1] Deng Ciping, Lu Xin, and Cui Yongqing, 'A branching unit of 8mm- and 4mm-band', Proceedings of National Conference on Millimeter Wave and Sub-millimeter Wave, 1988, Beijing, China.

[2] Deng Ciping, Li Zhen, and Lu Xin, 'A new type millimeter wave dual-reflector antenna fabricated easy', Proceedings of National Conference on Antenna, 1987, Nanjing, China.

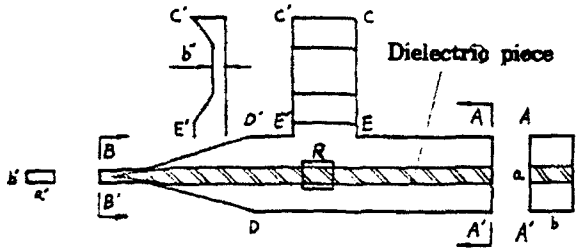

Fig.1 Configuration of the branching unit

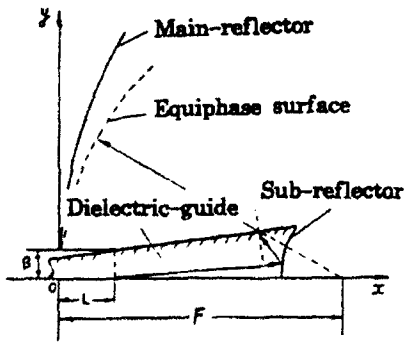

Fig.2 Geometrical relations of EM rays in dielectric-guide dual-reflector antenna

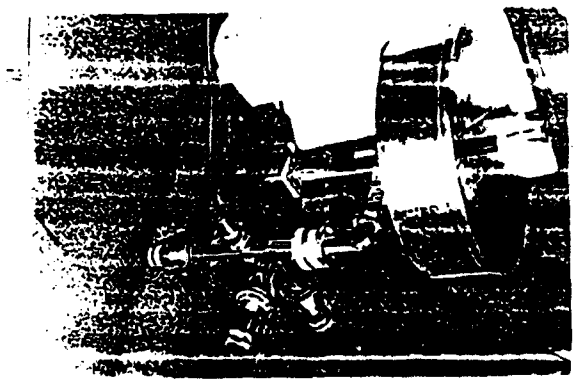

Fig.3 Photograph of dual-band (8mm & 4mm) dual-polarization MMW antenna feeding system

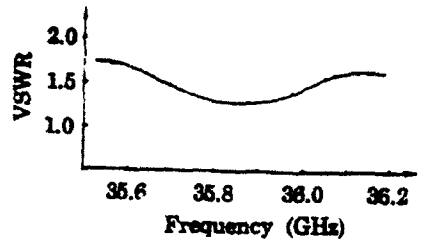

Fig.4 Experimental results of VSWR of the branching unit in 8mm-band

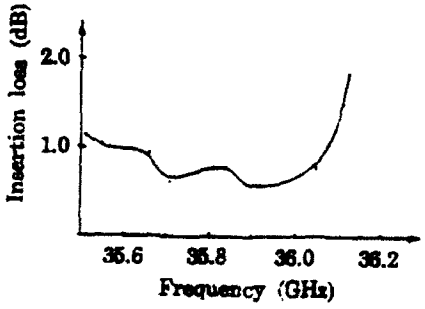

Fig.5 Experimental results of insertion loss of the branching unit in 8mm-band

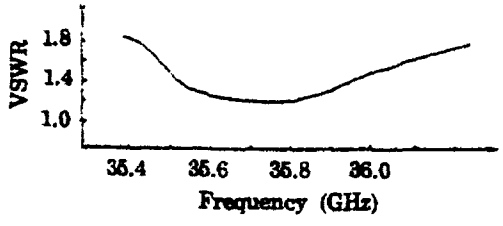

Fig.6 Experimental results of VSWR of the antenna feeding system in 8mm-band

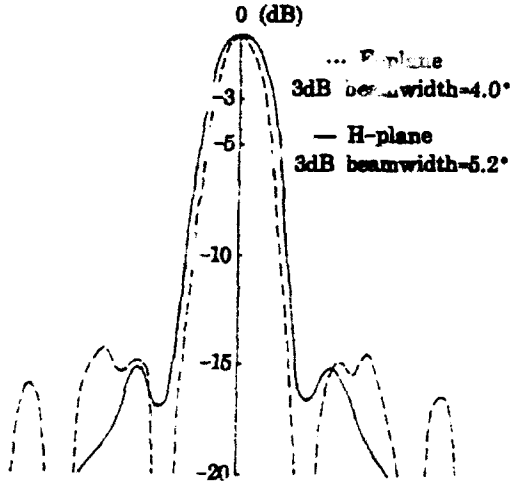

Fig.7 E- and H-plane patterns of the antenna at 35.7GHz

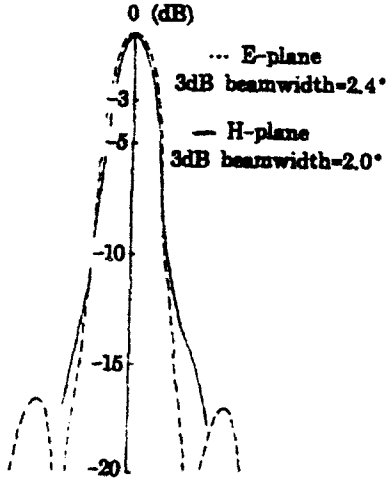

Fig.8 E- and H-plane patterns of the antenna at 72.0GHz

Table Experimental data of the branching unit at 35.9GHz and 74.0GHz

Frequency(GHz)	VSWR	Insertion loss(dB)	Isolation(dB)
35.9	1.20	0.62	25
74.0	1.25	0.70	23

Th5.5

NEW EXCITATION METHOD OF AUSTON SWITCH

Zhang Ling-qing and Wu Ke-qin
Shanghai millimeter- wave & submillimeter- wave Laboratory

ABSTRACT

We have presented a new method of excitation on photoconductive switch which can generate man-control ultrashort electrical pulses. The advantage of this method is that it relaxes the seriously dependence on free carrier lifetime of photoconductor on ultrafast optoelectronic devices.

INTRODUCTION

Since Jayaraman and Lee first observed the picosecond photoconductivity effect in 1972, there have been many application. One of the major applications has been in ultrafast switching which can be done with picoprecision. The switching of voltage pulses(Auston,1975)by using picosecond photoconductivity engendered ultrafast optoelectronics in which picosecond switching has been achieved. Auston switch has a rapid rise, but a long trail owing to the long lifetime of photoconductive material. This conditions has improved when new materials which have short carrier lifetime have developed, such as Cr.GaAs,amorphous silicon,radiation-damaged SOS. With fs laser source and "the sliding contact"excitation, subpicosecond electrical pulse can be obtained. The typical work in this area was done by D.R.Grischkowsky et al. recently shown in figure 1.

The laser source is a compensated colliding pulse, passively mode-locked dye laser producing pulses with 80fs width at a 100MHz repetition rate. The photoconductive material is heavily ion-implanted silicon-on sapphire(SOS) which has the carrier lifetime of a limit of 600fs. The electrical pulse short than 0.6ps on a coplanar transmission line had been obtained using a new method of pulse generation, "the sliding contact". We have generated electrical pulses of ps order as well by using radiation-damaged SOS as photoconductor and a similar microstrip circuit. In addition, Defonzo, Smith et al. using integrated planar antenna technique had generated the sub-picosecond electrical pulse radiation. Regardless of how were the ultrafast electrical pulses transmitted being generated, they all have the same way of excitation, that is, shorting the microstrip gap with one ultrafast optical pulse, as shown in figure 2(a).

The electrical pulse generated on Auston switch is determined by the laser pulse, the carrier lifetime in semiconductor, the capacitance of the switch. Recent work indicated that under some conditions, the effect of the laser pulsewidth and gap capacitance can neglect, as a result, the

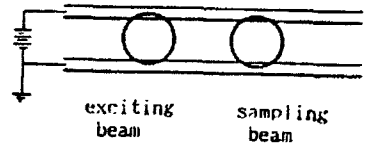

Fig.1 "Double sliding" contact

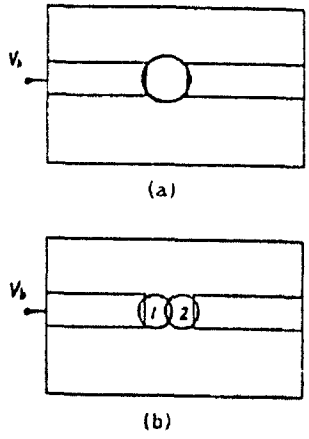

Fig.2 Different way of excitation on Auston switch.
(a)Traditional way of excitation. (b)Two-step excitation.

crucial aspect is the carrier lifetime. As for most fast optoelectronic devices, it is this factor that seriously limits the response speed. Although the carrier lifetime can be reduced to ps order using radiation-damage technology, it can not be short than 0.6ps of the limit lifetime. besides radiation-damage can not presently apply to most photoconductors which have carrier lifetime much larger than 1ps, therefore, it will undoubtly be a new research field in the future of how to break the limit which introduced by the carrier lifetime to response speed. For this reason we have prosed a new method of excitation, expecting to do some fundamental research work in area.

TWO-STEP PHOTOEXCITATION

Figure 2(b) shows the schematic diagram of two-step photoexcitation on a Auston switch. transforming one optical beam excitation to double optical beam excitation which have a relative delay(valid when shorter than carrier lifetime), each cover half of the gap, these are all the two-step photoexcitation meanings(on time and space). With this new method, one can generate electrical pulses with theirs pulsewidth being controled. Its operating principle as follow.

Assuming two optical beams (1) & (2) with a time interval of τ' illuminate on the gap shown in figure 2(b). Although the local photoconductivity of the gap illuminated by beam(1) would increase, the gap will hardly turn on because of only partialy excited. However, the electron-hole plasma induced by the beam(1) will decreases slowly (relative to the speed of plasma generating) as shown in figure 3(a). After a certain time τ', letting the beam(2) illuminate, the local photo-conductivity increases sharply owing to the high speed of plasma generating; As a result the photoconductivity of the whole gap increases sharply, the switch is open at once. While, the recombination of carriers owing to beam(1) is nearly completed, gap photoconductivity then decreases sharply; Hence, the switch turns off generating a transient signal narrow than the carrier lifetime shown in figure 3(b).

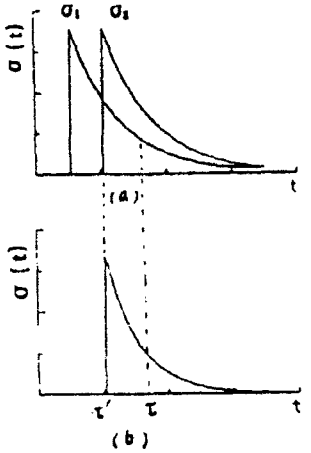

Fig.3 Schematic diagram of two-step excitation.

According to Auston's theory which is extremely general and applies to practically any transmission line configuration, the duration of the generated electrical pulse was given by the convolution of the laser pulse & the carrier lifetime. It is obvious that the photoconductive response can be improved by managing to reduce the carrier lifetime of photoconductor in the gap while the laser pulsewidth fixed.

In fig. 2(b), assuming the illumination is uniform(i.e., neglect dielectric relaxation), beam(1)illuminating at the zero moment, after delaying a certain time τ', letting the beam(2) illuminate, the photoconductivity are $\sigma_1(t)$,$\sigma_2(t)$ respectively. Neglecting retardation effect, and assuming exponential decays of carrier lifetime immediately after generation, then

$$\sigma_1(t) = (n_0 e\mu_n + p_0 e\mu_p)\exp(-\frac{t}{\tau}) \qquad (1)$$

$$\sigma_2(t) = \begin{cases} 0 & t<\tau' \\ (n_0 e\mu_n + p_0 e\mu_p)\exp(-\frac{t-\tau'}{\tau}) & t>\tau' \end{cases} \qquad (2)$$

where n_0, p_0 are the initial carrier densities, τ is carrier lifetime. The photoconductivity of the whole gap is

$$\frac{1}{\sigma(t)}=\frac{1}{\sigma_1(t)}+\frac{1}{\sigma_2(t)} \tag{3}$$

$$\sigma(t)=\frac{\sigma_1(t)\cdot\sigma_2(t)}{\sigma_1(t)+\sigma_2(t)} \tag{4}$$

Substituting Eqs.(1) & (2) into (4),we get

$$\sigma(t)=\begin{cases}0 & t<\tau' \\ (n_0e\mu_n+p_0e\mu_p)\dfrac{e^{-\frac{t-\tau'}{\tau}}}{1+e^{\tau'/\tau}} & t>\tau'\end{cases} \tag{5}$$

The curve of the photoconductivity $\sigma(t)$ is shown in figure 4 which has the same shape as that in figure 3(b).

The photoconductance can then be determined as:

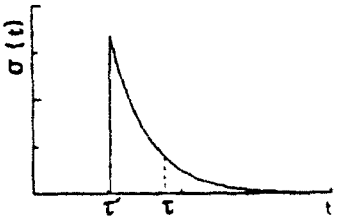

Fig.4 Theoretical(two-step way)

$$g(t)=\begin{cases}0 & t>\tau' \\ \dfrac{1}{V_g^2}\int dx^3\,(n_0e\mu_n+p_0e\mu_p)\dfrac{e^{-\frac{t-\tau'}{\tau}}}{1+e^{\tau'/\tau}}|E|^2 & t>\tau'\end{cases} \tag{6}$$

where V_g is the voltage across the gap, E is the electric field. The photoconductance is reduced by a factor of $(1+e^{\tau'/\tau})$ relative to that of one beam excitation.

Define $(\tau-\tau')$ being the effective lifetime of gap carriers by two-step excitation, expressed as τ_{eff}, we have:

$$\tau_{eff}=\tau-\tau' \tag{7}$$

Apparently, to control τ' is equivalent to control τ_{eff}, that is, the electric pulsewidth can be controlled at one's will. So, it break the limit to photoconductive response speed by the intrinsic carrier lifetime of photoconductive materials.

It should be noted that the fully understanding of the mechanism of the two-step excitation, especially some problems on the applied technology, needs more research work.

CONCLUSION

In summary, we have proposed and explained the principle and the advantages of a new photoexcitation—two-step excitation, and the photoconductance expression of the Auston switch has been evaluated. It is of significance using this method to improve the response ability of optoelectronic devices.

REFERENCS

(1) D.H.Auston,in Picosecond Optoelectronic Devices, edited by C.H.Lee (Academic, London, 1984), pp73-116.
(2) C.H.Lee and V.K.Mathur; IEEE J-QE, Vol.17,No.10,oct.,1981.
(3) Ketchen et al.; Appl.Phys.Lett.,Vol.48,No.12,24March,1986.
(4) F.E.Donay et al.; Appl.Phys.Lett.,50(8),23Feb.,1987.
(5) D.R.Grischkowsky et al.;IEEE J-QE,Vol.24,No.2,221-224,1988.

MILLIMETER WAVE ECM— A NEW FIELD OF ELECTRONIC COMBAT

JinXuan Gong
(Southwest Institute of Electronic Equipment, Chengdu, Sichuan, China)

ABSTRACT

In this paper, the features of mmW electronic countermeasure (ECM) are given. A system architecture of mmW radar ECM is proposed. And the stat-of-art, recent applications status and trends of mmW radar ECM systems abroad are briefly described.

THE FEATURES OF MMW ECM

In fact, the struggle between mmW ECM and ECCM is a struggle of energy. For example, in free space the ranges of ESM receiver and radar can be shown as:

$$P_{rmin} = P_t G_t^2 \lambda^2 \sigma / (4\pi)^3 R_r^4 \qquad \text{(radar)} \qquad (1)$$

$$P_{rmin} = P_t G_t G_j \lambda^2 / (4\pi)^2 R_j^2 \qquad \text{(ECM)} \qquad (2)$$

Illustrated by the equation, the intensity of signal received by the radar is in inverse proportion to R_r^4, while the intensity of signal received by the ESM receiver is in inverse proportion to R_j^2. That is to say, from the point of view of energy, a ESM receiver has certain advantages of range over a radar. Using the similar analysis method can result in a conclusion that, in high atmospheric attention, the radar jammer has certain advantages over a radar, too.
But in actual applications, the radar function is better than that of radar ECM system. The reasons are as follows:
1. MmW radar can use one or more narrow bands, while for mmW ESM receiving and jamming system, if there is no prior information available, it must cover the whole mmW band to intercept the radar targets and jam them.
2. Radar and communication systems may be operate on the same mmW frequency, so ESM receiver must be able to distinguish radar signals from non-radar signals in order to avoid interference from non-radar signals which have various modulations.
3. A mmW radar has short operation range, which shorten reconnaissance/jamming reaction time greatly. The reaction time from interception to jamming should be within only several decades of seconds.
4. Narrow Beam and High Antenna Gain. This forces the ESM receiver and jammer to exploit the same high-gain narrow-beam antenna, which will increase search time, and decrease the probability of radar reconnais-

sance and jamming.
5. A mmW radar has wide absolute bandwidth and may use extra-narrow pulse, so it has excellent ECCM capability and is very difficult to be detected and jammed. Also, the mmW radar has good range resolution, thus effect of chaff jamming is weakened.
6. Recently, conical scan mode is mainly explored in a mmW radar and the main jamming method used is angular deception. But it would be difficult to conduct wide bandwidth angular deception jamming in mmW bands.

SYSTEM ARCHITECTURE OF MMW ECM

In order to obtain relatively perfect ECM capabilities, mmW ECM should be integrated with current microwave and electro-optic ECM to form a comprehensive ECM system architecture, as shown in Fig.1. The EW intelligence sensor unit in Fig.1 is composed of microwave/mmW/optic multi-sensors and multi-sensor intelligence preprocessing subsystems.

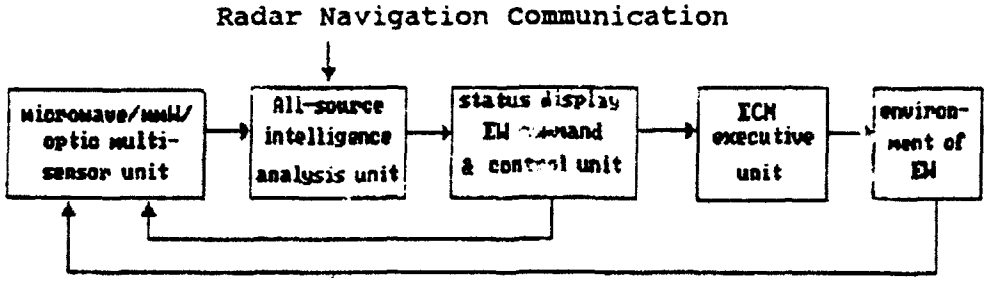

Fig. 1 System Architecture of mmW ECM

It is used to intercept and analyze various signal intelligence, measure various technical parameters and locate targets via passive multi-station location or time-of-arrival difference location. According to the tactical needs, the sensors can be deployed at proper positions and combined into a network in a single platform or multiple platforms. Standard data link interfaces should be used among sensors. All-source intelligence analysis unit fuses the information intercepted by multi-sensors and makes a coherent processing. Supported by the various data bases, it identifies and displays automatically the targets. The unit has standard data-transmission communications interfaces in conjunction with the microwave/mmW radar and communication systems to achieve information sharing.
The EW command and control unit is a command center of coordinated battle. Supported by decision-making bank, it can analyze and compare enemy situation, find the best operational concept, properly distribute various jamming assets, determine jamming frequency, power, direction and time, etc., control the ECM unit to implement its jamming mission and control spatial activities and searching program of the multi-sensor unit. A standard data link interface is used between this unit and the other parts.
The ECM executive unit is composed of microwave/mmW ECM, communication ECM, fuse ECM, optic ECM, ARM attack, etc. Controlled by the EW command and control unit, it can conduct coordinated countermeasure operations, which enable the system carry out effective jamming or ARM

attack against the multiple targets in optimal directions with the most suitable frequency, power, techniques and time.
The system illustrated in Fig.1 is relatively complete, full spectrum ECM system, it has a good versatility, and can be used in a special ECM aircraft, also it can be simplified to operate as a self-protect jamming system of a fighter, bomber, or AWACS aircraft. It can also be expanded to operate as shipboard EW system. In particular, when it is netted with other sensors on various platforms, this integrated ECM system can be used to detect those hardly-found targets such as stealth aircraft, cruise missiles, etc..

STATUS OF MMW ECM SYSTEM

As viewed from the whole developing progress of mmW ECM techniques abroad, mmW ESM system is developed rapidly with the mmW lower-power sources and low-noise devices becoming mature day by day. The types and achieved performances of mmW ESM receivers being developed or equipped are listed in table 1. At present, most of the developing

Table 1 Performances of mmW radar ESM receivers

	frequency (GHz)	sensitivity (dBm)	dynamic range (dB)	instantaneous bandwidth (MHz)	frequency accuracy (MHz)	environment density (10^4pps)
crystal video	2 - 40	-70 - -80	60	multi-octive	/	/
superhet	0.5 - 40	-75 - -100	70	10 - 1000	1 - 10	0.1 - 1
IFM	0.5 - 40	-55 - -70	60	2000 - 10000	0.5 -0.75	2 - 20
channelized	0.5 - 60	-80 - -100	70	multi-octive	1	10 - 50

activities of mmW ESM and warning system are concentrated on 18-40 GHz band, and few on 40-105 GHz bands. Typical systems such as the US MSQ-103A,WJ-1240, 1740 WJ-1925, APR-39A, UK "SUSIE", "Weasel", "KATIE" and Israel EL/L8310 etc. are all extended to 40 GHz. A channelized receiver is now being developed by Litton Industries INC., it operates from 26 to 100 GHz. NATO are now planning to develop a mmW radar warning system, which operates in 40-140 GHz. It is expected that by the year 2000, troops will be equipped with large number of mmW ESM and radar warning receivers.
As viewed from the primary features of mmW, it is even difficult to develop mmW radar jamming systems. To date, mmW jamming systems are being developed actively. For example, a mmW jammer is being developed for ALQ-131 jamming pods and SLQ-32 shipboard ECM system. Integrated EW system (INEWS) will cover microwave/mmW/laser band. US Army, Navy and Air Force are developing 20-95 GHz airborne radar jammers. US DOD is making a plan to develop mmW/microwave beam weapons. A low power beam weapon whose power will be 3 orders of magnitude higher than existing jammer. These beam weapons will be used to destruct stealth targets or jam onboard electronic equipment.

TREND OF MMW ECM TECHNIQUES

As mmW techniques develop, new mmW ECM systems are being developed. The key techniques being studied include:
1. Frequency Spread: Frequency range of radar ESM receiver is being

extended to 75-105 GHz and frequency range of radar jamming system is breaking through 40 GHz and 94 GHz windows.

2. Development of New mmW Solid-state Devices: The emphasis is placed on the development of high electron mobility transistors (HEMT) in 18-94 GHz. For low-noise devices, their gain is 1.7 dB at 36 GHz, 5 dB at 94 GHz, and they have potential gain at frequency up to 200 GHz. When used as power devices, they have output powers of 1 W and 100 mw at 30 GHz and 60 GHz respectively. Therefore it is possible that HEMT will become main mmW solid state devices.

3. Active Development of mmW monolithic IC (MIMIC): In order to actively promote mmW IC development, USA is implementing a MIMIC technique program to develop 1-100 GHz GaAs analog circuit chip for use in EW system. Now a number of MIMIC chips have been developed for use in ALQ-136, -165, INEWS ECM systems and Gen-X and AAED expendable decoy. Many MIMIC devices such as 94 GHz monolithic amplifiers, oscillators, etc. are all under mass production, and they will be used in mmW ECM systems.

4. Applications of Super-conductors in mmW ECM Systems: Recently, the most active development field lies on super-conducter mixers, super-conductor antennas, parametric amplifier, magnetic flux quantum-flow oscillators, Josephson detectors, and super-conductor ICs, etc. These devices provide low noise temperature and extrabroad band capabilities, so they are considered as a hopeful mmW, sub-mmW low noise and power devices. It is expected that use of super-conductor low-noise monolithic receivers can largely increased detection range and resolution of ESM/ELINT receivers, so they are especially suitable to extra-broad band ELINT reconnaissance and space surveillance. Multi-band mmW imaging array can be configurated by using super-conductor technique. It can detect targets with low observable signatures, such as stealth target.

CONCLUSION

In a word, with wide applications of the mmW technology to weapon systems, the military powers have brought mmW technology into programs of developing new weapon systems one after another, and made a series of plans about mmW military applications. The next generation of advanced weapon system based on mmW techniques is predicted to form the main threat in the 2000. Facing the threat from the coming mmW weapons, we must pay special attention to the developing trends of mmW technology, and develop mmW ECM equipment as quickly as possible. Some novel mmW ECM systems will arise after the 1990s.

REFERENCES

1. International Countermeasures Handbook, 1987 - 1990
2. JANE'S Weapon System, 1987 - 1990

INVESTIGATION OF FREQUENCY-SCANNING CHARACTERISTIC OF PERIODICALLY LOADED LEAKY-WAVE ANTENNA WITH METAL STRIPS

Li Guoding, Shi Changsheng, Zeng Zhihong
(Department of Electric Engineering,
Tsinghua University, Beijing China)

INTRODUCTION

The periodically loaded leaky-wave antenna with metal strips shown in Fig.1 has many advantages, snch as the antenna can be conveniently integrated with dielcctric-based planar integreted circuits and frequency-scanning applications can be realized at millimeter waves. In this paper we conduct theoretic and experimental investigation in frequency scanning characteristic of the leaky-wave antenna. By means of Green's function in the Fourier transform of spectral domain the dispersion equation of the leaky-wave antenna is deduced. The relation between the complex propagation constant along the leaky-wave structure and frequency, the geometry of the strncture and pesmittivity of dielectric-coated conductors is evaluated. The dispersion curve of the leaky-wave antenna shows that there is mode-coupling effeets between the spatial harmonics. The relation between the maximum radiation angle of n=-1 spatial harmonic and frequency is calculated and verified by experiment.

PROPAGATION CONSTANT OF THE PERIODICALLY LOADED LEAKY-WAVE ANTENNA

The structure shown in Fig. 1 is the periodically loaded, basically slow, traveling wave one. The thickness and the length of the dielectric slab are h and L, respectively. d is the length of the strip. 2w is width of the strip. The propagation constant of the leaky-wave antenna is the complx, The real part and imaginary part of the complex determine the maximun radiation direction and the pattern shape of the antenna, respectively.Therefor the real part determines froqueney scanning characteristic of the antenna. The strucfture is supposed to be infinite extent in Y-Z plane and only TE modes are excited. The current distribution on the strip in the Z-direction is supposed to be[1]

$$J_Y(z)=\{\exp(-jk_{z0}z)\ /(k_0(w^2-\bar{z}^2)^{\frac{1}{2}-j})\}\sum_{\nu=0}^{\infty}(-j)^{\nu}A_\nu\cos\{w_\nu(\bar{z}+w)\} \qquad (1)$$

Where $\bar{z}=z-nd$ $(n=0,\pm 1,\pm 2\ldots)$

$w_\nu=\nu\ \pi\ /(2w)$ $(0,1,2\ldots)$

A_ν is the coefficients of the Fourier series

$k_{z0}=\beta+j\alpha$ is the fundamental propagation constant

By means of Green's function in the Fourier transform of spectral domain the dispersion equation of the structure is[2]

$$\left| \sum_{n=-M}^{M} G(\zeta_n, k_{z0}) F_\nu(\zeta_n)(\zeta_n w \sin(\mu\pi/2-\zeta_n))/[(\mu\pi/2)^2-(\zeta_n w)^2] \right| = 0 \qquad (2)$$

$$(\nu = 0,1,2,3\ldots) \qquad (\mu = 0,1,2,3\ldots)$$

where $G(\zeta_n, k_{z0}) = (jk_{(0)} + k_{(1)} \operatorname{ctg}(k_{(1)} h))^{-1}$

$$F_\nu(\zeta_n) = (\pi/2)[J_0(\zeta_n w + (\nu\pi/2)) + (-1)^\nu J_0(\zeta_n w - (\nu\pi/2))]$$

$\zeta_n = 2n\pi/d$ $\qquad$ $J_0(x)$: the Bessel function

$k_{(0)}^2 = k_0^2 - (k_{z0} + \zeta_n)^2$ $\qquad$ $k_{(1)}^2 = \varepsilon_r k_0^2 - (k_{z0} + \zeta_n)^2$

K_0 is the free space propagation constant

The solution of complex k_{z0} satisfying Eq.(2) yields the desired complex wavenumber for the leaky-wave antenna. Plots of real part β and imaginary part α of the propagation constant k_{z0} from Eq.(2) are shown in Fig.2 where 2w=1mm, d=3mm, h=1.5mm ε_r=16. Fig.2 shows that there is mode-coupling effects between the spatial harmonics and the stop band appears. The dispersion curve for the dielectric slab on a perfectly conducting ground plane without any metal strips is given in same figure.

FREQENCY-SCANNING CHARACTERISTIC OF THE PERIODICALLY LOADED LEAKY-WAVE ANTENNA WITH METAL STRIPS

The leaky-wave antenna shown in Fig.1 is regarded as an array composed of thin metallic rectangular strips which is excited by the slow wave structure. Every strip is a radiation element. By theory of antenna array, the maximun radiation angle of n-th spatial harmonic is θ_n (See Fig.1) and

$$\theta_n = \sin^{-1}\left(\frac{\beta}{k_0} + \frac{\lambda_0}{d} n\right) \qquad n=0, \pm 1, \pm 2\ldots$$

In order that θ_n is located in visible region, β, k_0, λ_0, d and n must satisfy

$$\left| \frac{\beta}{k_0} + \frac{\lambda_0}{d} n \right| \leq 1 \qquad (3)$$

In the basically slow periodically structure $(\beta/k_0) > 1$, therefor, in equation (3) $n \leq 0$, i.e.

$$\left| \frac{\beta}{k_0} - |n| \frac{\lambda_0}{d} \right| \leq 1$$

$$\frac{|n|}{\frac{\beta}{k_0}+1} \leq \frac{d}{\lambda_0} \leq \frac{|n|}{\frac{\beta}{k_0}-1} \qquad (4)$$

We hope that only the pattern of n-th spatial harmonic is located

in visible region then

$$\frac{|n+1|}{\frac{\beta}{k_0}-1} < \frac{d}{\lambda_0} < \frac{|n-1|}{\frac{\beta}{k_0}+1} \qquad (5)$$

usually, n=-1 spatial harmonic is located in visible region, λ_0/d must satisfy

$$\frac{d}{\lambda_0} < \frac{2}{\frac{\beta}{k_0}+1} \qquad (6)$$

Condition (6) shows that when n=-1 spatial is located in fast wave reqion, other spatial hoarmonics are located in slow wave reqion in the Brillouin diagram. The relation between theoretical results of the angles θ_0 and frequencies are shown in Fig.3, The experimental values are given in same figures. As seen from Fig.3 the experimental results are in very good agreement with our theory and the rate of frequeney scanning, ten degrees per GHz, can be realize by use of the leaky-wave antenna.

CONCLUSION

The periodically loaded leaky-wave antenna with metal strips has good frequency scanning characfteristic. In this paper by means of Green's of spectral domain the dispersion equation of the leaky-wave antenna is deduced and the relation beftween the complex propagation constant and frequency is obtained. Condition of single pattern scanning is found. The relation between the maximun radiation angles θ_0 of n=-1 spatial harmonic and frequencies are computed and measured. The experimental results are very good agreement with theoritical results. Rate of frequency scanning, ten degrees per GHz, can be realize by use of the leaky-wave antenna.

REFERENCES

1. K. UCHIDA, T. NODA, and T. MATSUNAGA, " Numerical Analysis of Plane Wave Scattering by an Infinite Plane Grating Using Weighted Fourier Series " THE TRANSACTION OF THE IECE OF JAPAN, VOL.E 69, NO.2 FEBRUARY 1986.
2. Li Guoding, Si Changsheng, Mao Haihua, " INVESTIGATION OF PERIODICALY LOADED LEAKY-WAVE ANTENNA WITH INHOMOGENEOUS METAL STRIPS" 1990 Antennas and Propagation Symposium Digest Volumel PP. 517-520.

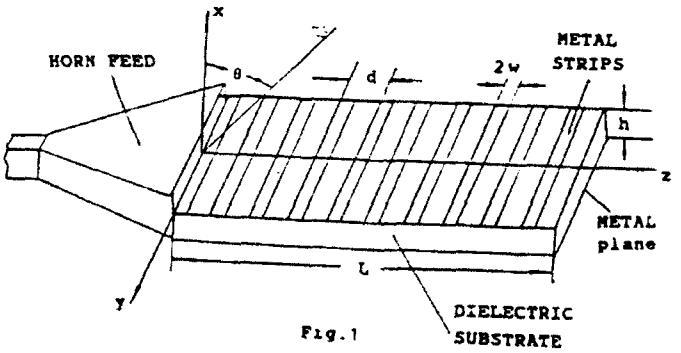

Fig.1

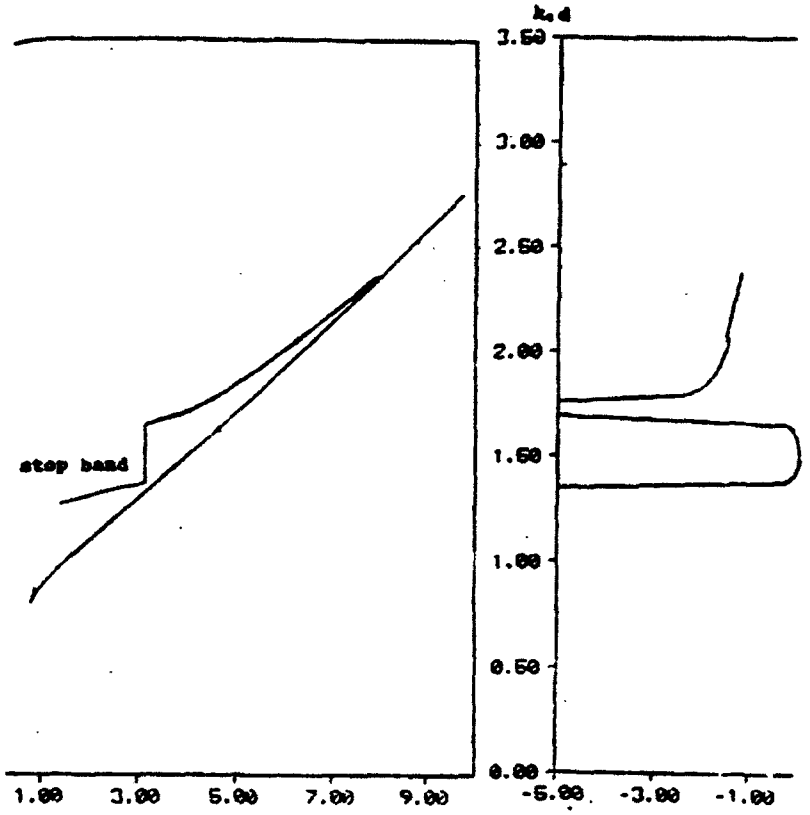
k₀ d
3.50
3.00
2.50
2.00
1.50
1.00
0.50
0.00
stop band
1.00
3.00
5.00
7.00
9.00
-5.00
-3.00
-1.00
β d
lg(ε d)

Fig.2

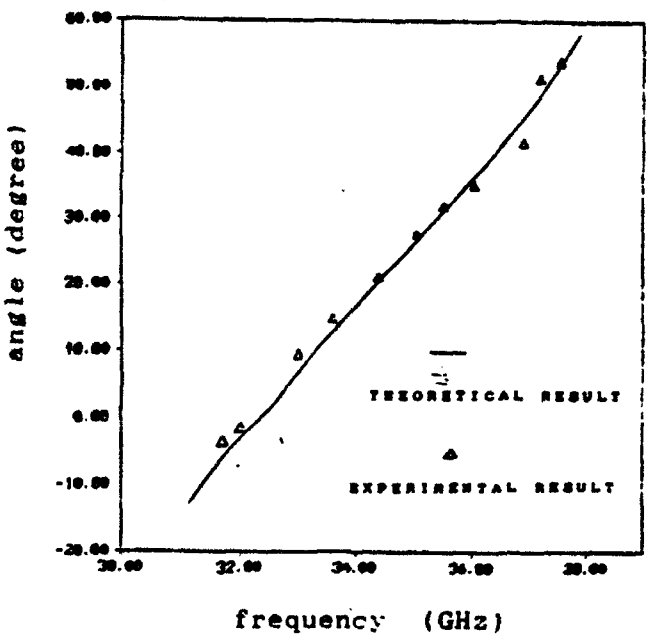
angle (degree)
THEORETICAL RESULT
EXPERIMENTAL RESULT
frequency (GHz)

Fig.3

INFLUENCE OF ELECTROMAGNETIC WAVE ON ENCAPSULATED SEMICONDUCTOR DEVICES

Kama Huang and Yongxue Yu
(Dempartment of Radio and Electronics of Sichuan University
Chengdu, 610064, Peopie's Republic of China)

Key TERMS

Electromagnetic wave(EMW), Semiconductor Devices, Parameters Degradation

ABSTRACT

This paper illustrates that electromagnetic waves radiations can cause the parameters degradations of encappulated sensitive semiconductor devices and decrease the preliminary failure time. It is also proved that we can make use of the electromagnetic wave radiation to get rid of the preliminary failure encapsulated semiconductor devices.

1. INTRODUCTION

More and more encapsulated semiconductor devices are applied and many of them work in the surroundings of electromagnetic radiation. But the influence of the radiation on these devices has not attracted enough attention. Experiments show that when some encapsulated semiconductor devices are radiated by electromagnetic wave with certain strength, their parameters may change and the preliminary failure time will decrease. Obviously, for some sensitive devices, the above changes will influence the reliability of these devices in the application. On the other hand, the influence also makes it possible for us to get rid of the preliminary failure semiconductor devices. Because the period of millimeter waves and submillimeter waves is comparable to the mean free time of the semiconductor material, it can be expected that some new results will be found when the semiconductor devices are radiation by millimeter and sub-millimeter waves.

2. INFLUENCE ON PARAMETERS OF SEMICONDUCTOR DEVICES

When encapsulated semiconductor devices are put in TEM cell and radiated by a standard even TEM wave, the parameters of them will change. It may be explained from the solutions of dynamic Eq. of carrires[1]:

$$d(m_n^*\vec{v}_d)/dt+m_n^*\vec{v}_d/T_m=-q(\vec{E}+\vec{v}_d x\vec{B}) \quad (1)$$

$$d(m_p^*\vec{v}_d)/dt+m_p^*\vec{v}_d/T_m=q(\vec{E}+\vec{v}_d x\vec{B}) \quad (2)$$

Where t_m is the mean free time, and are the masses of hole and electron respectively.

Supposing E is X-direction and B is Y-direction, if the angular frequency of electromagnetic wave is w $1/t_m$, the solutions of Eq. (1) and Eq. (2)are[1]: $X_{n,p}(w)=A_{n,p}(w)\exp(jwt)$

$$Y_{n,p}(w)=C_{n,p}(w)(1-\exp(-t/T_m))$$

Where $Z_{n,p}(w)=B_{n,p}(w)\exp(j2wt)$

$$A_{n,p}(w)=qE_oT_m/M_{n,p}^*(jw+1/T_m)-qE_oT_m/jwM_{n,p}^*$$

$$B_{n,p}(w)=jwqB_oT_m/(2jw+1/T_m)M_{n,p}^*-qB_oT_m^2/2M_{n,p}^* \cdot A_{n,p}(w)$$

$C_{n,p}$ is a constant decided by the experiment.

These solutions show that under the radiations of TEM wave, carriers in the semicondutor devices move in three directions. First, carriers move along Y-direction, this movement produces a charge accumulation effect 2 and forms an additional electric field and the changes of parameter. Second, carriers ocsillarate along X- and Z-directions and produce joule heat effect. The second effect leads to harmful temperature rise inside the devices. The changes of parameter of 3G1688 transistors under radiation of TEM waves are shown in table 1. In this table, fifty 3G1688 transistors in Group(A) are put in the TEM cell, while other fifty 3G-1688 transistors in Group B are preserved out of the cell.

3. INFULENCE ON THE RELIABILITY OF SEMICONDUCTOR DEVICES

Experiments show that the parameter degradation speed is decided by Arrhenius equation [2]. The two effects cause the parameter degradtion. First, carriers absorb energy from TEM waves and the activation energy decreases; Second, joule heat effect increases the temperature inside the devices. Arrhenius Eq. shows that both of the above effects can quicken the degradation of device parameters. The preliminary failure of 3G1688 transistor is shown in FIG.1. From FIG.1 we see that the preliminary failure time of the devices under the radiation of electromagnetic waves is obviously less than that in the high temperature enviornments. Therefore we may get rid of the preliminary failure devices with elec-

Table 1. 3G1688 transistor parameter changes under radiation of TEM wave

Experiment graps	Maximum Parameter degradation					Experiment condition
	h_{FE}	V_{Ces}	DV_{cbo}	DV_{ceo}	DV_{ebo}	
(A)	10%	4%	1%	6%	1%	f = 125 MHz E = 290v/M T = 17℃ t = 22 hours
(B)	2%	1%	1%	1%	1%	

Table 1.

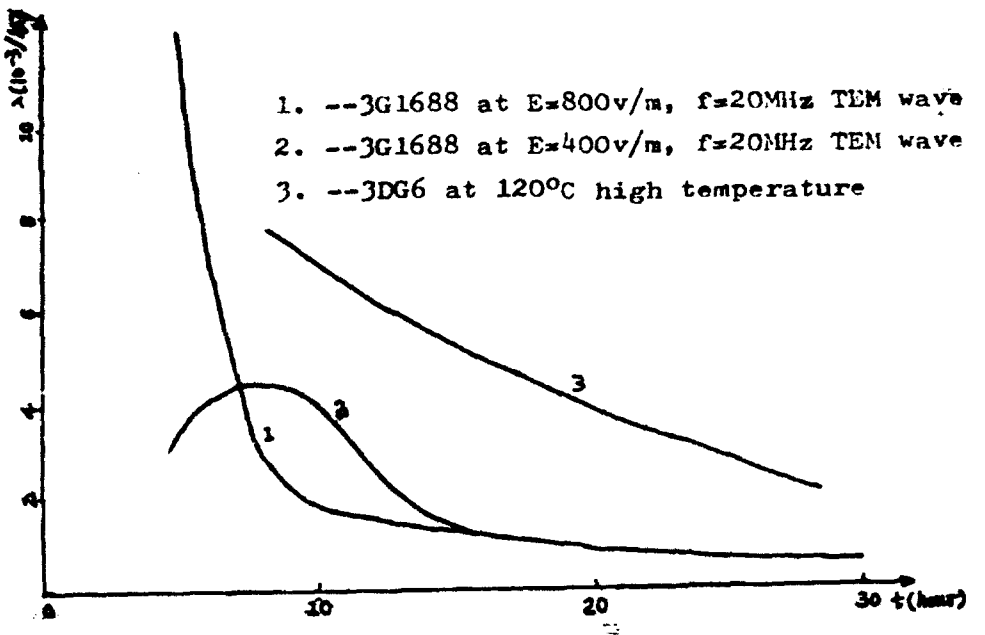

Fig.1. Preliminary failure time of 3G1688 at different conditions

tromagnetic waves.

4. CONCLUSION

In order to improve the reliability of semiconductor devices in electromagnetic enviornments, it is necessary to reaserch the influence of electromagnetic waves with different strength on the devices at different frequency. Because the period of millimeter and sub-millimeter waves is comparable to the mean free time of semiconductor, the condition $w \ll 1/t_m$ can not be satisfied, therefore those solutions based on Eq. (1) and Eq. (2) must be adjusted.

REFERENCE:

1 Kama Huang : " Using Electromagnetic wave to Get Rid of Preliminary Failure Semiconductor Devices " Journal of Microwaves Vol.26, No.3, 1991, PP 15-21.

2 Kama Huang : " Influence of Electromagnetic wave on Encapsulated Semiconductor Devices " Microwave and Optical Technology Letters Nov. 1990.

SOME TOPICS ON ECRM THEORY

Liu Shenggang

(*University of Electronic Science and Technology of China, Chengdu, Sichuan* 610054, *P. R. China*)

ABSTRACT

Three important topics on the theory of Electron cyclotron Resonance Maser have been studied and the main results are given in the paper. The topics are: Kinetic Theory of ECRM with Asymmetry Between Electron Beam and Cavity; Kinetic Theory of ECRM with Agimuthal Standing Wave and The Theory of Electron Bunching in the Drift Region with Adiabatical Increasing Magnetic Field.

INTRODUCTION

As the development of ECRM, the following required has been suggested in the design of gyrotrons:

- Output power of a gyromonotron is equal or greater than 1MW
- High efficiency
- Single mode operation

and so on.

This is a very critical condition for the design, manufacture and theoretical study of gyrotrons. When the operating wave length is very short with very high power output , whispering gallery modes should be applied. This results some important theoretical and practical problems:

When the azimuthal number of waves m is large, which one may be maintained in a ECRM ——azimuthal traveling waves or azimuthal standing waves?

On the other hand, when the operating wave length is very short with high output power, a single mode operation and high efficie cy is required. In this case, the condition that the hollow gyroting electron beam is in coincidence with the waveguide axial of the cavity is very critical. But in some cases, for example, some dis- coincidence has been observed and some interesting phenomena have been investigated experimentally in the Research Lab in KfK of Germany. So it seems very interesting to work out a theoretical description about the influence of this asymmetry on the characters on gyrotron.

Besides, the self-oscillation incluced by feedback is a serious problem in the development of gyroklystrons. When the author was giving lectures in University of Tennessee, Prof. I. Alexeff suggested the new idea of applying the gradient magnetic field in the drift region. It seems very interesting and important to study the azimuthal bunching of electron beam in this kind of drift region.

The paper concerns on the above three important theoretical problems, a detail analysis is taken out, and

ne important conclusions are obtained.

KINETIC THEORY OF ECRM WITH ASYMMETRY BETWEEN ELECTRON BEAM AND CAVITY

netic theory of ECRM and gyrotron with asymmetry between e-beam and cavity has been ... out in is section, considering the relation between the wave guide coordnate, electron beam coordinate and the iding centre coordinate, by applying the method of integration along the unperturbed trajectory, the rturbed distribution function of electron beam is derrived as:

$$f_1 = -k_c\mu_0 e\sum_q\sum_l\{J_q(k_c d)J_l(k_c r_c)J_{m-1}(k_c R_{g1})\cdot$$
$$\left[\frac{(\omega - k_{//}v_{//})}{\Omega_l}\frac{\partial f_0}{\partial P_\perp} + \frac{k_{11}v_\perp}{\Omega_l}\frac{\partial f_0}{\partial P_{//}}\right] - \frac{1}{m\omega_{c0}}$$
$$\left[J_q(k_c d)J_l(k_c r_c)J_{m-l-q}(k_c R_{g1}) + \frac{r_c\omega_c(m-q-l)}{R_{g1}\omega_{c0}}\right.$$
$$\left.J_q(k_c d)J_l(k_c r_c)J_{m-l-q}(k_c R_{g1})\frac{\partial f_0}{\partial R_{g1}}\right)\} \tag{1}$$

nere

$$\Omega_l = \omega - k_{//}v_{//} - l\omega_c$$

/ applying the method shown in [1~3], the dispersion equation may be carried out:

$$\frac{\omega^2}{c^2} - k_{//}^2 - k_c^2) = \frac{2k_c^2 v}{N_m\gamma_0}\sum_q\sum_l\{-\frac{\omega^2 - k_c^2c^2)}{\Omega_l^2}W_m$$
$$+\frac{(\omega - k_{//}v_{//})}{\Omega_l}\Omega_m + U_m\} \tag{2}$$

n the basis on the above results, the beam-wave interaction in a gyromontron has also been studied. By a eries complex derrivation , the starting current and frequency shift of a gyromontron with asymmetric etween electron beam and cavity are obtained:

$$I_m = -\frac{\pi k_c^2 a^2 v_{//}\gamma_o(1 - \frac{m^2}{k_c^2a^2})J_m^2(k_c a)}{\eta_o\mu_o(1 - \frac{s^2\lambda_o^2}{4L^2})Q_T(\sum_{i=1}^{4}Re(P_i))} \tag{3}$$

$$\frac{\Delta\omega}{\omega_o} = \frac{2\omega_\gamma^2(\frac{R_o r_\infty}{a^2})(1 - \frac{S^2\lambda_o^2}{4L^2})(\sum_{i=1}^{4}Im(P_i))}{k_c^2a^2(1 - \frac{m^2}{k_c^2a^2}J_m^2(k_c a)} \tag{4}$$

According to the above theory, Dr. Q. Dumbrajs of KfK in Germany has taken out a detail numerical nalysis. the results shown that the asymmetry influenced the operation of a gyrotron seriously.

KINETIC THEORY OF ECRM WITH AZIMUTHAL STANDING WAVES

The kinetic theory of ECRM and gyrotron with agimuthal standing waves has been carried out in this section . By applying the method similiar to [3~5], the dispersion equation has been derrived as:

$$(\frac{\omega^2}{c^2} - k_{//}^2 - k_c^2) = \frac{2k_c^2 v}{N_m\gamma_o}\{-\frac{(\omega^2 - k_{//}^2c^2)}{\Omega_l^2}W_m$$
$$-\frac{(\omega^2 - k_c^2c^2)}{(\Omega_l^-)^2}W_m + \frac{(\omega - k_{//}v_{//})}{\Omega_l}Q_m$$
$$\frac{(\omega - k_{//}v_{//})}{\Omega_l^-}Q_m^- + V_m + V_m^-\} \tag{5}$$

The azimuthal standing wave in an ECRM may be decomposed as two opposite rotating waves: the left-hand rotating wave and the right-hand rotating wave. The analysis shown that the right-hand rotating waves give the right-hand cyclotron harmonics and the left-hand rotating waves produce the left hand cyclotron harmonics . It turns out that the beam-wave interaction mechanisms of these two rotating waves are different from each other. From the above dispersion, it shown that the contribution of the left-hand rotating waves to the dispersion equation is less than that of the right-hand rotating waves. In particular, the growth rate of the instability due to the left-hand rotating waves is less than that due to the right-hand rotating waves . It turns out that the field pattern of the azimuthal standing waves could not remain unchange during the process of beam-wave interaction.

ELECTRON BUNCHING IN THE DRIFT REGION WITH ADIABATICAL INCREASING MAGNETIC FIELD

The author and Prof. I. Alexeff suggested a new kind of ECRM: Irrational Gyroklystron. The property of this kind of klystron is : The magnetic field in the drift region is adiabatical increasing . The azimuthal bunching of electron beam in this case has been carriced out here, the interaction power and oscillation frequency are also given. It shows that, there is not coupling between the input and output signals, because the input and output frequencies are irrational, the powwibility of self-oscillation inclucde by feedback is greatly reduced. So that, this kind of gyroklystron has much potential for practical application, and should be studied in detail.

CONCLUDSION

The influence of asymmetry between electron beam and carity on the ECRM, the azimuthal standing waves in ECRM and electron bunching in the drift region with adiabatical increasing magnetic field are three important topics in theorecal and practical applications. Theoretical studies on these topics are given in the paper a detail descussion has also been taken out, and some important conclusions are obtained.

REFERENCES

1. K. R. Chu, Phy. Fluids, (21)(1978)461
2. J. Y. Choe and S. Ahn, IEEE trans. EC-28(1)(1981)
3. Liu Shenggang, Acta Scientia Sinica, (8)(1970)902
4. Liu Shenggang, Acta scientia Sinica, (11)(1981)1402
5. Liu Shenggang, Relativistic Electronics Publication House of National Defence, P. R. China, 1987 (in chinese)
6. Wang C. et al. , Int. J. of IR/MM Waves
7. Liu Shenggang, IEEE ICOPS-18, 5A6, Williamsburg, USA, Jun 3~5, 1991
8. Liu Shenggang, IEEE ICOPS-18, 4P3, Williamsburg, USA, Jun 3~5, 1991

Investigation of a Free—Electron laser with an Electromagnetic Wiggler

Liang Zheng, Li Jiayin, Zhang Bin, Wu Jianqiang,
Ma Wenduo, Yang Ziqiang, Deng Tianquan,
Chen Xinyu, Zhou Xiaolan, Sun Jiahong and Liu Shenggang.
High Energy Electronics Research Institute
University of Electronic Science and Technology of China,
Chengdu 610054, Sichuan P. R. C

Digest

A great deal of attention has been focused on the free—electron laser with an electromagnetic wiggler (EM—FEL) in recent years due to the potential of shorter wavelength operation than the free—electron laser with a magnetostatic wiggler with electron beams of relatively modest energy. In principle, the EM—FEL can generate any given frequency radiation from microwaves to the ultraviolet with electron beam of modest energy using a variety of wavelengths' electromagnetic wiggler.

Theoretical analysis and experimental investigation of the EM—FEL with the relativistic microwave-devices as the electromagnetic wiggler have been deeply developed for the past ten years. The 0.4—mm laser was generated with 2—cm relativistic gyrotron as the electromagnetic wiggler. by V. L. Granatstein, et al. in 1977. In 1983 and 1984, Y. Carmel etal. and G. G. Denisov et al. observed the powerful radiation at millimeter wavelengths with a relativistic backward wave oscillator (BWO) at 3—cm as the electromagnetic wiggler, respectively. In 1985, Bratman et al. reported the general theory on stimulated emission of the powerful relativistic electron beam. And R. L. Kehs et al. studied experimentally the EM—FEL with BWO as the electromagnetic wiggler and observed the three—wave interaction mechanism involving cyclotron—harmonic idler waves.

In 1987 B. G. Danly et al. presented an EM—FEL configuration with mm—wavelength gyrotron as the pump source and simulated the parameters. Afterward some of theoretical questions of this configuration, such as electron orbits, linear gain and so on, was studied by H. P. Freund et al. In particular, T. S. Chu et al.. first reported the experimental results of the EM—FEL with a gyrotron as the electromagnetic wiggler, of which the operation wavelength was 2.4—mm and the normalized vector potential 0.0057.

Our experiment was designed to investigate stimulated Raman millimeter—wave scattering in the presence of a constant axial guide—magnetic field. The experiment arrangment is shown in Fig. 1. A voltage pulse (70ns, 0.6MV) is applied to a "cold" field—immersed cathode. A resultant 3~5 KA annular eletron beam is injected axially into the evacuated drift tube along the lines of the externally applied guide—magnetic field. The beam passes through the regions of the FEL interaction and the electromagnetic pump source, then is captured by the collector.

High powerful microwave is first generated by a BWO at 3cm in the region of EM pump source, then the same intense relativistic electron beam interaction with the electromagnetic wiggler in the region of FEL stimulates FEL radiation which can be detected by a detector in front of the output window.

The FEL output wavelength for an electromagnetic wiggler having a frequency ω_i is given by

$$\omega_s = \beta_{//}\gamma_{//}^2 CK\{1+\beta_{//}[1-(\frac{\omega_{c0}}{K\gamma_{//}\beta_{//}C})^2]^{1/2}\}, \tag{1}$$

where

$$K = \frac{\omega_i}{\beta_{//}C}(1+\frac{\beta_{//}}{\beta_{ph}}). \tag{2}$$

Here, $\beta_{//} = v_z/C$ (v_z denotes the axial eletron—beam velocity), $\gamma_{//} = (1-\beta_{//}^2)^{-1/2}$, C is light velocity, ω_{c0} represents the mode—dependent cutoff frequency of the interaction waveguide, and $\beta_{ph} = v_{ph}/C$, where v_{ph} is the phase velocity of the pump wave. The starting current I for the EM—FEL is governed by

$$I > \frac{1.7 \times 10^3 (S/\lambda L)^2 \gamma^4}{Q_c P(GW)} (KA), \tag{3}$$

where S is the area of the transverse cross－section of the interaction region, L the interaction length, λ wavelength of the pump wave, γ the relativistic factor, Q_c the oscillation quality of laser cavity and P the power of the pump wave.

The basic system of radiation diagnostics is shown in Fig. 2. In this scheme, the parameters of the pump wave drived by BWO is detected by 3－cm dispersive waveguide, the 8－mm radiation is measured by 8－mm dispersive waveguide, and the stimulated 3－mm scattering radiation is directly demonstrated by a 3－mm wave detector. The output signal waveforms of the EM－FEL are shown in Fig. 3 and Fig. 4. And Fig. 5, Fig. 6 as well as Fig. 7 show the corresponding waveforms of the pump wave generated by BWO, beam voltage and current, respectively.

The experimental results are given in Table 1.

Table 1 Experimental results of the EM－FEL developed in UESTC

	designed value	measured value
electron beam voltage	0.6MV	0.6MV
electron beam current	>2KA	3～5KA
wavelength of the pump wave	3.0cm	～3.0cm
power of the pump wave	>50MW	～100MW
mode of the pump wave	TM_{01}	TM_{01}
scattered wavelength of the FEL	～3mm	3～8mm
radiation power of the FEL	>10KW (at 3mm－band)	

The governing equations for the electron beam interaction with waves of the EM－FEL configuration shown in Fig. 1 are

$$\frac{dW}{dz} = Im[\bar{\omega}_i F_i a_i exp(i\theta_i) + \bar{\omega}_s F_s a_s exp(i\theta_s) + G a_s a_i^* exp(i(\theta_s - \theta_i))] \tag{4}$$

$$\frac{d\theta_i}{dz} = -\delta_i + \mu_i W \tag{5}$$

$$\frac{d\theta_s}{dz} = -\delta_s + \mu_s W \tag{6}$$

$$\rho_{m,n} = \frac{1}{(2\pi)^2} \iint_0^{2\pi} exp[-i(m\theta_i + n\theta_s)] d\theta_{i0} d\theta_{s0} \tag{7}$$

$$\frac{da_i}{dt} + \frac{\omega_i}{2Q_i} a_i = iM_i^m \int_0^{2\pi m} F_i \rho_{1,0} dz \tag{8}$$

$$\frac{da_s}{dt} + \frac{\omega_s}{2Q_s} a_s = iM_s^m \int_0^{2\pi m} (F_s \rho_{0,1} + G^* a_i \rho_{-1,1}) dz \tag{9}$$

Here, W denotes the lost energy of the electron in motion, θ_i and θ_s are electron phase corresponding to the pump wave and scattered wave, respectively; a_i and a_s normalized field-amplitudes.

The computative results by use of the equations (4)～(9) are shown in Fig. 8. It demonstrates the saturation times for the power of the pump wave and the FEL scattering <20ns.

The work reported here is the achievements in the EM－FEL developed in UESTC since 1987. On the basis of these work, new experimental configurations will be proposed for characterizing and optimizing the FEL emission.

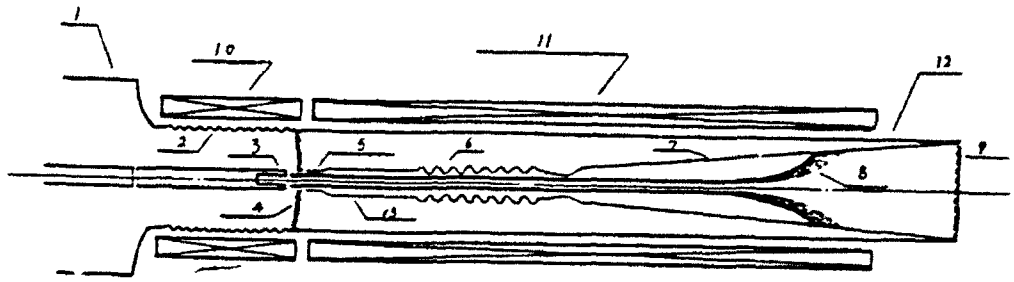

Fig. 1 The basic experimental configuration of the EM—FEL developed in UESTC.

1. pulseline accelerator 2. bellows 3. cathode 4. anode 5. wave cut—off region 6. slow—wave structure for BWO 7. output horn 8. relativistic electron beam 9. output window 10. cathode region magnetic — field 11. main magnetic field 12. vacuum cover 13. FEL interaction region

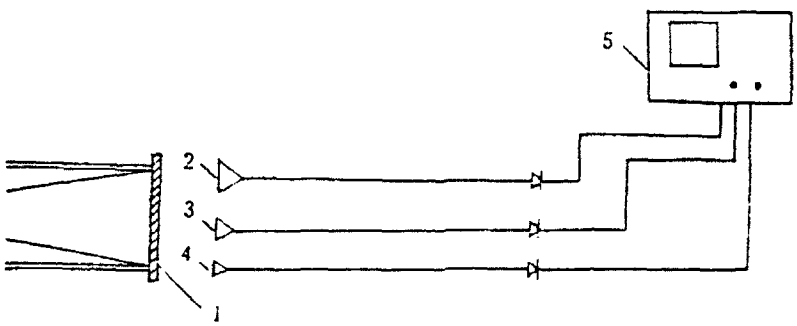

Fig. 2 The basic system of radiation diagnostics

1. output window 2. 3-cm dispersive waveguide 3. 8-mm dispersive waveguide 4. 3-mm wave detector 5. digital oscillator

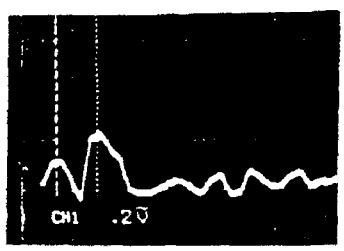

Fig. 3 Radiation signal detected by 8-mm dispersive waveguide corresponding to 0. 6MV beam voltage and 10KGs magnetic field.

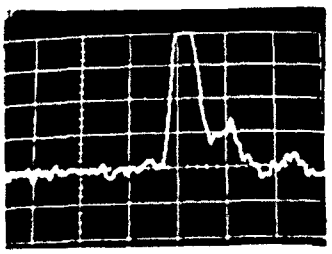

Fig. 4 3-mm FEL stimulated scattering signal.

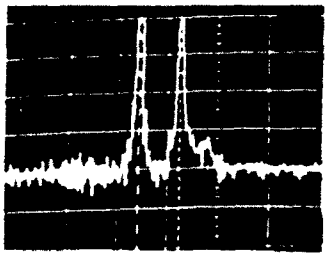

Fig. 5 The pump wave waveform out of BWO.

Electron beam voltage is 0. 6MV and axial guide magnetic—field 10KGs.

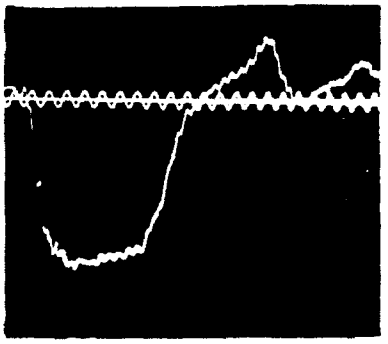

Fig. 6 Waveform of the electron beam voltage.

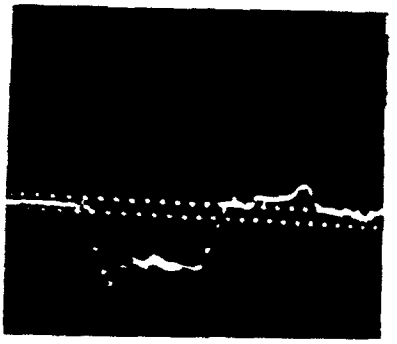

Fig. 7 Waveform of the electron beam current.

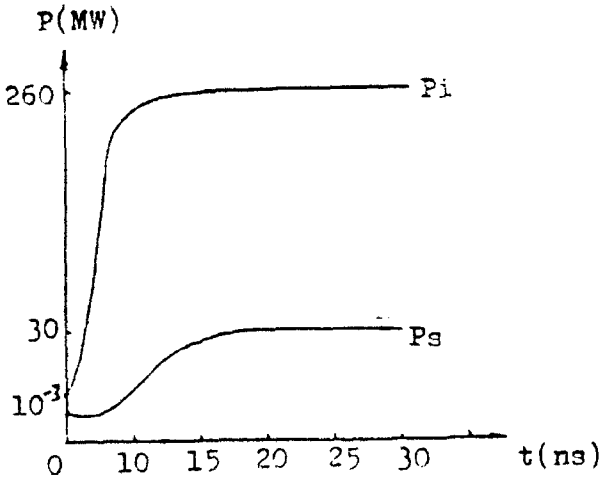

Fig. 8 The calculated starting charateristic suitable for the EM—FEL configuration shown in Fig. 1.

THE CLINOTRON

G. Ya.Levin, A. Ya. Kirichenko, A. I. Borodkin,
S. A. Churilova and A. Ya. Usikov.

Institute of Radiophysics and Electronics,
the Ukrainian Academy of Sciences
12, Acad. Proskura st., Kharkov, 310085 Ukraine

The clinotron belongs to a special class of millimeter wave sources. Soon after the invention of the backward-wave oscillator (BWO) it became clear that the same physical principles could not be applied to generating millimeter or submillimeter wavelength radiation, especially at medium and high power levels. Therefore, scientists and engineers had to reexamine the generation method and began seeking new ways of developing efficient and practicable systems.

In this paper, a new mechanism of beam-wave interaction is suggested which can allow to develop BWO-like devices for the use up to 10^{12}Hz. The authors have found that a "thick" electron beam slightly inclined with respect to the slow wave structure is capable of highly efficient interaction with the field, thus being suitable in millimeter and particularly submillimeter wave generators and amplifiers. This kind of interaction between a slow traveling electromagnetic wave and a finite-thickness electron beam has been named "clinotron interaction", and the tube making use of this mechanism is called the clinoton [1]. The Russian "clin" means "wedge". The oscillator described in this paper should be of interest to many readers because of such advantages as structural simplicity, sufficiently high output power, broad band electrical control and moderate requirements to power and magnetic field supplies.

Let us examine the disadvantages of the beam-wave interaction in a BWO. The maximum output power is obtained if the electron beam is parallel to the periodic system plane. Employment of a beam with a greater cross-section area than the effective r. f. modulation area leads to no effect. For this reason the microwave power transferred by the electron beam is limited at millimeter wavelengths.

In contrast to the TWT, the electron beam is introduced in the BWO in to a powerful field decreasing toward the collector. The drift of the electron beam down the tube is accompanied by formation of bunches

in the moving beam, with overbunching at times. The major part of electrons running immediately close to the circuit are intercepted by that because of their transverse velocities, which may be of thermal or other origin. As a result, an empty space appears between the beam and the slow wave structure. The majority of the beam electrons move at some distance from the slow wave structure, i.e. in a weak r.f. field.

Consider an electron beam of thickness d, inclined at an angle φ to the axis of the slow wave structure surface. The general geometry of the beam and the circuit are shown diagrammatically in Fig.1. Let the r. f. field be constant along the circuit, as well as and in the layer of thickness $\delta \simeq 1/2\beta$, where β is the propagation constant. Note the layer thickness to be about of $1/150\lambda$, where λ is the free-space wavelength. We further assume that the thick beam consists of n layers of thickness $\xi < \delta$, the interaction efficiency of each layer being P_i. The field - layer interaction length is the drift length l. The total interaction power of the whole beam is proportional to the product of the interaction power P_i for individual layers and the quantity of layers (n),

$$P = P_i \cdot n \qquad (1)$$

This allows increasing the generated power level from a few milliwatts to a few watts, avoiding overbunches in the moving charge. Provided the beam thickness has been chosen correctly, the optimum inclination angle φ_{opt} of the beam is

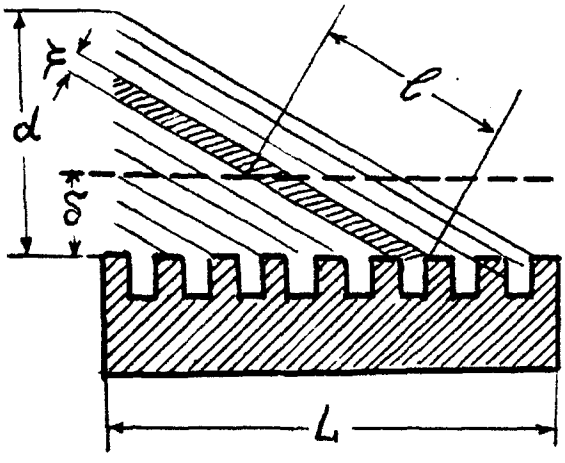

Fig.1

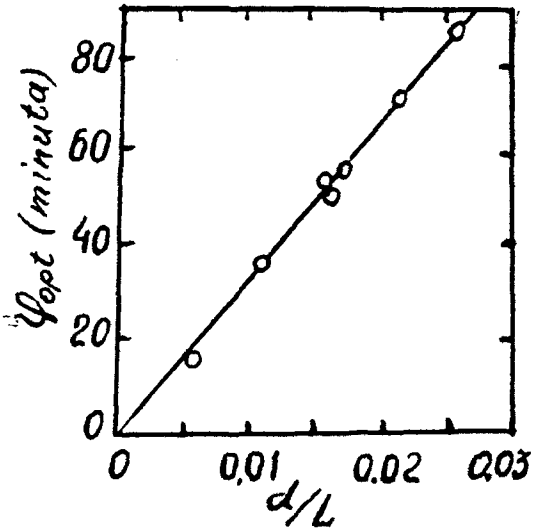

Fig.2

$$\varphi_{opt} = \text{arc tan } d/L, \qquad (2)$$

where L is length of the circuit. A maximum of radiated power is observed at the angle φ_{opt}.

In Fig.2, experimentally measured values of the optimum angle are given as a function of d/L. The solid curve is for $\varphi_{opt}(d/L)$ as calculated from equation (2).

Fig.3 shows experimental dependences of the generated power level P normalized to the maximum generated power P_{max} (in the clinotron mode) for different free space wavelengths λ, as functions of φ/φ_{opt}. The solid lines are only guides to the eye. It should be noted that the slope of $P/P_{max}(\varphi/\varphi_{opt})$ becomes greater as the free-space wavelength is decreases. Furthermore, the radiation power at $\lambda < 6$ mm of a beam parallel to the plane of the periodic circuit is equals to zero.

If the beam electrons drift along helical trajectories down the tube, then it is necessary to incline the electron flow at the angle ψ_{opt} with respect to elements of the periodic structure. The helix axis is in the plane parallel to that of the periodic structure.

The minimum starting current (I_{st}) and maximum output power (P) are achieved when the angle ψ equals $|\psi_{opt}|$. In Fig.5, we show the dependences of I_{st} and P on ψ (λ = 8,2 mm; H = 5 KGauss). The sign of ψ_{opt} (i.e. either plus or minus) depends on whether the "North" (solid curves) or "South" (dashed curves) pole of the magnet is placed near the collector. The optimum beam cline angle ψ_{opt} defined as

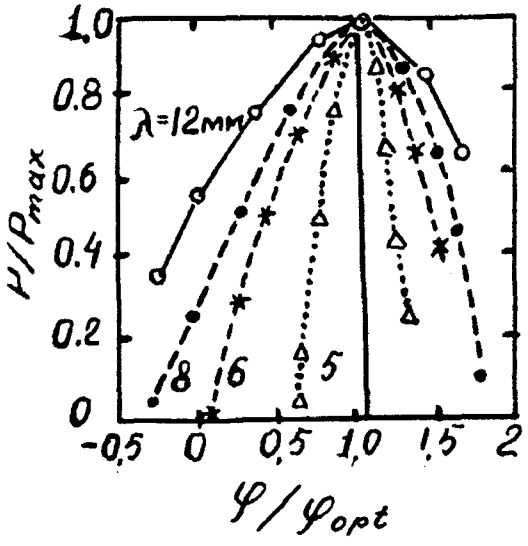

Fig.3

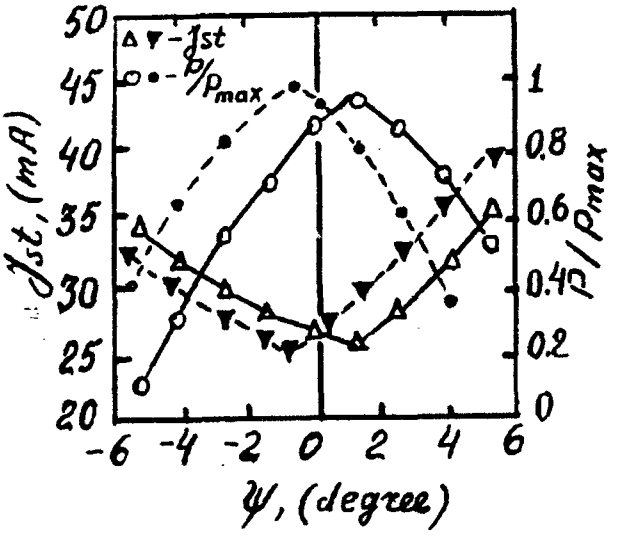

Fig.4

$$|\psi_{opt}| = \arctan \frac{r}{b} \frac{I_1(\beta r)}{I_0(\beta r)}, \qquad (3)$$

where r and b are the radius and length of the helical electron trajectory turn, respectively, and $I_0(\beta r)$ and $I_1(\beta r)$ are modified Bessel functions of the zeroth and first orders, respectively. This inclination of the beam may prove useful if a broad ($\geq m\lambda$) periodic circuit is used.

Normally, it is necessary to carefully shape the clinotron beam structure, in particular such elements as rectilinearity of electron trajectories, uniformity of the current density through the beam cross-section, the sharpness of the beam boundaries and constancy of the cross section area along the beam. All these requirements can be satisfied if the beam is placed asymmetrically in the interaction space as the effects of beam boundary pulsations and ionic destruction of the electron beam are removed.

The clinotron type interaction of an electron beam with electromagnetic waves has been investigated throughout the millimeter band and at submillimeter wavelengths. The basic specifications are given in the Table.

Tuning range Wavelength, mm	8÷8,7	4÷4,5	2÷2,3	1,5÷1,7	0,8	0,55
Operating voltage, kV	2,5	3,5	3,5	3,5	5,5	5,5
Beam current, A	0,25	0,25	0,25	0,25	0,2	0,2
Net output power, W	5÷30	3÷20	1÷5	0,5÷1,5	0,1÷0,5	0,03÷0,1
Magnetic field, kGs	3,0	3,5	3,5	5,0	7,0	9,0

As can be seen from the material presented, clinotrons are characterized by higher performance parameters and simplicity of embodiment compared, i.g. with the "O" type BWO (carcinotrons) of Thomson Tubes Electroniques.

1. A. I. Borodkin, A. Ya. Kirichemko, G. Ya. Levin, A. Ya. Usikov, S. A. Churilova. The Clinotron, 1992, Naukova Dumka Publ. Co., Kiev.

Th6.4

SYNCHRONOUS AND CHAOTIC OSCILLATIONS IN THE SMITH-PURCELL FREE-ELECTRON LASERS

Dmitry M. Vavriv

Institute of Radio Astronomy
4 Krasnoznamennaya St., 310002 Kharkov
Ukraine

Tel:(7-0572)448718 Fax:(7-0572)320273

ABSTRACT

The theory is developed for nonautonomous oscillation modes in the Smith-Purcell free-electron lasers and mechanisms of their locking with the aid of external signal are examined. An analysis is made of the synchronous oscillations stability when a locking signal spectrum includes more than one component and when a beam is low-frequency modulated. It is shown that the intensive chaotic oscillations may arise in these cases thereby resulting in the locking mode decay.

1. INTRODUCTION

The Smith-Purcell free-electron lasers are the effective sources of electromagnetic oscillations in a wide bandwidth - from the millimeter to optical ones. The oscillatory system of such lasers is an open resonator formed by two metal mirrors one of which is covered by a diffraction grating, the electron beam being passed nearby. The laser oscillations may be locked- in by supplying the external signal into the resonator [1-3].

In the present paper the results of theoretical studies are generalized concerning the locking modes in the lasers including an analysis of their stability to different perturbations. New instability mechanisms have been found and analyzed which can induce the chaotic oscillations.

2. THE MODEL

Being formulated as a self-consistent the problem was based on solving the Maxwell and particles motion equations simultaneously. Field effect of the beam charge had been also taken into account. When solving the system of equations a typical case has been considered when the following requirements are satisfied: a single-mode excitation of the open resonator is realized and radiative life time of particles is much less than the field relaxation time [1,2]. The study of resonator oscillation variations in amplitude and phase with time was reduced to an analysis of the system of ordinary differential equations and general integral representations are obtained for the coefficients entered into the equations.

3. SYNCHRONOUS OSCILLATIONS

In the case, when the laser mode locking occurs by harmonic oscillations the general expressions have been deduced for the locking bandwidth, amplitude and power of synchronous oscillations as a function of beam and resonator parameters. For the lasers under consideration, as well as for the classical oscillators, the locking bandwidth Δ_s may be expressed as follows

$$\Delta_s = K \frac{f_a}{Q}\left(\frac{P_s}{P_a}\right)^{1/2},$$

where f_a and P_a are the frequency and power of the self-excited laser oscillations, P_s, locking signal power, Q, Q-factor of oscillatory system, K, coefficient dependent on the other paramsters. The K value is found to be considerably greater in the Smith-Purcell lasers over other types of oscillators that may, in particular, be due to an

essential non-isochronism of the system. Fig.1 is an illustration of the time-varying field amplitude behavior at different values of frequency detuning $\delta = 2Q\,(f_s - f_a)/f_a$ corresponding to synchronous and asynchronous oscillations. Here, f_s is the frequency of external harmonic oscillations.

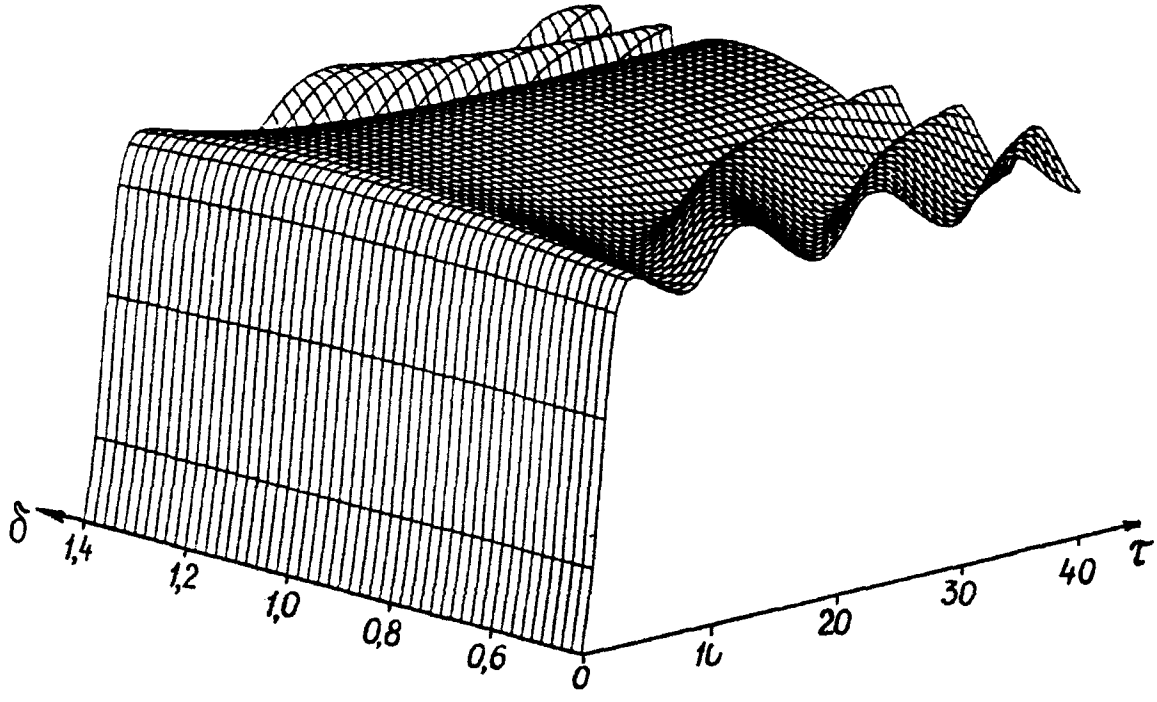

Fig.1. The time-varying field amplitude behavior at different values of frequency detuning δ corresponding to synchronous ($0.7 < \delta < 1.2$) and asynchronous oscillations.

4. CHAOTIC INSTABILITY

Systematic studies of locking mode stability have shown that such perturbations as additional spectral components of the external signal spectrum [4] and low-frequency parasitic beam modulation [5] present the most serious problems .In these cases the stochastic instability may arise causing the intensive oscillations even in the weakly nonlinear system.At multi frequency external signal , the

stochastic instability development appears to be the most probable if the spacing between frequencies approaches closely to Δ_s or is Δ_s - fold.

At low-frequency beam modulation, the chaotic instability may arise at the modulation frequencies even much more less then Δ_s which is in contradiction with a traditional representation that the chaotic oscillation should not arise as in this case the system turns to be adiabatic in its character. Not only are scenarios and conditions arising the chaotic oscillation in the cases considered being identified but the corresponding methods are developed to prevent their initiation.

REFERENCES

(1) D.M.Vavriv, and O.A.Tretyakov : "Nonautonomous oscillations in resonant generators with distributed interaction", Radiotekhnika i elektronika, **29**, 8, pp.1580-1588 (1984).

(2) D.M.Vavriv, and O.A.Tretyakov : "Synchronization of oscillations in resonant generators with distributed interaction", Radiotekhnika i elektronika, **29**, 9, pp.1798-1805 (1984).

(3) D.M.Vavriv: "Frequency transformation in resonant systems with distributed interaction", Izv. Vuzov - Radiofizika, **28**, 8, pp.1035-1042 (1985).

(4) A.B.Belogortsev, D.M.Vavriv, and O.A.Tretyakov: "Stochastic oscillations in quasi linear oscillatory systems", Zh. Tekh. Fiz.,**58**, 2, pp.284-293 (1988).

(5) S.A.Bulgakov, and D.M.Vavriv: "Interaction of low and high frequency oscillations in resonant distributed systems", Radiotekhnika i elektronika, **36**, 3, pp.520-527(1991).

RADIATIVE DAMPING OF TWO-DIMENSIONAL PLASMONS IN AN OPEN STRUCTURE WITH A METAL GRATING

O.R.Matov, O.V.Polishchuk, V.V.Popov
Institute of Radioengineering & Electronics of the Russian Academy of Sciences, Saratov branch, 410720 Saratov, Russia.

In experiments on resonant FIR absorption by two-dimensional (2D) plasmons in thin semiconductor space-charge layers [1] a metal grating (Fig.1) with periodicity $L<<\lambda_{FIR}$, here λ_{FIR} is the electromagnetic wave length, is used to couple FIR radiation to 2D plasmons having wave vectors $q=2\pi m/L$ $(m=1,2,3,...)$. This means that one observes 2D plasmons at the centre of the first Brillouin zone if we bear in mind the reduced band scheme of the periodic grating structure. As it is known [2], these plasma waves are subjected to additional damping via radiative decay.

In the FIR absorption experiments the width of the 2D plasmon resonance is about three times larger than the theoretical value defined by the dissipation of the plasmon energy in the 2D plasma layer. The radiative damping is expected to be one of the possible reasons for this. On the other hand, the radiative decay of non-equilibrium 2D plasma waves is a promising mechanism to be used for the development of a submillimeter electromagnetic wave radiator with the emission power of a milliwatt level [3].

In the weak coupling approximation it has been shown [2] that the radiative damping is expected to be small as compared to the dissipative one. But the experimental conditions [1] are much beyond the limits of the perturbation theory approach.

We have calculated the frequencies and the radiative damping for 2D plasma waves at the centre of the first Brillouin zone in

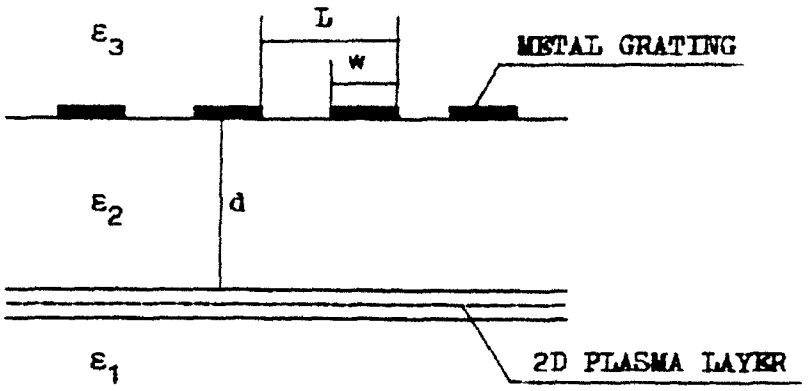

Fig.1 Structure under consideration. The two-dimensional plasma layer is separated from a metal grating by a dielectric slab with the thichness d. L and w are the grating periodicity and strip width, respectively. ε_1, ε_2 and ε_3 are the electrical permeabilities of the media.

the strict electromagnetic approach. Within the framework of this approach the metal grating is treated as a plane periodic array of perfectly conductive strips. Galerkin's method is used with the expansion of the current density distribution on the strips in terms of Chebyshev's polynomials to satisfy the edge conditions at the edges of the strips.

2D plasmons with a wave vector $q=2\pi/L$ are most strongly coupled to a radiation field [1] and corresponding resonance is well pronounced in the FIR absorption experiments. Fig.2a shows the frequency ω_1 and the radiative damping Γ_1 of 2D plasmons with a wave vector $q=2\pi/L$ as a function of the ratio d/L, where d is the thickness of the dielectric slab. The radiative damping is the most considerable ($\Gamma_1/\omega_1 \sim 0.15$) when $d/L \sim 10^{-4}$. for values

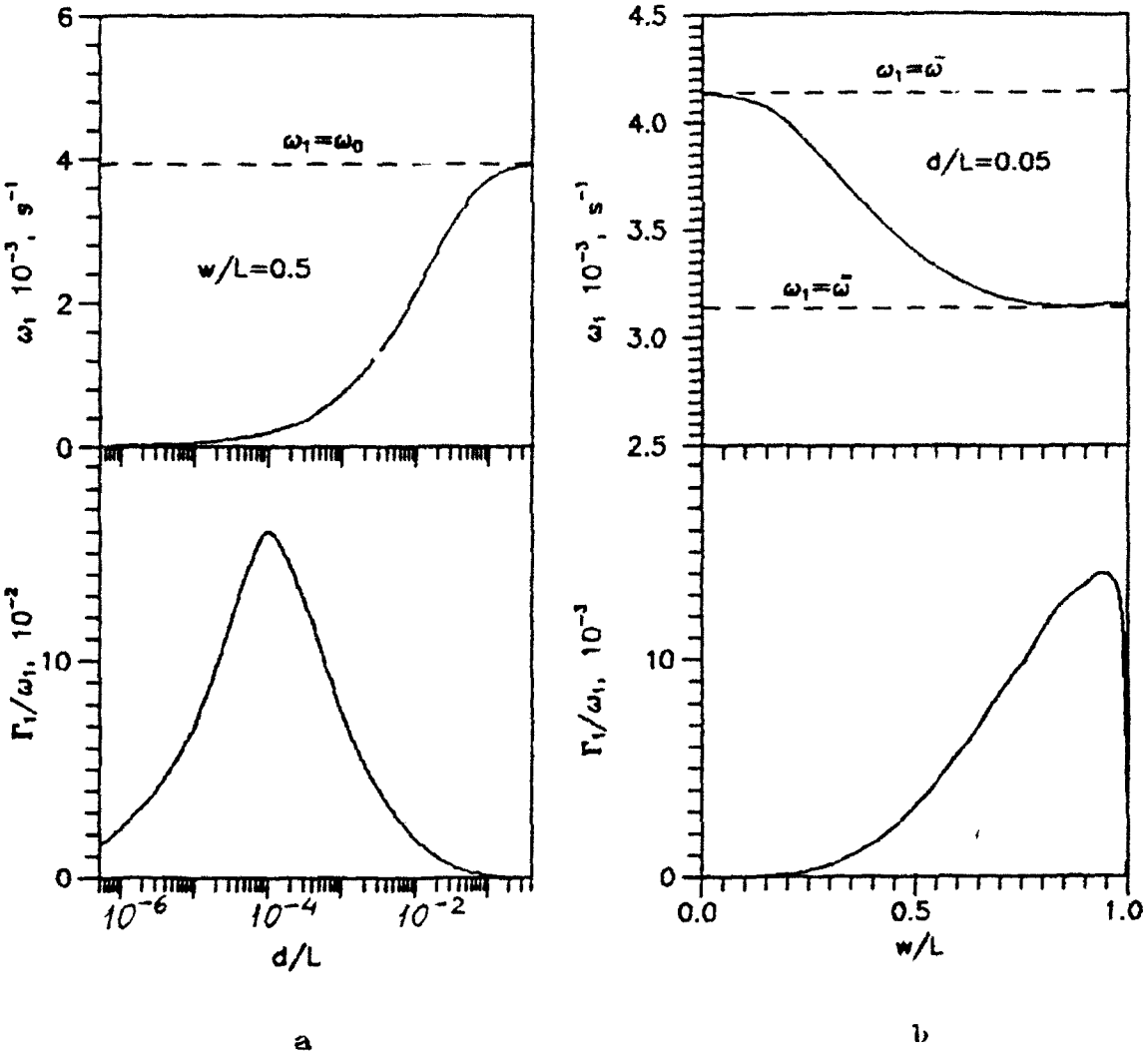

Fig.2. Frequency and radiative damping of 2D plasmons with a wave vector $q=2\pi/L$ as a function of the ratio d/L (a) and ratio w/L (b). $\varepsilon_1=1$, $\varepsilon_2=4$, $\varepsilon_3=12$, $N_s=1.5\times10^{11}cm^{-2}$, $L=2\times10^{-3}cm$. ω_0 is the frequency of 2D plasmon at the single interface of media 2 and 3. $\bar{\omega}$ and $\bar{\bar{\omega}}$ are the 2D plasmon frequencies for the structure without any grating and with a continious perfect screen, respectively.

$d/L \lesssim 0.1$ which are usually used in the FIR absorption experiments the greatest radiative damping $\Gamma_1/\omega_1 > 0.01$ takes place when the ratio $w/L \approx 0.95$, where w is the width of the grating strips (Fig.2b). This value of Γ_1/ω_1 is two orders of magnitude larger than expected from the perturbation theory [2]. It makes us conclude that the radiative damping may contribute a substantial part to the whole observed linewidth of the plasmon resonance. For the characteristic parameters of experiments [1] $\omega_1 = 3.5 \times 10^{12} s^{-1}$, $\varepsilon_1 = 1$, $\varepsilon_2 = 11.0$ (AlGaAs), $\varepsilon_3 = 12.8$ (i-GaAs), $L = 8.7 \times 10^{-5}$ cm, $d = 8 \times 10^{-6}$ cm, $w/L \sim 0.9$ and the areal density of electrons $N_s = 6.7 \times 10^{11} cm^{-2}$ we obtain $\Gamma_1/\omega_1 \sim 8 \times 10^{-3}$. This is roughly a half of the dissipative linewidth defined by the experimental value of the relaxation time $\tau = 7 \times 10^{-12}$ s. Nevertheless, this considerable radiative broadening can not explain the whole linewidth observed experimentally. The additional broadening may be caused by some other reasons, for example, ohmic losses in the metal grating strips and dielectric losses in the AlGaAs slab [1].

---

1. E. Batke, D. Heitmann, C.W. Tu, Phys. Rev., B34 (1986)6951.
2. M.V. Krasheninnikov, A.V. Chaplik, Zh. Eksperim. Teor. Fiz., V.88(1985)129.
3. T. Kobayashi, N. Okisu, Y. Sambe, In: High-Speed Electron. : Basic Phys. Phenom. and Device Princ. Int. Conf., Stockholm, Aug. 7-9, 1986.- Berlin, e.a. (1986), P.88.

THEORY AND DESIGN OF A NEW SMITH-PURCELL AMPLIFIER

Yuriy A. Romantsov

Institute of Radio Astronomy, 4 Krasnoznamennaya St.,
310002 Kharkov, Ukraine
Phone: (7-0572) 447-818 Fax: (7-0572) 322-320

ABSTRACT. A new promising type of the Smith-Purcell amplifiers of millimeter & submillimeter wave bands has been suggested. The main elements of construction are an open resonator with the distributed interaction and a special electronic gun with the field-emission cathode whose auto electronic emission current is modulated by the microwave input signal. The fundamentals of constructing such devices are discussed, the most promising designs being pointed out. On the basis of the theory developed, particle-field interaction in such devices are analyzed in details and the ultimate output parameters of the amplifiers are estimated.

INTRODUCTION. The creation of effective resonance amplifiers of millimeter & submillimetric waves is one of perspective directions in the development of electronic devices based on Smith-Purcell effect [1,2]. Due to the employment of an open resonators with distributed interaction the possible output characteristics of multi-resonator Smith-Purcell amplifiers surpass to a marked degree klystrons of millimeter wave band [3].

The main obstacle for the practical realization of this type devices is a large extension of an interaction space of input section, necessary for effective electron beam bunching by the injected signal. This essentially complicates opto-electronic & electrodynamic systems of a design. Therefore, at present time we have a prototype only of one-resonator regenerative amplifier on the base of orotron resonance system [4]. The report deals with the new type of Smith-Purcell amplifier - **orofemitron** (open resonator field emission microwave tube). It seems to us the perspectiveness of a **orofemitron** is stipulated by the use in one design of the most effective in millimeter & submillimeter wave band orotron

electrodynamic system and of the auto electronic cathode current microwave modulation phenomena [5]. This technique of electron beam current microwave modulation showed its effectiveness in **femitrons** -amplifiers & multipliers of X-band [5] as well as in gigatrons [6] & devices of vacuum micro electronics [7], developed at present time.

OROFEMITRONS DESIGN & PRINCIPLE OF OPERATION. The main elements of **orofemitrons** structure are an open resonator with the diffraction grating on one of the mirror and a special electron gun with the auto electronic emission cathode and input device of injected signal. It is designed for shaping of a strip electronic flow modulated in density by the input signal. The gain value of current modulation and its spectrum are controlled by the bias voltage Us at the auto cathode according to the **Fowler-Nordheim** rule of field emission [8]. Further, the modulated electron flow enters in output open resonator & exc : it due to the Smith-Purcell radiation which arises during the passage of electron beam above diffraction grating and distributed interaction of electrons with the periodic structure slow wave.

The input signal power increases due to the sharp slope of current-voltage characteristic of field-emission cathode and due to the effective distributed interaction of electron beam with the open resonator field ,as well as due to the increase of beam power under additional acceleration of shaped electron bunches between cathode and output resonator in the case when this acceleration is necessary for particle-slow wave synchronism.

THEORY & RESULTS. The theory of physical processes arising within the **orofemitron** and estimations of its output parameters are based on the well-known and reliable mathematical model of microwave modulation of field-emission current [5] and on joint solution of Maxwell's equations & equations of beam-particles motion for oscillating systems with distributed interaction [2].

For the amplification mode of low signal (input signal voltage Um << bias voltage Us) we observe the strong dependence of

maximum power gain factor of orofemitron

$$K_{max} \sim g_0^2 \, (Ua / Us) \, / (1-J)^2 \sim 30 \div 35 \text{ dB}$$

upon: the relative slope $g_0 = (Us/Ic(Us)) \, dIc/dUs$ of current-voltage auto emission cathode characteristic Ic(Us) ; the ratio J=Ic/Ist between Ic and current Ist of self-excited oscillations of output resonator if J<1 and acceleration voltage Ua to field cathode bias voltage Us ratio. The high quality factor Q~1000 of the open resonator in millimeter wave band and efficiency of distributed beam-field interaction allow to realize the values $J \sim 0.5 \div 0.8$ under beam current Ic ≤ 1A. The use of low -current electron beams not only increases the reliability of field-emission cathode operation ,but also allows to decrease the operating voltage Us in comparison with the Ua. These factors stipulate for the higher orofemitron design values K_{max} in comparison with the femitron where J<<1 & Ua/Us =1.

In the mode of power gain (Um/Us ~ 0.1 ÷ 0.5) the maximum achievable efficiency equal to ~ 70÷80 % of relativistic & nonrelativistic orofemitrons are reached not only due to the possibility of high bunching but also due to the optimal conditions of electron bunch - resonator field slow wave interaction. The results of numerical and analytical optimization of resonator & beam parameters [9] showed that maximum achievable efficiency of orofemitron is determined by four main parameters: particle velocity Vo, radius of a field spot R in an open resonator ,wave length of the signal λ and phase velocity of the slow wave Vph

$$\eta_{max} \simeq 2.4 \, (\lambda Vo/cR)[1. - 0.75 \, \gamma_f^4 \, \lambda Vo/cR/(1+2\gamma_f^2)] \, \gamma_f^4/(1+2 \, \gamma_f^2)$$

where: $\gamma_f = (1 - V_{ph}^2/c^2)^{-1/2}$; c- velocity of light; $Vo/V_{ph} \simeq 1 + 0.5/\gamma_f^2$. For open oscillating systems the condition R≥λ is satisfied, that's why maximum achieved efficiencies are determined mainly by the values of accelerating voltage (Vo) and parameters of diffraction grating (Vph).

CONCLUSION. The results of systematic analysis allow to make a conclusion that orofemitron is a promising amplifier of low

signals and of power in millimeter & submillimeter wave length bands .The latest achievements in the field of vacuum micro electronics and of miniature short-focus open resonators [10] used during development of orofemitron allow to create compact amplifiers of high stability with the gain coefficient K≃ 30 dB under output power Po≃1÷10kW and efficiency factor $\eta \simeq 50 \div 70$ % in the middle range of millimeter waves.

REFERENCES

(1) A.Gover & A.Yariv,Appl.Phys.,vol.16,p.121 (1978).

(2) D.M. Vavriv and O.A.Tretjakov,Theory of Resonance Amplifiers with distributed interaction,"Naukova Dumka",Kiev,Ukraine,1989.

(3) D.M. Vavriv & Yu.A. Romantsov:"Current status and furher progress in the Smith-Purcell amplifiers research",21st European Microwave Conference proceedings,vol.1,p.824 (1991).

(4) V.K.Korneenkov & V.S.Miroshnichenko,Izv.Vuzov.Radioelectronica, vol.26,no.3,p.93 (1983).

(5) F.M.Charbonnier,J.P.Barbour,L.F.Garret,W.P.Dyke, Proceedings of the IEER, vol.51, n.7, p.989, July 1963.

(6) H.M.Bizek ,P.M.McIntyre ,D. Raparia ,C.A. Swenson ,Trans.Plasma Sci.,vol.16,n.2,1988.

(7) First Int.Vacuum Micro electronics Conf.Williamsburg,Virginia, USA, 13-15 June 1988.

(8) R.H. Fowler & L.W.Nordheim,"Electron emission in intense electric fields" ,Proc.Roy.Soc.(London) A,vol.119,p.173;May, 1928.

(9) Yu.A.Romantsov ,"The investigation of relativistic particles dynamics in the resonant system with distributed interaction", Preprint n.47,Inst.of Radio Astronomy,Kharkov,Ukraine,1990.

(10) A.V.Nesterenko, A.I.Tsvyk, V.P.Shestopalov, Dokl.Ac.of.Sci. of USSR, vol.277,n.1,p.84,1984.

DISTRIBUTED INTERACTION OF OPEN RESONATOR FIELDS WITH SEMICONDUCTOR

V.A.Abdulkadyrov, I.D.Revin

Institute of Radiophysics and Electronics, Academy of Sciences of the Ukraine, 12 Acad. Proskura st., 310085 Kharkov, the Ukraine

The report presents some features of the interaction of a drifting flow of charge carriers in a semiconductor with space-inhomogeneous fields of the open resonators (OR). Diffraction grating is placed in the OR. Synchronous component of the S-th space garmonic has the form

$$E = A_S C_m C_n \Psi_m(x) \Psi_n(y) e^{-ih_s \cdot z + i\alpha_s y}, \qquad (1)$$

where

$$\Psi_m(X) = exp\left(-\frac{\kappa X^2}{2A_x}\right) H_m\left(\sqrt{\frac{\kappa}{A_x}} X\right); \quad \alpha_3 = \kappa \frac{C}{V_{phs}};$$

$$\Psi_n(y) = exp\left(-\frac{\kappa y^2}{2A_y}\right) H_n\left(\sqrt{\frac{\kappa}{A_y}} y\right); \quad h_s = \kappa \sqrt{\frac{C}{V_{phs}} - 1};$$

$$C_m = \sqrt[4]{\frac{A_x}{\kappa}} \left(\sqrt{m! \cdot 2^m \sqrt{\pi}}\right)^{-1}; \quad C_n = \sqrt[4]{\frac{A_y}{\kappa}} \left(\sqrt{n! 2^n \sqrt{\pi}}\right)^{-1};$$

$$A_{xy} = \sqrt{L(z_{xy_0} - L)};$$

V_{ph} is the phase of velocity of S-th space harmonic; H_m, H_n are the Hermite polynomials; A_s is the amplitude of S-th space harmonic; z_{xy_0} are the radii of the mirror's curvature.

An effective interaction of the drifting carriers flow in the semiconductor with a field (1) is possible when the conditions of synchronism are being fulfilled in space and time. It is easy to show that excitation of emergent radiation is also possible when the resonance between resonance and transit frequencies is being fulfilled.

$$w \simeq \frac{2\pi}{\ell} V_0 |S|,$$

here V_0 is the velocity of carriers drift, ℓ is the period of structure. The drifting flow is described in the frames of a quasi-

hydrodynamic model in a semiconductor. Determine the complex power of the interaction in the form

$$P = \frac{i\omega\Theta_n B_n g a_T}{16\pi h_p \gamma} \sum_{j=01} (1)^j \int_{-\infty}^{\infty} \frac{|\tilde{E}(K)|^2}{h_j - K} dK \qquad (2)$$

here Θ_n is the coefficient of using the drifting flow; B_n is the amplitude of average of the cross-section of flow of the synchronous harmonic's field, $\tilde{E}(K)$ is the spectral density of the synchronous field, K - is the spectral wave number:

$h_j = \left[h_o\left(1+i\frac{\nu}{2\omega}\right)+(-1)^j h_p\gamma\right]a_T$ - is the propagation constant of waves of the space charge (WSC): $h_o = \frac{\omega}{V_o}$; $h_p = \frac{\omega_p}{V_o}$;

$$\gamma = \left\{a_T - \frac{\omega^2}{\omega_p^2}\left[a_T\left(1+i\frac{\nu}{\omega}\right) - \left(1+i\frac{\nu}{2\omega}\right)\right]\right\}^{\frac{1}{2}};$$

ω, ω_p are the electromagnetic and plasma frequencies, correspondingly. The first addend (2) determines the efficiency of the power-exchange of slow WSC with space-inhomogeneous fields of OR, the second one is the quick WSC. To separate a real and imaginary parts of the expression (2) and an imaginary part of the expression (2) one may by means of the expansion of its analytical function determined by the cauchy integral along the real axis on degrees h''_j [1] and using the integral Gilbert transformation.

A complex power of the interaction of the drifting carriers flow in a semiconductor with a wave beam of OR at $\nu \simeq 2\omega_p$ one may represent in the following form

$$P = P_o \cdot F_m(\varphi, \varphi_\nu),$$

$$P_o = \frac{\omega g \Theta_n B_n^2 d_y^2}{8}, \quad \varphi_\nu = \frac{\nu}{2V_o} d_y$$

$$F_m(\varphi,\varphi_y)=\frac{\sqrt{\pi}}{2^{m+2}m!}\left\{\frac{2m\,H_{m-1}(z)}{H_m(z)}T_m(z)-\right.$$

$$\left.-\frac{H_m(z)}{H_{m+1}(z)}T_{m+1}(z)\right\};\qquad z=\frac{\varphi+i\varphi_y}{2\sqrt{2}};$$

$$T_m=H_m^2(z)\,w(z)+\frac{2}{\sqrt{\pi}}H_m(z)\sum(-1)^s C_m^n\cdot H_{m-s}(z)\cdot$$

$$\cdot H_{s-1}(-iz);\qquad C_m^n=\frac{m!}{(m-s)!}$$

$\varphi=\left(\frac{2\pi\varrho}{e}-\frac{h_o}{a_T}\right)$ – is the parameter of missynchronism; d_y is the diameter of the field's spot of the main oscillation type; $\nu=\sum_i \nu_i$, ν_i are the frequencies of collisions corresponding to the concrete mechanism of carriers scattering in a semiconductor; V_T is the heat velocity; $w(z)$ is the complex integral of probability.

In Fig. (a and b) are given graphs of functions $Re\,F_o(\varphi,\varphi_y)$ and $Im\,F_o(\varphi,\varphi_y)$ which determine the change of active and reactive power components of the interaction of the drifting electron flow of conductivity with the fields of the main type depending on the parameter of missynchronism for three meanings

1.-$\varphi_y=0$; 2. $\varphi_y=0.5$; 3.-$\varphi_y=1$.

In Fig. (c and d) analogous dependences corresponding to the first ($m=1$) highest type of OR oscillations are given-

References

1. Stix T. The Theory of Plasma Waves. M.1965 (in Russian).

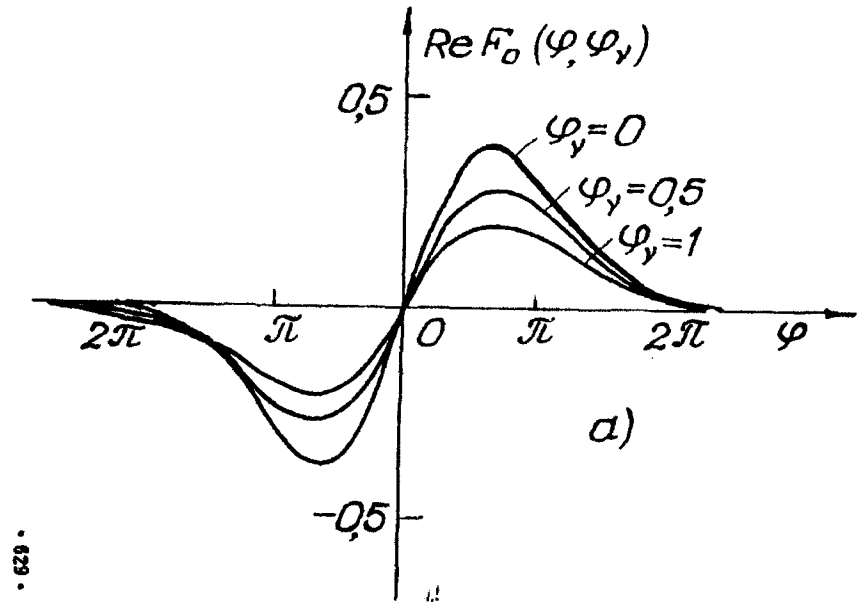
Re F₀ (φ, φᵧ)
0,5
φᵧ=0
φᵧ=0,5
φᵧ=1
2π
π
0
π
2π
φ
-0,5

а)

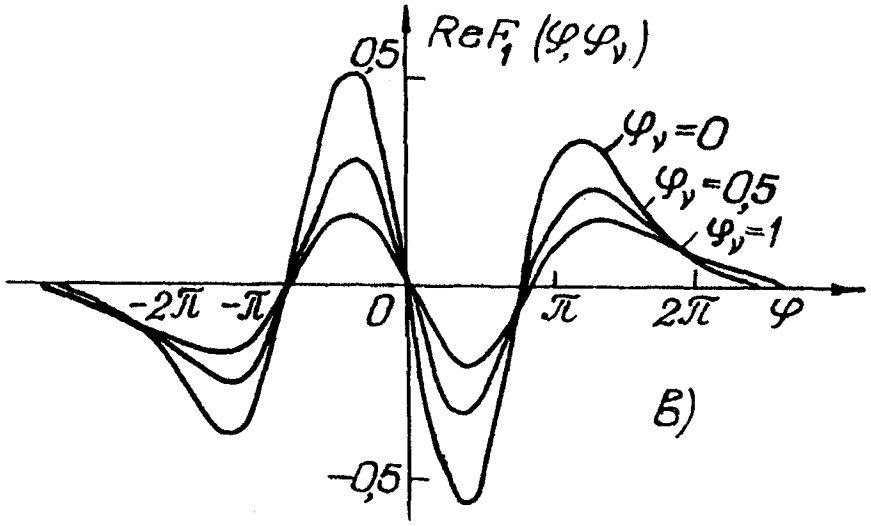
Re F₁ (φ, φᵧ)
0,5
φᵧ=0
φᵧ=0,5
φᵧ=1
-2π
-π
0
π
2π
φ
-0,5

б)

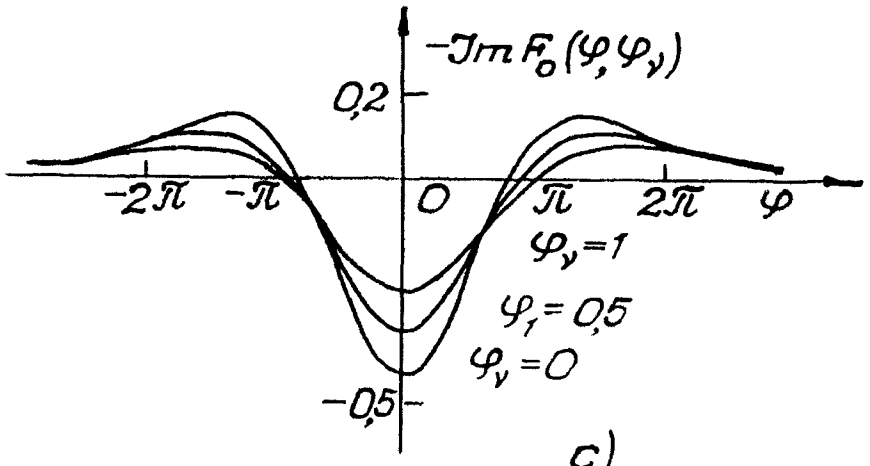
-Im F₀ (φ, φᵧ)
0,2
-2π
-π
0
π
2π
φ
φᵧ=1
φᵧ=0,5
φᵧ=0
-0,5

в)

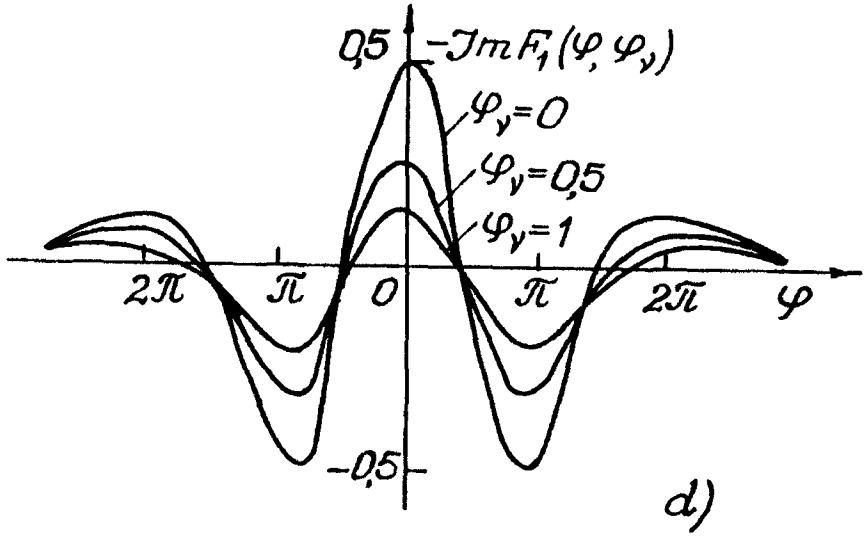
0,5
-Im F₁ (φ, φᵧ)
φᵧ=0
φᵧ=0,5
φᵧ=1
2π
π
0
π
2π
φ
-0,5

д)

· 629 ·

SUPERSLOW WAVES IN PERIODIC STRUCTURES

A.A.Bulgakov and V.D.Korolev

Institute of Radiophysics and Electronics,
Acad. of Science of Ukraine, 12 Proscura st.,
310085 Kharkov , Ukraine

It is known that developing of millimeter and submillimeter (MSM) wavebands is impossible without active elements. Up to date the devices using quantum superlattices and ballistic motion of carriers in submicrone structures are of first rate importance.

In this report we should like to attract attention on a possibility of the creation of semiconductor elements of MSM bands without complicated submicron technology. Distributed interaction of drift carriers in a semiconductor with slow electromagnetic waves is the mechanism which put into effect an instability of electromagnetic waves similar to that one in a travelling-wave tube or back-wave tube. In order to put into operation such interaction it is necessary to provide an equality of velocity of semiconductor drift carriers and propagation wave velocity. It is known that drift velocity is a less than heat velocity, i.e. it has an order of 10^7-10^8 cm/s. In addition, on electromagnetic wave in a solid state propagates with velocity $\sim c/\sqrt{\varepsilon}$ ($c = 3\times10^{10}$ cm/s is the vacuum light velocity, ε is the dielectric permeability), i.e. approximately is equal to 10^9 cm/s. Velocities of surface plasmons and magnetic plasmons also considerably exceed drift velocities [1]. Thus, it is necessary to increase carrier velocities by two or three orders or slow down an electromagnetic wave in order to obtain this synchronism. For increasing velocities it is possible to use ballistic motion of carriers in submicrone structures. In another case we propose to make use the layer-periodical structures consisting of semiconductor and dielectric layers [2].

In vacuum electronics comb-periodic structures became common use to obtain delay. The mechanism of delay in such structures is possible to consider as follows. A period of the structure is a resonator for the electromagnetic wave. The difference of oscillation phases between different resonators leads to propagation of a slow wave along the periodic structure. That velocity of propagation seems as low as we want in the case of almost zero phase difference between adjacent resonators, but it is difficult to realize this situation on account of wave damping calling into action phase erosion. Usually in the

periodic structures delay is of the order of 100.

There are some "resonant" types of waves in semiconductors: surface and volume plasmons and magnetic plasmons. Without damping velocities of these waves can be very low, but in practice damping is relatively high even in pure semiconductors. Therefore velocities of "resonant" waves differ slightly from the light velocity in vacuum. Another situation can be realized in the layer-periodic structure including the layers of a semiconductor ($\varepsilon_1 = \varepsilon_{01}\left[1 - \frac{\omega_p^2}{\omega(\omega + i\nu)}\right]$, where ε_{01} is the dielectric permeability of the lattice, ω_p is the plasmon frequency, ν is the effective frequency of collisions; d_1 is the thickness of the layer) and dielectric (ε_2, d_2). In Fig.1 dispersion curves for non-damping structures are shown

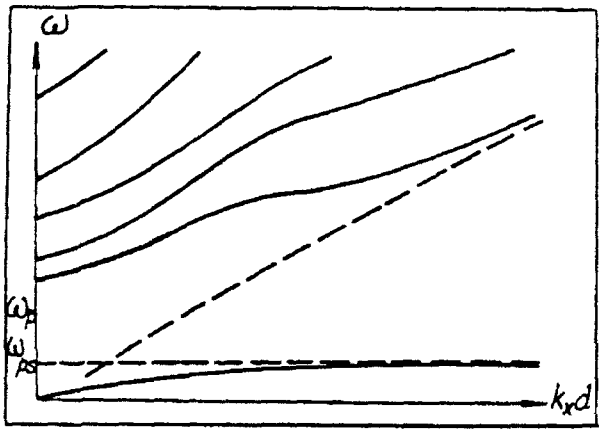

Fig.1.

(k_x is the component of the wave vector directed along layers, $d = d_1 + d_2$ is a period of the structure). It is shown that the lower curve asymptotically tends to the frequency of the surface plasmons $\omega_{ps} = \omega_0 / \sqrt{\varepsilon_{01} + \varepsilon_2}$ (ω_0 is lengmur frequency) propagating along boundaries of the dielectric and semiconductor. Another dispersion curves correspond to the frequency higher than ω_p. In this region the layer-periodic structure behaves like the dielectric lattice. The field structure of the lowest dispersion curve is schematically introduced in Fig.2a for volume and Fig.2b for the surface waves.

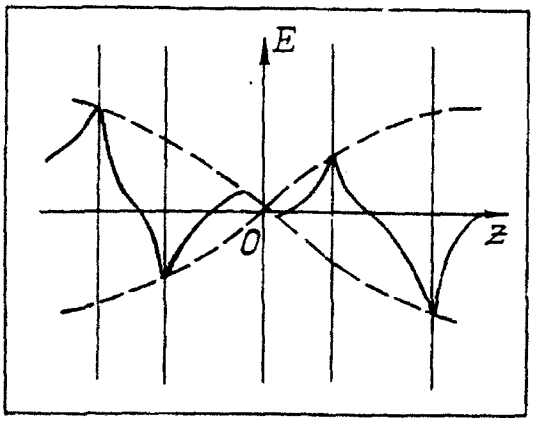

Fig.2a.

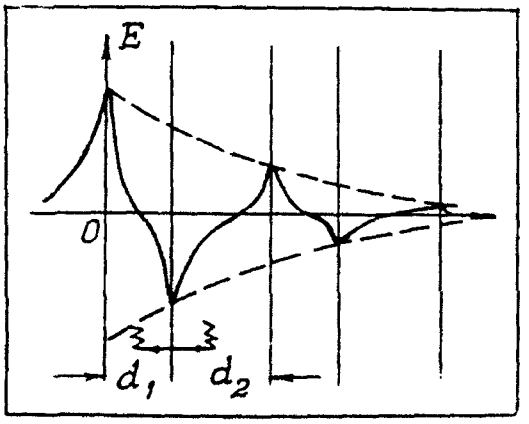

Fig.2b.

Dashed curves are envelopes for the field distributions inside the layers. It is shown from figures that in the infinite structure the field has a periodical character although inside a layer it decreases exponentially from the boundary. In the finite lattice the field decreases exponentially deep into the structure.

The dispersion curve changes its form if we take into account damping in semiconductor layers [3,4] (Fig.3). The longitudinal wave number can be written in form $k_x = k'_x + ik''_x$ and we find that

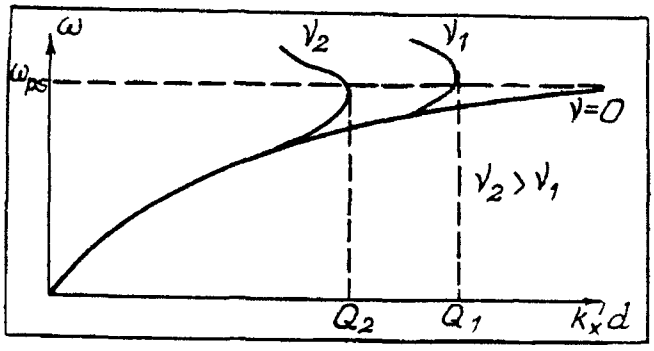

Fig.3.

$$k'_x d \simeq -\ln\left[\frac{\nu}{\omega_{ps}}\,\frac{\varepsilon_{oi}+\varepsilon_2}{\varepsilon_2}\right], \qquad (*)$$

$$k''_x d \simeq -\operatorname{arctg}\left[\frac{\omega_{ps}}{\nu}\right].$$

If frequency of collision $\nu \to 0$, than $k'_x d \to \infty$ and $k''_x d \to -\pi/2$. It is impossible that the value of $k'_x d$ is grater than the value given by formula (*). Let $(k'_x d)_{max} = Q$. The value of Q have been calculated for different structures with InSb as a semiconductor ($\varepsilon_{oi} = 16.7$, $\nu \simeq 10^{11}$ s^{-1}, $\omega_p \simeq 10^{12}$ s^{-1}) and dielectric layers ($\varepsilon_2 = 5$). We have obtained $Q = 2..4$ for the infinite structure, with the magnetic field $Q = 10..15$; for a surface wave in the semi-infinite structure $Q \simeq 50$; in the structure in a metal substrate $Q \simeq 50..70$.

Let us estimate the minimum phase velocity by the formula

$$\nu_{ph\ min} = \frac{\omega_{ps} d}{Q}.$$

The value of the structure period d is restricted by the formula application of the dielectric permeability. Therefore we have assumed $d \simeq 3..10$ μm for the estimations. In this case phase velocity $\nu_{phmin} \simeq 10^{6}..10^{8}$ cm/s with $\omega_{ps} \simeq 10^{12}$ s^{-1}. The great decay is obtained due to the fact that the investigated wave attenuation is less than in a homogeneous semiconductor since the wave energy concentrated in general in the low losses dielectric layers. In fact, the field in the semiconductor is proportional to $\exp(-\xi\sqrt{k_x^2 + |\varepsilon_1|\omega^2/c^2})$ and in the dielectric ~ $\exp(-\xi\sqrt{k_x^2 - \varepsilon_2\omega^2/c^2})$, where ξ is the coordinate counted from the boundary between the semiconductor and dielectric (see Fig.2). Thus, semiconductor layers define dispersion properties of the structure, and dielectric layers define wave

damping. As a result, the low damping electromagnetic wave propagation with the low phase velocity is possible.

1. Kaner E.A.,Yakovenko V.M. *Gidrodinamicheskie neustoichivosty v tverdotel'noy plasme*, Usp.Fis.Nauk , 1975, v.115, p.1,p.41.
2. Bass F.G.,Bulgakov A.A., and Tetervov A.P. *Visokochastotnie svoystva poluprovodnikov so sverhreshetkamy* , Moscow , Nauka, 1989, 288 p.
3. Alfano R.R. Damping effects on the polariton and plasmariton dispersion curves in *n*-GaAs, J.Opt.Soc. of Amer., 1970, v.60, N 1, p.66.
4. Covner G.S.,Alexander R.W., Bail R.G. and Jr.J. Surface electromagnetic waves with damping, Phys.Rev.B, 1976, v.14, N 4, p.1458.

FAR INFRARED AND MILLIMETER WAVES SPECTROSCOPY BY USING SYNCHROTRON RADIATION

Takao Nanba

Department of Physics, Faculty of Science, Kobe University, Nada-ku, Kobe 657, Japan

ABSTRACT

The synchrotron radiation from the electron storage ring is a powerful light source even in the far infrared and millimeter wave regions as in the vacuum ultra violet and X-ray regions. The actual utilization of the synchrotron radiation for the solid state spectroscopy on condensed matter in the far infrared and millimeter waves has started in 1986 at the UVSOR, the synchrotron radiation facility at Okazaki (Japan) and successively in 1989 at the NSLS (Brookhaven, USA). To demonstrate the advantage to use the synchrotron radiation instead of conventional black body sources , experiment under high pressure using a diamond anvil cell in the far infrared region and experiment on ionic super conductor in the millimeter wave region are described.

§1 INTRODUCTION

The synchrotron (SR) is a light source which covers continuously a very wide energy region from the microwave to the x-ray. However, the SR has not been employed until 1986 in the long wavelength spectroscopy although the SR has many excellent properties such as high brightness (photon numbers per unit area-solid angle product), continuous spectral distribution over the entire energy region, its precise time structure in the nano-second time domain and so on.

After preliminary experiments at the SRS (Daresbury, UK) [1] and the BESSY (Berlin, Germany) [2], spectroscopic system was constructed in 1985 at the beam line BL6A1, which is dedicated exclusively for the far infrared spectroscopy, of the UVSOR (Okazaki) and its practical utilization has started since 1986 [3] and successively at the NSLS since 1989 [4]. Many kinds of experiments at the UVSOR up to now proved that the SR delivers more intense photon flux over a high pressure mercury arc lamp in the far infrared and millimeter (MM) wave regions.

The purpose of the present paper is to describe the present status of the experiment on solid state spectroscopy in the far infrared and MM wave regions at the UVSOR.

§2 EXPERIMENT UNDER HIGH PRESSURE WITH A DAC

To compare the intensities of both sources, the SR and a 125 W high pressure mercury lamp, the light intensities from both sources were independently measured using the same spectroscopic system. The light intensity was measured as the function of the aperture at the sample position on which the light is focussed with

an optics of F/5.6 in the sample chamber.

Fig. 1 shows the ratios of the light intensity at 100 μm of the SR to that of the mercury lamp through different apertures. The intensities of the SR were normalized to that in operation of 100 mA. From this result, the boundary size of the aperture is 11 mm in diameter at which the intensity of the mercury lamp is equal to that of the SR at the ring current of 100 mA. This means that more photon flux with the SR than with the mercury lamp is acceptable into a detector in experiment where a sample acceptance is limited such as experiment under high pressure using a diamond anvil cell (DAC). We installed a spectroscopic system under high pressure using a DAC to perform study on a pressure-induced phase transition of condensed matters. The precise description of the spectroscopic system was described elsewhere[5,6]. Here, we describe the experimental outline in brief. We made a so-called lever-arm type of a DAC which is installed on the bottom of the liquid helium cryostat in the sample chamber. The pressure induced in the diamond anvil cell was measured by a conventional fluorescence measurement technique of a ruby. A ruby chip was immersed as a pressure sensor together with the sample in the liquid paraffin within the pressure cell. The light intensity through the DAC was detected by a liquid helium cooled bolometer.

By using this high pressure apparatus, we measured the transmission spectrum of alkali halide to know the change in the phonon spectrum of alkali halides due to the phase transition. It is well known from a x-ray diffraction measurement that alkali halide shows a first order phase transition from a B1 phase (rock salt structure) to a B2 (cesium chloride) under pressure as shown in Fig. 1. However, up to now, the observation of such spectrum under high pressure is quite rare because its difficulty of experiment.

Fig. 2 shows the development of the phonon spectra of Rubidium Iodide (RI) with the pressure (P) at room temperature. RI was evaporated in advance onto the culet surface of one of the diamond anvils which form the pressure cell. The thickness of the film was 2.8 μm. A stainless steel gasket was used. The thickness and the diameter of the pinhole were 0.2 and 0.7 mm. The pressure is shown in each spectrum. The sharp dip which corresponds to the TO phonon energy is shown by a downward arrow in each curve. The TO phonon showed a clear blue energy shift with the increase in the pressure in the B1 phase (lower three curves). The TO phonon energy was suddenly reduced after the phase transition to the B2 which occurs at 0.34 GPa [7]. In the B2 phase, the TO phonon showed a blue shift (higher three curves). From the energy shift of the TO phonon versus the pressure, the mode gruneisen parameters in the both B1 and B2 phases and the TO phonon energy in the B2 phase were reduced for the first time. The details of the experimental results on other alkali halides is also to be given.

§3 MM wave absorption of ionic super conductor

A collective motion of free carriers (electron or hole) in a conduction band is called as a plasmon. The onset of the absorption due to the excitation of the plasmon locates usually in the near infrared - visible region and its energy is a so-called plasma frequency which is given by the

equation

$$\omega_p^2 = 4\pi e^2 N / m^* \quad (1)$$

where N is a density of free carriers in the conduction band and m^* the effective mass of the carrier. A corresponding metallic reflectivity shows a sharp rise at the plasma frequency towards the lower energy. Super ionic conductor is an insulator at low temperature. However, ion becomes unstable and makes a thermal diffusion in the solid above the critical temperature , Tc. The diffussive motion of the ions may give an plasmon state (we call it as an "ionic plasmon"). Therefore, the reflectivity of a super ionic conductor is expected to show a sharp rise due to the excitation of the ionic plasmon at the temperature above the Tc. However, such sharp rise in the reflectivity is considered to appear in the MM wave region because the effective mass of the moving ion is much larger than that of an electron or a hole and consequently the ω_p becomes much smaller according to the eq. (1).

We measured the reflectivity of alkali silver iodide super ionic conductor $RbAg_4I_5$ of which Tc = 122 K [8]. The result is shown in Fig.3. As expected to an ionic plasmon, a sharp rise only in the spectrum at 300 K above the Tc was observed [9]. The fine structure in the spectrum above 20 cm^{-1} is due to the absorption by the phonon.

CONCLUSIONS

1) The practical utilization of the SR in the far infrared region has started since 1986 at the UVSOR facility of the Institute for Molecular Science at Okazaki (Japan). The available spectral region for the measurement covers 3 to 350 cm^{-1}.

2) The absorption measurement under high pressure using a DAC is available at the UVSOR. The change in the phonon spectrum of alkali halides under pressure was done to demonstrate the advantage of the utilization of the SR in the far infrared region. The mode gruneisen parameters and the TO phonon energy of alkali halides in the B1 and B2 phases were determined for the first time.

3) The reflectivity measurement on the super ionic conductor $RbAg_4I_5$ in the MM wave region was done and the sharp rise due to the excitation of the "ionic plasmon" was found.

ACKNOWLEDGMENTS

This work was done by the visiting researcher program of the UVSOR at the Institute for Molecular Science at Okazaki in collaboration with Professor M. Watanabe, Dr. K. Fukui (Fukui University at present) and Professor H. Inokuchi of the Institute for Molecular Science. The author is grateful to them for their useful discussions and encouragement through this work. The work on super ionic conductor was done in collaboration with Dr. T. Awano of Tohoku Gakuin University (Tagajo, Japan).

REFERENCES

[1] J. Yarwood, T. Shuttleworth, J. B. Hasted and T. Nanba: *Nature* 317 (1984) 743.

[2] E. Schweizer, J. Nagel, W. Braun, E. Lippert and A. M. Bradshow: Nucl. Instrum. Meth. A239 (1985) 630.

[3] T. Nanba, Y. Urashima, M. Ikezawa, M. Watanabe, E. Nakamura, K. Fukui and H. Inokuchi: Int. J. Infrared and Millimeter Waves 7 (1986) 1769.

[4] G. P. Williams, C. J. Hirschmugl, E. M. Kmeedler, E. A. Sullivan, D. P. Siddons, Y. J. Chabal, F. Hoffmann, and K. D. Moeller: Rev. Sci. Instrum. 60 (1989) 2176.
[5] T. Nanba: Rev. Sci. Instrum. 60 (1989) 1680.
[6] T. Nanba and M. Watanabe: J. Phys. Soc. Jpn. 58 (1989) 1535.
[7] S. N. Vaidya and G. C. Kennedy: J. Phys. Chem. Solids 32 (1971) 951.
[8] B. B. Owens and G. R. Argue: Science 157 (1967) 308.
[9] T. Awano, T. Nanba and M. Ikezawa: Solid State Ionics (1992).

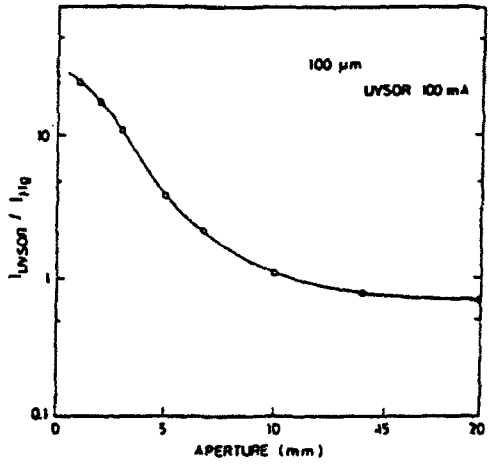

Fig. 1 The ratios of the light intensity of the SR at 100 μm to that of the mercury lamp which pass through the same aperture is shown versus the diameter of the aperture. The intensities of the SR were normalized to that in operation at 100 mA.

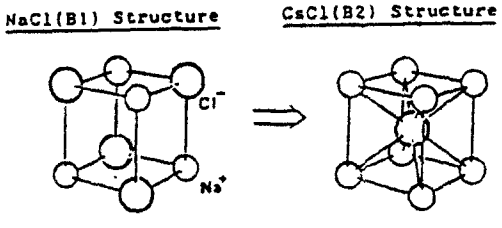

Fig. 2 The crystal structure of alkali halide at the NaCl(B1) and CsCl(B2) phase.

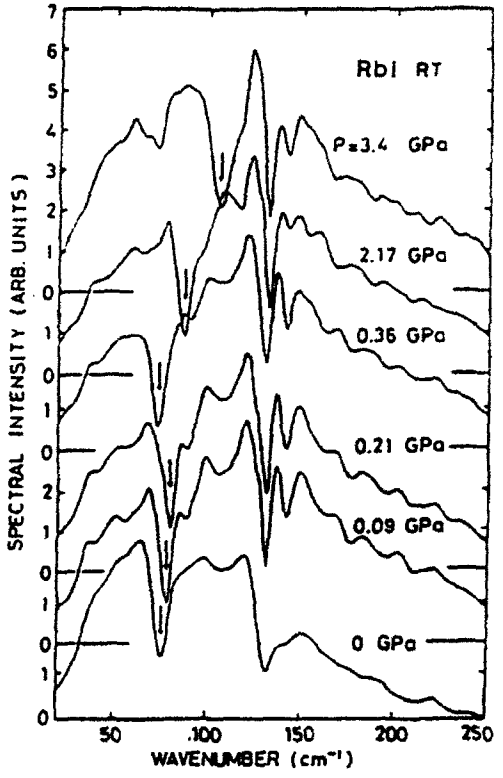

Fig. 3 Transmission spectra of RbI evaporated film of 2.8 μm thickness measured at room temperature under high pressure using a DAC. The sharp dip due to the absorption of the TO phonon mode of KI is shown by the downward arrow. A sharp dip at 132 cm^{-1} in each spectrum is due to the absorption of the cold crystalline quartz filters of the detector.

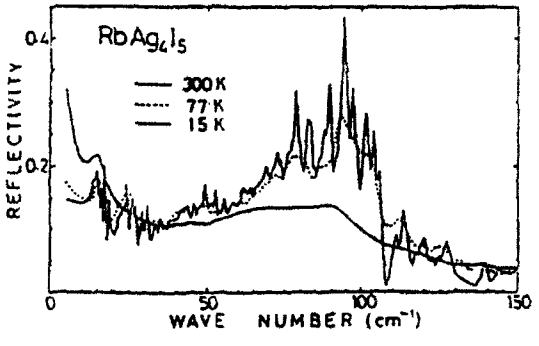

Fig. 4 The reflectivity of super ionic conductor $RbAg_4I_5$ at 15, 77, and 300 K.

Th7.2

PECULIARITIES OF FIR REFLECTION SPECTRA OF HgCdMnTe

Mazur Yu.I., Kriven S.I., Tarasov G.G., Shevchenko N.V.

Institute of Semiconductors of Academy of Sciences, Ukraine, Kiev

The main feature of lattice dynamics of multicomponent narrow gap semiconducting compounds is a great number of vibrational states with close or overlapping energy bands. Under proper symmetry conditions these states occur in resonance modifying the spectral distribution. One can reveal these modifications in IR reflection, absorption or Raman scattering spectra, their temperature and concentrational dependences. The resonance adjusting for narrow gap semiconductors is easily performed by compositional variation. It allows the lattice, band, relaxation parameters to be changed within broad limits. Another feature of interest is a proximity of electron and phonon energies leading to violation of adiabaticity criteria for such systems. New effects due to these circumstances are the subject of our $Hg_{1-x-y}Cd_xMn_yTe$ investigations.

$Hg_{1-x-y}Cd_xMn_yTe$ crystals of different compositions were synthesized by modified Bridgman technique at temperature gradient of 35 K/cm. Before measurements their surfaces were treated by mechanical polishing and subsequent bromide methanol etching. All crystals were of n-type conductivity and the free carrier concentration was varied from $n = 1\cdot10^{15} cm^{-3}$ to $n = 5\cdot10^{17} cm^{-3}$ at room temperature.

Reflection measurements in spectral range of 30-600 cm^{-1} were performed with IFS-113V spectrometer at temperatures 5K<T<300 K. The accuracy of wave numbers determination was about 1 - 2 cm^{-1} over all range measured. Kramers-Kronig transformation of reflection spectra defined the complex permittivity $\varepsilon(\omega)$. In view of strong influence of resonant plasmon-phonon interaction we firstly confined ourselves by the case of low Mn concentration ($y = 0.015$) and low free carrier concentration ($n = 1.9\cdot10^{15}$ cm^{-3}).

Fig. 1 presents $Hg_{0.655}Cd_{0.33}Mn_{0.0155}Te$ reflection spectra measured at various temperatures. Three parts can be picked out here: a) 80-120 cm^{-1}; b) 120-160 cm^{-1}; c) 160-220 cm^{-1} come from different physical sources. First part is usually refered to defect modes and strong spectrum modifications are observed here at temperature increasing, in particular, the broad band at ω = 105 - 115 cm^{-1} grows visibly. The second one corresponds to HgCdTe

LO - TO splitting, and the modes induced by Mn^{2+} dominate in the third part of reflection spectra.

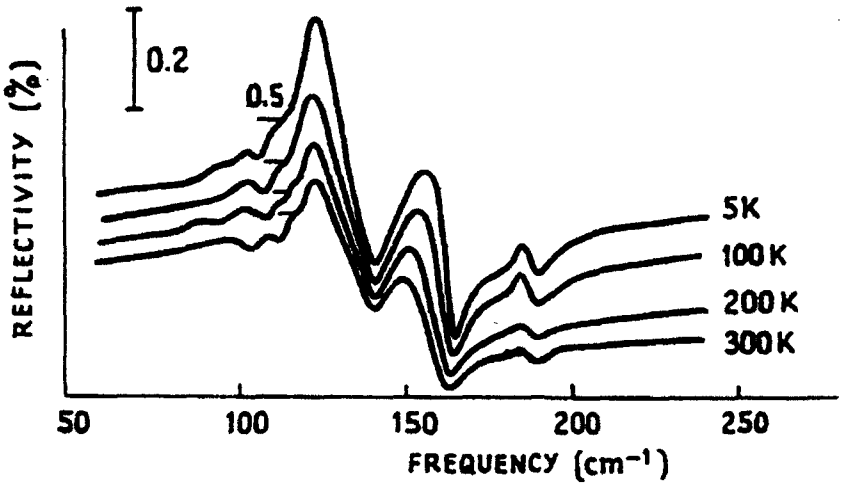

Fig. 1 Reflection spectra of HgCdMnTe at different temperatures

Due to Kramers-Kronig transformation we have identified the bands at ω = 141 cm^{-1} and ω = 160 cm^{-1} as HgTe- and CdTe-like LO modes and features at ω = 123 cm^{-1} and ω = 152 cm^{-1} as corresponding TO modes measured at helium temperature (T = 5 K). Under temperature increasing from T = 5 K to T = 300 K HgTe-like modes don't practically shift while the CdTe-like modes move to low energies on 3-4 cm^{-1}. It is very interesting behaviour, but our attention is further paid to analysis of fine structure of $\varepsilon''(\omega)$ and $Im(-\varepsilon^{-1}(\omega))$ spectra which is caused by lattice disordering. Within the range of reststrahlen rays we have found the band at ω = 135 cm^{-1}, which is shown in Fig. 2 for low temperature. It has a transverse polarization and can be attributed to clustering mode observed formerly under Raman investigations [1]. For ω > 160 cm^{-1} and low temperature (T = 5 K) the main feature is the peak at ω = 191 cm^{-1} with the strength proportional to Mn^{2+} content (Fig. 3). When the temperature is lifted up to T = 300 K the peak position shifts to low energies on 4 cm^{-1} and its halfwidth ($\Delta\omega$) grows substantially. At high temperature the dependence $\Delta\omega(T)$ can be approximated by $T^{2.5}$, but when the temperature lowers to T ≈ 80 K this dependence takes the form $\Delta\omega(T) \sim T^{0.8}$. The change of α in the dependence T^{α} points out the change of broadening mechanism for localized Mn-mode. If α > 2 the broadening, in the main, is determined by multiphonon decay or modulational process caused by quasielastic phonon scattering. At low temperature the main

contribution to the halfwidth is originated the single-phonon processes and inhomogeneity, and decreases the power α decreases to $\alpha \leqslant 1$.

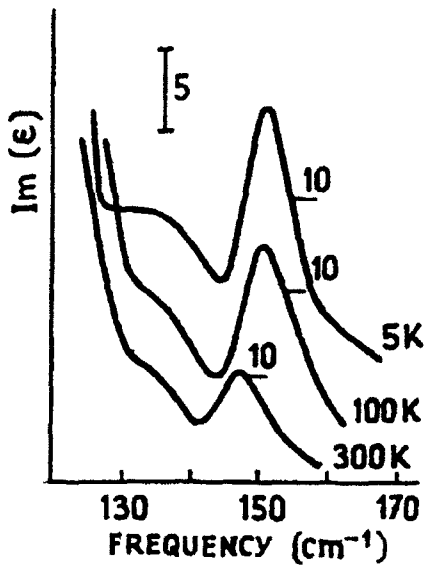

Fig. 2 The range of LO - TO splittings of HnCdTe at different temperatures

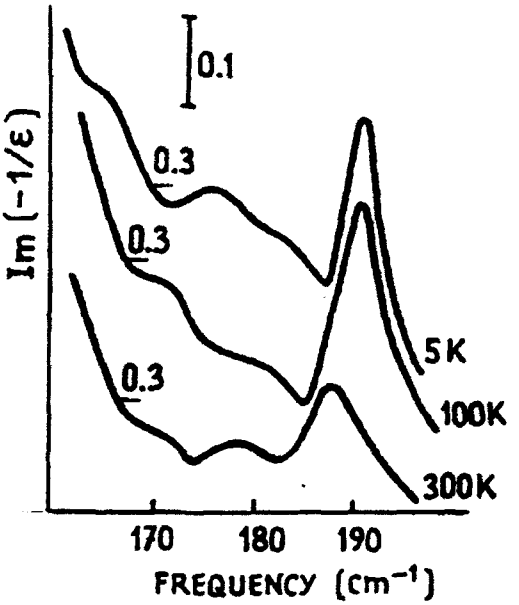

Fig. 3 Spectral dependence of $Im(-\varepsilon^{-1}(\omega))$ for the range of Mn-mode at different temperatures

Fig.3 shows also two shoulders at $\omega = 170$ cm^{-1} and $\omega = 180$ cm^{-1}. The feature at $\omega = 170$ cm^{-1} could be ascribed to LO mode of CdTe film, arising from the surface etching, but assignment of the second shoulder is problematically and needs more investigations.

From our point of view the range at 80-120 cm^{-1} is of most interest because here both defect modes and fundamental and combined lattice modes are arranged within small spectral interval. Fig. 4 presents the low frequency wing of $Im(-\varepsilon^{-1}(\omega))$ at different temperatures. The wing structure is observed up to $T \geqslant 300$ K and can be identified with the lattice vibrations for binary and ternary components known or discussed formerly [2-3]. The band at $\omega = 105$ cm^{-1} was firstly observed in HgTe and its solid solutions with low Cd content [2]. Due to strong temperature dependence this band has been supposed to be caused by subtractive LA-TA process allowed for zincblende structure at the L and X points of the Brillouin zone. For $\omega(LO) = 125$ cm^{-1} and $\omega(TA) = 20$ cm^{-1} Baars and Sorger have determined the energy of longitudinal acoustic mode $\omega(LA) = 112$ cm^{-1} correlated with the band $\omega = 113$ cm^{-1} observed in

Fig. 4. Analogous band was observed in HgCdTe, CdMnTe spectra and attributed to impurity-activated LA mode of CdTe, and what's more, due to estimations [4] small disordering is sufficient to activate LA vibrations in the spectral range $\omega < 120$ cm^{-1}. At last, the mode at $\omega = 95$ cm^{-1} corresponds to so-called G mode observed formerly in reflection spectra of HgMnTe. At temperature increase G mode moves to low energies, but at low temperature it falls into the gap between acoustic and optic branches of HgTe.

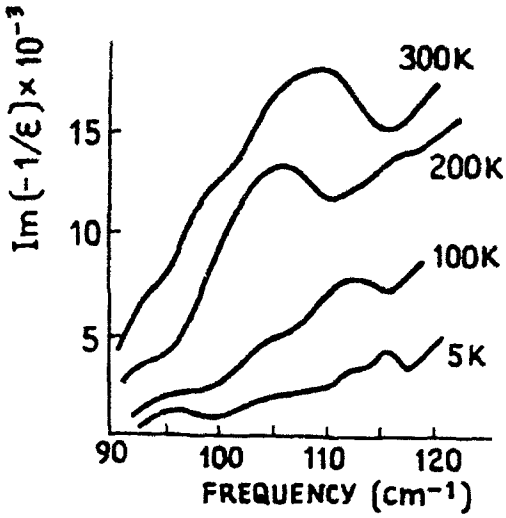

Fig. 4. Low-frequency wing of $Im(-\varepsilon^{-1}(\omega))$ for HgCdMnTe at different temperatures.

Immediate vicinity of different modes leads to peculiar behaviour of reflection peaked at $\omega = 105$ cm^{-1}. The latter has large oscillator strength and the temperature dependence usual for two-phonon processes. If the first property is characteristic for localized excitation, the second one applies to propagating excitation. To agree this inconsistency we propose the model of anharmonic resonant interaction of gap mode and subtractive lattice vibrations [5]. Due to interaction, the hybridization of wave functions takes place resulting in the modification of the spectral distribution in the range of resonating states as well as the probabilities of vibrational transitions. In this case the magnitude of reflection could be increased at the expence of local vibration but its temperature behaviour would be controled by two phonon process.

Thus, the reflection spectra analysis carried out allows to identify practically all vibrational states developed from the states of binary and ternary components of HgCdMnTe and find new features caused by energy bands crossing.

References

1. Tiong K.K. et al. Solid St. Commun. V. 50, 891, 1984
2. Baars J., Sorger F. Solid St. Commun. V. 10, 875, 1972
3. Lu W., et al. Phys. Rev. B, V. 40, 3383, 1989
4. Clayman B.P., et al. J. Appl. Phys. V. 66, 835, 1989
5. Kriven S.I., et al Fiz. tverd. tela, V. 34, 993, 1992

FIR TRANSMISSION OF $Hg_{1-x-y}Cd_xMn_yTe$

Mazur Yu.I., Kriven S.I., Tarasov G.G. and Shevchenko N.V.

Institute of Semiconductors of Academy of Sciences, Ukraine, Kiev

Phonon spectra of multicomponent mixed crystal $Hg_{1-x-y}Cd_xMn_yTe$ manifest a lot of features reflected the peculiarities of lattice dynamics which are of great interest for different applications. At small Mn content ($y < 0.05$) the phonon spectra change in accordance with two-mode behaviour under x variation. The overlapping ranges of LO-TO splitting for CdTe- and HgTe-like vibrations are easily separated from the reflection spectra with the LO-TO frequencies falling into the calibrated curves for $Hg_{1-x}Cd_xTe$ [1]. Clustering and surface modes from the range of LO-TO splittings are studied in detail by means of Raman spectroscopy [2] and, recently, by the technique of FIR reflection [3]. Out of the range of reststrahlen rays one finds different impurity modes, the modes induced by structural disordering, activated fundamental and combined lattice vibrations and so far. There is much less information about these excitations for HgCdTe, and for $Hg_{1-x-y}Cd_xMn_yTe$ it is quite absent. However these investigations could provide the data on degree of structural disordering, the role of Mn^{2+} in lattice stabilization, participation of compensated defects in lattice dynamics. Therefore we present here the data on transmission for $Hg_{1-x-y}Cd_xMn_yTe$ at different temperatures.

Fig. 1 shows the transmission spectra of $Hg_{0.65}Cd_{0.33}Mn_{0.02}Te$ (n-type, $n = 1.5 \cdot 10^{15}$ cm^{-3} at T=77 K, thickness $d \approx 0.2$ mm). Strong absorption occupies the spectral range from $\omega = 95$ cm^{-1} up to $\omega = 165$ cm^{-1}. Spectral interval from $\omega = 60$ cm^{-1} to $\omega = 95$ cm^{-1} corresponds to minimum values of single-phonon density of states for both the HgTe crystal and the CdTe one. Below $\omega = 60$ cm^{-1} the complicated structure of transmission is observed. Low-frequency features of single-phonon density of states fall into this spectral range also. Above $\omega \approx 165$ cm^{-1} and up to the range of two-phonon transitions the density of single phonon states approaches zero and the feature at $\omega = 190$ cm^{-1} corresponds to local vibration of Mn^{2+}. The ranges of transmission from $\omega \approx 240$ cm^{-1} to $\omega \approx 320$ cm^{-1} and $\omega > 320$ cm^{-1} refer to the two- and three-phonon processes respectively [4]. To analyse the transmission $T(\omega)$ the absorption coefficient $\alpha(\omega)$ is calculated with account on the reflection spectra measured formely.

Absorption coefficient of $Hg_{0.65}Cd_{0.33}Mn_{0.02}Te$ crystal is plotted in Fig. 2 at two different temperatures (dashed curves) for $\omega < 95$

cm^{-1}. Here the data of paper [5] are plotted also, which were obtained for $Hg_{0.67}Cd_{0.33}Te$ under the conditions similar to our. Comparing spectral features we conclude that the broad absorption band at $\omega \approx$ $\approx$ 30 - 45 cm^{-1} can be refered to the transverse acoustic modes of HgTe- and CdTe-type. These modes are activated by structural disordering of each of components as well as by impurity ions of Mn^{2+}. The latters can be responsible also for the band at ω = 53 cm^{-1} with strong temperature dependence which was ascribed by Shen et al.[5] to resonant vibration of Mn^{2+} in CdTe. It's worthwhile to note that the broad side-band of single-phonon density of states caused by TA modes in CdTe is also placed in this spectral range.

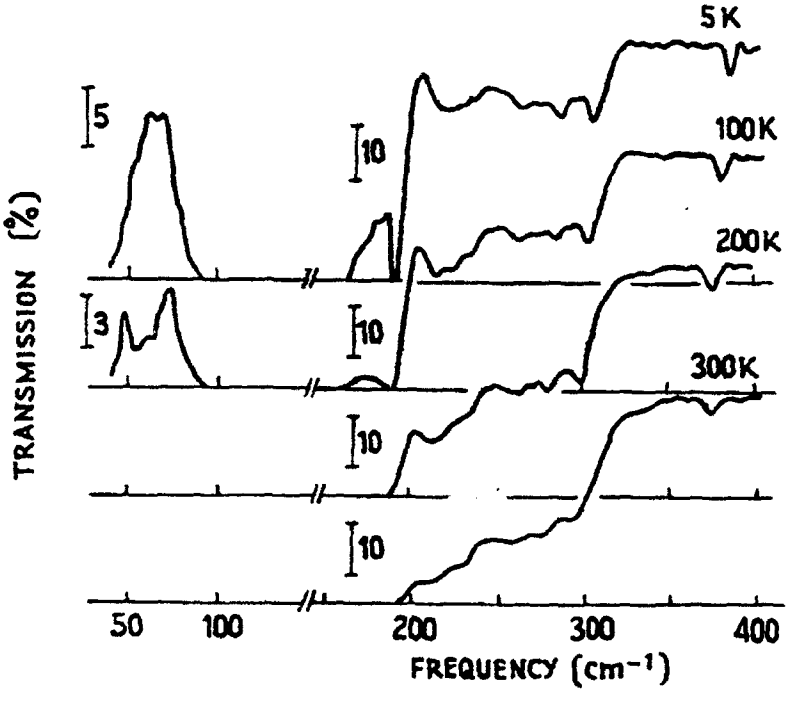

Fig. 1. FIR-transmission spectra of $Hg_{0.65}Cd_{0.33}Mn_{0.02}Te$ spectra at different temperatures

The strong absorption, as can be seen from Fig. 1, developes at ω = 95 cm^{-1}, much lower than ω = 118 cm^{-1}, which is low-energy limit of LO-TO ranges. We attribute this frequency to LA mode of HgTe activated by structural disordering of HgCdTe lattice, taking into account its polarization and energy position.

The band at ω = 190 cm^{-1} we refer to local vibration of Mn^{2+} because the magnitude of absorption peak is proportional to Mn-content and its temperature dependence is habitual for localized excitation. But in fact the situation is more complicated for this spectral range. The estimations show that different impurity modes could be active at this frequency. From theoretical analysis undertaken by Talwar and Vandevyver [6] it follows that undetectable impurities of Al, K, Fe substituting Cd in CdTe sublattice or Si, Na at the place of Hg in HgTe will generate a localized vibrational state at ω = 190 cm^{-1}. Be-

sides the 2LA(L) mode of HgTe can contribute to this band also.

Low-temperature absorption of the crystals investigated in the range of ω = 200 - 310 cm^{-1} has enriched structure (Fig. 3) due to both the multimode behaviour of HgCdMnTe and a number of defect modes. The band at ω = = 220 cm^{-1} keeps its complicated structure up to T = 300 K. Absorption at the band maximum is of 2 cm^{-1}. According to the selection rules for zinc-blend structure the next excitations can be actual for this band: overtone 2LA(L) of CdTe, compound combinations TO(X) + LA(X) (HgTe), LO(X) + LA(X) (HgTe), LO(L) + LA(L) (HgTe). It means that longitudinal acoustic modes, forbidden in infrared absorption and in Raman scattering, become of great importance for FIR transmission. Another explanation of strong (for a two-phonon spectra) absorption at ω = 220 cm^{-1} is the possibility of side-bands manifestation. In this case side-band of the vibration localized at ω = 190 cm^{-1} reflect the density of states from the range of transverse acoustic vibrations which is peaked at $\omega \approx$ 30 cm^{-1} for HgTe. The shift of absorption at ω = 220 cm^{-1} with the temperature increase corresponds to the shift of Mn^{2+} absorption peaks. The overtones and combined excitations for the frequencies from the range of LO-TO splittings of HgCdTe are placed within the interval $\omega \approx$ 240-320 cm^{-1}. Weak absorption at ω = 245 cm^{-1} is the limit of compound optical transitions and can be refered to 2TO(Γ)(HgTe). The temperature shift of absorption at ω = 304 cm^{-1} ($\sim$10 cm^{-1} under temperature increase from T = 5 K go T = 300 K) allows to ascribe this

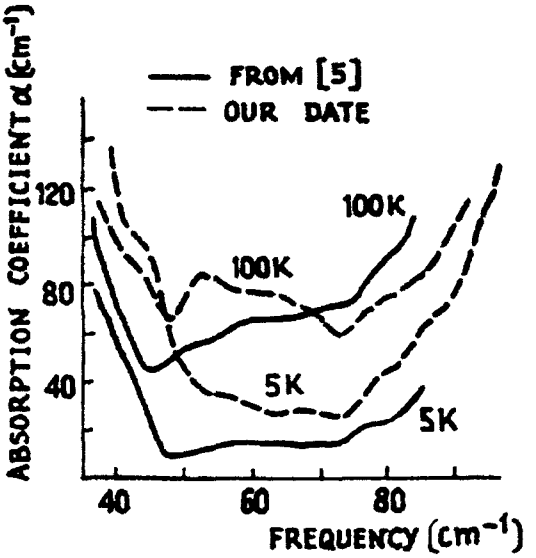

Fig. 2. Absorption coefficient of $Hg_{0.65}Cd_{0.33}Mn_{0.02}Te$ in the spectral range ω< 95 cm^{-1} at two temperatures.

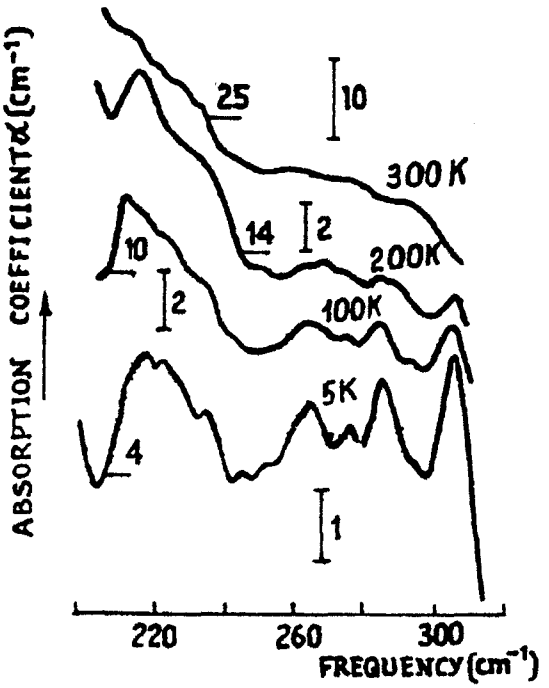

Fig. 3. Two-phonon absorption of $Hg_{0.65}Cd_{0.33}Mn_{0.02}Te$ at different temperatures

feature to 2TO(X) mode of CdTe-component. Really, the frequency of TO-mode of CdTe shifts on 5 cm^{-1} towards less values giving evidence for strong anharmonicity of vibration. The latter leads to the intensification of two-phonon absorption and to the correct value of its shift. We find the next classification for the other features under consideration in this spectral range: $\omega \approx 265$ cm^{-1} is 2LO(Γ) HgTe or TO(L) HgTe + TO(L) CdTe; $\omega = 276$ cm^{-1} is TO(Γ) HgTe + TO(Γ) CdTe.

To fit unambiguously the experimenta data the $\omega(\vec{k})$ dependences are necessary for HgCdTe. Note that two-phonon peaks with CdTe participation, as a rule, are more prominent that those with HgTe only.

Multiphonon absorption of HgCdMnTe is plotted in Fig. 4 from $\omega \approx 320$ cm^{-1} to $\omega = 400$ cm^{-1}. The striking feature is at $\omega = 380$ cm^{-1}. It is undoubtedly the overtone of local vibration at $\omega =$ $= 190$ cm^{-1}. The magnitude of peak is proportional of Mn-content, and the shift towards the lower energy is approximately twice of that for Mn-mode at temperature increase from T = 5 to T = 300 K. It should be noted a out-of-the-way modification of absorption lineshape with temperature increasing. The broad band at $\omega = 330$-350 cm^{-1} is caused by different combination of transverse optical vibrations which are of high dipole activity.

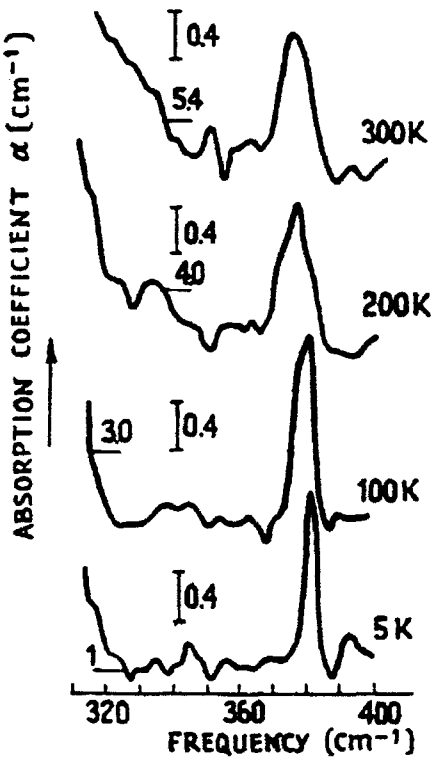

Fig. 4. Three-phonon absorption of $Hg_{0.65}Cd_{0.33}Mn_{0.02}Te$ at different temperatures

Thus, the analysis of acoustic and optical modes manifestation allows to conclude on the role of impurity atoms and structural defects in the change of dynamical properties of narrow gap solid solutions.

References

1. Baars J., Sorger F. Sol. St. Commun. V. 10, 875, 1972
2. Amirtharay P.M. et al. J. Vac. Sci. Technol. A, V. 3, 226, 1985
3. Kriven S.I. et al Fiz. tver. tela, V. 34, 893, 1992
4. Casselman T.W., Hansen G.L. J. Vac. Scin. Techn. A1, 1683, 1983
5. Shen S.C. et al. Sol. St. Commun., V. 48, 1017, 1983
6. Talwar D.N., Vandevyver M. J. Appl. Phys. V. 56, 1601, 1984

Th7.4

Polarization diplexing technique used for a FIR laser sideband heterodyne spectrometer

Daniel BOUCHER, Robin BOCQUET and Weidong CHEN
Laboratoire de Spectroscopie Hertzienne
Université des Sciences et Technologies de Lille
59655 Villeneuve d'Ascq, France

An improved version of a tunable far-infrared (FIR) laser sideband heterodyne spectrometer is reported in this article.

The generation of tunable coherent FIR laser sideband radiation is generally based on the modulation of a fixed frequency FIR laser radiation by a tunable microwave source in a nonlinear mixing component. Different detection methods lead to rather different spectrometer designs.

The FIR laser sideband spectrometer developped in Lille (France) uses a heterodyne detection system operating at room temperature [1].

The FIR source is a molecular laser optically pumped by a commercial PL6 CO_2 laser (Edinburgh Instruments). The CO_2 laser cavity length is locked to the point of maximum FIR laser output power, using the photoacoustic effect by means of a microphone signal originating from the FIR laser transition. The FIR laser radiation is extracted via a gold-coated dielectric silicon output coupler with a 8 mm-diam. hole in the center. The FIR laser system has been described in detail elsewhere [1].

The sideband generator is a GaAs Schottky barrier diode (Millitech Corporation, model MX-Q4), mounted in an open structure corner cube. As the sideband power level increases with input level, FIR laser power of at least 1 mW is required. A similar Schottky diode (Farran Technology Limited, model CIII) is used as the first mixer in the heterodyne receiver system. A local oscillator power of about 1 mW is generally needed to saturate the diode at the nonlinear mixing point.

In contrast to baseband detection, in which rigorous isolation of the laser radiation before the detector is a major constraint due to the poor conversion efficiency of the Schottky diode frequency modulator and the use of a corner cube, heterodyne detection needs unmodulated laser radiation as local oscillator for the heterodyne receiver, eliminating optical filtering in the spectrometer system.

The heterodyne detection method necessitates a division of the laser radiation into two beams directed to each Schottky diode corner cube. The principal problem is to develop an optical system which is able to realize the coupling of laser beam and of sideband radiation as efficiently as possible. The solution for the coupling of Gaussian beam results in a beam splitter, or in a dual-beam interferometer.

A beam splitter is placed in a resonator structure which is formed by a corner cube of the Schottky diode, a movable plane mirror, and an ellipsoidal focusing mirror [2]. The laser beam is divided by the beam splitter, then coupled to the sideband modulator and heterodyne receiver respectively. The sideband radiation coupling towards the interaction cell is optimized by adjusting the resonator cavity structure. However the simple structure of this setup offers only a sideband coupling efficiency of about 30%.

The dual-beam interferometer coupling system can be a Mach-Zehnder (M-Z) non-polarizing diplexer, or a Martin-Puplett (M-P) polarizing diplexer.

The non-polarization coupling technique, using two M-Z diplexers permits a coupling efficiency of ideally 100% ignoring the dielectric material losses. However the M-Z diplexer requires a thickness of the dielectric beam splitter adapted to the working frequency, so that its bandwidth is limited. In addition, the beam splitting of dielectric materials is always polarization dependent. Furthermore if we consider the constraint of beam truncation losses, a minimum non-overlap loss of -1.6 dB is not avoidable even if a diplexer of the confocal cavity structure is used with an enlarged beam waist.

The M-P interferometer, using polarization diplexing technique, couples two beams of different polarization. Its structure allows the use of the minimum diplexing path-length difference and an enlarged incident beam waist: the degree of non-overlap can thus be minimized.

A quasi-optical system using the polarization diplexing coupling technique has been developped for our FIR laser sideband heterodyne spectrometer. The schematic diagram of the experimental system is shown in Fig.1.

The FIR laser beam is enlarged at first by a frequency independent Gaussian beam telescope system consisting of a parabolic mirror M1 and an ellipsoidal mirror M2. Then the linearly polarized laser radiation is converted to circular polarization by a polarization

rotator MR1, which consists of a wire-grid polarizer and a plane mirror with an adjustable spacing. By a vertical wire-grid polarizer G1, the laser beam is divided between the transmitted beam which serves as local oscillator for the heterodyne receiver and the reflected beam which passes into the sideband generator after crossing the diplexer D1.

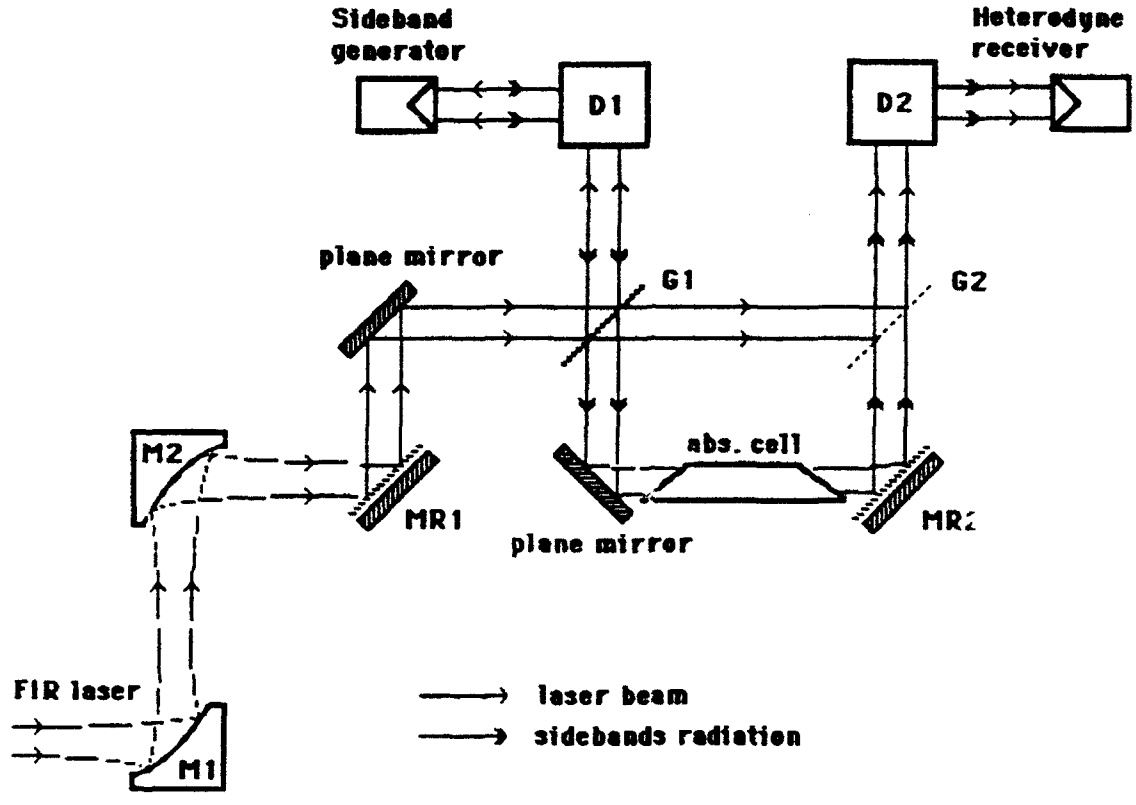

Fig. 1 Experimental optical system scheme

The diplexer D1 is a typical M-P interferometer. The interferometer path difference is tuned so that the sideband polarization is 90° with respect to that of the laser radiation towards the sideband generator, in order to separate sidebands from the laser carrier at G1. Another similar polarization rotator MR2 is used to rotate the polarization of the sideband beam through 90° again. The horizontal wire-grid polarizer G2 thus couples the unmodulated

laser radiation and the spectroscopic signal to the second diplexer D2 which recombines the two beams of different polarization onto the heterodyne detector.

Compared to an optical system using a non-polarization coupling technique, the non-overlap losses of the system which we have developped are very low, especially with an enlarged beam waist up to about 10 mm. The virtual losses of the entire optical system are about -0.5 dB at 1400 GHz.

The working frequency bandwidth of the system is determined by the performance of the wire-grid polarizer. With the present polarizers, whose wire parameters are: 2a=10 µm & g=40 µm (where 2a is the wire diameter, g the wire spacing), the optical system can operate over a wide spectral range from about 600 GHz to 2500 GHz. By using smaller wire parameters, the performance of the optical system at higher frequency could be improved.

In addition, this quasi-optical polarizing coupling system permits the FIR laser sideband heterodyne spectrometer to be used in single sideband.

REFERENCE

[1] Daniel BOUCHER, Robin BOCQUET, and Weidong CHEN
"Tunable heterodyne spectrometry using coherent submillimeter waves components and methods"
Conference Digest "16th International Conference on Infrared and Millimeter Waves", SPIE 1576, 240-243, 1991

[2] Weidong CHEN, Ph. D. Thesis, Université de Lille ! (France), 1991

Th7.5

MECHANISM AND DYNAMICS OF STIMULATED FAR-IR RADIATION OF HOT HOLES FROM COMPRESSED Ge

I.V.Altukhov, M.S.Kagan, K.A.Korol'ov, V.P.Sinis

Institute of Radioengineering and Electronics
Russian Academy of Sciences
Mokhovaya, 18, GSP-3, Moscow, 103907, Russia

Recently we have observed the stimulated emission of FIR hot-hole radiation from p-Ge under uniaxial compression with no magnetic field applied, which has been due to direct optical transitions between strain-split valence subbands [1]. In this report the experimental data concerning with the origin of population inversion of valence subbands and the evolution of stimulated radiation in space and time are presented.

The stimulated emission was observed at pressure both in the [111] and [100] crystallographic directions. The threshold compression P was about 9 kbar for [111] and 6 kbar for [100] and in both cases corresponded to the valence-subband separation energy Δ ($\Delta \propto P$) close to the optical phonon energy ε_o.

The spontaneous FIR hot-hole luminescence intensity at intermediate electric fields beginning at impurity breakdown was found to be dependent on stress as $\exp(-\alpha\Delta)$ with constant α both for [111] and [100]. At first sight, the exponential decreasing of spontaneous radiation intensity with stress may be explained by decreasing of hole concentration at the energies $\varepsilon > \Delta$ in the tail part of a distribution function. For the Maxwellian distribution function $\alpha^{-1} = kT_l$. T_l is the light-hole temperature. The field dependences of kT_l are shown in Fig.1 both for [111] and [100]. There is an interval of electric fields E at which T_l does not depend on E for both stress directions. On the other hand, the spontaneous radiation intensity increases with E increasing at P fixed. This points out increasing of hole concentration in the upper subband, i.e. increasing T_l. The contradiction means the distribution function is not Maxwellian. Besides it is clear from Fig.1 that T_l is higher and an initial field for T_l increasing is less for P $\parallel$ [100] than those for P $\parallel$ [111], although light holes having somewhat smaller effective masses in the [111] direction should be heated at lower fields. This fact shows the heating of light holes is affected by the presence of the heavy-hole band even at moderate fields.

The cause of non-Maxwellian distribution in unstressed semiconductor is known to be the run-away of holes, i.e. acoustic-phonon collisionless acceleration by the field, up to optical-phonon energy (streaming motion) [2]. Due to strong inelastic optical-phonon scattering the distribution function is

stretched in momentum space in the hole-drift direction. In stressed Ge the upper strain-split "heavy-hole" band may act as a similar limit for hole run-away up to the energy of Δ but with almost elastic scattering by acoustic phonons. If the probability of interband acoustic-phonon scattering is high enough in comparison to intraband one, the holes accelerated by the field to the energy of Δ may accumulate in the upper subband. This process may lead to inversion. The estimation [3] showed the condition for such hole sticking being $\mu E > s$ (μ is the light-hole mobility at $\varepsilon \cong \Delta$, s is the sound velocity) can be satisfied already at low fields close to shallow impurity-breakdown threshold in Ge. If the most of the holes are in the heavy-hole band as a result of light-hole run-away, the exponential decrease of spontaneous radiation intensity with stress have to depend on the hole temperature T_h in the upper band connected with T_l as $T_l \cong T_h \cdot (m_h/m_l - 1)$ (m_h and m_l are effective masses in the heavy-hole and light-hole subbands). The T_h values are marked on the right-hand scales of Fig.1. The heavy-hole temperature turns out to be higher than lattice temperature and is determined only by the intersubband scattering until the field heating begins. Since m_h in the [100] direction is less than that in the [111], so $T_{h2} > T_{h1}$ and heavy holes in [100] begin to be heated at lower fields than those in [111].

The field heating of heavy holes expands their energy distribution up to optical-phonon energy counted in stressed Ge from the bottom of the light-hole band, so the limiting energy is $\varepsilon_o - \Delta$. After optical-phonon emitting the holes are transferred to the lower band and then they run away to the upper one. Thus, all of the holes are in the energy range of $\varepsilon_o - \Delta$ (Fig.2). The highest energy of heavy holes depends on pressure in stressed Ge and may be done much less than that without stress (ε_o). As a result, the heavy-holes are in a narrow energy range when Δ is close to the optical-phonon energy. The inversion is strong in this case. The stimulated emission have been observed just at these conditions.

The uniaxial deformation is known to lead to the negative differential conductivity (NDC) caused by hot-hole transfer between strain-split valence subbands and, as a result, to high-field domain formation (see, f.i.,[4] and references cited). We have studied the interaction between high-field domains and stimulated radiation. The domain formation was observed at pressure above 4 kbar. There was two cases in dependence on sample contact conditions. In first case the static domain was formed at the negative sample electrode at voltages in NDC region and caused the current saturation (Fig.3,b). The capacitive probe mesurements showed the step-like field distribution in the specimen (Fig.3,a). The stimulated emission (curve 4 in Fig.3,a) arose and grew as the domain width increased with the voltage increasing reached some critical value. At large

enough radiation intensity the domain was destroyed and the field distribution became uniform (Fig.3,a). The generation (curve 5) and the uniform field distribution maintained at voltage diminishing during the same voltage pulse down to values much less than exciting voltages (Fig.3,a). The minimum supporting field was found to be about 200 V/cm which was somewhat larger than the field outside of the domain. These data show that high voltages necessary for stimulated emission exciting in this case are due to high-field domain formation because the out-of-domain field is insufficient for generation.

In second case the current oscillations caused by travelling domain formation appeared. At not too high voltages, however, the stimulated radiation arisen could coexist with Gunn oscillations. The stimulated emission and current oscillation magnitude were interdependent. The average current shown in Fig.4 illustrate domain evolution at FIR generation. At the pressure just before the stimulated emission threshold the current oscillations existed at all fields used and the average current saturated (curve 1). The oscillation frequency corresponded to the domain transit time with velocity about 10^7 cm/s. At stress above the threshold the average current (curve 2) changed similarly as the radiation intensity (curve 3) and the current oscillations became damped as the radiation inflamed and disappeared in the end. The travelling domain transformed to the static one as the radiation intensity increased considerably. The further evolution was in the same way as shown in Fig.3: next jump of emission intensity and current and conserving of stimulated radiation at uniform field at diminishing voltage. Thus, two possible stationary generation states with and without domains could exist in this case.

For some samples the stimulated radiation could appear beginning at the impurity-breakdown voltage all over the voltage range investigated with no current oscillations or static domain.

References

1. I.V.Altukhov, M.S.Kagan, V.P.Sinis. Sov.Phys.-JETP Lett.,V.47, 164 (1988); Proc.ICMWFT '90, Beijing, China, 439 (1990); Opt.Quant.Electr., V.23, S211 (1990)
2. A.A.Andronov. Infrared and Millimeter Waves, V.16, 149 (1986)
3. I.V.Altukhov, M.S.Kagan, K.A.Korol'ov, V.P.Sinis, F.A.Smirnov. Sov.Phys.-JETP, V.101, 360 (1992)
4. N.O.Gram, N.I.Meyer. Phys.Stat.Solidi, V.1, 237 (1971)

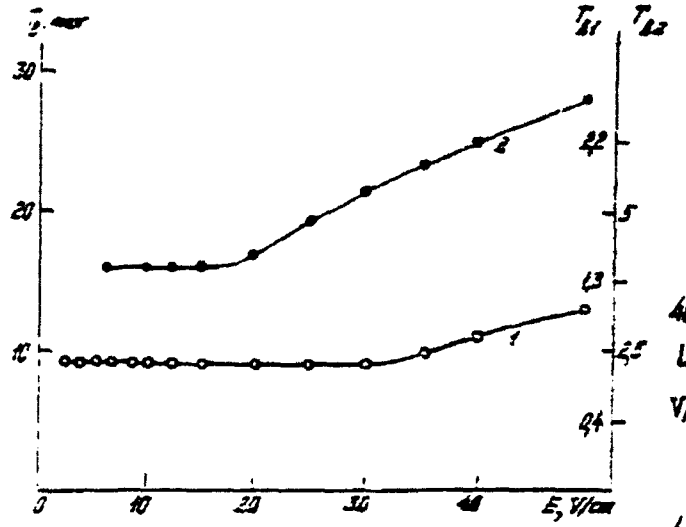

Fig. 1

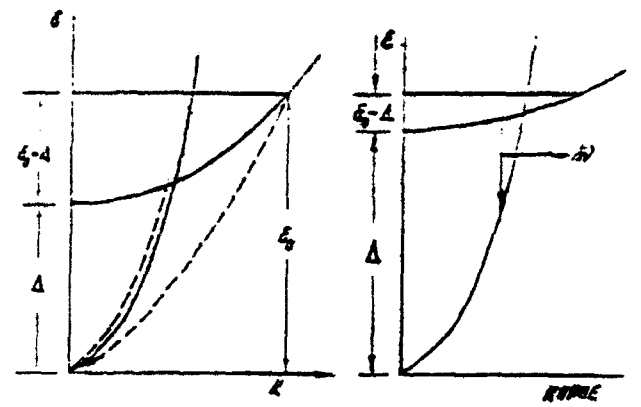

Fig. 2

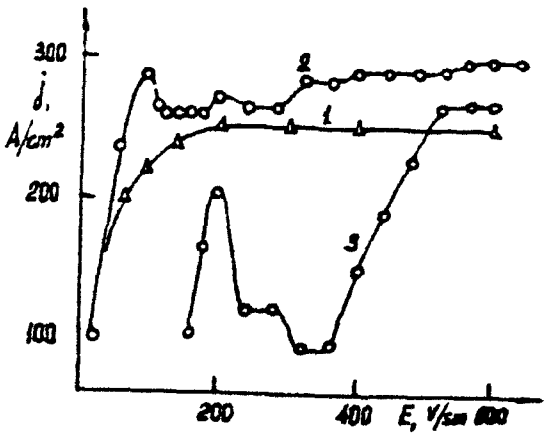

Fig. 4

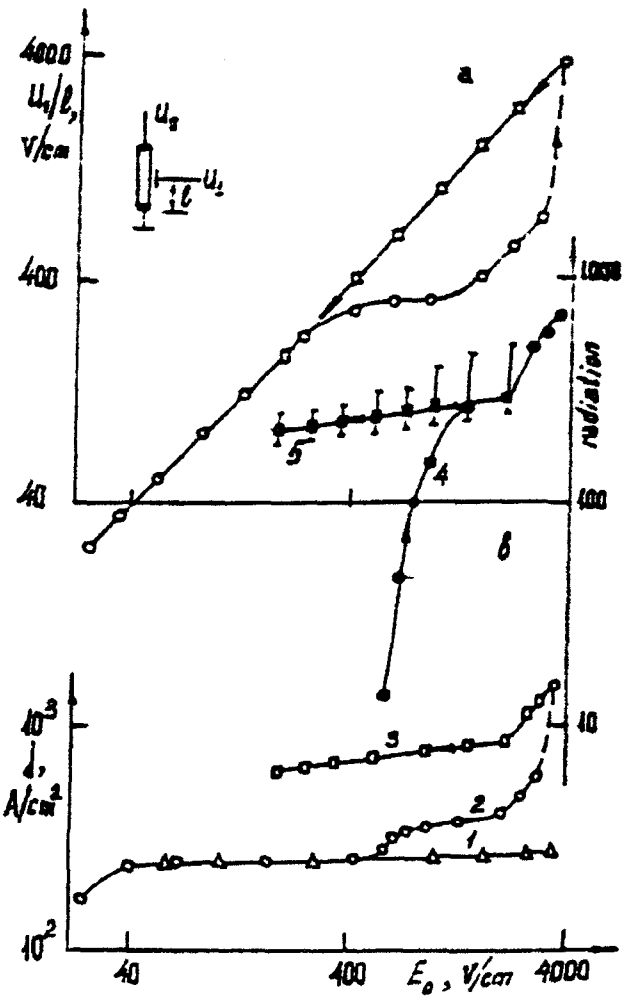

Fig. 3

Torsion-Rotation FIR Spectrum of O-18 Methanol

R.M. Lees[a], R.R.J. Goulding[b], Saibei Zhao[a], I. Mukhopadhyay[c], J.W.C. Johns[d], C.P. Chan[e], and W. Lewis-Bevan[f]

[a] CEMAID and Dept. of Physics, University of New Brunswick, Fredericton, N.B., Canada E3B 5A3

[b] Department of Physics, Memorial University of Newfoundland, St. John's, Nfld., Canada A1B 3X7

[c] Centre for Advanced Technology, Govt. of India,Dept. of Atomic Energy, Indore 452 013, M.P., India

[d] Herzberg Institute of Astrophysics, National Research Council of Canada, Ottawa, Canada K1A 0R6

[e] CEMAID and Dept. of Chemistry, University of British Columbia,Vancouver, B.C., Canada V6T 1Y6

[f] Dept. of Chemistry and Biochemistry, Southern Illinois University, Carbondale, IL 62901, U.S.A.

Abstract

Fourier transform spectra have been recorded for O-18 methanol in the far-infrared ground vibrational torsion-rotation band. Because the CH_3-rock and CO-stretch bands overlap well with the CO_2 laser bands, $CH_3{}^{18}OH$ is of interest as a source of optically-pumped FIR laser emission. From FIR assignments, accurate combination differences are obtained which allow confident assignment of the infrared CH_3-rock and CO-stretch series. This permits identification of IR pump transitions which are coincident with CO_2 laser lines, and thence can lead to assignments of the FIR laser lines. The FIR spectral measurements are also needed to check the identification of IR-pump/FIR-laser transition systems through IR/FIR combination loop relations. In this work, 57 subbranches in the ground state FIR spectrum of O-18 methanol have been assigned, and their approximate J-independent origins have been determined. These have been fitted to a model torsion-rotation Hamiltonian in order to determine a set of molecular constants for the ground state.

Introduction

In common with its normal CH_3OH parent, the O-18 isotopomer of methanol has two vibrational bands, the CO-stretching and in-plane CH_3-rocking bands, which overlap well with the CO_2 laser bands and lead to extensive optically-pumped far-infrared (FIR) laser emission [1]. Identification of the lasing transitions is an interesting spectroscopic puzzle, which has sparked much interest in recent years in methanol and its various species, and has led to a considerable increase in understanding of the energy level structure of both ground and excited vibrational states. The analysis of the IR vibrational bands depends heavily on a knowledge of combination differences in the vibrational ground state, hence detailed analysis of the torsion-rotation microwave and FIR ground-state spectra is an essential co-requisite for vibrational spectroscopy of the molecule.

Microwave spectra of $CH_3{}^{18}OH$ were first observed in an early study by Hughes et al. [2], then investigated more fully by Gerry et al. [3], who assigned a variety of transitions at low rotational quantum number and obtained a set of the J-dependent "*a*-type" parameters and certain of the J-independent or "*b*-type" parameters. Later, in order to explore the potential of O-18 methanol as an FIR laser source, Goulding et al. [4] looked at the optoacoustic spectrum with CO_2 laser excitation and discovered a number of promising coincidences between CO_2 laser lines and $CH_3{}^{18}OH$ IR absorptions. They predicted correctly that strong FIR laser lines would be pumped by the 10R(20) CO_2 line, but their specific proposed laser wavenumbers were not seen in practice when Ioli et al. [1] first investigated the FIR laser emission from this molecule. Following the report by Ioli et al., which also included a low-resolution

survey of the vibrational band structure comprising the IR spectrum [1], Lees et al. utilized the results of Goulding [5] along with further work on the high-resolution Fourier transform IR and FIR spectroscopy to assign a number of the reported IR-pump/FIR-laser transition systems involving both the CO-stretching [6] and CH_3-rocking [7] bands. Around the same time, Petersen and Choi [8] explored three transition systems with IR-radio-frequency and IR-IR double resonance and confirmed the assignments for those systems, including the more likely of the 10R(20) pumping schemes proposed by Goulding et al. [4].

In this paper, we report on our progress on the assignment of the ground state torsion-rotation FIR spectrum of O-18 methanol, and present our preliminary set of J-independent *b*-type constants as determined from approximate subbranch origins. If time permits, some applications of the results together with those from IR spectroscopy of the CO-stretching and CH_3-rocking bands to the identification of FIR laser transition systems will be discussed.

FIR Spectrum and Analysis

The FIR spectrum of $CH_3{}^{18}OH$ was originally recorded from 30-220 cm^{-1} on the DA3.002 Bomem spectrometer in Ottawa, at a resolution of 0.004 cm^{-1}. Analysis of this spectrum gave considerable information about the torsion-rotation energy level structure of the ground state [5], but there was still a lack of data for low rotational quantum numbers and for excited torsional transitions. Therefore, we ran the spectrum again recently in Ottawa from 15-470 cm^{-1} at higher pressure and sensitivity, using the modified Bomem instrument with 0.002 cm^{-1} resolution and similar conditions to those discussed briefly in our $^{13}CD_3OH$ study [9].

Analysis of the new spectrum is still in the early stages, but the increased resolution has permitted many of the highly overlapped Q branches to be followed almost to their initial lines, while the higher sensitivity has revealed numerous weak excited torsional branches much more clearly. So far, we have only worked our way up the spectrum to include Q branches with origins lying below 150 cm^{-1}, but it became clear almost immediately that the parameters we were using to predict the origins were giving discrepancies of several tenths of a cm^{-1}. To remedy this, we determined approximate experimental values for 57 FIR subbranch origins by extrapolating from the initial lines of the R, Q and P branches, and included 4 microwave Q-branch origins [3] to give a data set of 61 origin wavenumbers. These are listed in Table 1, and it can be seen that they cover a fairly wide range of rotational and torsional quantum numbers. It may also be noted that they are very irregularly distributed in the spectrum, due to the large and erratic effects of the torsional energy changes, hence reasonably accurate calculations are indeed of importance in locating and identifying the various P, Q and/or R subbranches.

We then fitted the subbranch origins by non-linear least squares to a set of *b*-type parameters, using the Kivelson-Kirtman formula [10] for the energy of state (nτK) as described for $^{13}CD_3OH$ [9]:

$$\begin{aligned} W(n\tau K) = {} & V_3 \langle 1-\cos 3\gamma\rangle/2 + F\langle P_\gamma^2\rangle + [A-(B+C)/2]\,K^2 + V_6\langle 1-\cos 6\gamma\rangle/2 \\ & - D_{KK}\,K^4 + k_1\,K^3\langle P_\gamma\rangle + k_2\,K^2\langle P_\gamma^2\rangle + k_3\,K\langle P_\gamma^3\rangle + k_4\langle P_\gamma^4\rangle \\ & + k_5\,K^2\langle 1-\cos 3\gamma\rangle + k_6\,K\langle P_\gamma\rangle + k_7\langle P_\gamma^2(1-\cos 3\gamma)\rangle \end{aligned}$$

In this notation, n is the torsional quantum number, τ is an index defining the A, E_1 or E_2 torsional symmetry, K is the component of the rotational angular momentum J along the *a*-axis, and P_γ is the torsional angular momentum [10]. As the constants F and A are both known functions of the axial moments of inertia, I_{a1} and I_{a2}, we fitted directly to the latter for convenience [11]. Also, we chose to constrain parameter k_6 to zero in the fit to avoid the linear dependence known to exist among the matrix elements for six of our parameters [10,11]. The FIR origins were equally weighted in the fit, but the

accuracies of the microwave origins were taken to be 10x better, giving them 100x the weight of the FIR origins. Table 1 includes the least squares residuals, and it can be seen that the 61 origins are quite well reproduced by the 11 *b*-type parameters, with the overall weighted standard deviation being 1.95 and the largest residual being 0.053 cm^{-1}. The values found for the parameters are given in Table 2 along with their rms errors. The values of the *a*-type parameters I_b, I_c, and I_{ab} were taken from the previous microwave study [3].The axial moments of inertia I_{a1} and I_{a2} and the torsional barrier height V_3 are well defined, and are similar to the previous microwave results [3], but some of the smaller torsion-vibration-rotation interaction parameters are not very well-determined in the the fit. We hope that extension of the assignments upward in wavenumber to include more origins with a wider range of torsional states, together with least-squares fitting of the subbranch line series to determine more precise origins, may improve the situation in future.

Acknowledgements

This work was made possible in part by a grant to the Centres of Excellence in Molecular and Interfacial Dynamics (CEMAID), funded by the Network of Centres of Excellence Programme in association with the Natural Sciences and Engineering Research Council of Canada. One of us (R.M.L.) also gratefully acknowledges operating support from NSERC and the University of New Brunswick Research Fund. We thank Mario Noël of the Herzberg Institute of Astrophysics for skillful technical assistance in operating the Bomem spectrometer.

References

1. N. Ioli, A. Moretti, D. Pereira, F. Strumia, and G. Carelli, "A New Efficient Far-Infrared Optically Pumped Laser Source: $CH_3{}^{18}OH$," *Appl. Phys. B* **48**, 299-304 (1989).
2. R.H. Hughes, W.E. Good, and D.K. Coles, *Phys. Rev.* **84**, 418 (1951).
3. M.C.L. Gerry, R.M. Lees and G. Winnewisser, "The Torsion-Rotation Microwave Spectrum of $^{12}CH_3{}^{18}OH$ and the Structure of Methanol," *J. Mol. Spectrosc.* **61**, 231-242 (1976).
4. R.R.J. Goulding, C. Young, R.M. Lees, W. Lewis-Bevan and J.W.C. Johns, "Doppler-Free Optoacoustic Spectroscopy of O-18 Methanol," *Infrared Phys.* **28**, 297-306 (1988).
5. R.R.J. Goulding, Ph.D. Thesis, University of New Brunswick, 1987.
6. R.M. Lees, W. Lewis-Bevan, J.W.C. Johns, R.R.J. Goulding, D.P. Donovan and C. Young, "IR Spectra and FIR Laser Assignments for O-18 Methanol," *13th Int. Conf. IR and MM Waves*, Honolulu, Hawaii, (ed. R.J. Temkin), *Proc. SPIE* **1039**, 356-357 (1988).
7. R.M. Lees, Saibei Zhao, M.A. Rommens, J.W.C. Johns, W. Lewis-Bevan, C. Young and T.J. Lees, "FIR Lasing and Spectroscopy in the CH_3-Rocking Band of O-18 Methanol," *15th Int. Conf. IR and MM Waves*, Orlando, Florida, (ed. R.J. Temkin), *Proc. SPIE* **1514**, 729-731 (1990).
8. J.C. Petersen and S.E. Choi, "Double Resonance Spectra of $CH_3{}^{18}OH$," *J. Opt. Soc. Am.B* , in press.
9. Li-Hong Xu, R.M. Lees and J.W.C. Johns, "Torsion-Rotation FIR Spectrum of $^{13}CD_3OH$," this conference.
10. R.M Lees and J.G. Baker, "Torsion-Vibration-Rotation Interactions in Methanol. I. Millimeter Wave Spectrum," *J. Chem. Phys.* **48**, 5299-5318 (1968).
11. R.M. Lees, "Linear Dependence in Least Squares Analysis, with an Application to Internal Rotation," *J. Mol. Spectrosc.* **33**, 124-136 (1970).

Table 1. Approximate (n'τ'K')←(n"τ"K") Subbranch Origins (cm^{-1}) in the FIR Spectrum of $CH_3{}^{18}OH$

(n'τ'K')	(n"τ"K")	TS [a]	ν_{obs}	ν_o-ν_c	(n'τ'K')	(n"τ"K")	TS [a]	ν_{obs}	ν_o-ν_c
(031)	(010)	A	9.974	0.004	(110)	(131)	A	67.185	0.002
(022)	(031)	A	16.075	0.003	(113)	(122)	A	66.826	-0.009
(013)	(022)	A	8.772	0.001	(116)	(125)	A	32.645	0.001
(034)	(013)	A	21.381	0.003	(134)	(125)	A	41.048	-0.015
(025)	(034)	A	39.983	0.002	(137)	(116)	A	111.171	0.026
(016)	(025)	A	39.208	-0.016	(1310)	(119)	A	83.455	-0.034
(037)	(016)	A	35.961	0.015	(133)	(124)	E_1	36.876	0.000
(028)	(037)	A	53.172	0.009	(115)	(124)	E_1	45.045	0.000
(019)	(028)	A	67.881	-0.001	(136)	(115)	E_1	112.395	-0.053
(0310)	(019)	A	62.043	-0.036	(111)	(120)	E_2	77.291	-0.003
(0211)	(0310)	A	65.241	0.029	(114)	(123)	E_2	56.742	-0.007
(033)	(012)	E_1	17.755	0.006	(135)	(114)	E_2	97.791	0.024
(024)	(033)	E_1	33.520	-0.001	(138)	(117)	E_2	104.415	0.046
(015)	(024)	E_1	28.258	-0.037	(210)	(131)	A	126.366	-0.017
(036)	(015)	E_1	30.096	0.007	(213)	(134)	A	122.253	0.018
(027)	(036)	E_1	49.426	0.006	(234)	(113)	A	150.918	-0.012
(018)	(027)	E_1	59.611	0.001	(237)	(128)	A	79.871	0.016
(039)	(018)	E_1	52.026	0.008	(212)	(133)	E_1	116.432	0.001
(0210)	(039)	E_1	60.638	-0.030	(236)	(127)	E_1	80.262	-0.006
(0111)	(0210)	E_1	80.081	0.029	(211)	(132)	E_2	115.495	-0.014
(032)	(011)	E_2	14.082	0.004	(235)	(126)	E_2	95.352	0.014
(023)	(032)	E_2	25.543	0.001	(231)	(210)	A	119.741	0.003
(014)	(023)	E_2	17.942	0.013	(222)	(213)	A	150.235	0.001
(035)	(014)	E_2	25.345	-0.015	(216)	(237)	A	109.317	-0.042
(026)	(035)	E_2	45.171	0.012	(221)	(212)	E_1	146.236	0.024
(017)	(026)	E_2	49.904	-0.003	(215)	(236)	E_1	100.746	0.017
(038)	(017)	E_2	43.214	-0.013	(220)	(211)	E_2	138.916	-0.000
(029)	(038)	E_2	56.787	0.005					
(0110)	(029)	E_2	74.619	-0.014					
(0311)	(0110)	E_2	72.837	0.001					
(021)	(030)	E_1	5.4956[b]	0.0011	(020)	(011)	E_2	5.0266[b]	0.0003
(012)	(021)	E_1	1.1314[b]	0.0010	(130)	(121)	E_1	6.2368[b]	0.0009

[a] Torsional symmetry. [b] Origin found from microwave results, and given 100x higher weight in the fit.

Table 2. J-Independent *b*-Type Parameters for the Ground Vibrational State of $CH_3{}^{18}OH$

Parameter	Matrix Element	Value [a]	Parameter	Matrix Element	Value [a]
I_{a1} (amu-Å^2)		0.760737(186)	k_1 (MHz)	$K^3\langle P_\gamma\rangle$	-1.503(593)
I_{a2} (amu-Å^2)		3.21143(60)	k_2 (MHz)	$K^2\langle P_\gamma^2\rangle$	-56.38(1.93)
V_3 (cm^{-1})	$\langle 1-\cos 3\gamma\rangle/2$	374.169(111)	k_3 (MHz)	$K\langle P_\gamma^3\rangle$	-160.84(3.33)
V_6 (cm^{-1})	$\langle 1-\cos 6\gamma\rangle/2$	-1.273(107)	k_4 (MHz)	$\langle P_\gamma^4\rangle$	-257.26(7.40)
D_{kk} (MHz)	$-K^4$	1.232(105)	k_5 (MHz)	$K^2\langle 1-\cos 3\gamma\rangle$	291.4(26.5)
I_b (amu-Å^2)		[21.37594]	k_6 (MHz)	$K\langle P_\gamma\rangle$	[0.00]
I_c (amu-Å^2)		[22.16858]	k_7 (MHz)	$\langle P_\gamma^2(1-\cos 3\gamma)\rangle$	-306.7(237.7)
I_{ab} (amu-Å^2)		[-0.15138]	S.D.[b]		1.95

[a] Standard deviations in the last figure are shown in parentheses. Values in brackets were fixed in the fit.

[b] Overall standard deviation of the fit, in weighted cm^{-1}.

Th7.7

Optical Study of Residual Donors in ZnSe/GaAs

H.Nakata, R.Komeda and T.Ohyama

Department of Physics, College of General Education

Osaka University, Toyonaka, Osaka 560 Japan

Far-infrared magneto-absorption and photoluminescene are observed for MOVPE grown ZnSe epitaxial layers. A far-infrared absorption peak at 4.2T for the wavelength of 57μm is assigned to transition from 1s to 2p$_+$ state of Cl donor in ZnSe. Free exciton and donor bound exciton are observed in photoluminescence measurement. The splitting of these peaks due to difference in thermal expansion coefficient leads us to estimate the strain in the ZnSe layer and the ionization energy of the residual donor is calculated from the splitting between the main peak and two electron satellite of the donor bound exciton.

1. Introduction

A ZnSe epitaxial layer has become an important semiconductor especially after the report on invention of the blue light emitting laser.[1] The control of residual impurities is inevitable to fabricate a p-ZnSe. Photoluminescence measurement has been widely applied to characterize residual impurities. In photoluminescence measurement, not only a free exciton but also a bound exciton can be observed.[2] The different residual impurities induce the bound exciton peaks at different peak positions. We can identify the residual impurities from the peak position in the bulk sample. Complexity comes to a ZnSe epitaxial layer because of strain in the ZnSe layer due to difference in thermal expansion coefficient between ZnSe layer and GaAs substrate.[3,4] Both free and bound exciton peak split because of the strain. We estimate the strain from the splitting of the free exciton peaks.

Two electron transition of the bound exciton is radiative recombination process like Auger effect.[2] The electron and hole in the bound exciton recombine each other and excite an electron to the excited state of the donor. We can easily estimate energy difference between the ground state and the excited state of the donor. We observed two electron transition in ZnSe/GaAs and estimated the energy difference. Far-infrared(FIR) magneto-absorption of dondrs in a ZnSe epitaxial layer was first reported by K.Saito et al..[5] They studied I doped ZnSe and observed an absorption peak at 5.3T for the wavelength of 57μm.

2.Experimental

The samples which we used in this study were ZnSe epitaxial layers grown on GaAs substrate by MOVPE (Metalorganic Vapor Phase Epitaxy) method. The sample thicknesses are 10 and 20μm . A CH_3OD laser with

the wavelength of 57μm was employed as a FIR source and the sample was placed in the magnetic field up to 5T in FIR magneto-absorption measurement.

An Ge doped with As was used as a detector. A xenon flash lamp was operated at 20Hz as an excitation source in photo-excitation measurement.

We made photo-luminescence measurement in a conventional way. A pulse N_2 laser with pulse width of 1ns and peak power of 10KW was employed as an excitation source. Luminescence was dispersed by a monochromator (SPEX 1269) and detected by a phot-multiplier. The signal was analyzed by a boxcar integrator.

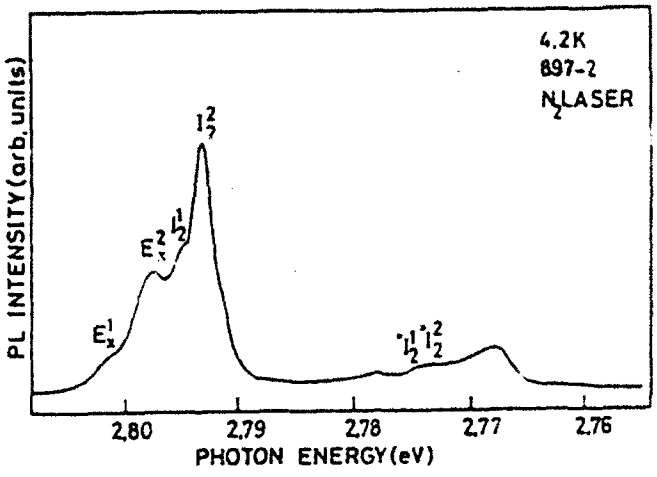

Fig.1 Photoluminescence spectrum of ZnSe/GaAs with thickness of 20μm. E_x and I_2 denote free exciton and donor bound exciton line, respectively.

3. Results and Discussion

Figure 1 shows photoluminescence spectra of the ZnSe epitaxial layer. E_x denotes a free exciton line and I_2 a donor bound exciton line. A two electron transition is possible in bound exciton recombination. The two electron transition is denoted $^*I_2$. Each line spilits into two lines by a residual tensile strain in plain due to difference in thermal expansion coefficient between ZnSe and GaAs.[3,4] The photon energies of emission lines are listed in Table 1. We can estimate a residual strain to be 7.2×10^{-4} from the energy separation 3.9meV of free exciton doublet E_x^1 and E_x^2.[4]

Table 1

Component	Transition energy (eV)
E_x^1	2.8012
E_x^2	2.7973
I_2^1	2.7947
I_2^2	2.7930
$^*I_2^1$	2.7745
$^*I_2^2$	2.7733

Energy separation between the main peak and the two electron satellite of donor

bound exciton gives us a energy difference between the ground state and the excited state of the donor. The separation between $^{*}I_2$ and I_2 lines is about 20meV. It is close to the energy difference of 19.66 meV between 1s and 2p states of Cl donor reported by Merz et al..[6]

Figure 2 shows FIR absorption of a donor in the ZnSe layer with the thinckness of 10μm. We observed a broad absorption peak at 4.2T. Saito et al. made the same kind of experiment for I doped ZnSe and reported one of peaks at 5.3T.[5] The peak position is different from ours. It means that our residual impurity is not an iodine. We assumed that the absorption peak is due to the transition from 1s to $2p_+$ state of an unknown residual donor. The energy difference between 1s and $2p_+$ state at zero magnetic field is estimated to be 20.0meV in linear Zeeman effect approximation with the electron effctive mass of $0.145m_0$.[7] The obtained value agrees well with that from photoluminescence measurement.

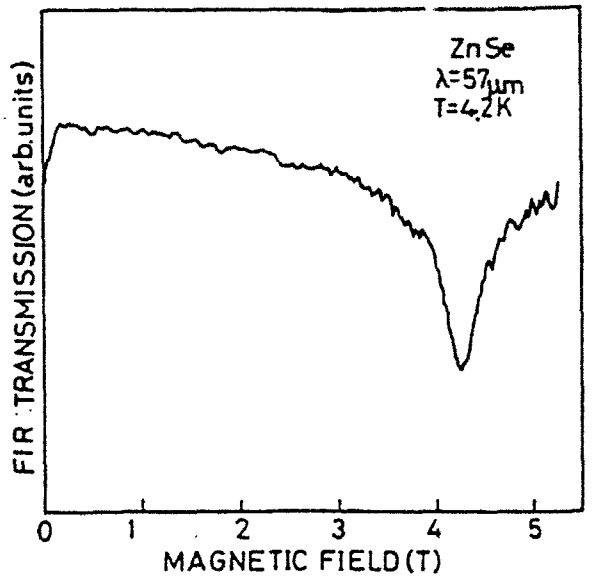

Fig.2 Far-infrared magneto-absorption of ZnSe/GaAs(t=10μm). An absorption peak at 4.2T corresponds to 1s to $2p_+$ transition of a residual donor.

The thick sample reveals a more sharp resonance at the same magnetic field. It means that it has a good crystal quality. When we elevates the bath temperature, the broadening of the peak occurs and the peak shifts to higher magnetic field as shown in Fig.3. The linewidth of the absorption peak changes from 51 to 61μeV at 4.2 to 20K. Residual strain induces the broading of $E_n D/E_g$, where E_n is the ionization energy of the nth level(=7meV), D is deformation potential(=4.1eV), is a strain and Eg is a energy gap(=2.8eV). The estimated broadening due to residual strain is about 7.6μeV. Other mechanisms are necessary to explain the linewidth.

Another interesting result is photo-modulated absorption experiment. In this experiment, a two channel boxcar integrator was used and one gate opened just after photoexcitation and another gate at enough delayed time. At 4.2T, FIR absorption decreases due to photoexcitation. In normal situation, photoexcitation creates electron-hole pair and ionized impurity captures free carriers to become a neutral impurities. In this case, photoexcitation ionizes neutral donors. Interface between ZnSe and GaAs may play a important role for this

mechanism.

4.Conclusions

We estimated residual strain of 7.2×10^{-4} the splitting of free exciton lines and assigned the residual donor to Cl impurity. The 1s to 2p+ transition of Cl impurity is observed at 4.2T in FIR absorption for the wavelength of 57μm. The estimated energy difference between 1s and 2p+ state at zero magnetic field agrees well with the result of photoluminescence. Temperature dependent line broadening and photoionization of donors are observed.

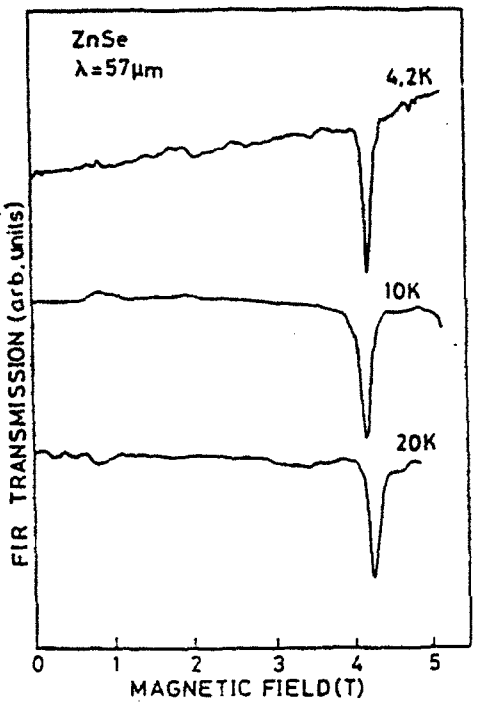

Fig.3 Temperature dependence of FIR magneto-absorption of ZnSe/GaAs(t=20μm). Linebroadening and peak shift are observed at higher temperatures.

5.Acknowledgements

We are indebted to Dr.Yodo for the supply of good quality samples. We are grateful to Dr.Yamada and Dr.Saito for useful discussions. One of authors (H.N.)acknowledges to the support from Nippon Sheet Glass Co. This work has been supported by the Subsidy for Special Equipment from the Ministry of Education, Science and Culture.

References

1.M.A.Haase, J.Qiu, J.M.DePuydt and H.Cheng : Appl. Phys. Lett.59 1272(1987).
2.M.Isshiki, T.Kyotani, K.Masumoto, W.Uchida, and S.Saito : Phys. Rev.B36 2568(1987).
3.K.Shahzad : Phys.Rev.B38 8309(1988).
4.M.Stoeher, F.Hamdani, J.P.Lascaray, and Maurin : Phys.Rev.B44 8912(1991).
5.K.Saito, S.Yamada, A.Ohki, and K,Ando : Jpn.J.Appl. Phys. 30 L74 (1991).
6.J.L.Merz, H.Kukimoto, K,Nassau, and J.W.Shiever : Phys. Rev.B6 545 (1972).
7.T.Ohyamam, K,Sakakibara, E.Otsuka, M.Isshiki and K.Igaki : Phys. Rev.B37 6153(1988).

Th7.8

NENP - A MODEL MATERIAL FOR MAGNETIC RESONANCE

S. Luther[a], W. Lu[b], J. Tuchendler[c], M. von Ortenberg[a], J. P. Renard[d]

[a]Institut für Halbleiterphysik und Optik
Hochmagnetfeldanlage
Technische Universität Braunschweig
D-3300 Braunschweig, Germany

[b]National Infrared Laboratory
Shanghai Institute of Technical Physics, Academia Sinica
Shanghai, P.R. China

[c]Laboratoire de Despositifs Infra-Rouge
Université Paris VI
F-75230 Paris, France

[d]Institut d'Electronique Fondamentale
Université Paris-Sud
F-91405 Orsay, France

We report on FIR-magneto transmission experiments on the model material NENP representing the most realistic system for the antiferromagnetic linear chain with S = 1. For such systems, Haldane made the conjecture that the excited triplet states of the system are separted from the singlet ground state by a nonzero gap in contrast to the case for S = 1/2[1]. After the first direct proof of the existence of the Haldane gap 2, we have investigated all possible transitions in the ideal system of infinite chains as well as the special effects due to ending and breaking of the chains. Impurity transitions are also observed. This implies that the selection rules of the ideal system are broken. The present data demonstrate the efficiency of FIR-spectroscopy in the investigation of complex spin systems.

1. F.D.M. Haldane, Phys. Rev. Lett. **50**, 1153 (1983).

2. W. Lu, J. Tuchendler, M. von Ortenberg, J. P. Renard, Phys. Rev. Lett. **67**, 3716 (1991).

HIGH FREQUENCY FIR-LASER MODULATION FOR PULSED HIGH MAGNETIC FIELD APPLICATION

R. Krevet, F. Roters and M. von Ortenberg

Institut für Halbleiterphysik und Optik
Technische Universität Braunschweig
D-3300 Braunschweig, Germany

We report on the first successful high frequency modulation of an optically pumped FIR-molecular gas laser in the range of 10^5 to 10^6 Hz. Such high modulation frequencies are necessary to apply a fast lock-in technique for the detection of FIR-magneto-optical spectra in high pulsed magnetic fields with pulse duration of the order of some msec. This high frequency lock-in technique has ben demonstrated to give, for magneto-transport measurements, the same signal-to-noise ratio as known from experiments in quasistationary fields as produced by superconducting or BITTER solenoids [1].

The modulation is provided by a Q-switch technique applying special piezo controlled mirror supports of the laser cavity. Using a high performance Piezo ceramic tandem configuration, we were able to displace the incoupling mirror of 4 cm diameter with a coupling hole of 3 mm at a resonance frequency of 195 k-Hz. In resonance, the displacement amplitude is sufficiently large to result in full modulation of the FIR-laser emission line.

The detection of the high frequency modulated radiation intensity is performed by a multi-element photoconductivity detector system as described in [2]. Magnetotransmission spectra obtained by this method are of the same quality obtained for those with modulation frequencies in the order of 10 to 100 Hz. The additional advantage of the modulation method is FIR-magneto-optics is the fact that, due to the modulation, the base line for zero transmission is well defined in contrast to the common experiments in pulsed magnetic fields, where only the magnetic field induced change is recorded without reference to the zero transmission value.

References:

1. M. von Ortenberg, W. Staguhn, F. Böbel, S. Takeyama, T. Sakakibara, N. Miura, J. Phys. E: Sci. Instrum. **22**, 359 (1989).

2. M. von Ortenberg and J. Geiger, Prof. 13th International Conference on Infrared and Millimeter Waves, Honolulu 1988, SPIE **1039**, 207 (1988).

FIR-Study of Rare Earth Compounds

P. Janssen, F. Herlach, L. Van Bockstal and J. Witters

Laboratorium voor Lage Temperaturen en Hoge - Veldenfysica
K. U. Leuven, Celestijnenlaan 200D, 3001 Leuven, Belgium

1. INTRODUCTION.

An ion with a partially filled shell has non-zero angular momentum and a corresponding magnetic moment. In a magnetic field, this leads to precession of the magnetic moment around the magnetic field with the Larmor frequency. If an oscillating magnetic field is applied, the orientation of the magnetic moment can be reversed. This phenomenon is well known as "Electron Paramagnetic Resonance" (EPR).

Resonance occurs when the frequency of the oscillating field is equal to the Larmor frequency. For a free ion this is:

$$\hbar\omega = g_L \mu_B B$$

(μ_B is the Bohr magneton). The Landé-factor g_L is given by:

$$g_L = 1 + \frac{J(J+1) - L(L+1) + S(S+1)}{2J(J+1)}$$

J, L and S are the quantum numbers for the total, total angular and total spin momentum respectively.

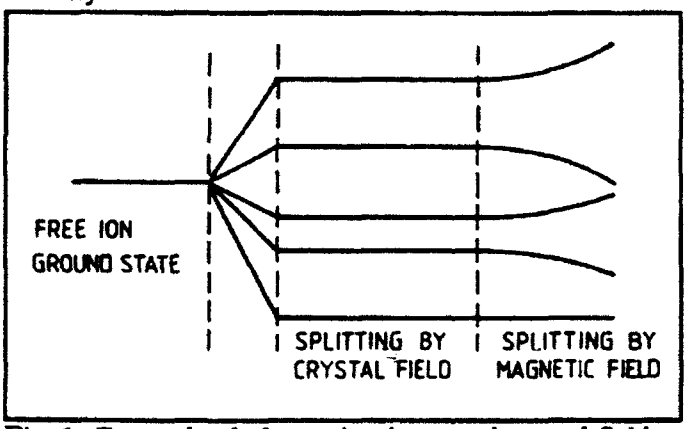

Fig. 1: *Energy levels for an ion in a weak crystal field.*

If the ion is inside a crystal it is subjected to the electrostatic influence of its neighbours, described by the crystal field. The energy levels are shifted, and the resonance condition changes accordingly. To appreciate this effect, one has to compare these changes in energy levels with other interactions. In the case of the rare earth ions the magnetic moment is due to the partially filled 4f-shell. This shell is surrounded by the

5s- and 5p- shells and these screen the crystal field very effectively (in contrast with e.g. the case of incomplete 3d-shells). Typical shifts produced in the energy levels are of the order of 10 to 100 cm^{-1}. The situation can thus be summarised as follows (see fig. 1):

- The ground state for a free ion is determined using Hund's rules. This yields the values for J, L and S. This ground state is (2J+1)-fold degenerate.
- This degeneracy will be lifted (partially) by the crystal field. How far the degeneracy is removed depends on the symmetry of the crystal field. However, if the number of electrons in the shell is odd, Kramers' theorem applies: the degeneracy cannot fully be lifted by an electric field. The remaining degeneracy is in this case at least twofold.
- An applied magnetic field will lift the remaining degeneracy. EPR between these split levels can be observed under suitable circumstances.

The difference in energy between the ground term, as given by Hund's rules, and the higher terms is much higher than the splitting induced by the crystal field. In most cases one can therefore ignore the higher terms completely at far-infrared (FIR) photon energies. The splittings caused by the crystal field however are right within the FIR region, which is therefore well suited for this studies.

2. THE USE OF HIGH MAGNETIC FIELDS.

In case of a large zero field splitting, even in very low magnetic fields, the use of FIR radiation may be necessary to observe EPR. There are a number of advantages in the use of high magnetic fields:

- Closely spaced lines can be resolved, resulting in a more accurate determination of the resonance field and easier study of line shapes.
- Many lines appear narrower in higher fields. This makes detection easier and can be of great help in separating different contributions to the line width (e.g. hyperfine lines).
- Evidently, the energy levels can be mapped over a wider field region.
- The difference between the applied magnetic field and the local field can be calculated in terms of a demagnetising field. This depends on the magnetisation in the sample, which in turn depends on the applied field. It is a definite advantage that in high fields the magnetisation can be saturated. Correct g-values can then be derived from the slope of the measured resonance condition (i.e. from a plot of photon energy versus applied field at resonance).

3. EXPERIMENTAL SET-UP.

We use two different spectrometers. They do not differ very much in principle, but are very different in the experimental arrangement. Both use an optically pumped FIR-laser as radiation source. A diagram of the spectrometer based on a superconducting magnet (up to 12 Tesla) is given in fig. 2. Due to the limited sweeping speed of the superconducting magnet a measurement with this spectrometer takes typically 15 minutes. As shown in the diagram, the radiation is chopped. Part of the beam is split off to stabilise the laser. The transmitted radiation is detected by a slow detector (e.g. a carbon bolometer), mounted under the sample.

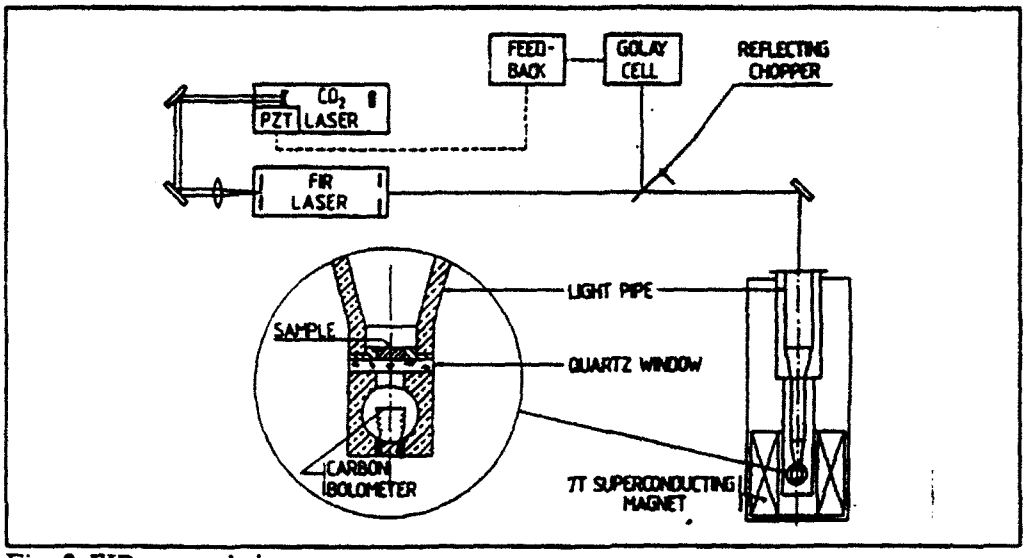

Fig. 2 *FIR transmission spectrometer*

The second spectrometer is based on a pulsed magnet. This technique produces much higher fields (over 50 Tesla), but on an entirely different time scale. The pulse duration is of the order of 10 milliseconds. High speed detectors (e.g. InSb hot electron bolometer) and high speed electronics (such as fast transient recorders) must be used. Experimental conditions, e.g. the stability requirements for the laser, are very different for both spectrometers.

4. SOME EXPERIMENTAL RESULTS.

The case of $TmVO_4$ [1] illustrates very well the lifting of the free ion degeneracy by the crystal field. As can be seen from fig. 3, not one (as expected) but several resonance lines are seen. The resonance condition (see fig. 4) was determined by repeating the measurement at different wavelengths. The $TmVO_4$ crystal is very easily distorted, and different distortions with different symmetries produce different splittings of the ground state. This explains the different lines, all with the same g-value but with different zero field splittings.

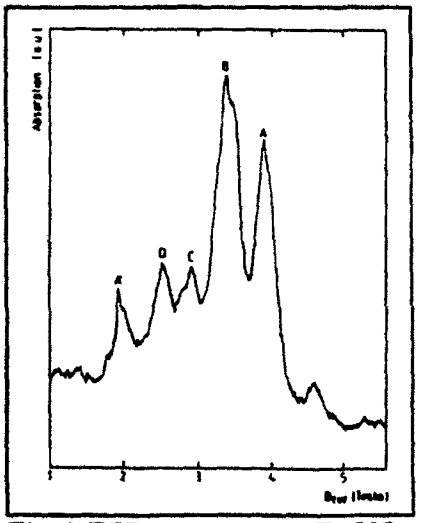

Fig. 3 EPR spectrum in $TmVO_4$

The case of DyAlG is more complicated. EPR in this material was, until now, only done in diluted materials. This has the advantage that interactions between the different magnetic moments are strongly reduced. However, in high fields, the study of the undiluted material can be undertaken. Here also, many lines were detected (see, e.g. fig. 5). The explanation given for $TmVO_4$ is not applicable, due to the Kramers theorem. The observed lines can roughly be grouped according to their g-values. Extra lines with a g-

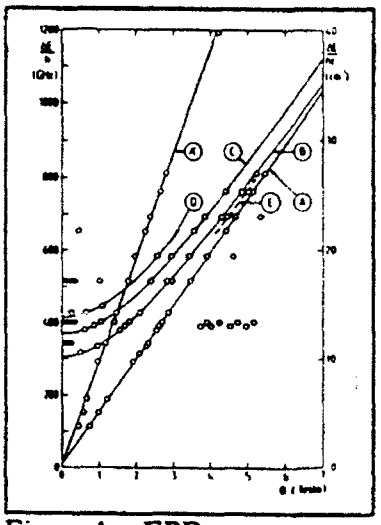

Fig. 4 EPR resonance condition for $TmVO_4$

value corresponding to the expected doublet splitting can be accounted for in terms of nearest neighbour interactions. Effects of non-stoichiometry can explain many of the other lines. We consider extra Dy^{3+} -ions occupying sites in the crystal normally occupied by Al^{3+} -ions. This has a double effect: some of the regular Dy^{3+} -ions see their crystal environment changed by this interchange. Furthermore, there can be signals caused by the irregularly placed Dy^{3+} -ions. Some of these lines show a g-factor which is much lower than expected. This effect does not account for all of the lines that are seen, but is, for a specific group of lines, consistent the angular variation of the spectra.

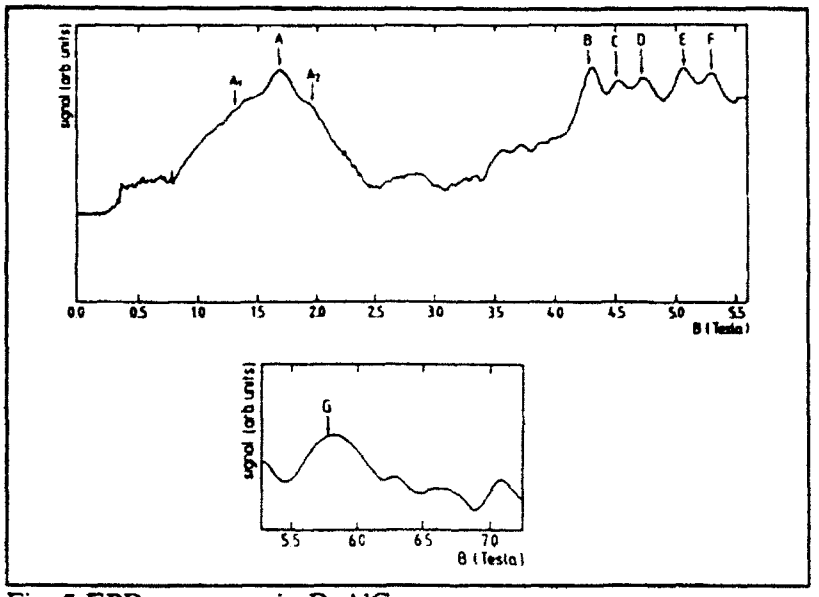

Fig. 5 EPR spectrum in DyAlG

Two more promising cases are $DyPO_4$ and $TbPO_4$. Both of these were until now not studied in the far infrared, but literature data on optical transitions generate interest in a FIR study of these materials as well. The results will be presented and discussed at the conference.

REFERENCES

[1] I. De Wolf, P. Janssen and B. Bleaney, Phys. lett., 108A, No 4, 221, 1985

[2] P. Janssen, M. Mahy and W. P. Wolf, Phys. rev. B, vol 37, No 10, 4851, 1988

Th8.1

OPTIMUM TRANSVERSE PARAMETERS OF MINI-OPFIRL

Li Yao and Lin Yikun
(Zhongshan University, Guangzhou, China)

ABSTRACT

Double-peak of the operating pressure had been found when the transverse feedback was strong enough. The density matrix for non-monochromatic signal fields was presented for calculation.

INTRODUCTION

The application of OPFIR lasers stimulated the study of the miniaturization of FIR sources[1,2]. A cw OPFIR laser with the cavity length as short as 5 cm was reported in 1986[3]. Miniature pulsed OPFIRLs with their cell length from 1 to 5 cm were delevoped[4] and the transverse feedback enhancement effect was found to be an active role in a mini-OPFIRL[5].

EXPERIMENTS

The experimental setup was a conventional OPFIRL system except the sample tubes were newly designed[5]. Different sample tubes made of three materials

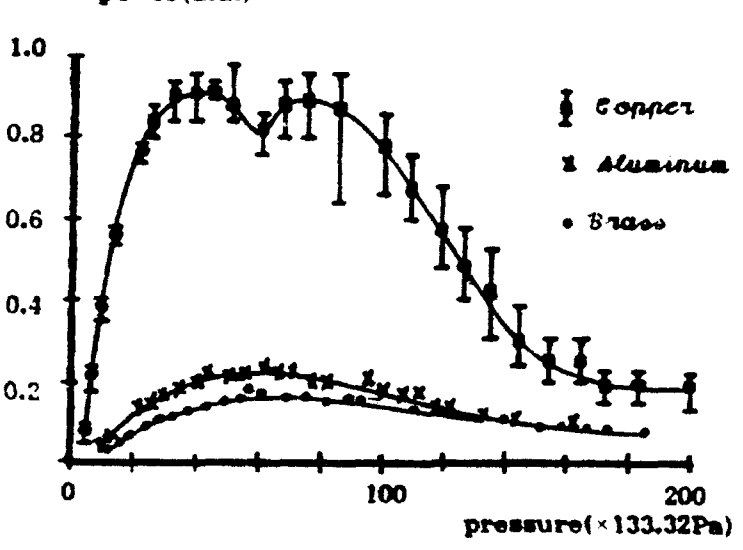

Fig.1 The output characteristic of mini-OPFIRL of three sample tubes with φ18mm ID.

Supported by Science Foundation of Zhongshan University

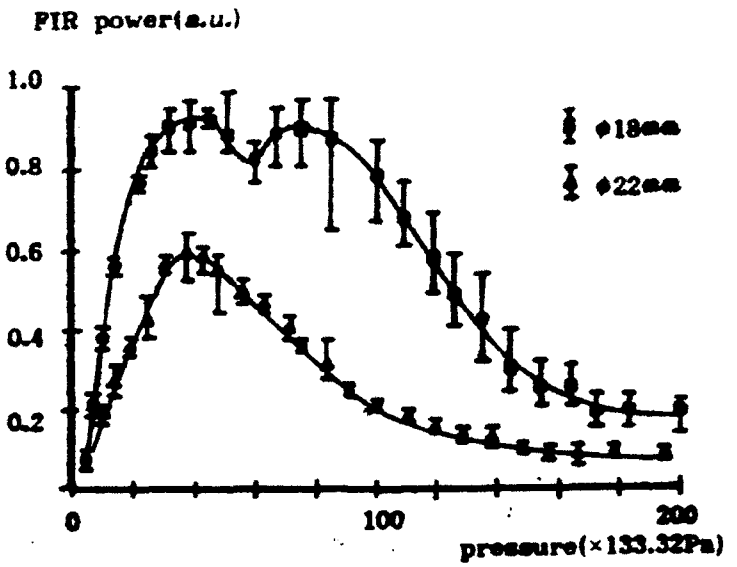

Fig.2 The output power of mini-OPFIRL with different inner diameters.

including aluminum, brass, copper with two different inner diameters (φ18mm and φ22mm) and the same length (39mm) were used to investigate the dependence of output power on the transverse parameters of the sample tube.

Fig.1 was the experimental curves of the output power versus the operating pressure of three sample tubes with the inner diameter of φ18mm. In the FIR region, the reflectivity of copper was the highest among these materials, and that of brass was the lowest. It was evident that the higher the reflectivity of the tube wall, the larger the output power of the mini-OPFIRL.

Fig.2 showed that the maximum output power of the copper sample tube with the inner diameter of φ18mm was larger than that of φ22mm, and furthermore, the output power of the latter dropped faster than the former when the operating pressure was higher than the optimum operating pressure.

The other result was that the optimum operating pressure of the mini-OPFIRL of φ18mm copper sample tube had two peaks, the first in P=40×133.32Pa and the other about in P=80×133.32Pa.

THE DENSITY MATRIX FOR NON-MONOCHROMATIC SIGNAL FIELDS

In a transverse feedback enhanced mini-OPFIR laser, there was interaction between the transverse feedback and the stimulated emission in the longitudinal direction. The conditions of the excitation and the emission between the two signals were different, so the production of the amplified spontaneous emissions were quite different. The density matrix for non-monochromatic signal fields should be considered.

It was assumed that the electric field interacting with the molecular system include the pump laser field and the signal laser field, where the pump laser was assumed to be monochromatic field with its frequency $\omega_p \approx \omega_{31}$ and the signal laser was the non-monochromatic field which was taken to consist of n

discrete frequency signals, $\omega_{s,n}$ ~ ω_{32} :

$$E(t)=\frac{1}{2}E_p\exp(i\omega_p t)+\frac{1}{2}\sum_n E_{s,n}\exp(i\omega_{s,n}t)+c.c.$$

With the rotating wave approximation and solving for the quasi-steady-state, the density matrix equation for three-level system was expanded as a set of *4N+5* complex linear equations, where *N* was the number of the discrete frequency signals concerned. By writng the equations in matrix form, the equations were solved and gain coefficients for *N* discrete signals were obtained:

$$\frac{P_{13I}}{B_p}=\frac{r_{31}^{*}-r_{23}^{*}\sum_n B_{s,n}^2(H_3')_n/(H_2)_{nn}}{h_1-B_p^2\sum_n B_{s,n}^2(H_3')_n^2/(H_2)_{nn}}$$

$$\frac{P_{32I,n}}{B_{s,n}}=\frac{r_{23}^{*}h_1-r_{31}^{*}B_p^2(H_3')_n}{h_1(H_2)_{nn}-B_p^2B_{s,n}^2(H_3')_n^2}$$

where

$$h_1=1+x^2+\sum_n B_{s,n}^2+4B_p^2-\sum_n B_{s,n}^2(-2x+y_n)/[1+(-x+y_n)^2+B_p^2+B_{s,n}^2]$$

$$(H_2)_{nn}=1+y_n^2+B_p^2+4B_{s,n}^2-B_p^2(-2y_n+x)^2/[1+(-x+y_n)^2+B_p^2+B_{s,n}^2]$$

$$(H_3')_n=-3-(-2x+y_n)(-2y_n+x)/[1+(-x+y_n)^2+B_p^2+B_{s,n}^2]$$

The gain coefficient for the FIR signal with the frequency $\omega_{s,n}$ was

$$G_{s,n}=-\frac{N_v\mu_s^2\tau}{\varepsilon_0 c\eta\hbar}\omega_{s,n}\mathrm{Im}(P_{32,n}/B_s)-\alpha$$

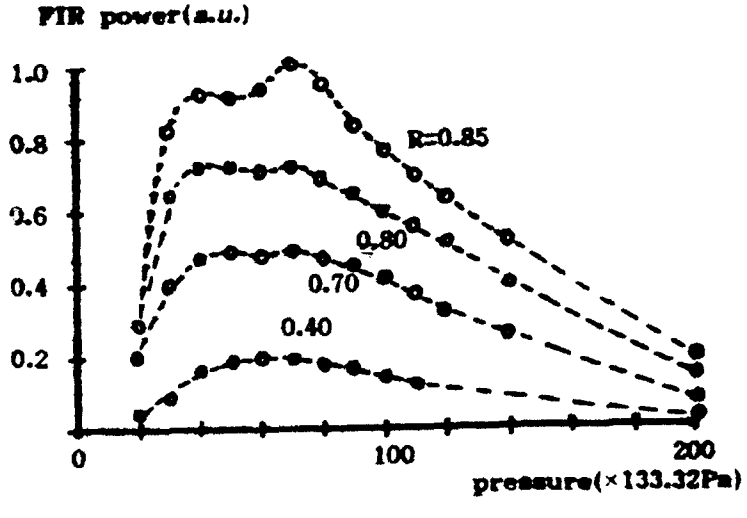

Fig.3 The calculated curves of a mini-OPFIRL, where **O** was the calculated point. The sample tube was 40mm long and ϕ18mm ID.

THEORETICAL CALCULATION ON MINI-OPFIRL

By means of the theoretical model[5] and the density matrix for non-monochromatic signal fields discussed above, the output power of the miniature OPFIR laser could be calculated by the iteration calculation method.

Fig.3 showed the calculated curves of the output power of the laser varying with the operating gas pressure, where the sample tube was 40mm long and ϕ18mm ID, the intensity of the input pump laser and the pump laser spot were 4MW/cm^2 and ϕ10mm, respectively. Three conclusions from the results could be obtained: i, The reflectivity of the side wall of the sample tube affected the output power of OPFIRL but not the optimum operating gas pressure. The higher the reflectivity, the higher the output power. ii, There were two optimum operating gas pressures when the reflection coefficient was greater than 80%, the first peak in P=40×133.32Pa and the second in P=70×133.32Pa. This was in agreement with the experiment of the copper sample tube as shown in Fig.1. iii, The shape of calculated curves was in agreement with that of experimental curves. When the operating gas pressure was lower than the optimum pressure, the output power increased rapidly as the operating pressure increased. When the operating presuure was higher than the optimum pressure, the output power decreased slowly as the operating pressure increased.

The double-peak phenomenon resulted from the interaction between the transverse feedback and the ASE signals along the optical axis. The first peak corresponded to the contribution of the transverse feedback and the second the ASE along the optical axis. These two signals enhanced each other. When the reflectivity became lower, the effect of the transverse feedback would be weaker and so would the enhancement to the longitudinal signal. Hence the second peak disappeared.

CONCLUSSION

The dependence of optimum operating pressure on the transverse parameters of the sample tube was studied. The mechanism of the processes in mini-OPFIRL was revealed, which was important for the development of the OPFIRL theory and the utillization of mini-OPFIRL.

REFERENCES

1. G.M. Rebeiz, et al., Int. J. IR-MMW, 8(1987), 1249.
2. M.A. Frerking, Ibid. 8(1987), 1211.
3. H.O. Everitt, et al., Appl. Phys. Phys. Lett. 49(1986), 16.
4. Lin Yikun et al., Int. J. IR-MMW. 10(1989), 1427.
5. Li Yao et al., Infrared Phys., 32(1991), 251.

Th8.2

CONFIRMATION AND PREDICTION OF OPTICALLY PUMPED FAR INFRARED LASER LINES IN METHANOL

I.Mukhopadhyay and P.K.Gupta
Laser Programme
Centre for Advanced Technology
Department of Atomic Energy
Indore 452 013, M.P.
India

and

R.M.Lees
Centre of Excellence in Molecular and
Interfacial Dynamics (CEMAID)
Physics Department
University of New Brunswick
Fredericton, N.B.
E3B 5A3, Canada

ABSTRACT

In this paper, the detailed analyses of high-resolution Fourier transform spectra of the infrared (IR) C-O stretch and far infrared (FIR) torsion-rotation bands of methyl alcohol have been applied to predict 30 potential FIR laser lines and to confirm previously proposed assignments of FIR emission lines optically pumped in the second and third excited torsional states of the C-O stretch state. The combination loop closure technique provided accurate frequencies for the observed and predicted FIR laser transitions.

CONFIRMATION AND PREDICTIONS

Over the last decade there has been a great deal of interest in the study of infrared (IR) and far infrared (FIR) spectra of methanol and its isotopic species [1-26]. This is mainly because of a large number of FIR laser lines obtained from these molecular species when pumped by a CO_2 laser. As far as FIR laser emission is concerned the high resolution spectroscopic study in the IR and FIR regions provide perhaps the best available method for identifying the quantum numbers involved in the abosrption and emission transitions. The ground state FIR transition assignments provide a powerful method for checking the correctness of the assignment scheme by the loop closure technique [17]. In the case when the emitted frequency is not measured precisely, the closed loop provides the frequency of the observed laser line with a precision which is atleast one order of magitude better than that can be obtained from usual wavelength measurements. Another aspect of the loop closure technique is that, one can predict the frequencies of yet unobserved FIR emission transitions possible from the same upper level with the same order of precision. The knowledge of quantum number assignments at FIR lasing transitions is not only of fundamental spectroscopic interest but also of importance for optimum operation of the FIR laser through the control of operating conditions.

In this work, an extensive analysis has been carried out on an IR spectrum of the C-O stretch fundamental band at a resolution of 0.002 cm^{-1} recorded on a BOMEM Fourier transform spectrometer at the Herzberg Institute of Astrophysics in Ottawa [18-19]. As an immediate application of this work, we provide valuable confirmation of recently proposed assignments for IR absorptions and FIR laser emissions pumped by four different CO_2 laser lines [13] viz. 9R(8), 9P(20), 9P(26) and 9P(4). Further, 24 potential FIR emission lines are predicted in CH_3OH which can be pumped by the following pump lines : sequence band 9R(9) and 13-CO_2 9R(4).

Another significant finding in the present work is the precise location of the highly down shifted first excited torsional C-O stretch transitions. It was found that alternative assignments are necessary for two recently proposed [22] IR pump/FIR laser systems involving transversely excited atmospheric (TEA) CO_2 laser lines.

ACKNOWLEDGEMENT

We are grateful to Dr.J.W.C.Johns of the Herzberg Institute of Astrophysics for the use of BOMEM Fourier transform spectrometer.

REFERENCES

[1] J.O.Henningsen, 'Molecular Spectroscopy by Far Infrared Laser Emission', University of Copenhagen (1984), ISBN 87-88318-06-0, and the references therein.

[2] M.Inguscio, F.Strumia and J.O.Henningsen, Rev. of IR and MM Waves, Vol. 2, 105-150 (1984) and the references therein.

[3] S.Kon, T.Kachi, Y,Tsunawaki and M.Yamanaka, Rev. of IR and MM Waves, Vol. 2, 159-192 (1984).

[4] R.M.Lees, I.Mukhopadhyay and J.W.C.Johns, Optics Commun. 55, 127-130 (1985).

[5] J.O.Henningsen, Int. J.IR and MM Waves, 7, 1605-1629 (1986).

[6] S.Petersen and J.O.Henningsen, Infrared Phys. 26, 55-71 (1986).

[7] I.Mukhopadhyay, R.M.Lees and J.W.C.Johns, IEEE J.Quantum Electron. QE-23, 1378-1384 (1987).

[8] I.Mukhopadhyay, R.M.Lees and J.W.C.Johns, Int.J.IR and MM Waves, 8, 1471-1482 (1987).

[9] I.Mukhopadhyay, R.M.Lees, J.W.C.Johns, W.Lewis-Bevan, F.Strumia and G.Moruzzi, Int.J.IR MM Waves, 8 1483-1502 (1987).

[10] I.Mukhopadhyay, R.M.Lees, J.W.C.Johns, Appl.Phys. B47, 319-324 (1988).

[11] R.R.J.Goulding, C.Young, R.M.Lees, W.Lewis-Bevan and J.W.C.Johns, Infrared Phys. 28, 297-306 (1988).

[12] I.Mukhopadhyay, R.M.Lees and J.W.C.Johns, Int. J.IR MM Waves, 9, 1119-1140 (1988).

[13] F.Tang, A.Olafsson and J.O.Henningsen, Appl.Phys. B47, 47-54 (1988).

[14] G.Moruzzi, F.Strumia, P.Carnesecchi, B.Carli and M.Carlotti, Infrared Phys. 29, 47-86 (1989).

[15] I.Mukhopadhyay, M.Mollabashi, R.M.Lees and J.W.C.Johns, J.Mol.Spectrosc. 138, 521-540 (1989).

[16] G.Moruzzi, F.Strumia, P.Carnesecchi, R.M.Lees, I.Mukhopadhyay and J.W.C.Johns, Infrared Phys. 29, 583-606 (1989).

[17] G.Moruzzi, F.Strumia, R.M.Lees and I.Mukhopadhyay, Infrared Phys.32, 333-347 (1991).

[18] I.Mukhopadhyay, R.M.Lees and K.V.L.N.Sastry, Infrared Phys. 30, 291-293 (1990).

[19] I.Mukhopadhyay, R.M.Lees and J.W.C.Johns, Optics Commun. 80, 425-434 (1991).

[20] I.Mukhopadhyay, I.Ozier and R.M.Lees, J.Chem. Phys. 93, 7049-7053 (1990).

[21] J.O.Henningsen, J.Mol.Spectrosc. 102, 399-415 (1983).

[22] Y.Nishi, Int. J.IR MM Waves, 8, 1189-1210 (1987).

[23] R.M.Lees and J.G.Baker, J.Chem. Phys. 48 5299-5318 (1986).

[24] G.Moruzzi, P.Riminucci, F.Strumia, B.Carli, M.Carlotti, R.M.Lees. I.Mukhopadhyay, J.W.C.Johns, B.P.Winnewisser and M.Winnewisser, J.Mol. Spectrosc. 44, 139-200 (1990).

[25] R.M.Percival, D.Devoy, G.Duxbury and H.Kato, J.Opt. Soc. Am.B4, 1188-1196 (1987).

[26] G.Moruzzi, F.Strumia, J.C.S.Moraes, R.M.Lees, I.Mukhopadhyay, J.W.C.Johns, B.P.Winnewisser and M.Winnewisser, J.Mol.Spectrosc., In Press.

Th8.3

STUDY OF MINIATURE OPTICALLY PUMPED FAR-INFRARED LASER

Luo Xizhang and Lin Yikun
(Zhongshan University, Guangzhou, China)

ABSTRACT

Five mini-OPFIRLs with sample tube 10cm, 5cm, 4.3cm, 3cm and 1.5cm in length, respectively, were built up and lase sucessfully. Power density and spectral characteristic of the mini-OPFIRL were studied theoretically and experimentaly.

I. INTRODUCTION

In recent years, far-infrared(FIR) has been used for radar and communication in outer-space[1]. The devices used in outer-space should be high efficent and small-sized. Many scholars have been engaged in the study of miniaturization of FIR devices. A CW optically pumped FIR laser(OPFIRL) cavity of 5cm in length was reported in 1986[2]. In the same year, Lin Yikun pointed out in his paper[3] that the optimum length of the sample tube of an OPFIRL was inversely proportional to the operating gas pressure of the laser and OPFIRL could be miniaturized if the laser operated at high gas pressure. In this paper, mini-OPFIRL with sample tube shorter than 10cm was studied theoretically and experimentally and discussion was given.

II. EXPERIMENTAL STUDY OF MINIATURE OPFIRL

The experimental system for the study of mini-OPFIRL was the same as that described in reference 4. NH_3 gas was chosen as the operating gas and 9R(16) from a TEA-CO_2 laser as the pumping source. Emission of pulsed OPFIRL was detected by a pyroelectric detector and recorded by model-7623 storage oscilloscope. Five mini-OPFIRLs, made of different materials, with the length of sample tube 10cm, 5cm, 4.3cm, 3cm and 1.5cm, respectively, were built up and tested. The results were shown in Table 1.

Table 1. Comparision of experimental and theoretical reesults of miniature OPFIRL

Length of sample tube(cm)	10	5	4.3	3	1.5
Material of sample tube	glass	glass	Al	Al	Al
Pumping power density(MW/cm^2)	6	6	4	4	4
Exp. optimum gas pressure($\times 10^3$ Pa)	7.3	10.7	9.3	10.2	6.7
Cal. optimum gas pressure($\times 10^3$ Pa)	7.7	10.6	9.3	10.7	14.6
Exp. FIR power density(W/cm^2)	2.2×10^3	0.2×10^3	0.1×10^3	50	8.1
Cal. FIR power density(W/cm^2)	142×10^3	3×10^3	38	2.7×10^{-3}	2.6×10^{-8}

III. THEORETICAL STUDY OF MINIATURE OPFIRL

The theoretical calculation was based on the semi-classical density matrix equations. For simplification, we assumed that the transition of NH_3 molecule in mini-OPFIRL system was confined within three energy levels. The three-level system assumption was accurate enough for the study of OPFIRL output characteristics.

The lasing process in an OPFIRL could then be described by density matrix equtions as follows:

$$\left.\begin{aligned} i\hbar\frac{\partial\rho_{ij}}{\partial t} &= \hbar\omega_{ij}\rho_{ij} - \frac{i\hbar}{\tau_{ij}}\rho_{ij} + [H',\rho]_{ij} \\ i\hbar\frac{\partial\rho_{jj}}{\partial t} &= \frac{i\hbar}{\tau_{jj}}(\rho^{0}_{jj} - \rho_{jj}) - [H',\rho]_{jj} \end{aligned}\right\} \qquad (1)$$

Applying the equations to the three-level system gave the following expression for FIR gain and IR absorption coefficent[5]:

$$\left.\begin{aligned} G_s &= -\frac{2N_v|\mu_s|^2}{\varepsilon_0\eta c\hbar B_s}(\omega_{32}T_a - y)\mathrm{Im}(P_{32}) \\ G_p &= -\frac{2N_v|\mu_p|^2}{\varepsilon_0\eta c\hbar B_p}(\omega_{31}T_a - x)\mathrm{Im}(P_{31}) \end{aligned}\right\} \qquad (2)$$

With relations (1) and (2), the output power density of an ASE OPFIRL with the length of sample tube L cm could be calculated numerically by iteration method[4]. Five mini-OPFIRLs mentioned above were calculted. The results were also listed in Table 1 for comparision, and the calculated frequency characteristic of a 10cm long OPFIRL with weak longitudinal feedbak was shown in Fig.1.

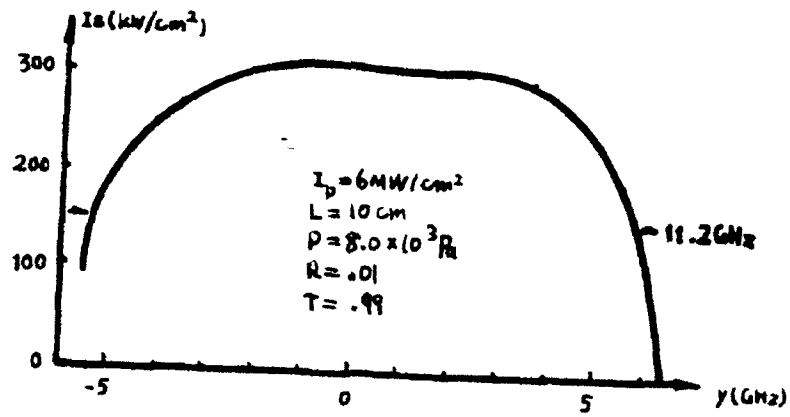

Fig.1 Frequency ccharacteristic of mini-OPFIRL with weak feedback

IV. DISCUSSION

1, It has been shown in our experiment and calculation that mini-OPFIRLs with sample tube as short as 10cm-1.5cm lase FIR eemission suceessfully.

2, Mini-OPFIRL operates at high gas pressure which is tens times of that for ordinary OPFIRL. The linewidth of mini-OPFIRL can be larger than 10GHz, this is because two AC Stark lines link together as the result of gas pressure broadening and saturation broadening effecc.s[6]. The widen laser line is of significance for frequency tunable FIR laser.

3, The deviations of optimum operating gas pressure and output power density between experimental and calculted results for very short OPFIRL suggest that transverse feedback from the side wall of the metallic sample tube plays an active role in mini-OPFIRL. The output FIR power dendity will be much enhanced. We call it transverse feedback effect. A detailed study of trawsverse feedback enhancement in mini-OPFIRL will be described in other paper.

REFERENCES

1. M.A. Frerking, Int. J. IR-MMW, 8(1987), 1211.
2. H.O. Everitt et al., Appl. Phys. Lett., 19(1986), 16.
3. Lin Yikun et al., 11th Int. Conf. IR-MMW, Oct.1986, Digest, p.26.
4. Luo Xizhang et al., Int. J. IR-MMW, 10(1989), 237
5. Li Yao et al., Ibid, 6(1985), 1075
6. Lin Yikun et al., Acta Scient. Natural. Universitat. Sunyat., 4(1988), 4.

FIR Laser Assignments and Predicted Frequencies for Optically Pumped $^{13}CD_3OH$

Li-Hong Xu[a], R.M. Lees[a] and J.W.C. Johns[b]

[a] CEMAID and Department of Physics, University of New Brunswick, Fredericton, N.B., Canada E3B 5A3

[b] Herzberg Institute of Astrophysics, National Research Council of Canada, Ottawa, Canada K1A 0R6

Abstract

High-resolution Fourier transform spectroscopy (FTS) of $^{13}CD_3OH$ has given insights into the far-infrared (FIR) laser emission observed when this molecule is optically pumped by a CO_2 laser. Six IR-pump/FIR-laser transition systems are considered, including two with completely new assignments plus four which have been presented previously but are discussed further with reference to recently reported experimental data. Five of the assignment schemes have been rigorously checked by forming closed combination loops, and accurate FIR laser wavenumbers have been obtained. The superiority in precision of the FIR laser wavenumbers determined from FTS combination loops over those from traditional wavelength measurements is demonstrated.

Introduction

The development of efficient FIR lasers with high output power is of interest for many practical applications, such as plasma diagnostics, scattering measurements, radio astronomy and a variety of solid-state semiconductor experiments. When a strong 127 μm FIR laser line was found for $^{13}CD_3OH$ optically pumped by the 10P(8) CO_2 laser line, and proved to be the second most efficient known [1,2], it was quickly utilized as a diagnostic on the Princeton tokamak. This discovery triggered our spectroscopic interest in this rather exotic isotopomer of methanol, and stimulated systematic high-resolution Fourier transform investigations of the spectra of $^{13}CD_3OH$ in various regions by our group. The scope of this present paper will be restricted to the two regions particularly relevant to the FIR laser assignment problem, namely the C-O stretching band centred at approximately 980 cm^{-1} in the infrared (IR) and the ground vibrational torsion-rotation band spread throughout the FIR. The former overlaps very well with the CO_2 laser bands so provides the IR pump transitions for the FIR lasers, while the latter gives essential information for the construction of frequency loops for confirmation or prediction of the FIR laser wavenumbers. As a consequence, many FIR laser emission lines have now been observed and a number of transitions assigned within the first excited C-O stretching state [1,3-8].

FT Spectrum and Experimental Details

High-resolution Fourier transform spectra of $^{13}CD_3OH$ were obtained from 15-240 and 815-1030 cm^{-1} at a resolution of 0.002 cm^{-1} on the modified DA3.002 Bomem spectrometer at the Herzberg Institute of Astrophysics in Ottawa. The spectra were recorded at room temperature using 4 transits of a 0.5 m multipass White cell (for a total path length of 2 m). The sample pressure was 40 mTorr for the FIR region and 100 mTorr for the C-O stretching region, giving minimal pressure broadening. The sample was supplied by MSD Isotopes of Montreal at 99 atom-% purity. To improve the signal-to-noise ratio, multiple scans were co-added for the final interferograms. The relative precision of recorded frequencies is believed to be of the order of ±0.0002 cm^{-1} or better for strong unblended lines, while the absolute accuracy based on calibration with naturally-present H_2O lines is estimated to be approximately ±0.0005 cm^{-1}.

FIR Laser Assignments for $^{13}CD_3OH$

The FIR laser transition identifications and wavenumber predictions for $^{13}CD_3OH$ were accomplished in two steps. First, the C-O stretch band was extensively analyzed and assigned to determine the coincidences between the parent IR absorptions and the CO_2 pump laser lines. Next, the ground state FIR information was brought in to combine with the IR pump and FIR laser data to form closed IR/FIR transition loops. The frequency combination relations from these loops provided rigorous checks on the FIR laser transition assignment schemes as well as yielding accurate predictions for the laser wavenumbers. A typical loop scheme is illustrated in Fig. 1 for the 10R(40) CO_2 pumping system at +132 MHz offset from the pump laser centre frequency. With the extensive closed loop diagrams that can be formed from the transitions shown in Fig. 1, the wavenumber of FIR laser line L_b is confirmed through three independent combination relations:

$$\begin{aligned} L_b &= P + d - h + i - I &&= 63.6125 \\ &= E + c - h + g - H &&= 63.6128 \quad \} \text{ Average } = 63.6125\ \text{cm}^{-1} \\ &= E + a - e + f - H &&= 63.6121 \end{aligned}$$

The self-consistency of these results along with the excellent agreement between our mean value of 63.6125 cm^{-1} and the direct frequency measurement value [7] of 63.61260 cm^{-1} serve as strong confirmation of our assignments. They also demonstrate clearly the superior precision of the FIR laser wavenumbers predicted from the combination loops over that obtainable from traditional wavelength measurement accuracies of typically ±0.5 μm (L_b was reported as 157.2 μm). This precision can be applied to the two further FIR laser lines, [L_a] (||) and L_c (||), associated with the scheme of Fig. 1. No observation of L_a has yet been reported, while for L_c only a wavelength measurement is available. From our loops, we predict wavenumbers for these lines as follows:

$$\begin{aligned} [L_a] &= P - A &&= 8.9122 \qquad & L_c &= P + d - G &&= 53.5039 \\ &= C - D &&= 8.9121 \qquad & &= E + a - F &&= 53.5040 \end{aligned}$$

In all, we have identified 15 IR-pump/FIR-laser transition systems so far with our FTS information, some of which have already been reported [8]. Our results for the six systems which are either new or have had additional FIR laser information reported recently [7] are collected in Table 1. Most of the assignments are rigorously confirmed with spectroscopic loop data, allowing accurate FIR laser wavenumbers to be deduced. In general, our calculated wavenumbers in Table 1 are in good agreement with those obtained from accurate laser frequency measurements [7].

Three further comments may be made. First, for System #3, the new observation of laser line L_b ties down the transition assignments nicely. Originally, there had been some uncertainty since only the single line L_a had been reported [4] and assigned as a $\Delta K=0$ *a*-type FIR laser line [8]. Such *a*-type lines are not very sensitive to quantum numbers other than J, so require caution in their identification. Our energy scheme for System #3 predicts that there should be a third FIR laser line, [L_c], at 10.8816 cm^{-1} with perpendicular polarization, as shown in Table 1. Secondly, we had originally presented System #5 with the 10R(8) CO_2 pump [8] only as a potential system for optical pumping and FIR lasing. The new observations [7] have confirmed this prediction, and have verified our proposed wavenumber for laser line L_f. Lastly, for System #4 involving n=2 second excited torsional levels, we have not yet identified all of the weak excited torsional series in the IR and FIR spectra necessary to form loops to confirm the assignments unambiguously. The plausibility of our proposed scheme, therefore, rests principally on the agreement between the reported wavenumber for laser line L_a and our best calculated value for this Q-branch transition in the excited state, together with the fact that the wavenumber difference of cm^{-1} between lines L_a and L_b is entirely consistent with the value of cm^{-1} calculated for a J=19→18 *a*-type transition using our mean observed n=2 excited-state B-value of cm^{-1}. We hope that further spectroscopic detective work will lead to the assignments needed to close a variety of combination loops to verify this proposal definitively in future.

Acknowledgements

This work was made possible in part by a grant to the Centres of Excellence in Molecular and Interfacial Dynamics (CEMAID), funded by the Network of Centres of Excellence Programme in association with the Natural Sciences and Engineering Research Council of Canada. One of us (R.M.L.) also gratefully acknowledges operating support from NSERC and the University of New Brunswick Research Fund. We thank Mario Noël of the Herzberg Institute of Astrophysics for his expert technical assistance in operating the Bomem spectrometer.

References

1. M. Inguscio, K.M. Evenson, F.R. Petersen, F. Strumia, and E. Vasconcellos, "A New Efficient Far Infrared Lasing Molecule: $^{13}CD_3OH$," *Int. J. Infrared and Millimeter Waves* **5**, 1289-1296 (1984).
2. N. Ioli, A. Moretti, and F. Strumia, "High Efficiency cw Far Infrared Lasers at 119 μm and 127 μm," *Appl. Phys. b* **48**, 305-309 (1989).
3. N. Ioli, A. Moretti, F. Strumia, and F. D'Amato, "$^{13}CH_3OH$ and $^{13}CD_3OH$ Optically Pumped FIR Laser: New Large Offset Emission and Optoacoustic Spectroscopy," *Int. J. Infrared and Millimeter Waves* **7**, 459-486 (1986).
4. D. Pereira, J.C.S. Moraes, A. Scalabrin, A. Moretti, and F. Strumia, "Measurement and Assignments of New FIR Laser Lines from $^{13}CD_3OH$," *15th Int. Conf. IR & MM Waves*, Lake Buena Vista, Florida, (ed. R.J. Temkin), *Proc. SPIE* **1514**, 735-737 (1990).
5. A. Scalabrin, D. Pereira, G. Carelli, N. Ioli, J.C.S. Moraes, A. Moretti, and F. Strumia, "Study of the Q-Branch of $^{13}CD_3OH$," *16th Int. Conf. IR & MM Waves*, Lausanne, Switzerland, (ed. M.R. Siegrist, M.Q. Tran, and T.M. Tran), *Proc. SPIE* **1576**, 254-255 (1991).
6. A. Scalabrin, D. Pereira, G.P. Galvão, and K.M. Evenson, "$^{13}CD_3OH$ and $^{13}CD_3OH$ Optically Pumped by a $^{13}CO_2$ Laser: Observation and Assignments of FIR Laser Lines," *16th Int. Conf. IR & MM Waves*, Lausanne, Switzerland, (ed. M.R. Siegrist, M.Q. Tran, and T.M. Tran), *Proc. SPIE* **1576**, 254-255 (1991).
7. J.C.S. Moraes, E.M. Telles, F.C. Cruz, A. Scalabrin, D. Pereira, G. Carelli, N. Ioli, A. Moretti, and F. Strumia, "New FIR Laser Lines and Frequency Measurements from Optically Pumped $^{13}CD_3OH$," *Int. J. Infrared and Millimeter Waves* **12**, 1475-1486 (1991).
8. Li-Hong Xu, R.M. Lees, I. Mukhopadhyay, and J.W.C. Johns, "Fourier Transform Spectroscopy of $^{13}CD_3OH$: Assignment of Far-Infrared Laser Lines," J. Mol. Spectrosc. **153** (Oka issue), in press.

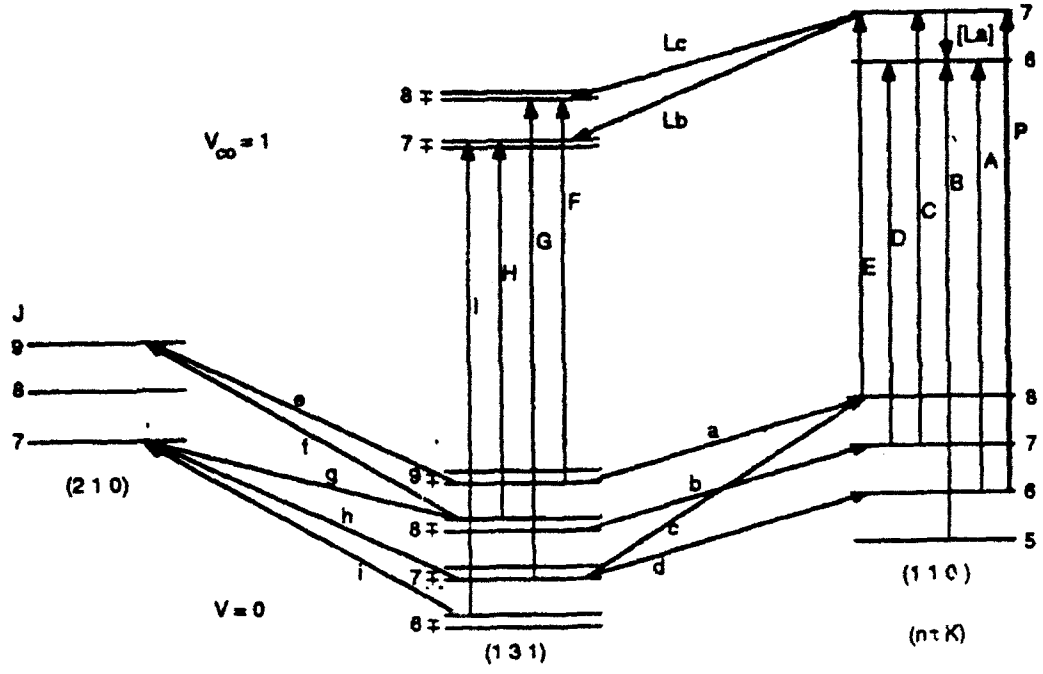

Fig. 1 Energy scheme for the 10R(40) + 132 MHz pump. Transition frequencies are (in cm-1): P=987.6229, A=978.7107(calc.), B=986.3961, C=978.6569(calc.), D=969.7447, E=968.4104, F=967.3763, G=989.1289, H=968.7298, I=987.9475, a=52.4700, b=53.7390, c=74.2222, d=55.0099, e=126.0844, f=137.5459, g=115.8029, h=126.0930, i=135.0201.

Table 1. Assignments of FIR laser lines in $^{13}CD_3OH$ optically pumped by a CO_2 laser.

System	CO_2 + Offset [ν in cm^{-1}]	IR Absorption [ν_{obs} in cm^{-1}]	FIR Laser Transitions[a] $(n'\tau'K',J')v'$ → $(n''\tau''K'',J'')v''$	Line Label	ν_{obs}[b] [cm^{-1}]	Rel Pol	$\nu_{pred.}$ [cm^{-1}]
#1	10P(24) + 20.5MHz	P(118,28)	(118,27)^{co} → (118,26)^{co}	L_a	34.37497*	∥	34.3737
	940.5488	940.5474	→ (127,27)^{co}	L_b	46.22017*	⊥	46.2180
			→ (127,26)^{co}	L_c	80.48092*	∥	80.4791
#2	10P(24) + 99MHz	P(015,29)	(015,28)^{co} → (015,27)^{co}	L_a	35.67851*	∥	35.6783
	940.5514	940.5517	→ (024,27)^{co}	L_b	43.88352*	∥	43.8825
			→ [(024,28)^{co}]	[L_c]		[⊥]	[8.2227]
#3	10P(24) - 155MHz	P(023,29)	(023,28)^{co} → (023,27)^{co}	L_a	35.63	∥	35.6582
	940.5429	940.5427	→ (032,27)^{co}	L_b	46.73	∥	46.7769
			→ (032,28)^{co}	[L_c]		[⊥]	[10.8816]
#4	10P(10) + 73MHz	P(225,19)	(225,18)^{co} → (216,18)^{co}	L_a	138.7	⊥	
	952.8833	952.8834	→ (216,19)^{co}	L_b	114.9	∥	
#5	10R(8) + 40MHz	P(039,10)	(039,9)^{co} → [(018,9)^{co}]	[L_a]		[⊥]	[24.0538]
	967.7086	967.7093	→ (018,8)^{co}	L_b	35.53816*	∥	35.5384
#6	10R(40) + 132MHz	R(110,6)	(110,7)^{co} → [(110,6)^{co}]	[L_a]		[∥]	[8.9122]
	987.6246	987.6229	→ (131-,7)^{co}	L_b	63.61260*	⊥	63.6125
			→ (131+,8)^{co}	L_c	53.19	∥	53.5040

[a] Transitions in brackets are predicted. Energy levels are labelled as $(n\tau K, J)^v$, where n is the torsional state, τ defines the torsional symmetry, K is the projection along the near-symmetry a-axis of the rotational angular momentum J, and v denotes the vibrational state.

[b] Wavenumbers with asterisks are converted from accurate frequency measurements [7], using c = 29979.2458 m/s.

Th8.5

NONSTATIONARY LASER BEAM SPATIAL STRUCTURE SIMULATION.

L. V. Yurchenko

Institute of Radiophysics and Electronics
of Ukrainian Academy of Science, Kharkov, Ukraine.

The effective numerical method for the approximate calculation of the evolution of the wave field from the moment of its excitation in the open resonator is proposed with the aim of the examination of nonstationary fields in the resonator of different configuration filled with nonlinear active media. This method is based on using the sequent integral transformations of the wave field completed with the account of the small correction of its amplitude and phase stimulated by the influence of the medium. The method mentioned is suitable for quasi-optical resonators of mm, sub mm and far infrared regions of waves.

By this method the following situations were considered: when the resonator is filled 1) with nonstationary medium that can be inhomogeneous in transversal and (or) longitudinal directions; 2) with nontationary weakly nonlinear medium; 3) with nonstationary inhomogeneous inverted medium in which a stimulated radiation appears; 4) with stationary anisotropic medium in which a short RF-impulse is propagating. Let's consider as the most interesting example the third case. In this case the method allows to calculate self-consistently the evolution of the transversal spatial structure and the angular dispersion of the radiation field of the laser with the different mechanism of the creation of the inversion of quantum level populations (chemical reaction, pumping by the RF-charge, optical pumping, etc.) taking into account the instabilities which can appear at any moment of the time, with the aim to optimize laser characteristics.

The application of the discussed method in this situation is based on the possibility to use the approximation of the frequency single-mode generation regime and the fact that the field changes slowly during the single pass through the resonator. Owing to this the field evolution during each pass mainly can be calculated by the solution of the linear wave equation for the complex amplitude of the field

$$\Delta U + \bar{\varepsilon}_r k^2 U = 0 \qquad (1)$$

in the form of Sommerfeld's integral. There $\bar{\varepsilon}_r$ is the middle value

of the complex permittivity during the pass, $k = \omega/c$ is the wave number in the vacuum. Additional field variation, which appear during the pass time (or some part of it) can be take into account in the form of corrections depending on the process predominating in the given moment of the time and the given part of the medium. These corrections can be calculated self-consistently depending on the field itself and they can take into account the nonstationarity of the external influences. So the correction to the amplitude of the field owing to nonlinear inhomogeneous amplification is calculated from the kinetic equations of the level populations, which in a number of cases of inverted medium have the following form

$$\partial N_2/\partial t = k_1(N - N_2)I - (k_2|U|^2 + k_3)N_2 \qquad (2)$$

where N is the concentration of the active centers, $N_2 = N_2(\rho, t, U)$ is the population of the upper quantum level, $I = I(\rho, t)$ is the pumping power, k_1, k_2, k_3 are the factors describing the transition probability that are defined by the Einstein's coefficients, ρ is the radius-vector in the cuvette cross section (axial symmetry of the pumping power and active medium was supposed).

The amplification coefficient of the field on given part of the medium is defined depending on N_2 by the following equation

$$\alpha(\rho, t, U) = \gamma N_2(\rho, t, U) \qquad (3)$$

where γ is the proportionality coefficient depending on the quantum energy, the radiation line width and the corresponding Einstein's coefficient.

The correction to the field phase is obtained from the equations describing the optical inhomogeneity appearing in the medium. In principle the method allows to take into account any sufficiently gradual inhomogeneity of a medium. Let us use here as an example the refraction index $n(\rho, t)$ the quadratic in the coordinate ρ

$$n(\rho, t) = n_o(1 + \beta(t)\,\rho^2/2) \qquad (4)$$

where the factor $\beta(t)$ describes the dynamics of the of the optical inhomogeneity variation due to excitation of the active medium.

Let us consider some results obtained by the mentioned method that describe the dynamics of the formation of the spatial mode structure of the laser radiation with the wavelength of $\lambda = 10.6$ μm under the influence of the short sufficiently power impulse of the pumping. The simulations carried out at the small levels of the pumping have demonstrated that in the cases of the weakly focusing or

defocusing medium the gradual localization or expansion of the field region is observed when compared with the convenient original mode of the empty resonator. The inhomogeneity of the amplification coefficient in these cases does not exert significant influence on the common shape of field distribution. More interesting phenomena take place at the large pumping power. If the medium becomes focusing one (this happens when the pumping energy is mostly absorbed near the cuvette walls) the localization of the field also takes place in the beginning of the process (Fig.a). However, with increasing the field amplitude owing to power stimulated radiation both the inversion and the amplification on the cuvette axis begin to decrease (Fig.b). As a result, the annular field distribution in the beam cross section is forming. The mechanism of the field spatial structure evolution described here is sufficiently universal and it can work in a lot of cases. In the same time, in the case of the defocusing medium this mechanism does not become apparent because of more homogeneous field distribution across the beam.

So in this work a simple effective and sufficiently universal method of the calculation of the fields in the resonators with the inhomogeneous and nonstationary medium which allows quickly to calculate the fields in a lot of practical physical situations has been developed.

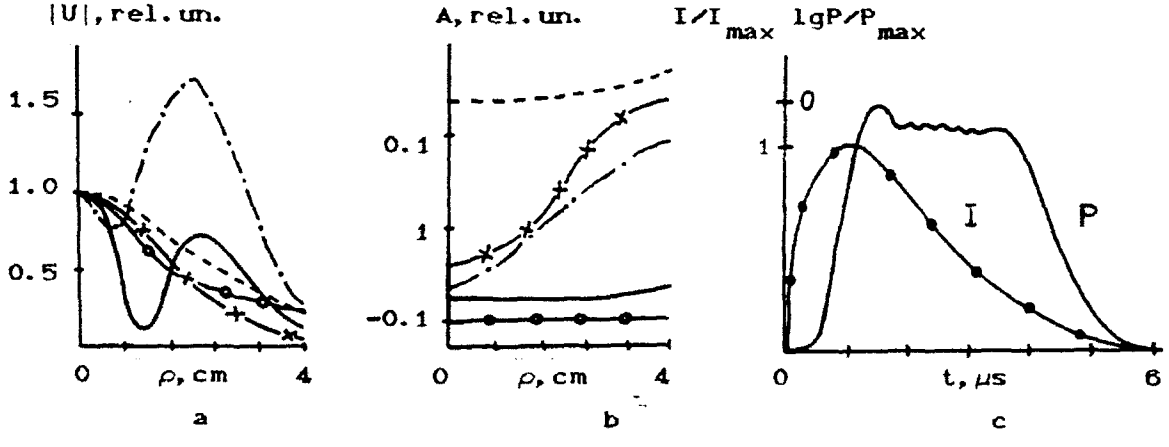

Fig. Dependences of the complex amplitude of the field (a) and the amplification (b) in the cuvette cross section and the total energy of radiation (c) during the pumping impulse (the resonator length L = 100 cm); -o- 0.1μs, --- 1μs, -x- 2.5μs, -·- 3μs, —— 6μs.

COMPLEX DIELECTRIC MEASUREMENTS OF MILLIMETER WAVE AND FAR-INFRARED MATERIALS*

Mohammed Nurul Afsar and Hua Chi

Department of Electrical Engineering
Tufts University
Medford, Massachusetts 02155 - 5528

ABSTRACT

The absorption coefficient of most low absorbing materials increases almost linearly with increasing frequency at millimeter wave frequencies. For ceramic boron nitride, the absorption also increases with increasing frequency atleast to about 600 GHz. Single crystal high resistivity silicon has the lowest absorption at room temperature in the entire millimeter wavelength region. Our new broadband continuous wave low temperature (6, 30, 76 K and 300 K) measurement on single crystal sapphire reveal that its absorption coefficient value shows a minimum around 180 GHz for low temperatures. Extra high resistivity silicon is by far the best window material as regards the absorption loss is concerned at room temperature.

INTRODUCTION

The search for an ideal window material for high power- high frequency gyrotron is still on [1- 3]. At millimeter wave frequency region, the absorption coefficient of most low-absorbing window materials increases with increasing frequency. This is because of the tail of lattice vibration or phonon absorption or various other absorption mechanisms present at submillimeter and far and mid infrared spectral region for solid crystalline and polycrystalline materials. For diamond and single crystal silicon, the monoatomic diamond crystal structure suggests the lattice vibration absorption to appear at frequencies in the infrared region. The entire mid-infrared, far-infrared, submillimeter and millimeter wave region therefore should be free from the tail effect of lattice or phonon absorption bands. Our highest resistivity (11,000 ohm-cm) compensated silicon also shows the absence of the microwave and millimeter wave free carrier absorption. We have an extra low- loss material but it is possible that we may have to improve its thermo-mechanical properties by coating it with diamond film evaporation. One expects to see a good room temperature low-absorption loss and mechanically strong window perhaps edge cooled by fluro-carbon fluid. The absorption coefficient of all presently used gyrotron window materials increases with increasing frequency. The cryo-edge-cooling would increase the complexity of a window system although it is expected that the absorption coefficient will decrease with decreasing temperature. At lower temperature a phonon or lattice vibration peak sharpens and the tail effect subsides or reduces significantly. So far we have found two potential room temperature low absorption coefficient materials for 140 and 280 GHz, but we need to improve mechanical and thermal characteristics of these two types of materials. For cryo-edge-cooling one would choose a temperature where the thermal conductivity has its highest value. It is difficult to measure extremely low loss tangent or absorption coefficient value. We have improved the sensitivity of our broadband dispersive Fourier transform spectrometers. We now can measure losses as low as 40 - microradians. In our dispersive Fourier transform spectroscopy we use a thick specimen in order to have higher transmissive loss through the specimen compared to its surface reflection losses. In an open resonator technique, the thickness restriction is different. The thickness of the specimen needs to be small and has to

* This research program is supported by the U.S. Department of Energy, Office of Fusion Research through Lawrence Livermore National Laboratory.

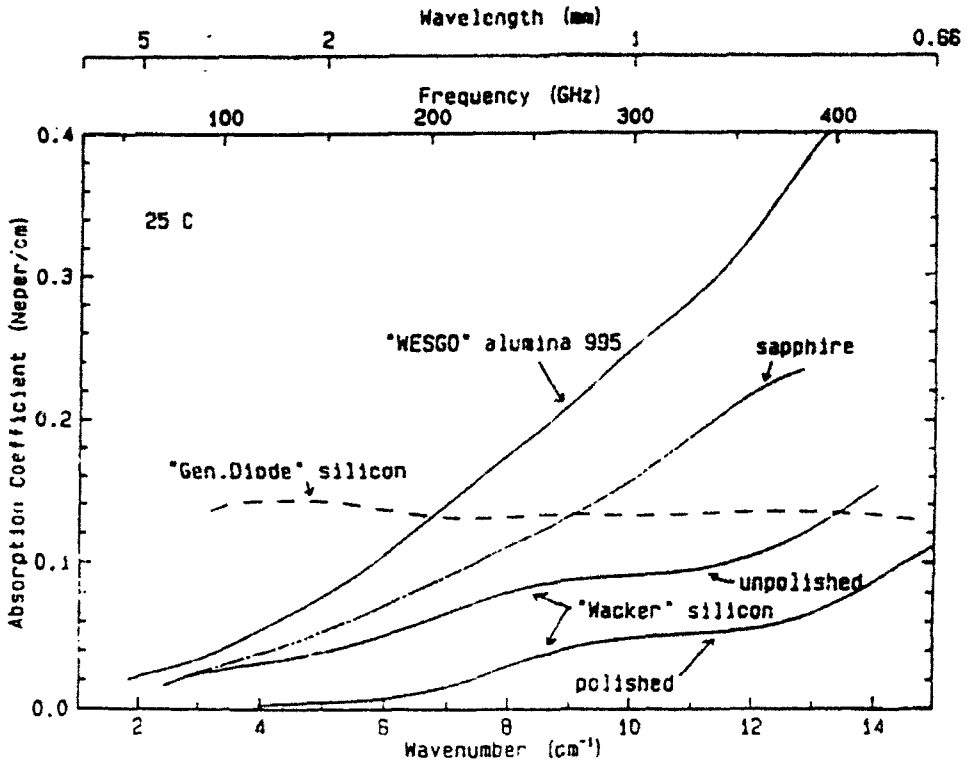

Figure 1 Comparison of absorption coefficient spectra of high resistivity silicon(resistivity = 11,000 ohm-cm), relatively low resistivity silicon ("general Diode" silicon resistivity = 1,500 ohm-cm), single crystal sapphire and alumina 995 at room tempertature

be approximately equal to an even multiple of guide wavelength inside the material. One needs to be extremely careful during measurements in such a system since the stability of such a system depends on stability of frequency, detection, cavity length and cavity Q. Effects such as vibration, temperature fluctuations can easily detoriate the measurement precision by a big factor. Both of our measurement systems are by far the most sensitive system available at millimeter wave and far-infrared frequencies. A comparison and agreement of data obtained by two different systems assure us the measurement accuracy for extra low absorption materials. Figure 1 shows the comparison of absorption coefficient spectra for several potential low loss dielectric materials over the frequency region 60 - 450 GHz. The absorption coefficient of single crystal extra high resistivity silicon is very small in the entire millimeter wave region. Around 120 GHz, it is so low that it is difficult to measure.

BROAD- BAND CONTINUOUS WAVE MEASUREMENT

We have used our dispersive Fourier transform spectroscopy together with a polarization two beam interferometer for the measurement of complex refractive index, complex dielectric permittivity and loss tangent at room temperature over the frequency range 60 - 450 GHz. The specimen was rotated until the maximum signal was attained (E- field perpendicular to the orientation of the drawing of the ceramic specimen. i.e ordinary ray). The specimen thickness was one inch. The interferogram signal with a thin specimen (0.125 inch) of the same boron nitride was used as a reference. The real part of the permittivity value for boron nitride is very low compared to silicon and sapphire. This is an advantage when a lower reflection loss is desired.

THE NEW LOW TEMPERATURE BROAD BAND FOURIER TRANSFORM SPECTROMETER

The vari-temp type dewar is well known for varying temperatures in the range 1.8 K to 300 K. The liquid helium exchange gas and heating mechanism were utilized to change the temperature in the range 1.8 to 300 kelvin. One can hold the temperature to within 0.5 degree kelvin. Two temperature sensors were used, one at the exchange gas controller and the other sensor (callibrated) at the specimen. The diameter of the cool working area of the dewar is about 80 mm. This allows us to insert a 3 inch diameter specimen inside the dewar. The interferometer optics size is 60 mm. The dispersive Fourier transform interferometry was adapted, so that the specimen arm acts as the fixed mirror arm. The dewar is mounted on a rail and it is easily detachable for specimen insertion. Free standing wire grid polarizers were used for beam splitting mechanism and indium antimonide hot electron bolometer detector was used for millimeter wave energy detection. Figure 2 compares the absorption coefficient spectra of single crystal sapphire at 6 K, 30K, 76K and 300 K

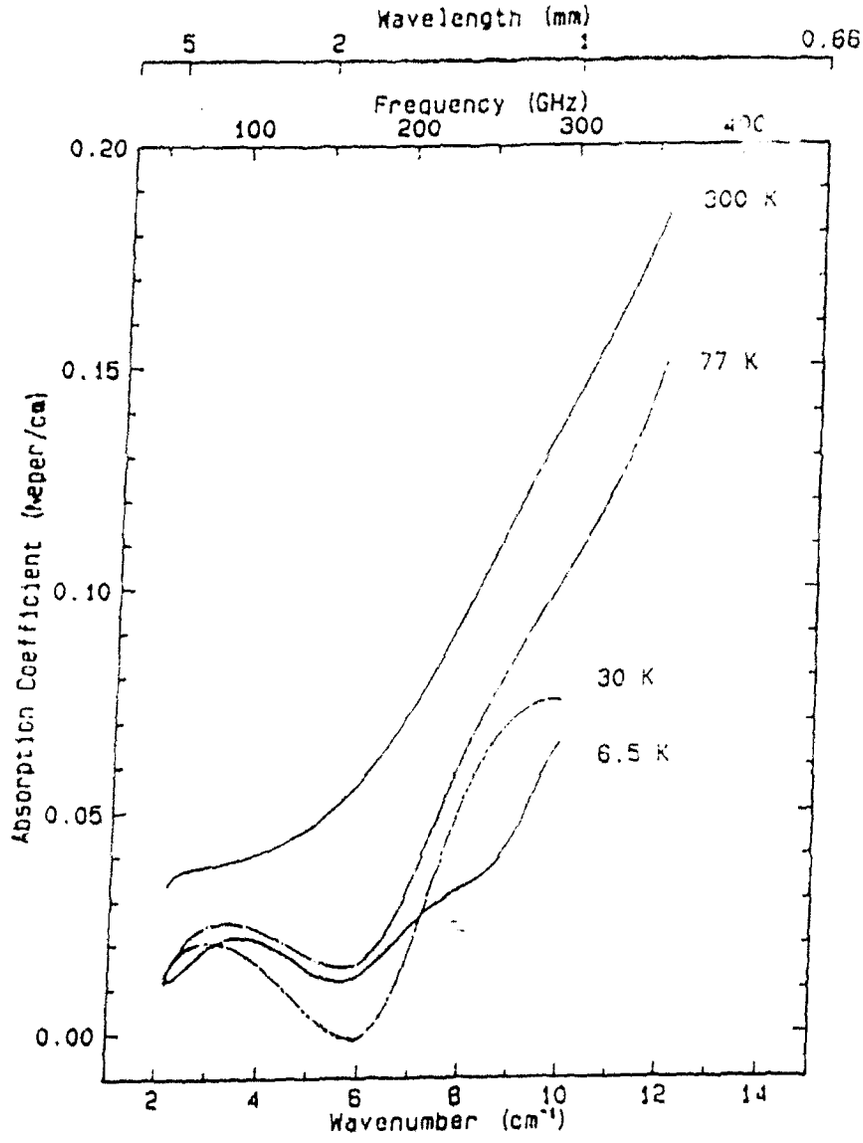

Figure 2 Comparison of absorption coefficient spectra of single crystal sapphire at 6.5 K , 30K, 77K and 300K

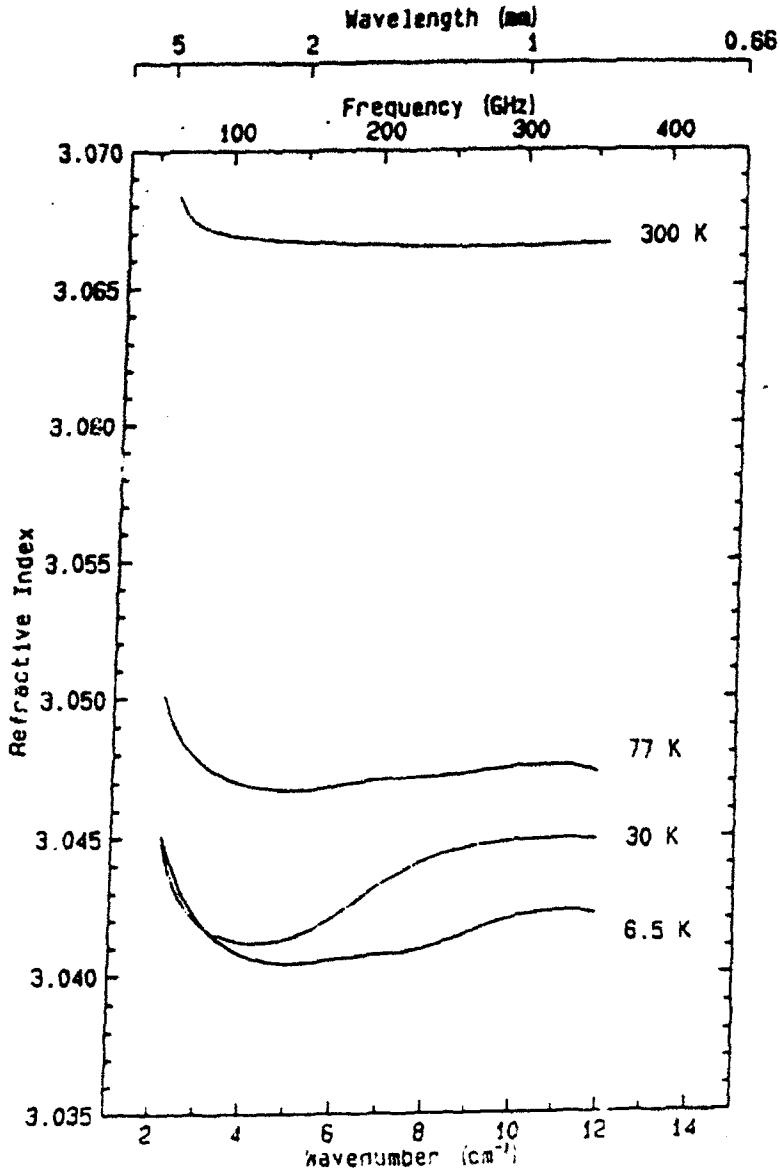

Figure 3 Comparison of refraction spectra for Sapphire at 6.5 K, 30K, 77 K and 300 K

REFERENCES

[1] M. N. Afsar, Xiaohui Li and Hua Chi, "An Automated 60 GHz Open Resonator System for Precision Dielectric Measurement", presented at the 1990 IEEE MTT-S International Microwave Symposium, May 8 - 10, 1990,Dallas, Texas, 1990 IEEE MTT-S Symposium Digest, vol.3, pages 1125 -1128, IEEE Catalog No. 90CH2848-0, ISSN 0149-645X, Library of Congress Catalog Card No. 77-645125

[2]. M. N. Afsar, Hua Chi and Xiaohui Li, "Precision Millimeter Wave Complex Refractive Index and Complex Dielectric Permittivity of Pure and Compensated Silicon", presented at the 1990 CPEM, 1990 IEEE Conference on Precision Electromagnetic Measurements, June 11 - 14, 1990, Ottawa, Canada, CPEM'90 Digest, pages 238-239, IEEE Cat.No.90CH2822-5, Library of Congress No.89-82032

[3]. M. N. Afsar, Xiaohui Li and Hua Chi, "An Automated 60 GHz Open Resonator System for Precision Measurement of LOss Tangent and Dielectric Permittivity", presented at the 1990 CPEM, 1990 IEEE Conference on Precision Electromagnetic Measurements. June 11 - 14, 1990, Ottawa, Canada, CPEM'90 Digest, pages 240-241, IEEE Cat. No. 90CH2822-5, Library of Congress No. 89-82032